MCEER
EARTHQUAKE ENGINEERING TO EXTREME EVENTS

ISSN 1520-295X

Development and Evaluation of Procedures for Analysis and Design of Buildings with Fluidic Self-Centering Systems

by
Shoma Kitayama and Michael C. Constantinou

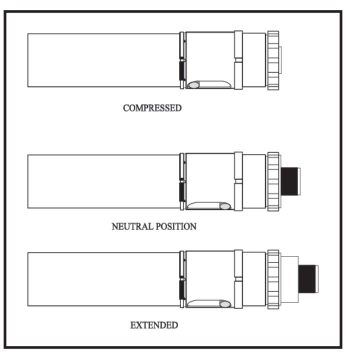

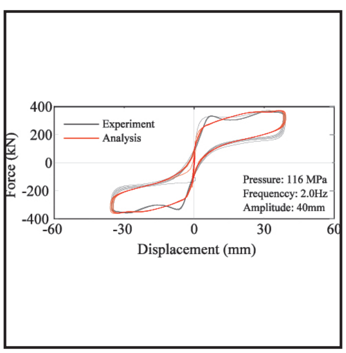

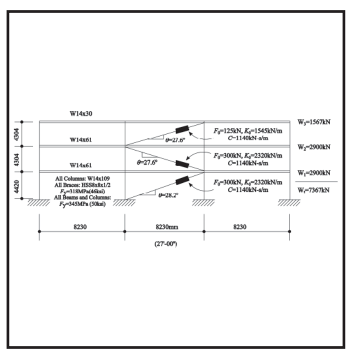

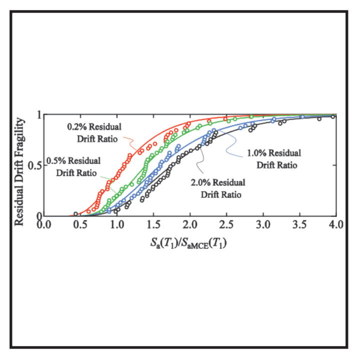

Technical Report MCEER-16-0003

July 21, 2016

This research was conducted at the University at Buffalo, State University of New York, and was supported by MCEER Thrust Area 3, Innovative Technologies.

MCEER
EARTHQUAKE ENGINEERING TO EXTREME EVENTS

Development and Evaluation of Procedures for Analysis and Design of Buildings with Fluidic Self-Centering Systems

by

Shoma Kitayama[1] and Michael C. Constantinou[2]

Publication Date: July 21, 2016
Submittal Date: January 10, 2016

Technical Report MCEER-16-0003

MCEER Thrust Area 3, Innovative Technologies

1 Ph.D. Candidate, Department of Civil, Structural and Environmental Engineering, University at Buffalo, State University of New York
2 SUNY Distinguished Professor, Department of Civil, Structural and Environmental Engineering, University at Buffalo, State University of New York

MCEER
University at Buffalo, State University of New York
212 Ketter Hall, Buffalo, NY 14260
E-mail: *mceer@buffalo.edu*; Website: *http://mceer.buffalo.edu*

PREFACE

MCEER is a national center of excellence dedicated to the discovery and development of new knowledge, tools and technologies that equip communities to become more disaster resilient in the face of earthquakes and other extreme events. MCEER accomplishes this through a system of multidisciplinary, multi-hazard research, education and outreach initiatives.

Headquartered at the University at Buffalo, State University of New York, MCEER was originally established by the National Science Foundation (NSF) in 1986, as the first National Center for Earthquake Engineering Research (NCEER). In 1998, it became known as the Multidisciplinary Center for Earthquake Engineering Research (MCEER), from which the current name, MCEER, evolved.

Comprising a consortium of researchers and industry partners from numerous disciplines and institutions throughout the United States, MCEER's mission has expanded from its original focus on earthquake engineering to one which addresses the technical and socioeconomic impacts of a variety of hazards, both natural and man-made, on critical infrastructure, facilities, and society.

MCEER investigators derive support from the State of New York, National Science Foundation, Federal Highway Administration, National Institute of Standards and Technology, Department of Homeland Security/Federal Emergency Management Agency, other state governments, academic institutions, foreign governments and private industry.

This report presents a study on the use of fluidic devices as elements of self-centering systems for buildings. The behavior of these devices is described based on experimental and analytical results for varying conditions of preload, history of motion and temperature. Mathematical models of the behavior of the devices are presented and validated by comparison to experimental results. Analyses of systems for a wide range of parameters are performed and the results are used to verify simplified methods of analysis and to develop design and analysis procedures for buildings with fluidic self-centering systems that follow the paradigm of Chapter 18 of the ASCE 7 Standard. Three and six-story buildings without and with self-centering systems are designed per the developed procedures and analyzed by nonlinear response history analysis with due considerations for the behavior of the devices and of the yielding structural system. The seismic risk-assessment of these buildings is also investigated in terms of collapse and residual drift for a particular site location by applying the probabilistic approach of FEMA P695. Finally, a pilot study of using fluidic self-centering devices instead of fluid damping devices as elements of seismic isolation systems is presented.

ABSTRACT

This report presents a study on the use of fluidic devices as elements of self-centering systems for buildings. These devices provide the functions of preload, stiffness and viscous damping incorporated in a single compact device. The main effect of these devices is a substantial reduction of residual displacements in earthquakes. Since they incorporate fluid damping, they also offer the benefit of reduction of drift. The report presents a description of the behavior of these devices and presents results on the behavior of small and large fluidic self-centering devices for varying conditions of preload, history of motion and temperature. Mathematical models of the behavior of the devices are presented and validated by comparison to experimental results. Analyses of systems for a wide range of parameters are performed and the results are used to validate simplified methods of analysis and to develop design and analysis procedures for buildings with fluidic self-centering systems that follow the paradigm of Chapter 18 of the ASCE 7-2010 Standard. Three and six-story buildings without and with self-centering systems are designed per the developed procedures and analyzed by nonlinear response history analysis with due considerations for the behavior of the devices and of the yielding structural system. The results demonstrate that the design of buildings with fluidic self-centering devices per the developed procedures offers benefits of substantial reduction in residual drift but also reduced peak drift, peak acceleration, peak shear and base shear forces, and reduced floor response spectra by comparison to the code-compliant buildings without fluidic self-centering devices.

The seismic collapse performance of these buildings is then quantified using the FEMA P695 procedures and is compared to the collapse performance of conventional buildings. It is concluded that buildings with fluidic self-centering devices designed by the procedures presented in this report have a collapse performance comparable to that of conventionally designed buildings. The study also determined that increases in the preload, increases in the displacement capacity or increases in the viscous damping constant of the self-centering devices have marginal or insignificant effects on the collapse margin ratio. Rather, an increase in the collapse margin ratio is obtained for frames having a device-braced system with increased ultimate capacity. Also, a study is conducted on the residual drift fragility of buildings with fluidic self-centering systems, which is calculated and compared to that of conventional buildings. It is shown that buildings with fluidic self-centering systems, designed per the procedures of this document, have substantial reduction of the probability of exceeding the residual drift limits of 0.2% and 0.5% for any level of earthquake. The buildings without and with fluidic self-centering systems are further analyzed to obtain information of the mean annual frequency of collapse, the mean annual frequency of exceeding the residual drift limits of 0.2%, 0.5%, 1% and 2%, and the related probability of collapse or of exceeding the residual drift limits in 50 years. It is concluded that all analyzed systems have a probability of collapse in 50 years

of about 1% or less, and that the structures with fluidic self-centering systems have much lower probabilities in 50 years of exceeding the residual drift limits of 0.2% and 0.5% than conventional structures. This information is of much interest to engineers, building officials, government officials, owners and insurers.

ACKNOWLEDGEMENTS

The authors acknowledge the financial support provided by the Japan Student Services Organization (JASSO) Student Exchange Support Program in the form of a Scholarship and Tuition Fee for Long-Term Study Abroad to the first author. This support is greatly appreciated. Moreover, the authors acknowledge support in the form of hardware, access to test facilities and time of engineering staff from Taylor Devices, Inc. of North Tonawanda, NY. The authors are grateful to Mr. Douglas P. Taylor, President and Mr. Alan Klembczyk, Vice President of Taylor Devices for their support and for many inspiring discussions during the course of the project.

TABLE OF CONTENTS

TABLE OF CONTENTS (CONT'D)

TABLE OF CONTENTS (CONT'D)

TABLE OF CONTENTS (CONT'D)

TABLE OF CONTENTS (CONT'D)

TABLE OF CONTENTS (CONT'D)

LIST OF FIGURES

LIST OF FIGURES (CONT'D)

LIST OF FIGURES (CONT'D)

LIST OF FIGURES (CONT'D)

LIST OF FIGURES (CONT'D)

LIST OF FIGURES (CONT'D)

LIST OF FIGURES (CONT'D)

LIST OF FIGURES (CONT'D)

LIST OF FIGURES (CONT'D)

LIST OF FIGURES (CONT'D)

LIST OF FIGURES (CONT'D)

LIST OF FIGURES (CONT'D)

LIST OF FIGURES (CONT'D)

LIST OF FIGURES (CONT'D)

LIST OF FIGURES (CONT'D)

LIST OF FIGURES (CONT'D)

LIST OF FIGURES (CONT'D)

LIST OF TABLES

LIST OF TABLES (CONT'D)

LIST OF TABLES (CONT'D)

LIST OF TABLES (CONT'D)

LIST OF TABLES (CONT'D)

SECTION 1
INTRODUCTION

The state-of-practice in the design of building structures is based on the allowance of inelastic action in pre-determined locations utilizing a variety of inelastic mechanisms such as yielding beams, yielding braces and specially detailed devices like buckling-restraint braces (BRB) and other yielding steel or other metallic devices (Constantinou et al., 1998, Christopoulos and Filiatrault, 2006). This approach reduces the force demand in the structural elements but at the expense of (a) structural damage to members supporting the weight or damage to replaceable parts or devices, and (b) permanent or residual deformations of the structure. Seismic protective systems such as seismic isolation and damping systems may provide increased protection by reduction of both force and displacement demands as a result of the lengthening of the period and an increase in damping (Naeim and Kelly, 1999, Ramirez et al., 2001, Constantinou et al., 2007). However, if inelastic action is allowed in the structural system, exclusive of the seismic isolation or damping system, residual deformation in the structural system will still occur. Only the technology of seismic isolation is capable of and has been used to economically eliminate inelastic action in the design earthquake and for important structures for the maximum earthquake. Some seismically isolated hospitals in California in the past few years have been designed to be essentially elastic in the maximum earthquake (e.g., analysis and design per ASCE 7-2010 (ASCE 7-10, 2010) using the maximum earthquake with R=1).

Residual deformations received increased attention in recent years (MacRae and Kawashima, 1997; Kawashima et al., 1998; Ruiz-Garcia and Miranda, 2006a and 2006b; Erochko et al., 2011). It is now recognized that residual drift is a performance index in building design as it affects building occupancy and repair following an earthquake. The guidelines in FEMA P-58 (FEMA, 2012) present more detailed information on the relation between the residual story drift and the damage state. Table 1-1 presents this information directly from FEMA P-58. The guidelines present the limit of 1% on the residual story drift as the threshold where it may be uneconomical and impractical to repair. Moreover, there is increasing evidence that a residual drift of 0.5% should be considered as the threshold beyond which a building may be more economical to replace rather than repair (McCormick et al., 2008, Erochko et al., 2011, Erochko, 2013). Another problem with permanent deformations is that they may accumulate to large values and result in collapse of the structure.

Table 1-1 Damage State and Residual Story Drift Ratio (FEMA, 2012)

Damage State	Description	Residual Story Drift Ratio Δ/h[1]
DS1	No structural realignment is necessary for structural stability; however, the building may require adjustment and repairs to nonstructural and mechanical components that are sensitive to building alignment (e.g., elevator rails, curtain walls, and doors).	0.2% (equal to the maximum out-of-plumb tolerance typically permitted in new construction)
DS2	Realignment of structural frame and related structural repairs required to maintain permissible drift limits for nonstructural and mechanical components and to limit degradation in structural stability (i.e., collapse safety)	0.5%
DS3	Major structural realignment is required to restore margin of safety for lateral stability; however, the required realignment and repair of the structure may not be economically and practically feasible (i.e., the structure might be at total economic loss).	1%
DS4	Residual drift is sufficiently large that the structure is in danger of collapse from earthquake aftershocks (note: this performance point might be considered as equal to collapse, but with greater uncertainty).	High Ductility Systems $4\% < 0.5V_{design}/W$
		Moderate Ductility Systems $2\% < 0.5V_{design}/W$
		Limited Ductility Systems $1\% < 0.5V_{design}/W$

Notes: (1) h is the story height

Self-centering systems were developed as means to minimize or eliminate permanent deformations and thus mitigate the problems associated with such deformations and achieving a higher performance level. Self-centering systems and devices are characterized by “flag-shaped” hysteresis; that is, they exhibit nonlinear-elastic behavior with some superimposed mechanism for energy dissipation. Many studies have demonstrated that systems with this type of behavior have about the same maximum drift as comparably designed conventional systems (bilinear hysteretic behavior) but with substantially less residual drift (Christopoulos et al., 2002a; Christopoulos et al., 2003; Pampanin et al., 2003, Tremblay et al., 2008, etc.). Notable examples of developed self-centering systems and devices are described in (Christopoulos and Filiatrault, 2006). The most recent work on the development of practical self-centering devices at sizes suitable for applications (Braconi et al. 2012, Erochko 2013, Erochko et al, 2013, Kammula et al, 2014, Chou and Chen, 2015) utilize pre-stressed tendons within large structural tubes to develop the preload, and friction devices to provide rigidity and the desired energy dissipation capability. The devices are meant to be used as braces. A full scale device that was built and tested (the Telescopic Self-Centering Energy Dissipating or T-SCED brace) had a length (excluding connections) of over 6500mm, section dimensions of about 300mm by 500mm, preload of about 400kN and force at the displacement capacity of 70mm equal to about 800kN. The large size of the device for the output force and displacement capacity is apparent. Its complexity is also noted due to a large number of tendons (16) and related anchorage details, bolted slotted connections and sliding interfaces. Its lifetime behavior is also unknown due to the expected relaxation of load on the frictional interfaces and uncertainties in friction.

Work in self-centering systems has overlooked that modern devices having the desired characteristic flag-shaped hysteresis have been in use in military and industrial applications over the last 50 years and that they have been experimentally and analytically studied as re-centering devices in seismic isolation systems some two decades ago. Fluidic self-centering devices operate on principles similar to those of fluid viscous dampers (Constantinou and Symans, 1992, 1993; Tsopelas and Constantinou, 1994) and utilize the same time-tested technologies. They are highly engineered manufactured products that also allow the development of a range of properties within the confined dimensions of a compact unit. For example, one such device tested as part of the work in this report was 750mm long (excluding connections), had a diameter of 180mm, adjustable preload of 40 to 180kN and maximum force at 50mm displacement equal to about 450kN (for the preload of 180kN). The device could be designed to deliver viscous damping of linear or nonlinear form and could also be configured to have different damping characteristics depending on the direction of motion (more when moving away from the neutral position and less when returning towards the neutral position or vice versa). Its major characteristics are compactness, capability to deliver a range of properties, ease in adjustability of properties (even in-situ) and reliability.

The development of self-centering devices began with the development of large fluidic damping devices when large breech loaded cannons were developed in the latter half of the 19th century. In 1862 the British Army was the first to use fluidic spring-dampers on gun carriages. At about the same time, the French mass-produced fluidic recoil dampers for their 75mm M1897 artillery piece. The device was a 1.2m stroke fluidic damper combined with spring action to attenuate recoil energy and return the gun to the battery (Taylor, 2014; Hogg, 1971). The device had all the elements of a modern fluidic spring-damper system, albeit for one directional motion and with primitive fluid sealing technology. A modern fluidic damper or a fluidic self-centering spring-damper device operates on the same principles but with modern seals that provide substantially greater life, higher fluid pressures and complex orificing to produce the desired damping functions (Taylor, 2014).

Self-centering devices as elements of seismic protective systems were analytically and experimentally studied at the University of California, Berkeley and the University at Buffalo starting in about 1990. Richter et al. (1990) described a mechanical device (Energy Dissipating Restraint or EDR) that had the desired flag-shaped hysteresis for a self-centering system. The device consisted of a steel tube with an integrated friction damper and a preloaded spring in the tube. Small scale tests were also reported (Aiken et al, 1992, 1993). The EDR device was never used and the reasons may be attributed to the inability to produce compact large force output devices and due to concerns with the longevity of the device (bronze on steel sliding interfaces). Aiken et al. (1992, 1993) also reported on testing of shape memory alloy devices as energy dissipation systems where they recognized that the flag-shaped hysteresis of these materials might be explored for providing limited self-centering capability. More recent studies on shape memory alloy devices have highlighted the potential of such materials in self-centering systems (Dolce et al., 2000, 2005; Miller et al., 2012; Eatherton et al., 2014).

Fluidic self-centering devices were used in combination with sliding bearings in the testing of a seismic isolation system with precise re-centering capability at the University at Buffalo (Taisei Corp., 1993; Tsopelas and Constantinou, 1994). (The two devices tested in 1992 at the University at Buffalo have been re-tested as part of the work presented in this report). The tested devices were virtually identical to the arresting centering spring-damper on the carrier-based Lockheed S-3Viking aircraft. Devices of this type and with force output up to 1500kN have been in use by the US Military since the 1970's as elements of shock isolation systems for missiles, submarines and ships. Moreover, compression-only versions of these devices have been in use as shock absorbers in industrial applications dating earlier than 1970. In the USA alone, thousands of fluidic devices with re-centering characteristics have been produced and are in use today in military and industrial applications. One building complex, the Quebec Iron and Titanium Smelter in Tracy, Canada was fitted in 1997 with fluidic self-centering devices as elements of a seismic protective system (Taylor Devices on-line catalog of projects).

Pekcan *et al*. (1995, 1999a) investigated the seismic performance of buildings with a self-centering device, called Elastomeric Spring Damper (ESD), which operated on principles similar to those of the fluidic device investigated by Tsopelas and Constantinou (1994) but the device utilized pressurized elastomer (with the substance of silly-putty) instead of oil. These devices were also based on proven hardware already in use in industrial applications as shock absorbers. Shake table tests of a concrete model with diagonally configured devices and a steel model with an innovative configuration system were conducted. Interestingly, the studies of Peckan et al. (1995, 1999a) and the earlier studies of Tsopelas and Constantinou (1994) have been completely ignored by investigations that followed despite the fact that they were based on existing proven technologies. Instead, efforts that followed concentrated on the development of new hardware and in studying the behavior of structures with flag-shaped hysteresis.

Filiatrault et al. (2000) investigated a self-centering device called the Friction Spring Seismic Damper (FSSD). The device, originally described in Kar et al. (1996), consisted of a stack of friction or ring springs enclosed in a cylinder. The rings consist of two groups, one outer group operated in tension and one inner group operated in compression so that preload, stiffness and friction force could be generated. The configuration of the device made it difficult to achieve high preload or to easily adjust the preload. For example, the device tested by Filatrault et al. (2000) had a preload of 9kN and a total force of 110kN at 25mm displacement. The device has a very high restoring force by comparison to the preload (ratio of 12) whereas a practical limit on the basis of practical large size devices is to have the force at the displacement capacity of the device about twice the preload (Erochko, 2013). Nevertheless, the device appears to have potential for application but for the issue of friction and its reliability when produced by the contact of metal on metal. Particularly, the use of the same metals in the two groups of friction rings ensures that friction will substantially change with time when the device is motionless due to cold welding (Rabinowicz, 1995). Even when dissimilar metals are used, corrosion becomes a major issue (British Standards Institution, 1990, Constantinou et al. 2007).

Starting in about 2000, a number of researchers looked at post-tensioned seismic-resistant connections and post-tensioned rocking walls (Ricles et al., 2001; Christopoulos et al., 2002b; Stanton and Nakaki, 2002; Kurama, 2000) which could be configured to produce flag-shaped hysteresis suitable for self-centering systems. Earlier studies of Priestley and Tao (1993) and MacRae and Priestley (1994) utilized un-bonded post-tensioning which provided self-centering capability but did not dissipate significant energy. Energy dissipation is now understood as an important component in self-centering systems.

A number of analytical studies since about 2001 have demonstrated the utility of self-centering systems in reducing or eliminating residual deformations and have explored the significance of energy dissipation and its form (Christopoulos et al., 2002a; Christopoulos et al., 2003; Pampanin et al., 2003; Christopoulos, 2004, Kam et al., 2008, Kam et al., 2010; Karavasilis and Seo, 2011; Eartherton and Haijjar, 2011).

More recently and having recognized that post-tensioning connections are cumbersome, the efforts concentrated on the development of self-centering bracing systems (Tremblay et al., 2008; Christopoulos et al., 2008; Erochko, 2013, Erochko et al., 2014a, 2014b; Eatherton et al., 2014, Kammula et al., 2014). These works resulted in the development of the Self-Centering Energy Dissipative Bracing System. The developed device consists of pre-stressed tendons within large structural tubes to develop the preload, and friction devices to provide rigidity and the desired energy dissipation capability. While they have the desired characteristics for a self-centering brace, they are clearly complex (many moving parts, large number of tendons, numerous connection details, frictional assemblies) and are very large in size. Moreover, the frictional assemblies, although consisting of materials that are much more reliable than the bimetallic interfaces of the EDR and FSSD, they are still subject to changes with time due to relaxation, aging and contamination.

This report concentrates on *Fluidic Devices* as elements of self-centering systems for buildings. It starts with a description of the behavior of these devices based on principles of mechanics. It proceeds with the presentation of test results on three devices, (a) a pair of small devices used in 1992 at the University at Buffalo in shake table testing of a model structure and re-tested to observe differences in behavior, (b) a large device tested under specific conditions of preload, initial temperature and a large number of cycles, and (c) a large device tested at three different levels of preload (easily accomplished by adjusting the initial pressure of the device) and various motion conditions. These test results are used to illustrate the behavior of the devices, to show the effects of time and temperature on their behavior, and to demonstrate ease in adjustability of their properties. Mathematical models of the behavior of the devices are presented and validated by comparison to experimental results. Analyses of single-degree-of-freedom systems for a wide range of parameters are performed and the results are utilized to (a) illustrate the effect of the added fluidic self-centering devices on the behavior of the structural system, and (b) to arrive at conclusions on the appropriate strategy for selection of the device properties in design. On the basis of these observations, a design strategy is developed that parallels the design strategy for buildings with damping systems as presented in ASCE 7-2010 (2010). Simplified methods of analysis are presented, again on the basis of the procedures for the design of buildings with damping systems (ASCE 7-10, 2010; Ramirez *et al*., 2001), and verified by comparison to rigorous response history analysis results. Three and six-story buildings without and with self-centering systems are designed per ASCE 7-10 (2010) procedures (for the conventional buildings) and per procedures developed in this report (for the buildings with self-centering fluidic devices). The response of the buildings is then obtained by simplified analysis and by nonlinear response history analysis with due considerations for the behavior of the devices and of the yielding structural system.

The seismic collapse performance of the two buildings is quantified using the FEMA P695 procedures (FEMA P695, 2009; Vamvatsikos and Cornell, 2002; Haselton, 2006; Haselton and Deierlein, 2007; Haselton et al., 2008; Liel et al., 2011; Lignos and Kranwinkler, 2011, 2013) and compared to that of conventional buildings. It is concluded that buildings with fluidic self-centering devices designed by the procedures presented in this report have a collapse performance comparable to that of conventionally designed buildings (in terms of the collapse margin ratio for the Maximum Earthquake). Moreover, the study varies the parameters of the fluidic devices, of the bracing system and of the strength of the frame. It is determined that increases in the preload, increases in the displacement capacity or increases in the linear viscous damping constant of the devices have marginal or insignificant effects on the collapse margin ratio. Rather, an increase in the collapse margin ratio was calculated for frames having a device-braced system with increased ultimate capacity and for frames with increased frame strength.

The study is then extended to study the residual drift fragility of buildings with fluidic self-centering systems and to compare them with those of conventional buildings. It is shown that buildings with fluidic self-centering systems, designed per the procedures of this document have substantial reduction of the probability of exceeding the residual drift limits of 0.2% and 0.5% for any level of earthquake.

Buildings without and with fluidic self-centering systems are further analyzed to obtain information of the mean annual frequency of collapse, the mean annual frequency of exceeding the residual drift limits of 0.2%, 0.5%, 1% and 2%, and the related probability of collapse or of exceeding the residual drift limits in 50 years (Medina and Krawinkler, 2004; Ibarra and Krawinkler, 2005; Krawinkler et at., 2006; Champion and Liel, 2012; Eads et al, 2013; Elkady and Lignos, 2014). This information is of much interest to engineers, building officials, government officials, owners and insurers. It is concluded that all analyzed systems have a probability of collapse in 50 years of about 1% or less, which is desirable. Also, the structures with fluidic self-centering systems have much lower probabilities in 50 years of exceeding the residual drift limits of 0.2% and 0.5% than conventional structures.

Finally, a study is presented on the effects of replacing viscous damping devices in seismic isolation systems by equivalent fluidic self-centering devices with identical damping characteristics and preload related to the minimum strength in the isolation system. It is observed that the use of the fluidic self-centering devices results in reduction of the residual displacements by four fold to six fold, in a small reduction of the peak isolator displacement and an increase in the peak floor accelerations and story drift ratio by as much as 15%.

SECTION 2
PRINCIPLES OF OPERATION AND MODELING OF FLUIDIC SELF-CENTERING DEVICES

2.1 Introduction

This section describes the principles of operation of the fluidic self-centering device. It is largely based on Tsopelas and Constantinou (1994) and Taylor and Lee (undated). The device is a compact compression-only fluidic spring-damper that is pressurized to develop preload. Spring force is developed by compressing the silicone oil in the device. Damping forces are developed by orificing the silicone oil at the time it is compressed. A mechanism is added to the compression-only device to maintain compression of the fluid whenever the device is in the compression or tension. (Details will be provided in the sequel). The device operates at high fluid pressure with special seal design. The seals consist of very soft material that flows under high pressure in order to seal microscopic surface roughness patterns and prevent oil leakage. Two devices manufactured by Taylor Devices and tested at the University at Buffalo in 1992 have been in storage without any leakage for 22 years. They were re-tested in 2014 and results will be presented in this report.

2.2 Principles of Operation

The principle of operation of the device is illustrated in Figure 2-1. A cylinder is completely filled with silicone oil.

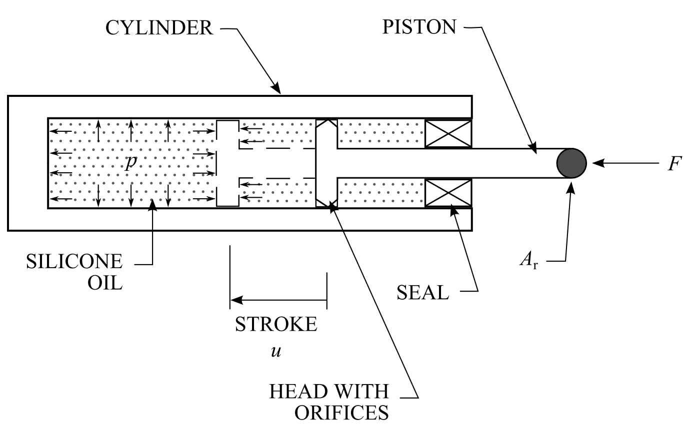

Figure 2-1 Principle of Operation of Fluidic Self-Centering Device

A rod of area A_r is forced into the cylinder so that the fluid volume is reduced by $\Delta V = A_r u$, where u is the imposed displacement of piston rod. The overpressure p in the cylinder is:

$$p = \frac{F}{A_r} \tag{2-1}$$

where F is the force acting on the rod. The overpressure p may be related to the change of volume using the volumetric relation:

$$p = K\frac{\Delta V}{V} \tag{2-2}$$

where K is the bulk modulus of the oil and V is the fluid volume. Equations (2-1) and (2-2) result in:

$$F = \frac{KA_r^2}{V}u \tag{2-3}$$

This relation is depicted in Figure 2-2 (a).

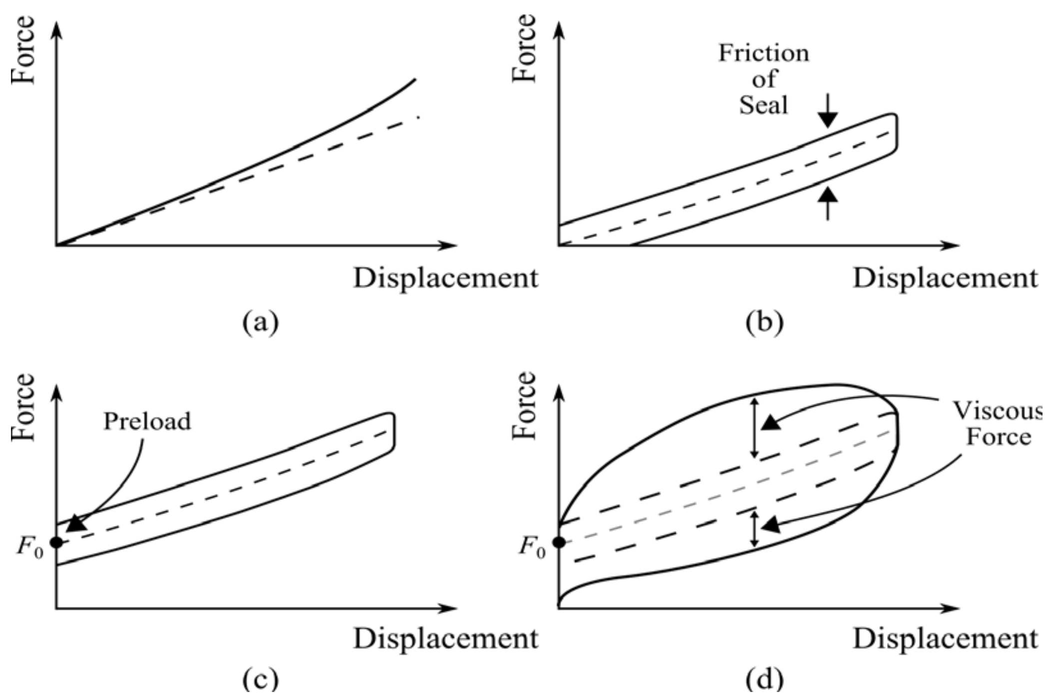

Figure 2-2 Components of Force in Fluidic Self-centering Device

Generally, this relation is nonlinear because the bulk modulus of the oil is dependent on the total pressure p_T (initial pressure plus instantaneous pressure) and the fact that the volume V reduces with increasing displacement so that V=V_0-$A_r u$, where V_0 is the initial fluid volume (at zero displacement). Therefore, more acurately:

$$F = \int \frac{K(p_T)A_r^2}{V_0 - A_r u} \tag{2-4}$$

where $K(p_T)$ is the pressure dependent bulk modulus of the oil. An example of an empirical relation for bulk modulus to pressure dependency of one silicone oil used in damping devices was given in Symans and Constantinou (1995):

$$K = 864 + 4.166p\left(MPa\right) \tag{2-5}$$

Note the bulk modulus relation to the pressure is nonlinear and Equation (2-5) is only valid in a specific range of pressure (about 50 to 110MPa). The bulk modulus also depends on temperature so that the above equation is representative for a narrow range of temperatures. Considering a pressure in the range of 73 to 116MPa (for which devices were tested and results are presented in this report), the values of the bulk modulus are in the range of about 1168 to 1347MPa, or about ±7% from the mean value. This indicates that the nonlinearity due to the dependency of the bulk modulus of the oil to the pressure is small. Based on data on the bulk modulus to pressure relation, it is known that nonlinearity in stiffness reduces as the initial pressure increases. However, larger nonlinearities may be obtained when there is significant reduction of the fluid volume, where the increase in force is further amplified by the increase in the bulk modulus of the compressed fluid. This may be desirable and also is easily controlled by the selection of the geometric parameters of the device: initial volume and area of piston.

Friction in the seal of the devices alters the force-displacement relation to the form depicted in Figure 2-2 (b). Note that the friction force in this device is typically very small (about 5% of preload F_0).
By pressurizing the device to an initial pressure p_0, a preload F_0 develops as:

$$F_0 = A_r p_0 \tag{2-6}$$

The preload F_0 must be exceeded for the rod to be moved. The resulting force-displacement relation is shown in Figure 2-2 (c).

The piston head supports the rod and provides resistance to fluid transfer across the head during stroking. The area and shape of the orifices on the piston head determine the level and nature of the developed viscous damping force. This viscous damping force is related to the velocity of the piston rod. A complete force-displacement loop is depicted in Figure 2-2 (d). It may be noted that the loop in this figure is shown with viscous force being more in the direction of motion away of the centered position than the opposite direction when the motion is towards the centered position (this is also seen in actual loops of the tested devices in this report-see Figure 2-6 for a sample). This behavior is desirable in cases of very high velocity motion when the piston rod re-centering may be delayed by the large damping force on reversal of motion. The effect of the form of the damping force is investigated in the studies presented in this report.

A schematic of the self-centering device, including the mechanism for compression-tension operation, is shown in Figure 2-3. The device consists of a compression-only spring-damper of which the cylinder is identified in the figure. The cylinder is encased in an external sleeve, denoted as cylinder sleeve in the figure. Note that in the neutral position the over-center pins bear against the edge of a slot that is cut out of the cylinder and sleeve. A view of one of the tested devices in the neutral position is also shown in the figure. The capacity for displacement of this device is 50 mm.

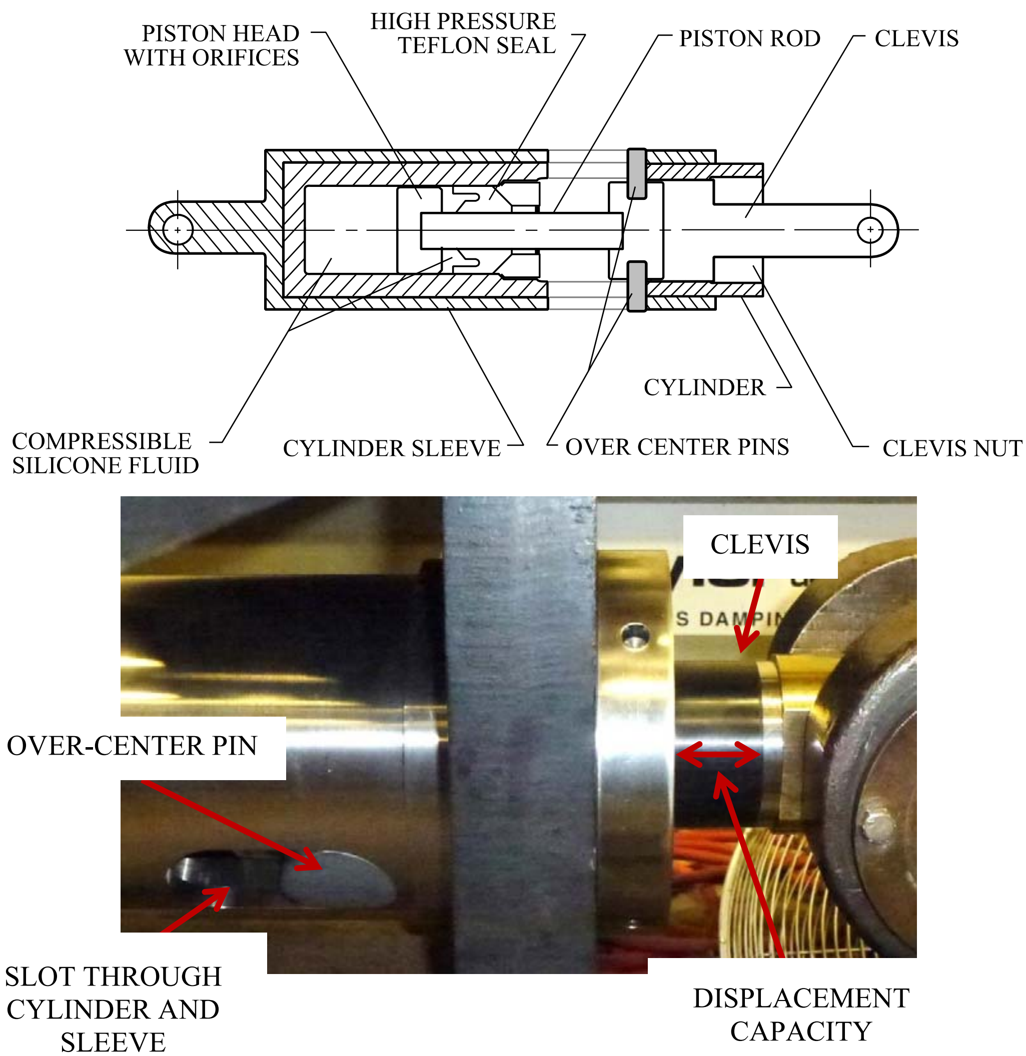

Figure 2-3 Schematic and View of Fluidic Self-Centering Device in Neutral Position

When the device operates in compression, the piston clevis moves as shown in Figure 2-4. A view of a device during testing in compression is included in the figure. Note that the over-center pin moves within a slot through the cylinder and sleeve.

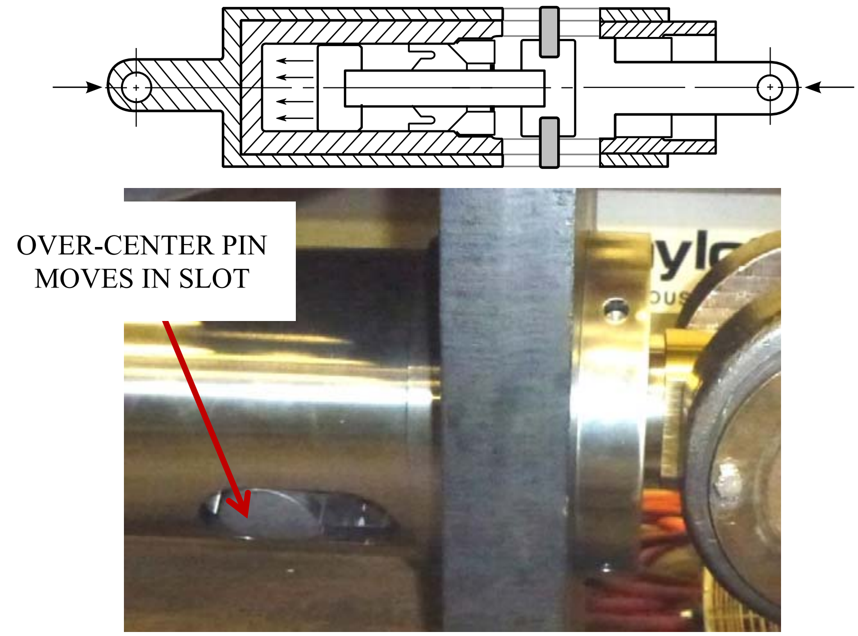

Figure 2-4 Operation of Fluidic Self-Centering Device in Compression

When the device operates in tension, the over-center pins react against the edge of the slot through the cylinder and sleeve so that the sleeve and cylinder move as shown in Figure 2-5.

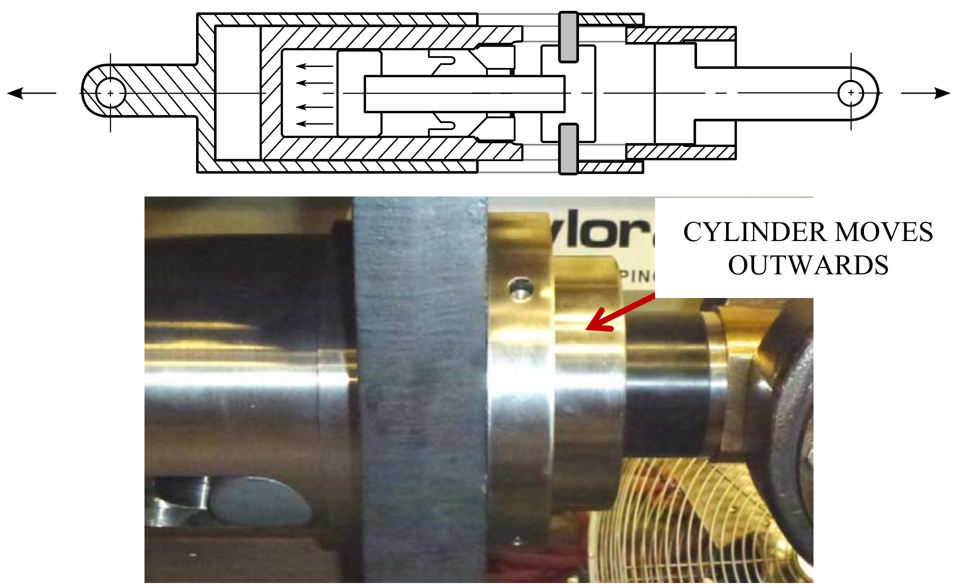

Figure 2-5 Operation of Fluidic Self-Centering Device in Tension

The schematic in Figure 2-6 provides a clearer illustration of the operation of the device.

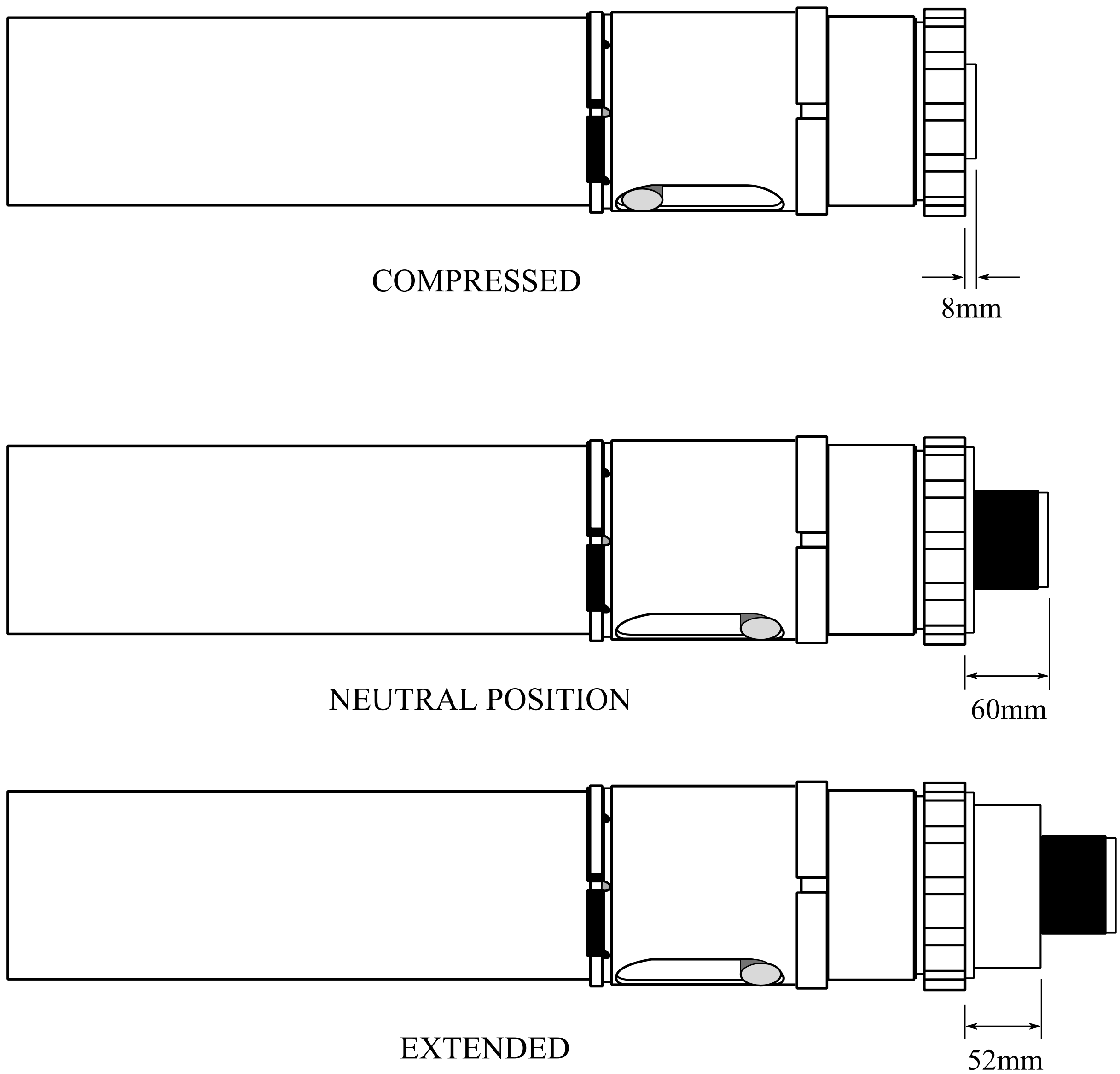

Figure 2-6 Illustration of Behavior of Device in Compression and Tension (dimensions shown are for the tested large size device of Section 3)

The compression-tension device has identical behavior in tension and compression owing to the fact that it only operates in compression. An example of force-displacement loops is shown in Figure 2-7 where the basic properties of preload F_0 and stiffness K_0 are identified. Note that the stiffness in this example is essentially independent of the displacement as a result of the selection of the fluid volume and piston area.

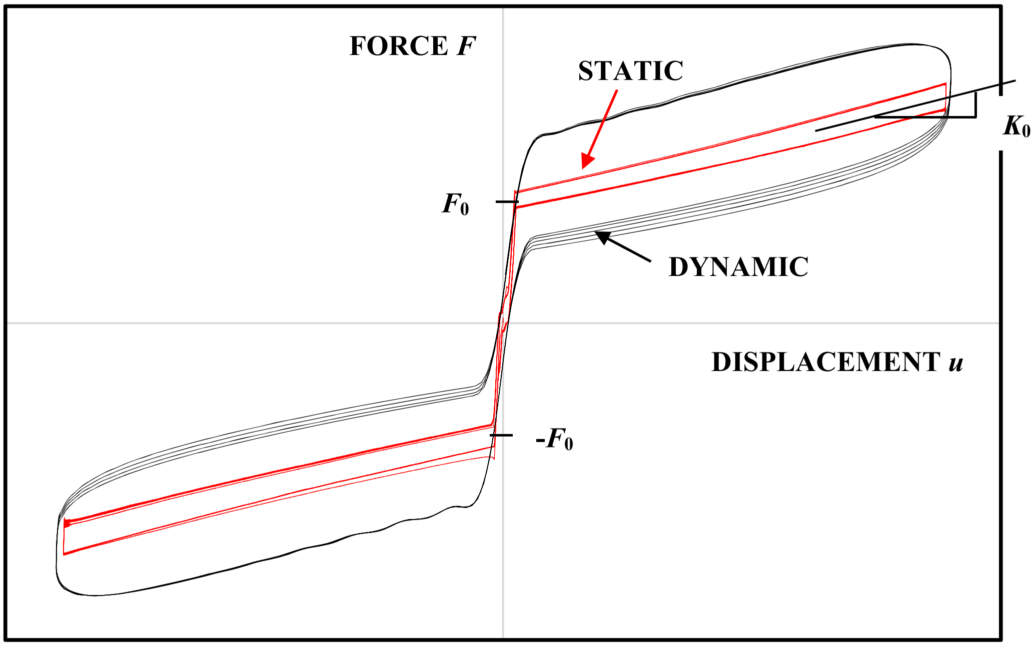

Figure 2-7 Typical Force-displacement Loops of Fluidic Self-Centering Device

2.3 Mathematical Modeling

The force in a fluidic self-centering device consists of the preload, the restoring force, the friction force in the seal and the fluid damping force. These four components are evident in the force-displacement loops of Figure 2-7. The following equation has been proposed by Tsopelas and Constantinou (1994) to describe the behavior of the device:

$$F = F_0\left[1-\exp\left(-\delta|u|\right)\right]\operatorname{sgn}\left(u\right)+K_0u+\left[F_{\min}+\zeta K_0|u|\right]Z_t+F_d\operatorname{sgn}\left(\dot{u}\right) \tag{2-7}$$

where the first term represents the preload, the second term the restoring force, the third term the seal friction force and the last term the fluid damping force.

The preload term could, for ideal conditions, be represented by a term $F_0\mathrm{sgn}(u)$, which presumes infinite stiffness at zero displacement. In reality, the stiffness of the device is not infinitely large at zero displacement. Rather, it has a large value which is dependent on the velocity of motion of the piston rod. This behavior is accounted for in the model by the exponential term for the preload. Note that the initial stiffness (at zero displacement) is given by $K_{in}=F_0\delta_0$ and that parameter δ is dependent on velocity and represents the inverse of a displacement at which the slope changes from the initial value K_{in} to K_0.

Tsopelas and Constantinou (1994) proposed an equation to describe the velocity dependence of parameter δ and, therefore, the initial stiffness. That equation was generalized as presented below (the original equation had $\delta_{\min}$=0):

$$\delta = \delta_{\min} + \left(\delta_0 - \delta_{\min}\right)\exp\left(-\delta_1 \left|\dot{u}\right|\right) \tag{2-8}$$

Equation (2-8) is generally valid for velocities less or equal to 600mm/sec. For larger values of velocity the limit value of δ calculated for the velocity of 600mm/sec should be used. Note that the initial stiffness for quasi-static conditions ($\dot{u} = 0$) is given by $F_0\delta_0$. The values of parameters δ_0, $\delta_{\min}$ and δ_1 are obtained experimentally. Values of parameters proposed by Tsopelas and Constantinou (1994) and based on observation of the behavior of a tested small size device is δ_0=1.78mm^{-1}, $\delta_{\min}$=0 and δ_1=0.00385sec/mm.

The second term in Equation (2-7) represents the restoring force. In general, the device has nonlinear restoring force but the nonlinearity typically is often too small to be of practical significance. In the test results of various devices presented in the next section, the nonlinear behavior is noticeable only in cases in which the initial pressure (preload) was low.

The third term in Equation (2-7) represents the seal friction. The sub-term $\zeta K_0|u|$ accounts for increased friction in the seal as a result of increased internal pressure during stroking. The value of ζ is obtained from observation of the force-displacement loops under quasi-static conditions. The increase in friction is not significant, so that a typical value for parameter ζ is zero. Parameter Z_t represents a continuous representation of sgn($\dot{u}$) and is based on modeling of sliding bearings (Constantinou et al, 1990). Parameter Z_t is governed by the following equation:

$$Y\dot{Z}_t + \gamma\left|\dot{u}\right|Z_t\left|Z_t\right|^{\eta-1} + \beta\dot{u}\left|Z_t\right|^{\eta} - A\dot{u} = 0 \tag{2-9}$$

where the parameters have the following values based on theoretical considerations Y=0.25 mm, A=1, β=0.1, γ=0.9, η=2.

The fourth term in Equation (2-7) represents the fluid viscous damping force. The device may be configured to produce damping force within a range of behaviors as described below:

$$F_d = \begin{cases} F_1 = C_1\left|\dot{u}\right|^{\alpha 1} & when \quad u\dot{u} > 0 \\ F_2 = C_2\left|\dot{u}\right|^{\alpha 2} & when \quad u\dot{u} < 0 \end{cases} \tag{2-10}$$

The damping force described by Equation (2-10) is nonlinear viscous and the values of parameter α_i can be reliably delivered in the range of 0.4 to 1.2. Also, Equation (2-10) describes a damping force that differs depending on the direction of motion, as expressed by the sign of the product of displacement and velocity. This is accomplished by utilization of a lower orifice area when stroke increases ($u\dot{u}>0$) than when the stroke decreases ($u\dot{u}<0$).

The various parameters in the model are graphically shown in Figure 2-8.

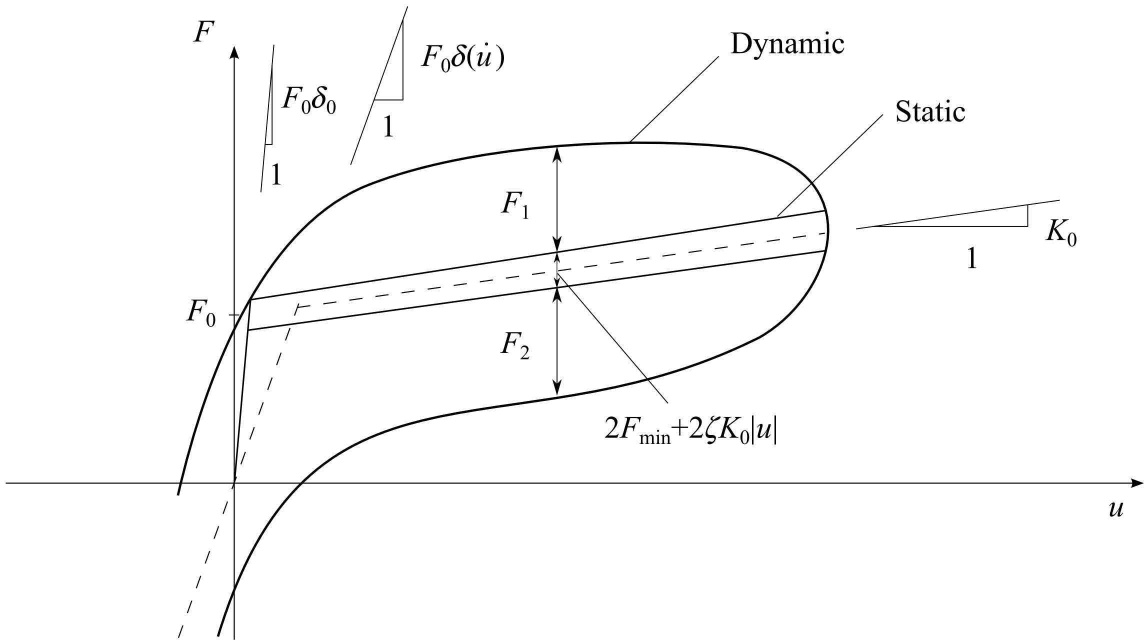

Figure 2-8 Definition of Terms in Model of Fluidic Self-centering Device

The mathematical model described in this section has been incorporated into program OpenSees (McKenna, 1997). Comparisons of experimental and analytical results are presented in Section 3.

SECTION 3
BEHAVIOR OF FLUIDIC SELF-CENTERING DEVICE AND MODEL VALIDATION

3.1 Introduction

This section presents experimental results on the behavior of two devices: (a) one small size device originally tested in 1992 (Tsopelas and Constantinou, 1994) and re-tested in 2014, and (b) a large size device of which two identical units were tested, one in 2009 and another in 2014. The latter device has been tested at three different values of initial pressure in the range of 29 to 116MPa, resulting in preload in the range of 44kN to 178kN. The devices were tested at temperature in the range of zero to 50ºC to reveal the effect of temperature on their behavior.

The experimental results are compared with analytical predictions based on the model presented in Section 2. The comparison serves the purpose of validating the analytical model.

3.2 Small Size Device

Two small size devices were used in 1992 in the shake table testing of a precise-positioning seismic isolation system (Taisei, 1993, Tsopelas and Constantinou, 1994). These two devices were kept in storage since 1994 and were re-tested in 2014. Figure 3-1 shows a drawing and a photograph of one of the devices.

The device is virtually identical to the arresting centering spring-damper on the carrier-based Lockheed S-3 Viking aircraft. Figure 3-2 shows an S-3 Viking aircraft during an approach to land on a carrier. The arresting hook is visible. The S-3 was retired from front-line fleet service aboard aircraft carriers in 2009.

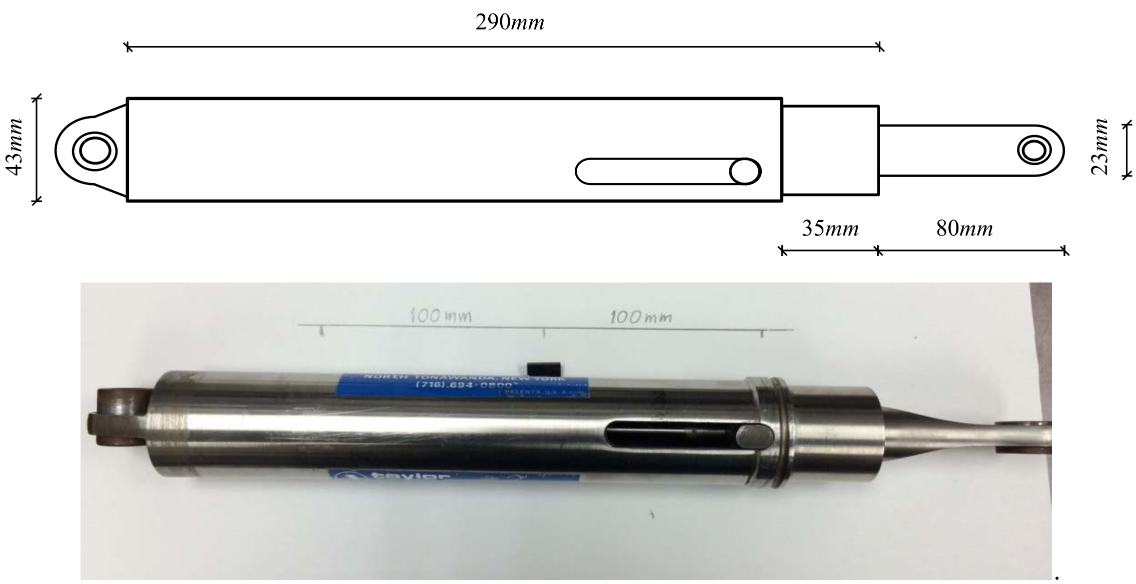

Figure 3-1 Tested Small Size Fluidic Self-Centering Device (manufactured in 1992)

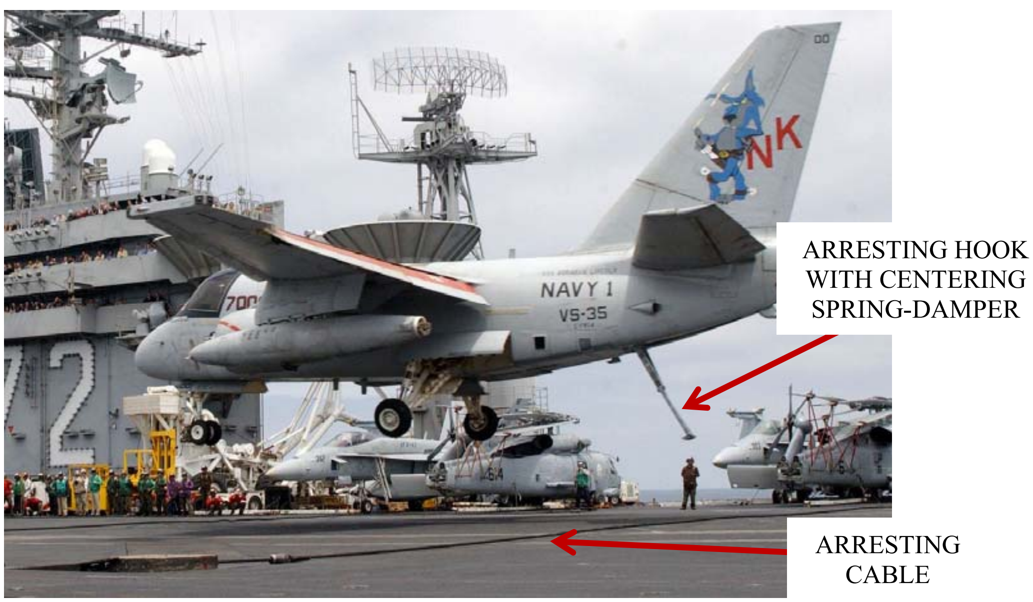

Figure 3-2 S-3 Viking Aircraft during Landing (arresting hook with centering spring-damper is visible) (http://www.navy.mil/view_image.asp?id=7171)

The two devices were tested in accordance with the test matrix of Table 3-1.

Table 3-1 Test Matrix for Small Size Device

Test No.	Device No.	Frequency Hz	Amplitude mm	Number of Cycles	Recorded Temperature at Start of Test ℃
1	1	0.01	45	5	21
2	1	0.5	45	5	21
3	1	1.0	12.5	5	24
4	1	1.0	25	5	24
5	1	1.0	37.5	5	24
6	1	1.0	45	5	24
7	1	0.01	45	5	51
8	1	1.0	45	5	52
9	1	0.01	45	5	1
10	1	1.0	45	5	2
11	2	0.01	45	5	21
12	2	0.5	45	5	21
13	2	1.0	12.5	5	23
14	2	1.0	25	5	23
15	2	1.0	37.5	5	23
16	2	1.0	45	5	21

Testing was conducted by imposing five cycles of sinusoidal history of displacement with specified amplitude and frequency. The surface temperature of the device at the start of each experiment was recorded. Sufficient idle time between tests was allowed for any heating effects to diminish. Figure 3-3 shows a view of the test set-up. Note that the load cell is mounted at the reaction frame so that it measures the reaction (so that the measured force did not include any inertia effects of the moving actuator parts). Also note that the arrangement shown is for the testing at elevated temperature (hence the heating tape). The low temperature tests were conducted with a plastic bag containg ice placed around the device.

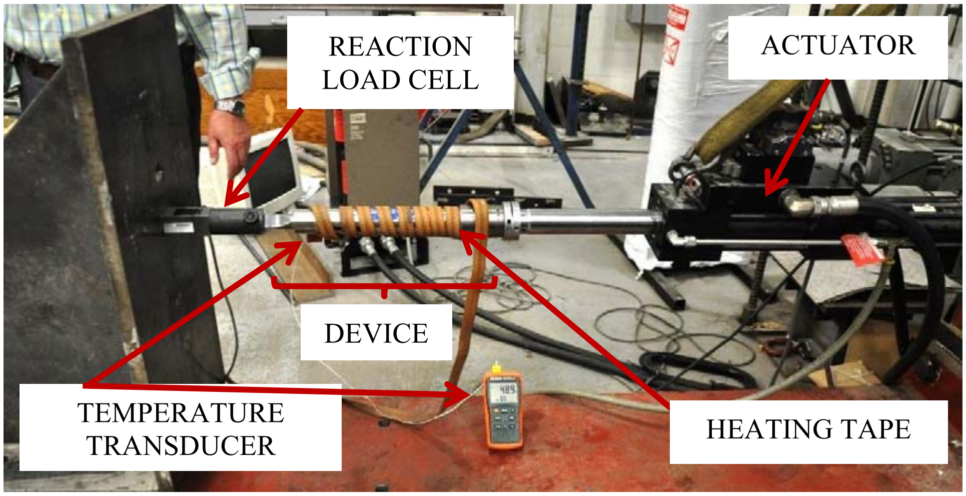

Figure 3-3 Test Set-up for Small Size Device

Figure 3-4 present the recorded force-displacement loops of devices No. 1 and 2 at normal temperature. Note that device No. 2 has a slightly lower preload than device No. 1. Unfortunately, data from the 1992 testing were available for only one of the two devices and unknown for which of the two devices. Thus, it is not known if the difference existed since the manufacturing of the devices or it is the result of 22-year aging. The difference is small and within the typical ±15% of tolerance in properties allowed in production.

Figure 3-5 compares the force-displacement loops of both devices tested in 2014 to the loops of the one device available from the testing in 1992. Note that it was not known which of the two devices was tested in 1992. The test data of device No.1 are essentially the same as those of the device tested in 1992. We presume that this was device No. 1 and, therefore, there was insignificant change in behavior over a period of 22 years.

Figure 3-6 compares the recorded force-displacement loops of device No. 1 for various values of the temperature at the start of the test (about 1°C, 20°C and 50°C). It is evident that temperature affects the value of preload but not the stiffness or the fluid damping force. This is due to changes in the initial pressure of the device, which proportionally affects the preload but only marginally affects the stiffness and damping force. The relation of preload F_0 and temperature T is essentially linear (for the tested device, $F_0=4.4+(T-20)$ in units of kN and degrees centigrade). The relation will be further discussed in the testing of a large device later in this section.

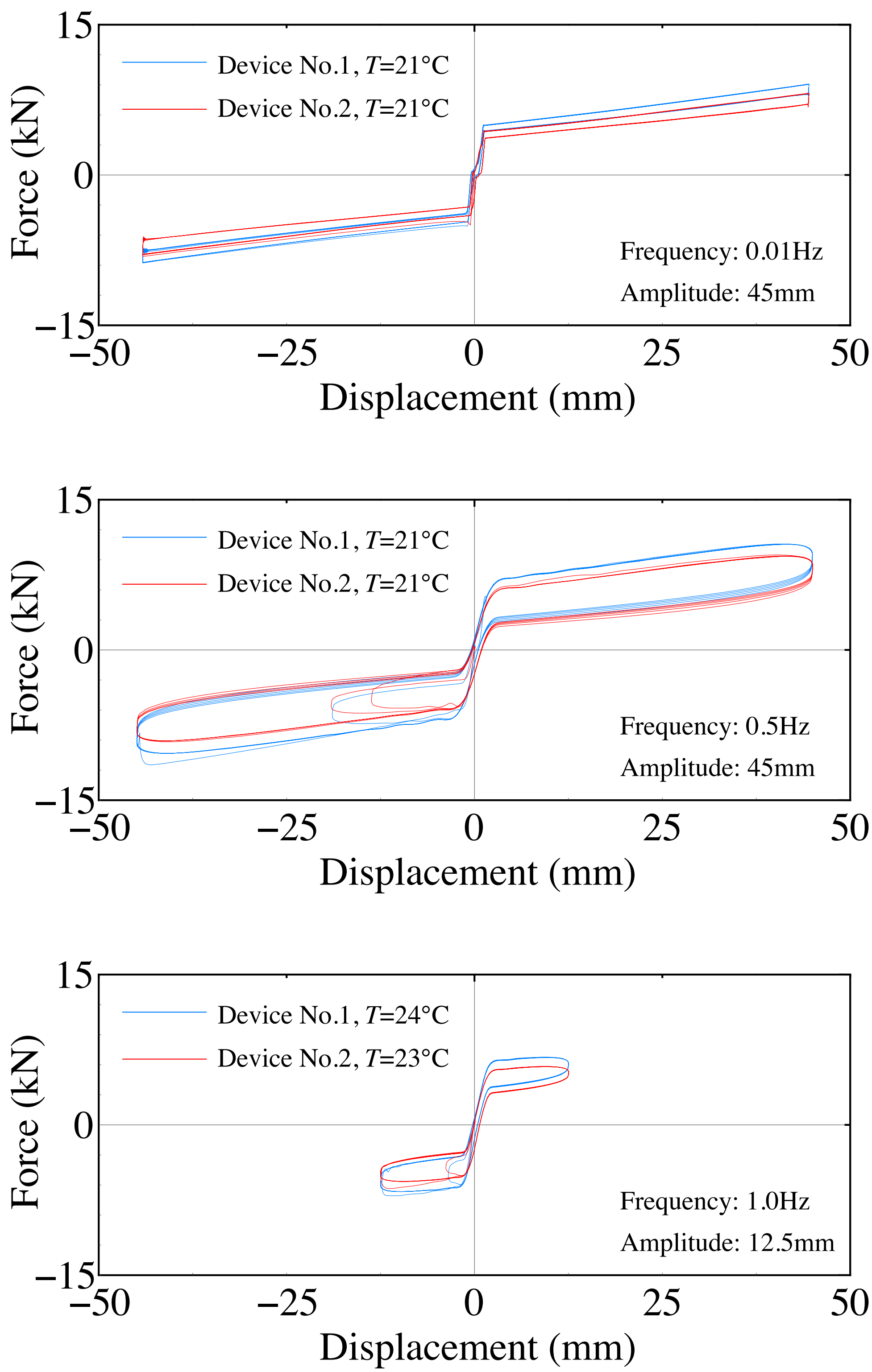

Figure 3-4 Recorded Force-Displacement Loops of Devices No. 1 and 2

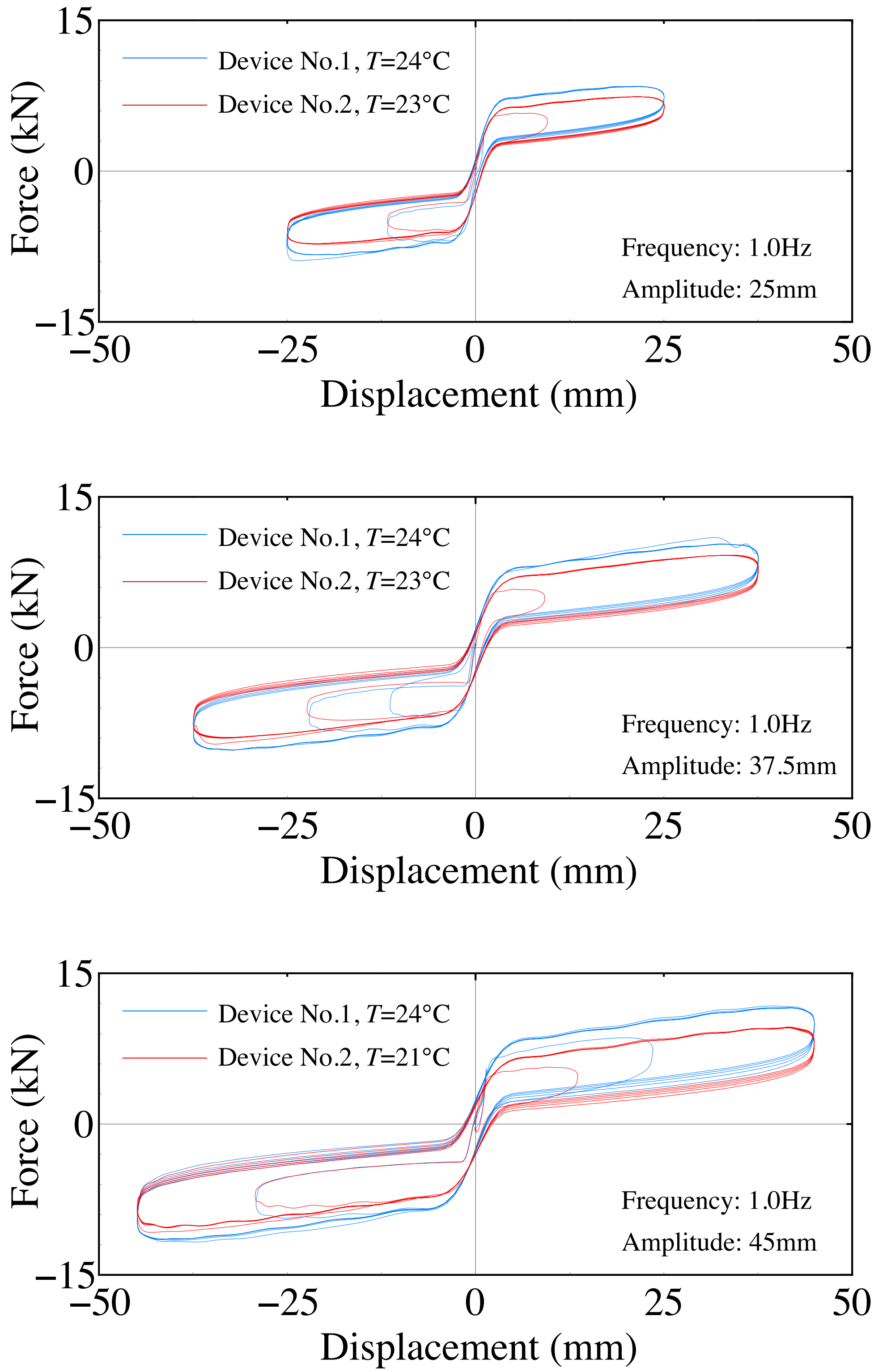

Figure 3-4 (Continued)

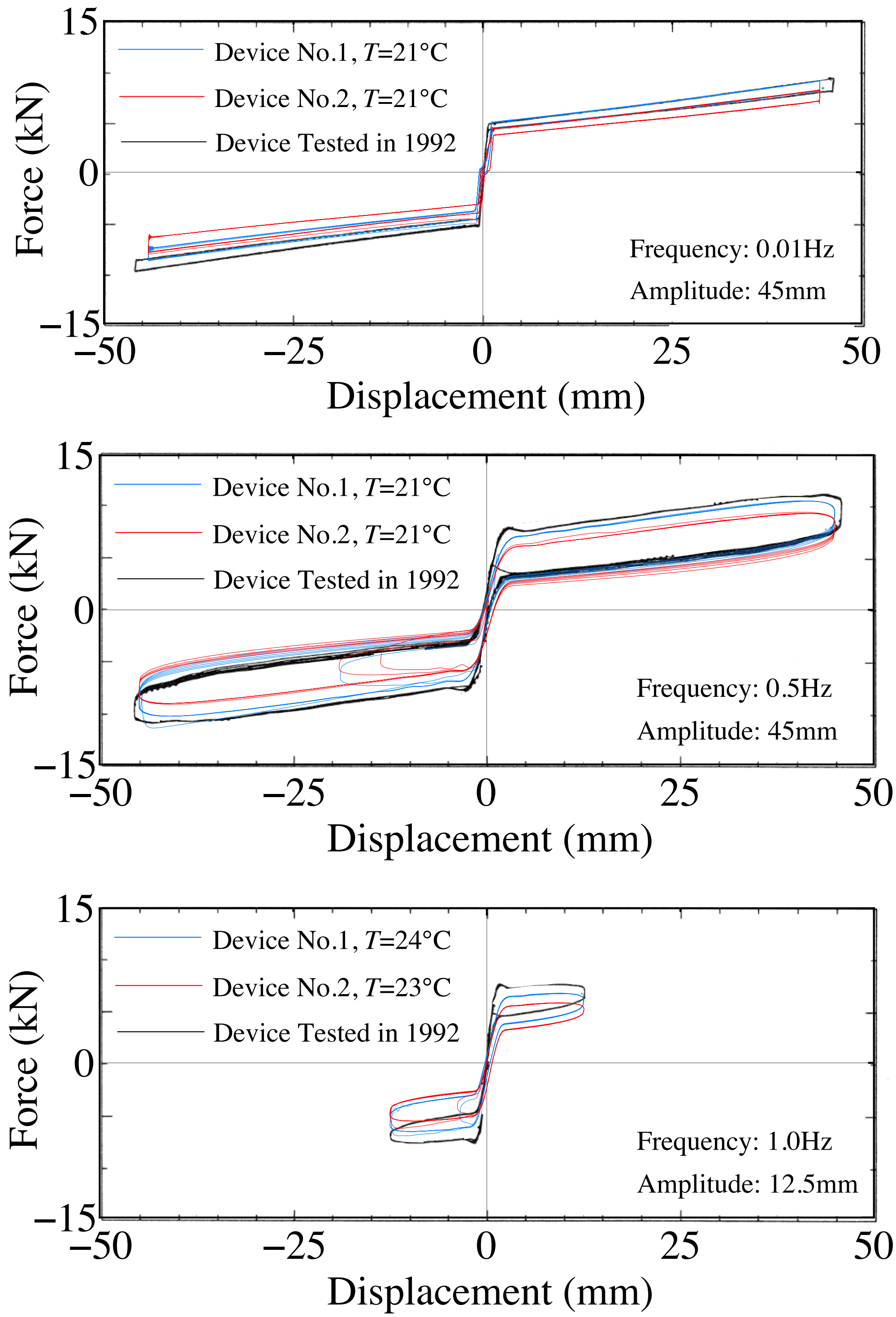

Figure 3-5 Comparison of Force-Displacement Loops of Devices No. 1 and 2 Tested in 2014 and Device Tested in 1992

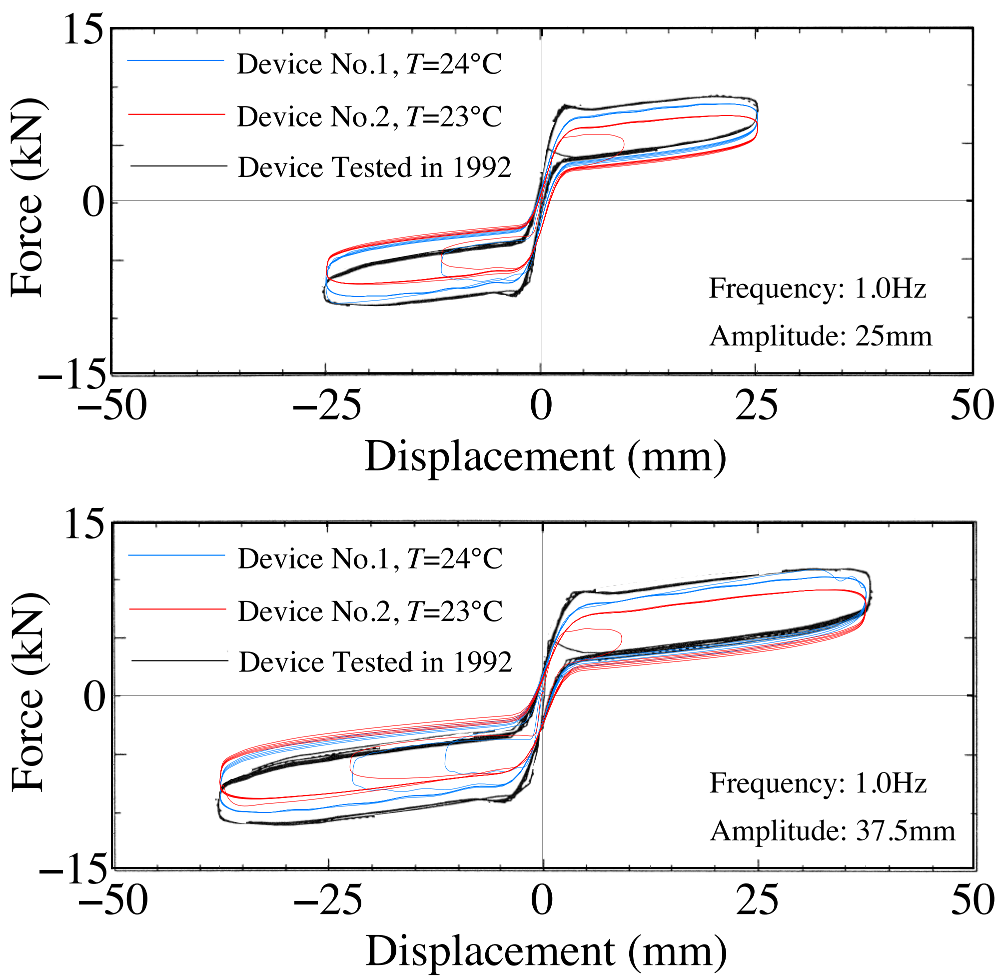

Figure 3-5 (Continued)

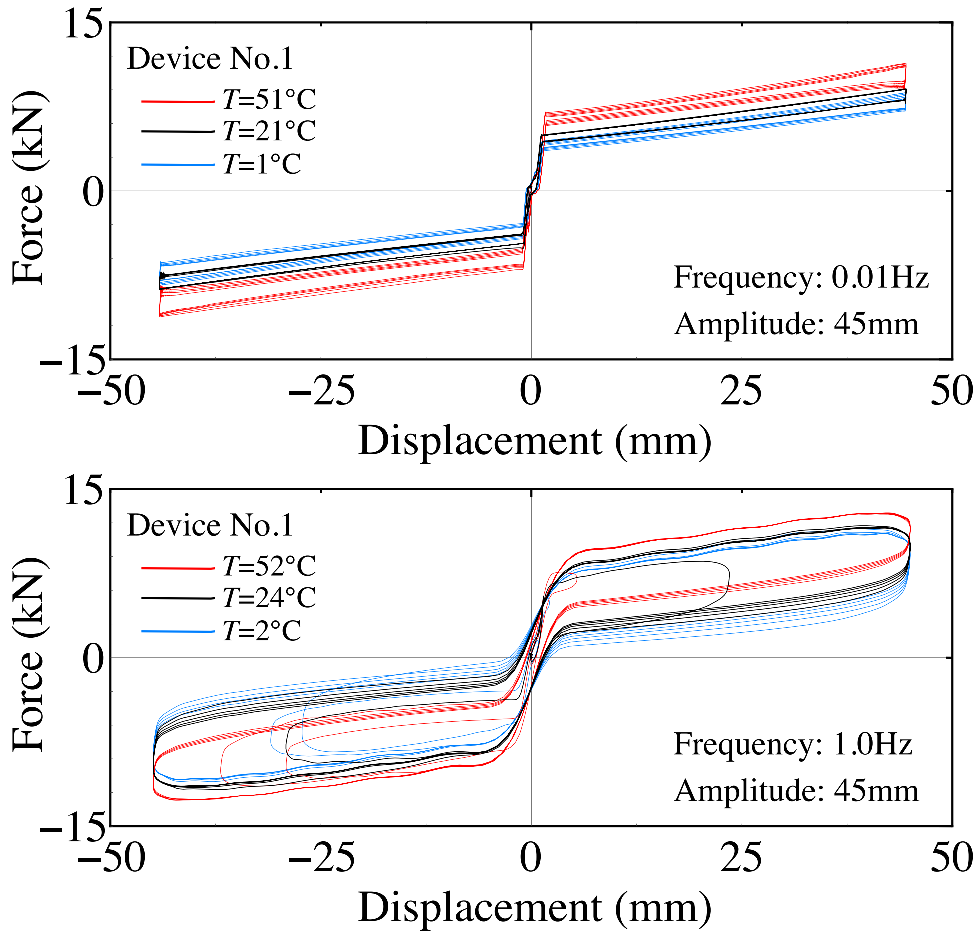

Figure 3-6 Effect of Temperature on Behavior of Device No. 1

3.3 Large Size Device

Two identical units of a large size device were tested at the testing facility of Taylor Devices in North Tonawanda, NY. Figure 3-7 shows a drawing of the device and a view of one of the devices during testing. Note that the force is measured by a load cell mounted on the moving actuator rod. The weight of the moving parts (including those of the device, actuator head and half of load cell) equaled 1500N when moving in compression and to 1785N when moving in tension. The resulting peak inertia force during testing was less than 2.7kN based on the highest recorded acceleration of 1.5g. When the recorded force was corrected for inertia effects, there was no observable difference in the results.

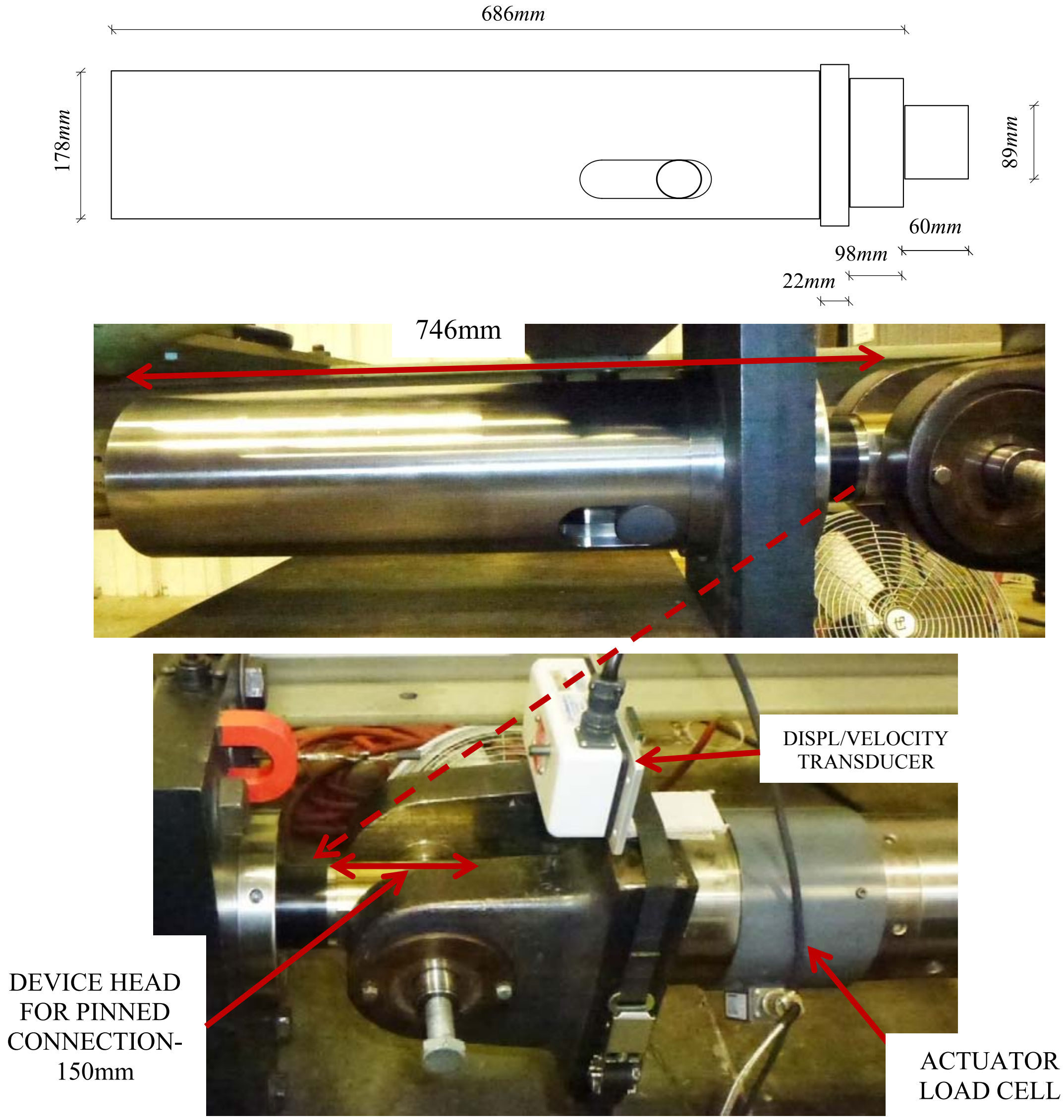

Figure 3-7 Tested Large Size Fluidic Self-Centering Device

The first unit was a production device for an application in a military shock isolation system of which the details are unknown to the authors of this report. The device had an initial pressure of 73MPa at the temperature 20°C. The piston rod area was 1534mm^2 (diameter of piston rod equal to 1.74in or 44.2mm) and the displacement capacity was ±50mm. The device was tested quasi-statically at three different temperatures (-1, 20 and 51°C at the start of testing) to reveal the effect of temperature on the preload and seal friction. Results are presented in Figure 3-8. The device was conditioned in an environmental chamber for a minimum of 18 hours and then moved to the testing equipment and tested within 30 minutes. Note that the temperature shown in the graphs was recorded at the start of each test.

The data demonstrate a linear relation between preload and temperature, which for the tested device is given by F_0=113+1.6(T-20) in units of kN and degrees centigrade. This relation is predictable by assuming that the change of temperature does not result in any change of volume of the device cylinder (the coefficient of linear thermal expansion of the 17-4 Precipitation Hardening stainless steel used for the cylinder is 1.1x10^{-5}/^{o}C or about 80 times smaller than the volumetric thermal expansion coefficient of the silicone oil). Accordingly, the change in preload is given by

$$\Delta F_0 = \alpha K A_r \Delta T \tag{3-1}$$

where α is the volumetric thermal expansion coefficient of the silicone oil (=0.0009/^{o}C), K is the bulk modulus of the fluid, A_r is the piston rod area and ΔT is the change in temperature. Using Equation (2-5) and initial pressure of p_0=73MPa at the temperature of 20^{o}C, K=1168MPa, and for the piston area of 1534mm^2 (piston rod diameter 44.2mm), we calculate a preload F_0=p_0A_r=112kN and αKA_r=1.61kN/^{o}C, which agree very well with the experimental values of 113kN and 1.6kN/^{o}C, respectively.

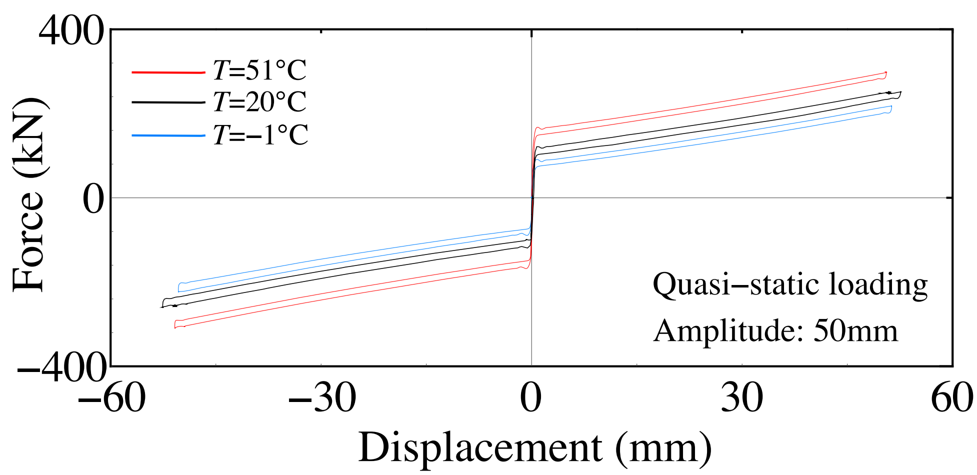

Figure 3-8 Effect of Temperature on Force-Displacement Loops of Large Size Fluidic Self-Centering Device under Quasi-static Conditions

The second large size unit was manufactured as an extra device during manufacturing of production devices for an unknown military application. The device was identical in geometry and materials as the previously tested device but the internal pressure was adjusted in order to demonstrate the effect on behavior. The device was pressurized to three different pressures, 29, 72.5 and 116MPa, and testing was conducted at a temperature of about 23^{o}C. The process of pressurizing the device and testing (total of 12 tests) took a total of two hours. This demonstrates the ease by which the internal pressure and preload can be adjusted.

Figures 3-9 to 3-11 present the recorded force-displacement loops in the testing of the device for the three cases of initial pressure. For each case, a quasi-static test was conducted at amplitude of 50mm, followed by three dynamic tests, each of 5 cycles at amplitude of 38mm and frequency of 0.5, 1.0 and 2.0Hz. The figures also include analytically predicted force-displacement loops, for which the analysis will be described in the sequel. Note that the loops show some fluctuation in the force. This is due to fluctuations in the velocity of the imposed motion, which was not of perfect sinusoidal form. For example, Figure 3-12 shows the imposed histories of displacement and velocity in the test of the device at pressure of 116MPa and frequency of 2Hz.

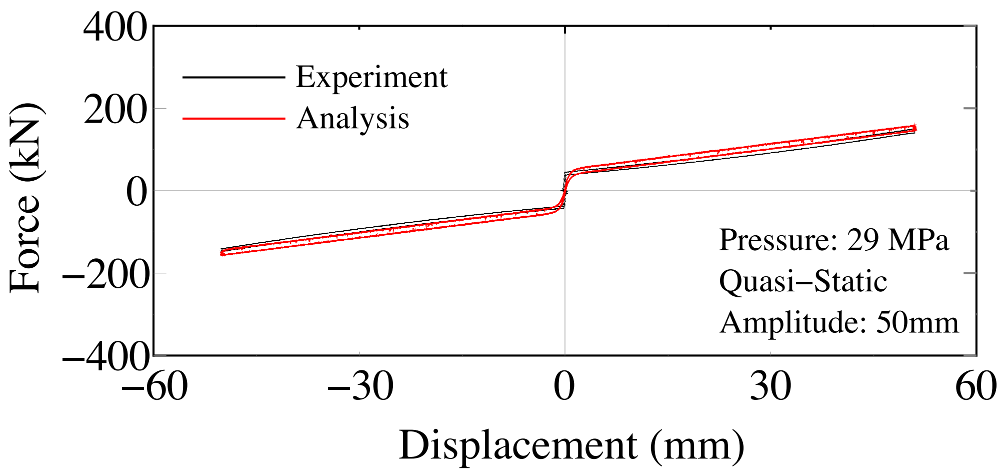

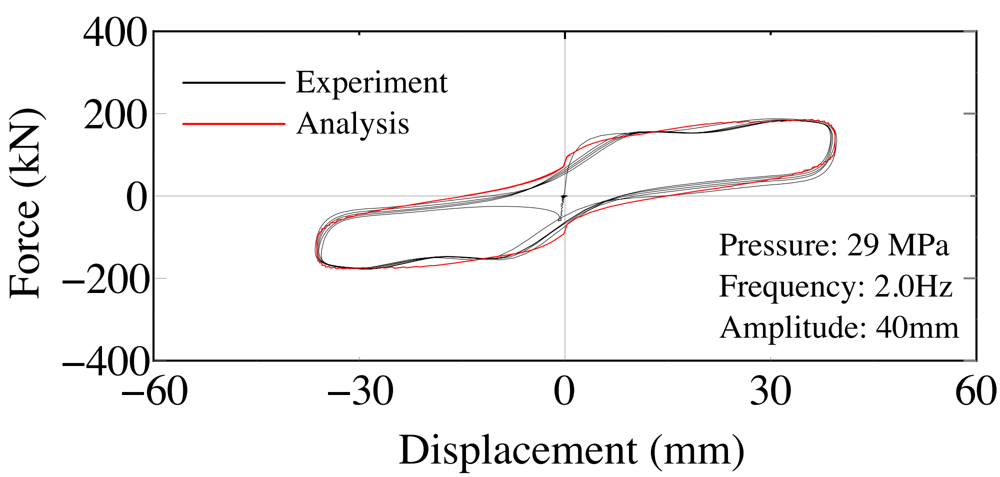

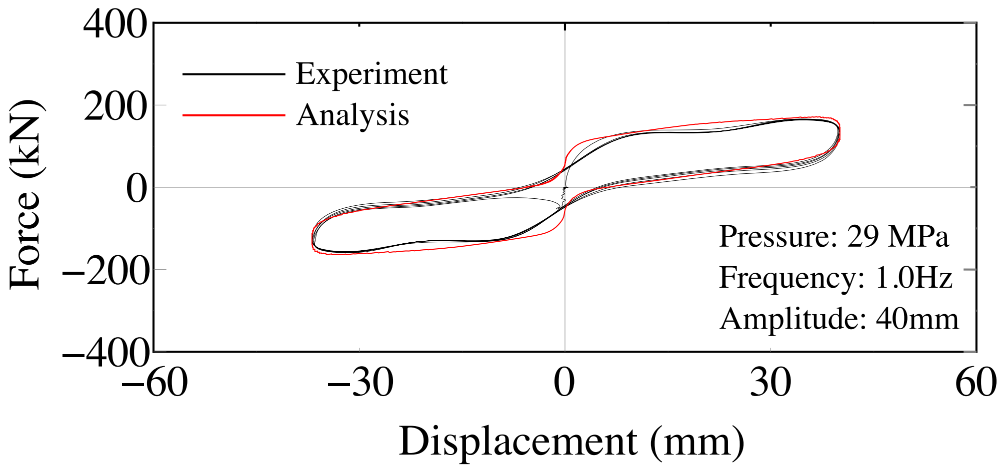

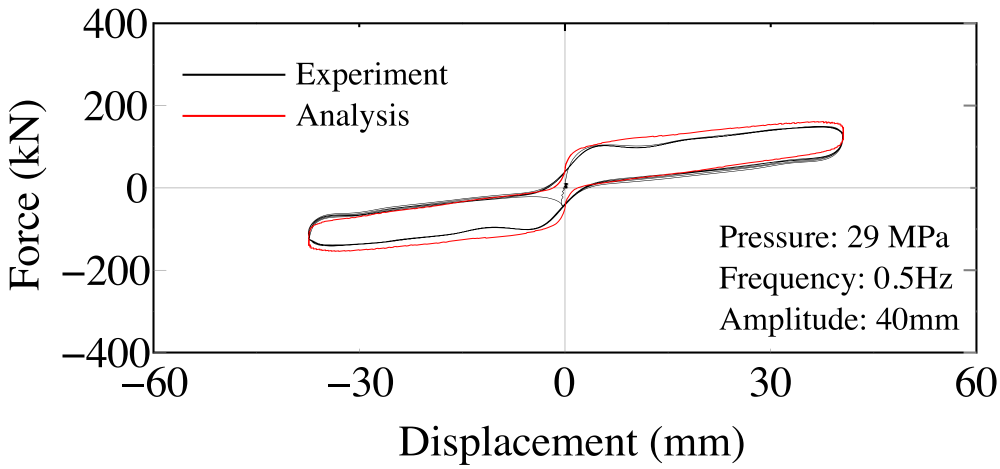

Figure 3-9 Recorded Force-Displacement Loops of Device at Initial Pressure of 29MPa

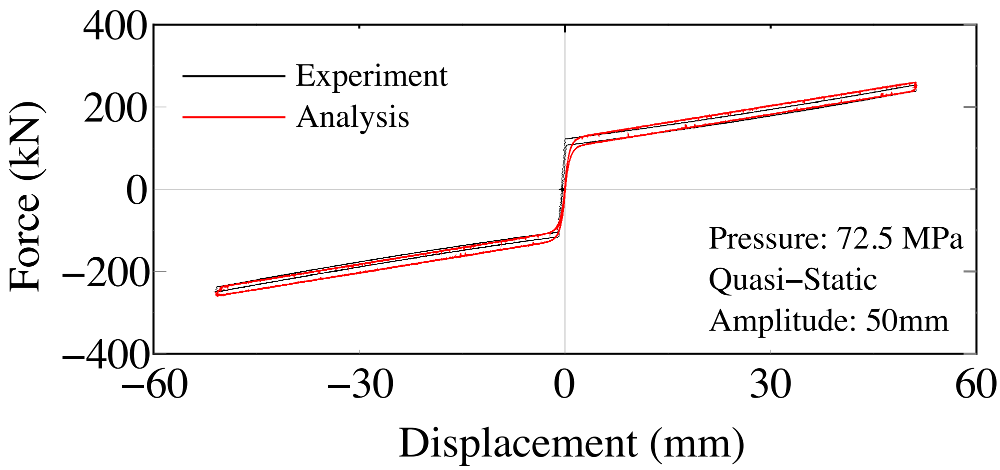

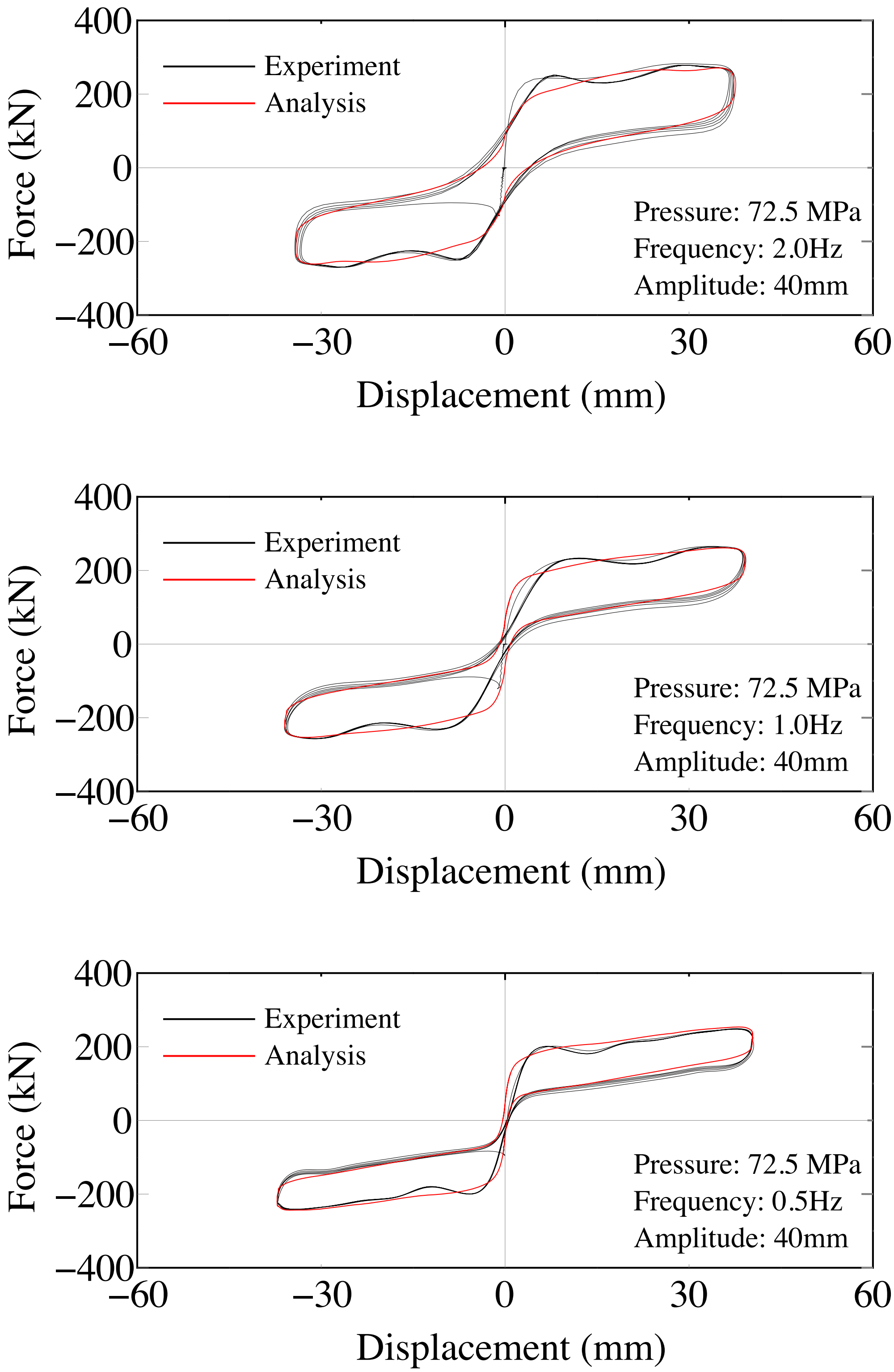

Figure 3-10 Recorded Force-Displacement Loops of Device at Initial Pressure of 72.5MPa

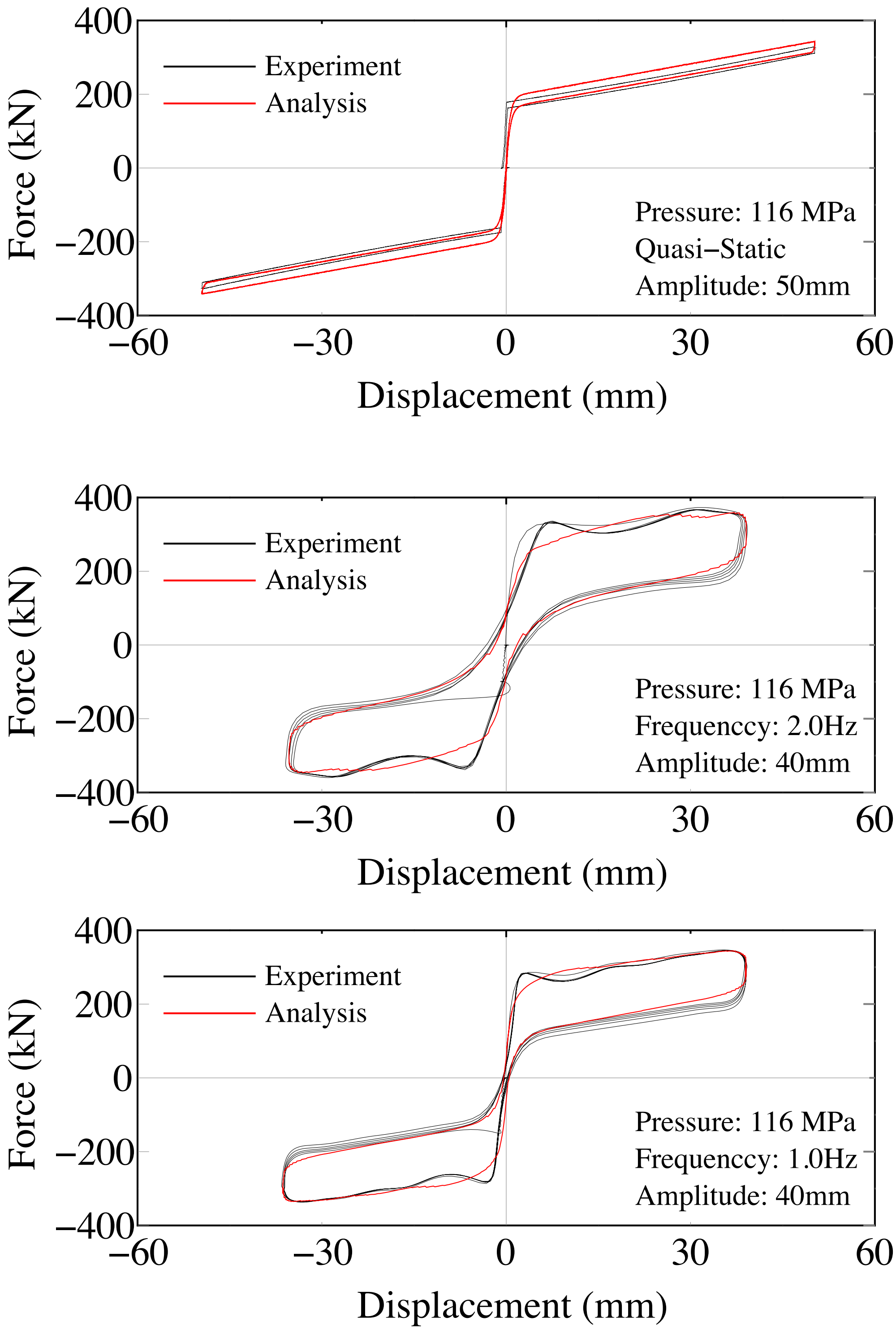
400
200
0
−200
−400
−60
−30
0
30
60
Force (kN)
Displacement (mm)
Experiment
Analysis
Pressure: 116 MPa
Quasi−Static
Amplitude: 50mm
400
200
0
−200
−400
−60
−30
0
30
60
Force (kN)
Displacement (mm)
Experiment
Analysis
Pressure: 116 MPa
Frequenccy: 2.0Hz
Amplitude: 40mm
400
200
0
−200
−400
−60
−30
0
30
60
Force (kN)
Displacement (mm)
Experiment
Analysis
Pressure: 116 MPa
Frequenccy: 1.0Hz
Amplitude: 40mm

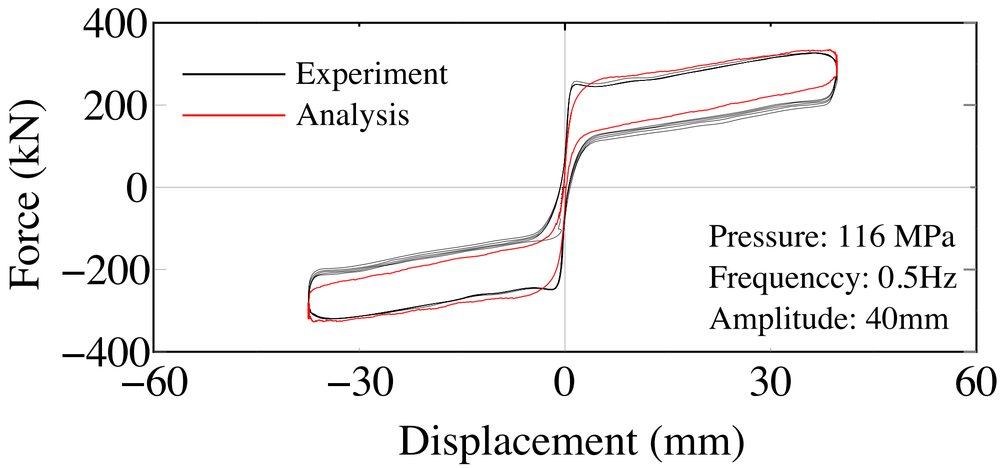

Figure 3-11 Recorded Force-Displacement Loops of Device at Initial Pressure of 116MPa

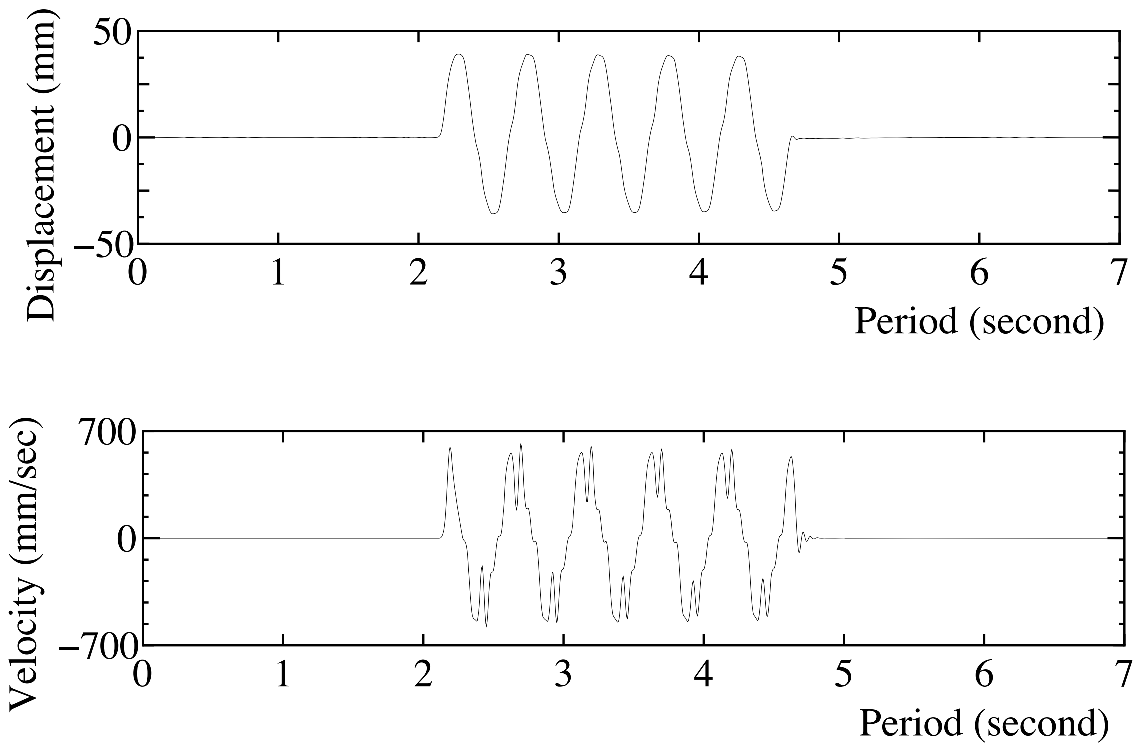

Figure 3-12 Recorded Histories of Imposed Displacement and Velocity in Test of Device at Pressure of 116MPa and Frequency of 2Hz

The analytical prediction of the force-displacement loops of the tested device in Figures 3-9 to 3-11 was based on the model of Equations 2-7 to 2-10 and using the parameters in Table 3-1. The values of parameters in this table were obtained as follows:

(1) The preload is the nominal value obtained by use of Equation (2-6) with the nominal value of pressure and a piston road area A_r=1535mm^2. Note that the nominal pressure in the table has a tolerance of ±0.7MPa. The value of preload is thus predictable within a range. For example, for the device at pressure of 29MPa, the range of values of preload is 43.4 to 45.6kN.

(2) The friction force F_{min} was assigned a value equal to 0.06 times the nominal value of the preload. The value of 0.06 is consistent with observations of behavior of devices of small and large size.

(3) The value of the stiffness K_0 was based on the test data under quasi-static conditions. The value is simply the peak force at maximum displacement minus the preload and divided by the maximum displacement (=50mm). This provides a representative effective stiffness, whereas the actual stiffness may have some nonlinear relation to the displacement. This is evident in the force-displacement loops of the device at the lowest pressure of 29MPa in Figure 3-9. The stiffness can be predicted by theory on the basis of Equations (2-3) and (2-4) but with corrections to account for the effect the cylinder deformation under the action of the fluid pressure and using a detailed representation of the bulk modulus to pressure relation. The manufacturer of the device actually predicted the value of stiffness with good accuracy but detailed calculations are proprietary and therefore not be presented in this report. Specifically, the predicted values of stiffness (based on the nominal pressure) were 1.9kN/mm, 2.6kN/mm and 3.4kN/mm. Note that the predicted values are within ±15% of the actual values determined in the experiment, which is the typical manufacturing tolerance.

(4) The damping force was based on prediction by the manufacturer of the devices (the calculations are highly empirical and proprietary). The form of the damping force followed the model of Equations (2-10) with nominal values C_1=7.32 kN (sec/mm)$^{0.4}$, C_2=5.86 kN (sec/mm)$^{0.4}$, and $\alpha_1=\alpha_2$=0.4. The manufacturing drawings indicated that the damping force is given by Equations (2-10) with a tolerance of ±10%. Accordingly, constants C_1 and C_2 are expected to be in the range of 6.6 to 8.1 kN (sec/mm)$^{0.4}$ and 5.3 to 6.5 kN (sec/mm)$^{0.4}$, respectively.

(5) Other parameters were assigned the values ζ=0, δ_0=1.78mm^{-1}, δ_{min}=0 and δ_1=0.00385sec/mm on the basis of recommendations by Tsopelas and Constantinou (1994).

Table 3-2 Parameters in Analytical Model of Large Size Fluidic Self-Centering Device

Nominal Pressure (MPa)	F_0 (*kN*)	F_{min} (*kN*)	K_0 (*kN/mm*)
29.0	44.4	2.6	2.1
72.5	111.2	6.7	2.7
116.0	177.9	10.7	3.0

The analytically determined force-displacements loops of the device in Figures 3-9 to 3-11 are in good agreement with the experimental loops. Given that the analytical prediction was based on theory and experience without actual use of the test results (apart for the values of stiffness K_0), the model used may be declared validated. Note that the use of theory and experience can predict the values of peak forces within a typical range of ±15% of the peak forces predicted by use of the nominal values of the model properties. Within the context of bounding analysis, analyses need to be performed with upper and lower bound values of properties in the model to obtain bounds on the response of the analyzed structural system. This would require application of factors of 1.15 and 0.85 (per ASCE 7-2016 terminology-see McVitty and Constantinou, 2015- these will be the λ_{test} values) on the values of preload F_0, stiffness K_0, and coefficients C_1 and C_2. Other parameters may be assigned the values used in the model in this report (see item 5 above) and a value of F_{min}=0.06 F_0.

SECTION 4

SEISMIC RESPONSE OF SINGLE-DEGREE-OF-FREEDOM SYSTEM WITH FLUIDIC SELF-CENTERING DEVICES

4.1 Introduction

A number of studies investigated and compared the behavior of structural systems having bilinear hysteretic behavior and flag-shaped hysteretic behavior by analyzing single-degree-of-freedom representations (Christopoulos et al., 2002a, 2003; Christopoulos 2004; Kam et al, 2010; Karavasilis and Seo, 2011; Eatherton and Hajjar, 2011). The studies utilized generic representations of conventional structural systems and self-centering systems in which the conventional structural system behavior was modelled as bilinear hysteretic (perfect or deteriorating) and the self-centering system was modelled as bilinear elastic with added energy dissipation capability in hysteretic or viscous forms. Also, the studies utilized different ground motion suites, with some studies only considering far-field motions and others considering both far-field and near-fault motions. Invariably, these studies demonstrated that self-centering systems reduce or eliminate residual deformations. Some studies also showed that the self-centering systems generate higher peak acceleration response (or peak shear force) than that of comparable elasto-plastic systems and that they result in residual deformations that are not sensitive to decreasing values of post-yielding stiffness.

The study reported in this section of the report follows the paradigm of these studies but concentrates on the behavior of inelastic structural systems with *added* fluidic self-centering having the behavior described in Section 3 of this report. That is, the fluidic self-centering devices are viewed as devices similar to *damping devices* that are added to a structural system that has by itself resistance to lateral loads. Furthermore, it considers viscous damping behavior not previously contemplated as possible but readily deliverable with fluidic devices such as asymmetric force (e.g., more on loading than on unloading) and with linear and nonlinear dependency on the velocity of motion. Moreover, the study (a) considers seismic motions with far-field and near-fault characteristics, (b) distinguishes between motions with pulse-like and non-pulse-like characteristics based on contemporary classifications (Baker, 2007), (c) distinguishes between design level and maximum earthquake level, and (d) selects and scales motions on the basis of the currently applicable ASCE 7-2010 standard.

Results are presented with the particular intention of (a) identifying values of preload as a fraction of the structural system's strength exclusive of the self-centering devices that result in acceptably low residual deformations, (b) observing the effect of the form of viscous damping (linear, nonlinear and asymmetric) on the response, and (c) comparing the ductility demand, peak displacement, residual displacement and peak acceleration of systems with and without fluidic self-centering devices.

4.2 Selection and Scaling of Earthquake Ground Motions

Analysis of generic single-degree-of-freedom systems with fluidic self-centering devices was conducted with seismic motions selected from historic events and scaled to represent in an average sense particular response spectra at the design and the maximum earthquake levels. A Risk-Targeted Maximum Considered Earthquake (MCE_R) response spectrum was constructed per ASCE 7, 2010 for a location in California (latitude 37.8814°N, longitude 122.08°W) with characteristic values of S_{MS}=1.875g and S_{M1}= 0.9g. The Design level response spectrum (DE) has characteristic values equal to 2/3 of those of the MCE_R, so S_{DS}=1.25g and S_{D1}= 0.6g. The spectra of the two levels of earthquake are shown in Figure 4-1.

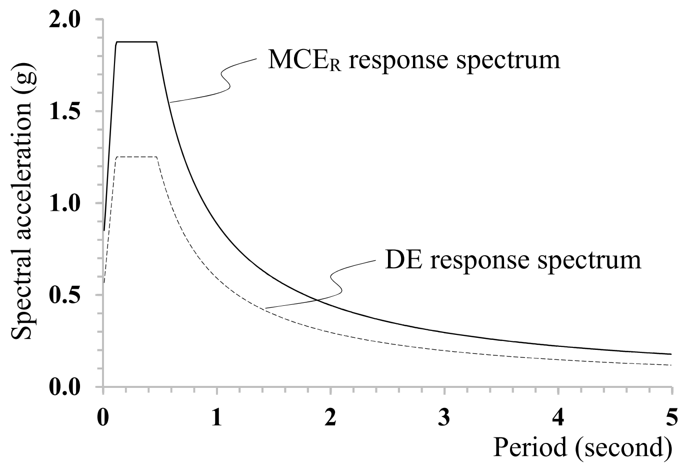

Figure 4-1 MCE_R and DE Response Spectra (5-% damped) Considered in Study

Sets of motions representative of the MCE_R spectrum and with near-fault pulse-like, near-fault non-pulse-like or far-field ground characteristics were used in the study. The distinction between pulse-like and non-pulse-like motions was necessitated by the recognition that substantially larger displacement demands occur in the case of pulse-like motions than in the case of non-pulse-like motions when systems with large effective period are considered (Pant et al., 2013). The selection of the near-fault ground motions was based on the procedure described in Pant et al. (2013), which was based on the classification of Baker (2007). The selection of far-field ground motions was based on FEMA (2009). The ground motions selected and some of their characteristics are presented in Tables 4-1 to 4-3 for the near-fault pulse-like motions, the near-fault non-pulse-like motions and the far-field motions, respectively. Note that each selected ground motion was rotated along the fault-normal and fault-parallel directions and that only the fault normal components were used in the analysis (the fault-parallel components are typically less intense and disregarded in this study). Each of the three ensembles of motions consisted of seven components.

The selected ground motions were spectrally matched to the MCE_R response spectrum using procedures described in Hancock *et al*. (2006). The average of the scaled motions is compared to the target MCE_R spectrum in Figures 4-2 to 4-4 for near-fault pulse-like, near-fault non-pulse-like and far-field ground motions, respectively. Histories of the scaled ground motions are shown in Figure 4-5 for the near-fault pulse-like and non-pulse-like cases and Figure 4-6 for the far-field ground motions. Note that each of the scaled motions was lengthened with 15 seconds of zeroes to allow for the calculation of the free vibration response and any residual deformation.

Table 4-1 Near-Fault Pulse-Like Ground Motions (Fault Normal Components)

No.	Event	Year	Station	Magnitude	Site class	PGA [g]	PGV [cm/s]
1	Imperial Valley	1979	El Centro Array #7	6.5	D	0.46	108.8
2	Loma Prieta	1989	LGPC	6.9	C	0.94	96.8
3	Loma Prieta	1989	Saratoga, W. Valley Coll.	6.9	C	0.40	71.2
4	Northridge	1994	Jensen Filter Plant	6.7	C	0.52	67.6
5	Northridge	1994	Sylmar, Converter Sta. East	6.7	C	0.84	116.2
6	Kobe, Japan	1995	Takarazuka	6.9	D	0.65	72.7
7	Duzce, Turkey	1999	Bolu	7.1	D	0.78	55.0

Table 4-2 Near-Fault Non-Pulse-Like Ground Motions (Fault Normal Components)

No.	Event	Year	Station	Magnitude	Site class	PGA [g]	PGV [cm/s]
1	Gazli, USSR	1976	Karakyr	6.8	C	0.60	64.9
2	Imperial Valley	1979	Bonds Corner	6.5	D	0.76	44.2
3	Northridge	1994	LA-Sepulveda VA Hospital	6.7	C	0.73	63.2
4	Northridge	1994	Pacoima Kagel Canyo	6.7	C	0.53	56.0
5	Kobe, Japan	1995	Nishi-Akashi	6.9	C	0.48	33.7
6	Chi-Chi, Taiwan	1999	TCU067	7.6	C	0.56	91.7
7	Hector Mine	1999	Hector	7.1	C	0.34	37.0

Table 4-3 Far-Field Ground Motions (Fault Normal Components)

No.	Event	Year	Station	Magnitude	Site class	PGA [g]	PGV [cm/s]
1	Superstition Hills	1987	El Centro Imp. Co.	6.5	D	0.36	46.0
2	Loma Prieta	1989	Capitola	6.9	D	0.53	35.0
3	Kobe, Japan	1995	Shin-Osaka	6.9	D	0.24	38
4	Kocaeli, Turkey	1999	Duzce	7.5	D	0.36	59
5	Kocaeli, Turkey	1999	Arcelik	7.5	C	0.22	40
6	Friuli, Italy	1976	Tolmezzo	6.5	C	0.35	31
7	Northridge	1994	Canyon Country – WLC	6.7	D	0.48	45.0

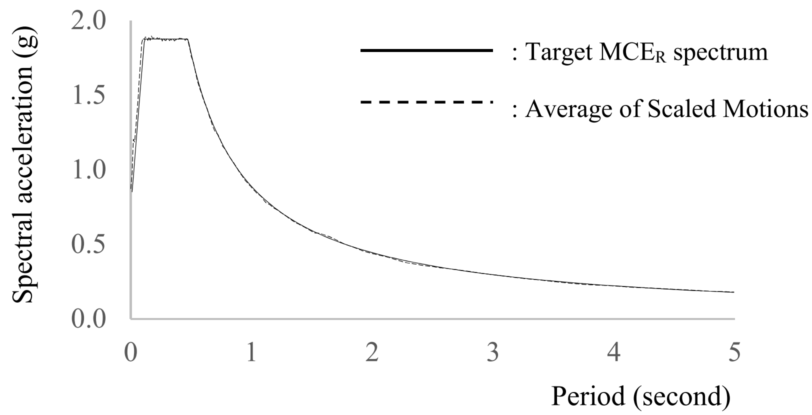

Figure 4-2 Comparison of Response Spectra of Scaled Near-Fault Pulse-Like Motions and Target Spectrum

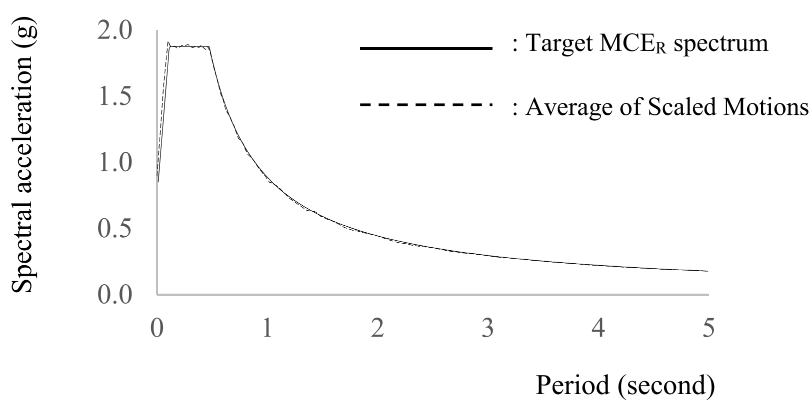

Figure 4-3 Comparison of Response Spectra of Scaled Near-Fault Non-Pulse-Like Motions and Target Spectrum

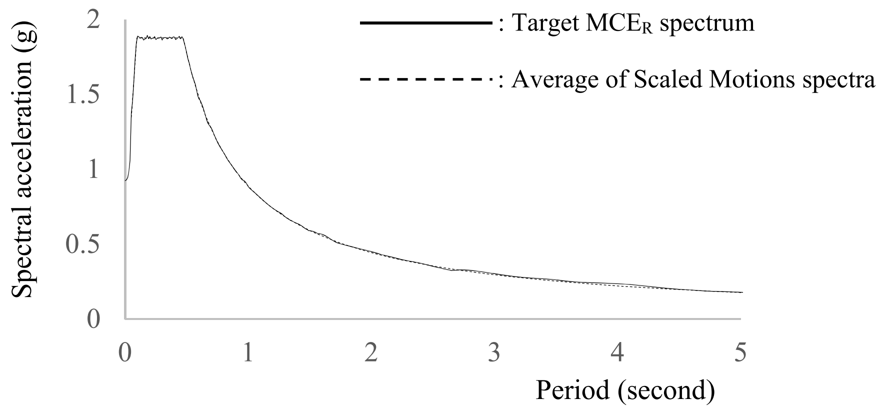

Figure 4-4 Comparison of Response Spectra of Scaled Far-Field Motions and Target Spectrum

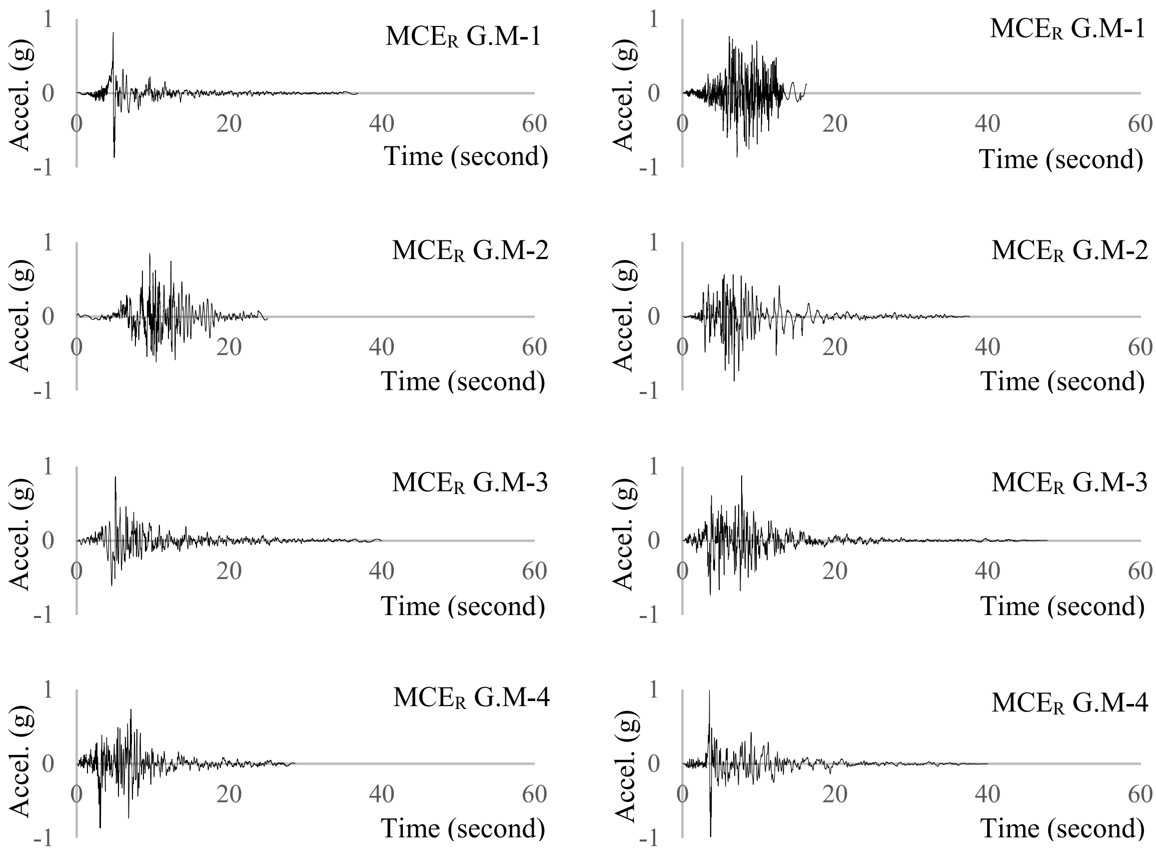

Figure 4-5 Histories of Acceleration of Scaled Near-Fault Motions

(Left Column: Pulse-Like, Right Column: Non-Pulse-Like)

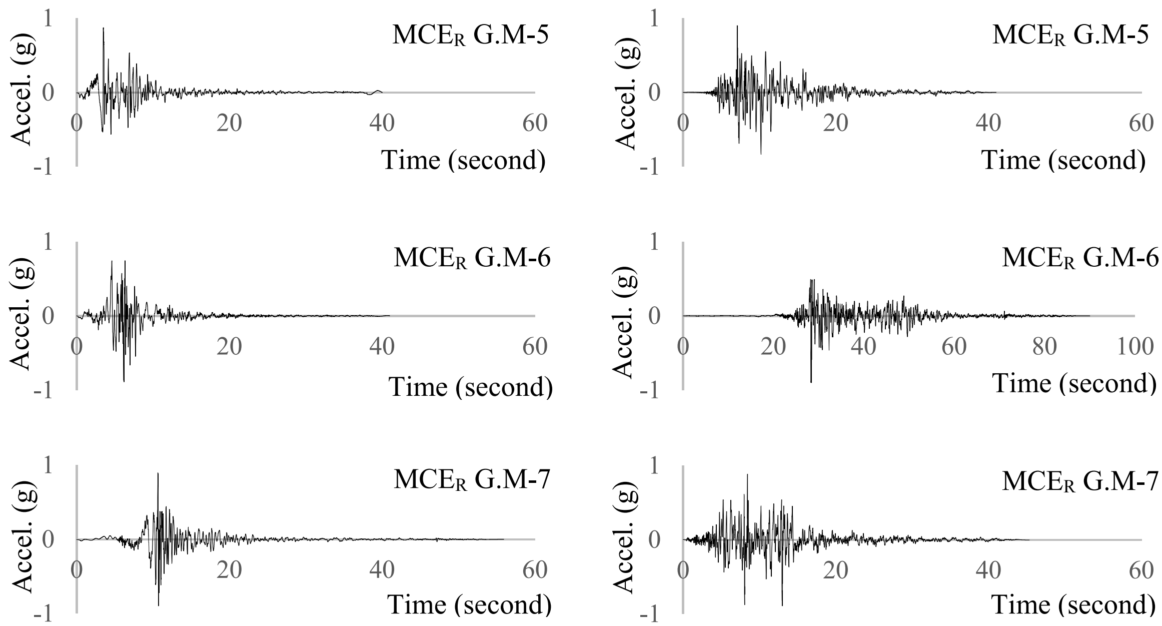

Figure 4-5 (Continued)

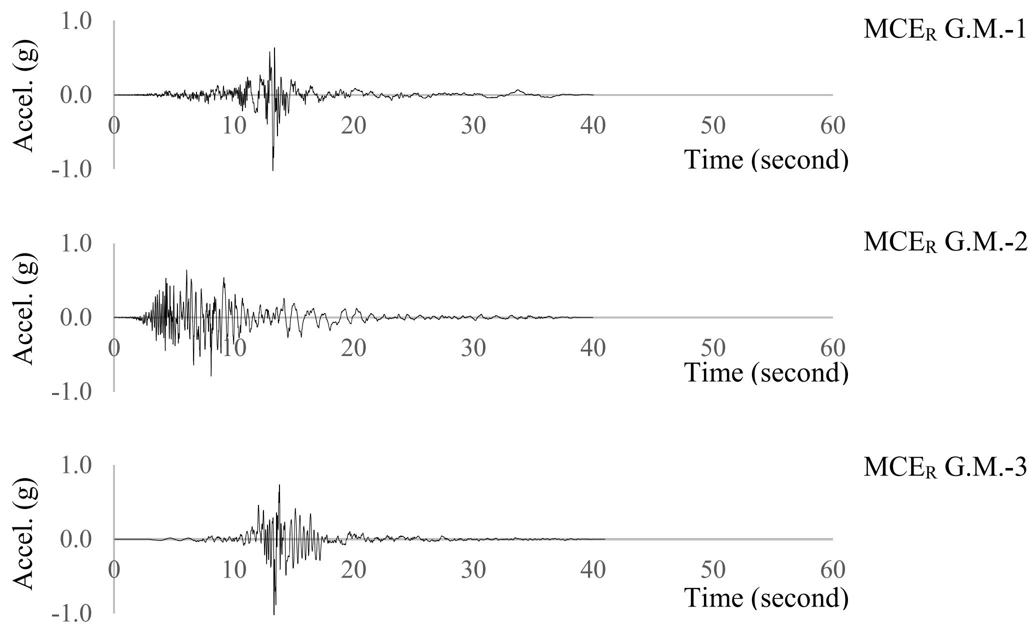

Figure 4-6 Histories of Acceleration of Scaled Far-Field Motions

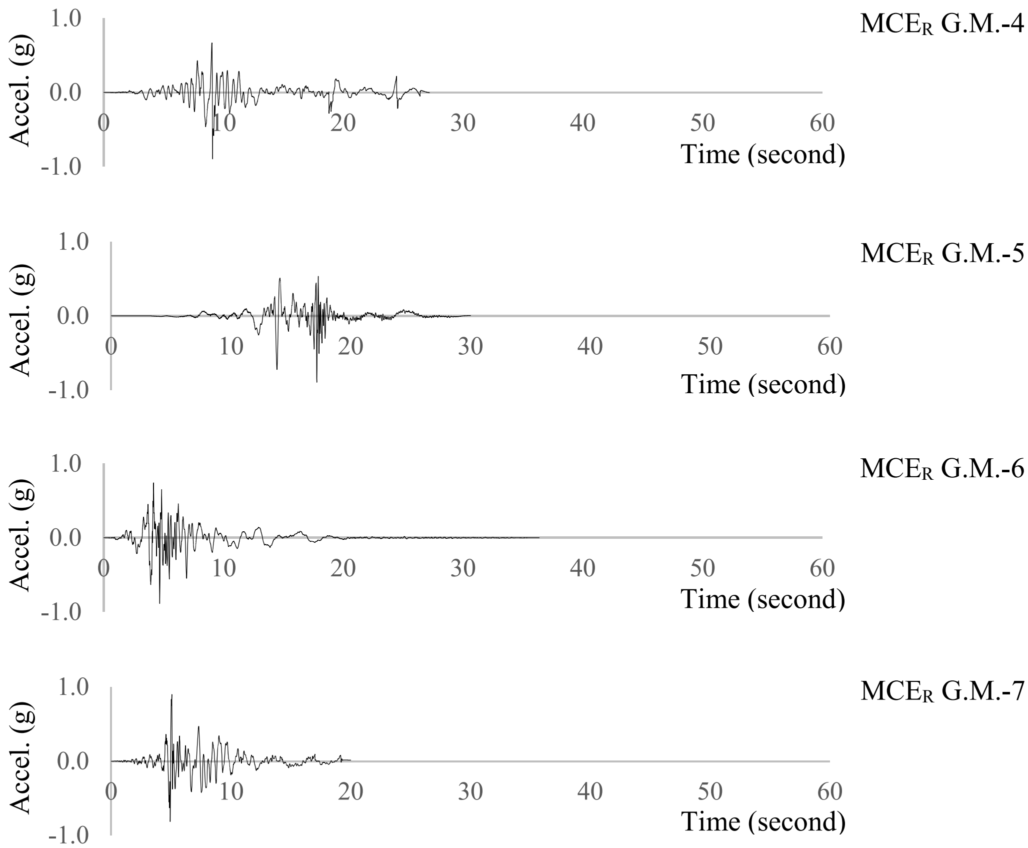

Figure 4-6 (Continued)

4.3 Analyzed Single-Degree-of-Freedom Systems

The analyzed system consisted of a SDOF system with smooth bilinear hysteretic behavior representing the primary structural system and with added fluidic self-centering devices. The selection of parameters of the primary structural system followed the paradigm of Ramirez et al (2001) in the study of damping systems. Figure 4-7 shows the lateral force-displacement relation of the primary system. The system is represented as a SDOF system with mass m, elastic stiffness K_e, base shear (yield) strength F_y, yield displacement D_y, and inherent damping ratio β_I. The post-elastic stiffness is expressed as a fraction of the elastic stiffness and given by αK_e.

When fluidic self-centering devices are added to the primary structural system, the force-displacement relation is shown in Figure 4-8. The basic parameters of the fluidic self-centering devices are the preload F_0, the stiffness K_0, the friction force F_{min} and the damping force, which will be described in more detail later in this section.

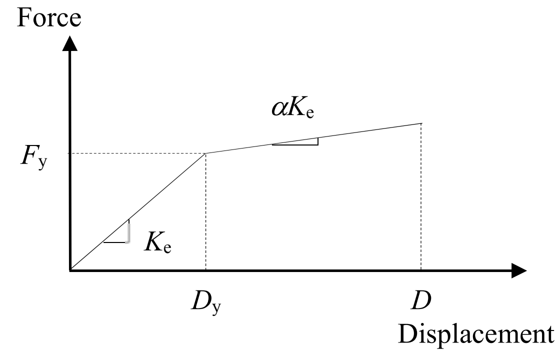

Figure 4-7 Force-displacement Relation of Primary Structural System

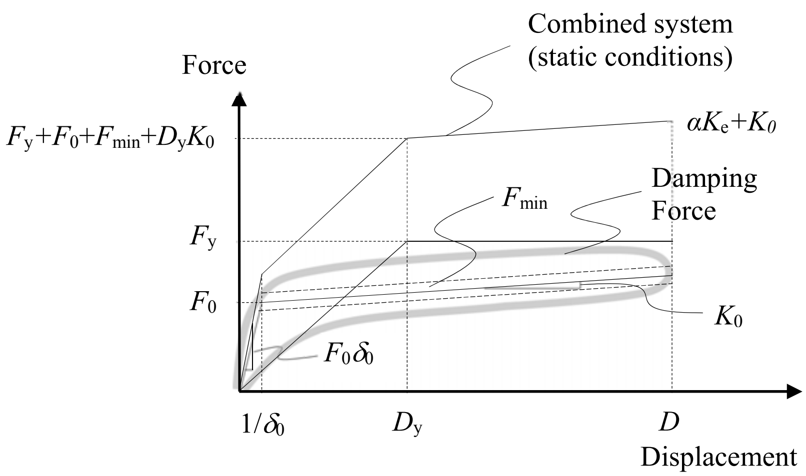

Figure 4-8 Force-displacement Relation of System with Added Fluidic Self-centering Device

The equation of motion of a single-degree-of-freedom system with these characteristics may be written as follows:

$$m\ddot{u}(t) + F_{PS}(t) + C_{effi}\dot{u}(t) + F_{FSC}(t) = -ma_g(t) \tag{4-1}$$

where m is the mass, $\dot{u}$ is the relative velocity, $\ddot{u}$ is the relative acceleration, a_g is the ground acceleration, C_{effi} is the inherent damping constant to produce a damping ratio β_i, F_{FSC} is the force from the fluidic self-centering device, and F_{PS} is the force from inelastic bilinear hysteretic primary structural system. Importance in this equation is the description of inherent damping, which is described as linear viscous with damping ratio equal to β_i. This ratio is defined with respect to the effective (or secant) stiffness K_{eff} of the primary system (equal to the peak force in the primary system divided by the peak displacement). The use of the inherent damping ratio defined in this way is important in avoiding amplification of the inherent damping as the system undergoes inelastic action (Tsopelas *et al*., 1997, Ramirez *et al*., 2001). The inherent damping ratio β_i is constant regardless of the amplitude of motion and set in the analysis equal to 0.05. This requires iterative analysis (e.g., Tsopelas *et al*., 1997) or some simplification as implemented in this report and described below.

The behavior of the primary structural system is described by the following parameters:

(a) Elastic period, T_e:

$$T_e = 2\pi \left(\frac{D_y}{A_y} \right)^{1/2} \tag{4-2}$$

where A_y represents the acceleration at yield of the primary system ($=F_y/m$).

(b) Post-yielding to elastic stiffness ratio: α

(c) Ductility-based portion of the R-factor

$$R_\mu = \frac{S_{ae}(T_e, \beta_i)}{A_y} \tag{4-3}$$

where $S_{ae}(T_e, \beta_i)$ is the spectral acceleration in the Design Earthquake (DE) at period T_e and damping ratio β_i=0.05 (elastic conditions).

R_μ and T_e are taken as variable parameters. 1, 2, 3, 4 and 5 are used for R_μ and 0.3, 0.5, 0.7, 1.0, 1.5, 2.0 and 3.0 are used for T_e.

To avoid iterative analysis in the calculation of the inherent damping constant, the assumption is made that the effective period $T_{eff} = T_e\sqrt{\mu} = T_e\sqrt{R_\mu}$ where $\mu = D / D_y$ (ductility ratio) and that the ductility ratio is equal to the ductility-based portion of the R-factor. This is consistent with observations in the analysis of a large number of systems in Ramirez *et al*. (2001) provided that the structural system is flexible enough (T_e larger than about 0.3sec). This assumption is important in the simplified method of analysis (Equivalent Lateral Force procedure) of ASCE 7, 2010 for structures with damping systems. This leads to:

$$C_{\mathrm{effi}} = \frac{4\pi m \beta_{\mathrm{i}}}{T_{\mathrm{e}}\sqrt{R_{\mu}}} \tag{4-4}$$

The behavior of the fluidic self-centering device added to the primary structural system is described by the following parameters:

(d) Ratio of preload to strength of the primary structural system: $\dfrac{F_0}{F_{\mathrm{y}}}$

(e) Ratio of device friction force to preload: $\dfrac{F_{\min}}{F_0}$

(f) Stiffness after overcoming the preload: K_0

The stiffness is assumed zero as this appears to be the most desirable value for resulting in the least acceleration. The implications of this assumption are assessed by considering realistic values of stiffness in selected analyses.

(g) Damping force, considered to have one of four different types: linear-viscous damping, non-linear-viscous damping, upper-half viscous damping and lower-half viscous damping. The four types are illustrated in Figure 4-9. In general, the damping force will be described by parameters β_{v} and α that are discussed below.

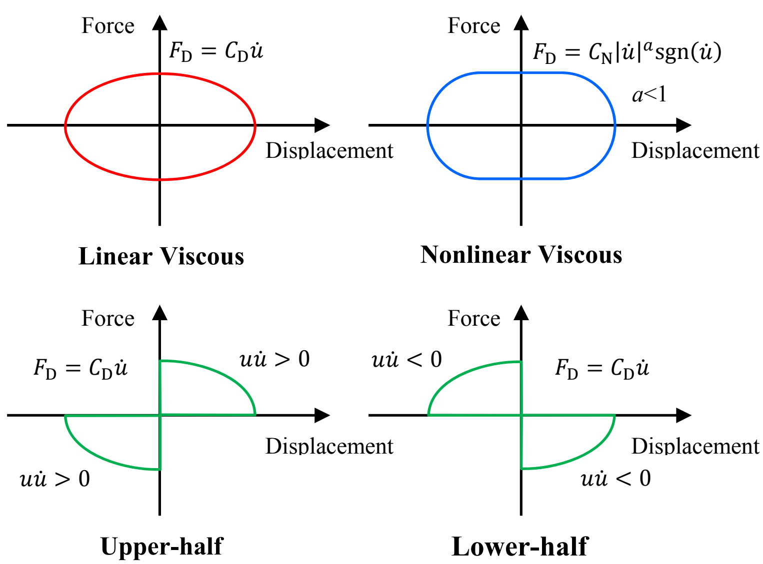

Figure 4-9 Forms of Viscous Damping Force Considered

Note that the upper half viscous damping force is an idealization of actual behavior where the damping force is less when the device piston rod moves towards the neutral position than when it moves away from the neutral position (see Section 3 for test data). This behavior is desirable in high speed shock isolation applications where the piston rod needs to quickly return to the neutral position. Moreover, this form of damping may result in further reduction of the residual deformation by comparison to either linear or nonlinear viscous damping. In three of the four cases (linear, upper half and lower half), the damping force is described by:

$$F_{\mathrm{D}} = C_{\mathrm{D}}\dot{u} \tag{4-5}$$

in which the damping constant is related to a damping ratio β_{v} under elastic conditions (note that the damping ratio is defined for the primary structural system under elastic conditions) by:

$$C_{\mathrm{D}} = \frac{4\pi m\beta_{\mathrm{v}}}{T_{\mathrm{e}}} \tag{4-6}$$

It should be noted that for a given value of the damping ratio β_{v}, constant C_{D} is the same for the three cases of damping type. The distinction between the three cases has been illustrated in Figure 4-9. In the fourth case, the damping force is described as nonlinear viscous (Ramirez *et al.*, 2001):

$$F_{\mathrm{D}} = C_{\mathrm{N}}\left|\dot{u}\right|^{a}\operatorname{sgn}\left(\dot{u}\right) \tag{4-7}$$

Parameter C_{N} is again related to an effective damping ratio β_{v} defined for the primary system under elastic conditions (see Ramirez *et al.*, 2001):

$$C_{\mathrm{N}} = \frac{2\pi m\beta_{\mathrm{v}}\omega_{\mathrm{n}}\left(\omega_{\mathrm{n}}D\right)^{1-a}}{\lambda} \tag{4-8}$$

$$\lambda = 4\cdot 2^{a}\,\frac{\Gamma^{2}\left(1+a/2\right)}{\Gamma\left(2+a\right)} \tag{4-9}$$

Note that D is the maximum displacement of the primary system (exclusive of the self-centering system) in the Design Earthquake at period T_{e} and damping ratio $\beta_{\mathrm{i}}+\beta_{\mathrm{v}}$. That is,

$$D = S_{\mathrm{ae}}(T_{\mathrm{e}},\beta_{\mathrm{i}})T_{\mathrm{e}}^{2}/(4\pi^{2}B) \tag{4-10}$$

in which B is a parameter to account for the effect of damping $\beta_{\mathrm{i}}+\beta_{\mathrm{v}}$ that is different than 5% of critical on the maximum displacement. Parameter B is given in Table 18.6-1 of ASCE 7-2010. Also, Γ(-) is the gamma function.

For dynamic analysis, the force of the fluidic self-centering device is described by Equations (2-7) to (2-9) and using the following values of parameters: F_{min}/F_0=0.05, δ_0=2mm^{-1}, δ_{min} =0, δ_1 =0.004 sec/mm, ζ=0, Y=0.25mm, A=1, β=0.1, γ=0.9 and η=2. Note that the values of these parameters are those used in modeling the behavior of tested devices per Sections 2 and 3 (or closely rounded values). Also, for the case of nonlinear viscous damping only the case of exponent a=0.5 was considered. Analysis was conducted with a range of values of the other parameters as presented in Table 4-4. A total of 6,300 different systems were considered (5 values of R_μ, 7 values of period, 5 values of damping ratio, 9 values of ratio of preload to strength and 4 different cases of viscous damping force). However, not all cases were analyzed when it became evident that high values of the preload to strength ratio were undesirable so that for some cases the value of this ratio was limited to 0.25. Also, in many cases the values of parameter R_μ were limited to 1, 2 and 5 as it become evident that higher resolution was not necessary to observe trends in the key response quantities considered. For each case, 42 response history analyses were conducted using the 3 groups of scaled motions described in Section 4.2, for the Design Earthquake and again for the Maximum Earthquake. A total of over 200,000 analyses were conducted.

Table 4-4 Values of Parameters of Primary Structural System and Fluidic Self-Centering Device

R_μ	T_e (sec)	β_v	F_0/F_y
1	0.3	0.00	0.00
2	0.5	0.05	0.05
3	0.7	0.10	0.10
4	1.0	0.15	0.15
5	1.5	0.20	0.20
	2.0		0.25
	3.0		0.50
			0.75
			1.00

Post-elastic to elastic stiffness ratio (primary structural system) α=0.05
Nonlinear damping exponent a=0.5
ζ=0, β_i=0.05, F_{min}/F_0=0.05, δ_0=2mm^{-1}, δ_{min} =0, δ_1 =0.004 sec/mm,
Y=0.25mm, A=1, β=0.1, γ=0.9, η=2
K_0=0 unless otherwise noted

4.4 Results on Peak Response of Primary Structural System

Results are presented in terms of the average of the peak response quantities obtained in the 7 analyses in each group of scaled motions:

1) Absolute acceleration A_{max}.
2) Displacement or drift D_{max}.
3) Residual displacement D_{Res}.
4) Ductility ratio μ_f, defined as follows and calculated using the value of D_{max}:

$$\mu_{\mathrm{f}} = \frac{D_{\max}}{D_y} = \frac{4\pi^2 D_{\max} R_{\mu}}{T_{\mathrm{e}}^2 S_{\mathrm{ae}}(T_{\mathrm{e}}, \beta_{\mathrm{i}})} \tag{4-11}$$

5) Floor response spectra.

4.4.1 Structural System without Fluidic Self-Centering Devices

A total of 1,470 non-linear response history analyses were conducted for the structure exclusive of any self-centering system and without any viscous damping force (other than inherent damping) for 5 values of R_{μ}, 7 values of elastic period T_{e}, 21 ground motions and 2 types of earthquake level (DE and MCE). Figures 4-10 to 4-12 present the peak calculated response for the three cases of near-fault pulse-like, near-fault non-pulse-like and far-field motions, respectively. For each figure, the graphs on the left are for the DE level and the graphs on the right are for the MCE level.

The results in Figures 4-10 to 4-12 represent the benchmark by which the results of the system with the fluidic self-centering devices will be compared. The results also demonstrate the significance of motions with pulse-like characteristics as they result in larger maximum displacements and larger residual displacements that when non-pulse-like and far-field motions are considered. This is particularly pronounced for systems with period larger than about 2sec. The importance of considering the Maximum Earthquake is also evident in the results of these figures. Note that the design is based on the Design Earthquake (values of parameter R_{μ} are based on the DE spectrum).

Most important observations in the results that for the MCE the response in terms of ductility demand is excessive for some systems. Also, the residual displacement is very large as it is about half of the maximum displacement for the pulse-like motions but only about a fifth of the maximum displacement for the non-pulse-like and far-field motions.

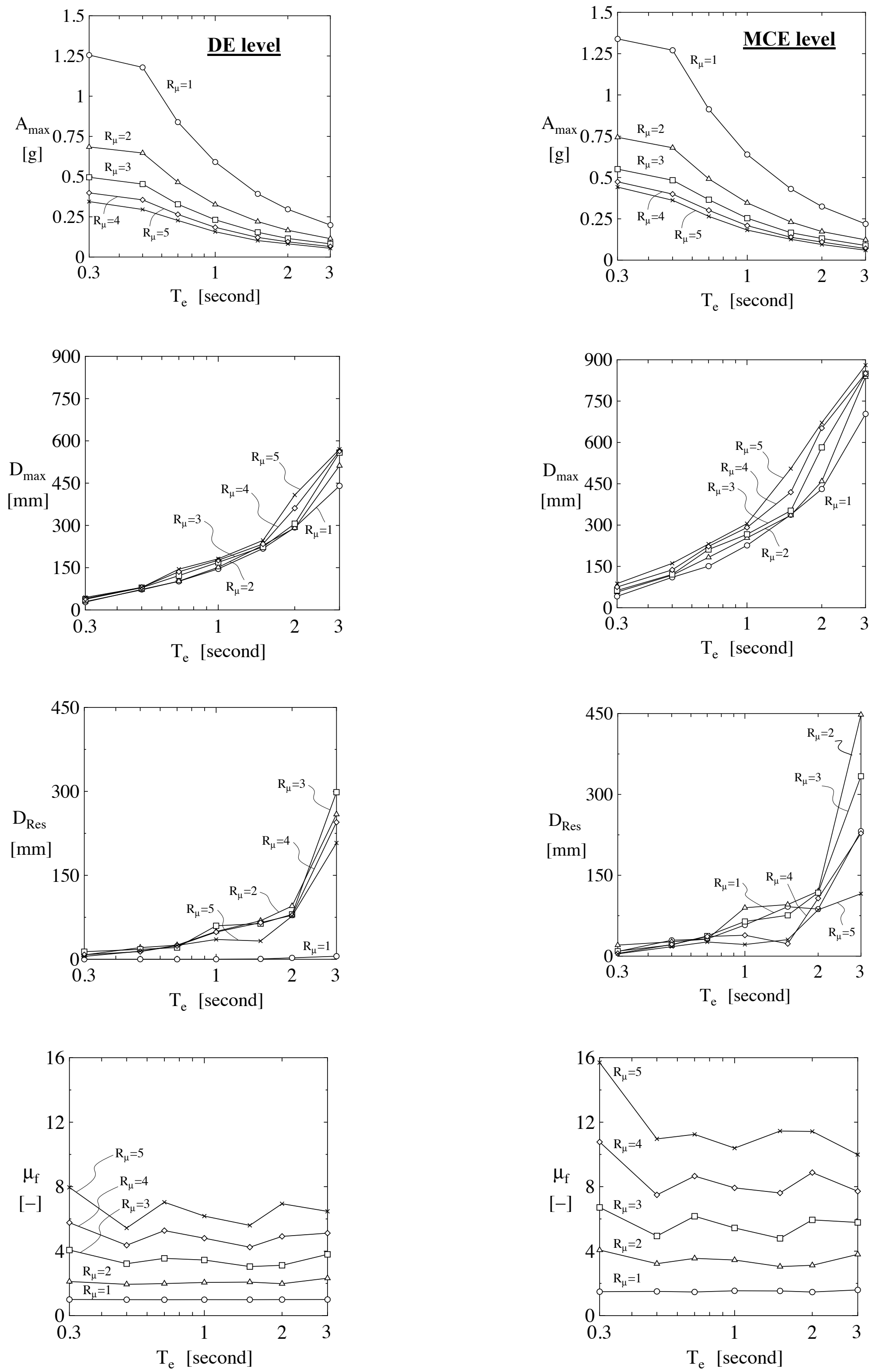

Figure 4-10 Peak Response of System without Self-Centering Devices for Near-Fault Pulse-Like Motions

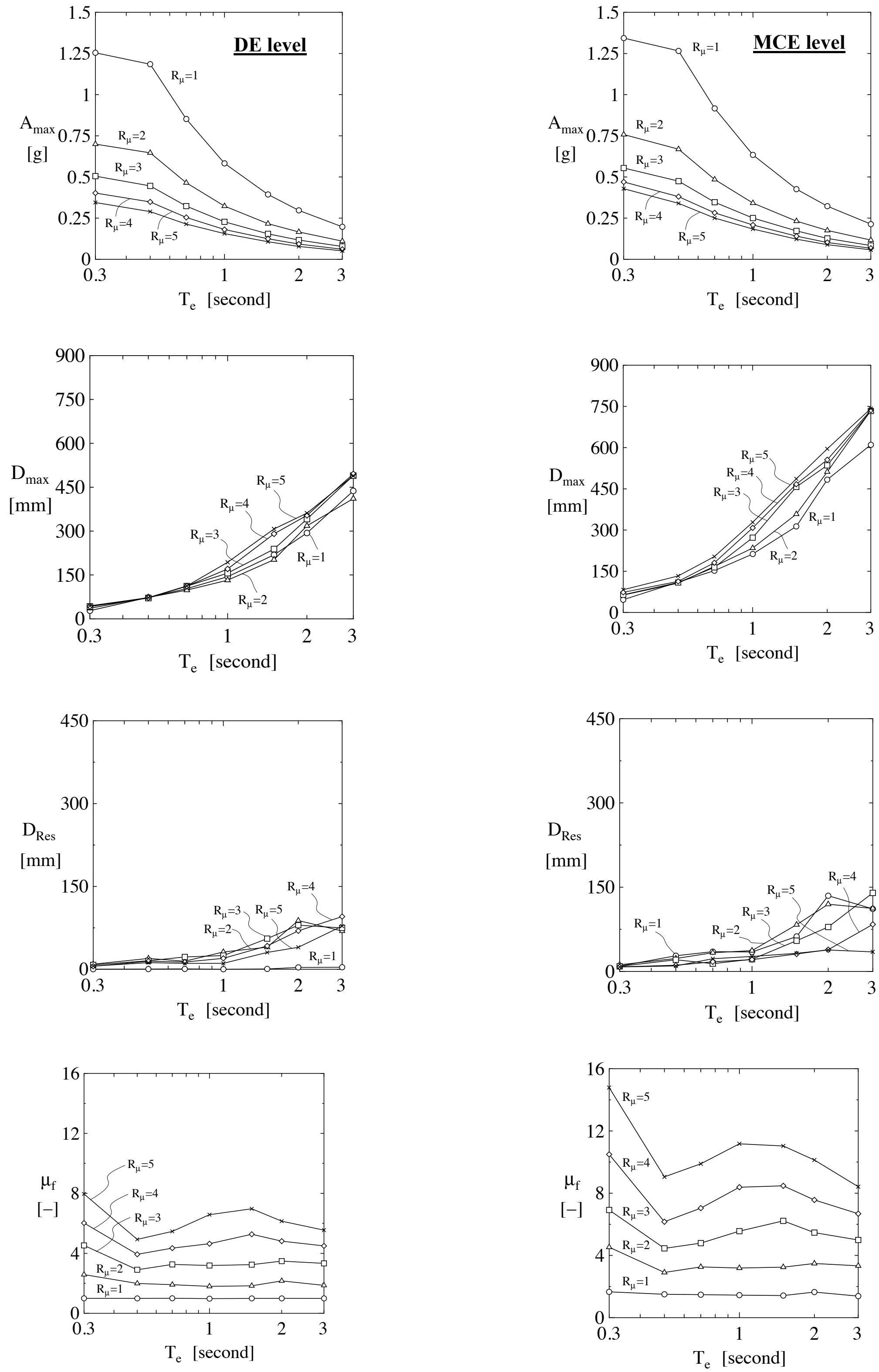

Figure 4-11 Peak Response of System without Self-Centering Devices for Near-Fault Non-Pulse-Like Motions

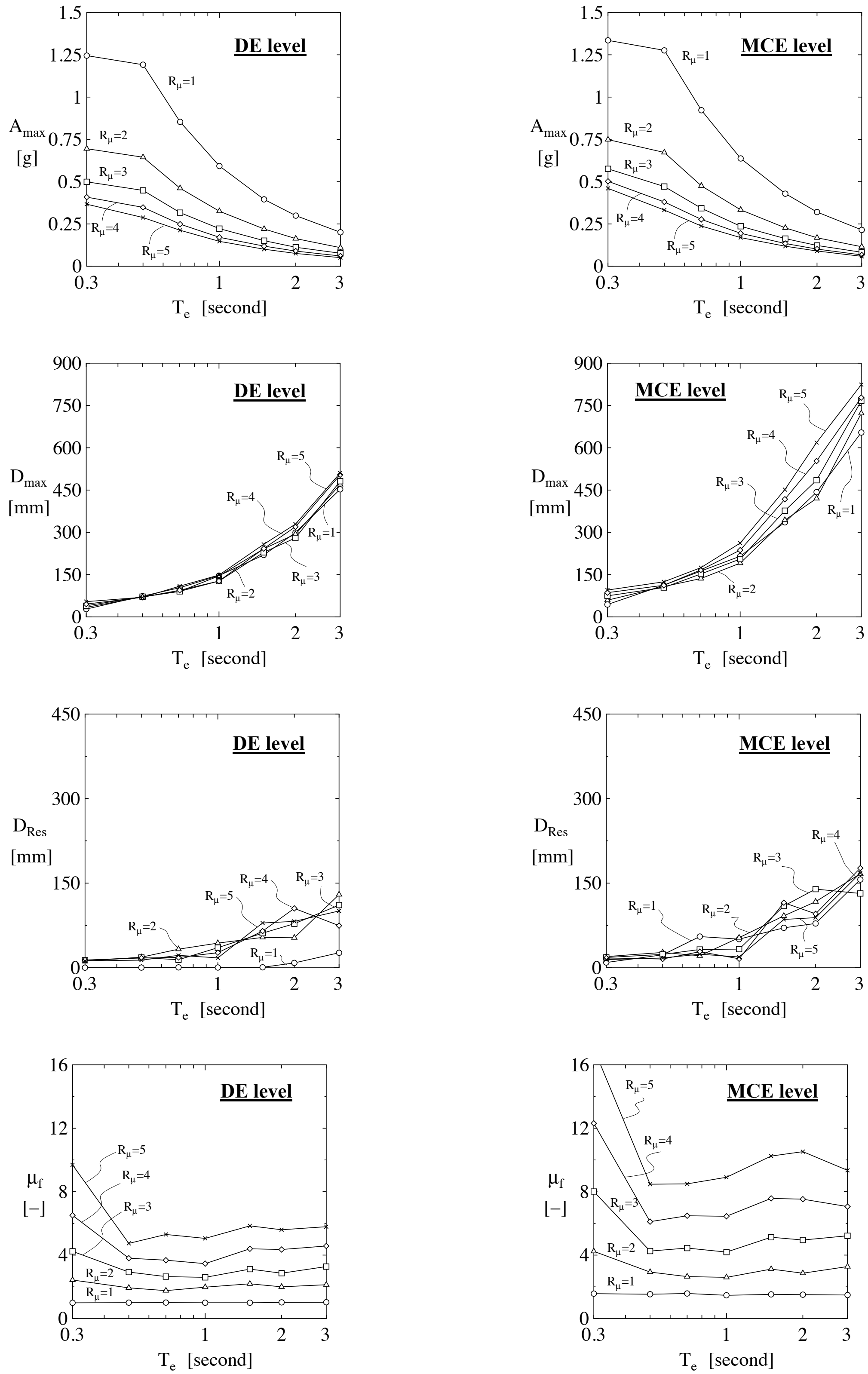

Figure 4-12 Peak Response of System without Self-Centering Devices for Far-Field Motions

4.4.2 Structural System with Fluidic Self-Centering Devices

More than 200,000 non-linear response history analyses were conducted for values of R_μ equal to 1, 2 and 5, other parameters as in Table 4-4 and DE and MCE earthquake levels. Results for all analyzed cases are presented in Appendix A. Selected results are presented in this section by concentrating on the following cases: (a) near-fault pulse-like motions that resulted in the largest displacements and residual displacements, (b) linear viscous damping with β_v=0.10 and (c) preload to strength ratio F_0/F_y=0.20. This combination of parameters resulted in sufficiently low residual displacements. Results are also shown that demonstrate that the form of damping does not have a significant effect (but for some special cases), that higher damping results in improved performance, and that larger values of preload result in less residual displacement but larger acceleration. Also, results are compared for the case where the stiffness of the fluidic self-centering system is considered to have realistic values to the case where the stiffness is assumed to be zero.

Figure 4-13 compares the peak response of the analyzed system with and without the fluidic self-centering system for the case of near-fault pulse-like motions, linear viscous damping with β_v=0.10 and preload to strength ratio F_0/F_y=0.20. It is evident that the addition of the fluidic self-centering device results in (a) reduction of the maximum displacement, and proportionally the ductility demand, (b) reduction in the residual displacement so that is essentially trivial for the DE level (but for the case of R_μ=2 and elastic period larger than 2sec) and (c) some small increase in acceleration when R_μ>1. To further illustrate the effect of the added fluidic self-centering device, Figure 4-14 compares the calculated maximum and residual displacements for the three cases of motion (pulse-like, non-pulse-like and far-field) for the MCE level and for two cases of R_μ=2 and 5. It may be seen that the type of motion affects the maximum displacement and the residual displacement especially for flexible structures. The effect of pulse-like near-fault motions on the displacement demand in flexible systems was known (e.g., Pant et al., 2013) but the effect on residual displacement is newly observed. Note that one would intuitively expect more residual displacement for the case of R_μ=5 than the case of R_μ=2 but this is not always true.

The effect of the form of damping and its value is illustrated in Figure 4-15 where the response of the system with F_0/F_y=0.2 and R_μ=2 is compared for three types of damping (linear, nonlinear and upper linear) and two values of damping ratio (β_v=0.1 and 0.2) in the case of the pulse-like, near fault motions at the MCE level.

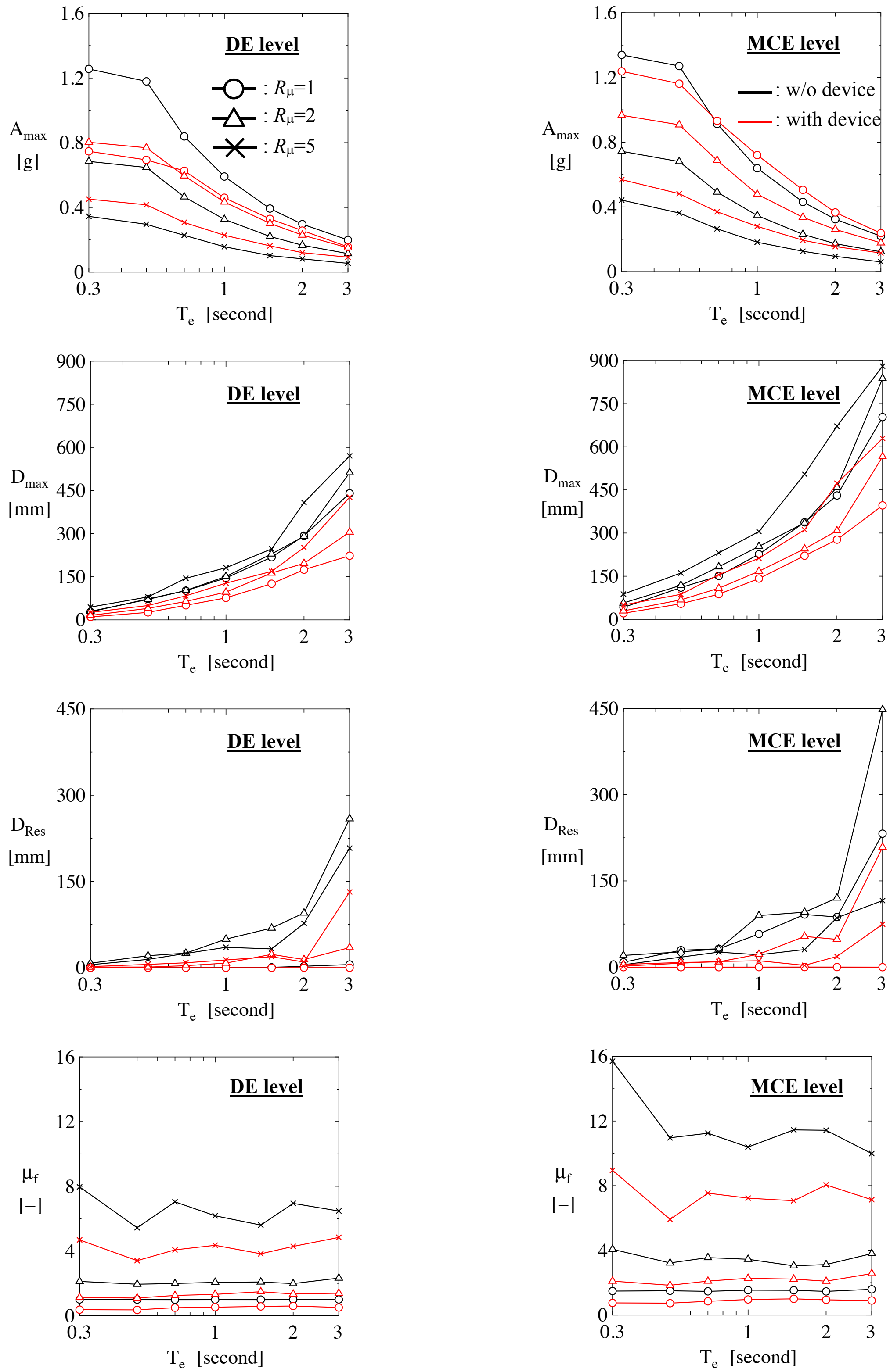

Figure 4-13 Comparison of Response of Structure with and without a Self-Centering System for Near-Fault Pulse-Like Motions, Linear Viscous Damping with β_v=0.10 and F_0/F_y=0.20

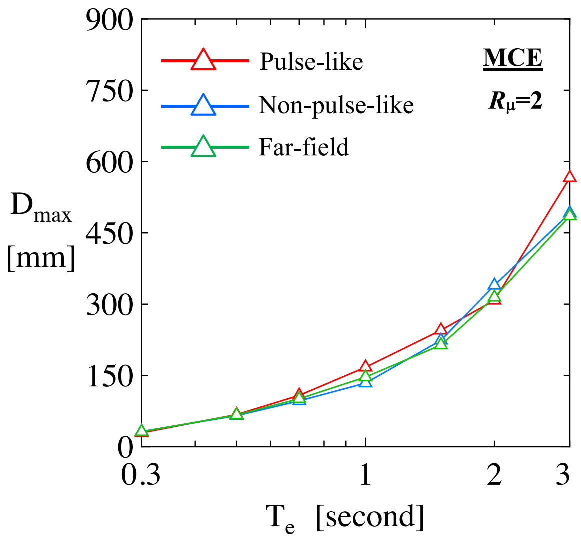

(a) Maximum dislacement, R_μ=2

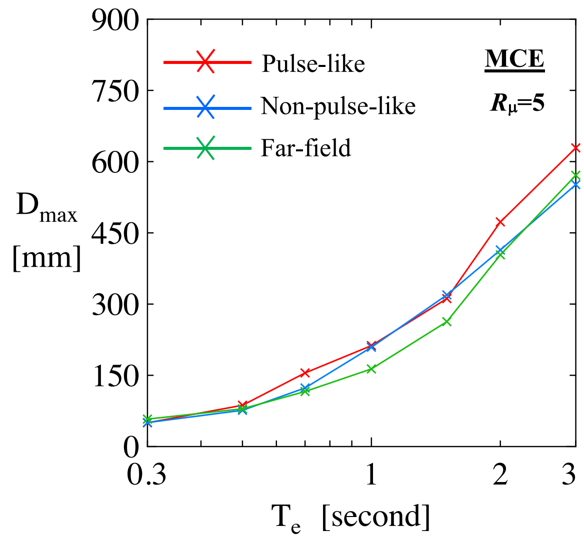

(b) Maximum dislacement, R_μ=5

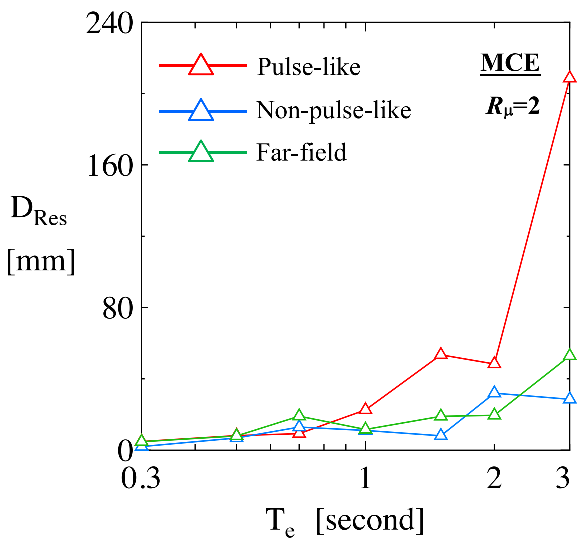

(c) Residual dislacement, R_μ=2

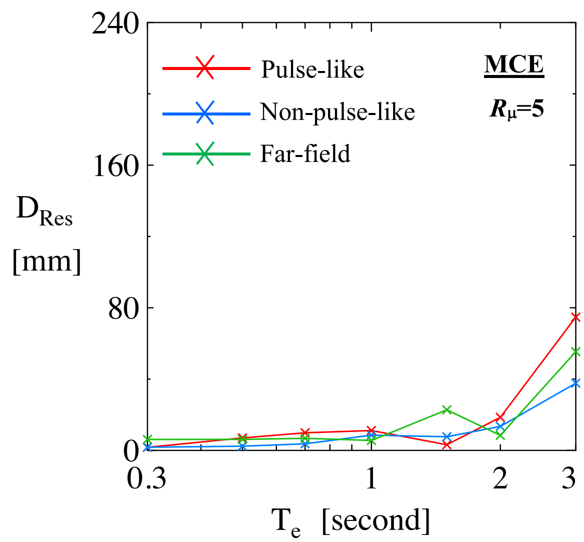

(d) Residual dislacement, R_μ=5

Figure 4-14 Effect of Ground Motion Type on Maximum and Residual Displacements in MCE for Case of Linear Viscous Damping with β_v=0.10, R_μ=2 and 5 and F_0/F_y=0.20

The results in Figure 4-15 show that the form of damping has minor effects on the calculated response (but for the residual displacement) and that an increase of damping from the value of β_v=0.10 to 0.20 results in a reduction of maximum displacement and residual displacement and a proportionally lesser increase in acceleration. What is interesting is that the upper half damping results in a noted reduction in residual displacement for flexible systems when combined with increased damping (see case of T_e=3sec and β_v=0.2). This is understandable as the upper half damping allows for quick re-centering as the damping force vanishes when the system moves towards the neutral position.

Note that the lower half damping type was found to be undesirable as illustrated in Figure 4-16, where the lower half damping form is shown to result is a general increase in displacement response by comparison to the linear damping, and some minor reduction of acceleration in cases of large values of R_μ.

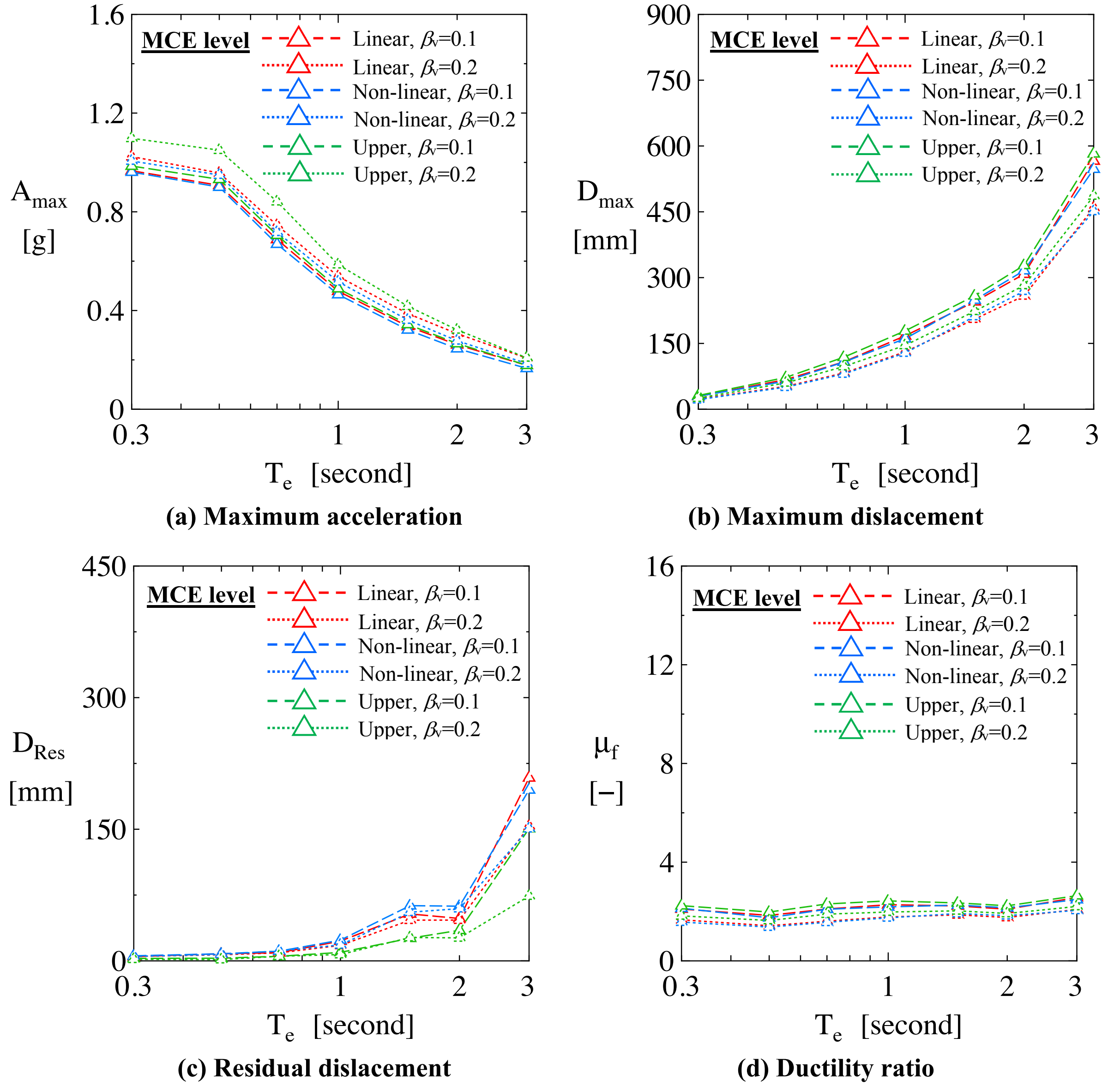

Figure 4-15 Effect of Type of Damping and Damping Value (β_v=0.10 and 0.20) on Peak Response in MCE Level Pulse-Like, Near-Fault Motions for F_0/F_y=0.20 and R_μ=2

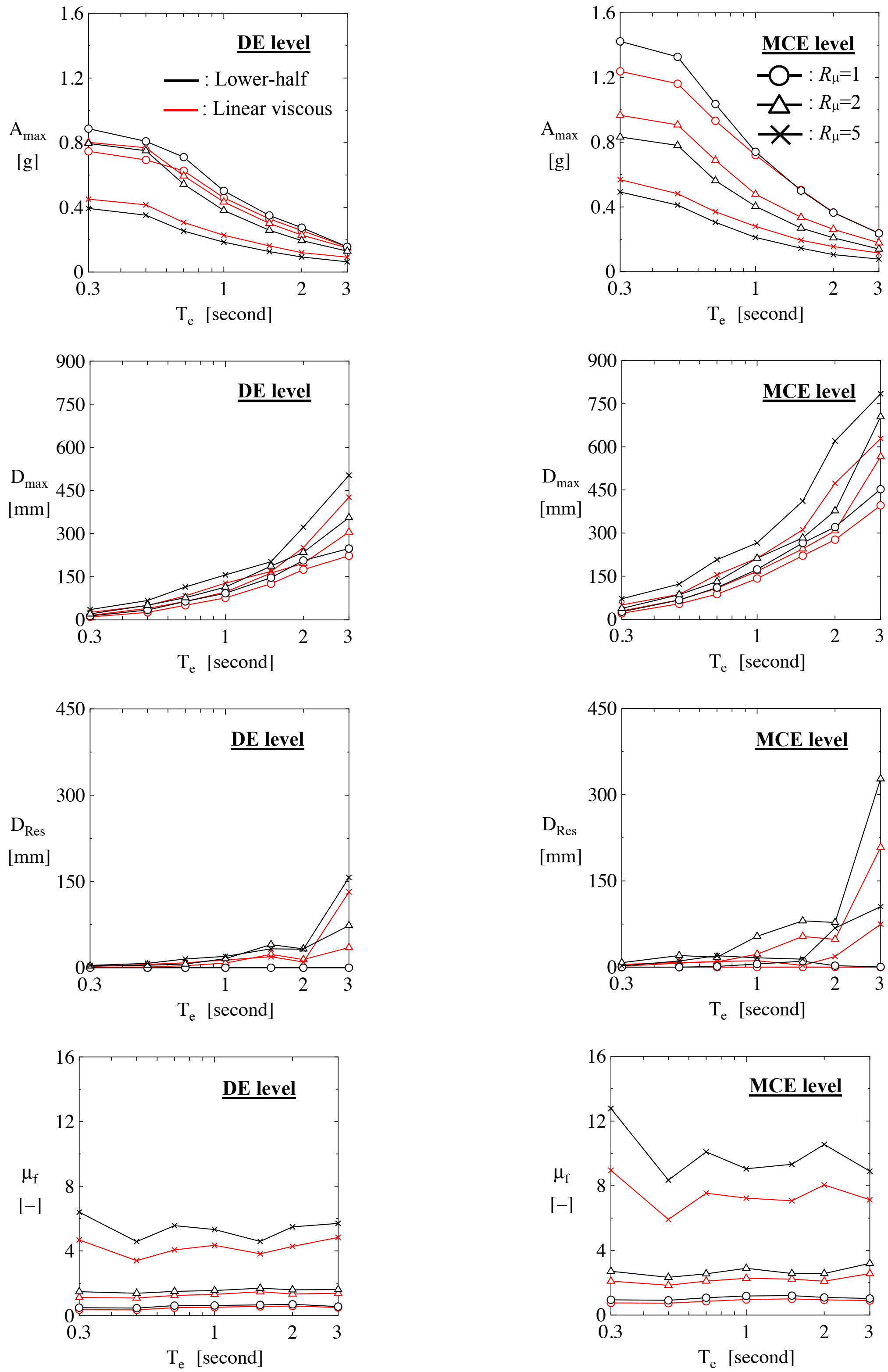

Figure 4-16 Comparison of Peak Response of System with Linear and Lower Half Damping both with β_v=0.10 in MCE Level Pulse-Like, Near-Fault Motions for F_0/F_y=0.2

Results presented in this section were exclusively for the case of preload to strength ratio F_0/F_y=0.20. This is based on the fact that this value of preload resulted in acceptable residual displacements as illustrated in the numerous results of Appendix A. A sample of these results is presented in Figure 4-17 where the effect of the preload on the residual displacement is compared in the case near-fdault pulse-like motions, R_μ=2 and the three types of useful damping with β_v=0.10. Evidently, the case F_0/F_y=0.5 results in nil residual displacements but the value F_0/F_y=0.2 systematically results in low values of residual displacements in the DE and acceptably low values in the MCE.

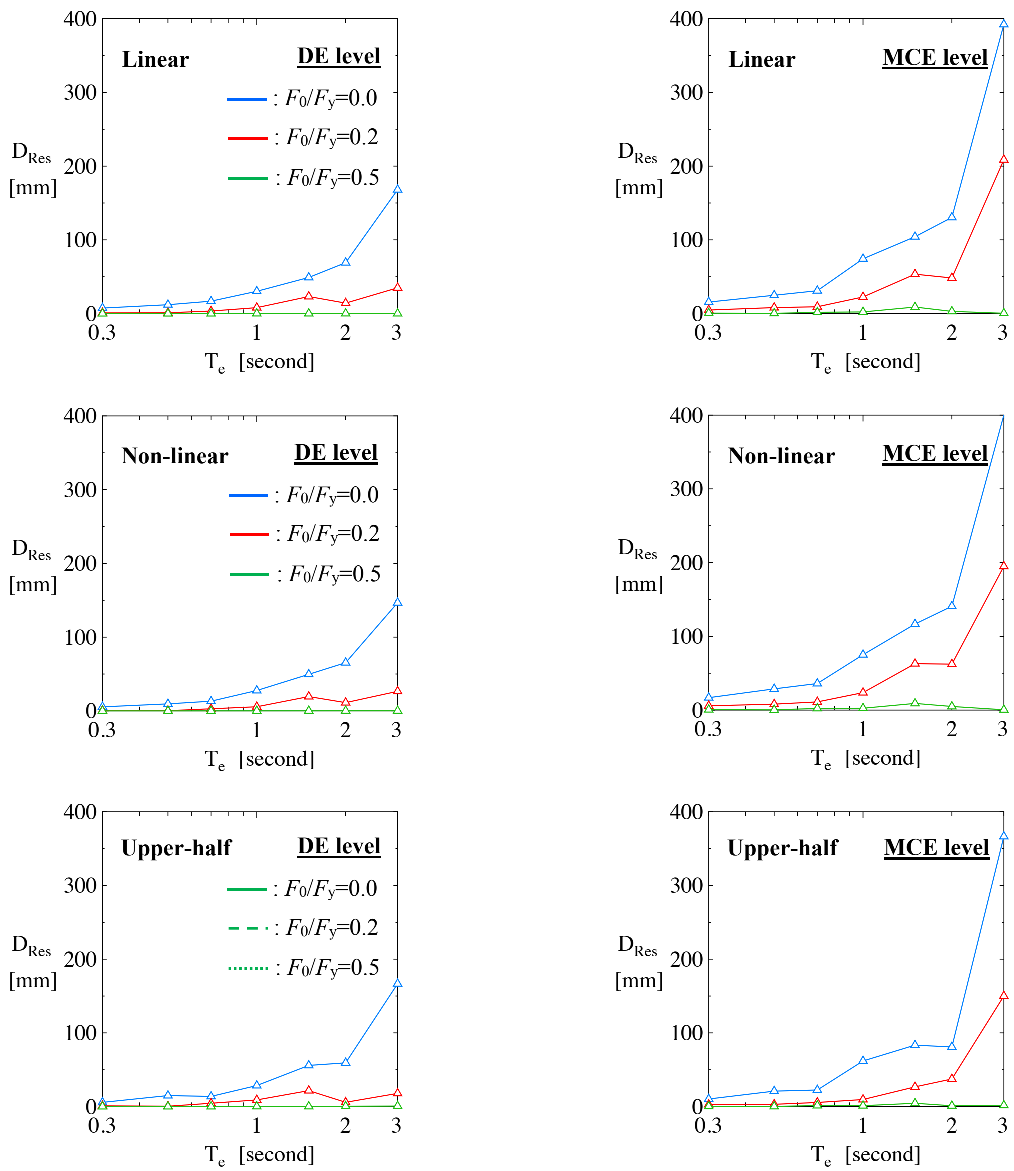

Figure 4-17 Effect of Preload on the Residual Displacement in Pulse-Like, Near-Fault Motions for R_μ=2 and Three Types of Useful Damping with β_v=0.10

Additional results in Figures 4-18 demonstrate the effect on the residual displacement of the amount and type of viscous damping for the three useful cases of damping in pulse-like, near-fault motions for F_0/F_y=0.2 and R_μ=2. It is evident that linear and nonlinear damping has essentially the same effect but the upper half damping offers some small advantage in flexible systems subjected to pulse like, near-fault motions (see also Appendix A).

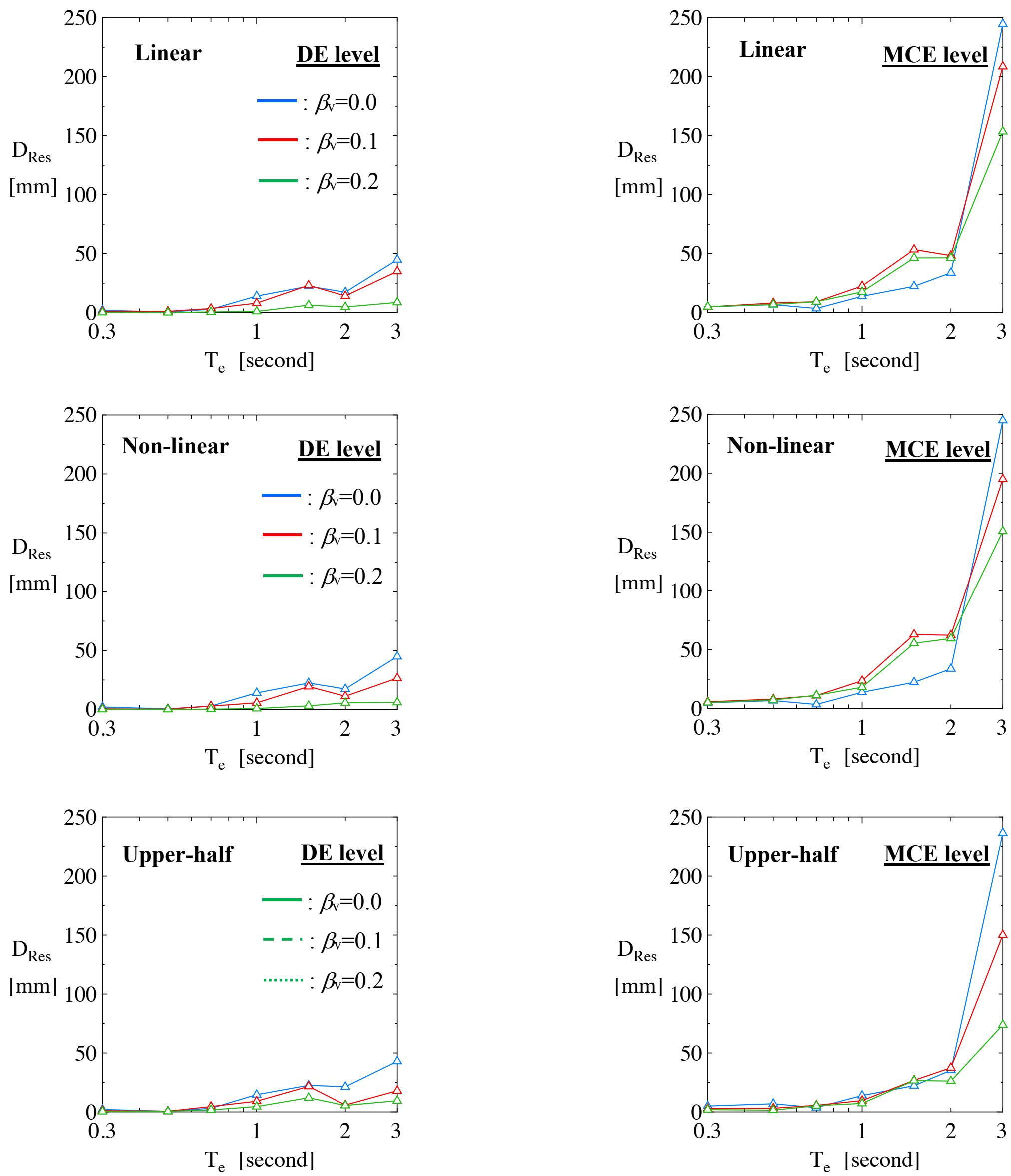

Figure 4-18 Effect of Amount and Type of Damping on the Residual Displacement of System in Pulse-Like, Near-Fault Motions for R_μ=2 and F_0/F_y=0.2

Figure 4-19 compares the peak responses of (a) a structure without a self-centering system and R_{μ}=2 and (b) a structure with a fluidic self-centering system but R_{μ}=3, F_0/F_y=0.2 and upper half damping with β_v=0.1, all in the case of near-fault pulse-like motions at the DE and MCE level. Note that it has been already determined that a preload to strength ratio F_0/F_y=0.2 and upper half damping with β_v=0.1 result in acceptable residual displacements. Also, and on the basis of the procedures followed for the design of structures with damping systems (see ASCE 7-2010 and Ramirez et al, 2001), a structure with a self-centering system will be designed for a strength (exclusive of the self-centering system) that is less than that of the conventional structure. Hence, the comparison of response for two different values of R_{μ}. Note that based on the values of R_{μ}, the strength of the structure with the self-centering system (but exclusive of the self-centering devices) is 2/3 or 0.66 times that of the conventional structure. Based on this comparison, the structure with the self-centering system has the same ductility ratio and acceleration as the conventional structure but less drift, and less residual displacement by a factor of 2 to 3. Note that the structure with the self-centering system has lesser peak displacement but the same ductility as the conventional structure of the same elastic period. This is due to the fact that for the same elastic period, the conventional structure has large yield displacement. Actually, the conventional structure with larger strength will also be stiffer so that the yield displacement will be less, leading to increased ductility demand for the conventional structure (see Ramirez et al., 2001 for a similar observation in the case of damped structures).

This indicates that the design of the structures with self-centering systems could be based on lateral forces that are 0.66 of those prescribed for conventional structures and it is expected that they will have a comparable performance in terms of ductility demand but substantially less residual displacements. This approach will be followed in the design of structures with fluid self-centering devices, but in similarity to the approach followed for structures with damping systems in ASCE 7-2010, the factor used will be 0.75 instead of 0.66.

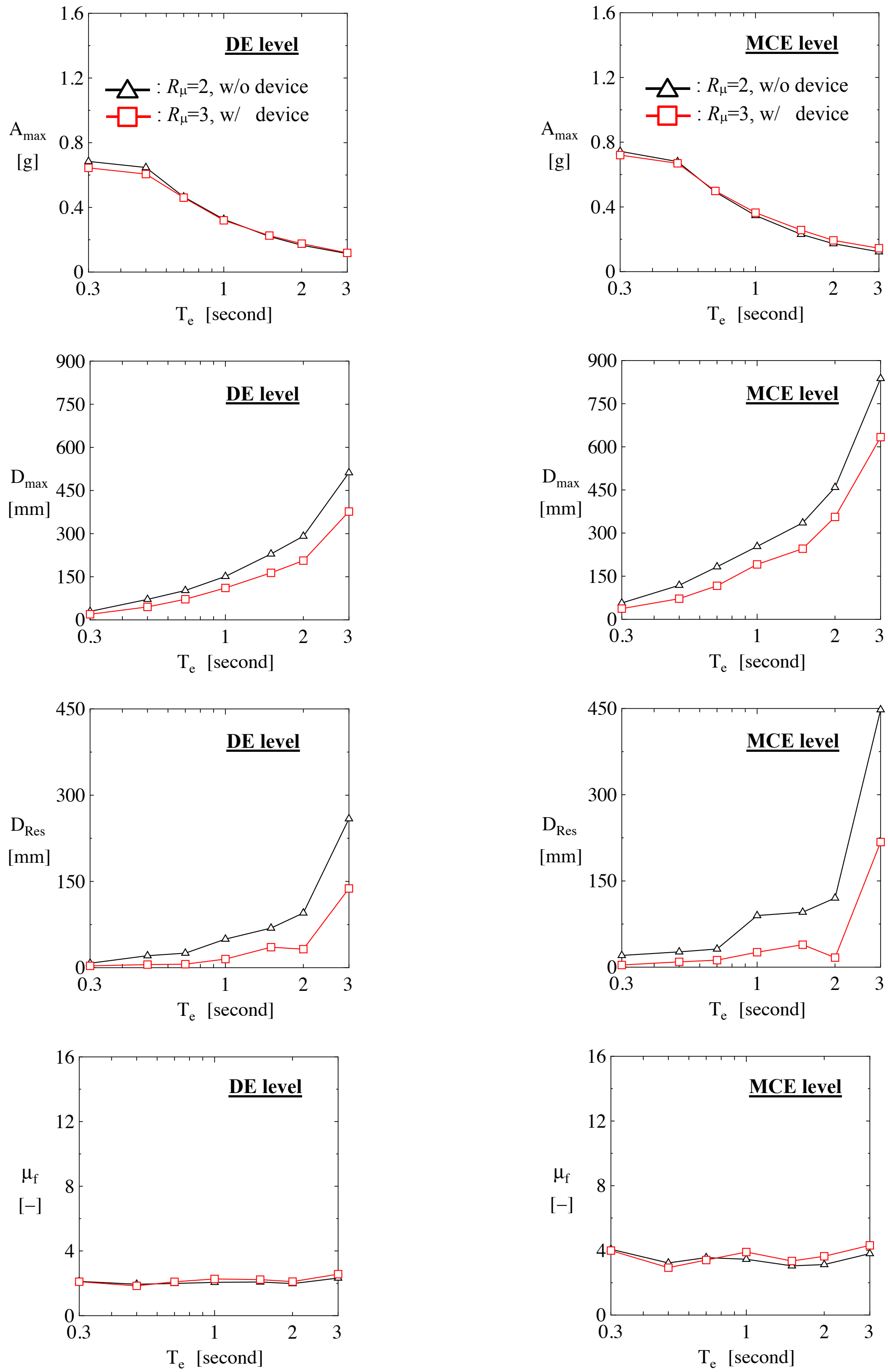

Figure 4-19 Comparison of Peak Responses in Near-Fault Pulse-Like Motions of Structure without and with Fluidic Self-Centering System with F_0/F_y=0.2 and Linear Damping with β_v=0.1

4.5 Non-Structural Response

Results presented so far concentrated on the structural response. Some results related to the response of non-structural elements are presented in this section by presenting floor response spectra calculated from the acceleration histories. For brevity, the presented spectra are limited to selected results for the structure with elastic period T_e=0.5 or 1.0*sec* and with a fluidic self-centering system having preload to strength ratio F_0/F_y=0, 0.2 or 0.50, viscous damping with β_v=0, 0.1 or 0.2, and stiffness K_0=0. All floor spectra are constructed for 5% damping ratio.

Figures 4-20 to 4-25 present comparisons of floor spectra to illustrate the effects of (a) the addition of the self-centering system (Fig. 4-20 and 4-21), (b) the type of input motion (Fig. 4-22), (c) the type of damping (Fig. 4-23), (d) the level of preload (Fig. 4-24) and (f) the amount of damping (4-25). The results demonstrate the following expected effects:

(1) The addition of the self-centering system causes an increase in effective stiffness and damping in the system as evident by the shift in the location of the peaks of the spectra and in the widening of the spectra. There is an increase in spectral acceleration values in the high frequency range for inelastic structural systems (R_μ>1) when the self-centering devices are added (for same value of R_μ for the conventional and self-centering systems).

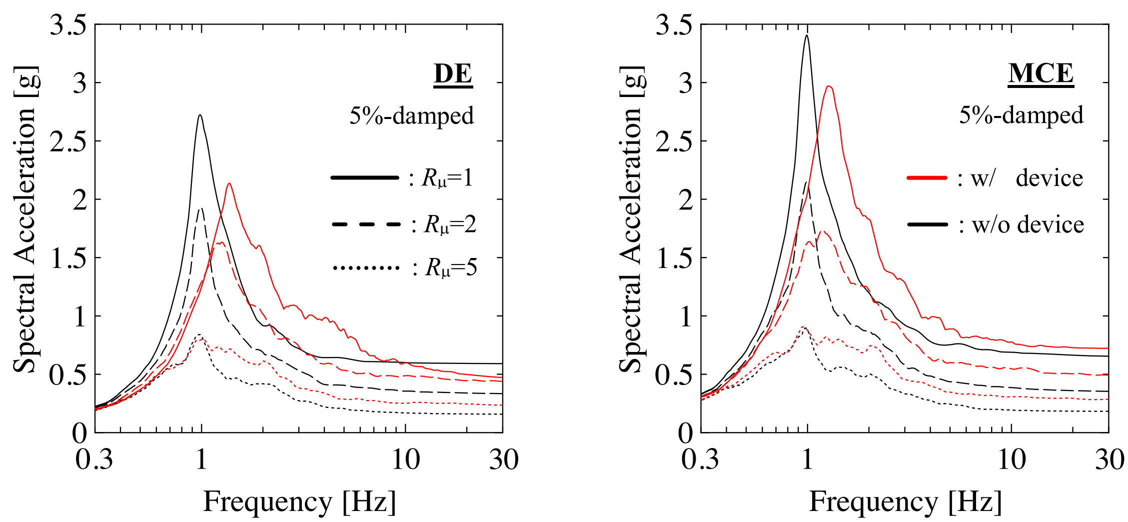

Figure 4-20 Comparisons of Floor Spectra of Structures without and with Self-Centering Devices for F_0/F_y=0.20, Linear Damping with β_v=0.1 and T_e=1.0*sec* in Near-Fault Pulse-Like Motions

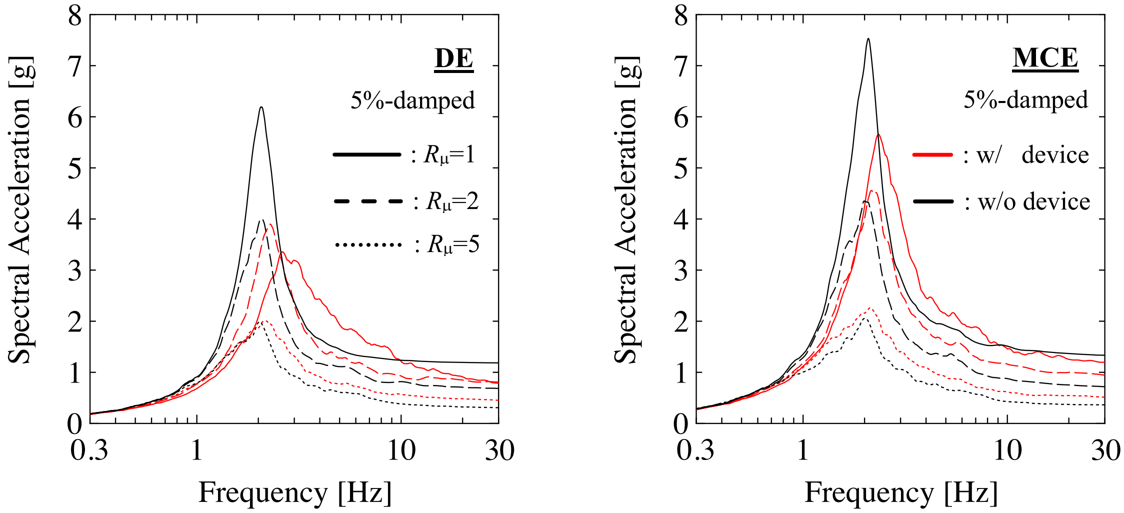

Figure 4-21 Comparisons of Floor Spectra of Structures without and with Self-Centering Devices for F_0/F_y=0.20, Linear Damping with β_v=0.1 and T_e=0.5*sec* in Near-Fault Pulse-Like Motions

(2) There is some but not significant difference in floor spectra obtained in the far-field, near-fault non-pulse- like and near-fault pulse-like seismic motions.

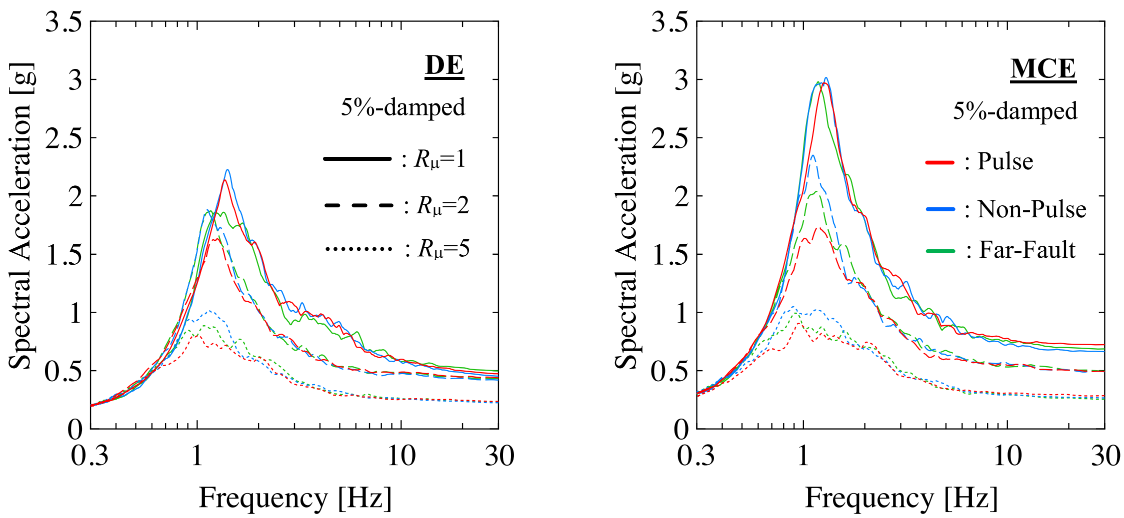

Figure 4-22 Effect of Ground Motion Type on Floor Spectra of Structures with Self-Centering Devices for F_0/F_y=0.20, Linear Damping with β_v=0.1 and T_e=1.0 *sec*

(3) The upper half damping type results in slightly higher floor spectra. The other three types result in similar floor spectra for all practical purposes.

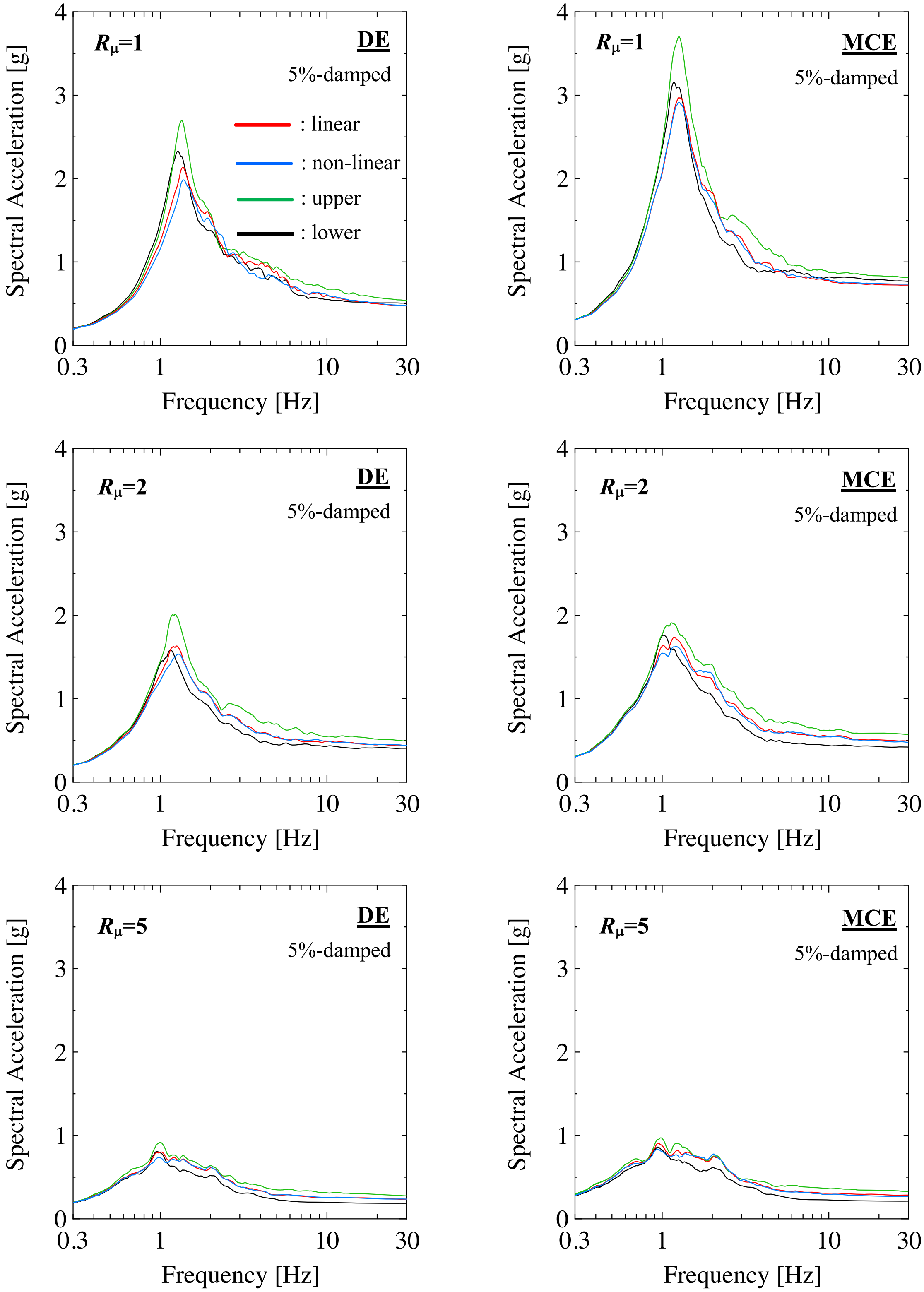

Figure 4-23 Effect of Damping Type on Floor Spectra of Structures with Self-Centering Devices for F_0/F_y=0.20, β_v=0.1 and T_e=1.0 *sec* in Near-Fault Pulse-Like Motions

(4) Increases in preload result in marked increases in the floor spectral values.

(5) Increases the damping ratio results in reduction in floor spectral accelerations is the resonance range and minor increases in spectral accelerations in the large frequency range.

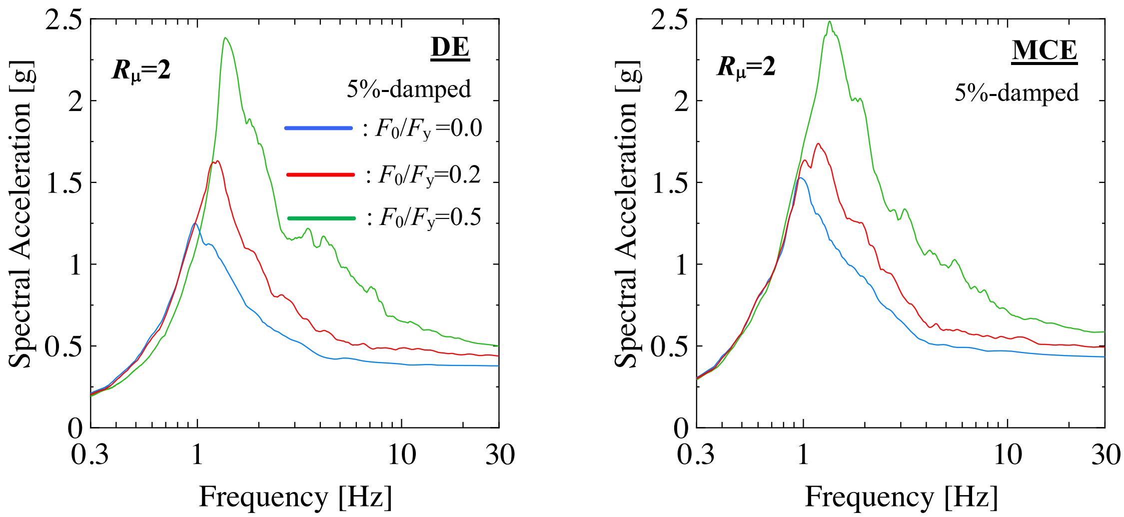

Figure 4-24 Effect of Preload on Floor Spectra of Structures with Self-Centering Devices for Linear Damping with β_v=0.1 and T_e=1.0*sec* in Near-Fault Pulse-Like Motions

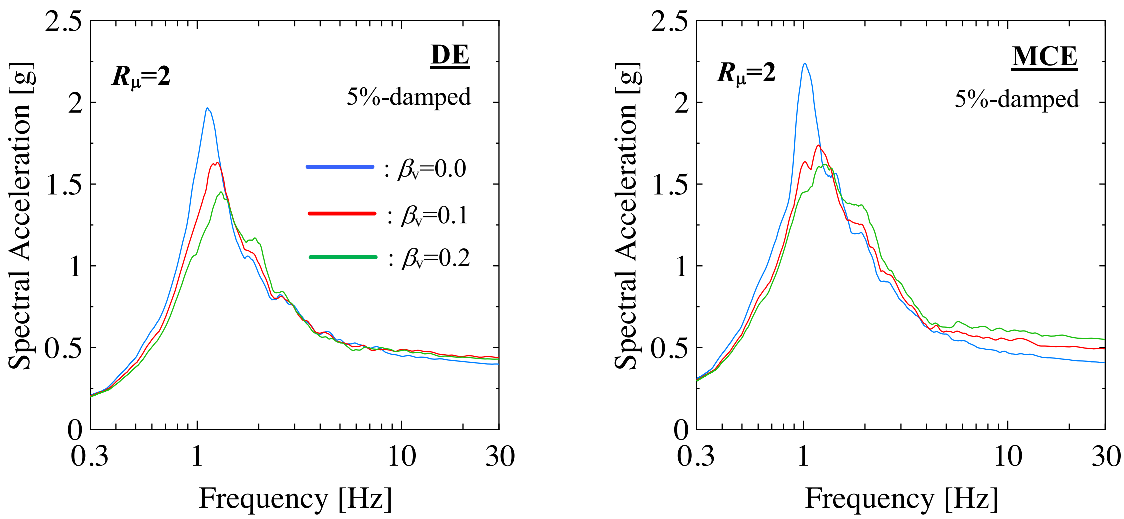

Figure 4-25 Effect of Amount of Linear Viscous Damping on Floor Spectra of Structures with Self-Centering Devices for F_0/F_y=0.20, T_e=1.0*sec* in Near-Fault Pulse-Like Motions

4.6 Effect of Stiffness of Fluidic Self-Centering Device on Response

The results presented in the preceding sections applied for the case of the fluidic self-centering device having stiffness K_0 zero. As discussed in Section 2, a fluidic self-centering device will have stiffness. Low stiffness is possible but would require a large volume of fluid and thus a large size device. Economy and compact size typically result in a restoring force that at the displacement capacity of the device is about equal to or larger than the preload. The implications of having non-zero stiffness are investigated in this section.

The stiffness of the fluidic self-centering device in the studies of this section is selected so that:

$$K_0 = \frac{F_0}{D_{max}}$$

where F_0 is the preload and D_{max} is maximum displacement obtained as the average of the analyses for the seven motions used to represent the response spectrum. This value of displacement was obtained from the analysis with stiffness K_0=0. This method of describing the device stiffness was thought to be a better descriptor of actual behavior rather than arbitrarily selecting stiffness values and performing parametric studies.

Figure 4-26 illustrates the stiffness relation and how it was incorporated in the model for analysis.

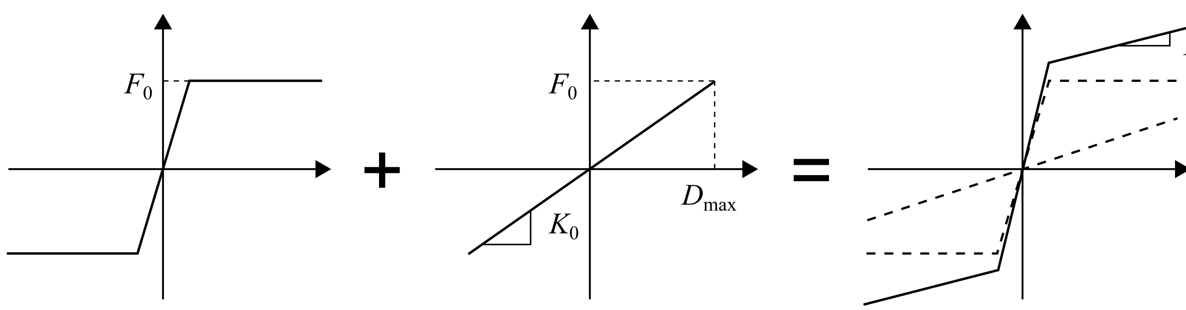

Device hysteresis (K_0=0) **Device stiffness K_0** **Device hysteresis ($K_0 \neq 0$)**

Figure 4-26 Inclusion of Stiffness in Model of Fluidic Self-Centering Device

Figure 4-27 compares the response of the structure with the fluidic self-centering device having stiffness zero or different than zero as described above, for near-fault pulse-like motions, preload to strength ratio F_0/F_y=0.2 and linear viscous damping with β_v=0.1 (other parameters per Table 4-4). Evidently, the stiffness causes a minor increase in acceleration for elastic structure conditions (R_μ=1), whereas the maximum displacement and ductility are the same. Interestingly, the stiffness results in reduced residual displacement, a very desirable effect.

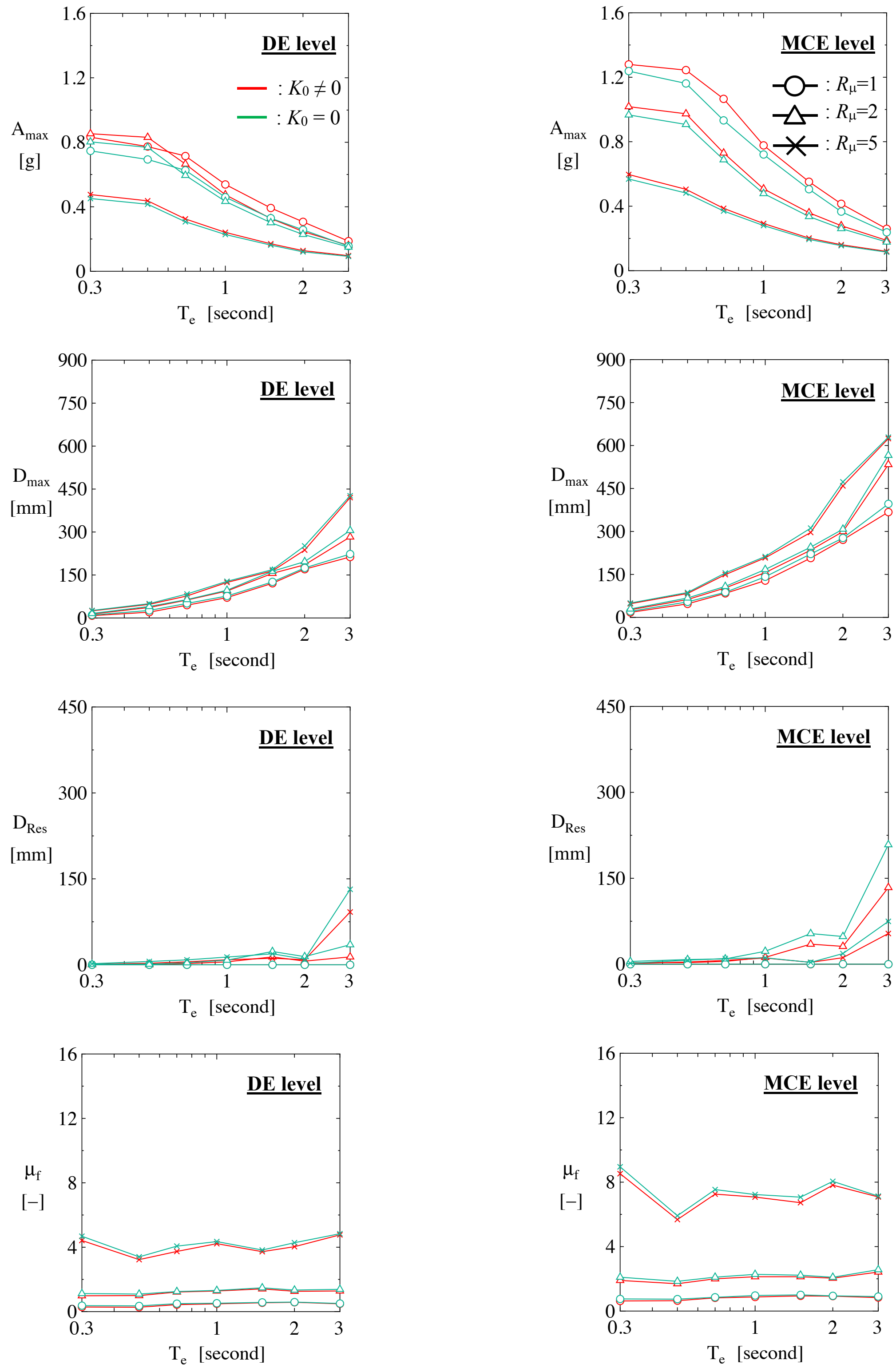

Figure 4-27 Comparison of Peak Responses in Near-Fault Pulse-Like Motions of Structure with Self-Centering System of Stiffness $K_0 = 0$ or $K_0 \neq 0$, F_0/F_y=0.2 and Linear Damping with β_v=0.1

Figure 4-28 compares the response of the structure with and without a self-centering system having $K_0 \neq 0$, F_0/F_y=0.20 and linear viscous damping with β_v=0.10 in the near-fault pulse-like motions. Evidently the addition of the fluidic self-centering system results in a substantial reduction of maximum displacements, ductility demands and residual displacements. It also results in an increase in acceleration, which is slightly more for elastic structure conditions than the case of zero stiffness (K_0=0).

Figure 4-29 compares floor response spectra of the system with fluidic self-centering devices with zero and non-zero stiffness, F_0/F_y=0.20 and linear viscous damping with β_v=0.10 in the near-fault pulse-like motions. The system with stiffness has higher floor spectra under elastic structure conditions (R_μ=1)-with the differences diminishing as the structure undergoes increasing inelastic action (increasing R_μ).

The floor spectra of the structure with the fluidic self-centering system with nonzero stiffness ($K_0 \neq 0$) are compared to those of the structure without a self-centering system in Figure 4-30 when F_0/F_y=0.2, linear viscous damping with β_v=0.1, T_e=1.0*sec* in near-fault, pulse-like motions. Also, the addition of the self-centering system results in an increase in floor spectral acceleration for the same value of elastic period and R_μ.

4.7 Conclusions

The results of this study show that the addition of a fluidic self-centering system to an inelastic structural system offers important advantages in reduction of maximum displacement, ductility demand and residual displacement. The acceleration and floor spectral acceleration will generally increase or remain about the same for the two systems having the same elastic period and strength to elastic demand ratio (R_μ). Based on the results, the following parameters for the structural system and the self-centering system provide the desired performance in terms of reduction or elimination of residual displacements, reduction of maximum displacement, and reduction of ductility without having a significant increase in accelerations:

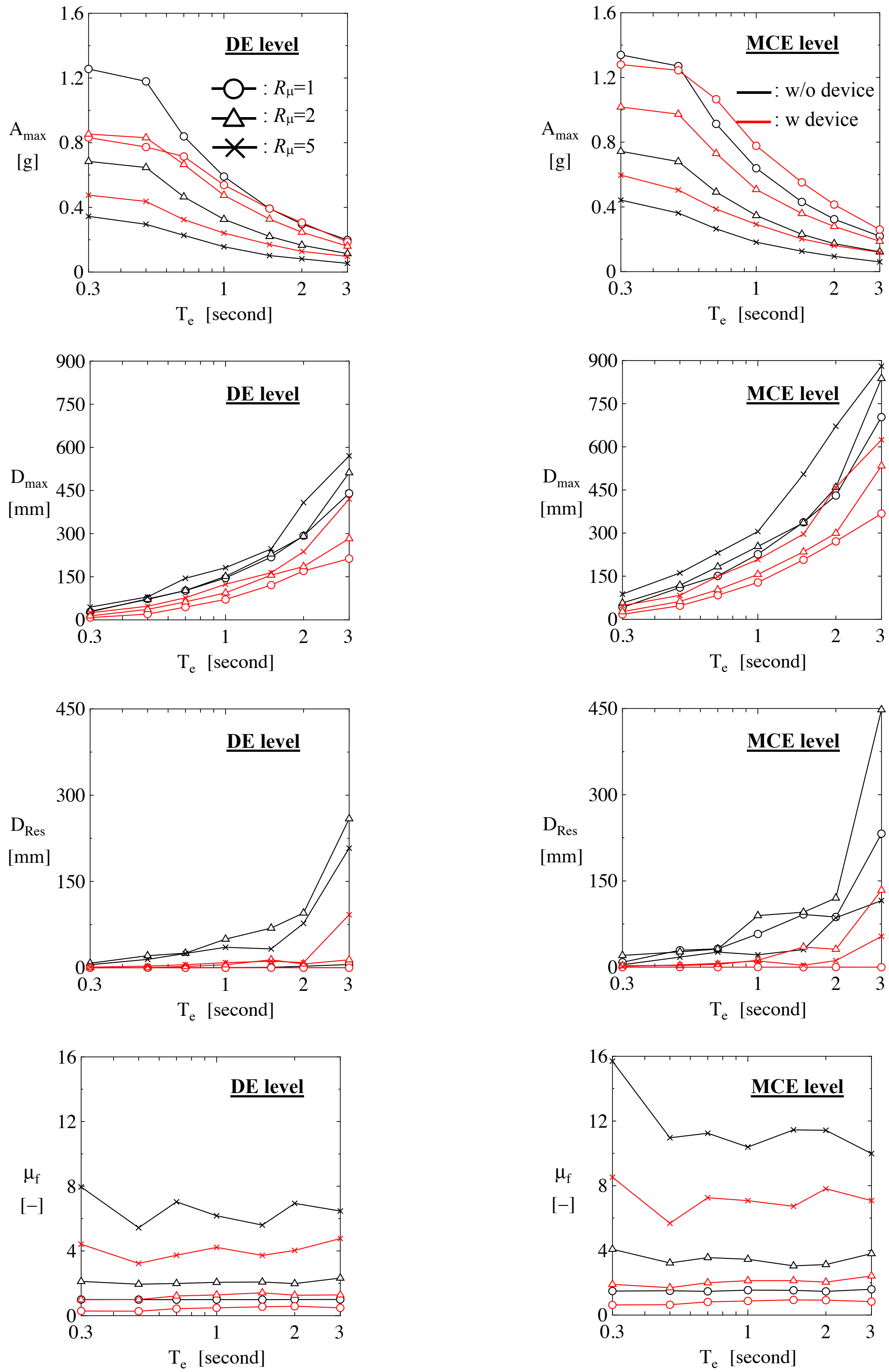

Figure 4-28 Comparison of Response of Structure with and without a Self-Centering System with $K_0 \neq 0$ for Near-Fault Pulse-Like Motions, Linear Viscous Damping with β_v=0.10 and F_0/F_y=0.20

(1) Self-centering system with preload to strength ratio F_0/F_y=0.20 and viscous damping of linear, nonlinear or upper half type with effective damping ratio β_v=0.10. The upper half damping offers a small advantage in further reducing the residual displacements when the structure is flexible and the input motion has pulse-like characteristics. Slightly higher values of preload (say F_0/F_y=0.25) and of damping ratio (say 0.15) may further improve the performance.

(2) Structural system exclusive of the self-centering system design for lateral forces that are equal to 0.75 or larger of those prescribed for conventional structures on the basis of ASCE 7-2010.

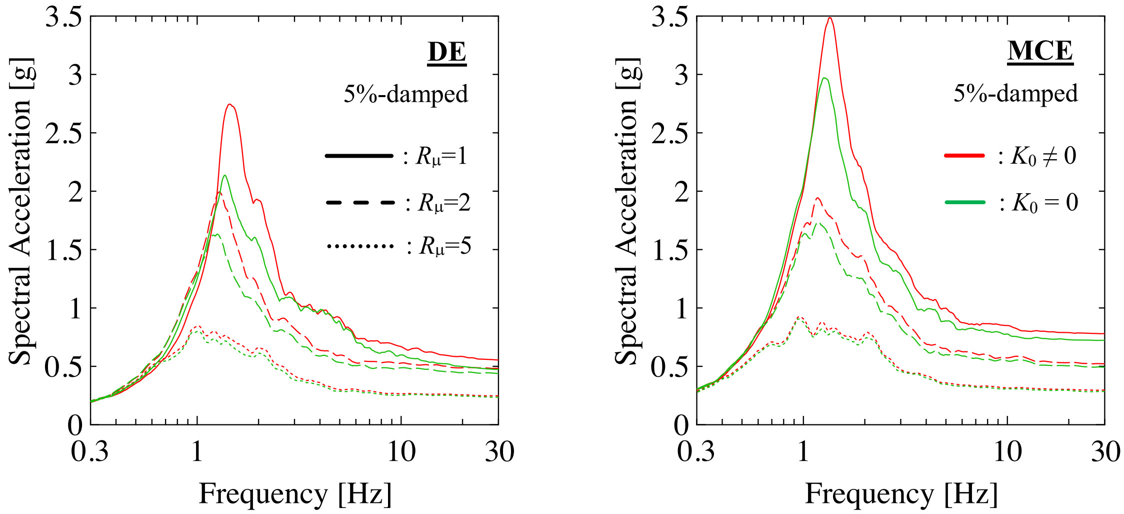

Figure 4-29 Effect of Stiffness of Device (K_0=0 or K_0≠0) on Floor Spectra of Structures with Self-Centering Devices for Linear Damping with β_v=0.1 and T_e=1.0*sec* in Near-Fault Pulse-Like Motions

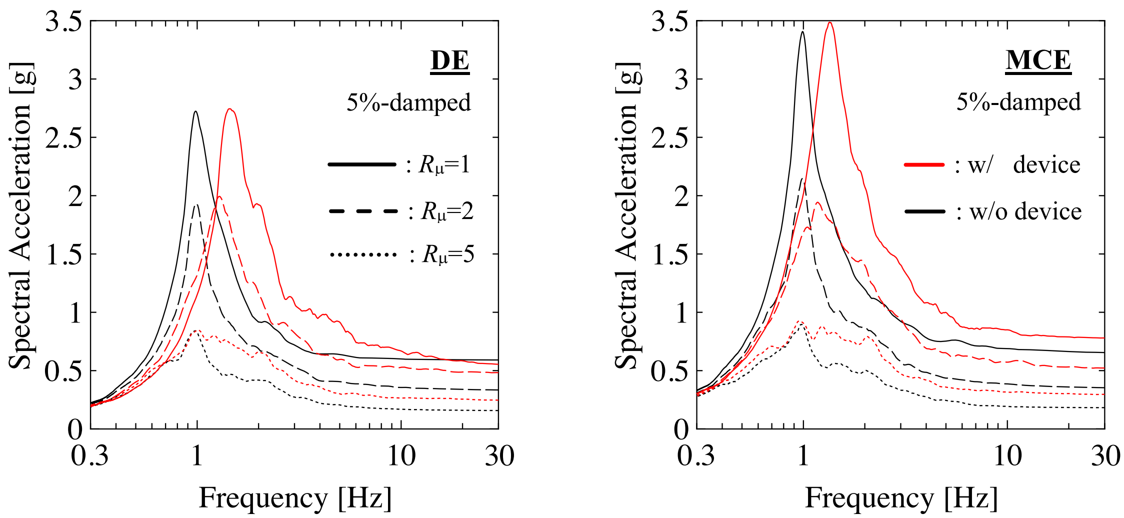

Figure 4-30 Comparisons of Floor Spectra of Structure without and with a Fluidic Self-Centering Device having F_0/F_y=0.2, Linear Damping with β_v=0.1, T_e=1.0*sec* and K_0≠0 in Near-Fault, Pulse-Like Motions

SECTION 5
EVALUATION OF SIMPLIFIED METHOD OF ANALYSIS OF YIELDING SINGLE-DEGREE-OF-FREEDOM SYSTEMS WITH FLUIDIC SELF-CENTERING DEVICES

5.1 Introduction

Simplified methods of analysis are important in the development of design and analysis methods for buildings with fluidic self-centering devices. The intent is to develop design and analysis methodologies that follow the paradigm of the methods for buildings with damping systems in ASCE 7-2010 and which were developed and evaluated in Ramirez et al. (2001). The analysis method is either the Equivalent Lateral Force (ELF) method, which treats the structural system analyzed as a single-degree-of-freedom system with an additional residual mode of vibration, or the Response Spectrum Analysis (RSA) method, which accounts for all important modes of vibration. A first step in the evaluation of the validity and degree of accuracy of the simplified methods is the analysis of single-degree-of-freedom systems. The next step, presented in Section 6, is to describe the design philosophy for buildings with fluidic self-centering devices and perform analysis in selected examples to estimate the force and displacement demands so that an assessment of adequacy may be performed. Then nonlinear response history analysis is conducted to validate the design and to assess the accuracy of the simplified analysis.

The simplified method used for yielding structures with self-centering devices is the one utilized in ASCE 7-2010 for structures with damping systems. It is based on the replacement of the yielding structure with the added fluidic self-centering device with an equivalent linear elastic and linear viscous system. The calculation of the maximum displacement is obtained iteratively by use of the design response spectrum (5%-damped) as modified for the increased damping. The calculation of the maximum acceleration and maximum velocity is based on the simplified procedures described in Ramirez et al. (2001).

5.2 Analyzed System

The analyzed system is depicted in Figures 4-7 and 4-8 and is described by Equations (4-1) to (4-10). Specifically, Equation (4-1) is used to perform response history analysis using the scaled groups of motions described in Section 4 and obtain the peak response of the system. The average of each of the seven analyses in the response history analysis is compared with the results of the simplified analysis. The parameters of the analyzed system are presented in Table 5-1. Figure 5-1 illustrates the fluidic self-centering device as a combination of a bilinear elastic element with preload $F_0 = mA_0$, a bilinear hysteretic element with strength equal to $F_{min} = mA_{min}$ (seal friction), elastic stiffness K_0 and a linear or nonlinear damping element. Figure 5-2 illustrates the behavior of the primary structural system. Note that m is the mass and the quantities A, A_y, A_0 and A_{min} have units of acceleration.

Table 5-1 Parameters of Analyzed SDOF System with Fluidic Self-Centering Devices

Primary Structural System				Self-Centering Device			
R_μ	T_e (sec)	β_i	α	β_v	a	F_0/F_y	K_0
1	0.3	0.05	0.05	0.1	1.0 (linear damping)	0.10	$\neq 0$[1]
2	0.5			0.2	0.5 (nonlinear damping)	0.20	
3	0.7						
4	1.0						
5	1.5						
	2.0						
	3.0						
1: Stiffness such that the force equals the preload F_0 at the maximum displacement D							

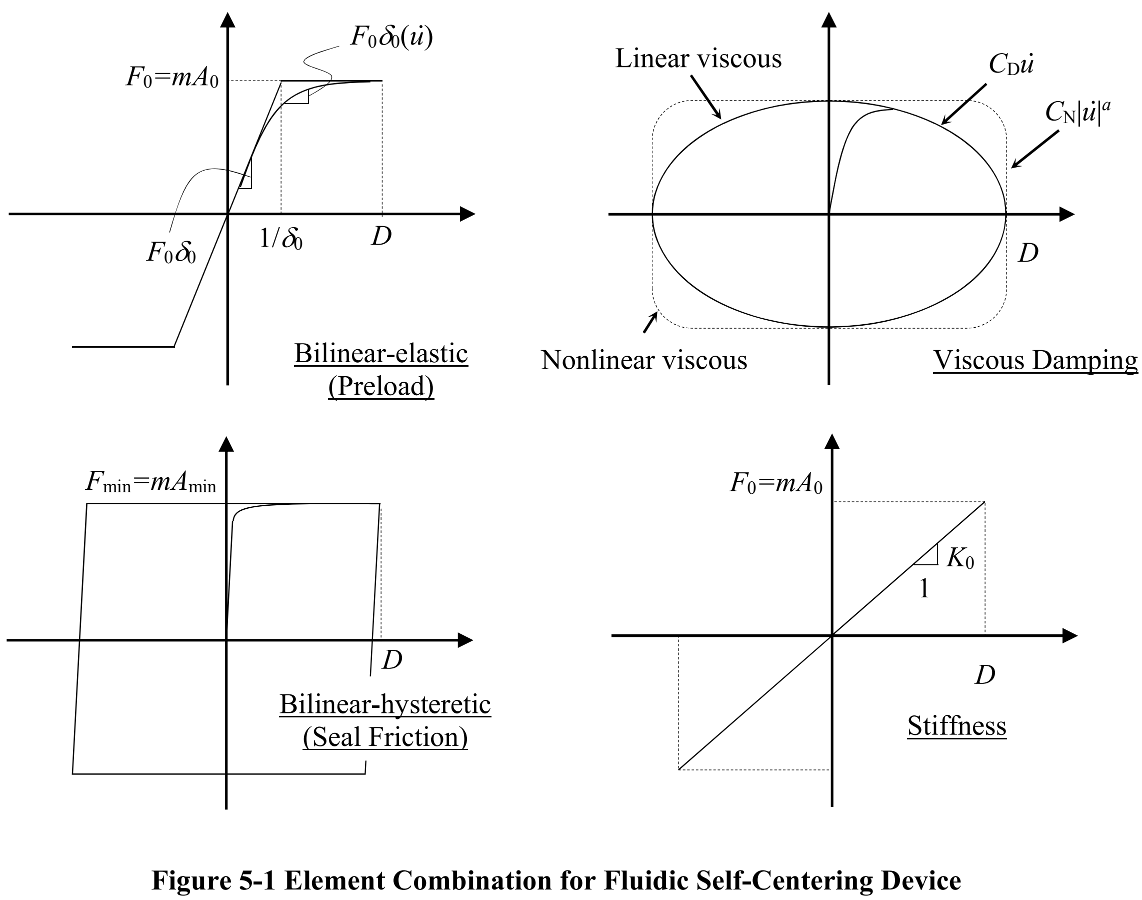

Figure 5-1 Element Combination for Fluidic Self-Centering Device

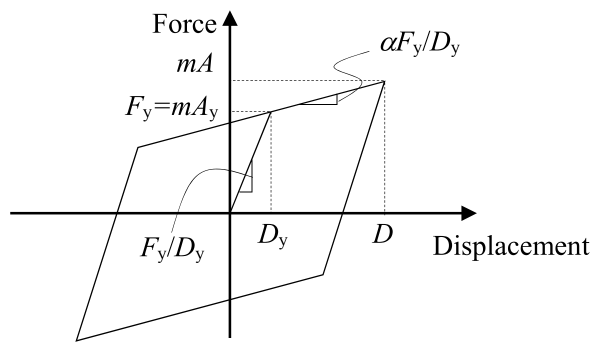

Figure 5-2 Behavior of Primary Structural System

In addition to the values of parameters in Table 5-1, the following values of other parameters were used (see also Section 4): ζ=0, δ_0=2mm^{-1}, δ_{min} =0, δ_1 =0.004 sec/mm, Y=0.25mm, A=1, β=0.1, γ=0.9 and η=2.

5.3 Simplified Method of Analysis

The simplified method of analysis is based on the replacement of the analyzed system with an equivalent linear elastic and linear viscous representation having an effective period T_{eff} and an effective damping ratioβ_{eff}. The calculation of these quantities is described below:

Effective Period T_{eff}

$$T_{\text{eff}} = 2\pi \left(\frac{D}{A + A_{\text{min}} + A_0 + {K_0 D}/{m}} \right)^{1/2} \tag{5-1}$$

Note that quantity A+A_{min}+A_0+(K_0D)/m is the acceleration of system (primary plus added fluidic self-centering device) at the instance of maximum displacement D. Quantity m is the mass. Quantity A is illustrated in Figure 5-2 and given by Equation (5-2):

$$A = \begin{cases} A_y \cdot \dfrac{D}{D_y} & \left(D \le D_y\right) \\ A_y + \alpha \dfrac{A_y}{D_y}\left(D - D_y\right) & \left(D \ge D_y\right) \end{cases} \tag{5-2}$$

Note that the yield displacement D_y is related to A_y and T_e by Equation (4-2). Also, note that Equation (5-1) includes the general form of the device stiffness. For the specific case analyzed where the spring force at the maximum displacement D equals to the preload, quantity A_0+K_0D/m simplifies to 2A_0.

Effective Damping Ratio β_{eff}

The effective damping ratio is calculated by the procedures described in Ramirez *et al*. (2001) and is given below:

$$\beta_{\text{eff}} = \beta_{\text{i}} \left(\frac{A}{A + A_{\min} + A_0 + {K_0 D}/{m}} \right)^{1/2} + \beta_{\text{v}} \left(\frac{T_{\text{eff}}}{T_{\text{e}}} \right)^{2-a} + \frac{2q_{\text{H}}\left(A_{\text{y}}D - AD_{\text{y}}\right) + 2A_{\min}\left(D - Y\right)}{\pi\left(A + A_{\min} + A_0 + {K_0 D}/{m}\right)D} \tag{5-3}$$

Here, β_{i} is inherent damping ratio of the primary structural system, which we set equal to 0.05 under elastic or inelastic conditions and β_{v} is added viscous damping ratio (linear when a=1). Note that the inherent damping in the combined system (first term in Equation 5-3) has been reduced due to the increase in stiffness under elastic conditions. The third term in Equation (5-3) is valid for $D \geq D_{\text{y}}$. If $D \leq D_{\text{y}}$ quantity ($A_{\text{y}}D$-AD_{y}) in the third term is set equal to zero.

The damping ratio is related to the parameters of the system by:

$$\beta_{\text{v}} = \frac{C_{\text{N}}\lambda}{2\pi m} D^{a-1} \left(\frac{2\pi}{T_{\text{e}}} \right)^{a-2} \tag{5-4}$$

$$\lambda = 4 \cdot 2^a \frac{\Gamma^2\left(1 + {a}/{2}\right)}{\Gamma\left(2 + a\right)} \tag{5-5}$$

Here Γ(-) is the gamma function. Equation (5-4) simplifies for the case of linear viscous damping to:

$$\beta_{\text{v}} = \frac{C_{\text{D}}T_{\text{e}}}{4\pi m} \tag{5-6}$$

D_{y} is yield displacement of the primary structural system (see Figure 5-2 above) and is related to the other parameters as follows, where S_{ae} is the spectral acceleration at period T_{e}:

$$D_{\text{y}} = \frac{S_{\text{ae}}T_{\text{e}}^2}{4\pi^2 R_{\mu}} \tag{5-7}$$

The third term in Equation (5-3) includes the contribution of the yielding primary structural system (plus seal friction from the fluidic device), which when perfect bilinear hysteretic has factor q_{H}=1.0. This factor, called the hysteresis loop adjustment factor is used to reduce the area under the perfect bilinear hysteretic loop to better represent the behavior of real structural systems. In ASCE 7-2010, the value of q_{H} is defined as in Equation (5-8) (see Ramirez *et al.*, 2001 for justification):

$$q_{\text{H}} = 0.67\frac{T_{\text{s}}}{T_{\text{e}}} \tag{5-8}$$

Here T_{s} is the value of period at which the response spectrum regions of constant acceleration and constant velocity intersect and is equal to the ratio $S_{\text{M1}}/S_{\text{MS}}$ in units of second. According to the ASCE 7-2010, the value of q_{H} shall not be taken as greater than 1.0 and need not be taken as less than 0.5. In this study, q_{H}=1.0 is used as the analyzed system has perfect bilinear hysteresis. Also, note that Equations (5-1) and (5-3) are valid for the general case of fluidic self-centering device stiffness. For the specific case analyzed in this section, the stiffness is such that the spring force at maximum displacement D is equal to the preload, so that the term A_0+(K_0D)/m in these equations is equal to 2A_0.

An additional parameter is needed to obtain the spectral acceleration from the response spectrum when the effective damping is different than 5-percent. This is obtained by the standard procedure per ASCE 7-2010 where the 5%-damped spectral acceleration is divided by the damping parameter B:

$$S_{\text{ae}}\left(T_{\text{eff}}, \beta_{\text{eff}}\right) = \frac{S_{\text{ae}}\left(T_{\text{eff}}, \beta = 0.05\right)}{B} \tag{5-9}$$

Parameter B is given in Table 5-2. Moreover, the analysis needs to determine the maximum values of velocity and acceleration. The maximum velocity is calculated as pseudo-velocity times a correction factor *CFV* per equation (5-10).

$$V_{\max} = \frac{2\pi}{T_{\text{eff}}} \cdot D \cdot CFV \tag{5-10}$$

Factor *CFV* was determined by Ramirez et al (2001) based on the analysis of yielding systems with added viscous damping and is presented in Table 5-3.

Table 5-2 Damping Parameter B

Effective Damping (% of critical)	B
≤2	0.8
5	1.0
10	1.2
20	1.5
30	1.8
40	2.1
50	2.4
60	2.7
70	3.0
80	3.3
90	3.6
≥100	4.0

Table 5-3 Velocity Correction Factor *CFV* per Ramirez *et al* (2001)

Effective Period (second)	Effective Damping Ratio									
	0.10	0.20	0.30	0.40	0.50	0.60	0.70	0.80	0.90	1.00
0.3	0.72	0.70	0.69	0.67	0.63	0.60	0.58	0.58	0.54	0.49
0.5	0.75	0.73	0.73	0.70	0.69	0.67	0.65	0.64	0.62	0.61
1.0	0.82	0.83	0.86	0.86	0.88	0.89	0.90	0.92	0.93	0.95
1.5	0.95	0.98	1.00	1.04	1.05	1.09	1.12	1.14	1.17	1.20
2.0	1.08	1.12	1.16	1.19	1.23	1.27	1.30	1.34	1.38	1.41
2.5	1.05	1.11	1.17	1.24	1.30	1.36	1.42	1.48	1.54	1.59
3.0	1.00	1.08	1.17	1.25	1.33	1.42	1.50	1.58	1.67	1.75
3.5	1.09	1.15	1.22	1.30	1.37	1.45	1.52	1.60	1.67	1.75
4.0	0.95	1.05	1.15	1.24	1.38	1.49	1.60	1.70	1.81	1.81

An expression for the velocity correction factor has been derived by Pekhan et al. (1999b) based on the analysis of elastic systems. Ramirez et al. (2001) reported that the simpler expression of Pekhan et al. (1999b) provided a good and simple corrector for the pseudo-velocity. This expression is:

$$CFV = \left(\frac{T_{\text{eff}}}{T_{\text{s}}}\right)^{0.455\beta_{\text{Veff}}+0.132} \tag{5-11}$$

Note that in Equation (5-11) (but not in Table 5-3) the damping ratio is interpreted as the portion of the effective damping contributed by viscous damping. This is given by the first two terms of Equation (5-3):

$$\beta_{\mathrm{veff}} = \beta_{\mathrm{i}} + \beta_{\mathrm{v}}\left(\frac{T_{\mathrm{eff}}}{T_{\mathrm{e}}}\right)^{2-a} \tag{5-12}$$

The maximum acceleration is calculated as the acceleration at maximum displacement $(A + A_{\min} + A_0 + \frac{K_0 D}{m})$ times a factor and (5-13). Again for the analyzed case in this section, $A_0 + \frac{K_0 D}{m} = 2A_0$. Note that Equation (5-13) is adopted from Ramirez et al. (2001).

$$A_{\max} = \left(A + A_{\min} + A_0 + \frac{K_0 D}{m}\right)\cdot\left(CF_1 + \frac{2\pi\beta_{\mathrm{veff}}}{\lambda}\cdot CF_2\right) \tag{5-13}$$

In this equation, CF_1 and CF_2 are load combination factors used to calculate the response at the time of maximum acceleration by combining the peak accelerations at the time of maximum drift and at the time of maximum velocity. These factors are calculated as follows (Ramirez *et al*., 2001):

$$CF_1 = \begin{cases} \cos\delta & \text{when } \; D < D_{\mathrm{y}} & \text{(5-14a)} \\ \mu\cos\delta & \text{when } \; D > D_{\mathrm{y}} \;\; \mu\cos\delta < 1 & \text{(5-14b)} \\ 1 & \text{when } \; D > D_{\mathrm{y}} \;\; \mu\cos\delta \geq 1 & \text{(5-14c)} \end{cases}$$

$$CF_2 = (\sin\delta)^a \tag{5-15}$$

$$\delta = \tan^{-1}(2\beta_{\mathrm{veff}}) \tag{5-16}$$

In these equations μ is the ductility ratio defined by $\mu = \frac{D}{D_{\mathrm{y}}}$.

The procedure for simplified analysis follows the steps below:

1. Given are the system parameters T_{e}, R_{μ}, damping ratio β_{v}, damping exponent α, preload to yield strength ratio F_0/F_{y}, stiffness to mass ratio K_0/m, friction to preload ratio $F_{\min}/F_0$ and inherent damping β_{i}.
2. Calculate A_{y} using Equation (4-3) and D_{y} using Equation (4-2).
3. Calculate $A_{\min}=F_{\min}/m=A_{\mathrm{y}}(F_0/F_{\mathrm{y}})(F_{\min}/F_0)$.
4. Calculate $A_0=A_{\mathrm{y}}(F_0/F_{\mathrm{y}})$.
5. Assume the maximum displacement of the system D.
6. Calculate the effective period T_{eff} using Equation (5-1).
7. Calculate the effective damping ratio β_{eff} using Equation (5-3).
8. Calculate the damping parameter B using Table 5-2.
9. Obtain the maximum acceleration $S_{\mathrm{ae}}(T_{\mathrm{eff}}, \beta_{\mathrm{i}}=0.05)$ from the 5%-damped response spectrum.
10. Calculate the spectral displacement S_{d}:
$$S_{\mathrm{d}} = \left(\frac{T_{\mathrm{eff}}}{2\pi}\right)^2 \cdot \frac{S_{\mathrm{ae}}(T_{\mathrm{eff}}, \beta = 0.05)\, g}{B} \tag{5-17}$$
where g is the gravity acceleration.
11. Compare the assumed displacement D to the calculated displacement S_{d}. Repeat the steps 5 to 10 until the assumed displacement value is sufficiently close to the calculated value.
12. Calculate the maximum velocity using Equation (5-10).
13. Calculate the maximum acceleration using Equations (5-12) to (5-16).

5.4 Comparison of Results of Simplified Analysis to Results of Response History Analysis

The availability of a large collection of response history analysis results from Section 4 facilitates comparison to simplified analysis results. The figures that follow compare the average of the peak response calculated in the response history analysis (distinguished by the type of excitation used: far-field, near-fault pulse-like and near-fault non-pulse-like; and DE and MCE level) to the simplified analysis results. Typical in all figures is that the vertical axis of each graph shows the response history analysis results and the horizontal axis the simplified analysis results.

Figure 5-3 compares the peak acceleration, displacement and velocity for all analyzed cases with linear viscous damping of $\beta_v = 0.1$ and $F_0/F_y = 0.2$ (all values of period T_e and R_μ).

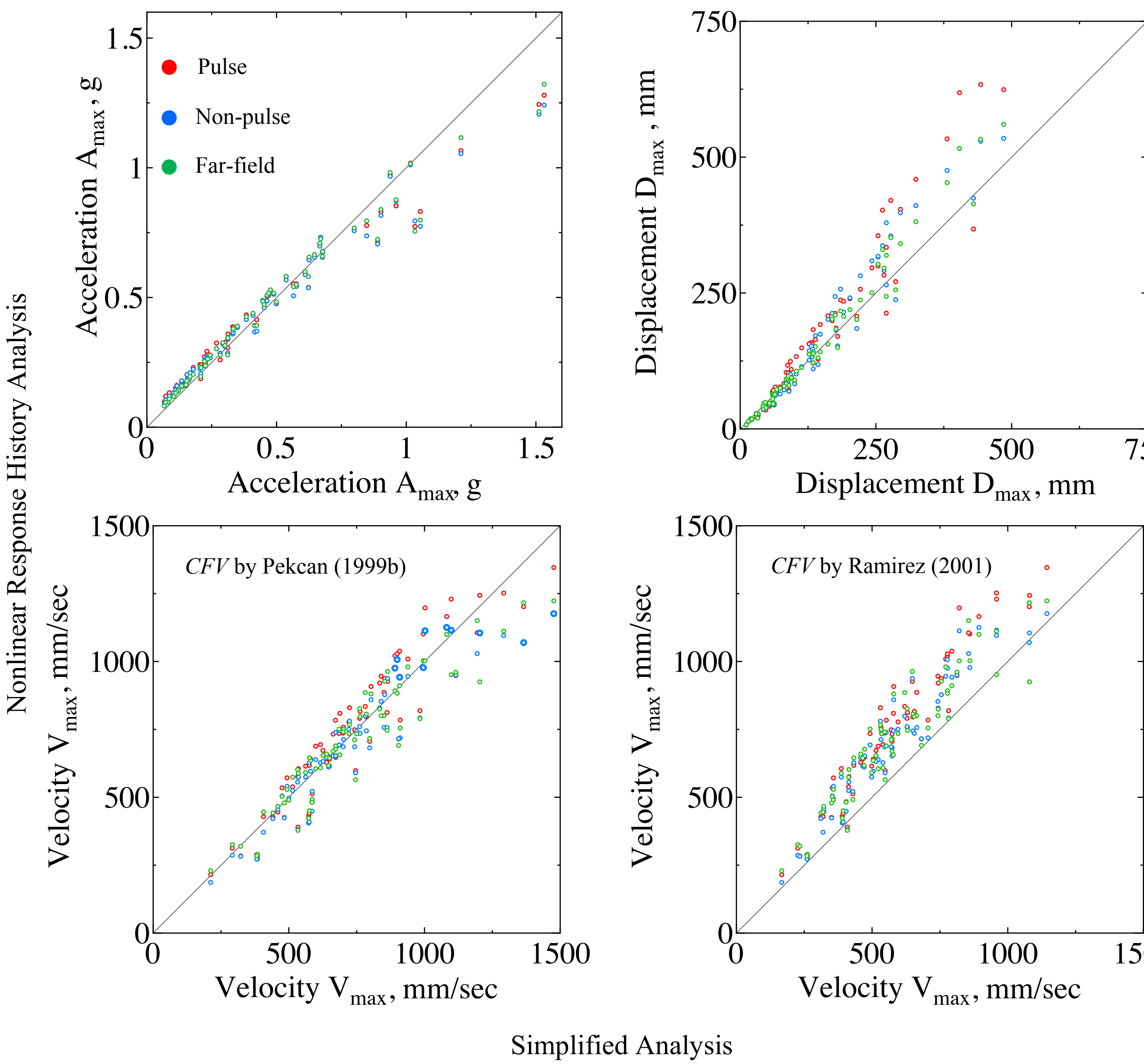

Figure 5-3 Comparison of Response History Analysis Results to Simplified Analysis Results for all Cases with Linear Viscous Damping, $\beta_v = 0.1$ and $F_0/F_y = 0.2$. Distinction by Type of Motion (DE and MCE, Pulse-like, Non-Pulse-like, Far-field)

The peak velocity correction factors of Ramirez et al (2001) and of Pekhan et al (1999b) are utilized. The data in Figure 5-3 are distinguished by the type of motion: far-field, near-fault pulse-like and near-fault non-pulse-like. Figures 5-4 and 5-5 show the same results but the distinction is based on the value the elastic period and of R_μ, respectively.

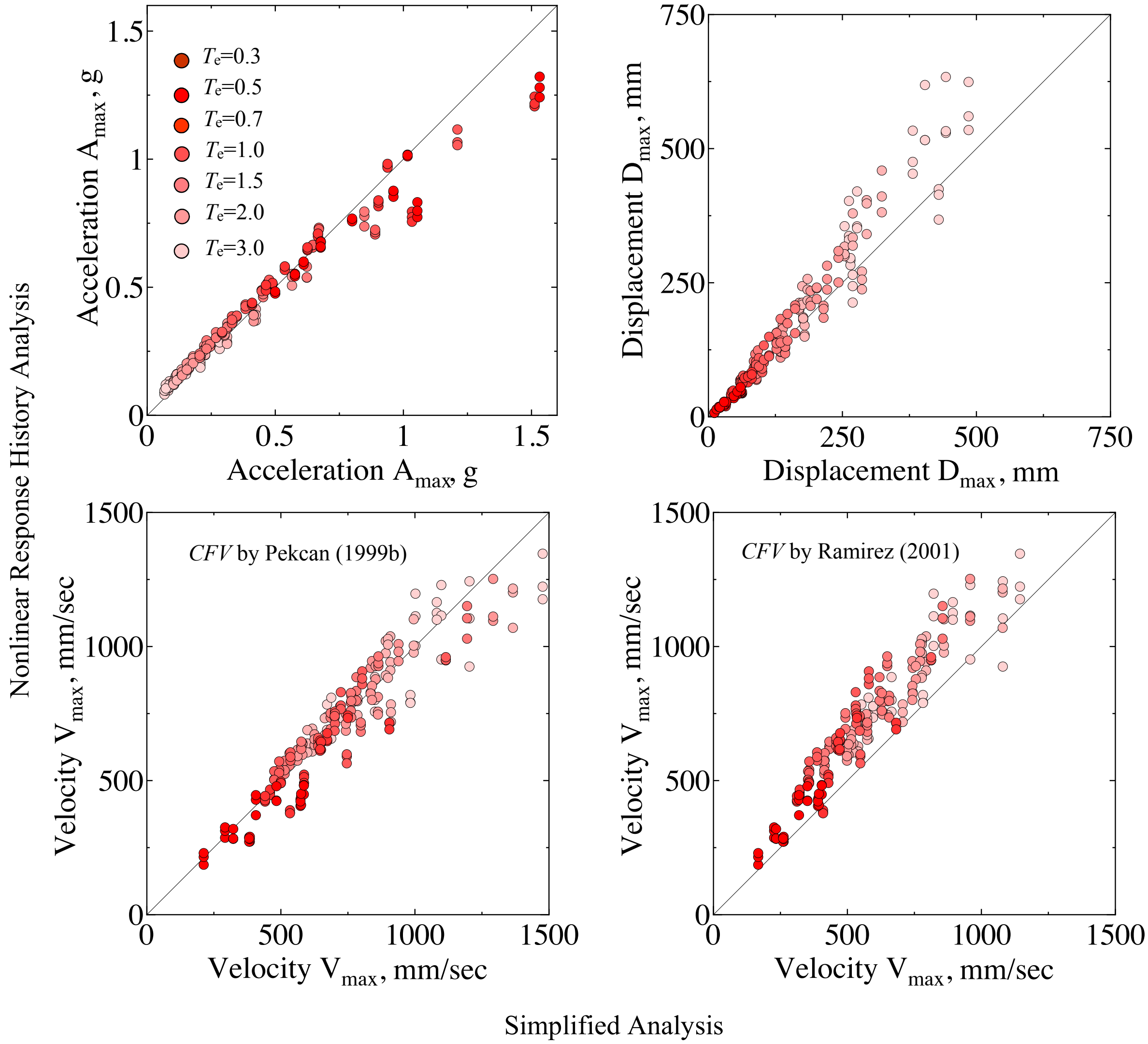

Figure 5-4 Comparison of Response History Analysis Results to Simplified Analysis Results for all Cases with Linear Viscous Damping, β_v = 0.1 and F_0/F_y = 0.2. Distinction by Value of Elastic Period (DE and MCE, Pulse-like, Non-Pulse-like, Far-Field)

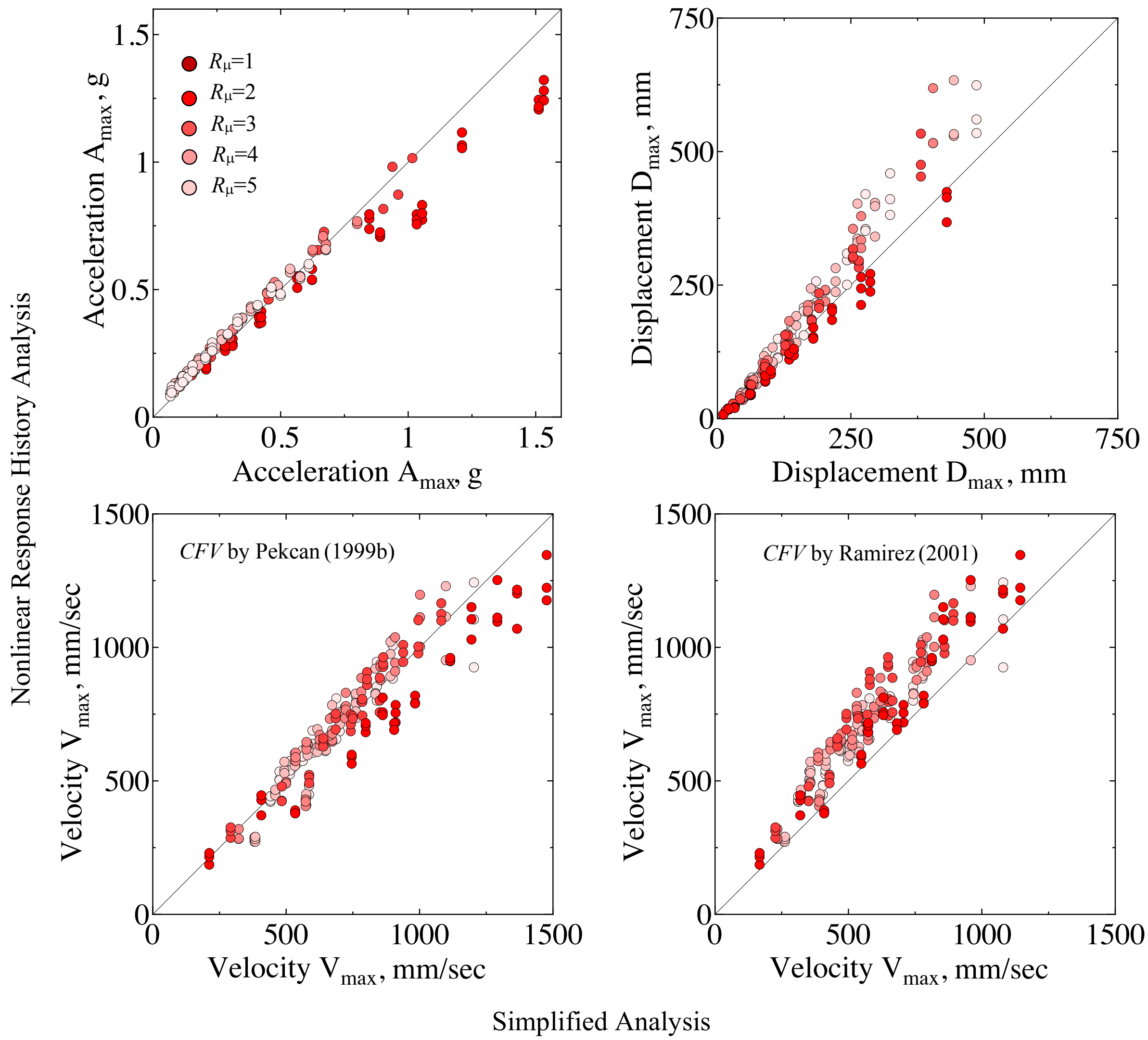

Figure 5-5 Comparison of Response History Analysis Results to Simplified Analysis Results for all Cases with Linear Viscous Damping, β_v = 0.1 and F_0/F_y = 0.2. Distinction by Value of R_μ (DE and MCE, Pulse-like, Non-Pulse-like, Far-field)

Similar to Figures 5-3 to 5-5, Figures 5-6 to 5-8 compare peak response for the same parameters but with F_0/F_y = 0.1 instead of 0.2.

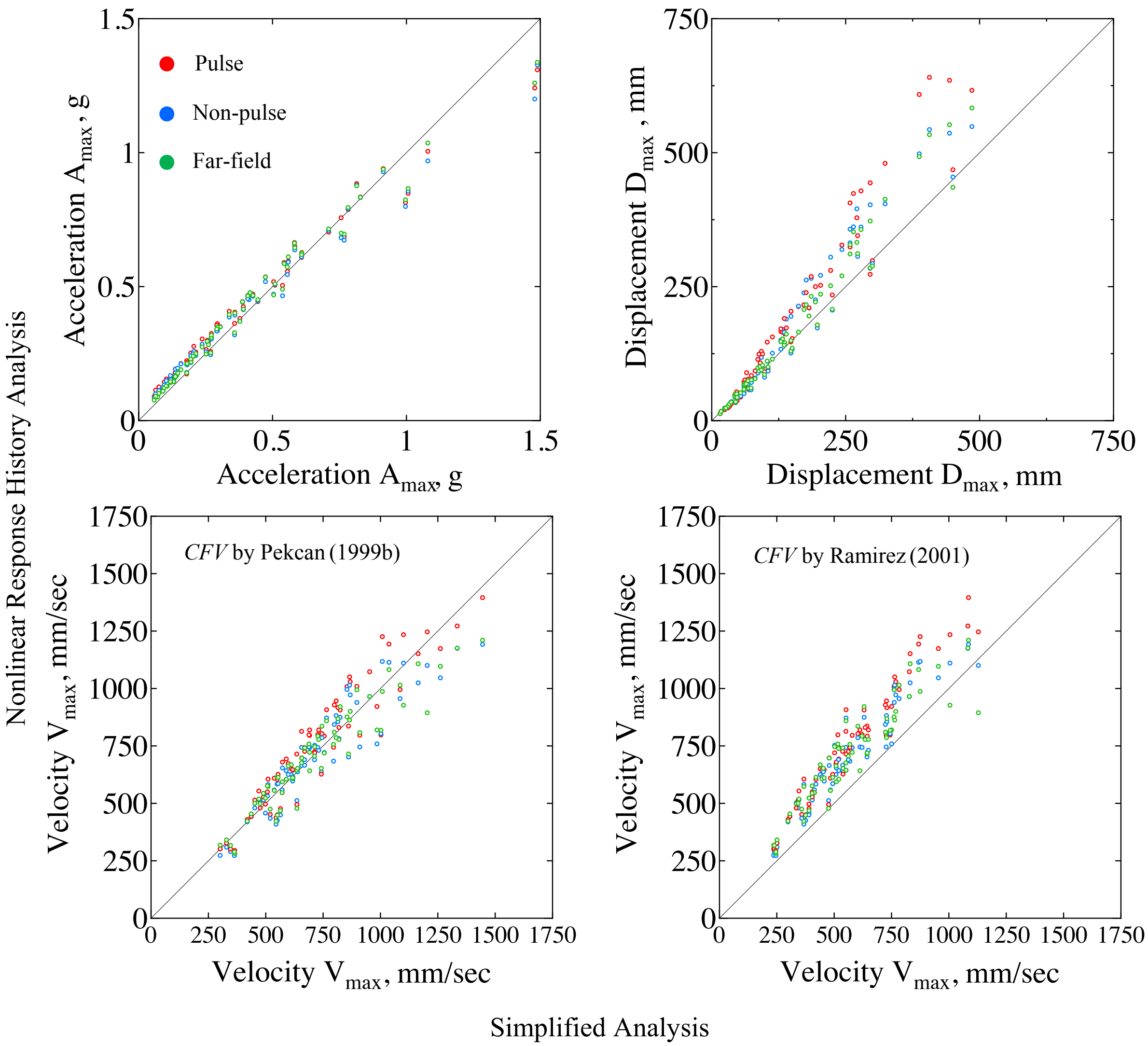

Figure 5-6 Comparison of Response History Analysis Results to Simplified Analysis Results for all Cases with Linear Viscous Damping, $\beta_v = 0.1$ and $F_0/F_y = 0.1$. Distinction by Type of Motion (DE and MCE, Pulse-like, Non-pulse-like, Far-field)

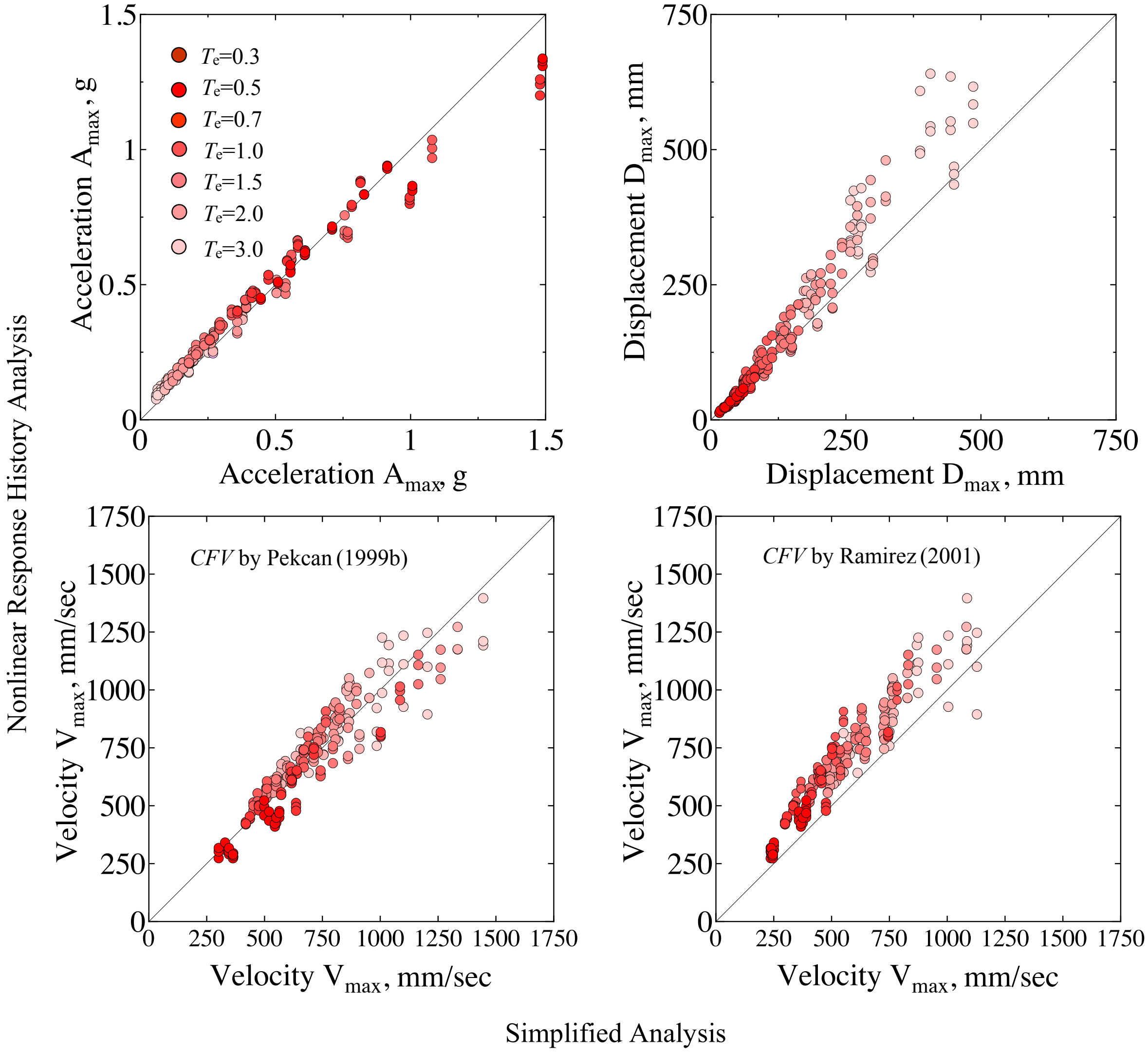

Figure 5-7 Comparison of Response History Analysis Results to Simplified Analysis Results for all Cases with Linear Viscous Damping, β_v = 0.1 and F_0/F_y = 0.1. Distinction by Value of Elastic Period (DE and MCE, Pulse-like, Non-pulse-like, Far-field)

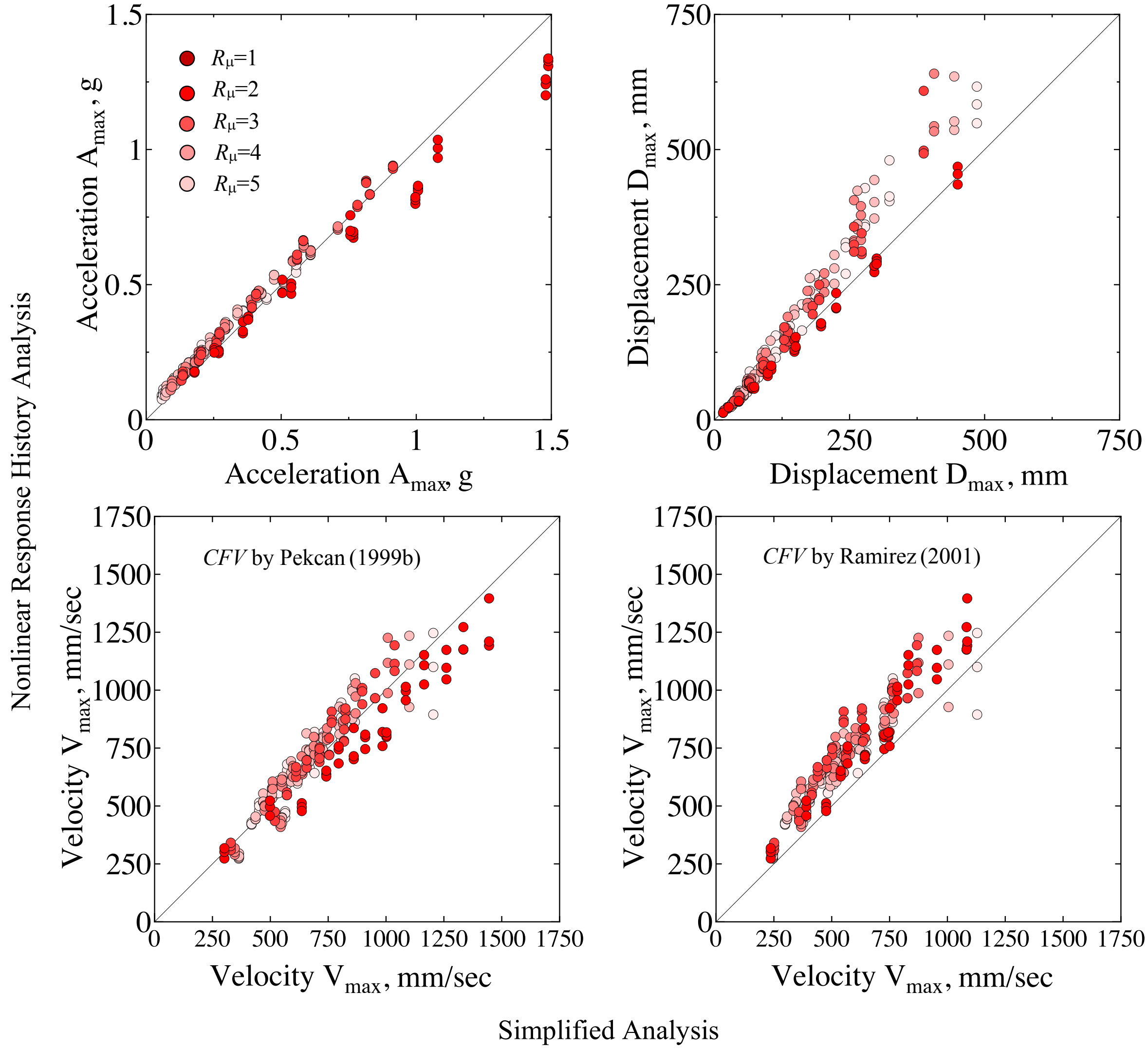

Figure 5-8 Comparison of Response History Analysis Results to Simplified Analysis Results for all Cases with Linear Viscous Damping, β_v = 0.1 and F_0/F_y = 0.1. Distinction by Value of R_μ (DE and MCE, Pulse-like, Non-pulse-like, Far-field)

Figures 5-9 to 5-11 present a comparison of results for the cases of linear viscous damping with β_v = 0.2 and F_0/F_y = 0.2 and again distinguishing the results by the type of motion, value of elastic period and value of R_μ.

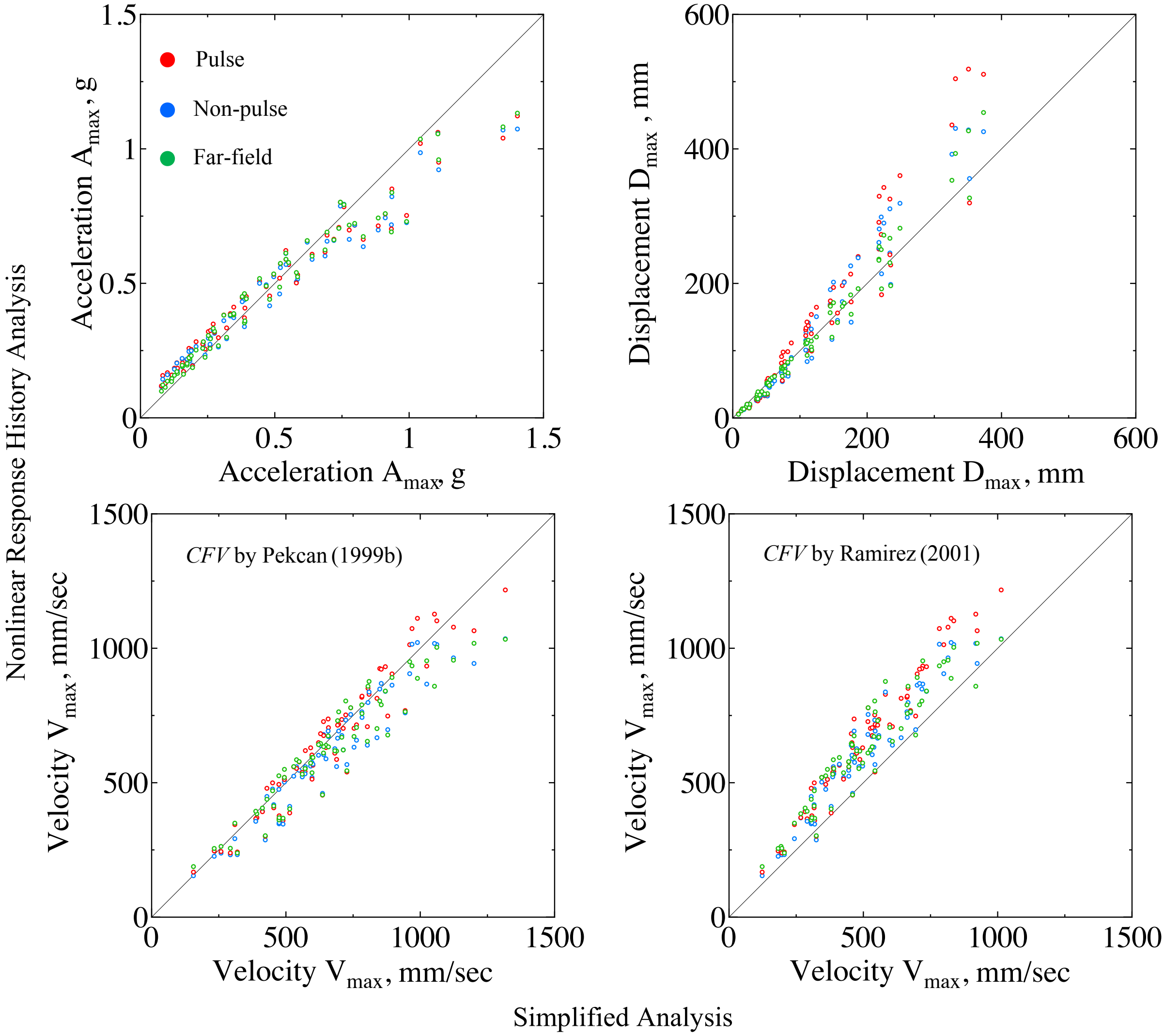

Figure 5-9 Comparison of Response History Analysis Results to Simplified Analysis Results for all Cases with Linear Viscous Damping, β_v = 0.2 and F_0/F_y = 0.2. Distinction by Type of Motion (DE and MCE, Pulse-like, Non-pulse-like, Far-field)

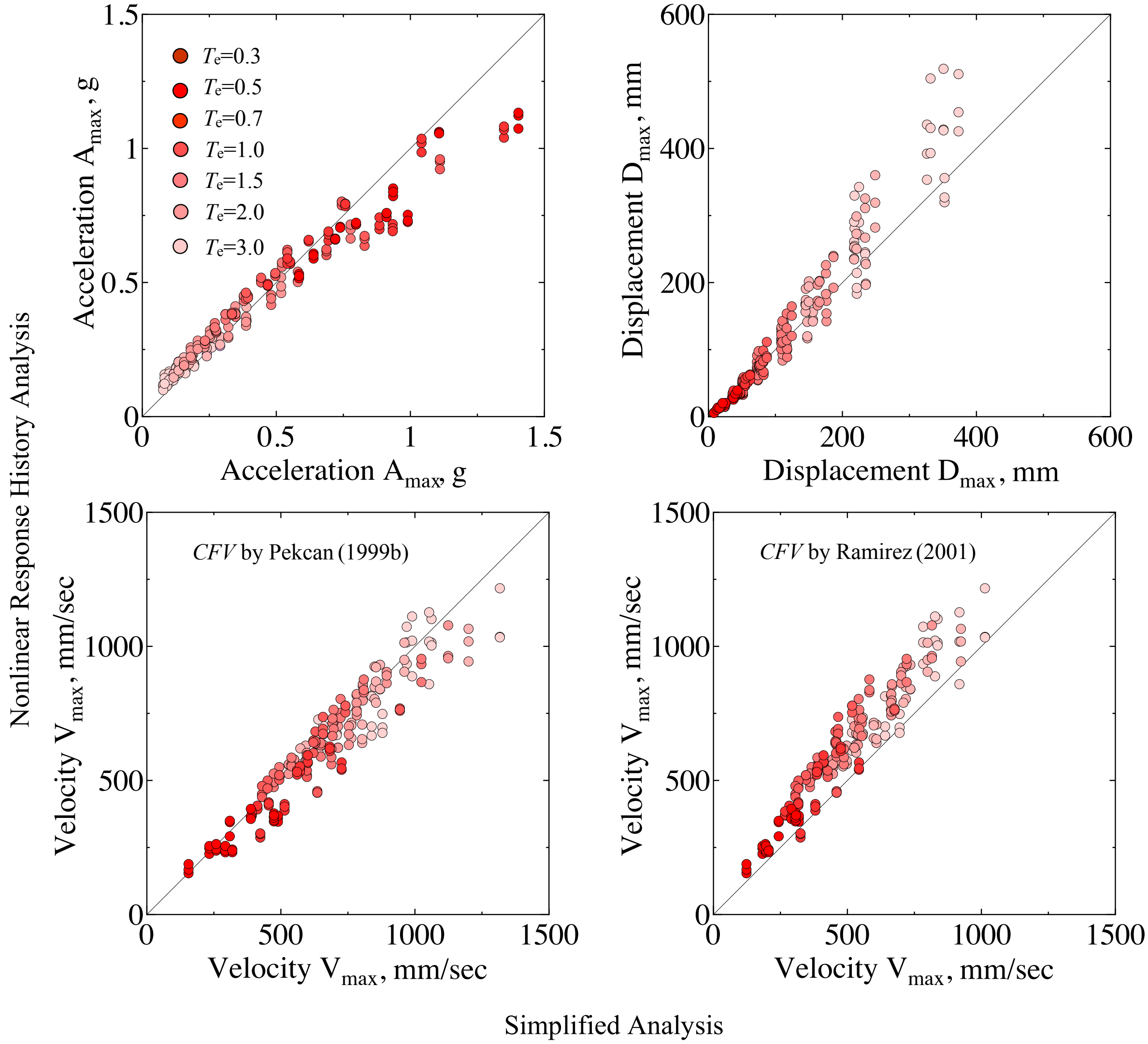

Figure 5-10 Comparison of Response History Analysis Results to Simplified Analysis Results for all Cases with Linear Viscous Damping, β_v = 0.2 and F_0/F_y = 0.2. Distinction by Value of Elastic Period (DE and MCE, Pulse-like, Non-pulse-like, Far-field)

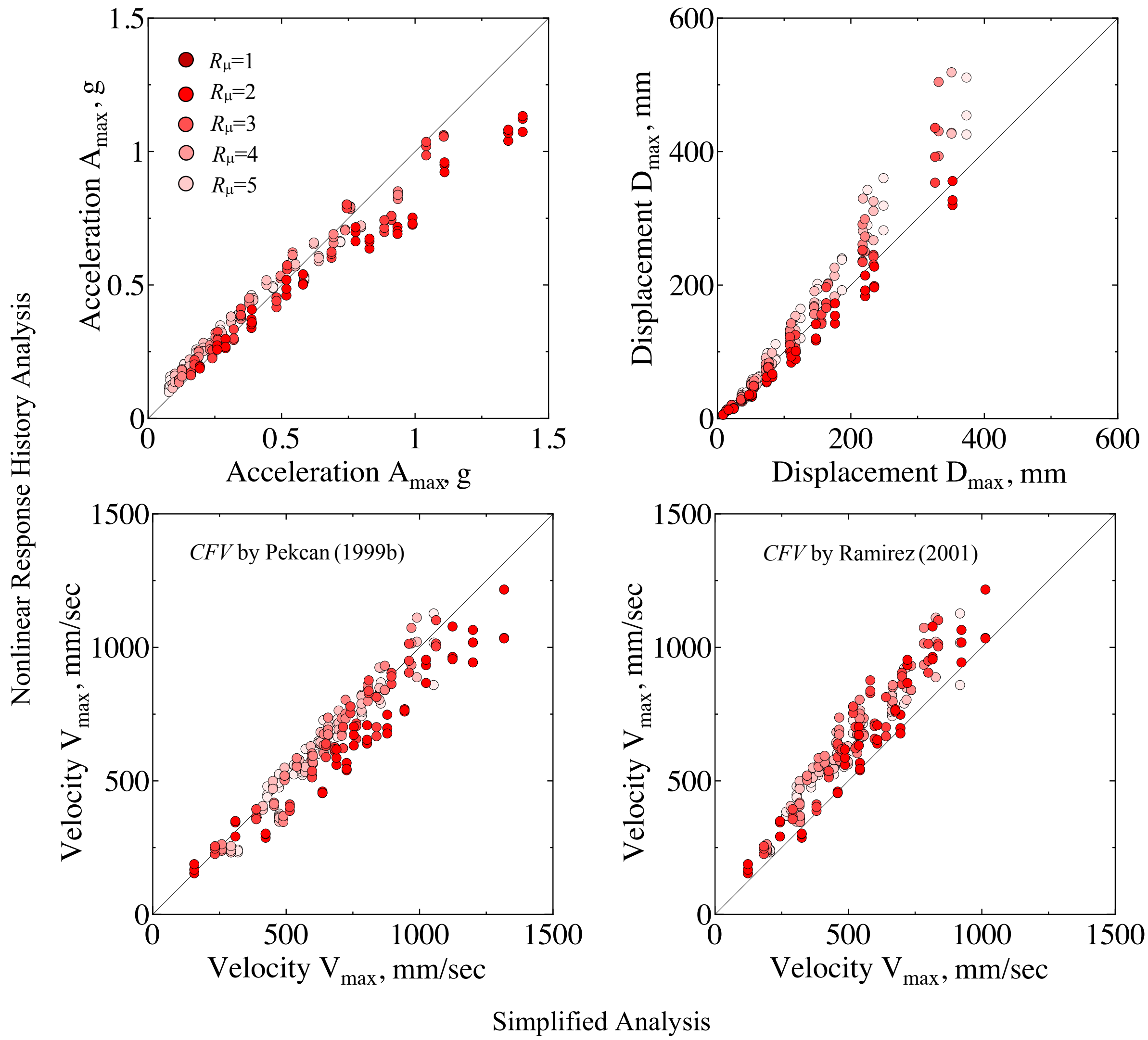

Figure 5-11 Comparison of Response History Analysis Results to Simplified Analysis Results for all Cases with Linear Viscous Damping, β_v = 0.2 and F_0/F_y = 0.2. Distinction by Value of R_μ (DE and MCE, Pulse-like, Non-pulse-like, Far-field)

Figures 5-12 to 5-14 present a comparison of results for the cases of nonlinear viscous damping with β_v = 0.1 and F_0/F_y = 0.2 and again distinguishing the results by the type of motion, value of elastic period and value of R_μ.

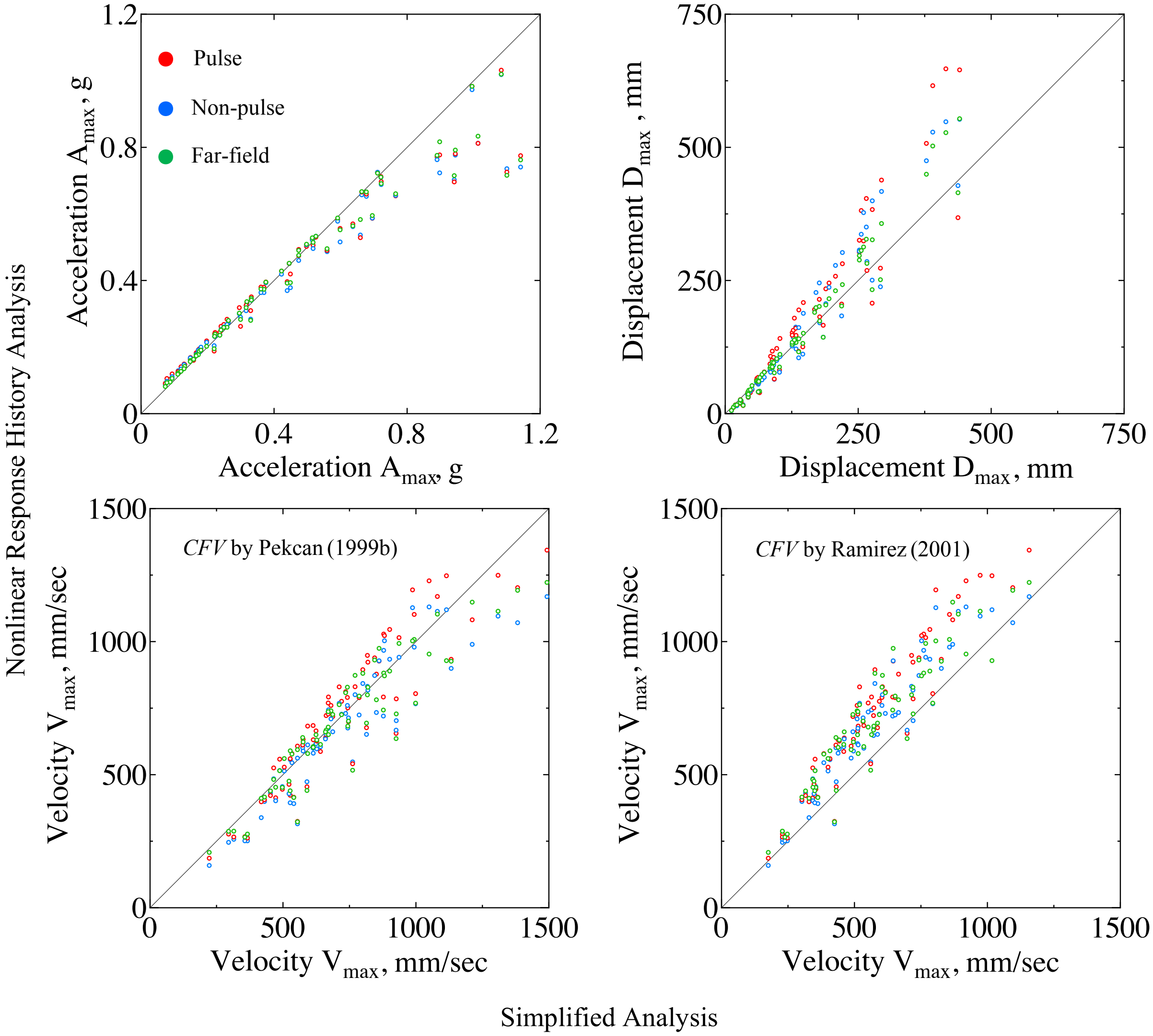

Figure 5-12 Comparison of Response History Analysis Results to Simplified Analysis Results for all Cases with Nonlinear Viscous Damping, β_v = 0.1 and F_0/F_y = 0.2. Distinction by Type of Motion (DE and MCE, Pulse-like, Non-pulse-like, Far-field)

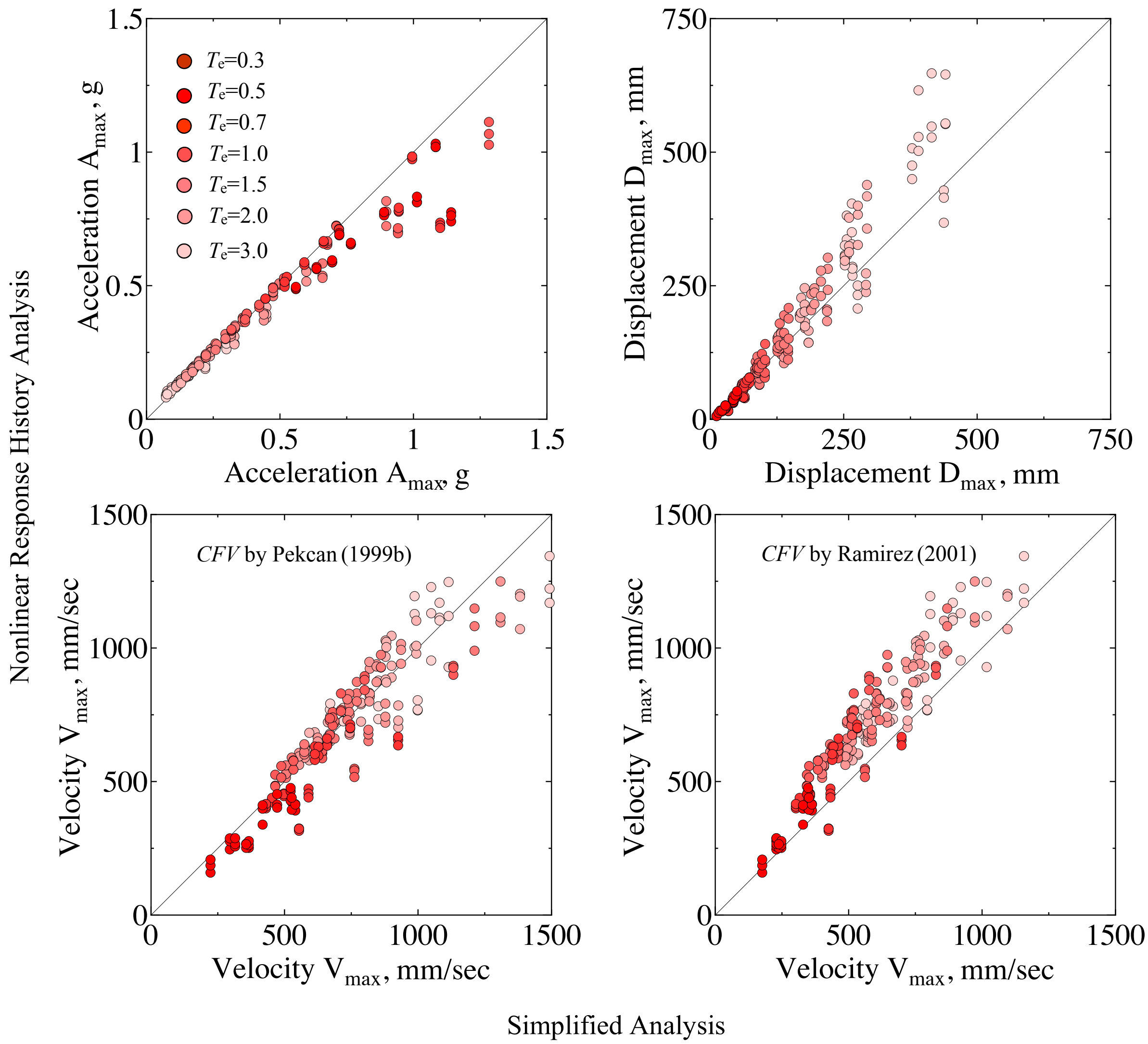

Figure 5-13 Comparison of Response History Analysis Results to Simplified Analysis Results for all Cases with Nonlinear Viscous Damping, β_v = 0.1 and F_0/F_y = 0.2. Distinction by Value of Elastic Period (DE and MCE, Pulse-like, Non-pulse-like, Far-field)

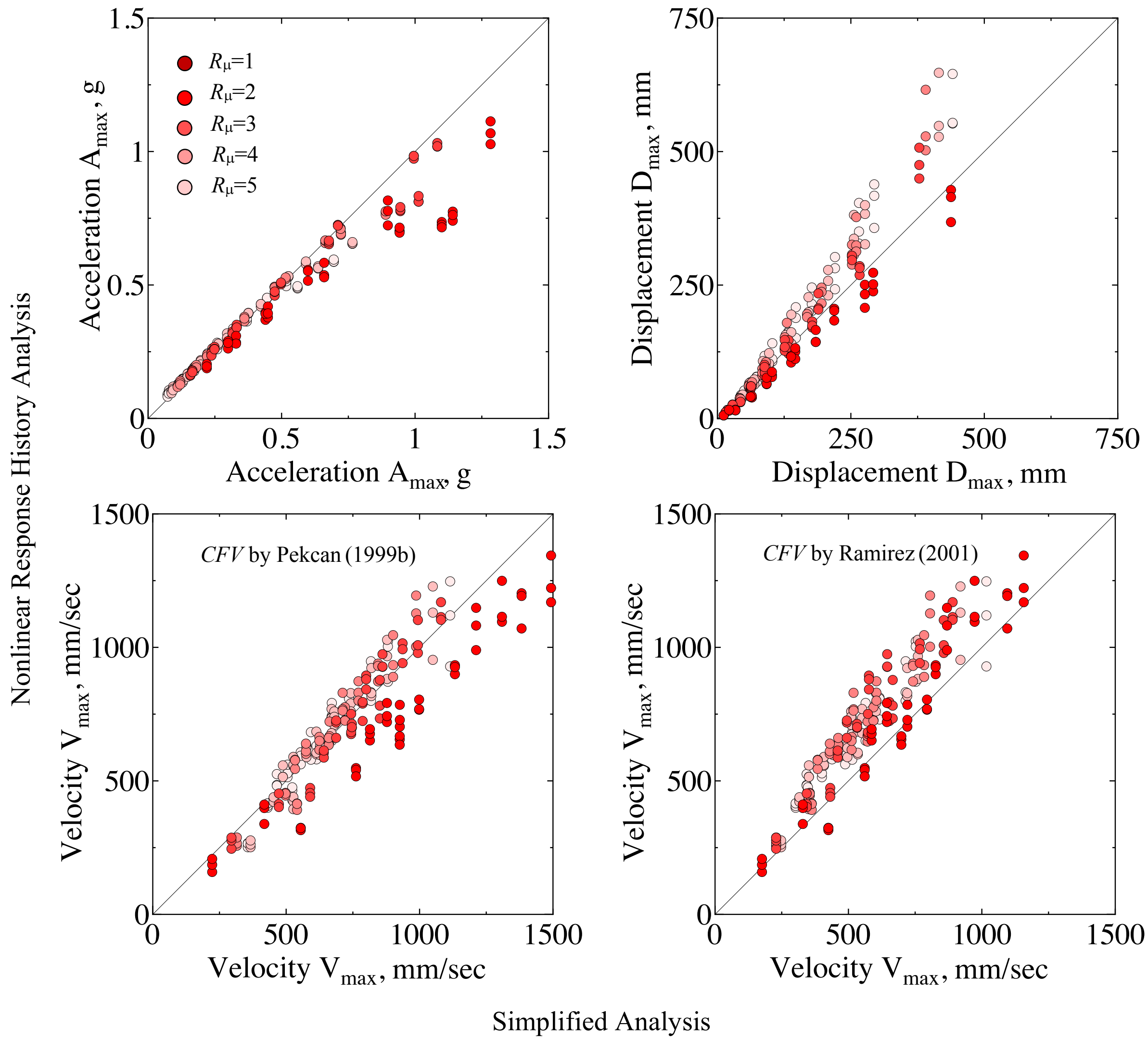

Figure 5-14 Comparison of Response History Analysis Results to Simplified Analysis Results for all Cases with Nonlinear Viscous Damping, β_v = 0.1 and F_0/F_y = 0.2. Distinction by Value of R_μ (DE and MCE, Pulse-like, Non-pulse-like, Far-field)

The results show a systematic conservatism in the simplified analysis prediction of the peak acceleration, which appears to increase with increasing ratio of F_0/F_y. This is explained by the fact that Equation (5-13) is based on the assumption of elasto-plastic behavior, which is true only when the self-centering system stiffness K_0=0. In the case of the analyzed system with stiffness such that the spring force at the maximum displacement is equal to the preload and when F_0/F_y=0.2, Equation (5-13) may be revised to approximately be

$$A_{\max} = \left(0.85A_{\mathrm{D}} + 0.15A_{\mathrm{D}}\cos\delta\right)\cdot CF_1 + 0.85A_{\mathrm{D}}\cdot\frac{2\pi\beta_{\mathrm{veff}}}{\lambda}\cdot CF_2 \quad (5\text{-}18)$$

where

$$A_{\mathrm{D}} = A + A_{\min} + A_0 + \frac{K_0 D}{m} \quad (5\text{-}19)$$

Equation (5-18) is based on the fact that the maximum viscous damping force occurs when the displacement is equal to $D \cos\delta$ (Ramirez *et al*., 2001) and that the ratio of the lateral force, excluding the viscous component, at displacement $D\cos\delta$ to the lateral force at displacement D is about equal to 0.85 (for the system with stiffness such that the spring force at the maximum displacement is equal to the preload and when F_0/F_y=0.2). Equations (5-18) and (5-19) predict slightly less acceleration than Equation (5-13). However, the difference is not significant and the conservatism of Equation (5-13) is preferred for a simplified analysis method.

5.5 Conclusions

The results in Figures 5-3 to 5-14 systematically show that the simplified methods predict accurately or conservatively the peak acceleration for all cases. The peak displacement is also predicted well by the simplified method except for the cases of flexible systems (elastic period of 3sec) in near-fault, pulse-like motions where the simplified method under-predicts the displacement. This is consistent with the observations of Pant et al. (2013) who studied displacement demands in seismic isolation systems. Interestingly, the peak velocity tends to be predicted well or overestimated when the correction factor of Pekhan et al. (1999b) is used and it tends to be predicted well or underestimated when the correction factor of Ramirez et al. (2001) is used. The average of the two correction factors provides a better corrector for the pseudo-velocity to predict the peak velocity in all cases. This is shown in Figure 5-15 where the maximum velocity calculated by the response history analysis and the simplified analysis are again compared for the four cases analyzed. In the simplified calculation, the *CFV* used was the average of the *CFV* obtained from Equation (5-11) and from Table 5-3.

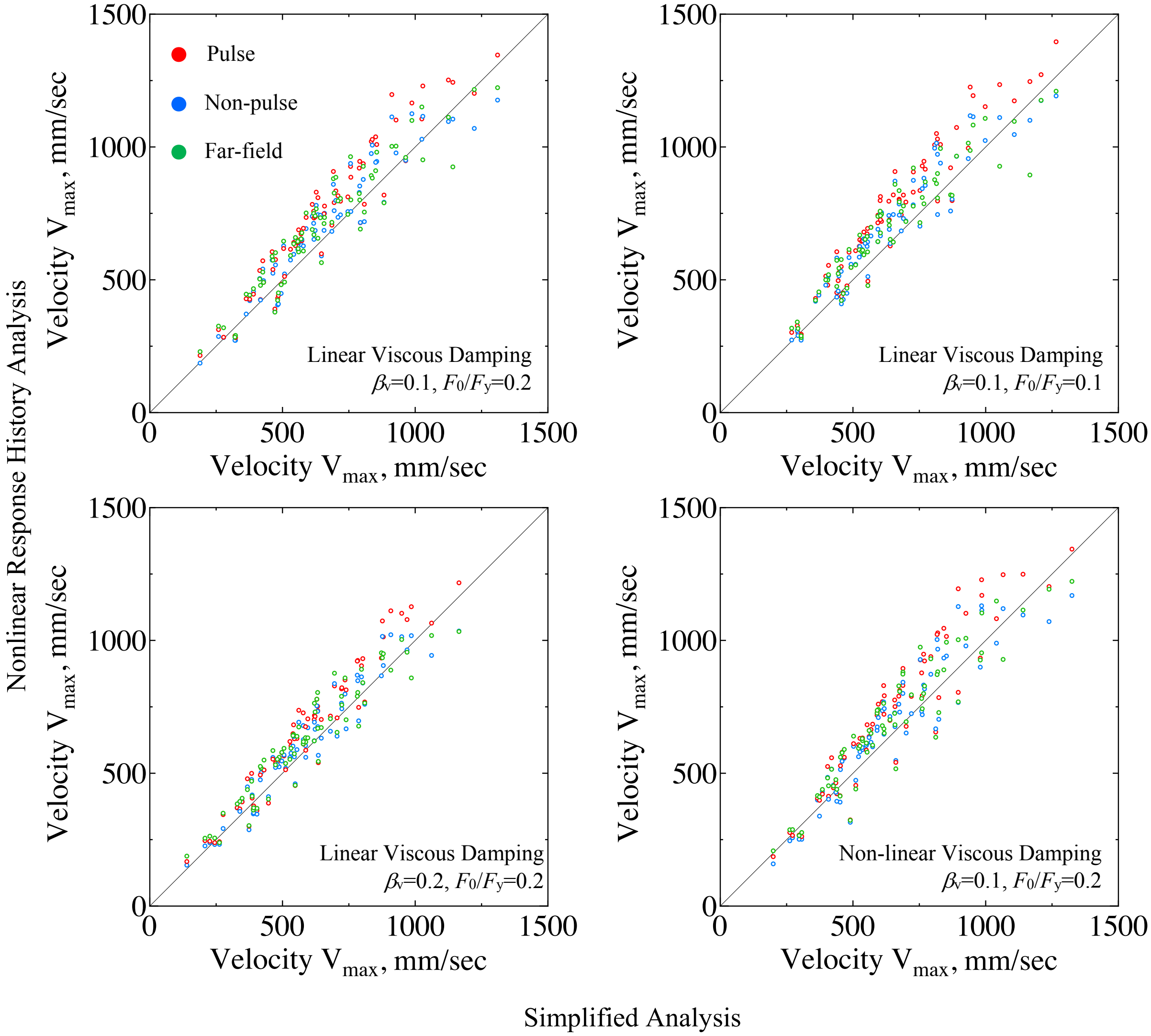

Figure 5-15 Comparison of Peak Velocity Calculated by Response History and Simplified Analysis for all Cases and using Average Values of *CFV*. Distinction by Type of Motion (DE and MCE, Pulse-like, Non-pulse-like, Far-field).

SECTION 6

DEVELOPMENT OF EQUIVALENT LATERAL FORCE AND RESPONSE SPECTRUM ANALYSIS PROCEDURES FOR NEW BUILDINGS WITH FLUIDIC SELF-CENTERING DEVICES

6.1 Introduction

This section presents an approach for the design and analysis of buildings with fluidic self-centering devices. The approach parallels that of buildings with damping systems in Chapter 18 of ASCE 7-2010, the development of which is described in Ramirez et al. (2001).

The fluidic self-centering devices are added to the primary structural system which is designed for prescribed forces exclusive of the added self-centering system. The primary structural system need not meet any criteria for drift. The addition of the self-centering system provides a prescribed minimum amount of preload to minimize or eliminate any residual deformations. The preload and the additional stiffness and damping provided by the self-centering system result in acceptable drifts. The presented Equivalent Lateral Force (ELF) and Response Spectrum Analysis (RSA) procedures can then be used to calculate the displacement and force demands so that an adequacy assessment of the building is performed.

The ELF and RSA procedures require the following assumptions, which are common to the procedures used for buildings with damping systems:

1) The building is designed to have a proper collapse mechanism so that the distribution of drift may be reasonably estimated on the basis of either eigenvalue analysis under elastic conditions or simple assumptions (like inverted triangular distribution).
2) The building is analyzed in each principal direction with a single degree of freedom per floor.
3) The behavior can be represented by an elasto-plastic model.
4) The yield strength of the building can be obtained by (a) plastic analysis, (b) pushover analysis, or (c) using a specified minimum seismic base shear and values of the response modification factor (R), the system over-strength factor (Ω) and the deflection amplification factor (C_d).

6.2 Minimum Allowable Base Shear, Minimum Preload and Minimum Damping

Buildings codes (e.g., standard ASCE 7) specify a base force for the design of the lateral seismic force-resisting system. The value of the base shear is dependent on the design spectrum, the response modification factor R, the risk category (importance factor) and the period of the structure. Moreover, the building codes specify drift limits, and prescribe procedures of how to distribute the force for analysis and how to calculate the drift.

For buildings with damping systems, ASCE 7-2010 prescribes a minimum allowable base shear force that is equal to $0.75V$, where V is the base shear prescribed for the building exclusive of the damping system. The rationale for this minimum value was presented and justified in Ramirez *et al*. (2001). In the simplest possible terms, factor 0.75 is the inverse of parameter B=1.35 per Table 5-2 corresponding to a damping ratio of 0.15. That is, an added viscous damping β_V=0.10 under elastic conditions would be required for a total, including inherent damping, of 0.15.

The same approach is recommended for the design of buildings with fluidic self-centering devices. Moreover, a minimum value of preload is recommended as described below. That is, the recommended approach for design of buildings with fluidic self-centering devices is:

1) Design the building exclusive of the self-centering system for a base shear force not less than V_{min} given by Equation (6-1) where V is determined in accordance with Section 12.8 of ASCE 7-2010 for the structural system selected.

$$V_{\min} = 0.75V \tag{6-1}$$

2) Provide a preload at each story level in each principal direction equal to or larger than 0.2 times of the story shear yield strength. The story shear yield strength is defined as the shear force at which gross inelastic action commences. It is determined by plastic or pushover analysis.

3) Provide viscous damping in linear or nonlinear form with damping ratio $\beta_V \geq 0.10$ in the fundamental mode of vibration, under elastic conditions and in each principal direction of the building. The damping may be shaped as upper half or similar to upper half as described in Sections 2 and 3 of this report. The calculation of the damping ratio is presented later in this report.

The rationale for providing a preload at least equal to 0.20 times the story shear yield strength is based on the results of analysis in Section 4 where such a preload resulted in very small or trivial residual deformations in the Design Earthquake and acceptably small residual deformations in the Maximum Earthquake. The minimum damping ratio of 0.10 justifies the use of Equation (6-1) and is consistent with observations in the results of analysis in Section 4 related to the effect of viscous damping on the maximum displacement.

Equation (6-1) provides the seismic base shear which is the result of lateral forces acting on the building when the first plastic hinge forms. When the design of the seismic-force-resisting system is based on plastic analysis principles, the required base shear strength V_y is needed. The definition of parameters and the relation between parameters is illustrated in Figure 6-1 (adapted from Figure 7-1 of Ramirez *et al.*, 2001). Note that T_1 is the period of the building under elastic conditions.

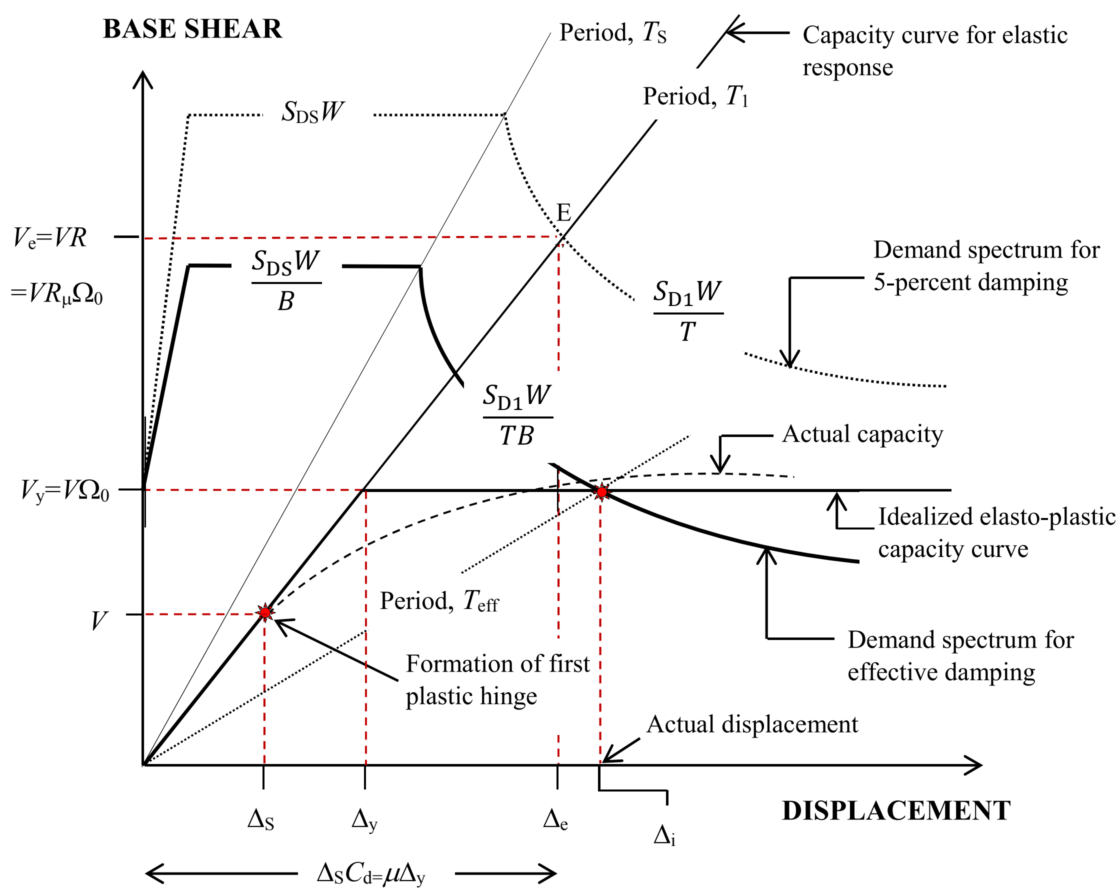

Figure 6-1 Force-displacement Relations, Demand Curves and Structural Response Parameters

Based on Figure 6-1, the lateral load and corresponding displacement at the formation of the first plastic hinge in the frame are V and Δ_S, respectively. The yield strength and yield displacement of the idealized building frame are V_y and Δ_y, respectively. The required elastic strength and maximum elastic displacement are V_e and Δ_e, respectively; and the maximum inelastic displacement is Δ_i. As drawn, the maximum inelastic displacement is greater than the elastic displacement Δ_e (and thus at odds with the displacement calculated using the ASCE 7 deflection amplification factor C_d, which is less than factor R). Note that lateral load V is equal to the design lateral force that is given by V_e divided by R. Simple relationships for the idealized yielding system have been presented in Ramirez *et al*. (2001) but are repeated below to aid in the presentation. The displacement ductility ratio (μ), response modification factor (R), over-strength factor (Ω_0), ductility-based portion of the R factor (R_μ), and the deflection amplification factor (C_d) are equal to

$$\mu = \frac{\Delta_i}{\Delta_y} \tag{6-2}$$

$$R_\mu = \frac{V_e}{V_y} \tag{6-3}$$

$$\Omega_0 = \frac{V_y}{V} \tag{6-4}$$

$$R = \frac{V_e}{V} = R_\mu \cdot \Omega_0 \tag{6-5}$$

$$C_d = \frac{D_i}{D_s} = \mu \cdot \Omega_0 \tag{6-6}$$

On the basis of Equations (6-1) and (6-4), $V_y = V_{min}\Omega_0$. However, this equation would be valid if factors R and C_d were correctly specified to be equal. Until such inconsistency in the values of R and C_d is eliminated, ASCE 7-2010 (based on Ramirez *et al*., 2001) presents equations which imply that

$$V_y = V_{min}\Omega_0 \frac{C_d}{R} \tag{6-7}$$

Equation (6-7) is used in the examples presented in this report to arrive at the required base shear strength of the example buildings. Plastic analysis principles are then used to size the seismic-force-resisting system to have base shear strength V_y and an acceptable collapse mechanism.

The displacement ductility ratio μ is related to factors R and Ω_0 as follows. In the constant velocity region of the spectrum ($T_1 \geq T_S$), the equal displacement assumption may be used (Newmark and Hall, 1982), so that $D_i = D_e$. It follows that

$$\mu = R_\mu,\ T_1 \geq T_s \tag{6-8}$$

In the constant acceleration region of the spectrum ($T<T_s$), the equal energy assumption may be used, so that

$$\mu = \frac{1}{2}\left(R_\mu^2 + 1\right) \quad , T_1 < T_s \tag{6-9}$$

Utilizing (6-5) and introducing the importance factor I_e (per ASCE 7-2010, Section 11.5.1) the maximum effective ductility demand is

$$\mu_{max} = \frac{R}{\Omega_0 \cdot I_e}, \quad T_{eff} \geq T_s \tag{6-10}$$

$$\mu_{max} = \frac{1}{2}\left[\left(\frac{R}{\Omega_0 I_e}\right)^2 + 1\right], \quad T_{eff} \leq T_s \tag{6-11}$$

Note that in (6-10) and (6-11), the effective period T_{eff} is introduced. This is the period of the fundamental mode of vibration of the structure in the direction of interest including the effect of the added self-centering system. The effective period will be described later in this report but in short is the effective period at the displaced position in the design earthquake.

6.3 Simplified Analysis of Elastic Buildings with Fluidic Self-Centering Devices

The analysis of buildings with fluidic self-centering devices follows the approach for buildings with damping systems developed in Ramirez *et al*. (2001) and implemented in ASCE 7-2010. The only difference is in the calculation of the period under elastic conditions.

Period T_1 and other modal parameters are obtained in analysis of the structure with the added fluidic self-centering devices where each device is represented by an effective stiffness $K_{eff,i}$ as shown in Figure 6-2. The stiffness is calculated as the force consisting of the preload plus the spring force at a device relative displacement corresponding to a story drift equal to the story yield displacement divided by the yield displacement. This will be further explained later in Section 6.4.

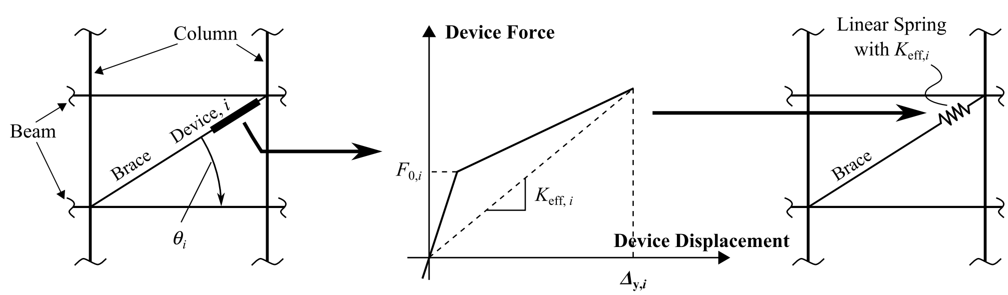

Figure 6-2 Definition of Effective Stiffness of Fluidic Self-Centering Device for Calculation of Period T_1, Inclusive of the Self-Centering System Effect

What follows is based on ASCE 7-2010 and Ramirez *et al*. (2001) together with a presentation of background information.

In general, a model of analysis of the building needs to be developed, including the preload and spring force effects of the fluidic self-centering devices as discussed above and illustrated in Figure 6-2, and excluding any viscous damping effects. An eigenvalue analysis needs to be performed to determine the frequencies (periods) of free vibration, mode shapes, seismic modal weights and modal participation factors.

The equations of motion may be written in the general form (Chopra, 2012)

$$\left[M\right]\{\ddot{u}\}+\left[K\right]\{u\}=-\left[M\right]\{l\}\,a_{\mathrm{g}} \tag{6-12}$$

where [M] is the mass matrix (diagonal with elements w_i/g if the degrees of freedom consist of only the horizontal displacements of masses w_i/g in the horizontal direction, where w_i is the reactive weight associate with degree of freedom u_i), [K] is the stiffness matrix, {u} is a vector containing displacements u_i, $\{\ddot{u}\}$is a vector of accelerations, $\ddot{u}_i$, {l} is the influence vector which becomes a unity vector when vector {u} consist of only the horizontal displacements of masses w_i/g and a_{g} is the horizontal ground acceleration.

The solution of the eigenvalue problem of (6-12) results in frequencies ω_m (the corresponding period, T_m *is* $2\pi/\omega_m$) and mode shapes $\{\phi\}_m$, where m varies between *1* and the number of degrees of freedom, *N*. The dynamic response of the building can be obtained by modal analysis as the superposition of modal responses by substituting in (6-12)

$$\{u\}=[\Phi]\{y\} \tag{6-13}$$

where {y} is the vector of modal displacements, [Φ] is a matrix having vectors $\{\phi\}_m$ as columns. Note that in (6-13), [Φ] is defined to be dimensionless so that {y} has dimensions of displacement. The use of the orthogonality conditions results in decomposition of (6-12) into N uncoupled equations of the form

$$\ddot{y}_m+\omega_m^2 y_m=-\Gamma_m a_{\mathrm{g}} \tag{6-14}$$

where Γ_m is the modal participation factor given by

$$\Gamma_m=\frac{\{\phi\}_m^T[M]\{l\}}{\{\phi\}_m^T[M]\{\phi\}_m} \tag{6-15}$$

Note that Equation (6-15) simplifies to the following form when vector {u} consist of only the horizontal displacements of masses w_i/g:

$$\Gamma_m = \frac{\sum_{i=1}^{N} w_i \cdot \phi_{im}}{\sum_{i=1}^{N} w_i \cdot \phi_{im}^2} \tag{6-16}$$

where ϕ_{im} is the element of mode shape m corresponding to degree of freedom u_i.

Equation (6-14) is used to calculate the peak values of y_m from the 5%-damped response spectrum of motion a_g (the modification of this approach for damped systems is discussed later in this report). Let the spectral displacement of motion a_g (5%-damped, frequency ω_m) be S_d and the corresponding spectral acceleration be S_a (note that $S_a = \omega_m^2 \cdot S_d$). It follows that the contribution to the displacement vector from mode m is

$$\{u\}_m = \Gamma_m \{\varphi\}_m S_d = \Gamma_m \{\varphi\}_m \frac{S_a}{\omega_m^2} \tag{6-17}$$

Moreover, the peak lateral inertia forces on the building contributed by mode m are given by

$$\{F\}_m = [M]\{\varphi\}_m \Gamma_m S_a \tag{6-18}$$

The result of these inertia forces or base shear is given by

$$V_m = \frac{\overline{W}_m S_a}{g} \tag{6-19}$$

where $\overline{W}_m$ is the m^{th} modal weight (or effective modal weight)

$$\overline{W}_m = \frac{(\{\phi\}_m^{\mathrm{T}}[M]\{l\})^2}{\{\phi\}_m^{\mathrm{T}}[M]\{\phi\}_m} \tag{6-20}$$

Equation (6-20) simplifies to the following form when vector $\{u\}$ consist of only the horizontal displacements of masses w_i/g:

$$\overline{W}_m = \frac{\left(\sum_{i=1}^{N} w_i \phi_{im}\right)^2}{\sum_{i=1}^{N} w_i \phi_{im}^2} = \Gamma_m \left(\sum_{i=1}^{N} w_i \phi_{im}\right) \tag{6-21}$$

It may be shown that

$$\sum_{m=1}^{N} \overline{W}_m = \sum_{i=1}^{N} w_i = W \tag{6-22}$$

That is, the sum of the modal weights equals the total weight W of the building. Moreover, it may be shown that for any i = 1 to N

$$\sum_{m=1}^{N} \phi_{im} \Gamma_m = 1 \tag{6-23}$$

Hereafter the mode shapes $\{\phi\}_m$ are normalized so that ϕ_{im} is equal to 1 at the roof level. Under this condition it can be shown that

$$\sum_{m=1}^{N} \Gamma_m = 1 \tag{6-24}$$

Equations (6-22) to (6-24) allow for a theoretically consistent simple definition of the residual mode that is used to approximate the contribution of the modes of vibration higher than the first mode. Specifically, the equivalent lateral force procedure for buildings with damping systems and also used herein for buildings with self-centering devices utilizes the contribution from the first mode and a residual mode of which the associated frequency is arbitrarily selected but the modal weight, modal participation factor and mode shape are determined on the basis of (6-22) to (6-24):

$$\overline{W}_{\mathrm{R}} = W - \overline{W}_1 \tag{6-25}$$

$$\Gamma_R = 1 - \Gamma_1 \tag{6-26}$$

$$\{\varphi\}_{\mathrm{R}} = \frac{1}{\Gamma_{\mathrm{R}}}\{1\} - \frac{\Gamma_1}{\Gamma_{\mathrm{R}}}\{\varphi\}_1 \tag{6-27}$$

Note that the residual mode shape $\{\varphi\}_{\mathrm{R}}$, as defined by (6-27), satisfies the orthogonality conditions. Per ASCE 7-2010, the period of the residual mode is arbitrarily defined as:

$$T_{\mathrm{R}} = 0.4T_1 \tag{6-28}$$

Consider now the effect of viscous damping in the fluidic self-centering devices. The damped system is non-classically damped and its frequencies (eigenvalues) and mode shapes (eigenvectors) are not those determined by eigenvalue analysis of the un-damped system. Nevertheless, the use of the un-damped frequencies and mode shapes together with energy-based calculation of the damping ratios provides good estimates of the seismic response of the damped structure. This is particularly true for buildings with complete vertical distributions of viscous damping devices (Constantinou and Symans, 1992). It may also be valid for cases of incomplete vertical distributions or cases of concentration of damping devices, whereas Constantinou and Symans (1992) demonstrated the validity of the approach in some cases of incomplete vertical distribution of damping devices.

The damping force in self-centering device j is given by the following relation for the of linear viscous damping

$$F_{\mathrm{D}j} = C_j \dot{u}_{\mathrm{D}j} \tag{6-29}$$

where C_j is the damping coefficient, $u_{\mathrm{D}j}$ is the device relative displacement and $\dot{u}_{\mathrm{D}j}$ is the relative velocity between the ends of the device along the axis of the device. Moreover, the relation between the device relative displacement and the inter-story drift $\Delta_{\mathrm{r}j}$ is

$$u_{\mathrm{D}j} = \Delta_{\mathrm{r}j} \cos\theta_j \tag{6-30}$$

where θ_j is the angle of inclination of device j (see Figure 6-2).

Modal damping ratios in a building can be calculated using energy principles (Chopra, 2012)

$$\beta = \frac{W_{\mathrm{D}}}{4\pi W_{\mathrm{s}}} \tag{6-31}$$

Following Ramirez *et al*. (2001), it is assumed that the building undergoes harmonic vibration such that

$$\{u\} = \Delta_{\mathrm{R}} \{\phi\}_m \sin\left(\frac{2\pi t}{T_m}\right) \tag{6-32}$$

where Δ_R is the amplitude of roof displacement; T_m is the m^{th} period of vibration; and $\{\phi\}_m$ is the m^{th} mode shape (normalized so that ϕ_{im} = 1 for i corresponding to the roof displacement), the energy dissipated by the damping system per cycle of motion in mode m is

$$W_{\mathrm{D}} = \frac{2\pi^2}{T_m} \sum_j C_j \cos^2\theta_j \Delta_{\mathrm{R}}^2 \phi_{\mathrm{r}j}^2 \tag{6-33}$$

where

$$\phi_{\mathrm{r}j} = \phi_{jm} - \phi_{(j-1)m} \tag{6-34}$$

Quantity $\phi_{\mathrm{r}j}$ the difference between the m^{th} modal ordinates associated with degrees of freedom j and (j-1). Note that (6-33) is based on $\Delta_{\mathrm{r}j} = \Delta_{\mathrm{R}}\phi_{\mathrm{r}j}$. The maximum strain energy W_{s} is calculated as the maximum kinetic energy,

$$W_{\mathrm{s}} = \frac{2\pi^2}{T_m^2} \sum_i \left(\frac{w_i}{g}\right) \Delta_{\mathrm{R}}^2 \phi_{im}^2 \tag{6-35}$$

The viscous damping ratio in mode m is given by

$$\beta_{\mathrm{v}m} = \left(\frac{T_m}{4\pi}\right) \frac{\sum_j C_j \cos^2\theta_j \phi_{\mathrm{r}j}^2}{\sum_i \left(\frac{w_i}{g}\right) \phi_{im}^2} \tag{6-36}$$

where the summation over i extends over all reactive weights and the summation over j extends over all damping devices. Equation (6-36) is identical to that given in Ramirez *et al*. (2001) except that $\cos\theta_j$ is used in lieu of the more general displacement amplification factor f_j.

Equation (6-36) may be also written in the following form where $[C]$ is the damping matrix formed by the contribution of linear viscous damping elements with respect to the vector of velocities $\{\dot{u}\}$ corresponding to the vector of displacements $\{u\}$ in Equation (6-12).

$$\beta_{\mathrm{v}m} = \left(\frac{T_m}{4\pi}\right)\frac{\{\phi\}_m^{\mathrm{T}}[\mathrm{C}]\{\phi\}_m}{\{\phi\}_m^{\mathrm{T}}[M]\{\phi\}_m} \tag{6-37}$$

For the case of nonlinear viscous damping, the force in each self-centering device is given by

$$F_{\mathrm{D}j} = C_{\mathrm{N}j}\left|\dot{u}_{\mathrm{D}j}\right|^{a_j}\,\mathrm{sgn}\left(\dot{u}_{\mathrm{D}j}\right) \tag{6-38}$$

where $C_{\mathrm{N}j}$ is the damping coefficient and a_j is the damping exponent. Equation (6-31) is still used to calculate the damping ratio, but the value will be amplitude-dependent. Based on vibration in the form of Equation (6-32),

$$W_{\mathrm{D}} = \sum_j \left(\frac{2\pi}{T_m}\right)^{a_j} C_{\mathrm{N}j}\lambda_j\left(\Delta_{\mathrm{R}}\cos\theta_j\phi_{\mathrm{r}j}\right)^{1+a_j} \tag{6-39}$$

where λ_j is given by (4-9) as function of the exponent a_j. Equation (6-35) is still valid so that the damping ratio for mode m=1 is given by

$$\beta_{\mathrm{v}1} = \frac{\sum_j (2\pi)^{a_j}\cdot T_1^{2-a_j}\cdot\lambda_j C_{\mathrm{N}j}\cos\theta_j^{1+a_j}\Delta_{\mathrm{R}}^{a_j-1}\phi_{\mathrm{r}j}^{1+a_j}}{8\pi^3\sum_i\left(\frac{w_i}{g}\right)\phi_{i1}^2} \tag{6-40}$$

Equation (6-40) reduces to (6-36) when a_j = 1 (linear viscous damping, for which $\lambda_j = \pi$).

When damping is of the upper half, linear or nonlinear viscous type, the damping ratio is determined by the same procedures as for the corresponding full damping cases. This is based on the observations of Section 3 analyses where the upper half damping case had an insignificant effect on the peak displacement demand by comparison to the full damping case. It had, however, a measurable effect in reducing the residual displacement so that it is useful.

Equations (6-36) or (6-37) and (6-40) are utilized for the simplified analysis of yielding buildings with self-centering devices by replacing period T_1 by the effective period T_{eff} in an approach that parallels that of buildings with damping systems.

6.4 Effective Period and Effective Damping of Yielding Buildings with Self-centering Devices

Analysis of the building with the self-centering system under inelastic structure conditions requires the use of the effective period and the effective damping at the calculated displacement demand. This analysis requires conversion of the pushover curve of the building to the spectral capacity curve.

For a multi-degree-of-freedom building, conversion of the pushover curve to a spectral capacity curve per Figure 6-3 results in:

$$A_y = \frac{V_y g}{\overline{\overline{W}}_1} \tag{6-41}$$

$$D_y = \frac{A_y T_1^2}{4\pi^2} = \frac{\Delta_{yR}}{\Gamma_1} \tag{6-42}$$

where V_y is the yield strength established by pushover or plastic analysis of the building using a pattern of lateral loads proportional to the first mode shape of the building for elastic conditions, D_y is the yield displacement in the spectral capacity curve, Δ_{yR} is the yield displacement in the pushover curve (the subscript R denotes roof displacement), Γ_1 is the first mode participation factor and T_1 is the fundamental mode period.

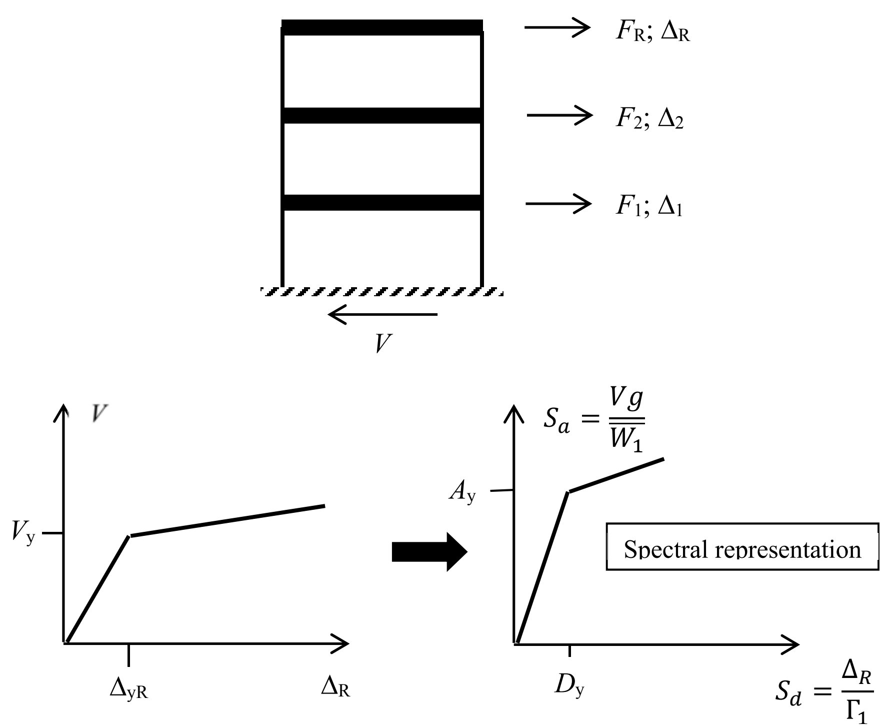

Figure 6-3 Transformation of Force-Displacement Relation to Spectral Capacity Relation

For a building with a fluidic self-centering system the shear force-roof displacement relation is shown in Figure 6-4. Note that the self-centering system viscous force effect is not depicted in this relation. This effect will be accounted for by increased damping of the building. Three force-displacement relations are shown in Figure 6-4: the relation of the building exclusive of the self-centering system, the effect of the self-centering system and the relation of the combined building and self-centering system. The dashed line represents an effective stiffness representation of the self-centering system effect as discussed in Section 6.3 and depicted in Figure 6-2. Note that it is assumed that the addition of the self-centering system does not affect the yield displacement Δ_{yR}. Accordingly, period T_1 calculated by the procedure described in Section 6.3 (and depicted in Figure 6-2) is the period of the building including the self-centering system effect valid for elastic building conditions.

Note that based on the design procedure described in Section 6.2, the preload is equal to 0.2 times the yield strength of the story, so that the effect of the preload on the base shear is equal to $F_{01}=0.2V_y$. Also, based on common configurations of fluidic self-centering devices (see Section 3), the spring force at maximum displacement is about equal to the preload. This simplifies the force at maximum displacement and results in a simple expression for the effective period.

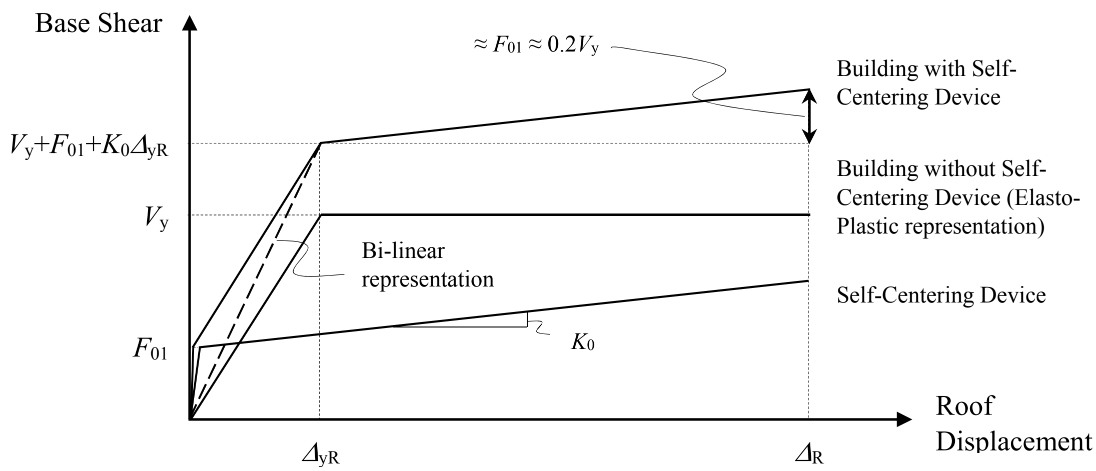

Figure 6-4 Force-Displacement Relations of Building with Fluidic Self-Centering System

The effective period (in the first mode of vibration) is given by the following equation in the spectral representation form

$$T_{\text{eff}} = 2\pi\sqrt{\frac{D}{A}} \tag{6-43}$$

where A is the spectral acceleration at maximum spectral displacement D. Based on Figure 6-4 and Equations (6-41) and (6-42), $A=(V_y+2F_{01})g/\overline{W}_1$ and $D=\Delta_R/\Gamma_1$, resulting in

$$T_{\mathrm{eff}} = T_1\sqrt{\mu}\sqrt{\frac{A_{\mathrm{y}} + A_{\mathrm{F0}}}{A_{\mathrm{y}} + 2A_{\mathrm{F0}}}} \tag{6-44}$$

In Equation (6-44), T_1 is the first mode period for elastic conditions and including the effect of the self-centering system as discussed in Section 6.3 and illustrated in Figure 6-2, A_{y} is defined by Equation (6-41) for the primary structural system (exclusive of the self-centering system), A_{F0} is defined by Equation (6-45) and μ is the displacement ductility ratio, defined by Equation (6-46):

$$A_{\mathrm{F0}} = \frac{F_{01}g}{\overline{\overline{W}}_1} \tag{6-45}$$

$$\mu = \frac{D}{D_{\mathrm{y}}} \tag{6-46}$$

Note that Equation (6-44) is based on the assumption that the ground floor self-centering system spring force at the maximum displacement is equal to the ground floor preload. If the spring force is zero, then term $\sqrt{(A_{\mathrm{y}} + A_{\mathrm{F0}})/(A_{\mathrm{y}} + 2A_{\mathrm{F0}})}$ should be replaced by unity. If the spring force is different than assumed, factor 2 in the denominator of the term should be accordingly adjusted.

For linear viscous damping in the self-centering system, the effective damping is based on Equation (5-3) but simplified to:

$$\beta_{\mathrm{eff}} = \beta_{\mathrm{i}} + \beta_{\mathrm{v1}}\frac{T_{\mathrm{eff}}}{T_1} + \frac{1.42q_{\mathrm{H}}}{\pi}\left(1 - \frac{1}{\mu}\right) \tag{6-47}$$

In this equation, β_{v1} is calculated by Equation (6-36) or (6-37). There are a number of simplifications in Equation (6-47) by comparison to Equation (5-3): (a) the reduction of the inherent damping due to the added stiffness by the self-centering system is too small and was ignored, (b) the primary structural system is assumed elasto-plastic so that A=A_{y}, (c) the self-centering system spring force, which is equal to K_0D/m, is assumed equal to A_0 per common behavior of fluidic self-centering devices, (d) A_0 is set equal to 0.2A_{y} per the design procedure of Section 6.2, and (e) the friction parameter A_{min} is set equal to 0.05A_0=0.01A_{y} per common behavior of fluidic self-centering devices and parameter Y=0. The latter simplification leads to a 0.014 contribution to β_{eff} from the device seal friction and is neglected. Also, per ASCE 7-2010 and to avoid overestimation of the contribution of inherent damping, the term 2/π in Equation (6-47) should be replaced by (0.64-β_{i}). Parameter q_{H} is given by Equation (5-8) but using the period of the first mode:

$$q_{\mathrm{H}} = 0.67\frac{T_{\mathrm{s}}}{T_1} \tag{6-48}$$

In the examples of this report the structural system is assumed to have perfect bilinear hysteretic behavior so that parameter q_H is set equal to unity.

Variables T_{eff} and β_{eff} are the effective period and damping in the first mode. Higher modes of the yielded building may be conservatively assumed to possess the properties of the higher modes of the elastic building. That is, the periods are equal to T_m and the damping ratios are given by

$$\beta_m = \beta_i + \beta_{vm} \tag{6-49}$$

where $m \geq 2$, and β_{vm} is given by (6-36) or (6-37). This is the approach followed in ASCE 7-2010 for buildings with damping systems.

When a residual mode is used together with the first mode of vibration, the effective period of the residual mode may arbitrarily be assumed to be some multiple of T_1. Following ASCE 7-2010, T_R is set to be equal to $0.4T_1$. The effective damping in the residual mode may be conservatively assumed to be

$$\beta_R = \beta_i + \beta_{vR} \tag{6-50}$$

where β_{vR} is given by (6-36) or (6-37) with m=R.

When the viscous damping in the self-centering system is nonlinear, the effective period is still given by Equation (6-44) and the effective damping is given by

$$\beta_{eff} = \beta_i + \beta_{v1}\left(\frac{T_{eff}}{T_1}\right)^{2-a} + \frac{1.42 q_H}{\pi}\left(1 - \frac{1}{\mu}\right) \tag{6-51}$$

where β_{v1} is the damping ratio determined from (6-40) for m=1 (note that calculation of β_{v1} requires knowledge of the roof displacement, Δ_R) and all other terms were defined previously. Equation (6-51) also assumes that damping in all self-centering devices is described by the same exponent $a_j = a$.

The calculation of the damping ratio in the higher modes or the residual mode is complicated by the fact that (6-40) is not applicable to higher modes. To circumvent this difficulty, Seleemah and Constantinou (1997) resorted to a physical interpretation of the higher mode response. They viewed the higher mode response as a small amplitude high frequency motion centered about the first mode response. Accordingly, one could define an effective damping constant C_{effj} for each nonlinear viscous element as being the slope of the force-velocity curve of the device at the calculated device velocity in the first mode, $\dot{u}_1$ (see Ramirez *et al.*, 2001 for more details) (quantity $\dot{u}_1$ is calculated later in this report by Equation 6-58 as quantity ∇_{j1}):

$$C_{\mathrm{eff}j} = a_j C_{\mathrm{N}j} \dot{u}_1^{a_j - 1} \quad (6\text{-}52)$$

Accordingly, the effective damping in the higher modes is given by

$$\beta_m = \beta_{\mathrm{i}} + \beta_{\mathrm{v}m} \text{ and } \beta_{\mathrm{R}} = \beta_{\mathrm{i}} + \beta_{\mathrm{vR}} \quad (6\text{-}53)$$

where $\beta_{\mathrm{v}m}$ and β_{vR} are calculated using (6-36) or (6-37) with $C_{\mathrm{eff}j}$ in place of C_j.

6.5 Step-by Step Design and Analysis Procedures

A step-by-step procedure for the design and analysis of a building with a fluidic self-centering system is presented. Analysis procedures by the Response Spectrum and the Equivalent Lateral Force procedures are described.

Design

The design procedure described below follows the paradigm of Ramirez et al (2001) for buildings with damping systems. The steps are:

1) Based on the seismic force-resisting system of the building, exclusive of the self-centering devices (most likely a moment-resisting frame system), select values parameters R, Ω_0 and C_d per Table 12.2-1 of ASCE 7-2010. Observe height limitations.

2) Calculate the seismic base shear V per equations 12.8-1 to 12.8-10 of ASCE 7-2010.

3) Design the seismic force-resisting system, exclusive of the self-centering devices, for a seismic base shear at least equal to $V_{\min}$=0.75V. Account for torsion per section 12.8.4 of ASCE 7-2010. For this,

    a. Design the building to have base yield strength per Equation (6-7) and account for torsion per item 3 above.
    b. Distribute the force over height per ASCE 7-2010 equations 12.8-11 and 12.8-12.
    c. Establish the redundancy factor ρ per ASCE 7-2010 section 12.3.4. For Seismic Design Categories D to F, ρ=1.3 but likely the value ρ=1.0 can be used based on ASCE 7-2010 section 12.3.4.2 provided that the building with the self-centering system is classified as a braced frame in which the loss of any brace (one self-centering device) will result in less than 33% loss in story strength. The loss in strength will be the loss of preload which is limited to

20% of the story strength for all devices. Since at least two devices will be used in each direction, the loss of strength (preload) will be less than or equal to 10% of the story strength.

4) There is no need to check the drift criteria as those will be checked when analysis of the building including the self-centering system is conducted.

5) Conduct plastic or pushover analysis of the building, exclusive of the self-centering system, to establish the lateral force-displacement relations of each story and determine the shear yield strength and the effective yield displacement of each story.

6) Add fluidic self-centering devices to provide in each principal horizontal direction a total preload equal to 20% or larger of the story shear yield strength.

7) Conduct preliminary design the bracing system for the self-centering devices based on the assumption of a maximum device force equal to 3 times the preload and a displacement of the device corresponding to a drift equal to the one permitted by ASCE 7-2010, Table 12.12-1 times $1.5R/C_d$. Note that the factor R/C_d intends to obtain a real estimate of the maximum drift (as R should be equal to C_d, but is not) and the factor 1.5 intends to scale the drift to the maximum earthquake level. Also, the multiplier of 3 on the preload to obtain the maximum force intends to produce a reasonably conservative estimate of the total force.

Response Spectrum Analysis (RSA) Procedure

The analysis is performed in order to obtain estimates of peak story displacement and drifts, peak member forces and peak self-centering device forces and displacements. Also, peak floor accelerations may be determined. The response spectrum procedure utilizes modal analysis principles with the exception that the first mode response contributions account for inelastic action in the primary structural system and nonlinear behavior in the self-centering devices. This requires an iterative analysis procedure as the effective properties are amplitude dependent. What follows is based on the theory presented in Section 6.3. The steps below are based on calculating the response in the Design Earthquake. The same procedure is followed in the analysis for the Maximum Earthquake. First procedures are presented for the case of linear viscous damping and then separately for the case of nonlinear viscous damping.

1) Develop a model of analysis of the building with each self-centering device represented by an effective spring defined per Section 6.3 and depicted in Figure 6-2. The effective stiffness is

defined as the force in the device at a displacement corresponding to the story effective yield displacement obtained for the building exclusive of the self-centering devices (item 5 above) divided by that displacement. Note that the effective yield displacement of each story is determined by plastic analysis or pushover analysis.

2) Conduct an eigenvalue analysis of the building to obtain the frequencies (periods T_m) and mode shapes $\{\phi\}_m$. Calculate the modal participation factors Γ_m and modal weights $\overline{W}_m$ per Equations (6-15) or (6-16) and (6-20) or (6-21), respectively.

3) For the case of <u>linear viscous damping</u>, calculate the damping ratio under elastic conditions β_{vm} in each mode m using Equation (6-36) or (6-37). The value of the damping constants C_j, j=1 to N (N=number of devices used) should be such that the damping ratio in the first mode β_{v1} is about 0.10 or larger.

4) Calculate the effective yield displacement D_y where Δ_{yR} is the effective yield displacement of the first story obtained from the pushover curve as shown in Figures 6-3 and 6-4

$$D_{\mathrm{y}} = \frac{\Delta_{\mathrm{yR}}}{\Gamma_1} \tag{6-54}$$

5) Assume the value of displacement D in the single-degree-of-freedom spectral representation of the pushover curve. Calculate the displacement ductility ratio μ using Equation (6-46).

6) Calculate the effective period T_{eff} and effective damping β_{eff} using Equations (6-44) and (6-47), respectively.

7) Using the Design Earthquake response spectrum, calculate the displacement D as

$$D_{\mathrm{D}} = \frac{T_{\mathrm{eff}}^2 S_{\mathrm{a}}(T_{\mathrm{eff}}, \beta = 0.05)}{4\pi^2 B} \tag{6-55}$$

where factor B is calculated for the value of the effective damping β_{eff} using Table 5-2 and S_{a} is the spectral acceleration value at the effective period of the 5%-damped Design Earthquake response spectrum. Repeat the displacement calculation by using the elastic period T_1 instead of T_{eff} and the damping ratio β_{v1} (Equation (6-26) or (6-37)) instead of β_{eff}. If the calculated displacement under elastic conditions is larger than the displacement calculated based on Equation (6-55), use the elastic displacement value.

8) If the value of the displacement calculated by Equation (6-55) is larger than the elastic displacement, repeat the process of steps 5 to 7 until the calculated value of the displacement is sufficiently close to the assumed value. Let this value be D_D.

9) Calculate the distribution of displacements contributed by the fundamental mode using

$$\{u\}_1 = \Gamma_1 \{\phi\}_1 D_D \tag{6-56}$$

This distribution of displacements should then be used to calculate story drifts Δu_{j1} for story j contributed by the fundamental mode.

10) Calculate the contribution to the displacements of the higher modes of vibration (m≥2) using

$$\{u\}_m = \frac{\Gamma_m \{\phi\}_m T_m^2 S_a(T_m, \beta = 0.05)}{4\pi^2 B} \tag{6-57}$$

where factor B is calculated for the value of the damping ratio β_m using Table 5-2 and S_a is the spectral acceleration value at the period T_m of the 5%-damped Design Earthquake response spectrum. Calculate the story drifts Δu_{jm} for story j contributed by mode m=2, 3, etc.

11) Use an appropriate combination rule (e.g., SRSS) to obtain the total floor displacements and story drifts using the calculated contributions of each mode. These are actual drift values and not the design story drift values obtained from analysis of the elastic structure for loads divided by factor R and then multiplied by factor C_d as described by ASCE 7-2010. For checking drift, the calculated total drift values are multiplied by factor C_d/R and then compared to the allowable values in Table 12.12-1 of ASCE 7-2010.

12) For the case of nonlinear viscous damping, perform steps 1, 2, 4 and 5 above. Then skip step 6 and replace with step 13 below:

13) Calculate the effective period T_{eff} and effective damping β_{eff} using Equations (6-44) and (6-51), respectively. Damping ratio β_{v1} is calculated using Equation (6-40) with Δ_R=$\Gamma_1 D$. The value of the damping constants C_{Nj}, j=1 to N (N=number of devices used) should be such that the damping ratio in the first mode β_{v1} is about 0.10 or larger.

14) Follow steps 7 to 11 but calculate the damping ratio β_{vm} ($m \geq 2$) using Equation (6-36) or (6-37) with constant C_j replaced by C_{effj} given by Equation (6-52). The calculation of velocity $\dot{u}_1 = \nabla_{j1}$ is described in step 15 below.

This completes the calculation of the displacement demands. The steps below apply for both linear and nonlinear damping cases. The steps provide information on the calculation of the inertia forces at the instant of maximum displacement (from where accelerations may be calculated) and peak self-centering device velocities (for calculation of damping forces).

15) Calculate the self-centering device peak velocities ∇_{jm} contributed by each mode $m \geq 1$ using the story drift Δu_{jm}, the device orientation θ_j (see Figure 6-2) and multiplying by the effective frequency for the first mode and the frequency for each other mode $m \geq 2$ and the correction factor for velocity determined as described in Section 5 (Table 5-3) using the calculated values of T_{eff} and β_{eff} (or T_1 and β_{v1} depending on the calculation of displacement D_D-inelastic or elastic) for the first mode and period and damping ratio T_m and β_{vm} for each mode $m \geq 2$.

$$\nabla_{j1} = \frac{2\pi}{T_{eff}} \Delta u_{j1} \cos\theta_j \bullet CFV(\mathrm{T}_{eff}, \beta_{eff}) \tag{6-58}$$

$$\nabla_{jm} = \frac{2\pi}{T_m} \Delta u_{jm} \cos\theta_j \bullet CFV(\mathrm{T}_m, \beta_m)\text{, m} \geq 2 \tag{6-59}$$

Note that the quantity $u_{D,j} = \Delta u_{jm} \cos\theta_j$, m=1, 2, etc. is the displacement of self-centering device j.

16) Calculate peak values of device displacements $u_{D,iT}$ and velocities ∇_{iT} by using the peak quantities contributed by each mode and some appropriate combination rule (e.g., SRSS).

17) Calculate the self-centering device peak damping force. For linear viscous damping, this force is given by

$$F_{\mathrm{V},i} = C_i \cdot \nabla_{i\mathrm{T}} \tag{6-60}$$

18) Calculate the peak self-centering device force as the maximum value of the following expression as quantity u is varied between zero and $u_{D,iT}$.

$$F_{\mathrm{D},i\mathrm{MAX}} = F_{\mathrm{min},i} + F_{0,i} + K_{0,i}u + F_{\mathrm{v},i}\sqrt{1-\left(u/u_{\mathrm{D},i\mathrm{T}}\right)^2} \tag{6-61}$$

Figure 6-5 illustrates the principle for calculating the total force. Note that the figure applies for the case of linear damping for which the damping force-displacement relation is elliptical.

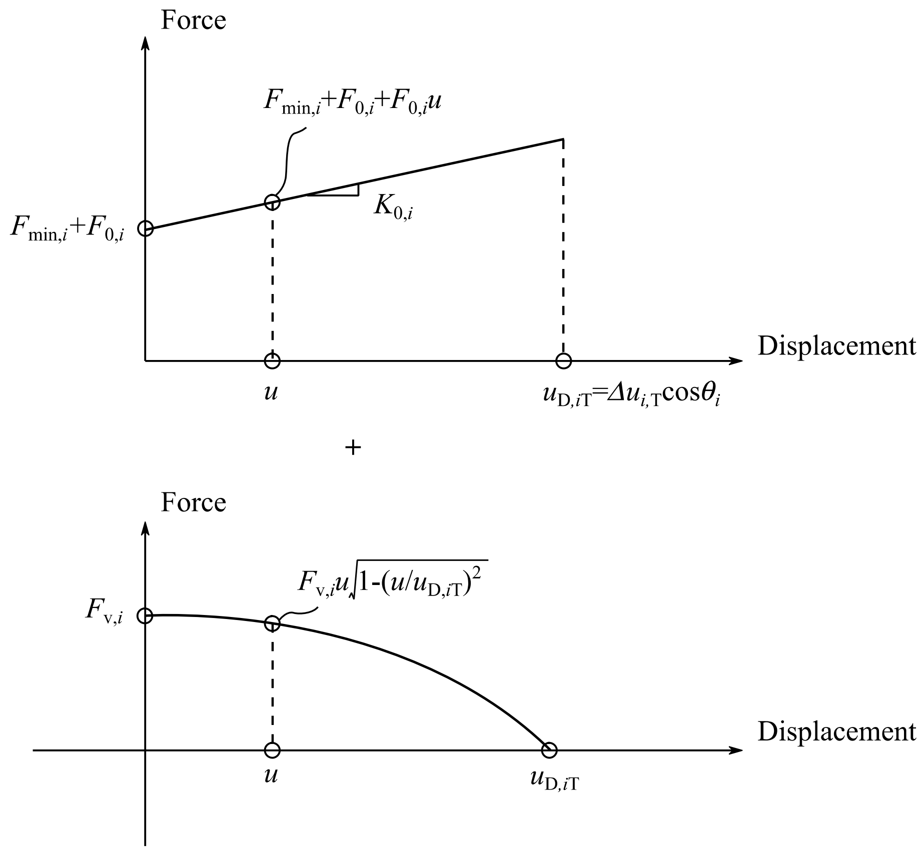

Figure 6-5 Calculation of Peak Force in Fluidic Self-Centering Device

A different expression is needed for the case of nonlinear damping. It is not possible to derive a simple expression for nonlinear damping along the lines of Equation (6-61). It has to be calculated numerically by considering a cycle of harmonic motion at amplitude of displacement $u_{D,iT}$ and amplitude of velocity ∇_{iT}.

19) Calculate the peak shear force in each story as the story shear strength (here it is assumed that the story has yielded) plus the component of force $F_{D,iMAX}$ in the horizontal direction $F_{D,iMAX}\cos\theta_i$.

Equivalent Lateral Force (ELF) Procedure

The Equivalent Lateral Force procedure may be applied following the steps of the Response Spectrum Analysis procedure for the first mode contribution and then only considering the contribution of an additional artificial mode-the residual mode. The steps are as follows:

1) Step 1 in RSA procedure.
2) Step 2 above but only calculate the period T_1, the mode shape $\{\phi\}_1$ and the modal participation factor Γ_R. Calculate the residual mode period T_R, the mode shape $\{\phi\}_R$ and the modal participation factor Γ_R using Equations (6-28), (6-27) and (6-26), respectively.
3) Step 3 above for linear viscous damping to calculate the damping ratio β_{vm} but only for m=1 and m=R.
4) Steps 4 to 11 above but in step 10 calculate the displacements only for m=R.
5) Steps 12 and 13 for the case of nonlinear viscous damping.
6) Step 14 but only calculate the damping ratio β_{vm} for m=R.
7) Step 15 to 19 above but only for modes m=1 and m=R.

The ELF procedure described above requires in step 1 an eigenvalue analysis of the structure including the stiffening effect of the self-centering devices. While this is simple, the entire process cannot be cast into the typical form for an ELF procedure as in Chapter 18 of the ASCE 7-2010. For that the period T_1 and the mode shape $\{\phi\}_1$ need to be prescribed rather than calculated. One option is to utilize the period T_1 using the procedures of Section 12.8.2 of ASCE 7-2010 to calculate the fundamental period of the building excluding the effect of the self-centering devices and then make an adjustment on the basis of simple considerations for the effect of the devices. However, the procedures in ASCE 7 apply for a building that meets the criteria of ASCE 7 in terms of minimum base shear and drift, whereas the building excluding the self-centering devices does not. Use of the ASCE 7 procedures would have underestimated the period and thus resulted in underestimation of drift. This report does not address this issue and does not attempt to develop a simple approach at estimating the fundamental period of a building with self-centering devices. Accordingly, the ELF procedure implemented in the examples of this report utilizes eigenvalue analysis to estimate the modal properties of the fundamental mode, which is the recommended procedure.

SECTION 7
EVALUATION OF METHODS OF ANALYSIS AND DESIGN OF BUILDINGS WITH FLUIDIC SELF-CENTERING DEVICES

7.1 Introduction

This section presents examples of design and analysis of buildings with damping systems. Design and analysis were performed using the procedures of Section 6, which are based on the ASCE 7-10 (2010) Equivalent Lateral Force (ELF) and Response Spectrum Analysis (RSA) methods.

The examples presented below involve three-story and six-story special steel moment frame buildings with fluidic self-centering devices installed in diagonal configurations. Each of these frames was designed based on the procedures of Section 6 and ASCE 7-10 (2010) for base shear of $0.75V$, where V is minimum base shear force per ASCE 7 (2010). Fluidic self-centering devices were added with characteristics based on the design procedures of Section 6. Analysis was performed using the ELF and RSA procedures of ASCE 7 (2010) as modified in Section 6, and by nonlinear dynamic response history analysis following ASCE 7 (2010). The seismic excitation was described by the response spectrum of ASCE 7-10 with parameters S_{DS}=1.25, S_{D1}=0.6 and T_s=0.48 sec (see Figure 4-1 in this report).
The results of response history analysis are compared to the results of the simplified ELF and RSA analysis procedures.

7.2 Design of 3-Story and 6-Story Reference Frames

The reference frames are conventional special steel moment frames in 3-story and 6-story buildings. These frames were designed to meet the minimum required strength (Section 12.8.1.1) and drift limits (Section 12.12.1) of ASCE 7-2010. Later in this section, the behavior and response of these frames are compared with those of the corresponding frames with fluidic self-centering devices in order to ascertain the benefits offered by the fluidic self-centering systems designed by the procedures of Section 6.
Appendix B presents a description of the geometry, the design parameters and loads for the example buildings. Figures B-1, B-2 and B-3 the plan view and elevations of the 3-story and 6-story buildings of the examples. The lateral force-resisting system is composed of two special steel moment frames in each direction. For such frames, ASCE 7-10 (2010) assigns factors R=8, C_d=5.5 and Ω_0=3. Also presented in Appendix B are calculations for the design of the 3-story and 6-story reference frames that satisfy the ASCE 7-10 drift limit Δ_a=0.02h_{sx}, where h_{sx} is the story height.

The 3-story reference building has a fundamental period equal to 1.07 sec and the 6-story reference building has a fundamental period equal to 1.90 sec (determined by eigenvalue analysis using program OpenSees (2014)). The base shear strength of each frame of the two building has been determined by pushover analysis (analysis in program OpenSees using a vertical force distribution proportional to the lateral forces per ASCE 7-2010 equations 12.8-11 and 12.8-12, and including P-Δ effects) to approximately be 1300 kN for the 3-story frame and 1750 kN for the 6-story frame.

7.3 Design of 3-Story and 6-Story Frames with Fluidic Self-Centering Devices

Frames with fluidic self-centering devices were designed using the procedures of Section 6. According to these procedures, and in similarity to Chapter 18 of ASCE 7-2010 on "Seismic Requirements for Structures with Damping Systems," the frames were designed for a seismic base shear of $0.75V$, where V is the seismic base shear in accordance with ASCE 7-2010, Section 12.8 (required for a conventional frame without a damping system). Detailed calculations are provided in Appendices C and D. The designed frames and details of the fluidic self-centering devices are shown in Figures 7-1 and 7-2. These frames are classified as 3*S*-75 and 6*S*-75, respectively. Note that for the 6*S*-75 frame the shown bracing is the original bracing per Appendix D prior to the modification based on the results of the response history analysis (see Appendix D).

Table 7-1 presents a summary of the characteristics of the four frames (two reference frames and the two frames with the fluidic self-centering system) in terms of the base shear strength and the fundamental period. Detailed information on the reference frames is provided in Appendix B. Evidently, the frames of the building with the fluidic self-centering devices have a much lower strength and a larger fundamental period. The period is still larger in the buildings with the fluidic devices even when the stiffening effect of the fluidic devices is approximately accounted for. The increased flexibility and the reduced strength of the buildings with the fluidic devices indicate potential for reduced inertia forces and reduced forces transmitted to the foundation.

Table 7-1 Characteristics of Example Frames

Frame	Number of Stories	Base Shear Strength[1] (kN)	Fundamental Period[2] (sec)
3*S*-75	3	1300	1.50 (1.31)
6*S*-75	6	1750	2.30 (2.06)
3*S*-Reference	3	2300	1.07 (NA)
6*S*-Reference	6	2450	1.90 (NA)

1 Calculated by pushover analysis in OpenSees using a lateral force distribution in accordance with ASCE 7 equations 12.8-1 and 12.8-2, and including P-Δ effects

2 Value is period of frame without the self-centering system. Value in parenthesis is period including the effect of the self-centering devices, modelled as elastic elements with effective stiffness calculated at a story drift displacement equal to the story yield displacement

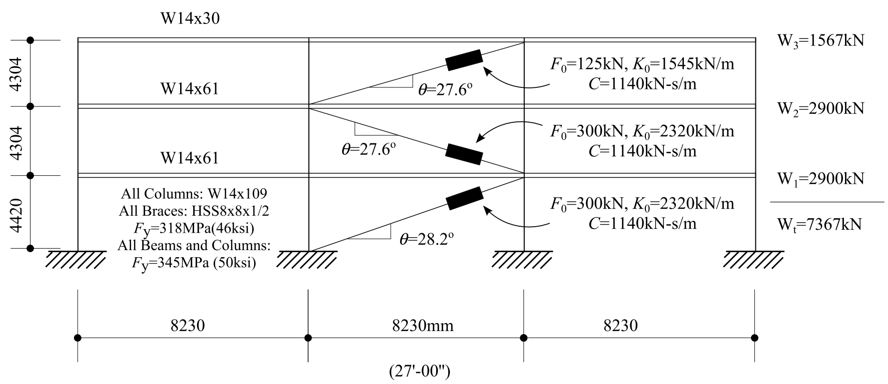

Figure 7-1 3-Story Frame 3*S*-75 with Fluidic Self-Centering Devices

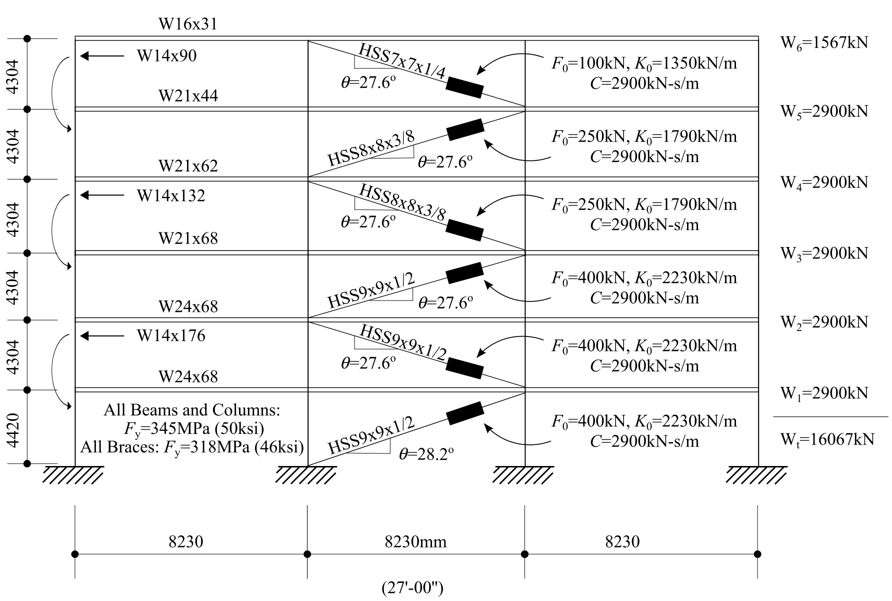

Figure 7-2 6-Story Frame 6*S*-75 with Fluidic Self-Centering Devices

7.4 Analytical Modeling of Buildings with Fluidic Self-Centering Devices

Each of the buildings with fluidic self-centering devices was modelled and analyzed in program OpenSees (2014) using the following features:

1) Each building was represented by a single frame in a two-dimensional analysis.
2) The seismic excitation was horizontal only; i.e. no vertical excitation was included.
3) Inherent damping in the analyzed frame was modelled as Rayleigh damping with 5% of critical damping in the first two modes of vibration.
4) Plastic hinges in beams and columns were modelled as having the bilinear moment-curvature relation shown in Figure 7-3. Plastic hinges in beams were located at the column face. Plastic hinges in columns were located at beam faces. Plastic hinges at column bases were located at a distance of equal to the column depth from the base.

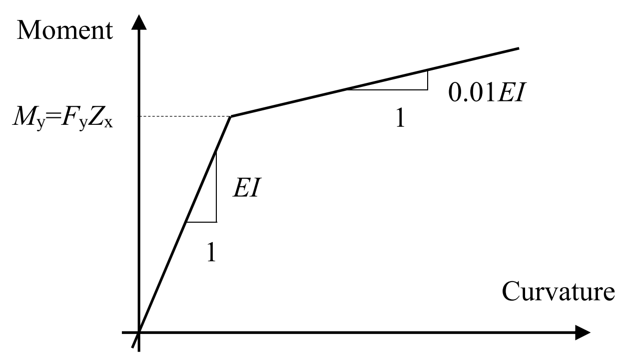

Figure 7-3 Bilinear Moment-Curvature Relation for Plastic Hinges

5) Each fluidic self-centering device and its brace were modeled as illustrated in Figure 7-4 (based on work by Choi et al, 2008 on another self-centering device). The brace is modeled as a linear and elastic element of unlimited strength (buckling or yielding is not modelled in this study but is accounted for later when an evaluation of performance is conducted. Figure 7-5 shows a representative force-displacement relation obtained by this element in OpenSees when imposing motion of 45mm amplitude at frequency of 1Hz.

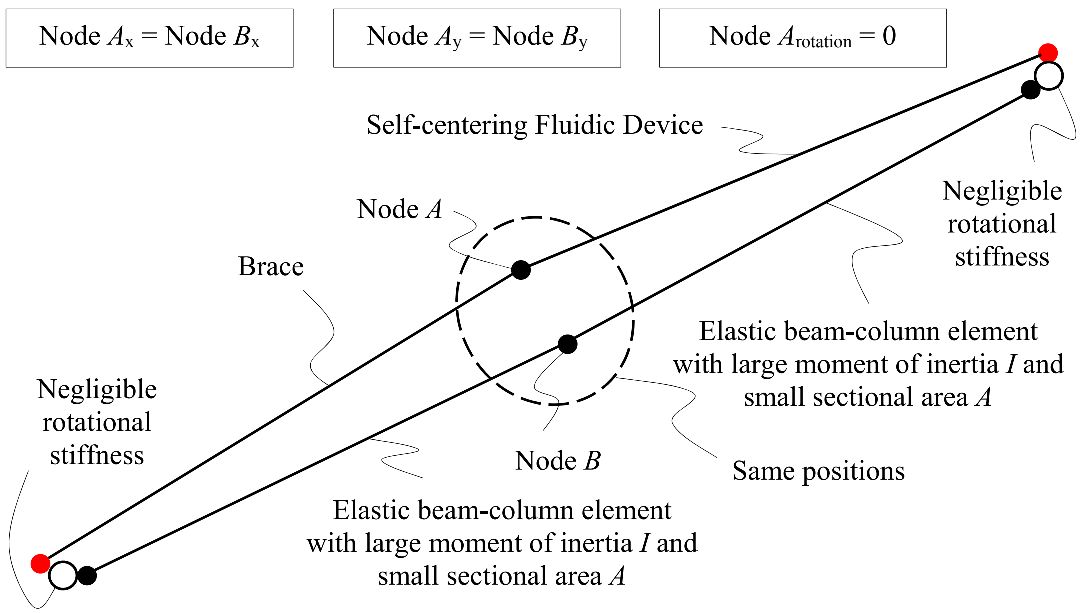

Figure 7-4 Modeling of Fluidic Self-Centering Device and its Brace in OpenSees

6) The behavior of the fluidic self-centering device was modeled by the procedures described in Section 3.
7) The numerical integration utilized the average acceleration Newmark-Beta scheme with a time step equal to 0.001sec.

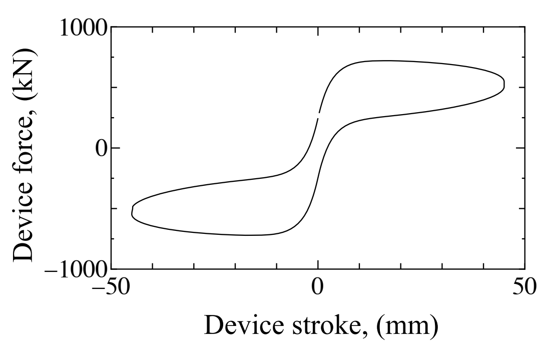

Figure 7-5 Representative Force-Displacement Relation of Element of Fluidic Self-Centering Device Obtained in OpenSees

8) The analysis model included a leaning column carrying portion of the weight of the building within the tributary area of the analyzed frame. This was necessary in order to better account for P-Δ effects. Figure 7-6 illustrates the model for the 3-story building. Note that the weights shown represent only the seismic weight, which was taken as the dead load plus half of the live load.

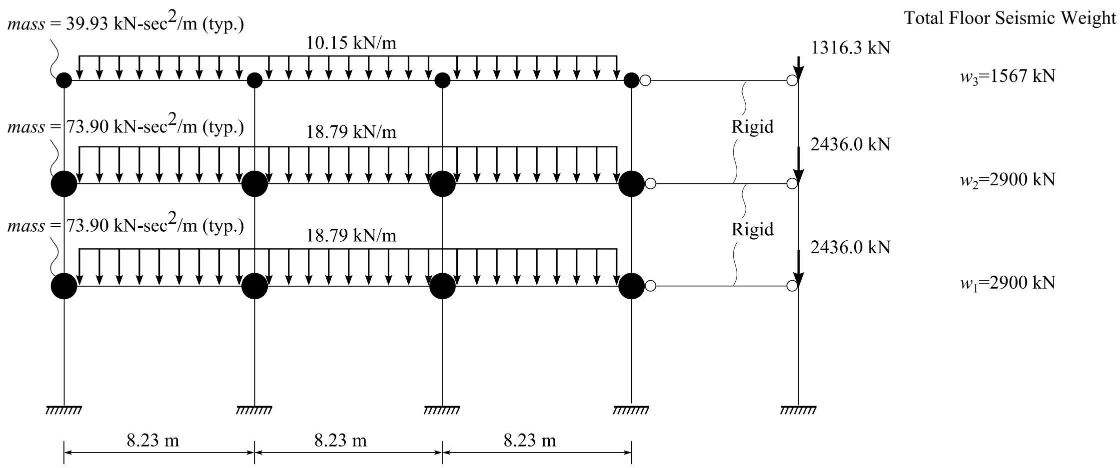

Figure 7-6 Model of Analysis for 3-story Frame in Program OpenSees Illustrating Mass and Seismic Weight Distribution and the use of a Leaning Column (bracing omitted for clarity)

7.5 Nonlinear Response History Analysis

Frames 3*S*-75 and 6*S*-75 were analyzed in the Design Earthquake (DE) and in the Maximum Considered Earthquake (MCE) using suites of scaled ground motions. Each suite consisted of 7 motions. Three different suites were selected, to respectively represent far-field, near-fault without pulse-like effects and near-fault with pulse-like effects. Thus a total of 21 analyses were performed for the DE and another 21 analyses for the MCE. The motions used and the scaling procedures employed have been described in Section 4 of this report (Tables 4-1 through 4-3 for Near-Fault Pulse-Like, Near-Fault Non-Pulse-Like and Far-Field, respectively). The MCE consisted of the DE acceleration histories multiplied in amplitude by factor of 1.5. Peak response quantities were obtained for each motion and average values have been calculated and are presented herein.

7.6 Results of Nonlinear Response History Analysis and Comparison to Results of ELF and RSA Procedures

Comparisons of results obtained by the simplified methods of analysis of Section 6 (ELF and RSA) and nonlinear response history analysis are presented in Tables 7-2 and 7-3 for 3S-75 frame in the DE and MCE, respectively, and in Tables 7-4 and 7-5 for the 6S-75 frame in the DE and MCE, respectively. The presented results include:

1) Peak floor displacement with respect to the ground.
2) Peak story drift.
3) Peak self-centering device velocity.
4) Peak self-centering device force.

5) Peak story shear force.

The results in Tables 7-2 to 7-5 reveal the following:

1) The response history analysis results depend on the type of seismic motion used (far-field, near-fault non-pulse-like and near-fault pulse-like). Of course, the results of the ELF and RSA procedures do not.
2) For the case of the 3-story example, the ELF and RSA procedures mostly predicted conservative estimates of floor displacement and drift. Even when compared to response history analysis results in the case of the near-fault, pulse-like motions, the RSA and ELF procedures provided good predictions of displacement responses within about 15% of the response history analysis results. Results for the device velocities obtained by nonlinear response history analysis in the three types of motions used and by the RSA and ELF procedures varied significantly among procedures and types of motion. Nevertheless, the maximum among the RSA and ELF procedures calculated velocity for any device in the critical MCE was conservatively estimated or was very close to the maximum calculated value among the three types of motion in the response history analysis. Also, the peak device forces calculated by the RSA and ELF procedures were of acceptable accuracy and with values typically conservative or very close to the results of the response history analysis.
3) For the case of the 6-story example, the RSA and ELF procedures resulted in predictions which are comparable to those of the response history analysis in a manner similar to that of the 3-story example. However, the simplified methods occasionally over-predict or under-predict the device velocities and forces although this does not have any effect in the presented example given that the devices in all stories are the same.
4) Given that both the RSA and the ELF procedures are based on the same initial steps of pushover analysis, modal analysis and first mode response calculations, and given the errors it may introduce, it appears that the ELF procedure does not provide any important benefit in terms of reduction of calculation effort to warrant its use.
5) Interestingly, the results of the RSA and ELF procedures on the total story shear force are occasionally predicted accurately and occasionally are over-predicted or under-predicted. This appears to be unanticipated for some cases as the devices' forces are predicted well by the simplified procedures and the frames yield so that the contribution to the shear force from the frame is known. These are the basic reasons for the difference:
    a. The behavior of the frames as shown in the pushover curves of Appendices C and D are not elasto-plastic as assumed in the RSA and ELF procedures but have a trilinear behavior, which results in lower values of story shear strength when drift is less than a

certain limit. For example, Figure 7-7 presents the story shear force-story drift relationships of frame 3*S*-75 determined in pushover analysis using a lateral load distribution based on the ASCE 7 equations 12.8-11 and 12.8-12. The drift calculated as the average of response history analysis in the far-field DE and MCE motions is denoted in the graphs of Figure 7-7. Evidently, while inelastic action commences, the drift is in most cases less than the level at which the shear force equals the shear strength.

b. The frames in the dynamic analysis do not always develop plastic hinges in all beams as postulated in the simplified analysis procedures. For example, Figures 7-8 and 7-9 present information on the plastic hinge development in the 3-story 3S-75 frame in one of the scaled motions used in the analysis for the DE and the MCE, respectively. Evidently, not all beams develop plastic hinges.

c. The pushover curves depend on the distribution of lateral forces. The pushover curves used in the ELF and RSA procedures were based on a lateral force pattern following the prescribed lateral forces per ASCE 7, whereas other distributions may have been more appropriate. For example, Figures 7-10 and 7-11 present pushover curves for the two frames exclusive of the fluidic self-centering system obtained using a pattern of loads in accordance with ASCE 7 equations 12.8-11 and 12.8-12 (used in ELF and RSA procedures) (called modal pattern), using a pattern of loads in proportion to the floor mass (called uniform pattern) and using a pattern of lateral loads in proportion to the first mode (called first mode pattern). Considerably different base shear strengths are calculated by the three patterns of load. Note that the ELF and RSA procedures may be repeated using the pushover curve obtained in the uniform pattern in order to obtain bounds on response as done in Ramirez et al. (2001) for structures with damping systems and also recommended in FEMA 356 (FEMA, 2000). Note that the pushover curves are shown to have a roof displacement of about 10% of the frame height. Two graphs also denote the displacement at 2% of the frame height, which is a better indicator of the behavior in the MCE.

Table 7-2 Comparison of Results of ELF and RSA Procedures to Nonlinear Response History Analysis for 3*S*-75 Frame with Fluidic Self-Centering Device in the DE

Response Quantity	Story	Simplified Analysis		Nonlinear Response History Analysis		
		RSA	ELF	Near-Fault Pulse	Near-Fault Non-Pulse	Far-Field
Floor Displacement (mm)	3	198.4	198.3	182.5	153.3	160.8
	2	134.9	134.6	129.9	108.9	111.4
	1	55.6	60.5	57.0	47.9	46.9
Story Drift (mm)	3	68.7	65.9	57.1	50.6	53.5
	2	80.6	84.1	75.0	64.4	66.5
	1	55.6	60.5	57.0	47.9	46.9
Device Velocity (mm/sec)	3	352.2	286.7	437.4	404.4	393.3
	2	323.8	365.8	433.9	391.4	383.4
	1	240.5	295.6	302.3	268.0	261.5
Device Force (kN)	3	543.6	470.3	586.6	561.7	555.0
	2	719.6	766.4	732.7	695.3	712.3
	1	611.8	674.0	631.1	619.7	603.0
Story Shear Force (kN)	3	1031.7	966.8	790.5	735.4	730.4
	2	1737.7	1779.2	1499.7	1405.1	1448.2
	1	1839.2	1894.0	2016.7	1912.6	1826.9

Table 7-3 Comparison of Results of ELF and RSA Procedures to Nonlinear Response History Analysis for 3*S*-75 Frame with Fluidic Self-Centering Device in the MCE

Response Quantity	Story	Simplified Analysis		Nonlinear Response History Analysis		
		RSA	ELF	Near-Fault Pulse	Near-Fault Non-Pulse	Far-Field
Floor Displacement (mm)	3	297.7	297.6	270.7	240.9	238.3
	2	202.4	201.9	202.3	178.7	173.4
	1	83.3	90.7	97.6	86.2	79.4
Story Drift (mm)	3	103.1	98.9	80.2	71.8	76.5
	2	121.0	126.2	107.5	96.7	95.6
	1	83.3	90.7	97.6	86.2	79.4
Device Velocity (mm/sec)	3	527.9	429.9	523.8	540.5	526.5
	2	486.1	549.3	525.4	533.6	515.0
	1	360.2	443.6	434.6	401.4	394.5
Device Force (kN)	3	749.4	639.7	663.2	721.2	715.2
	2	922.4	992.8	891.8	862.8	889.1
	1	759.5	853.6	854.8	780.6	753.7
Story Shear Force (kN)	3	1214.1	1116.9	938.8	959.9	970.6
	2	1917.4	1979.8	1791.1	1718.2	1768.6
	1	1969.3	2052.3	2473.3	2347.9	2322.6

Table 7-4 Comparison of Results of ELF and RSA Procedures to Nonlinear Response History Analysis for 6*S*-75 Frame with Fluidic Self-Centering Device in the DE

Response Quantity	Story	Simplified Analysis		Nonlinear Response History Analysis		
		RSA	ELF	Near-Fault Pulse	Near-Fault Non-Pulse	Far-Field
Floor Displacement (mm)	6	315.3	314.0	280.4	294.1	269.3
	5	276.9	277.0	254.9	269.9	248.1
	4	223.8	223.4	212.1	231.0	213.2
	3	163.6	162.7	160.9	178.0	165.3
	2	98.5	100.9	99.8	111.4	104.6
	1	38.1	57.6	39.8	44.1	41.2
Story Drift (mm)	6	45.7	37.6	29.4	26.3	26.1
	5	58.0	54.8	47.5	42.5	42.5
	4	62.7	63.1	59.8	56.7	55.0
	3	66.2	67.6	67.3	70.7	65.2
	2	60.6	61.1	62.5	69.7	64.8
	1	38.1	57.6	39.8	44.1	41.2
Device Velocity (mm/sec)	6	214.5	118.6	200.1	190.0	217.8
	5	211.8	172.5	251.4	232.9	272.1
	4	205.6	198.8	255.6	248.8	278.7
	3	206.7	213.1	273.1	261.3	277.5
	2	192.4	192.7	269.5	256.8	267.1
	1	129.2	265.2	200.2	199.0	203.2
Device Force (kN)	6	769.4	451.8	533.1	501.6	578.3
	5	883.6	770.3	806.6	744.1	837.0
	4	867.0	847.6	848.5	777.5	776.2
	3	1033.5	1052.3	1057.1	1036.1	978.8
	2	990.7	991.7	1066.3	1113.7	1027.7
	1	802.1	1197.4	915.5	950.9	899.1
Story Shear Force (kN)	6	1081.8	800.4	609.8	579.6	655.5
	5	1783.0	1682.6	1259.0	1113.3	1149.6
	4	2018.3	2001.1	1772.6	1634.3	1623.5
	3	2465.9	2482.6	2145.1	2081.1	2051.2
	2	2578.0	2578.8	2454.5	2529.0	2460.6
	1	2456.9	2805.3	2986.5	3074.5	2914.4

Table 7-5 Comparison of Results of ELF and RSA Procedures to Nonlinear Response History Analysis for 6*S*-75 Frame with Fluidic Self-Centering Device in the MCE

Response Quantity	Story	Simplified Analysis		Nonlinear Response History Analysis		
		RSA	ELF	Near-Fault Pulse	Near-Fault Non-Pulse	Far-Field
Floor Displacement (mm)	6	473.0	471.1	424.6	453.1	398.8
	5	415.4	415.4	395.5	423.3	373.0
	4	335.7	335.1	344.7	372.3	328.4
	3	245.4	244.0	274.0	298.3	260.7
	2	147.7	151.3	181.6	194.9	167.2
	1	57.1	86.4	77.2	81.3	67.7
Story Drift (mm)	6	68.7	56.5	34.8	32.0	31.8
	5	87.0	82.1	60.2	56.0	53.9
	4	94.1	94.6	82.1	83.8	75.1
	3	99.2	101.4	103.5	110.9	97.5
	2	90.9	91.8	107.4	115.2	101.0
	1	57.1	86.4	77.2	81.3	67.7
Device Velocity (mm/sec)	6	321.6	178.1	223.0	231.5	248.1
	5	317.7	258.7	284.1	296.4	323.6
	4	308.4	298.2	312.3	309.0	338.7
	3	309.4	319.7	351.6	334.2	360.7
	2	288.3	289.1	363.2	357.2	372.7
	1	193.4	397.8	293.7	300.0	303.3
Device Force (kN)	6	1041.5	625.9	592.7	607.3	661.0
	5	1194.7	1023.9	911.5	905.3	983.2
	4	1171.8	1140.2	1001.2	925.7	974.4
	3	1347.0	1368.5	1320.0	1268.0	1231.4
	2	1288.5	1277.8	1366.2	1417.4	1333.5
	1	996.9	1586.0	1244.2	1284.6	1115.7
Story Shear Force (kN)	6	1323.0	954.7	670.5	684.1	734.9
	5	2058.7	1907.4	1432.0	1323.0	1389.4
	4	2288.5	2260.4	2041.0	1888.5	1871.9
	3	2743.7	2762.8	2482.5	2423.3	2352.8
	2	2841.9	2832.4	2934.9	2946.5	2818.8
	1	2628.6	3147.7	3685.3	3720.5	3455.7

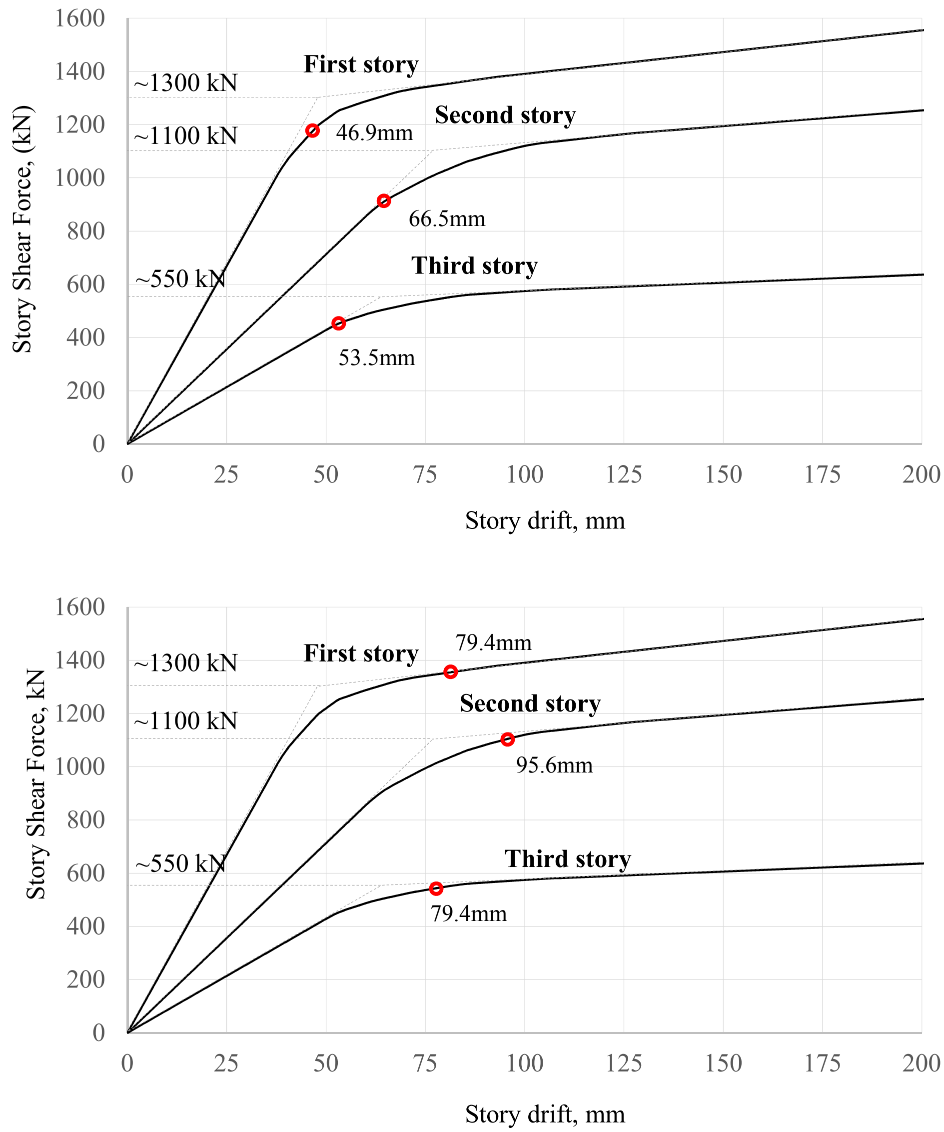

Figure 7-7 Story Shear Force versus Story Drift Relations for Frame 3*S*-75 (calculated by pushover analysis using a pattern of loads in proportion to prescribed loads in ASCE 7) and Average Drift in DE and MCE Calculated for Far-Field Motions in Response History Analysis

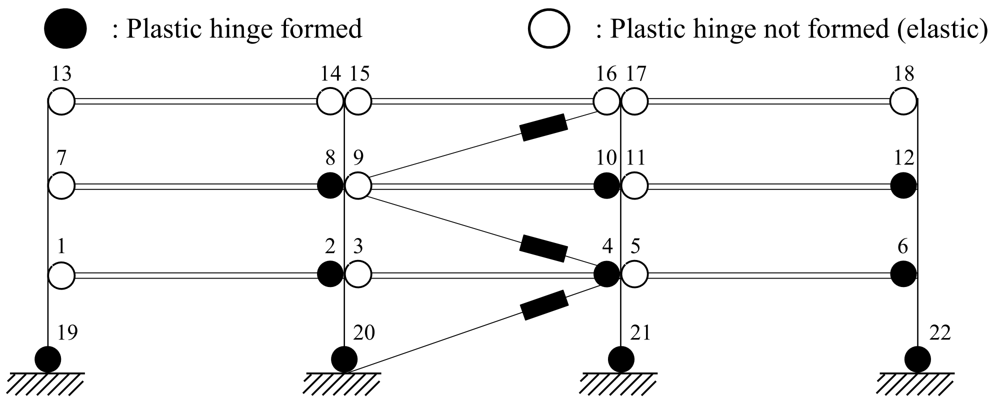

Figure 7-8 Formation of Plastic Hinges in Frame 3*S*-75 in Scaled Far-field Ground Motion Kocaeli, Duzce Station in the DE

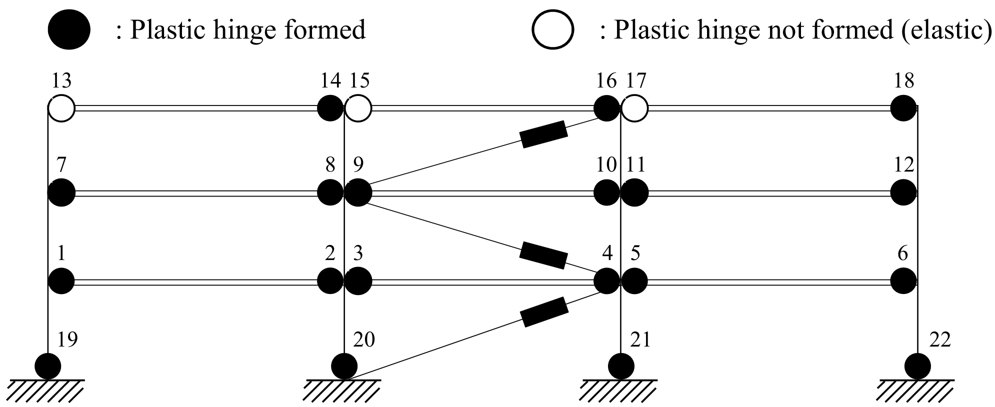

Figure 7-9 Formation of Plastic Hinges in Frame 3*S*-75 in Scaled Far-field Ground Motion Kocaeli, Duzce Station in the MCE

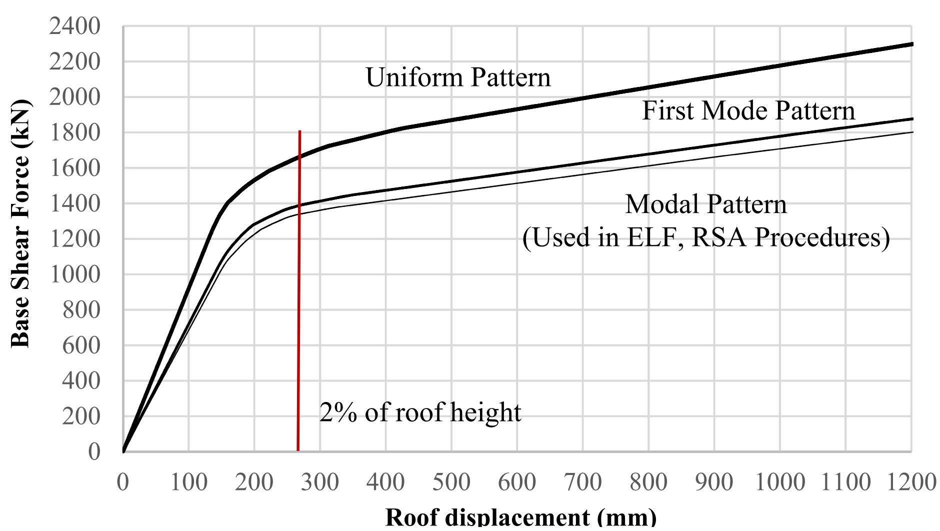

Figure 7-10 Pushover Curves of 3-story Frame 3*S*-75 Exclusive of the Fluidic Self-centering System Obtained by Various Patterns of Lateral Load

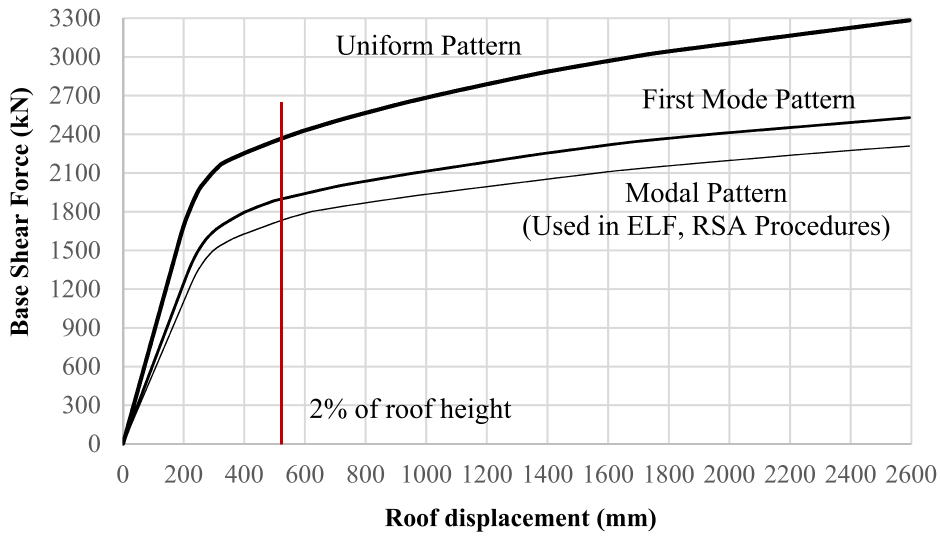

Figure 7-11 Pushover Curves of 6-story Frame 6*S*-75 Exclusive of the Fluidic Self-Centering System Obtained by Various Patterns of Lateral Load

7.7 Conclusions

The simplified methods of analysis provide good and most often conservative estimates of drift and good predictions of fluidic self-centering device forces. Story shear forces can also be accurately predicted but that requires the use of the appropriate push-over curve. To accomplish this, it would be required to obtain bounds of the response by utilizing pushover curves based on modal and uniform load patterns.

The quality of prediction by the simplified methods is better for the shorter structures (herein a 3-story example) than for taller structures (herein a 6-story example). Nevertheless, the simplified methods provide means for developing a design and assessing its adequacy prior to performing nonlinear response history analysis.

Since both the RSA and the ELF procedures require the execution of pushover analysis and then modal analysis as their first step, the ELF procedure does not offer any significant advantage in terms of simplicity to warrant its use over the RSA procedure.

SECTION 8
ADDITIONAL RESULTS AND COMPARISON OF RESPONSE OF CONVENTIONAL BUILDINGS AND BUILDINGS WITH FLUIDIC SELF-CENTERING DEVICES

8.1 Introduction

This section presents a comparison of the response, as calculated by nonlinear response history analysis, of the 3- and 6- story conventional buildings (Appendix B) and the corresponding buildings with fluidic self-centering devices (Appendices C and D, and Figures 7-1 and 7-2). The response is calculated for the DE and MCE using the scaled motions of Section 4 representing far-field, near-fault without pulse-like effects and near-fault with pulse-like effects, and following the procedures described in Section 7.

8.2 Comparison of Response

Results are presented in terms of peak response quantities (average of 7 analyses) for the story drift, residual story drift, floor total velocity, floor acceleration, and base shear force in Tables 8-1 to 8-4, distinguished by the building height (3- or 6- story) and the earthquake level (DE or MCE).

Tables 8-1 and 8-2 compare the response calculated for the 3-story structure with and without the fluidic self-centering system in the DE and MCE level motions, respectively. The results are distinguished by the three types of ground motions used in the analysis (near-fault pulse, near-fault non-pulse and far-field). Similarly, tables 8-3 and 8-4 compare results for the 6-story structure with and without the fluidic self-centering system in the DE and MCE level motions, respectively.

Figures 8-1 to 8-4 present floor acceleration spectra of 3-story and 6-story frames with and without the fluidic self-centering system for the case of ground motions characterized as near-fault, pulse-like. The floor spectra were calculated from the recorded floor acceleration histories (average of 7 spectra) for a damping ratio of 5-percent.

Note that the buildings with the fluidic self-centering system were designed on the basis of the procedures of Section 6 which are based on the criteria of ASCE 7, Chapter 18 “Seismic Requirements for Structures with Damping Systems” in terms of base shear strength and story drift for the DE. There was no specific attempt to reduce drift although this may be accomplished by the combination of added damping and preload.

The results of Tables 8-1 to 8-4 clearly demonstrate the benefits offered by the fluidic self-centering system as designed by the procedures of Section 6: (a) substantial reduction of the residual drift in the DE and MCE, (b) essentially elimination of the residual drift in the DE, (c) reduction of peak drift in the MCE, (d) reduction of base shear force, (e) reduction of peak floor accelerations, and (f) reduction of peak floor total velocities. The reduction in acceleration and total velocities are particularly pronounced in the upper floors of the analyzed structures.

Moreover, the floor spectra of Figures 8-1 to 8-4 demonstrate that the floor spectral accelerations in the buildings with the fluidic self-centering system can be substantially less than those of the comparable conventional buildings over a wide range of frequencies. This, together with the observed reduction of total floor velocities, provides evidence of potential for improved performance of secondary systems for which the response is sensitive to acceleration (e.g., suspended ceilings, sprinkler systems, etc.) or total velocity (e.g., free standing objects than can overturn).

Note that the base shear force is the ultimate shear force for the design of the foundation. Reduction of this force should transform into benefits for the foundation design.

These benefits emanate from the combination of (a) the added preload, stiffness and viscous damping by the self-centering system, (b) the reduction of strength of the structure, and (c) the reduction of stiffness (increase of period) of the structure (see Table 7-1 for information).

8.3 Additional Results for 3-story and 6-story Buildings with Fluidic Self-Centering System

Additional results of response history analysis are presented to illustrate the effects of increased damping, the form of damping (linear or nonlinear), increased preload and reduced device stiffness on the calculated response. The results serve the purpose of showing the effects on the response in the MCE and are also used to size the bracing system for the fluidic devices and determine its ultimate characteristics. These ultimate characteristics are used in Sections 9 and 10 in evaluating the seismic performance and how this performance is affected by the design parameters.

Table 8-5 presents results of response history analysis in the MCE for the 3-story frame 3S-75 equipped with fluidic self-centering devices providing a damping ratio in the fundamental mode under elastic conditions equal to 0.10 (case already shown in Table 8-2) and damping ratio of 0.15. The only difference between the two compared cases is the value of the damping constant of each device, C=1710kN-sec/m versus C=1140kN-sec/m for all three stories.

On the basis of the results in Table 8-5, the peak device force is 1107kN and the brace is selected to have a capacity of 1.3 times the force. A HSS8x8x5/8 structural tube section is selected which has a capacity in compression for an effective length of 8535mm (28ft) equal to 1435kN. This force is used as the ultimate force in both compression and tension for the device-brace system in the collapse performance assessment in Section 9.

The results in Table 8-5 also demonstrate the effect of increased damping: reduction in peak drift and increase in device peak force. Also, the residual drift is affected with small reduction in some locations and small increase in other locations.

Table 8-6 presents results of response history analysis in the MCE for the 3-story frame 3*S*-75 equipped with fluidic self-centering devices providing a damping ratio in the fundamental mode under elastic conditions equal to 0.10 and having preload of about 20% of the story strength (case already shown in Table 8-2) and another case in which the preload is increased by a factor of 1.3, whereas the damping constant remains the same (C=1140kN-sec/m). The effect of increased preload is to reduce the peak drift and the residual drift at the expense a small increase in the device peak force. On the basis of the calculated peak device force, an HSS8x8x5/8 structural tube section is selected for bracing which has a capacity in compression for an effective length of 8535mm (28ft) equal to 1435kN. This force is used as the ultimate force in both compression and tension for the device-brace system in the collapse performance assessment in Section 9.

Table 8-7 presents results of response history analysis in the MCE for the 3-story frame 3*S*-75 equipped with fluidic self-centering devices with nonlinear viscous damping, designed to provide a damping ratio in the fundamental mode in the DE equal to 0.10 and 0.15. The other parameters of preload and stiffness for each device are the same as those of the 3*S*-75 frame case of balanced configuration. The damping properties of the devices were selected on the basis of the procedures in Section 6.5 and specifically step 13 of the RSA method, with the devices having the nonlinear viscous behavior of equation (6-38) with exponent α=0.5. This resulted in the damping constant of each device to be C_N=551.3kN-(sec/m)$^{1/2}$ and C_N= 666.4kN-(sec/m)$^{1/2}$, respectively, for all three stories. On the basis of the results on the peak device force, the bracing was selected to be HSS8x8x1/2 for both cases.

It may be noted in the results of Table 8-7 that the increase in nonlinear damping has a small effect on the peak drift in the MCE. The increase of damping had a larger effect on the DE response, but unlike the case of linear damping, the effect is not proportional in the MCE as the dampers have nonlinear behavior.

To further illustrate the difference between linear and nonlinear viscous behavior, Table 8-8 presents a comparison of the MCE response of the 3S-75 frame for linear and nonlinear viscous behavior, both having a fundamental mode damping ratio of 0.10 in the DE. It may be noted that linear damping is a little more effective than nonlinear damping in reducing drift in the MCE (but not in the DE) at the expense of a higher device peak force. While this is desirable for the MCE response, it may affect the collapse fragility as the device force increases substantially with increasing intensity of the earthquake.

Table 8-9 compares the response of the 3*S*-75 frame with increased nonlinear viscous damping of 0.15 in the fundamental mode in the DE under elastic conditions for the frame and with two different sets of values of the fluidic device stiffness. One set is the originally used set of values as determined in the design of the devices and the second set of stiffness values is arbitrarily set to be ten times less. Evidently, the reduction in stiffness has some small beneficial effect on accelerations, shear forces and device forces but it results in an increase in the residual drift, an undesirable effect.

Finally, Table 8-10 compares the response of the original 6-story frame 6*S*-75 (linear viscous damping with damping ratio β_{v1}=0.10) to the response of the same frame but with increased nonlinear damping (β_{v1}=0.15 in DE under elastic frame conditions). The increase of damping has a minor beneficial effect on the calculated response, including the peak drift and the residual drift. To further investigate the effect of increased nonlinear viscous damping, Figures 8-5 and 8-6 were prepared to compare the floor acceleration response in the DE and the MCE (only case of near-fault pulse-like motions) of the 6*S*-75 frame in the two cases of damping. Clearly, the increased damping and the conversion to nonlinear still offers significant benefits. The spectral accelerations are about the same as those of the linearly-damped system and are much less than those of the conventional 6*S*-Reference frame for a wide range of frequencies (compared to Figures 8-3 and 8-4).

8.4 Conclusions

The results of this section demonstrate substantial benefits in buildings designed by the procedures of Section 6 and equipped by fluidic self-centering devices, as compared to conventional buildings, in terms of reduction (or near elimination) of residual drift, reduction of accelerations, floor velocities and base shear forces. Note that this assessment was based on the comparison of response of two buildings, one 3-story and one 6-story, when analyzed for the effects of the Design Earthquake and the Maximum Considered Earthquake as characterized by a particular response spectrum and three different scenarios in terms of proximity to fault.

Additional results are presented in Sections 9 and 10 where building systems with fluidic self-centering devices are formally evaluated using the procedures of FEMA P695 (FEMA, 2008) for quantification of the building collapse performance and of the residual drift performance.

Table 8-1 Comparison of Response Calculated in Response History Analysis for 3-story Structure with and without Fluidic Self-Centering System in DE

Response Quantity	Story	With Fluidic Self-Centering System			Without Fluidic Self-Centering System		
		Near-Fault Pulse	Near-Fault Non-Pulse	Far-Field	Near-Fault Pulse	Near-Fault Non-Pulse	Far-Field
Peak Story Drift (mm)	3	57.1	50.6	53.5	84.6	76.4	77.8
	2	75.0	64.4	66.5	86.6	79.1	86.1
	1	57.0	47.9	46.9	47.6	47.6	45.8
Residual Story Drift (mm)	3	0.4	0.1	0.2	14.3	6.7	10.2
	2	0.9	0.4	0.4	10.9	5.8	8.3
	1	4.0	1.7	0.8	4.8	4.0	4.0
Base Shear Force (kN)	3	790.5	735.4	730.4	1430.5	1302.7	1335.8
	2	1499.7	1405.1	1448.2	2003.8	1920.7	1930.7
	1	2016.7	1912.6	1826.9	2639.4	2793.3	2544.3
Peak Floor Acceleration (g)	3	0.532	0.497	0.489	0.925	0.832	0.857
	2	0.410	0.401	0.390	0.572	0.607	0.505
	1	0.423	0.430	0.475	0.593	0.592	0.592
Peak Absolute Floor Velocity (mm/sec)	3	1216.4	1197.4	1270.9	1460.1	1521.8	1476.2
	2	1098.7	1073.1	1190.6	1188.8	1163.3	1241.3
	1	1088.2	1021.7	1119.8	1140.3	1098.7	1185.6

Table 8-2 Comparison of Response Calculated in Response History Analysis for 3-story Structure with and without Fluidic Self-Centering System in MCE

Response Quantity	Story	With Fluidic Self-Centering System			Without Fluidic Self-Centering System		
		Near-Fault Pulse	Near-Fault Non-Pulse	Far-Field	Near-Fault Pulse	Near-Fault Non-Pulse	Far-Field
Peak Story Drift (mm)	3	80.2	71.8	76.5	132.0	117.3	114.0
	2	107.5	96.7	95.6	128.8	116.2	115.3
	1	97.6	86.2	79.4	82.9	74.7	64.7
Residual Story Drift (mm)	3	6.2	2.1	2.4	28.3	12.0	19.9
	2	8.4	2.7	2.3	27.3	10.7	16.8
	1	12.2	5.9	6.4	26.2	10.0	13.0
Base Shear Force (kN)	3	938.8	959.9	970.6	1819.7	1699.3	1760.1
	2	1791.1	1718.2	1768.6	2347.8	2289.2	2168.9
	1	2473.3	2347.9	2322.6	3111.2	3164.4	3052.9
Peak Floor Acceleration (g)	3	0.634	0.663	0.661	1.154	1.085	1.129
	2	0.466	0.525	0.516	0.763	0.747	0.653
	1	0.573	0.627	0.651	0.829	0.854	0.856
Peak Absolute Floor Velocity (mm/sec)	3	1689.4	1638.2	1844.1	1938.2	1936.6	2097.7
	2	1562.6	1526.6	1722.4	1668.8	1620.9	1784.0
	1	1578.8	1513.4	1645.1	1653.7	1597.8	1755.7

Table 8-3 Comparison of Response Calculated in Response History Analysis for 6-story Structure with and without Fluidic Self-Centering System in DE

Response Quantity	Story	With Fluidic Self-Centering System			Without Fluidic Self-Centering System		
		Near-Fault	Near-Fault Non-Pulse	Far-Field	Near-Fault	Near-Fault Non-Pulse	Far-Field
Peak Story Drift (mm)	6	29.4	26.3	26.1	68.1	60.6	61.7
	5	47.5	42.5	42.5	83.2	76.2	73.1
	4	59.8	56.7	55.0	91.5	82.1	79.5
	3	67.3	70.7	65.2	80.3	86.2	80.9
	2	62.5	69.7	64.8	62.2	71.2	69.1
	1	39.8	44.1	41.2	35.5	38.9	38.9
Residual Story Drift (mm)	6	0.3	0.4	0.3	12.6	8.3	9.1
	5	0.7	0.5	0.4	15.1	11.8	10.1
	4	2.0	1.4	1.0	16.0	14.5	10.5
	3	2.4	3.4	1.8	14.8	15.6	11.6
	2	2.4	5.1	2.7	10.5	12.3	10.6
	1	1.4	2.5	1.5	3.7	6.2	5.2
Base Shear Force (kN)	6	609.8	579.6	655.5	1194.0	1172.2	1199.6
	5	1259.0	1113.3	1149.6	1796.0	1692.4	1732.1
	4	1772.6	1634.3	1623.5	2356.8	2085.1	2115.9
	3	2145.1	2081.1	2051.2	2446.2	2491.7	2465.4
	2	2454.5	2529.0	2460.6	2771.5	2842.6	2805.3
	1	2986.5	3074.5	2914.4	3357.5	3356.3	3282.2
Peak Floor Acceleration (g)	6	0.420	0.397	0.442	0.769	0.755	0.769
	5	0.322	0.291	0.323	0.504	0.427	0.387
	4	0.319	0.316	0.333	0.482	0.423	0.469
	3	0.381	0.422	0.389	0.473	0.476	0.489
	2	0.392	0.450	0.434	0.492	0.508	0.515
	1	0.451	0.461	0.467	0.496	0.492	0.482
Peak Absolute Floor Velocity (mm/sec)	6	1170.5	1213.3	1353.9	1469.4	1442.4	1631.8
	5	1098.5	1149.0	1293.2	1174.2	1237.2	1403.1
	4	1024.8	1068.0	1210.2	1121.4	1137.8	1282.2
	3	1018.7	1021.9	1140.0	1125.7	1030.7	1185.7
	2	1048.5	1000.5	1103.2	1125.3	1029.6	1169.7
	1	1081.7	1011.7	1083.8	1122.9	1026.8	1123.4

Table 8-4 Comparison of Response Calculated in Response History Analysis for 6-story Structure with and without Fluidic Self-Centering System in MCE

Response Quantity	Story	With Fluidic Self-Centering System			Without Fluidic Self-Centering System		
		Near-Fault Pulse	Near-Fault Non-Pulse	Far-Field	Near-Fault Pulse	Near-Fault Non-Pulse	Far-Field
Peak Story Drift (mm)	6	34.8	32.0	31.8	101.4	105.5	88.9
	5	60.2	56.0	53.9	110.7	117.3	100.7
	4	82.1	83.8	75.1	121.5	129.9	108.8
	3	103.5	110.9	97.5	115.6	130.8	114.6
	2	107.4	115.2	101.0	99.3	109.0	98.2
	1	77.2	81.3	67.7	61.0	63.9	56.2
Residual Story Drift (mm)	6	0.6	0.4	0.3	27.0	26.0	19.4
	5	3.0	1.8	1.1	24.5	23.7	17.2
	4	8.8	5.6	3.1	24.4	21.1	16.5
	3	8.5	7.1	4.4	24.7	18.8	15.2
	2	7.5	8.4	6.4	21.7	17.7	14.4
	1	11.5	12.6	9.2	16.2	15.4	10.7
Base Shear Force (kN)	6	670.5	684.1	734.9	1515.2	1487.7	1568.3
	5	1432.0	1323.0	1389.4	2060.1	1936.0	1978.4
	4	2041.0	1888.5	1871.9	2753.2	2521.5	2361.6
	3	2482.5	2423.3	2352.8	2785.6	2916.6	2877.1
	2	2934.9	2946.5	2818.8	3200.9	3259.9	3133.9
	1	3685.3	3720.5	3455.7	3864.7	3886.7	3713.0
Peak Floor Acceleration (g)	6	0.464	0.475	0.502	0.960	0.951	1.004
	5	0.349	0.353	0.376	0.637	0.584	0.474
	4	0.352	0.364	0.393	0.640	0.589	0.640
	3	0.431	0.477	0.478	0.609	0.670	0.674
	2	0.505	0.571	0.548	0.680	0.705	0.759
	1	0.640	0.653	0.656	0.715	0.709	0.708
Peak Absolute Floor Velocity (mm/sec)	6	1571.2	1608.5	1843.9	1888.2	1896.8	2128.4
	5	1511.8	1534.8	1795.2	1577.9	1605.0	1840.1
	4	1465.1	1430.0	1713.4	1569.6	1517.7	1754.5
	3	1445.5	1413.1	1630.9	1558.7	1433.8	1669.2
	2	1485.4	1428.5	1616.1	1595.7	1489.2	1702.3
	1	1566.6	1484.9	1612.7	1626.2	1522.6	1668.1

Table 8-5 Comparison of Response Calculated in Response History Analysis for 3-story Structure with Fluidic Self-Centering System in MCE and two Cases of Linear Viscous Damping (β_{v1}=0.10 and 0.15)

Response Quantity	Story	C=1140 kN-s/m, β_{v1}=0.10			C=1710 kN-s/m, β_{v1}=0.15		
		Near-Fault Pulse	Near-Fault Non-Pulse	Far-Field	Near-Fault Pulse	Near-Fault Non-Pulse	Far-Field
Peak Story Drift (mm)	3	80.2	71.8	76.5	69.5	61.8	64.0
	2	107.5	96.7	95.6	99.7	88.0	87.7
	1	97.6	86.2	79.4	91.9	78.9	73.2
Residual Story Drift (mm)	3	6.2	2.1	2.4	3.5	1.0	0.8
	2	8.4	2.7	2.3	7.1	1.9	1.7
	1	12.2	5.9	6.4	13.2	5.6	6.7
Peak Device Velocity (mm/sec)	3	523.8	540.5	526.5	445.2	454.7	448.0
	2	525.4	533.6	515.0	507.6	503.3	494.7
	1	434.6	401.4	394.5	419.3	391.6	379.6
Peak Device Force (kN)	3	663.2	721.2	715.2	789.9	852.6	853.2
	2	891.8	862.8	889.1	1069.1	1049.9	1107.0
	1	854.8	780.6	753.7	996.0	939.0	899.0
Peak Floor Acceleration (g)	3	0.634	0.663	0.661	0.598	0.613	0.611
	2	0.466	0.525	0.516	0.471	0.506	0.512
	1	0.573	0.627	0.651	0.571	0.601	0.621
Peak Story Shear Force (kN)	3	938.8	959.9	970.6	918.7	886.6	893.1
	2	1791.1	1718.2	1768.6	1832.0	1712.5	1798.3
	1	2473.3	2347.9	2322.6	2586.6	2431.0	2392.7

Table 8-6 Comparison of Response Calculated in Response History Analysis for 3-story Structure with Fluidic Self-Centering System in MCE and two Cases of Preload (damping constant C=1140kN-s/m)

Response Quantity	Story	$F_{0,1}$=300kN, $F_{0,2}$=300kN, $F_{0,3}$=125kN			$F_{0,1}$=390kN, $F_{0,2}$=390kN, $F_{0,3}$=160kN		
		Near-Fault Pulse	Near-Fault Non-Pulse	Far-Field	Near-Fault Pulse	Near-Fault Non-Pulse	Far-Field
Peak Story Drift (mm)	3	80.2	71.8	76.5	78.1	70.7	74.8
	2	107.5	96.7	95.6	105.9	93.0	91.7
	1	97.6	86.2	79.4	95.2	80.4	76.6
Residual Story Drift (mm)	3	6.2	2.1	2.4	3.7	1.1	1.5
	2	8.4	2.7	2.3	4.9	1.1	1.3
	1	12.2	5.9	6.4	8.5	3.4	4.7
Peak Device Velocity (mm/sec)	3	523.8	540.5	526.5	553.0	557.3	538.4
	2	525.4	533.6	515.0	550.5	543.7	520.0
	1	434.6	401.4	394.5	431.9	399.6	382.2
Peak Device Force (kN)	3	663.2	721.2	715.2	726.3	770.4	761.6
	2	891.8	862.8	889.1	978.0	952.8	966.3
	1	854.8	780.6	753.7	933.0	875.1	835.6
Peak Floor Acceleration (g)	3	0.634	0.663	0.661	0.696	0.695	0.681
	2	0.466	0.525	0.516	0.523	0.561	0.547
	1	0.573	0.627	0.651	0.614	0.646	0.666
Peak Story Shear Force (kN)	3	938.8	959.9	970.6	1021.2	1010.5	988.0
	2	1791.1	1718.2	1768.6	1849.2	1769.0	1827.0
	1	2473.3	2347.9	2322.6	2552.6	2411.5	2363.1

Table 8-7 Response Calculated in Response History Analysis for 3-story Structure with Fluidic Self-Centering System in MCE and two Cases of Nonlinear Viscous Damping (β_{v1}=0.10 and 0.15 in DE)

Response Quantity	Story	Non-Linear Damping, C_N= 551.3kN-(sec/m)$^{1/2}$ (β_v=0.10 in DE)			Non-Linear Damping, C_N= 666.4kN-(sec/m)$^{1/2}$ (β_v=0.15 in DE)		
		Near-Fault Pulse	Near-Fault Non-Pulse	Far-Field	Near-Fault Pulse	Near-Fault Non-Pulse	Far-Field
Peak Story Drift (mm)	3	84.3	78.7	83.2	78.9	73.3	77.4
	2	109.6	95.1	94.7	106.4	91.0	91.4
	1	97.0	84.7	76.7	94.6	81.2	73.6
Residual Story Drift (mm)	3	7.8	2.3	4.1	6.1	1.7	3.0
	2	9.2	2.7	2.8	8.6	2.4	2.5
	1	13.0	6.3	6.3	13.4	6.1	6.6
Peak Device Velocity (mm/sec)	3	605.1	606.9	578.4	574.6	568.6	542.5
	2	558.6	557.9	535.9	557.8	549.3	530.8
	1	445.6	410.8	393.9	440.5	409.2	386.8
Peak Device Force (kN)	3	551.8	577.3	576.3	623.4	645.6	643.4
	2	798.1	759.0	780.5	861.0	825.2	846.9
	1	781.3	727.0	709.1	837.0	786.9	760.8
Peak Floor Acceleration (g)	3	0.733	0.749	0.740	0.765	0.789	0.725
	2	0.518	0.576	0.548	0.552	0.570	0.542
	1	0.612	0.628	0.644	0.602	0.613	0.637
Peak Story Shear Force (kN)	3	1098.4	1107.5	1105.0	1080.2	1080.6	1075.6
	2	1860.2	1792.5	1821.4	1872.1	1790.4	1842.5
	1	2431.7	2326.2	2290.3	2474.1	2353.3	2314.4

Table 8-8 Comparison of Response Calculated in Response History Analysis for 3-story Structure with Fluidic Self-Centering System in MCE and Cases of Linear and Nonlinear Viscous Damping (β_{v1}=0.10 in DE)

Response Quantity	Story	Linear Damping C=1140 kN-s/m			Non-Linear Damping C_N= 551.3kN-(sec/m)$^{1/2}$		
		Near-Fault Pulse	Near-Fault Non-Pulse	Far-Field	Near-Fault Pulse	Near-Fault Non-Pulse	Far-Field
Peak Story Drift (mm)	3	80.2	71.8	76.5	84.3	78.7	83.2
	2	107.5	96.7	95.6	109.6	95.1	94.7
	1	97.6	86.2	79.4	97.0	84.7	76.7
Residual Story Drift (mm)	3	6.2	2.1	2.4	7.8	2.3	4.1
	2	8.4	2.7	2.3	9.2	2.7	2.8
	1	12.2	5.9	6.4	13.0	6.3	6.3
Peak Device Velocity (mm/sec)	3	523.8	540.5	526.5	605.1	606.9	578.4
	2	525.4	533.6	515.0	558.6	557.9	535.9
	1	434.6	401.4	394.5	445.6	410.8	393.9
Peak Device Force (kN)	3	663.2	721.2	715.2	551.8	577.3	576.3
	2	891.8	862.8	889.1	798.1	759.0	780.5
	1	854.8	780.6	753.7	781.3	727.0	709.1
Peak Floor Acceleration (g)	3	0.634	0.663	0.661	0.733	0.749	0.740
	2	0.466	0.525	0.516	0.518	0.576	0.548
	1	0.573	0.627	0.651	0.612	0.628	0.644
Peak Story Shear Force (kN)	3	938.8	959.9	970.6	1098.4	1107.5	1105.0
	2	1791.1	1718.2	1768.6	1860.2	1792.5	1821.4
	1	2473.3	2347.9	2322.6	2431.7	2326.2	2290.3

Table 8-9 Response Calculated in Response History Analysis for 3-story Structure with Fluidic Self-Centering System in MCE and two Cases of Fluidic Device Stiffness and Increased Nonlinear Viscous Damping (β_{v1}=0.15 in DE)

Response Quantity	Story	Non-Linear Damping, High Stiffness, $K_{0,1}=K_{0,2}$=2320, $K_{0,3}$=1545kN/m			Non-Linear Damping, Low Stiffness, $K_{0,1}=K_{0,2}$=232, $K_{0,3}$=155kN/m		
		Near-Fault Pulse	Near-Fault Non-Pulse	Far-Field	Near-Fault Pulse	Near-Fault Non-Pulse	Far-Field
Peak Story Drift (mm)	3	78.9	73.3	77.4	82.5	74.3	80.6
	2	106.4	91.0	91.4	107.9	94.0	93.3
	1	94.6	81.2	73.6	95.3	84.6	75.1
Residual Story Drift (mm)	3	6.1	1.7	3.0	8.5	2.5	3.8
	2	8.6	2.4	2.5	11.3	3.4	3.1
	1	13.4	6.1	6.6	15.2	8.2	8.2
Peak Device Velocity (mm/sec)	3	574.6	568.6	542.5	553.4	574.0	551.5
	2	557.8	549.3	530.8	531.5	546.5	537.2
	1	440.5	409.2	386.8	434.1	407.9	386.7
Peak Device Force (kN)	3	623.4	645.6	643.4	588.1	623.7	619.6
	2	861.0	825.2	846.9	758.3	763.1	782.9
	1	837.0	786.9	760.8	729.2	713.9	701.6
Peak Floor Acceleration (g)	3	0.765	0.789	0.725	0.731	0.748	0.708
	2	0.552	0.570	0.542	0.548	0.563	0.537
	1	0.602	0.613	0.637	0.604	0.609	0.653
Peak Story Shear Force (kN)	3	1080.2	1080.6	1075.6	1009.1	1039.4	1033.8
	2	1872.1	1790.4	1842.5	1758.7	1699.2	1755.8
	1	2474.1	2353.3	2314.4	2360.8	2273.1	2246.2

Table 8-10 Comparison of Response Calculated in Response History Analysis for 6-story Structure with and without Fluidic Self-Centering System in MCE and Cases of Linear (β_{v1}=0.10) and Nonlinear (β_{v1}=0.15 in DE) Damping

Response Quantity	Story	Linear Damping C=2900 kN-s/m			Non-Linear Damping, C_N= 1433 kN (sec/m)$^{1/2}$		
		Near-Fault Pulse	Near-Fault Non-Pulse	Far-Field	Near-Fault Pulse	Near-Fault Non-Pulse	Far-Field
Peak Story Drift (mm)	6	34.8	32.0	31.8	28.6	24.9	25.9
	5	60.2	56.0	53.9	54.3	47.4	47.5
	4	82.1	83.8	75.1	76.8	75.4	69.3
	3	103.5	110.9	97.5	97.8	104.6	90.6
	2	107.4	115.2	101.0	103.3	111.4	96.5
	1	77.2	81.3	67.7	73.3	79.2	65.4
Residual Story Drift (mm)	6	0.6	0.4	0.3	0.5	0.5	0.4
	5	3.0	1.8	1.1	2.1	1.2	0.8
	4	8.8	5.6	3.1	8.4	5.3	2.6
	3	8.5	7.1	4.4	10.3	8.1	4.5
	2	7.5	8.4	6.4	9.7	9.8	6.7
	1	11.5	12.6	9.2	12.5	13.7	9.4
Peak Device Velocity (mm/sec)	6	223.0	231.5	248.1	198.8	189.0	217.7
	5	284.1	296.4	323.6	303.5	293.8	335.4
	4	312.3	309.0	338.7	337.9	341.7	389.1
	3	351.6	334.2	360.7	384.5	370.4	407.9
	2	363.2	357.2	372.7	381.6	376.1	389.5
	1	293.7	300.0	303.3	295.0	300.5	303.7
Peak Device Force (kN)	6	592.7	607.3	661.0	679.9	657.8	722.2
	5	911.5	905.3	983.2	988.4	958.8	1026.9
	4	1001.2	925.7	974.4	1036.0	1012.8	1072.6
	3	1320.0	1268.0	1231.4	1295.6	1292.3	1264.8
	2	1366.2	1417.4	1333.5	1307.6	1356.1	1288.4
	1	1244.2	1284.6	1115.7	1246.9	1281.2	1179.0
Peak Floor Acceleration (g)	6	0.464	0.475	0.502	0.450	0.452	0.473
	5	0.349	0.353	0.376	0.387	0.363	0.388
	4	0.352	0.364	0.393	0.408	0.403	0.476
	3	0.431	0.477	0.478	0.491	0.503	0.570
	2	0.505	0.571	0.548	0.559	0.615	0.618
	1	0.640	0.653	0.656	0.626	0.662	0.703
Peak Story Shear Force (kN)	6	670.5	684.1	734.9	673.4	655.2	715.8
	5	1432.0	1323.0	1389.4	1487.7	1351.0	1467.6
	4	2041.0	1888.5	1871.9	2103.3	1945.1	1965.7
	3	2482.5	2423.3	2352.8	2568.3	2527.4	2482.8
	2	2934.9	2946.5	2818.8	3007.3	3038.0	2897.7
	1	3685.3	3720.5	3455.7	3649.4	3715.2	3474.6

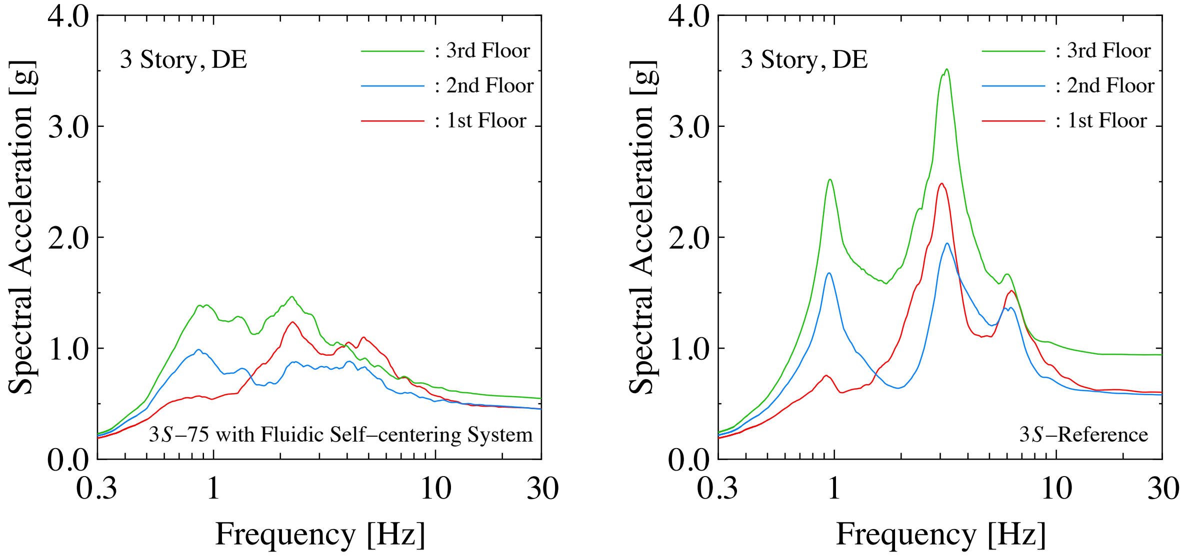

Figure 8-1 Floor Acceleration Spectra (5%-damped) of 3-story Frame 3*S*-75 with Fluidic Self-Centering System and Conventional Frame 3*S*-Reference for Near-Fault Pulse-like Motions in DE

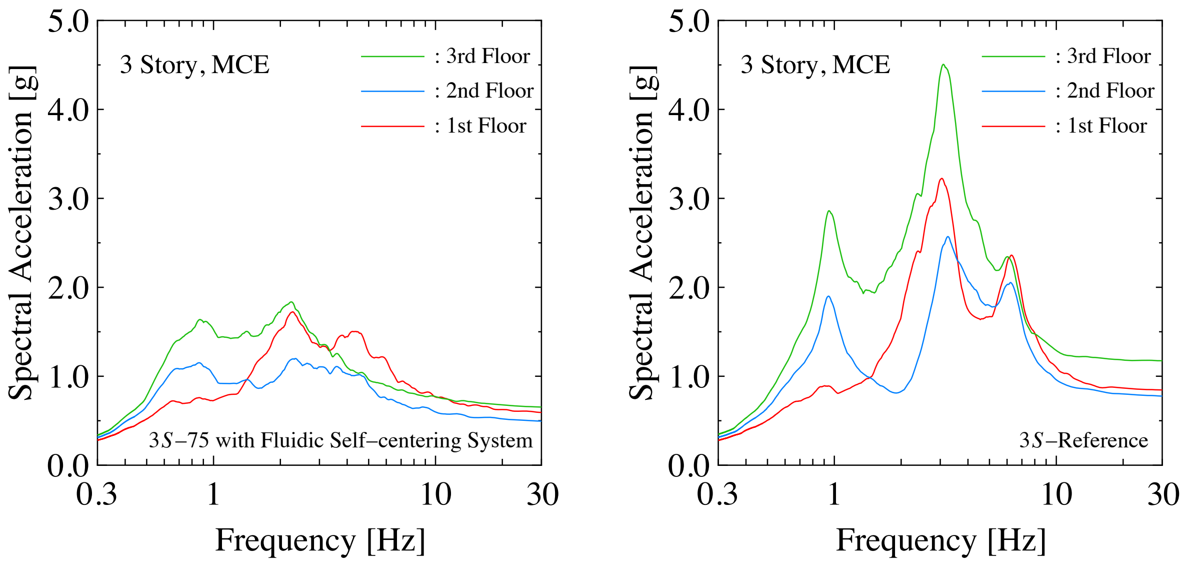

Figure 8-2 Floor Acceleration Spectra (5%-damped) of 3-story Frame 3*S*-75 with Fluidic Self-Centering System and Conventional Frame 3*S*-Reference for Near-Fault Pulse-like Motions in MCE

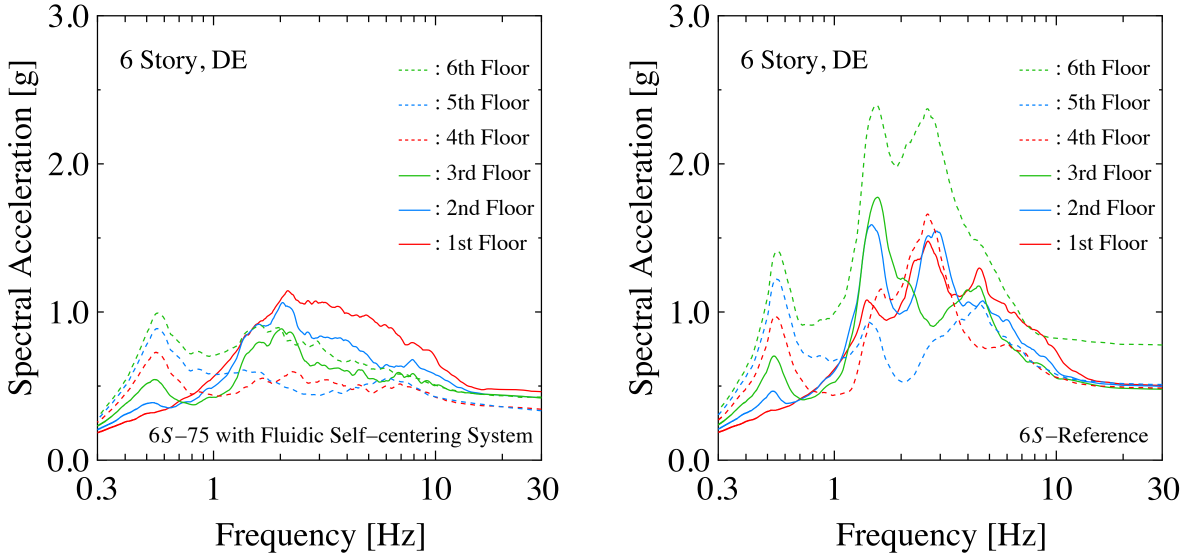

Figure 8-3 Floor Acceleration Spectra (5%-damped) of 6-story Frame 6*S*-75 with Fluidic Self-Centering System and Conventional Frame 6*S*-Reference for Near-Fault Pulse-like Motions in DE

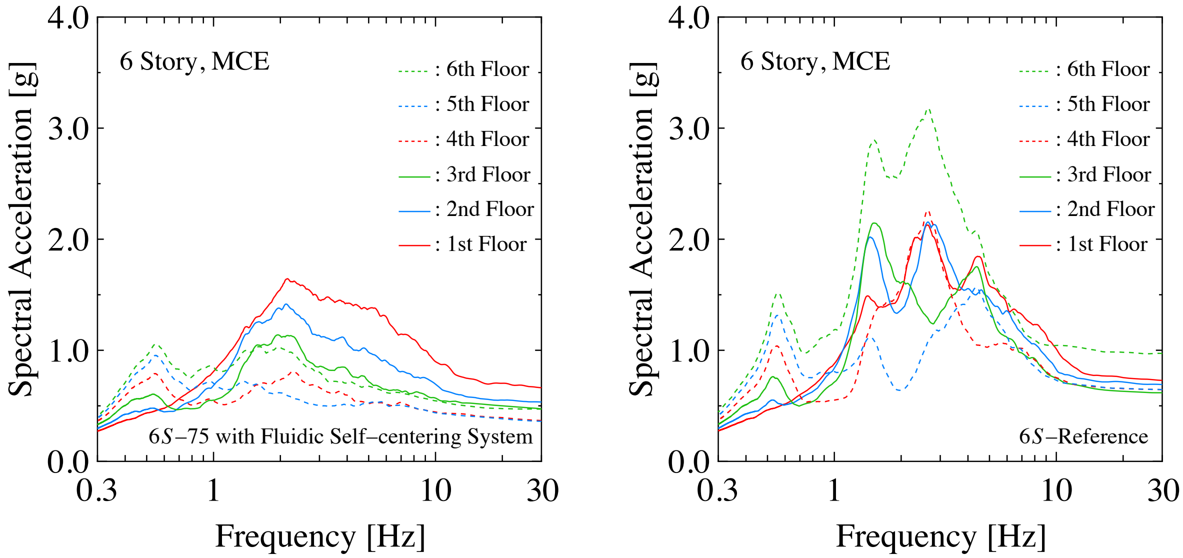

Figure 8-4 Floor Acceleration Spectra (5%-damped) of 6-story Frame 6*S*-75 with Fluidic Self-Centering System and Conventional Frame 6*S*-Reference for Near-Fault Pulse-like Motions in MCE

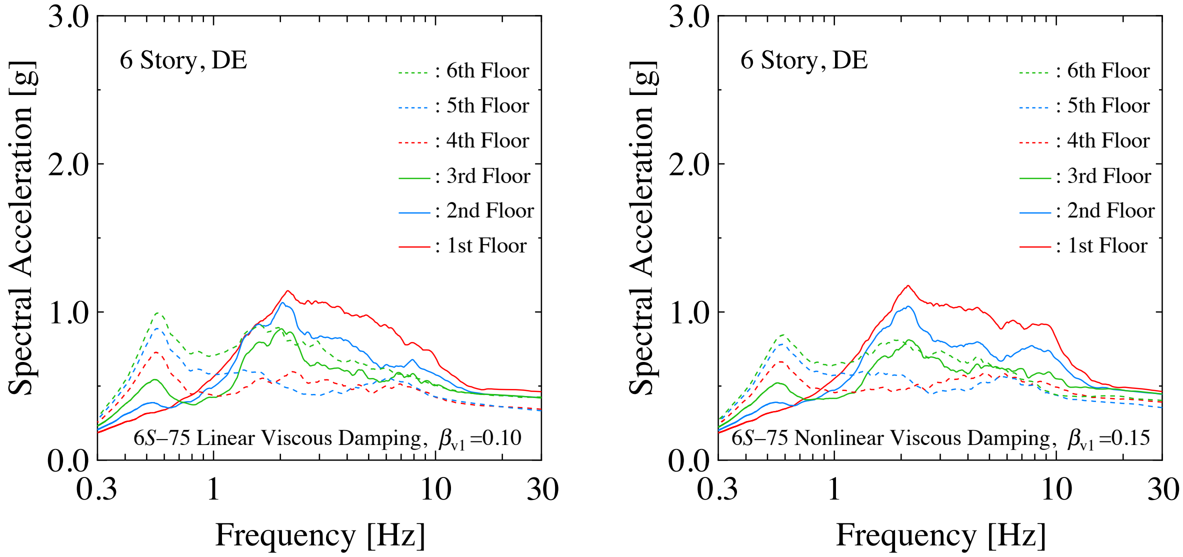

Figure 8-5 Floor Acceleration Spectra (5%-damped) of 6-story Frame 6*S*-75 with Fluidic Self-Centering System in Two Cases of Damping for Near-Fault Pulse-like Motions in DE (left figure is for linear viscous damping with β_{v1}=0.10; right figure is for nonlinear viscous damping with β_{v1}=0.15 in the DE)

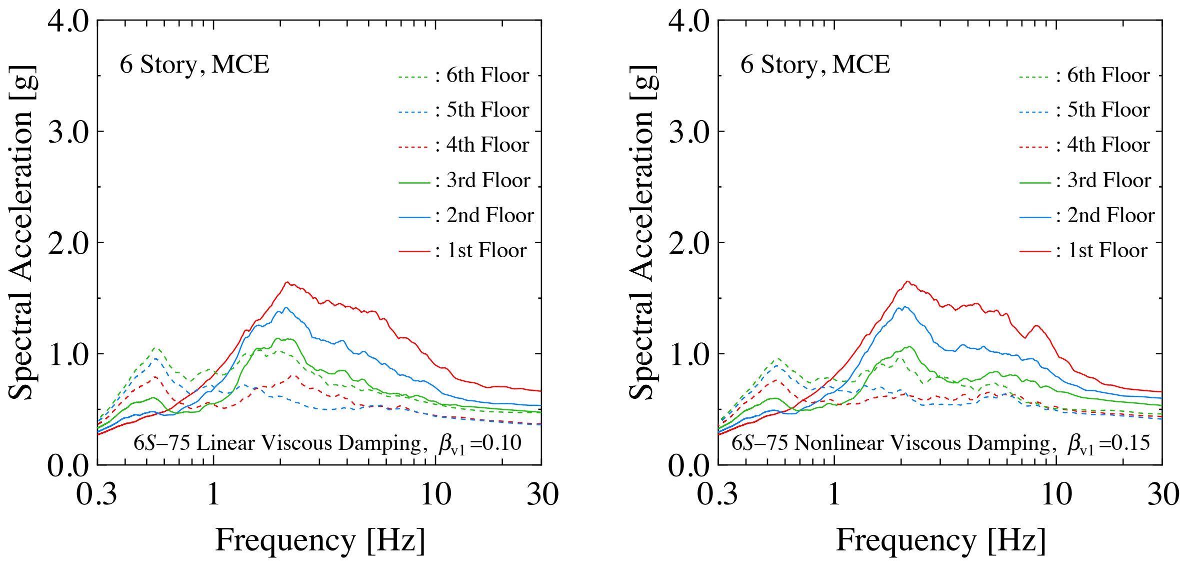

Figure 8-6 Floor Acceleration Spectra (5%-damped) of 6-story Frame 6*S*-75 with Fluidic Self-Centering System in Two Cases of Damping for Near-Fault Pulse-like Motions in MCE (left figure is for linear viscous damping with β_{v1}=0.10; right figure is for nonlinear viscous damping with β_{v1}=0.15 in the DE)

SECTION 9

COLLAPSE PERFORMANCE EVALUATION OF BUILDINGS WITH FLUIDIC SELF-CENTERING DEVICES

9.1 Introduction

The comparison of performance of buildings with and without a fluidic self-centering system in Section 8 demonstrated important benefits provided by the self-centering system in the Design Earthquake and the Maximum Considered Earthquake. Apart from the expected reduction or near elimination of the residual drift, the benefits included reduction in the base shear and reductions in the floor peak accelerations, peak total velocities and floor response spectra, with the reductions being particularly pronounced at the upper floors. These benefits resulted from the design of the structure exclusive of the fluidic self-centering system to have a reduced strength based on the procedures presented in Section 6, and to have added preload, stiffness and viscous damping with the addition of the fluidic devices, again based on the procedures described in Section 6.

The improved performance of the buildings with the fluidic self-centering system in the DE and MCE analyses documented in Section 8 does not necessarily imply that the buildings have acceptable seismic performance in terms of the "collapse margin ratio" on the basis of the contemporary procedures of FEMA P695 (FEMA, 2009). Such evaluations are presented in this section and compared to evaluations of the seismic performance of conventional buildings without a self-centering system and designed to meet the criteria of ASCE 7-2010.

Seismic performance evaluation based on the procedures of FEMA P695 (2009) requires conducting incremental dynamic analysis and simulating collapse of the analyzed structure (Vamvatsikos and Cornell, 2002; Haselton, 2006; Haselton and Deierlein, 2007; Haselton *et al*., 2008; Liel *et al*., 2011; Lignos and Kranwinkler, 2013). The procedure in this section follows the formality of the FEMA P695 procedure but concentrates on buildings identified in the previous sections as 3*S*-Reference, 6*S*-Reference, 3*S*-75 and 6*S*-75 with the latter two cases enhanced to include the failure mechanism of the fluidic self-centering system. Inclusion of the failure characteristics of the fluidic device-bracing system is important in the assessment of seismic performance as extensively discussed and analyzed in Miyamoto *et al*. (2010, 2011) for the case of fluid viscous dampers, although other studies have ignored the ultimate characteristics of dampers in seismic performance assessments (Wanitkerkul and Filiatrault, 2008; Seo *et al*., 2014).

The study of Seo *et at*. (2014) investigated the performance of 4-story steel moment resisting frames with viscous dampers in five different configurations: steel moment resisting frame (SMRF) building, SMRF with viscous dampers (reduced shear strength at 75% of the minimum required per ASCE 7, story drift criteria of 2%), SMRF with viscous dampers (un-reduced shear strength, story drift criteria of 2%), SMRF with viscous dampers (reduced shear strength, story drift criteria of 1.5%), and SMRF with viscous dampers (un-reduced shear strength, story drift criteria of 1.5%). The study concluded that the viscously damped SMRF building with reduced design strength did not achieve the same level of collapse resistance as the conventional SMRF buildings. Also, the study concluded that viscously damped buildings with reduced design strength may achieve a higher collapse performance than conventional SMRF buildings when the drift is limited to 1.5% rather than 2% per ASCE 7 criteria.

The conclusions of the study of Seo *et al*. (2014) have relevance and implications in the assessment of seismic performance of buildings with fluidic self-centering devices as the design procedure followed (see Section 6) is based on reduced shear strength of the building excluding the self-centering system (75% of the minimum required per ASCE 7-2010). However, the addition of the self-centering system with preload and stiffness effectively increases the shear strength and, together with viscous damping, controls drift (e.g., the results of Section 8 show the drift to be less than 1.7% in the DE for the two buildings analyzed) so that it would be expected that the seismic performance is about the same or better than that of conventionally designed buildings.

The study of Miyamoto *et al*. (2011) that considered the ultimate behavior of the fluidic damping devices in assessing the seismic performance utilized symmetric damper configurations that required two dampers per frame per story (with the exception of a 1-story structure studied). It also assumed that the devices had an ultimate capacity between 1.0 and 1.3 times the maximum force calculated in the MCE. Sections 18.7.1.2 to 18.7.1.4 in ASCE 7-2010 specify the requirements for the design of damping systems and their connections. They have to be designed to resist the forces, displacements and velocities calculated in the MCE and assessed using strength design criteria with a redundancy factor $\rho=1$ and a resistance factor $\phi=1$. Fluid damping devices, and by extension fluidic self-centering devices, are typically designed by reputable manufacturers to have a capacity much larger than the one required by ASCE 7. Rather, the ultimate capacity is determined by buckling in compression of the device-brace system and by failure of the connections in tension. While it is possible for the engineer to design the connections to fail at a force equal to the calculated force in the MCE (hence the “safety factor” of unity in the study of Miyamoto et al, 2011), it will likely be the maximum force calculated in the required 7 analyses and not the average force calculated in the MCE that will be used. In practice, this typically means using a force equal to 1.3 times the calculated average value of the 7 analyses in order to avoid underestimating the maximum force when motions based on spectral matching are used in the analysis.

In general, the ultimate characteristics of a fluidic self-centering system or a damping system in general will be different in compression (controlled by buckling) and in tension (controlled by design of connections). This may lead to "unbalanced" behavior where the push-over curves differ depending on the direction of the applied lateral forces. The effects of such a behavior on the seismic performance will be investigated in this section. Also, various approaches at enhancing the seismic performance in terms of increasing the collapse margin ratio will be investigated, including increases in displacement capacity, viscous damping, preload and ultimate force capacity of the fluidic self-centering system.

9.2 Modeling the Behavior of Structural Components for Collapse Resistance Assessment

The model of analysis was the same as that used in response history analysis as described in Section 7 (and depicted for the 3-story case in Figure 7-6) but modified to represent the ultimate behavior of the components as described below. Note that the model is two-dimensional with only horizontal ground motion and response considered. The model accounted for P-Δ effects. The OpenSees program (2013) was used to develop the analytical model.

The Modified Ibarra-Krawinkler bilinear-hysteretic model (Lignos and Krawinkler, 2011) is used to represent beam deteriorating moment-rotation hysteresis along the lines of related studies (Miyamoto et al., 2011; Seo et al., 2014; Hamidia et al., 2014). The hysteresis model is shown in Figure 9-1. Characteristic points of the moment-rotation relation are the yield point [θ_y, M_y], the capping point [θ_c, M_c], the amount of rotation between the yield and the capping points θ_p, the post-capping plastic rotation θ_{pc}, the residual strength M_r and the ultimate rotation capacity θ_u. Moment M_y is the effective yield strength, calculated as the product of the plastic section modulus, the material yield stress σ_y ($M_{y,p}$=$Z\sigma_y$) and a coefficient (=$M_y/M_{y,p}$) which accounts for isotropic hardening. Moment M_c is calculated considering strength increase beyond yielding. Moment M_r is a residual moment strength and is taken as a portion κ of moment M_y. Failure occurs at ultimate rotation capacity θ_u. Details of the model and its parameters are presented in Lignos and Krawinkler (2011). The version of the model utilized in this study assumes zero residual moment so that the value of θ_u is set equal to a large value and the moment-rotation relation is the one depicted in Figure 9-1 by the dashed line.

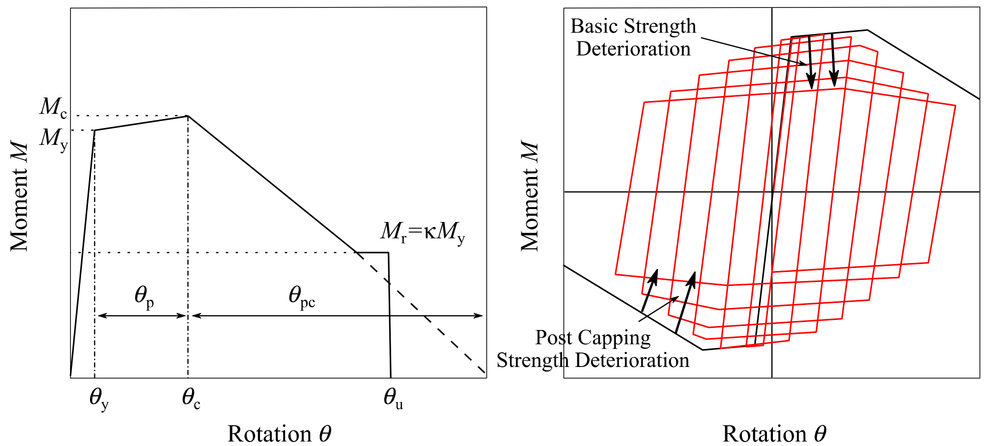

Figure 9-1 Modified Ibarra-Krawinkler used for Beams (left monotonic, right cyclic)

Columns are modeled using a concentrated plasticity bi-linear hysteretic model without strength or stiffness deterioration and with a ratio of elastic to post-elastic stiffness equal to 0.002.

The fluidic self-centering device and its connecting brace were modeled using the mathematical model described in Sections 3 and 7 after enhancing to account for its ultimate behavior. Two limit states are included in the analytical model: a displacement limit (device stroke limit) and a force limit. Figure 9-2 illustrates the assumed behavior of the device, where for the illustration the viscous force is excluded. In this figure, F_0 is the preload, K_0 is the stiffness based on compression of the fluid column and $D_{Capacity}$ is the displacement capacity of the device. The ultimate force in compression is the force at which the device-brace system buckles. Given that typically the length of this system is large (the effective length was 8535mm in the analyzed structures, with the end conditions being perfect pins), the ultimate compression load is determined by elastic buckling. The ultimate force in tension is controlled either by the strength of the connections or the tensile strength of the device. Typically, such devices are designed to have an ultimate strength at least twice that of the maximum force expected during operation. Connections are designed for the maximum force calculated in the MCE analysis, which typically implies design for 1.3 times the average force calculated in seven analyses for the MCE. This limit typically controls the behavior in tension.

The stiffness of the device beyond displacement $D_{Capacity}$ may be calculated based on the geometric and material properties of the device and the effect of bracing (Miyamoto *et al.*, 2011 have done this in fluid dampers), however this would require details that are only known to the manufacturer. In this study, this stiffness was set to have a large value that was 1000 times the value of stiffness K_0 of device.

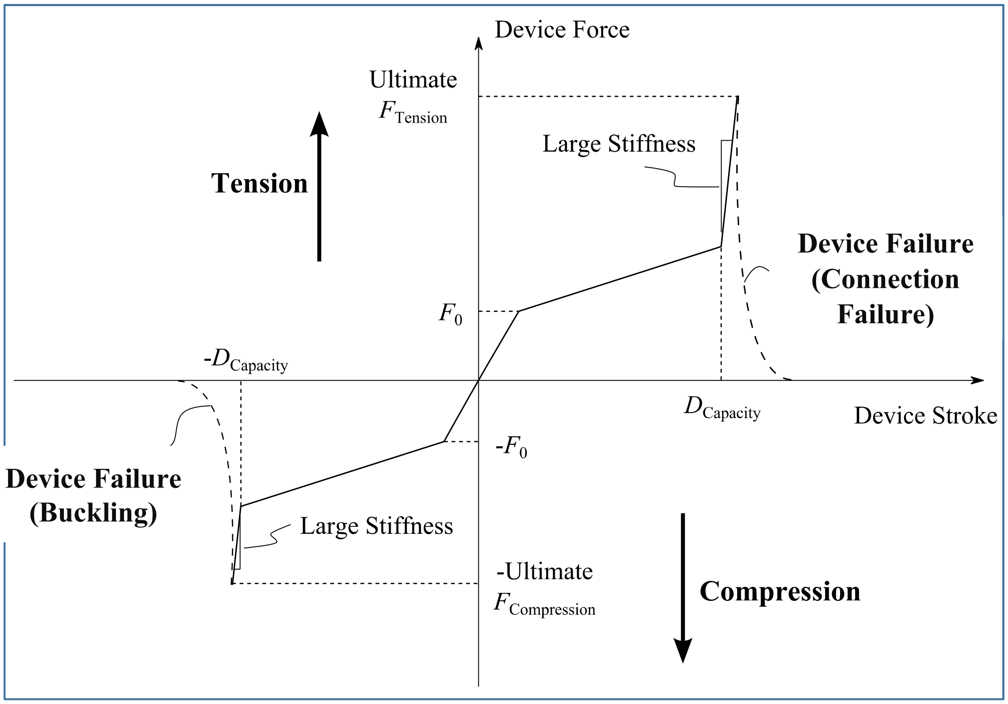

Figure 9-2 Ultimate Behavior of Self-Centering Fluidic Device-Brace System

The post-failure behavior of the device was defined in a manner that would (a) be physically meaningful and (b) avoid numerical instability in the analysis program. The behavior modeled is illustrated in Figure 9-3. The force is dependent on the time step. It is reduced at each time step by an amount equal to 10% of the value at the previous step. This force is essentially nil after about 100 steps. For example, if the time steep is 0.001sec, the force reduces to about 0.006 of the ultimate force in 50 steps or 0.05 sec.

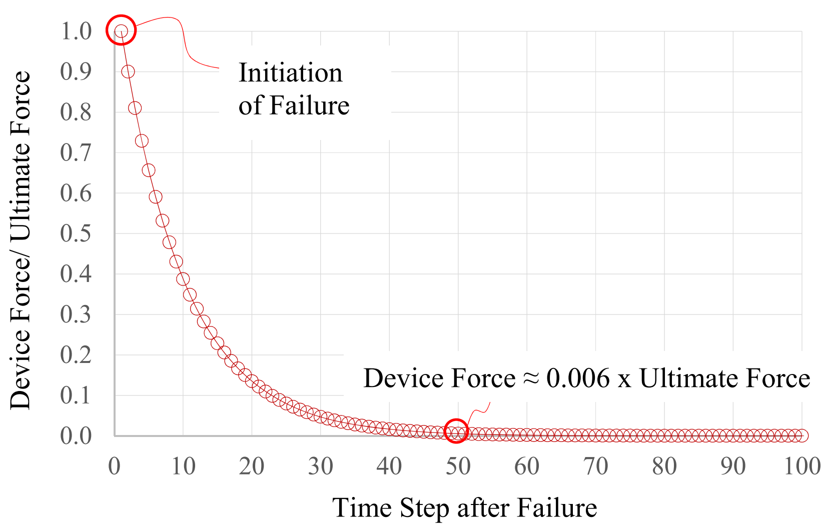

Figure 9-3 Post-failure Behavior of Fluidic Self-Centering Device-Brace System

An example of the behavior generated by this model is shown in the hysteresis curves of Figure 9-4 generated by dynamic analysis of a single-degree-of-freedom system for specified cyclic input. The device parameters are arbitrary and the hysteresis loops are only shown to illustrate the difference between models without and with consideration of the ultimate behavior of the device.

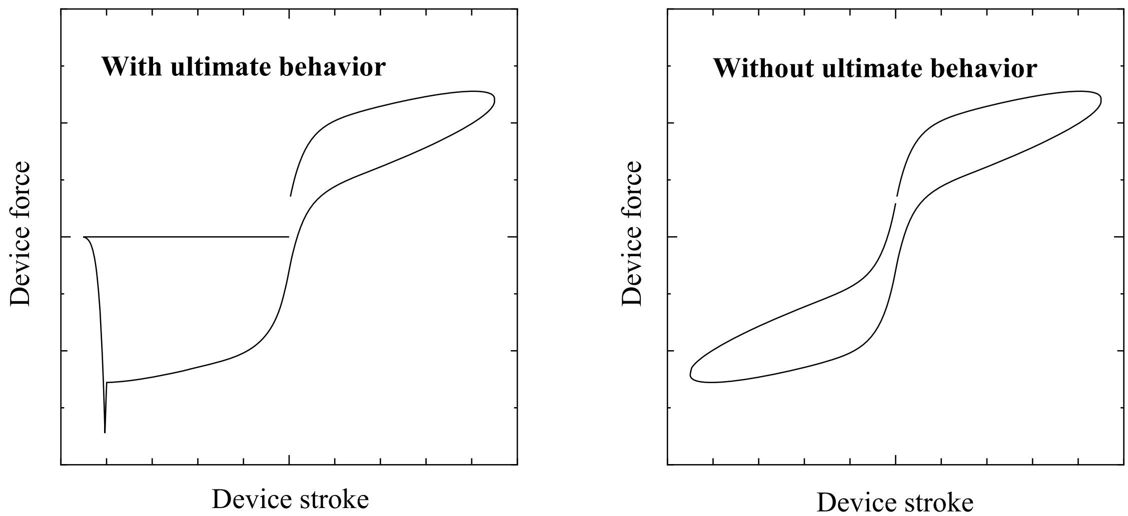

Figure 9-4 Force-displacement Relations of Fluidic Self-Centering Device-Brace System with and without Consideration of Ultimate Behavior

9.3 Properties of 3-story Buildings with and without Fluidic Self-Centering Devices

Frame 3*S*-75 with the self-centering system and the conventional 3*S*-Reference were analyzed. Details are presented in Appendices B and C. Figure 9-5 compares the two frames. Note that the tributary weights are assumed the same for the two frames. The model for analysis is illustrated in Figure 7-6.

The parameters of the fluidic self-centering system are summarized in Table 9-1. The ultimate force in compression is the buckling load of the HSS8x8x1/2 brace for an effective length of 8535mm. The ultimate force in tension is calculated as 1.3 times the average force calculated in the MCE (which is 891.8kN per Table 7-3, case of near-fault, pulse-like motions). Also in Table 9-1, F_0 is the preload, K_0 is the stiffness and C is the linear viscous damping constant. The stiffness for displacements larger than the displacement capacity is set 1000 times larger than K_0. It may be noted that the ultimate forces in tension and in compression are essentially the same. This leads to what it will be termed "balanced" behavior that results in pushover curves that are the same (or nearly so in this case) regardless of the direction of application of the lateral loads.

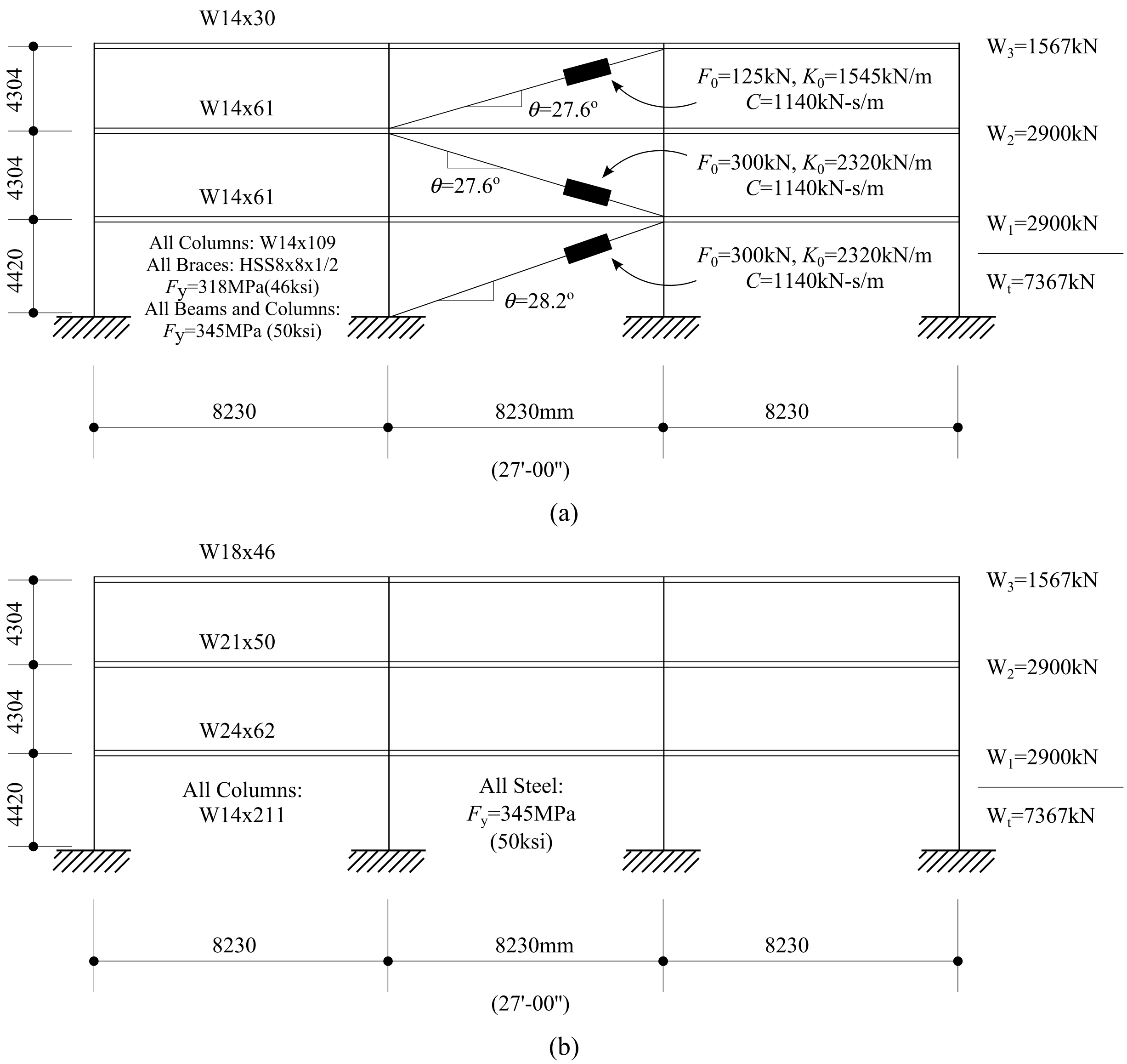

Figure 9-5 Frames (a) 3*S*-75 and (b) 3*S*-Reference

Table 9-1 Parameters of Fluidic Self-Centering Device-Brace System for Frame 3*S*-75 in "Balanced" Configuration

Story	F_0 [kN]	K_0 [kN/m]	Braces	C [kN-s/m]	$D_{Capacity}$ [mm]	Ultimate $F_{Tension}$ [kN]	Ultimate $F_{Compression}$ [kN]
3rd	125	1545	HSS8×8×1/2	1140	165	1160	1215
2nd	300	2320	HSS8×8×1/2	1140	165	1160	1215
1st	300	2320	HSS8×8×1/2	1140	165	1160	1215

Pushover curves for the 3-story frames are presented below to reveal the characteristics of the analyzed structures and to discuss issues related to the distribution of forces in the pushover analysis. It should be noted that the pushover curves used for the frame designs (see Appendices B and C, and Section 7) were based on forces distributed in proportion to the lateral force prescribed in ASCE 7-2010 (termed modal distribution in Section 7). However, FEMA P695 (FEMA, 2009) recommends the use of a different distribution of lateral forces in which the lateral forces are proportional to the product of the floor mass and first mode floor displacement. This is expressed as:

$$F_x \sim m_x \phi_{1,x} \tag{9-1}$$

where F_x is the lateral force at floor x, m_x is the mass x and $\phi_{1,x}$ is the first mode displacement at level x. For comparison, the ASCE 7 lateral force pattern is expressed as:

$$F_x \sim \frac{w_x h_x^k}{\sum_{i=1}^{n} w_i h_i^k} \tag{9-2}$$

where w_x is the story seismic weight at floor x, h_x is the height of floor x and k is a factor depending on the period of the structure.

Figure 9-6 presents pushover curves of the 3*S*-75 frame exclusive and inclusive of the fluidic self-centering system, and of frame 3*S*-Reference for the two lateral force distributions: FEMA P695 and ASCE 7-modal. The distribution of lateral force calculated by Equations (9-1) and (9-2) is presented in Table 9-2. Forces were applied on the left side of the frames shown in Figure 9-5.

Table 9-2 Lateral Force Distribution in Pushover Analysis of 3-Story Frames

Story	3*S*-75 Inclusive of Fluidic Self-centering System		3*S*-75 Exclusive of Fluidic Self-centering System		3*S*-Reference	
	FEMA P695	ASCE 7-modal	FEMA P695	ASCE 7-modal	FEMA P695	ASCE 7-modal
3	1.000	1.000	1.000	1.000	1.000	1.000
2	1.260	1.054	1.249	1.014	1.211	1.105
1	0.507	0.405	0.490	0.467	0.454	0.461

It is noted that the pushover curves are marginally affected by the pattern of load used despite the differences in load patterns seen in Table 9-2. Accordingly, pushover curves shown in the sequel are based on the FEMA P695 distribution of loads.

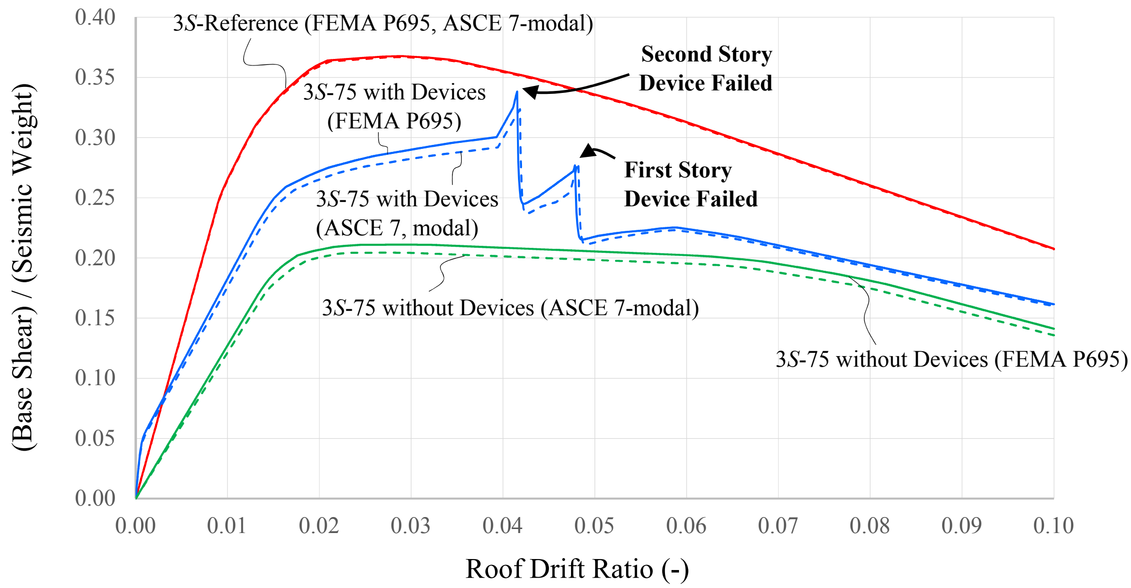

Figure 9-6 Push-Over Curves of 3*S*-Reference and 3*S*-75 Frames

The effect of the self-centering device configuration on the pushover curves is illustrated in the graphs of Figure 9-8 based on the configurations of Figure 9-7. Note that the device properties are those of Table 9-1 for which the behavior of the self-centering devices is balanced. Accordingly, the four different configurations of Figure 9-7 result in essentially the same pushover curves with the same sequence of device failure. The small differences seen in the pushover curves of Figure 9-8 are due to the small difference in the compression and tension capacities of the devices in this balanced design. Accordingly, it is expected that any of the configurations of Figure 9-7 will produce essentially the same results on performance.

To illustrate the importance of the balanced design, consider a case in which the connections of the self-centering devices in the 3-story frame are designed to fail at a force equal to twice the capacity in compression. This leads to an "unbalanced" design with the properties presented in Table 9-3.

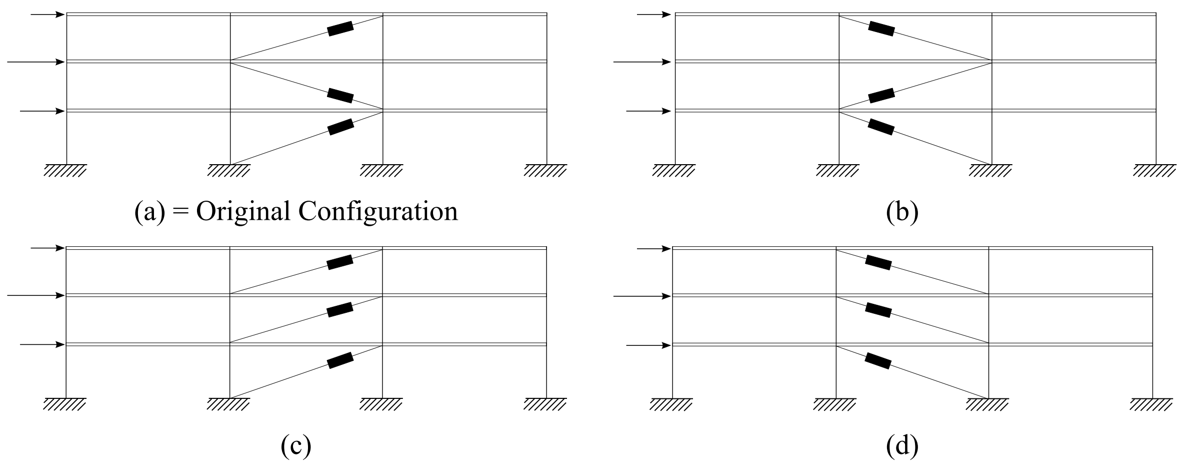

Figure 9-7 Self-Centering Device Configurations Analyzed

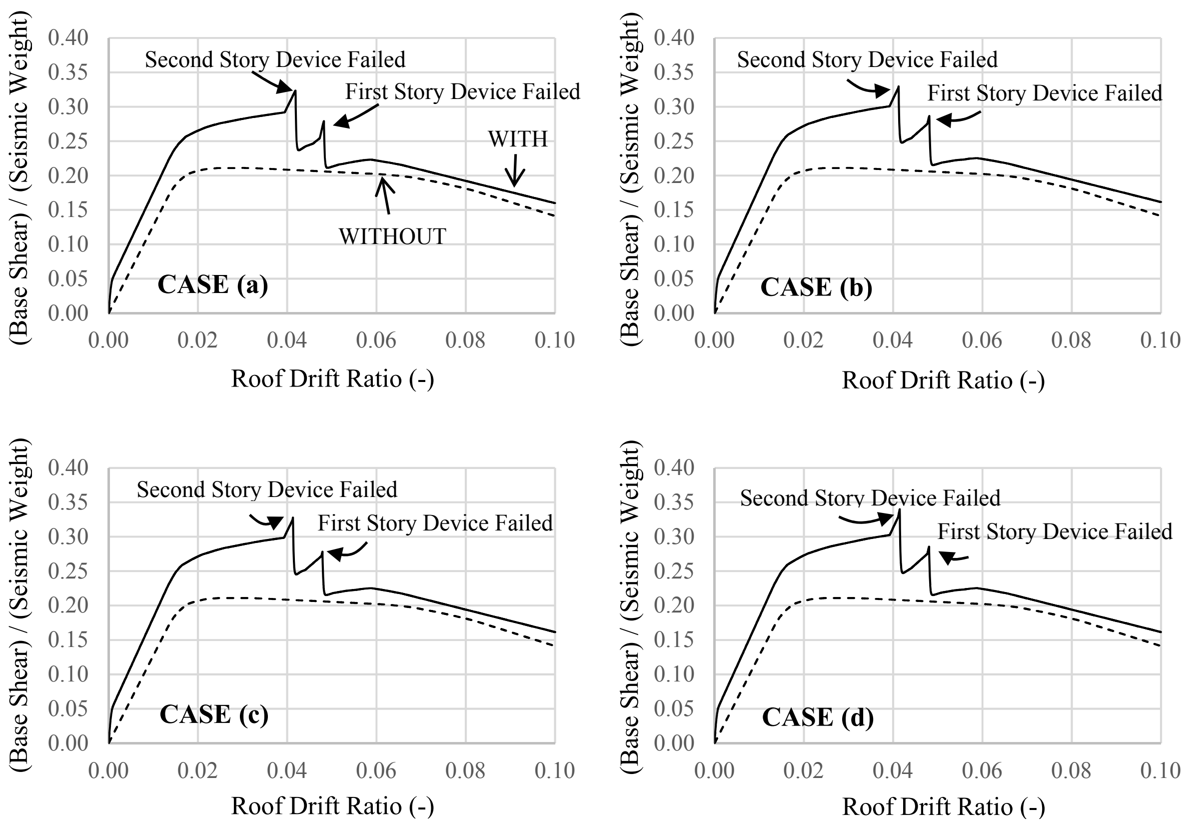

Figure 9-8 Pushover Curves of 3-Story Frame 3*S*-75 with Balanced Self-Centering Devices per Configurations of Figure 9-7 (FEMA P695 distribution of load)

Table 9-3 Parameters of Fluidic Self-Centering Fluidic Device-Brace System for Frame 3*S*-75 in "Unbalanced" Configuration

Story	F_0 [kN]	K_0 [kN/m]	Braces	C [kN-s/m]	$D_{Capacity}$ [mm]	Ultimate $F_{Tension}$ [kN]	Ultimate $F_{Compression}$ [kN]
3rd	125	1545	HSS8×8×1/2	1140	165	2430	1215
2nd	300	2320	HSS8×8×1/2	1140	165	2430	1215
1st	300	2320	HSS8×8×1/2	1140	165	2430	1215

The pushover curves for the unbalanced design in the four configurations of Figure 9-7 are presented in Figure 9-9. There are notable differences in the pushover curves and in the sequence of device failures among the four configurations. These differences are expected to lead to differences in the collapse resistance and are thus worthy of investigation.

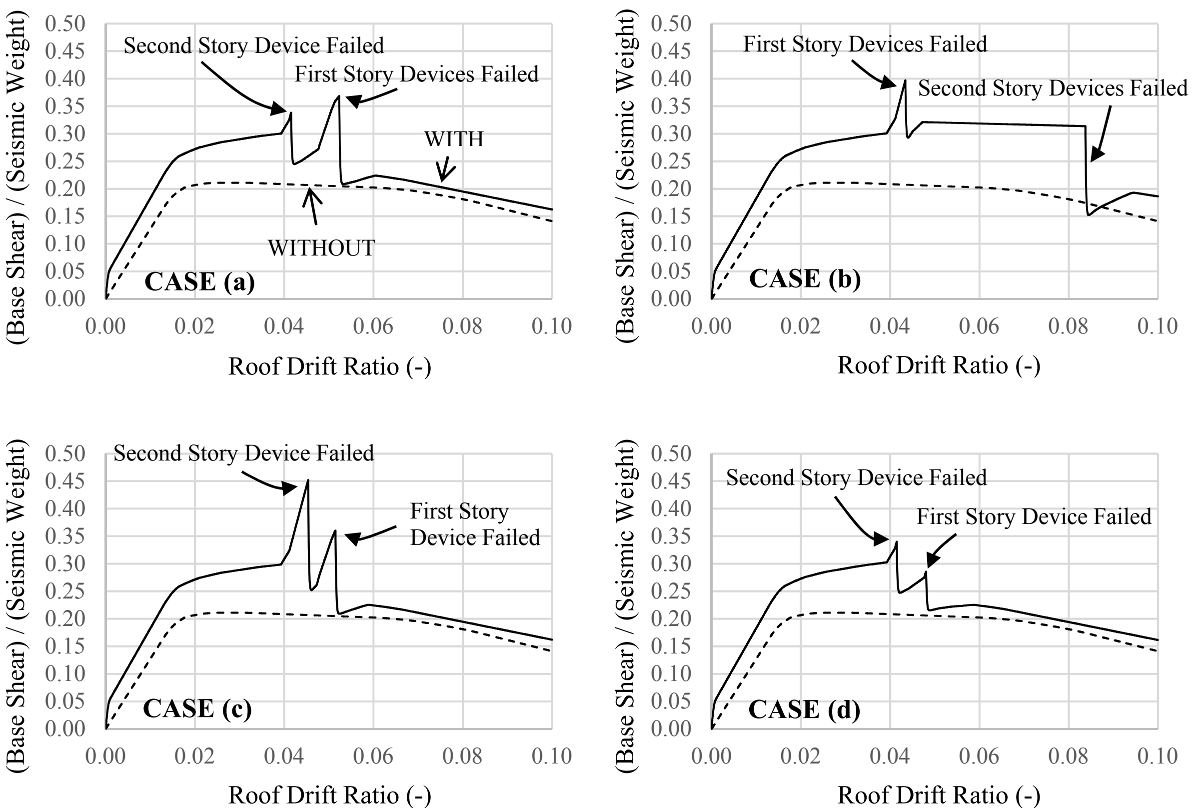

Figure 9-9 Pushover Curves of 3-Story Frame 3*S*-75 with Unbalanced Self-Centering Devices per Configurations of Figure 9-7 (FEMA P695 distribution of load)

9.4 Properties of 6-story Buildings with and without Fluidic Self-Centering Devices

The properties of the 6-story buildings are presented based only on the original device configuration. Figure 9-10 presents the two frames analyzed: 6*S*-75 with fluidic self-centering devices and 6*S*-Reference. The properties of the fluidic self-centering devices under ultimate conditions are presented in Table 9-4. Note that the model used in the collapse resistance assessment includes the modified bracing as determined following the response history analysis (see end of Appendix D). The ultimate force in compression has been calculated as the design strength in compression for an effective length of 8535mm and a factor ϕ=1 (see Appendix D). The ultimate force in tension has been calculated as 1.3 times the average force calculated in the seven analyses for the MCE (per Table 7-4).

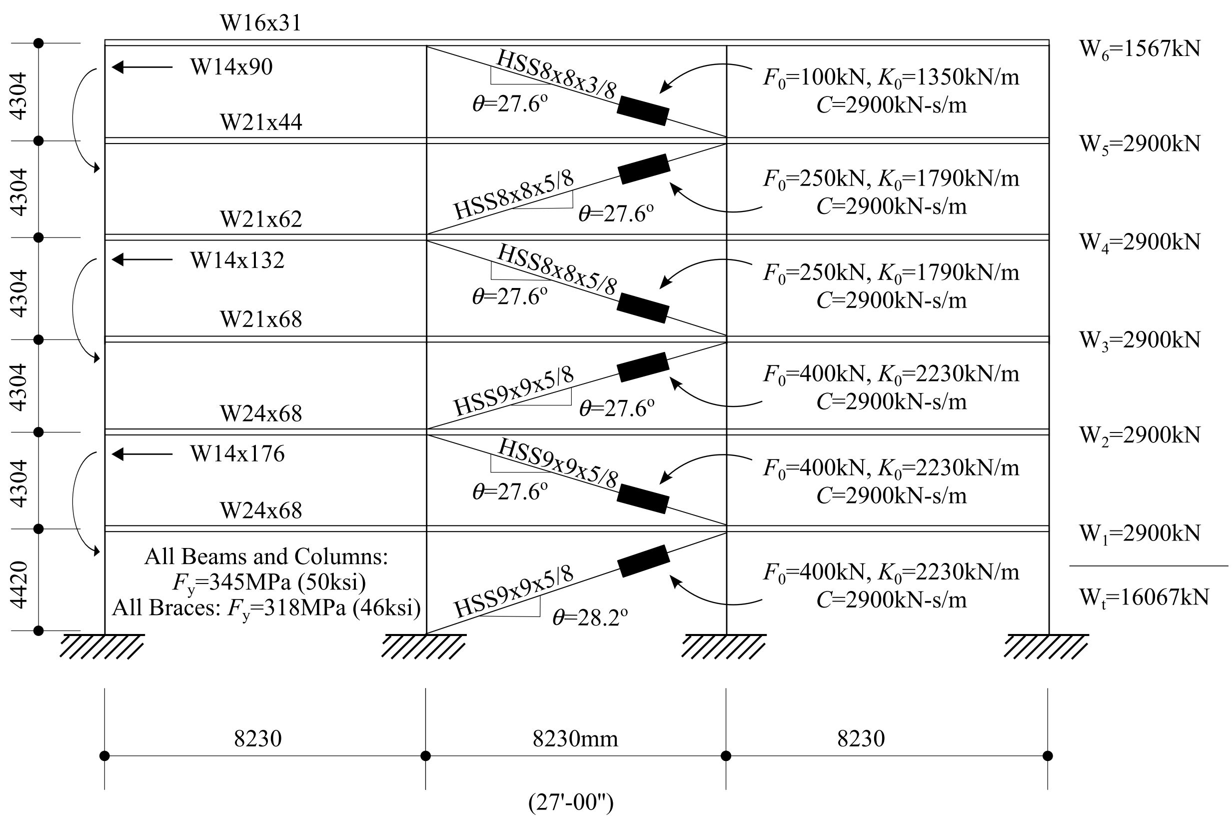

(a)

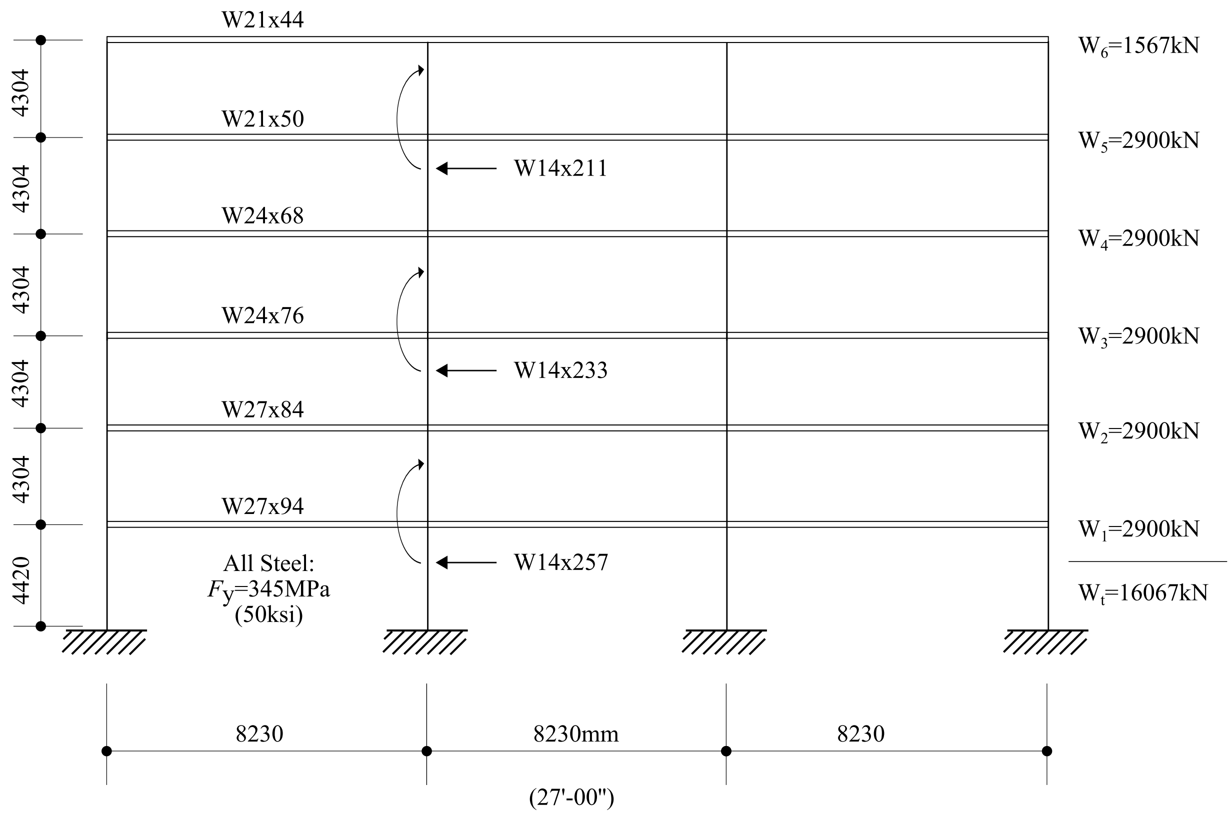

(b)

Figure 9-10 Frames (a) 6*S*-75 and (b) 6*S*-Reference

Table 9-4 Parameters of Fluidic Self-Centering Fluidic Device-Brace System for Frame 6*S*-75

Story	F_0 [kN]	K_0 [kN/m]	Braces	C [kN-s/m]	$D_{Capacity}$ [mm]	Ultimate $F_{Tension}$ [kN]	Ultimate $F_{Compression}$ [kN]
6th	100	1350	HSS8x8x3/8	2900	165	859	964
5th	250	1790	HSS8×8×5/8	2900	165	1302	1434
4th	250	1790	HSS8×8×5/8	2900	165	1302	1434
3rd	400	2320	HSS9x9×5/8	2900	165	1843	1983
2nd	400	2320	HSS9x9×5/8	2900	165	1843	1983
1st	400	2320	HSS9x9×5/8	2900	165	1843	1983

Figure 9-11 presents pushover curves of the 6*S*-75 frame exclusive and inclusive of the fluidic self-centering system, and of frame 6*S*-Reference for the two lateral force distributions: FEMA P695 and ASCE 7-modal. The distribution of lateral force calculated by Equations (9-1) and (9-2) is presented in Table 9-5. Forces were applied on the left side of the frames.

Table 9-5 Lateral Force Distribution in Pushover Analysis of 6-Story Frames

Story	6*S*-75 Inclusive of Fluidic Self-centering System		6*S*-75 Exclusive of Fluidic Self-centering System		6*S*-Reference	
	FEMA P695	ASCE 7-modal	FEMA P695	ASCE 7-modal	FEMA P695	ASCE 7-modal
6	1.000	1.000	1.000	1.000	1.000	1.000
5	1.634	1.339	1.621	1.310	1.615	1.360
4	1.320	0.905	1.297	0.861	1.286	0.932
3	0.957	0.541	0.938	0.500	0.913	0.574
2	0.568	0.264	0.551	0.234	0.532	0.290
1	0.217	0.079	0.209	0.063	0.197	0.091

It is noted that the pushover curves are affected by the pattern of load used but the effects does not seem to be significant for the cases of the reference frame and the frame with the fluidic self-centering system.

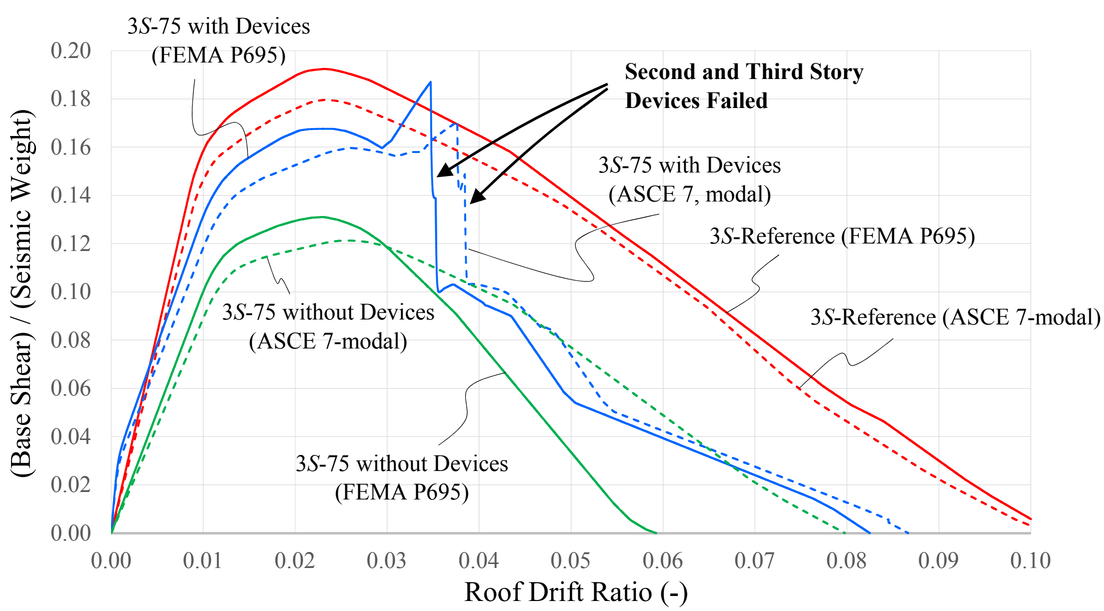

Figure 9-11 Push-Over Curves of 6*S*-Reference and 6*S*-75 Frames

9.5 Selection and Scaling of Input Ground Motions

The collapse resistance assessment requires performing Incremental Dynamic Analysis (IDA), which is used to assess the probability of collapse for a particular set of motions (Vamvatsikos and Cornell, 2002; FEMA P695, 2009). The suite of motions used in the analysis is the set of 44 individual components of far-field ground motions utilized in the FEMA P695 (2009) project. The ground motions were all recorded from sites located greater than or equal to 10 km from fault rupture, had a peak ground acceleration (PGA) larger than 0.2*g*, a peak ground velocity (PGV) larger than 150mm/sec and a magnitude M larger than 6.5. Two methods of scaling these ground motions are used in this study: 1) S_a-Component Scaling and 2) Peak Ground Velocity (PGV) Normalization. The two scaling methods are briefly described below.

The S_a-Component scaling method has been used in the study of Seo *et al*. (2014) and other recent studies of collapse resistance assessment (e.g., Champion and Liel, 2012, Elkady and Lignos, 2014). In this scaling approach, the ground motions are scaled in amplitude so that the 5%-damped spectral accelerations of each of the ground motions are equal at the fundamental period of the analyzed structure. Figure 9-12 shows an example of this scaling method.

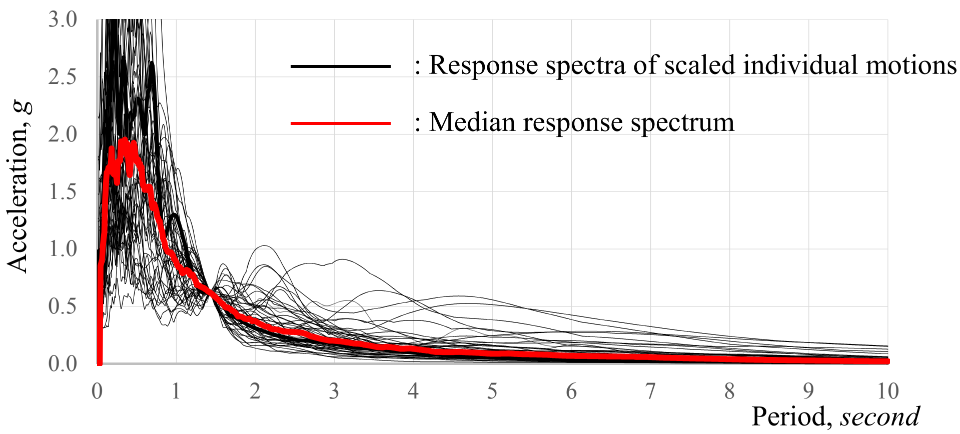

Figure 9-12 Example of S_a-Component Scaling

The Peak Ground Velocity (PGV) Normalization scaling method is used in the FEMA P695 (2009) document and has been used in the related study of Miyamoto *et al*. (2011). In this approach each ground motion is normalized by a factor numerically equal the PGV of the motion so that effectively all scaled motions have the same PGV. Figure 9-13 shows an example of this scaling method.

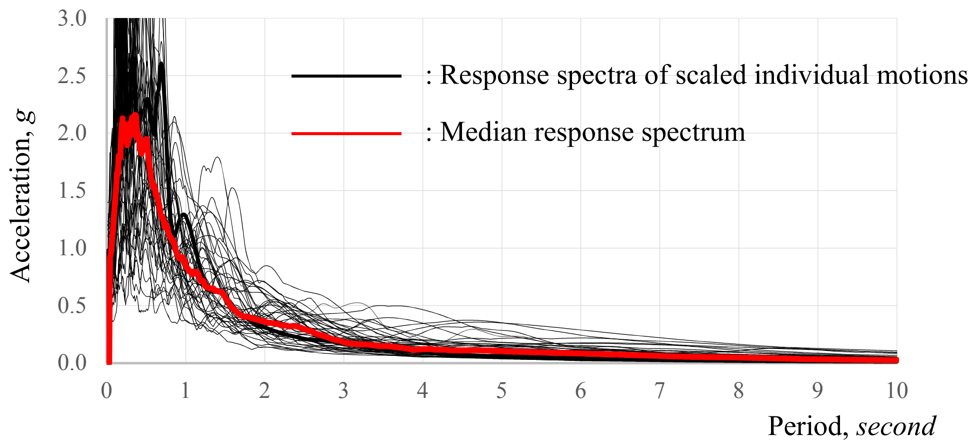

Figure 9-13 Example of PGV Normalization Scaling

Values of the fundamental period used in the scaling are presented in Table 9-6. Note that the periods of 3*S*-75 and 6S-75 frames were calculated by including the effect of the self-centering devices, modelled as elastic elements with an effective stiffness determined at a story drift displacement equal to the story yield displacement (see Sections 6 and 7, Table 7-1).

Table 9-6 Values of Fundamental Period used for Scaling Motions

Frame	Number of Stories	Fundamental Period (sec)
3*S*-75	3	1.31
3*S*-Reference	3	1.07
6*S*-75	6	2.06
6*S*-Reference	6	1.90

9.6 Collapse Fragility

9.6.1 Definition of Collapse Criteria

Incremental dynamic Analysis (IDA) is utilized to assess the collapse fragility of the frames with and without the fluidic self-centering system. In this method, the scaled motions are used to repeatedly analyze the frames by systematically increasing the intensity so that the spectral acceleration of the scaled motions at the fundamental period $S_a(T_1)$ increases by increments of 0.05g until the frame "collapses" under the combined action of the lateral earthquake forces and gravity. Collapse is defined as one of the following events:

1) The maximum story drift ratio exceeds 10%.
2) There is instability detected by termination of the analysis program.

3) The slope of the $S_a(T_1)$ vs maximum story drift ratio (the IDA curve) in the current step of analysis is less than 10% of the slope of the same curve in the first step of analysis.

9.6.2 Fragility Analysis Results

Figure 9-14 presents the IDA curves of the 3*S*-75 (including the fluidic self-centering system in the balanced configuration of Table 9-1) and 3*S*-Reference frames computed using motions scaled by the S_a-Component scaling approach. Each of these curves corresponds to a particular ground motion (out of the 44 used) and each dot on curve represents the result of one nonlinear response history analysis. The dots are connected by lines to represent the IDA curves, distinguish between ground motions and detect "collapse" when the slope of the curve is less than 10% of the slope of the initial IDA curve slope.

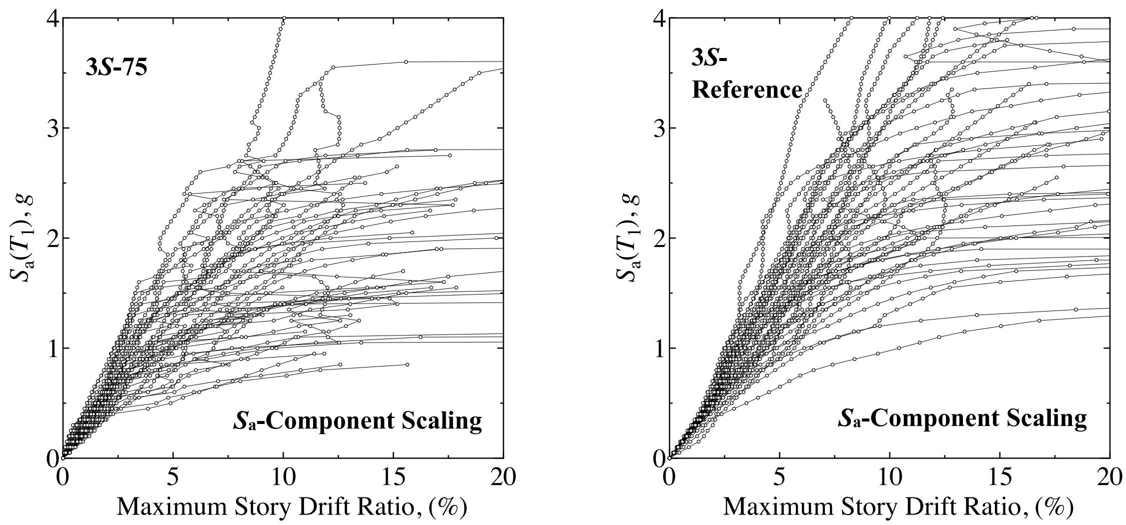

Figure 9-14 IDA Curves for 3*S*-75 and 3*S*-Reference Frames for Motions based on S_a-Component Scaling

Figure 9-15 presents the empirical collapse fragility curves for the two frames (cumulative distribution function or probability of collapse vs the intensity measure of $S_a(T_1)$ normalized by the spectral acceleration in the MCE at the fundamental period T_1 of each frame, where the probability of collapse was determined at each intensity level as the number of analyses that resulted in collapse divided by the total number of analyses, 44). The fitted lognormal cumulative distribution functions are also shown in Figure 9-15. The median collapse value $S_{aCOL}(T_1)$ (spectral acceleration at which at least half of the analyses result in collapse), the dispersion factor β and the spectral acceleration in the MCE at the fundamental period T_1 are also shown in the figure. Note that the cumulative distribution function *CDF* is given by:

$$CDF(x) = \int_{-\infty}^{x} \frac{1}{s\beta\sqrt{2\pi}} \exp\left[-\frac{\{\ln s - \ln m\}^2}{2\beta^2}\right] ds \tag{9-3}$$

In this equation, x is the random variable (the spectral acceleration at the fundamental period of the structure) and m is the median collapse value $S_{aCOL}(T_1)$ divided by $S_{aMCE}(T_1)$.

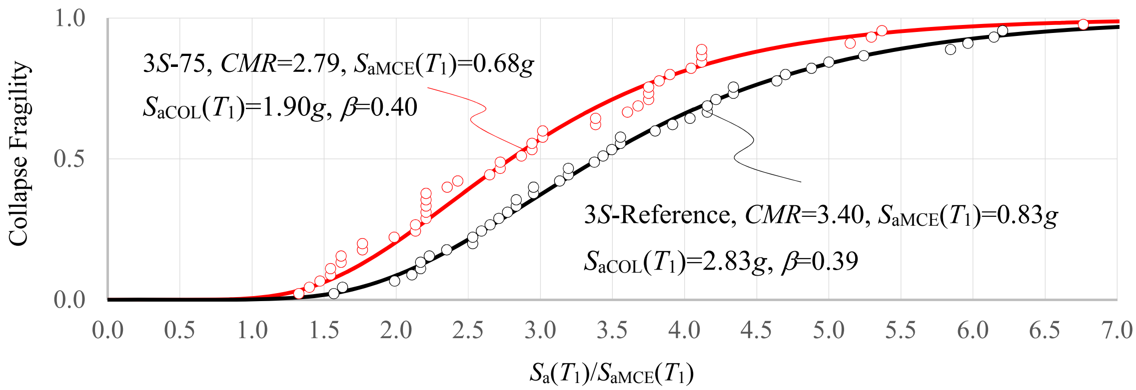

Figure 9-15 Collapse Fragility (or cumulative distribution function) for 3*S*-75 and 3*S*-Reference Frames for Motions based on S_a-Component Scaling

Figures 9-16 and 9-17 show the IDA curves and the collapse fragility curves of the 3*S*-75 and 3*S*-Reference frames obtained using motions scaled by the *PGV* Normalization scaling approach.

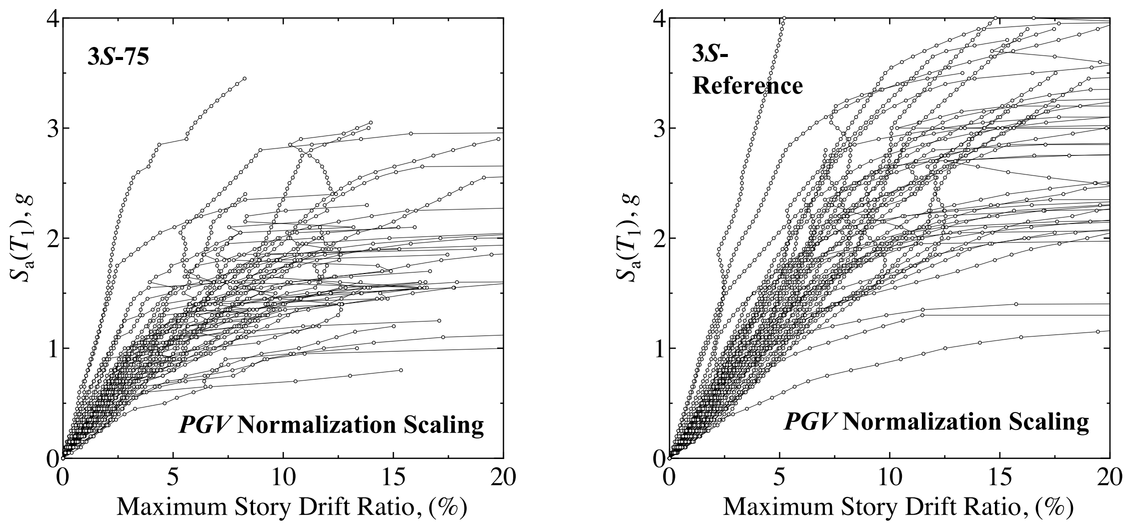

Figure 9-16 IDA Curves for 3*S*-75 and 3*S*-Reference Frames for Motions based on PGV Normalization Scaling

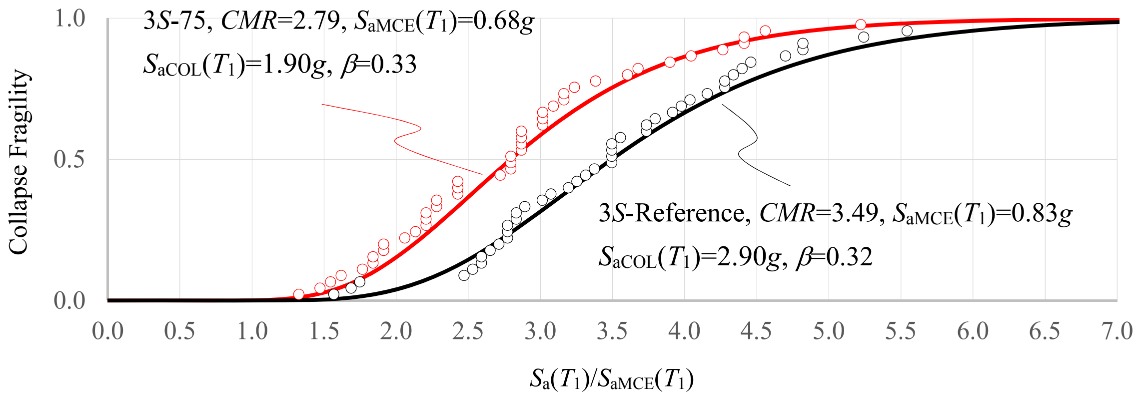

Figure 9-17 Collapse Fragility (or cumulative distribution function) for 3*S*-75 and 3*S*-Reference Frames for Motions based on *PGV* Normalization Scaling

Figures 9-18 to 9-21 show the IDA and collapse fragility curves of the 6*S*-75 and 6*S*-Reference frames obtained by using the two methods of scaling.

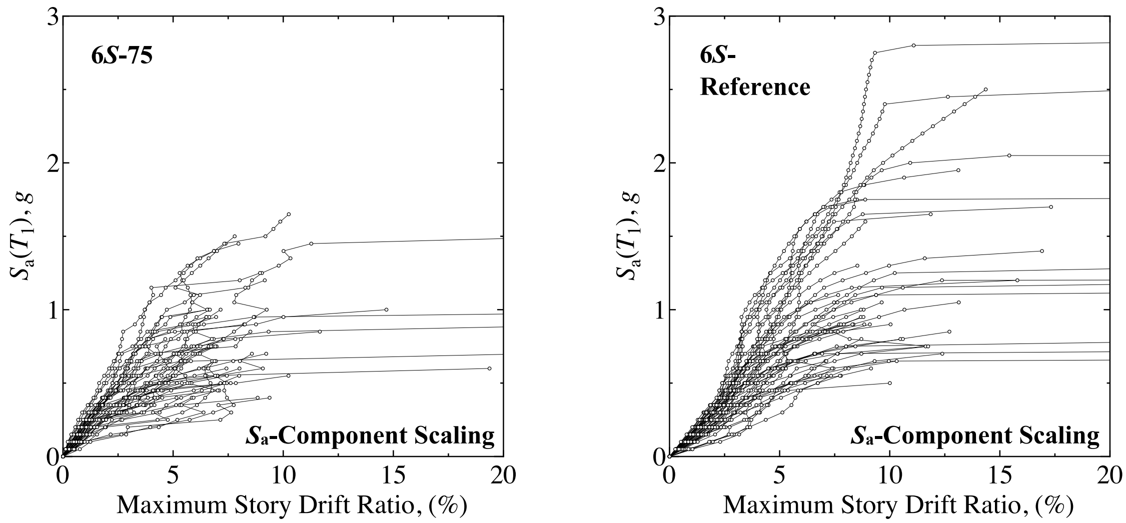

Figure 9-18 IDA Curves for 6*S*-75 and 6*S*-Reference Frames for Motions based on S_a-Component Scaling

Note that the collapse fragility curves are presented as function of the spectral acceleration at the fundamental period normalized by the spectral acceleration in the MCE at the fundamental period. This is done for the purpose of comparison of the curves shown on the same graph. A more detailed presentation of results of the IDA curves and of the collapse fragility curves as function of the earthquake intensity $S_a(T_1)$ is presented in Appendix E for all analyzed cases.

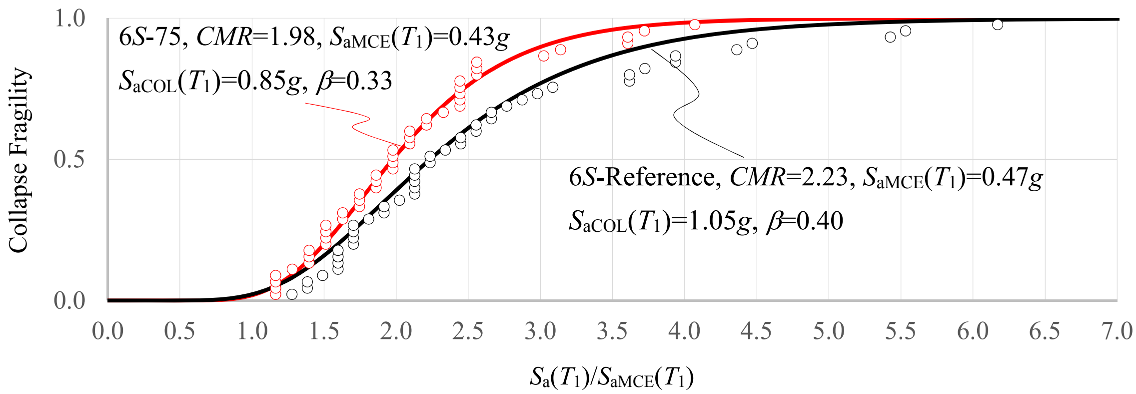

Figure 9-19 Collapse Fragility (or cumulative distribution function) for 6*S*-75 and 6*S*-Reference Frames for Motions based on S_a-Component Scaling

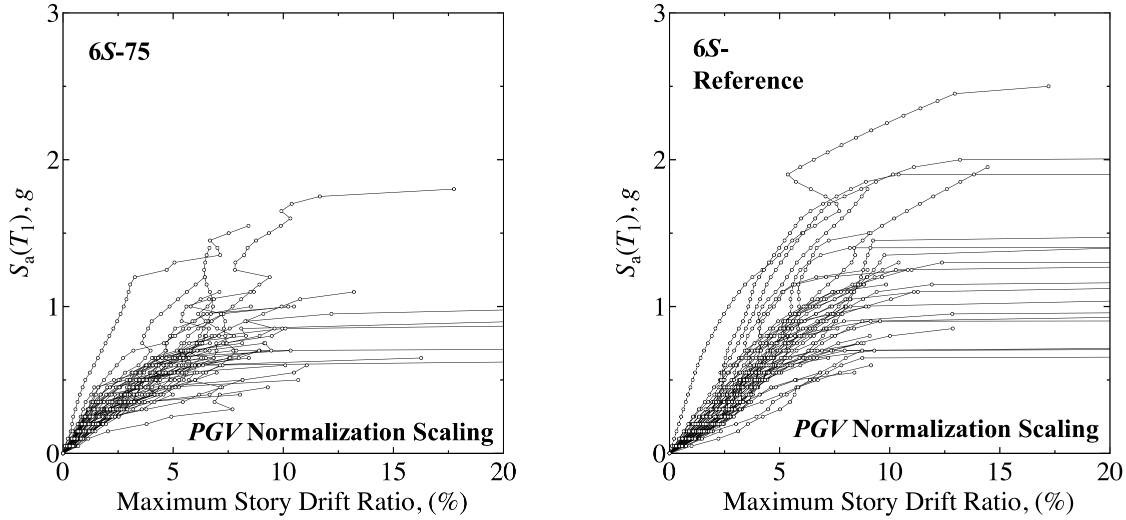

Figure 9-20 IDA Curves for 6*S*-75 and 6*S*-Reference Frames for Motions based on PGV Normalization Scaling

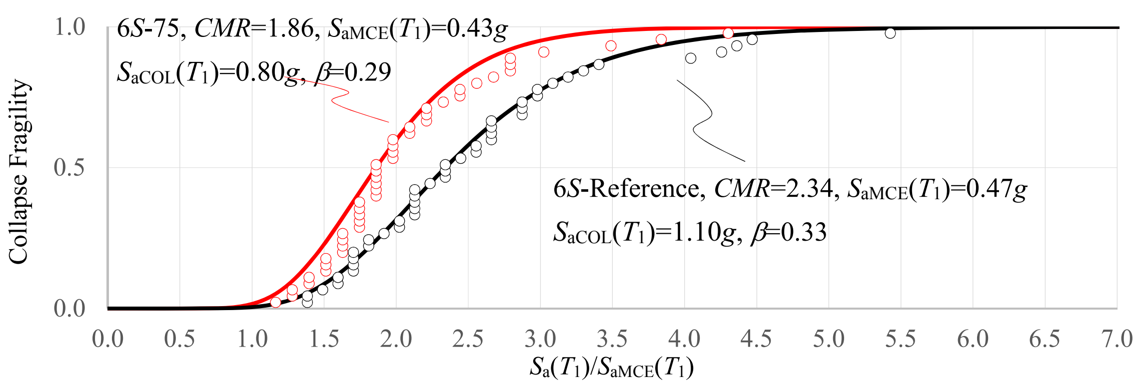

Figure 9-21 Collapse Fragility (or cumulative distribution function) for 6*S*-75 and 6*S*-Reference Frames for Motions based on *PGV* Normalization Scaling

Tables 9-7 and 9-8 present values of the following parameters calculated for the 3-story and 6-story buildings using the data in the collapse fragility curves:

1) The spectral acceleration at the fundamental period when collapse occurs (or median), $S_{aCOL}(T_1)$,
2) The spectral acceleration at the fundamental period at the MCE level, $S_{aMCE}(T_1)$,
3) The collapse margin ratio, CMR defined as

$$CMR = \frac{S_{aCOL}(T_1)}{S_{aMCE}(T_1)} \tag{9-4}$$

Note that the CMR accounts for the random nature of the ground motions (aleatory uncertainty) but it does not account for variability in the structural properties and uncertainty in the analysis model (epistemic uncertainty). The FEMA P695 procedure (FEMA, 2009) presents a systematic approach to account for epistemic uncertainty and for correcting for the effects of the spectral shape, resulting in the *adjusted collapse margin ratio* (ACMR). Generally, the ACMR is larger than the CMR. While the ACMR could be calculated, the use of just the CMR and the probability of collapse in the MCE enabled comparison of the designs with and without the self-centering system, and also allowed for investigating the effect of various design parameters on the collapse vulnerability.

4) The probability of collapse at the MCE, defined as the ratio of the number of collapses at an intensity corresponding to $S_{aMCE}(T_1)$ divided by the total number of analyses (used 45 instead of 44 to avoid a probability of 1-certainty), and
5) The dispersion factor β.

Table 9-7 Collapse Margin Ratio, Probability of Collapse in the MCE and other Parameters in Case of Motions based on S_a-Component Scaling

	$S_{aCOL}(T_1)$ or median (g)	$S_{aMCE}(T_1)$ (g)	*CMR*	Collapse Probability at MCE (*%*)	β
3*S*-75	1.90	0.68	2.79	0.6	0.40
3*S*-Reference	2.83	0.83	3.40	0.1	0.39
6*S*-75	0.85	0.43	1.98	1.9	0.33
6*S*-Reference	1.05	0.47	2.23	2.2	0.40

Table 9-8 Collapse Margin Ratio, Probability of Collapse in the MCE and other Parameters in Case of Motions based on *PGV* Normalization Scaling

	$S_{aCOL}(T_1),g$	$S_{aMCE}(T_1),g$	*CMR*	Collapse Probability at MCE, *%*	β
3*S*-75	1.90	0.68	2.79	0.1	0.33
3*S*-Reference	2.90	0.83	3.49	0.0	0.32
6*S*-75	0.80	0.43	1.86	1.6	0.29
6*S*-Reference	1.10	0.47	2.34	0.5	0.33

In discussing the results of the seismic collapse assessment it is noted that the analyzed frames with the fluidic self-centering system had the ultimate properties in Tables 9-1 and 9-4 for the 3-story and 6-story frames respectively, and the configurations of the devices were those shown in Figures 9-5(a) and 9-10(a). The ultimate properties of the frames are essentially the same in the two directions (forces towards the right or forces towards the left) in what was termed "balanced" conditions. Additional studies will follow with "unbalanced" conditions.

The results in Figures 9-14, 9-16, 9-18 and 9-20 and in Tables 9-7 and 9-8 demonstrate the following:

1) The collapse fragility curves of the frames with the fluidic self-centering system show a shift to the left when compared to those of the conventional reference frames. This results in a lower collapse margin ratio (*CMR*), as shown in Tables 9-7 and 9-8 that indicates an increase in vulnerability to collapse for the weaker 3*S*-75 and 6*S*-75 frames. This reduction in *CMR* is relatively small and it will be shown that there is a variety of measures that can improve it.
2) The probability of collapse at the MCE is very small. Note that the probability of collapse was determined by analytical means using the fitted lognormal distribution to the empirical data (by comparison the CMR is directly based on the empirical data). The empirical data show zero probability of collapse in the MCE. This is consistent with the design of the frames in which the columns were provided with increased section properties in order to prevent plastic hinge formation in the columns and to sustain additional axial loads.
3) The reduction of the CMR in the 3*S*-75 and 6*S*-75 frames is consistent with the observations of Seo *et al*. (2014) in the study of collapse fragility of structures with viscous damping systems. However, the actual values of CMR are higher and values of the probability of collapse in the

MCE are lower in this study than in the study of Seo *et al*. (2014). This is attributed to the stronger column design in this study.

4) There is a small effect of the ground scaling approach on the computed CMR and probabilities of collapse in the MCE.

9.7 Effect of Fluidic Self-Centering System Design on Collapse Fragility of 3-Story Structure

A number of studies of collapse fragility are conducted to investigate the following:

1) Effect of the fluidic self-centering system design in terms of ultimate characteristics in the "balanced" and "unbalanced" configurations, and configurations of high strength.
2) Effect of displacement capacity of the fluidic self-centering system.
3) Effect of the amount and type of viscous damping (linear or nonlinear) provided by the fluidic self-centering system.
4) Effect of the preload in the fluidic self-centering system.
5) Effect of stiffness of the fluidic self-centering system.
6) Effect of increased strength of the frame.

The studies concentrate on the 3-story 3*S*-75 frame analyzed using ground motions scaled by the S_a-component scaling approach. One more study with frame 3*S*-85 is reported. Summaries of the results are presented in Tables 9-9 and 9-10.

9.7.1 Effect of Ultimate Characteristics of Fluidic Self-Centering System on Collapse Fragility

Figure 9-22 presents the IDA curves for the 3*S*-75 frame in the unbalanced configuration (see Table 9-3 for properties) and Figure 9-23 presents the empirical collapse fragility curves (cumulative distribution function or probability of collapse vs the intensity measure of $S_a(T_1)$ normalized by the spectral acceleration in the MCE at the fundamental period T_1 of each frame) for the 3*S*-75 frame in the balanced configuration of Table 9-1 and the unbalanced configuration of Table 9-3. The fragility curve for the 3*S*-Reference frame is also shown for comparison. The results demonstrate a small but clear increase in the collapse margin ratio in the unbalanced configuration, which is the result of the increased ultimate capacity of the device-brace system in one direction (tension). This indicates that increasing the ultimate capacity of the brace-device system should improve the collapse margin ratio. Note that the capacity is increased by increasing the section of the structural tubing used to support the fluidic self-centering device and by increasing the strength of the connections of the tubing to the frame and the device. The device itself typically has high capacity in both tension and compression by a factor of 2 on the maximum force in the MCE.

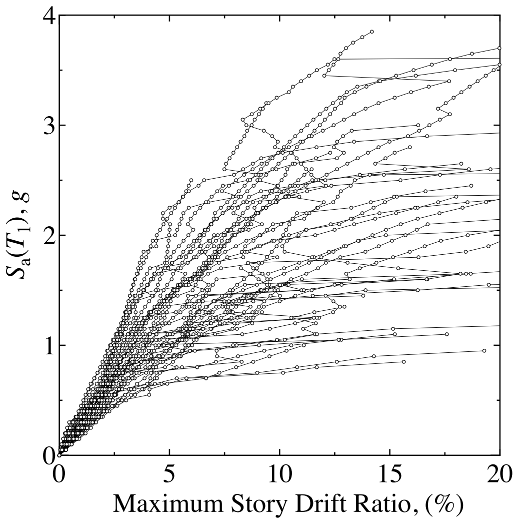

Figure 9-22 IDA Curves for 3*S*-75 in Unbalanced Configuration for Motions based on S_a-Component Scaling

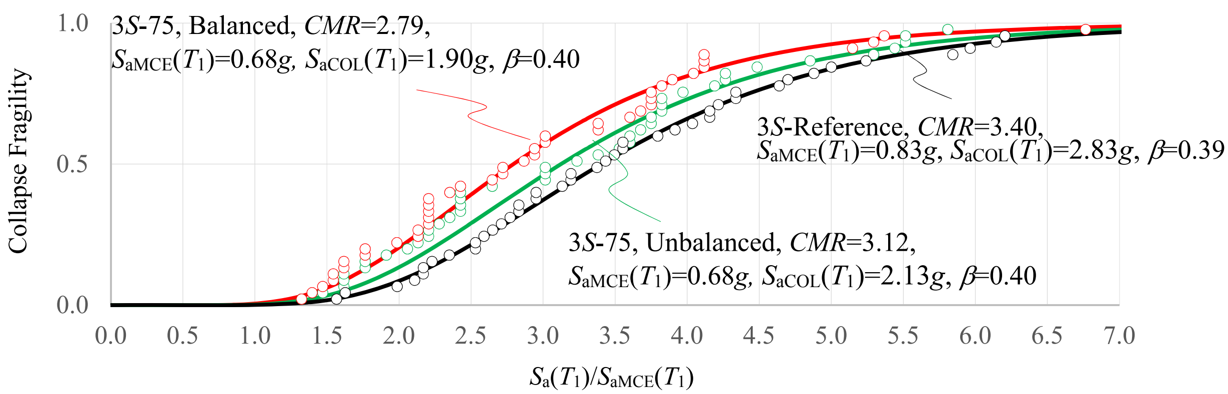

Figure 9-23 Collapse Fragility (or cumulative distribution function) for 3*S*-75 Frame in Balanced and Un-Balanced Configurations and for 3*S*-Reference Frame for S_a-Component Scaled Motions

To demonstrate the effect of increased ultimate capacity of the self-centering device-brace system, the ultimate capacity is increased by designing the brace and the connections for a force equal to twice the device peak force calculated in the MCE or 1784kN. A brace of section HSS9x9x5/8 used for these devices has a capacity of 1983kN in compression for effective length of 8535mm (28ft). This capacity is used for both compression and tension and is presumed that the devices have at least as much force capacity. The parameters of the new 3-story frame are the same as those in Table 9-1 but the ultimate capacity in tension and in compression is equal to 1983kN. The empirical collapse fragility curves of the new frame and those of the 3S-75-balanced and of the 3S-Reference frames are shown in Figure 9-24 together with information on the collapse margin ratio. Motions scaled by the S_a-component procedure have been used in the analysis. Evidently, the ultimate capacity of the device-brace system has a marked effect on the fragility curve and the collapse margin ratio, resulting in a large increase on the collapse margin ratio.

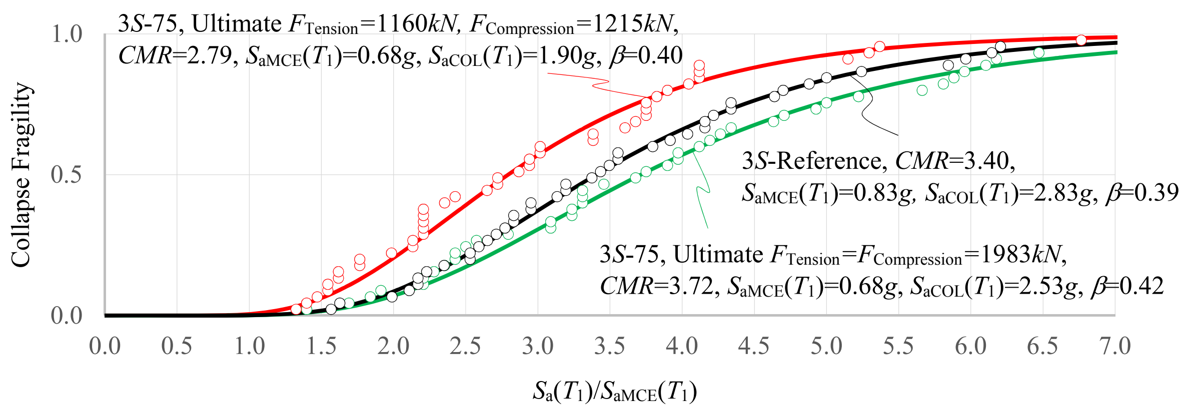

Figure 9-24 Collapse Fragility for 3S-75 Frame in Balanced (capacity 1.3 times the peak force) and Increased Capacity (2 times the peak force) Configurations and for 3S-Reference Frame for S_a-Component Scaled Motions

9.7.2 Effect of Displacement Capacity of Fluidic Self-centering System on Collapse Fragility

The effect of increased displacement capacity of the self-centering system on the collapse fragility is investigated by analyzing the 3S-75 frame with the properties of Table 9-1 (balanced configuration) but with the displacement capacity increased to 215mm, which is 30% larger than the original displacement capacity of the devices. Note that when the displacement capacity of the fluidic devices increases, the volume of fluid is also increased and the stiffness of the device is reduced. This has not been considered in this study so that only the effect of the device displacement capacity is revealed.

The empirical collapse fragility curves of the frame with increased displacement capacity of the devices and those of the 3S-75 with 165mm displacement capacity and of the 3S-Reference frames are shown in Figure 9-25 together with information on the collapse margin ratio. Motions scaled by the S_a-component procedure have been used in the analysis. Evidently, the displacement capacity of the fluidic self-centering devices has no effect on the fragility curve and the collapse margin ratio.

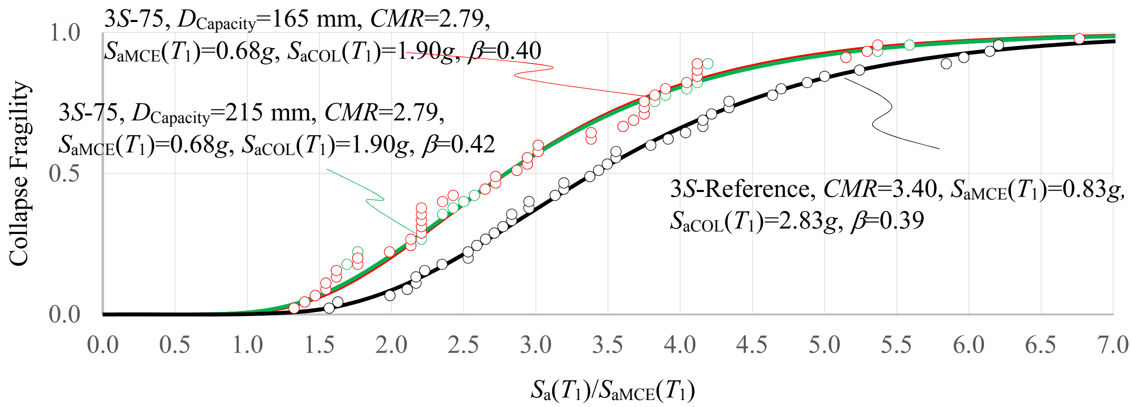

Figure 9-25 Collapse Fragility for 3*S*-75 Frame in Balanced Configurations with Displacement Capacity of 165mm and 215mm and for 3*S*-Reference Frame for S_a-Component Scaled Motions

9.7.3 Effect of Damping Provided by the Fluidic Self-Centering System on Collapse Fragility

The effect of increased linear viscous damping of the self-centering system on the collapse fragility is investigated by analyzing the 3*S*-75 frame with the properties of Table 9-1 (balanced configuration) but with the damping constant C=1710(kN-sec/m) instead of C=1140(kN-sec/m) so that the damping in the fundamental mode is 0.15 instead of 0.10. The results of analysis of this frame for the MCE are presented in Table 8-5 from where the peak device force was used to select the size of the bracing. The braces are HS8x8x5/8 with capacity in compression for effective length of 8535mm (28ft) equal to 1425kN. The ultimate capacity of the device-brace system of the frame with increased damping is taken as 1425kN in both tension and in compression.

The empirical collapse fragility curves of the frame with increased damping and those of the 3*S*-75 with damping of 0.10 and of the 3*S*-Reference frames are shown in Figure 9-26 together with information on the collapse margin ratio. Motions scaled by the S_a-component procedure have been used in the analysis. Evidently, the increase in linear viscous damping of the fluidic self-centering system results in a small decrease of the collapse margin ratio. This is due to the fact that the damping force increases without bound as the earthquake intensity increases beyond the MCE, leading to failure of the device-brace system at a lower level of intensity.

The negative effect of increased linear viscous damping on the collapse fragility suggests that the use of increased nonlinear viscous damping (for which the damping force does not increase as much as velocity increases) could improve the collapse fragility. This is investigated next by analyzing the 3*S*-75 frame in the balanced configuration of Table 9-1 but converting the dampers to nonlinear per equation (6-38) with exponent α=0.5 and damping constant C_N= 551.3kN-(sec/m)$^{1/2}$ or C_N= 666.4kN-(sec/m)$^{1/2}$ so that the effective damping ratio β_{v1} per equation (6-40) (step 13 of RSA procedure of Section 6.5) is 0.10 or 0.15, respectively, in the DE (see Section 8.3). The two frames with the self-centering system of nonlinear viscous behavior were analyzed for the effects of the MCE and the response was reported in Section 8, Tables 8-7 and 8-8. The fragility curves are presented in Figures 9-27 and 9-28 together with information on the collapse margin ratio. Motions scaled by the S_a-component procedure have been used in the analysis. Evidently, increases in nonlinear viscous damping result in increases in the collapse margin ratio as expected.

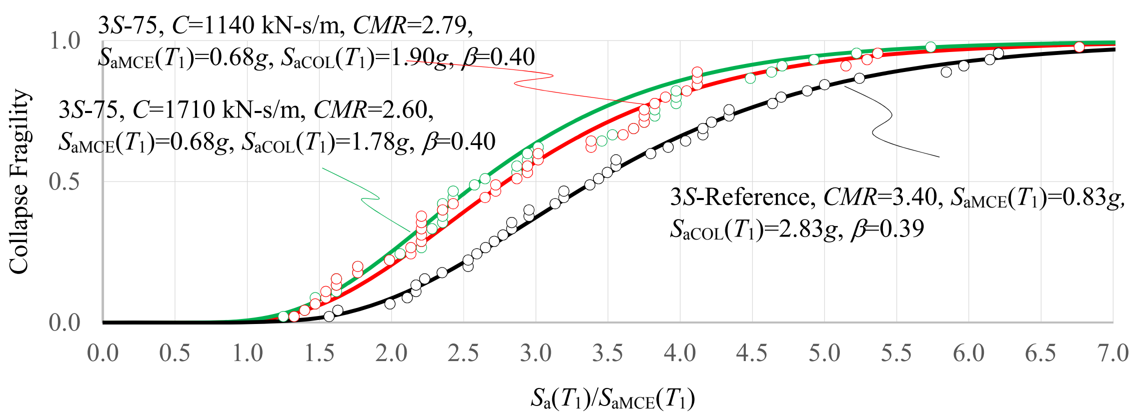

Figure 9-26 Collapse Fragility for 3*S*-75 Frame in Balanced Configurations with Linear Viscous Damping Ratio of 0.10 (*C*=1140kN-s/m) and 0.15 (*C*=1710kN-s/m), and for 3*S*-Reference Frame for S_a-Component Scaled Motions

A further analysis is conducted on the 3*S*-75 frame with increased nonlinear viscous damping (exponent α=0.5, damping constant C_N= 666.4kN-(sec/m)$^{1/2}$, effective damping ratio in the DE for elastic conditions β_{v1}=0.15) and with increased size of bracing so that the ultimate capacity in both tension and compression is 1983kN (HSS9x9x5/8, designed for capacity of about twice the peak device force in the MCE). Results are presented in Figure 9-28, again for the S_a-component scaled motions, and compared to the case of the same frame with nonlinear viscous damping of β_{v1}=0.15 in the balanced configuration (HSS8x8x1/2 bracing with capacity of 1160kN in tension and 1215kN in compression) and to the 3*S*-reference frame. Evidently, the increased capacity has a marginal effect on the collapse margin ratio, which may be explained by the nonlinear nature of the viscous force.

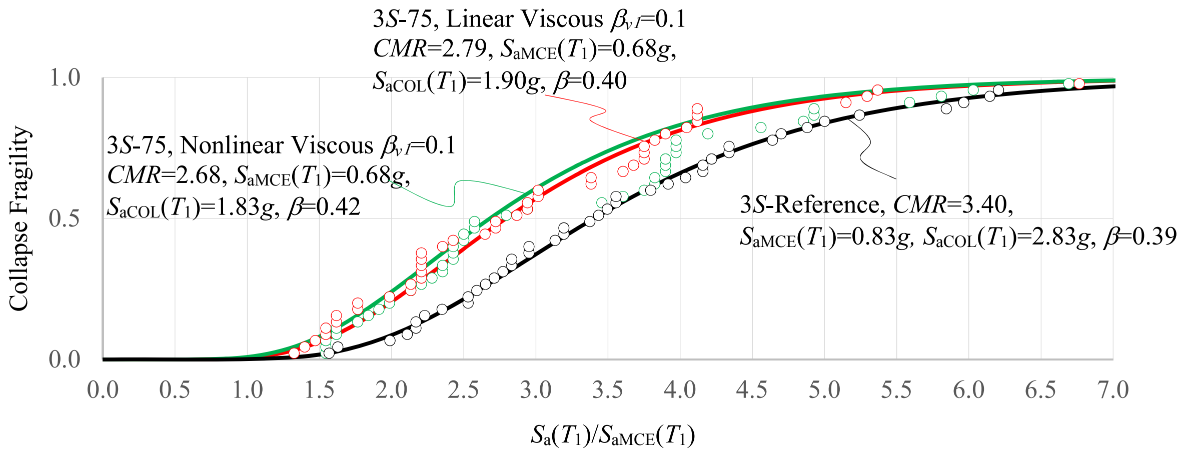

Figure 9-27 Collapse Fragility for 3*S*-75 Frame in Balanced Configuration with Nonlinear Effective Viscous Damping Ratio of 0.10 in the DE (C_N= 551.3 kN-(sec/m)$^{1/2}$), Linear Viscous Damping Ratio of 0.10 (*C*=1140 kN-sec/m), and for 3*S*-Reference Frame for S_a-Component Scaled Motions

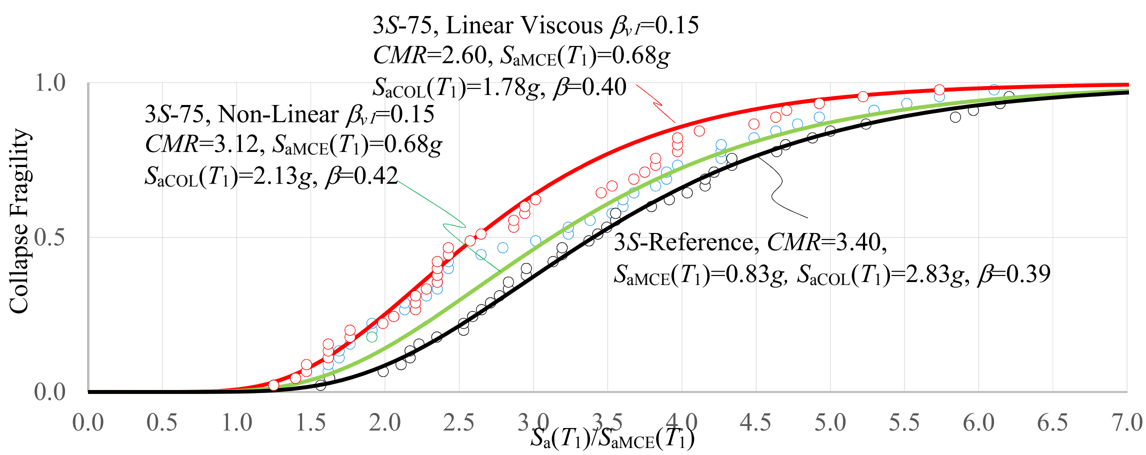

Figure 9-28 Collapse Fragility for 3*S*-75 Frame in Balanced Configuration with Nonlinear Effective Viscous Damping Ratio of 0.15 in the DE (C_N= 666.4 kN-(sec/m)$^{1/2}$), Linear Viscous Damping Ratio of 0.15 (*C*=1710 kN-sec/m), and for 3*S*-Reference Frames for S_a-Component Scaled Motions

However, it should be noted in the empirical data on the collapse fragility in Figure 9-29 show that the two 3*S*-75 frames have essentially the same spectral acceleration at collapse ($S_{aCOL}(T_1)$) but the frame with the larger ultimate capacity has lower probability of collapse for ground motions with intensity less than the one corresponding to $S_{aCOL}(T_1)$. For example, consider an intensity of 2.5 times that at the MCE. The probability of collapse for the frame with lower capacity is about 50% larger that of the frame with higher ultimate capacity. Yet they both have a collapse probability of 0.5 at the intensity of about 3.2 times the

MCE intensity. This indicates the complexity of the problem considered in which we attempt to describe the performance using only the measures of average response in the DE and MCE and of the collapse margin ratio.

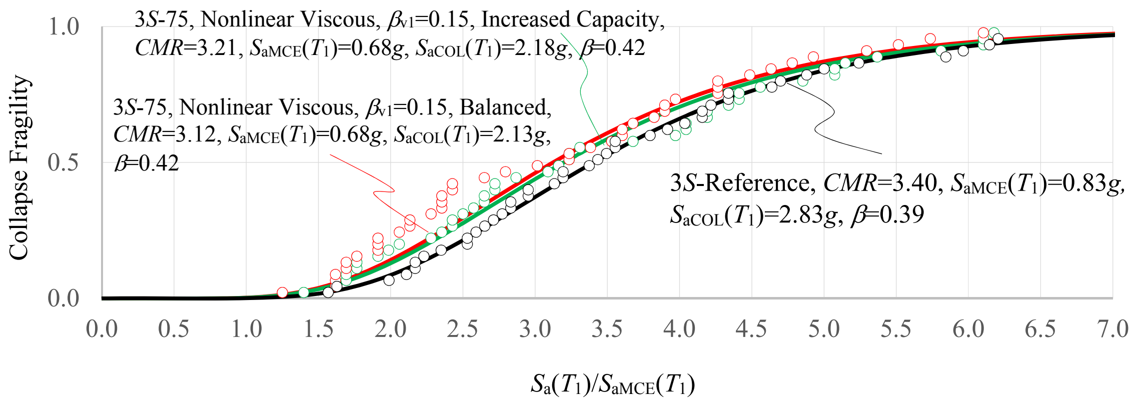

Figure 9-29 Collapse Fragility for 3*S*-75 Frame with Nonlinear Effective Viscous Damping Ratio of 0.15 in the DE (C_N= 666.4 kN-(sec/m)$^{1/2}$) in Balanced Configuration (ultimate capacity about 1.3 of force in MCE) and in Increased Ultimate Capacity (about twice of force in MCE), and for 3*S*-Reference Frames for S_a-Component Scaled Motions

9.7.4 Effect of Preload Provided by the Fluidic Self-Centering System on Collapse Fragility

The effect of increased preload of the self-centering devices on the collapse fragility is investigated by analyzing the 3*S*-75 frame with the properties of Table 9-1 (balanced configuration) but with the preload in each device selected to be about 1.3 times higher than the recommended amount of approximately 20% of the story strength. This led to preload of 160kN, 390kN and 390kN for the devices in stories 3, 2 and 1, respectively (was 125, 300 and 300kN). The change in preload will cause some small change in the stiffness (see Table 3-1 for changes when preload is changed by a significant amount). This change is ignored in this study. Also, the change in preload caused a small reduction of the fundamental period T_1 (calculated per Section 6.3) from 1.31sec to 1.28 sec. This change was too small to require re-scaling of the ground motions for analysis but was used in the calculation of the collapse margin ratio. Moreover, the damping constant for each device was kept at 1140kN-sec/m so that, effectively due to the reduction of period, there is a small reduction in effective damping in the fundamental mode from 0.10 to 0.098.

The modified 3*S*-75 frame was analyzed for the MCE and results have been presented in Table 8-6, where it is noted that the increased preload had an insignificant effect on the peak drift, caused a decrease in residual drift and a small increase in the peak device force that necessitates a change in the brace from an

HSS8x8x1/2 section to an HSS8x8x/5/8 section. The new brace-device system has increased capacity, calculated to be 1425kN (compression capacity of the tube section for effective length of 8535mm) for both compression and tension.

The empirical collapse fragility curves of the frame with increased preload and those of the original 3S-75 with preload of about 20% of the story strength and of the 3S-Reference frames are shown in Figure 9-30 together with information on the collapse margin ratio. Motions scaled by the S_a-component procedure have been used in the analysis. Evidently, the increase in preload of the fluidic self-centering system results in a marginal increase in the collapse margin ratio. This increase is likely caused by the marginal increase in the ultimate capacity.

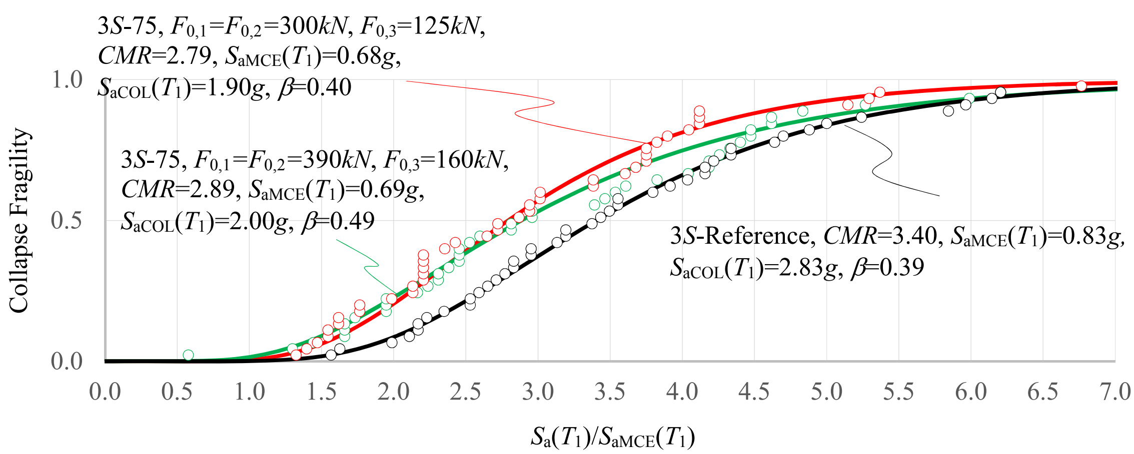

Figure 9-30 Collapse Fragility of 3*S*-75 Frame with Increased Preload ($F_{0,1}$=$F_{0,2}$=390kN, $F_{0,3}$=160kN), Frame 3*S*-75 in Balanced Configuration (preload of $F_{0,1}$=$F_{0,2}$=390kN, $F_{0,3}$=125kN) and 3*S*-Reference Frame for S_a-Component Scaled Motions

9.7.5 Effect of Stiffness of the Fluidic Self-Centering System on Collapse Fragility

The effect of the stiffness of the fluidic self-centering devices on the collapse fragility is investigated by analyzing the 3*S*-75 frame, case of nonlinear damping with effective damping ratio β_{v1}=0.15 (exponent α=0.5, damping constant C_N= 661.4kN-(sec/m)$^{1/2}$) and all other properties the same as previous analyses per Table 9-1 but for the stiffness of the devices that is assumed to be equal to 1/10th of the value used in all previous analyses. Such low stiffness is technologically possible but it can be achieved at an increased cost of the fluidic devices as the volume of the fluid needs to be substantially increased and, therefore, the volume and cost of the device will increase too.

The empirical collapse fragility curves of the 3S-75 frame with low and high fluidic device stiffness (nonlinear effective viscous damping ratio of 0.15 in the DE, exponent α=0.5, C_N= 661.4 kN-(sec/m)$^{1/2}$) and of the 3S-Reference frames are shown in Figure 9-31 together with information on the collapse margin ratio. Motions scaled by the S_a-component procedure have been used in the analysis. Evidently, the low stiffness results in a reduction of the collapse margin ratio by comparison to the case of high device stiffness and same nonlinear viscous damping properties. This is caused by the increase in story drift due to the low stiffness of the system.

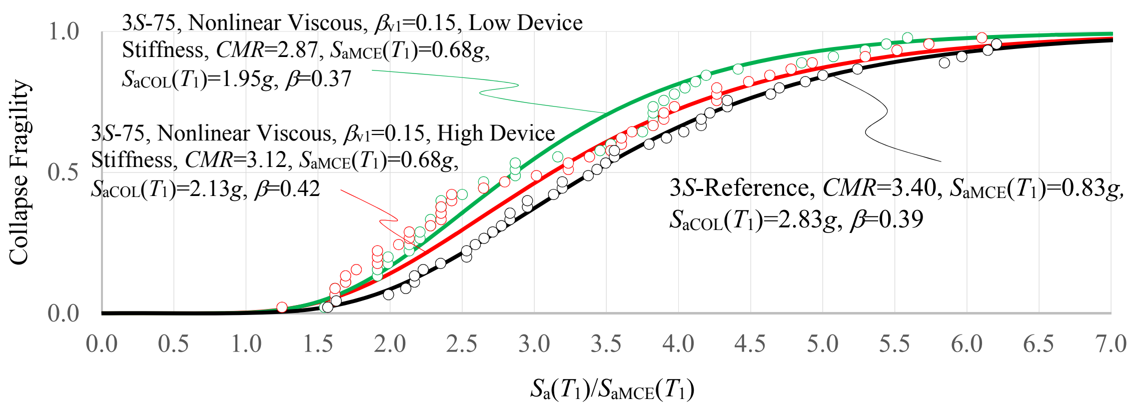

Figure 9-31 Collapse Fragility of 3S-75 Frame with High and with Low Fluidic Device Stiffness and with Nonlinear Effective Viscous Damping Ratio of 0.15 in the DE (α=0.5, C_N= 666.4 kN-(sec/m)$^{1/2}$), and for 3S-Reference Frame for S_a-Component Scaled Motions

9.7.6 Effect of Increased Strength of Frame on Collapse Fragility

The effect of increased strength of the frame on the collapse fragility is investigated by analyzing the 3S-85 frame (see Appendix C). This frame has each section larger by one step by comparison to the 3S-75 frame with balanced brace configuration. Note that this frame has been designed for a base shear strength equal to 85% of the minimum base shear. Also, the fluidic self-centering system has linear viscous damping with β_{v1}=0.10. The empirical collapse fragility curves of (a) the 3S-85 frame, (b) the 3S-75 frame with balanced brace configuration, (c) the 3S-75 frame with increased ultimate capacity of the device-brace system, and (d) the 3S-Reference frames are shown in Figure 9-32 together with information on the collapse margin ratio. Motions scaled by the S_a-component procedure have been used in the analysis. Evidently, the increase results in an increase of the collapse margin ratio by comparison to the case of frame 3S-75, although not as large an increase as that caused by an increase in the ultimate capacity of the fluidic self-centering device-brace system.

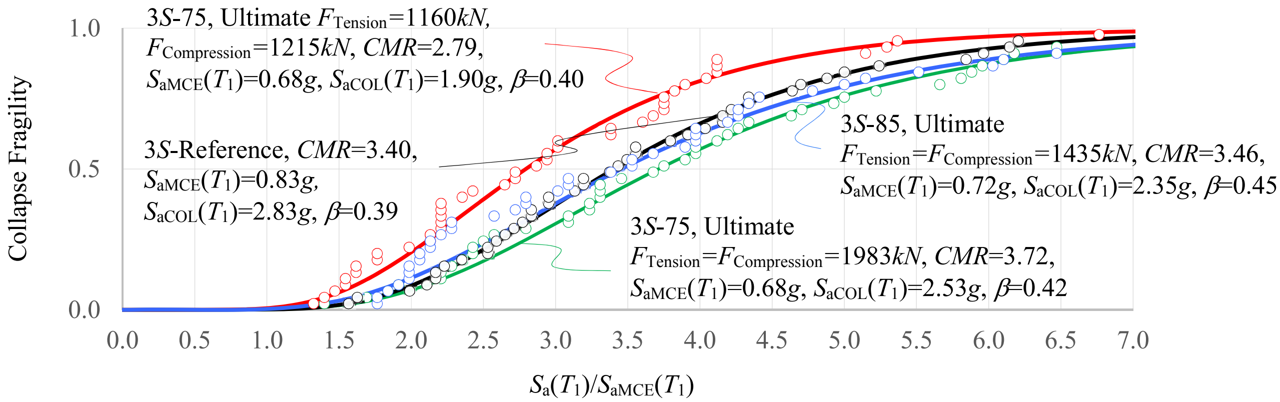

Figure 9-32 Collapse Fragility for 3*S*-85 Frame with the Comparisons to other Frames for S_a-Component Scaled Motions

Table 9-9 Parameters of Fluidic Self-Centering Fluidic Device-Brace System for Frames 3*S*-75, 3*S*-85 and 3*S*-Reference and Collapse Margin Ratio for S_a-Scaled Motions (parameters are the same for all stories except for the preload and stiffness; damping is linear viscous unless noted otherwise)

Configuration	F_0 [kN]	K_0 [kN/m]	Braces	C or C_N [kN-(s/m)$^\alpha$]	$D_{Capacity}$ [mm]	Ultimate $F_{Tension}$ [kN]	Ultimate F_{Compr} [kN]	*CMR*
3*S*-75 Balanced T_1= 1.31sec	125/300/300	1545/2320/2320	HSS8×8×1/2	1140	165	1160	1215	2.79
3*S*-75 Unbalanced T_1= 1.31sec	125/300/300	1545/2320/2320	HSS8×8×1/2	1140	165	2430	1215	3.12
3*S*-75 Increased Capacity T_1= 1.31sec	125/300/300	1545/2320/2320	HSS9×9×5/8	1140	165	1983	1983	3.72
3*S*-75 Increased Displacement Capacity T_1= 1.31sec	125/300/300	1545/2320/2320	HSS8×8×1/2	1140	215	1160	1215	2.79
3*S*-75Increased Linear Damping T_1= 1.31sec	125/300/300	1545/2320/2320	HSS8×8×5/8	1710	165	1435	1435	2.60
3*S*-75 Increased Preload T_1= 1.28sec	160/390/390	1545/2320/2320	HSS8×8×5/8	1140	165	1435	1435	2.89
3*S*-75 Nonlinear Damping β_{v1}=0.10 (α=0.5) T_1= 1.31sec	125/300/300	1545/2320/2320	HSS8x8x1/2	551.3	165	1160	1215	2.68
3S-75 Increased Nonlinear Damping β_{v1}=0.15 (α=0.5) T_1= 1.31sec	125/300/300	1545/2320/2320	HSS8x8x1/2	666.4	165	1160	1215	3.12
3S-75 Increased Capacity Increased Nonlinear Damping β_{v1}=0.15 (α=0.5) T_1= 1.31sec	125/300/300	1545/2320/2320	HSS9x9x5/8	666.4	165	1784	1784	3.21
3*S*-75 Low Stiffness Nonlinear Damping β_{v1}=0.15 (α=0.5) T_1= 1.31sec	125/300/300	155/232/232	HSS8x8x1/2	666.4	165	1160	1215	2.87
3*S*-85 Increased Strength T_1= 1.23sec	150/350/350	1545/2320/2320	HSS8×8×5/8	1220	165	1435	1435	3.46
3*S*-Reference T_1= 1.07sec	-	-	-	-	-	-	-	3.40

Table 9-10 Selected Response Parameters in DE and MCE (case of near-fault, pulse like motions) and Collapse Margin Ratio of Frames 3*S*-75, 3*S*-85 and 3*S* -Reference

Configuration	Peak Story Drift DE (mm)	Maximum Residual Story Drift DE (mm)	Maximum Residual Story Drift MCE (mm)	Peak Floor Acceleration DE (g)	Peak Device Force MCE (kN)	*CMR*
3*S*-75 Capacity 1.3F_{MCE} Linear Viscous Damping β_{v1}=0.10 T_1= 1.31sec	75.0	4.0	12.2	0.532	891.8	2.79
3*S*-75 Increased Preload Capacity 1.3F_{MCE} Linear Viscous Damping β_{v1}=0.10 T_1= 1.28sec	71.0	3.0	8.5	0.566	978.0	2.89
3*S*-75 Increased Capacity 2.0 F_{MCE} Linear Viscous Damping β_{v1}=0.10 T_1= 1.31sec	73.7	3.7	12.1	0.523	890.4	3.72
3*S*-75 Capacity 1.3F_{MCE} Increased Linear Damping β_{v1}=0.15 T_1= 1.31sec	69.4	3.3	13.2	0.497	1069.1	2.60
3*S*-75 Capacity 1.3F_{MCE} Nonlinear Damping β_{v1}=0.10 in DE (α=0.5) T_1= 1.31sec	73.2	3.7	13.0	0.607	798.1	2.68
3*S*-75 Capacity 1.3F_{MCE} Increased Nonlinear Damping β_{v1}=0.15 in DE (α=0.5), T_1= 1.31sec	70.7	3.5	13.4	0.671	861.0	3.12
3*S*-75 Capacity 2.0F_{MCE} Increased Nonlinear Damping β_{v1}=0.15 in DE (α=0.5), T_1= 1.31sec	70.7	3.5	13.4	0.671	861.0	3.21
3*S*-75 Capacity 1.3F_{MCE} Low Stiffness Nonlinear Damping β_{v1}=0.15 in DE (α=0.5), T_1= 1.31sec	72.2	3.6	15.2	0.656	758.3	2.87
3*S*-85 Increased Strength Linear Viscous Damping β_{v1}=0.10, T_1= 1.23sec	68.9	2.8	11.4	0.576	959.7	3.46
3*S*-Reference T_1= 1.07sec	86.6	14.3	28.3	0.925	NA	3.40

9.8 Effect of Fluidic Self-Centering System Design on Collapse Fragility of 6-Story Structure

The 6-story frame 6*S*-75 with the fluidic self-centering system is further analyzed to determine information on its collapse fragility for two additional cases: (a) increased nonlinear viscous damping (β_{v1}=0.15 in the DE) and all other parameters the same as those of the frame analyzed in Section 9.6 (ultimate strength about equal to 1.3 times the peak device force in the MCE), and (b) increased ultimate strength of the device-brace system (about equal to twice the peak device force in the MCE) and all other parameters the same as those of the frame analyzed in Section 9.6 (linear viscous damping β_{v1}=0.10 in the DE). Motions scaled by the S_a-component procedure have been used in the analysis. Figures 9-33 and 9-34 present the fragility curves for the two additional cases, together with those of the 6*S*-Reference frame and the originally analyzed 6S-75 frame. Table 9-11 summarizes the properties of the analyzed frames, including the one analyzed in Section 9.6 and the 6S-Reference frame, and also includes the calculated collapse margin ratio. Table 9-12 presents key response quantities of the 6-story frames in the DE and the MCE (from data in Section 8).

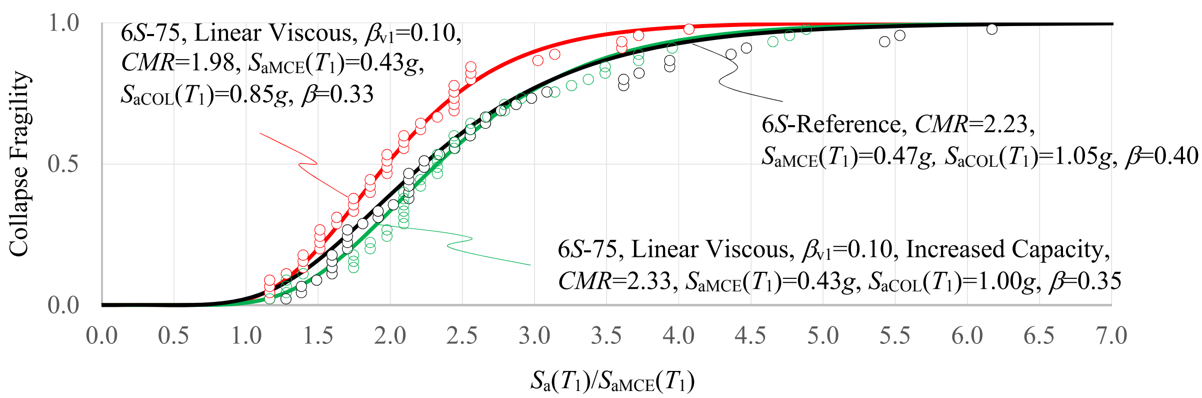

Figure 9-33 Collapse Fragility for 6*S*-75 frame in Configurations with Ultimate Capacity of 1.3 times the Peak Device Force and Increased Capacity (2 times the peak force) and for 6*S*-Reference Frame for S_a-Component Scaled Motions

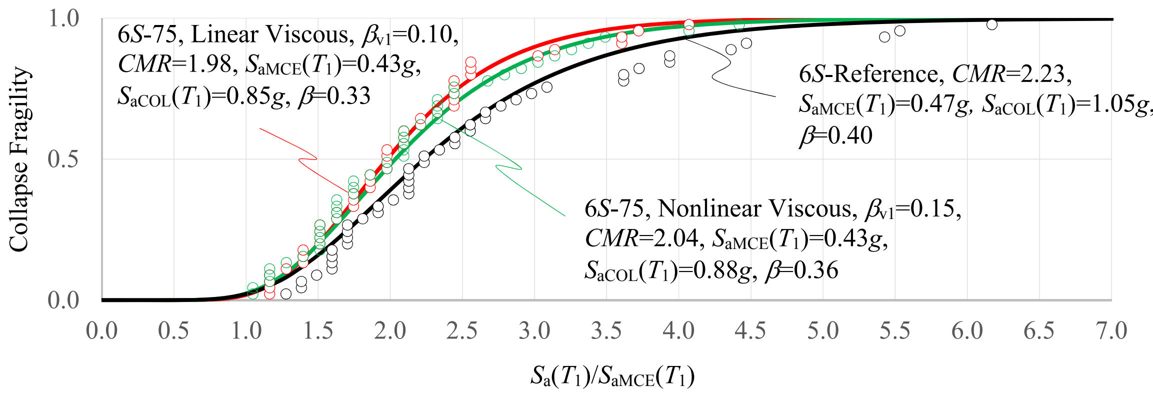

Figure 9-34 Collapse Fragility for 6*S*-75 Frame in Configurations with Ultimate Capacity of 1.3 times the Peak Device Force, with Nonlinear Effective Viscous Damping Ratio of 0.15 in the DE or Linear Viscous Damping Ratio of 0.10 and for 3*S*-Reference Frame for S_a-Component Scaled Motions

The increase in the ultimate strength of the device-brace system resulted in marked increase in the collapse margin ratio. However, the increase in damping and its conversion to nonlinear viscous damping did not have any noticeable increase (some 5% increase by comparison to the linear viscous case-recall that in the case of the 3*S*-75 frame, the increase in the CMR was also small at about 10%).

9.9 Summary

The collapse fragility of several 3-story and 6-story frames with and without a fluidic self-centering system has been evaluated. The study first resulted in the observation that frames with a fluidic self-centering system designed per the minimum requirements described in Section 6 and a device-brace ultimate capacity equal to about 1.3 times the peak force (average of 7 analyses) in the device calculated in the MCE have insignificant probability of collapse in the MCE but have a collapse margin ratio which, while acceptable, is less than that of comparable frames designed without a self-centering system to meet the criteria of ASCE 7-2010.

The study then concentrated on the 3-story frame with the fluidic self-centering system and varied the parameters of the fluidic devices, of the bracing system and of the strength of the frame. A total of 10 cases having the properties presented in Table 9-9 were analyzed. It was determined that increases in the preload, increases in the displacement capacity or increases in the linear viscous damping constant of the devices have marginal or insignificant effects on the collapse margin ratio (values are summarized in Table 9-9). Rather, an increase in the collapse margin ratio was calculated for frames having a device-braced system with increased ultimate capacity (the example was for a capacity equal to twice the peak force calculated in the MCE) and for frames with increased frame strength (85% of minimum base shear strength).

Table 9-11 Parameters of Fluidic Self-Centering Fluidic Device-Brace System for 6-Story Frame

Configuration	Story	F_0 [kN]	K_0 [kN/m]	Braces	C or C_N [kN-(s/m)$^\alpha$]	$D_{Capacity}$ [mm]	Ultimate $F_{Tension}$ [kN]	Ultimate $F_{Compression}$ [kN]	*CMR*
Linear Damping β_{v1}=0.10 Ultimate Capacity 1.3F_{MCE} T_1= 2.06sec	6th	100	1350	HSS8x8x3/8	2900	165	859	964	1.98
	5th	250	1790	HSS8×8×5/8	2900	165	1302	1434	
	4th	250	1790	HSS8×8×5/8	2900	165	1302	1434	
	3rd	400	2230	HSS9x9×5/8	2900	165	1843	1983	
	2nd	400	2230	HSS9x9×5/8	2900	165	1843	1983	
	1st	400	2230	HSS9x9×5/8	2900	165	1843	1983	
Increased Nonlinear Damping β_{v1}=0.15 in DE (α=0.5) Ultimate Capacity 1.3F_{MCE} T_1= 2.06sec	6th	100	1350	HSS8x8x3/8	1433	165	859	964	2.04
	5th	250	1790	HSS8×8×5/8	1433	165	1302	1434	
	4th	250	1790	HSS8×8×5/8	1433	165	1302	1434	
	3rd	400	2230	HSS9x9×5/8	1433	165	1843	1983	
	2nd	400	2230	HSS9x9×5/8	1433	165	1843	1983	
	1st	400	2230	HSS9x9×5/8	1433	165	1843	1983	
Linear Damping β_{v1}=0.10 Ultimate Capacity 2.0F_{MCE} T_1= 2.06sec	6th	100	1350	HSS9x9x3/8	2900	165	1305	1305	2.33
	5th	250	1790	HSS9×9×5/8	2900	165	1983	1983	
	4th	250	1790	HSS9×9×5/8	2900	165	1983	1983	
	3rd	400	2230	HSS12x12×1/2	2900	165	3026	3026	
	2nd	400	2230	HSS12x12×1/2	2900	165	3026	3026	
	1st	400	2230	HSS12x12×1/2	2900	165	3026	3026	
6*S*-Reference Frame T_1= 1.90sec	6th	-	-	-	-	-	-	-	2.23
	5th	-	-	-	-	-	-	-	
	4th	-	-	-	-	-	-	-	
	3rd	-	-	-	-	-	-	-	
	2nd	-	-	-	-	-	-	-	
	1st	-	-	-	-	-	-	-	

Table 9-12 Selected Response Parameters in DE and MCE (case of near-fault, pulse like motions) and Collapse Margin Ratio of Frame 6*S*-75 in Various Configurations and 6*S*-Reference Frame

Configuration	Peak Story Drift DE (mm)	Maximum Residual Story Drift DE (mm)	Maximum Residual Story Drift MCE (mm)	Peak Floor Acceleration DE (g)	Peak Device Force MCE (kN)	CMR
Capacity 1.3F_{MCE} Linear Viscous Damping β_{v1}=0.10 T_1= 2.06sec	70.7	5.1	12.6	0.467	1366.2	1.98
Capacity 1.3F_{MCE} Increased Nonlinear Damping β_{v1}=0.15 in DE (α=0.5) T_1= 2.06sec	63.2	3.4	13.7	0.489	1356.1	2.04
Capacity 2.0F_{MCE} Linear Damping β_{v1}=0.10 in DE T_1= 2.06sec	65.7	2.3	11.7	0.455	1363.6	2.33
6*S*-Reference T_1=1.90sec	91.5	16.0	27.0	0.769	NA	2.23

Also, some marginal increase of the collapse margin ratio was calculated for frames with devices having increased nonlinear viscous damping. Benefits on the collapse margin ratio were realized even when only the tension capacity was increased in an un-balanced configuration. This result is attributed to the fact that the fluidic device force increases with increasing intensity of the earthquake due to increases in both displacement (linear stiffness) and increases in velocity, particularly for the case linear viscous damping.

Table 9-10 compares key response parameters in the DE and MCE (case of motions with near-fault, pulse-like characteristics) and the collapse margin ratio for the important configurations of the 3*S*-75 and the 3*S*-85 frames studied. The information was obtained from the tables of Sections 7 and 8, and Appendix C.

A further limited study on the 6-story frame was conducted in which either the ultimate capacity of the device-brace system was increased or the damping was converted to nonlinear viscous and increased to 0.15 in the DE. The results are summarized and compared to those of the 6*S*-Reference frame in Table 9-11. Also Table 9-12 compares key response parameters in the DE and MCE (case of motions with near-fault, pulse-like characteristics) and the collapse margin ratio for the important configurations of the 6*S*-75 frame studied. Again it is observed that increases in the ultimate capacity result in increases in the collapse margin ratio and that increases in nonlinear viscous damping have marginal beneficial effects on the collapse margin ratio.

While this section concentrated on the collapse margin ratio, the collapse fragility analysis provides additional information that is revealed in some of the data presented in the figures of collapse fragility curves and in the detailed data of analysis. Detailed information on the collapse fragility analysis results is presented in Appendix E for each analyzed case. The data may be used to obtain additional information such as the probability of collapse given the MCE or any other level of earthquake.

An increased device-brace ultimate capacity has no effect on the response in the DE or the MCE but has an important effect on the collapse margin ratio. The increase in cost for the increased ultimate capacity is primarily due to an increase in the bracing size, whereas the fluidic devices are typically designed for high capacity. For example, a change of the bracing in the 3*S*-75 frame from HSS8x8x1/2 to HSS9x9x5/8 and the design of connections in tension to result in a balanced ultimate capacity (approximately the same in tension and compression), would amount to approximately \$10,000 increase in cost for the 3-story structure (4 frames, 12 devices) in 2015 costs in the US, or less than \$1,000 per device-brace system. While the size of the brace has no effect on the DE and MCE response, it has a marked effect on the collapse margin ratio and thus is should be considered in design.

The study in this section only considered collapse in quantifying the seismic performance and used this performance index to derive conclusions on the effect of various design parameters. Other important parameters may be used to quantify the seismic performance. This is investigated in the next section where the procedures used in this section are utilized but the performance index is defined to be a limit value of the residual drift.

SECTION 10
RESIDUAL DRIFT PERFORMANCE EVALUATION OF BUILDINGS WITH FLUIDIC SELF-CENTERING DEVICES

10.1 Introduction

The improved performance of the buildings with fluidic self-centering systems in the DE and MCE has been documented in Section 8 and summarized again in Section 9. This improvement included reductions of the peak story drift, substantial reductions in the residual drift, reductions in peak accelerations and reductions in floor spectral accelerations over all frequencies. The collapse performance assessment in Section 9 established that structures with fluidic self-centering systems designed by the minimum procedures of Section 6 have acceptable collapse margin ratio which is comparable to that of conventional structures designed by the minimum criteria of ASCE 7-2010. The analyses in Section 9 also provided information on how to improve the collapse margin ratio and, more generally, how to reduce the probability of collapse given a particular level of earthquake intensity. In general, the probability of collapse can be reduced by increasing the force ultimate capacity of the brace-fluidic device system, whereas other modifications, such as increased displacement capacity, increased preload and increased damping, had small or insignificant effects on the collapse fragility.

However, increases in preload and damping have important effects in reducing the peak story drift and the residual drift. The latter is of particular interest today and is considered an important performance index (MacRae and Kawashima, 1997; Kawashima *et al*., 1998; McCormick *et al*., 2008; Ruiz-Garcia and Miranda, 2006a and 2006b; Erochko et al., 2011; Erochko, 2013). This section concentrates on an evaluation of the performance of structures without and with fluidic self-centering systems based on the residual drift. Specifically, the methodology of FEMA P695 (FEMA, 2009) is employed but the limit state is defined as a specific value of the peak residual drift. Fragility curves and related information are calculated, presented and discussed in this section for several systems out the many analyzed in Section 9 for the limit states of residual drift ratio equal to 0.2%, 0.5%, 1% and 2%. These four limits were selected as they are directly related to a description of damage in FEMA P58 (FEMA, 2012). Specifically, the limit of 0.2% may require some adjustments and repairs to nonstructural systems, the limit of 0.5% will require realignment and repair of the structural system, whereas the limit of 1% will require major realignment and it may be more economical to demolish rather than repair. The limit of 2% indicates that the structure is in danger of collapse in aftershocks. Other studies suggest that the limit of 0.5% may be considered as the threshold beyond which it may be uneconomical and impractical to repair. For example, a comparison of performance of frames with Buckling Restraint Braces to Steel Moment Resisting Frames (Erochko *et al*., 2011) utilized the limit of 0.5%. A study by Ramirez and Miranda (2012) on the economic impact of the residual drift assumed that the probability of having to demolish a building that has not collapsed given the residual drift is log-normally distributed with a median of 0.015 and a logarithmic standard deviation of 0.3. That is, the probability to demolish is approximately 0.10 for a residual drift of 1%, is 0.50 for a residual drift of 1.5% and is nearly 1.0 for a residual drift of 3%.

10.2 Residual Drift Performance Evaluation Results

Selected 3*S*-75 and 6*S*-75 frame configurations, the 3*S*-85 frame and the 3*S*-Reference and 6*S*-Reference frames were analyzed. Table 10-1 presents basic information on the analyzed systems with more details presented in Tables 9-9 and 9-11 and Figures 9-5 and 9-10 and Appendix C. Analysis was conducted using the 44 motions scaled by the S_a-component scaling approach. Incremental dynamic analysis was conducted until either a prescribed limit on the residual drift was exceeded or the analysis was terminated based on the collapse criteria defined in Section 9.6.1, whichever occurred first. IDA curves were constructed showing the intensity of the seismic motion versus the value of the maximum (among all stories) residual drift. An example of an IDA collection of curves is shown in Figure 10-1 for the case of frame 3*S*-75, case of linear damping with β_v=0.1 and device-brace system capacity equal to about 1.3 times the average force calculated in the MCE. A complete collection of results, including IDA graphs, fragility curves and empirical data, is presented in Appendix F.

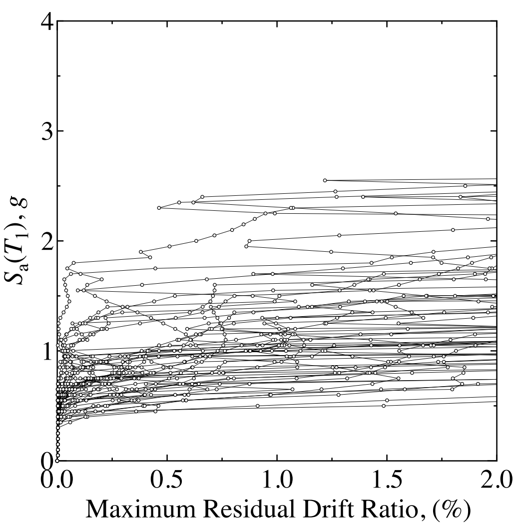

Figure 10-1 IDA Curves for 3-Story Frame 3*S*-75, Linear Viscous Damping β_v=0.1 and Device-Brace System Capacity Equal to 1.3F$_{MCE}$

Table 10-1 Analyzed Frames for Residual Drift Fragility, Selected Response Parameters in DE and MCE (case of near-fault, pulse like motions) and Fragility Analysis Results

Configuration	Maximum Residual Story Drift DE (mm)	Maximum Residual Story Drift MCE (mm)	Residual Drift Median $S_a(T_1)/S_{aMCE}(T_1)$-β			
			0.2%	0.5%	1.0%	2.0%
3*S*-75, Capacity 1.3F_{MCE} Linear Viscous Damping β_{v1}=0.10 T_1=1.31sec	4.0	12.2	1.01 - 0.338	1.25 - 0.322	1.44 - 0.347	1.60 - 0.329
3*S*-75, Increased Preload Capacity 1.3F_{MCE} Linear Viscous Damping β_{v1}=0.10 T_1=1.28sec	3.0	8.5	1.10 - 0.413	1.39 - 0.367	1.59 - 0.396	1.75 - 0.396
3*S*-75, Increased Capacity 2.0F_{MCE} Linear Viscous Damping β_{v1}=0.10 T_1=1.31sec	3.7	12.1	1.10 - 0.382	1.66 - 0.378	1.93 - 0.313	2.32 - 0.316
3*S*-75, Capacity 1.3F_{MCE} Increased Nonlinear Damping β_{v1}=0.15 in DE (α=0.5) T_1=1.31sec	3.7	13.0	1.01 - 0.289	1.19 - 0.294	1.37 - 0.275	1.68 - 0.301
3*S*-85, Capacity 1.3F_{MCE} Linear Viscous Damping β_{v1}=0.10 T_1=1.23sec	2.8	11.4	1.08 - 0.390	1.55 - 0.370	1.60 - 0.335	1.82 - 0.338
3*S*-Reference T_1=1.07sec	14.3	28.3	0.59 - 0.391	0.85 - 0.393	1.36 - 0.381	1.98 - 0.369
6*S*-75, Capacity 1.3F_{MCE} Linear Viscous Damping β_{v1}=0.10 T_1= 2.06sec	5.1	12.6	0.74 - 0.469	0.86 - 0.471	0.98 - 0.492	1.19 - 0.460
6*S*-75, Capacity 1.3F_{MCE} Increased Nonlinear Damping β_{v1}=0.15 in DE (α=0.5) T_1= 2.06sec	3.4	13.7	0.47 - 0.447	0.63 - 0.438	0.83 - 0.456	1.27 - 0.481
6*S*-75, Capacity 2.0F_{MCE} Linear Damping β_{v1}=0.10 in DE T_1= 2.06sec	2.3	11.7	1.05 - 0.373	1.39 - 0.415	1.78 - 0.400	1.86 - 0.367
6*S*-Reference T_1= 1.90sec	16.0	27.0	0.47 - 0.406	0.70 - 0.503	1.23 - 0.612	1.60 - 0.480

Figures 10-2 to 10-11 present the fragility curves for each of the cases of Table 10-1 and for the four values of the residual drift: 0.2%, 0.5%, 1% and 2%. Each graph shows the empirical data (also tabulated in Appendix F) and the log-normal representation of the fragility curve. Note that the intensity of the seismic motion is normalized by the spectral acceleration at the fundamental period in the MCE. The probability of exceeding any of the four limit values of the residual drift given a particular level of seismic intensity may be read as the ordinate of each graph at a particular level of seismic intensity of which the MCE level is at $S_a(T_1)/S_{aMCE}(T_1)=1$ and the DE level is at $S_a(T_1)/S_{aMCE}(T_1)=0.67$. The log-normal distribution is described by Equation (9-3). Values of the dispersion factor β and the value of $S_a(T_1)/S_{aMCE}(T_1)$ corresponding to a probability of exceedance equal to 0.5 are presented in Table 10-1 (note that the median "*m*" of the log-normal distribution-see Equation 9-3 is the median value of $S_a(T_1)/S_{aMCE}(T_1)$).

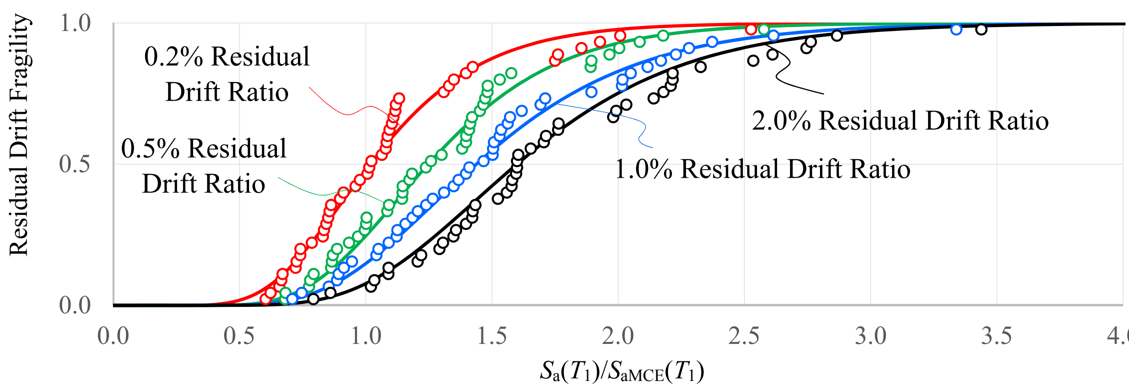

Figure 10-2 Residual Drift Fragility (or cumulative distribution function) for 3*S*-75 Frame, Linear Viscous Damping β_v=0.1, Device-Brace System Capacity Equal to 1.3F$_{MCE}$ and S_a-Component Scaled Motions

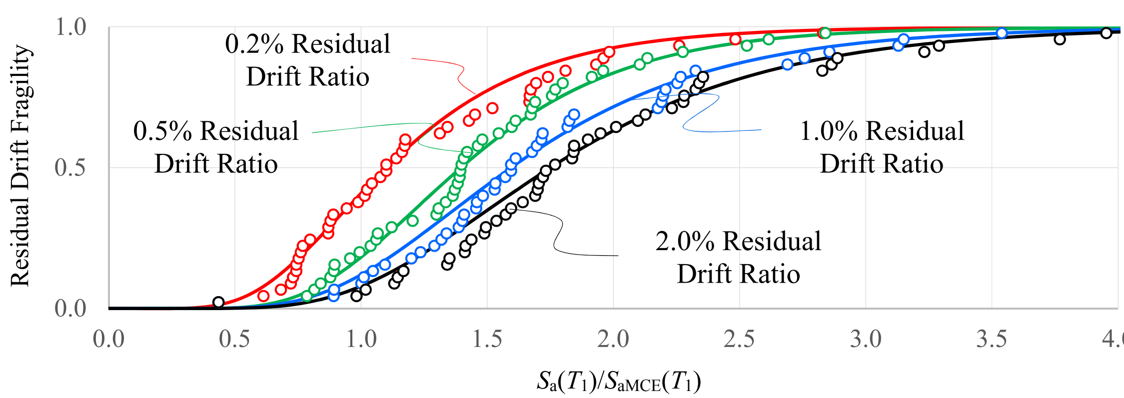

Figure 10-3 Residual Drift Fragility (or cumulative distribution function) for 3*S*-75 Frame, Increased Preload, Linear Viscous Damping β_v=0.1, Device-Brace System Capacity Equal to 1.3F$_{MCE}$ and S_a-Component Scaled Motions

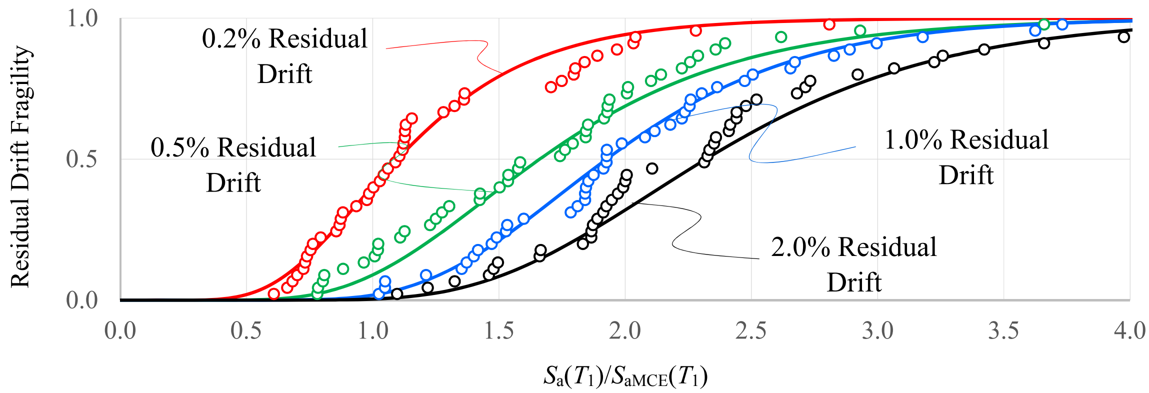

Figure 10-4 Residual Drift Fragility (or cumulative distribution function) for 3*S*-75 Frame, Linear Viscous Damping β_v=0.1, Device-Brace System Capacity Equal to 2.0F$_{MCE}$ and S_a-Component Scaled Motions

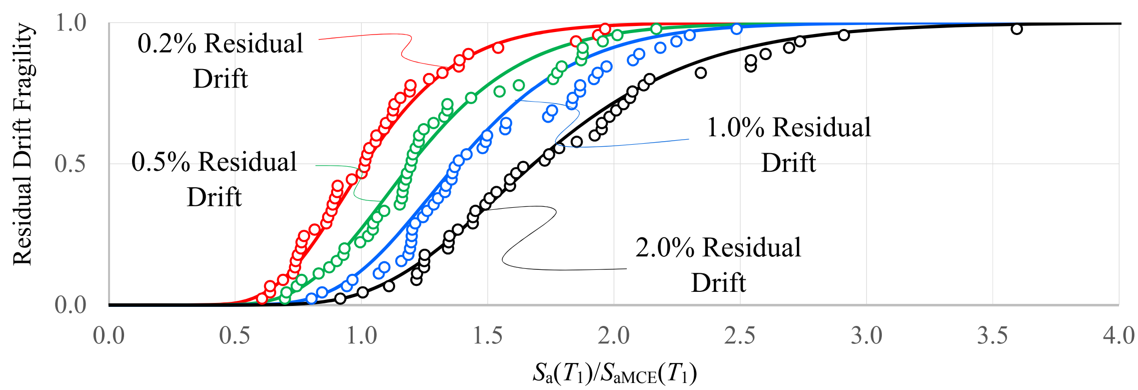

Figure 10-5 Residual Drift Fragility (or cumulative distribution function) for 3*S*-75 Frame, Nonlinear Viscous Damping β_v=0.15 in DE, Device-Brace System Capacity Equal to 1.3F$_{MCE}$ and S_a-Component Scaled Motions

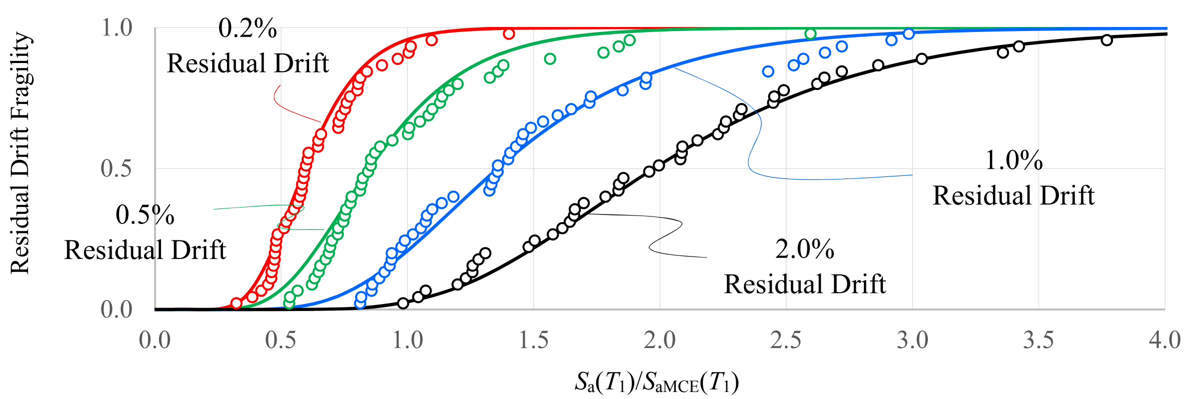

Figure 10-6 Residual Drift Fragility (or cumulative distribution function) for 3*S*-Reference Frame in S_a-Component Scaled Motions

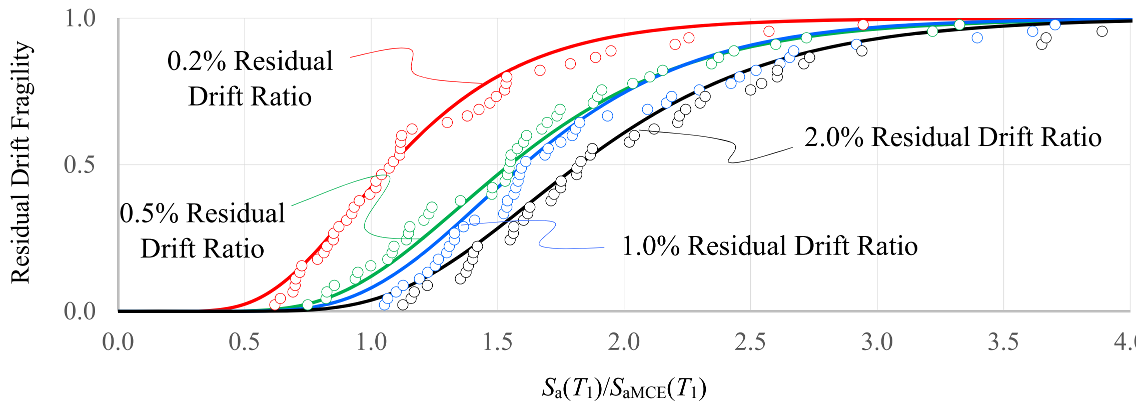

Figure 10-7 Residual Drift Fragility (or cumulative distribution function) for 3*S*-85 Frame, Linear Viscous Damping β_v=0.1, Device-Brace System Capacity Equal to 1.3F$_{MCE}$ and S_a-Component Scaled Motions

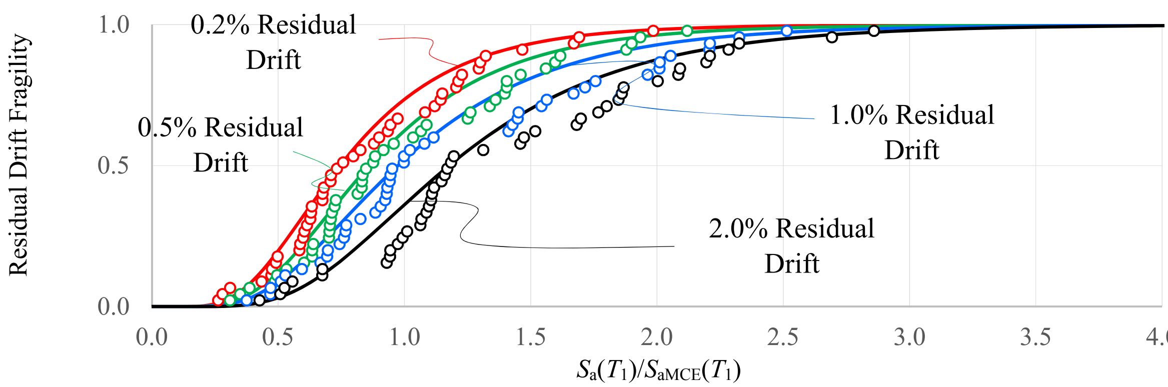

Figure 10-8 Residual Drift Fragility (or cumulative distribution function) for 6*S*-75 Frame, Linear Viscous Damping β_v=0.1, Device-Brace System Capacity Equal to 1.3F$_{MCE}$ and S_a-Component Scaled Motions

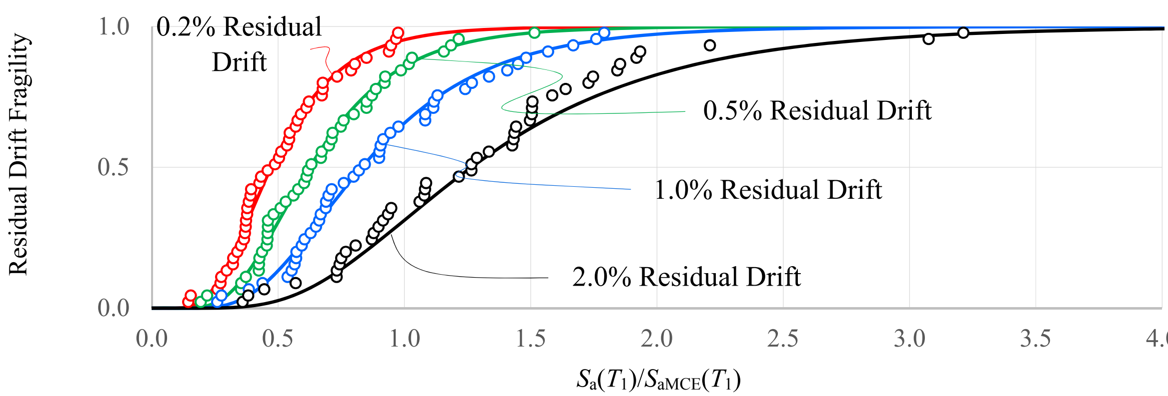

Figure 10-9 Residual Drift Fragility (or cumulative distribution function) for 6*S*-75 Frame, Nonlinear Viscous Damping β_v=0.15 in DE, Device-Brace System Capacity Equal to 1.3F$_{MCE}$ and S_a-Component Scaled Motions

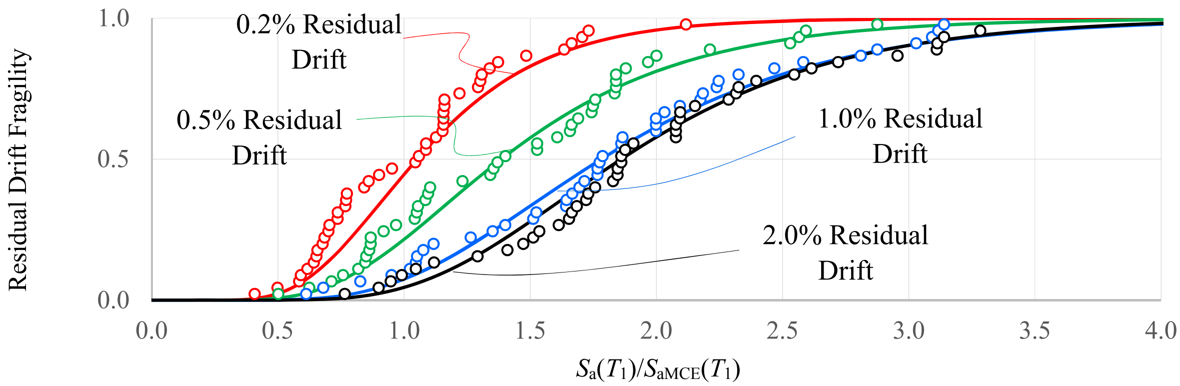

Figure 10-10 Residual Drift Fragility (or cumulative distribution function) for 6*S*-75 Frame, Linear Viscous Damping β_v=0.1, Device-Brace System Capacity Equal to 2.0F_{MCE} and S_a-Component Scaled Motions

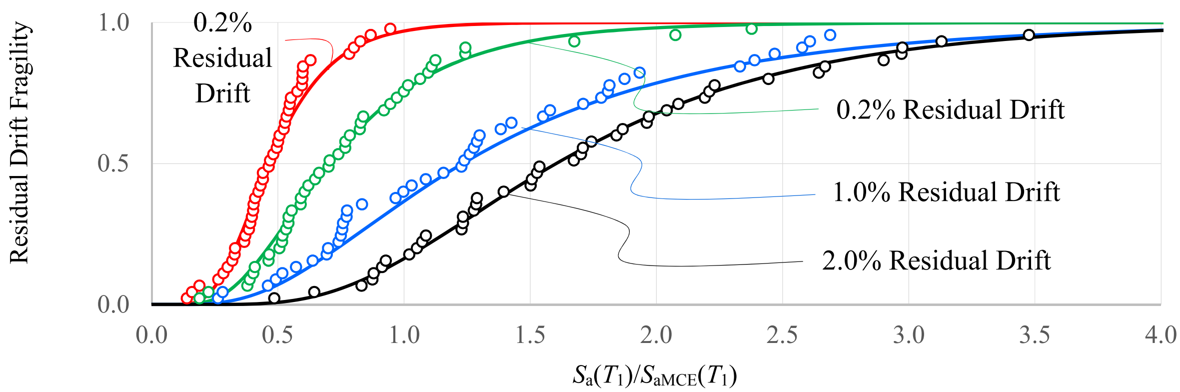

Figure 10-11 Residual Drift Fragility (or cumulative distribution function) for 6*S*-Reference Frame in S_a-Component Scaled Motions

10.3 Summary

The results on the residual drift fragility presented in this section demonstrate substantial reduction of the probability of exceeding the residual drift limits of 0.2% and 0.5% when the fluidic self-centering system is used. For example, in the case of the 3-story frame the probability of exceeding the limit value of 0.5% of the residual drift given the DE (p(Residual Drift>0.5% | $S_a(T_1)/S_{aMCE}(T_1)$=0.67) is less than about 0.05 for all cases of the analyzed 3*S*-75 and 3*S*-85 frames with fluidic self-centering devices and is less than about 0.25 for the case of the conventional frame 3*S*-Reference. In the case of the 3*S*-75 frame with fluidic devices of increased preload, the probability is near zero (Figure 10-3). For the same case, the probability of exceeding the limit of 0.5% given the MCE, p(Residual Drift>0.5% | $S_a(T_1)/S_{aMCE}(T_1)$=1), is 0.2, whereas for the conventional 3*S*-Reference frame (Figure 10-6) the same probability is 0.67.

However, the probability of exceeding the residual drift limits of 1% and 2% given any level of seismic intensity for the structures with the fluidic self-centering system are about the same or higher than those of the conventional structures. The reason for this difference is the fact the structures with the fluidic self-centering system may experience collapse before they have large residual drift. This is rectified by increasing the ultimate capacity of the fluidic device-brace system, as seen in the results for the system with ultimate capacity of $2.0F_{MCE}$.

SECTION 11
ASSESSMENT OF COLLAPSE RISK AND RESIDUAL DRIFT RISK FOR BUILDINGS WITH FLUIDIC SELF-CENTERING DEVICES

11.1 Introduction

The fragility curves in Section 9 present information on the probability of collapse for specific levels of earthquake intensity. Similarly, the fragility curves in Section 10 present information on the probability of exceeding certain residual drift ratio values for specific levels of earthquake intensity. This information is very useful and obtained in computationally intensive analysis. However, engineers, building officials, government officials, owners and insurers are interested in assessing risk, defined in this case as the mean annual frequency of collapse, λ_C, or the mean annual frequency of exceeding a specified limit of residual drift, λ_{RD}. The mean annual frequency is related to another important parameter, the probability of collapse for a given number of years *n*, P_C (*n* years), or the probability of exceeding a specified value of residual drift for a given number of years *n*, P_{RD} (*n* years). Assuming that the earthquake occurrence follows a Poisson distribution, the following equations relate the mean annual frequency to the probability of collapse or probability of exceedance of a specified limit of residual drift ratio in *n* years:

$$P_C(n\_years) = 1 - e^{-\lambda_C n} \tag{11-1}$$

$$P_{RD}(n\_years) = 1 - e^{-\lambda_{RD} n} \tag{11-2}$$

The calculation of the mean annual frequency requires consideration of the hazard from all possible seismic events. The hazard data are obtained from the USGS website (http://geohazards.usgs.gov/hazardtool/application.php) in the form of the annual frequency of exceedance λ_{Sa} as function of the spectral acceleration S_a for specific values of the period (zero, 0.1, 0.2, 0.3, 0.5, 0.75, 1.0, 2.0, 3.0, 4.0 and 5.0 second). Values of the annual frequency of exceedance at intermediate values of period are typically obtained by linear interpolation in the logarithmic space.

The calculation of the mean annual frequency of collapse, λ_C, and the mean annual frequency of exceeding a specified limit of residual drift, λ_{RD}, requires integration of the collapse or the residual drift fragility of the structure over the seismic hazard curve (Medina and Krawinkler, 2004; Ibarra and Krawinkler, 2005; Krawinkler *et at*., 2006; Champion and Liel, 2012; Eads *et al*., 2013; Elkady and Lignos, 2014):

$$\lambda_C = \int_0^\infty (P_C \,|\, \mathrm{S}_a) \cdot \left| \frac{d\lambda_{S_a}}{d(\mathrm{S}_a)} \right| \cdot d(\mathrm{S}_a) \tag{11-3}$$

$$\lambda_{RD} = \int_0^\infty (P_{RD} \,|\, \mathrm{S}_a) \cdot \left| \frac{d\lambda_{S_a}}{d(\mathrm{S}_a)} \right| \cdot d(\mathrm{S}_a) \tag{11-4}$$

In Equations (11-3) and (11-4) $|d\lambda_{Sa}(S_a)/d(S_a)|$ is the absolute value of the slope of the seismic hazard curve.

This section presents data on the mean annual frequency of collapse, λ_C, and the mean annual frequency of exceeding specified limits of the residual drift, λ_{RD} (residual drift ratio of 0.2%, 0.5%. 1.0% and 2.0%) for the 3*S*-75, 3*S*-85, 3*S*-Reference, 6*S*-75 and 6*S*-Reference structures of Table 10-1 for the site considered in Section 4 (latitude 37.8814°N, longitude 122.08°W, site class D). Figure 11-1 presents the seismic hazard curves for the site (annual frequency of exceedance versus the value of spectral acceleration for the relevant periods of 1.0, 2.0 and 3.0 second, 5%-damped). Based on these curves, curves for the fundamental period of the structures (1.07, 1.23, 1.28, 1.31, 1.90 and 2.06 second, 5%-damped) were constructed using linear interpolation in the logarithmic space and are shown in Figure 11-2.

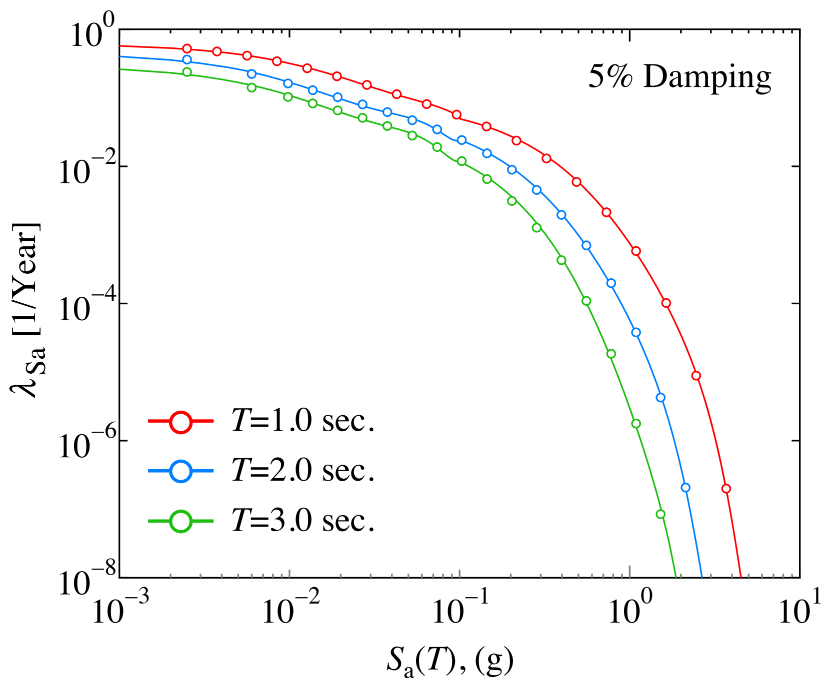

Figure 11-1 Seismic Hazard Curves at Site of Latitude 37.8814°N and Longitude 122.08°W, Site Class D for Periods of 1.0, 2.0 and 3.0 second (source USGS)

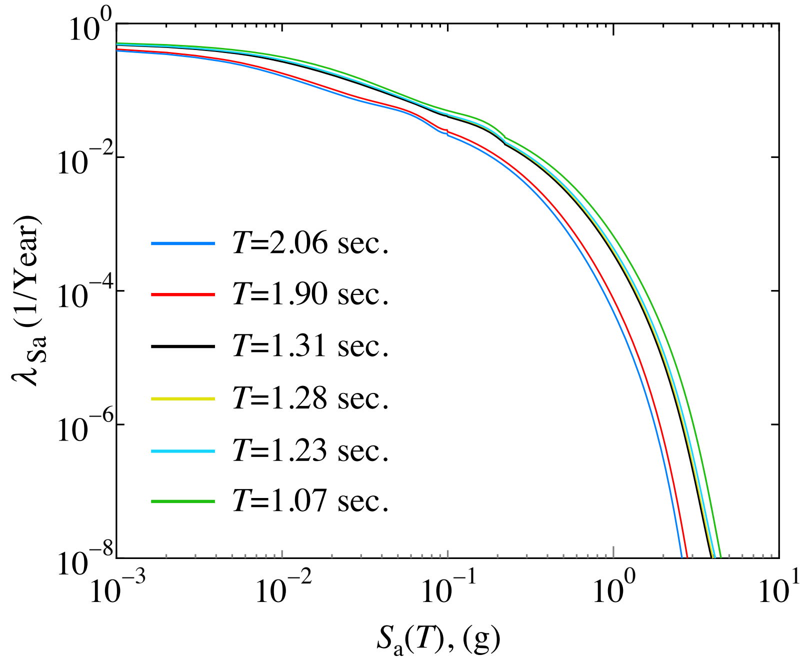

Figure 11-2 Seismic Hazard Curves at Site of Latitude 37.8814°N and Longitude 122.08°W, Site Class D for Periods of 1.07, 1.23, 1.28, 1.31, 1.90 and 2.06 second obtained by Linear Interpolation in Logarithmic Space of Data of Figure 11-1

Each of the curves in Figure 11-2 was approximated by polynomials in the logarithmic space that agreed with the values of the annual frequency of exceedance, $\lambda_{Sa}(S_a)$. As an example, the curve for period of 1.0 sec in Figure 11-1 was approximated as $\log_{10}[\lambda_{Sa}(S_a)]=1190.8S_a^4-851.9S_a^3+208.6S_a^2-23.7S_a-0.26$ for $1.0\times10^{-3}g\leq S_a\leq 2.2\times10^{-1}g$ and $\log_{10}[\lambda_{Sa}(S_a)]=0.01S_a^4-0.15S_a^3+0.65S_a^2-2.45S_a-1.16$ for $2.2\times10^{-1}g \leq S_a\leq 6.2\times10^0 g$. In general, the approximation is in the form:

$$\log_{10}(\lambda_{S_a}) = \sum_{i=0}^{N} a_i S_a^i \tag{11-5}$$

The derivative is then obtained as

$$\frac{d\lambda_{S_a}}{dS_a} = \lambda_{S_a}\frac{1}{\log_{10} e}\sum_{i=1}^{N} i a_i S_a^{i-1} \tag{11-6}$$

An example of the process in calculating the mean annual frequency is presented in Figure 11-3. In this case the figure illustrates the process by using actual data for frame 3S-75 with a fluidic self-centering system, case of linear viscous damping β_{v1}=0.10 and ultimate brace force equal to 1.3F_{MCE}. The top graph is the collapse fragility curve for the frame calculated in Section 9 (Figure 9-22, balanced case), $P_C|S_a$. The middle graph is the slope of the seismic hazard curve for period T_1=1.31sec, $|d\lambda_{Sa}(S_a)/d(S_a)|$, calculated using Equation (11-6). The bottom graph is the product of the other two graphs, $P_C|S_a \cdot |d\lambda_{Sa}(S_a)/d(S_a)|$. The mean annual frequency of collapse, λ_C, is the area under the line of the bottom graph per Equation (11-3), which is numerically calculated.

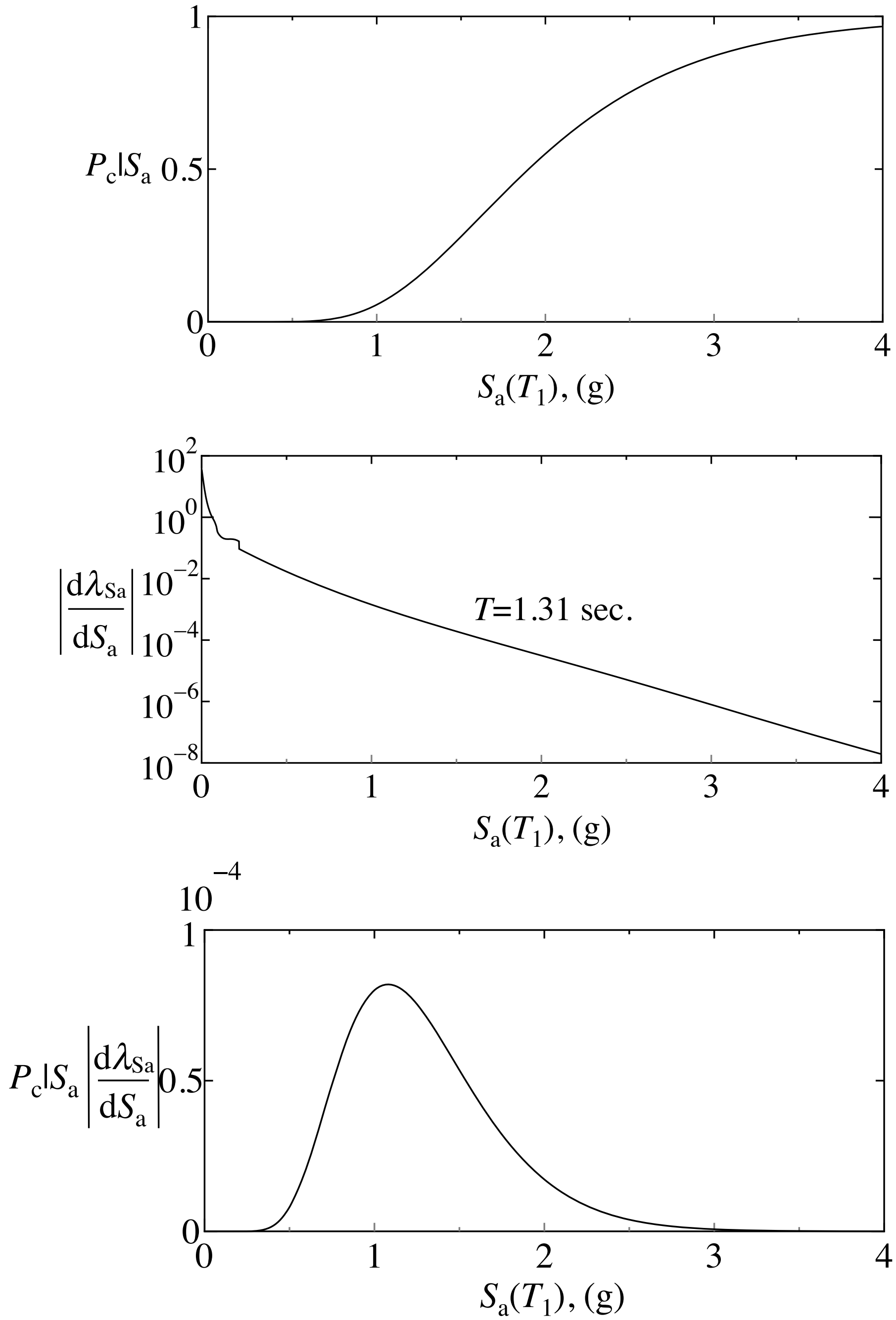

Figure 11-3 Example of Calculation of Mean Annual Frequency of Collapse for Frame 3*S*-75, Case of Linear Viscous Damping β_{v1} =0.10 and Ultimate Brace Force equal to 1.3F_{MCE}. Top Graph is the Collapse Fragility Curve, Middle Graph is the Slope of the Seismic Hazard Curve and Bottom Curve is the Product of the Two

11.2 Calculated Mean Annual Frequencies and Related Probabilities in 50 years

The 3-story and 6-story structures without and with fluidic self-centering systems in Table 10-1 have been further analyzed to obtain information of the mean annual frequency of collapse, the mean annual frequency of exceeding the residual drift limits of 0.2%, 0.5%, 1% and 2%, and the related probability of collapse or of exceeding the residual drift limits in 50 years. The procedure described in Section 11.1 was followed and detailed data for the fragility curves, seismic hazard curves and the de-aggregation curves are presented in Appendix G for each of the analyzed cases. Table 11-1 presents the calculated results. Note that λ_C is the mean annual frequency of collapse, λ_{RD} is the mean annual frequency of exceeding the specified residual drift ratio, P_C is the probability of collapse in 50 years and P_{RD} is the probability of exceeding any of the specified residual drift limits in 50 years.

These results provide additional information beyond the data in Sections 9 and 10 that were conditional on the level of the seismic intensity (say DE or MCE). Importantly, all analyzed systems have a probability of collapse in 50 years of about 1% or less, which is desirable. Also, the structures with fluidic self-centering systems have much lower probabilities in 50 years of exceeding the residual drift limits of 0.2% and 0.5% but they have about the same or higher probabilities of exceeding the limits of 1% and 2%. The reason for this difference is the fact the structures with the fluidic self-centering system may experience collapse before they have large residual drift. This is rectified by increasing the ultimate capacity of the fluidic device-brace system, as seen in Table 11-1 in the results for the system with device-brace capacity of $2.0F_{MCE}$.

Table 11-1 Mean Annual Frequency of Collapse, Mean Annual Frequency of Exceeding Specified Residual Drift Limits and Related Probabilities of Exceedance in 50 Years (probabilities in %)

System	Parameter	0.2% Res. Drift	0.5% Res. Drift	1.0% Res. Drift	2.0% Res. Drift	Collapse
3*S*-75, Capacity 1.3F_{MCE} Linear Viscous Damping β_{v1}=0.10 T_1= 1.31sec	λ_C or λ_{RD}	1.91×10^{-3}	1.04×10^{-3}	7.19×10^{-4}	4.80×10^{-4}	8.25×10^{-5}
	P_C or P_{RD}	9.10	5.07	3.53	2.37	0.41
3*S*-75, Increased Preload Capacity 1.3F_{MCE} Linear Viscous Damping β_{v1}=0.10 T_1= 1.28sec	λ_C or λ_{RD}	1.84×10^{-3}	8.49×10^{-4}	6.15×10^{-4}	4.55×10^{-4}	1.20×10^{-4}
	P_C or P_{RD}	8.78	4.16	3.03	2.25	0.60
3*S*-75, Increased Capacity 2.0 F_{MCE} Linear Viscous Damping β_{v1}=0.10 T_1= 1.31sec	λ_C or λ_{RD}	1.70×10^{-3}	4.97×10^{-4}	2.31×10^{-4}	1.10×10^{-4}	2.65×10^{-5}
	P_C or P_{RD}	8.17	2.46	1.15	0.55	0.13
3*S*-75, Capacity 1.3F_{MCE} Increased Nonlinear Damping β_{v1}=0.15 in DE (α=0.5) T_1= 1.31sec	λ_C or λ_{RD}	1.77×10^{-3}	1.11×10^{-3}	6.79×10^{-4}	3.67×10^{-4}	5.53×10^{-5}
	P_C or P_{RD}	8.48	5.39	3.34	1.82	0.28
3*S*-85, Capacity 1.3F_{MCE} Linear Viscous Damping β_{v1}=0.10 T_1= 1.23sec	λ_C or λ_{RD}	1.80×10^{-3}	6.04×10^{-4}	4.80×10^{-4}	3.09×10^{-4}	5.76×10^{-5}
	P_C or P_{RD}	8.62	2.98	2.37	1.53	0.29
3*S*-Reference T_1= 1.07sec	λ_C or λ_{RD}	5.93×10^{-3}	2.90×10^{-3}	8.44×10^{-4}	2.16×10^{-4}	2.62×10^{-5}
	P_C or P_{RD}	25.67	13.51	4.13	1.08	0.13
6*S*-75, Capacity 1.3F_{MCE} Linear Viscous Damping β_{v1}=0.10 T_1= 2.06sec	λ_C or λ_{RD}	4.64×10^{-3}	3.50×10^{-3}	2.81×10^{-3}	1.72×10^{-3}	2.42×10^{-4}
	P_C or P_{RD}	20.70	16.07	13.10	8.24	1.20
6*S*-75, Capacity 1.3F_{MCE} Increased Nonlinear Damping β_{v1}=0.15 in DE (α=0.5) T_1= 2.06sec	λ_C or λ_{RD}	9.70×10^{-3}	6.17×10^{-3}	3.70×10^{-3}	1.51×10^{-3}	2.47×10^{-4}
	P_C or P_{RD}	38.43	26.54	16.87	7.27	1.22
6*S*-75, Capacity 2.0F_{MCE} Linear Damping β_{v1}=0.10 in DE T_1= 2.06sec	λ_C or λ_{RD}	1.92×10^{-3}	1.01×10^{-3}	4.56×10^{-4}	3.49×10^{-4}	1.45×10^{-4}
	P_C or P_{RD}	9.13	4.94	2.25	1.73	0.72
6*S*-Reference T_1= 1.90sec	λ_C or λ_{RD}	9.95×10^{-3}	5.46×10^{-3}	2.16×10^{-3}	8.07×10^{-4}	2.07×10^{-4}
	P_C or P_{RD}	39.20	23.90	10.26	3.95	1.03

SECTION 12

FLUIDIC SELF-CENTERING DEVICES AS ELEMENTS OF SEISMIC ISOLATION SYSTEMS TO REDUCE RESIDUAL DISPLACEMENTS

12.1 Introduction

Fluidic self-centering devices may be used as elements of seismic isolation systems to provide re-centering capability and damping. The original experimental study of Tsopelas and Constantinou (1994) with fluidic self-centering devices explored the use of these devices as elements of an isolation system to completely eliminate residual displacements. The study presented in this section explores the use of fluidic self-centering devices to replace fluid viscous dampers in seismic isolation systems for the benefit of eliminating or substantially reducing residual displacements in the isolation system. For the purpose of the study, a seismically isolated building with Triple Friction Pendulum (FP) isolators and linear fluid viscous dampers is analyzed. The properties of the isolators and dampers are extracted from production test data of isolators and dampers used in actual projects. Similarly, the site-specific spectra and the scaled motions used in analysis are based on the spectra and motions used in the analysis of an actual seismically isolated building in California.

A second study is then conducted that parallels the study of the seismically isolated building but with the viscous damping devices designed to provide a nominal preload equal to 0.02 times the weight of the building, and a viscous damping function and displacement capacity (±36inch) identical to those of the fluid viscous dampers. The design of the devices was performed by the manufacturer of the damping devices, who also provided the dimensions and the stiffness of the device. The selection of the preload of 0.02 times the weight is based on the upper bound friction coefficient under quasi-static conditions for the inner surfaces of the Triple FP isolators, which was 0.023. Under these conditions, the fluidic self-centering devices are expected to substantially reduce residual deformations. The effects on other response parameters, like isolators peak displacements, story drift and accelerations are then investigated in the study.

12.2 Description of Analyzed Seismically Isolated Building

The analyzed seismically isolated building is the 4-story steel moment frame used in the examples of Sarlis and Constantinou (2010). The structure is illustrated in Figures 12-1 and 12-2. The structure is supported on 18 Triple Friction Pendulum (FP) isolators of the geometry shown in Figure 12-3. The isolation system also features 12 linear fluid viscous dampers (6 dampers in each principal direction) of the geometry shown in Figure 12-4. The weight is lumped at the joints as shown in Figure 12-2 so that each isolator carries a load (dead plus seismic live) of 3,338kN (or 750kip). The total weight of the isolated structure is 60,075kN (or 13,500kip). Note that the structure consists of three identical frames as shown in Figure 12-2. These frames are interconnected by W26×245 beams (at 1, 2 and 3 stories and roof) and by W26×300 (at base mat) beams in the transverse direction. All connections are rigid.

The analyzed isolated structure is imaginary but the isolators and dampers are actual devices used in construction for which the prototype and production test data were used to extract the properties used in the analysis of this example. Specifically, test data on 72 identical isolators at load of 3,338kN (750kip) and high velocity were available. The data for the first 18 of these isolators were used to obtain the lower and upper bound properties of the isolators using the procedures described in McVitty and Constantinou (2015). The properties are listed in Table 12-1 (see Sarlis and Constantinou, 2010 and McVitty and Constantinou, 2015 for nomenclature and definition of parameters). Note that since production test data at high speed are available, there is no production-related uncertainty in the values of friction. Also heating effects are included in the test data. Only contamination and aging effects are considered.

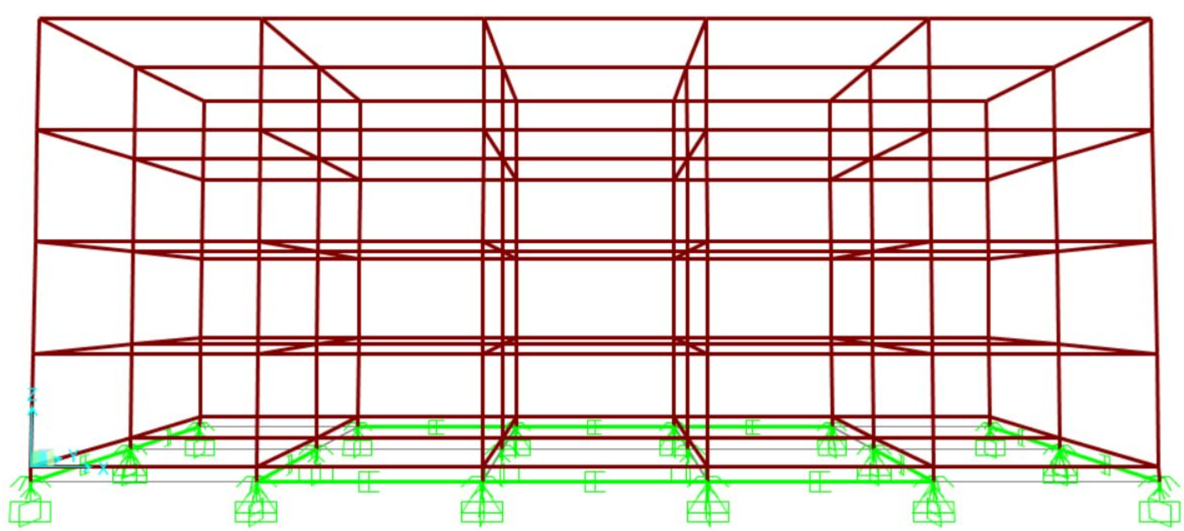

Figure 12-1 Three-Dimensional View of Analysis Model of Isolated Building in SAP2000

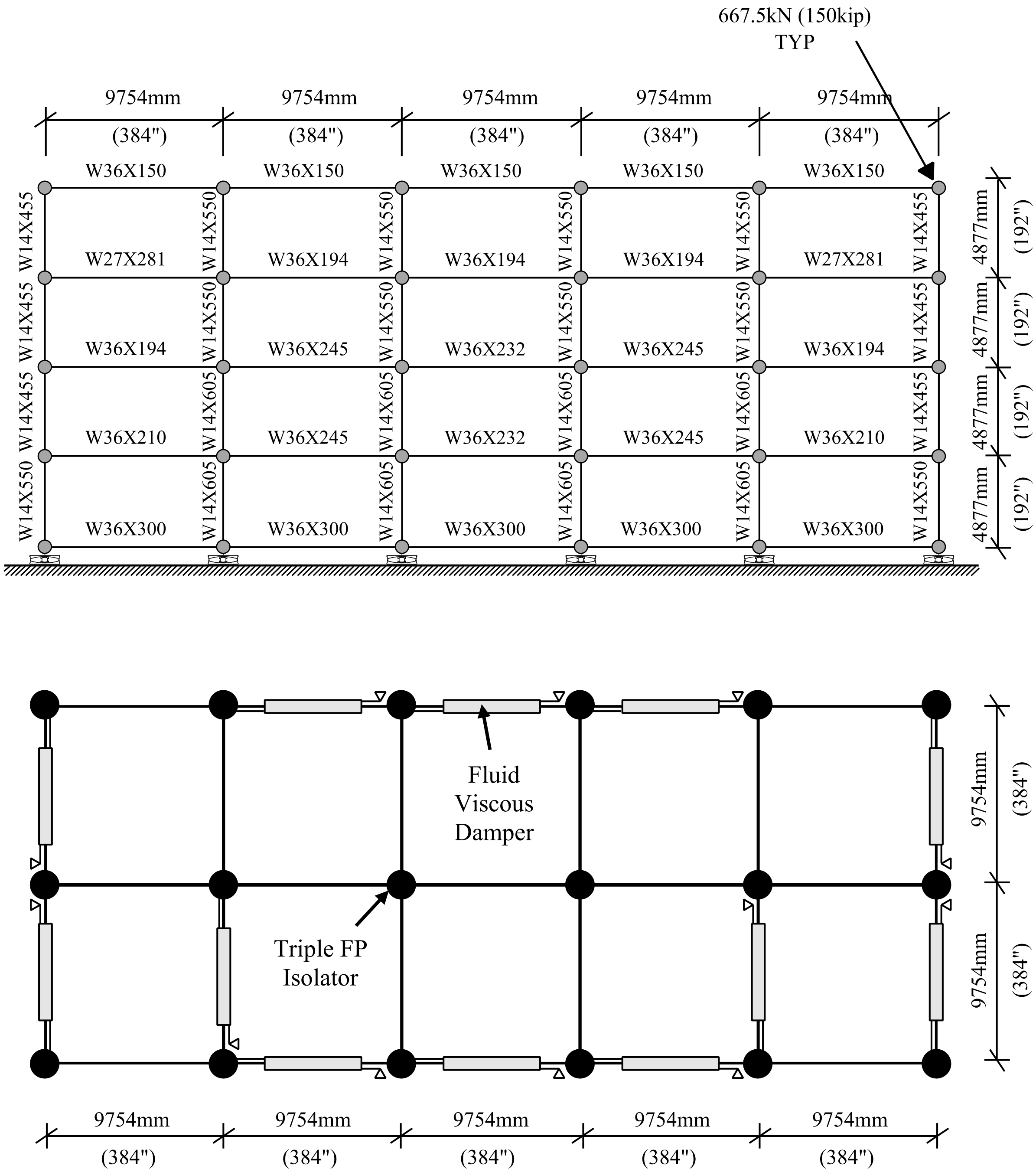

Figure 12-2 Elevation of Building and Plan of Isolation System

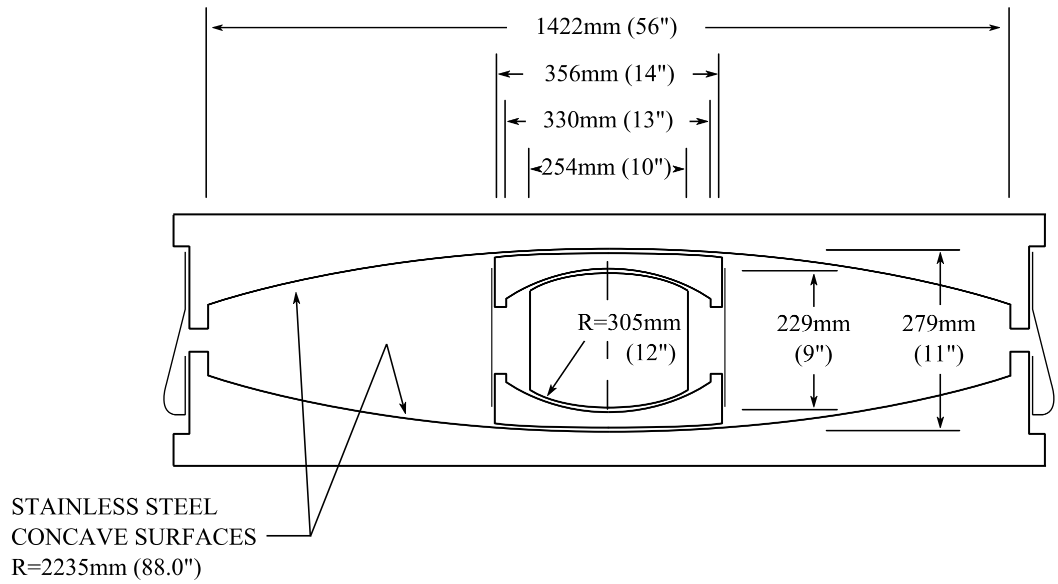

Figure 12-3 Section of Triple FP Isolator

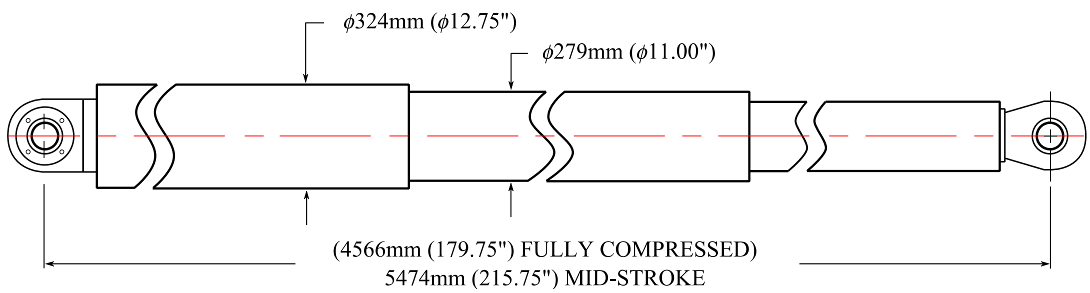

Figure 12-4 Plan View of Viscous Damping Device

Table 12-1 Properties of Triple FP Isolators

$R_{eff_1} = R_{eff_4}$	2096mm (82.5inch)	
$R_{eff_2} = R_{eff_3}$	191mm (7.5inch)	
$d_1^* = d_4^*$	500mm (19.67inch)	
$d_2^* = d_3^*$	24mm (0.94inch)	
$\mu_1 = \mu_4$	Upper Bound	0.075
	Lower Bound	0.058
$\mu_2 = \mu_3$	Upper Bound	0.034
	Lower Bound	0.030
$a_1 = a_2 = a_3 = a_4$	0.1sec/mm (2.54sec/in)	
Friction coefficients μ_1 to μ_4 are for fast velocity conditions. Zero velocity friction values are assumed to be 2/3 of the fast velocity values.		

The viscous dampers are of linear viscous damping devices with the force F related to the velocity V via $F=CV$. Thirty two of these devices were tested for a project. The properties of the first twelve of these devices were reduced based on the procedures in McVitty and Constantinou (2015) and found the average value of the damping constant to be C=0.93kN-sec/mm (5.3kip-sec/in). Note that again this value includes the heating effects. Aging is not considered as the dampers cannot change properties provided that they are maintained with the internal pressure checked to be at the specified level.

The structure was modelled for analysis in program SAP2000 (version 17). The parallel model was used in the modeling of the isolators per procedures in Sarlis and Constantinou (2010). Structural damping was modeled based on the guidelines of Sarlis and Constantinou (2010) as Rayleigh damping with 2% of critical damping ratio anchored at frequencies of 1.9 and 11.9Hz. Also, structural damping was set equal to zero for frequencies less than 0.24Hz using the “Rayleigh damping with override” option in the program in order to avoid leakage of damping in the isolation system. Table 12-2 presents numerical values of the parallel model parameters of each isolator as implemented in SAP2000.

Table 12-2 Values of Parameters of Parallel Model of Isolators in SAP2000

Elements		FP1	FP2
Element Height		406mm (16inch)	406mm (16inch)
Shear Deformation Location- (distance from top joint of FP element)		203mm (8inch)	203mm (8inch)
Element Mass		4.4×10^{-4} kN-s^2/mm (0.0025 kip-s^2/inch)	4.4×10^{-4} kN-s^2/mm (0.0025 kip-s^2/inch)
Supported Weight		1668kN (375kip)	1668kN (375kip)
Vertical Stiffness		6232.5kN/mm (35588.4kip/inch)	6232.5kN/mm (35588.4kip/inch)
Elastic Stiffness	Upper Bound	214.5kN/mm (1225.0kip/inch)	8.8kN/mm (50.0kip/inch)
	Lower Bound	188.3kN/mm (1075.0kip/inch)	
Yield Displacement		4.0×10^{-4}mm (0.01inch)	-
Effective Stiffness		0	0.8kN/mm (4.5kip/in)
Friction Coefficient SLOW	Upper Bound	0.0453	0.0497
	Lower Bound	0.04	0.0339
Friction Coefficient FAST	Upper Bound	0.068	0.0745
	Lower Bound	0.06	0.0509
Radius		0	2096mm (82.5inch)
Rate Parameter		0.05mm/sec (1.27inch/sec)	0.05mm/sec (1.27inch/sec)
Rotational/Torsional Stiffness (R1,R2,R3)		0	0
Rotational Moment of Inertia		56.5kN-mm-sec^2 (0.5 kip-in-sec^2)	56.5kN-mm-sec^2 (0.5 kip-in-sec^2)

12.3 Ground Motions Used in Analysis

The ground motions used in the analysis are based on the motions selected and scaled for the analysis of an actual seismically isolated structure in California. Table 12-3 presents the seed motions selected for scaling. Each of these motions was rotated and components were obtained along the fault-normal and fault-parallel directions. Each of the rotated components was then spectrally matched to site-specific fault-normal and fault-parallel spectra representing the maximum considered earthquake. Figure 12-5 shows the site-specific spectra and the average spectra of the scaled motions in the fault-normal and fault-parallel directions. Table 12-4 includes information of the peak ground acceleration (PGA) and the peak ground velocity (PGV) of the scaled motions in the fault-normal (FN) and fault-parallel (FP) directions. Each of the scaled motions was also lengthened with 10 seconds of zeroes to allow for the calculation of any residual isolator displacement. For the analysis, the fault-normal components of the scaled motions were applied in the transverse building direction.

Table 12-3 Seed Ground Motions and Recorded Characteristics

Motion	Earthquake	Magnitude/ Fault	Recording Station / Site Class	Recorded PGA (g) H1/H2	Scaled PGA (g) FN/FP	Scaled PGV (mm/sec) FN/FP
1	1999 Kocaeli, Turkey	7.4 / Strike-Slip	Duzce / USGS – C	0.31/0.36	0.84/0.83	1819/1219
2	1992 Erzincan, Turkey	6.7 / Strike-Slip	Erzincan / USGS – C	0.50/0.52	0.85/0.84	1608/1643
3	1992 Landers, USA	7.3 / Strike-Slip	Lucerne / USGS – A	0.72/0.79	0.85/0.85	1963/1755
4	1989 Loma Prieta, USA	6.9 / Reverse Oblique	Saratoga-Aloha Ave / Alluvium	0.51/0.32	0.87/0.87	1654/1676
5	1995 Kobe, Japan	6.9 / Strike-Slip	Takarazuka / USGS – D	0.69/0.69	0.85/0.85	2189/1316
6	1992 Landers, USA	7.3 / Strike-Slip	Yermo Fire Station / Alluvium	0.24/0.15	0.85/0.84	2040/1143
7	1999 Kocaeli, Turkey	7.4 / Strike-Slip	Yarimca / USGS – C	0.27/0.35	0.85/0.82	1908/1166

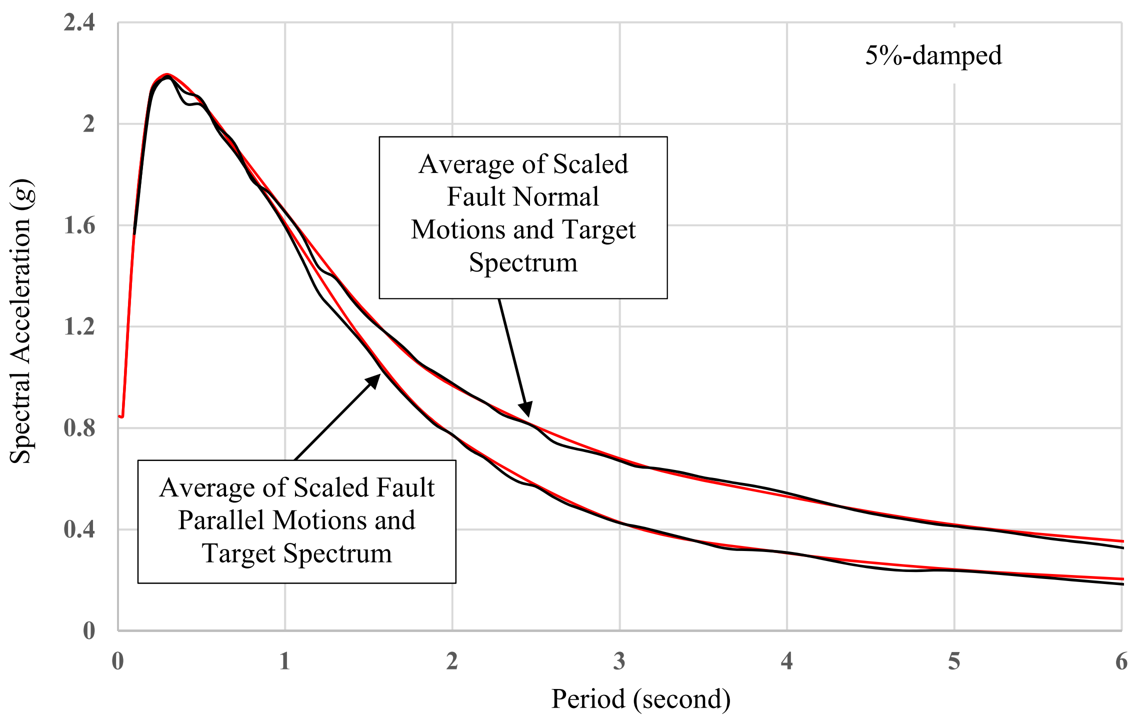

Figure 12-5 Site-Specific Spectra and Average Spectra of Fault Normal and Fault Parallel Scaled Motions

12.4 Analysis Results for Isolated Building with Fluid Viscous Dampers

Response history analysis was conducted in the isolator lower bound and upper bound conditions per properties of Table 12-1. The damper constant *C* was 0.93kN-sec/mm (5.3kip-sec/in) for both types of analyses. Results are presented in Tables 12-4 to 12-6 in terms of the resultant peak isolator displacements, resultant isolator residual displacement, resultant peak base shear force normalized by the weight (*W*=60,075kN or 13,500kip), damper peak displacement and peak force, peak roof acceleration and peak story drift ratio (resultant acceleration and drift, not along principal building directions). Note that the displacement at initiation of stiffening of the isolators in the lower bound conditions is 1008mm (39.7inch) and the displacement capacity of the isolators is 1046mm (41.2inch). Based on the average analysis results for the isolator displacement (Table 12-4), the peak displacement demand is 902mm (35.5inch) so that there is no initiation of stiffening.

Table 12-4 Peak Isolator Displacements, Residual Displacements and Base Shear Force

Motion	Lower Bound Friction		
	Isolator Disp. (mm)	Residual Disp. (mm)	Base Shear /*W*
1	934.7	49.3	0.352
2	779.8	30.0	0.305
3	970.3	17.8	0.367
4	937.3	9.4	0.409
5	899.2	34.8	0.337
6	901.7	8.1	0.331
7	889.0	38.4	0.314
Average	**901.7**	**26.9**	**0.345**

Motion	Upper Bound Friction		
	Isolator Disp. (mm)	Residual Disp. (mm)	Base Shear/*W*
1	873.8	56.9	0.352
2	706.1	39.9	0.327
3	944.9	43.2	0.383
4	886.5	24.1	0.412
5	858.5	50.8	0.341
6	825.5	4.3	0.325
7	807.7	28.2	0.324
Average	**843.3**	**35.3**	**0.352**

Table 12-5 Peak Damper Displacements and Forces

Motion	Lower Bound Friction	
	Damper Displacement (mm)	**Damper Force (kN)**
1	904.2	1385.6
2	744.2	1839.8
3	815.3	1819.8
4	896.6	2292.2
5	914.4	1987.5
6	901.7	1501.7
7	886.5	1878.5
Average	**866.1**	**1814.9**

Motion	Upper Bound Friction	
	Damper Displacement (mm)	**Damper Force (kN)**
1	843.3	1299.8
2	675.6	1842.5
3	779.8	1817.1
4	843.3	2165.8
5	866.1	1903.8
6	828.0	1381.2
7	805.2	1874.0
Average	**805.2**	**1754.8**

Table 12-6 Peak Roof Accelerations and Story Drift Ratios

Motion	Lower Bound Friction				
	Roof Acceleration (g)	Story Drift Ratio (%)			
		1	2	3	4
1	0.555	0.763	0.727	0.559	0.316
2	0.469	0.573	0.595	0.470	0.270
3	0.578	0.658	0.663	0.568	0.337
4	0.527	0.713	0.727	0.604	0.334
5	0.570	0.729	0.685	0.550	0.313
6	0.540	0.663	0.646	0.519	0.295
7	0.522	0.671	0.644	0.522	0.298
Average	**0.537**	**0.682**	**0.670**	**0.542**	**0.309**

Motion	Upper Bound Friction				
	Roof Acceleration (g)	Story Drift Ratio (%)			
		1	2	3	4
1	0.594	0.761	0.726	0.557	0.311
2	0.532	0.638	0.662	0.523	0.286
3	0.647	0.693	0.709	0.588	0.353
4	0.559	0.734	0.757	0.633	0.355
5	0.587	0.729	0.691	0.580	0.344
6	0.584	0.655	0.641	0.519	0.298
7	0.535	0.673	0.649	0.532	0.304
Average	**0.577**	**0.698**	**0.691**	**0.562**	**0.322**

More analyses were conducted only for the upper bound friction properties and for motions being weaker (i.e., half in acceleration amplitude) than the scaled motions representing the maximum considered earthquake. These motions are representative of an earthquake with a much larger probability of occurrence than the maximum considered earthquake. The calculated residual displacements were less than those reported in Table 12-6 so that it is concluded that the residual isolator displacements for the analyzed isolated building are about 35.6mm (or 1.4inch, average value) with values in the analysis ranging from nearly zero to 57.2mm (or 2.25inch).

12.5 Analysis Results for Isolated Building with Fluidic Self-Centering Devices

The manufacturer of the fluid viscous dampers (Taylor Devices, Inc.) was consulted and was asked to develop a design for a fluidic self-centering device having preload of 200kN (45kip), linear viscous damping with constant C=0.93kN-sec/mm (5.3kip-sec/in), displacement capacity of ±914mm (36inch), peak force of 2002kN (450kip) and peak velocity of 2159mm/sec (or 85in/sec); these are the characteristics of the fluid viscous damping devices. Note that the preload of 200kN (or about 10% of the peak force) corresponds to a total force (for 6 devices in each direction) of 1202kN (270kip) or 0.02 of the weight of the building (=60,075kN or 13,500kip), which is just less than the quasi-static value of friction force in the upper bound case of the inner surfaces of the Triple FP isolators is 0.023 of the weight (per Table 12-1, values for $\mu_2 = \mu_3$, see footnote). Thus, the residual displacements are expected to be very small.

The device has dimensions close to those of the damper of Figure 12-4, but diameter is 305mm (12inch) and pin-to-pin center mid-stroke length is approximately 4572mm (180inch) when the stiffness is 0.75kN/mm (4.3kip/inch) and is approximately 5080mm (200inch) when the stiffness is 0.51kN/mm (2.9kip/inch). Calculations were performed for the case of device stiffness equal to 0.51kN/mm and results are presented in Tables 12-7 to 12-9 for both lower and upper bound values of the friction coefficients.

The device model used in the analysis in program SAP2000 is illustrated in Figure 12-6. The stiffness, viscous damping and preload components of the force are modelled using standard SAP2000 elements. Friction in the seals is neglected as it is very small and is included in the viscous damping force. The preload component of the force is modeled by a bilinear elastic element with displacement at which the preload force of 2002kN (450kip) is reached equal to 25.4mm (1.0 inch). The stiffness and damping functions are modelled using the standard linear and damper elements.

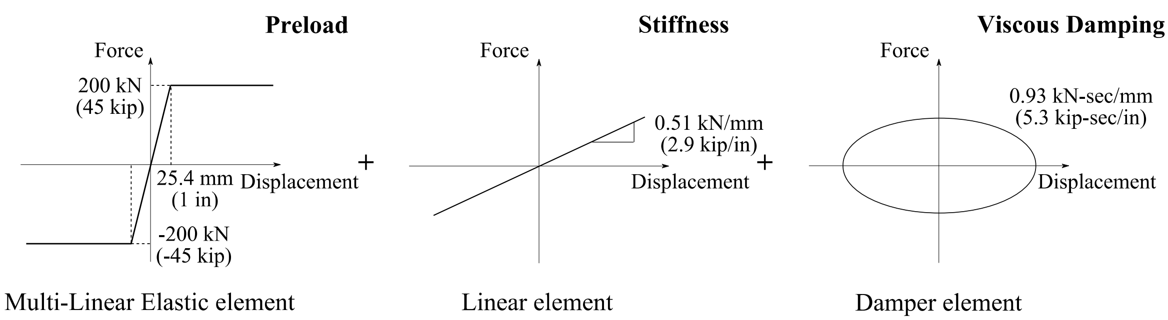

Figure 12-6 Force-Displacement Components for Fluidic Self-Centering Device

Table 12-7 Peak Isolator Displacements, Residual Displacements and Base Shear Force in Isolation System with Fluidic Self-Centering Devices

Motion	Lower Bound Friction		
	Isolator Disp. (mm)	**Residual Disp. (mm)**	**Base Shear /*W***
1	891.5	8.4	0.398
2	721.4	6.4	0.389
3	919.5	5.8	0.420
4	962.7	3.6	0.477
5	947.4	3.6	0.420
6	769.6	1.5	0.336
7	792.5	13.7	0.378
Average	**858.5**	**6.1**	**0.403**

Motion	Upper Bound Friction		
	Isolator Disp. (mm)	**Residual Disp. (mm)**	**Base Shear/*W***
1	838.2	10.2	0.397
2	703.6	9.1	0.406
3	909.3	6.1	0.437
4	906.8	3.6	0.476
5	899.2	2.0	0.421
6	703.6	1.8	0.332
7	774.7	14.5	0.387
Average	**820.4**	**6.6**	**0.408**

Table 12-8 Peak Damper Displacements and Forces in Isolation System with Fluidic Self-Centering Devices

Motion	Lower Bound Friction	
	Device Displacement (mm)	Damper Force (kN)
1	878.8	1790.0
2	701.0	2149.4
3	749.3	2112.0
4	919.5	2564.0
5	975.4	2263.7
6	769.6	1770.4
7	800.1	2183.2
Average	**828.0**	**2119.1**

Motion	Upper Bound Friction	
	Device Displacement (mm)	Damper Force (kN)
1	823.0	1724.1
2	624.8	2132.5
3	731.5	2123.1
4	861.1	2454.5
5	922.0	2186.7
6	706.1	1647.2
7	782.3	2184.1
Average	**779.8**	**2064.4**

Table 12-9 Peak Roof Accelerations and Story Drift Ratios in Isolation System with Fluidic Self-Centering Devices

Motion	Lower Bound Friction				
	Roof Acceleration (g)	Story Drift Ratio (%)			
		1	2	3	4
1	0.591	0.864	0.824	0.629	0.357
2	0.559	0.661	0.636	0.500	0.325
3	0.713	0.743	0.792	0.735	0.430
4	0.666	0.878	0.838	0.703	0.418
5	0.581	0.876	0.794	0.586	0.340
6	0.630	0.712	0.673	0.509	0.312
7	0.686	0.793	0.713	0.632	0.399
Average	**0.632**	**0.790**	**0.753**	**0.614**	**0.369**

Motion	Upper Bound Friction				
	Roof Acceleration (g)	Story Drift Ratio (%)			
		1	2	3	4
1	0.614	0.448	0.429	0.327	0.184
2	0.576	0.734	0.698	0.532	0.333
3	0.728	0.763	0.809	0.753	0.439
4	0.687	0.864	0.863	0.736	0.435
5	0.645	0.860	0.778	0.650	0.371
6	0.678	0.701	0.665	0.508	0.327
7	0.681	0.813	0.726	0.631	0.394
Average	**0.658**	**0.741**	**0.710**	**0.591**	**0.355**

The results demonstrate that the addition of the fluidic self-centering devices with characteristics equivalent in the damping function to those of fluid viscous damper results in a substantial reduction of the residual displacements (by about 80% in the presented example) and a small reduction in the peak isolator displacement (about 5%). This comes at the expense of an increase in the peak story drift and peak floor accelerations by as much as 15%.

To further demonstrate the benefits offered by the fluidic self-centering devices, a case is investigated in which the isolated building is reanalyzed in the upper case friction properties and with the device preload equal to either 151kN or 227kN (34kip or 51kip) (that is, equal to either 0.015W or 0.0227W, W=60,075kN or 13,500kip, for the 6 devices). Note that in the case of preload equal to 227kN, the total preload is equal to the zero velocity friction force in the inner surfaces of the isolators. Accordingly, one would expect the 227kN preload case to further reduce the residual displacement and that the case of preload of 151kN will result in larger residual displacement. All other isolator, damper and self-centering device parameters are the same. Results are presented in Table 12-10. Evidently, even small amounts of preload, but close to the friction force in the inner surfaces of the Triple FP isolators, result in substantial reduction in residual isolator displacements. Nevertheless, it is recognized that for this example, the residual displacements were generally small to be of concern.

Table 12-10 Average Isolator Peak Displacement, Residual Displacement, Peak Device Displacement and Force, Peak Roof Acceleration and Peak Story Drift Ratio in Isolation System with Viscous Dampers and with Fluidic Self-Centering Devices of 151, 200 and 227kN (34, 45 and 51kip) Preload, Case of Upper Bound Friction

System	Isolator Displacement (mm)	Residual Displacement (mm)	Damper/ Device Displace-ment (mm)	Damper/ Device Force (kN)	Story Drift Ratio (%)	Roof Acceleration (g)
Fluid Viscous Dampers	843.3	35.3	805.2	1755	0.698	0.577
Fluidic Self -Centering Devices, Preload=151kN	820.4	8.9	782.3	2024	0.786	0.625
Fluidic Self -Centering Devices, Preload=200kN	820.4	6.6	779.8	2064	0.741	0.658
Fluidic Self -Centering Devices, Preload=227kN	817.9	5.8	777.2	2089	0.807	0.676

12.6 Summary

It has been demonstrated that replacing viscous damping devices with equivalent fluidic self-centering devices in seismic isolation systems results in substantial reduction of residual isolator displacements. The studied system employed Triple FP isolators and linear viscous dampers which were then replaced by fluidic self-centering devices having a total preload equal to or less than the friction force in the inner surfaces of Triple FP isolators. The result was a 4-fold to 6-fold reduction in residual displacement together with a small decrease in peak isolator displacement and up to a 15% increase in story drift and peak floor acceleration. Reduction of residual displacements to the level demonstrated in the examples is such that the remaining residual offset cannot affect serviceability of the isolated structure. In general, isolation systems with large residual displacements need to be detailed to be able to accommodate these displacements as they may affect the serviceability of the structure and the functionality of elements crossing the isolation plane, such as fire-protection and weather proofing elements, egress/entrance details, elevators, and joints of primary piping systems (see Commentary of ASCE 7-2016).

SECTION 13
SUMMARY AND CONCLUSIONS

The work presented in this report is primarily a study on the use of fluidic devices as elements of self-centering systems for buildings and secondarily as devices to replace fluid viscous dampers in seismic isolation systems. These devices operate on principles similar to those of fluid viscous dampers and fluid springs, and have a 50-year history of extensive applications in the military and industry. They provide the functions of preload, stiffness and viscous damping incorporated in a single compact device. The main effect of these devices is a substantial reduction of residual displacements in earthquakes. Since they incorporate fluid damping, they also offer the benefit of reduction of drift.

The report presented a description of the behavior of these devices based on principles of mechanics, and presented results on the behavior of small and large fluidic self-centering devices for varying conditions of preload, history of motion and temperature. It also investigated the behavior of two devices tested over a period of 22 years. Mathematical models of the behavior of the devices have been presented and validated by comparison to experimental results.

Analyses of single-degree-of-freedom systems for a wide range of parameters were performed and the results were utilized to demonstrate the effect of the added fluidic self-centering devices on the behavior of the structural system, and to derive conclusions on a strategy for the selection of the device properties in design. On the basis of these observations, a design strategy was presented that parallels the design strategy for buildings with damping systems as presented in ASCE 7-2010. This strategy calls for the design of the primary structural system for a base shear force not less than 75% of the base shear force prescribed in ASCE 7-2010 for the building exclusive of the self-centering system, a preload equal to about (or more) than 20% of the story shear yield strength and a viscous damping ratio of at least 10% of critical under elastic frame conditions. Moreover, simplified methods of analysis were presented, again similar to the procedures for the analysis and design of buildings with damping systems in ASCE 7-2010, and verified by comparison to rigorous response history analysis results.

Three and six-story buildings without and with self-centering systems were designed per ASCE 7-2010 procedures (for the conventional buildings) and per the procedures developed in this report (for the buildings with self-centering fluidic devices). The response of the buildings was then obtained by the presented simplified analysis procedures and by nonlinear response history analysis with due considerations for the behavior of the devices and of the yielding structural system. The results demonstrated that the design of buildings with fluidic self-centering devices per the developed procedures offers benefits of substantial reduction in residual drift but also reduced peak drift, peak acceleration, peak shear and base shear forces, and reduced floor response spectra by comparison to the code-compliant buildings without fluidic self-centering devices. Also, the study established the validity of the simplified methods of analysis and determined its range of accuracy. Specifically, the simplified methods of analysis provide good and most often conservative estimates of drift and good predictions of fluidic self-centering device forces. It was determined that the presented Response Spectrum Analysis (RSA) simplified method provides sufficient means for developing a design and assessing its adequacy prior to performing nonlinear response history analysis.

The seismic collapse performance of two buildings, one 3-story and one 6-story, designed per the developed procedures when fluidic self-centering devices are used, was quantified using the FEMA P695 procedures and was compared to the collapse performance of conventional buildings designed per the minimum requirements of ASCE 7-2010. It was concluded that buildings with fluidic self-centering devices designed by the procedures presented in this report have a collapse performance comparable to that of conventionally designed buildings (in terms of the collapse margin ratio for the Maximum Earthquake). The study then varied the parameters of the fluidic devices, of the bracing system and of the strength of the frame in order to obtain information on how the design strategy affects the collapse performance. It was determined that increases in the preload, increases in the displacement capacity or increases in the viscous damping constant of the self-centering devices have marginal or insignificant effects on the collapse margin ratio. Rather, an increase in the collapse margin ratio was calculated for frames having a device-braced system with increased ultimate capacity and for frames with increased frame strength. It was concluded that designing the device-brace system for an ultimate capacity of about twice the calculated peak device force in the Maximum Earthquake (average of 7 analyses) while the frame is designed for a base shear force equal to 75% of the minimum prescribed base shear force per ASCE 7-2010 results in the best collapse performance.

The study then concentrated on the residual drift fragility of buildings with fluidic self-centering systems and calculated and compared them to those of conventional buildings. It was shown that buildings with fluidic self-centering systems, designed per the procedures of this document have substantial reduction of the probability of exceeding the residual drift limits of 0.2% and 0.5% for any level of earthquake.

Buildings without and with fluidic self-centering systems were further analyzed to obtain information of the mean annual frequency of collapse, the mean annual frequency of exceeding the residual drift limits of 0.2%, 0.5%, 1% and 2%, and the related probability of collapse or of exceeding the residual drift limits in 50 years. It was concluded that all analyzed systems have a probability of collapse in 50 years of about 1% or less, which is desirable. Also, the structures with fluidic self-centering systems have much lower probabilities in 50 years of exceeding the residual drift limits of 0.2% and 0.5% than conventional structures. This information is of much interest to engineers, building officials, government officials, owners and insurers.

Finally, a study was conducted on the effects of replacing viscous damping devices in seismic isolation systems by equivalent fluidic self-centering devices with identical damping characteristics and preload related to the minimum strength in the isolation system. It was observed that the use of the fluidic self-centering devices results in reduction of the residual displacements by four fold to six fold, in a small reduction of the peak isolator displacement and an increase in the peak floor accelerations and story drift ratio by as much as 15%.

SECTION 14
REFERENCES

Aiken I. D., Nims D. K., Kelly J. M. (1992). “Comparative Study of Four Passive Energy Dissipation Systems.” *Bulletin of the New Zealand National Society for Earthquake Engineering*, **25**(3): 175-192.

Aiken I. D., Nims D. K., Whittaker A. S., Kelly J. M. (1993). “Testing of Passive Energy Dissipation Systems.” *Earthquake Spectra*, **9**(3): 335-370.

American Institute of Steel Construction (2010). “Steel Construction Manual, 14th Ed., Third Printing (Hardbound).” AISC: Chicago, IL.

American Society of Civil Engineers (2010). “Minimum Design Loads for Buildings and other Structures.” (ASCE standard 7-10). ASCE: Reston, VA.

American Society of Civil Engineers (2016). “Minimum Design Loads for Buildings and other Structures.” (ASCE standard 7-16). ASCE: Reston, VA.

Baker J. W. (2007). “Quantitative Classification of Near-Fault Ground Motions Using Wavelet Analysis.” *Bulletin of the Seismological Society of America*, **97**(5): 1486-1501, October.

Braconi A., Morelli F., Salvatore W. (2012). “Development, Design and Experimental Validation of a Steel Self-Centering Device (SSCD) for Seismic Protection of Buildings.” *Bulletin of Earthquake Engineering*, **10**(6): 1915-1941.

British Standards Institution (1990). “Commentary on Corrosion at Bimetallic Contacts and its Alleviation.” PD 6484:1979.

Champion C., Liel A. (2012). "The Effect of Near-Fault Directivity on Building Seismic Collapse Risk." *Earthquake Engineering and Structural Dynamics*, **41**(10): 1391-1409.

Chopra A. K. (2012). “Dynamics of Structures”, 4th Edition, Prentice Hall, Englewood Cliffs, N.J.

Chou C.-C., Chen Y.-C. (2015). “Development of Steel Dual-Core Self-Centering Braces: Quasi-staticand Cyclic Tests and Finite Element Analyses.” *Earthquake Spectra*, **31**(1): 247-272.

Christopoulos C., Filiatrault A., Folz B. (2002a). “Seismic Response of Self-Centering Hysteretic SDOF Systems.” *Earthquake Engineering and Structural Dynamics*, **31**(5): 1131-1150.

Christopoulos C., Filiatrault A., Uang C.-M., Folz B. (2002b). “Posttensioned Energy Dissipating Connections for Moment-Resisting Steel Frames.” *Journal of Structural Engineering*, **128**(2): 1111-1120.

Christopoulos C., Pampanin S., Priestley M. J. (2003). “Performance-Based Seismic Response of Frame Structures Including Residual Deformations. Part I: Single-Degree of Freedom Systems.” *Journal of Earthquake Engineering*, **7**(1): 97-118.

Christopoulos C. (2004). “Frequency-Response of Flag-Shaped SDOF Hysteretic Systems.” *Journal of Engineering Mechanics*, **130**(8): 894-903.

Christopoulos C., Filiatrault A. (2006). “Principles of Passive Supplemental Damping and Seismic Isolation.” IUSS Press, Intituto Universitario di Studi Superiori di Pavia.

Christopoulos C., Tremblay R., Kim H.-J., Lacerte M. (2008). “Self-Centering Energy Dissipative Bracing System for the Seismic Resistance of Structures: Development and Validation.” *Journal of Structural Engineering*, **134**, SPECIAL ISSUE: Design and Analysis of Structures with Seismic Damping Systems, 96–107.

Constantinou M. C., Mokha A. Reinhorn A. (1990). “Teflon Bearing in Base Isolation II: Modeling.” *Journal of Structural Engineering*, **116**(2), 455-474.

Constantinou M. C., Symans M. D. (1992). “Experimental and Analytical Investigation of Seismic Response of Structures with Supplemental Fluid Viscous Dampers.” *NCEER-92-0032*, Multidisciplinary Center for Earthquake Engineering Research, Buffalo, NY**.**

Constantinou M. C., Symans M. D. (1993). "Seismic Response of Structures with Supplemental Damping." *Structural Design of Tall Buildings*, **2**(2): 77-92.

Constantinou M. C., Soong T. T., Dargush G. F. (1998). “Passive Energy Dissipation Systems for Structural Design and Retrofit.” *MCEER-98-MN01*, Multidisciplinary Center for Earthquake Engineering Research, Buffalo, NY.

Constantinou M. C., Whittaker A. S., Kalpakidis Y., Fenz D. M. and Warn G. P. (2007). “Performance of Seismic Isolation Hardware under Service and Seismic Loading.” *MCEER-07-0012*, Multidisciplinary Center for Earthquake Engineering Research, Buffalo, NY.

Dolce M., Cardone D., Marnetto R. (2000). “Implementation and Testing of Passive Control Devices Based on Shape Memory Alloys.” *Earthquake Engineering and Structural Dynamics*, **29**(7): 945-968.

Dolce M., Cardone D., Ponzo F. C., Valente C. (2005). “Shaking Table Tests on Reinforced Concrete Frames without and with Passive Control Systems.” *Earthquake Engineering and Structural Dynamics*, **34**(14): 1687-1717.

Eads L., Miranda E., Krawinkler H., Lignos D. G. (2013). “An Efficient Method for Estimating the Collapse Risk of Structures in Seismic Regions.” *Earthquake Engineering and Structural Dynamics*, **42**(1): 25-41.

Eartherton M. R., Hajjar J. F. (2011). “Residual Drifts of Self-Centering Systems Including Effects of Ambient Building Resistance.” *Earthquake Spectra*, **27**(3), 719-744.

Eatherton M. R., Fahnestock L. A., Miller D. J. (2014). “Computational Study of Self-Centering Buckling-Restrained Braced Frame Seismic Performance.” *Earthquake Engineering and Structural Dynamics*, **43**(11): 1897–1914.

Elkady A., Lignos D. G. (2014). “Modeling of the Composite Action in Fully Restrained Beam-to-Column Connections: Implications in the Seismic Design and Collapse Capacity of Steel Special Moment Frames.” *Earthquake Engineering and Structural Dynamics*, **43**(13): 1935–1954.

Erochko J., Christopoulos C., Tremblay R., Choi H. (2011). “Residual Drift Response of SMRFs and BRB Frames in Steel Buildings Designed according to ASCE 7-05.” *Journal of Structural Engineering*, **137**(5), 589-599.

Erochko J. (2013). “Improvements to the Design and Use of Post-Tensioned Self-Centering Energy-Dissipative (SCED) Braces.” Doctoral Thesis, University of Toronto, Toronto, Ontario.

Erochko J., Christopoulos C., Tremblay R., Kim H.-J. (2013). “Shake Table Testing and Numerical Simulation of a Self-Centering Energy Dissipative Braced Frame.” *Earthquake Engineering and Structural Dynamics*, **42**(11): 1617–1635.

Erochko J., Christopoulos C., Tremblay R. (2014)[a] “Design and Testing of an Enhanced-Elongation Telescoping Self-Centering Energy-Dissipative Brace.” *Journal of Structural Engineering*, **141**(6): 04014163.

Erochko J., Christopoulos C., Tremblay R. (2014)[b] “Design, Testing, and Detailed Component Modeling of a High-Capacity Self-Centering Energy-Dissipative Brace.” *Journal of Structural Engineering*, **141**(8), 04014193.

Federal Emergency Management Agency (2000). “Prestandard and Commentary for the Seismic Rehabilitation of Buildings. No. 356.” FEMA: Washington, D.C.

Federal Emergency Management Agency (2009). “Quantification of Building Seismic Performance Factors P695/June 2009.” FEMA: Washington DC.

Federal Emergency Management Agency (2012). “Seismic Performance Assessment of Buildings. P-58/September.” FEMA: Washington DC.

Filiatrault A., Tremblay R., Kar R. (2000). “Performance Evaluation of Friction Spring Seismic Damper.” *Journal of Structural Engineering*, **126**(4), 491-499.

Hamidia M., Filiatrault A., Aref A. (2014). “Simplified Seismic Sidesway Collapse Analysis of Frame Buildings.” *Earthquake Engineering & Structural Dynamics*, **43**(3): 429-448.

Hancock J., Lamprey J. W., Abrahamson N. A., Bommer J. J., Markatis A., McCoyh E., Mendis R. (2006). “An Improved Method of Matching Response Spectra of Recorded Earthquake Ground Motion Using Wavelets”. *Journal of Earthquake Engineering*, **10**, Special Issue 1: 67-89.

Haselton C. B. (2006). “Assessing Seismic Collapse Safety of Modern Reinforced Concrete Moment Frame Buildings” *Ph.D. Thesis*, Department of Civil and Environmental Engineering, Stanford University. USA.

Haselton C. B., Deierlein G. G. (2007). “Assessing Seismic Collapse Safety of Modern Reinforced Concrete Frame Buildings” *Blume Earthquake Engineering Research Center Technical Report No. 156*, Stanford University, USA.

Haselton C. B., Mitrani-Reiser J., Goulet C. A. , Deierlein G. G., Beck J. L., Porter K. A., Stewart J. P., Taciroglu E. (2008). “An Assessment to Benchmark the Seismic Performance of a Code-Conforming Reinforced-Concrete Moment-Frame Building” *PEER Report 2007/12*, Pacific Engineering Research Center, University of California, Berkeley, California, USA.

Hogg I. V. (1971). “Guns 1914/18 (History of 1st World War).” Ballantine Books, Inc., New York, New York.

Ibarra L. F., Krawinkler H. (2005). “Global Collapse of Frame Structures under Seismic Excitations.” PEER Report 2005/06; Pacific Earthquake Engineering Research Center College of Engineering University of California, Berkeley.

Kam W. Y., Pampanin S., Carr A. J. (2008). “Design Procedure and Behavior of Advanced Flag-Shape (AFS) MDOF Systems.” *2008 NZSEE Conference*, Paper Number 38.

Kam W. Y., Pampanin S., Palermo A., Carr A. J. (2010). “Self-Centering Structural Systems with Combination of Hysteretic and Viscous Energy Dissipations.” *Earthquake Engineering and Structural Dynamics*, **39**(10): 1083-1108.

Kammula V., Erochko J., Kwon O.-S., Christopoulos C. (2014). “Application of Hybrid-Simulation to Fragility Assessment of the Telescoping Self-Centering Energy Dissipative Bracing System.” *Earthquake Engineering and Structural Dynamics*, **43**(6): 811-830.

Kar R., Rainer J. H. (1996). “New Damper for Seismic Control of Structures.” *Proc. 1st Struct. Spec. Conf.*, Canadian Society of Civil Engineering, Edmonton, Alta., Canada, 835–842.

Karavasilis T. L., Seo C.-Y. (2011). "Seismic Structural and Non-Structural Performance Evaluation of Highly Damped Self-Centering and Conventional System." *Engineering Structures*, **33**(8): 2248-2258.

Kawashima K., MacRae G. A., Hoshikuma J., Nagaya K. (1998). "Residual Displacement Response Spectrum." *Journal of Structural Engineering*, **124**(5): 523-530.

Krawinkler H., Zarein F., Medina R. A., Ibarra L. F. (2006). "Decision Support for Conceptual Performance-Based Design." *Earthquake Engineering and Structural Dynamics*, **35**(1): 115-133.

Kurama Y. C. (2000). "Seismic Design of Unbonded Post-Tensioned Precast Concrete Walls with Supplemental Viscous Damping." *ACI Structral Journal*, 07/2000, **97**(4): 648-658.

Liel, A. B., C. B. Haselton, and G. G. Deierlein (2011). "Seismic Collapse Safety of Reinforced Concrete Buildings: II. Comparative Assessment of Non-Ductile and Ductile Moment Frames," *Journal of Structural Engineering* **134** (7): 492-502.

Lignos G. L., Krawinkler H. (2011). "Deterioration Modeling of Steel Components in Support of Collapse Prediction of Steel Moment Frames under Earthquake Loading." *Journal of Structural Engineering*, **137**(11): 1291-1302.

Lignos G. L., Krawinkler H. (2013). "Development and Utilization of Structural Component Databases for Performance-Based Earthquake Engineering." *Journal of Structural Engineering*, **139** SPECIAL ISSUE: NEES 2: Advances in Earthquake Engineering, 1382-1394.

MacRae G. A., Priestley M. J. N. (1994) "Precast Post-Tensioned Ungrouted Concrete Beam-Column Subassemblage Tests." *SSRP-94/10*, La Jolla, Calif. Dept. of Applied Mechanics & Engineering Sciences, University of California, San Diego, Report (Structural Systems Research Project).

MacRae G. A., Kawashima K. (1997). "Post-Earthquake Residual Displacements of Bilinear Oscillators." *Earthquake Engineering and Structural Dynamics*, **26**(7): 701-716.

McCormick J., Aburano H., Ikenaga M., Nakashima M. (2008). "Permissible Residual Deformation Levels for Building Structures Considering both Safety and Human Elements." *The 14th World Conference on Earthquake Engineering*, Octorber 12-17, Beijing, China.

McKenna F. T. (1997). “Object-Oriented Finite Element Programming: Frameworks for Analysis, Algorithms and Parallel Computing.” Ph.D. Thesis, Department of Civil and Environmental Engineering, University of California, Berkeley, CA.

McVitty W. J. and Constantinou M. C. (2015). “Property Modification Factors for Seismic Isolators: Design Guidance for Buildings”. *MCEER-15-0005*, Multidisciplinary Center for Earthquake Engineering Research, Buffalo, NY.

Medina R. A., Krawinkler H. (2004). “Seismic Demands for Nondeteriorating Structures and Their Dependence on Ground Motions.” *PEER Report 2003/15*, Pacific Earthquake Engineering Research Center College of Engineering University of California, Berkeley, CA.

Miller D. J., Fahnestock L. A. and Eatherton M. R. (2012). “Development and Experimental Validation of a Nickel-Titanium Shape Memory Alloy Self-Centering Buckling-Restrained Brace.” *Engineering Structures*, **40**: 288-298.

Miyamoto H. K., Gilani A. S. J., Wada A., Ariyaratana C. (2010). “Limit States and Failure Mechanisms of Viscous Dampers and the Implications for Large Earthquakes.” *Earthquake Engineering and Structural Dynamics*, **39**(11): 1279-1297.

Miyamoto H. K., Gilani A. S. J., Wada A., Ariyaratana C. (2011) “Identifying the Collapse Hazard of Steel Special Moment-Frame Buildings with Viscous Dampers using the FEMA P695 Methodology” *Earthquake Spectra*, **27**(4): 1147-1168.

Naeim F. and Kelly J. M. (1999). “Design of Seismic Isolated Structures: From Theory to Practice.” John Wiley & Sons, Inc.

National Earthquake Hazard Reduction Program (1997). “NEHRP Recommended Provisions for Seismic Regulations for New Buildings and Other Structures.” Federal Emergency Management Agency, Report No. FEMA 302: Washington, D. C.

Newmark, N. M. and Hall, W. J. (1982). “Earthquake Spectra and Design”, Earthquake Engineering Research Institute, Oakland, CA.

Pampanin S., Christopoulos C., Priestley M. J. (2003). “Performance-Based Seismic Response of Frame Structures Including Residual Deformations. Part II: Multi-Degree of Freedom Systems.” *Journal of Earthquake Engineering*, **7**(1): 119-147.

Pant D. R., Constantinou M. C., Wijeyewickrema A. C. (2013). “Re-evaluation of Equivalent Lateral Force Procedure for Prediction of Displacement Demand in Seismically Isolated Structures.” *Engineering Structures*, **52**: 455-465.

Pekcan G., Mander J. B., Chen S. S. (1995). “Experimental Performance and Analytical Study of a Non-Ductile Reinforced Concrete Frame Structure Retrofitted with Elastomeric Spring Dampers.” *MCEER-95-0010*, Multidisciplinary Center for Earthquake Engineering Research, Buffalo, NY.

Pekcan G., Mander J. B., Chen S. S. (1999a). “Experimental Investigation and Computational Modeling of Seismic Response of a 1:4 Scale Model Steel Structure with a Load Balancing Supplemental Damping System.” *MCEER-99-0006*, Multidisciplinary Center for Earthquake Engineering Research, Buffalo, NY.

Pekcan G., Mander J. B., Chen S. S. (1999b). “Design and Retrofit Methodology for Buildings Structures with Supplemental Energy Dissipating Systems.” *MCEER-99-0021*, Multidisciplinary Center for Earthquake Engineering Research, Buffalo, NY.

Priestley M. J. N., Tao J. R. (1993). “Seismic Response of Precast Prestressed Concrete Frames with Partially Debonded Tendons.” *PCI Journal*, **38**(1): Jan/Feb 1993, 58-59.

Rabinowicz E. (1995). “Friction and wear of materials.” New York, Wiley, 2nd ed.

Ramirez C. M., Miranda E. (2012). “Significance of Residual Drifts in Building Earthquake Loss Estimation.” *Earthquake Engineering and Structural Dynamics*, **41**(11): 1477-1493.

Ramirez O. M., Constantinou M. C., Kircher C. A., Whittaker A. S., Johnson M. W., Gomez J. D., Chrysostomou C. Z. (2001). “Development and Evaluation of Simplified Procedures for Analysis and Design of Buildings with Passive Energy Dissipation Systems.” *MCEER-00-0010*, Multidisciplinary Center for Earthquake Engineering Research, Buffalo, NY.

Richter P. J., Nims D. K., Kelly J. M., Kallenbach R. M. (1990). “The EDR-Energy Dissipating Restraint, A New Device for Mitigating Seismic Effects.” *Proceedings of the 1990 Structural Engineers Association of California Convention*, Lake Tahoe, September.

Ricles J. M., Sause R., Garlock M. M., Zhao C. (2001). “Posttensioned Seismic-Restraint Connections for Steel Frames.” *Journal of Structural Engineering*, **127**(2): 113-121.

Ruiz-Garcia J., Miranda E. (2006a). “Residual Displacement Ratios for Assessment of Existing Structures.” *Earthquake Engineering and Structural Dynamics*, **35**(3): 315-336.

Ruiz-Garcia J., Miranda E. (2006b). “Evaluation of Residual Drift Demands in Regular Multi-Storey Frames for Performance-Based Seismic Assessment.” *Earthquake Engineering and Structural Dynamics*, **35**(13): 1609-1629.

Sarlis A. A. S., Constantinou M. C. (2010). “Modeling Triple Friction Pendulum Isolators in Program SAP2000.” *Personal Communication*, University at Buffalo, State University of New York.

Seleemah A. A., Constantinou M. C. (1997). “Investigation of Seismic Response of Buildings with Linear and Nonlinear Fluid Viscous Dampers”, *NCEER-97-004*, National Center for Earthquake Engineering Research, University at Buffalo, State University of New York, Buffalo, NY.

Seo C.-Y., Karavasilis T. L., Ricles J. M., Sause R. (2014). “Seismic Performance and Probabilistic Collapse Resistance Assessment of Steel Moment Resisting Frames with Fluid Viscous Dampers.” *Earthquake Engineering and Structural Dynamics*, **43**(14): 2135-2154.

Stanton J. F., Nakaki S. D. (2002). “Design Guidelines for Precast Concrete Structural Systems.” *PRESSS Report No. 01/03-09*, Department of Civil Engineering, University of Washington, Seattle, WA.

Symans M. D., Constantinou M. C. (1995). “Development and Experimental Study of Semi-Active Fluid Damping Devices for Seismic Protection of Structures.” *NCEER-95-0011*, Multidisciplinary Center for Earthquake Engineering Research, Buffalo, NY.

Taisei Corporation. (1993). “Taisei-NCEER Complementary Research Report on the Development of Seismic Isolation Systems for Bridges: Shake Table Experiment of Passive Sliding Bearing Isolation System.” *Technical Report*, Taisei Corporation, Technical Research Institute (in Japanese).

Taylor D. P. (2014). *Personal communication*.

Taylor D. P and Lee D. (undated). “Precise Positioning Shock Isolators.” Available at Taylor Devices website: http://taylordevices.com/literature.html .

Tremblay T., Lacerte M., Christopoulos C. (2008). “Seismic Response of Multistory Buildings with Self-Centering Energy Dissipative Steel Braces.” *Journal of Structural Engineering*, **134**(1): 108-120.

Tsopelas P., Constantinou M. C. (1994). “NCEER-Taisei Research Program on Sliding Seismic Isolation Systems for Bridges: Experimental and Analytical Study of a System Consisting of Sliding Bearings and Fluid Restoring Force/Damping Devices.” *NCEER-94-0014*, Multidisciplinary Center for Earthquake Engineering Research, Buffalo, NY.

Tsopelas P., Constantinou M. C., Kircher C. A., Whittaker A. S. (1997). “Evaluation of Simplified Methods of Analysis for Yielding Structures.” *NCEER-97-0012*, Multidisciplinary Center for Earthquake Engineering Research, Buffalo, NY.

Vamvatsikos D., Cornell C. A. (2002). “Incremental Dynamic Analysis.” *Earthquake Engineering and Structural Dynamics*, **31**(3): 491-514.

Wanitkorkul A., Filiatrault A. (2008). “Influence of Passive Supplemental Damping Systems on Structural and Nonstructural Seismic Fragilities of a Steel Building.” *Engineering Structures*, **30**(3): 675-682

APPENDIX A

SUPPLEMENTAL RESULTS ON SINGLE-DEGREE-OF-FREEDOM SYSTEM WITH AND WITHOUT FLUIDIC SELF-CENTERING DEVICES

This appendix presents a collection of results in the analysis of the SDOF system with and without fluidic self-centering devices. Results are presented for (a) the three types of motion (near fault pulse-like, near fault non-pulse-like and far-field), (b) DE and MCE level of earthquake, (c) damping ratio in the range of β_v=0.0 to 0.20, (d) strength to elastic demand ratio R_μ=1, 2 and 5, (e) elastic period T_e in the range of 0.3 to 3.0sec, (f) stiffness K_0=0 or $K_0 \neq 0$ and such that the spring force at maximum displacement is equal to the preload, and (g) preload over strength ratio F_0/F_y = 0.00 to 1.00. The figures below are grouped as follows:

A.1.1: Linear viscous damping, K_0=0, Near-fault Pulse-like motions
A.1.2: Non-linear viscous damping, K_0=0, Near-fault Pulse-like motions
A.1.3: Upper-half viscous damping, K_0=0, Near-fault Pulse-like motions
A.2.1: Linear viscous damping, K_0=0, Near-fault Non-pulse-like motions
A.2.2: Non-linear viscous damping, K_0=0, Near-fault Non-pulse-like motions
A.2.3: Upper-half viscous damping, K_0=0, Near-fault Non-pulse-like motions
A.3.1: Linear viscous damping, K_0=0, Far-field motions
A.3.2: Non-linear viscous damping, K_0=0, Far-field motions
A.3.3: Upper-half viscous damping, K_0=0, Far-field motions
A.4: Linear viscous damping, $K_0 \neq 0$, Near-fault Pulse-like motions
A.5: Linear viscous damping, $K_0 \neq 0$, Near-fault Non-pulse-like motions
A.6: Linear viscous damping, $K_0 \neq 0$, Far-field motions

Tables A-1 and A-2 present symbols and lines used in the figures to distinguish the analyzed cases.

Table A-1 Legend (Lines)

Structures without self-centering device	
Structures with self-centering device	

Table A-2 Legend (Markers)

R_μ=1	○
R_μ=2	△
R_μ=5	×

A.1 Seismic Response under Near-Fault Pulse-Like Ground Motions

A.1.1 Structure with Linear Viscous Damping and K_0=0 for Near-Fault Pulse-Like Ground Motions

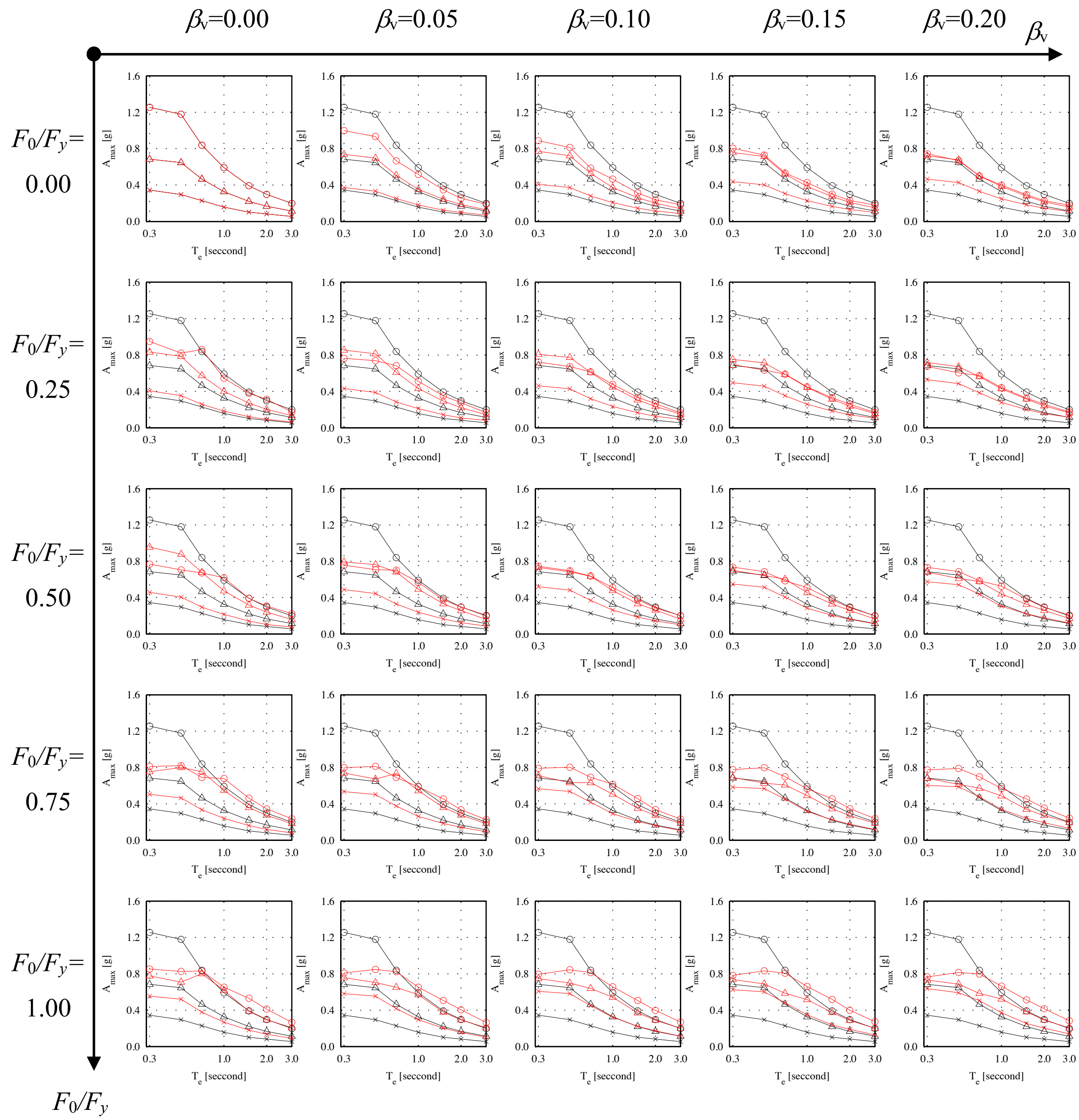

Figure A-1 Acceleration in DE, Near-Fault Pulse-like Motions, Linear Viscous Damping, Stiffness K_0=0, R_μ=1, 2 and 5

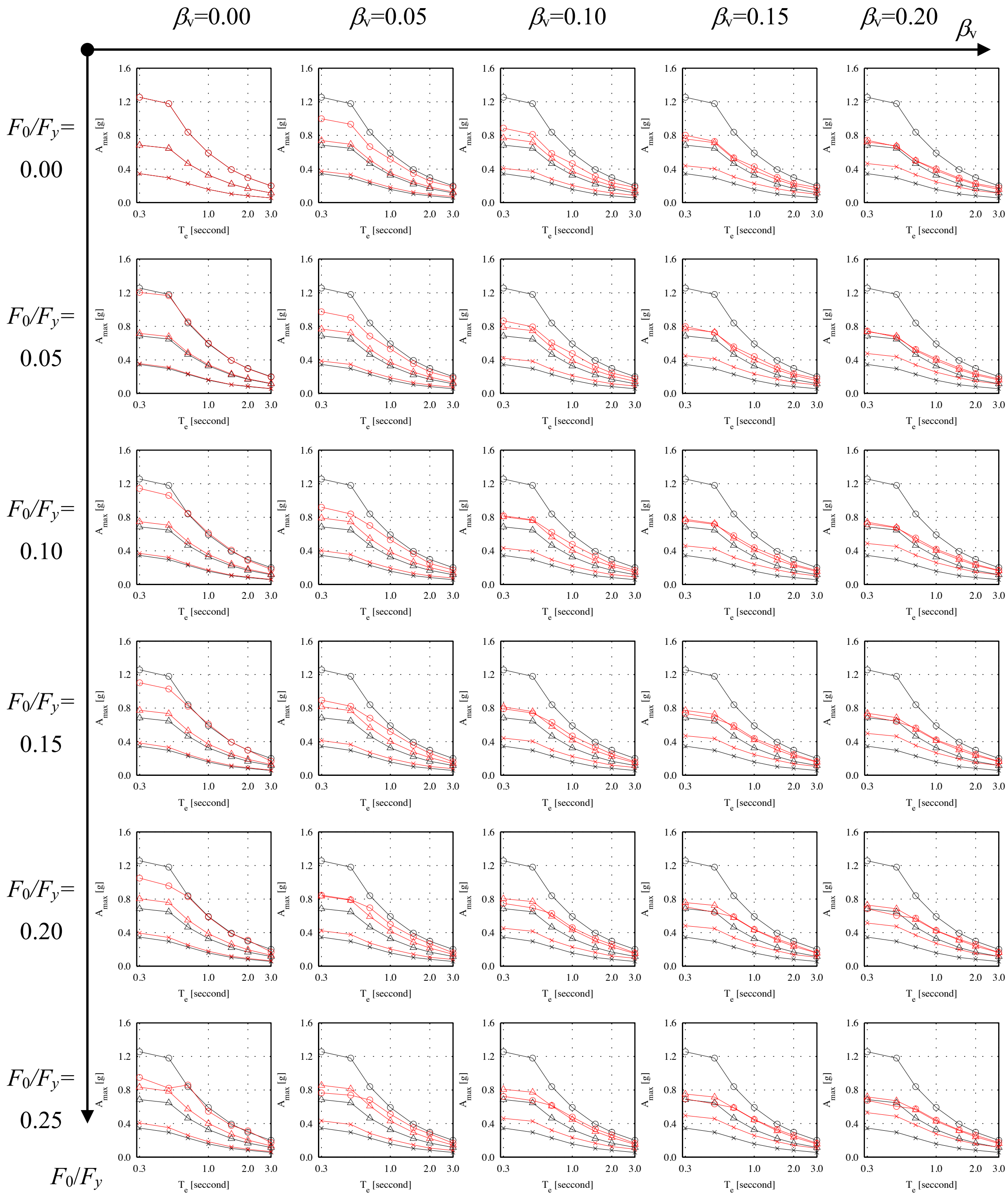

Figure A-1 (Continued)

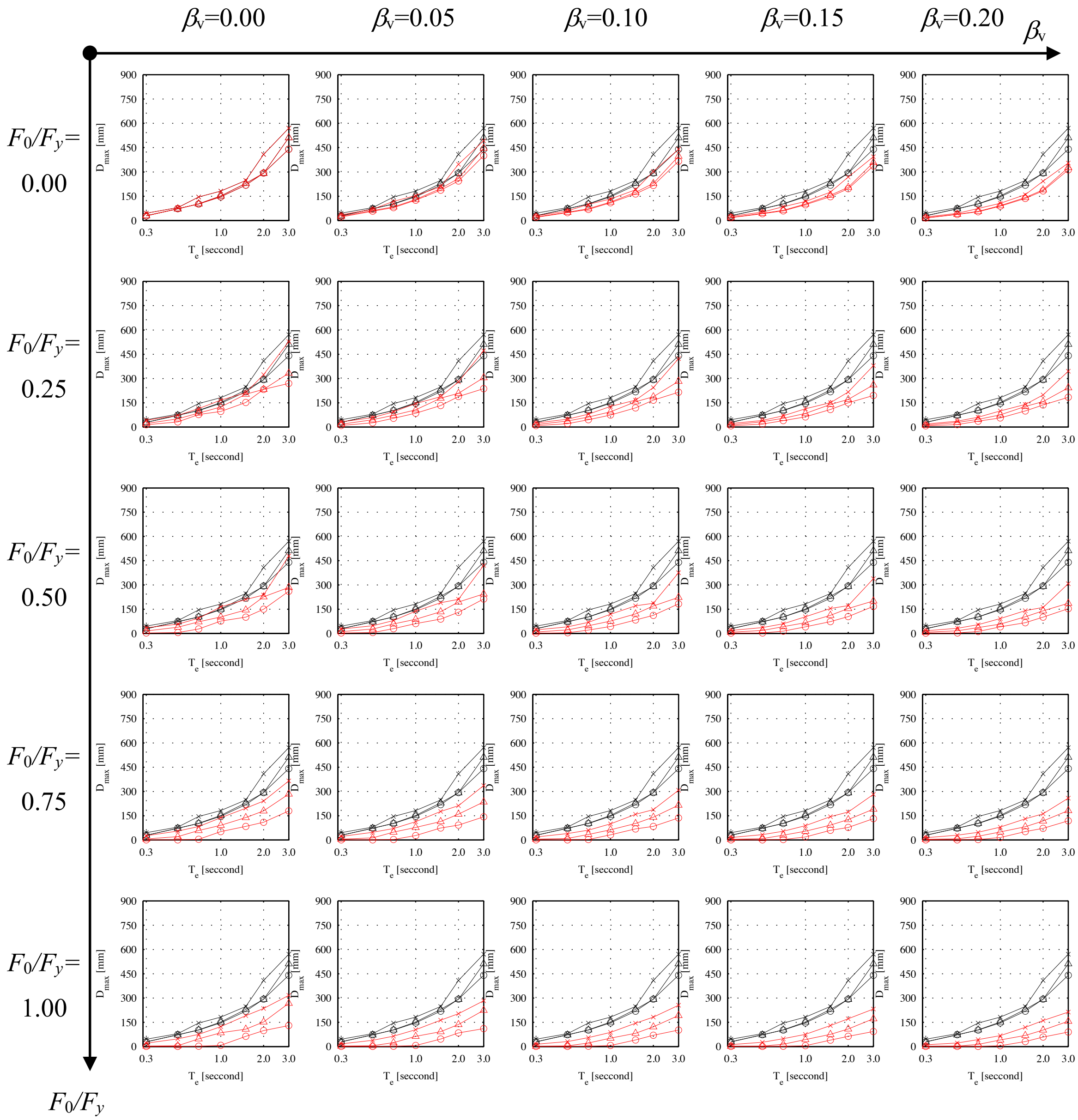

Figure A-2 Displacement in DE, Near-Fault Pulse-like Motions, Linear Viscous Damping, Stiffness K_0=0, R_μ=1, 2 and 5

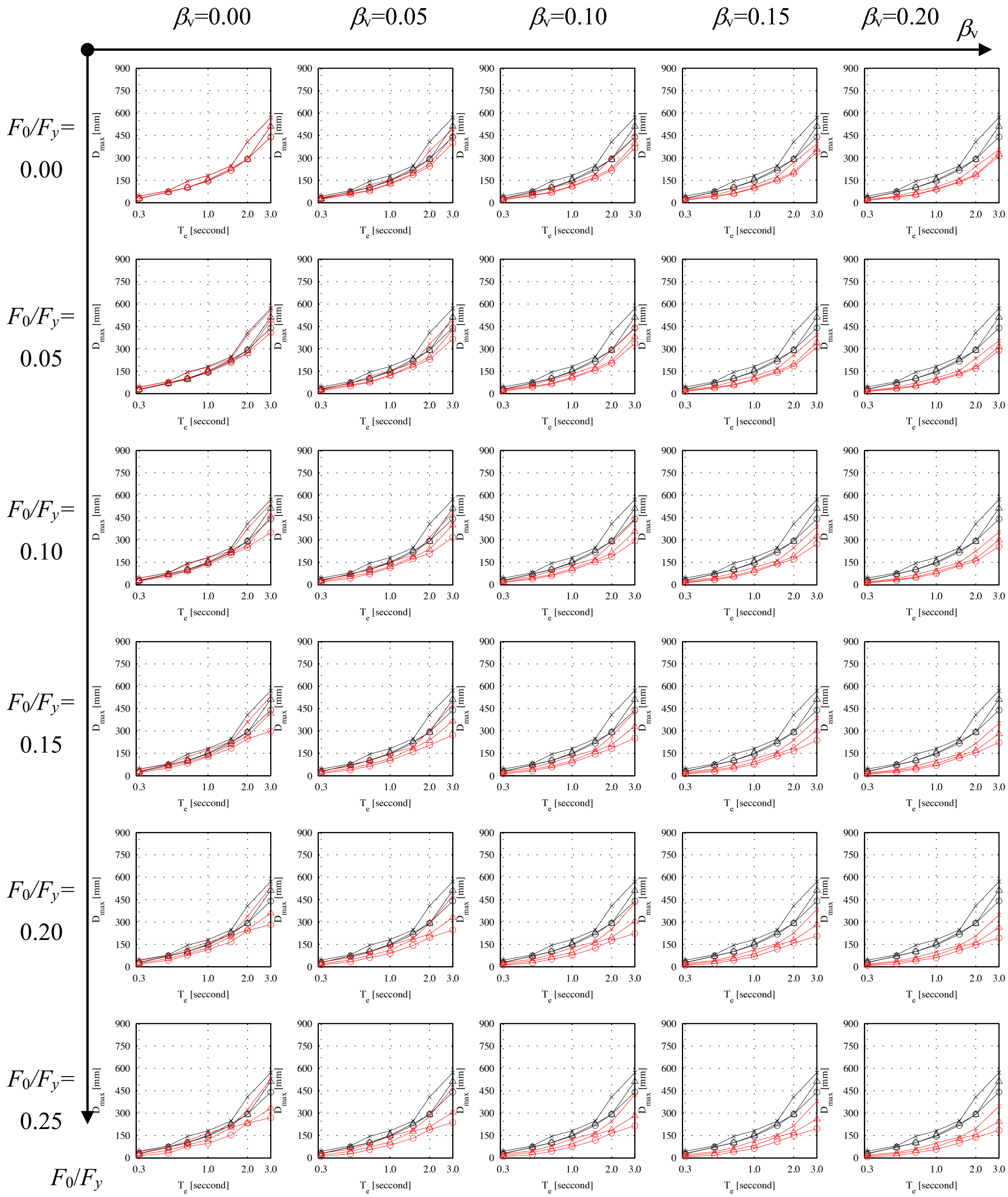

Figure A-2 (Continued)

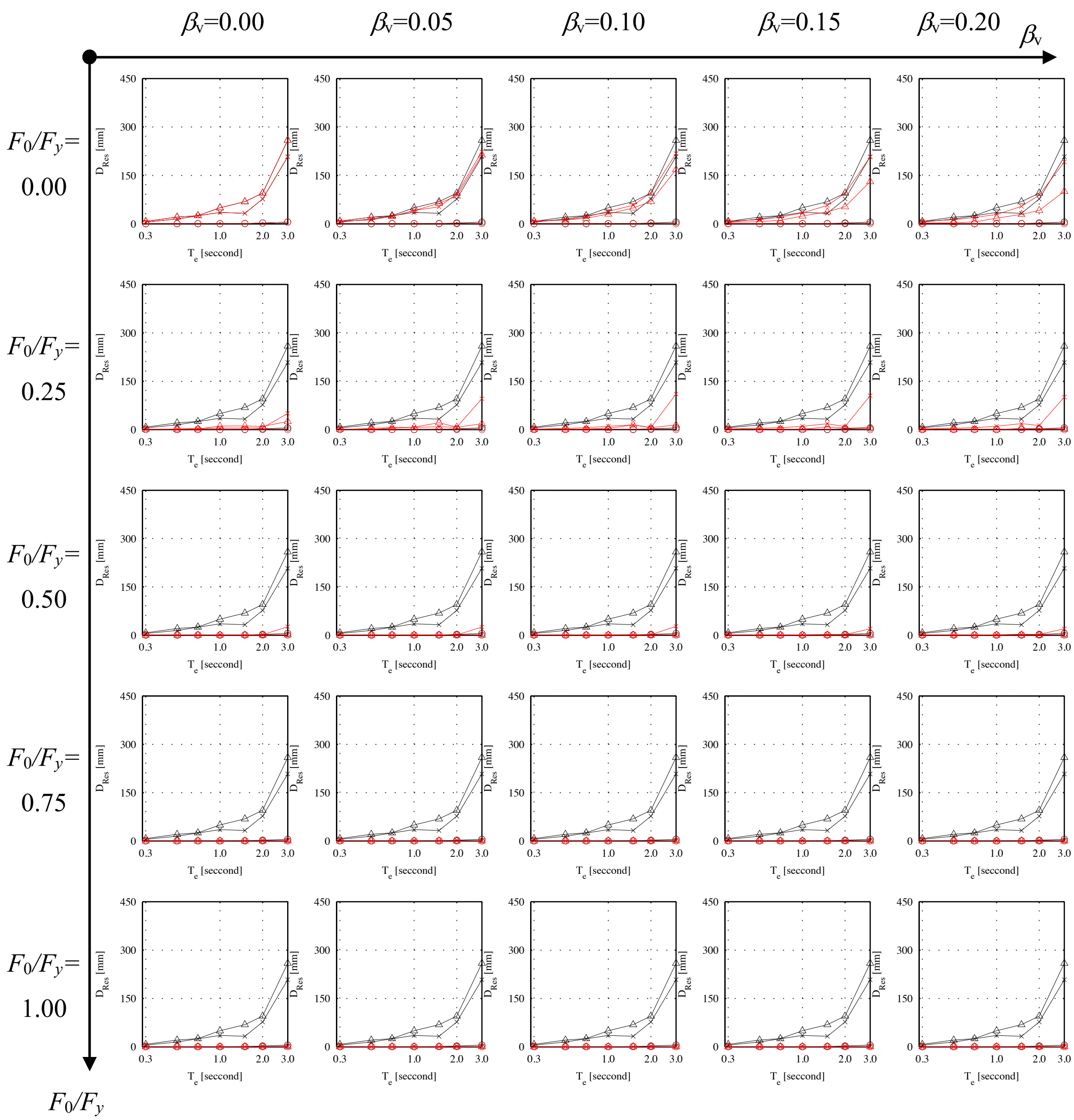

Figure A-3 Residual Displacement in DE, Near-Fault Pulse-like Motions, Linear Viscous Damping, Stiffness K_0=0, R_μ=1, 2 and 5

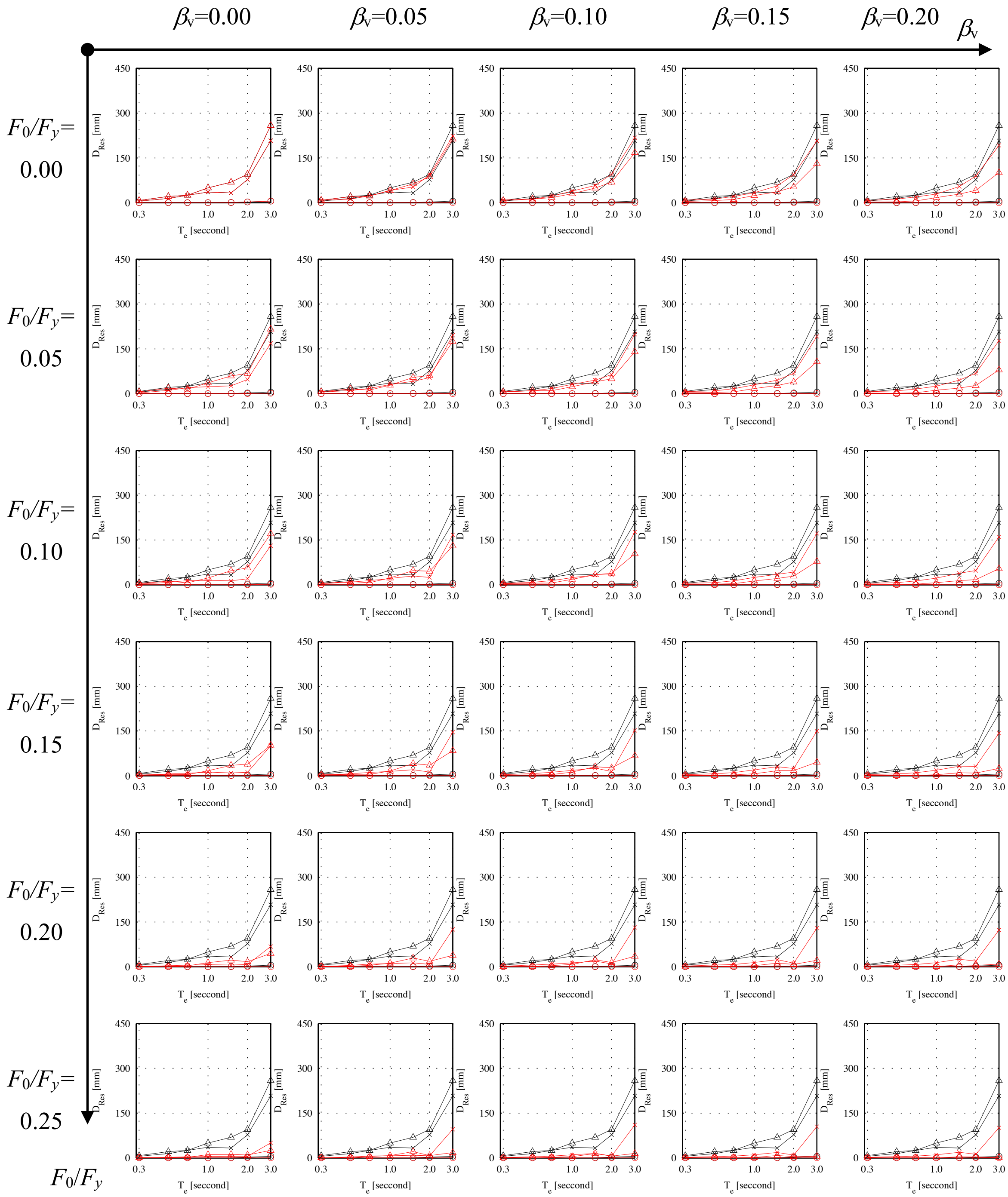

Figure A-3 (Continued)

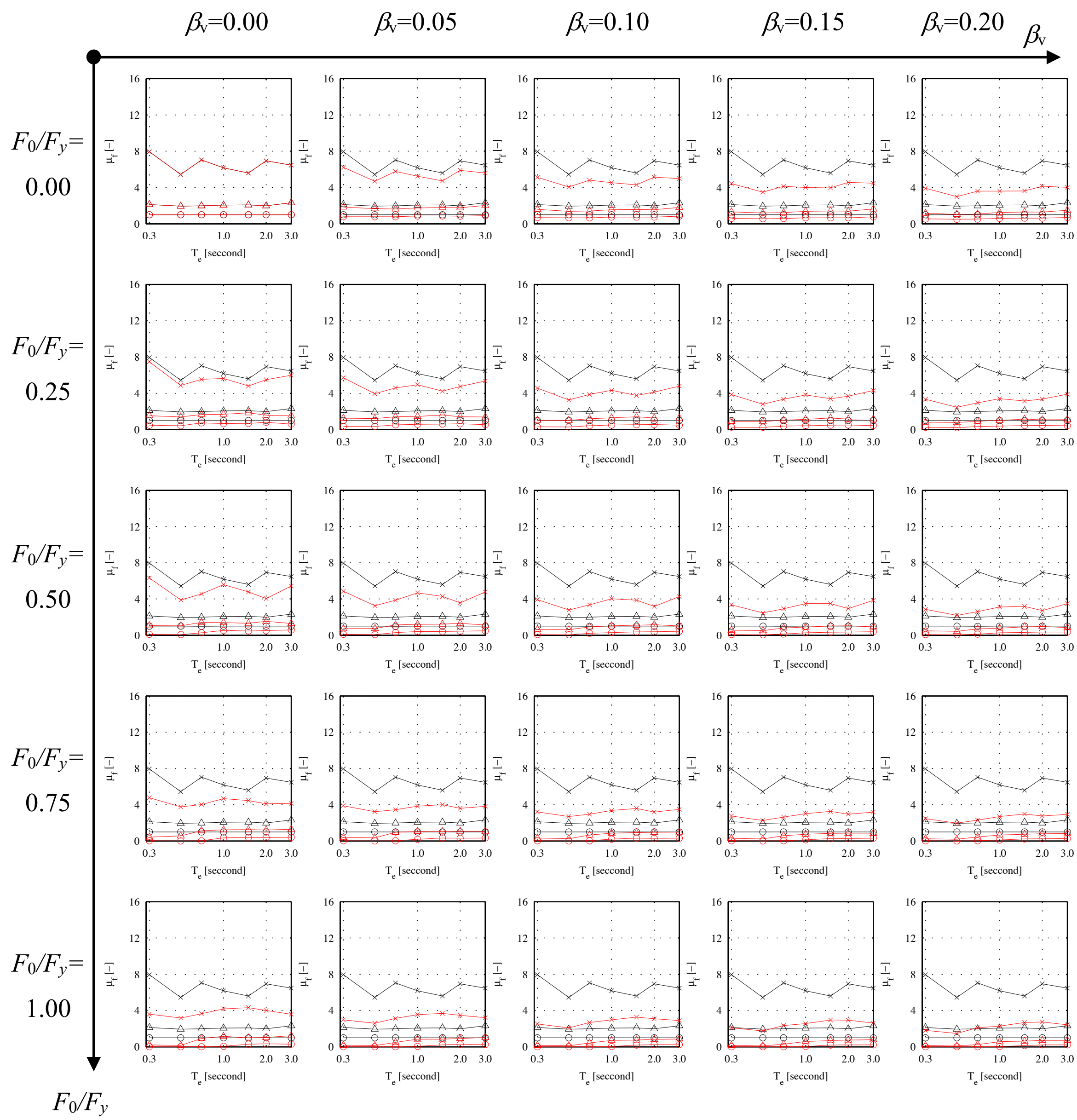

Figure A-4 Ductility Ratio in DE, Near-Fault Pulse-like Motions, Linear Viscous Damping, Stiffness K_0=0, R_μ=1, 2 and 5

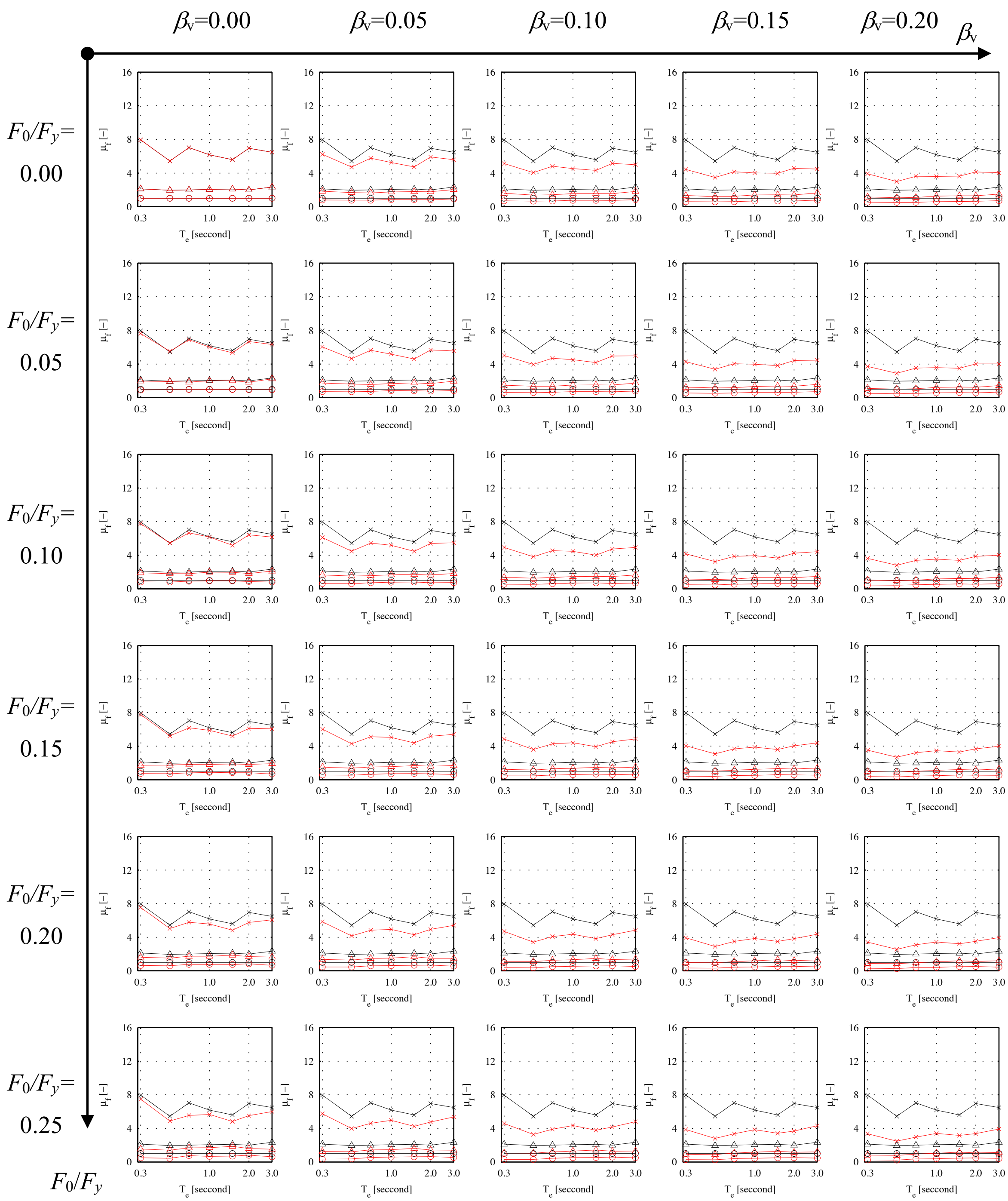

Figure A-4 (Continued)

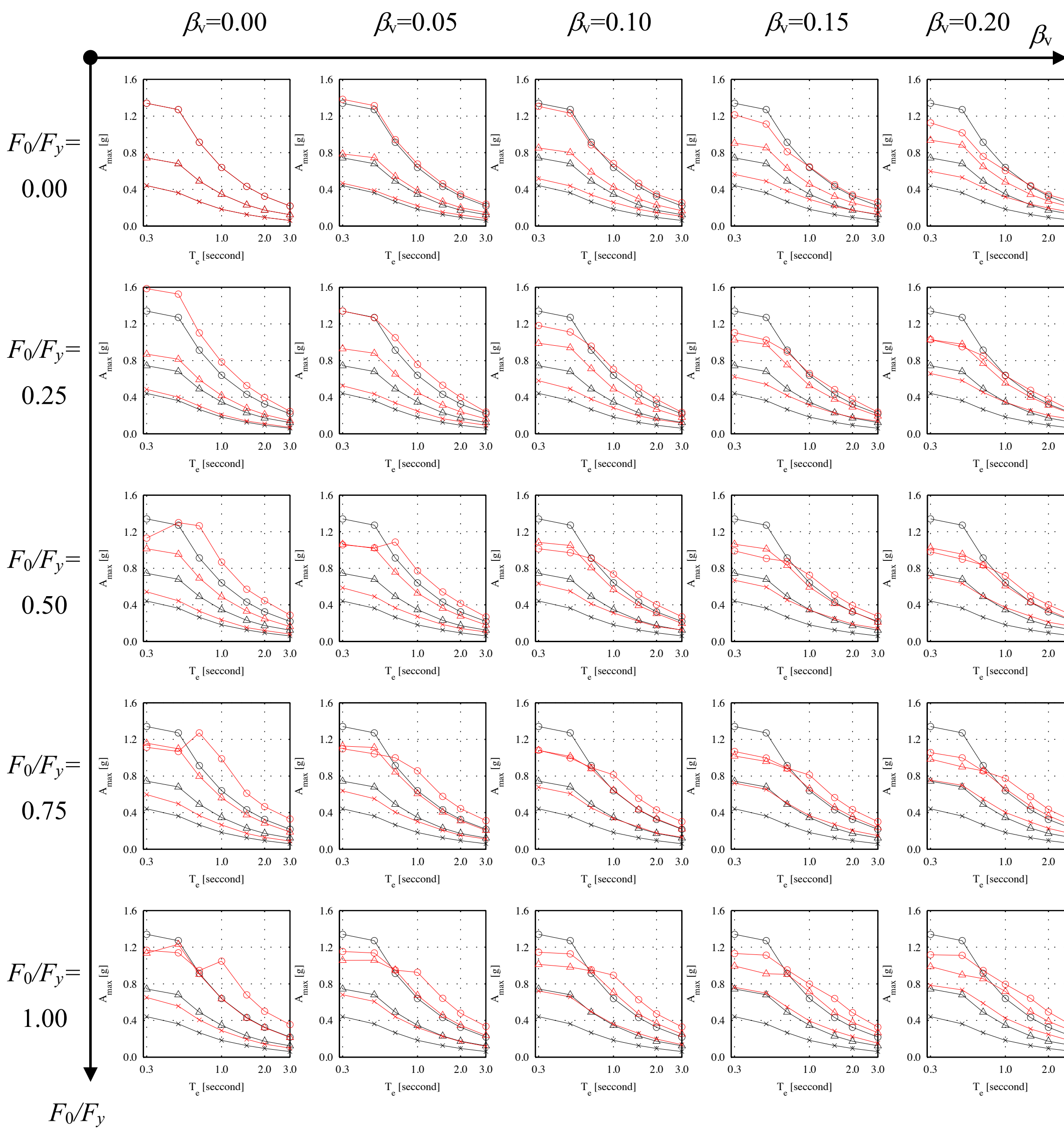

Figure A-5 Acceleration in MCE, Near-Fault Pulse-like Motions, Linear Viscous Damping, Stiffness K_0=0, R_μ=1, 2 and 5

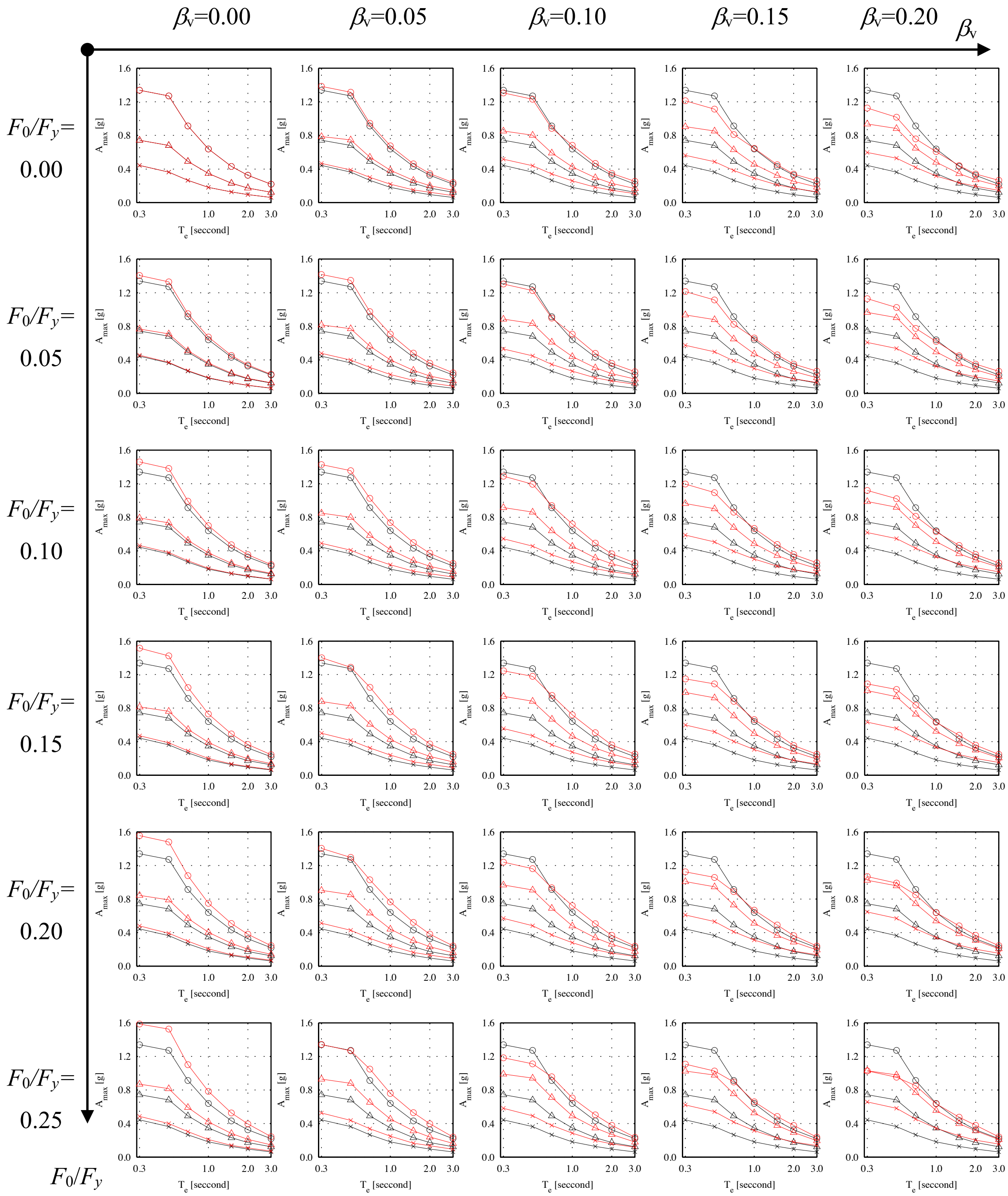

Figure A-5 (Continued)

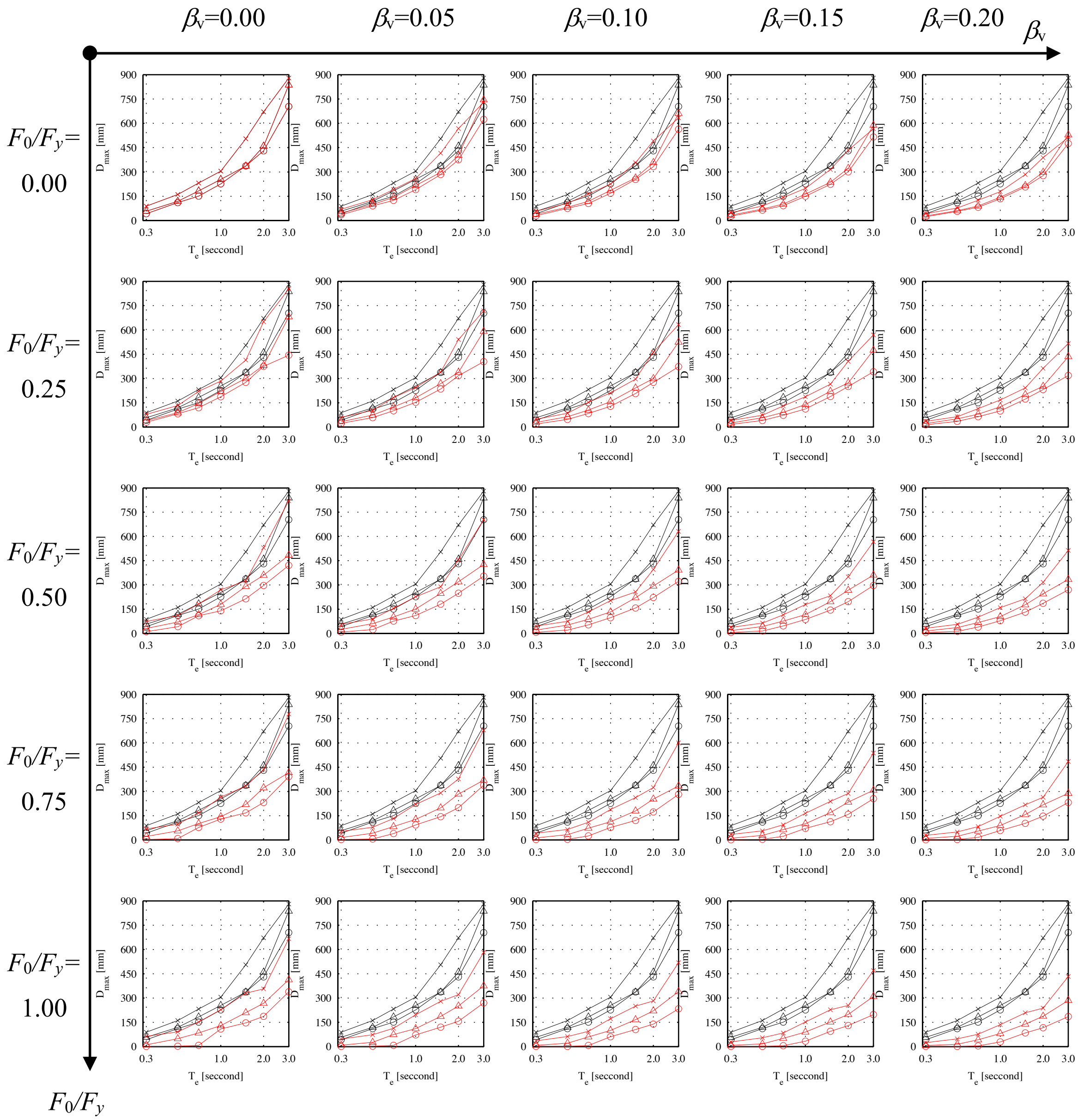

Figure A-6 Displacement in MCE, Near-Fault Pulse-like Motions, Linear Viscous Damping, Stiffness K_0=0, R_μ=1, 2 and 5

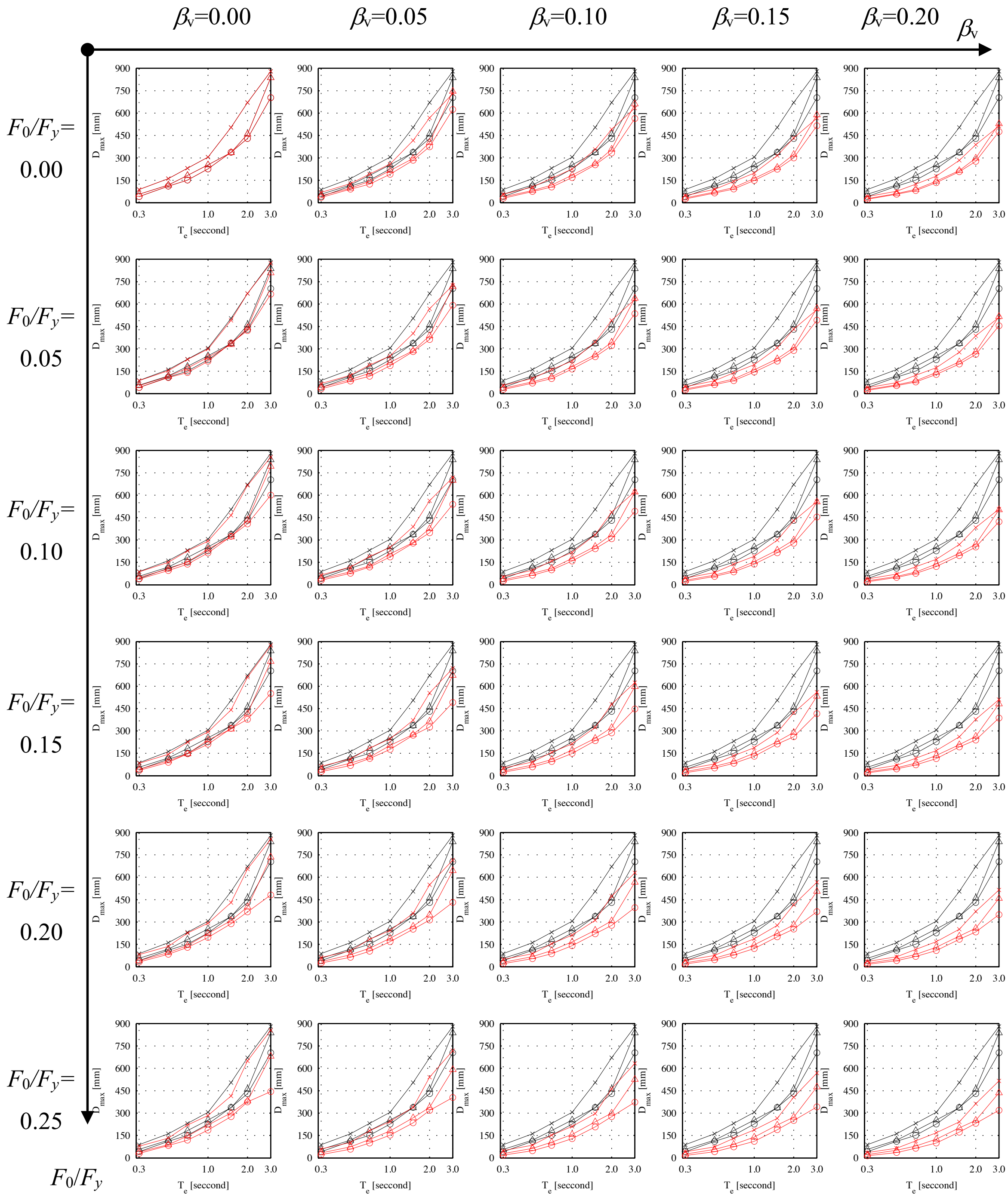

Figure A-6 (Continued)

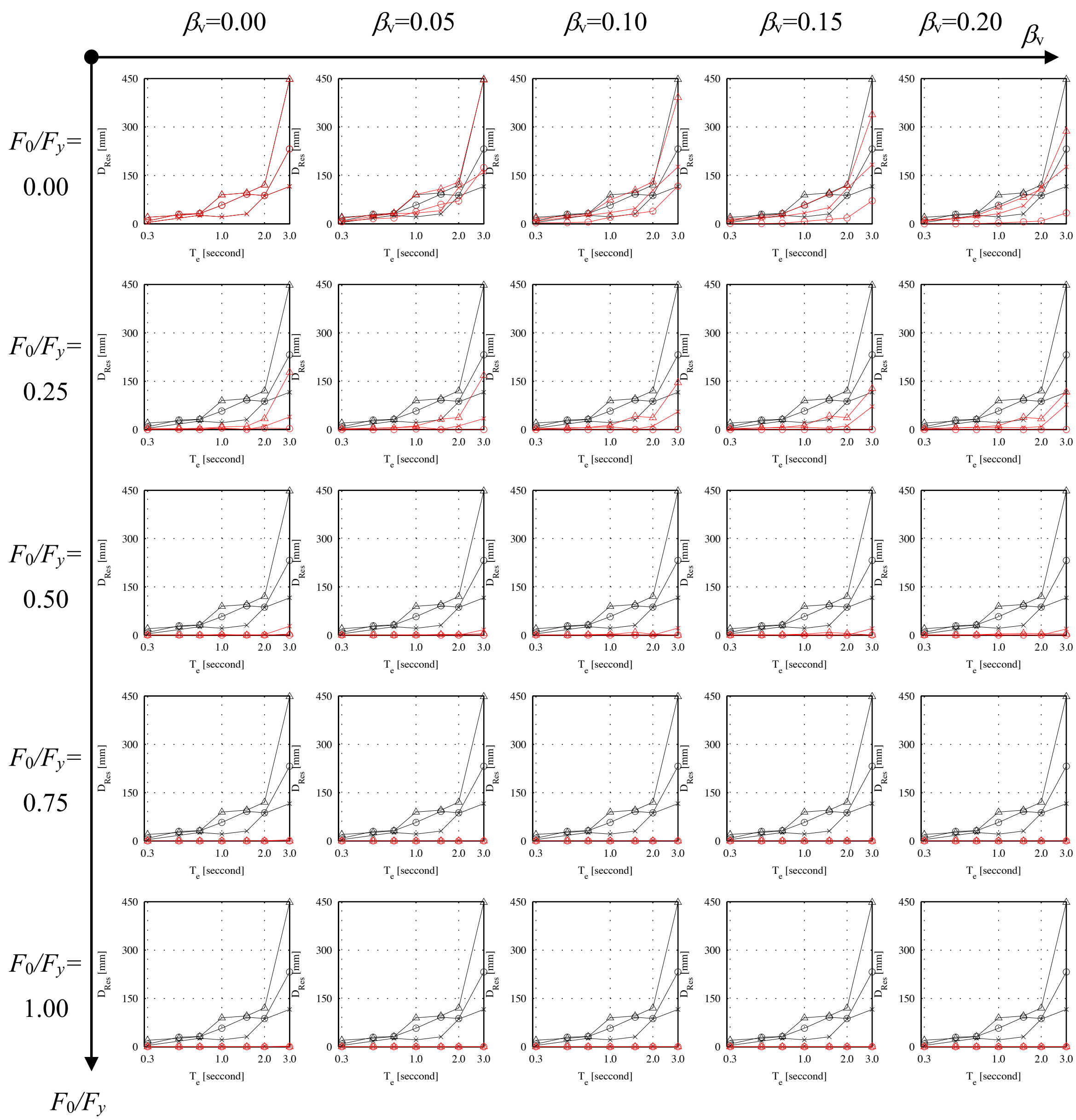

Figure A-7 Residual Displacement in MCE, Near-Fault Pulse-like Motions, Linear Viscous Damping, Stiffness K_0=0, R_μ=1, 2 and 5

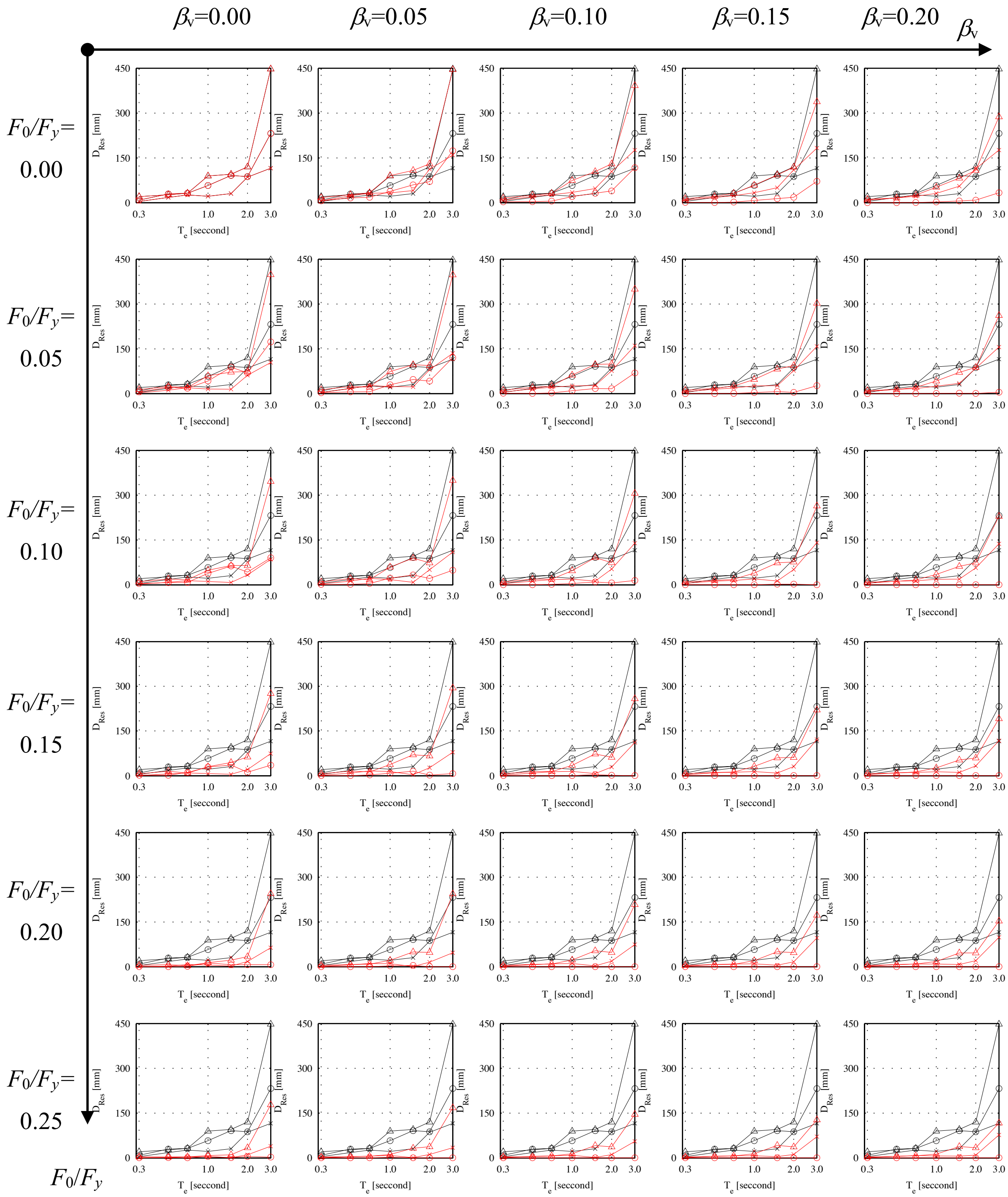

Figure A-7 (Continued)

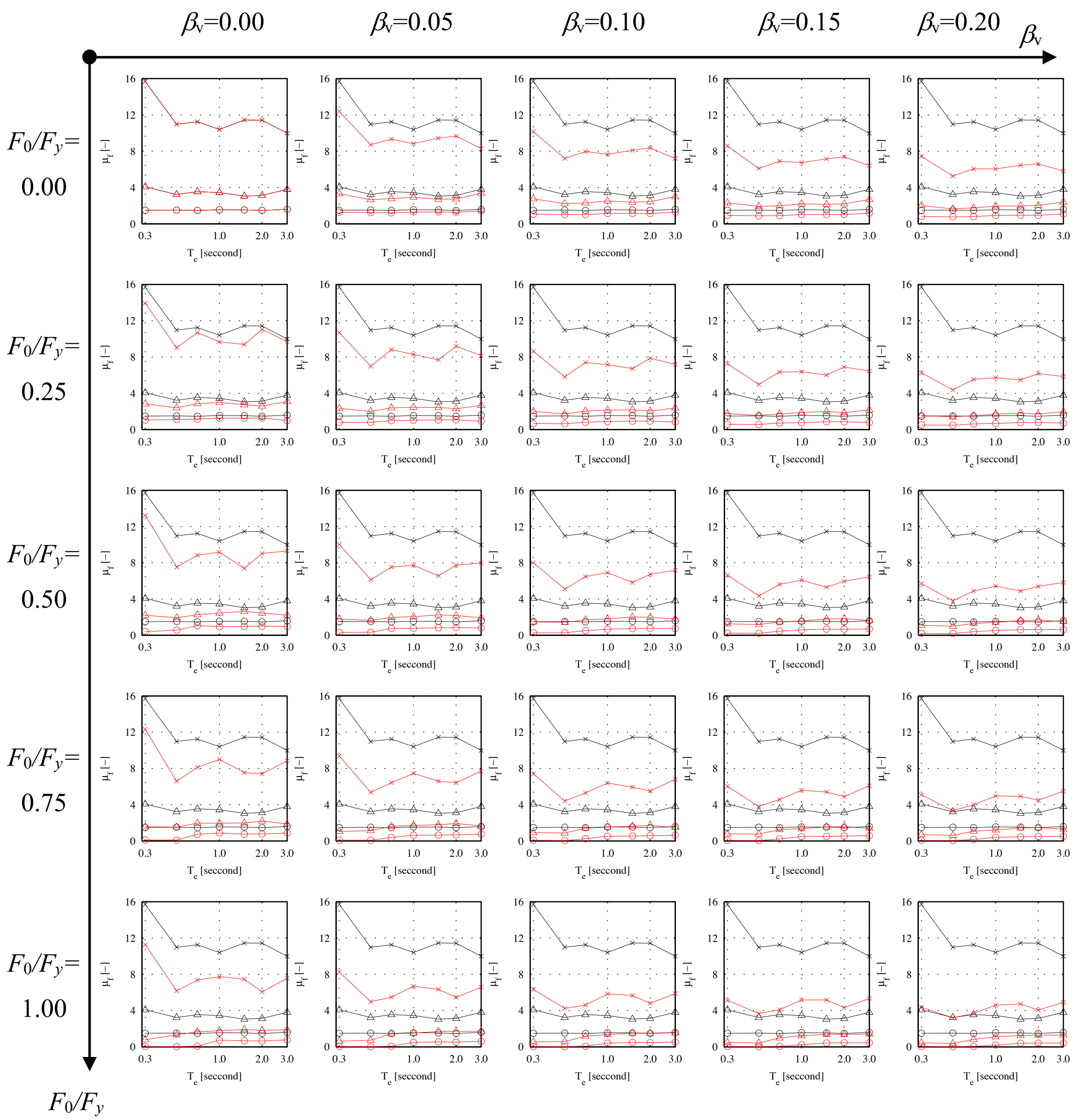

Figure A-8 Ductility Ratio in MCE, Near-Fault Pulse-like Motions, Linear Viscous Damping, Stiffness K_0=0, R_μ=1, 2 and 5

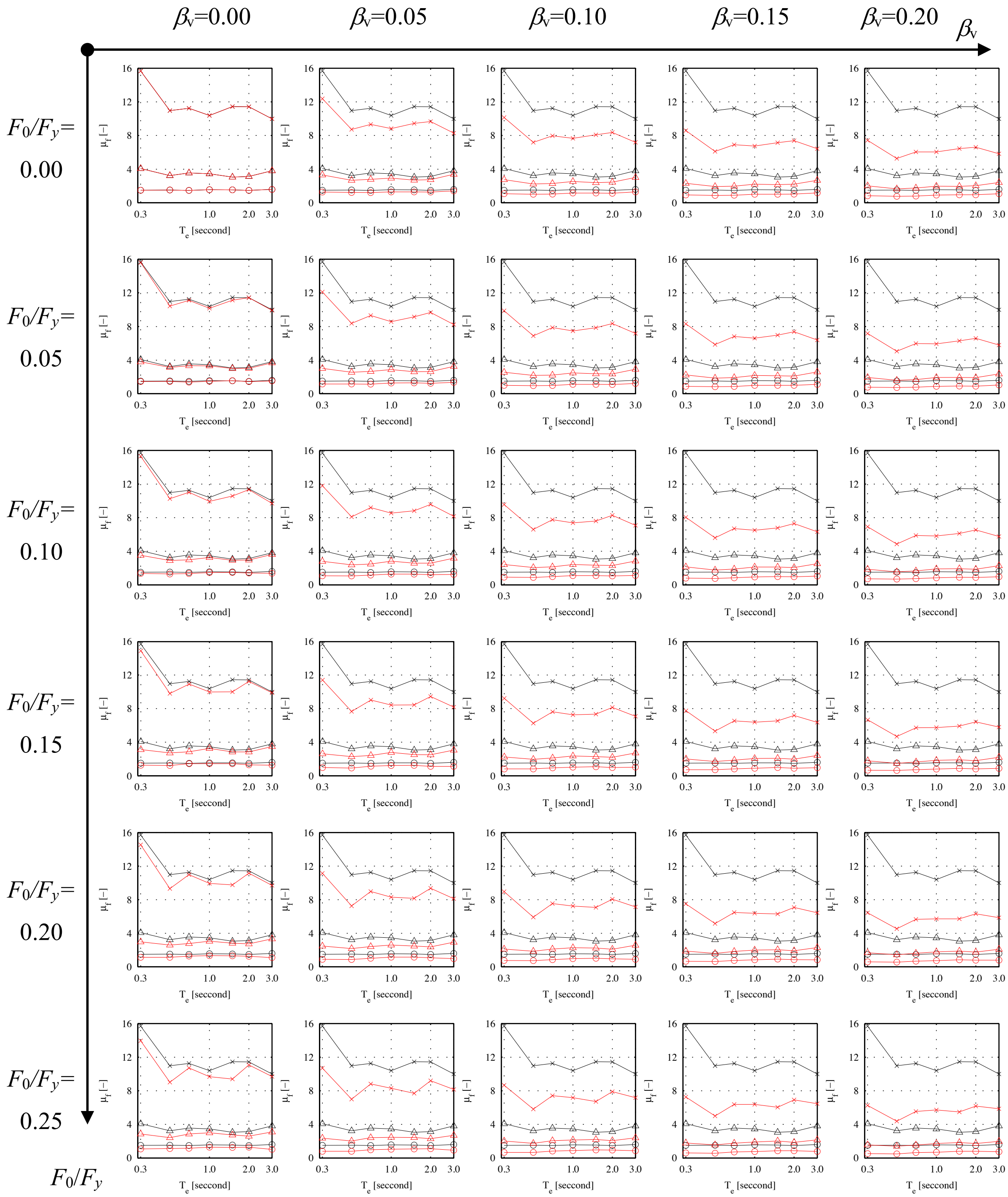

Figure A-8 (Continued)

A.1.2 Structure with Non-Linear Viscous Damping and K_0=0 in Near-Fault Pulse-Like Ground Motions

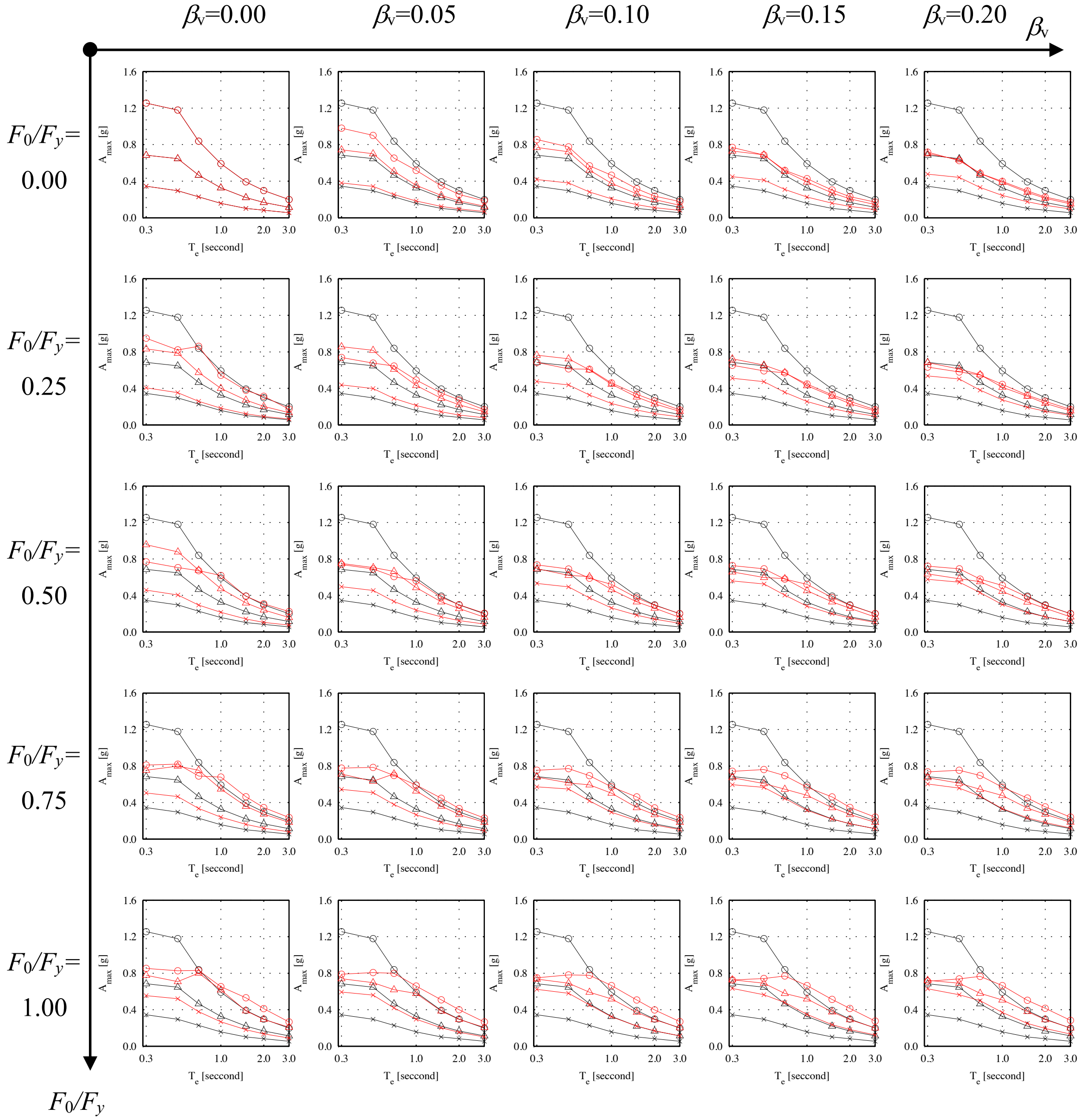

Figure A-9 Acceleration in DE, Near-Fault Pulse-like Motions, Non-linear Viscous Damping, Stiffness K_0=0, R_μ=1, 2 and 5

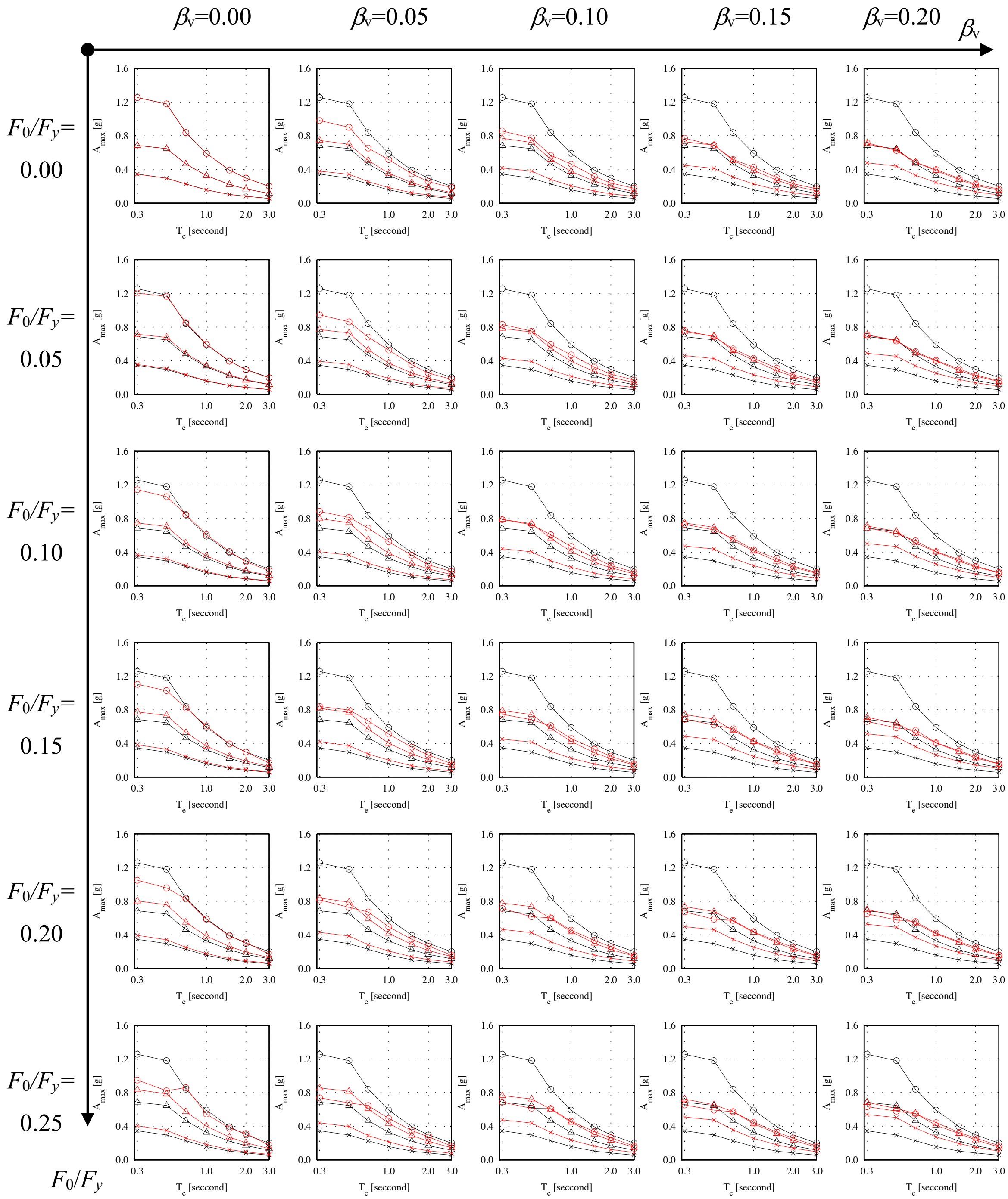

Figure A-9 (Continued)

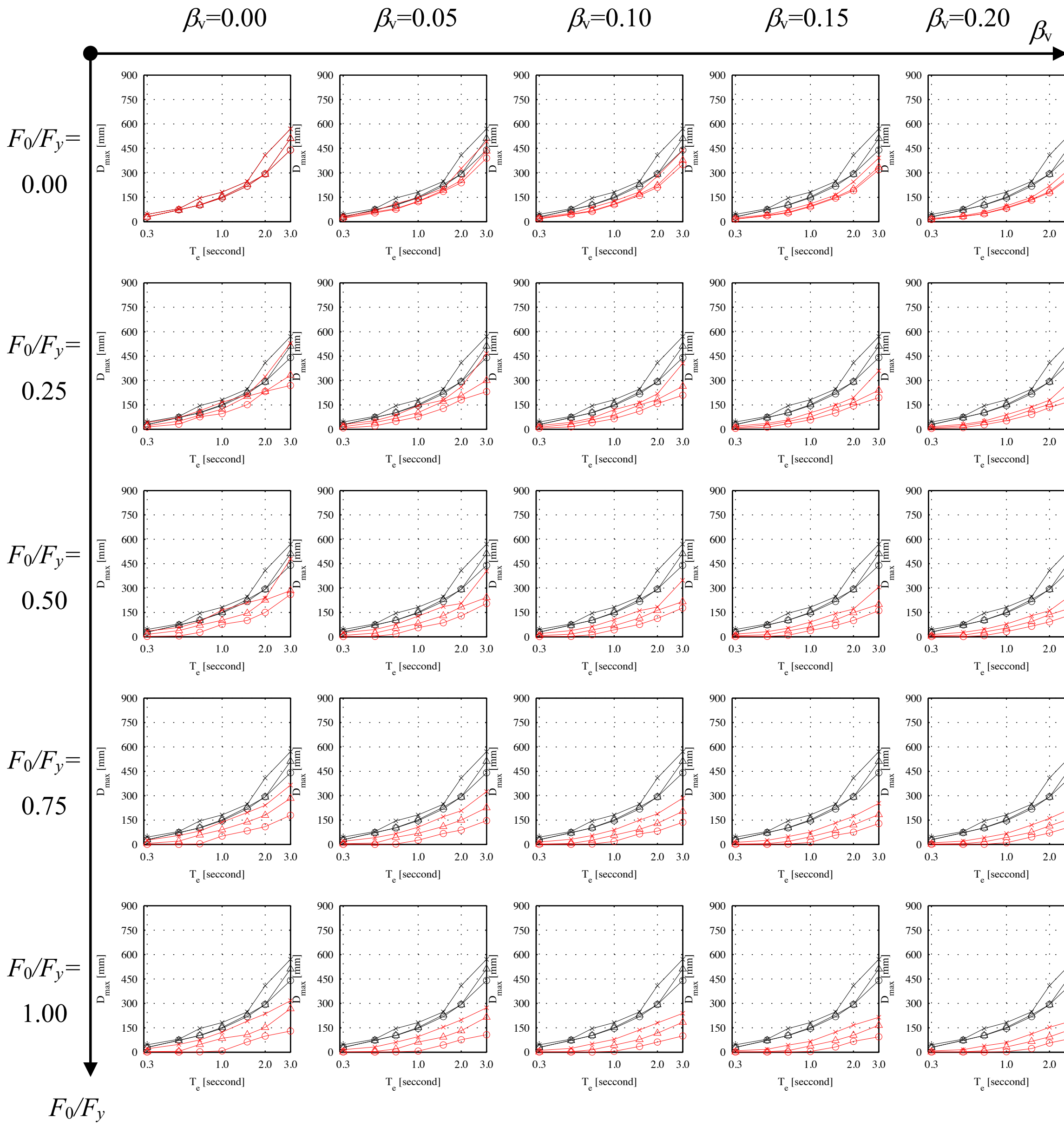

Figure A-10 Displacement in DE, Near-Fault Pulse-like Motions, Non-linear Viscous Damping, Stiffness K_0=0, R_μ=1, 2 and 5

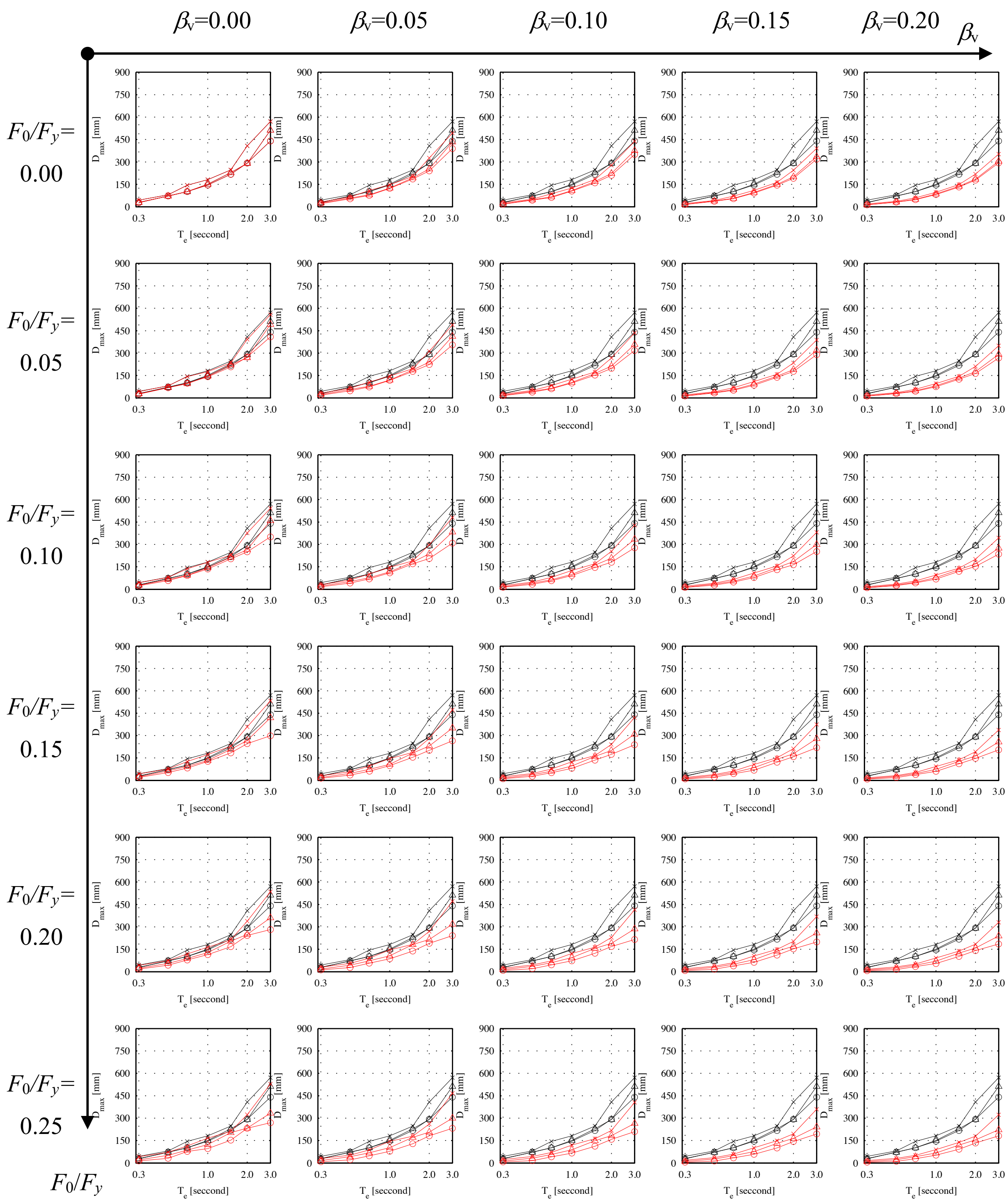

Figure A- 10 (Continued)

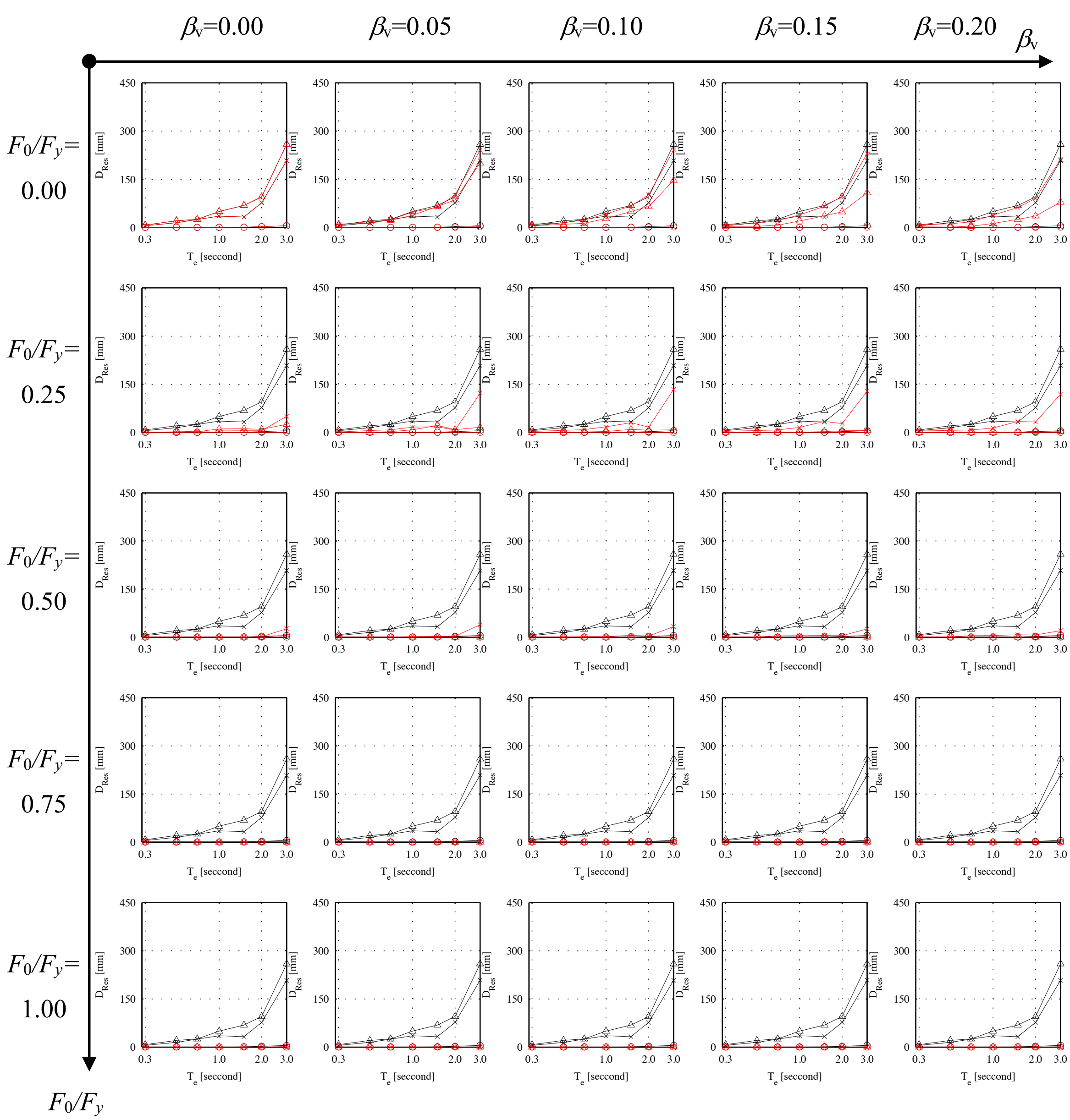

Figure A-11 Residual Displacement in DE, Near-Fault Pulse-like Motions, Non-linear Viscous Damping, Stiffness K_0=0, R_μ=1, 2 and 5

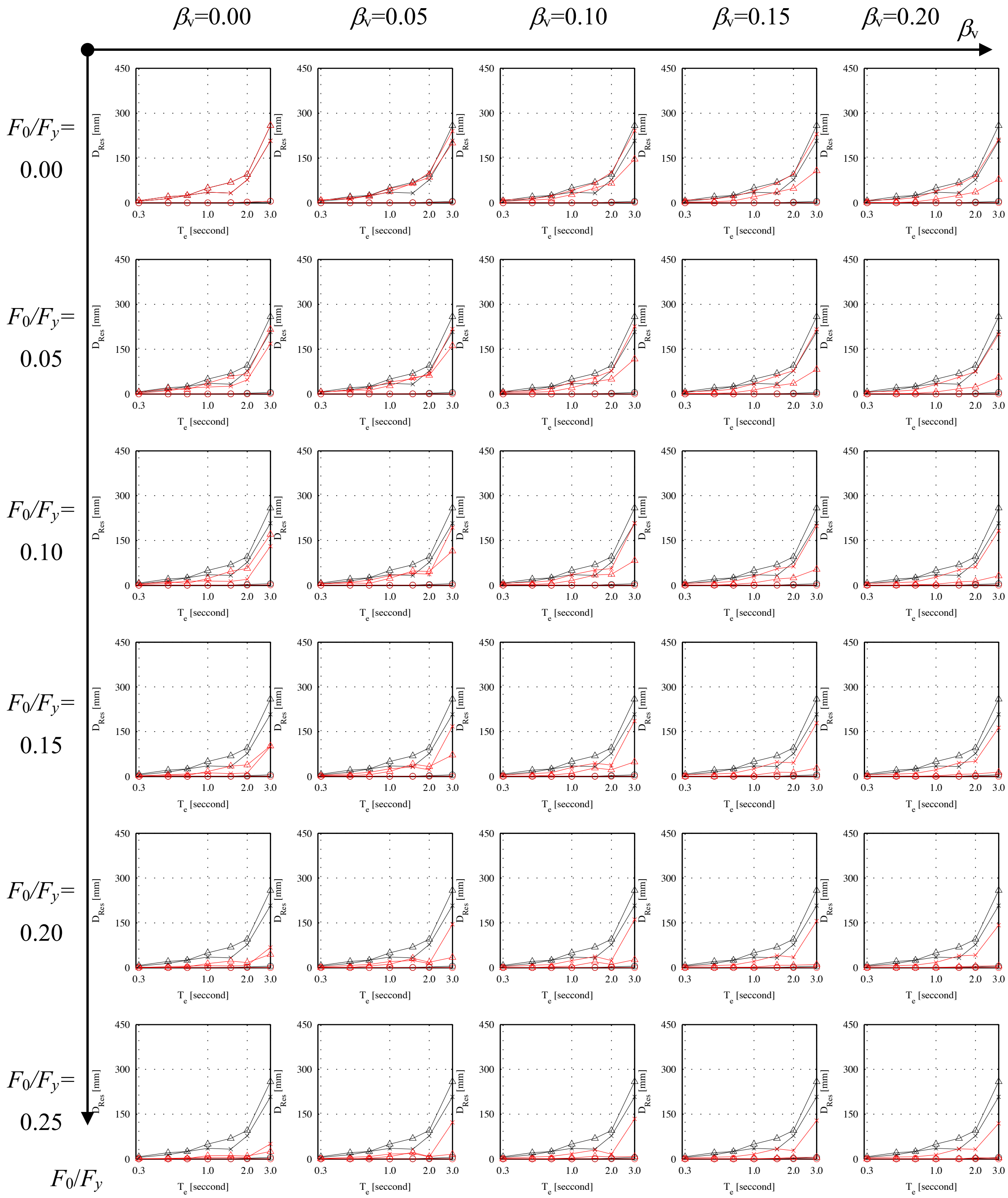

Figure A-11 (Continued)

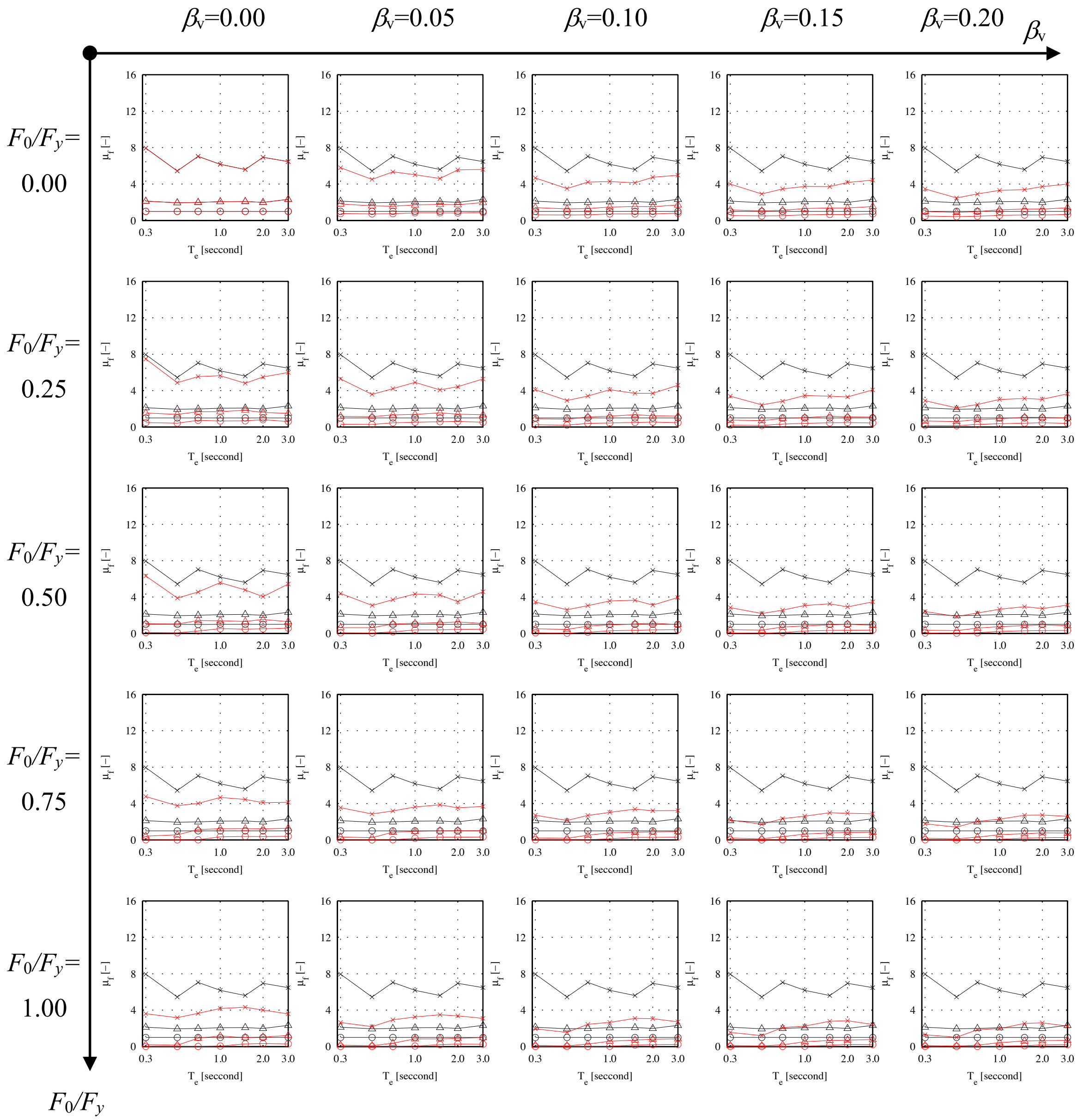

Figure A-12 Ductility Ratio in DE, Near-Fault Pulse-like Motions, Non-linear Viscous Damping, Stiffness K_0=0, R_μ=1, 2 and 5

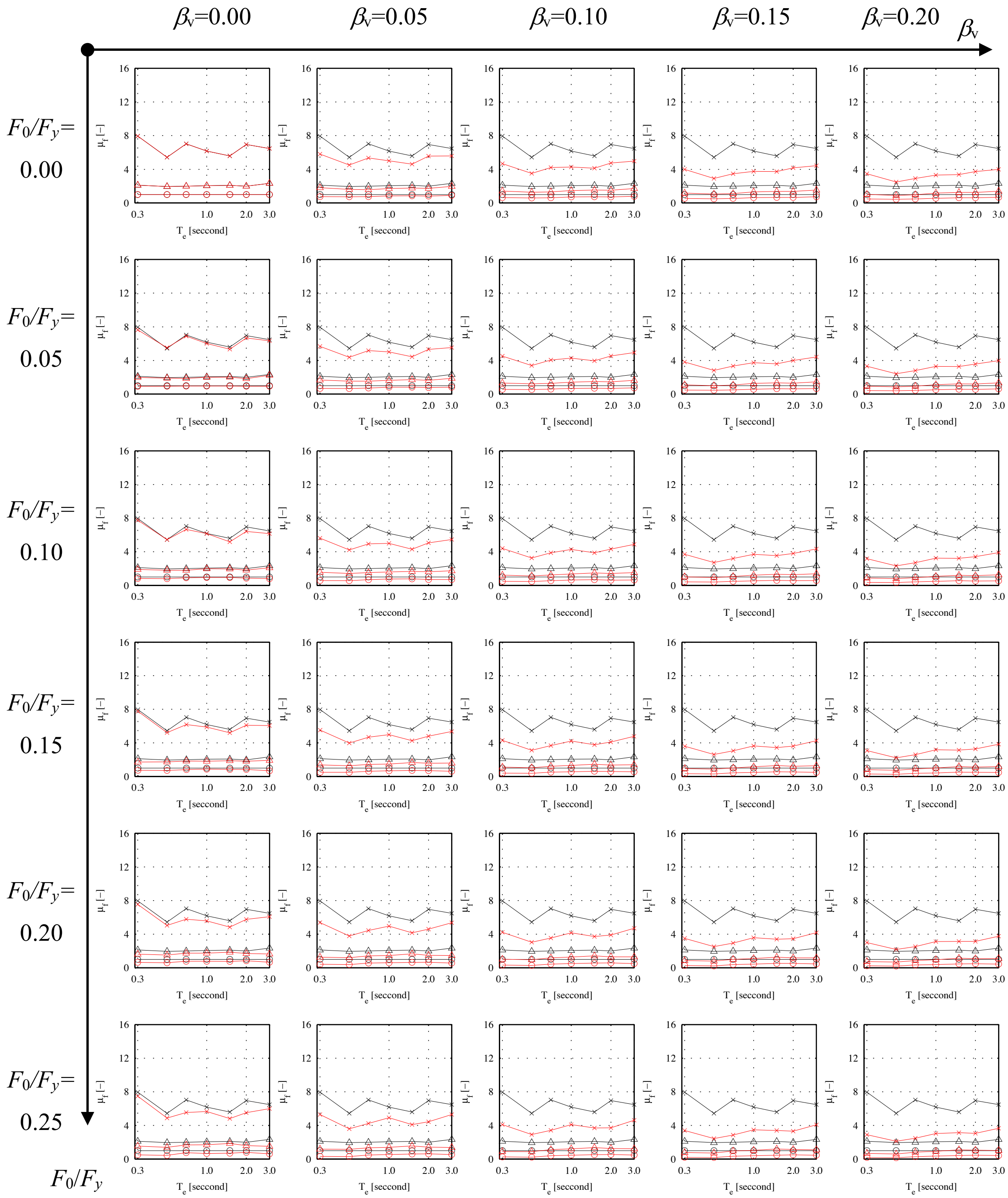

Figure A-12 (Continued)

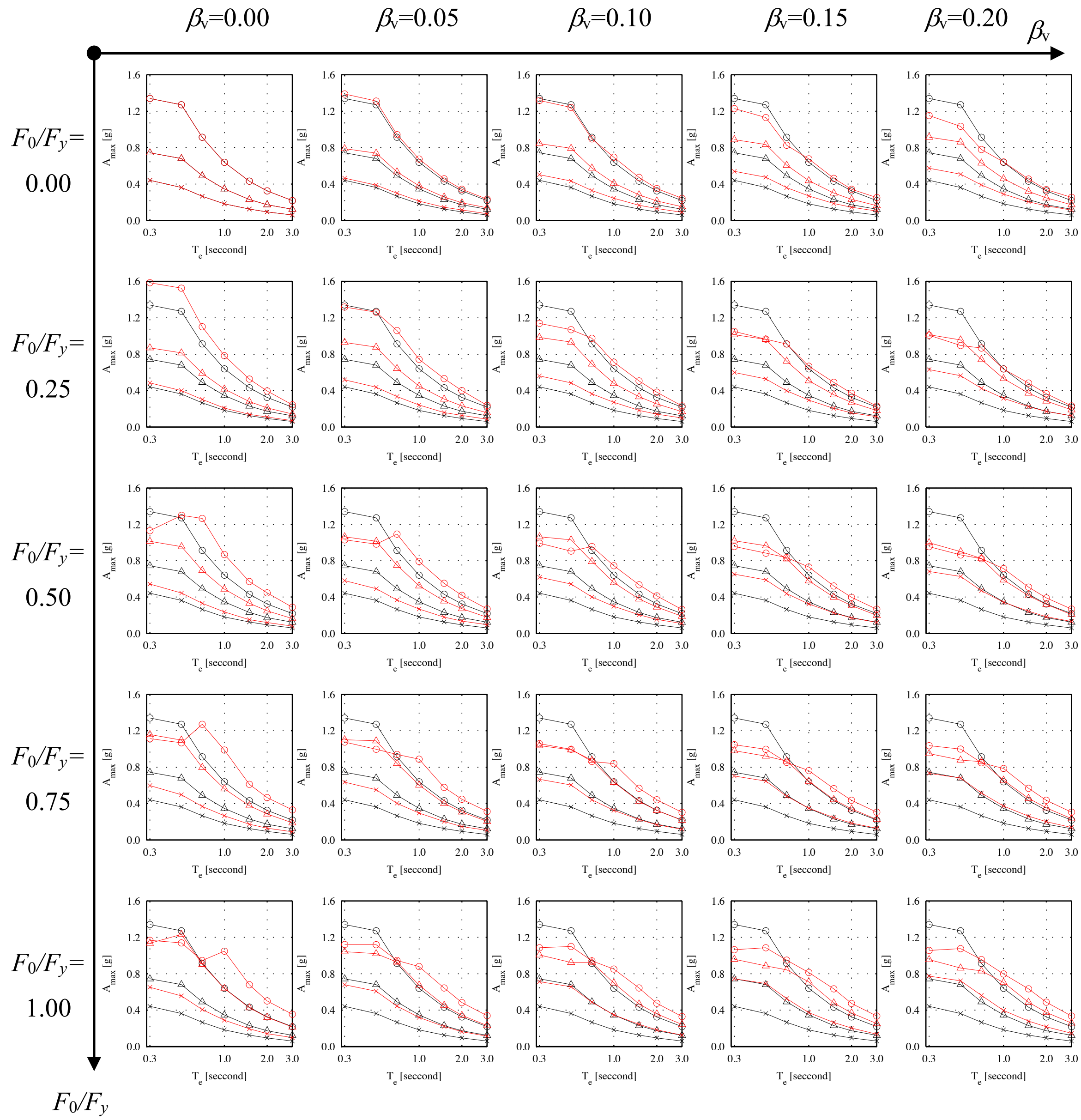

Figure A-13 Acceleration in MCE, Near-Fault Pulse-like Motions, Non-linear Viscous Damping, Stiffness K_0=0, R_μ=1, 2 and 5

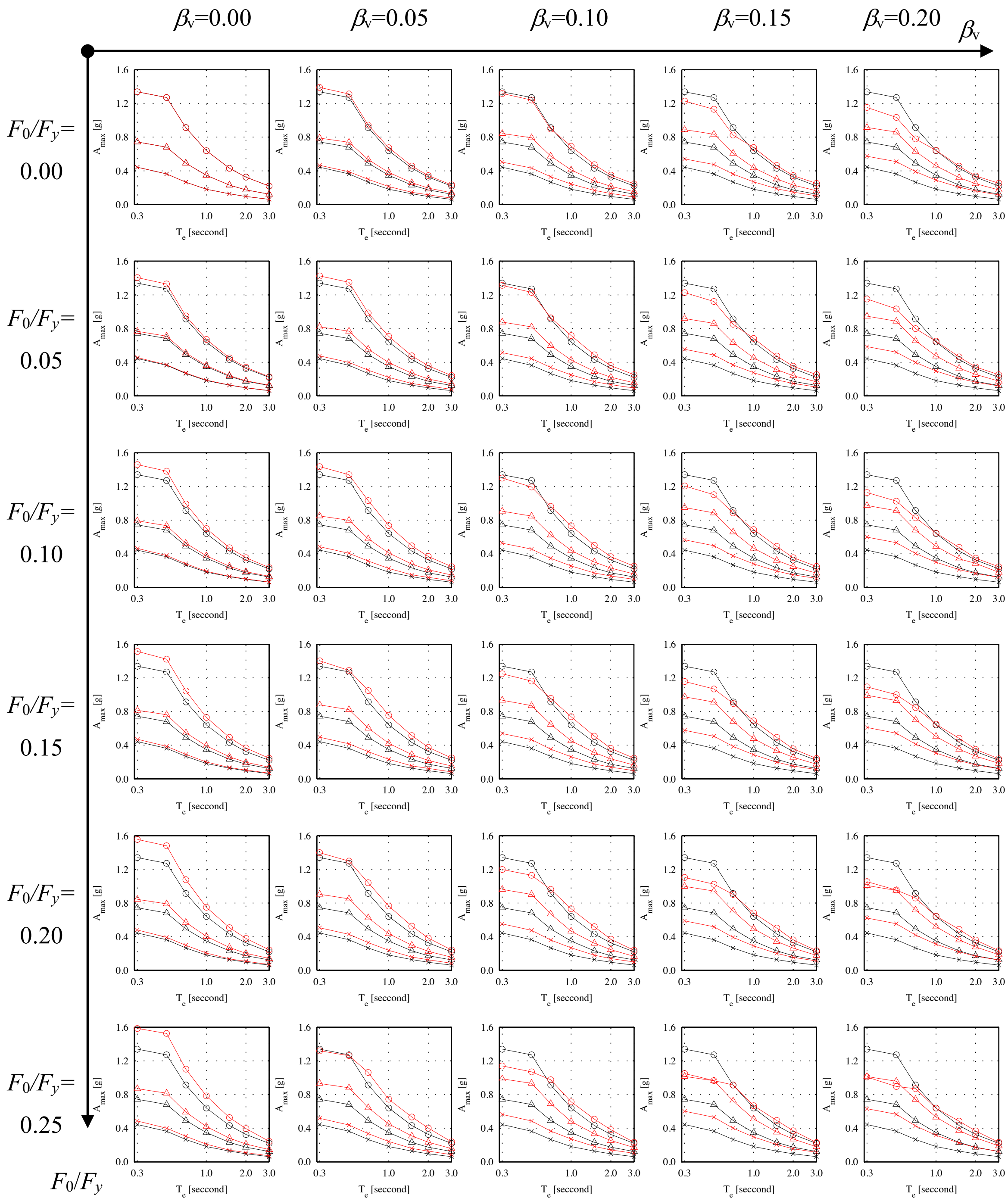

Figure A-13 (Continued)

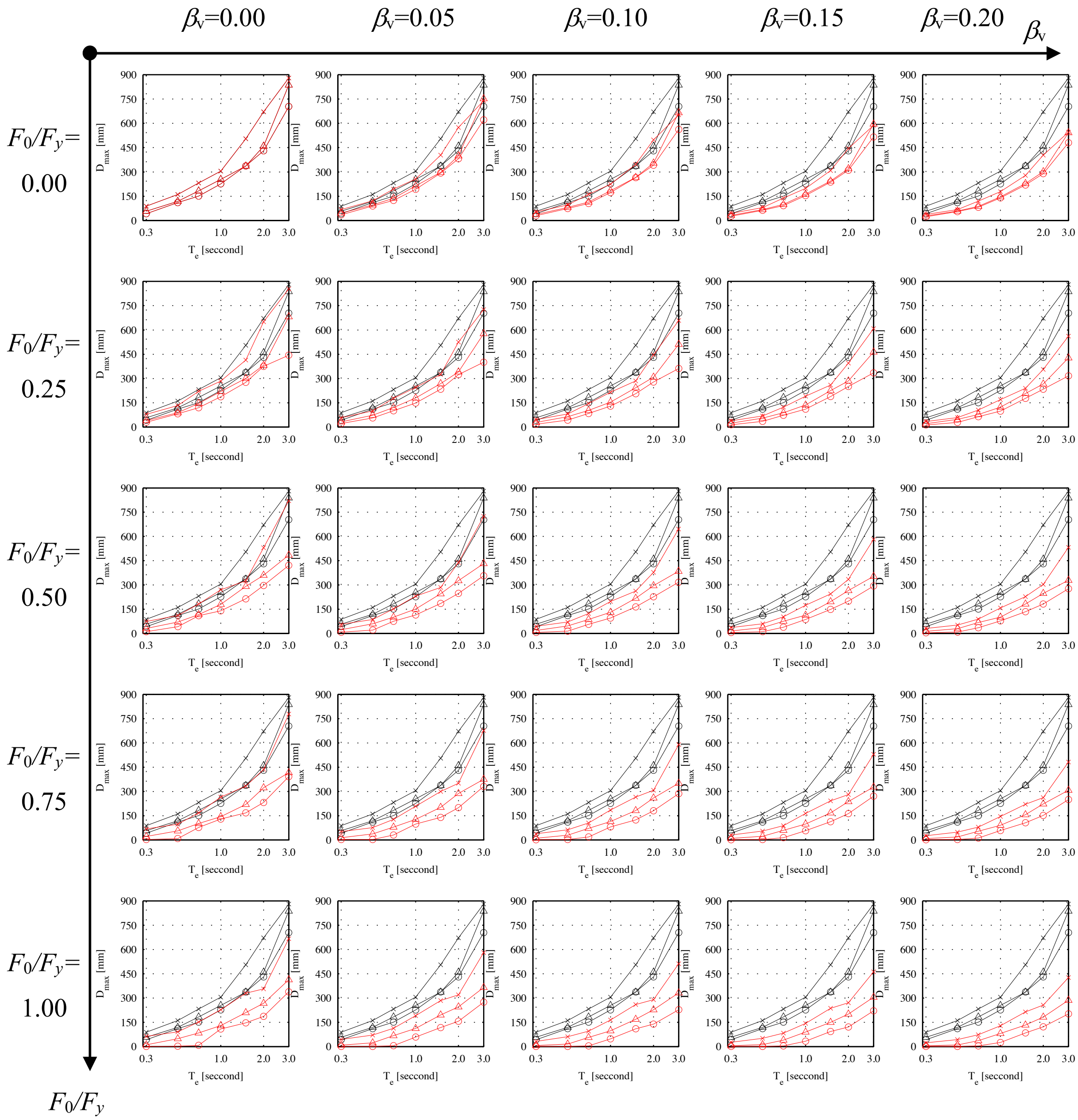

Figure A-14 Displacement in MCE, Near-Fault Pulse-like Motions, Non-linear Viscous Damping, Stiffness K_0=0, R_μ=1, 2 and 5

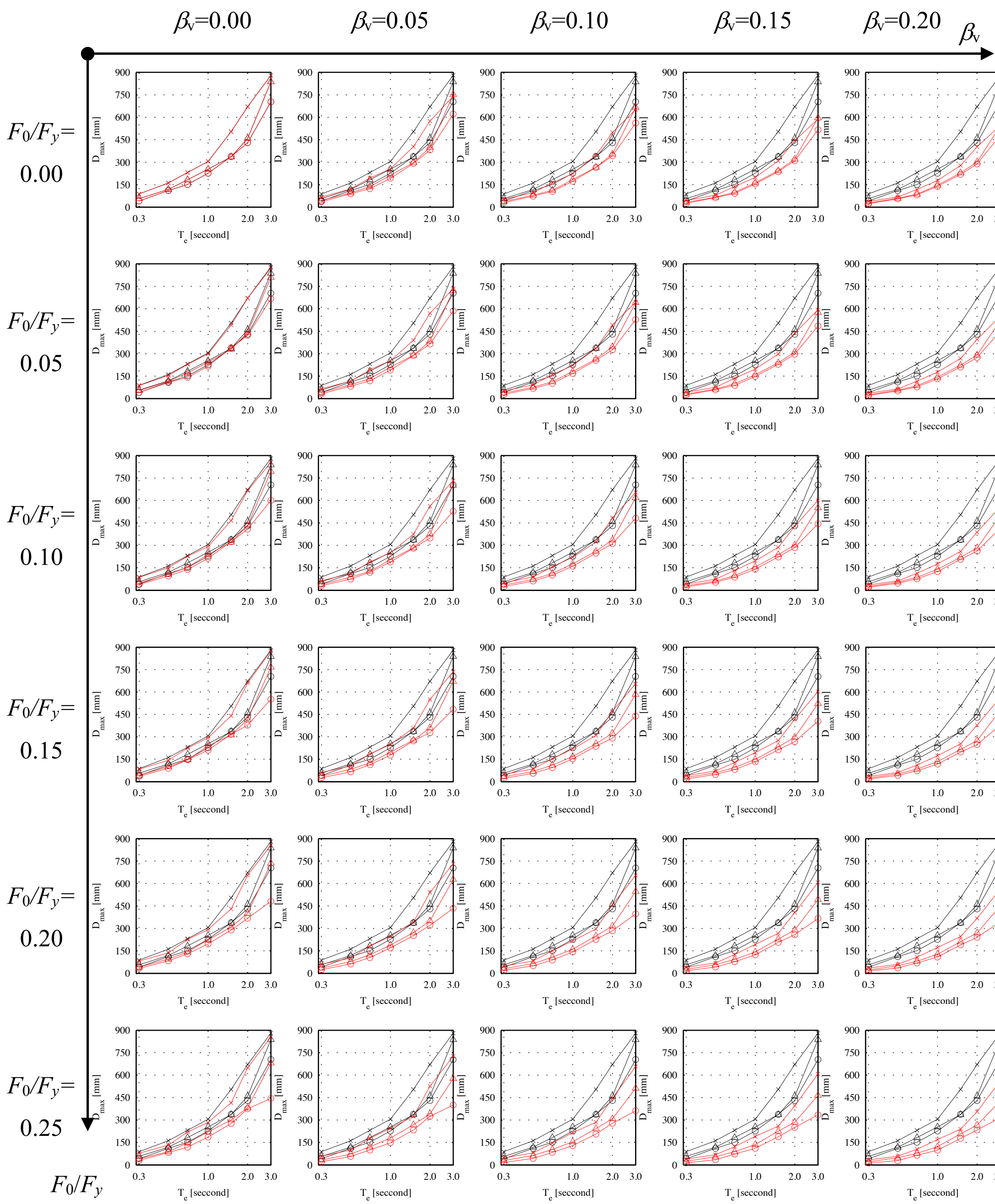

Figure A-14 (Continued)

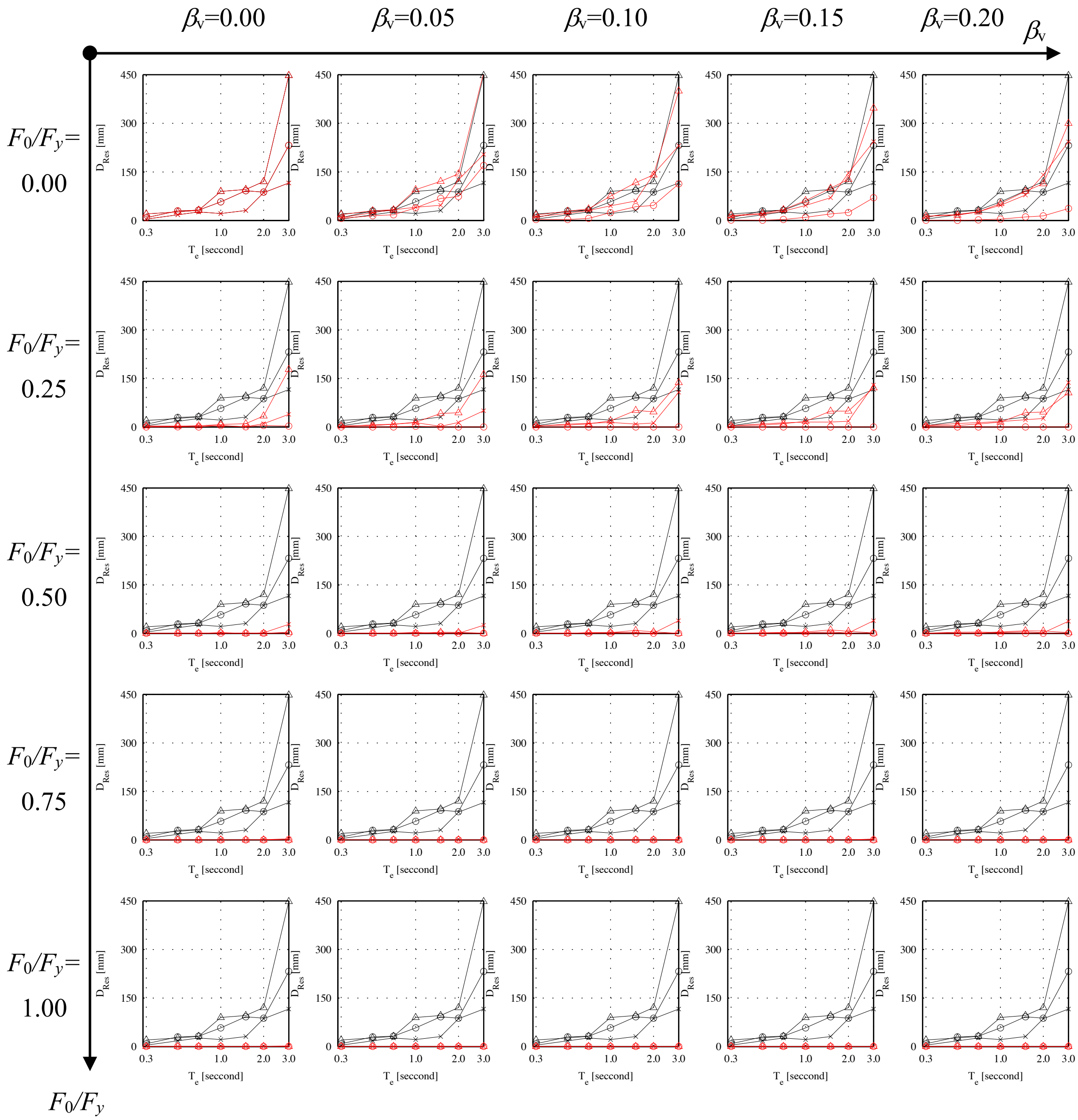

Figure A-15 Residual Displacement in MCE, Near-Fault Pulse-like Motions, Non-linear Viscous Damping, Stiffness K_0=0, R_μ=1, 2 and 5

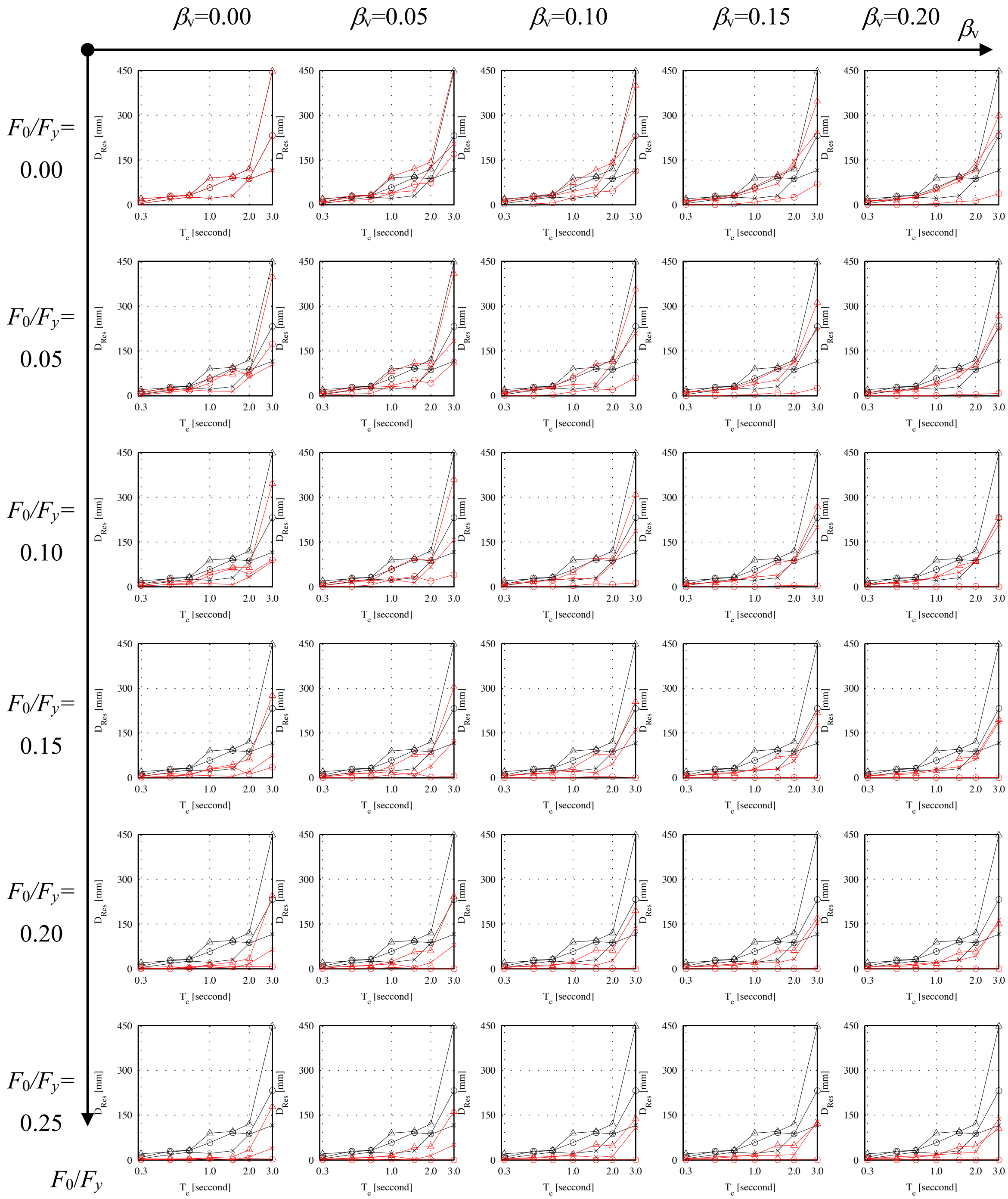

Figure A-15 (Continued)

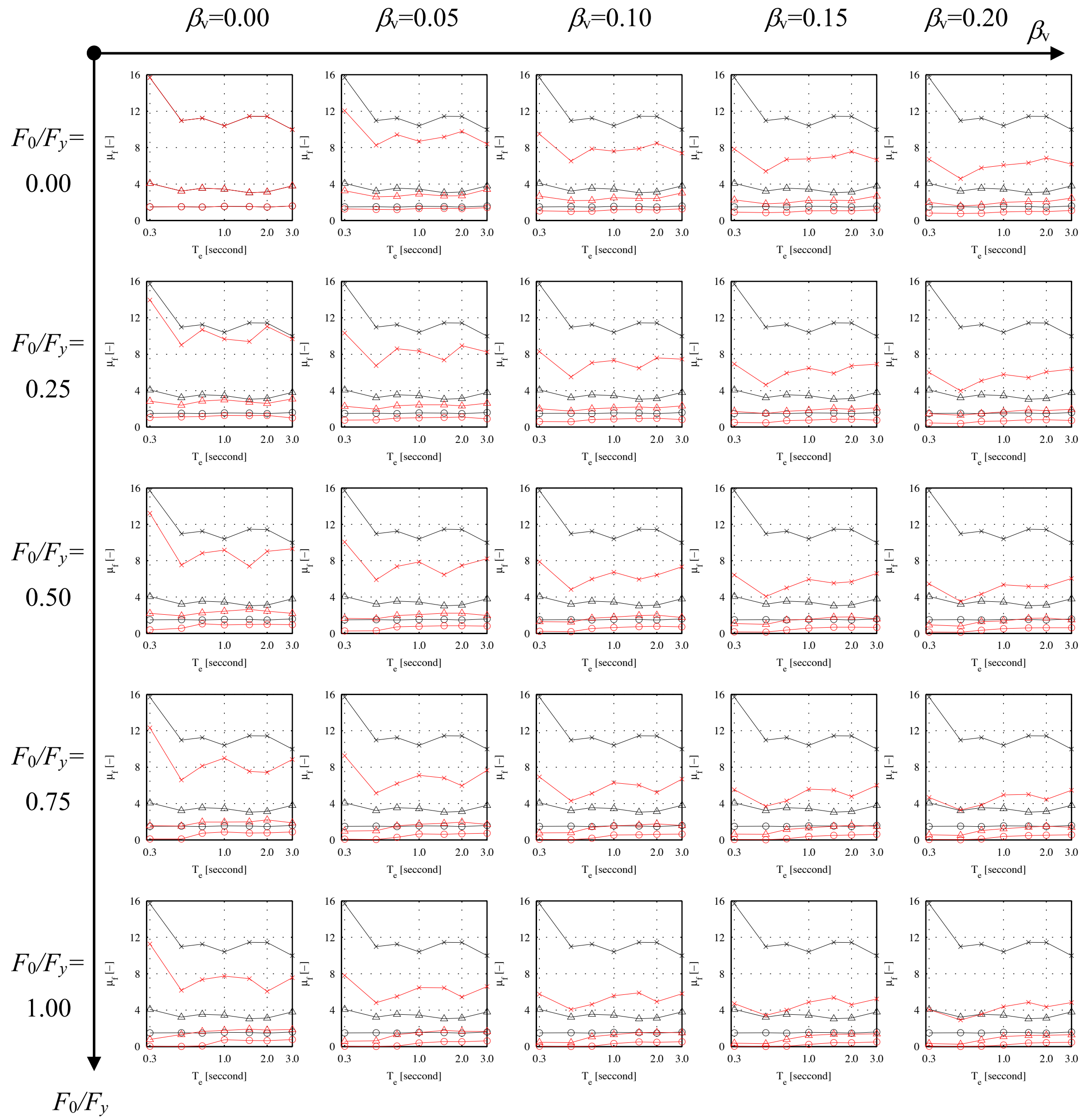

Figure A-16 Ductility Ratio in MCE, Near-Fault Pulse-like Motions, Non-linear Viscous Damping, Stiffness K_0=0, R_μ=1, 2 and 5

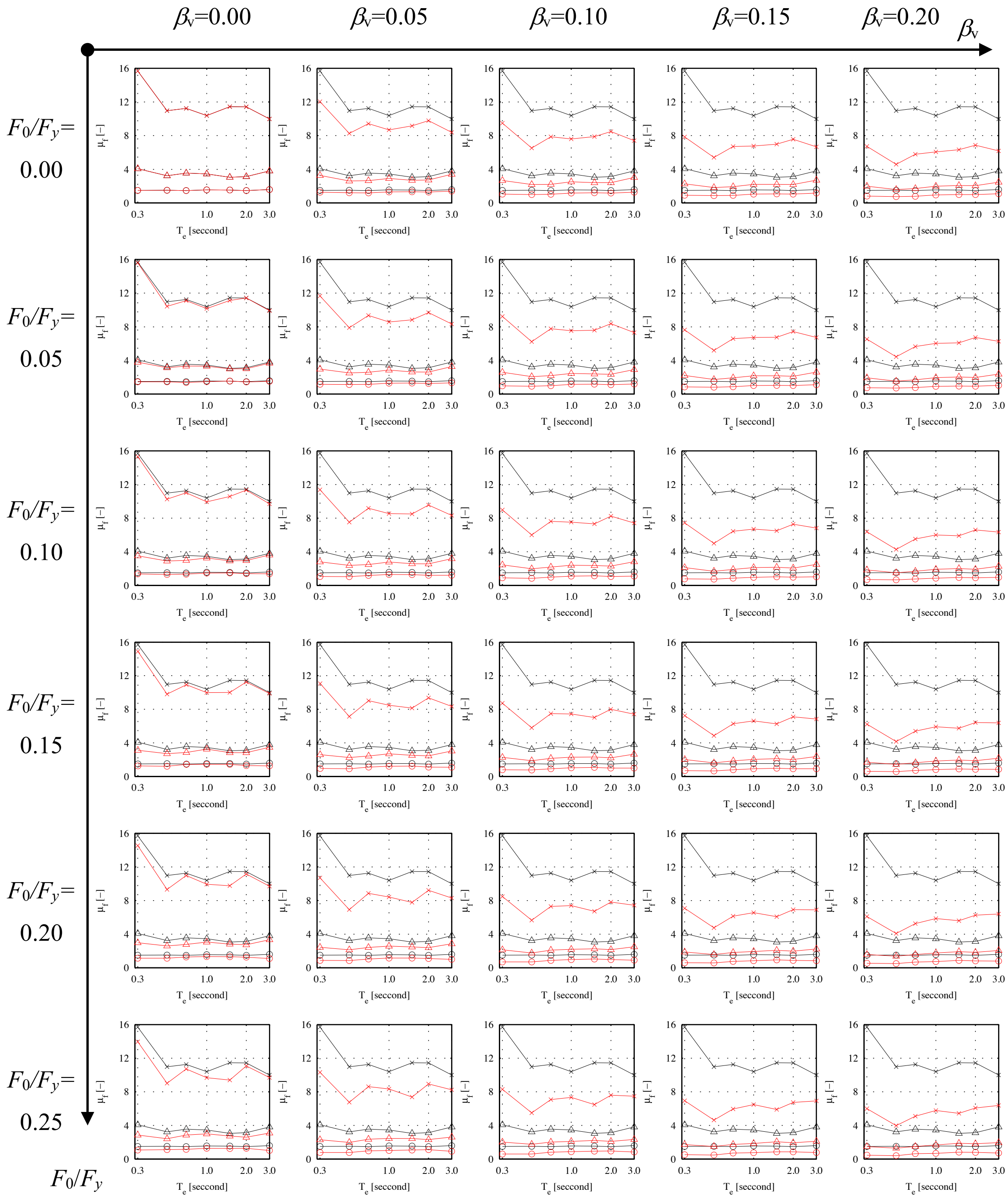

Figure A-16 (Continued)

A.1.3 Structure with Upper-Half Viscous Damping and K_0=0 in Near-Fault Pulse-Like Ground Motions

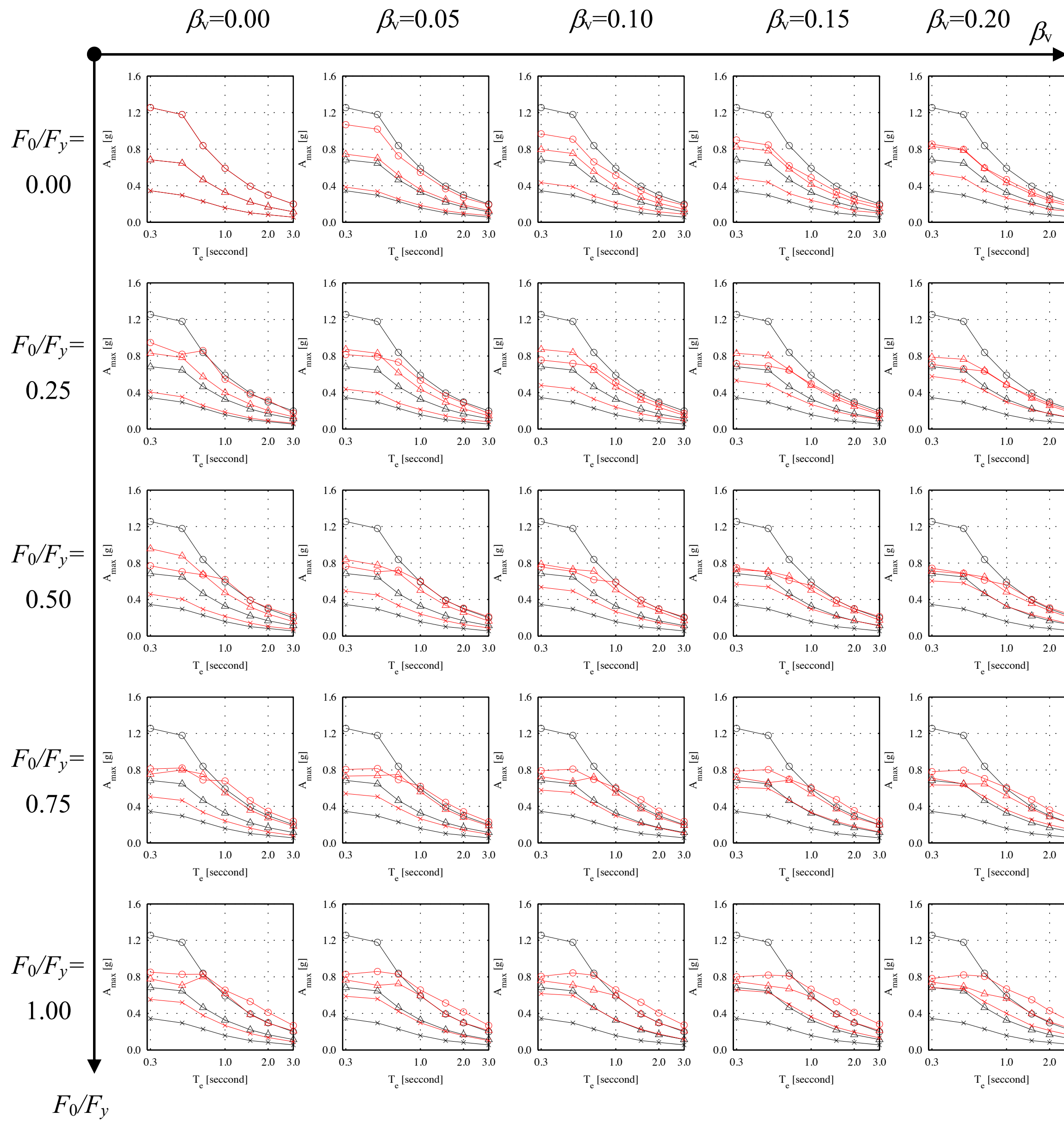

Figure A-17 Acceleration in DE, Near-Fault Pulse-like Motions, Upper-half Viscous Damping, Stiffness K_0=0, R_μ=1, 2 and 5

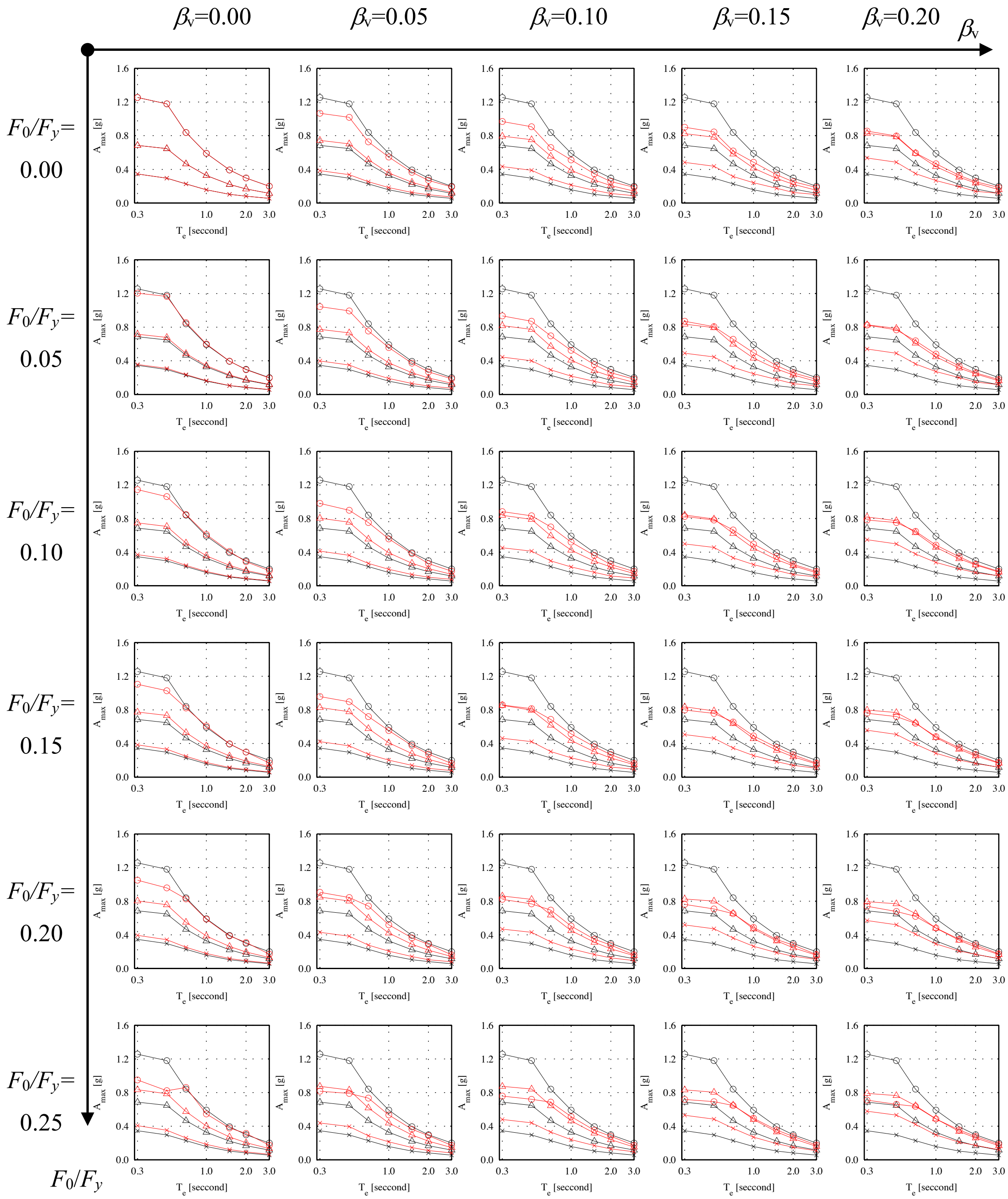

Figure A-17 (Continued)

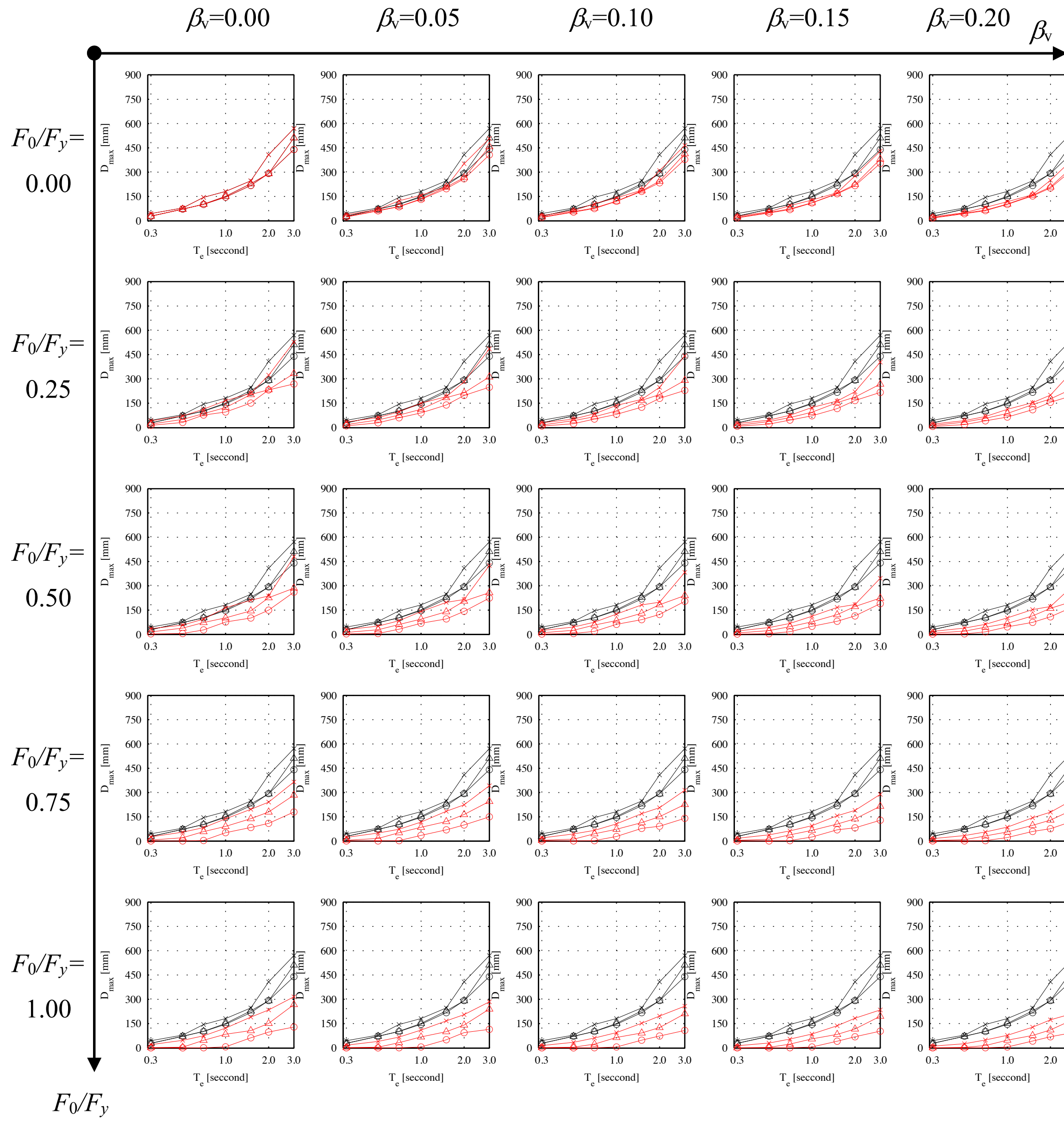

Figure A-18 Displacement in DE, Near-Fault Pulse-like Motions, Upper-half Viscous Damping, Stiffness K_0=0, R_μ=1, 2 and 5

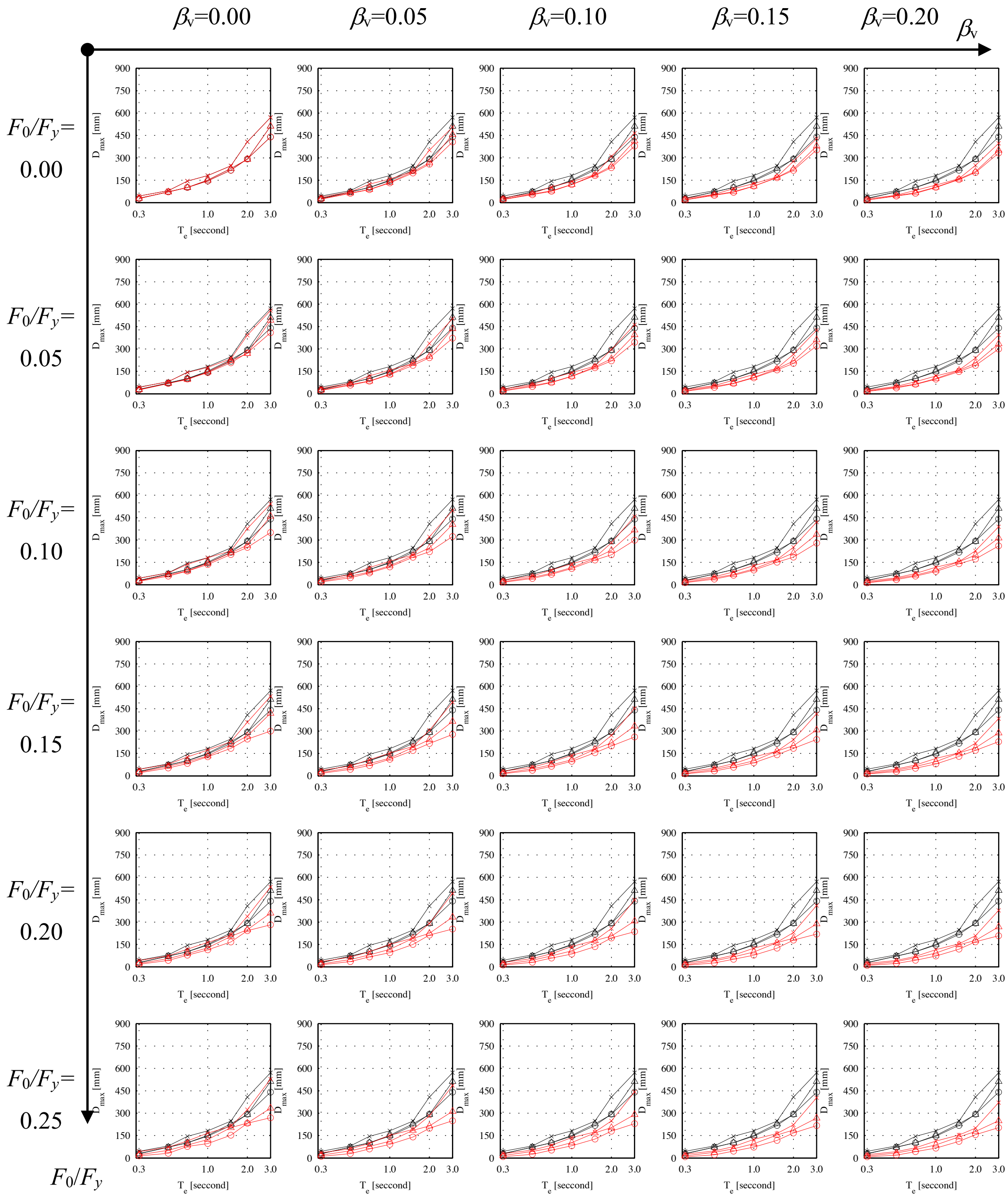

Figure A-18 (Continued)

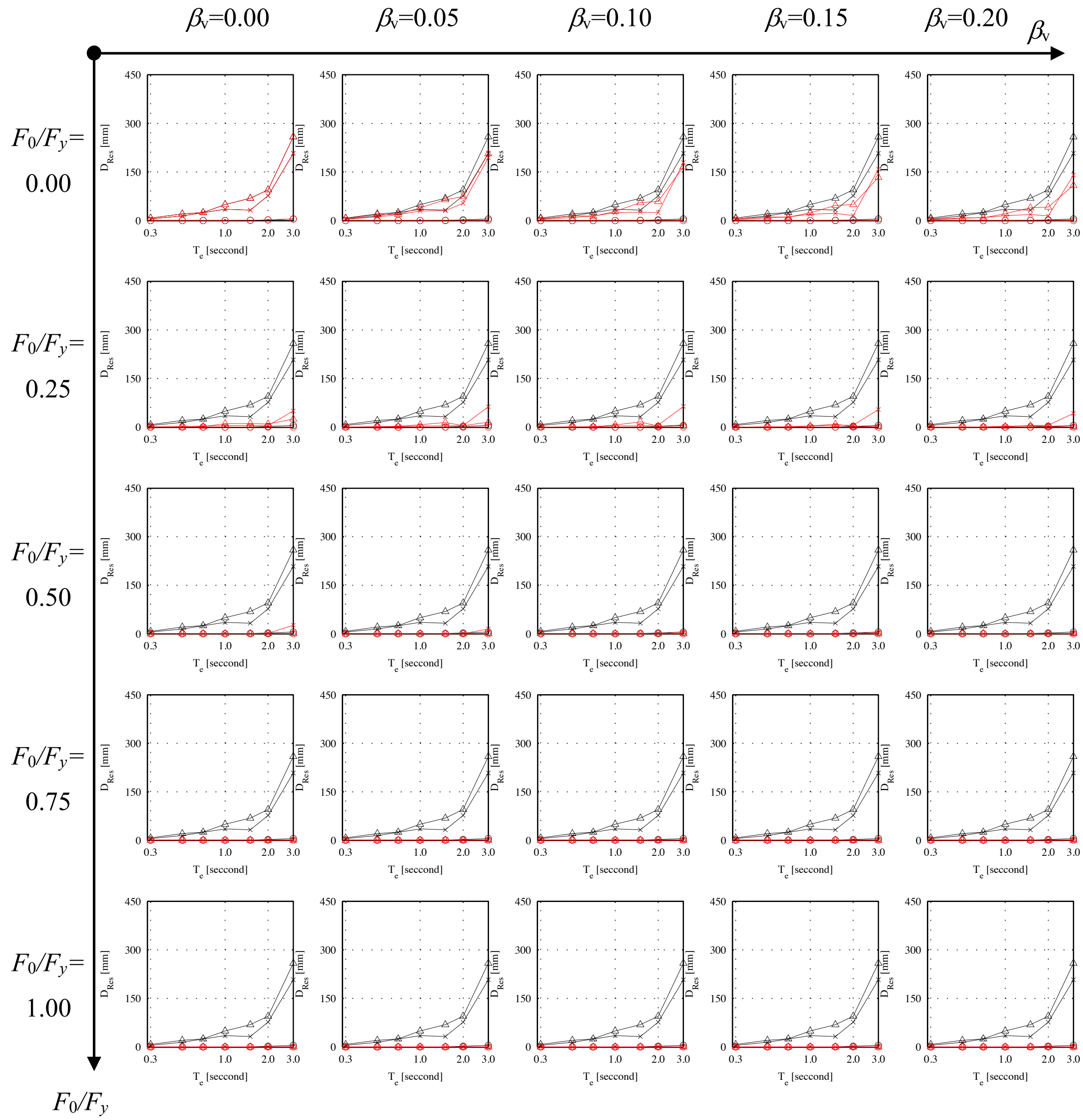

Figure A-19 Residual Displacement in DE, Near-Fault Pulse-like Motions, Upper-half Viscous Damping, Stiffness K_0=0, R_μ=1, 2 and 5

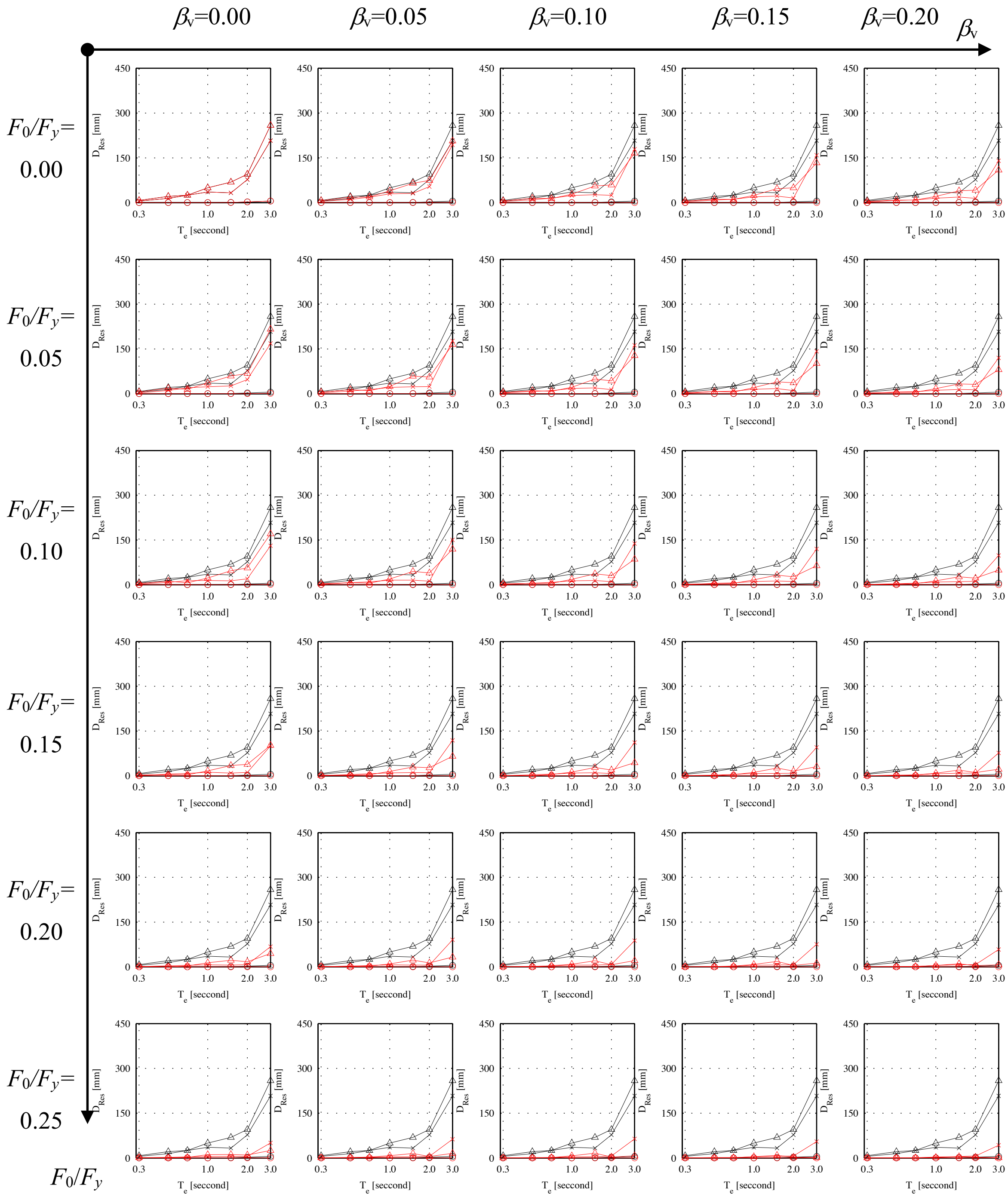

Figure A-19 (Continued)

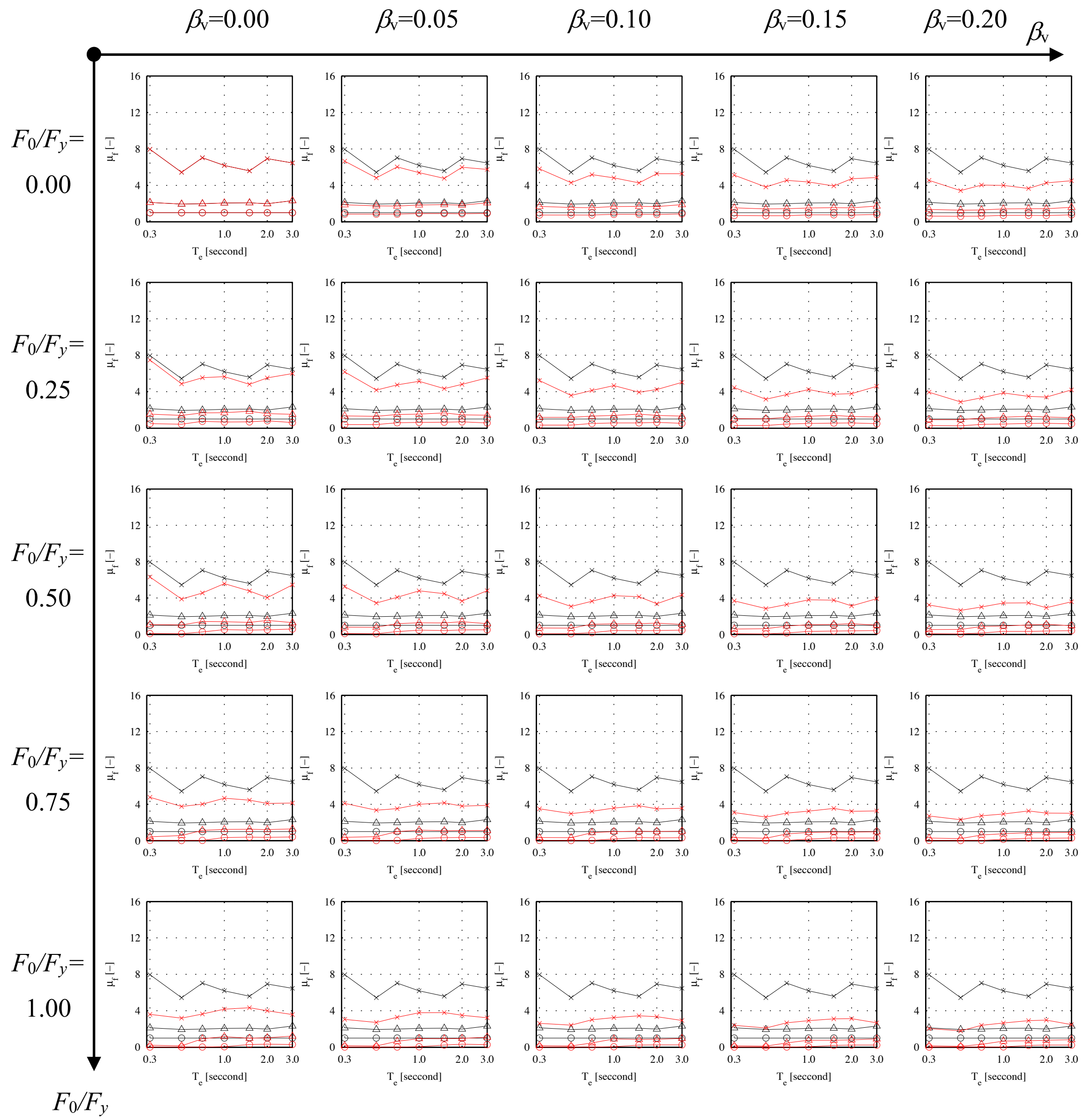

Figure A-20 Ductility Ratio in DE, Near-Fault Pulse-like Motions, Upper-half Viscous Damping, Stiffness K_0=0, R_μ=1, 2 and 5

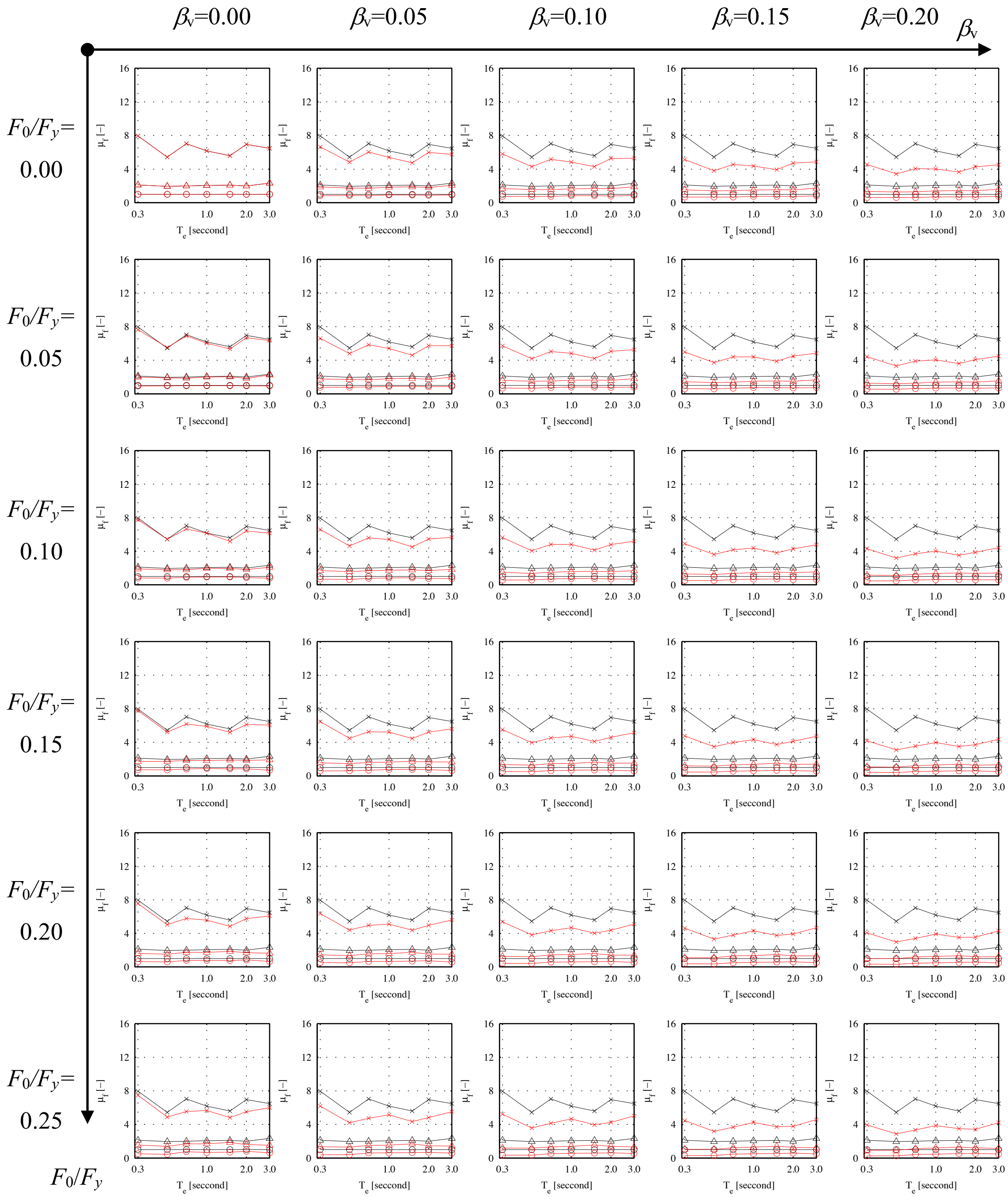

Figure A-20 (Continued)

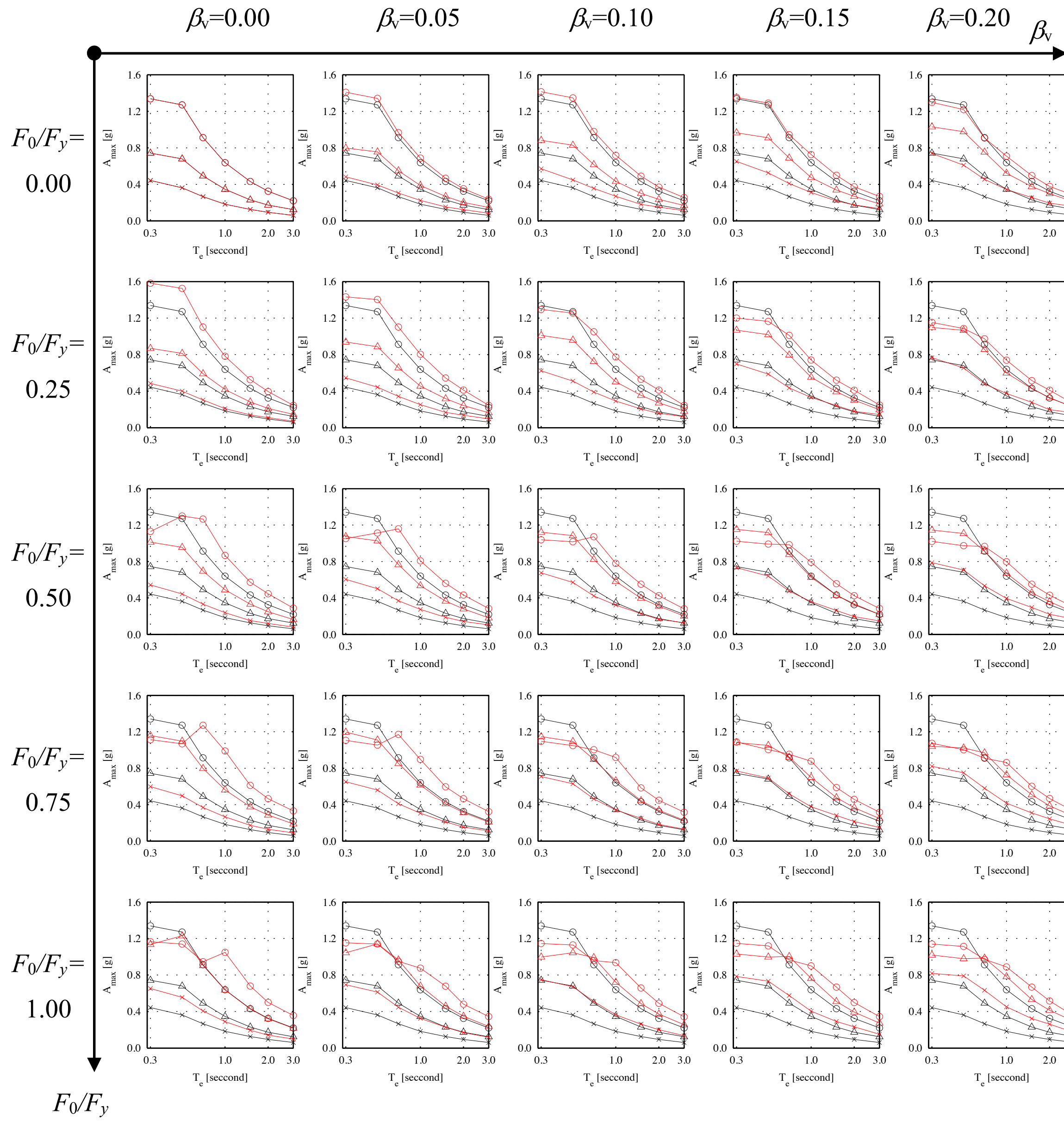

Figure A-21 Acceleration in MCE, Near-Fault Pulse-like Motions, Upper-half Viscous Damping, Stiffness K_0=0, R_μ=1, 2 and 5

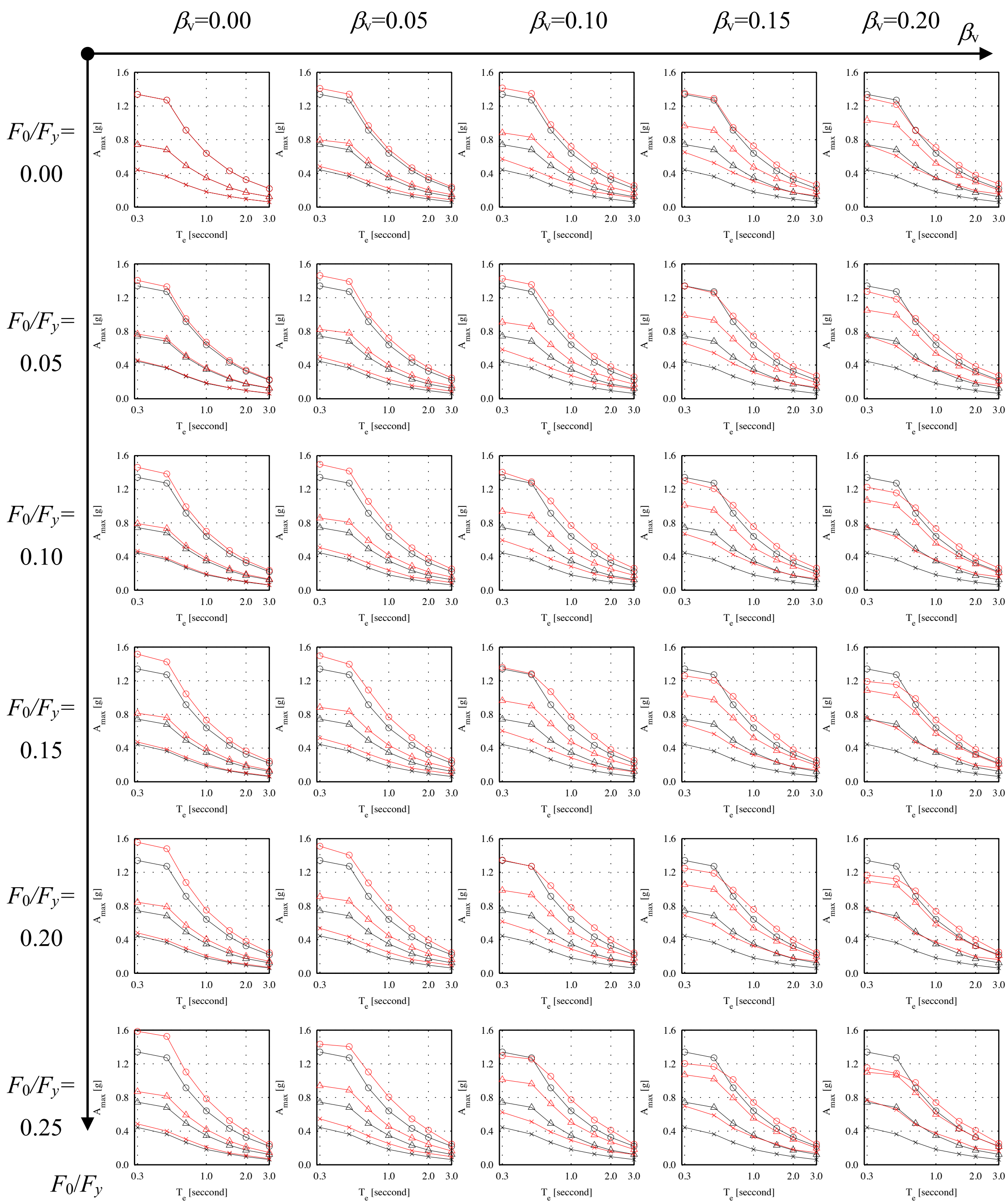

Figure A-21 (Continued)

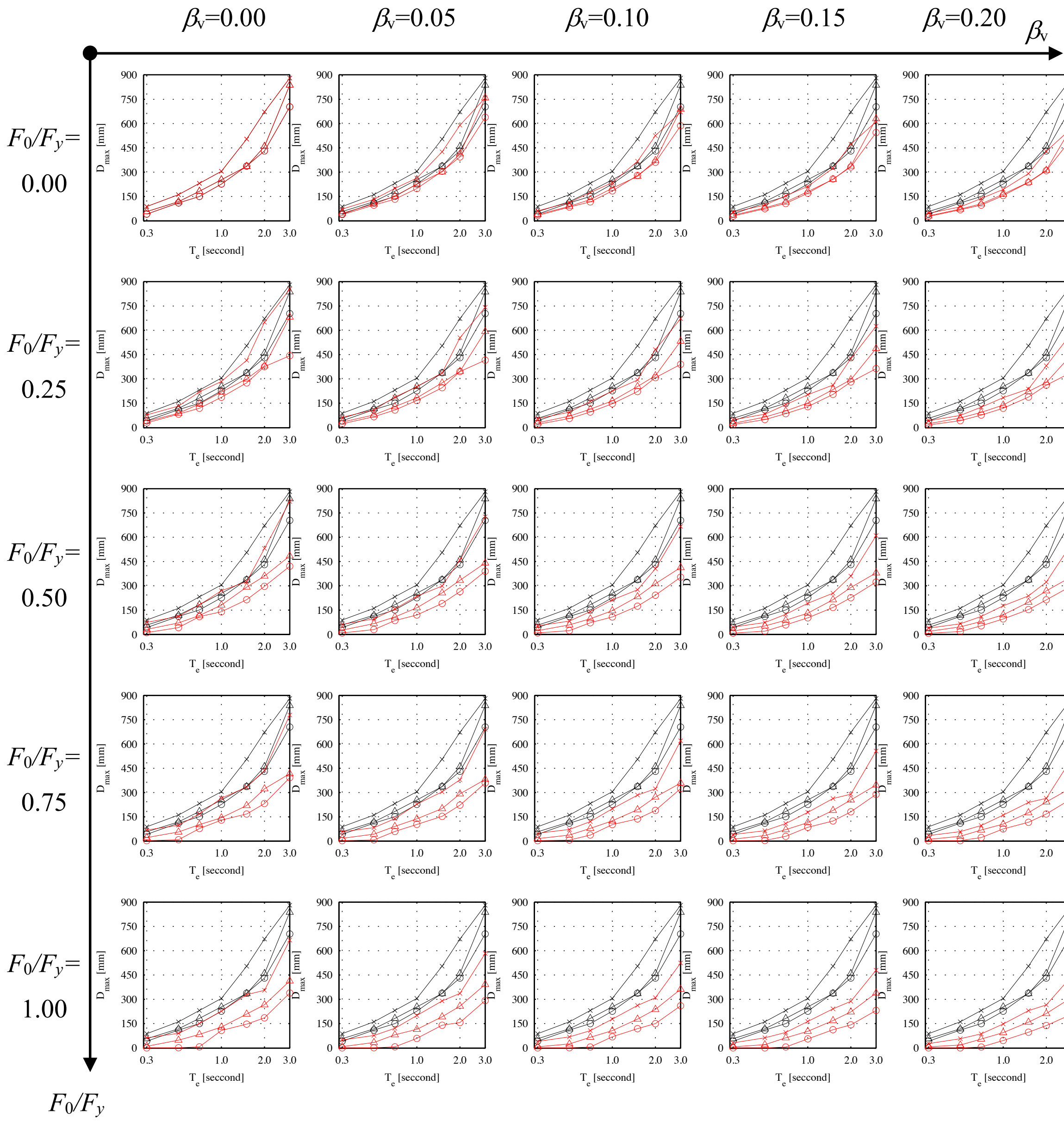

Figure A-22 Displacement in MCE, Near-Fault Pulse-like Motions, Upper-half Viscous Damping, Stiffness K_0=0, R_μ=1, 2 and 5

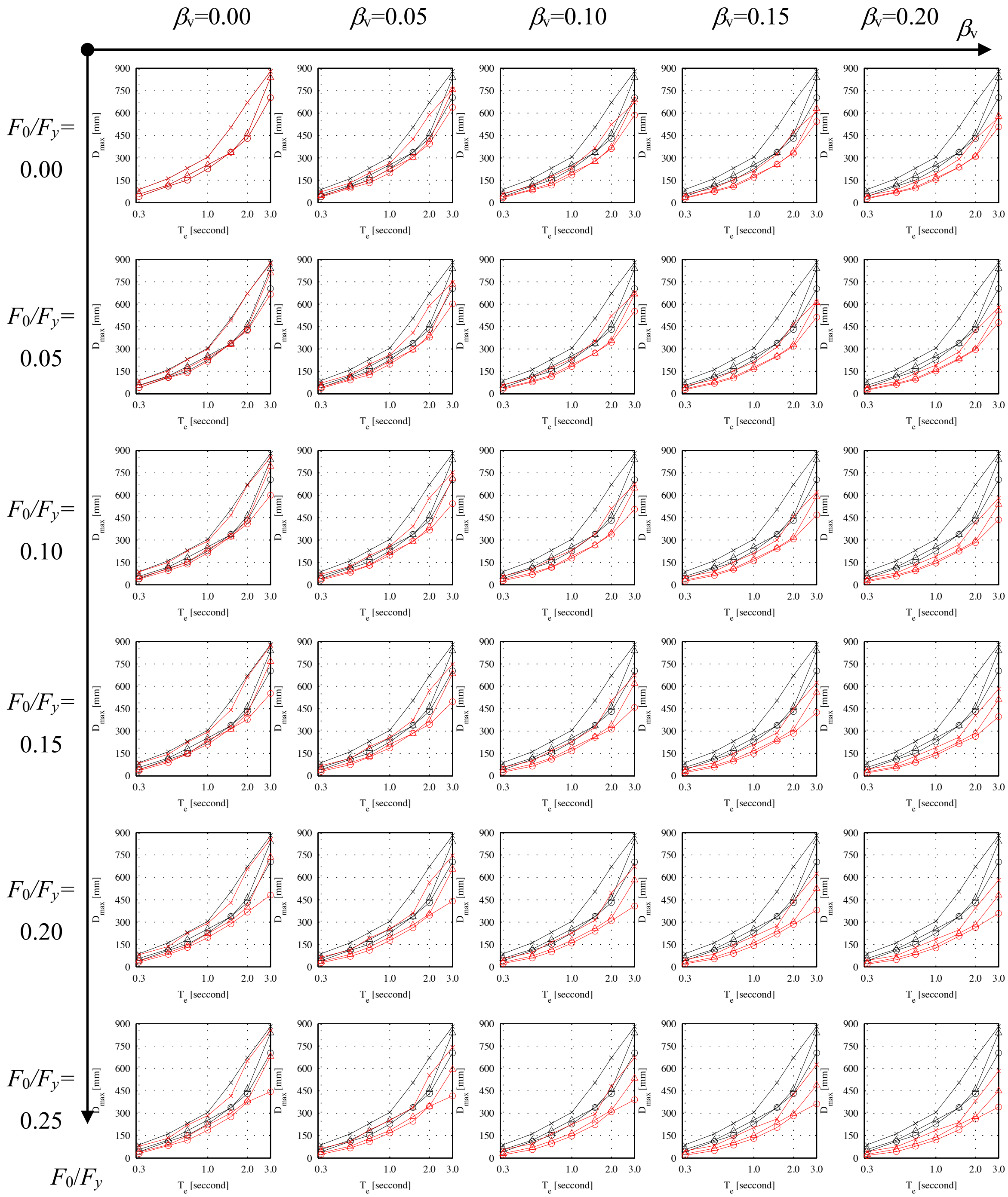

Figure A-22 (Continued)

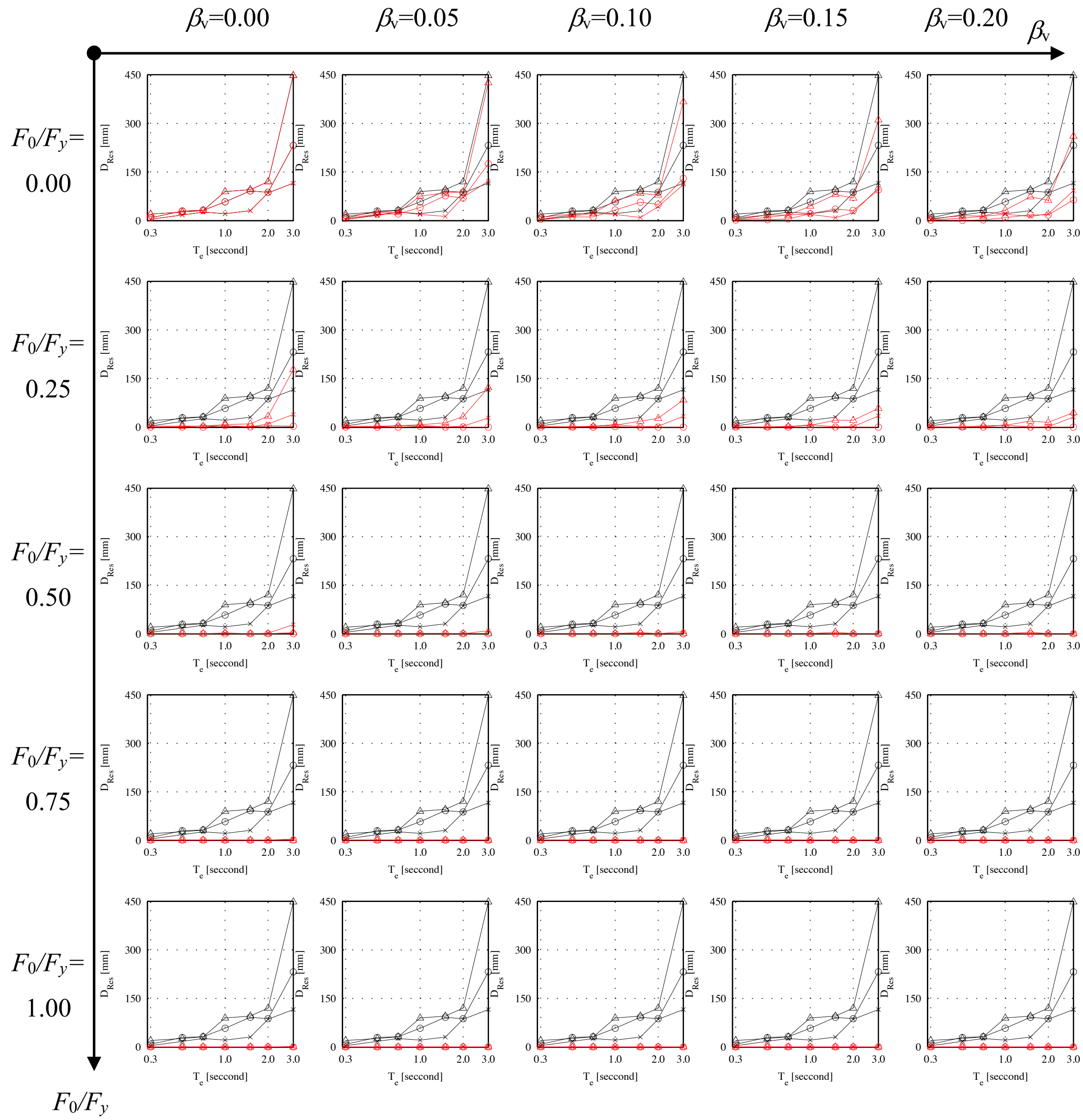

Figure A-23 Residual Displacement in MCE, Near-Fault Pulse-like Motions, Upper-half Viscous Damping, Stiffness K_0=0, R_μ=1, 2 and 5

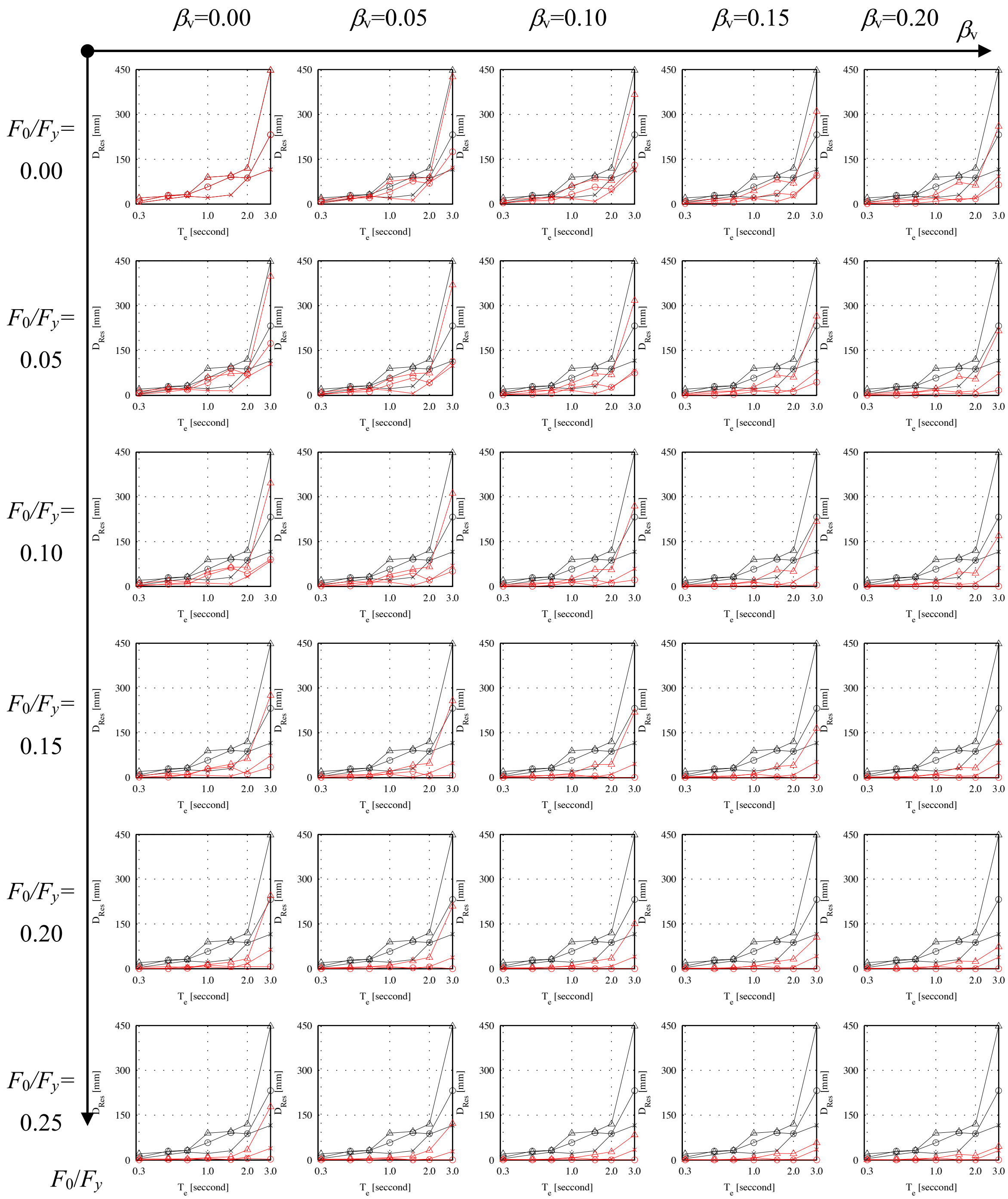

Figure A-23 (Continued)

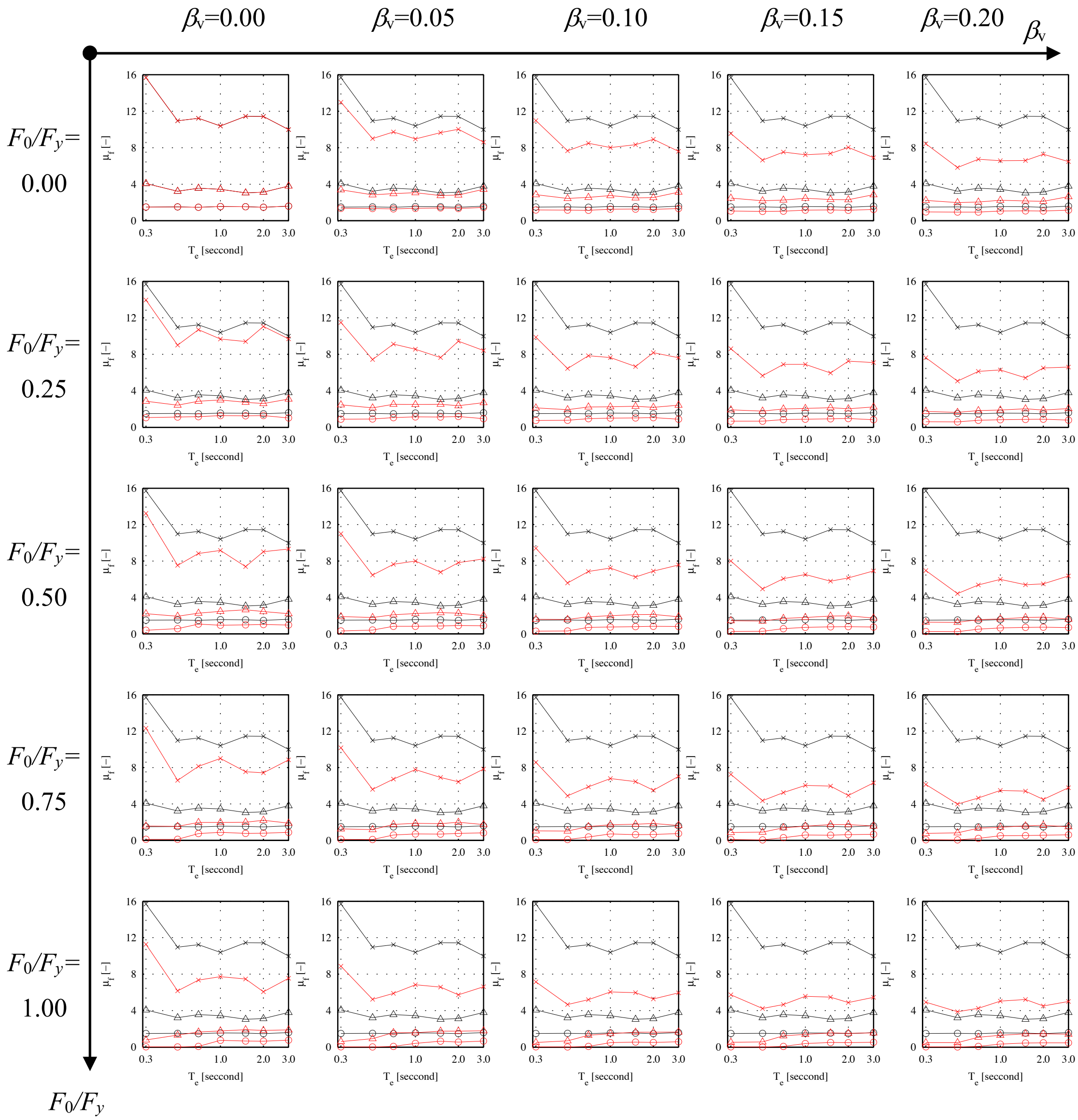

Figure A-24 Ductility Ratio in MCE, Near-Fault Pulse-like Motions, Upper-half Viscous Damping, Stiffness K_0=0, R_μ=1, 2 and 5

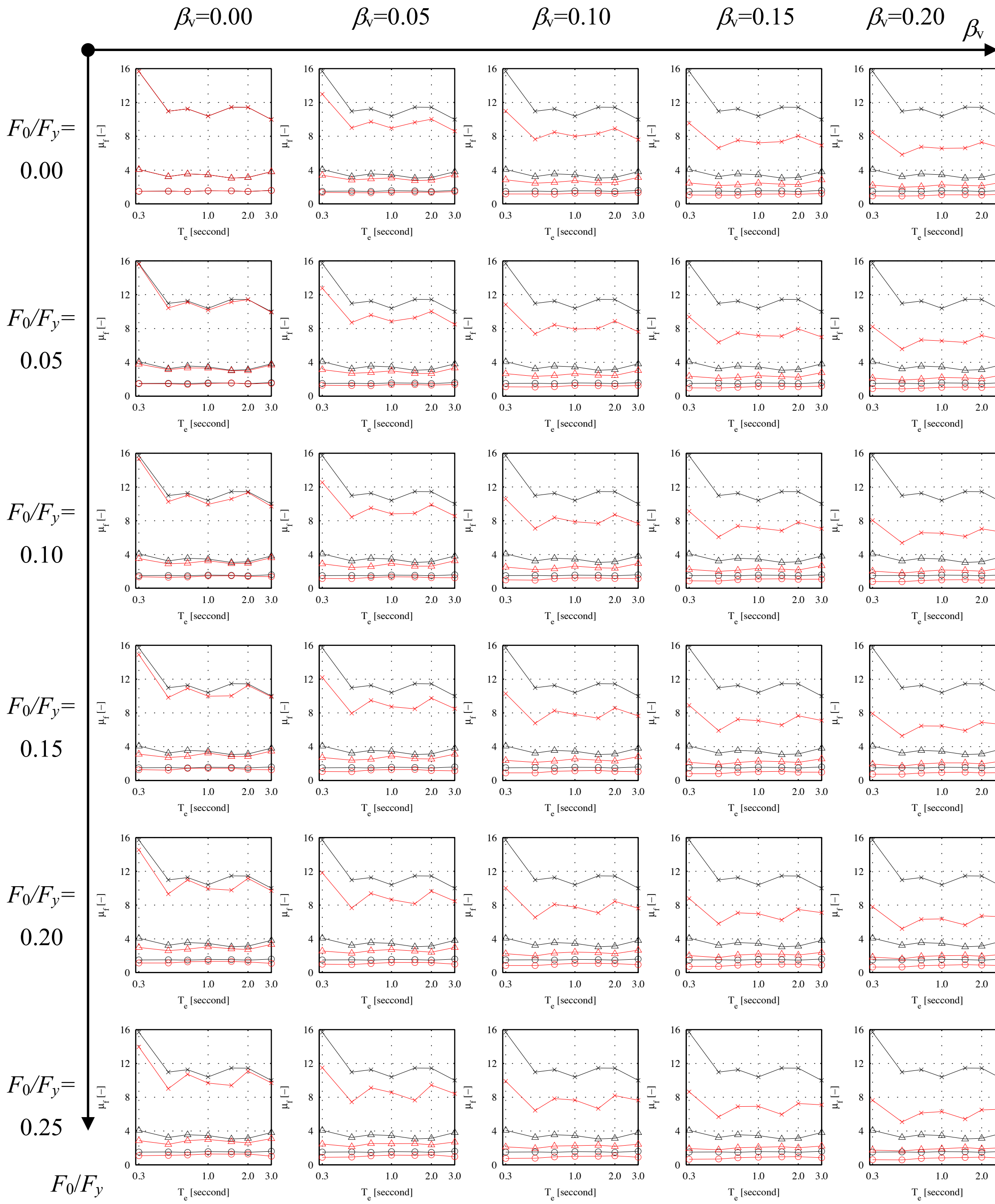

Figure A-24 (Continued)

A.2 Seismic Response under Near-Fault Non-Pulse-Like Ground Motions

A.2.1 Structure with Linear Viscous Damping and K_0=0 for Near-Fault Non-Pulse-Like Ground Motions

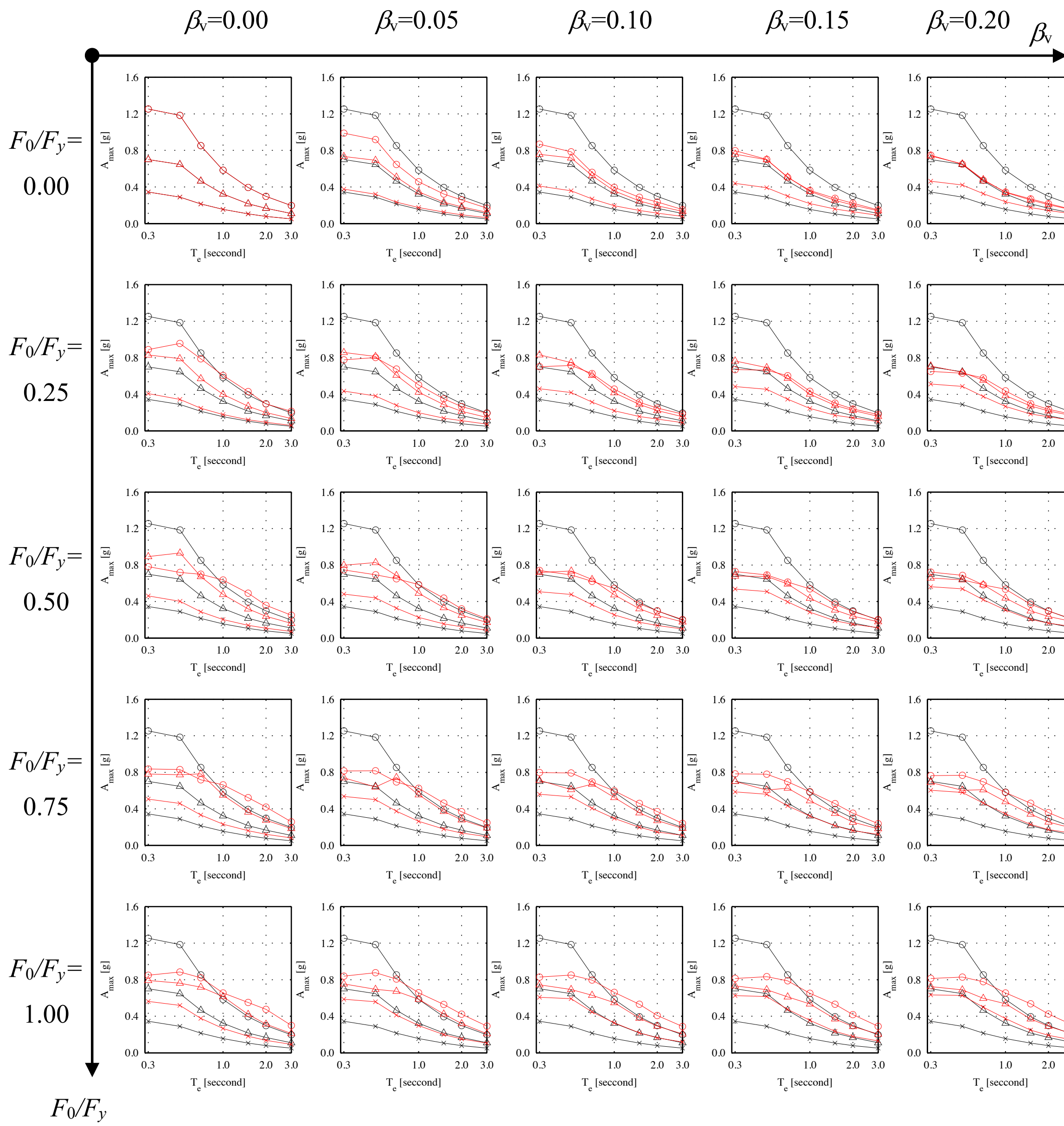

Figure A-25 Acceleration in DE, Near-Fault Non-Pulse-like Motions, Linear Viscous Damping, Stiffness K_0=0, R_μ=1, 2 and 5

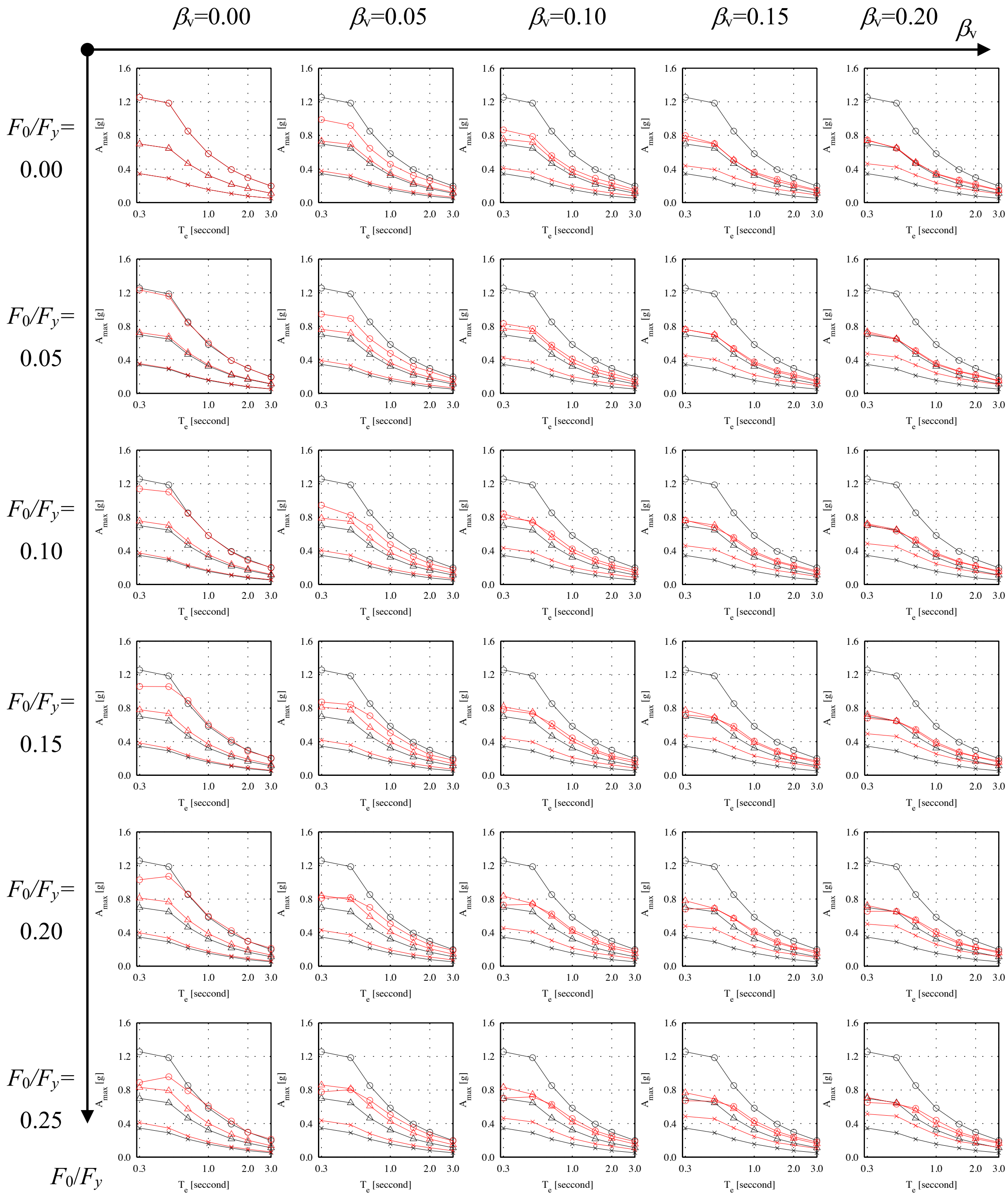

Figure A-25 (Continued)

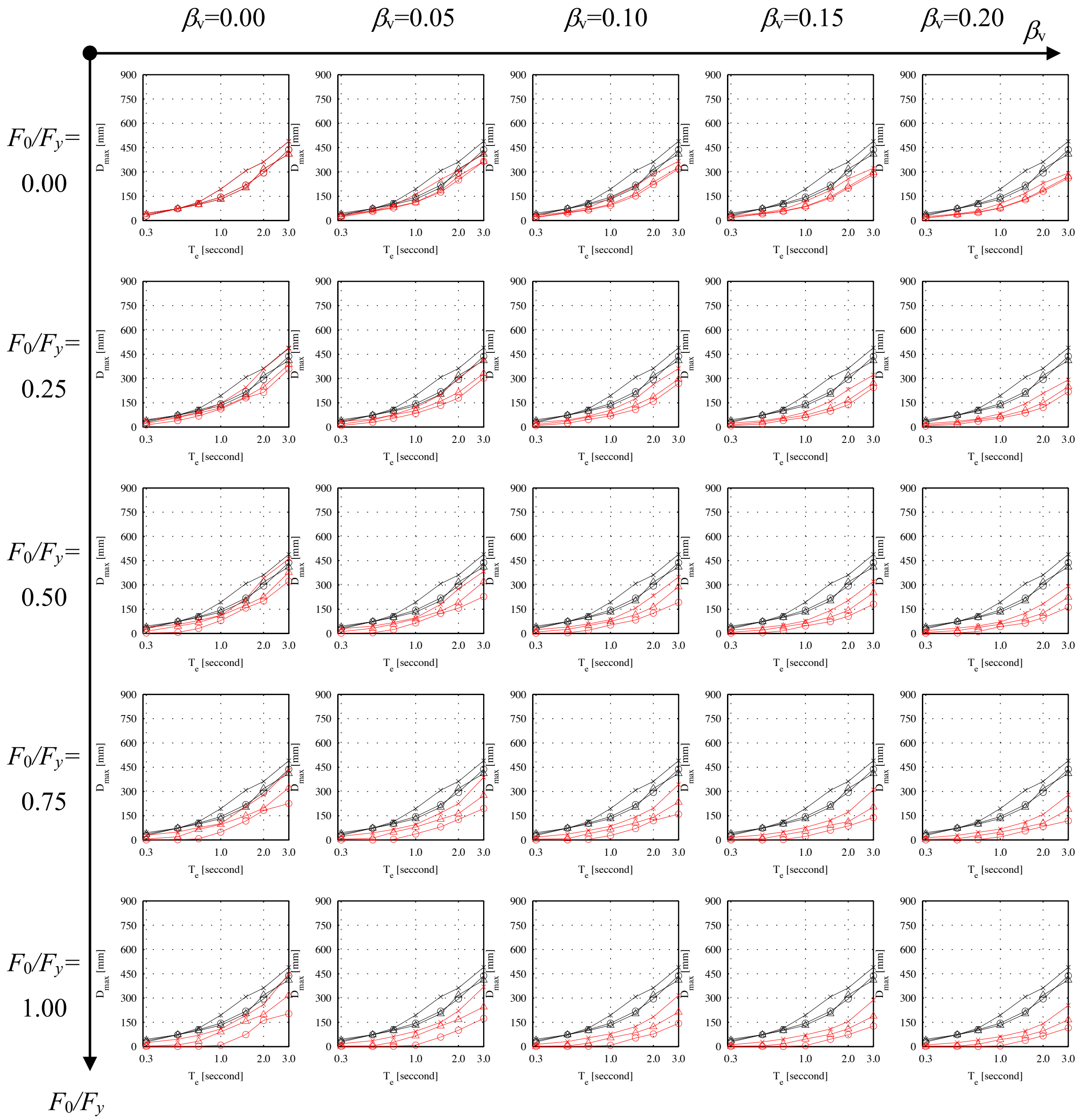

Figure A-26 Displacement in DE, Near-Fault Non-pulse-like Motions, Linear Viscous Damping, Stiffness K_0=0, R_μ=1, 2 and 5

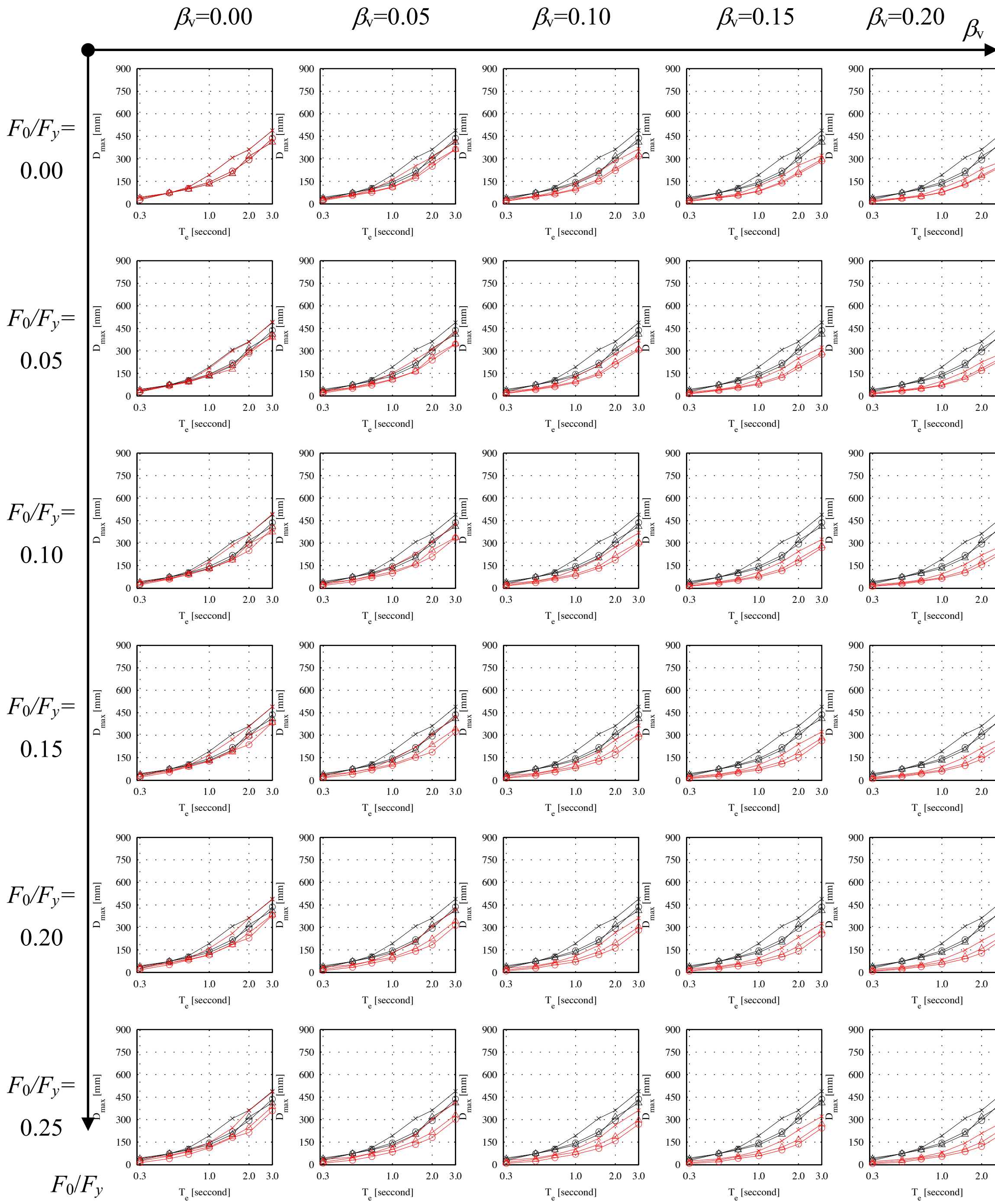

Figure A-26 (Continued)

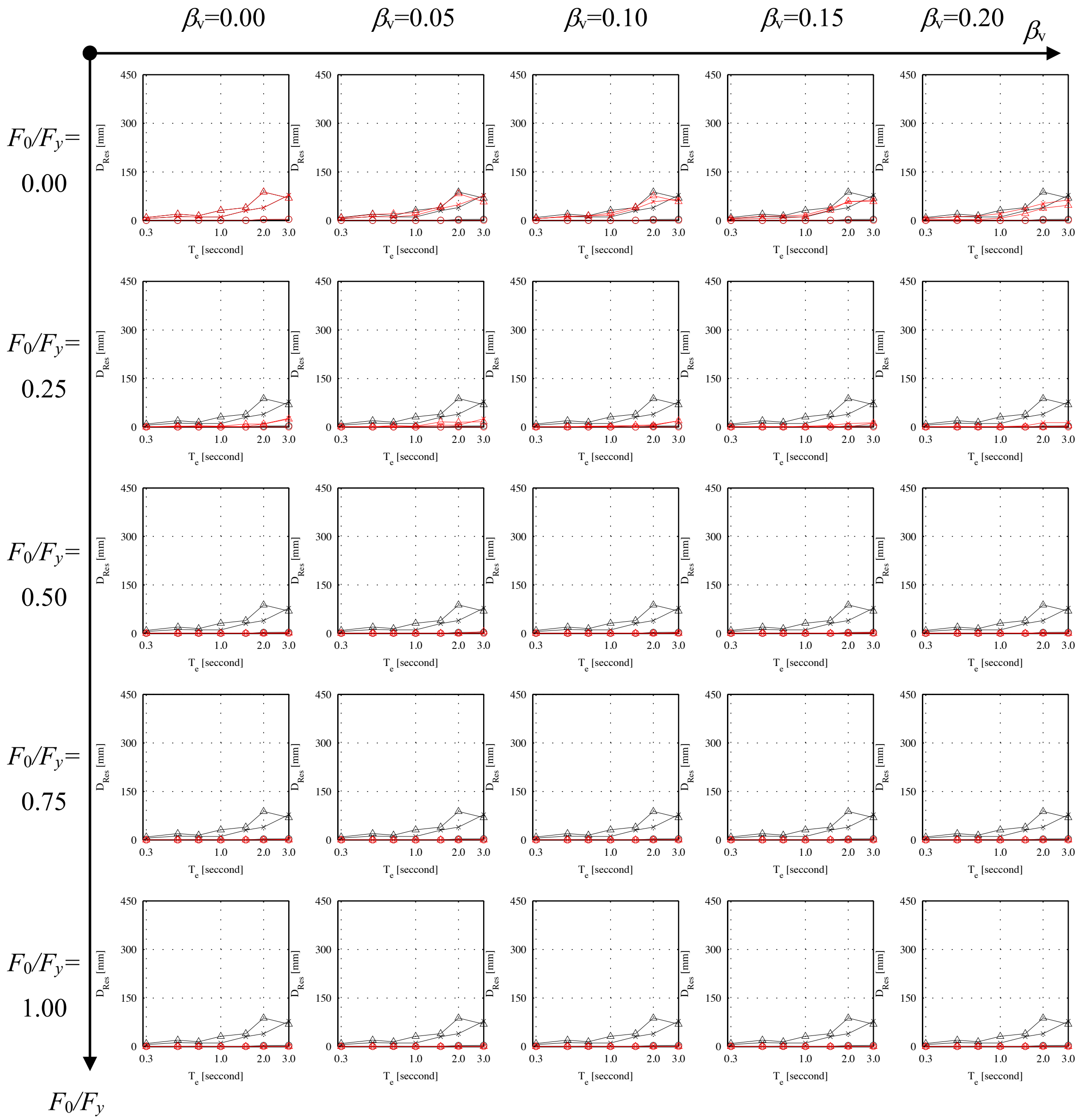

Figure A-27 Residual Displacement in DE, Near-Fault Non-pulse-like Motions, Linear Viscous Damping, Stiffness K_0=0, R_μ=1, 2 and 5

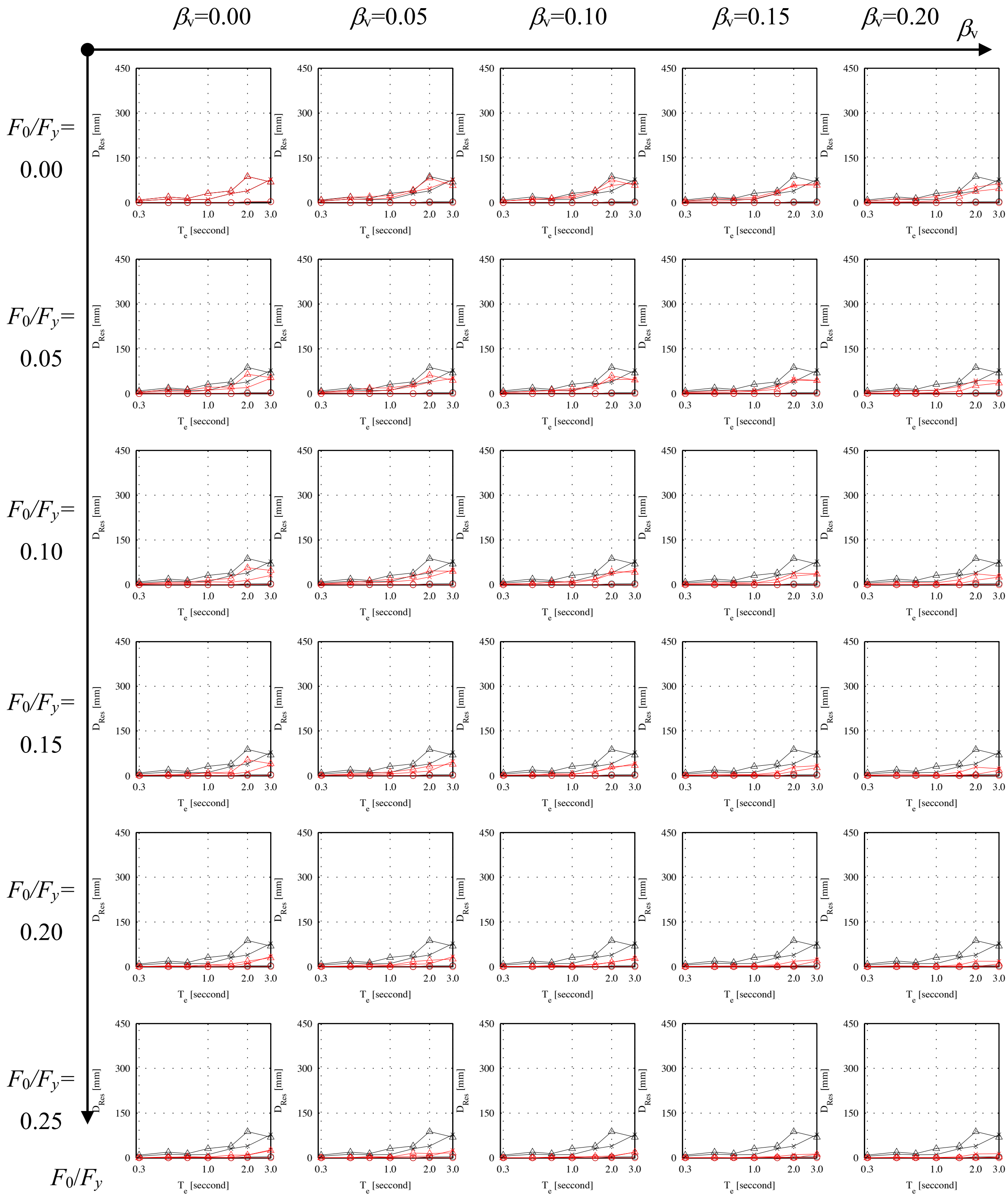

Figure A-27 (Continued)

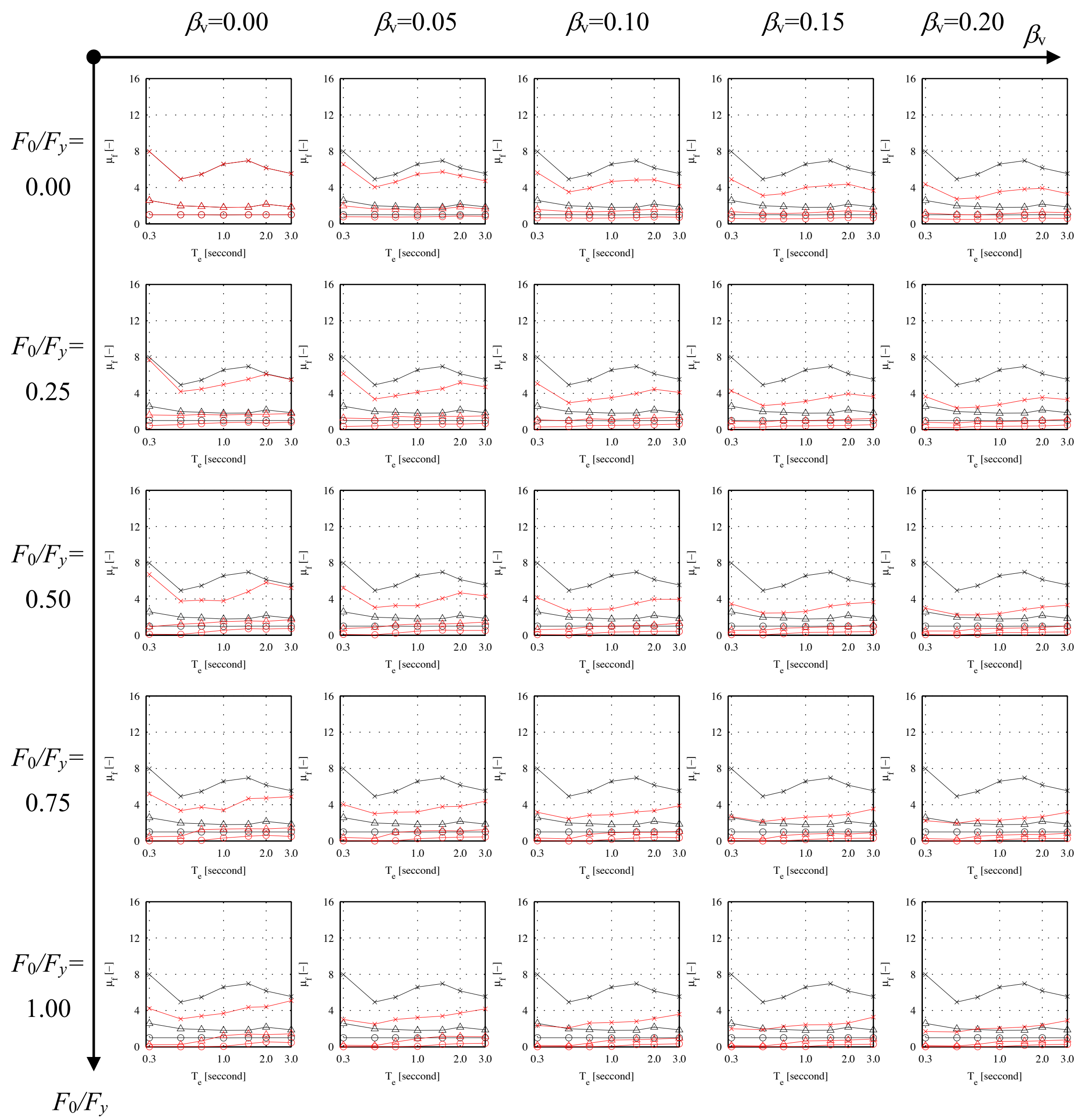

Figure A-28 Ductility Ratio in DE, Near-Fault Non-pulse-like Motions, Linear Viscous Damping, Stiffness K_0=0, R_μ=1, 2 and 5

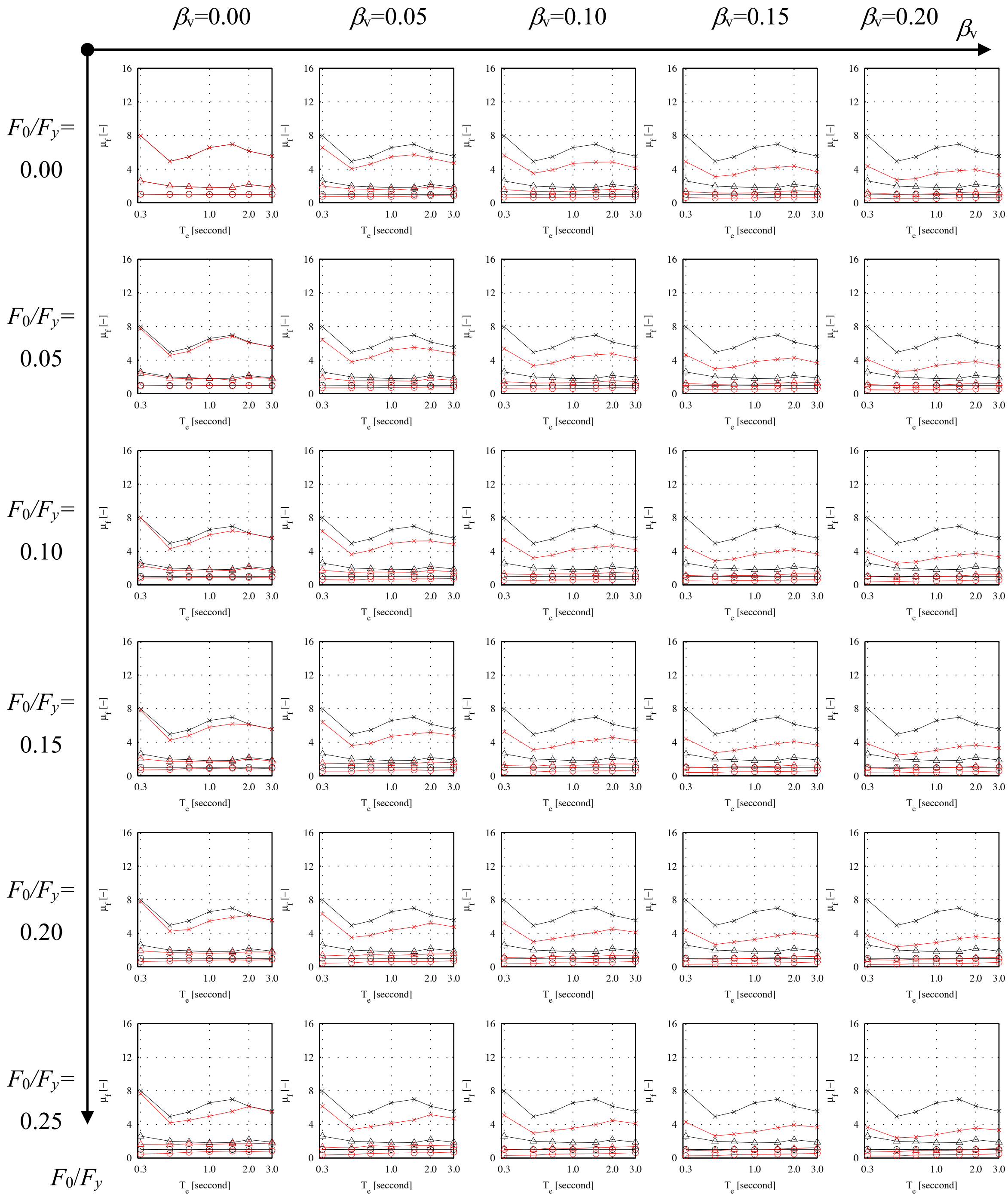

Figure A-28 (Continued)

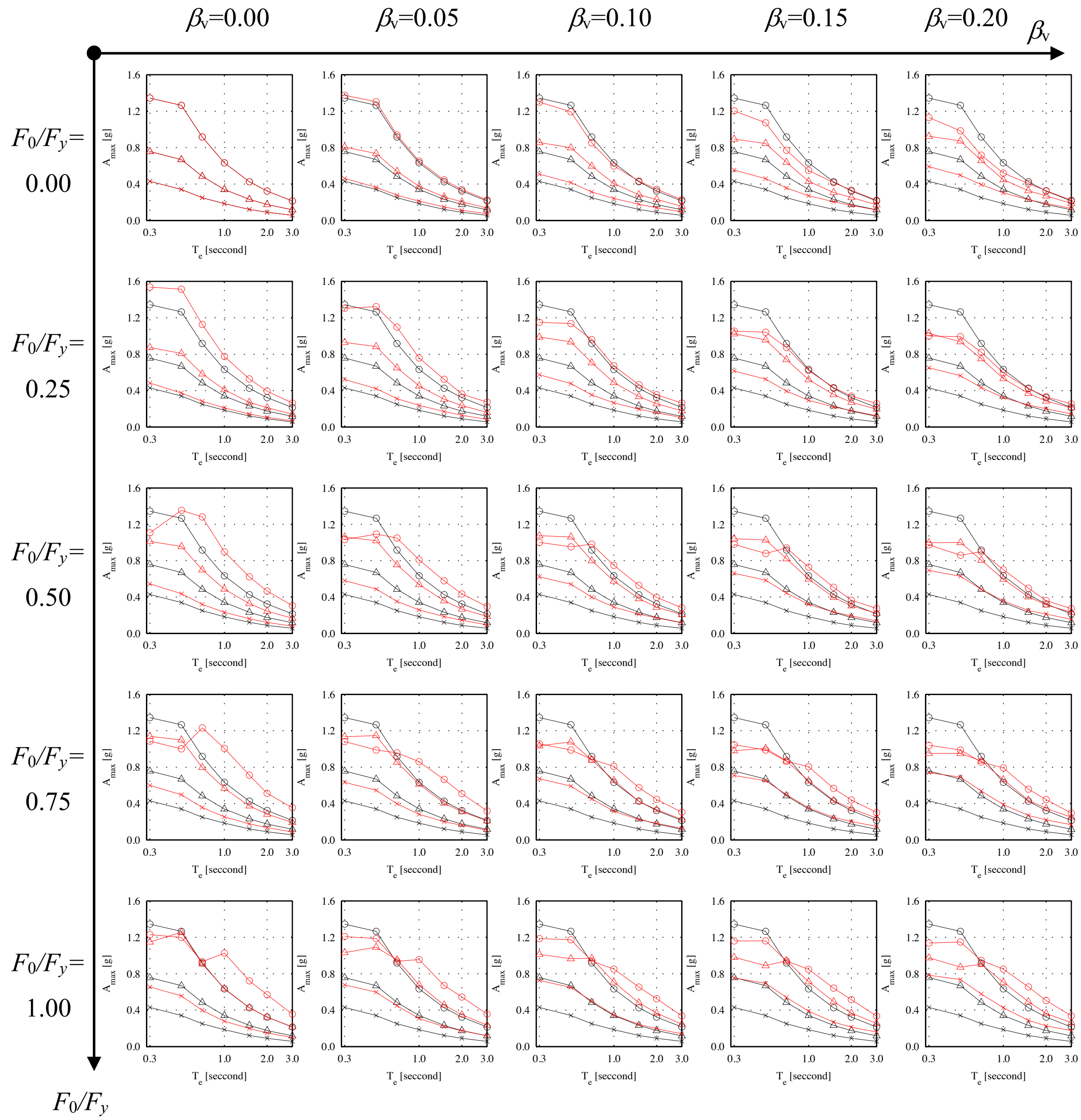

Figure A-29 Acceleration in MCE, Near-Fault Non-Pulse-like Motions, Linear Viscous Damping, Stiffness K_0=0, R_μ=1, 2 and 5

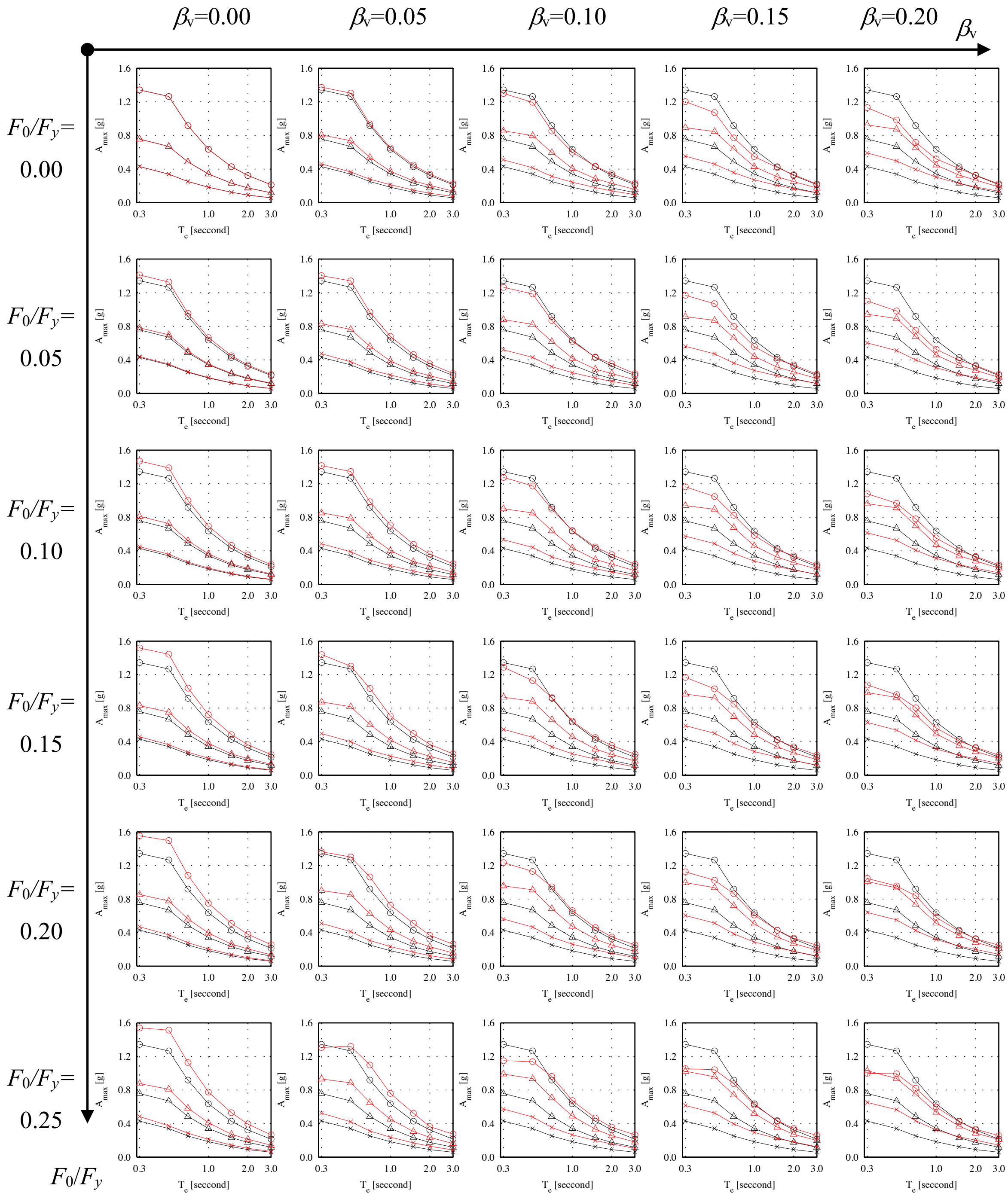

Figure A-29 (Continued)

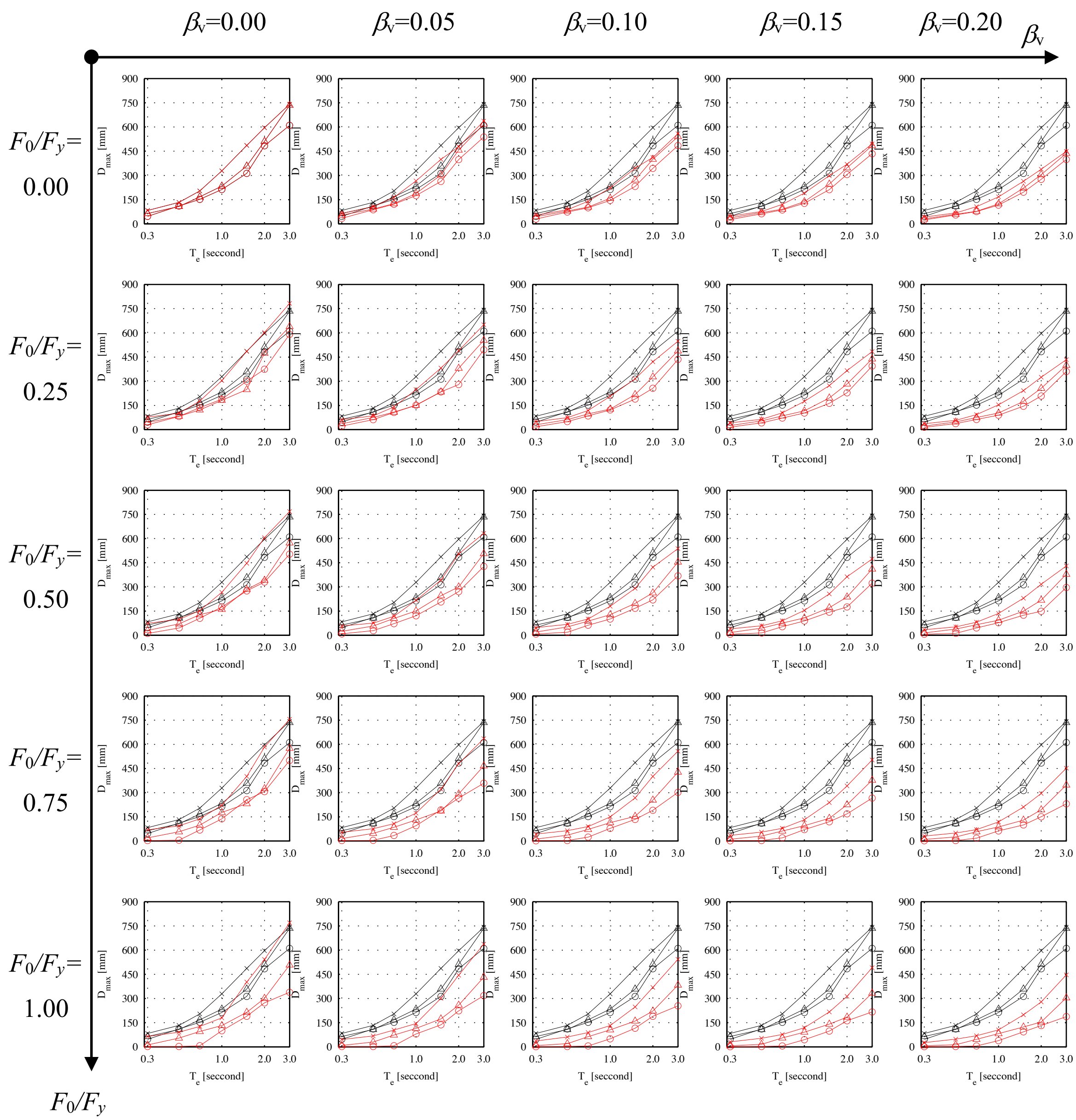

Figure A-30 Displacement in MCE, Near-Fault Non-Pulse-Like Motions, Linear Viscous Damping, Stiffness K_0=0, R_μ=1, 2 and 5

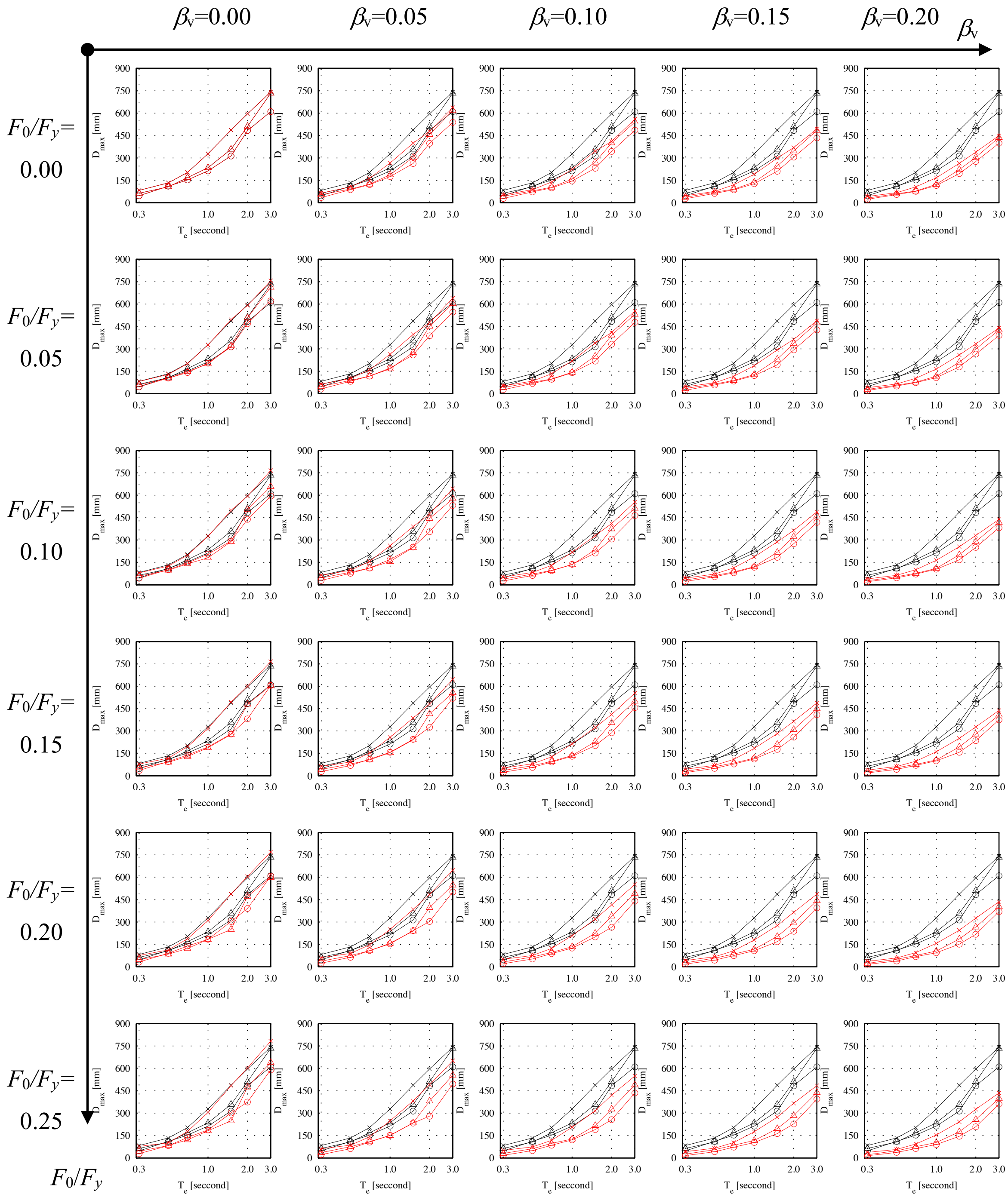

Figure A-30 (Continued)

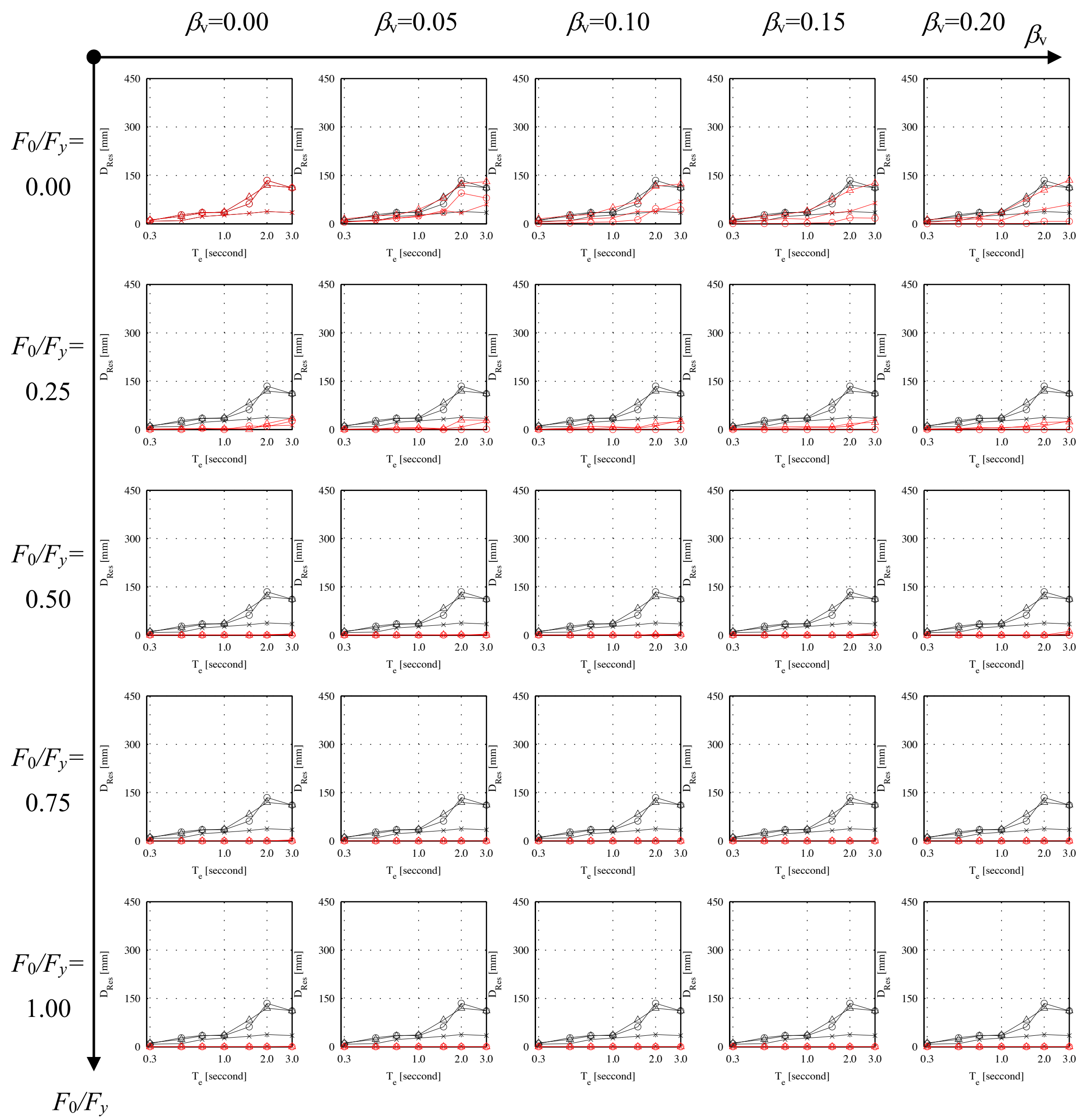

Figure A-31 Residual Displacement in MCE, Near-Fault Non-Pulse-Like Motions, Linear Viscous Damping, Stiffness K_0=0, R_μ=1, 2 and 5

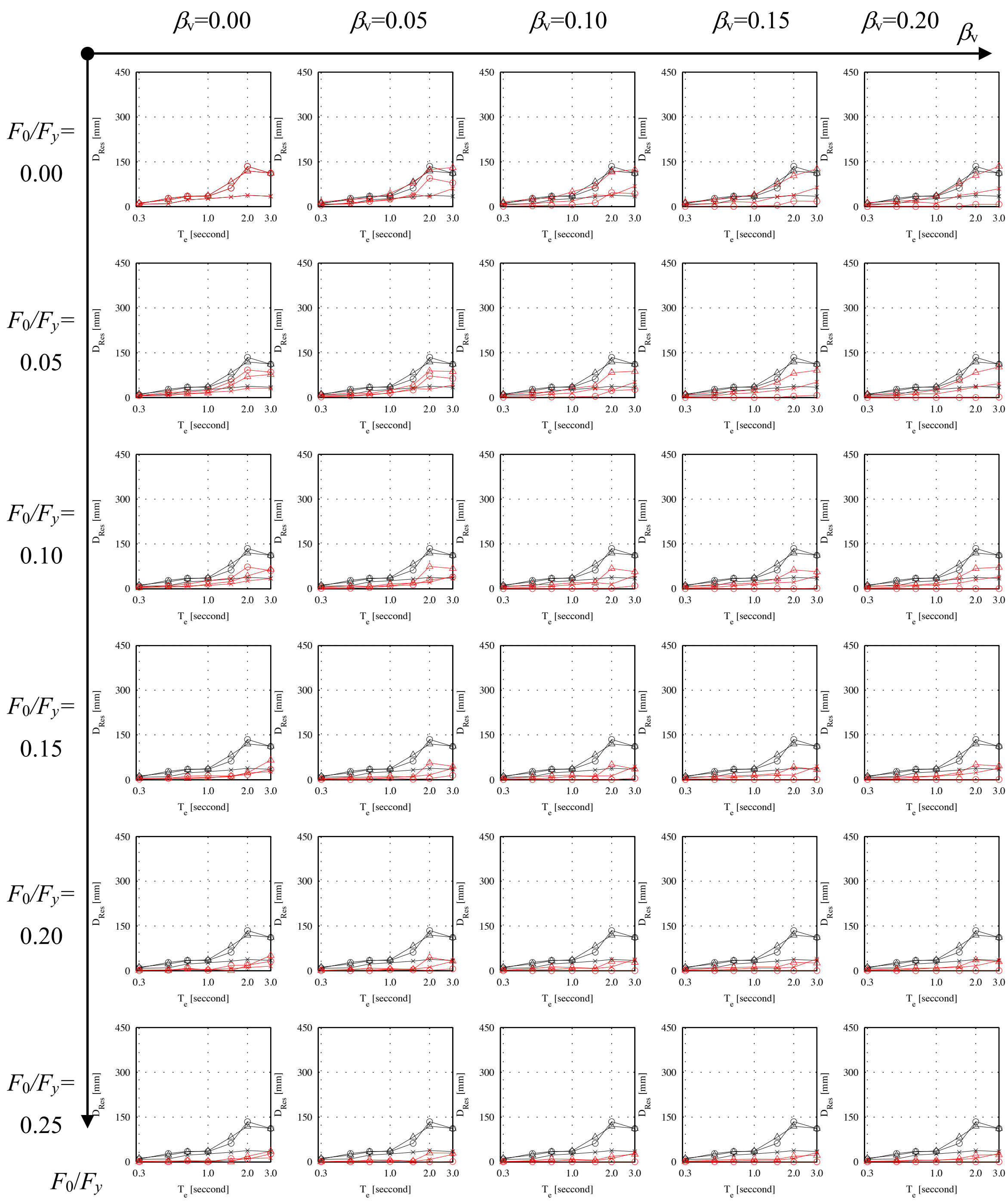

Figure A-31 (Continued)

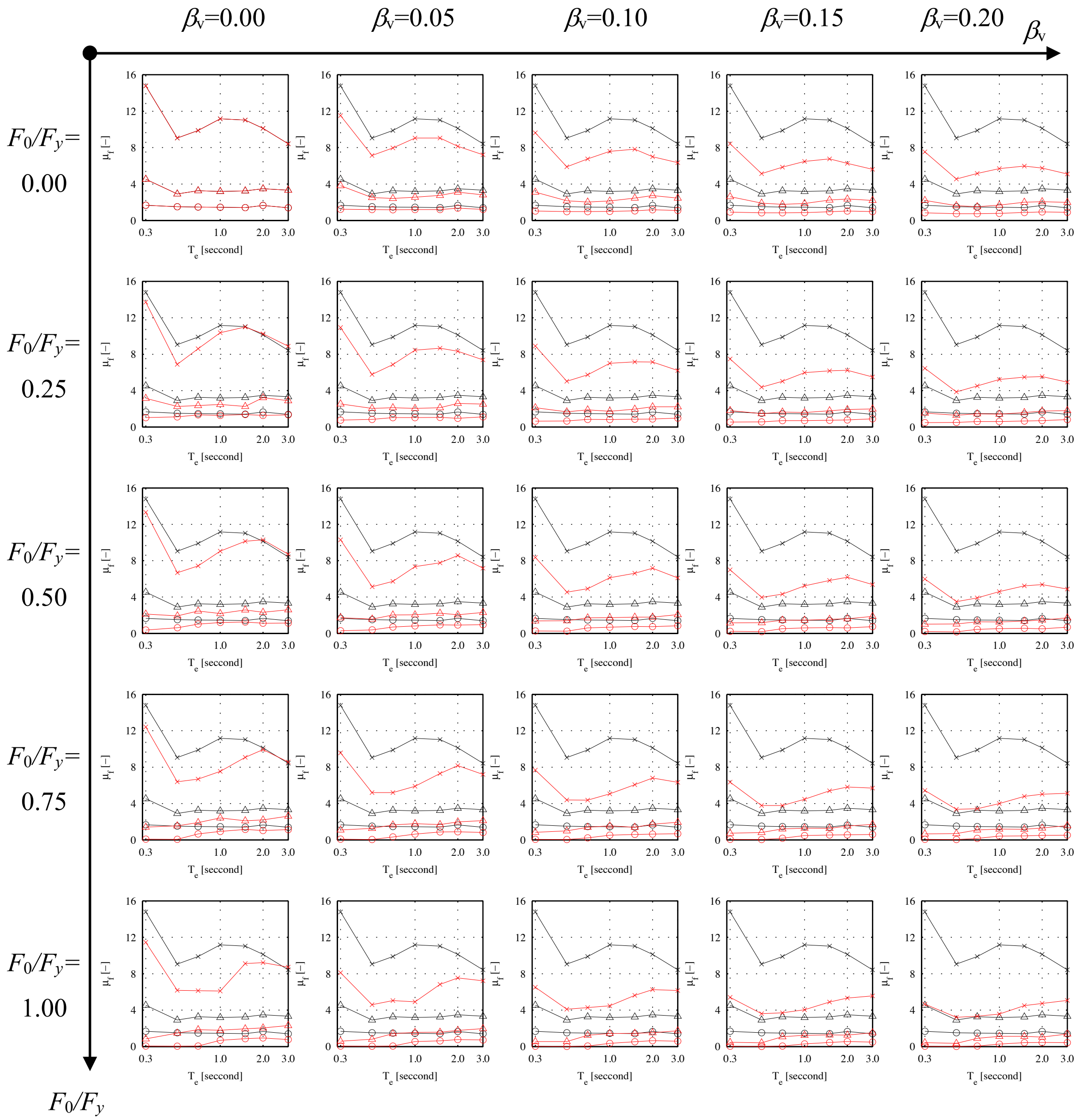

Figure A-32 Ductility Ratio in MCE, Near-Fault Non-Pulse-like Motions, Linear Viscous Damping, Stiffness K_0=0, R_μ=1, 2 and 5

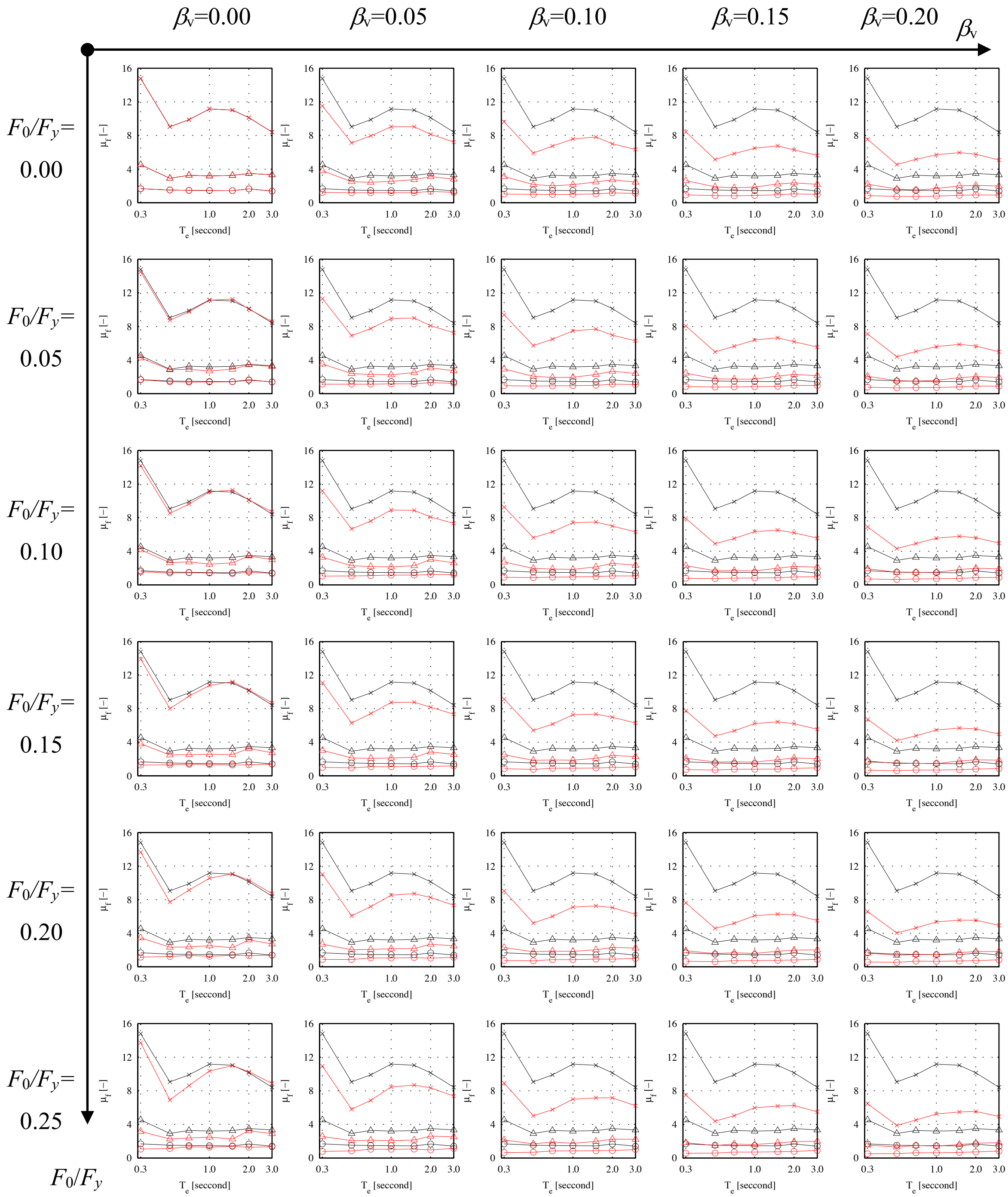

Figure A- 32 (Continued)

A.2.2 Structure with Non-Linear Viscous Damping and K_0=0 in Near-Fault Non-Pulse-like Ground Motions

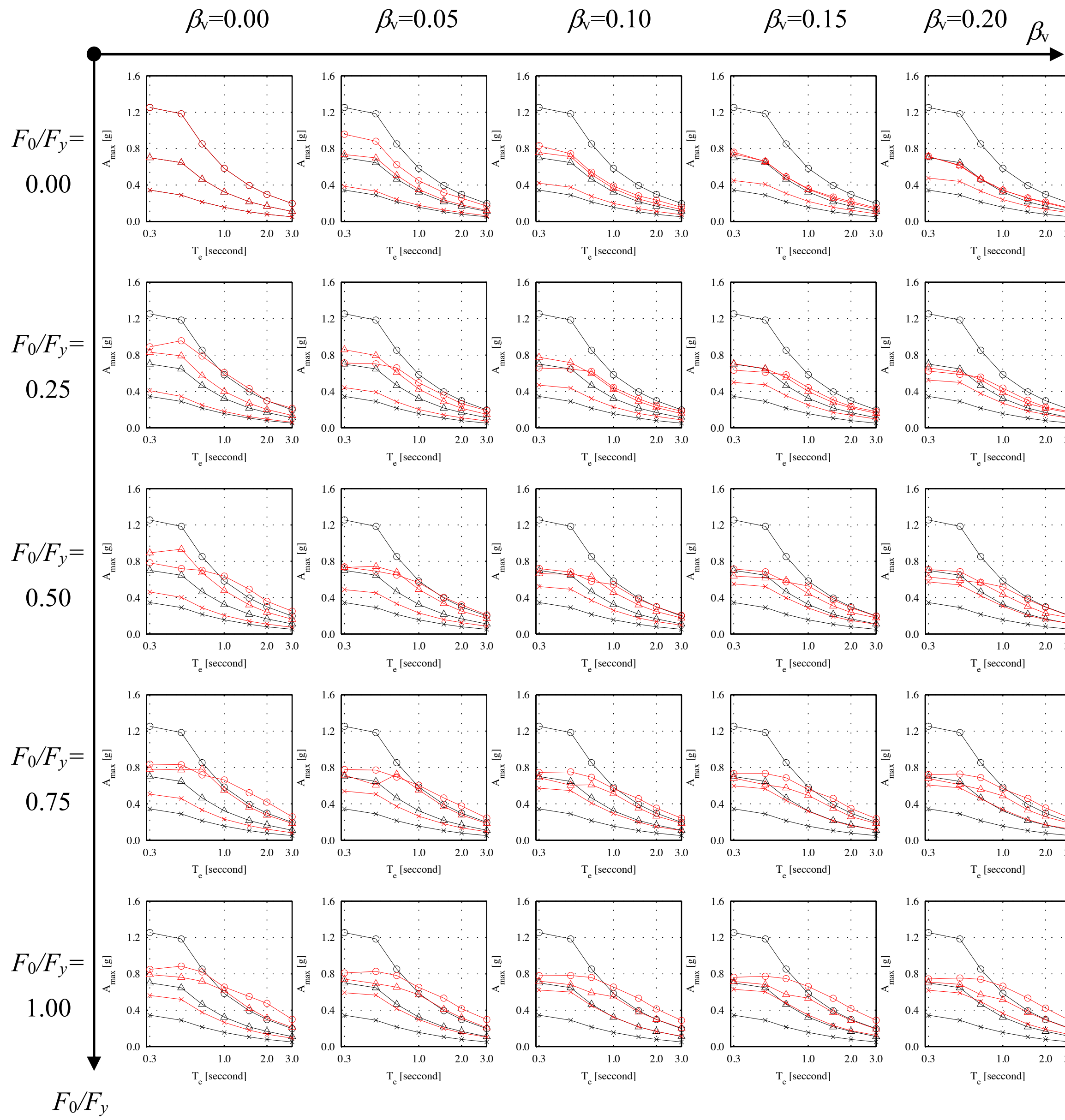

Figure A-33 Acceleration in DE, Near-Fault Non-Pulse-like Motions, Non-linear Viscous Damping, Stiffness K_0=0, R_μ=1, 2 and 5

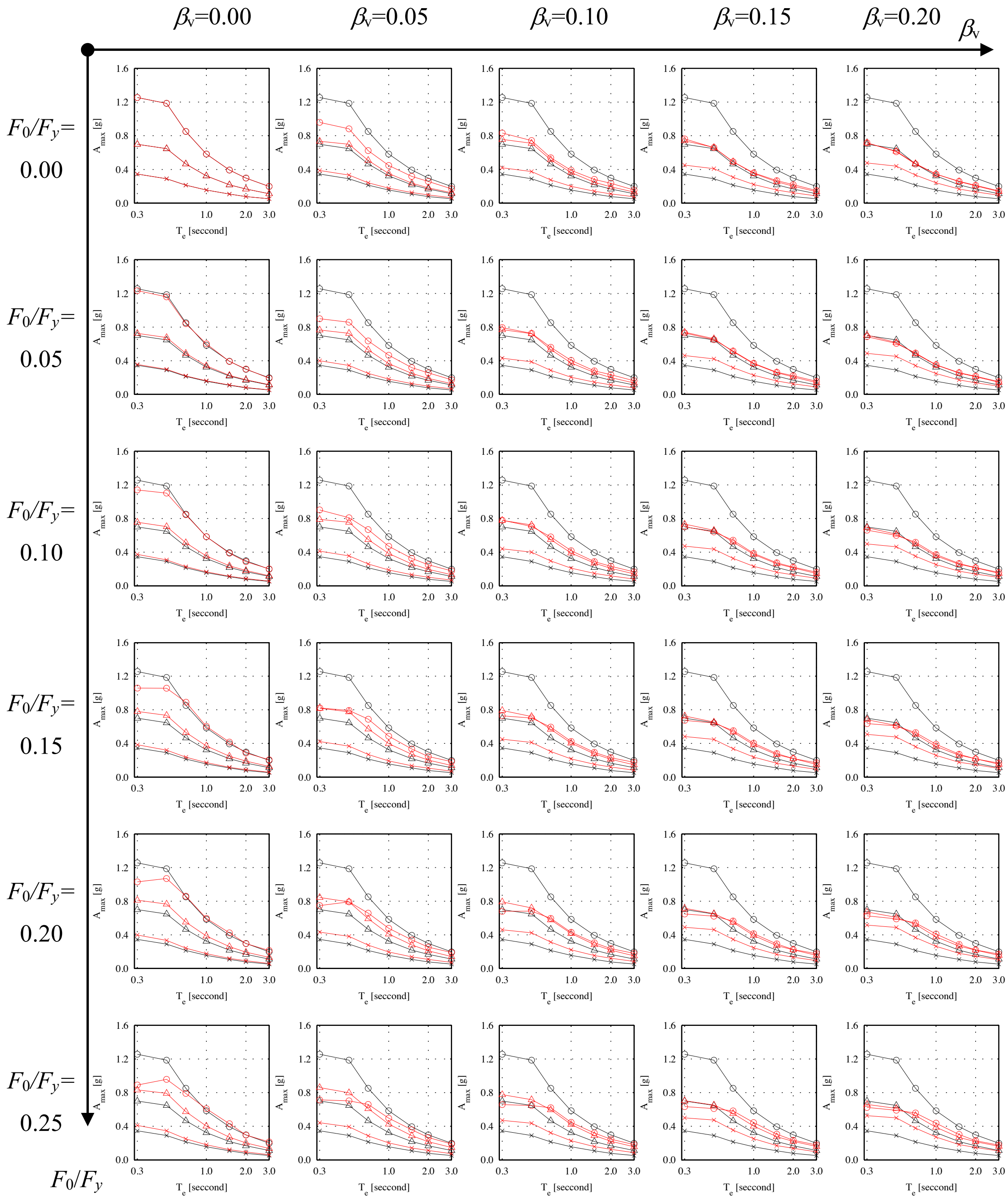

Figure A-33 (Continued)

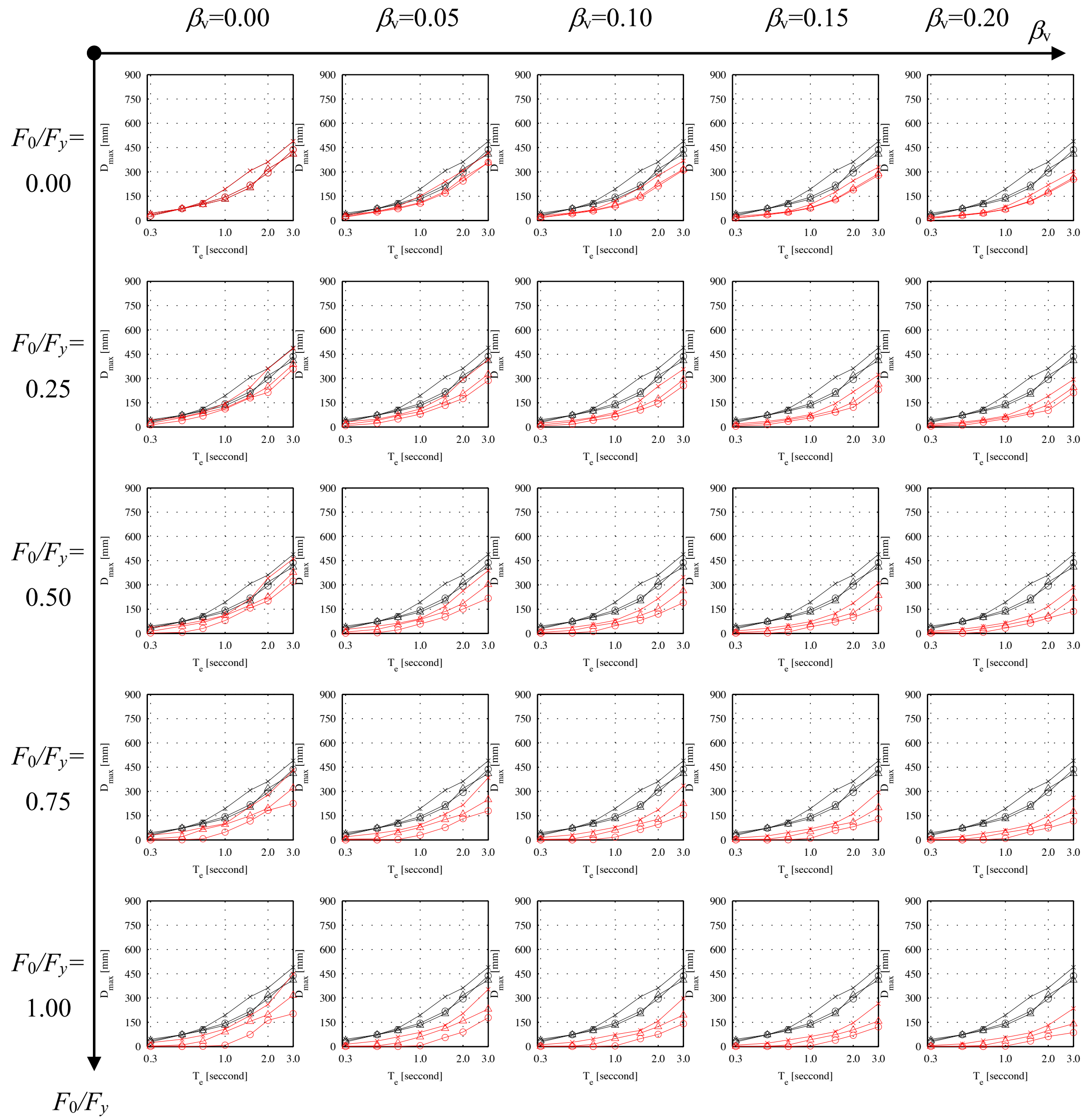

Figure A-34 Displacement in DE, Near-Fault Non-Pulse-like Motions, Non-linear Viscous Damping, Stiffness K_0=0, R_μ=1, 2 and 5

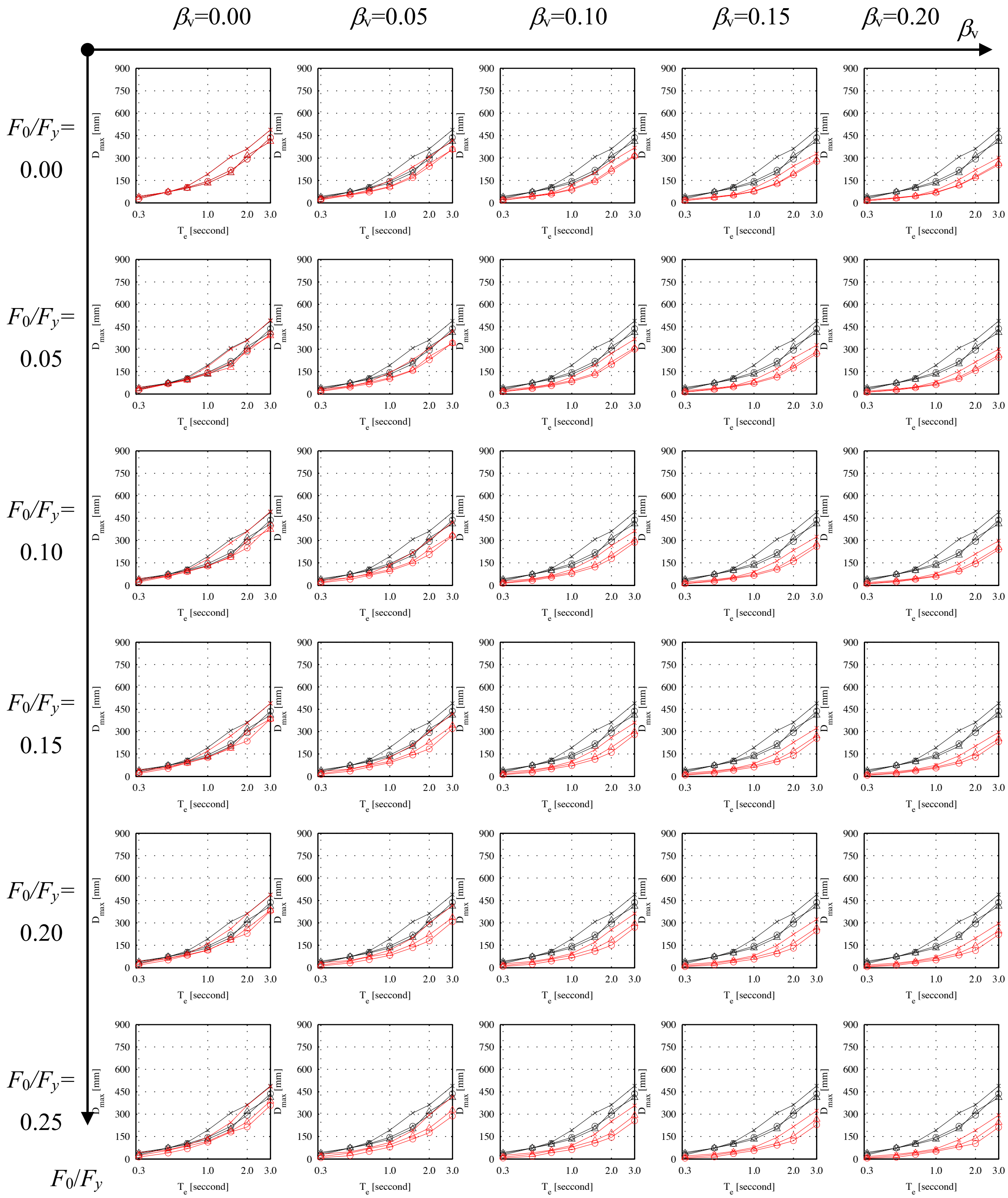

Figure A-34 (Continued)

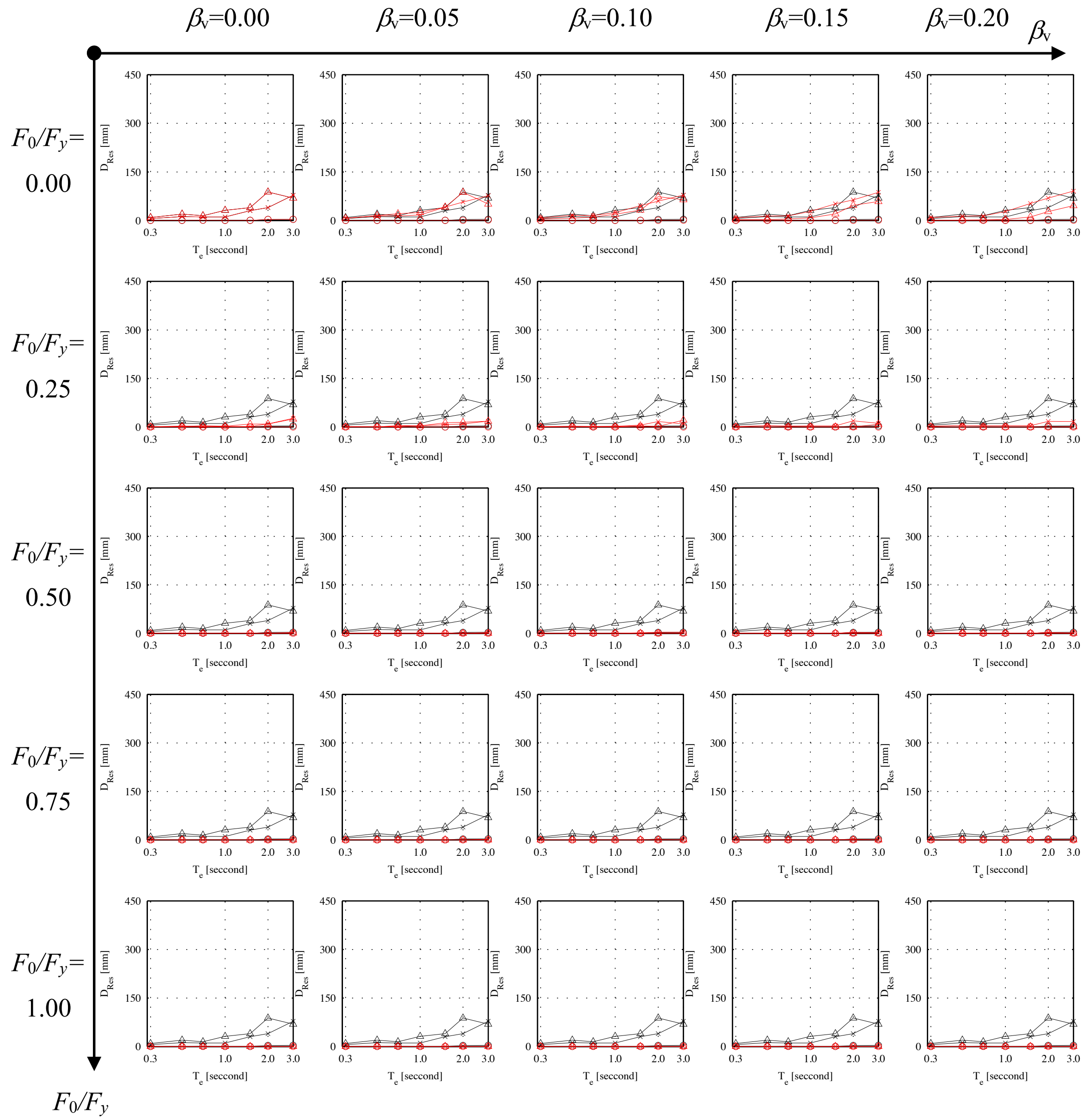

Figure A-35 Residual Displacement in DE, Near-Fault Non-Pulse-like Motions, Non-linear Viscous Damping, Stiffness K_0=0, R_μ=1, 2 and 5

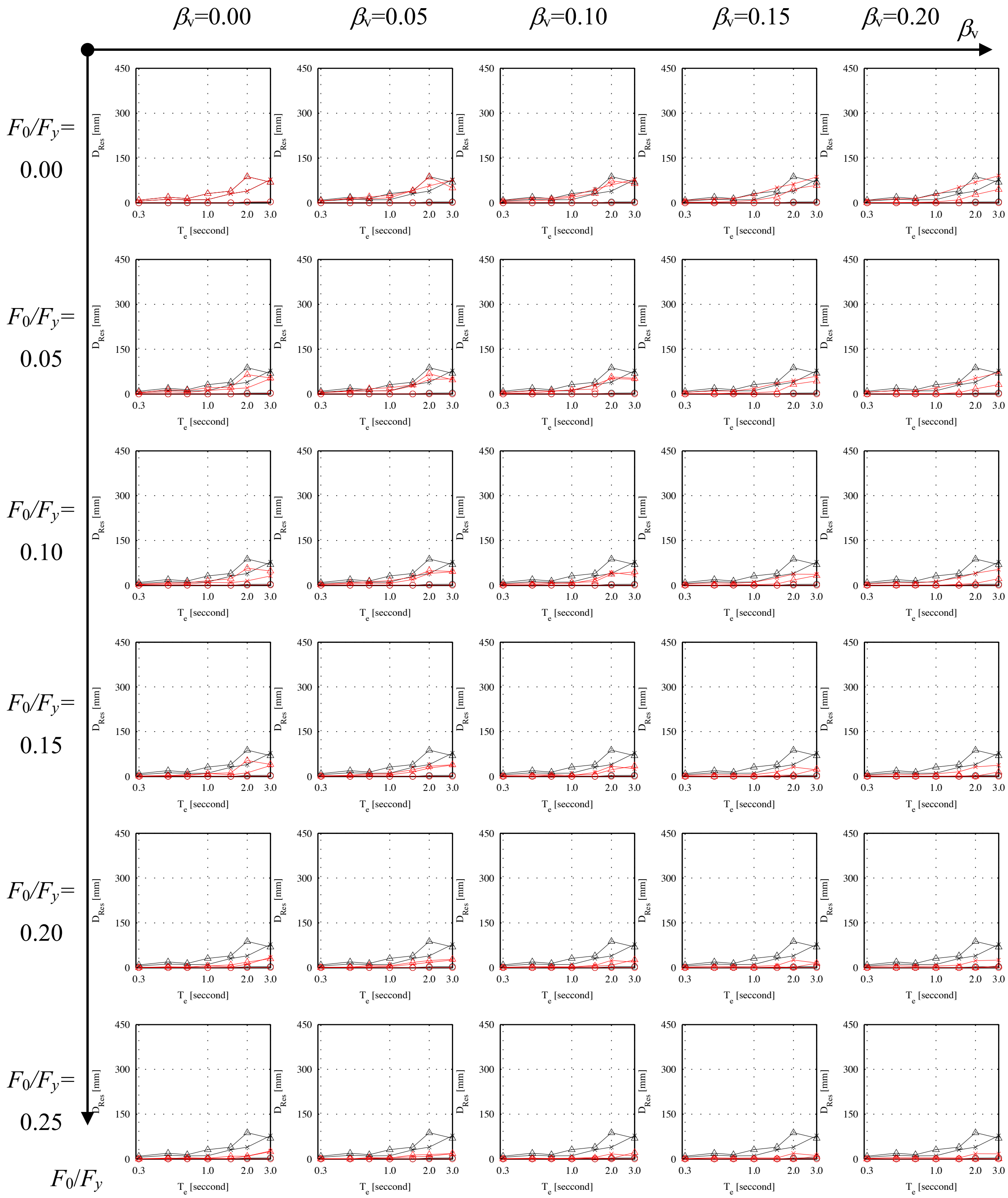

Figure A-35 (Continued)

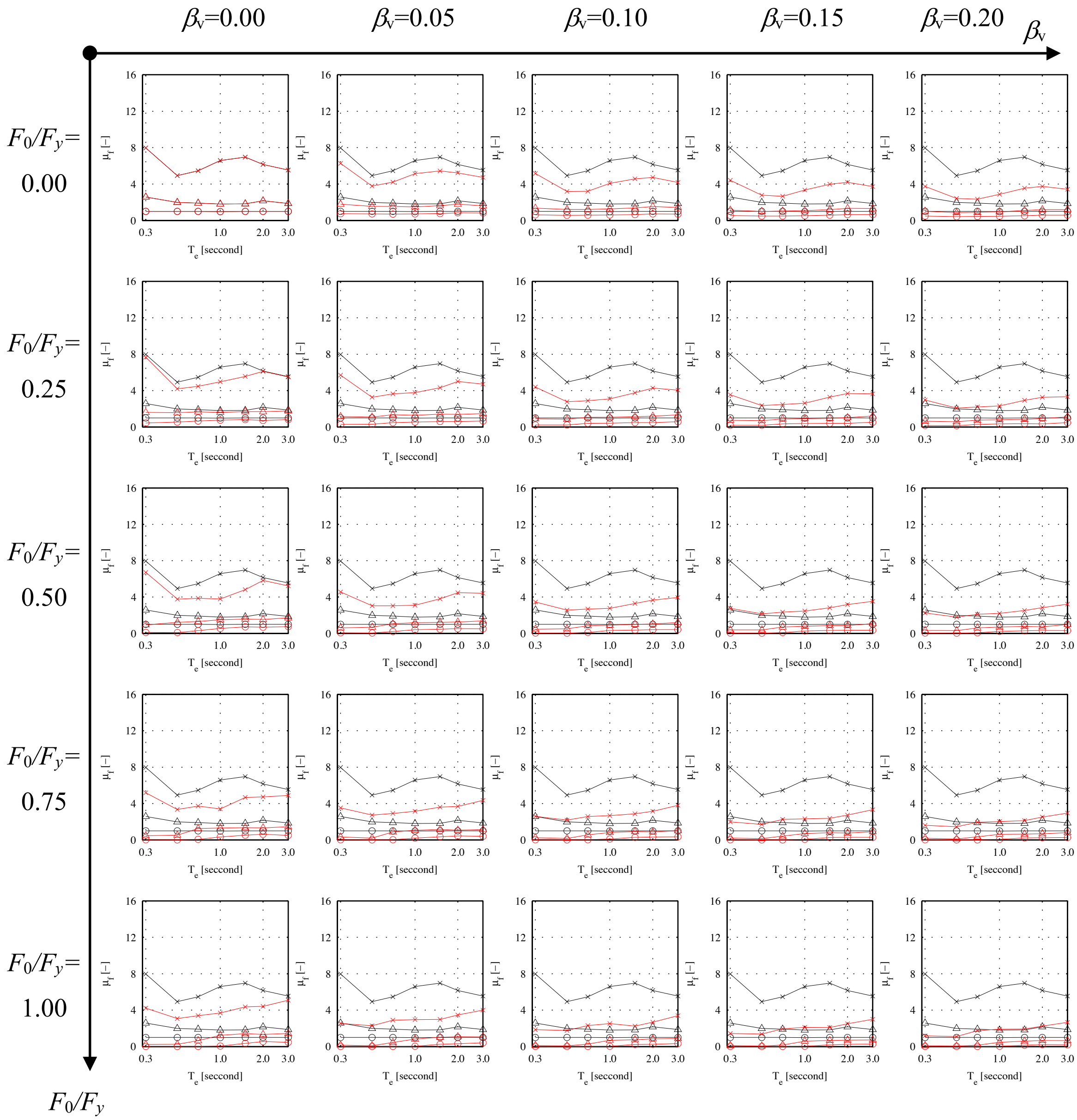

Figure A-36 Ductility Ratio in DE, Near-Fault Non-Pulse-like Motions, Non-linear Viscous Damping, Stiffness K_0=0, R_μ=1, 2 and 5

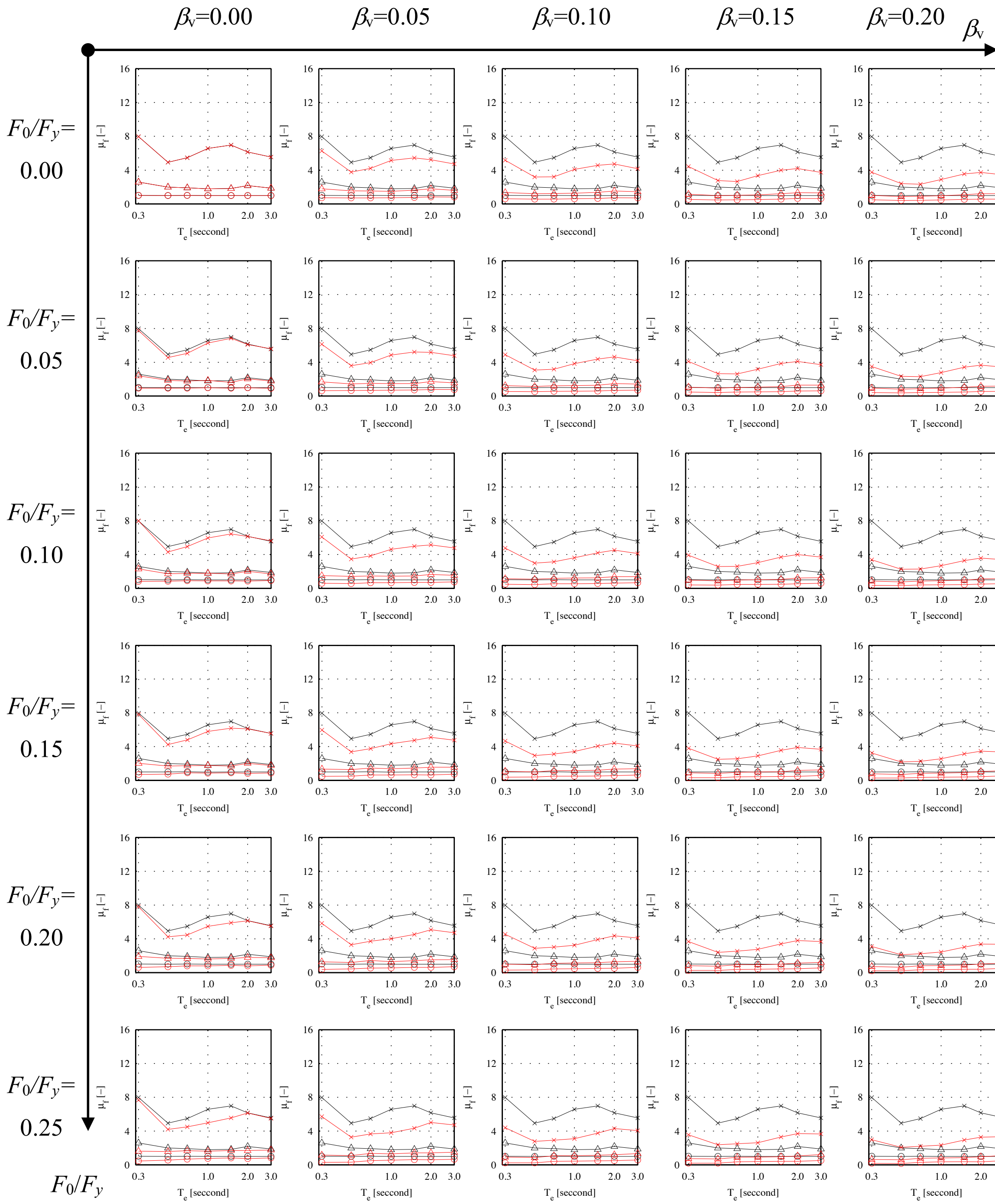

Figure A-36 (Continued)

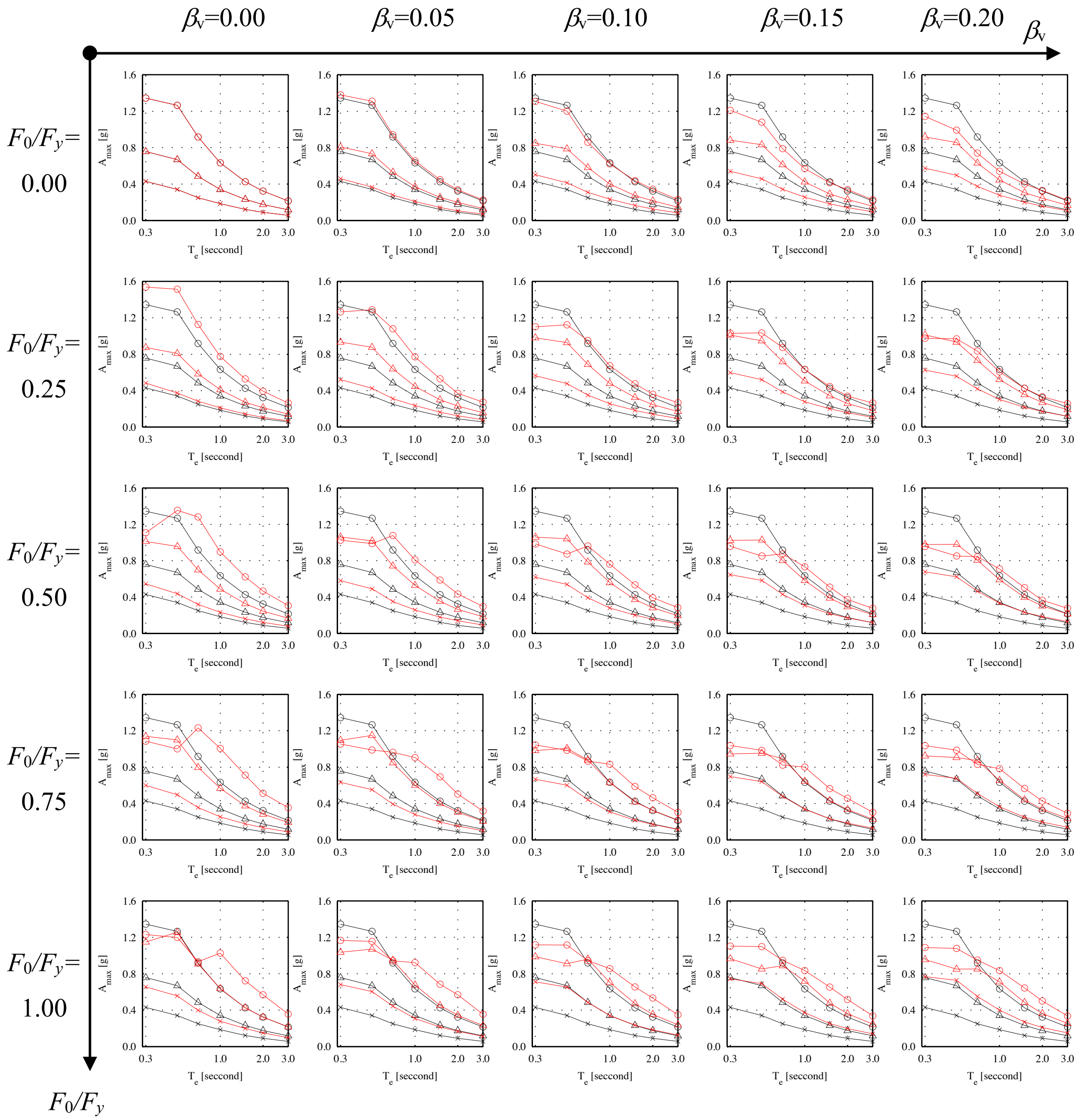

Figure A-37 Acceleration in MCE, Near-Fault Non-Pulse-like Motions, Non-linear Viscous Damping, Stiffness K_0=0, R_μ=1, 2 and 5

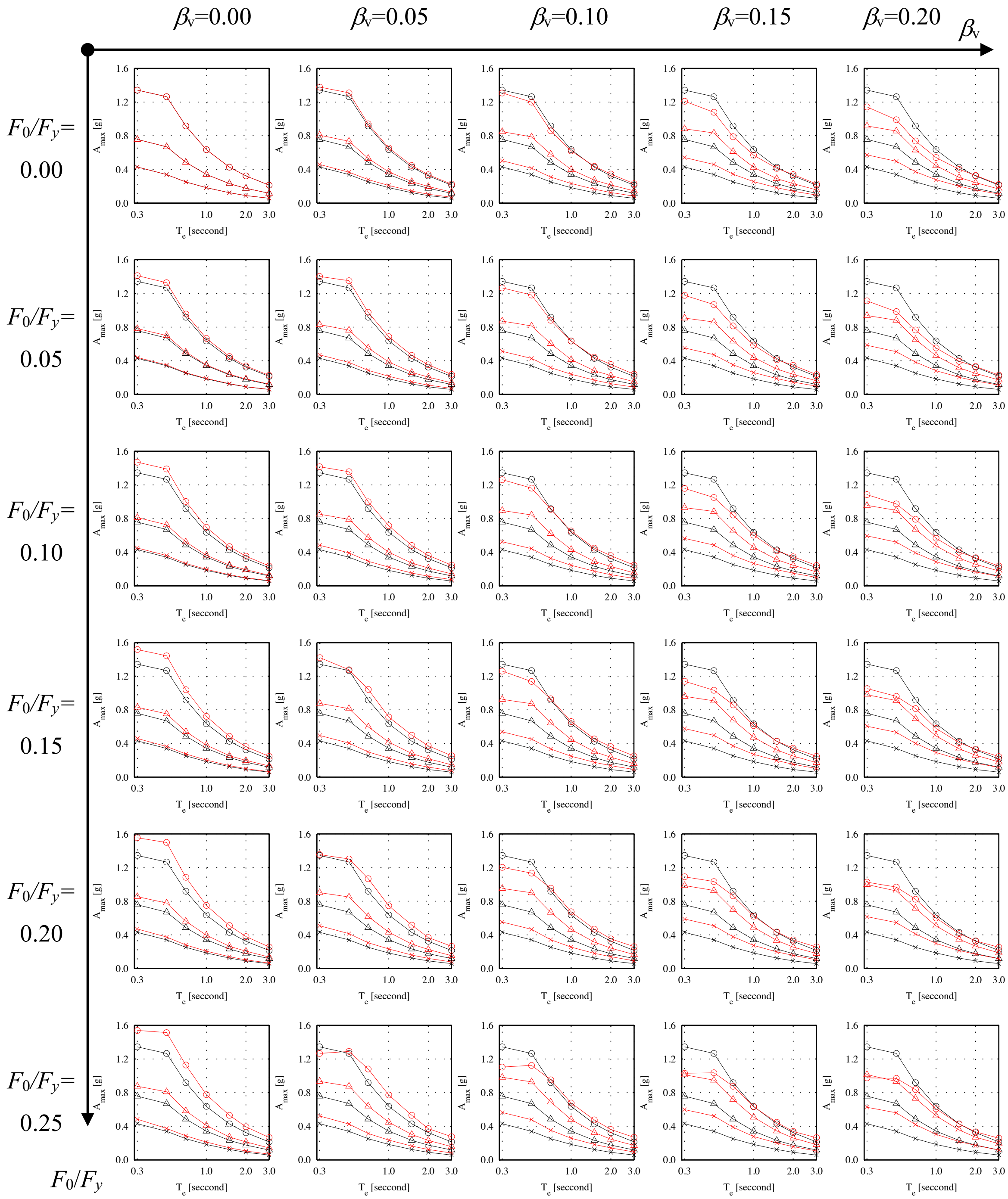

Figure A-37 (Continued)

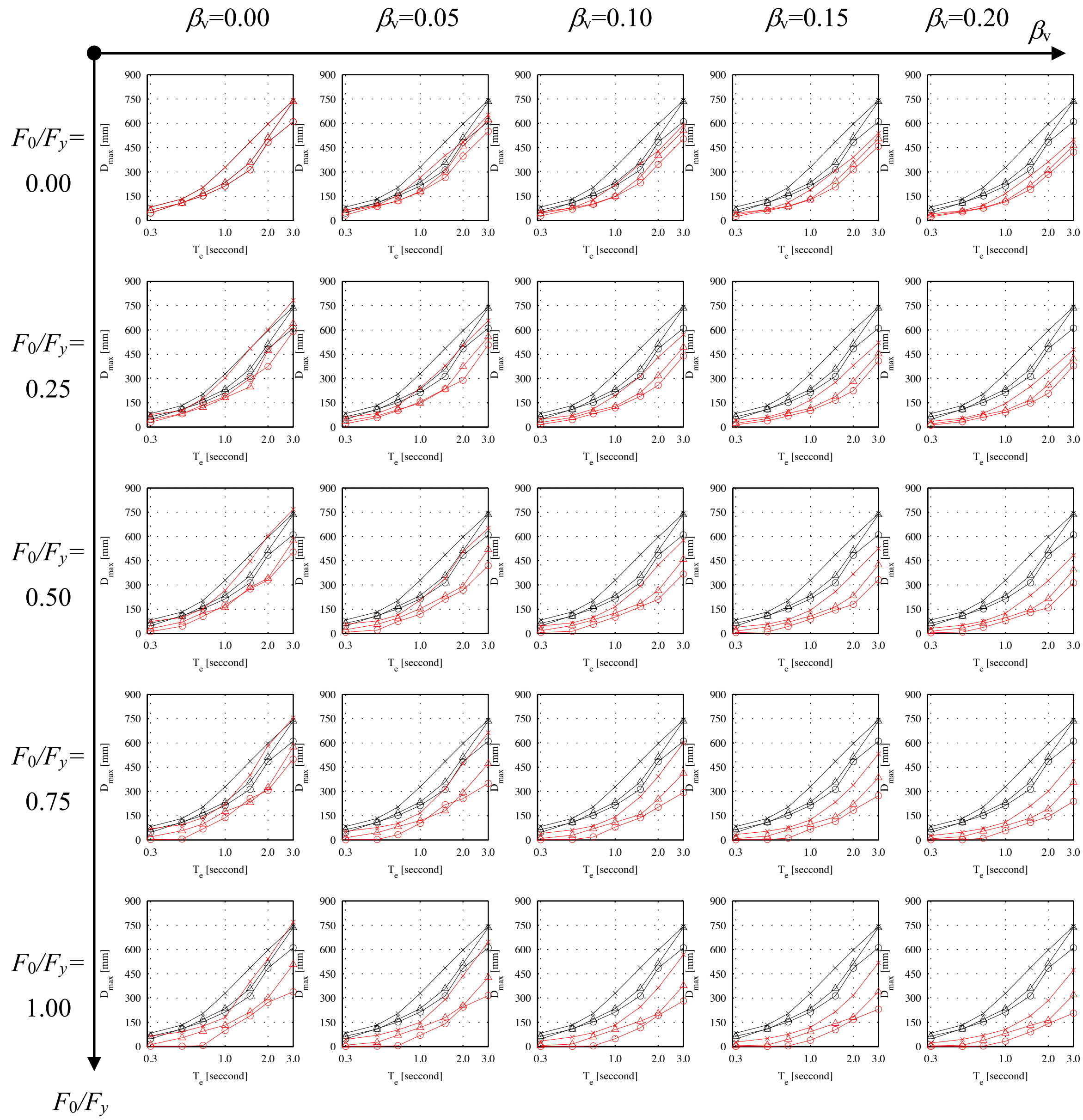

Figure A-38 Displacement in MCE, Near-Fault Non-Pulse-like Motions, Non-linear Viscous Damping, Stiffness K_0=0, R_μ=1, 2 and 5

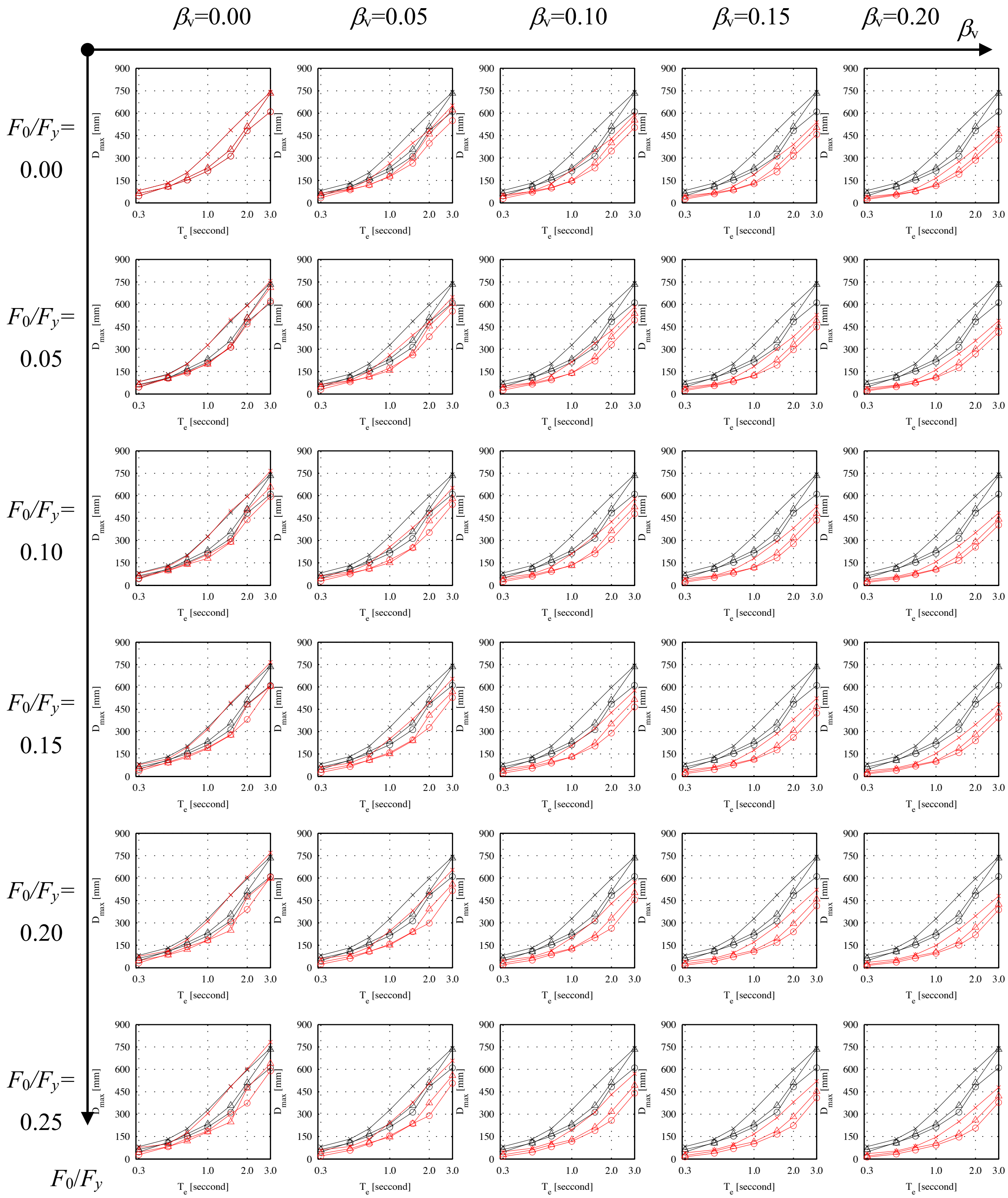

Figure A-38 (Continued)

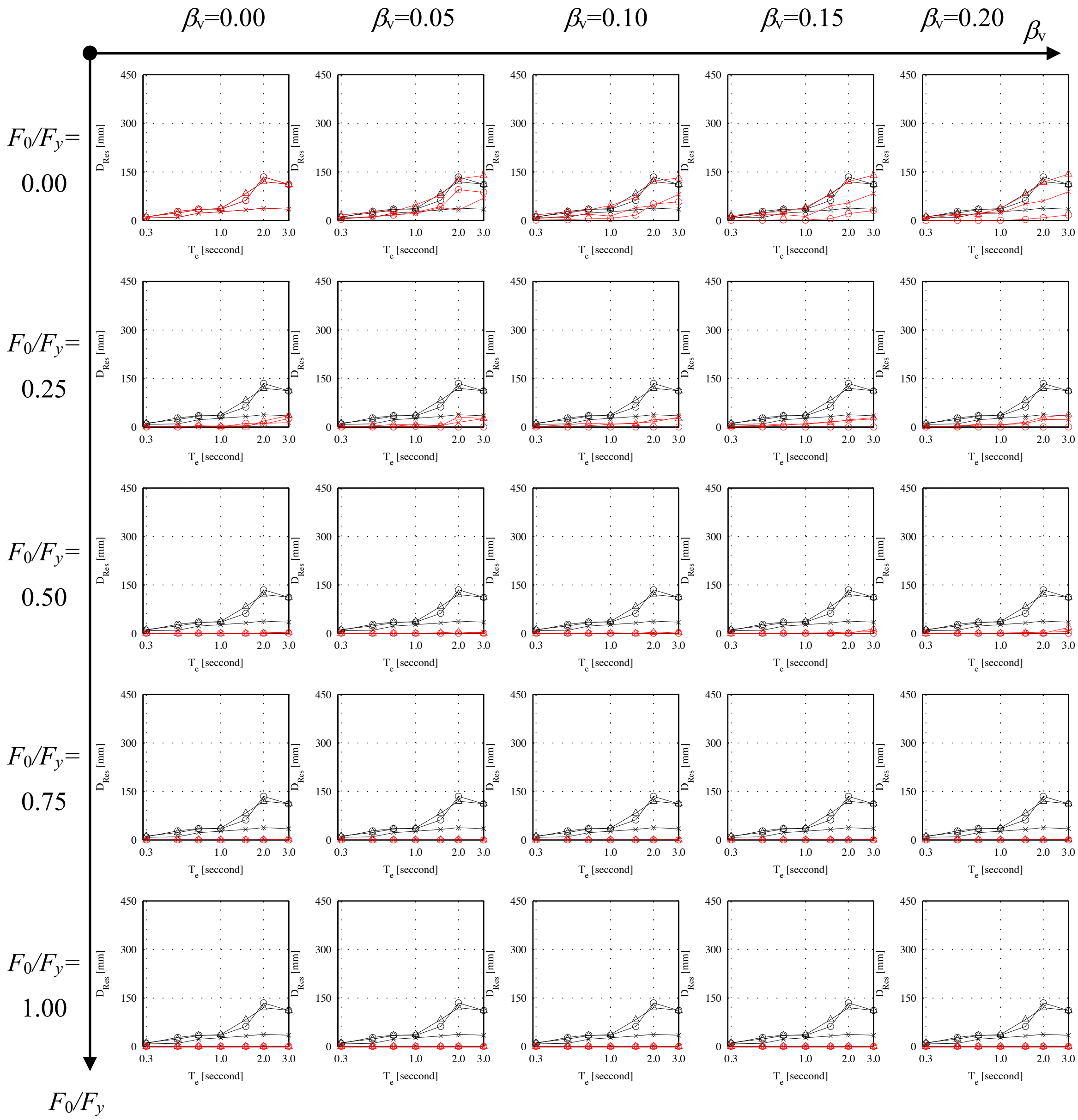

Figure A-39 Residual Displacement in MCE, Near-Fault Non-Pulse-like Motions, Non-linear Viscous Damping, Stiffness K_0=0, R_μ=1, 2 and 5

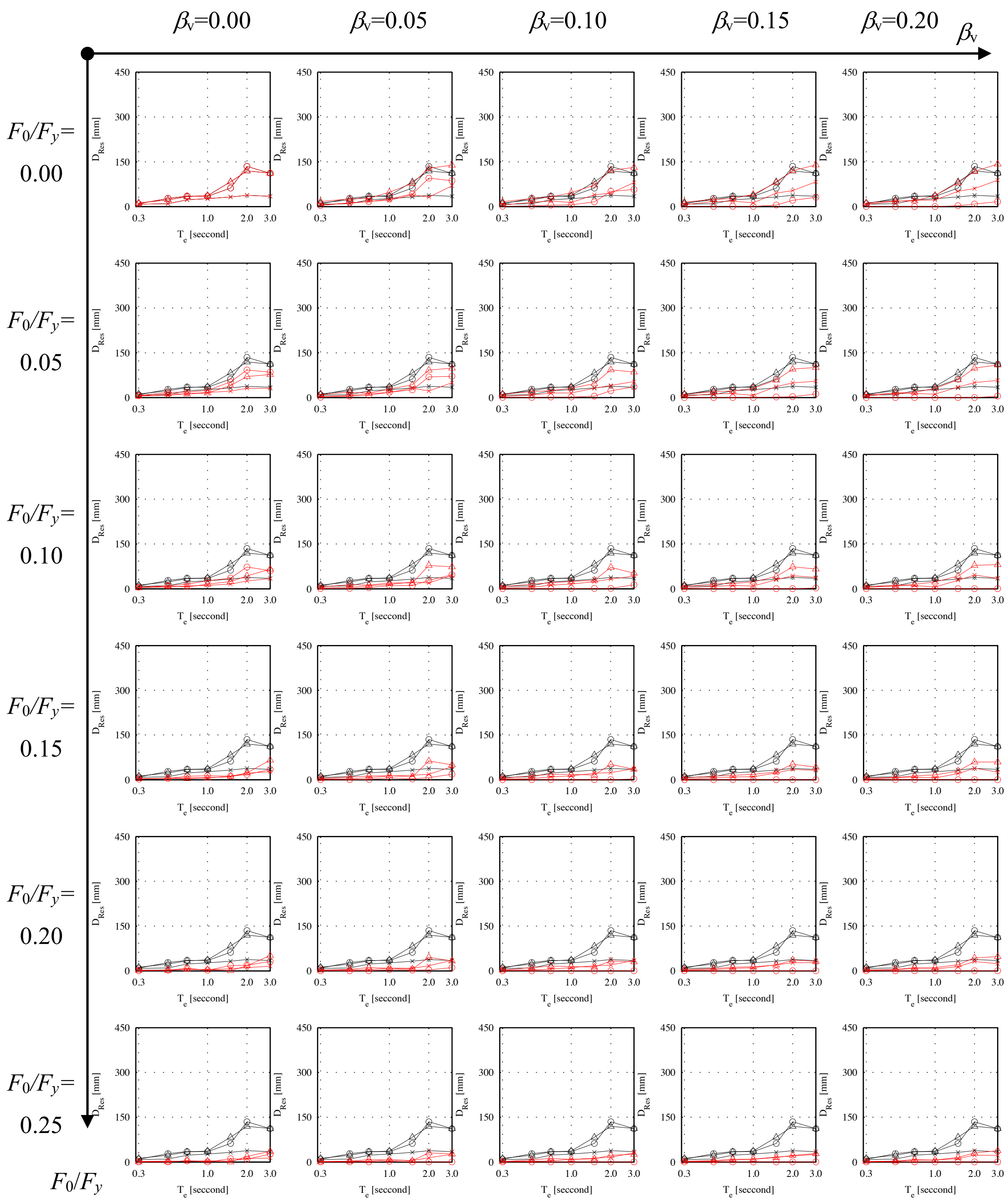

Figure A-39 (Continued)

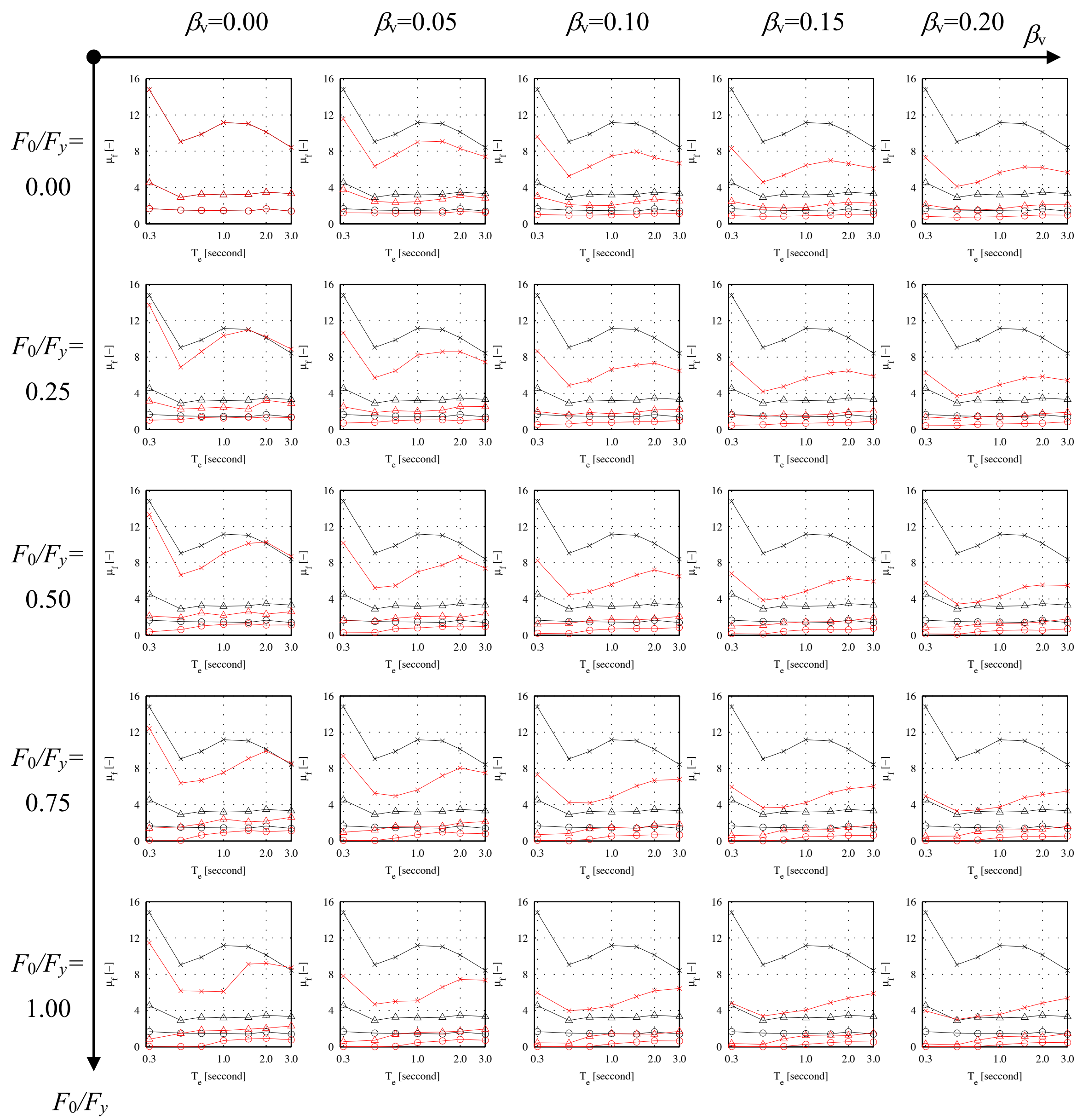

Figure A-40 Ductility Ratio in MCE, Near-Fault Non-Pulse-like Motions, Non-linear Viscous Damping, Stiffness K_0=0, R_μ=1, 2 and 5

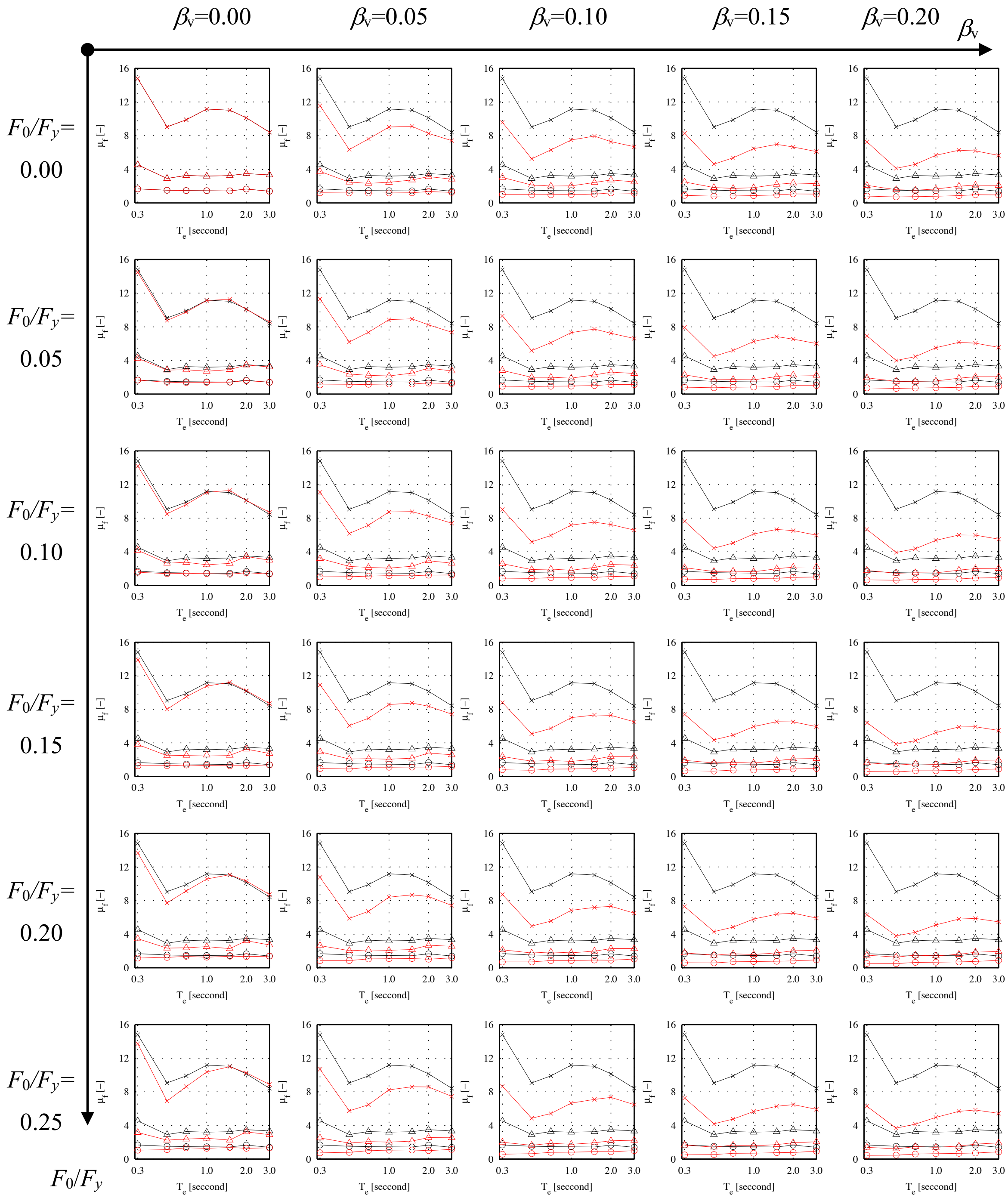

Figure A-40 (Continued)

A.2.3 Structure with Upper-Half Viscous Damping and K_0=0 in Near-Fault Non-Pulse-Like Ground Motions

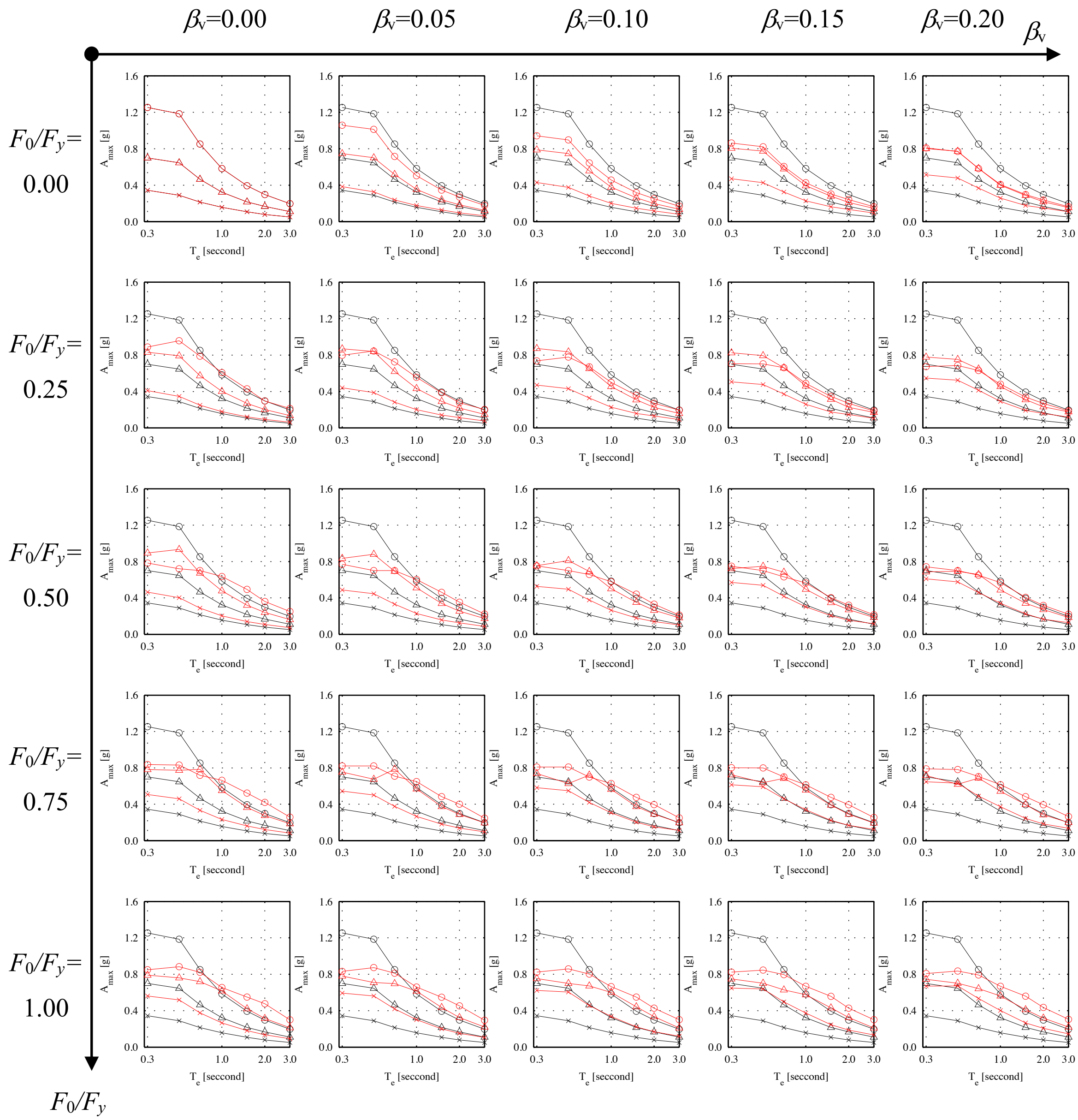

Figure A-41 Acceleration in DE, Near-Fault Non-Pulse-like Motions, Upper-half Viscous Damping, Stiffness K_0=0, R_μ=1, 2 and 5

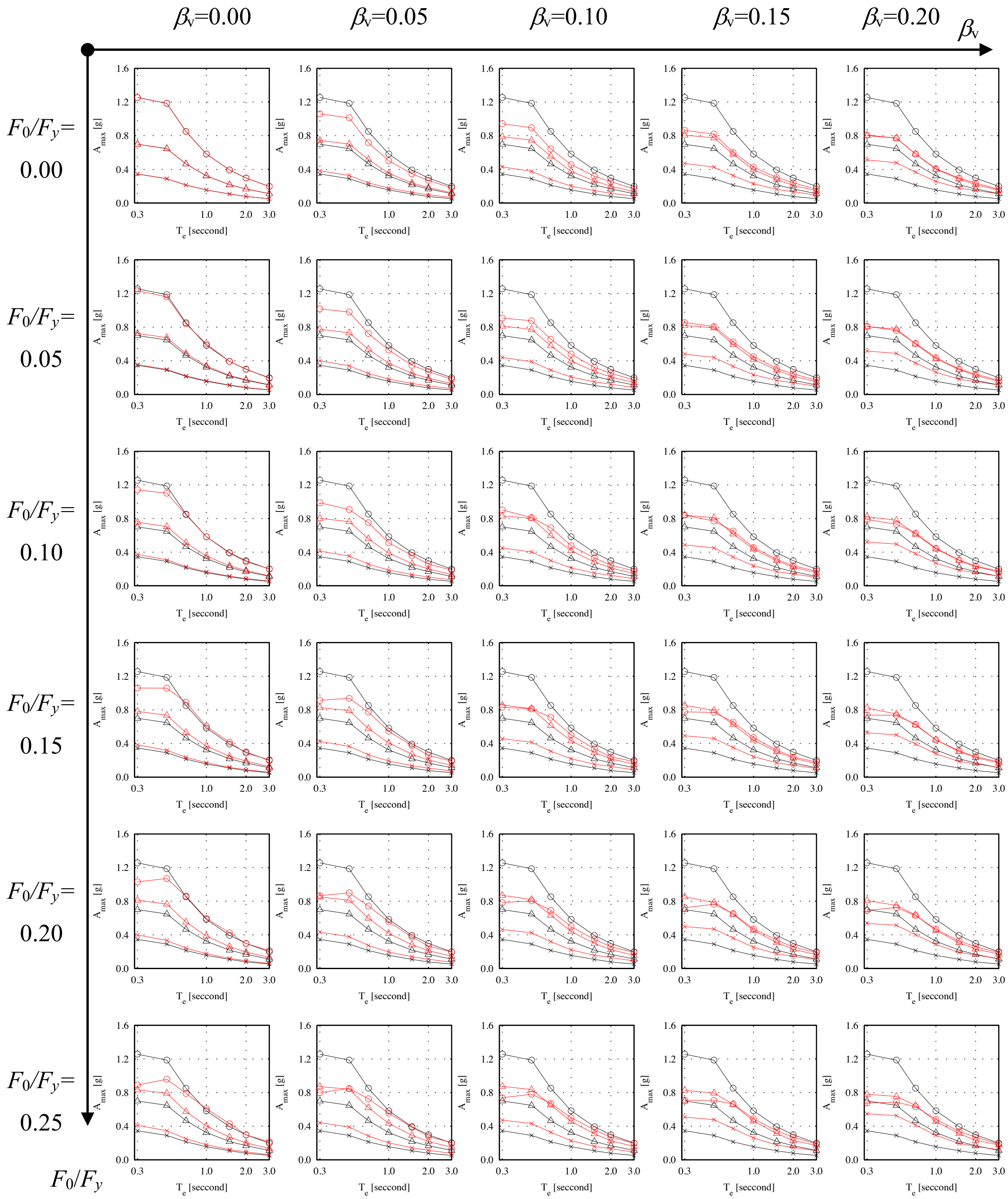

Figure A-41 (Continued)

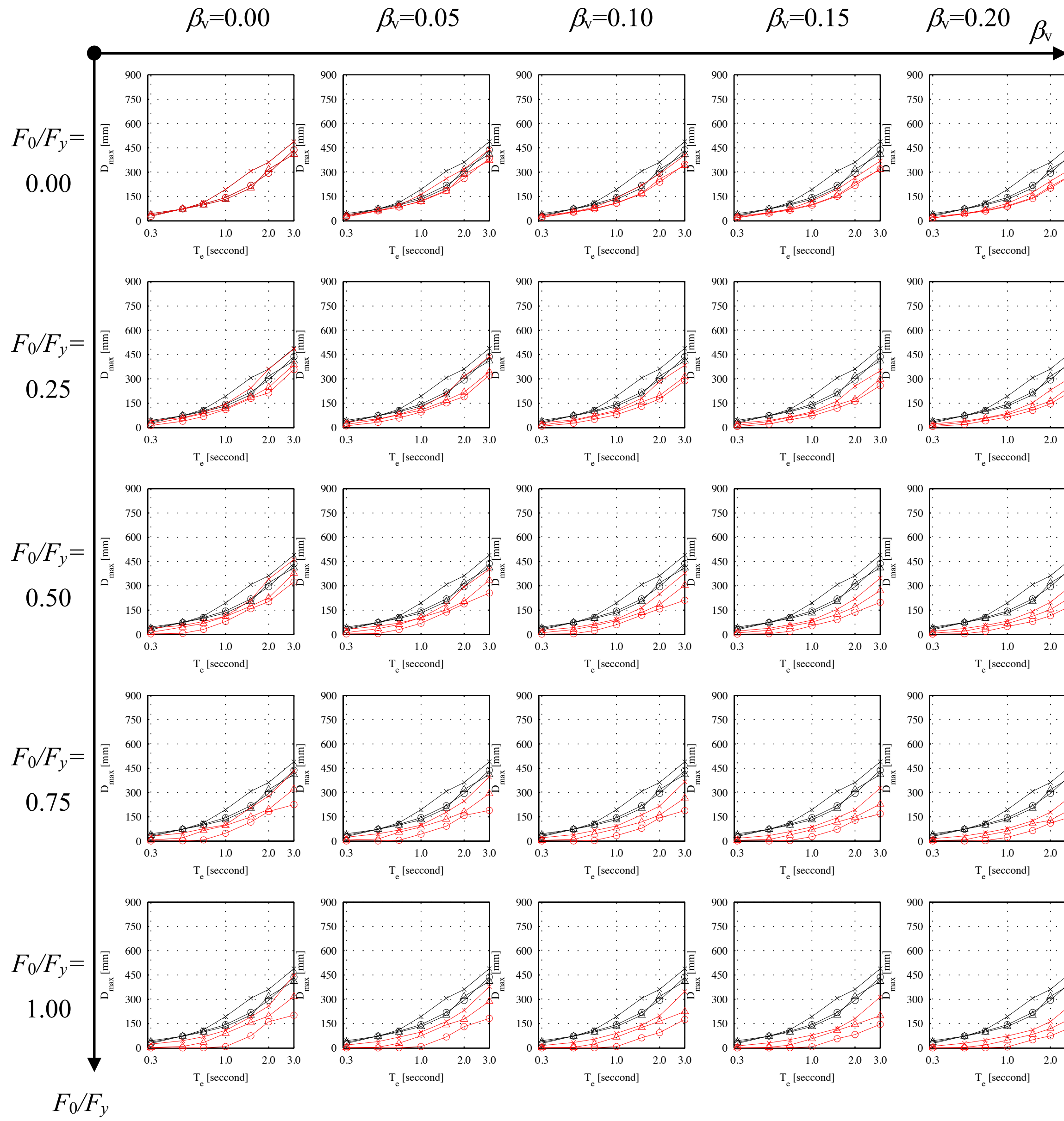

Figure A-42 Displacement in DE, Near-Fault Non-Pulse-like Motions, Upper-half Viscous Damping, Stiffness K_0=0, R_μ=1, 2 and 5

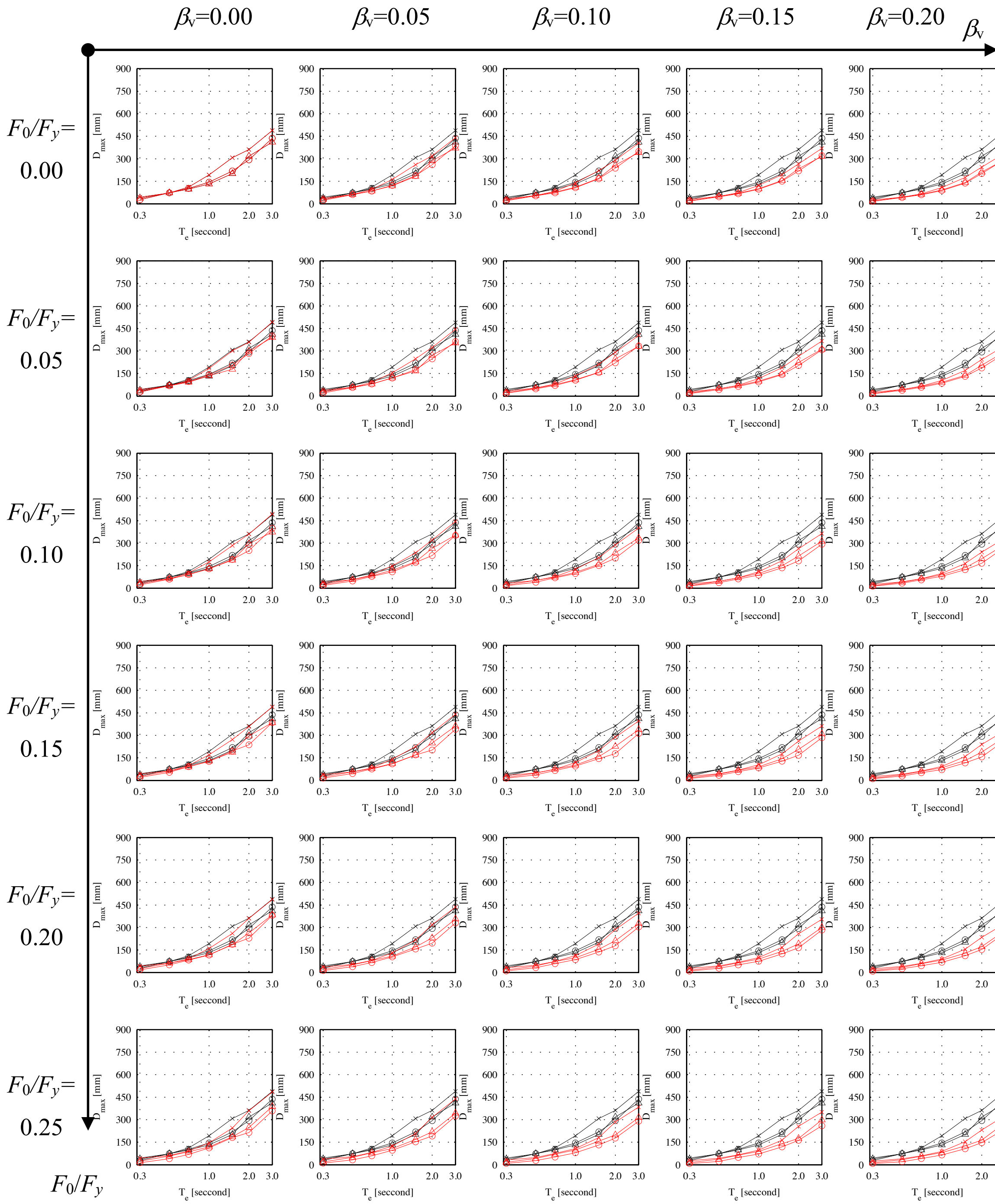

Figure A-42 (Continued)

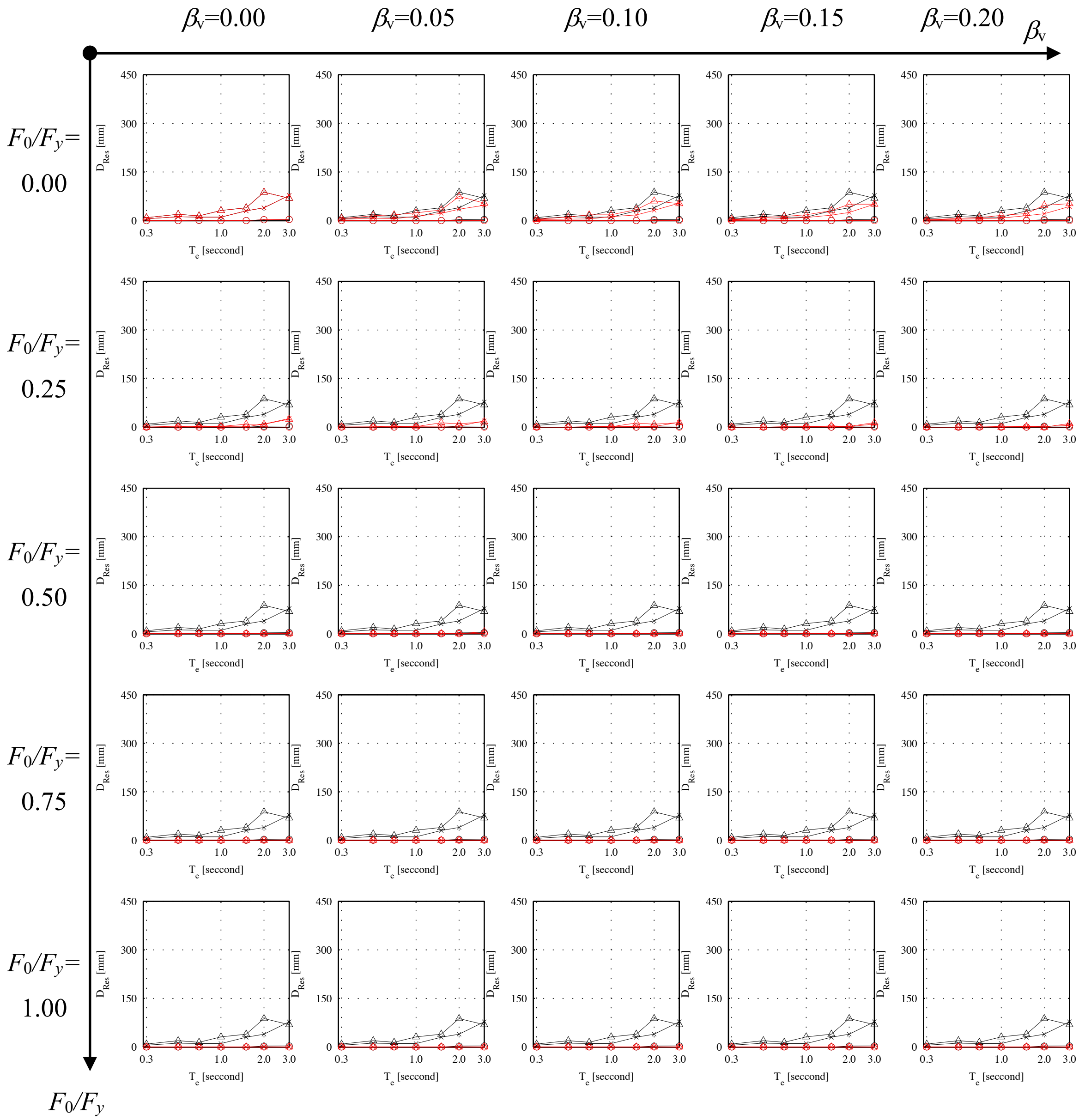

Figure A-43 Residual Displacement in DE, Near-Fault Non-Pulse-like Motions, Upper-half Viscous Damping, Stiffness K_0=0, R_μ=1, 2 and 5

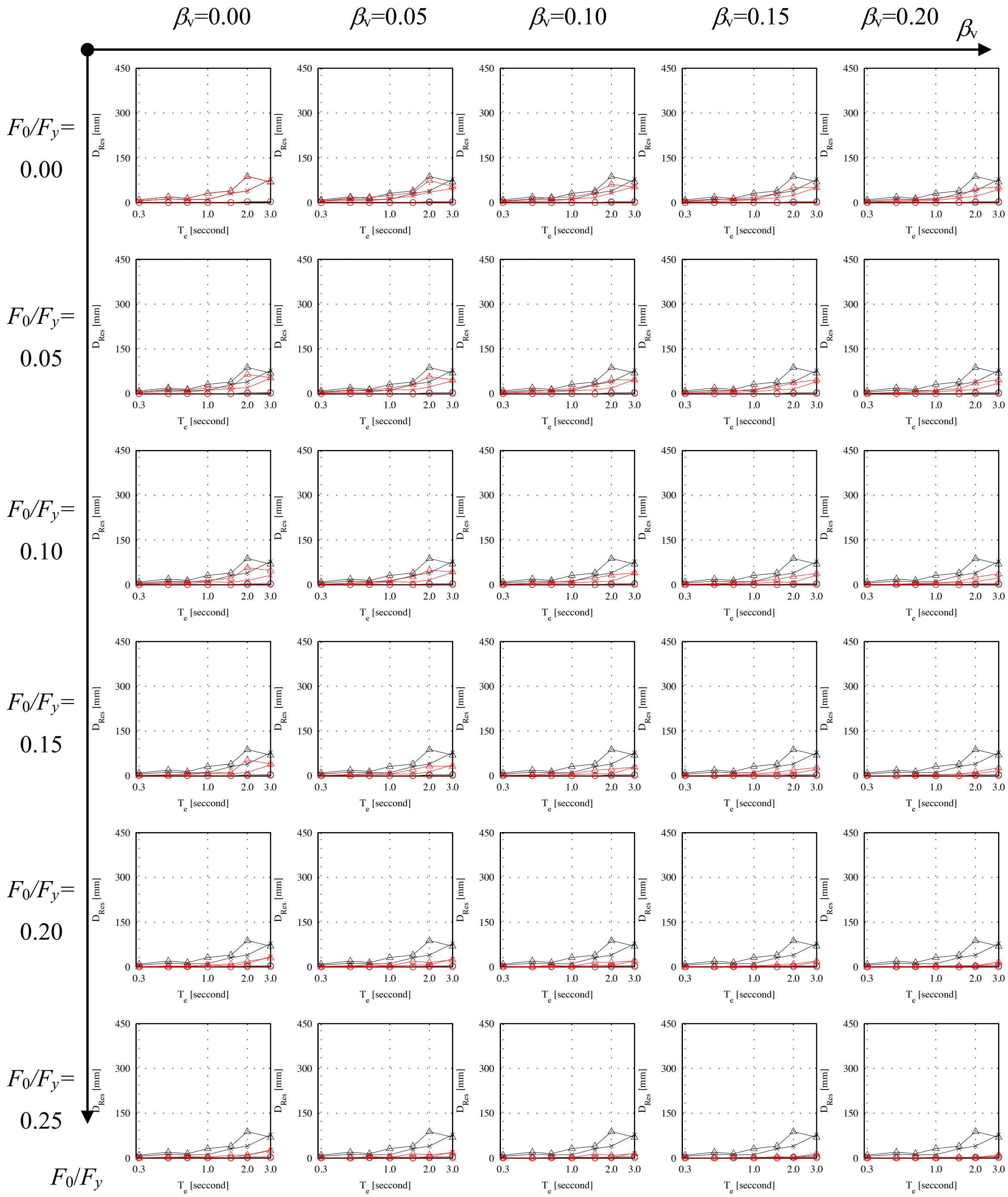

Figure A-43 (Continued)

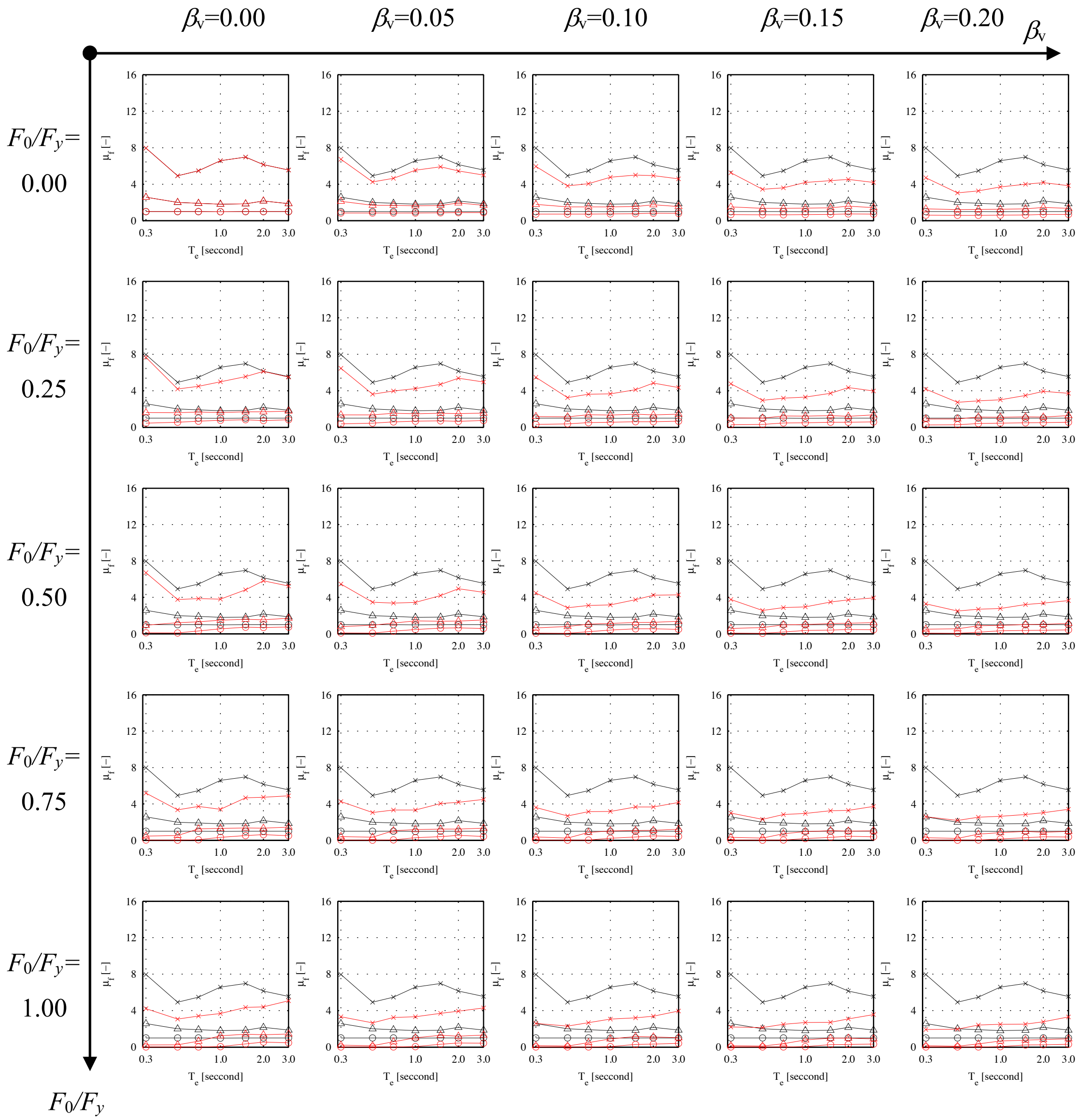

Figure A-44 Ductility Ratio in DE, Near-Fault Non-Pulse-like Motions, Upper-half Viscous Damping, Stiffness K_0=0, R_μ=1, 2 and 5

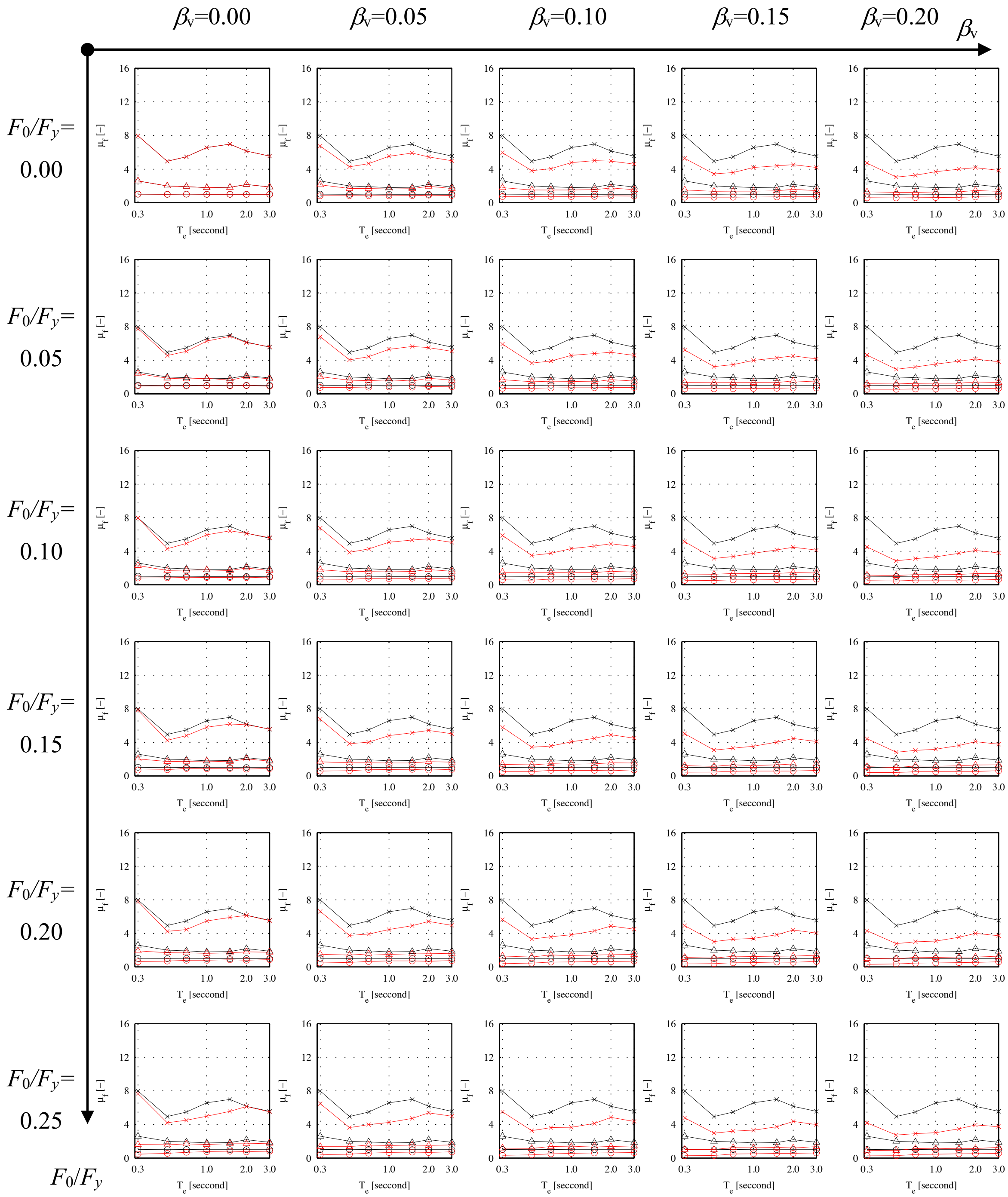

Figure A-44 (Continued)

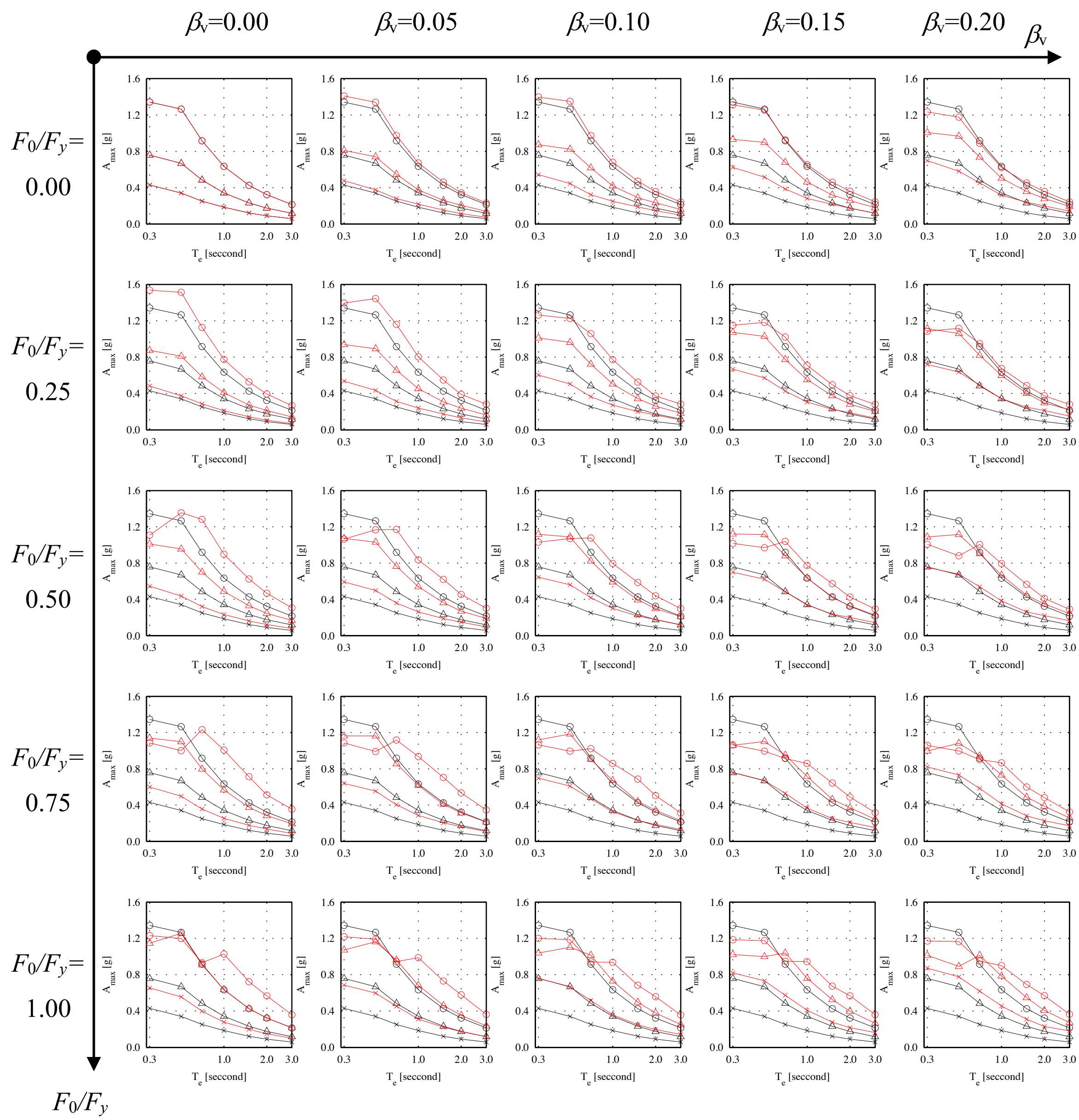

Figure A-45 Acceleration in MCE, Near-Fault Non-Pulse-like Motions, Upper-half Viscous Damping, Stiffness K_0=0, R_μ=1, 2 and 5

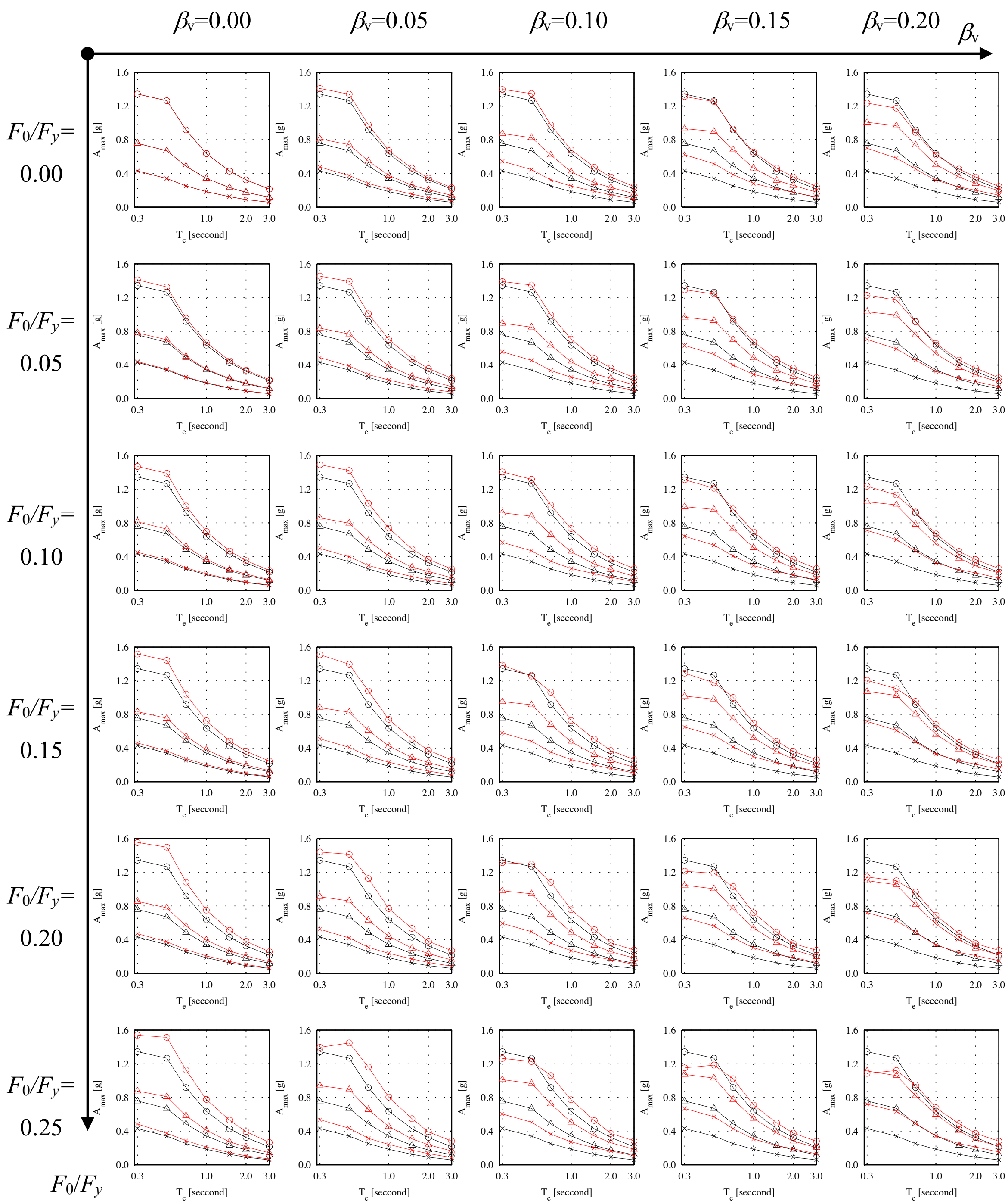

Figure A-45 (Continued)

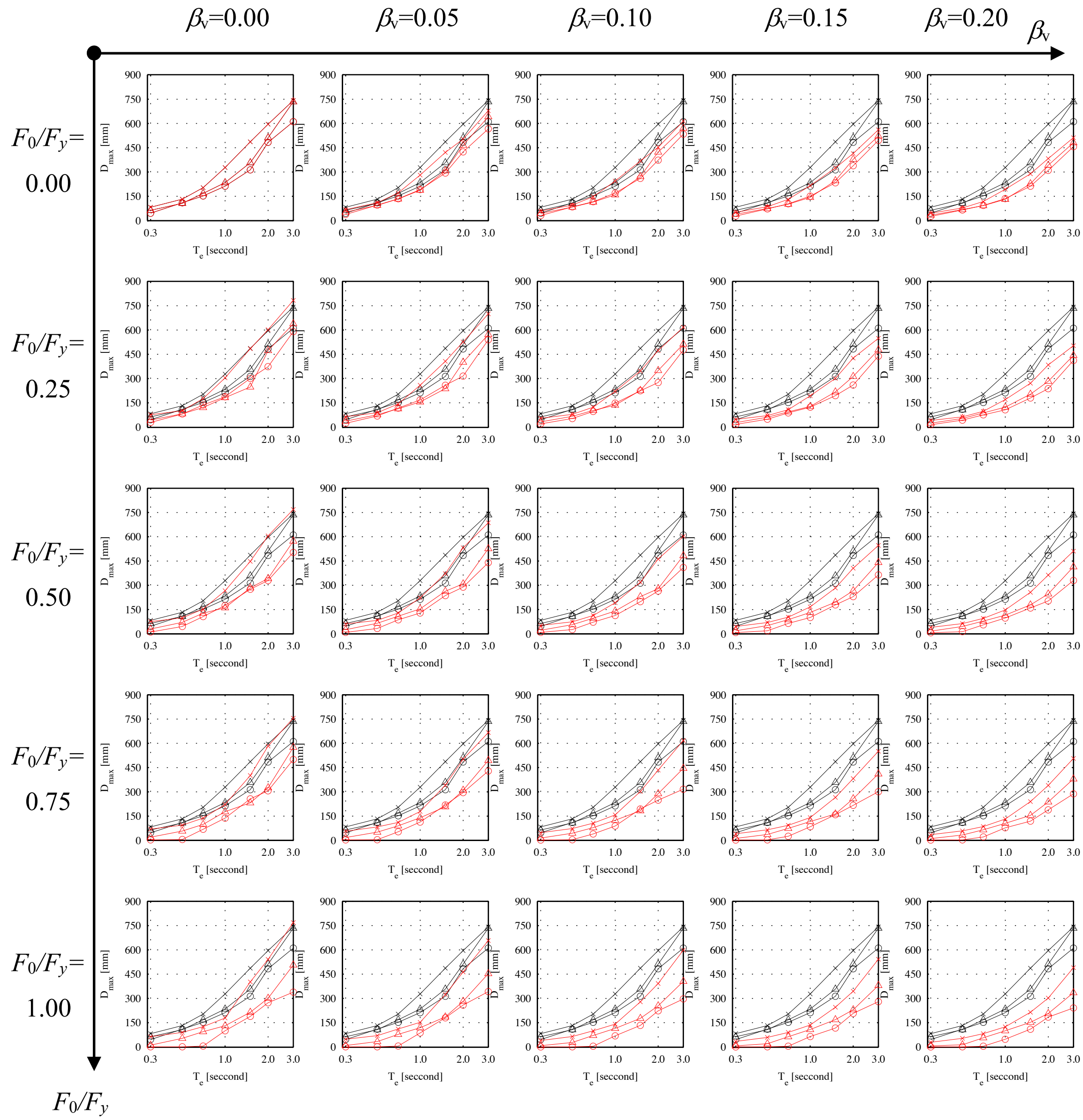

Figure A-46 Displacement in MCE, Near-Fault Non-Pulse-like Motions, Upper-half Viscous Damping, Stiffness K_0=0, R_μ=1, 2 and 5

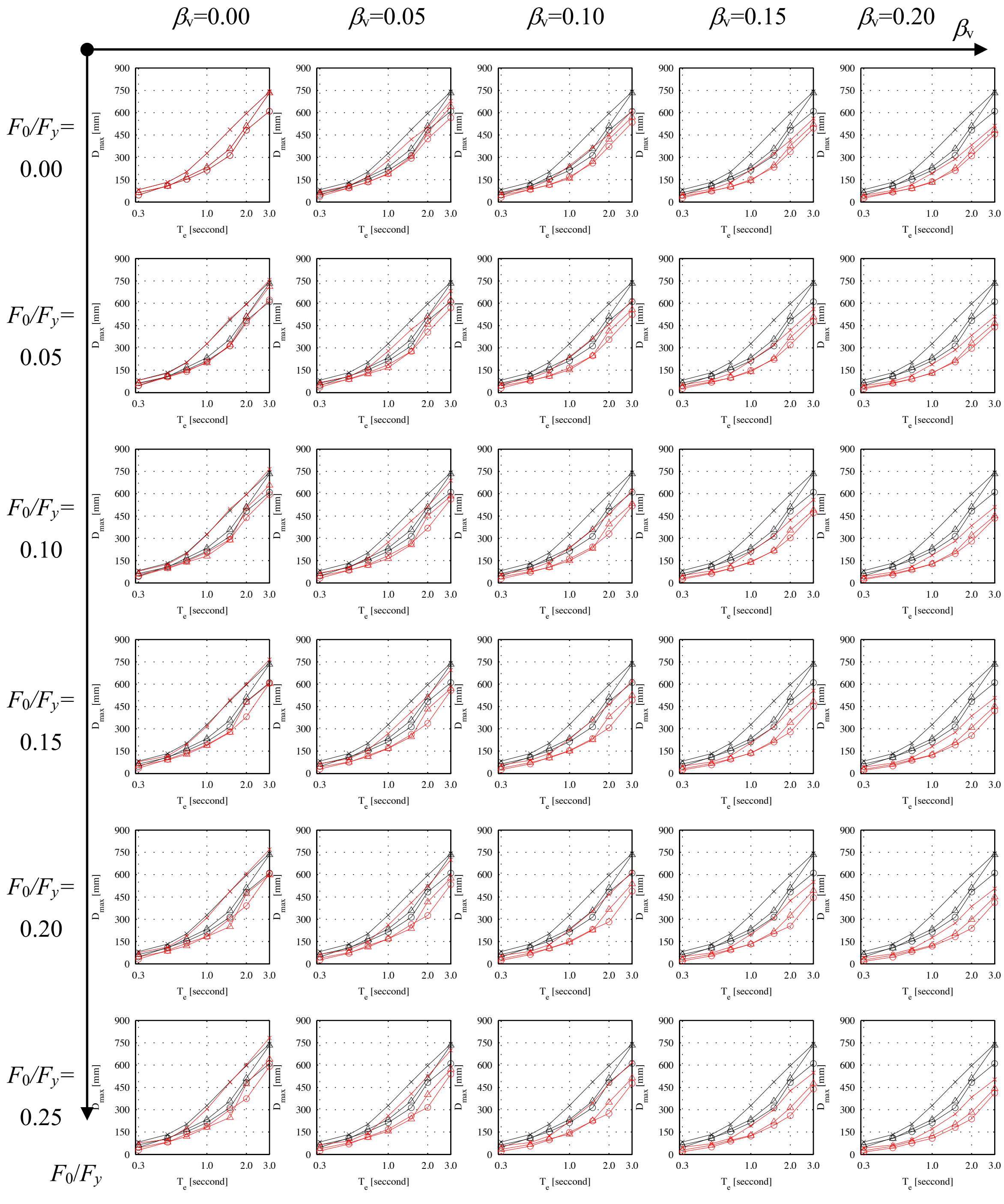

Figure A-46 (Continued)

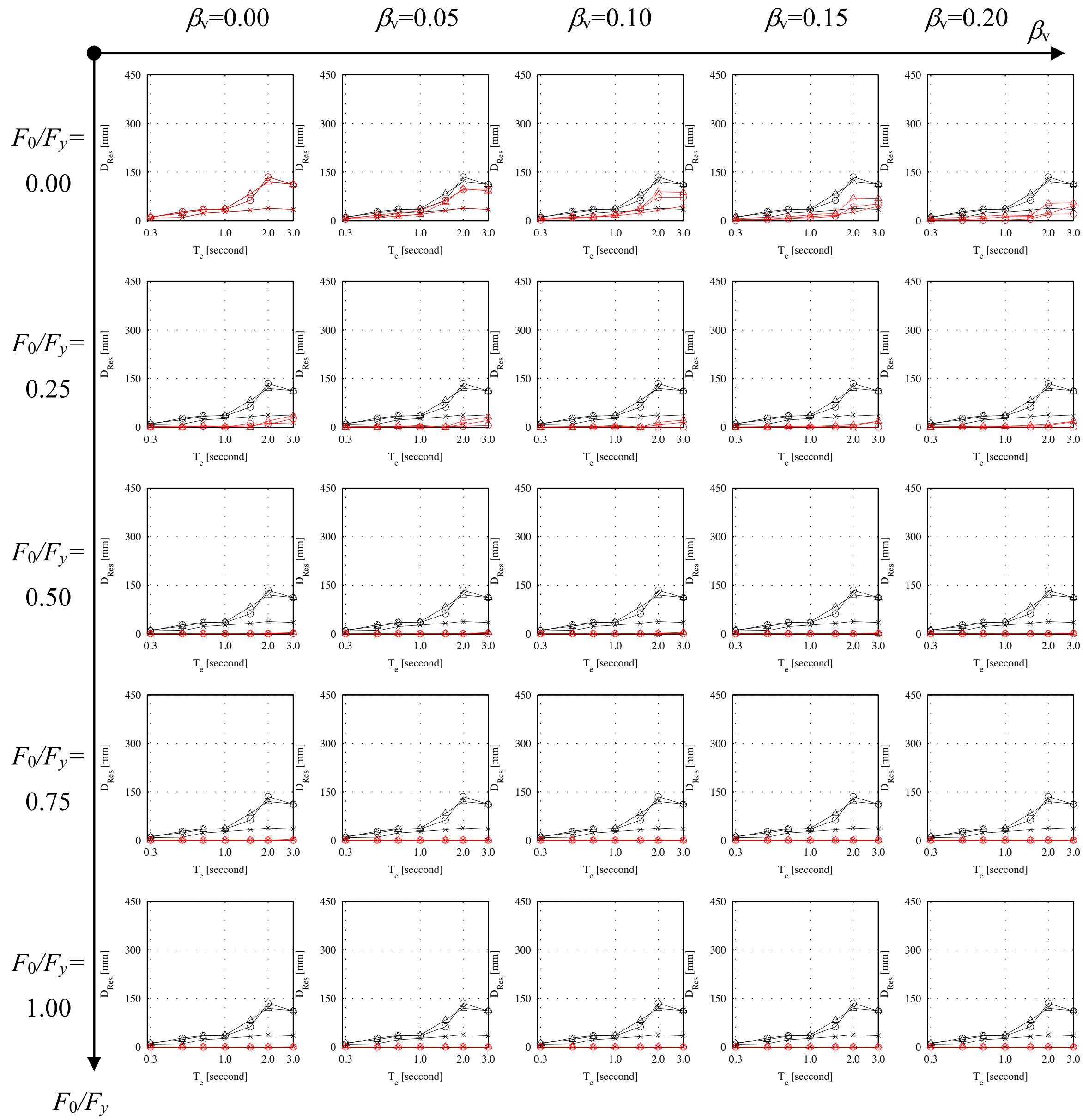

Figure A-47 Residual Displacement in MCE, Near-Fault Non-Pulse-like Motions, Upper-half Viscous Damping, Stiffness K_0=0, R_μ=1, 2 and 5

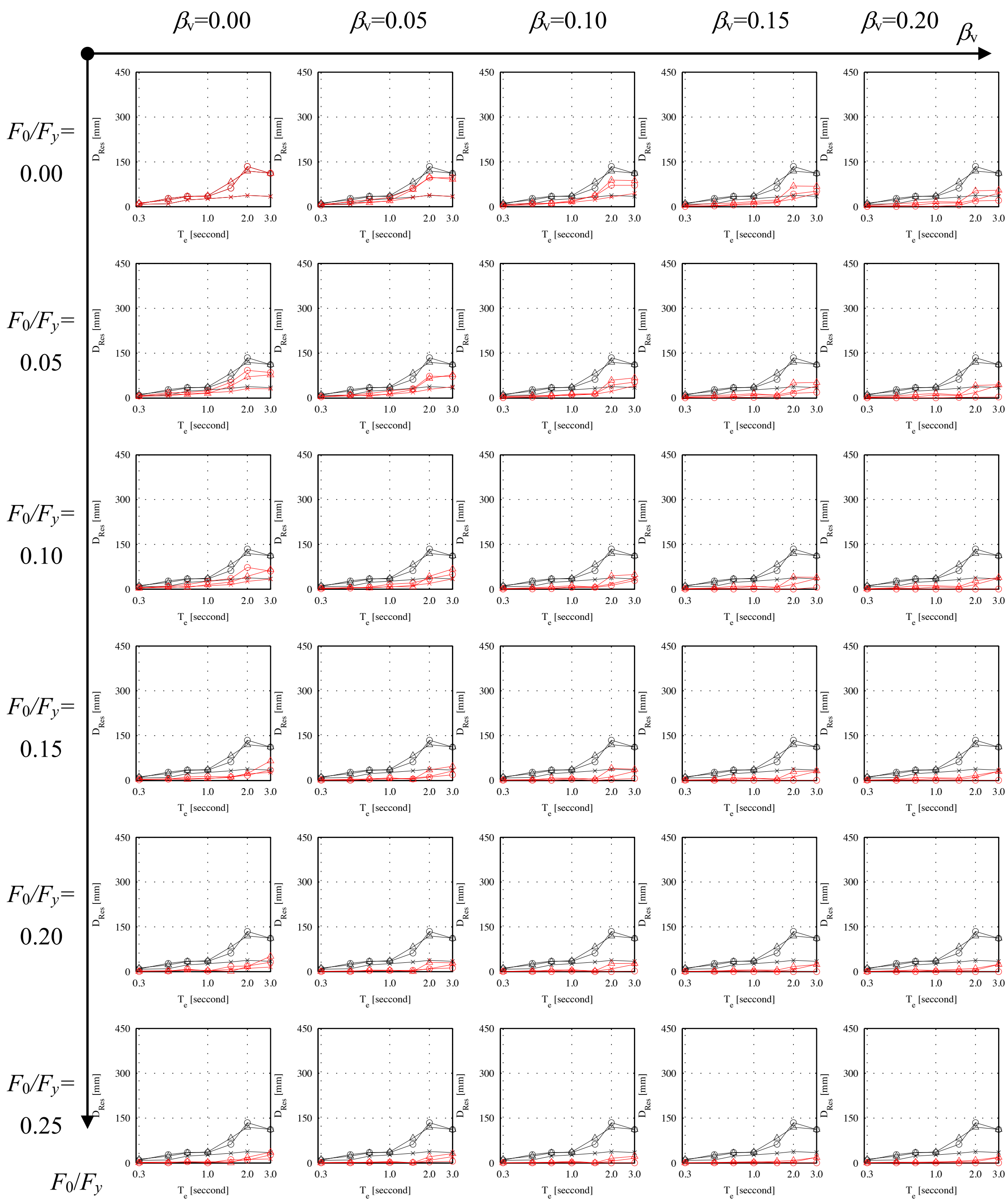

Figure A-47 (Continued)

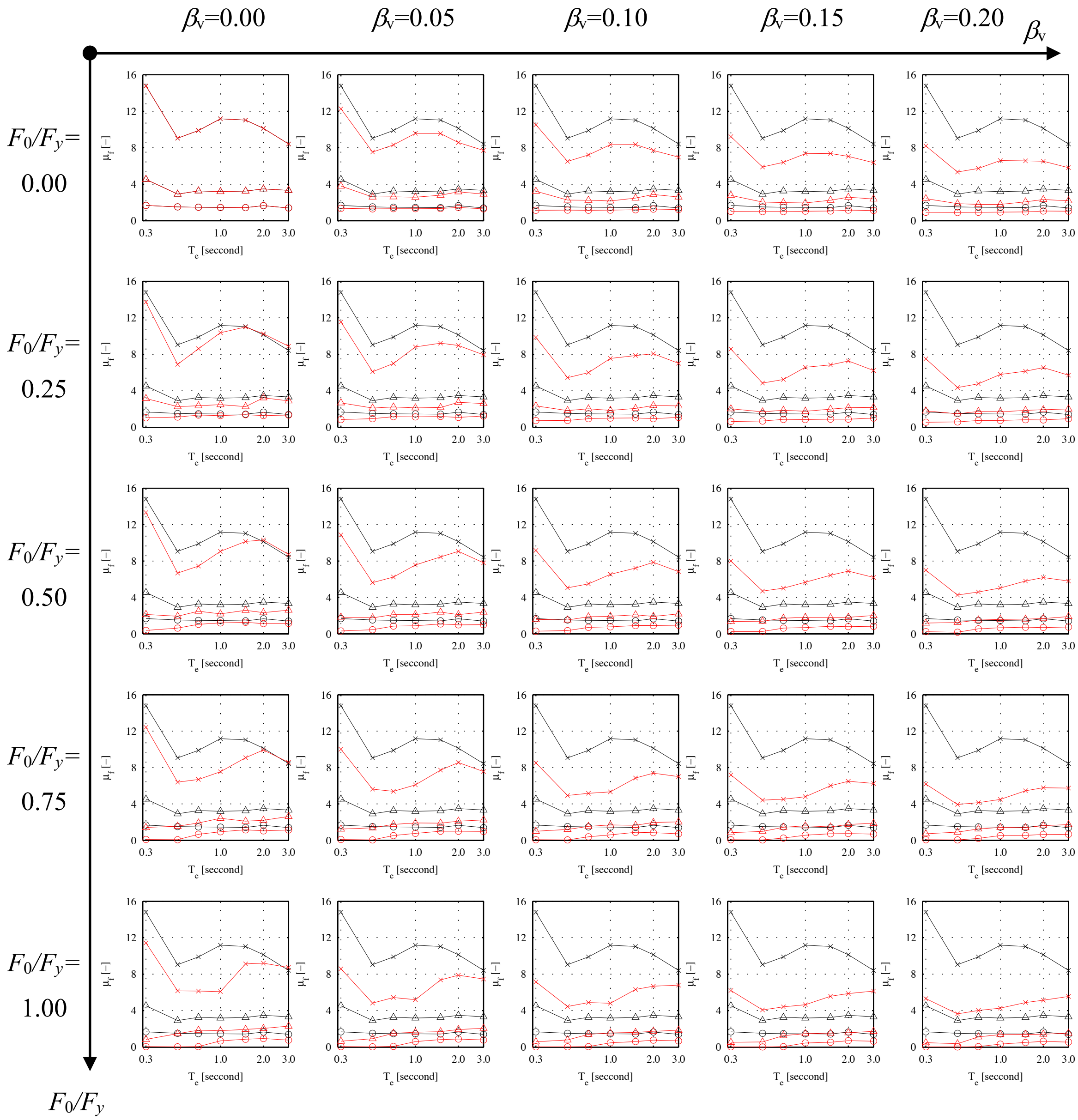

Figure A-48 Ductility Ratio in MCE, Near-Fault Non-Pulse-like Motions, Upper-half Viscous Damping, Stiffness K_0=0, R_μ=1, 2 and 5

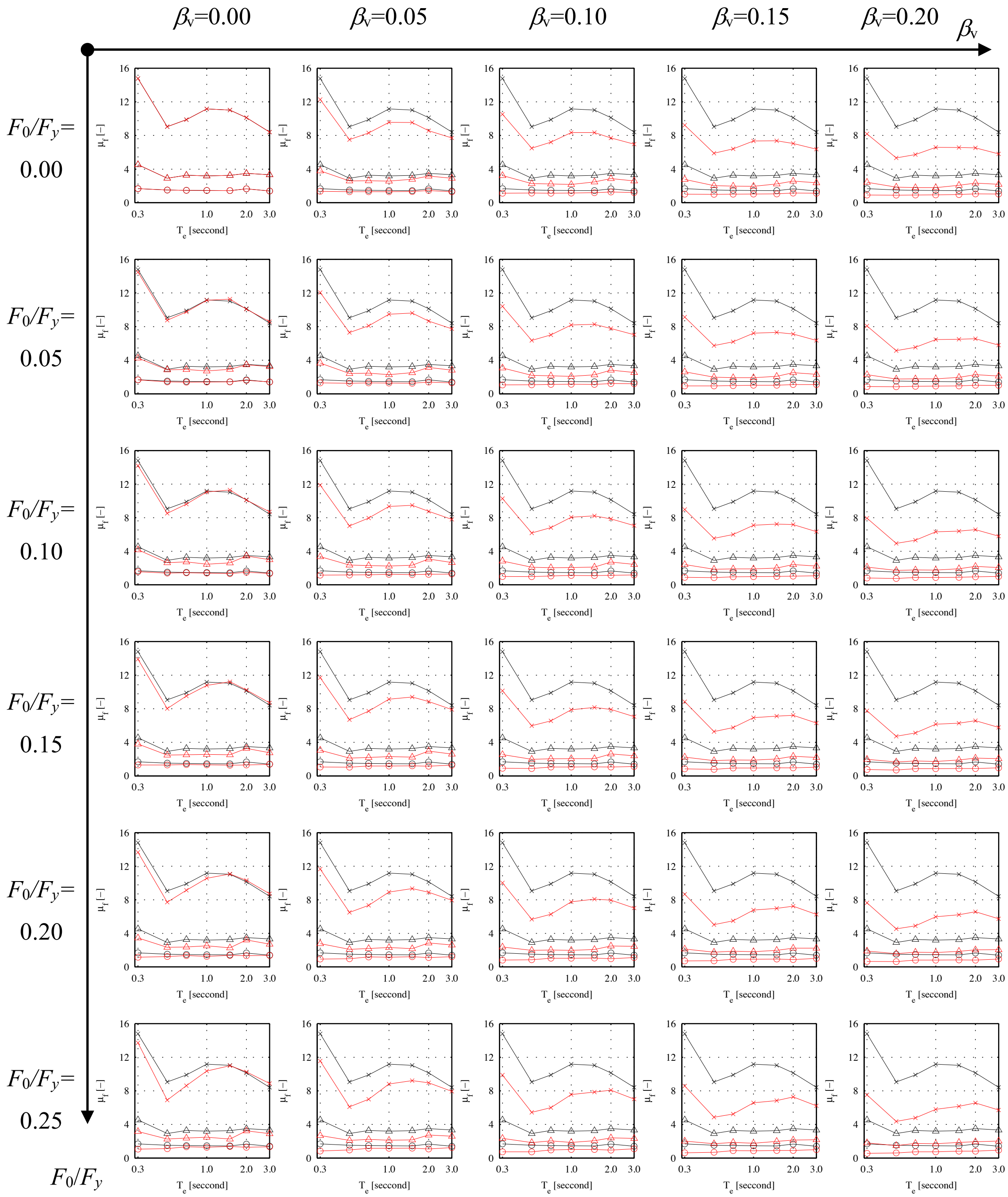

Figure A-48 (Continued)

A.3 Seismic Response under Far-Field Ground Motions

A.3.1 Structure with Linear Viscous Damping and K_0=0 for Far-Field Ground Motions

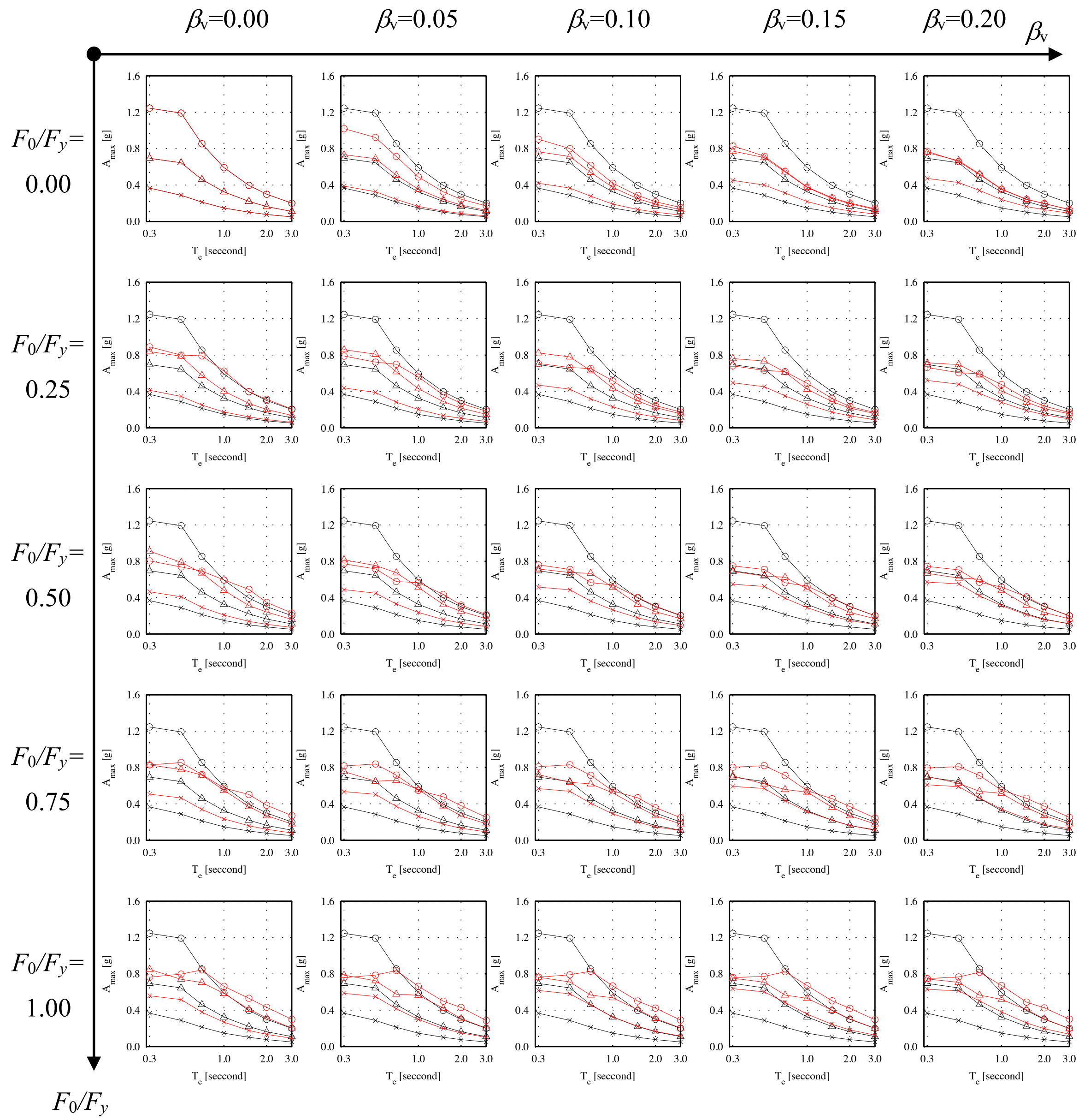

Figure A-49 Acceleration in DE, Far-Field Motions, Linear Viscous Damping, Stiffness K_0=0, R_μ=1, 2 and 5

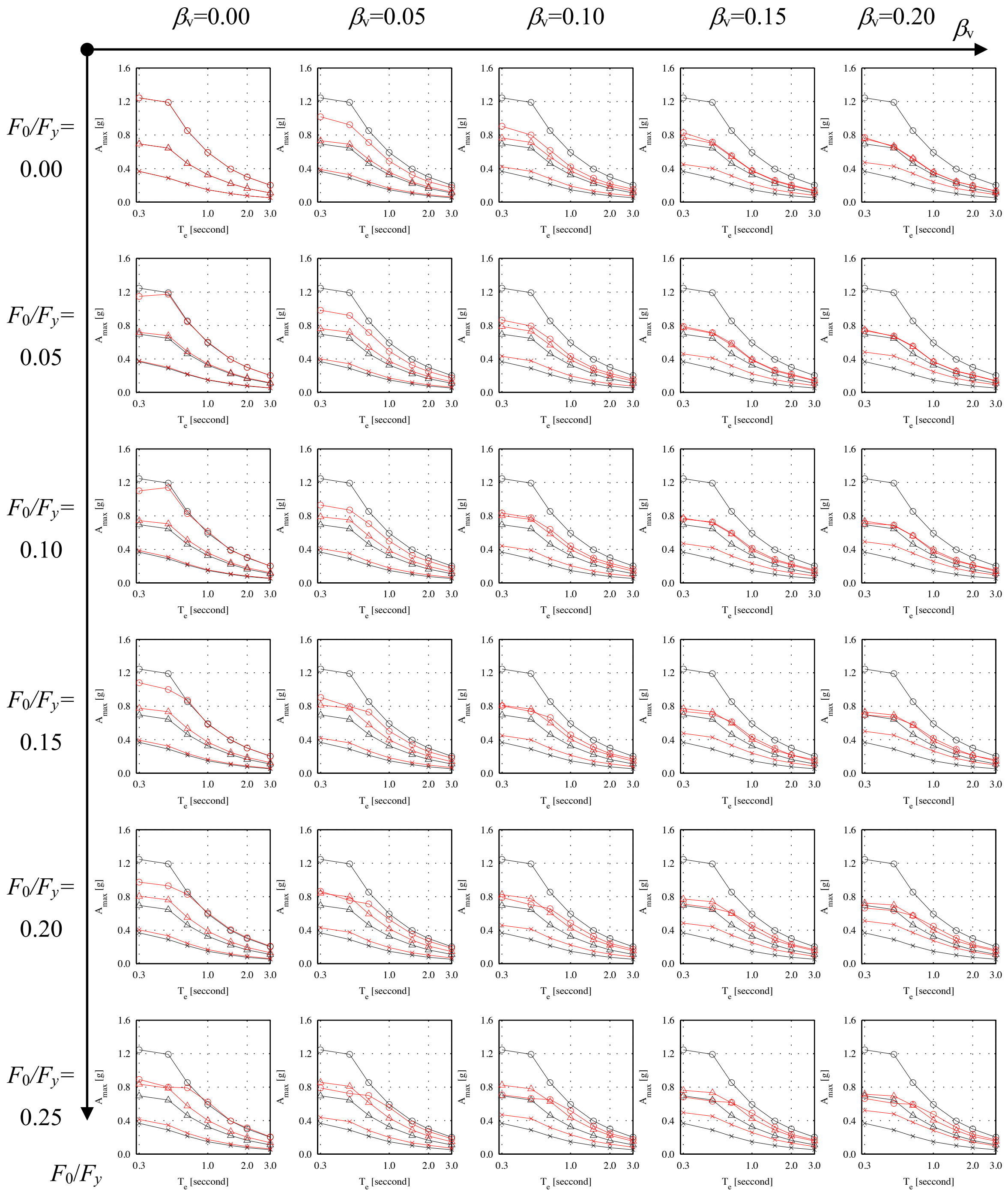

Figure A-49 (Continued)

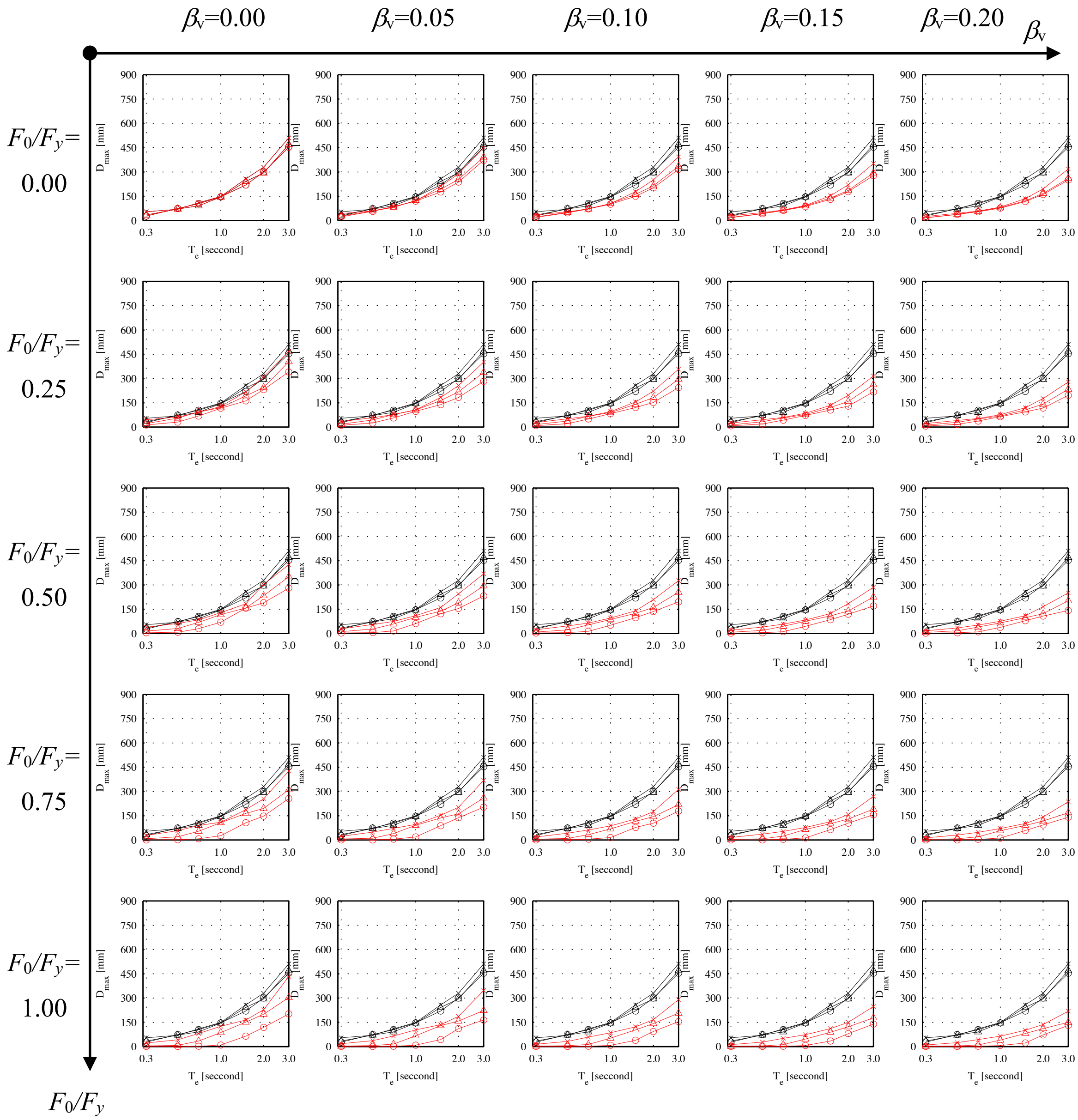

Figure A-50 Displacement in DE, Far-Field Motions, Linear Viscous Damping, Stiffness K_0=0, R_μ=1, 2 and 5

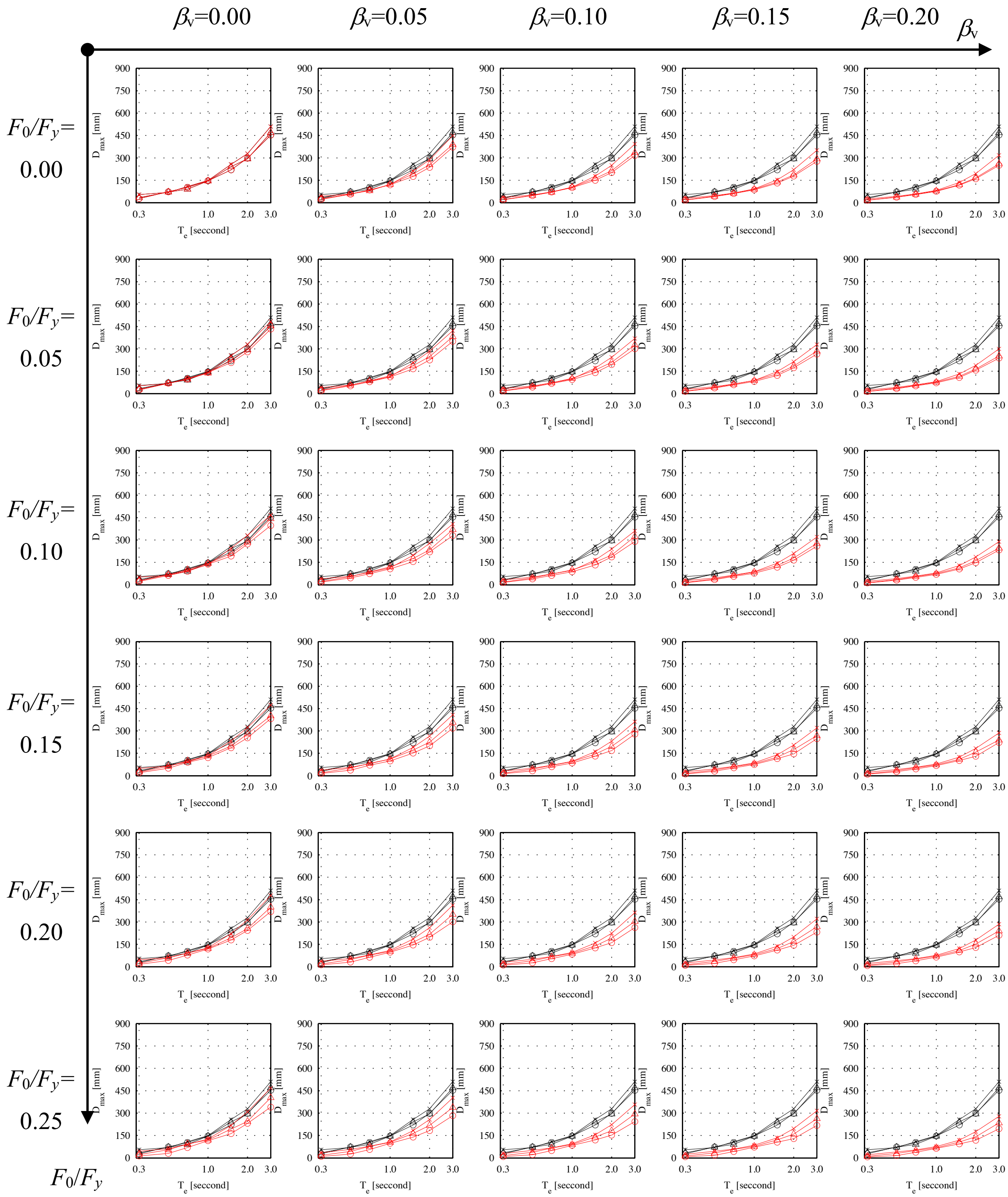

Figure A-50 (Continued)

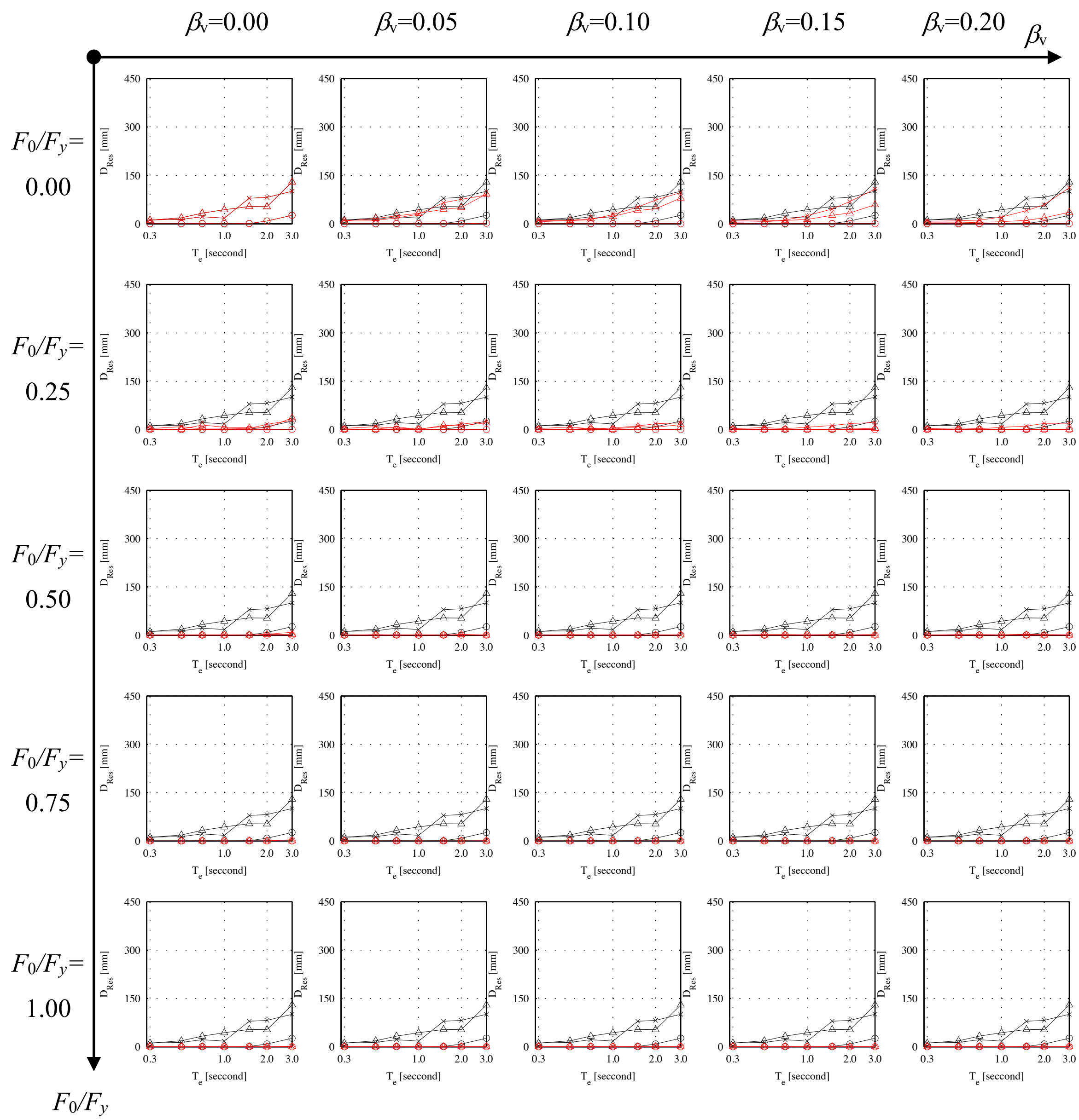

Figure A-51 Residual Displacement in DE, Far-Field Motions, Linear Viscous Damping, Stiffness K_0=0, R_μ=1, 2 and 5

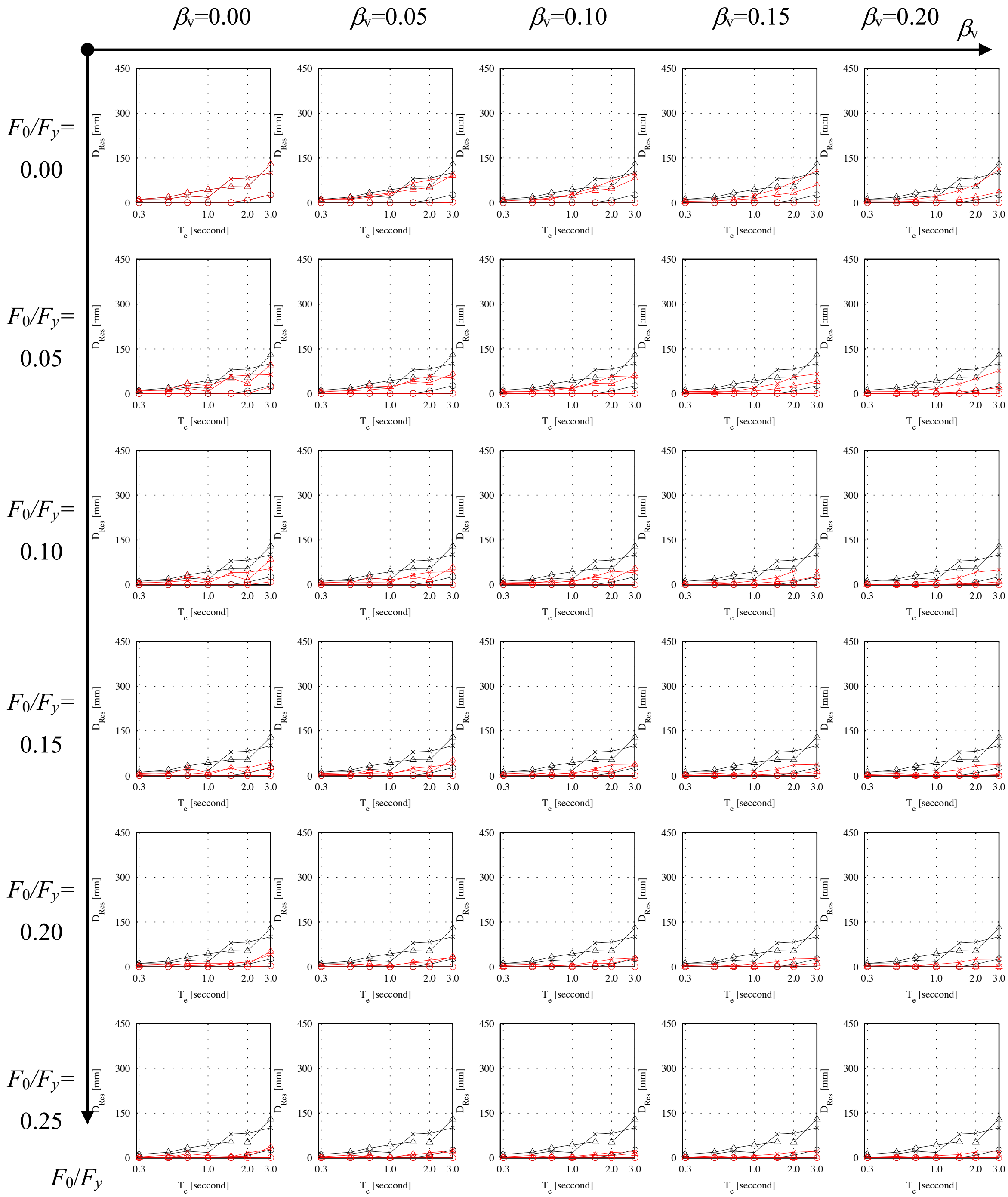

Figure A-51 (Continued)

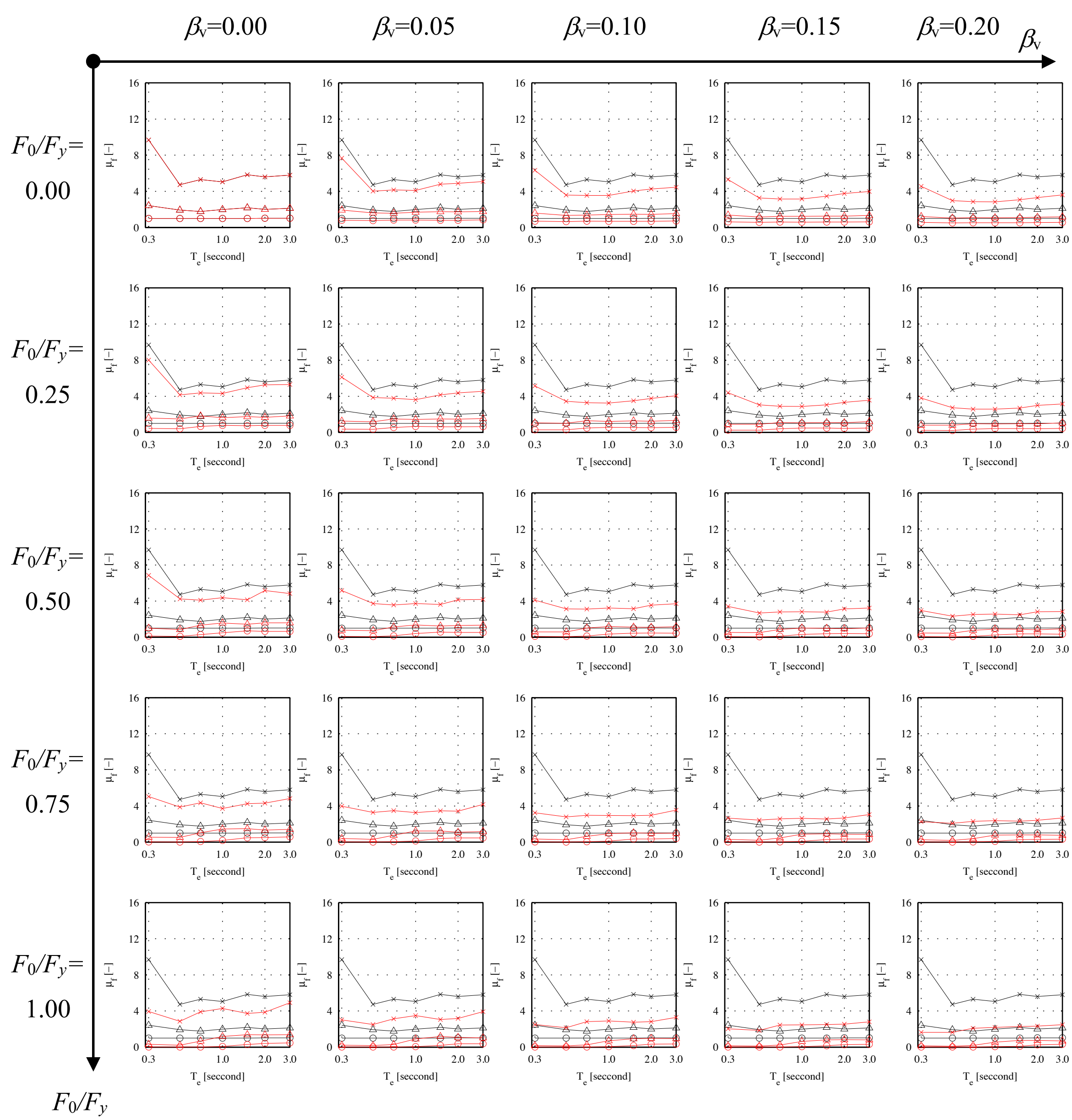

Figure A-52 Ductility Ratio in DE, Far-Field Motions, Linear Viscous Damping, Stiffness K_0=0, R_μ=1, 2 and 5

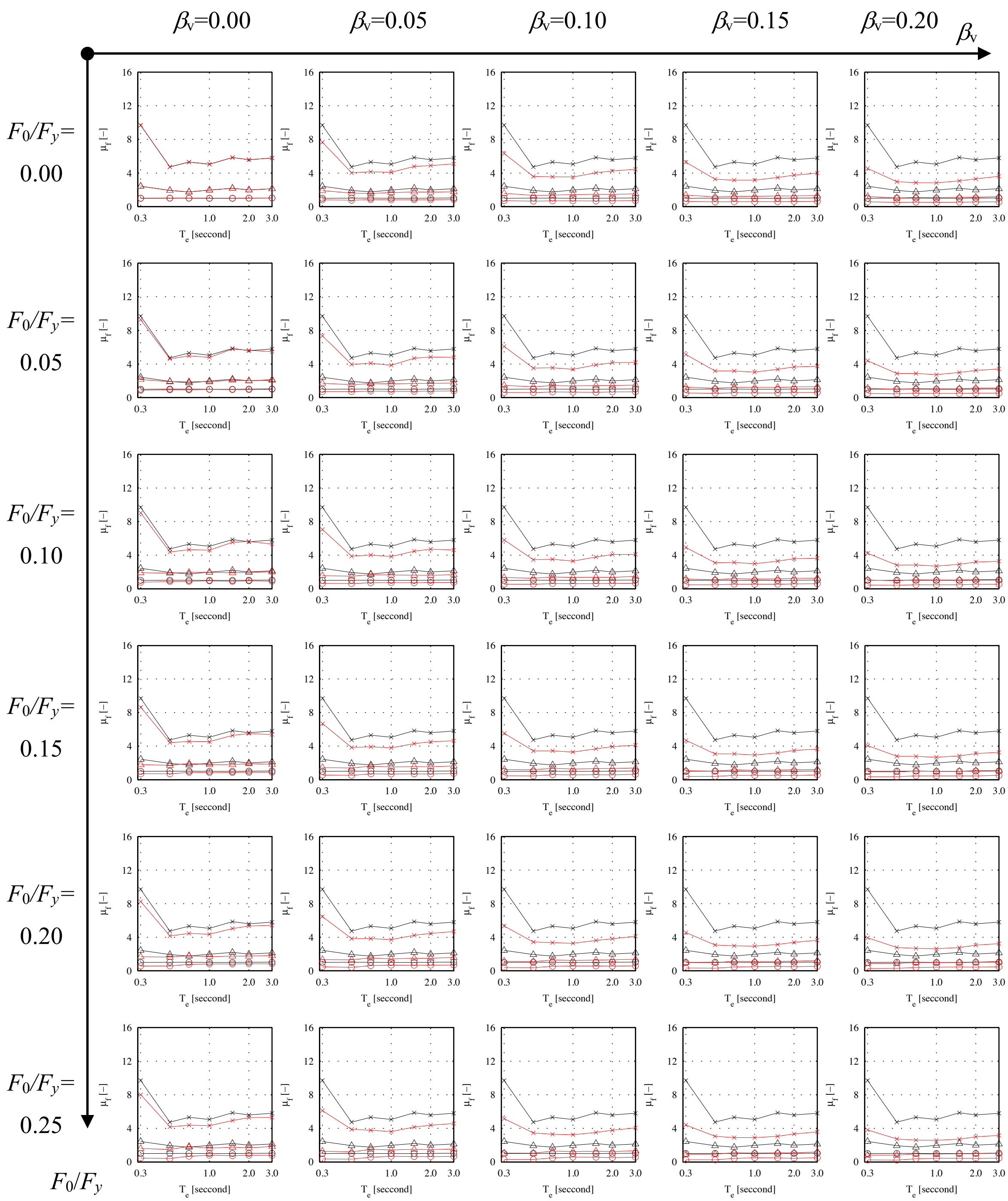

Figure A-52 (Continued)

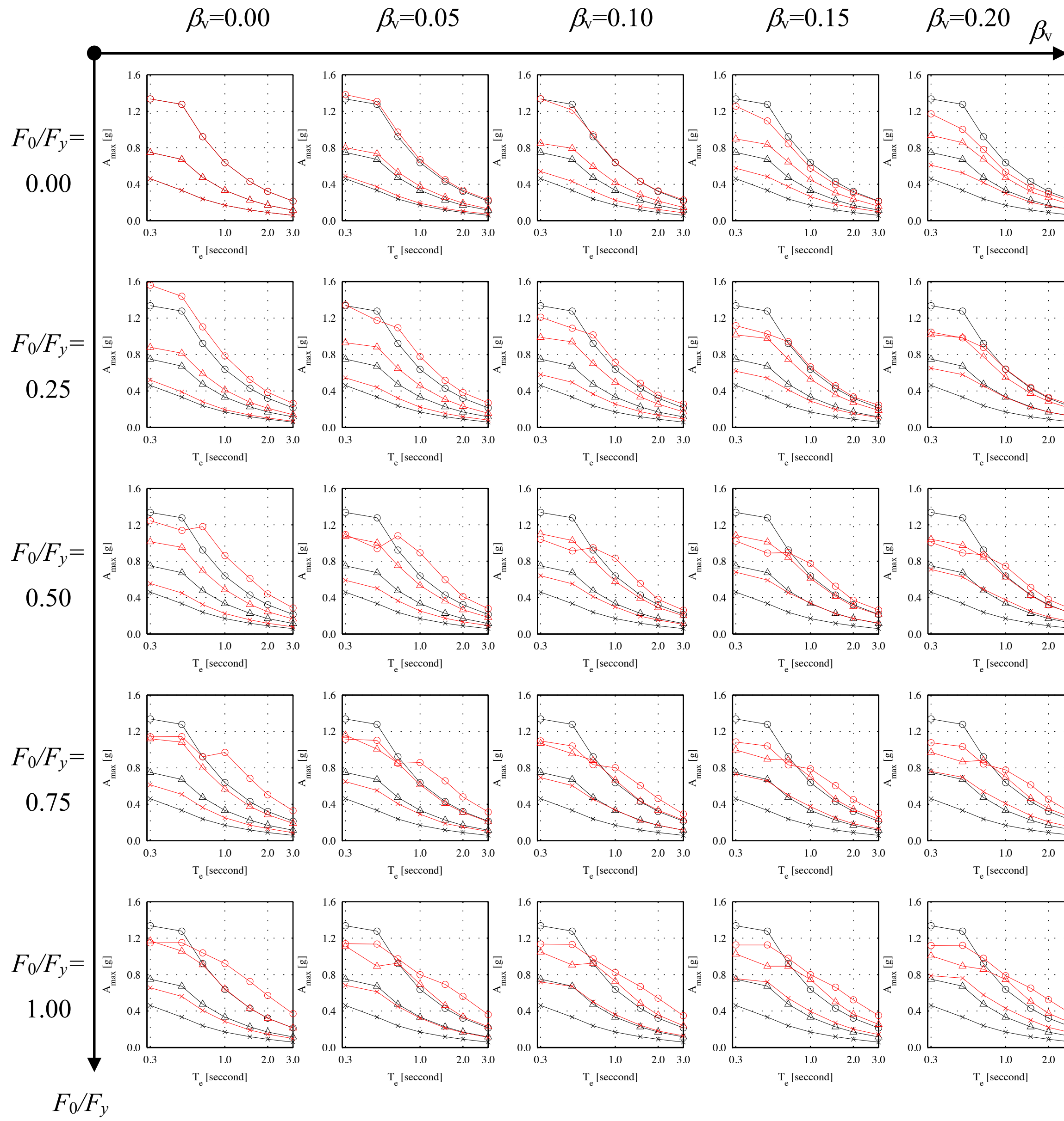

Figure A-53 Acceleration in MCE, Far-Field Motions, Linear Viscous Damping, Stiffness K_0=0, R_μ=1, 2 and 5

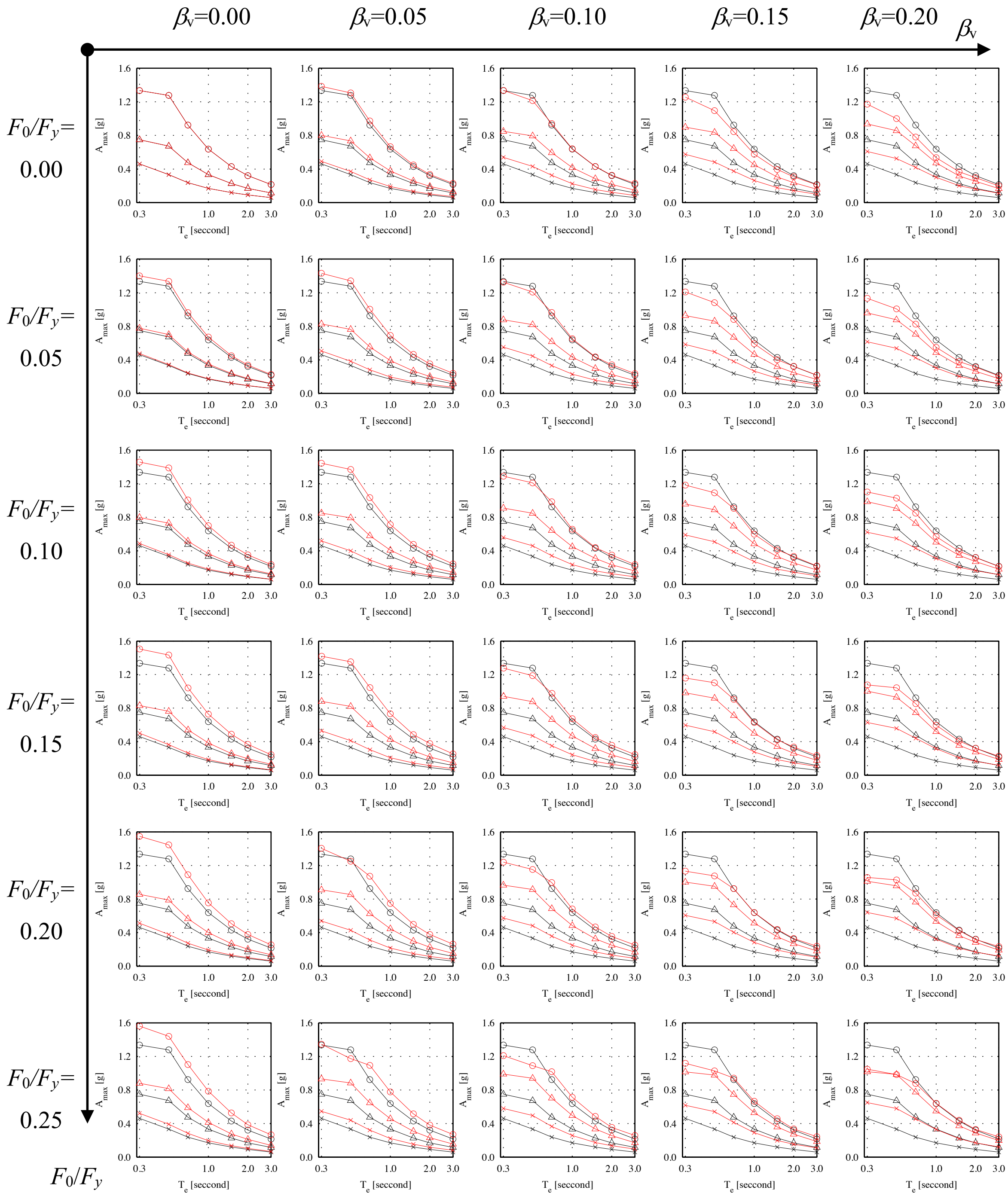

Figure A-53 (Continued)

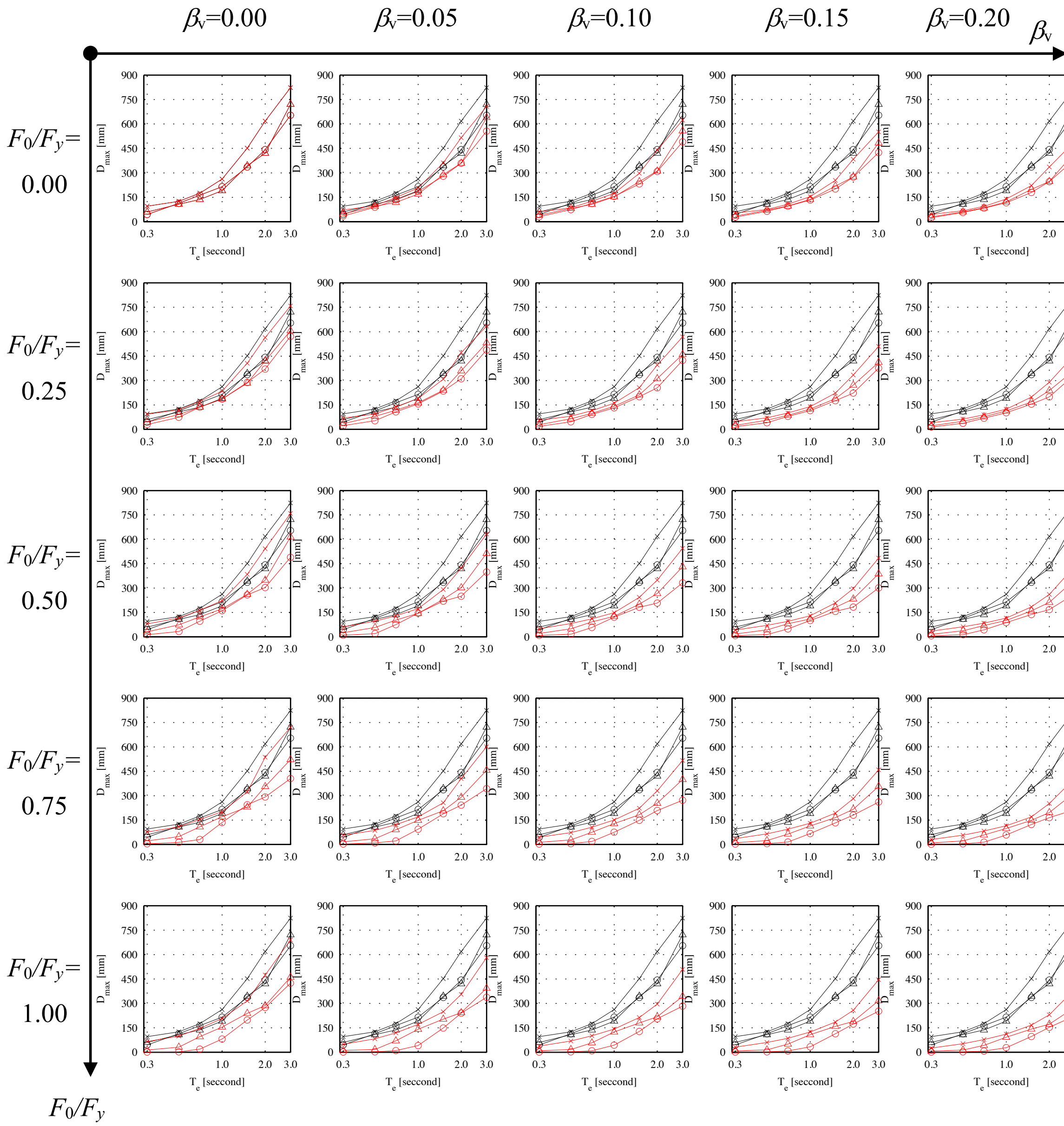

Figure A-54 Displacement in MCE, Far-Field Motions, Linear Viscous Damping, Stiffness K_0=0, R_μ=1, 2 and 5

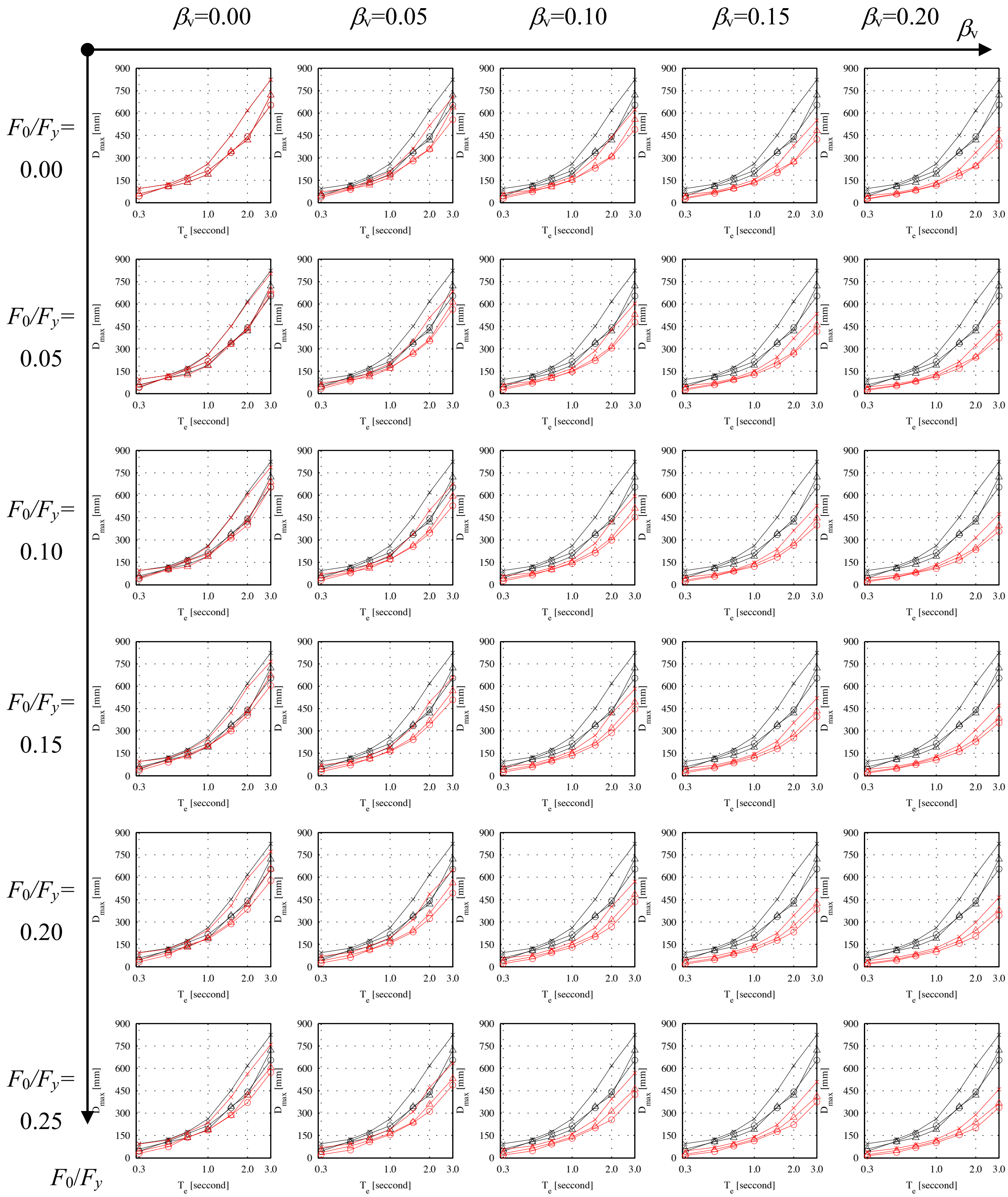

Figure A-54 (Continued)

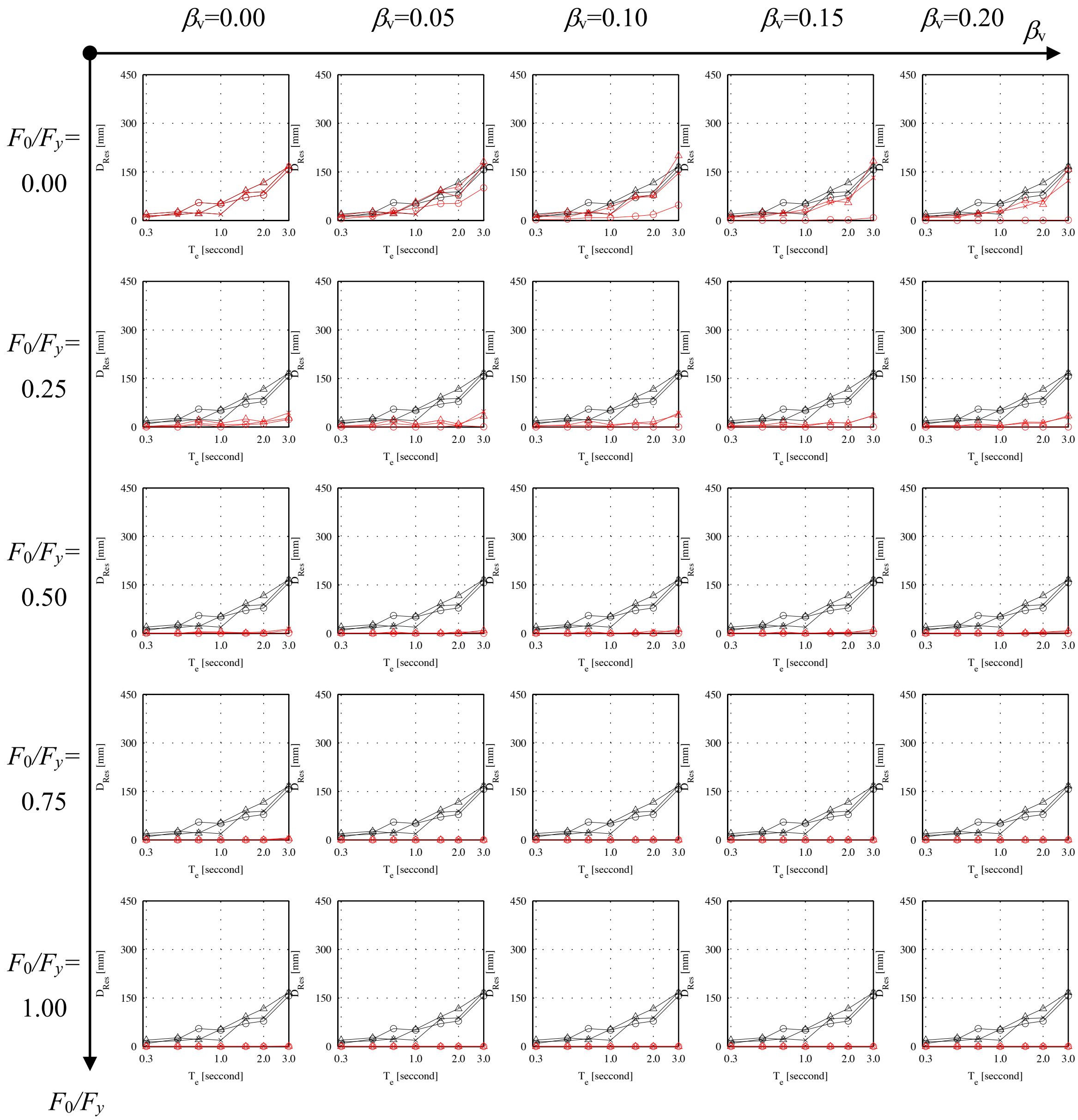

Figure A-55 Residual Displacement in MCE, Far-Field Motions, Linear Viscous Damping, Stiffness K_0=0, R_μ=1, 2 and 5

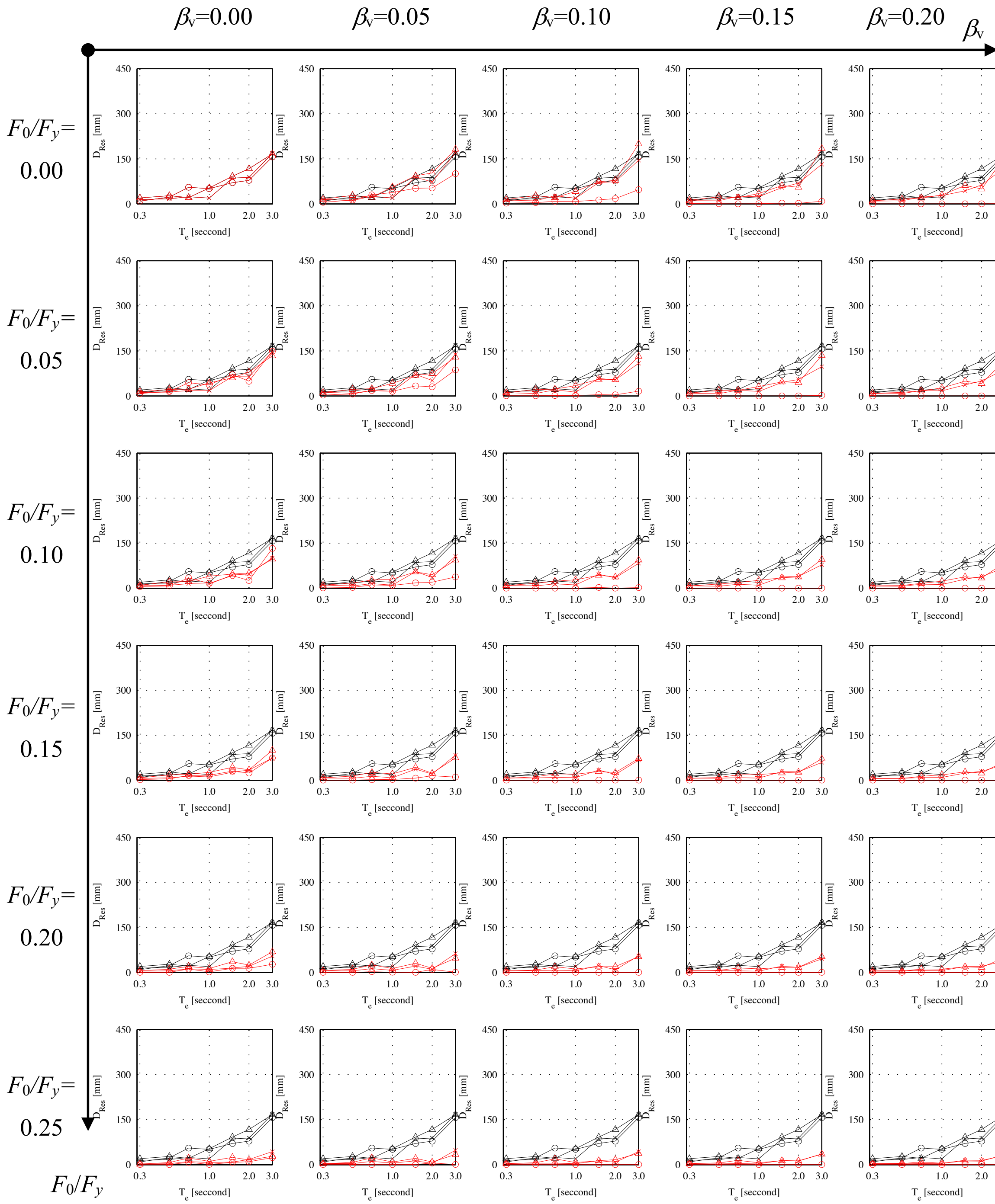

Figure A-55 (Continued)

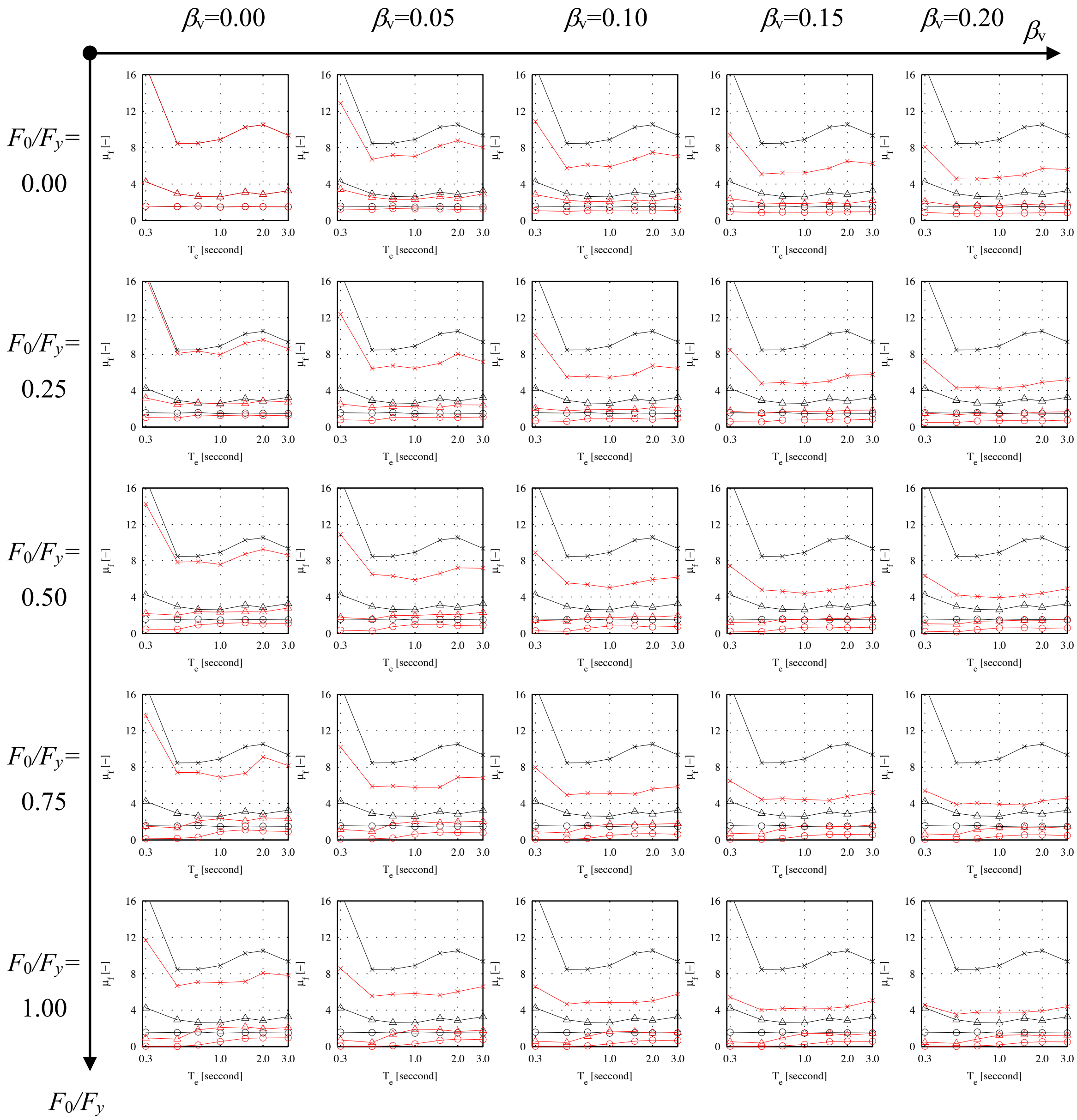

Figure A-56 Ductility Ratio in MCE, Far-Field Motions, Linear Viscous Damping, Stiffness K_0=0, R_μ=1, 2 and 5

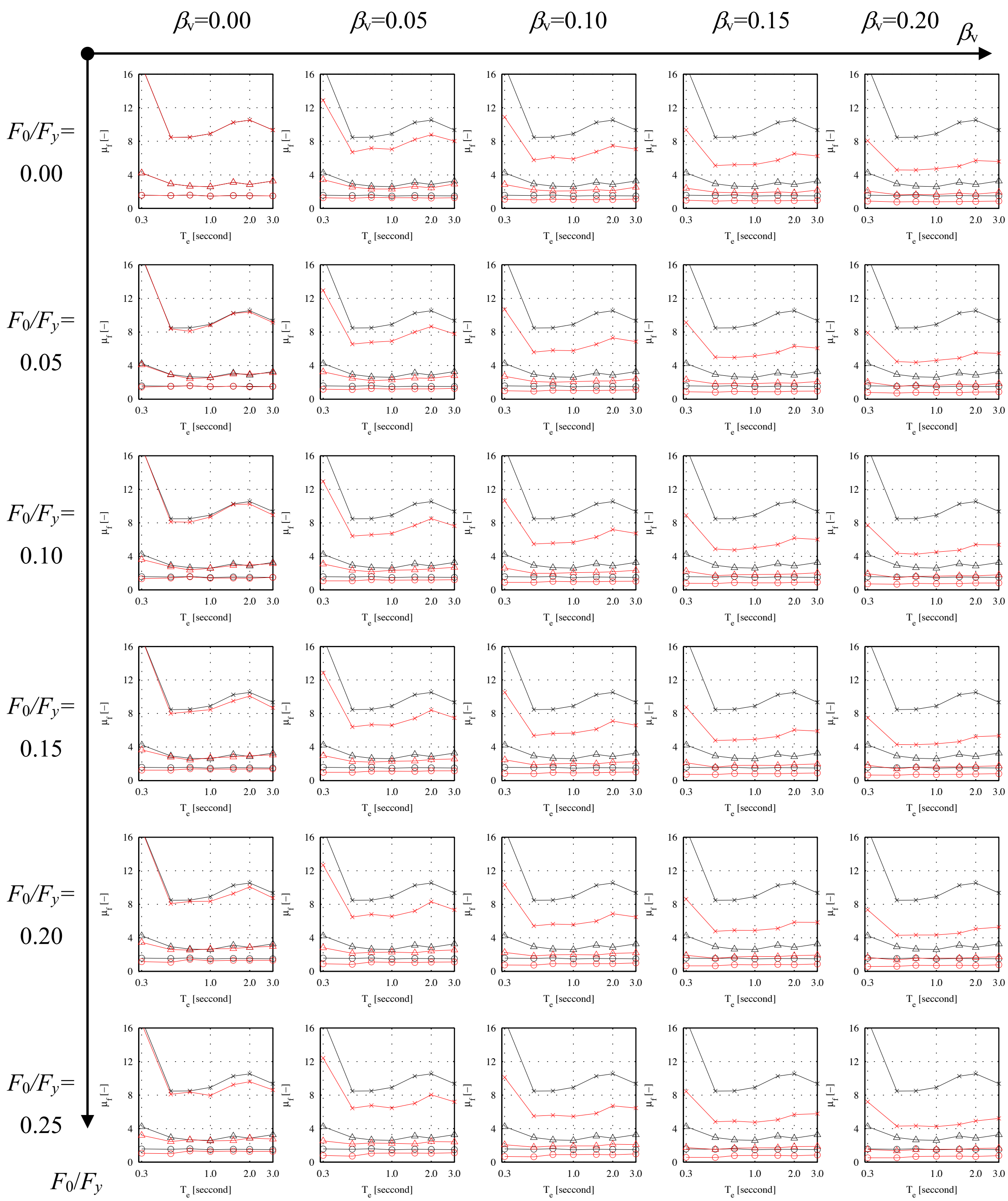

Figure A-56 (Continued)

A.3.2 Structure with Non-Linear Viscous Damping and K_0=0 in Far-Field Ground Motions

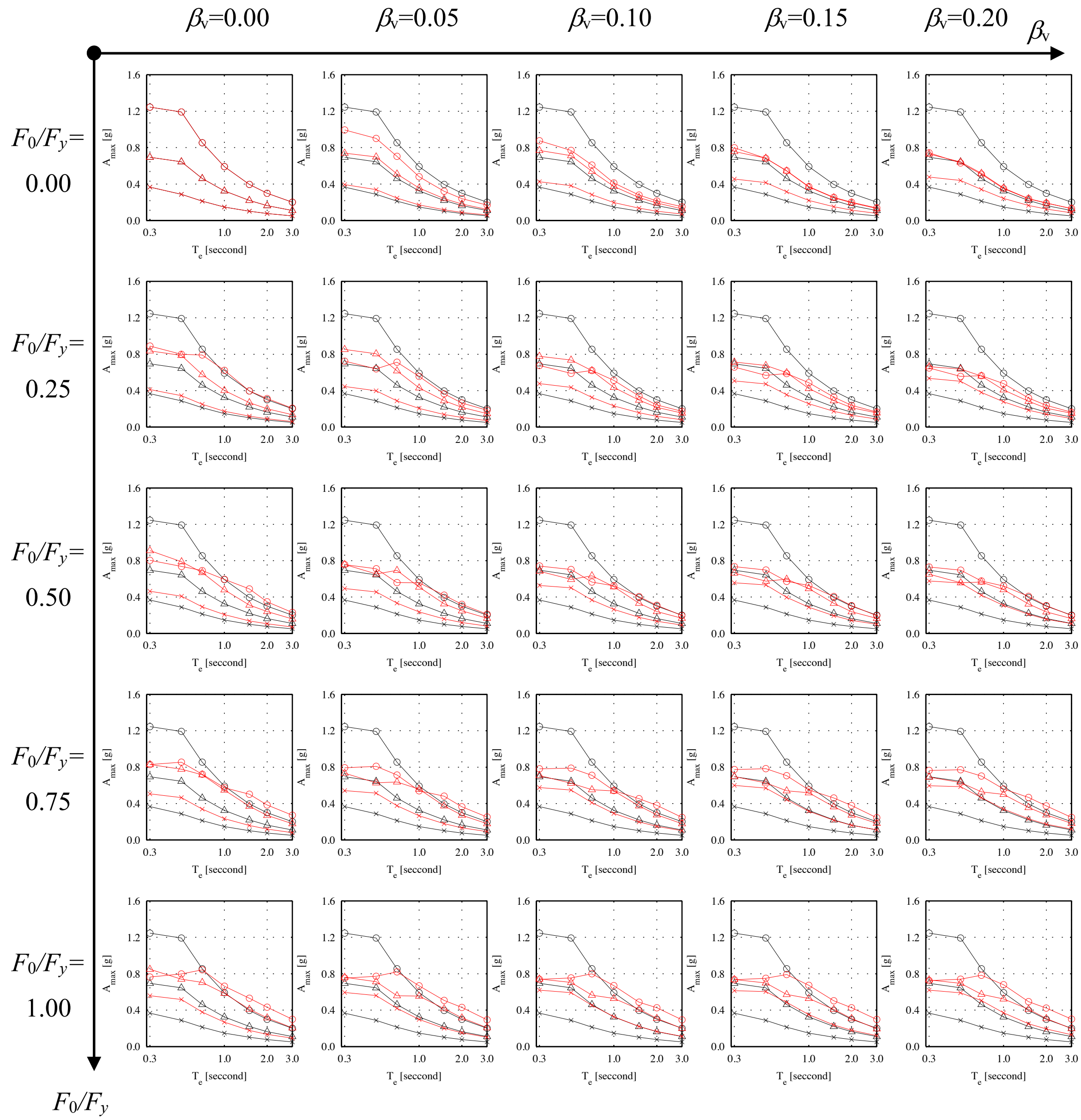

Figure A-57 Acceleration in DE, Far-Field Motions, Non-linear Viscous Damping, Stiffness K_0=0, R_μ=1, 2 and 5

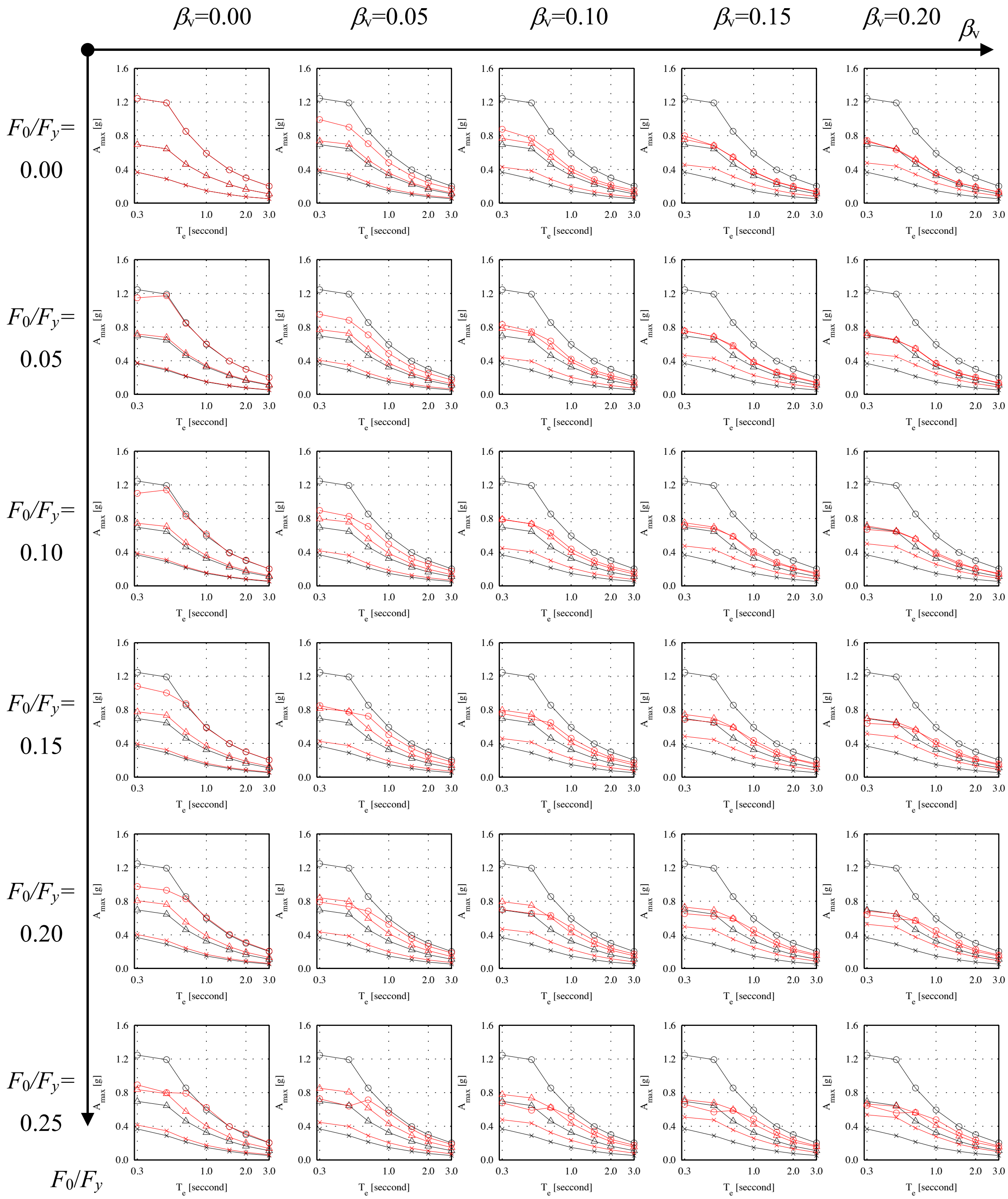

Figure A-57 (Continued)

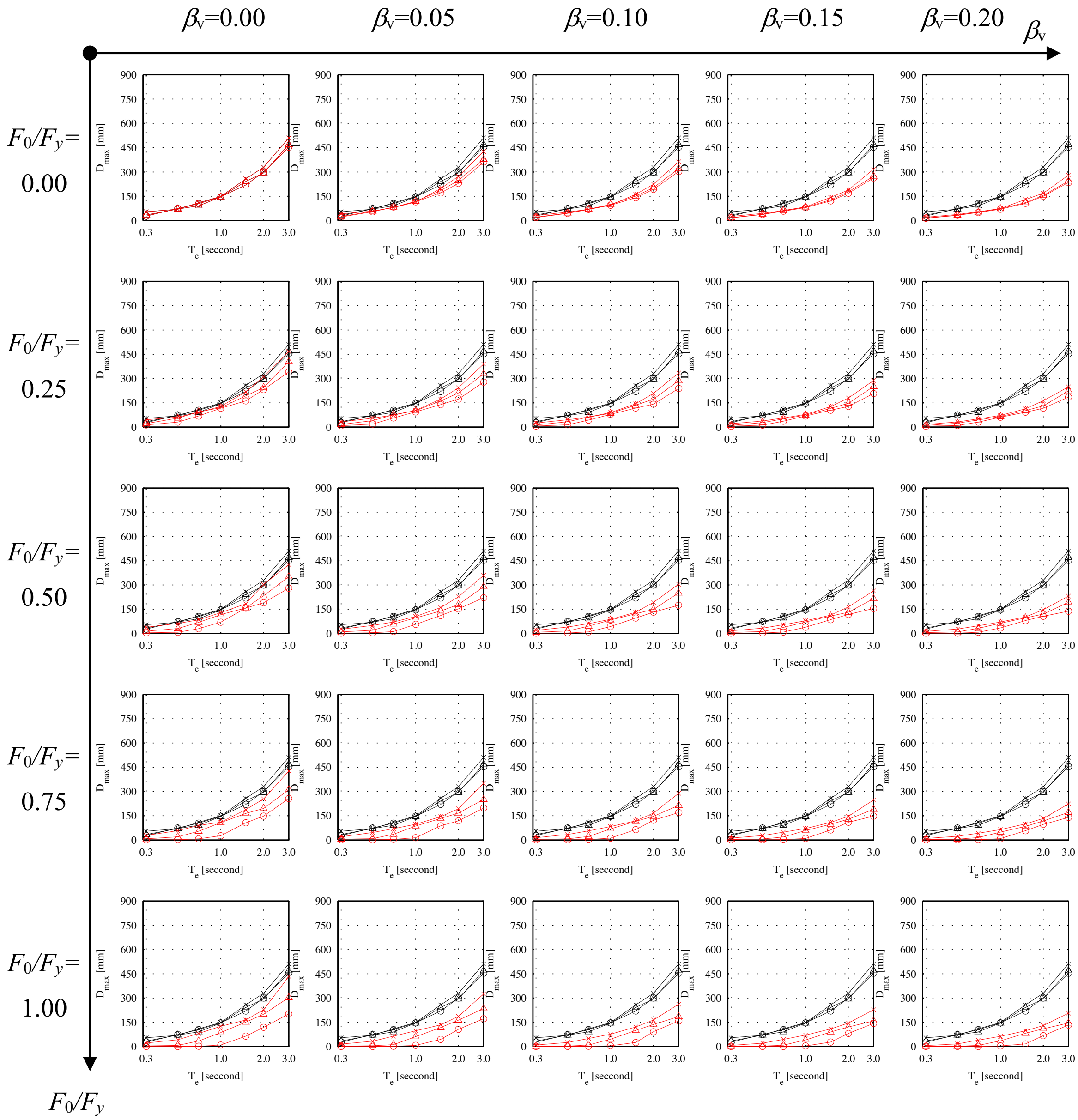

Figure A-58 Displacement in DE, Far-Field Motions, Non-linear Viscous Damping, Stiffness K_0=0, R_μ=1, 2 and 5

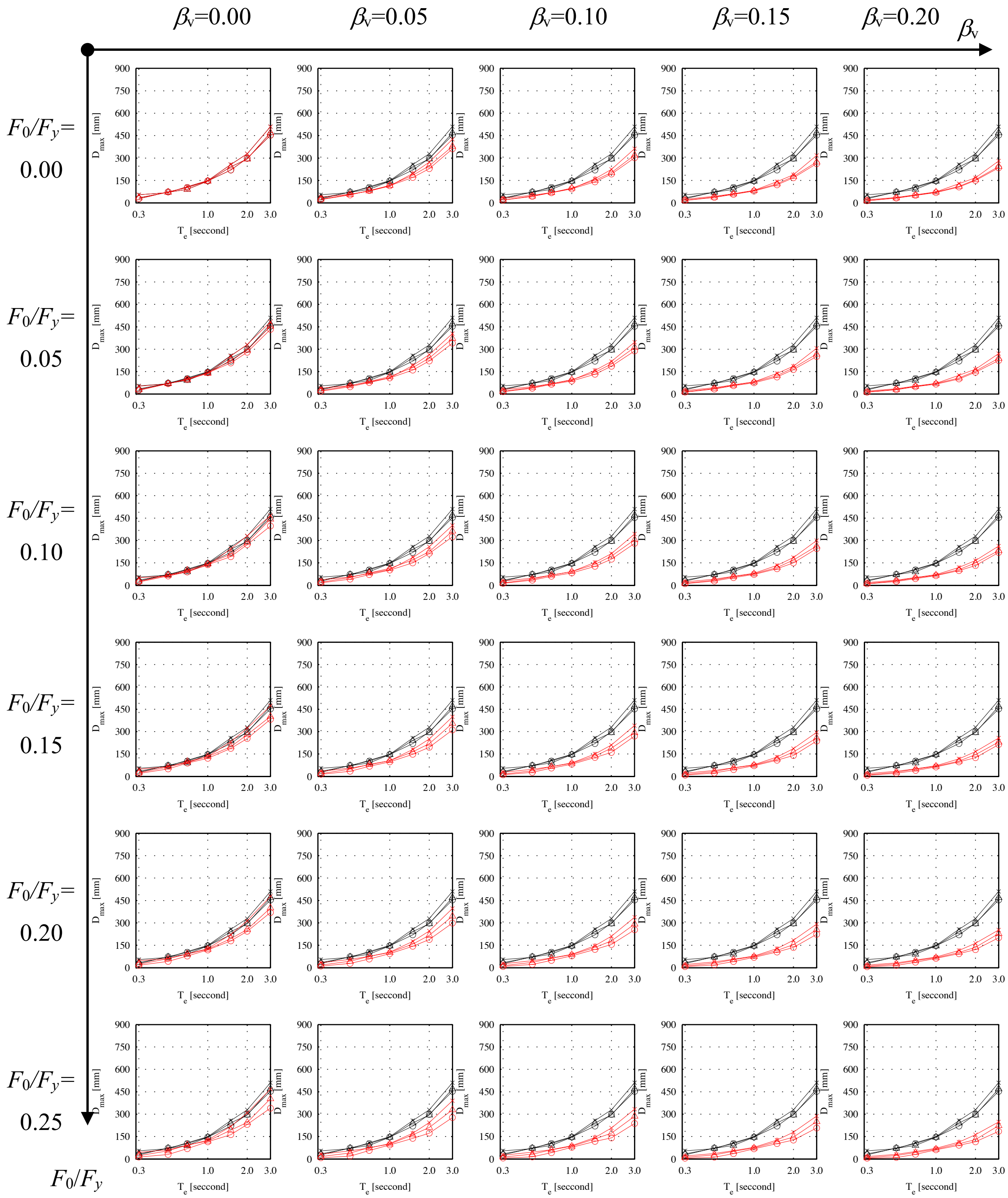

Figure A-58 (Continued)

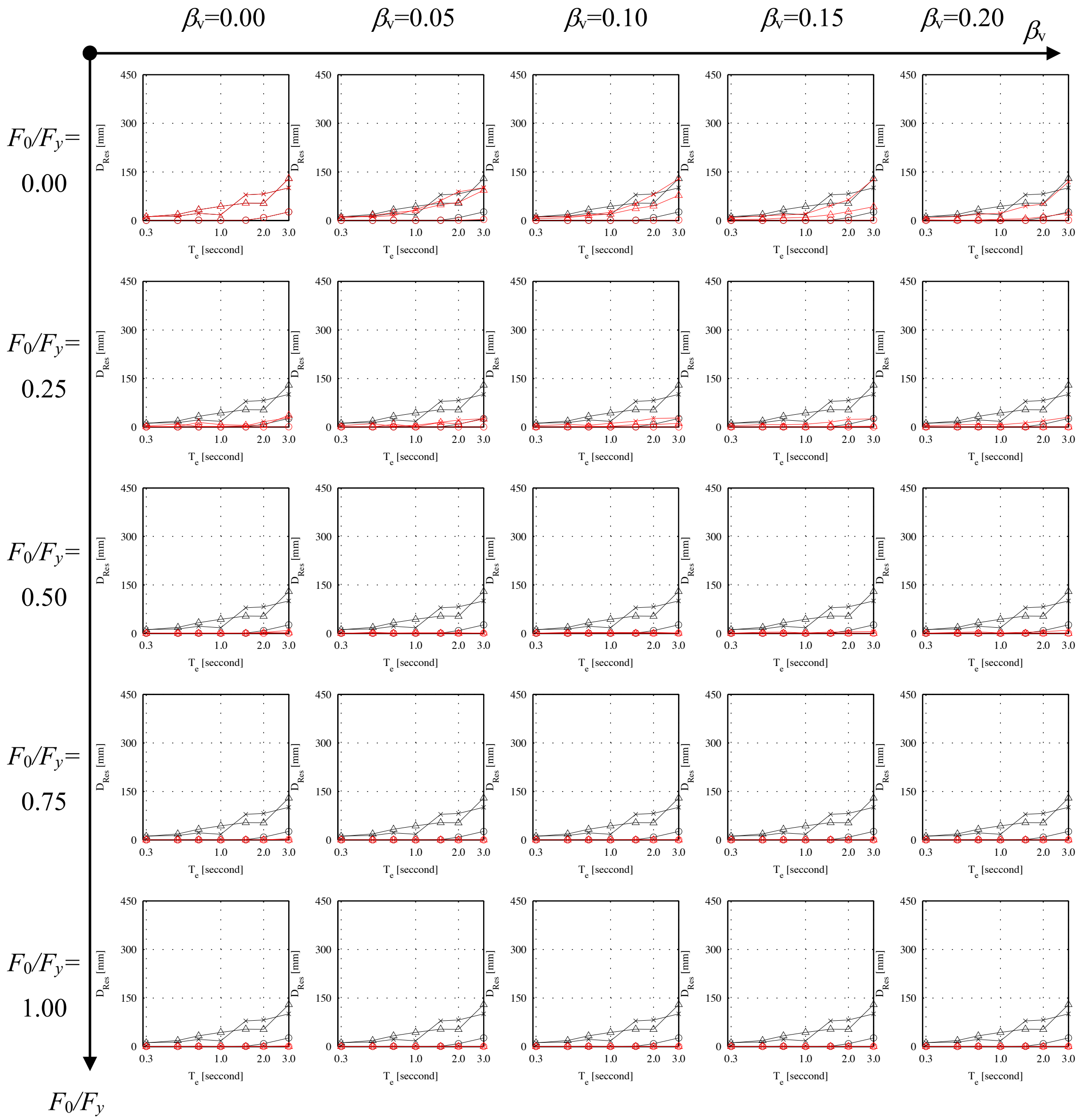

Figure A-59 Residual Displacement in DE, Far-Field Motions, Non-linear Viscous Damping, Stiffness K_0=0, R_μ=1, 2 and 5

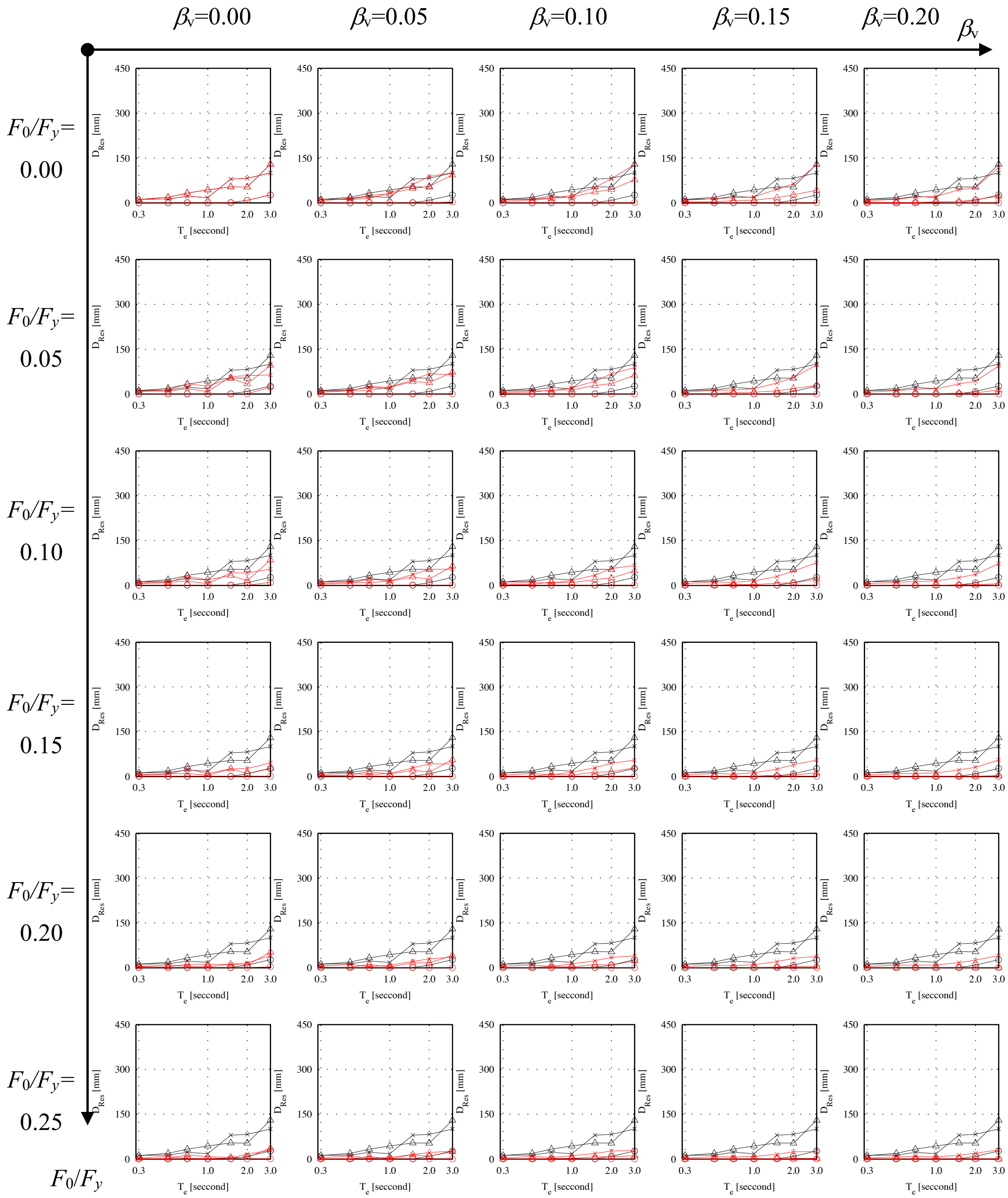

Figure A-59 (Continued)

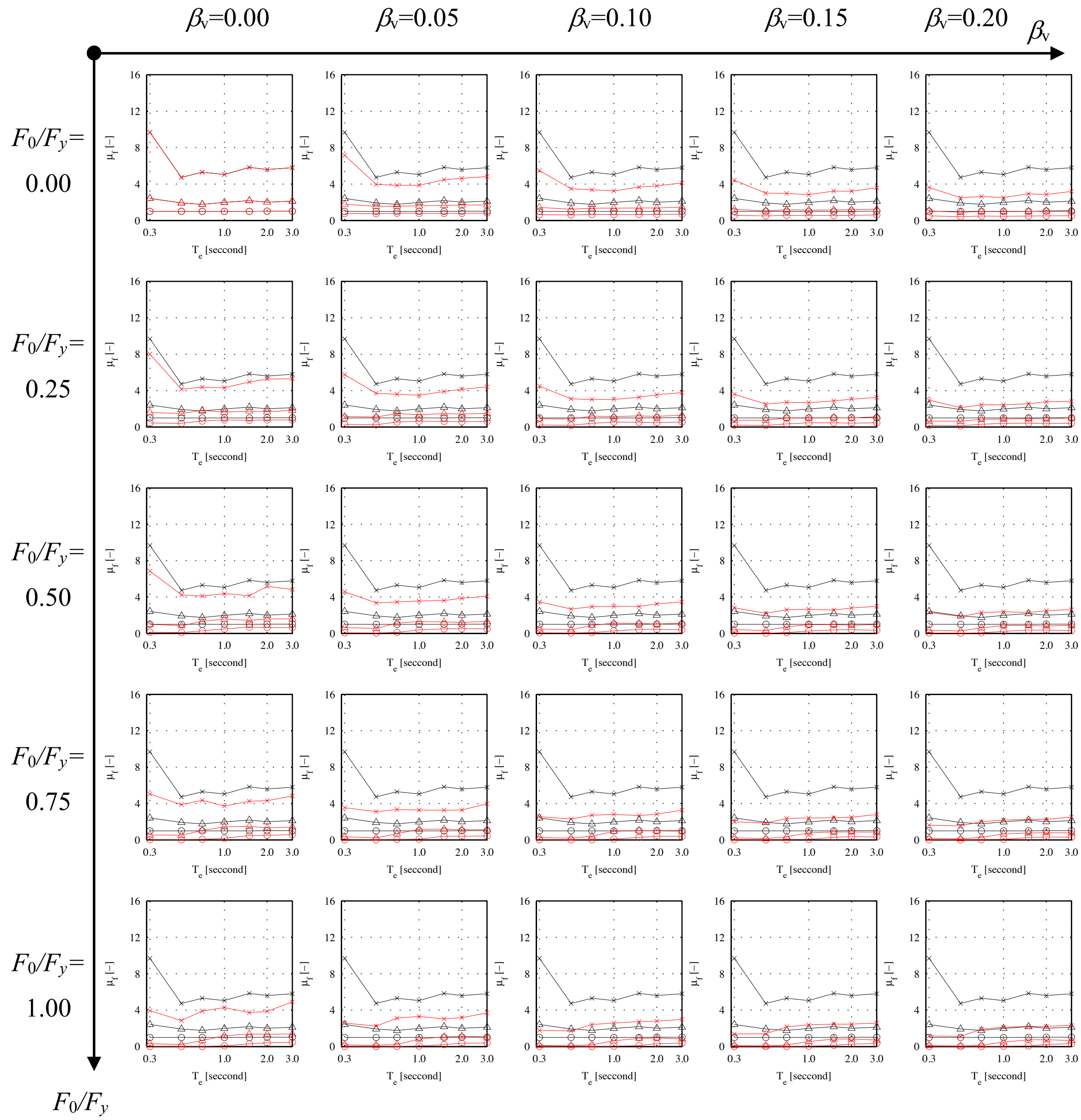

Figure A-60 Ductility Ratio in DE, Far-Field Motions, Non-linear Viscous Damping, Stiffness K_0=0, R_μ=1, 2 and 5

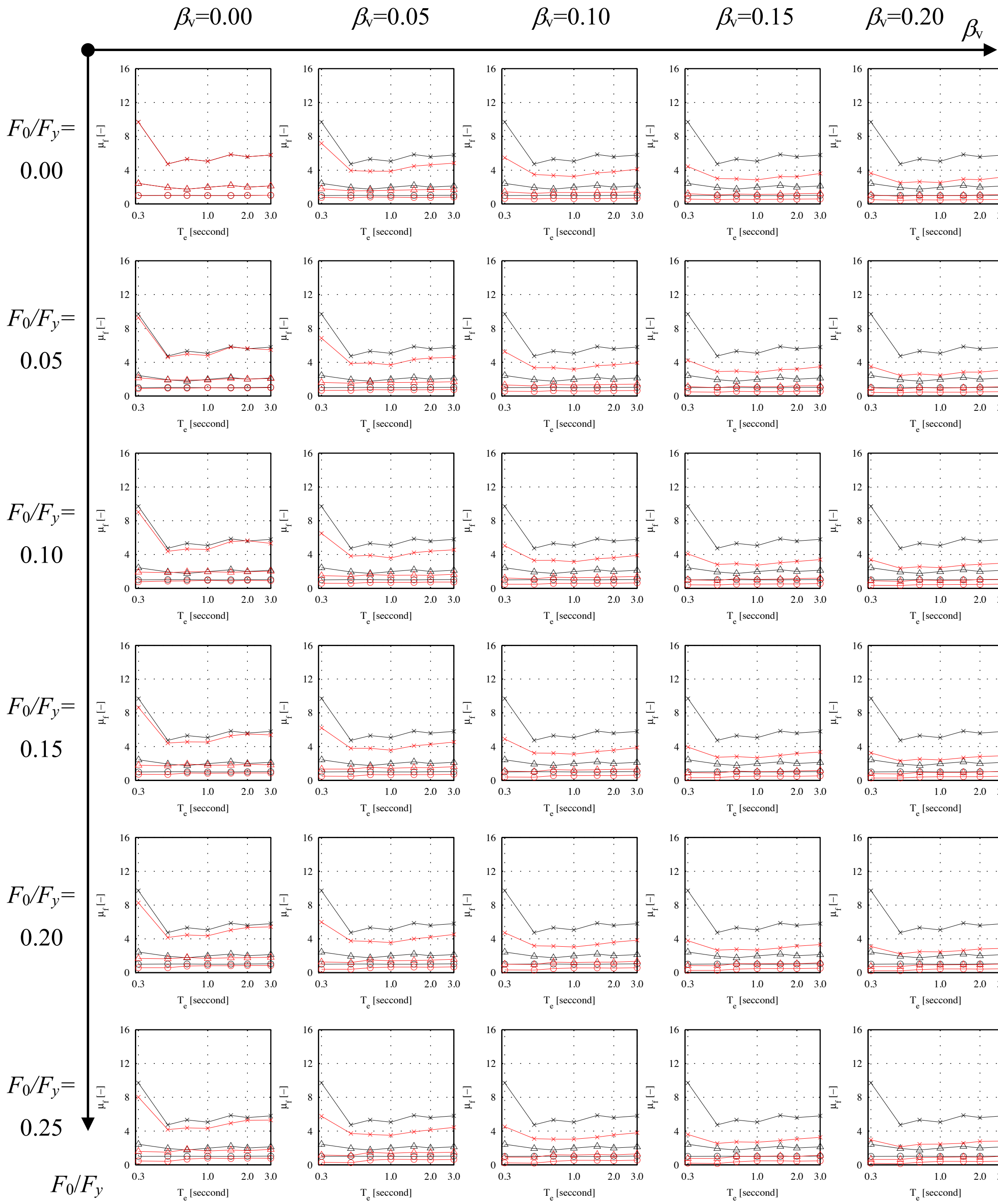

Figure A-60 (Continued)

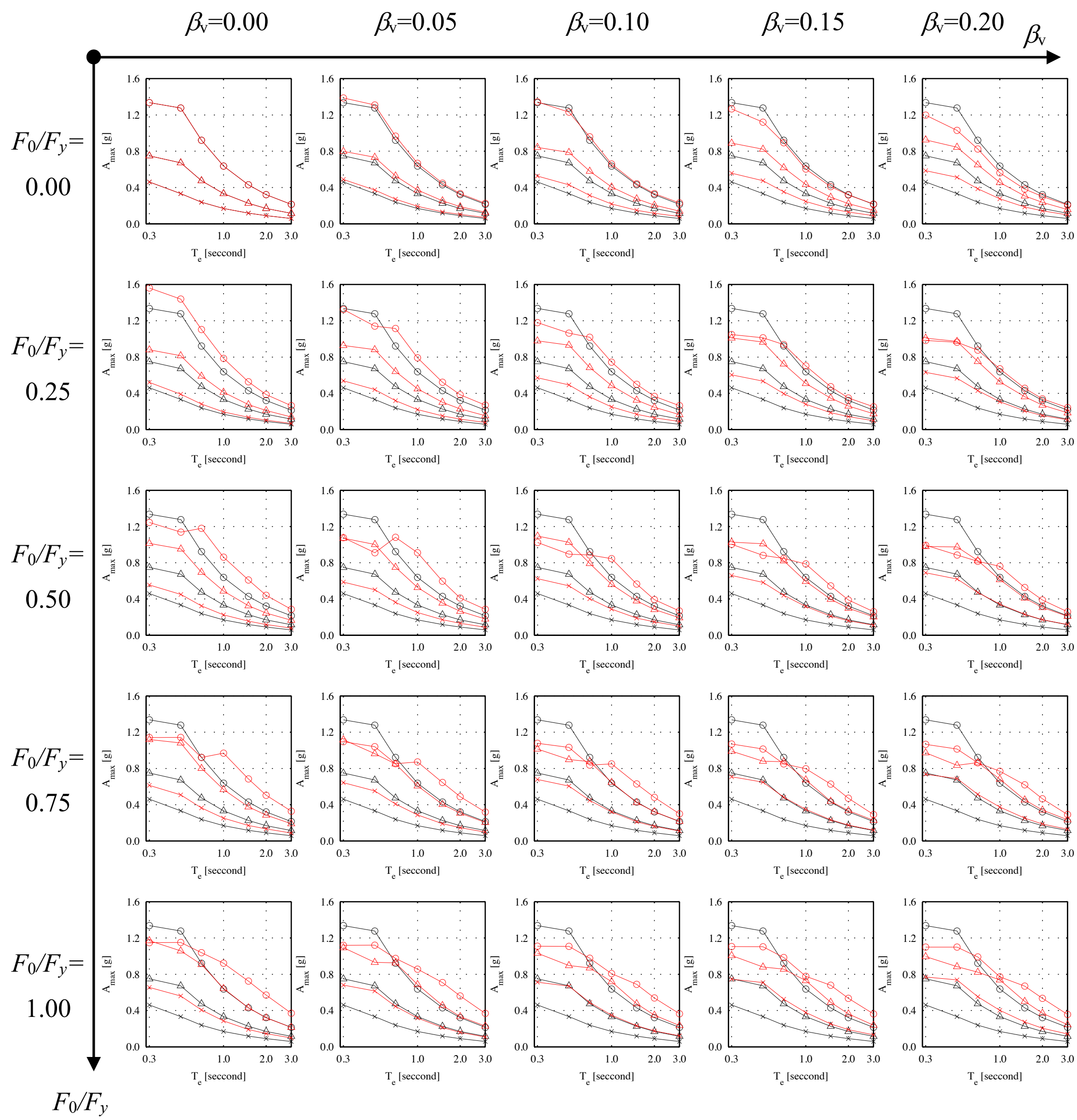

Figure A-61 Acceleration in MCE, Far-Field Motions, Non-linear Viscous Damping, Stiffness K_0=0, R_μ=1, 2 and 5

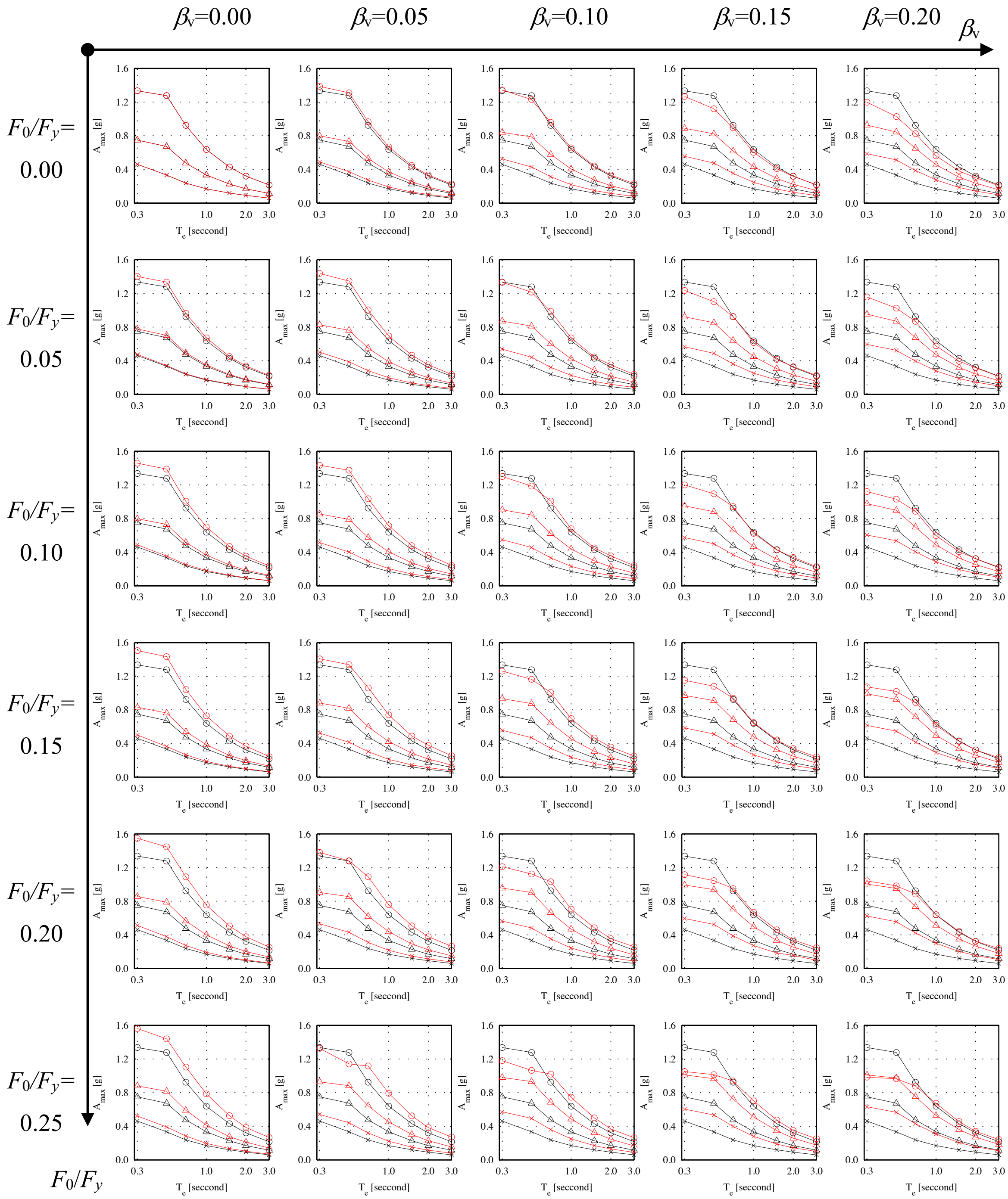

Figure A-61 (Continued)

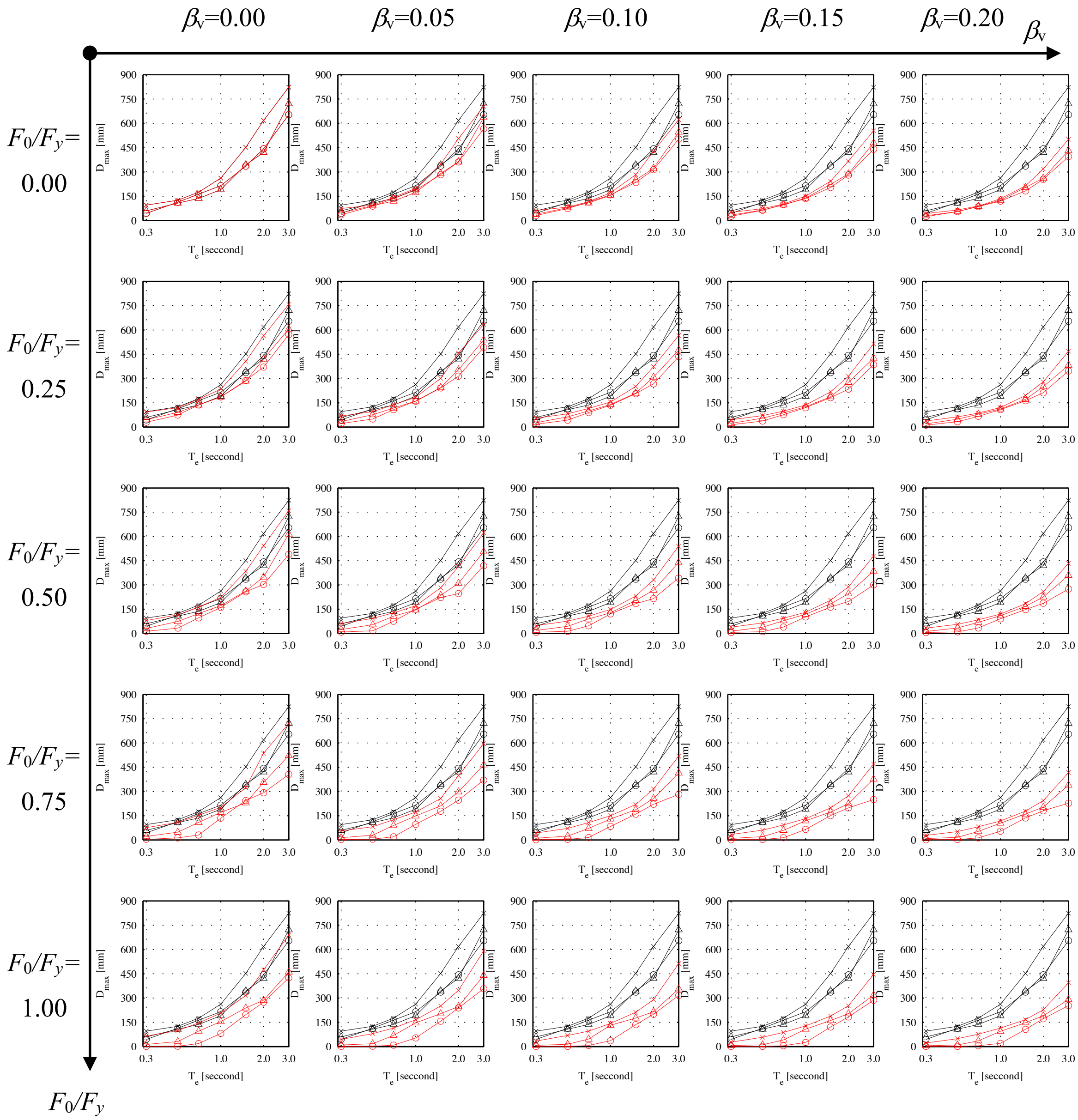

Figure A-62 Displacement in MCE, Far-Field Motions, Non-linear Viscous Damping, Stiffness K_0=0, R_μ=1, 2 and 5

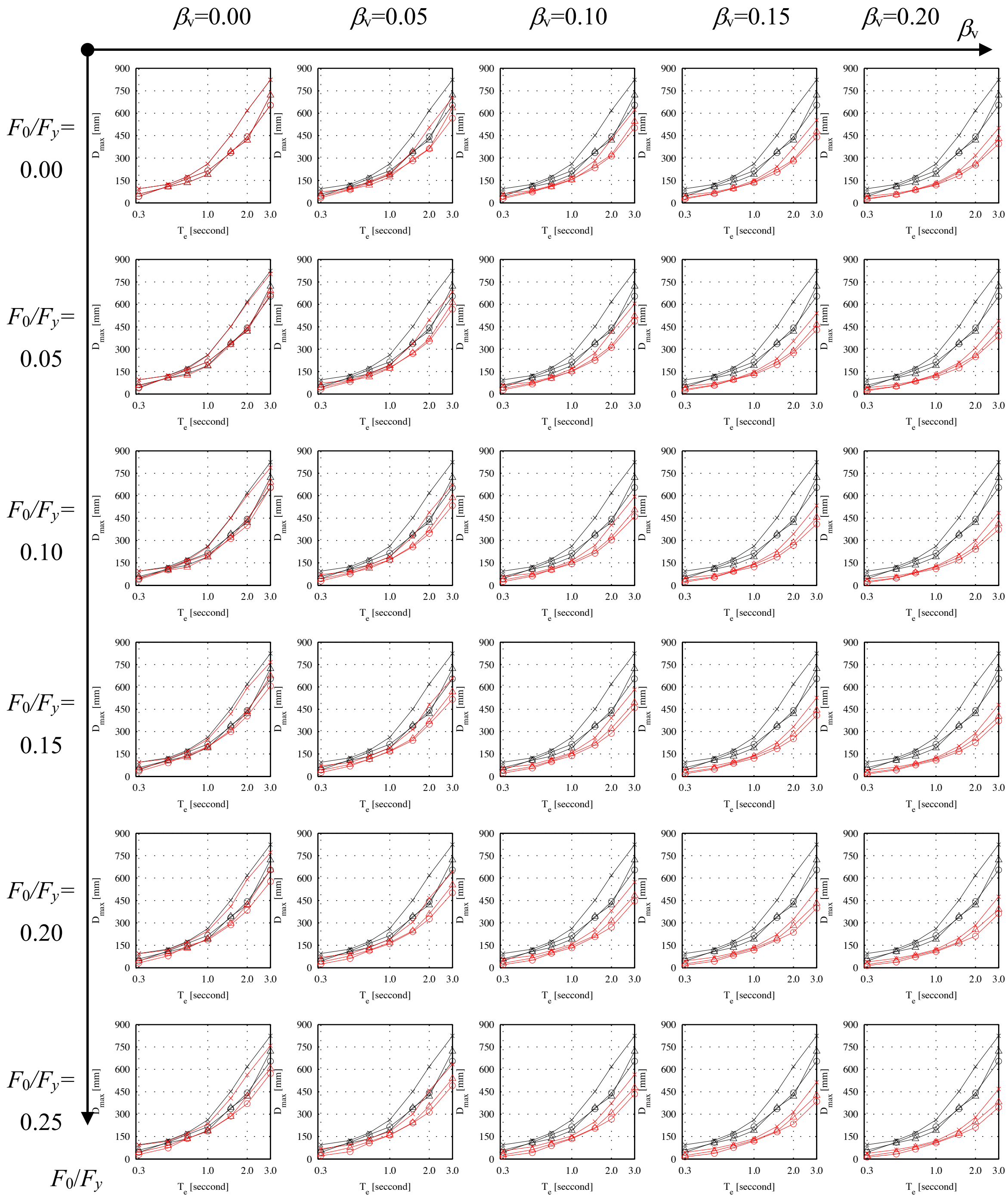

Figure A-62 (Continued)

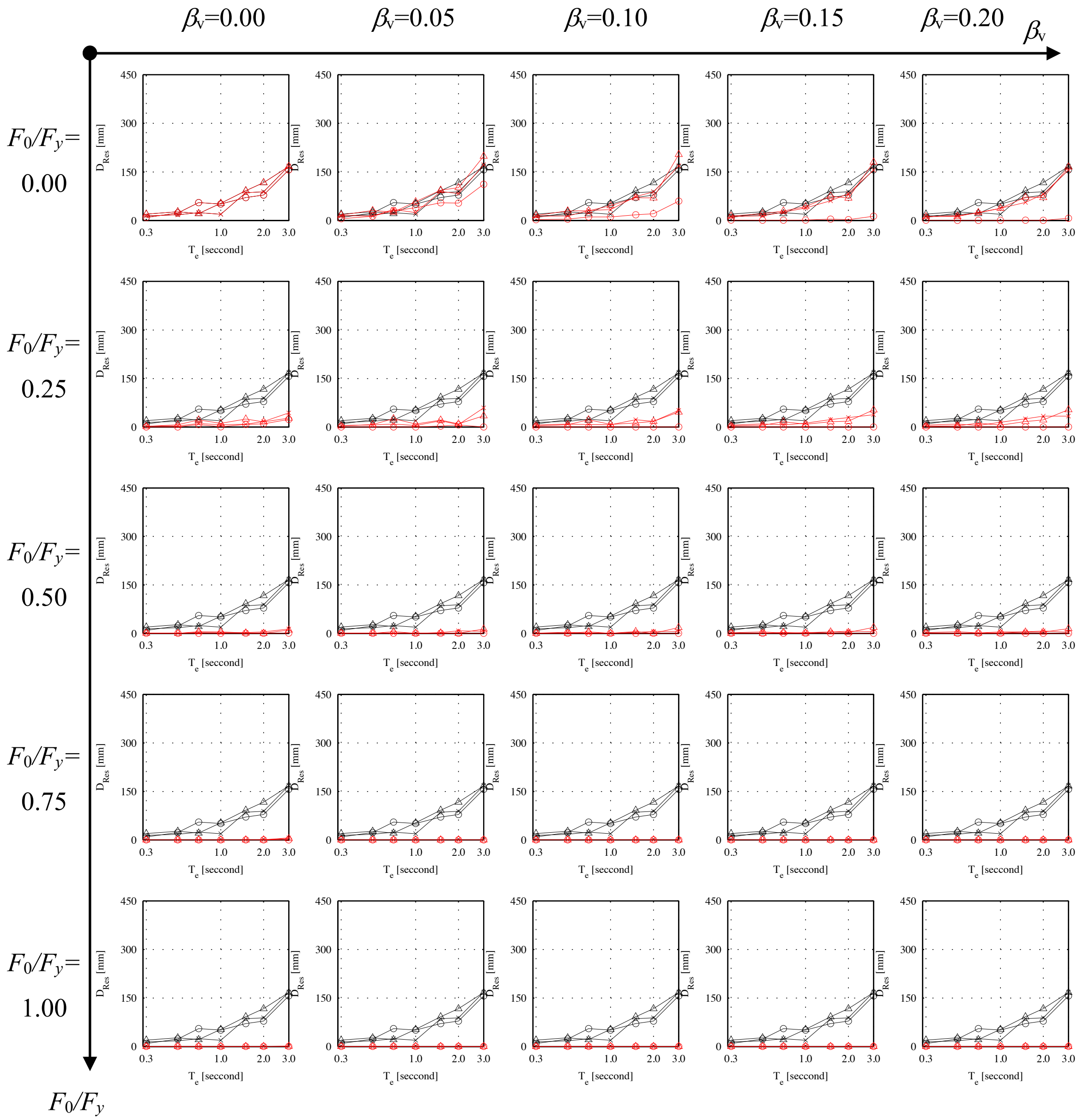

Figure A-63 Residual Displacement in MCE, Far-Field Motions, Non-linear Viscous Damping, Stiffness K_0=0, R_μ=1, 2 and 5

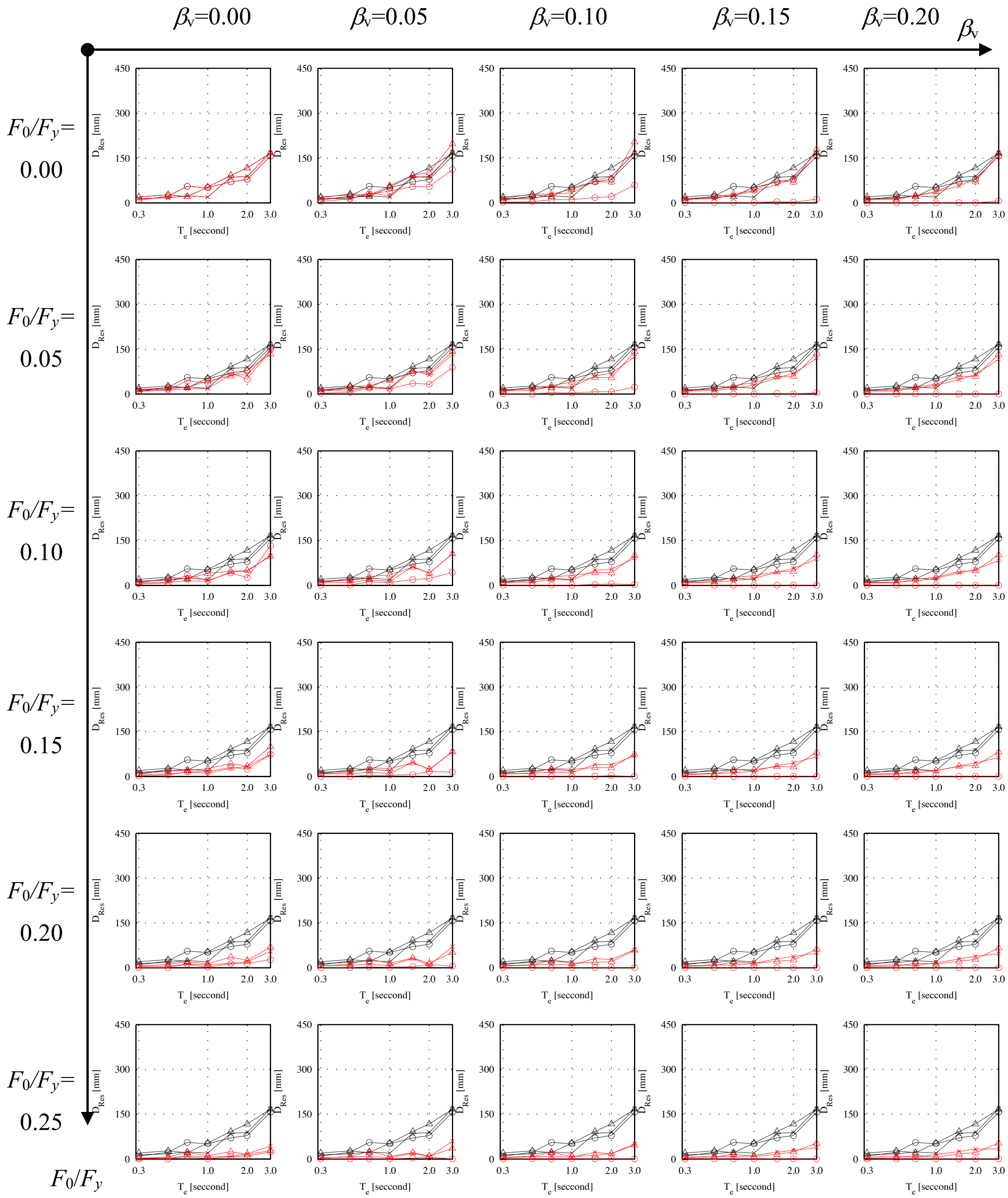

Figure A-63 (Continued)

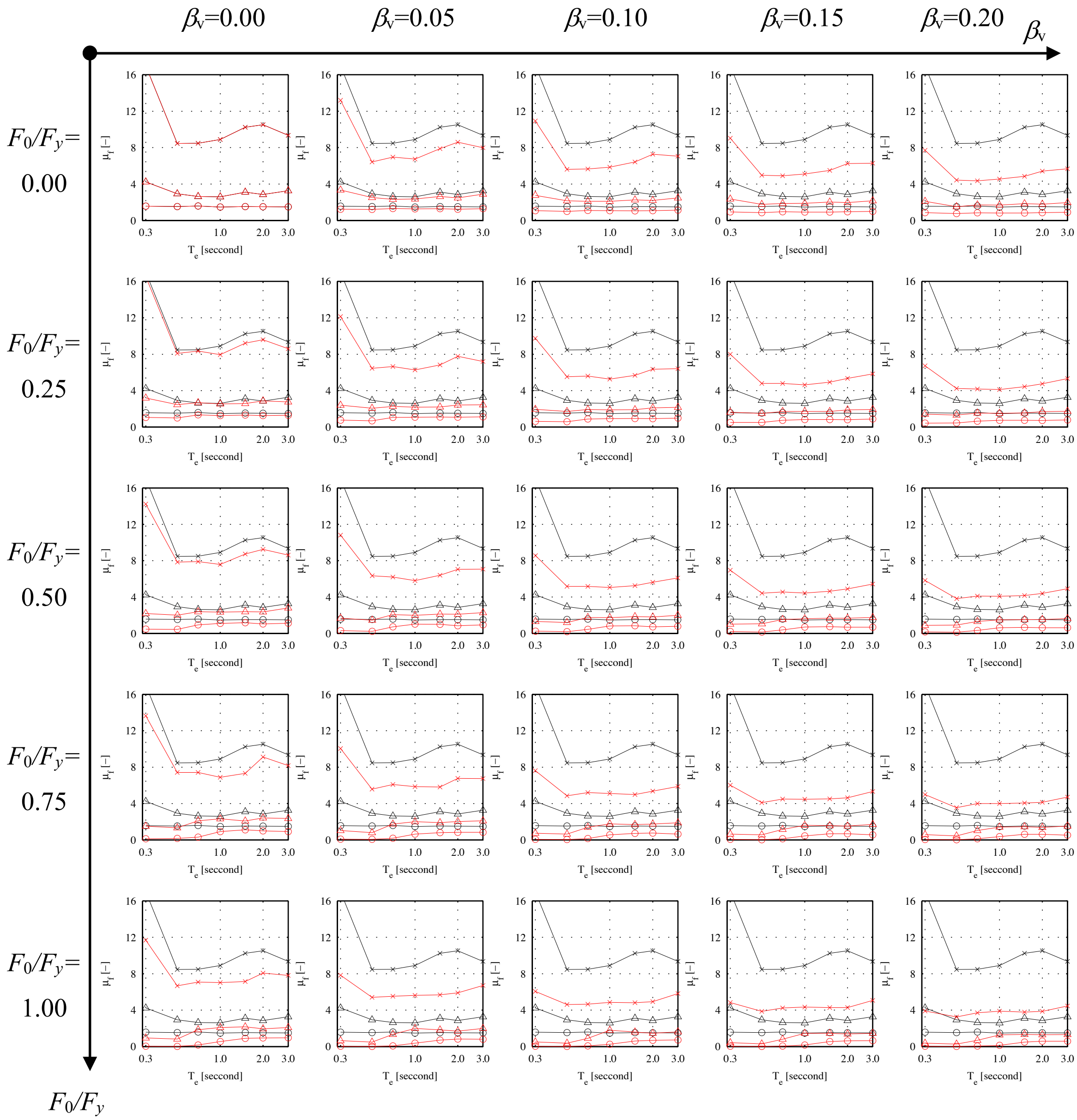

Figure A-64 Ductility Ratio in MCE, Far-Field Motions, Non-linear Viscous Damping, Stiffness K_0=0, R_μ=1, 2 and 5

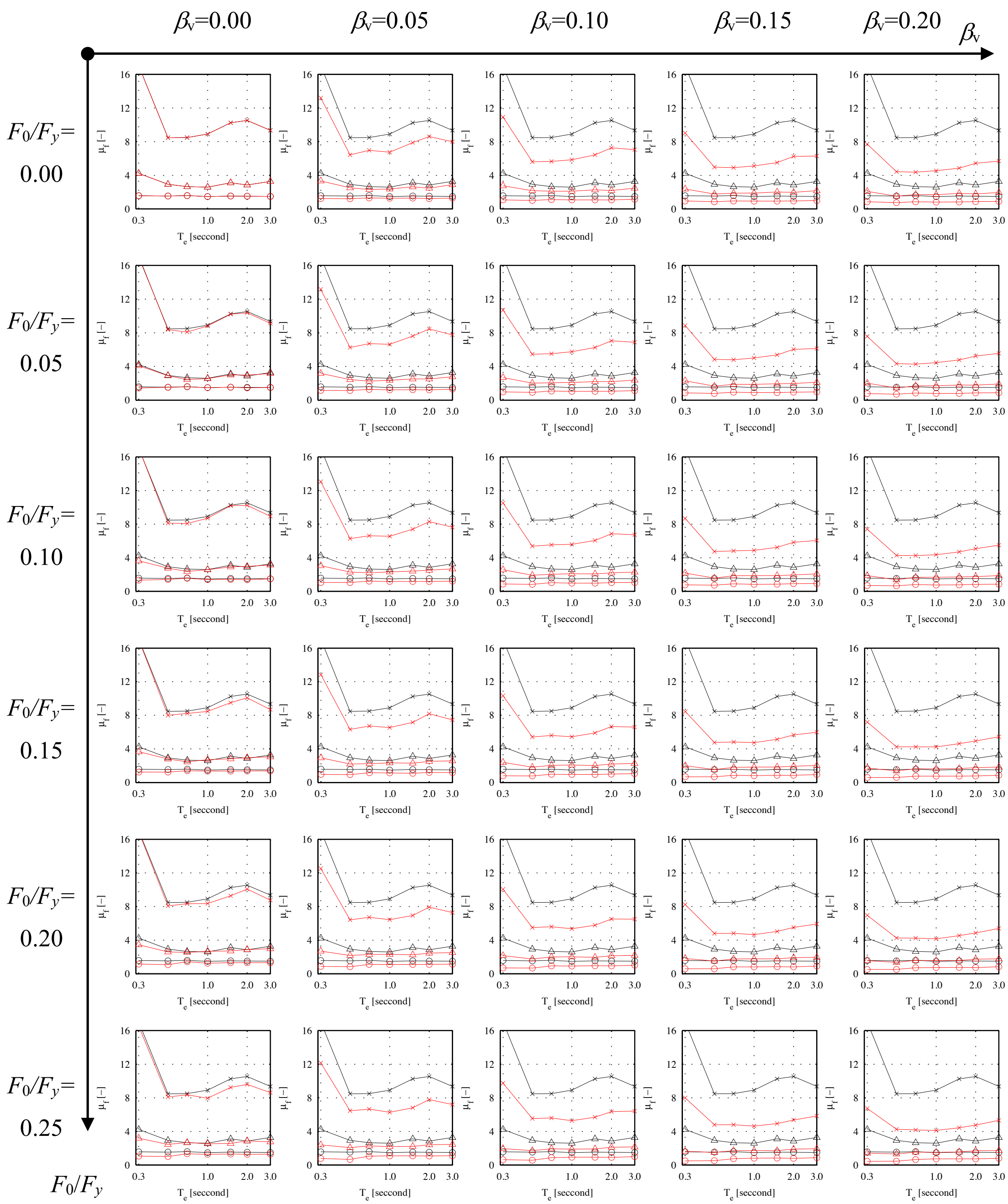

Figure A-64 (Continued)

A.3.3 Structure with Upper-Half Viscous Damping and K_0=0 in Far-Field Ground Motions

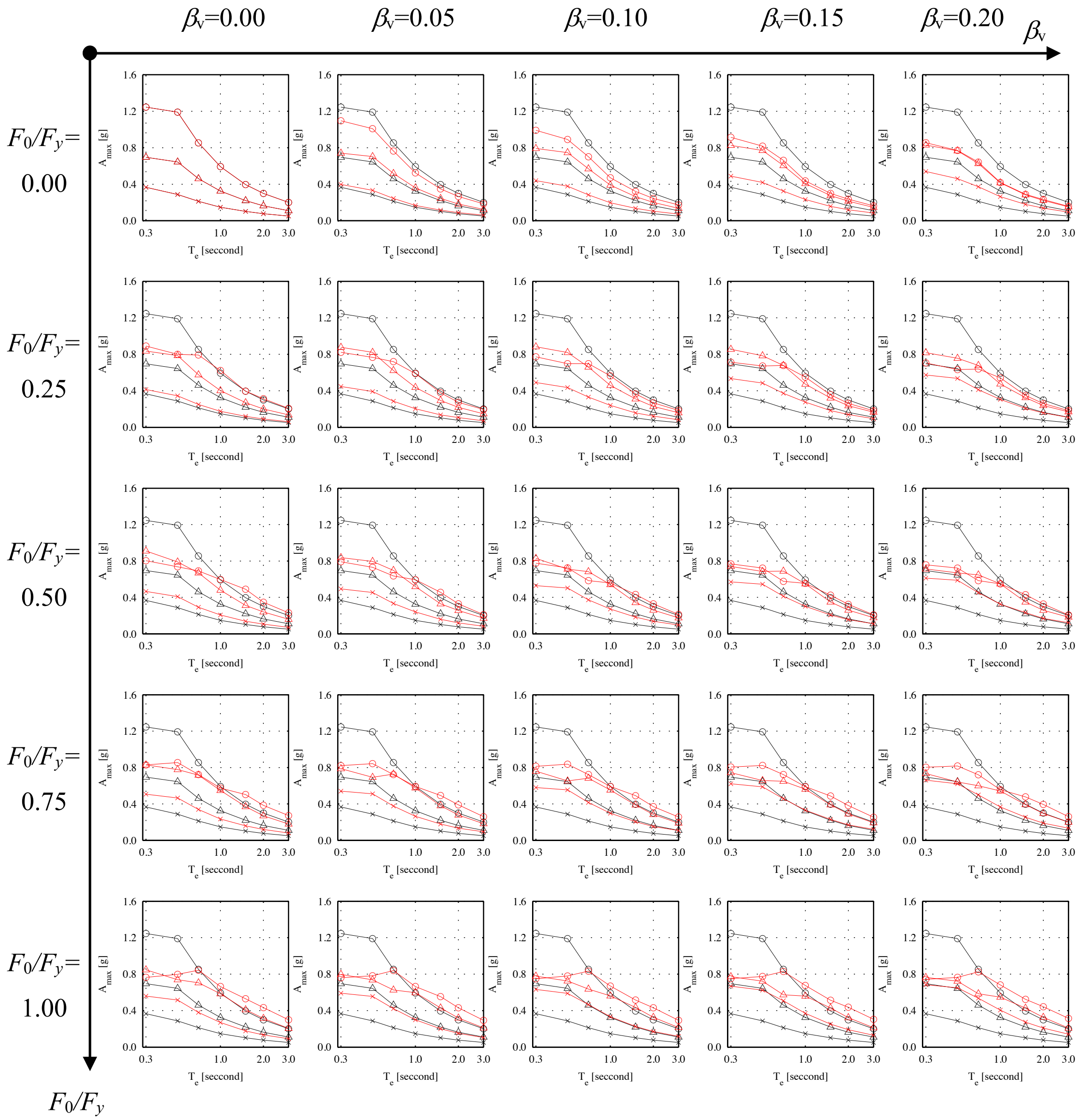

Figure A-65 Acceleration in DE, Far-Field Motions, Upper-half Viscous Damping, Stiffness K_0=0, R_μ=1, 2 and 5

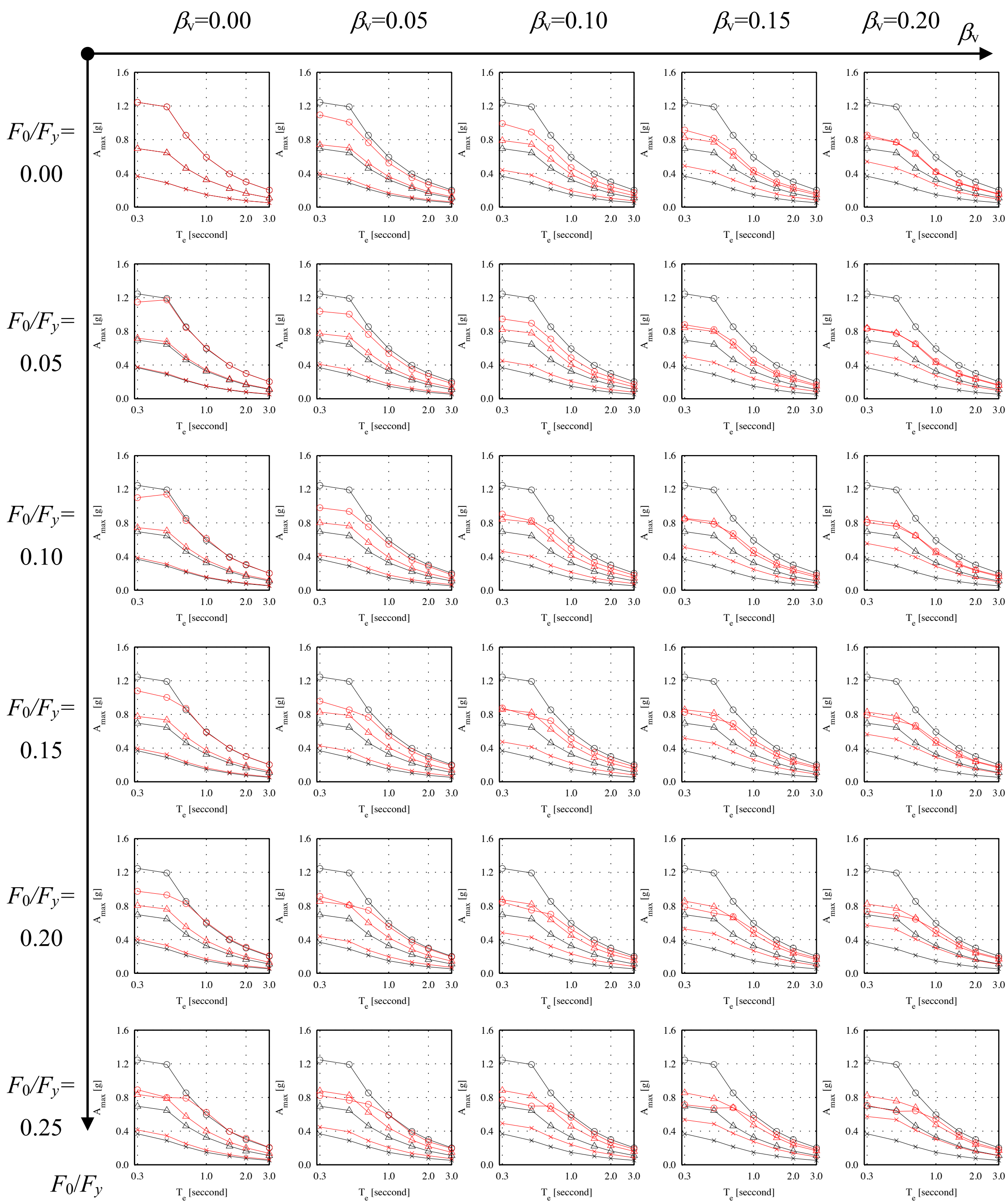

Figure A-65 (Continued)

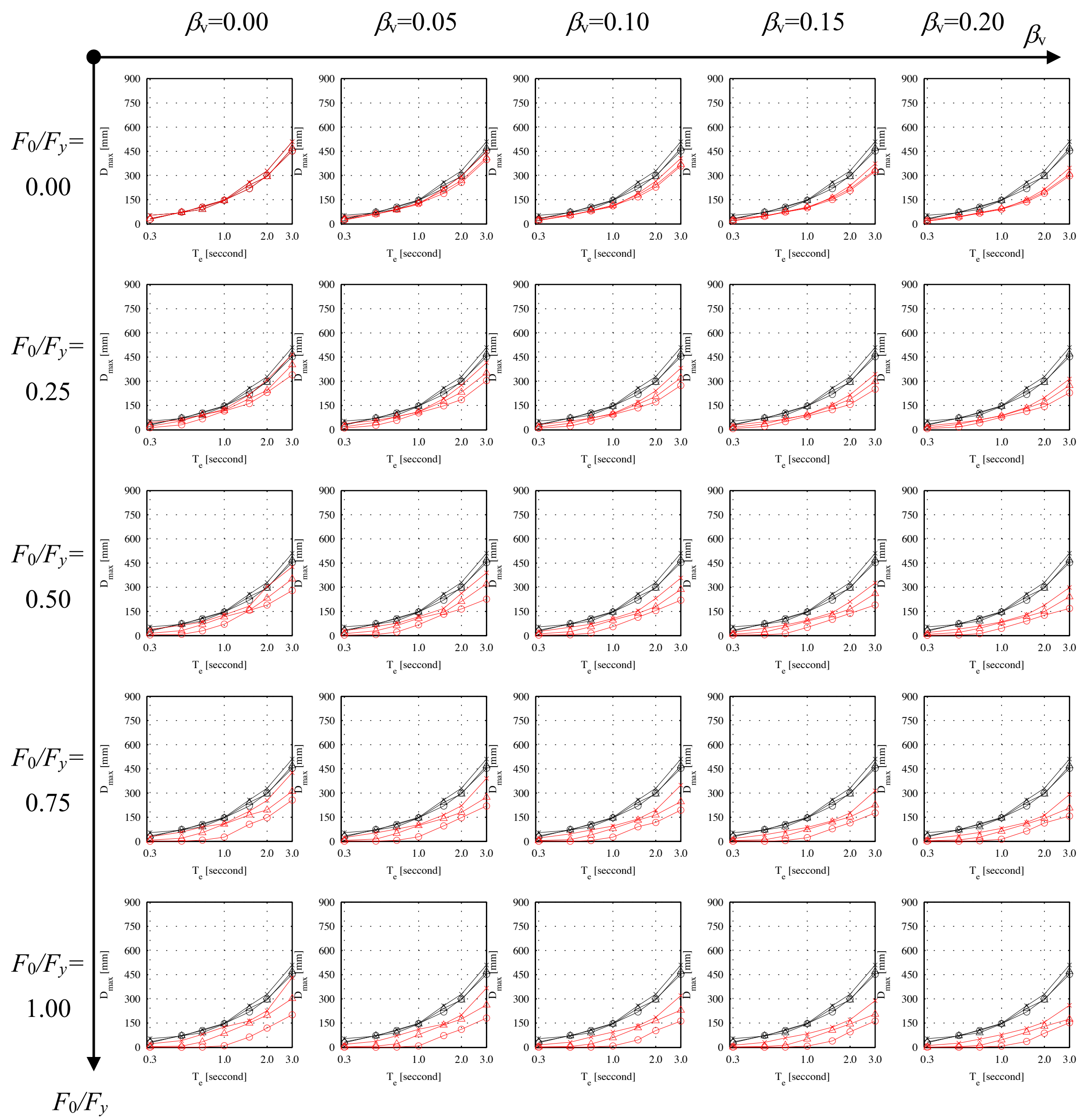

Figure A-66 Displacement in DE, Far-Field Motions, Upper-half Viscous Damping, Stiffness K_0=0, R_μ=1, 2 and 5

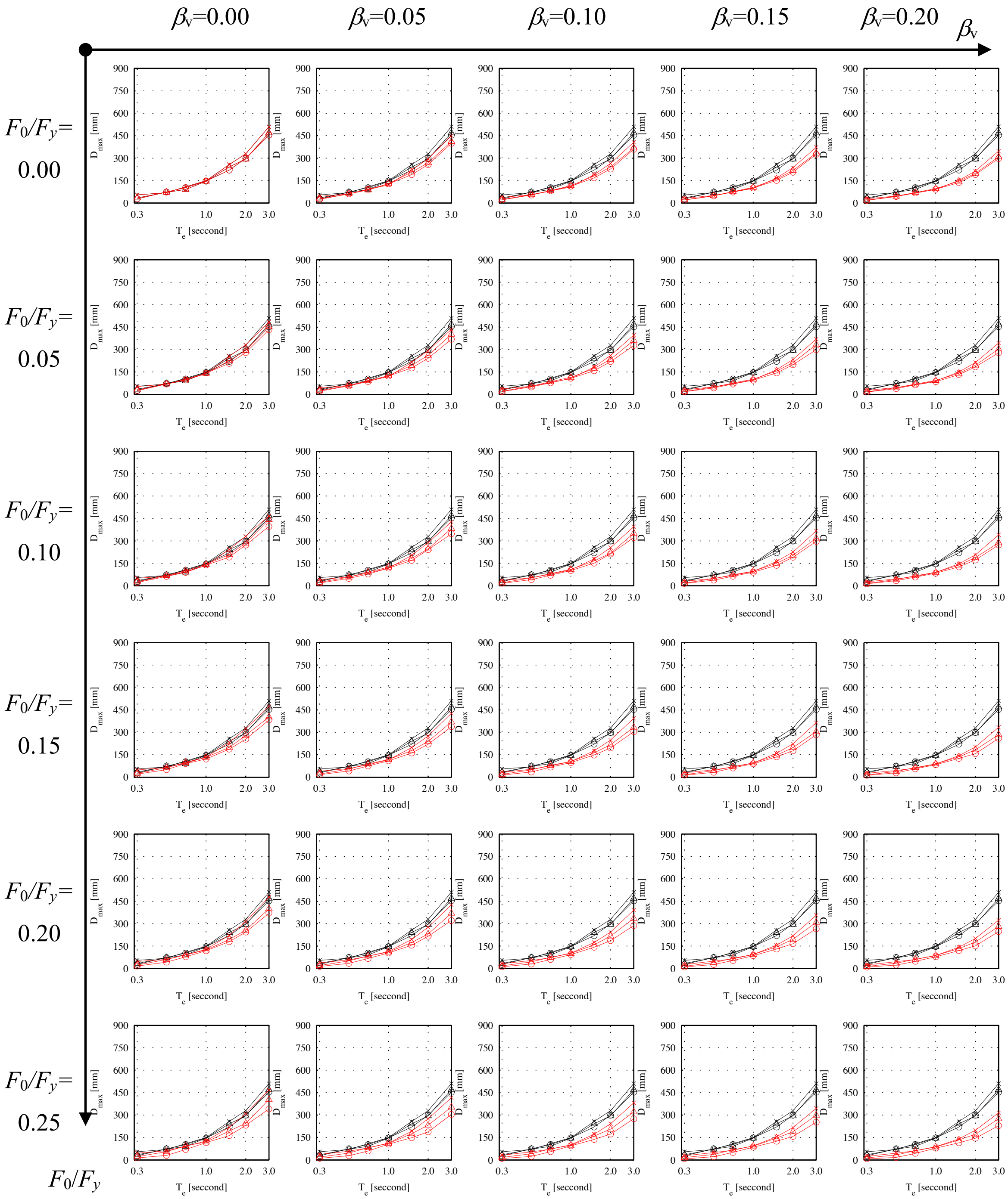

Figure A-66 (Continued)

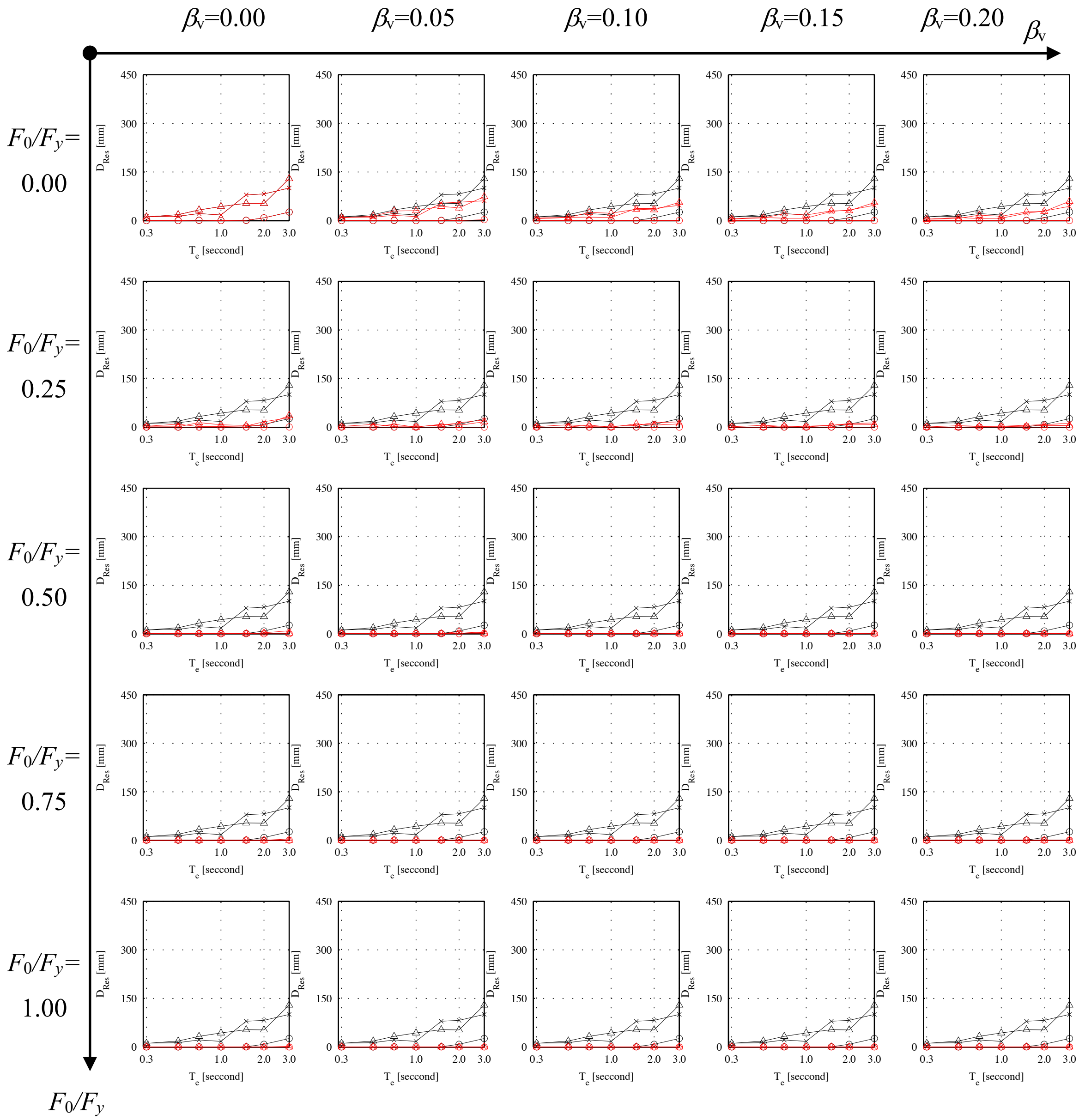

Figure A-67 Residual Displacement in DE, Far-Field Motions, Upper-half Viscous Damping, Stiffness K_0=0, R_μ=1, 2 and 5

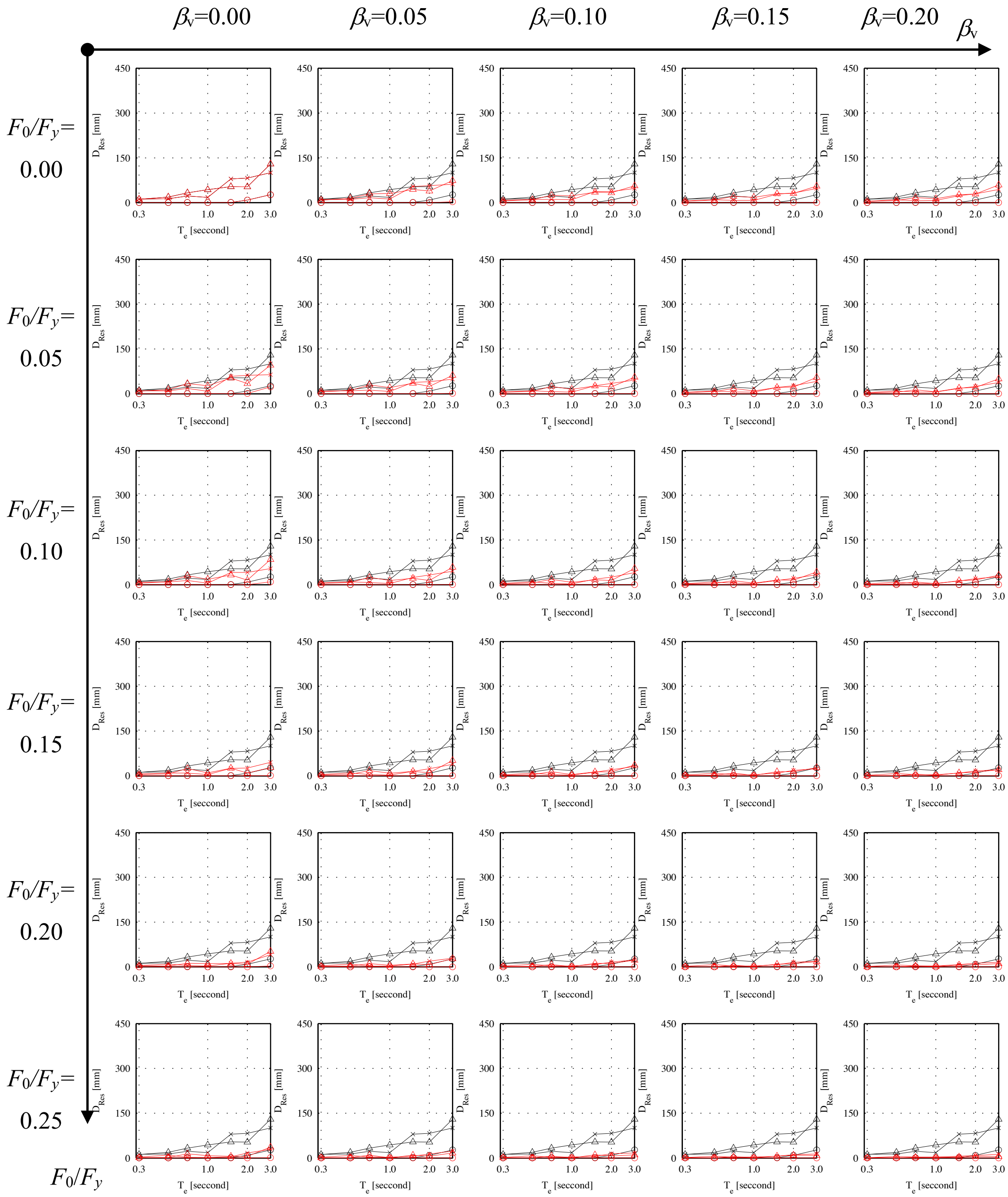

Figure A-67 (Continued)

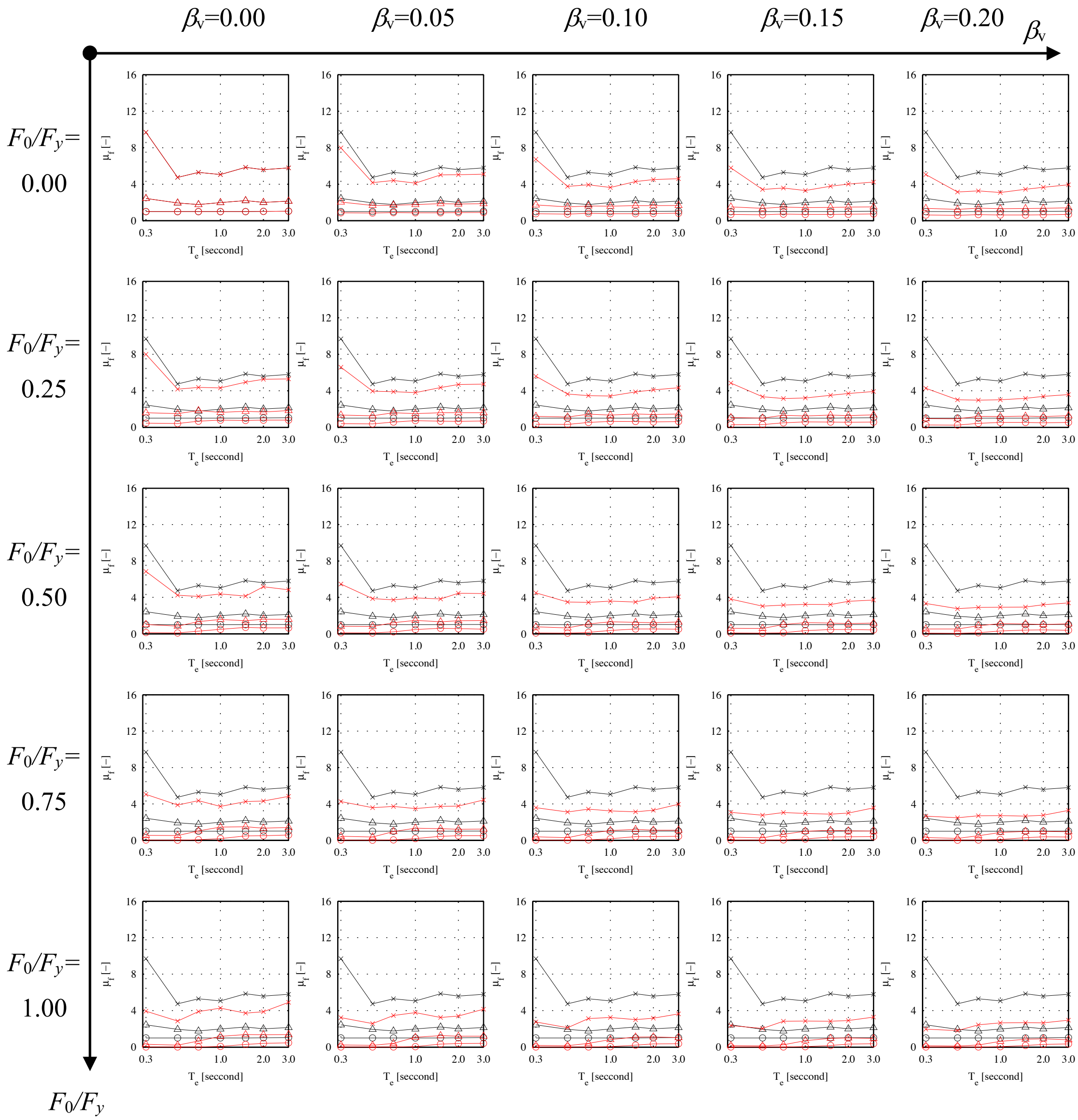

Figure A-68 Ductility Ratio in DE, Far-Field Motions, Upper-half Viscous Damping, Stiffness K_0=0, R_μ=1, 2 and 5

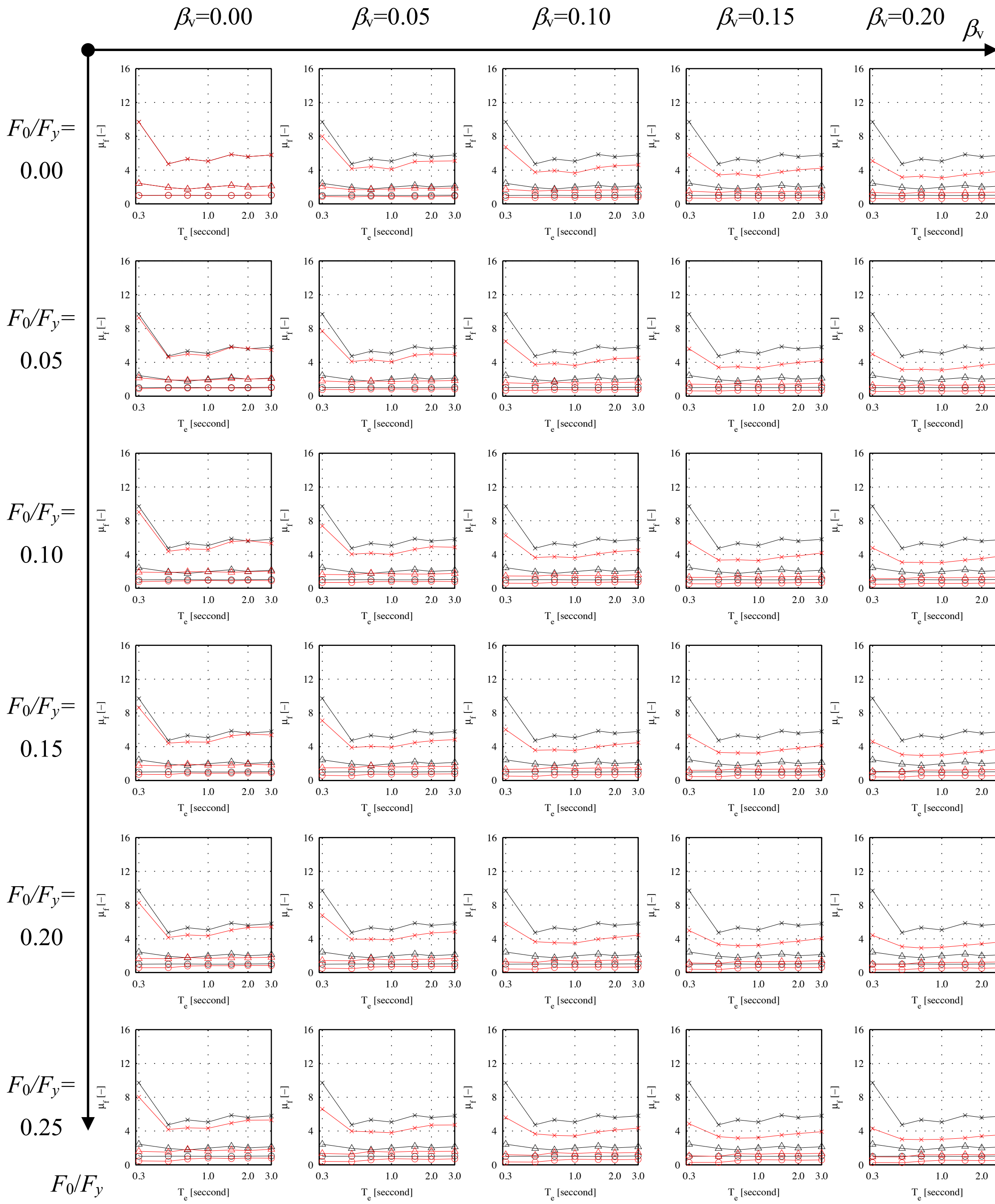

Figure A-68 (Continued)

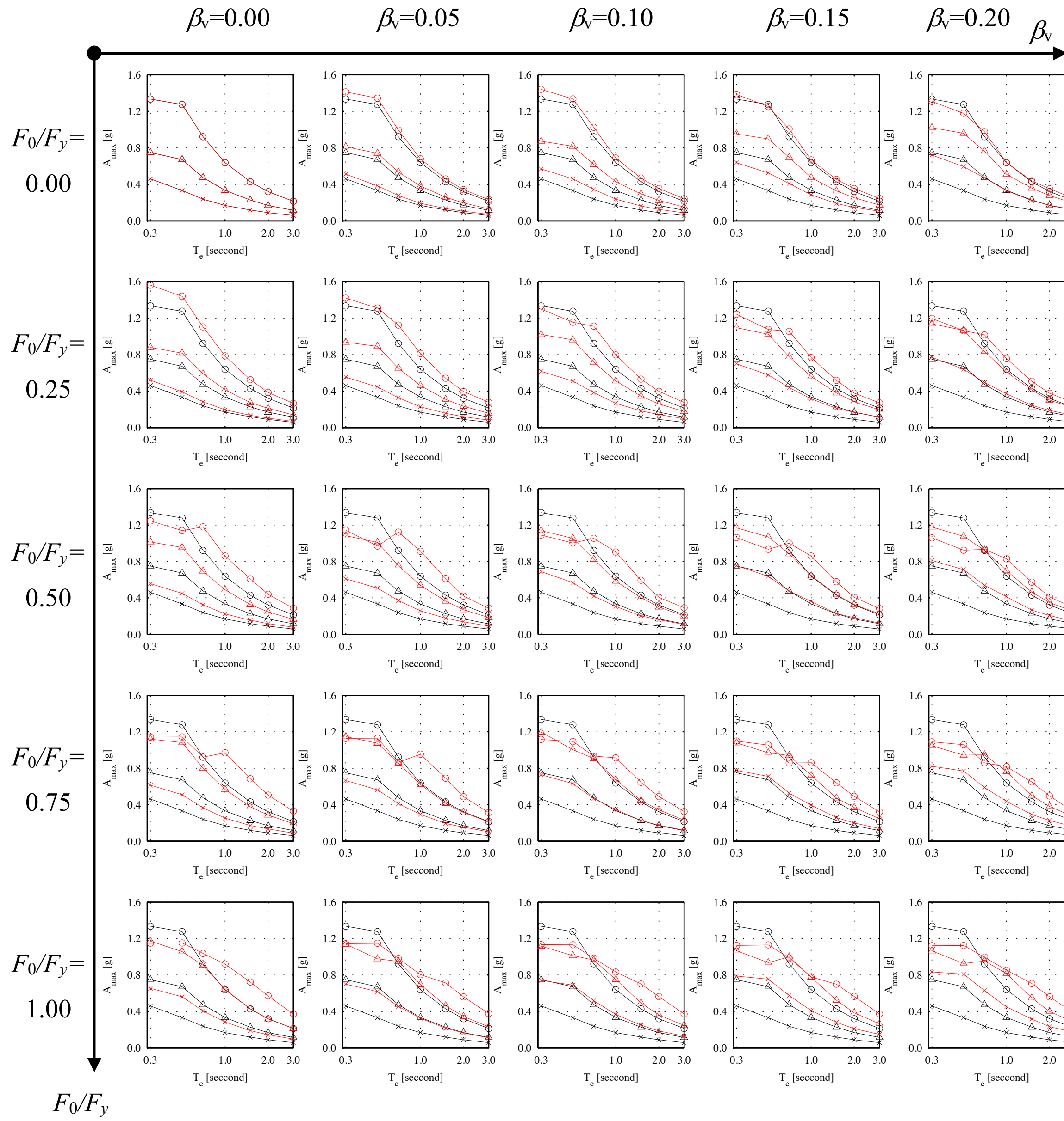

Figure A-69 Acceleration in MCE, Far-Field Motions, Upper-half Viscous Damping, Stiffness K_0=0, R_μ=1, 2 and 5

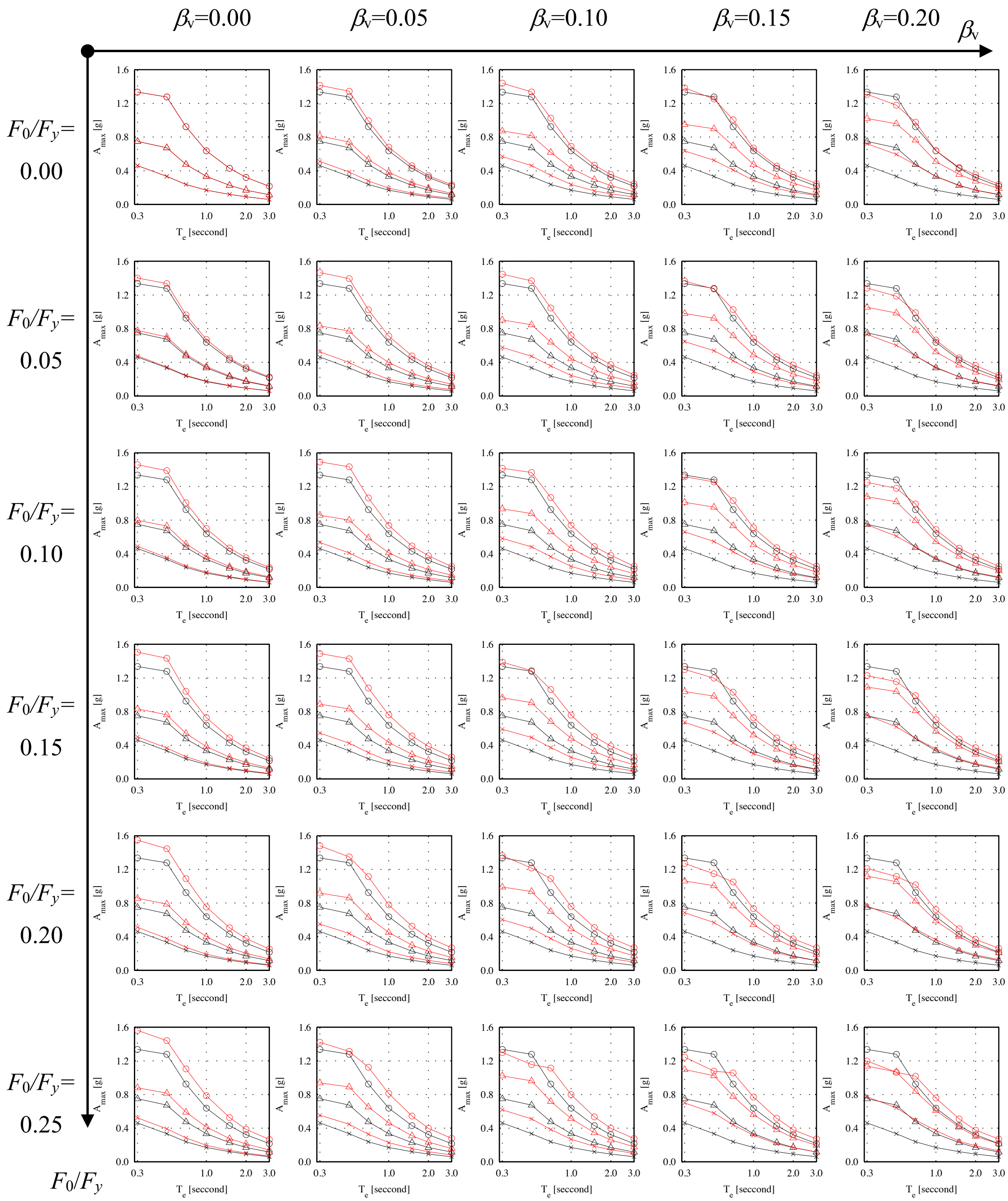

Figure A-69 (Continued)

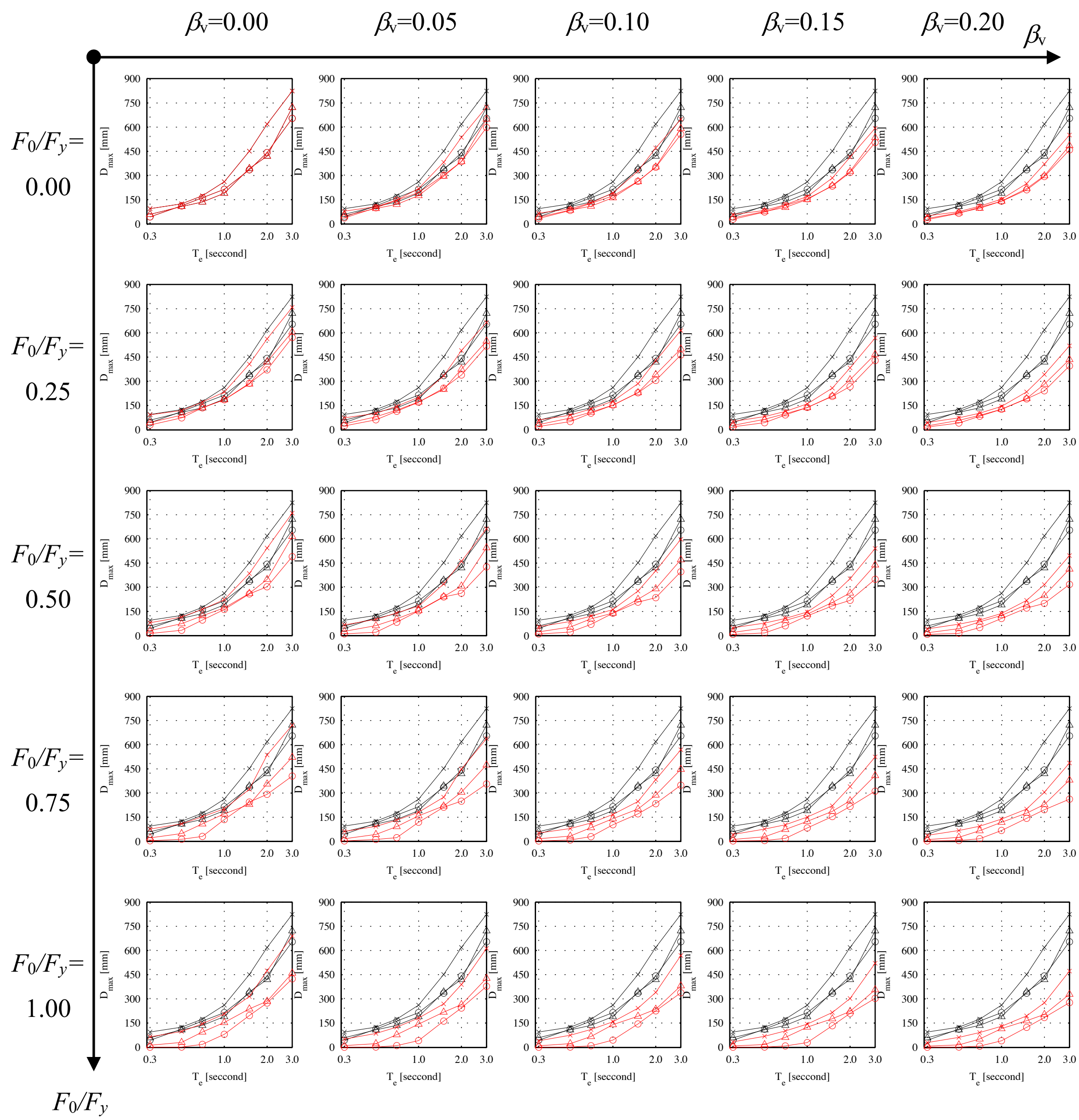

Figure A-70 Displacement in MCE, Far-Field Motions, Upper-half Viscous Damping, Stiffness K_0=0, R_μ=1, 2 and 5

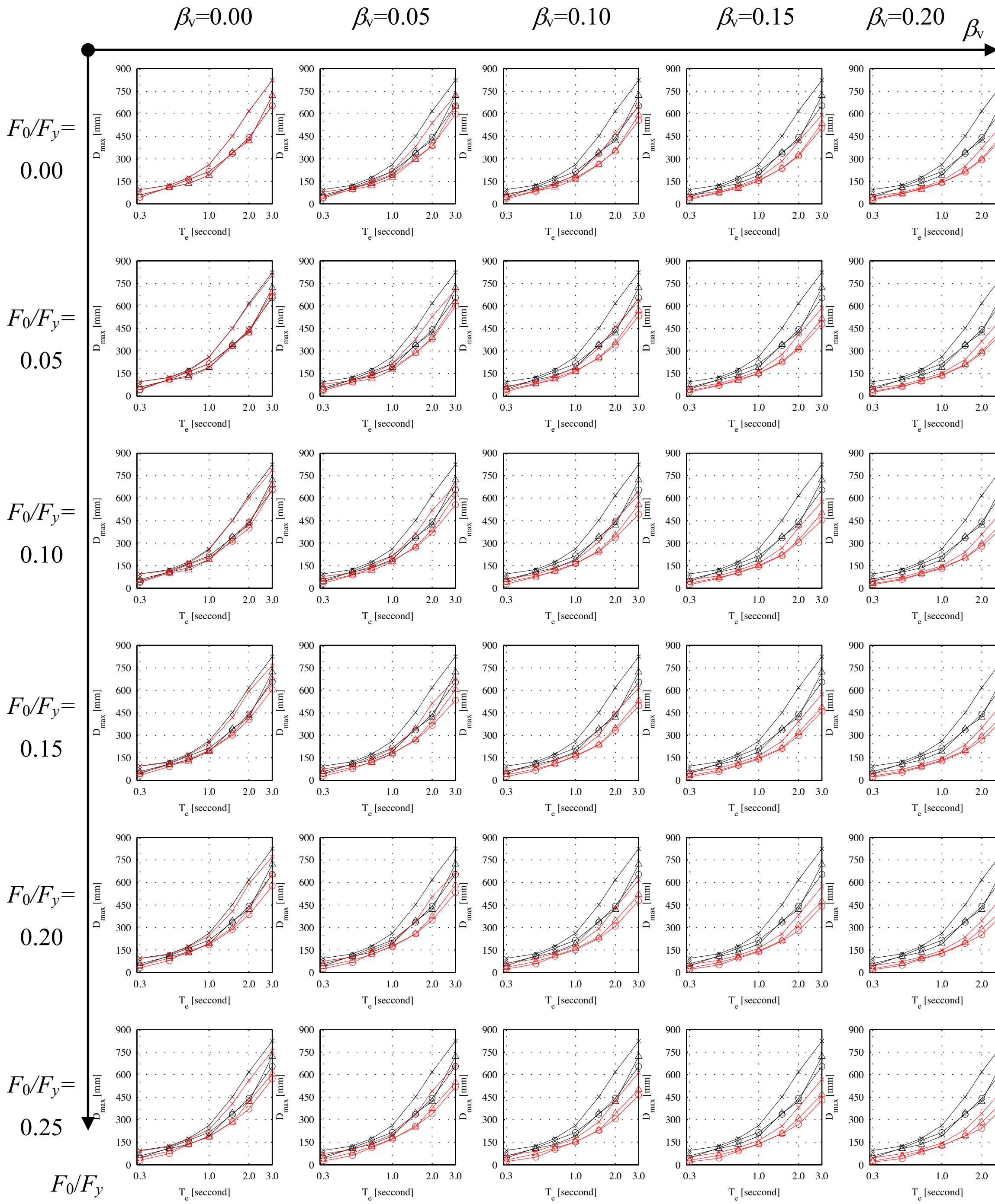

Figure A-70 (Continued)

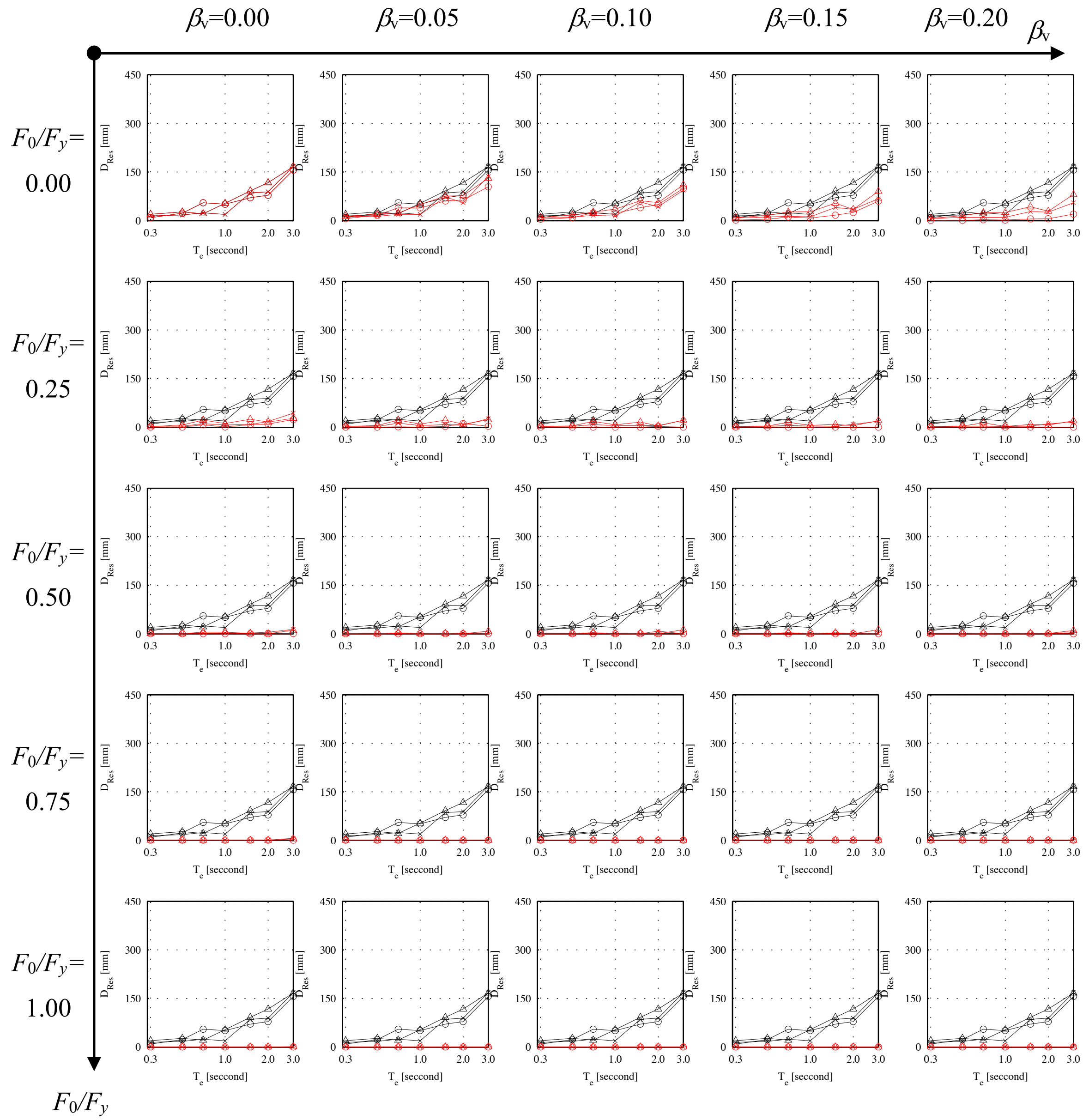

Figure A-71 Residual Displacement in MCE, Far-Field Motions, Upper-half Viscous Damping, Stiffness K_0=0, R_μ=1, 2 and 5

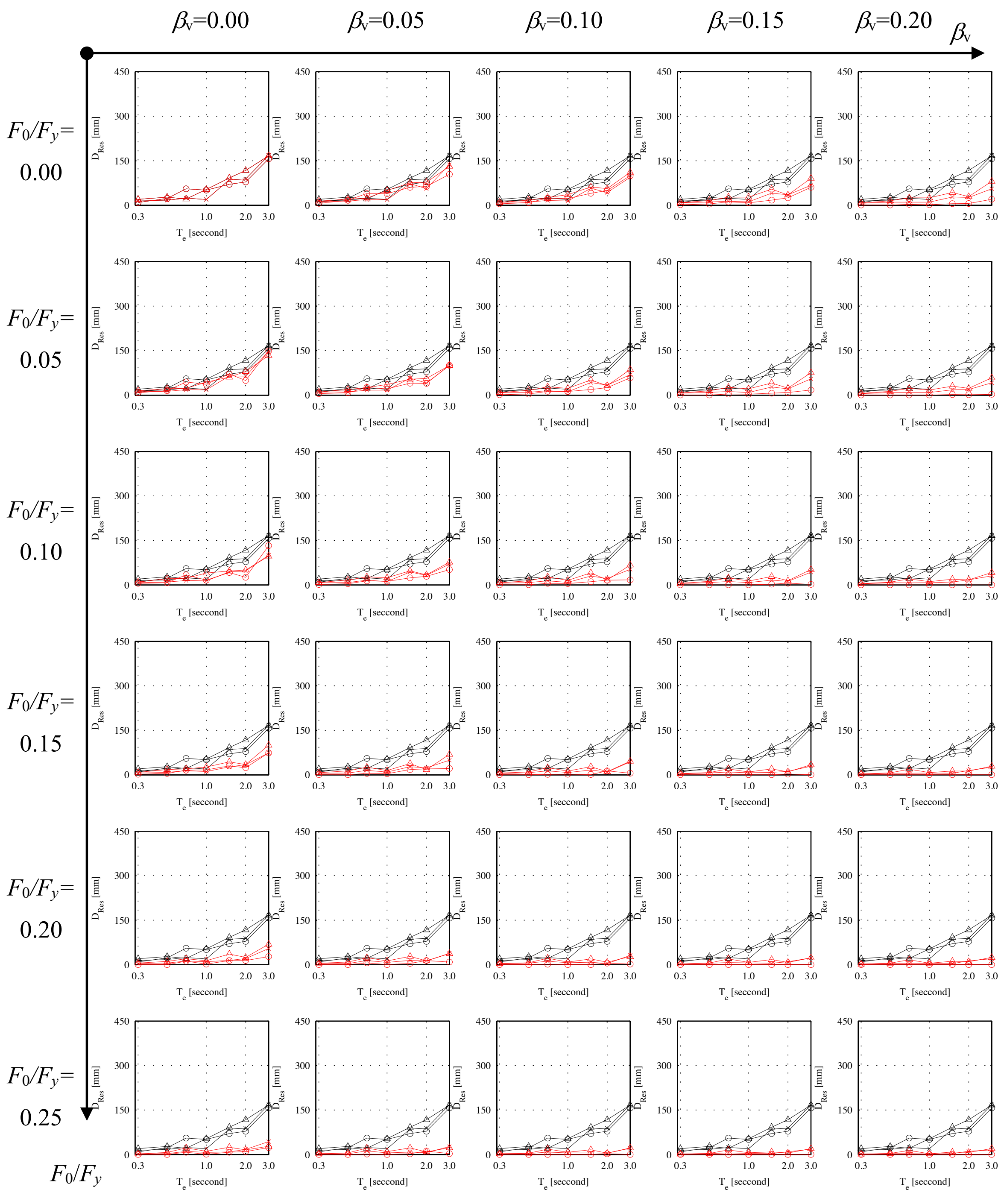

Figure A-71 (Continued)

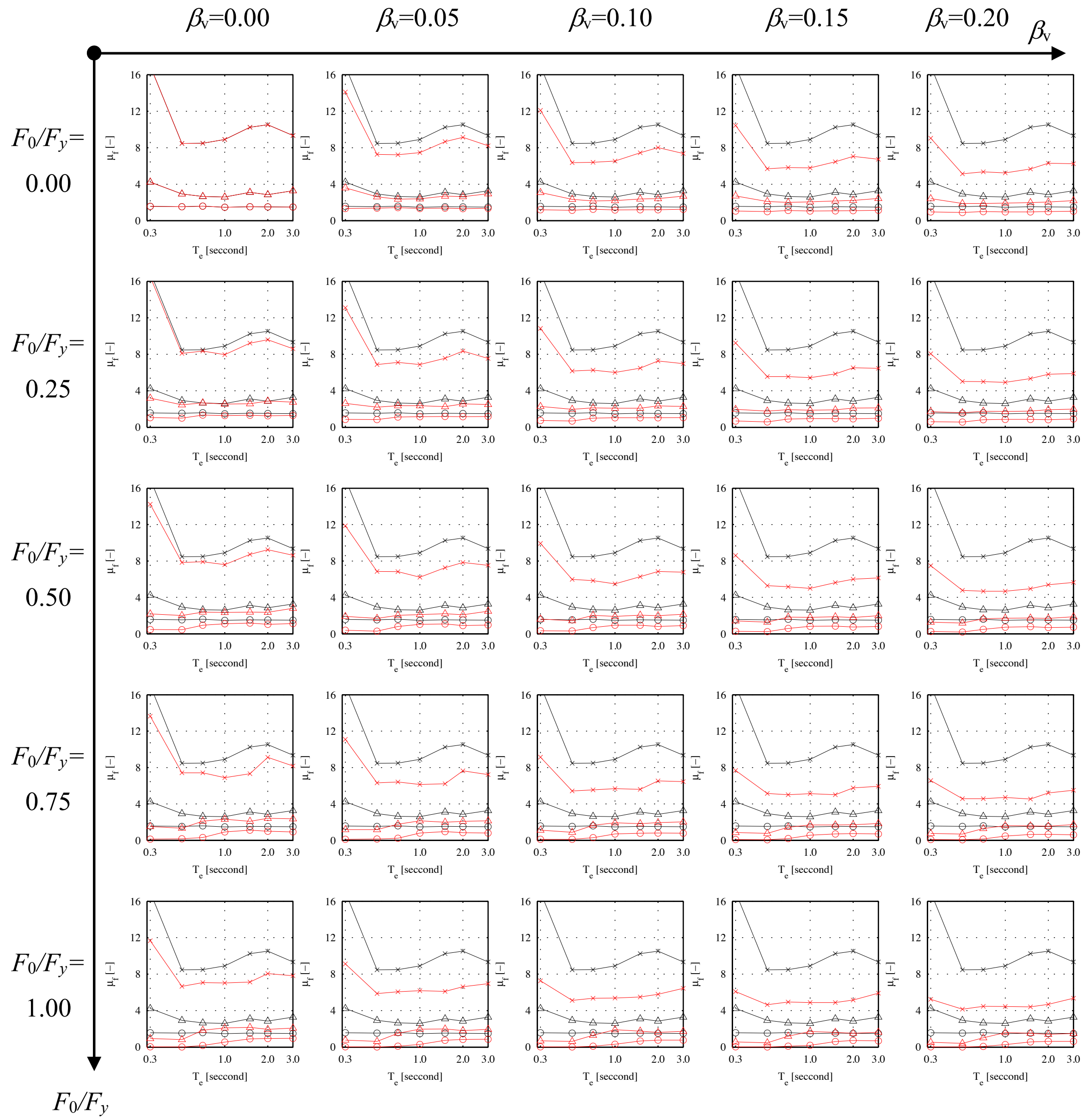

Figure A-72 Ductility Ratio in MCE, Far-Field Motions, Upper-half Viscous Damping, Stiffness K_0=0, R_μ=1, 2 and 5

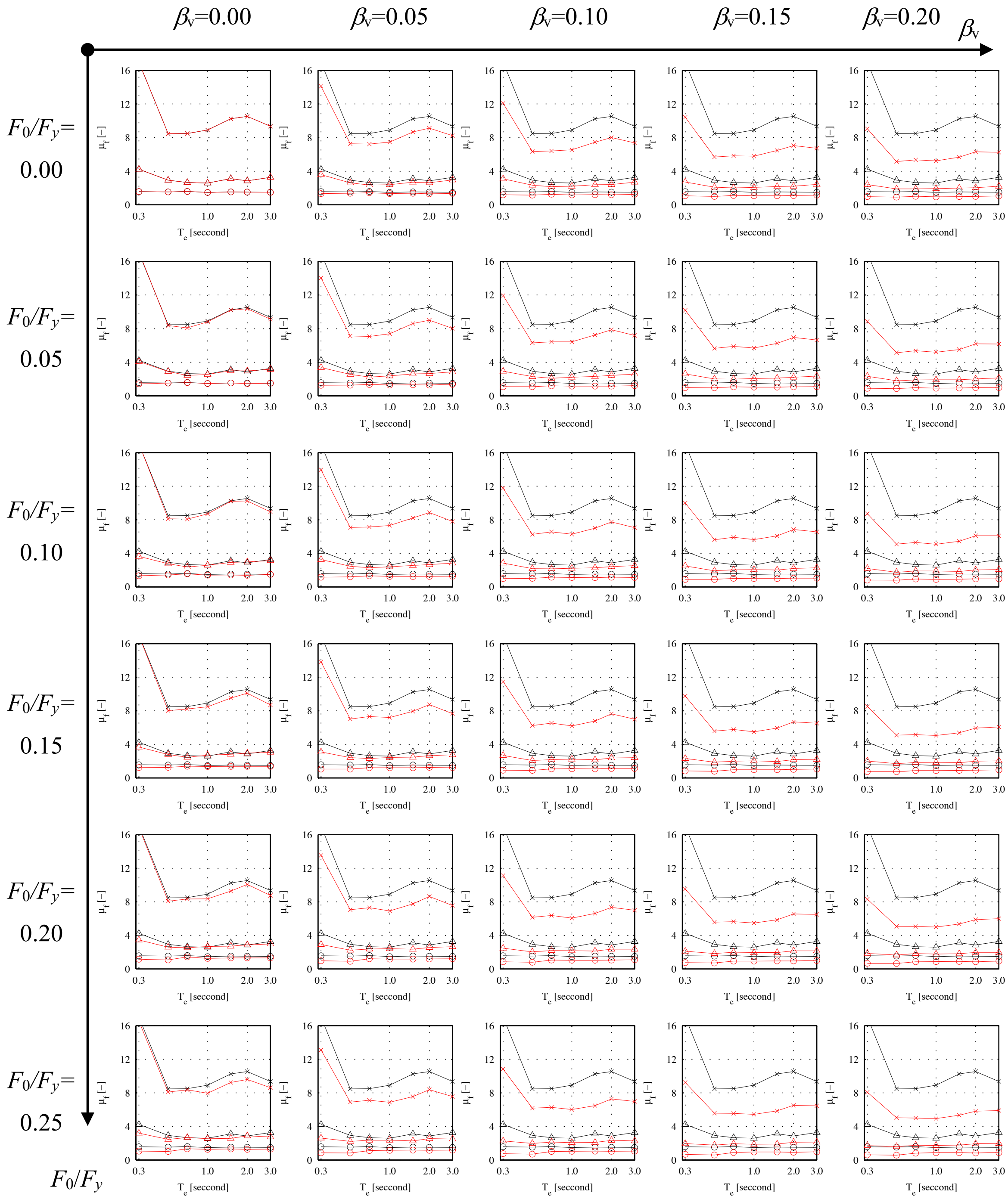

Figure A-72 (Continued)

A.4 Structure with Linear Viscous Damping and $K_0 \neq 0$ in Near-Fault Pulse-Like Ground Motions

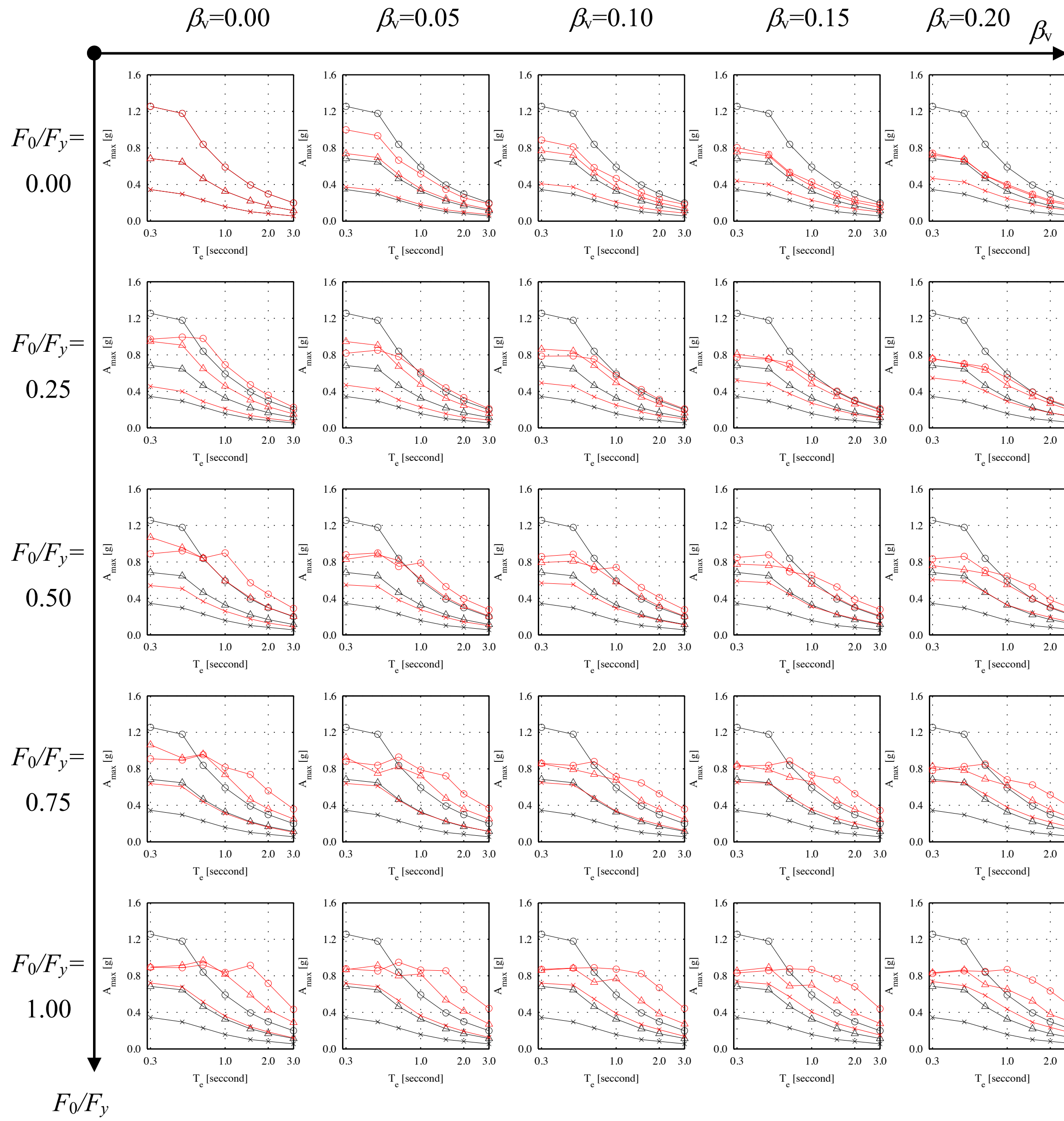

Figure A-73 Acceleration in DE, Near-Fault Pulse-like Motions, Linear Viscous Damping, Stiffness $K_0 \neq 0$, R_μ=1, 2 and 5

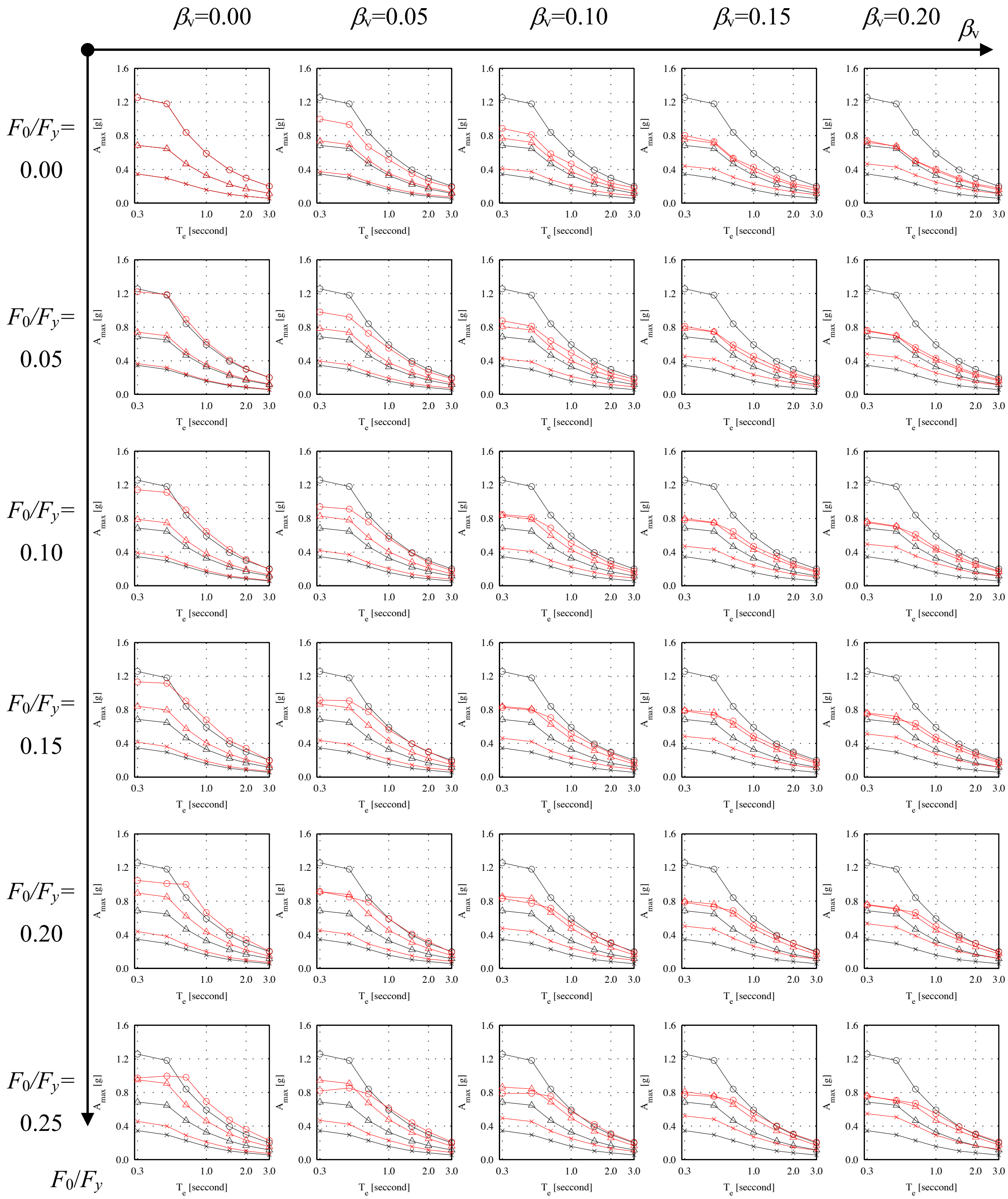

Figure A-73 (Continued)

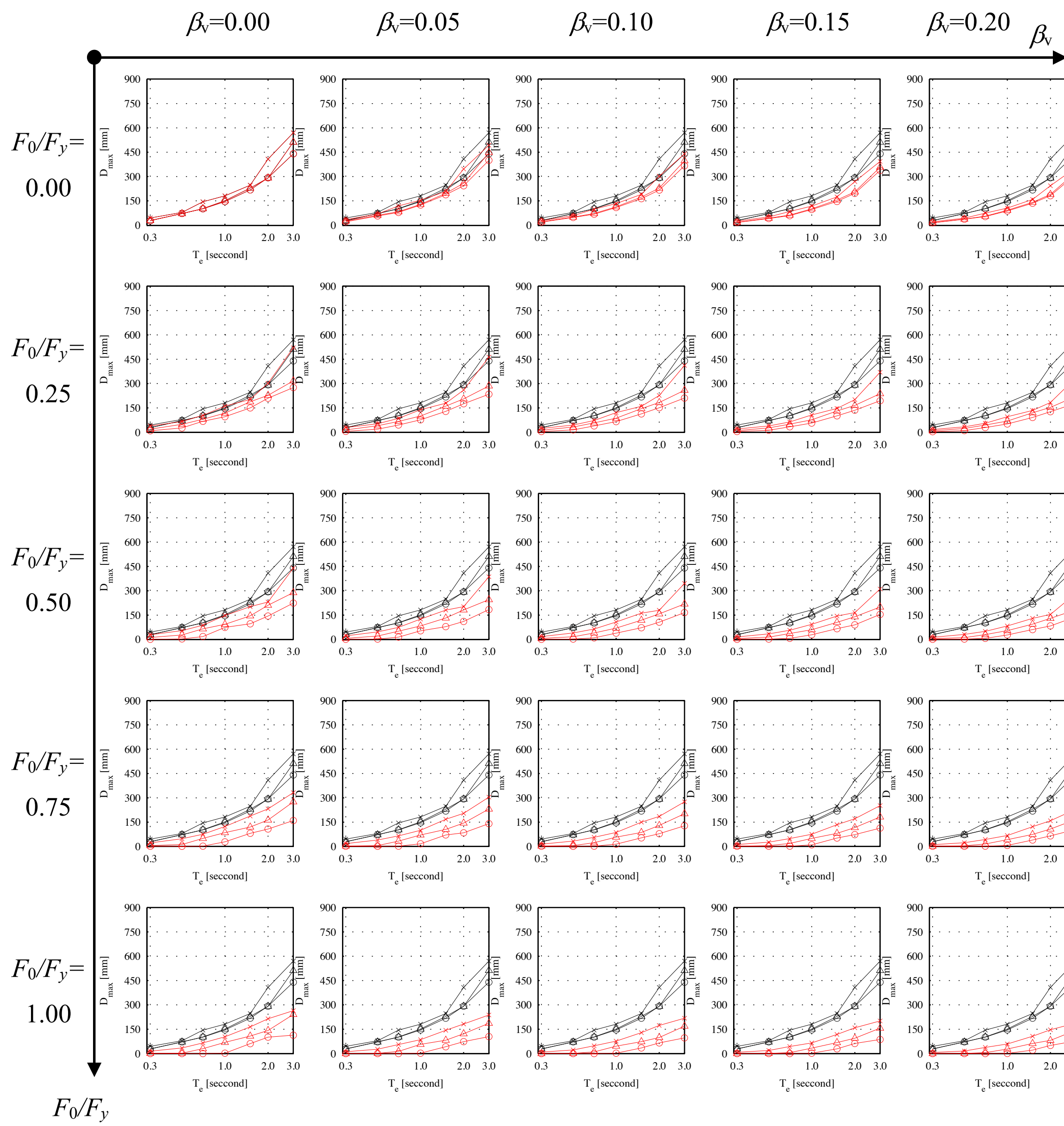

Figure A-74 Displacement in DE, Near-Fault Pulse-like Motions, Linear Viscous Damping, Stiffness $K_0 \neq 0$, R_μ=1, 2 and 5

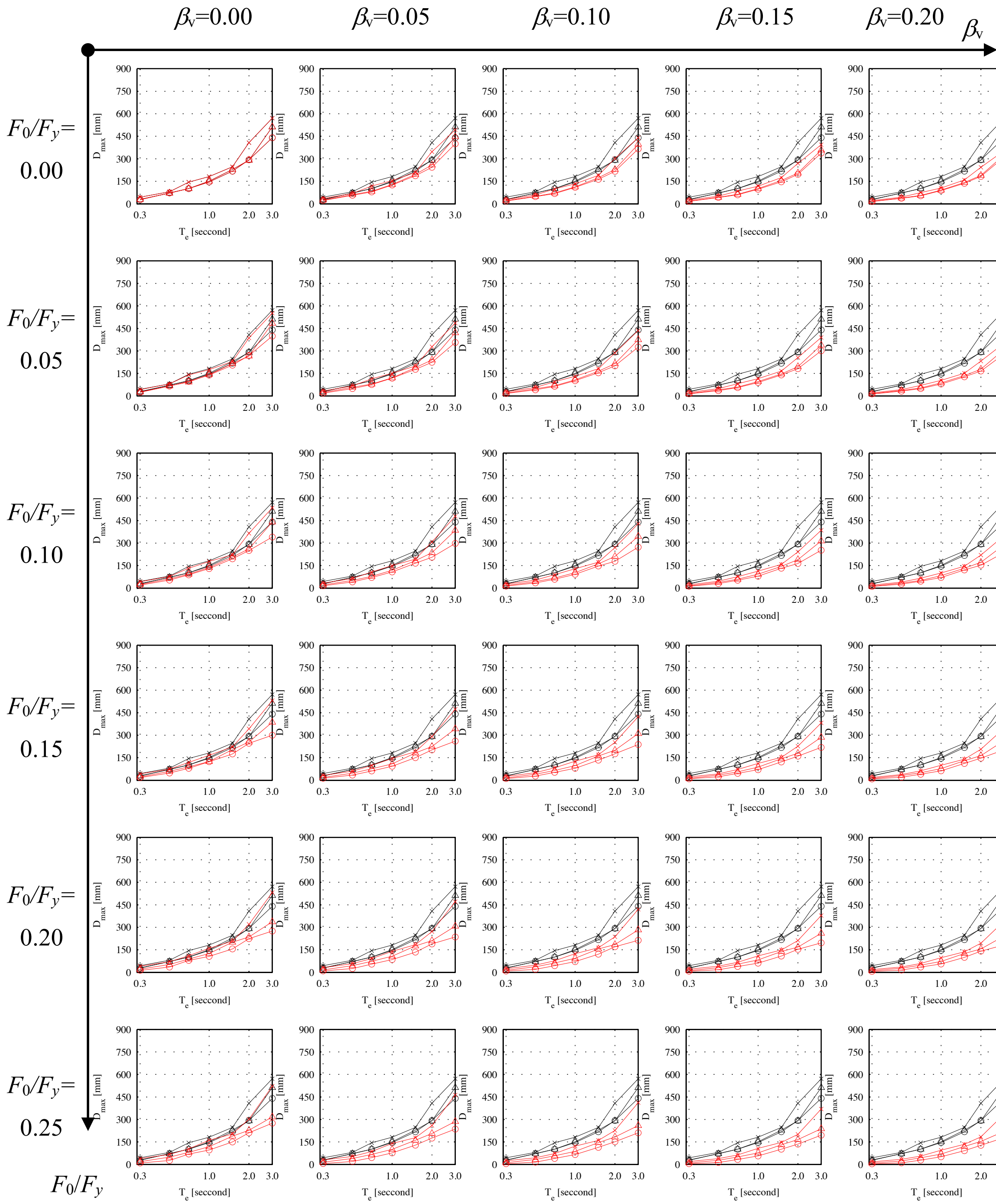

Figure A-74 (Continued)

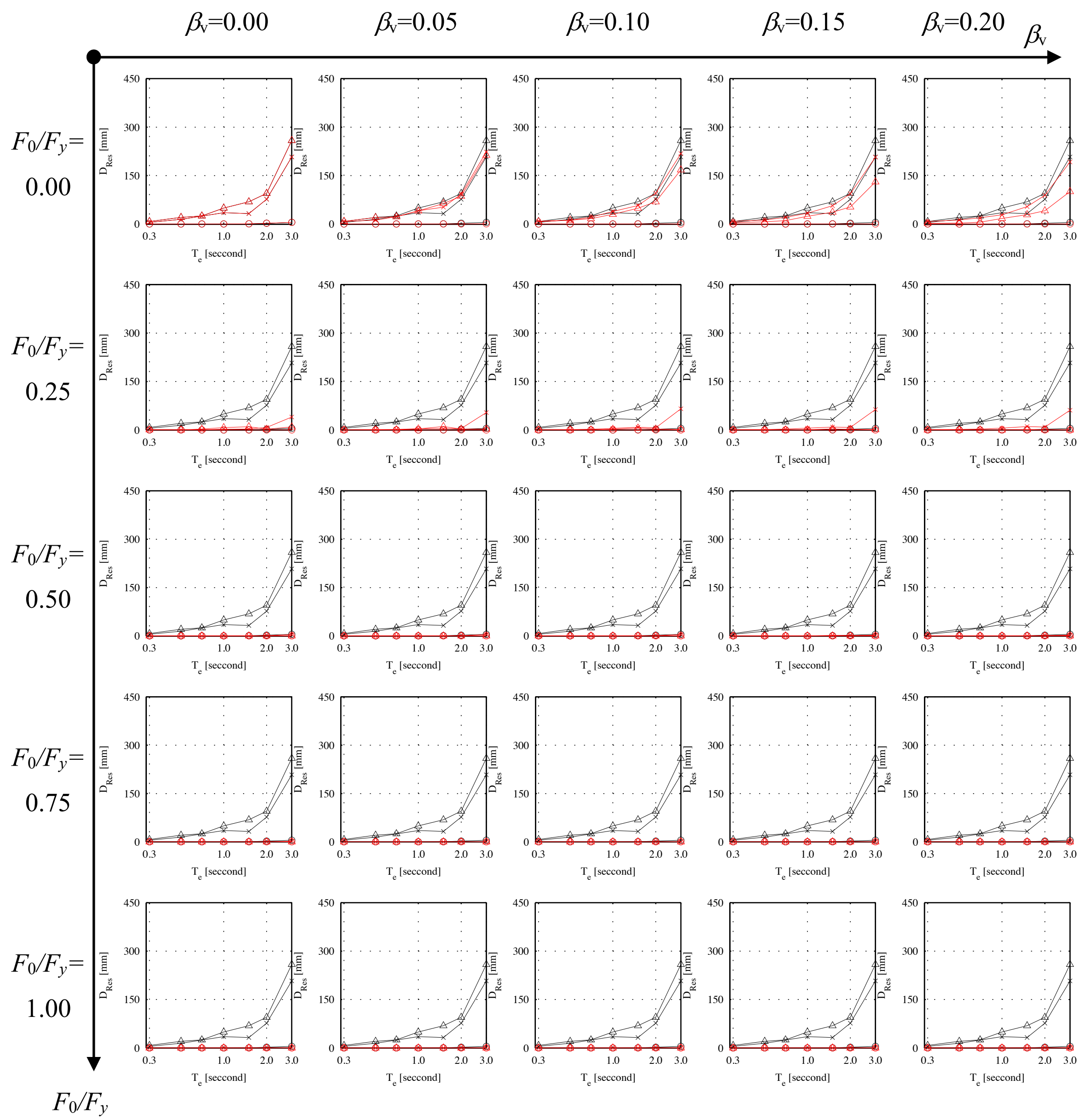

Figure A-75 Residual Displacement in DE, Near-Fault Pulse-like Motions, Linear Viscous Damping, Stiffness K_0≠0, R_μ=1, 2 and 5

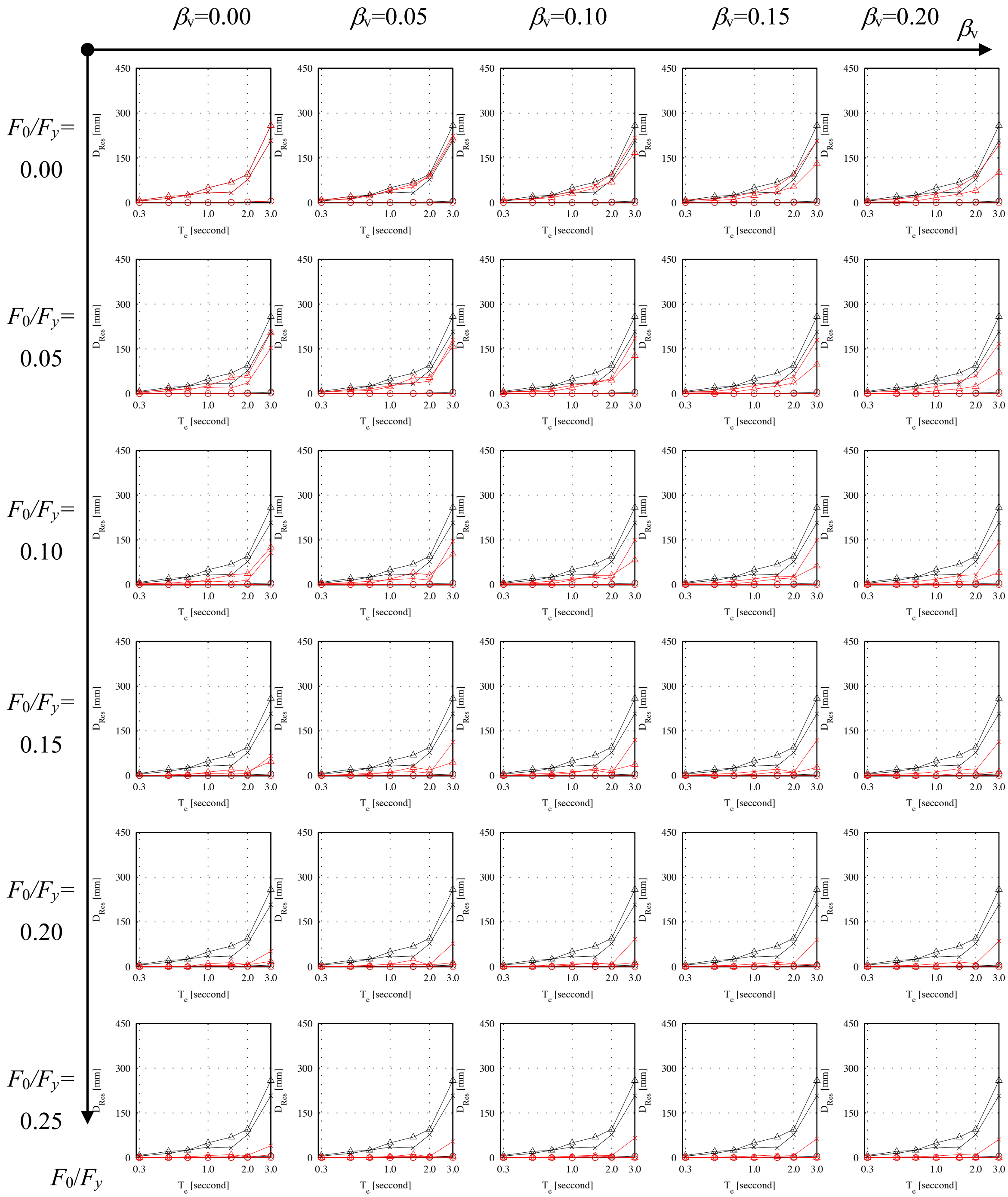

Figure A-75 (Continued)

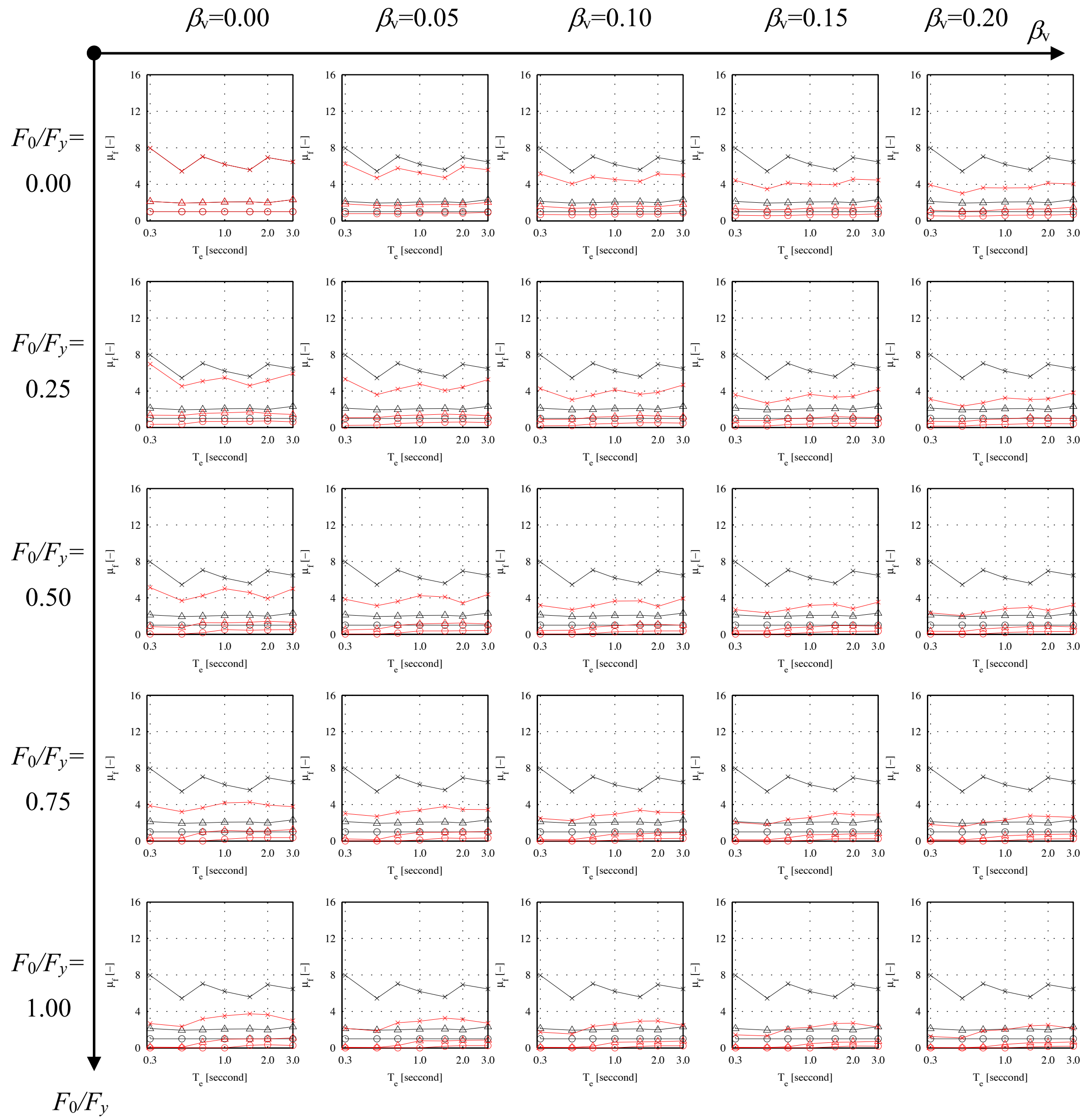

Figure A-76 Ductility Ratio in DE, Near-Fault Pulse-like Motions, Linear Viscous Damping, Stiffness $K_0 \neq 0$, R_μ=1, 2 and 5

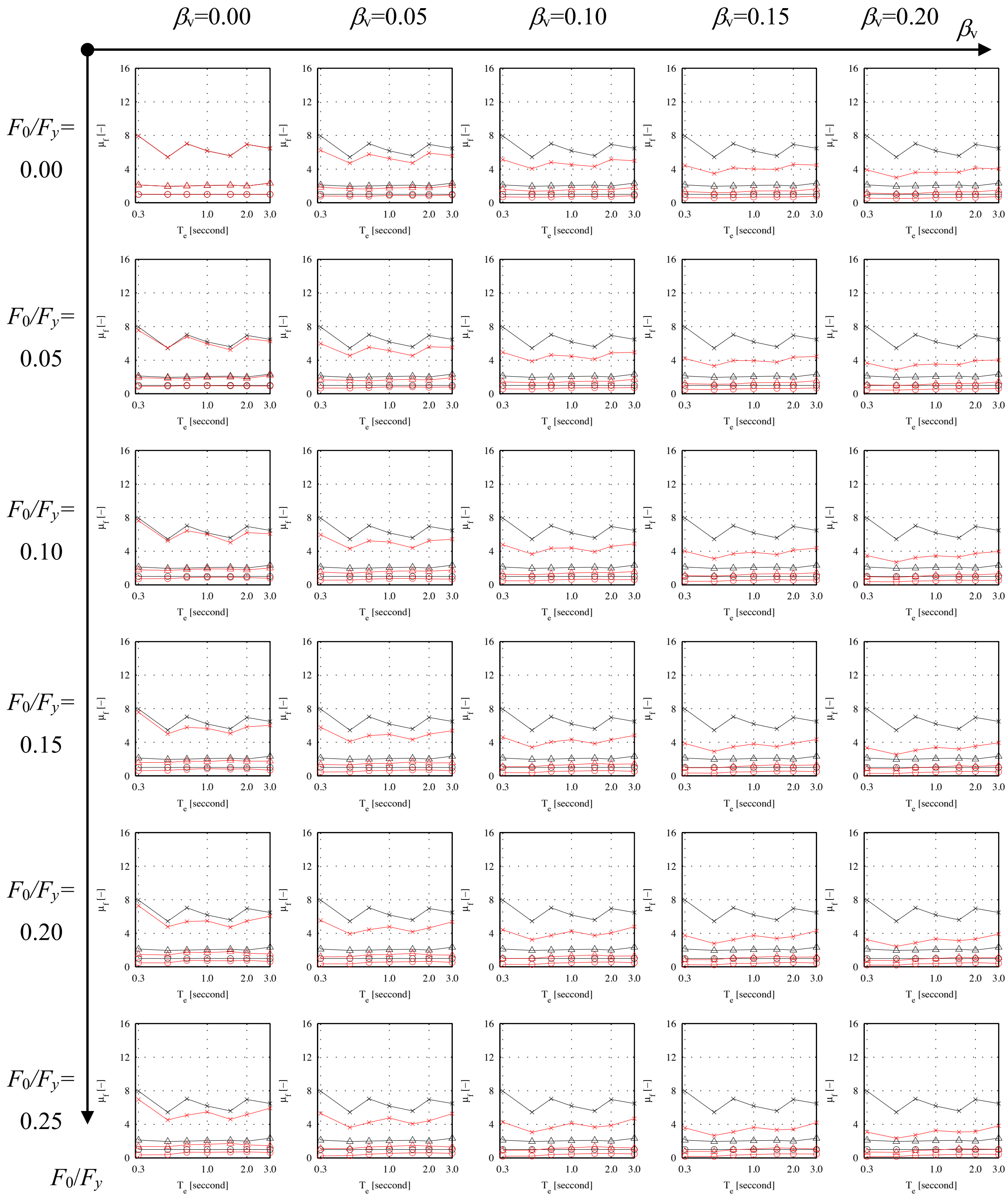

Figure A-76 (Continued)

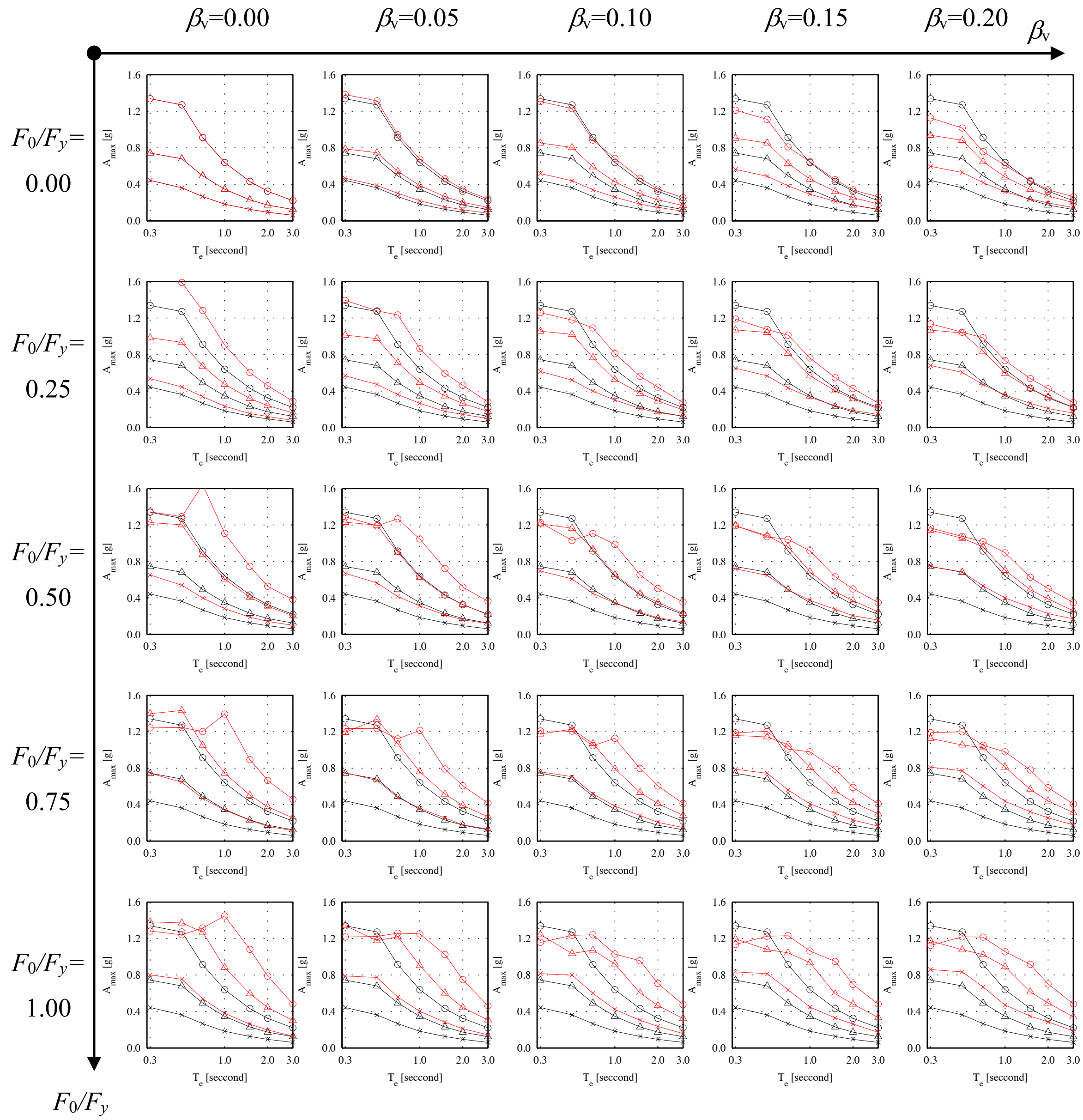

Figure A-77 Acceleration in MCE, Near-Fault Pulse-like Motions, Linear Viscous Damping, Stiffness $K_0 \neq 0$, R_μ=1, 2 and 5

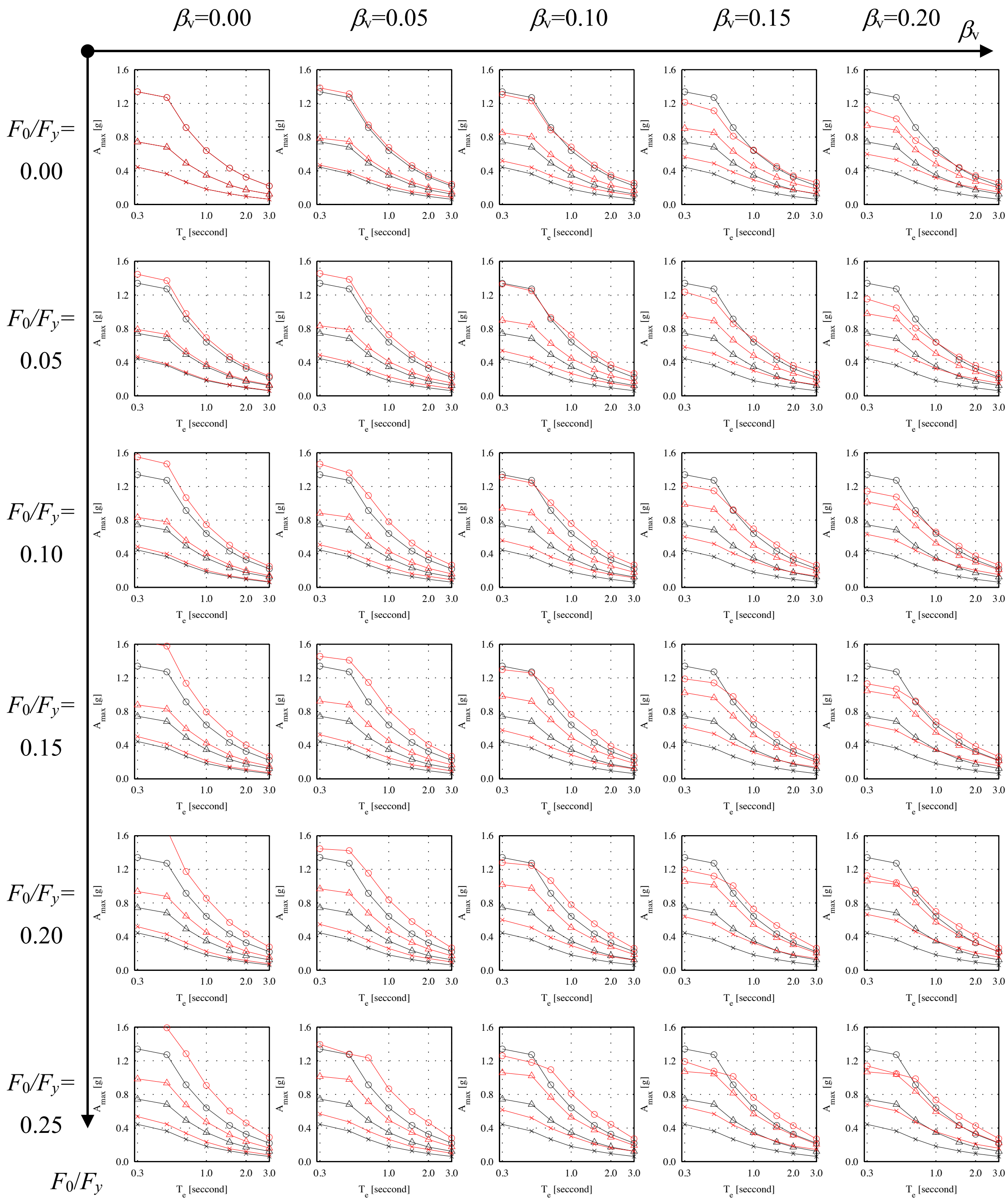

Figure A-77 (Continued)

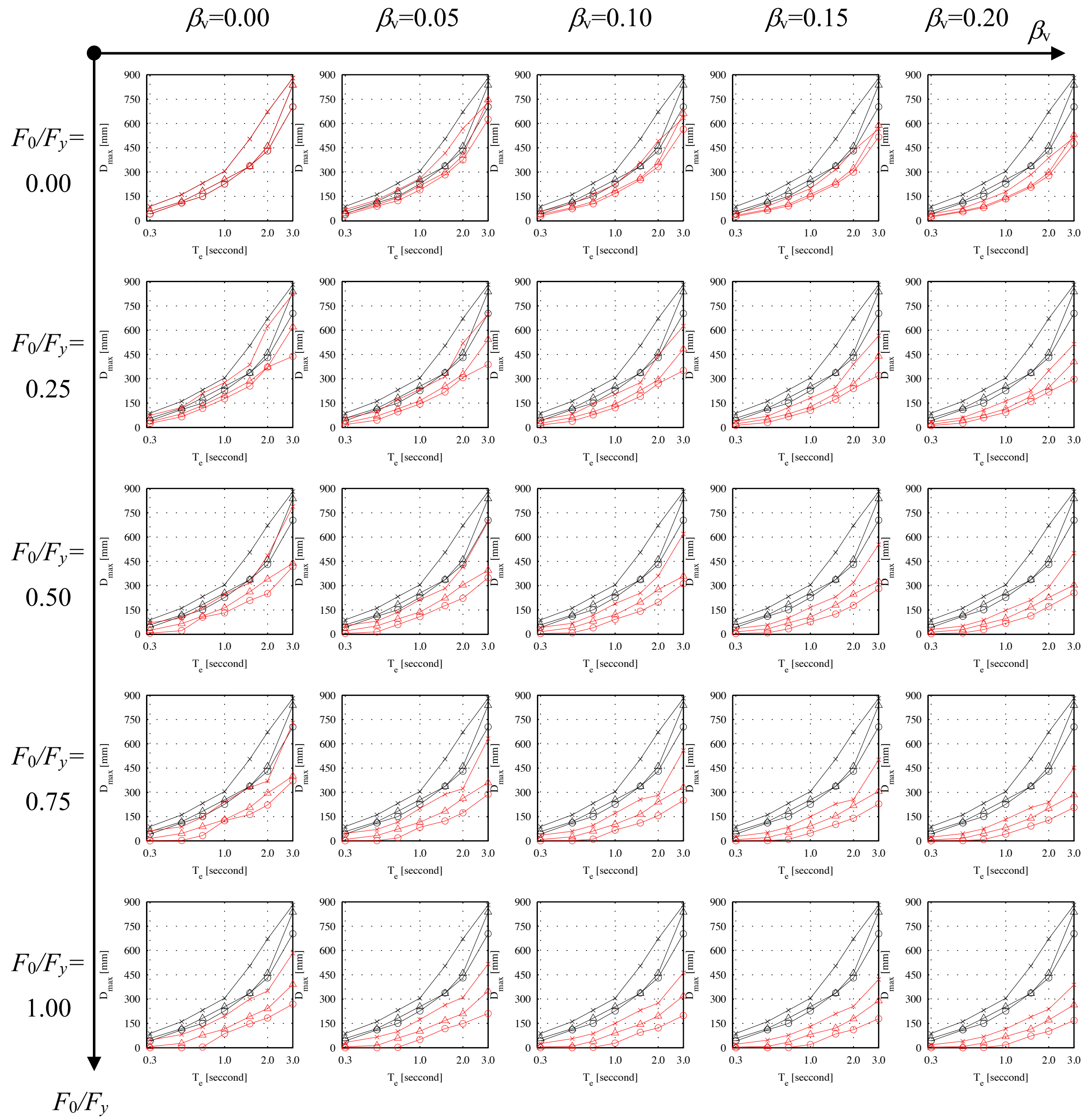

Figure A-78 Displacement in MCE, Near-Fault Pulse-like Motions, Linear Viscous Damping, Stiffness K_0≠0, R_μ=1, 2 and 5

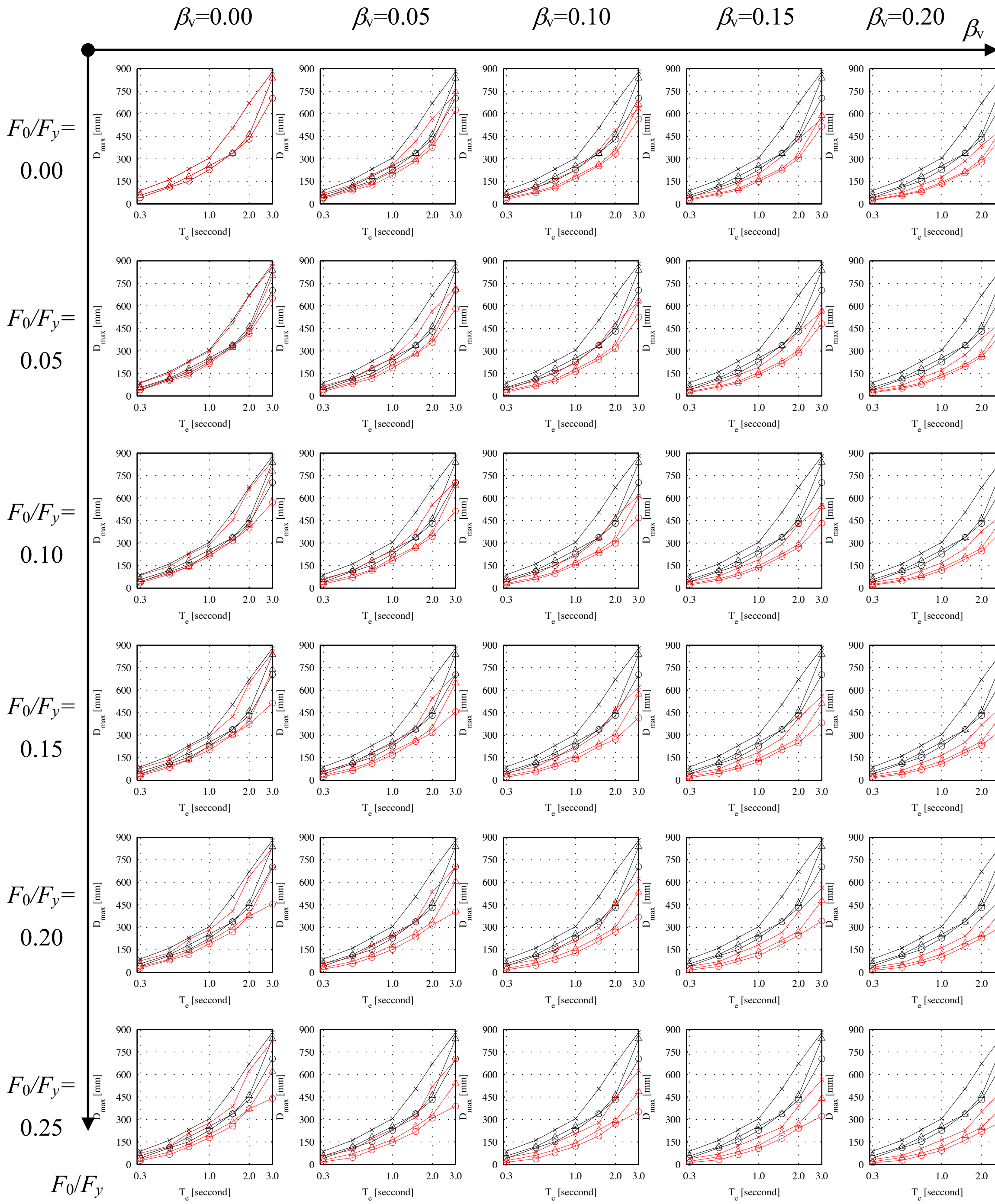

Figure A-78 (Continued)

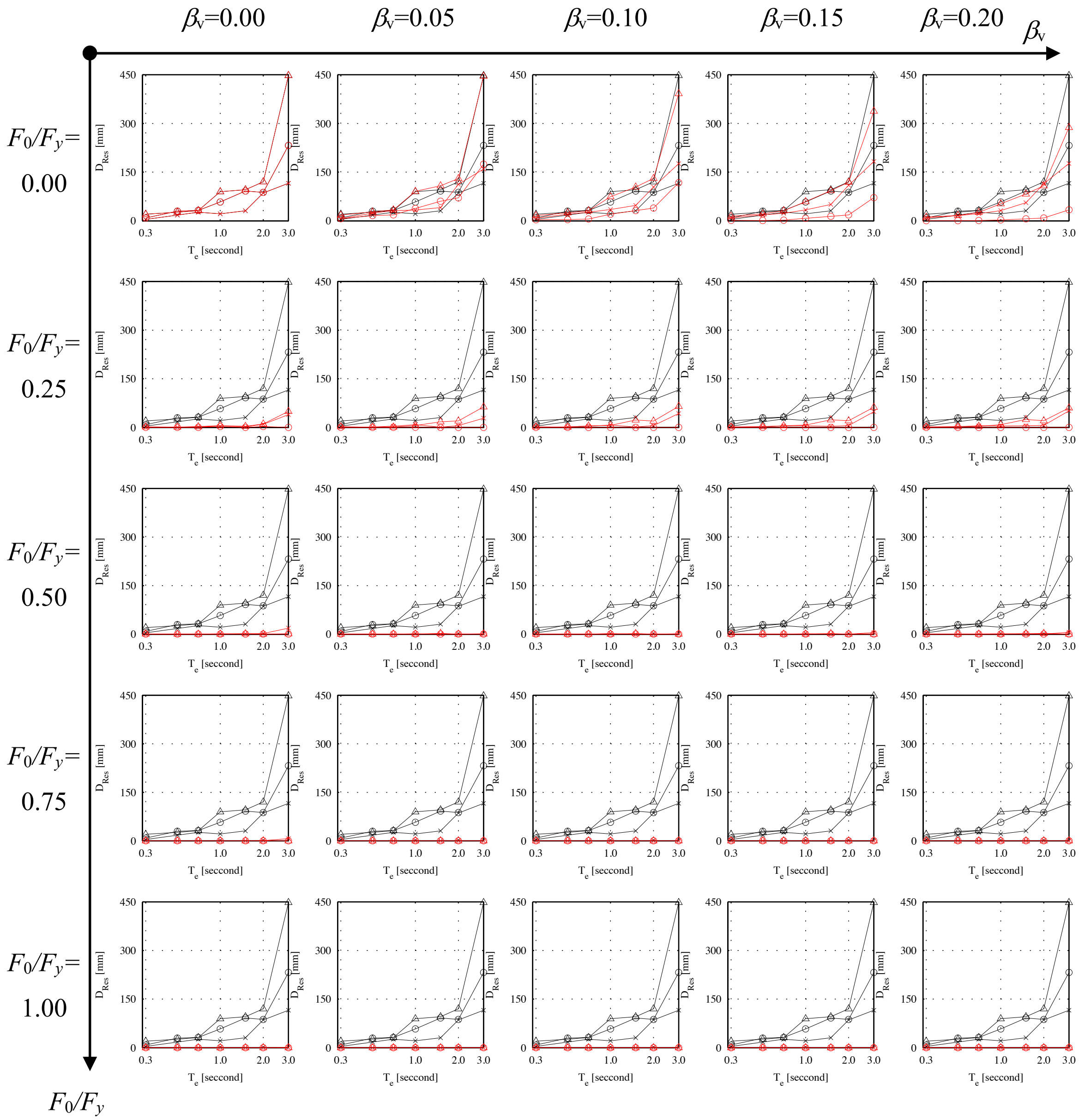

Figure A-79 Residual Displacement in MCE, Near-Fault Pulse-like Motions, Linear Viscous Damping, Stiffness $K_0 \neq 0$, R_μ=1, 2 and 5

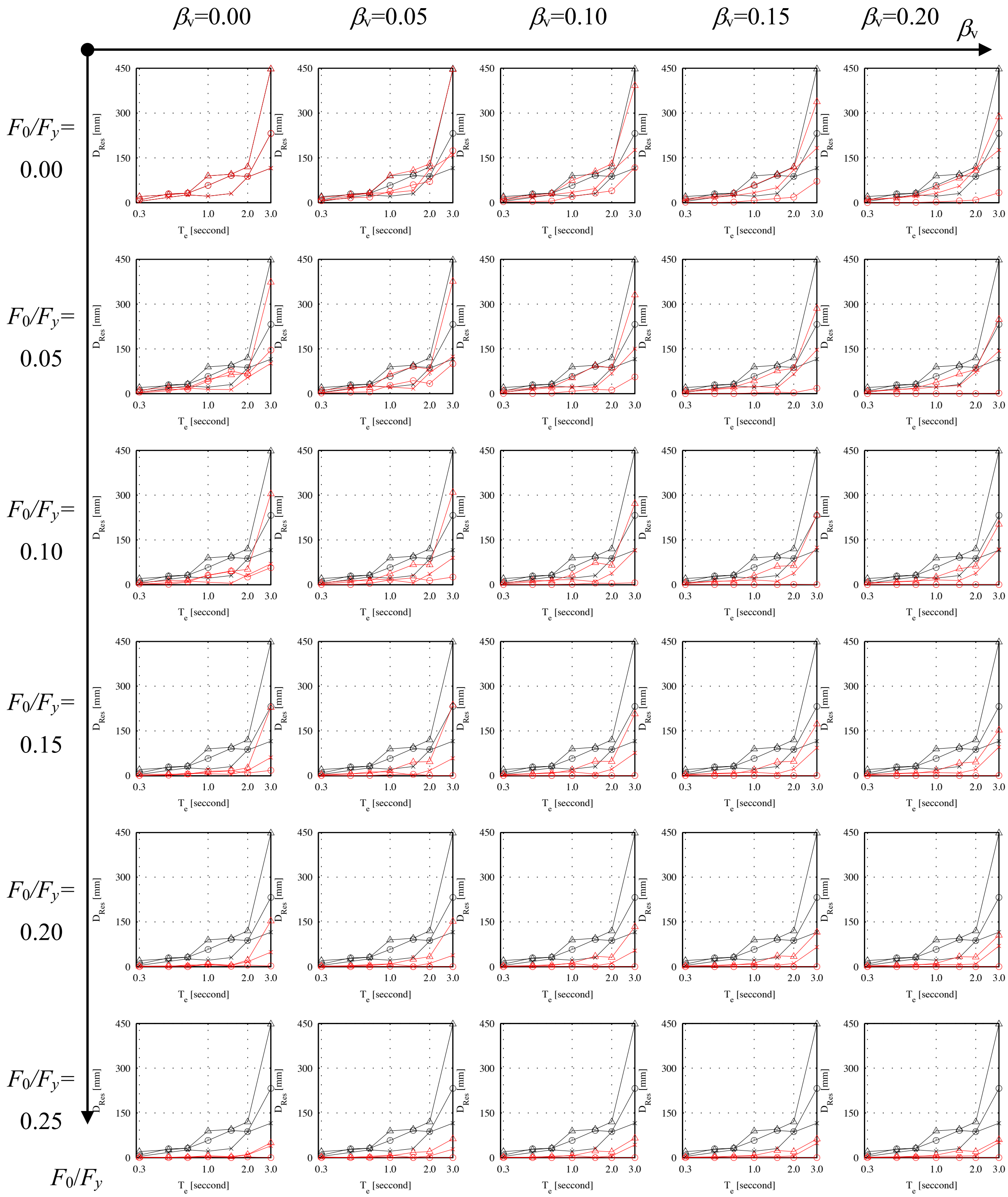

Figure A-79 (Continued)

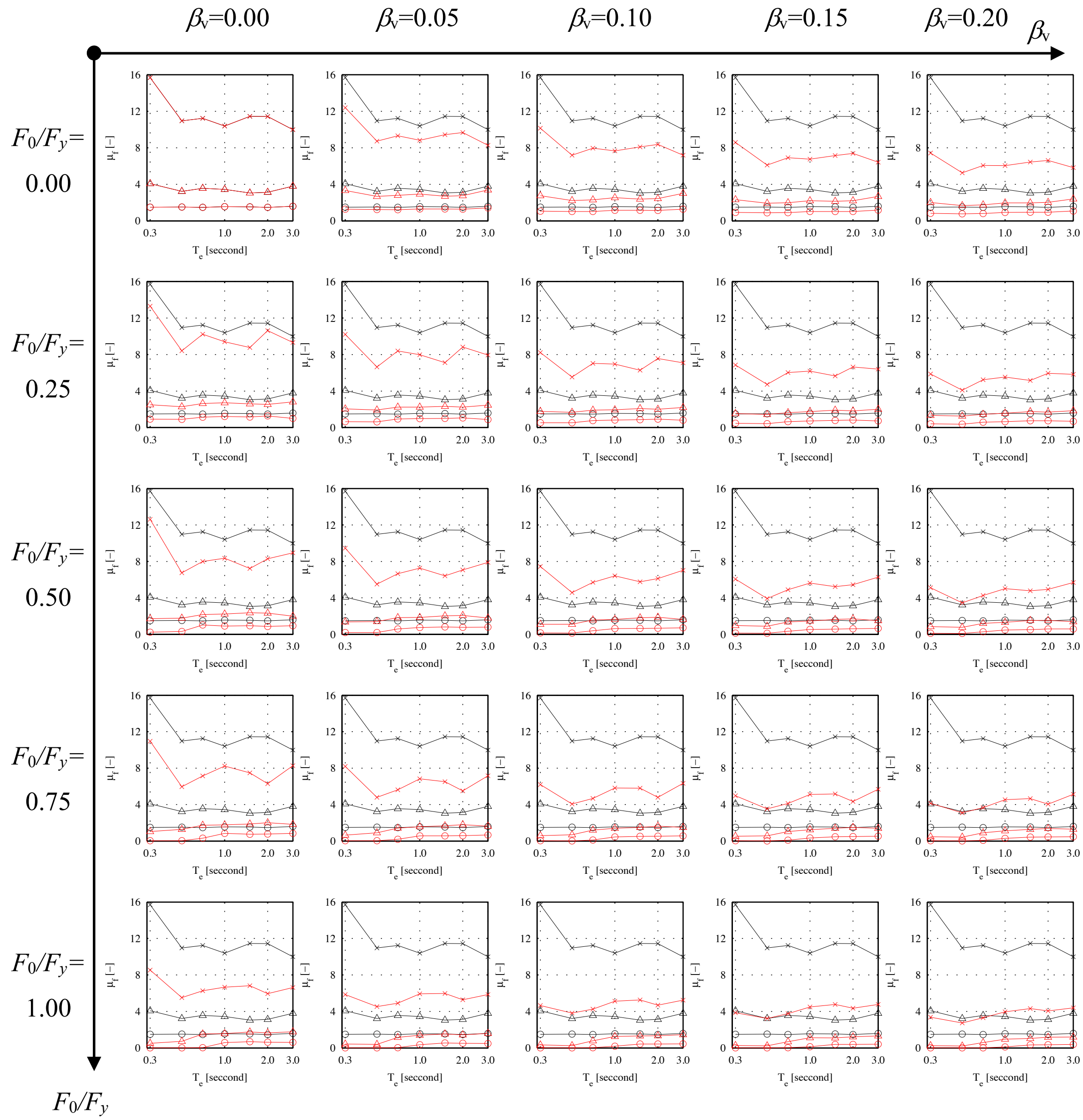

Figure A-80 Ductility Ratio in MCE, Near-Fault Pulse-like Motions, Linear Viscous Damping, Stiffness $K_0 \neq 0$, R_μ=1, 2 and 5

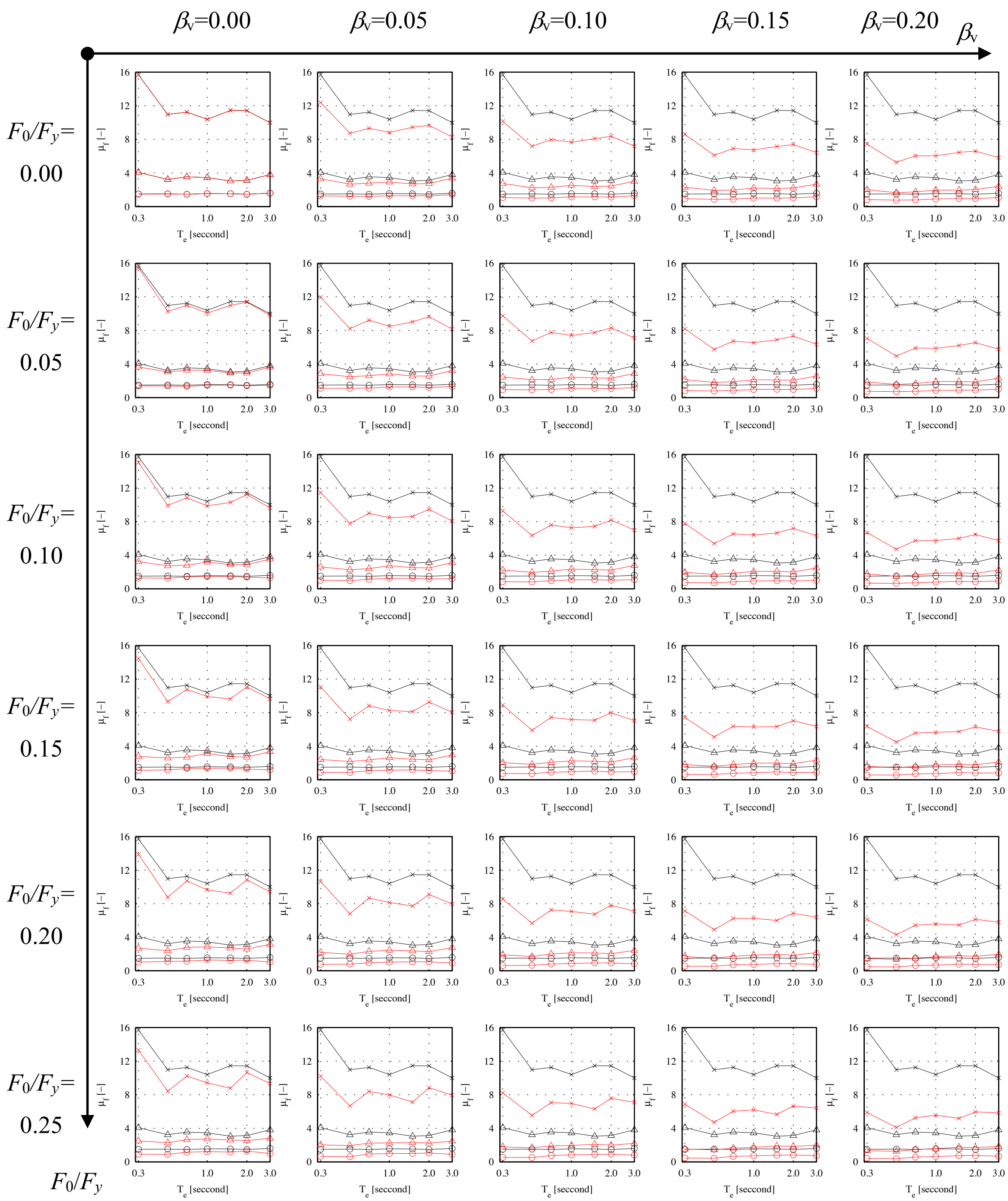

Figure A-80 (Continued)

A.5 Structure with Linear Viscous Damping and $K_0 \neq 0$ in Near-Fault Non-Pulse-Like Ground Motions

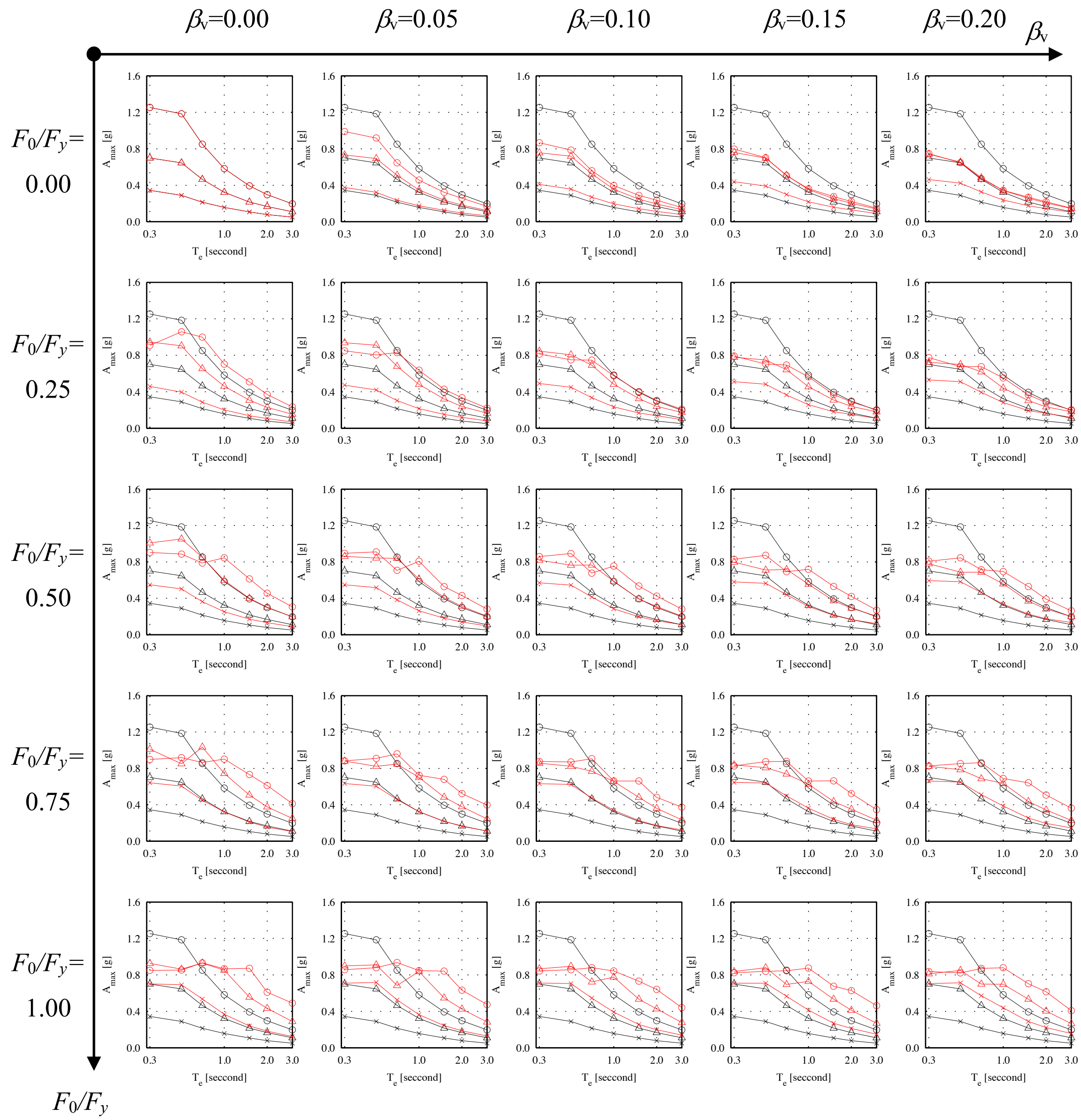

Figure A-81 Acceleration in DE, Near-Fault Non-Pulse-like Motions, Linear Viscous Damping, Stiffness $K_0 \neq 0$, R_μ=1, 2 and 5

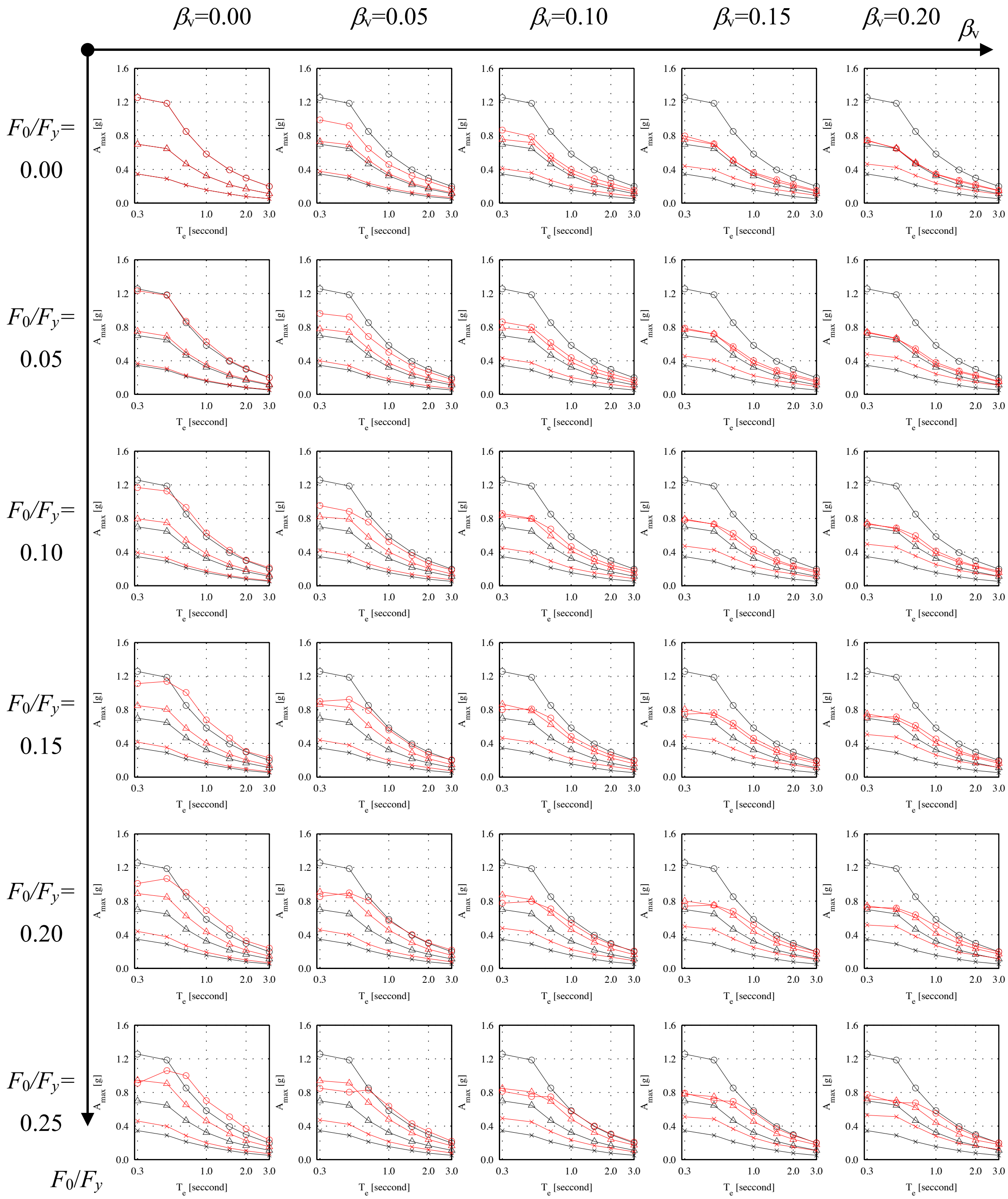

Figure A-81 (Continued)

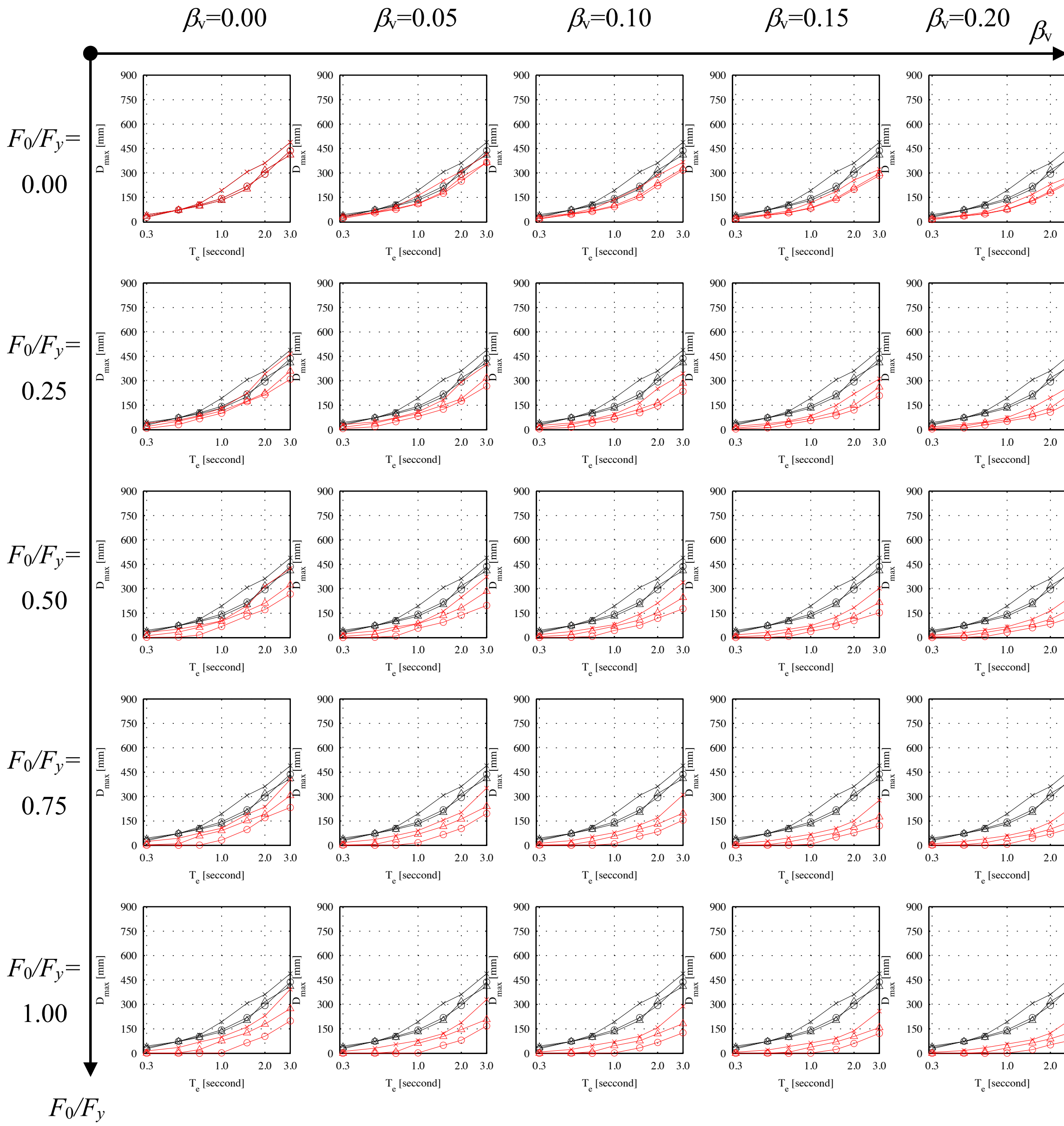

Figure A-82 Displacement in DE, Near-Fault Non-Pulse-like Motions, Linear Viscous Damping, Stiffness K_0≠0, R_μ=1, 2 and 5

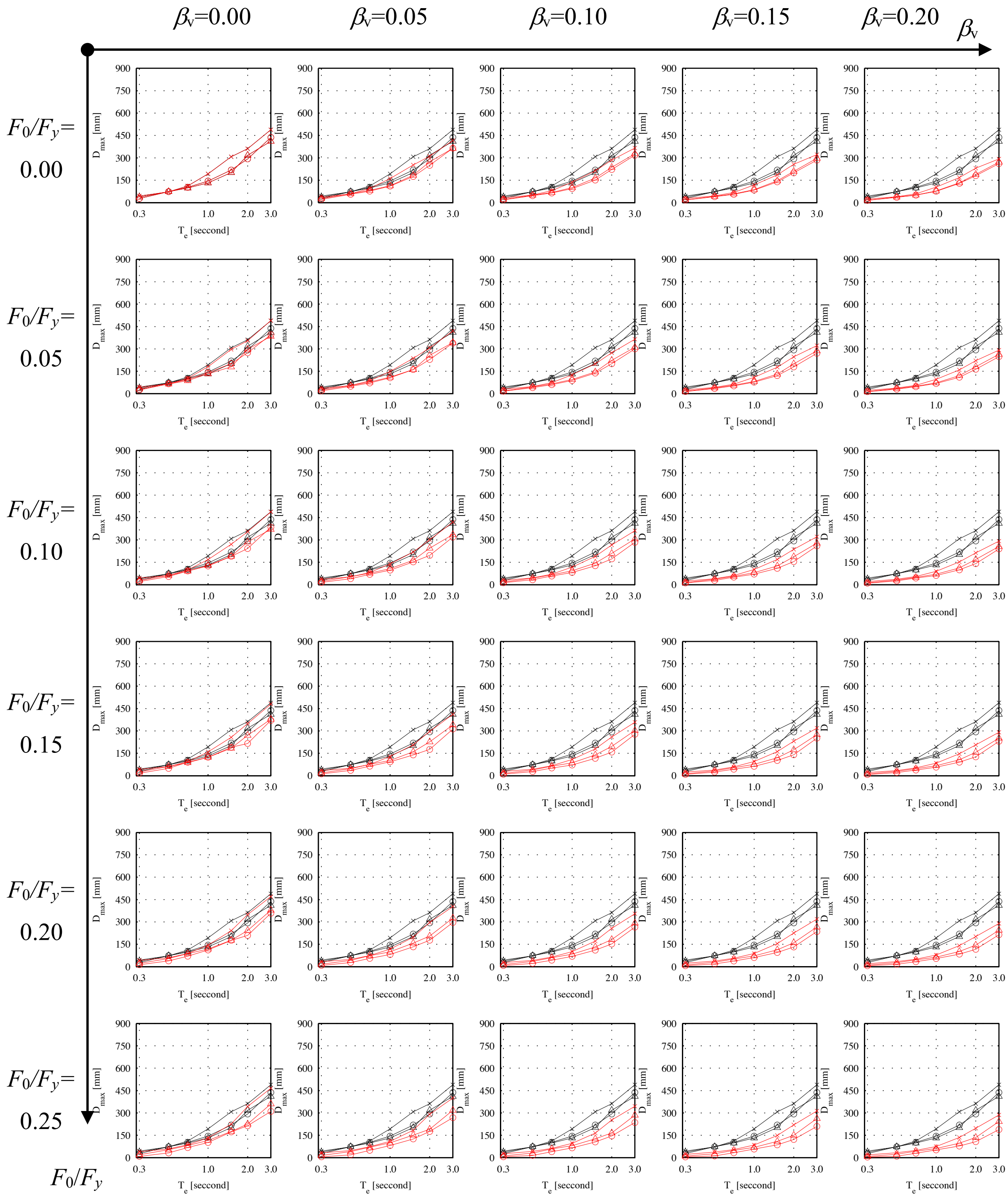

Figure A-82 (Continued)

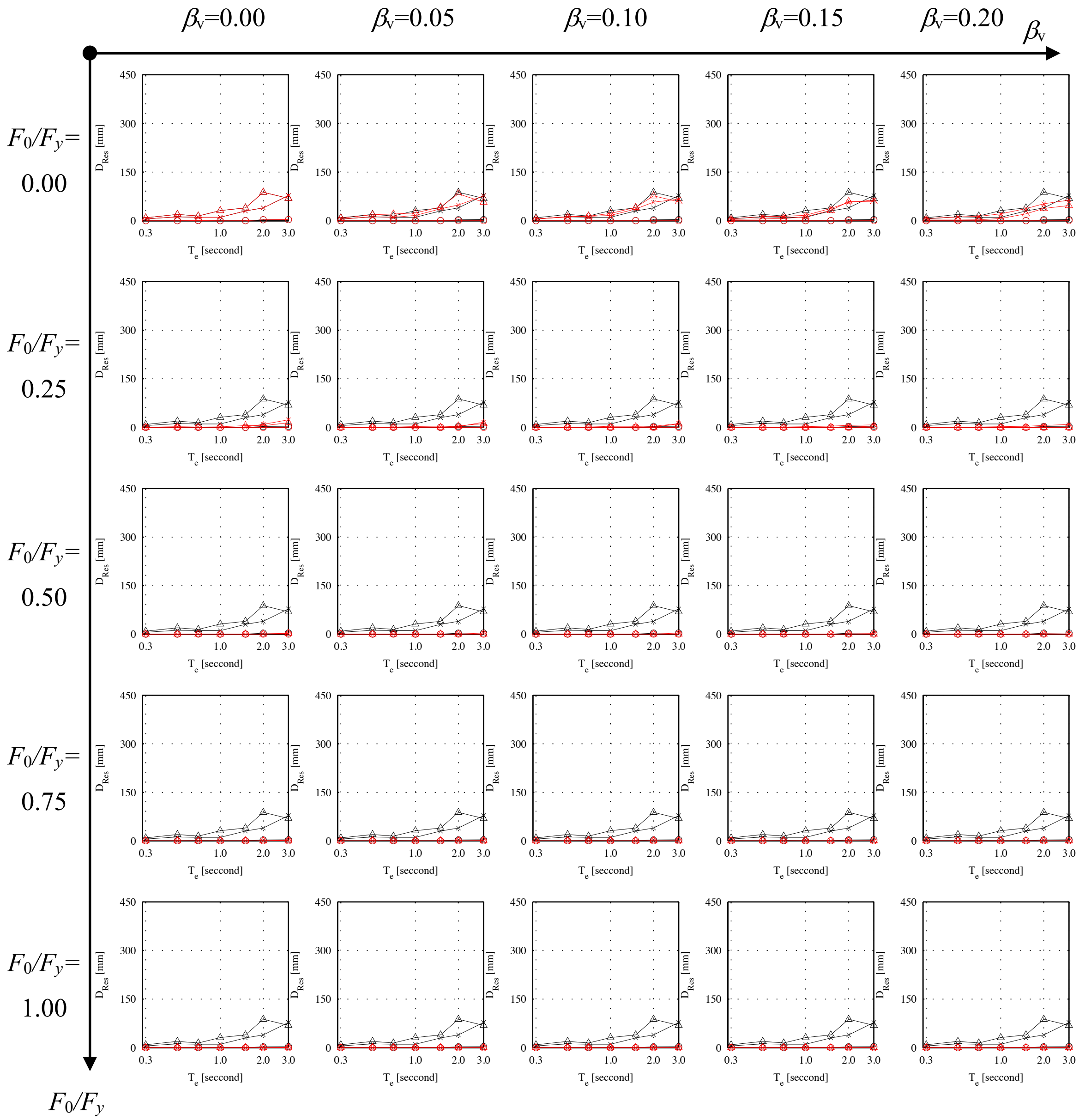

Figure A-83 Residual Displacement in DE, Near-Fault Non-Pulse-like Motions, Linear Viscous Damping, Stiffness $K_0 \neq 0$, R_μ=1, 2 and 5

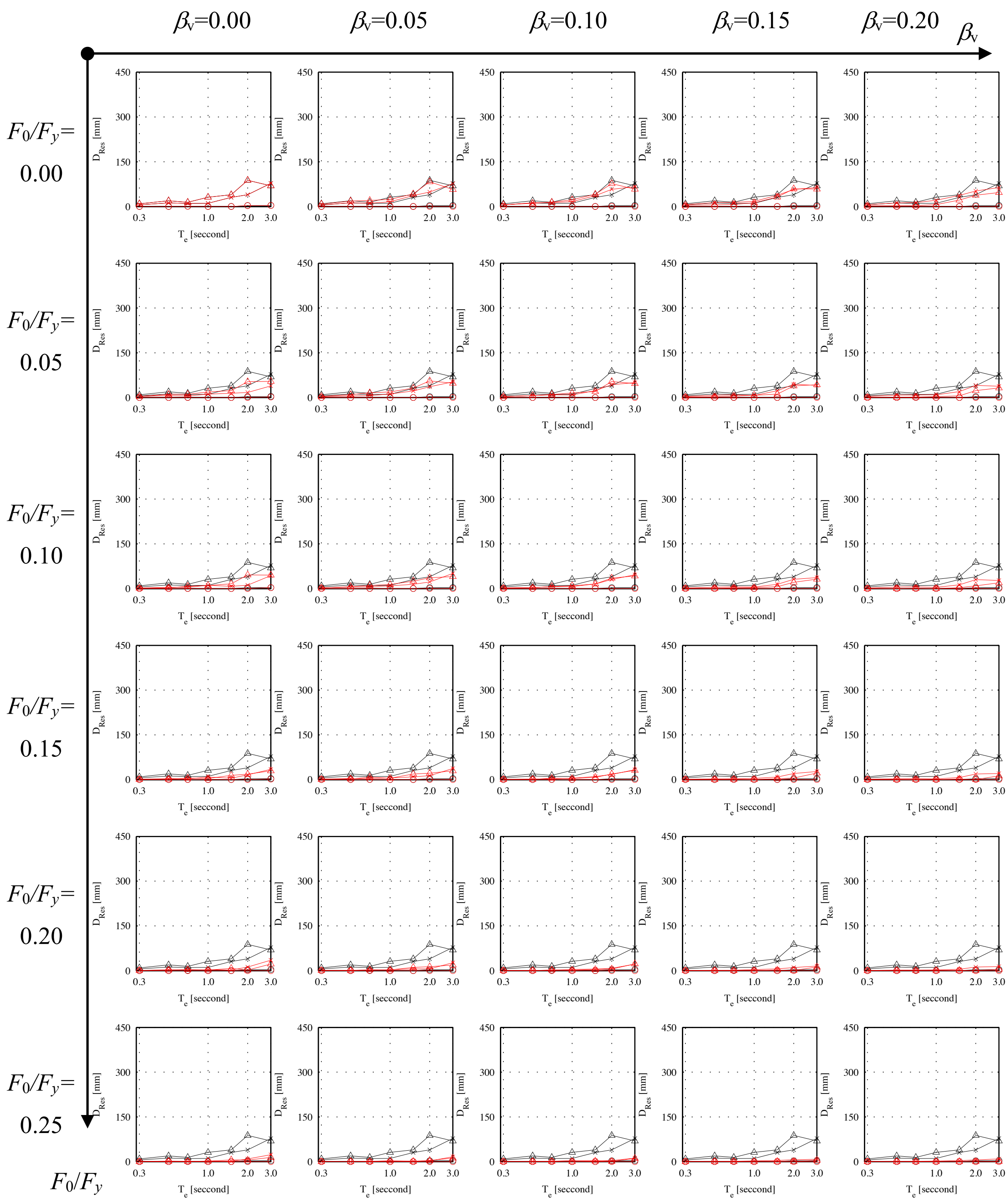

Figure A-83 (Continued)

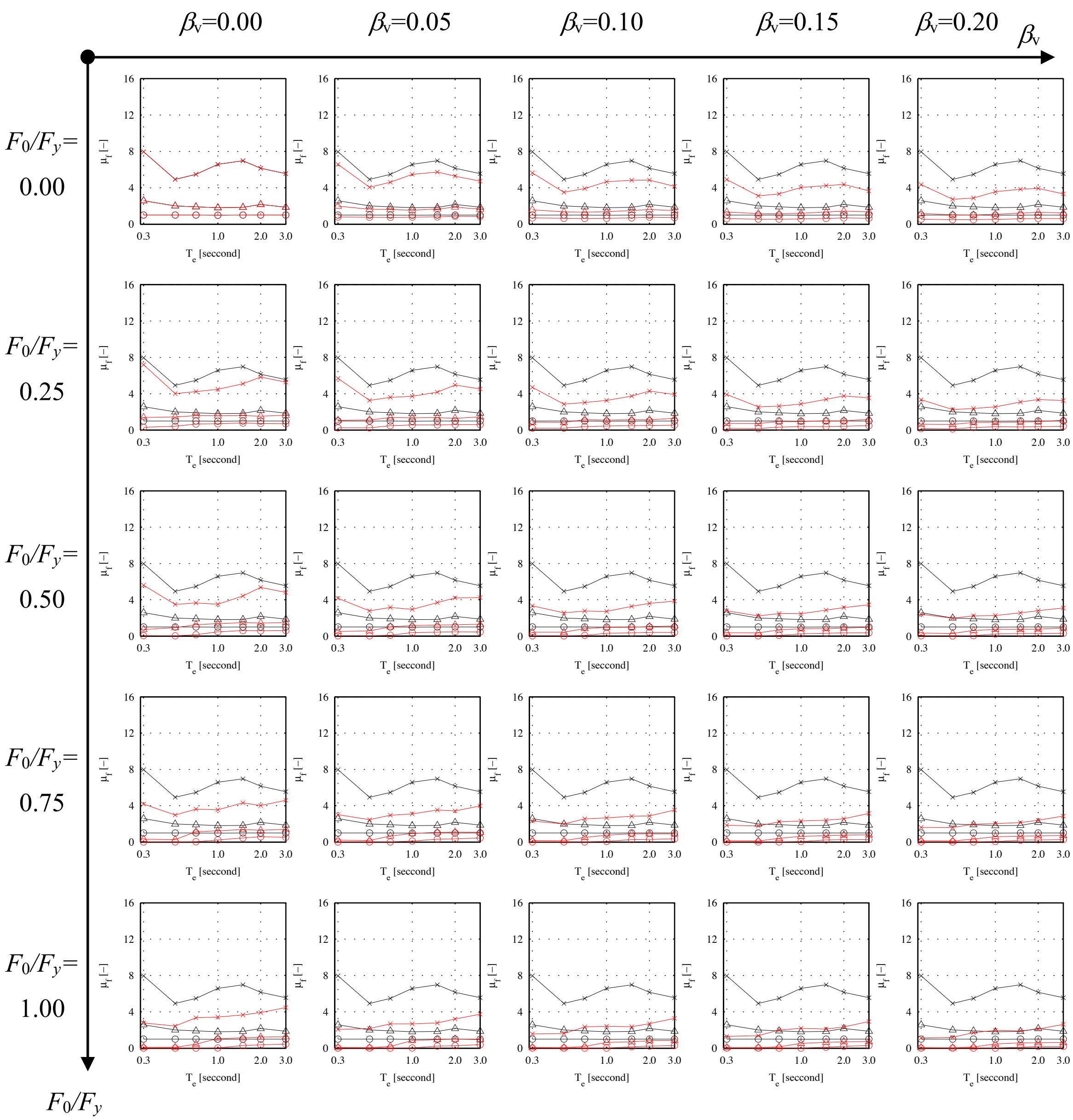

Figure A-84 Ductility Ratio in DE, Near-Fault Non-Pulse-like Motions, Linear Viscous Damping, Stiffness $K_0 \neq 0$, R_μ=1, 2 and 5

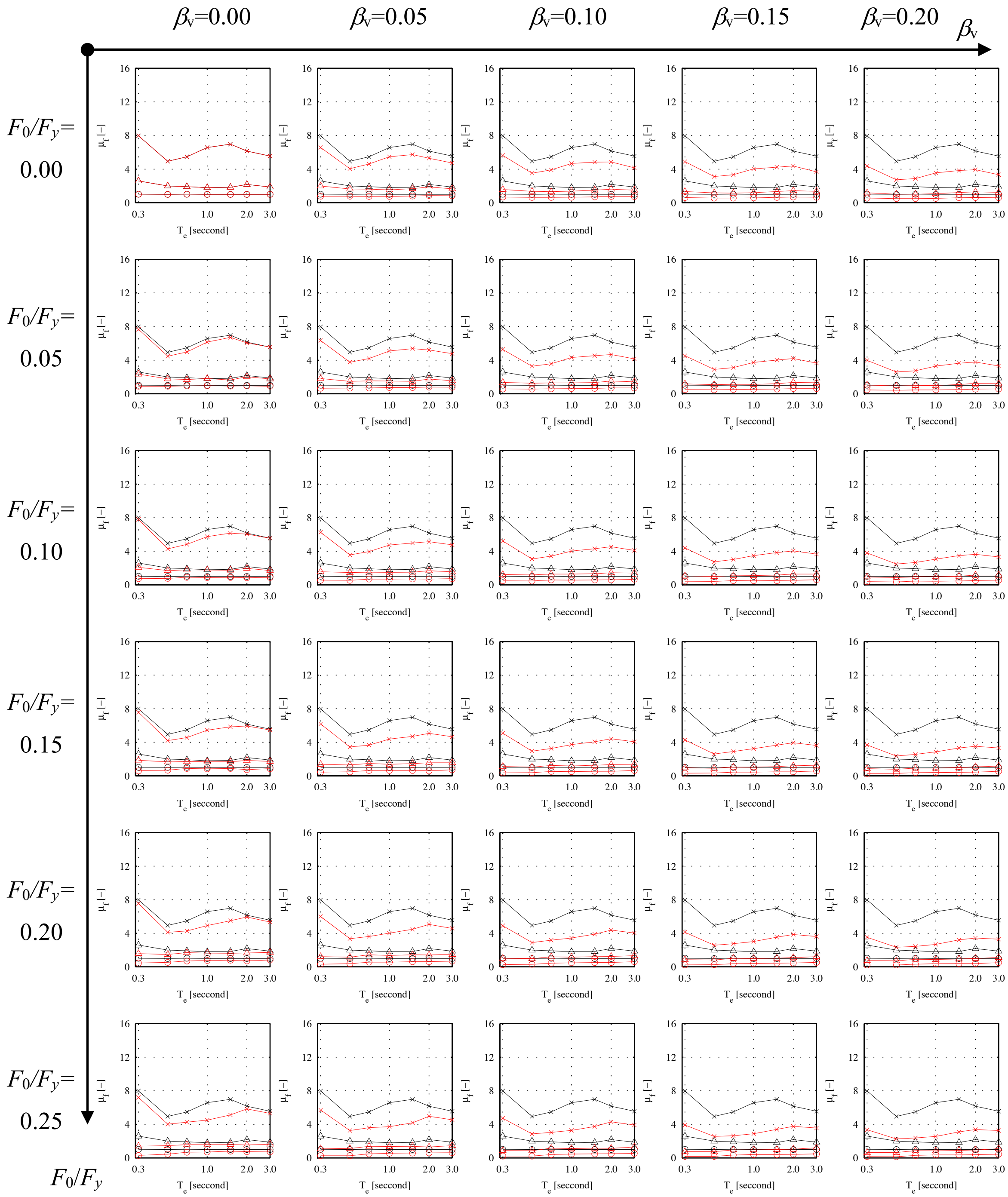

Figure A-84 (Continued)

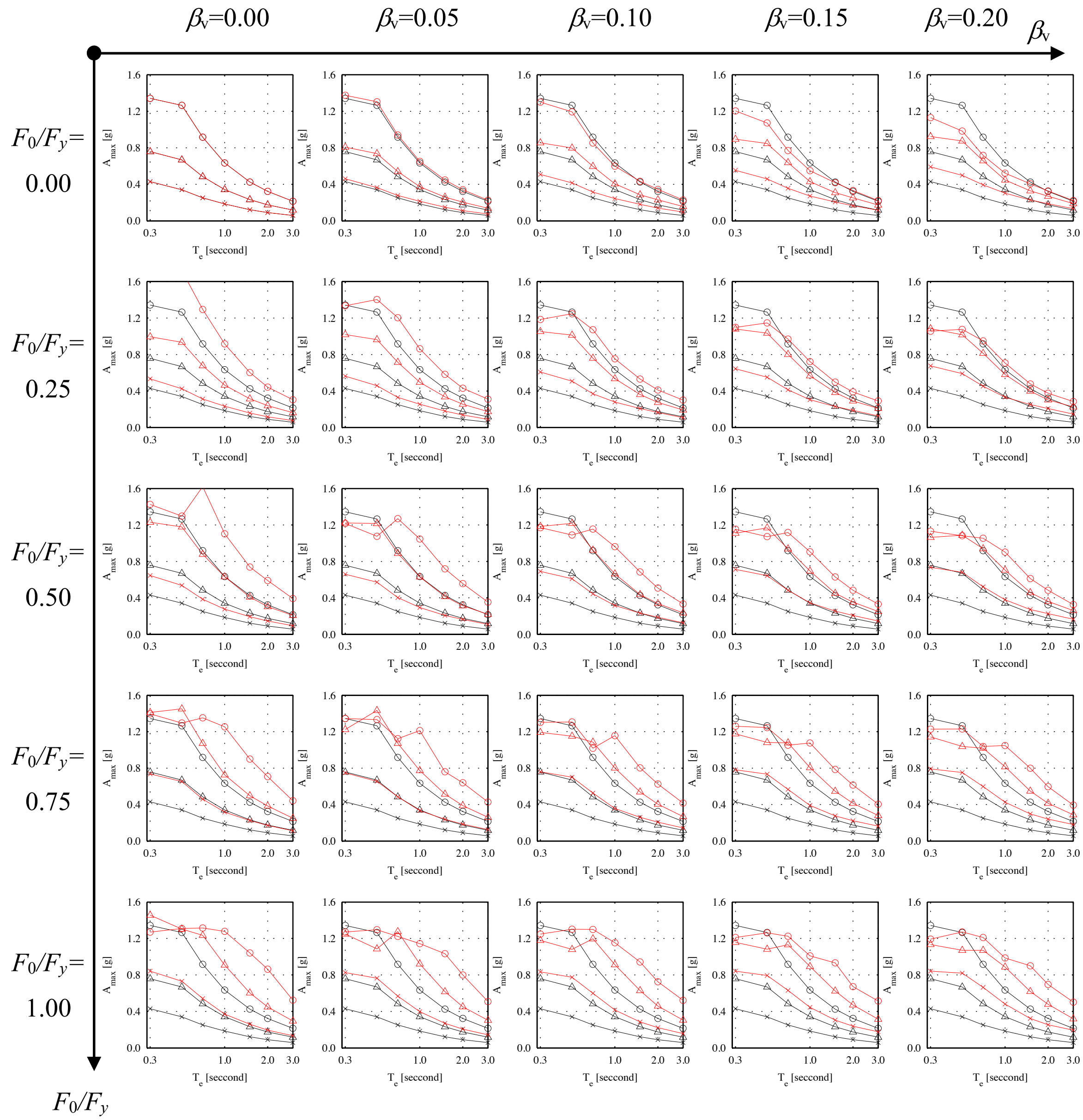

Figure A-85 Acceleration in MCE, Near-Fault Non-Pulse-like Motions, Linear Viscous Damping, Stiffness $K_0 \neq 0$, R_μ=1, 2 and 5

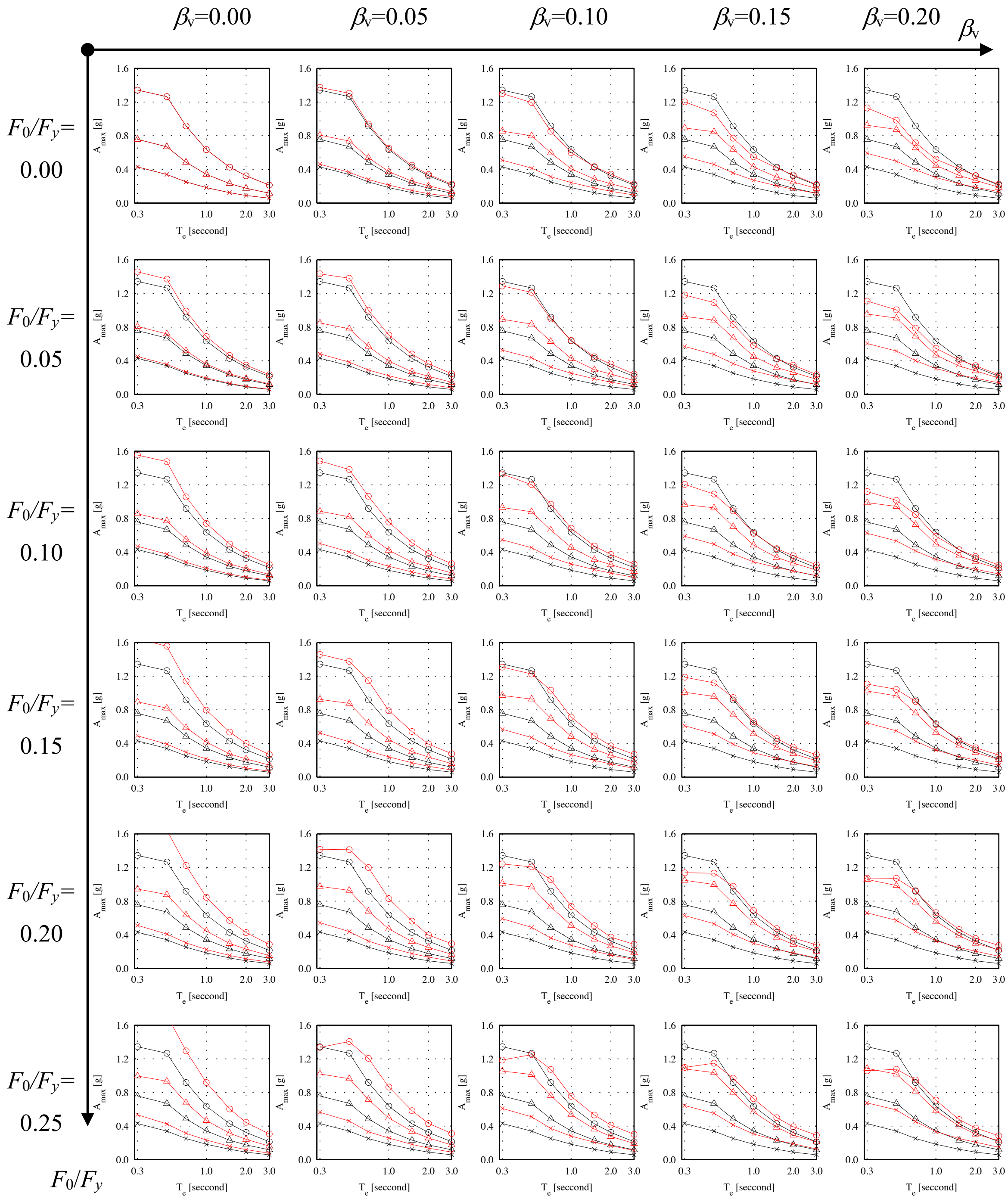

Figure A-85 (Continued)

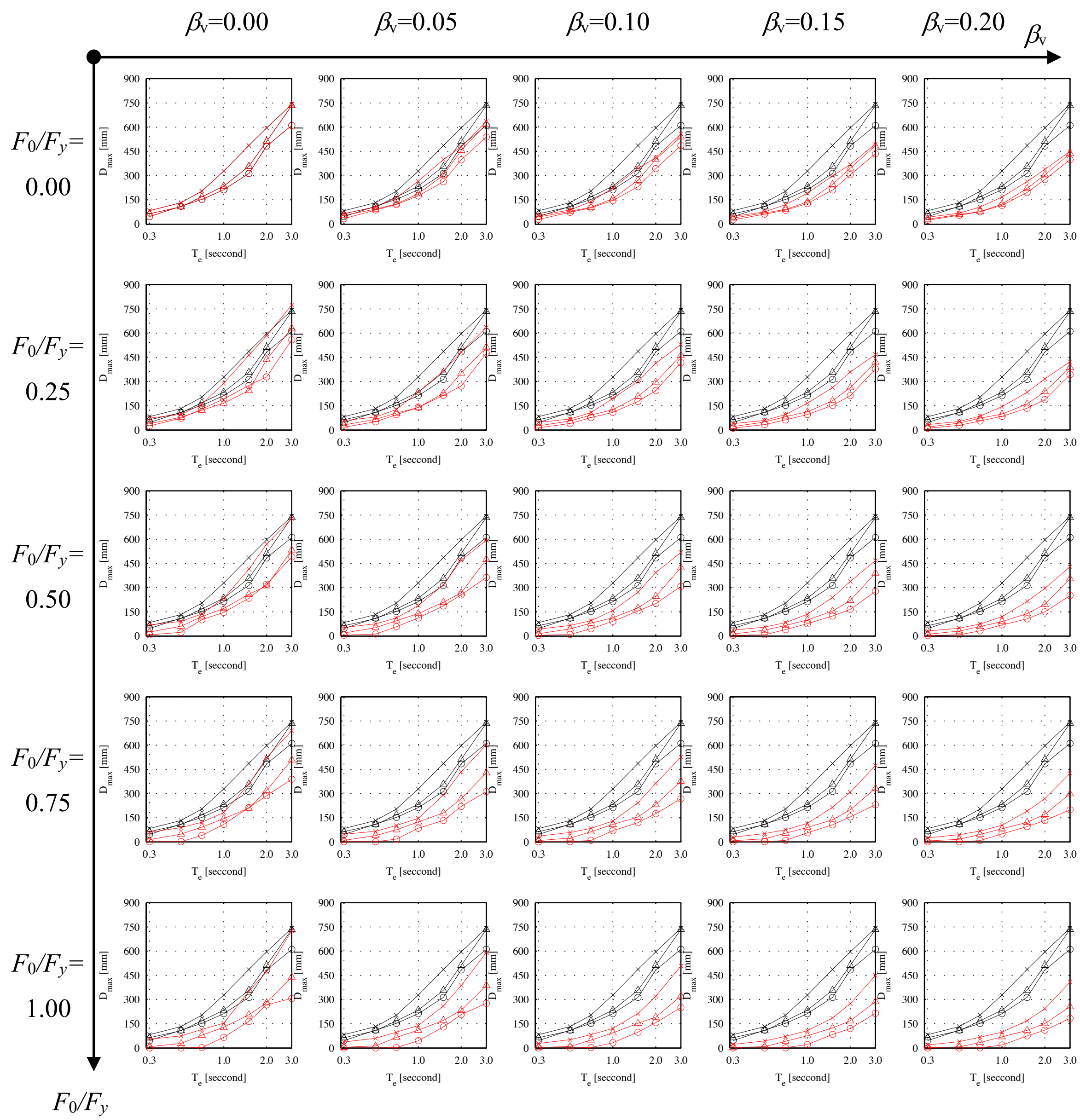

Figure A-86 Displacement in MCE, Near-Fault Non-Pulse-like Motions, Linear Viscous Damping, Stiffness $K_0 \neq 0$, R_μ=1, 2 and 5

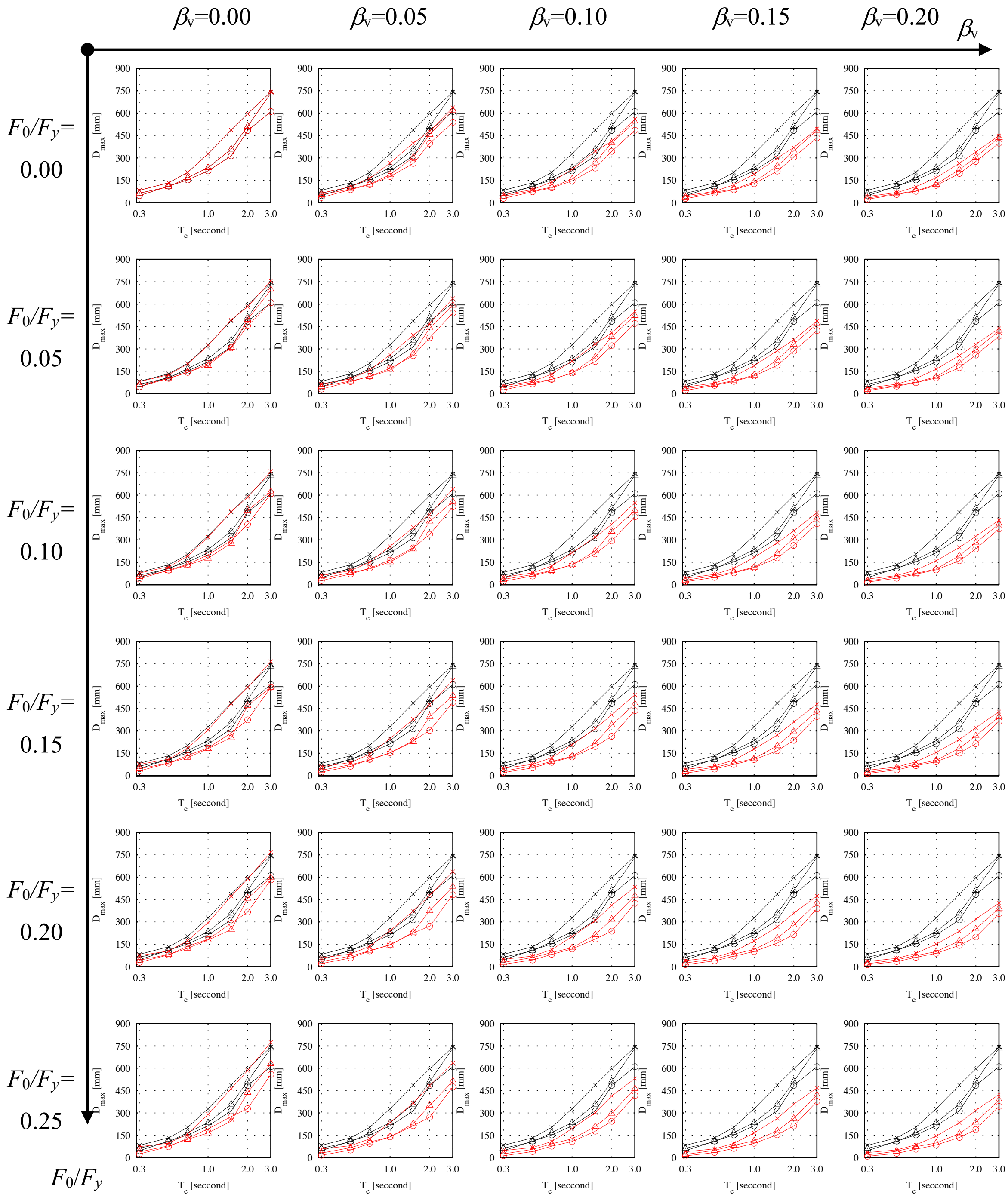

Figure A-86 (Continued)

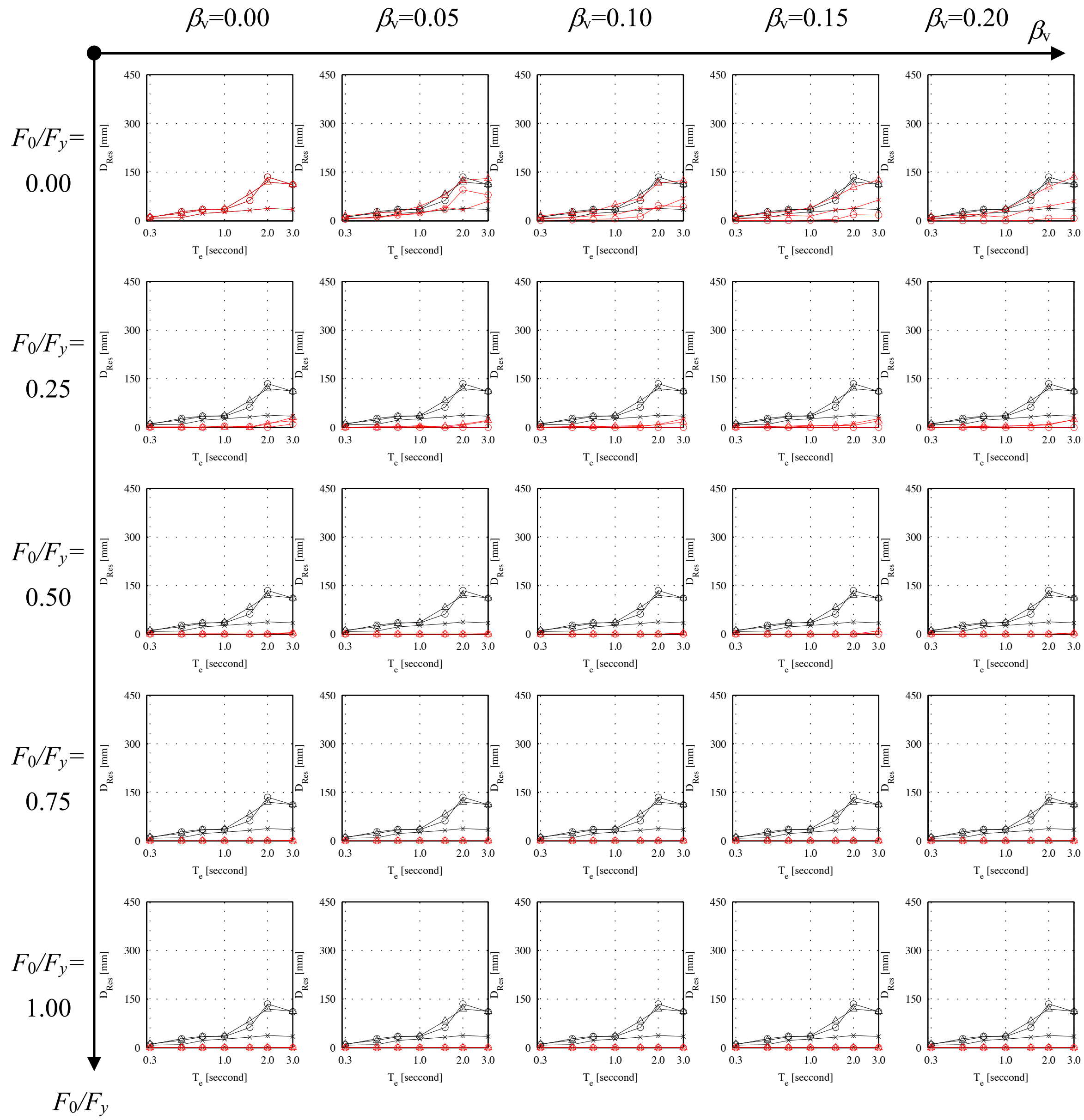

Figure A-87 Residual Displacement in MCE, Near-Fault Non-Pulse-like Motions, Linear Viscous Damping, Stiffness K_0≠0, R_μ=1, 2 and 5

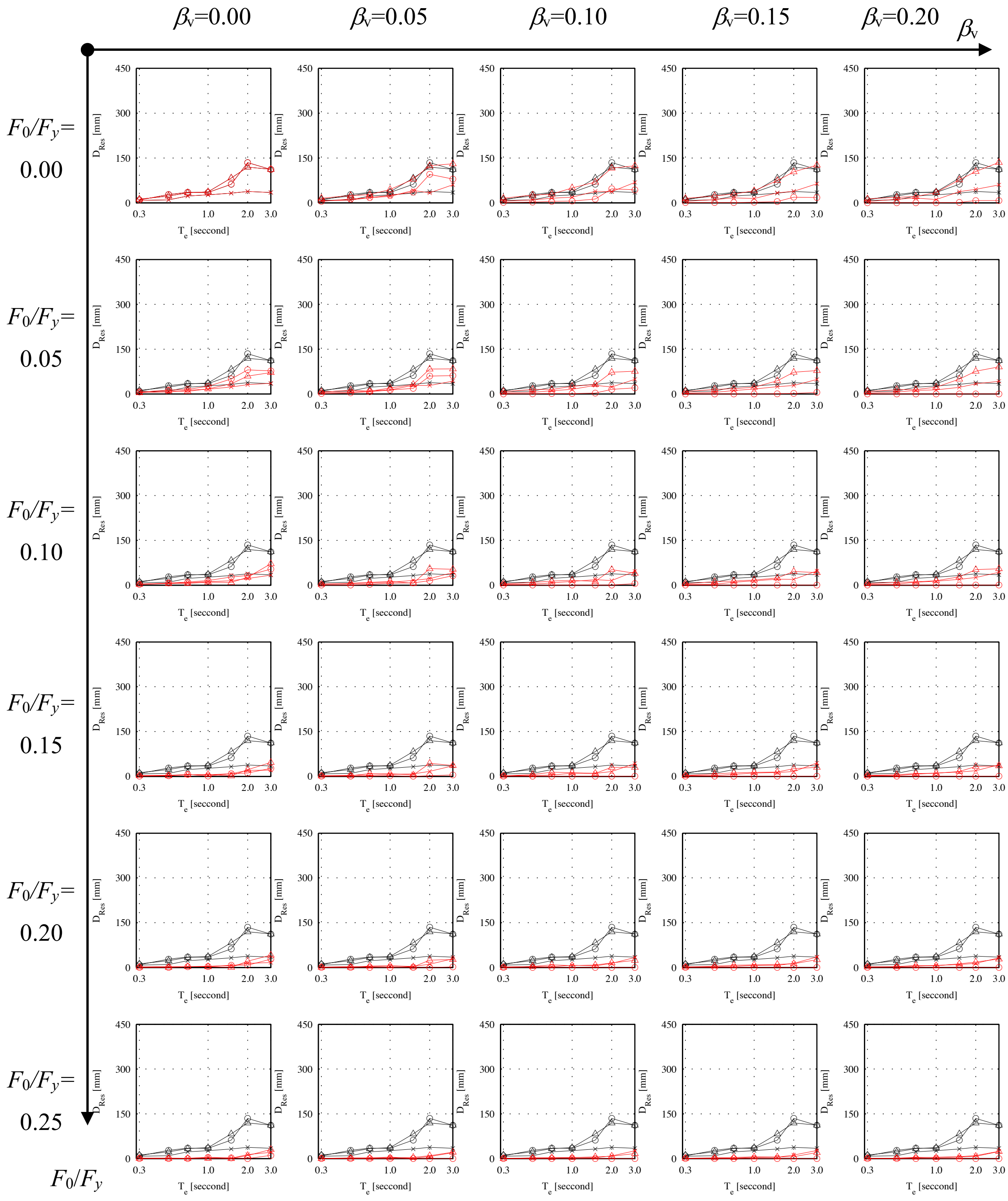

Figure A-87 (Continued)

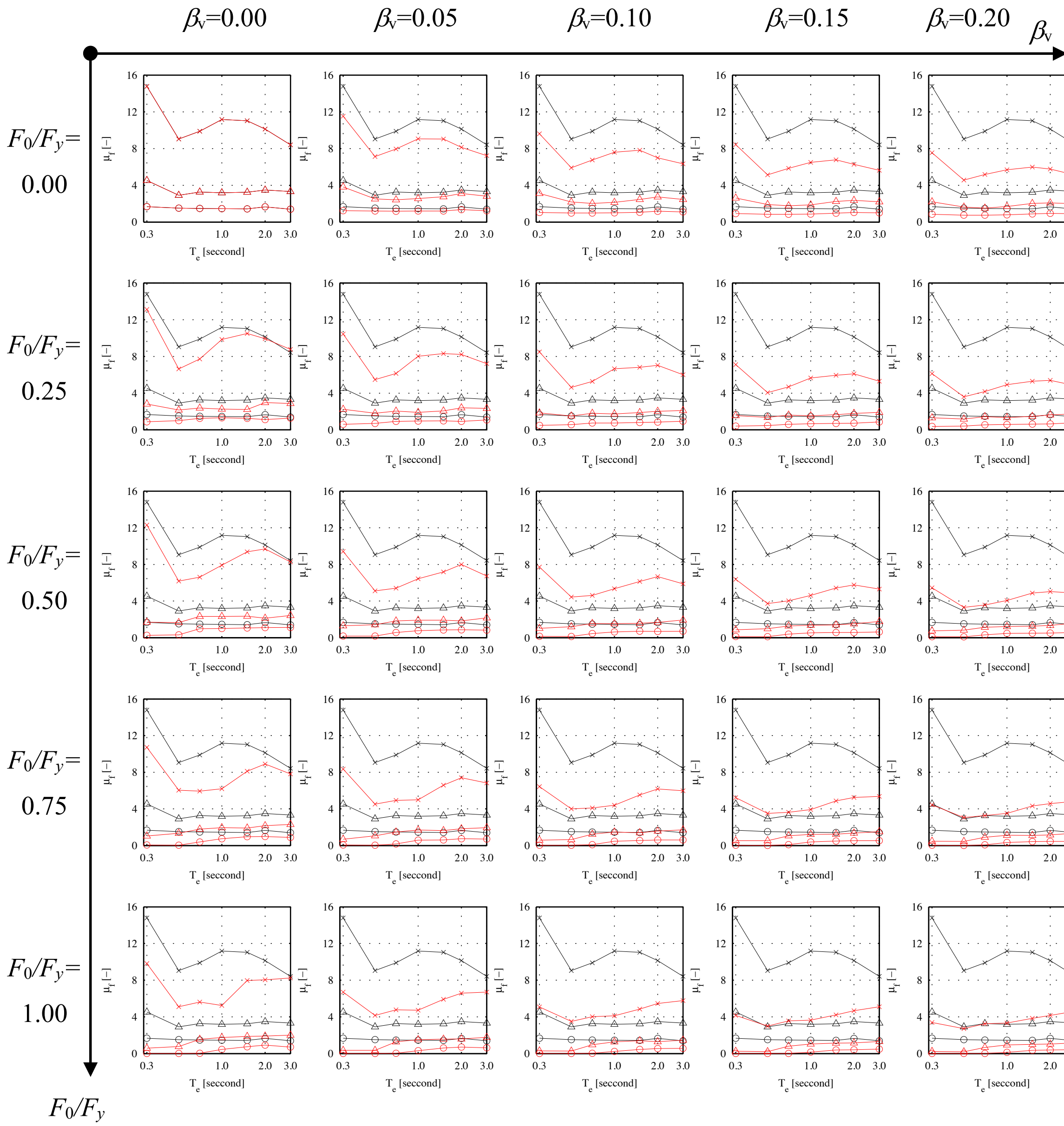

Figure A-88 Ductility Ratio in MCE, Near-Fault Non-Pulse-like Motions, Linear Viscous Damping, Stiffness K_0≠0, R_μ=1, 2 and 5

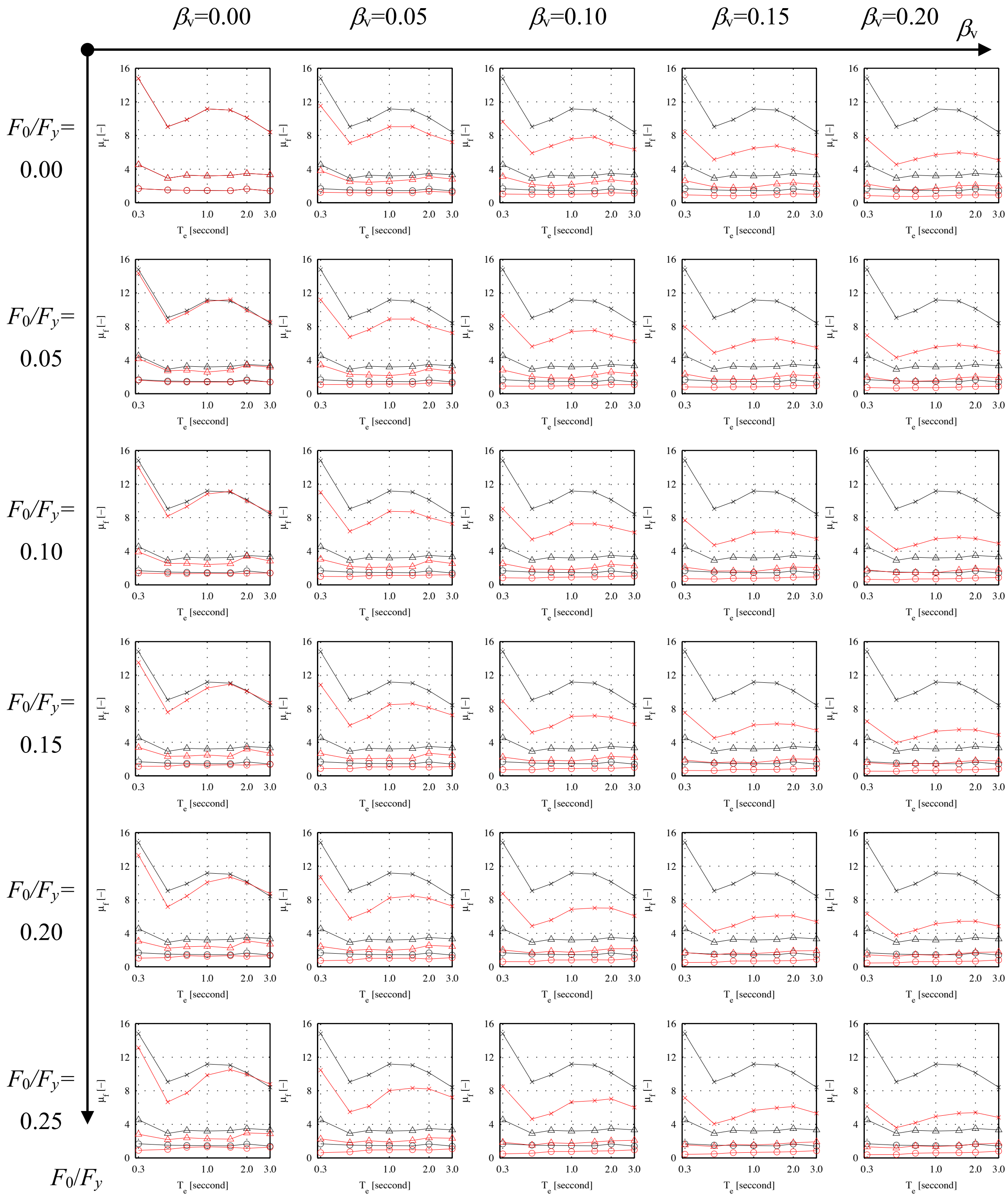

Figure A-88 (Continued)

A.6 Structure with Linear Viscous Damping and $K_0 \neq 0$ in Far-Field Ground Motions

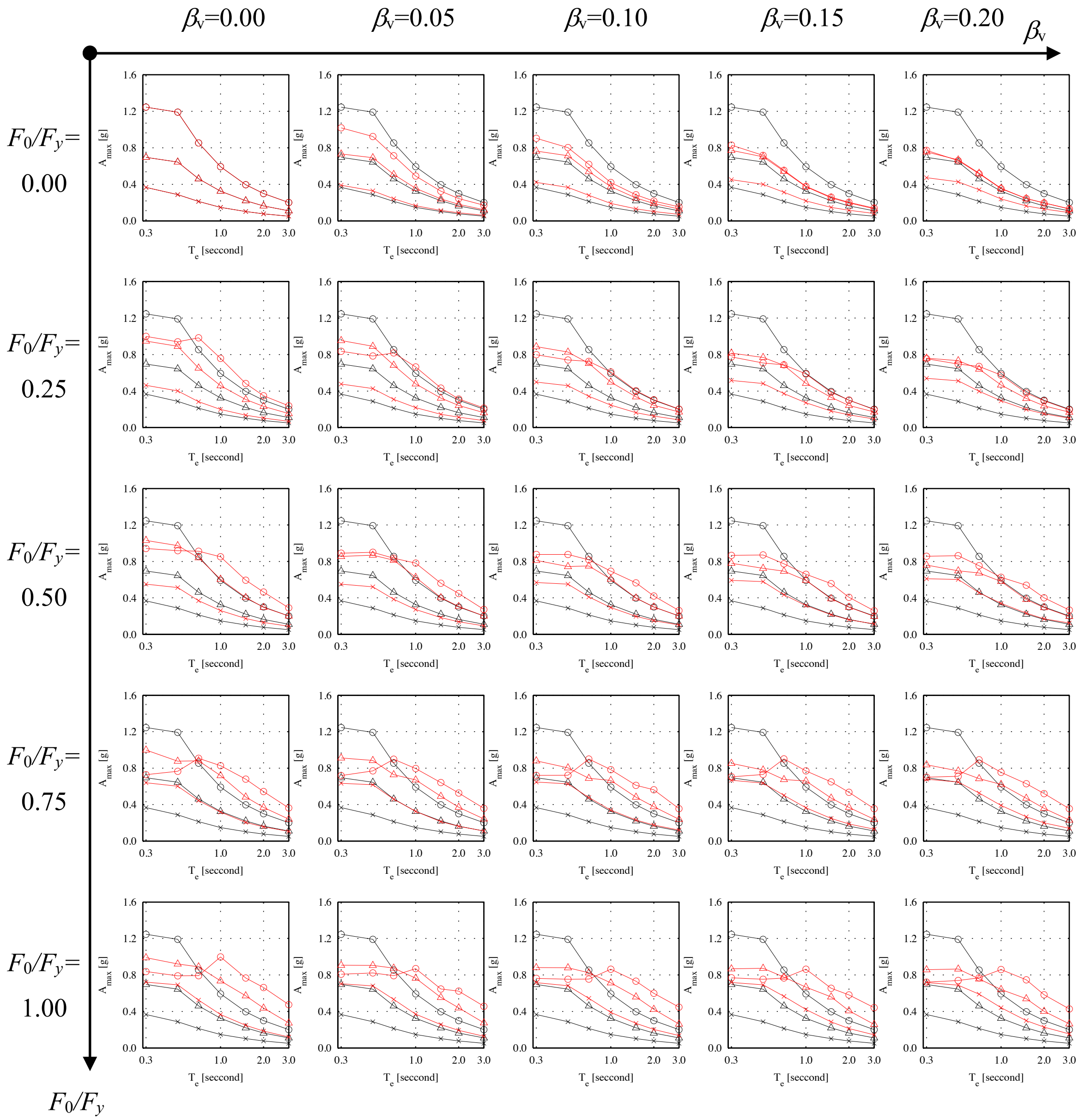

Figure A-89 Acceleration in DE, Far-Field Motions, Linear Viscous Damping, Stiffness $K_0 \neq 0$, R_μ=1, 2 and 5

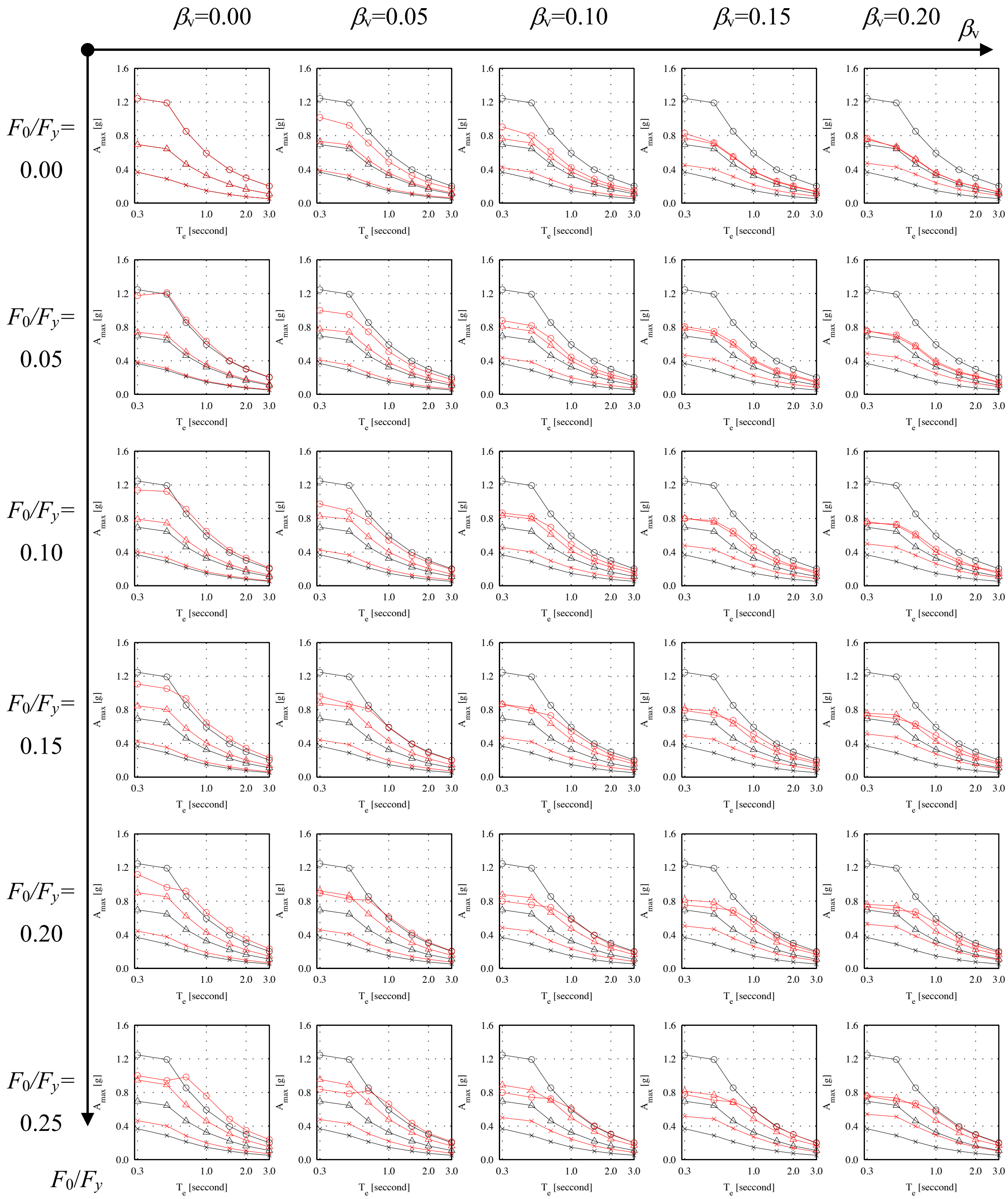

Figure A-89 (Continued)

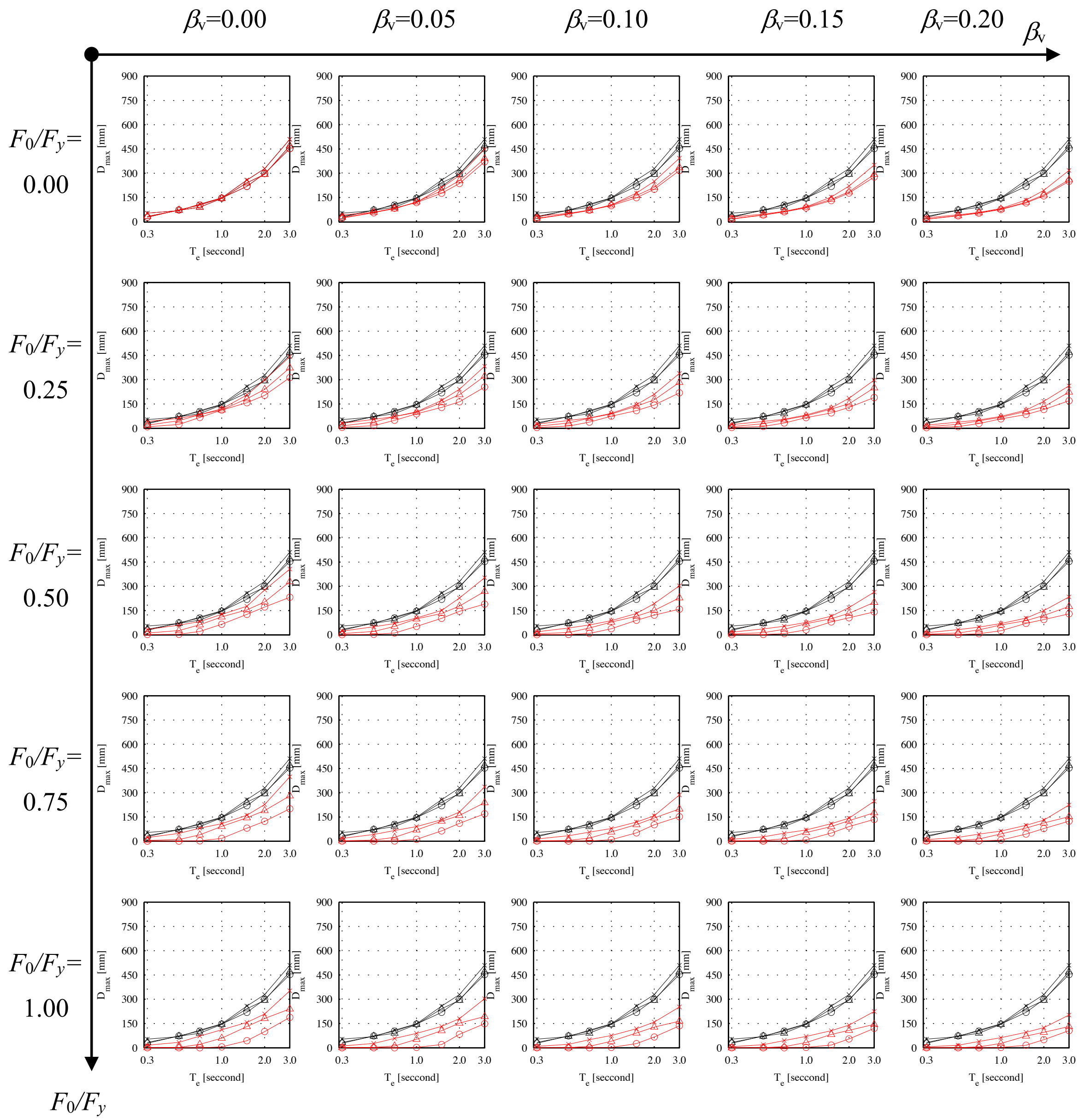

Figure A-90 Displacement in DE, Far-Field Motions, Linear Viscous Damping, Stiffness K_0≠0, R_μ=1, 2 and 5

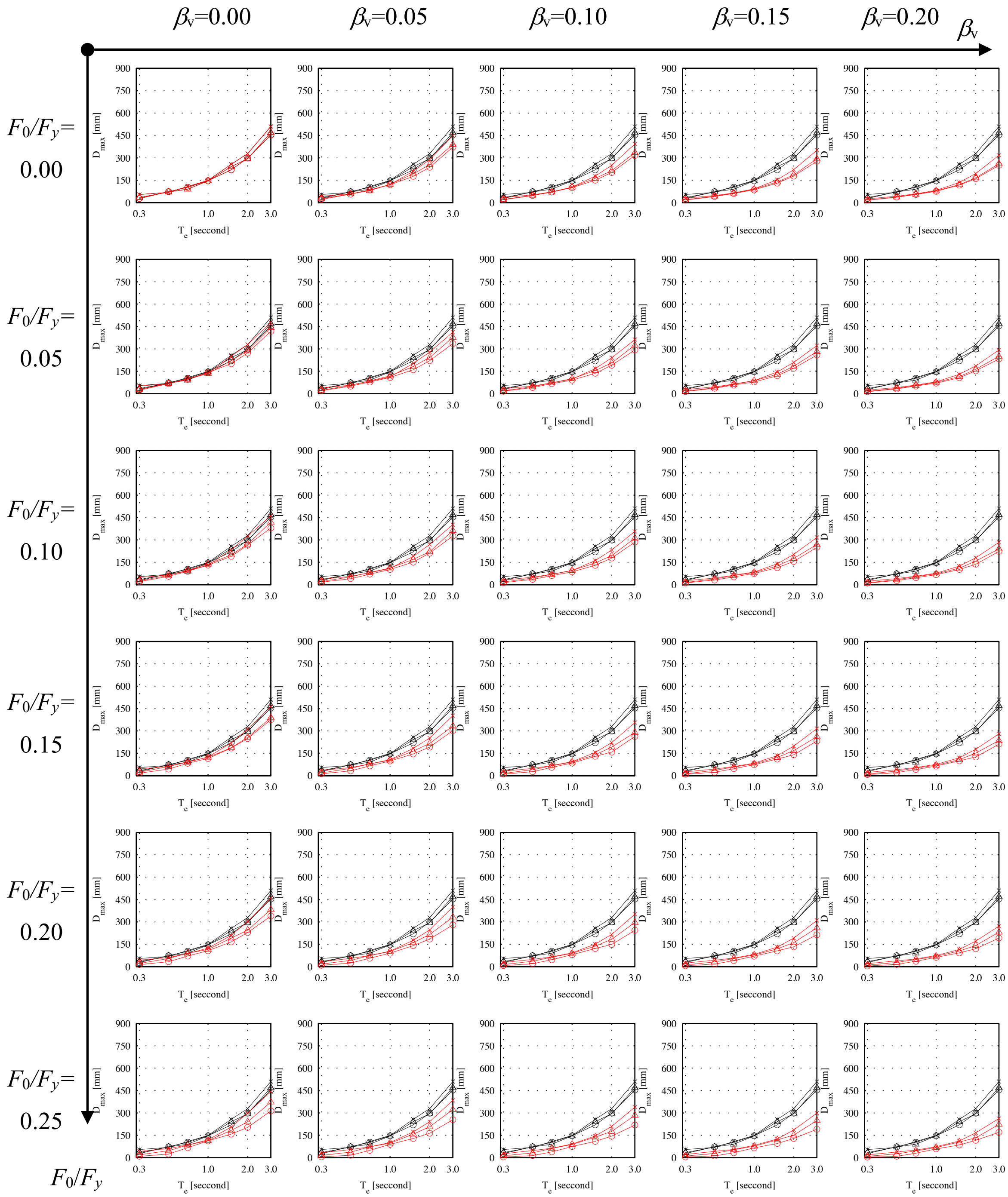

Figure A-90 (Continued)

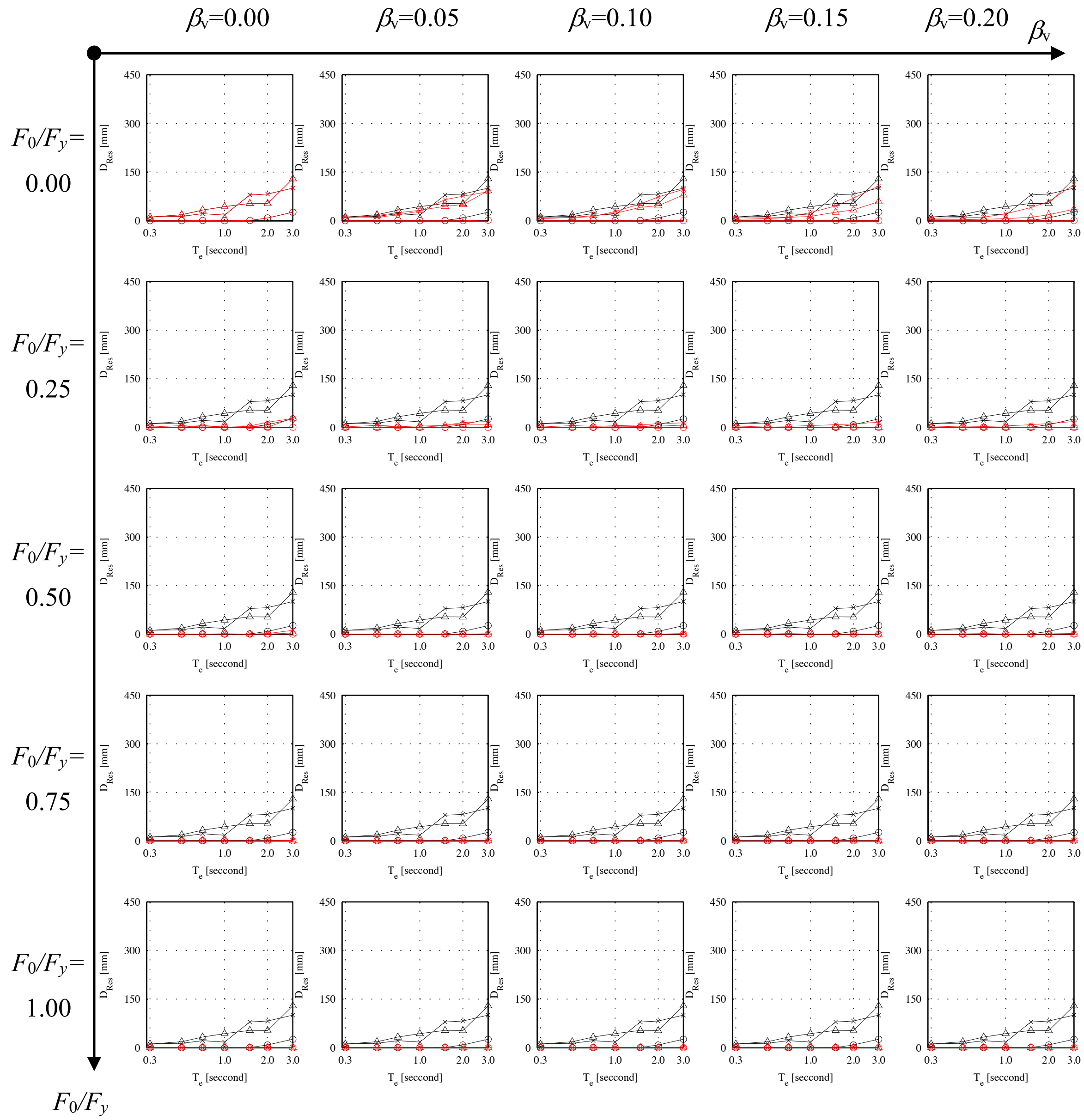

Figure A-91 Residual Displacement in DE, Far-Field Motions, Linear Viscous Damping, Stiffness $K_0 \neq 0$, R_μ=1, 2 and 5

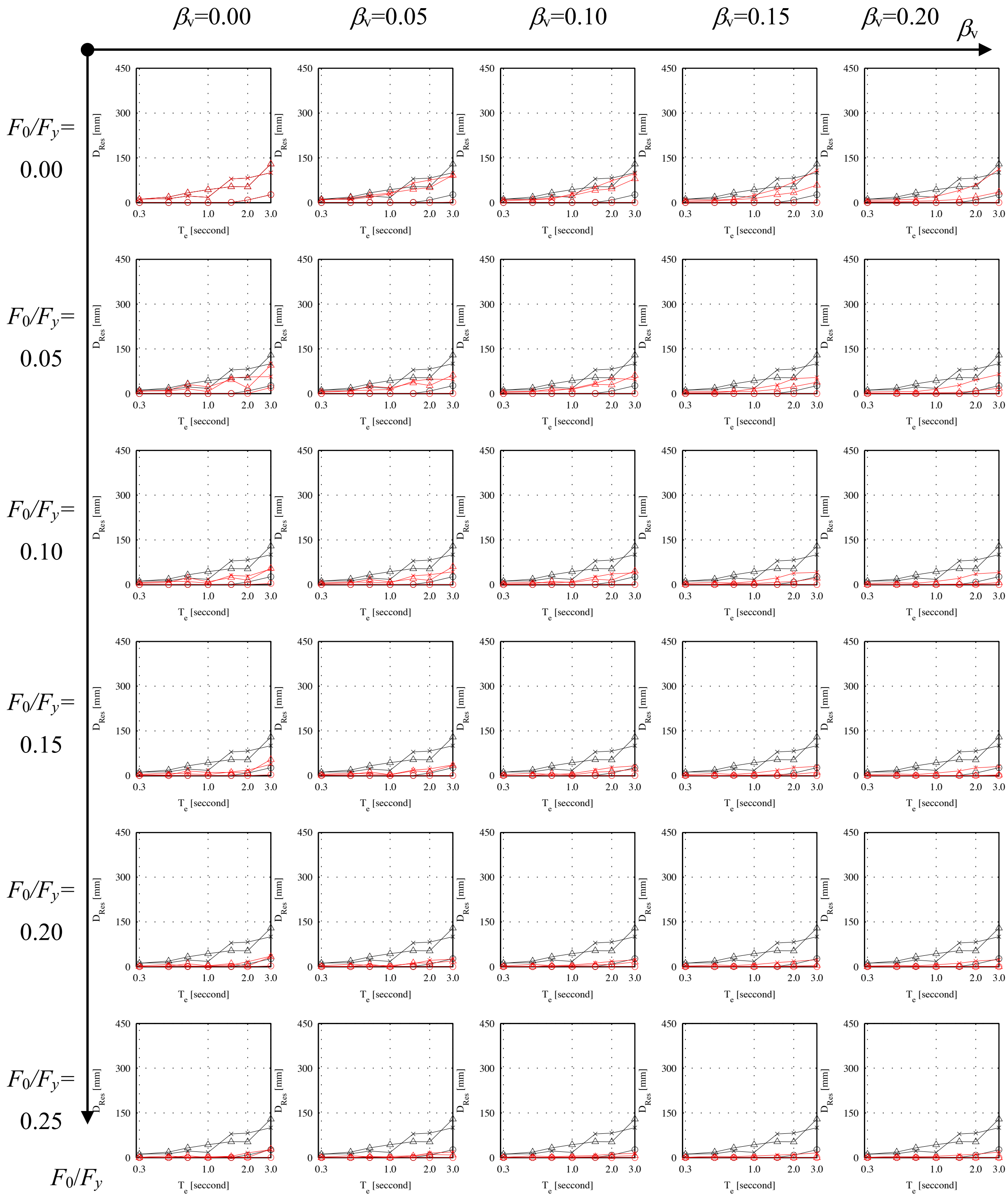

Figure A-91 (Continued)

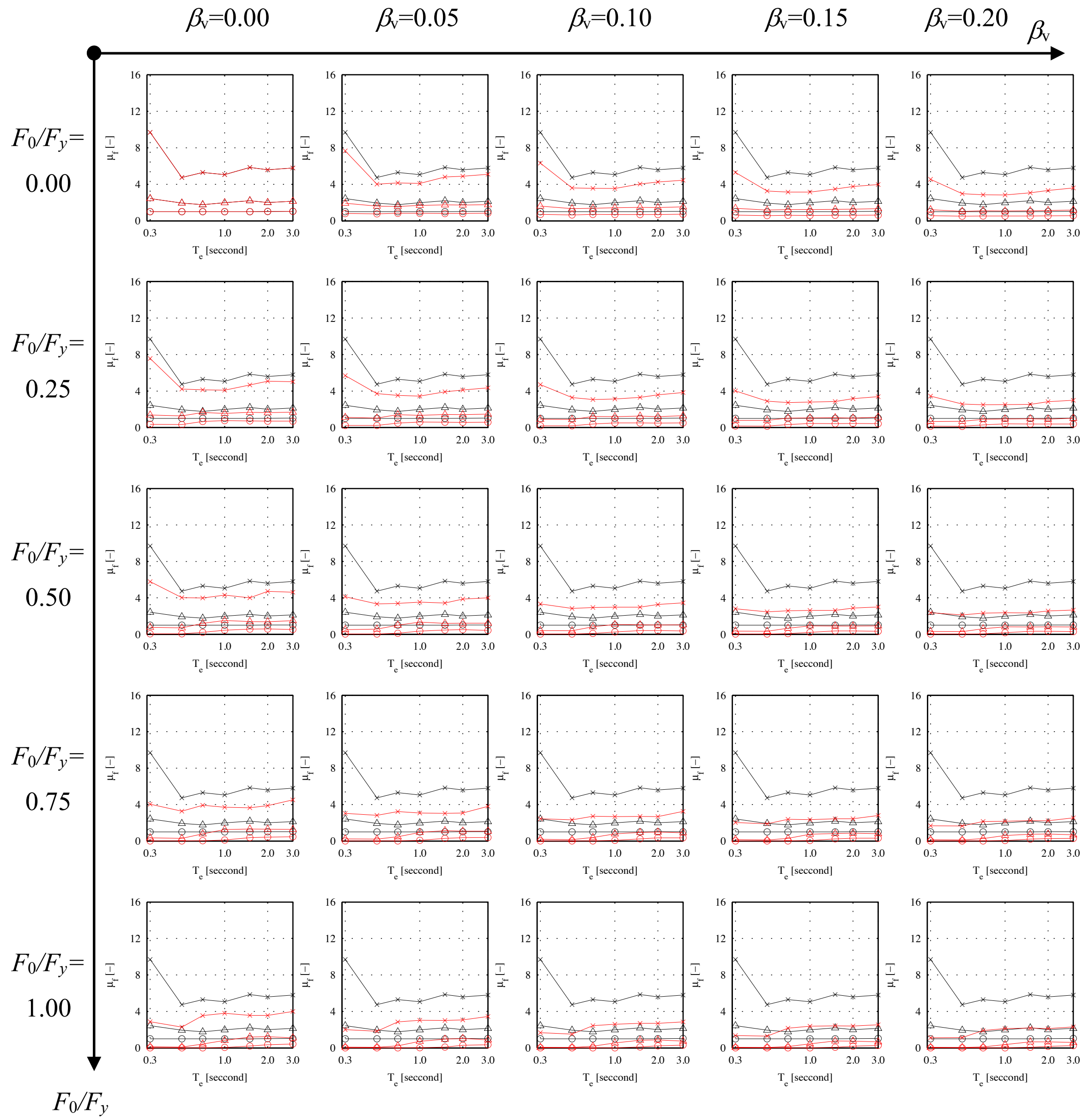

Figure A-92 Ductility Ratio in DE, Far-Field Motions, Linear Viscous Damping, Stiffness $K_0 \neq 0$, R_μ=1, 2 and 5

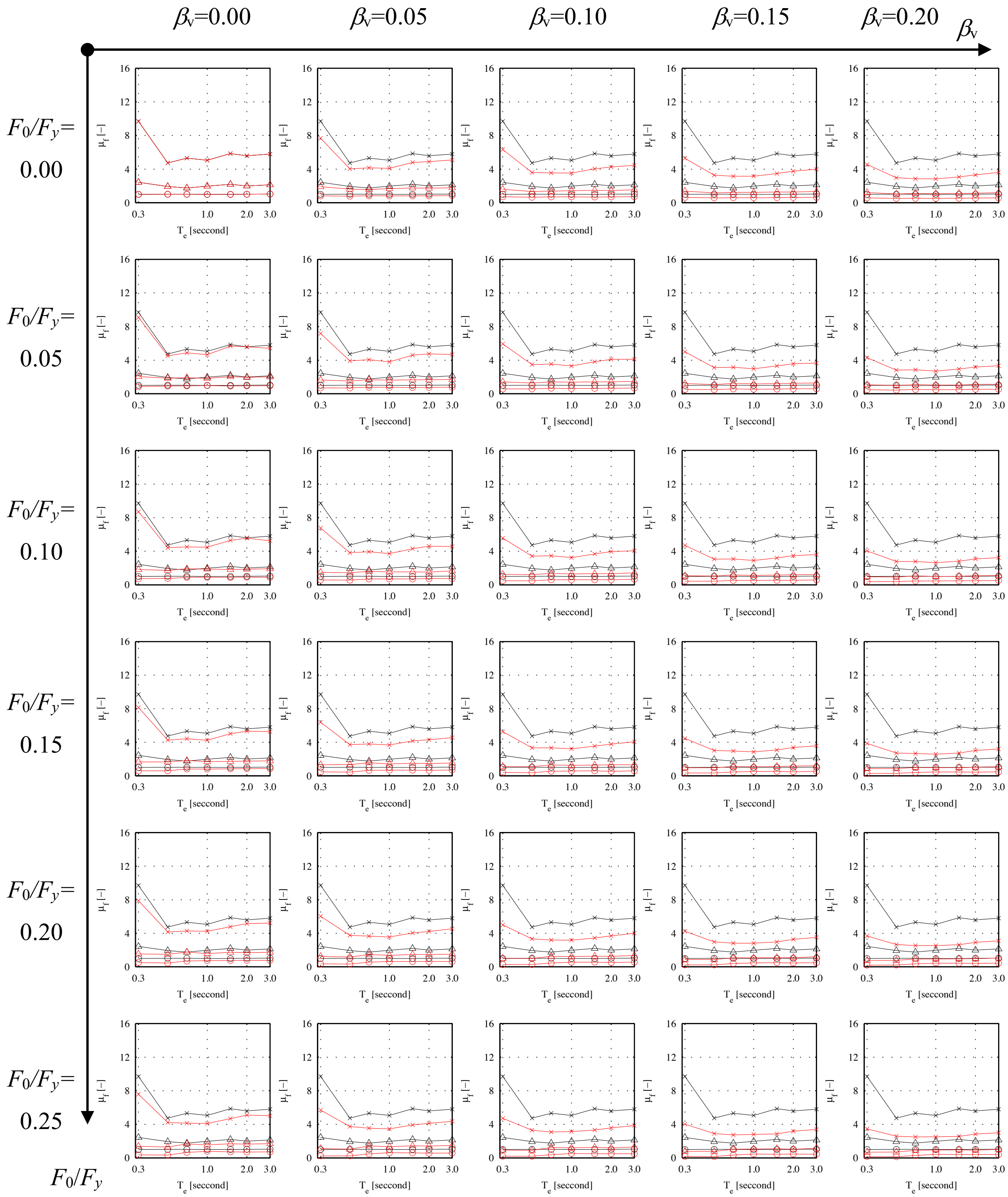

Figure A-92 (Continued)

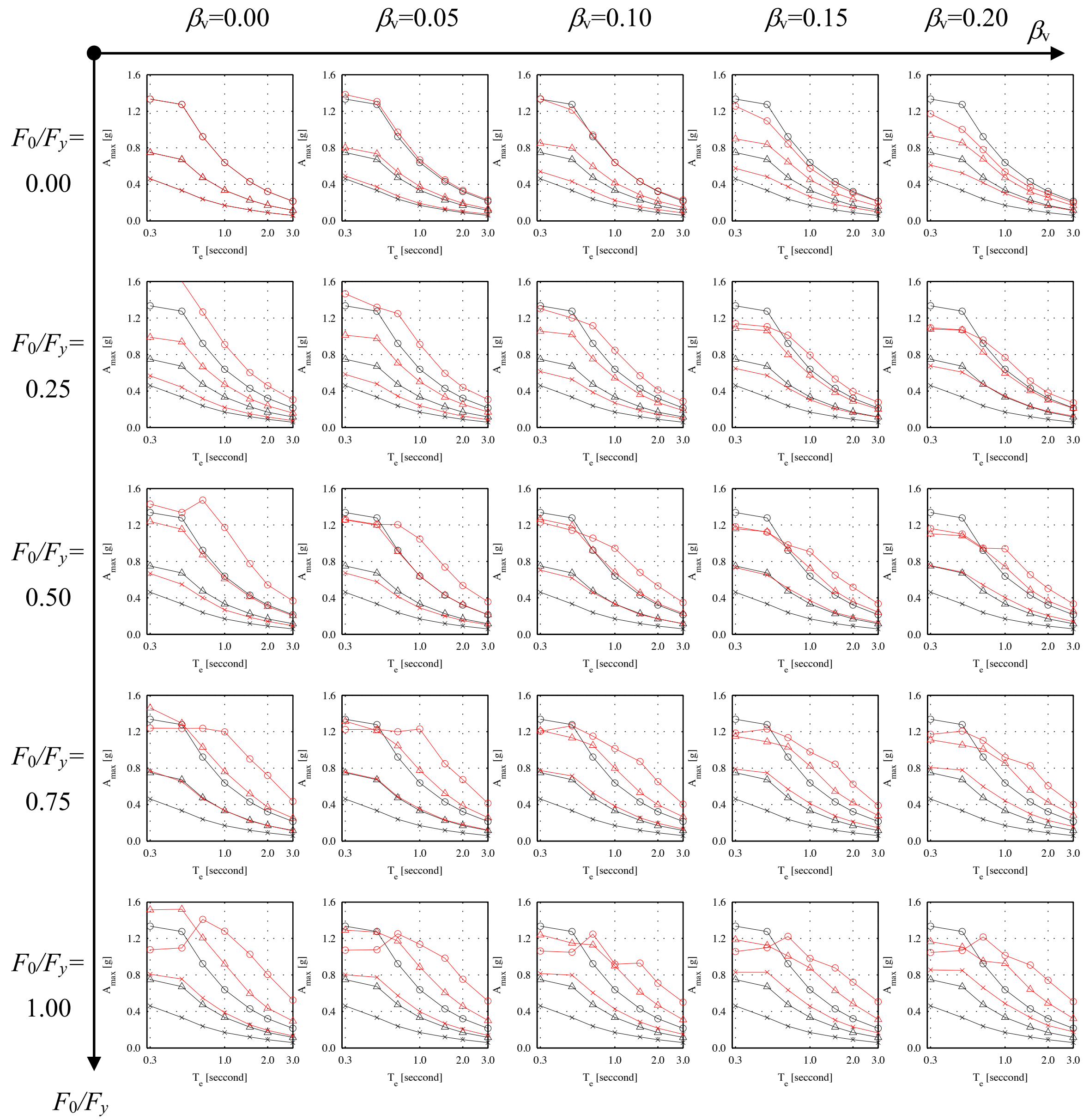

Figure A-93 Acceleration in MCE, Far-Field Motions, Linear Viscous Damping, Stiffness $K_0 \neq 0$, R_μ=1, 2 and 5

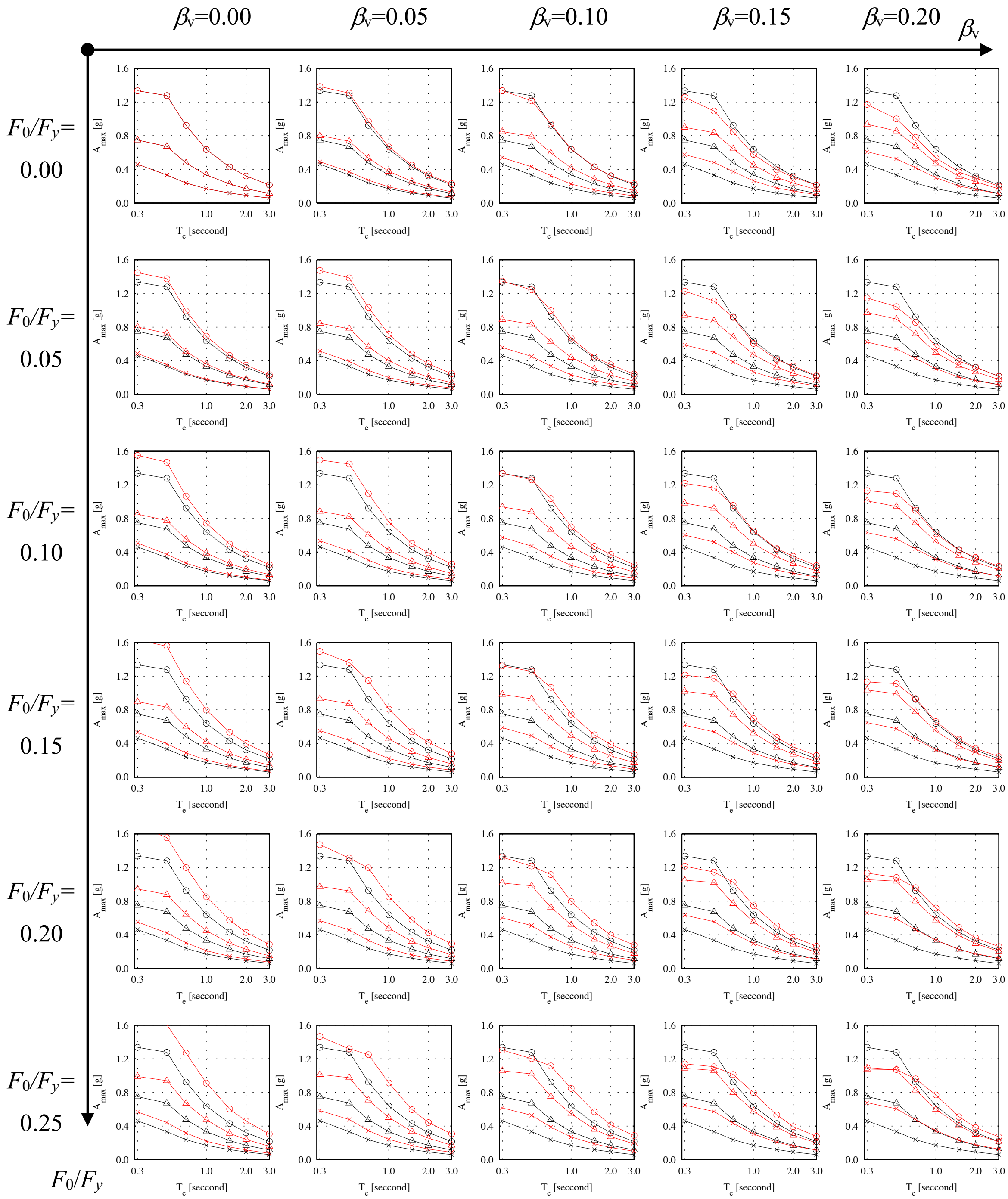

Figure A-93 (Continued)

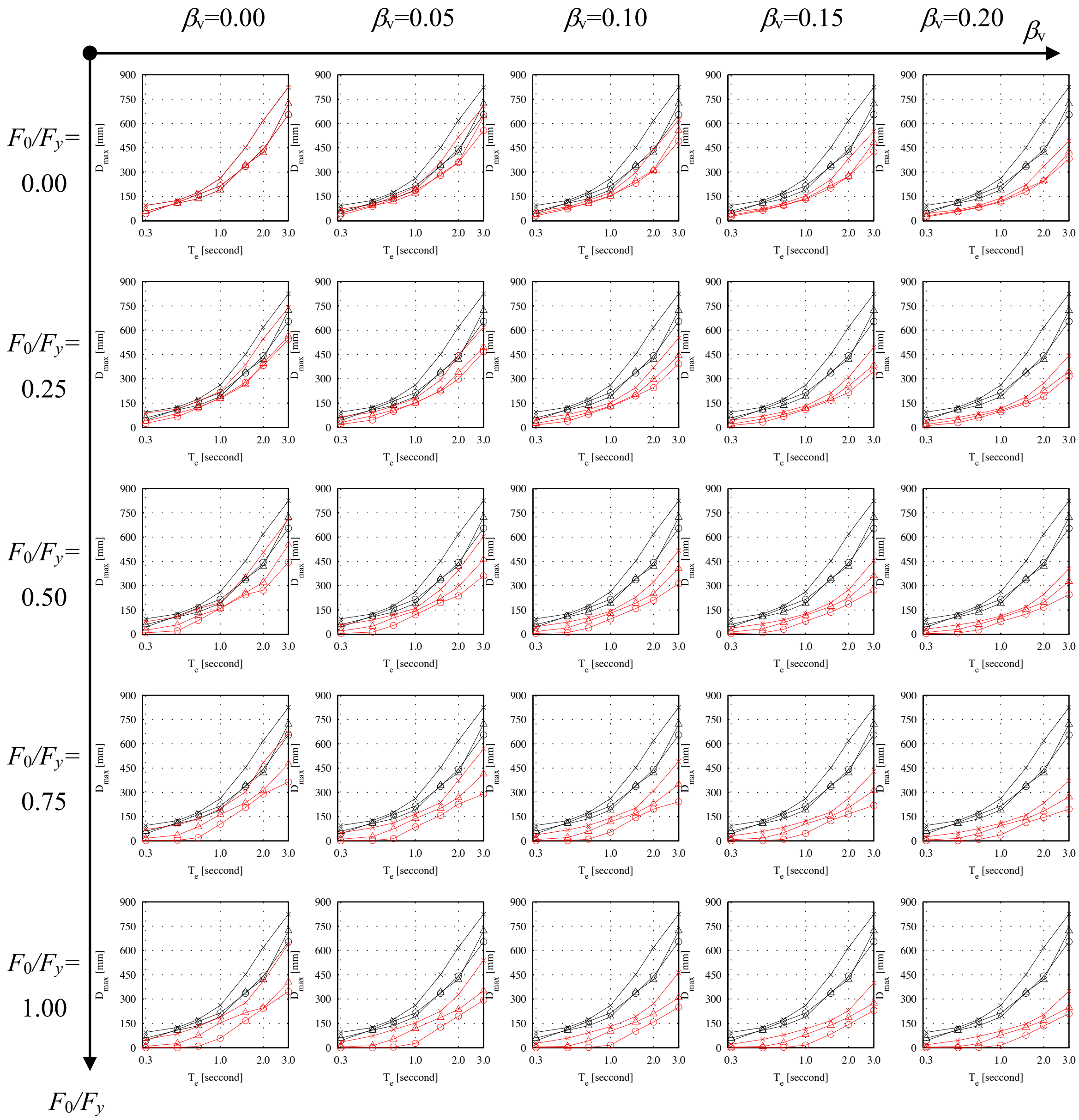

Figure A-94 Displacement in MCE, Far-Field Motions, Linear Viscous Damping, Stiffness K_0≠0, R_μ=1, 2 and 5

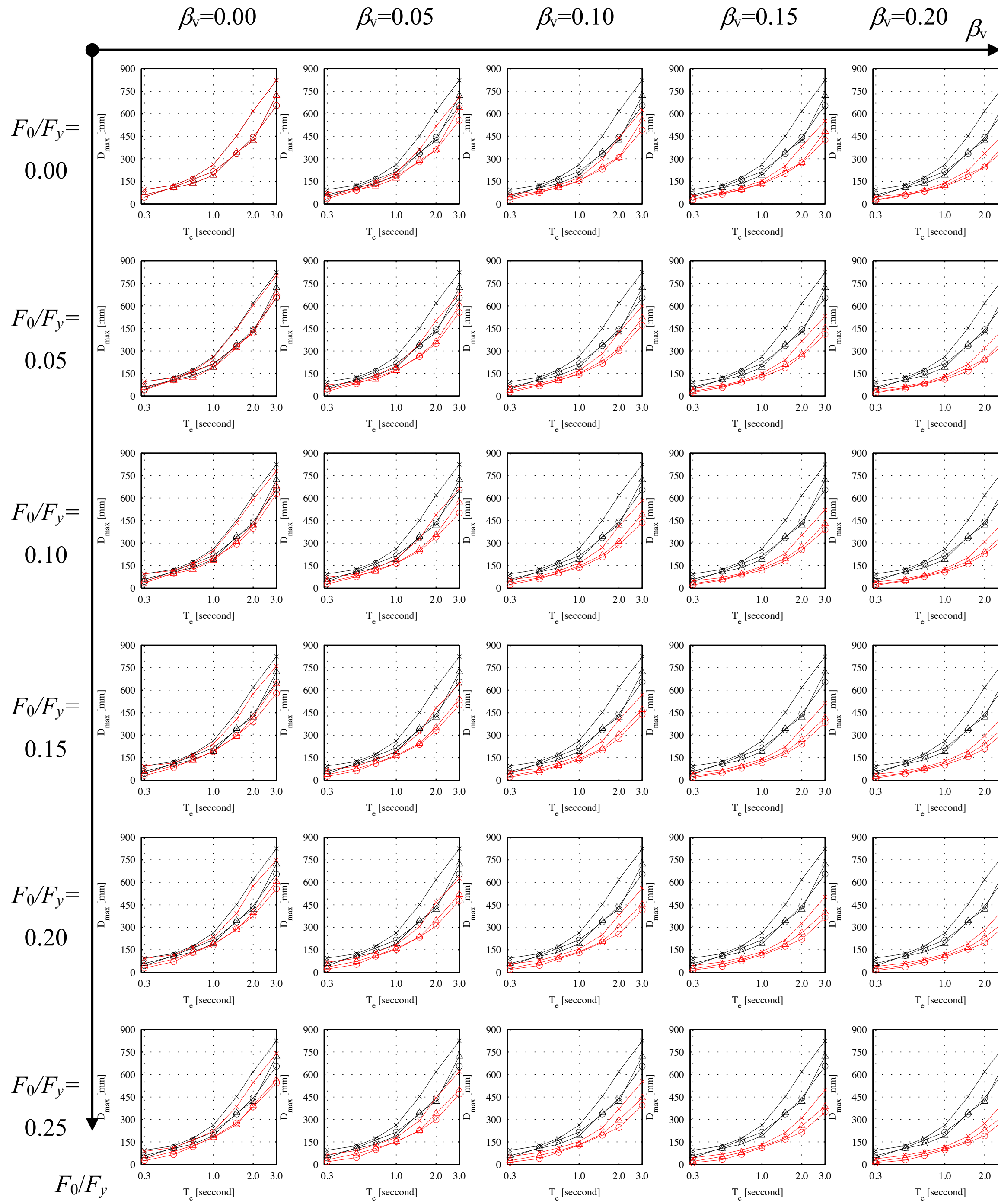

Figure A-94 (Continued)

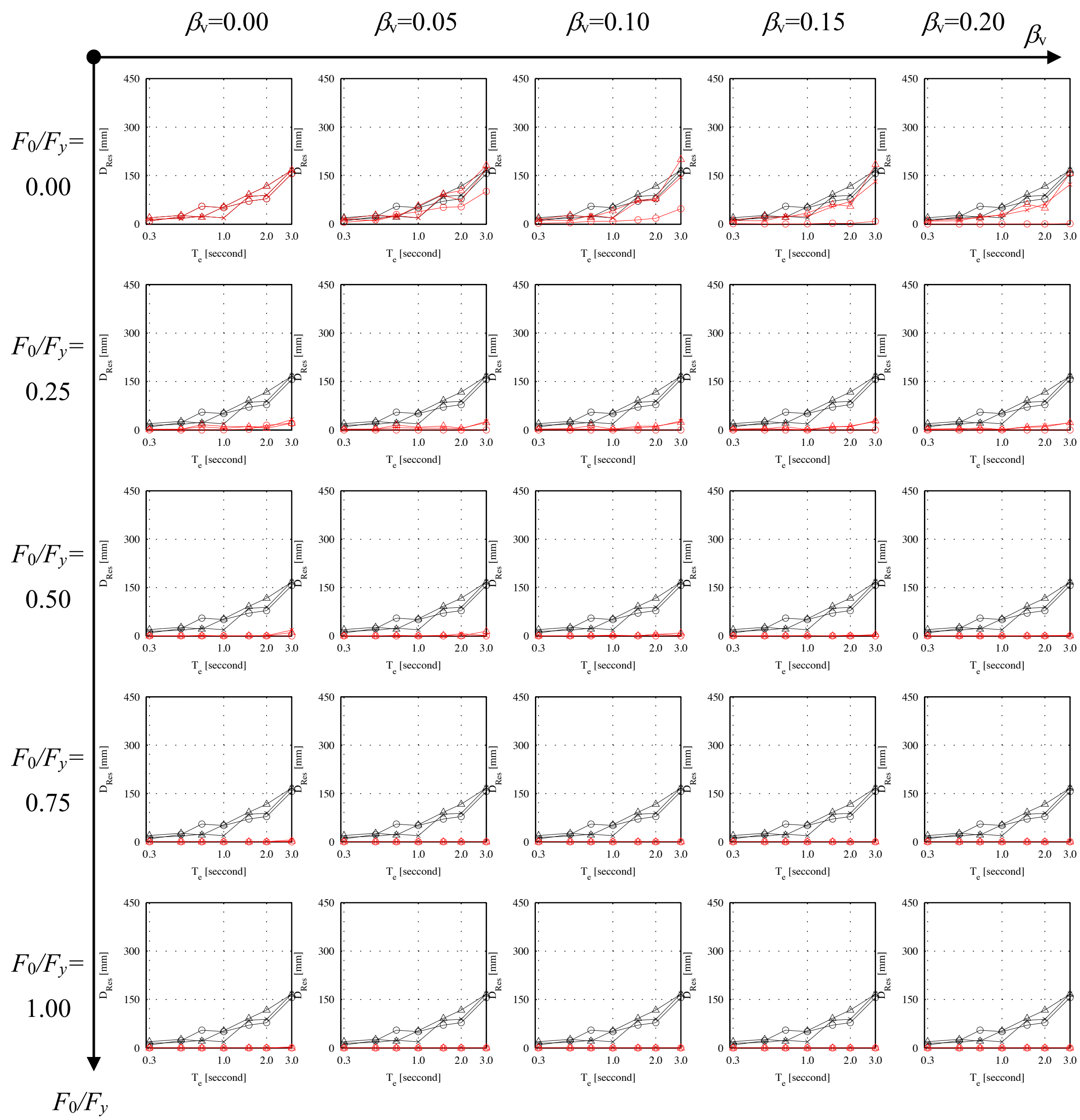

Figure A-95 Residual Displacement in MCE, Far-Field Motions, Linear Viscous Damping, Stiffness $K_0 \neq 0$, R_μ=1, 2 and 5

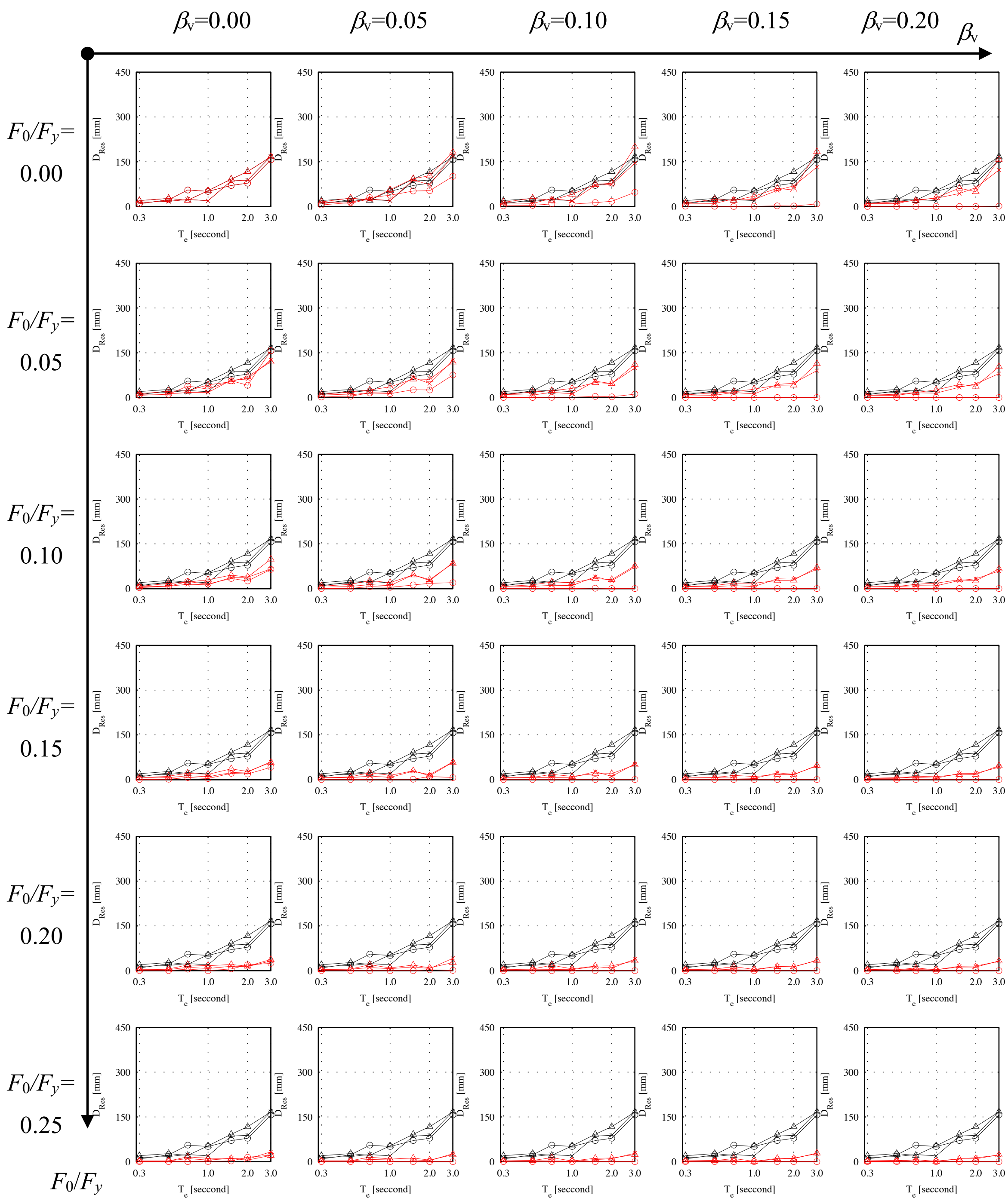

Figure A-95 (Continued)

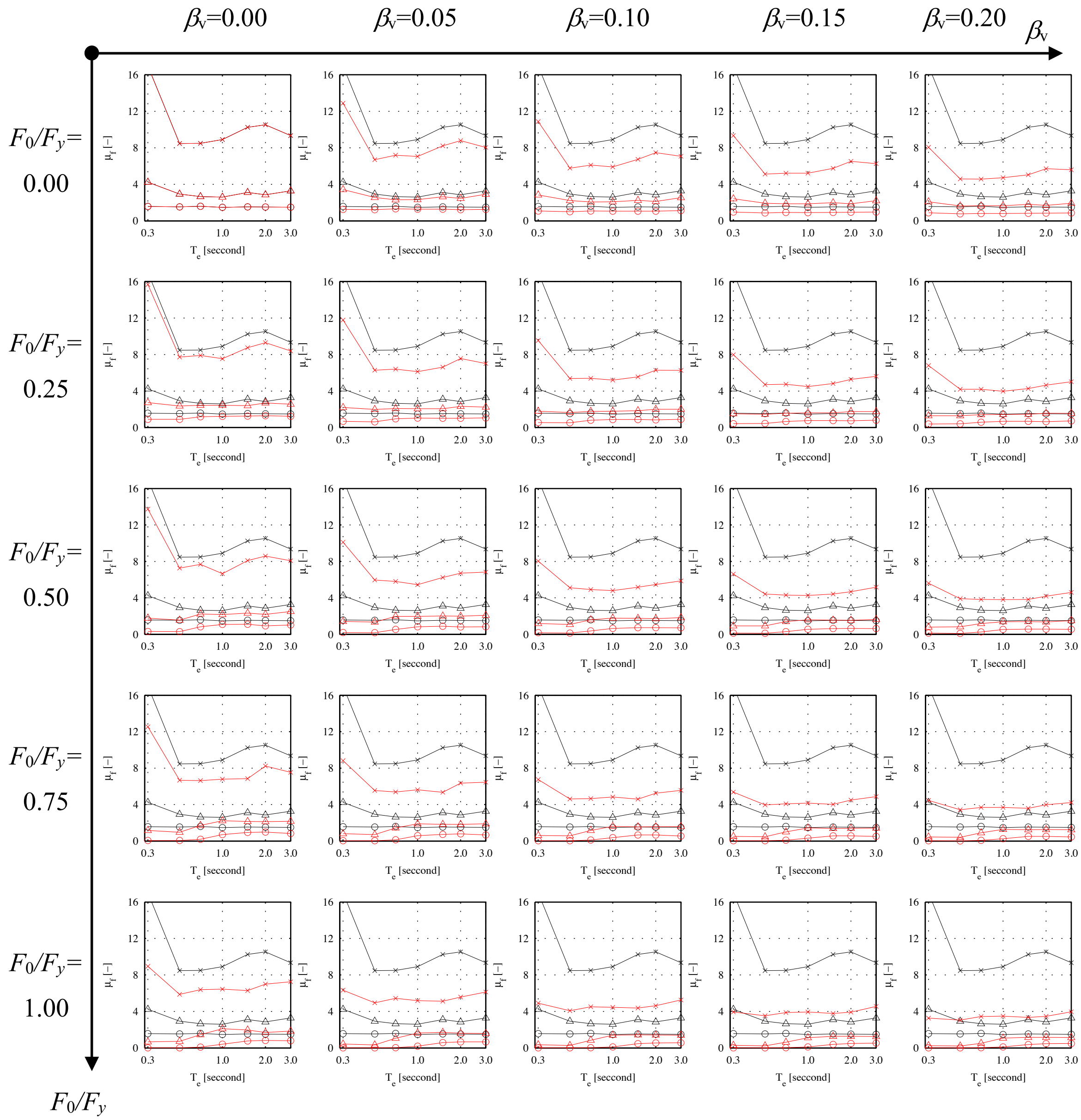

Figure A-96 Ductility Ratio in MCE, Far-Field Motions, Linear Viscous Damping, Stiffness K_0≠0, R_μ=1, 2 and 5

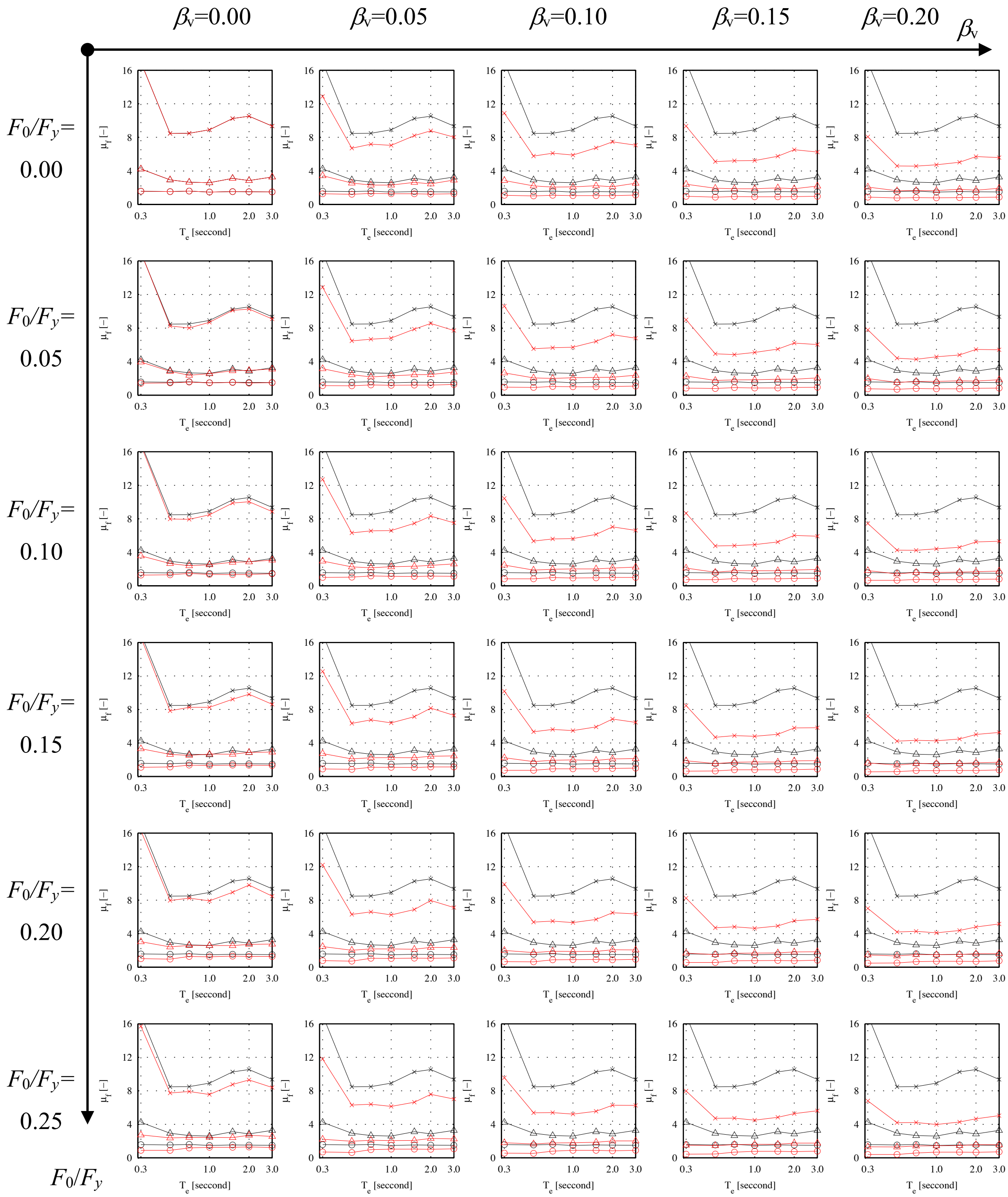

Figure A-96 (Continued)

APPENDIX B

DESCRIPTION OF EXAMPLE CONVENTIONAL BUILDINGS AND DESIGN OF LATERAL FORCE RESISTING SYSTEMS PER ASCE 7-2010

B.1 Introduction

This appendix presents a description of a 3-story and a 6-story building that are utilized in the development of design examples for structures with fluidic self-centering systems. The examples follow the paradigm in the corresponding appendix in Ramirez et al (2001) but the procedures and adequacy criteria follow ASCE 7-2010 instead of NEHRP (1997). The appendix presents the design of special steel moment frames for these buildings without any fluidic self-centering system to meet the strength and drift criteria of ASCE 7-2010. A comparison of these frames to those of the same buildings with fluidic self-centering devices illustrates the benefits and drawbacks offered by the self-centering systems.
The two designed frames are termed *3S-Reference* and *6S-Reference* frames.

B.2 Description of 3-Story Building

This building is residential in use and is of regular configuration, constructed of steel, 41.15 m (135′) x 41.15 m (135′) in plan, and 13.028 m (42′-9″) high. A typical floor plan and a typical elevation are shown in Figure B-1. Columns are spaced at 8.23 m (27′-0″) o.c. Wind and earthquake resistance is provided by two three-span special moment frames in each direction, located on the perimeter of the building and are indicated by heavy lines in Figure B-1. Floors are assumed to behave as rigid diaphragms. The site of the buildings is considered to be in California and having a Risk-Targeted Maximum Considered (MCE_R) response spectrum constructed per ASCE 7-2010 to have the characteristic values of S_{MS}=1.875g and S_{M1}= 0.9g. The Design level response spectrum (DE) has characteristic values equal to 2/3 of those of the MCE_R, so S_{DS}=1.25g and S_{D1}= 0.6g. The spectra of the two levels of earthquake are shown in Figure 4-1.

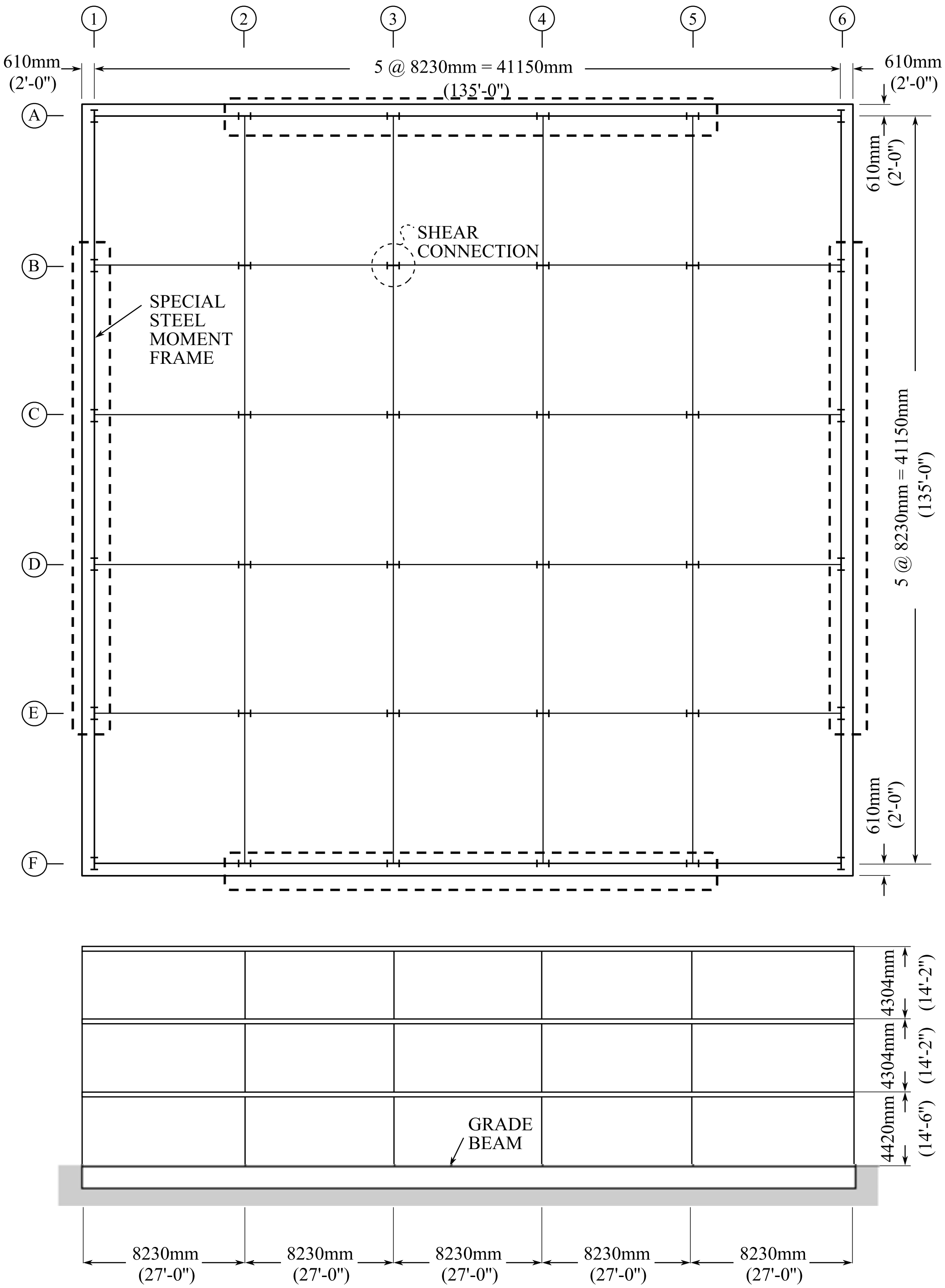

Figure B-1 Plan and Elevation of 3-Story Building

Design Parameters

The building is designed to meet the criteria of the ASCE 7-2010 Standard: Minimum Design Loads for Buildings and Other Structures.

Loads

Roof Dead Load:	*1.68 kN/m² (35 psf)*
Roof Live Load:	*0.96 kN/m² (20 psf)*
Floor Dead load:	*3.35 kN/m² (70 psf)*
Floor Live Load:	*1.68 kN/m² (35 psf)*
Cladding:	*1.20 kN/m² (25 psf)*

Reduced floor live load of 35 psf is assumed for all floors for convenience. Unreduced live load is 40 psf.

Material

Steel with yield strength: $F_y = 345\ MPa\ (50\ ksi)$

Weight of the Building

Third Floor (roof):	$w_3 = 3{,}134\ kN$
Second Floor:	$w_2 = 5{,}800\ kN$
First Floor:	$w_1 = 5{,}800\ kN$
Total	$W_T = 14{,}734\ kN$

Design Coefficients per Table 12.2.1, ASCE 7-2010

For Steel Special Moment Frame

Response Modification Factor:	$R = 8.0$
System Over-strength Factor:	$\Omega_0 = 3.0$
Deflection Amplification Factor:	$C_d = 5.5$

Importance Factor per Table 1.5-2, ASCE 7-2010

I_e=1 for Risk Category I or II

Allowable Story Drift per Table 12.12.1, ASCE 7-2010

For Seismic Group I or II, all other Structures: $\Delta_a = 0.02 h_{sx}$

Evaluation of Design Gravity Loads

Gravity loads on beams are summarized in Table B-1 using the loads described in Section B.3.1 and the tributary width to each beam of the special steel moment frame.

Table B-1 Uniform Gravity Loads on Beams of Typical Steel Special Moment Frame

Floor	Tributary Width (m)	Floor Dead Load (kN/m)	Cladding (kN/m)	Total Dead Load (kN/m)	Live Load (kN/m)
3	4.725	7.9	2.6	10.5	4.5
2	4.725	15.8	5.2	21.0	8.0
1	4.725	15.8	5.2	21.0	8.0

B.3 Design of Typical 3-Story Steel Special Moment Frame

Seismic Base Shear *V* and Minimum Required Base Shear Strength V_y

Fundamental Period of the Structure, *T* (per Chapter 12.8.2, ASCE 7-2010)

Approximate fundamental period T_a (eq. 12.8-7):

$$T_a = C_t\left(h_n\right)^{0.8}$$

$$C_t = 0.028$$

$$T_a = 0.028\left(42.74\right)^{0.8} \qquad \therefore T_a = 0.565\,\text{sec}$$

$$T \le C_u \cdot T_a$$

$$C_u = 1.4 \qquad (\text{For } S_{D1} > 0.4g, \text{ Table 12.8-1})$$

$$T \le 1.4 \times 0.565 = 0.79\,\text{sec} \qquad \therefore\ T = 0.79\,\text{sec}$$

Seismic Response Coefficient, C_s (eq. 12.8-3)

$$C_s = \frac{S_{D1}}{R\left(T/I_e\right)} = \frac{0.6}{8\times\left(0.79/1.0\right)} = 0.095$$

(Limits per equations 12.8-5 and 12.8-6 of ASCE 7-2010 do not govern)

Seismic Base Shear, *V* (eq. 12.8-1)

$$V = C_s \cdot W_T$$

$$V = 0.095x14,734 \qquad \therefore V = 1,400\ \text{kN}\ (315\ \text{kip})$$

The seismic base shear of each frame is 0.525*V* where *0.5V* is the share of *V* by one of two frames and *0.025V* is the additional force due to an accidental eccentricity of 5% of the plan dimension. The seismic base shear per frame, including the effects of torsion, is *V= 735 kN* (*165 kip*).

Accordingly, the minimum required base shear strength for each frame V_y (see Section 6 herein) is

$$V_y = V \cdot \frac{C_d \cdot \Omega_o}{R} = 735 \times \frac{5.5 \times 3.0}{8} = 1{,}516\,kN\,(341kip)$$

Vertical Distribution of Seismic Forces

The vertical distribution of the seismic forces is described in Chapter 12.8.3 of ASCE 7-2010. The base shear is V=735kN.

$$C_{vx} = \frac{w_x h_x^k}{\sum_{i=1}^{n} w_i h_i^k} \qquad \text{For } T = 0.79\text{sec} \qquad k = 1.145$$

Per Chapter 12.3.4.2, the redundancy factor is taken as equal to 1.3.

$$\rho = 1.3$$

The lateral seismic forces are presented in Table B-2.

Table B-2 Lateral Seismic Forces for 3-Story Frame

Floor	w_x^* (kN)	h_x (m)	$w_x h_x^k$	C_{vx}	F_x (kN)
3	1567	13.03	29627	0.3697	271.7
2	2900	8.72	34617	0.4319	317.5
1	2900	4.42	15900	0.1984	145.8

***:** Reactive weight of each frame $\sum_{i=1}^{N} w_i h_i^k = 80{,}144$

Preliminary Design of Beams and Columns

The critical loading combination for this frame is (1.2+0.2S_{DS})D+ρQ_E+0.5L per ASCE 7-2010 Section 12.4.2.3, where D is dead load, L is live load and Q_E is seismic load from the lateral forces F_x in Table B-2. Given that S_{DS}=1.25, the critical loading case is 1.45D+0.5L+1.3Q_E. This loading combination controls the requirements for the strength design of the frame. Accordingly, the assessment of adequacy starts with a preliminary design that is identical to the one of Ramirez et al. (2001) for the 3-story reference frame. This frame has W14x211 column sections and W18x46, W21x50 and W24x62 beam sections from top to bottom. Static analysis of the frame for the critical loading combination for strength shows that all members have a required strength that is substantially less than the design strength. This was expected as the drift criteria control the design. For the calculation of the drift the seismic forces based on the computed fundamental period of the structure, without use of the upper limit C_uT_a=0.79sec, are used.

The fundamental period of the trial frame was calculated by eigenvalue analysis in program OpenSees to be T=1.07sec. The seismic response coefficient is C_s=S_{D1}/(RT)=0.6/(8x1.07)=0.07. The seismic base shear is V=0.525C_sW_T=0.525x0.07x14734=541.5kN.

The lateral loads are then recalculated based Section 12.8.3 of ASCE 7-2010 and the values are presented in Table B-3. Note that for T=1.07sec, the exponent k is equal to 1.285. Floor displacement are calculated as the displacement δ_{xe} due to the lateral loads shown times C_d/I_e=5.5. The drift criteria are satisfied.

Table B-3 Calculation of Story Drifts of 3-Story Frame

Level	h_i (m)	w_i (kN)	$w_i h_i^k$	C_{vx}	F_{xi} (kN)	δ_{Xe} (mm)	$C_d\delta_{xe}/I_e$ (mm)	Δ_i (mm)	Δ/h_{sx}
3	13.03	1567	42440	0.3897	211.0	36	197.5	68.8	0.016
2	8.72	2900	46877	0.4305	233.1	24	128.7	80.6	0.019
1	4.42	2900	19578	0.1798	97.4	9	48.1	48.1	0.011

$$\sum w_i h_i^k = 108{,}895$$

Figure B-2 shows the frame geometry, section properties and tributary weights.

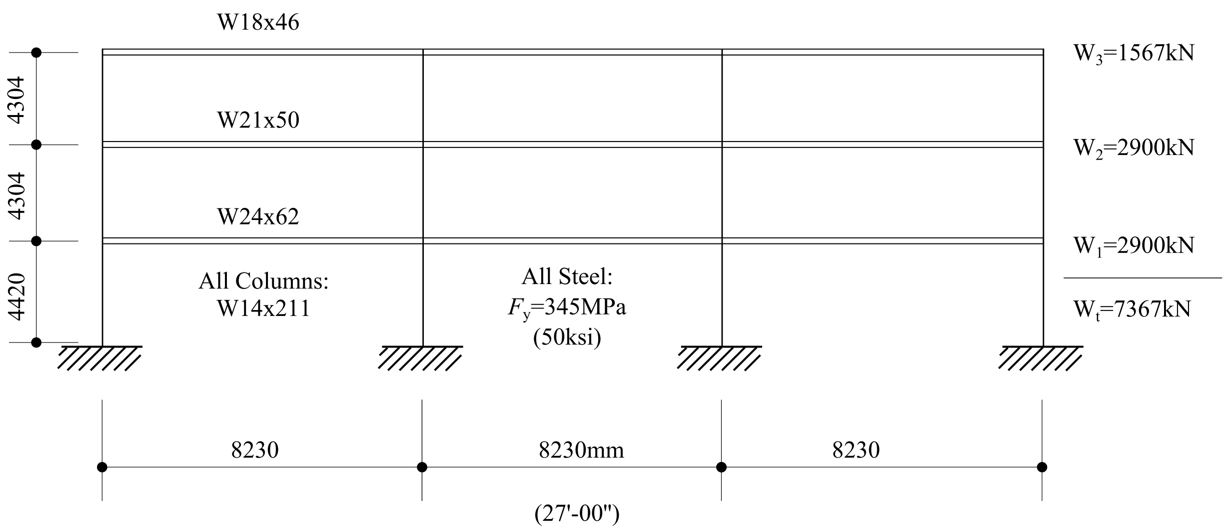

Figure B-2 3S-Reference Frame Geometry, Section Properties and Tributary Weights

B.4 Design of 6-Story Special Steel Moment Frame

Consider that the building of Figure B-1 has six stories. Assume that the number and distribution of special steel moment frames remains as shown. Furthermore, assume that the interstory height and floor weights also remain unchanged. This section presents the design of the 6-story special steel moment frame following the same approach as in the 3-story example. The allowable story drift is 0.02 times the story height (Table 12.12.1, ASCE 7-2010). Same gravity loads are assigned for the 6-story building as for the 3-story building shown in Table B-1 for the typical floors and the top floor.

Seismic Base Shear V and Minimum Required Strength V_y

Fundamental Period of the Structure, T (per Chapter 12.8.2, ASCE 7-2010)

Height of the structure: $h_n = 4420 + 5 \times 4304 = 25940mm$ (85.1′)

Approximate period: $T_a = 0.028\left(85.1'\right)^{0.8} = 0.98sec$

Upper bound period: $T_1 = 1.4 \times 0.98 = 1.372sec$

Seismic Response Coefficient, C_s

$$C_s = \frac{0.6}{8 \times 1.372} = 0.0547$$

C_s shall not be less than (Eq. 12.8-5, ASCE-2010) $C_S = 0.044 S_{DS} I_e \geq 0.01$

Here, C_s=0.044$S_{DS}I_e$=0.044x1.25x1.0=0.055≥0.0547, thus C_s=0.055 governs.

Seismic Base Shear, V (eq. 12.8-1)

$$V = C_s \cdot W_T$$

$$V = 0.055 \times 32134 \qquad \therefore V = 1767.4kN(397.2kip)$$

The seismic base shear of each frame, including the torsional effect is $V= 927.9\ kN$ ($208.5\ kip$). Accordingly, the minimum required base shear strength for each frame V_y (see Section 6 herein) is

$$V_y = V \cdot \frac{C_d \cdot \Omega_o}{R} = 927.9 \times \frac{5.5 \times 3.0}{8} = 1{,}913.8kN\,(430.1kip)$$

Vertical Distribution of Seismic Forces

Exponent k (for $T=1.372\ sec$): $k = 1.436$

Redundancy reliability factor (per 12.3.4.2 in ASCE 7-2010): $\rho = 1.3$

Calculations of the vertical distribution of seismic forces per frame are presented in Table B-4.

Table B-4 Lateral Seismic Forces for 6-Story Frame

Level	w_i (kN)	h_i (m)	$w_i h_i^k$	C_{vxi}	F_{xi} (kN)
6	1567	25.94	168085	0.2135	198.1
5	2900	21.63	239629	0.3044	282.5
4	2900	17.33	174306	0.2214	205.4
3	2900	13.03	115733	0.1470	136.4
2	2900	8.72	65010	0.0826	76.6
1	2900	4.42	24503	0.0311	28.9

$$\sum_{i=1}^{N} w_i h_i^k = 787,266$$

Preliminary Design of Beams and Columns

Beams are proportioned for the maximum of the bending moments obtained from critical seismic loads according to load combination of $1.45D+0.5L+1.3Q_E$. Similar to the 3-story building, the assessment of adequacy started with a preliminary design that is identical to the one of Ramirez et al. (2001) for the 6-story reference frame. This frame has W14x211, W14x233 and W14x257 column sections from top to bottom, each spanning for two stories, and W21x44, W21x50, W24x68, W24x76, W27x84 and W27x94 beam sections from top to bottom, each spanning over the entire floor. Static analysis of the frame for the critical loading combination for strength shows that all members a required strength that is much larger than needed. Drift is calculated using seismic forces calculated based on the computed fundamental period of the structure without use of the upper limit value of C_uT_a=1.372sec.

The fundamental period of the trial frame was calculated by eigenvalue analysis in program OpenSees to be T=1.90sec. The seismic response coefficient is $C_s=S_{D1}/(RT)$=0.6/(8x1.90)=0.0395. The seismic base shear is $V=0.525C_sW_T$=0.525x0.0395x32134=666.4kN.

The lateral loads are recalculated based on Section 12.8.3 of ASCE 7-2010 and the values are presented in Table B-5. Note that the exponent k is equal to 1.7. Floor displacements are calculated as the displacement δ_{xe} due to the lateral loads shown and then multiplied by C_d/I_e=5.5. The drift criteria are satisfied.

Table B-5 Calculation of Story Drifts of 6-Story Frame

Level	w_i (kN)	h_i (m)	$w_ih_i^k$	C_{vx}	F_{xi} (kN)	δ_{xe} (mm)	$C_d\delta_{xe}/I_e$ (mm)	Δ_i (mm)	Δ_i/h_{sx}
6	1567	25.94	397025	0.2354	156.9	73.0	401.6	55.5	0.013
5	2900	21.64	539927	0.3202	213.4	62.9	346.1	75.1	0.017
4	2900	17.33	370131	0.2195	146.2	49.3	271.0	81.8	0.019
3	2900	13.03	227931	0.1352	90.1	34.4	189.2	81.0	0.019
2	2900	8.72	115153	0.0683	45.5	19.7	108.2	68.9	0.016
1	2900	4.42	36276	0.0215	14.3	7.2	39.4	39.4	0.009

$$\sum_{i=1}^{N} w_i h_i^k = 1,686,443$$

Figure B-3 shows the frame geometry, section properties and tributary weights.

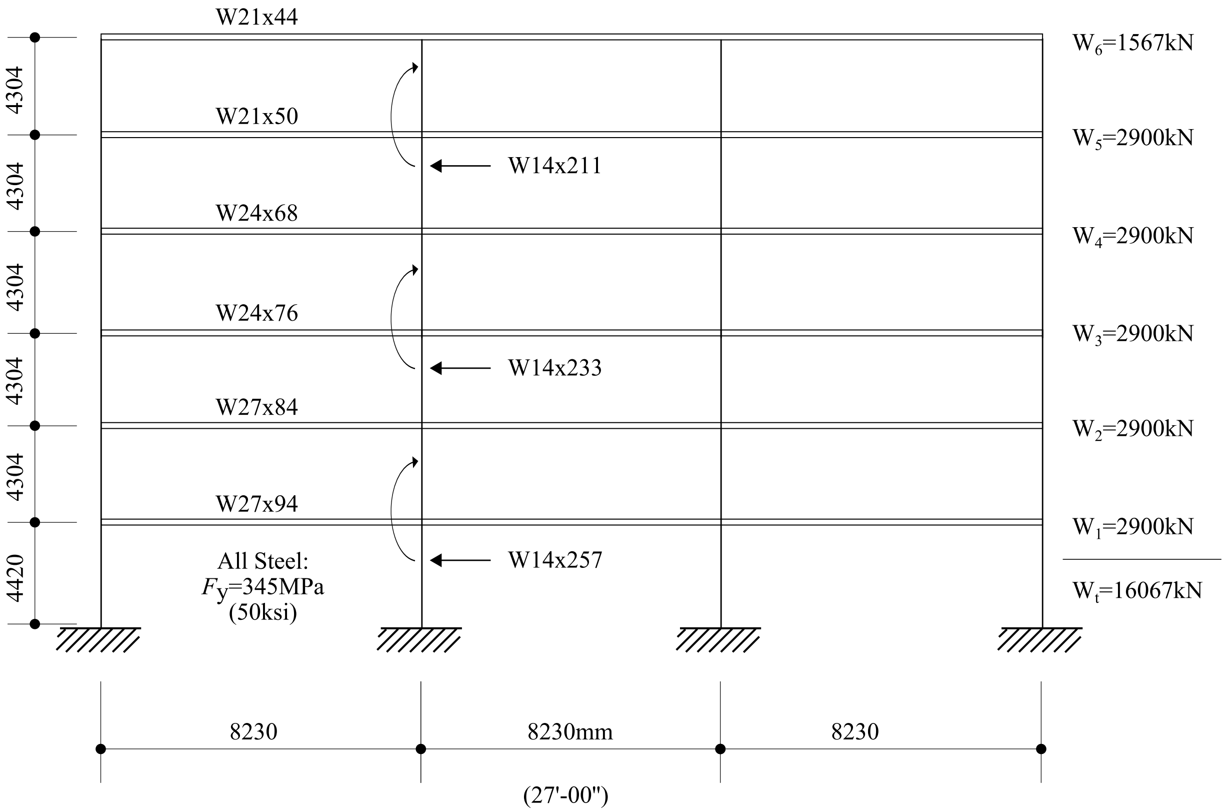

Figure B-3 6-Story Special Moment Frame Designed to Meet ASCE 7-2010 Criteria without a Self-Centering Damping System (6*S*-Reference)

APPENDIX C

DESIGN AND ANALYSIS OF EXAMPLE 3-STORY BUILDING WITH FLUIDIC SELF-CENTERING DEVICES

This appendix presents the design and simplified analysis of an example 3-story building with fluidic self-centering devices. The building is the one shown in Figure B-1 of Appendix B and consists of two steel special moment frames in each principal direction. Each frame is designed for a base shear equal to $0.75V$, where V is determined in accordance with Section 12.8 of ASCE 7-2010 per design procedures of Section 6 of this report. This frame is designated as *3S-75*. Fluidic self-centering devices are added as diagonal elements to this frame. Alternatively, the fluidic self-centering devices may be added to another frame (e.g., along lines 2, 5, B and E of plan in Figure B-1 of Appendix B) that is designed to remain elastic and with all simple connections. This is a preferred arrangement as it results in less force in the special moment frame and allows for easier assessment of adequacy of the structural system.

The frame exclusive of the fluidic self-centering system is first designed per procedures of Section 6 of this report. Then fluidic self-centering devices are added per procedures of Section 6 and analysis is performed again following the simplified ELF and RSA procedures of Section 6.

At the end of this appendix there is a brief presentation on the design of a stronger 3-story frame. Designated as 3S-85, the frame is designed for a base shear equal to $0.85V$, where V is determined in accordance with Section 12.8 of ASCE 7-2010 per design procedures of Section 6 of this report. The frame is of interest in studying its response and its collapse fragility by comparison to those of the 3S-75 and the 3S-References frames.

C.1 Design of Frame 3*S*-75

The geometry, material and gravity loading of the 3*S*-75 frame are the same as those of the 3*S*-Reference of Appendix B. Only difference between the two frames is the size of the member sections. Figure C-1 shows the geometry, section properties and the tributary weights of the 3*S*-75 frame. Note that the beam sections are slightly larger than those of the frame used by Ramirez et al. (2001) for buildings with damping systems and also designated as frame 3*S*-75. The reasons for the slight difference are: (a) the lateral and distribution of lateral forces are slightly different, (b) the redundancy factor is larger in ASCE 7 than in the older version of NEHRP, and (c) the vertical earthquake and accidental torsion effects have been accounted for in the current design.

Analysis following Chapter 12.8 of ASCE 7-2010 and presented in Appendix B established the seismic base shear for a single 3*S*-Reference frame, including the effect of torsion, to be V=735kN. The minimum base shear allowed for the 3*S*-75 frame per procedures of Section 6 is 0.75V=551.3kN. The required minimum base shear strength for the frame is

$$V_y = V \cdot \frac{C_d \cdot \Omega_o}{R} = 551.3 \times \frac{5.5 \times 3.0}{8} = 1{,}137\, kN\, (255.5 kip)$$

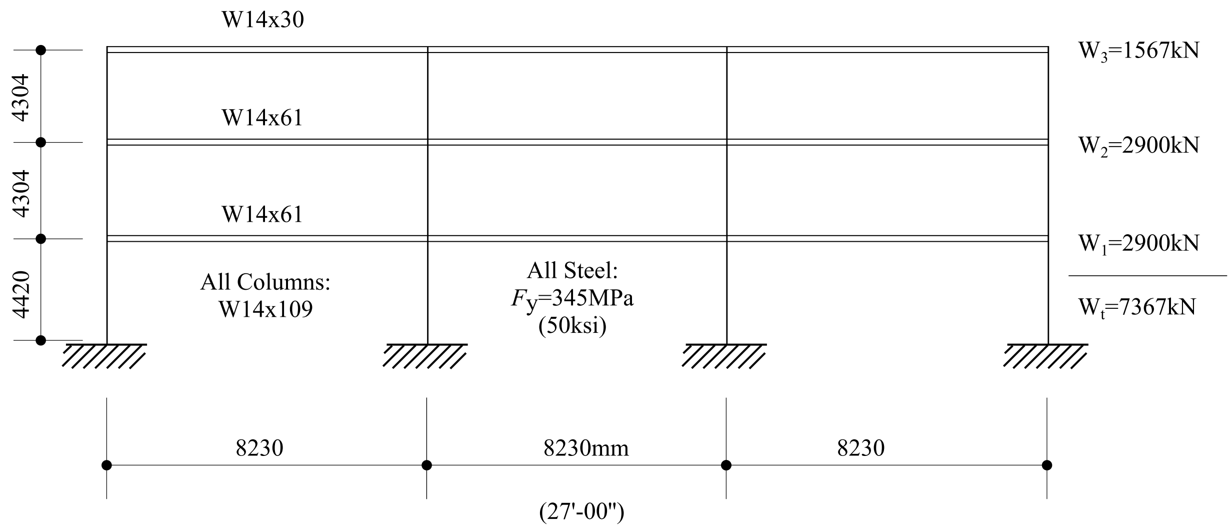

Figure C-1 Frame 3*S*-75 Geometry, Section Properties and Tributary Weights

Verification of the design is described below based on the procedures of Appendix B following ASCE 7-2010 and then by pushover analysis to obtain the force-displacement characteristics and verify the base shear strength. The parameters are: R=8, Ω_0=3, C_d=5.5, I_e=1.0, ρ=1.3, S_{MS}=1.875g, S_{M1}=0.9g, S_{DS}=1.25g and S_{D1}=0.6g. Also, the period for calculations of internal forces per ASCE 7-2010 is T=0.79sec (see Appendix B).

The seismic base shear for a single frame V=551.3kN is distributed vertically using ASCE 7-2010 equations 12.8-11 and 12.8-12:

$$F_y = C_{vx} V \tag{C-1}$$

$$C_{vx} = \frac{w_x h_x^k}{\sum_{i=1}^{n} w_i h_i^k} \tag{C-2}$$

The value of parameter k has been determined in Appendix B to be k =1.145. The calculated lateral seismic forces are summarized in Table C-1. Quantity $\sum_{i=1}^{n} w_i h_i^k$ is equal to 80,144.

Table C-1 Lateral Seismic Forces for 3-Story Frame 3*S*-75

Floor	w_i [kN]	h_i [m]	$w_i h_i^k$	C_{vx}	F_x [kN]
3	1567	13.03	29627	0.3697	203.8
2	2900	8.72	34617	0.4319	238.1
1	2900	4.42	15900	0.1984	109.4

Analysis of the frame for the critical loading combination $(1.2+0.2S_{DS})D+0.5L+\rho Q_E$ (which is equal to $1.45D+0.5L+1.3Q_E$) resulted in the required strengths of the members of the frame. The required bending moment strengths are as follows: (a) third floor beam 202kN-m, (b) second floor beam 467kN-m, (c) first floor beam 495kN-m, and (d) columns 656kN-m. The factored compressive axial force in the interior columns is P_u=695kN, prior to the use of the Ω_0 factor.

C.2 Construction of Push-Over Curve of 3*S*-75 based on Plastic Analysis

Plastic analysis may be used to calculate the base shear strength of the frame. Then with information on the fundamental mode period and mode shape, the push-over curve may be constructed. The method was detailed in Ramirez et al. (2001) and is reproduced below with minor modifications and some condensation.

Consider the N-story, n-bay moment frame subjected to an arbitrary distribution of lateral load as shown in Figure C-2(a). Arbitrary span length, story height, and corresponding beam and column ultimate bending capacities are assumed at any level. The base shear strength of the frame, V_y, is defined as the resultant lateral force at the collapse stage (Figure C-2(b)).

The base shear strength is calculated by equating the work done by the forces applied to the structure to the energy dissipated at plastic hinge locations, that is,

$$\sum_{i=1}^{N} F_i \cdot D_i = \sum_{k=1}^{K} M_{pck} \cdot \theta + 2\sum_{i=1}^{N}\sum_{j=1}^{n} M_{pbij} \cdot \beta_{ij} \qquad \text{(C-3)}$$

where F_i = lateral load applied at level i, D_i = lateral displacement of level i, M_{pck} = plastic moment at base of first-story column at column line k, M_{pbij} = plastic moment of beam at level i and span j, β_{ij} = rotation of beam plastic hinge at level i and span j, and θ = rotation of plastic hinge at base of columns. From Figure C-2(c), β_{ij} can be calculated by

$$\beta_{ij} = \theta \cdot \left(\frac{1}{1 - 2\alpha_{ij}} \right) \tag{C-4}$$

where α_{ij} = length factor for beam hinge location at level i and span j (see Figure C-2(c)).

Equilibrium of forces in the horizontal direction of the whole structure at the collapse stage requires that the sum of lateral forces must equal the base shear strength, V_y, that is,

$$\sum_{i=1}^{N} F_i = \sum_{i=1}^{N} \lambda_i V_y = V_y \tag{C-5}$$

where the lateral force at any level, F_i, are expressed as a fraction of the base shear strength, $F_i = \lambda_i V_y$. Parameter λ_i is a force distribution factor that depends on the lateral force pattern (first mode, modal, uniform, etc.) utilized in the pushover analysis of the structure.

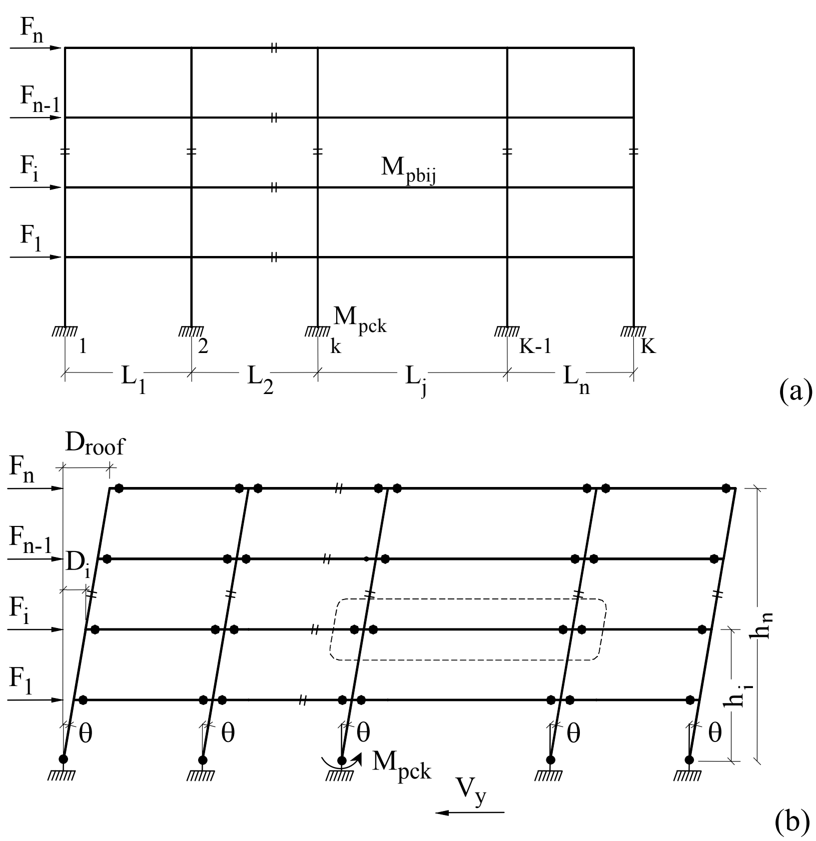

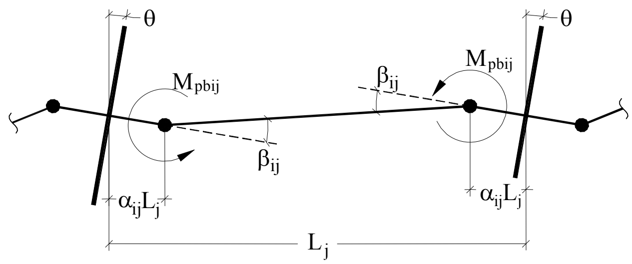

Figure C-2 Plastic Analysis of Moment Frame for Calculation of Base Shear Strength

Substitution of (C-5) and (C-4) into (C-3) results in

$$V_y = \frac{1}{\sum_{i=1}^{N}\left(\lambda_i \cdot h_i\right)} \cdot \left\{ \sum_{k=1}^{K} M_{pck} + \left[2\sum_{i=1}^{N}\sum_{j=1}^{n}\left(M_{pbij} \cdot \chi_{ij}\right) \right] \right\} \tag{C-6}$$

where, h_i = height of level i above the hinge at the base of the structure as shown in Figure C-2(b), and

$$\chi_{ij} = \frac{1}{1 - 2\alpha_{ij}} \tag{C-7}$$

Equation (C-4) may be further simplified when all first story columns have the same section, so that $M_{pck} = M_{pc}$, and all beams in a floor have the same section, so that $M_{pbij} = M_{pbi}$. Accordingly $\chi_{ij}=\chi_i=1/(1-2\alpha_i)$ and (C-6) simplifies to:

$$V_y = \frac{1}{\sum_{i=1}^{N}\left(\lambda_i \cdot h_i\right)} \cdot \left\{ \left(n+1\right) M_{pc} + 2n \cdot \sum_{i=1}^{N}\left(M_{pbi} \cdot \chi_i\right) \right\} \tag{C-8}$$

An idealized elasto-plastic representation of the pushover curve of a moment frame is characterized by the base shear strength, V_y, as given by equation C-6 or C-8 and a yield displacement, Δ_{yR}, which is the roof displacement when the plastic collapse mechanism develops. The latter is calculated by use of equations (6-41) and (6-42) as:

$$\Delta_{yR} = \left(\frac{g}{4\pi^2}\right) \cdot \Gamma_1 \cdot \left(\frac{V_y}{\overline{W}_1}\right) \cdot T_1^2 \tag{C-9}$$

where Γ_1 is the first mode participation factor given by equation (6-15), $\overline{W}_1$ is the first modal weight and T_1 is the fundamental period of the frame under elastic conditions.

The method is applied for constructing the push-over curve for frame 3*S*-75 of Figure C-1.

Frame parameters

Number and length of spans: n=3; L_b=8230 mm

Number of stories: N=3;

Material properties: F_y=345 MPa (50 ksi)

Column sections: W14×109 (d_c = 363 mm; $M_{pc}= Z_x \times F_y$ = 1086.8 kN-m)

Beam properties:

3rd floor: W14×30 (d_b = 351 mm; $M_{pc} = Z_x \times F_y$ = 267.4 kN-m)

2nd floor: W14×61 (d_b = 353 mm; $M_{pc}=Z_x \times F_y$= 576.2 kN-m)

1st floor: W14×61 (d_b = 353 mm; $M_{pc}=Z_x \times F_y$= 576.2 kN-m)

Floor weights: w_3=1567kN; w_2=w_1=2,900kN

Story heights: h_3=12928 mm; h_2=8624 mm; h_1=4320 mm

Eigenvalue analysis: T_1=1.50*sec*; $\{\phi_1\}^T$=[1.000, 0.675, 0.265]; $\overline{W}_1$=5959.2kN; Γ_1=1.4

It is assumed that plastic hinges form in the beams at a point located at a distance of half the depth of the column section $d_c/2$ from the column center (i.e., $\alpha_i= (d_c/2)/L_i$). Also, in columns a plastic hinge develops near the base at a distance of one depth (d_c) of the column section from the base of the frame.

Evaluation of parameters α_i, χ_i, and $M_{pbi}\chi_i$

Parameters are presented in Table C-2.

Table C-2 Parameters α_i, χ_i, and $M_{pbi}\chi_i$

Level	M_{pbi} (kN-m)	α_i	χ_i	$M_{pbi}\chi_i$ (kN-m)
3	267.4	0.022	1.05	279.7
2	576.2	0.022	1.05	602.8
1	576.2	0.022	1.05	602.8
				$\Sigma M_{pbi}\chi_i$=1485.3 kN-m

From Table C-2, the term $(n+1)M_{pc} + 2n\sum_{i=1}^{N}(M_{pbi} \cdot \chi_i)$ in equation (C-8) is calculated as:

$$(n+1)M_{pc} + 2n\sum_{i=1}^{N}(M_{pbi} \cdot \chi_i) = (3+1)\cdot 1086.8 + 2\cdot 3\cdot 1485.3 = 13259.0 \quad \text{kN}\cdot\text{m}$$

The term $\sum_{i=1}^{N}(\lambda_i h_i)$ in equation (C-8) depends on the horizontal shear distribution λ_i. In this study, λ_i=C_{vx} as defined in section 12.8-12 in ASCE 7-2010. Thus,

$$\lambda_i = \frac{w_i h_i^k}{\sum_{m=1}^{N} w_m h_m^k} \tag{C-10}$$

Here, k is calculated to be k=1.5 (ASCE 7, 2010) based on the period of 1.50sec. Calculations are summarized in Table C-3.

Table C-3 Calculation of $\lambda_i h_i$

Level	w_i (kN)	h_i (mm)	$w_i h_i^k \times 10^6$	λ_i	$\lambda_i h_i$ (mm)
3	1567	13027	2329.9	0.420	5471.3
2	2900	8724	2363.0	0.426	3716.4
1	2900	4420	852.2	0.154	680.7
			$\Sigma w_i h_i^k \times 10^6$=5545.1		$\Sigma \lambda_i h_i$=9868.4

Thus, V_y is calculated from equation (C-8) as:

$$V_y = \frac{13259.0 \times 10^3}{9868.4} = 1343.2 \quad \text{kN} \tag{C-11}$$

Δ_{yR} is calculated from equation (C-9) as:

$$\Delta_{yR} = \left(\frac{g}{4\pi^2}\right) 1.4 \left(\frac{1343.2}{5959.2}\right) 1.50^2 = 176.4 \quad \text{mm} \tag{C-12}$$

C.3 Push-Over Analysis of 3*S*-75 Frame and Comparison to Results of Plastic Analysis

A pushover analysis of frame 3*S*-75 was conducted in program OpenSees and the base shear-roof displacement relation was constructed. Lateral loads in the pushover analysis were distributed in proportion to parameter λ_i as shown in Table C-3. Figure C-3 presents the pushover curves computed in OpenSees with and without consideration of P-Δ effects and the pushover curve obtained in plastic analysis. The latter does not include P-Δ effects. Also, the computation when P-$\varDelta$ effects are accounted for considers a small post-elastic stiffness of members (ratio of post-elastic to elastic stiffness equal to 0.01).

Evidently, plastic analysis predicts well the pushover curve of the frame when P-Δ effects are neglected. Note that the calculated (OpenSees) base shear strength of 1,400kN without P-Δ effects exceeds the minimum required for this frame, which is 1,137kN. Also, it is observed that the pushover curve is affected by P-Δ effects and this behavior will be accounted for in the analysis of the frame with added fluidic self-centering devices. The base shear strength including P-Δ effects is equal to about 1,300kN, thus slightly more than the minimum required.

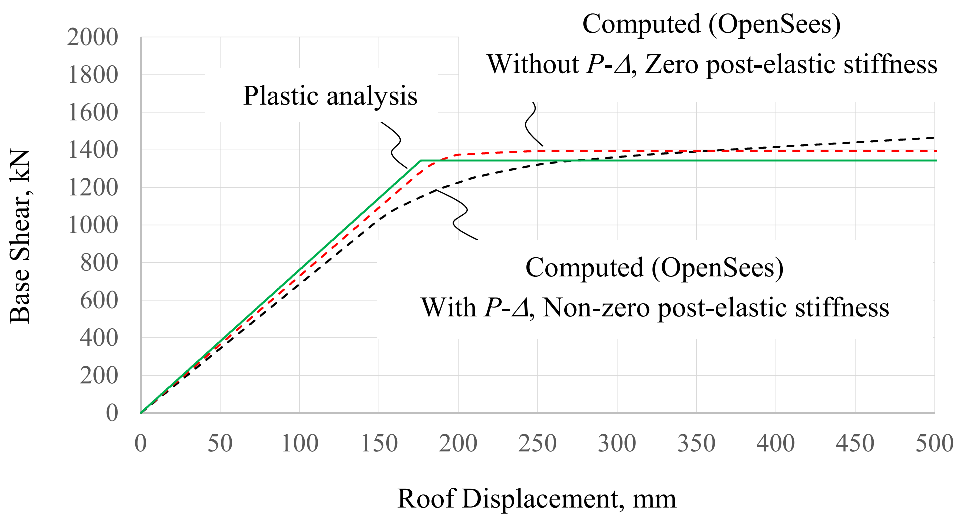

Figure C-3 Comparison of Pushover Curves of Frame 3*S*-75

C.4 Design and Simplified Analysis of 3*S*-75 Frame with Fluidic Self-Centering Devices

The procedures of Section 6.5 are applied. The first step is to conduct a pushover analysis and determine the story shear-story drift relations of each story so that the story shear yield strengths are determined. This may be obtained by plastic analysis as described in Section C.3 but computational analysis including P-Δ effects is preferred to better capture the frame behavior. This analysis has been performed (see Section C.3) and Figure C-4 presents the results. Based on this figure, the story yield strengths are obtained as : $F_{y,1}$=1,300 kN, $F_{y,2}$=1,110 kN and $F_{y,3}$=550 kN. Note that the pushover curves in Figure C-4 have some small post-elastic stiffness so that the yield strength was defined as the force at initiation of inelastic action in bilinear representations of the pushover curves.

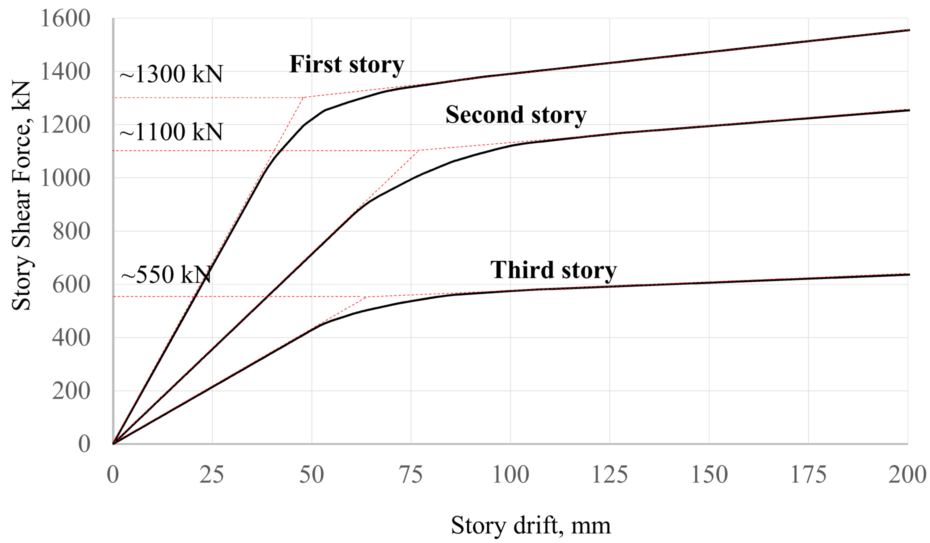

Figure C-4 Story Shear Force Versus Story Drift Relations for Frame 3*S*-75

Parameters for fluidic self-centering devices

The component of preload in the horizontal direction is selected to be approximately equal to a 20% of the story shear yield strength. One device will be used at each story placed in a diagonal configuration at an angle θ. The preload for the device at story i, $F_{0,i}$ is calculated as:

$$F_{0,i} = \frac{0.2 \times F_{y,i}}{\cos\theta} \tag{C-13}$$

Accordingly,

$$F_{0,1} = \frac{0.2 \times F_{y,1}}{\cos 28.2°} = \frac{0.2 \times 1300}{\cos 28.2°} = 295.0kN \qquad \text{(select 300 kN)}$$

$$F_{0,2} = \frac{0.2 \times F_{y,2}}{\cos 27.6°} = \frac{0.2 \times 1100}{\cos 27.6°} = 248.2kN \qquad \text{(select 300 kN)}$$

$$F_{0,3} = \frac{0.2 \times F_{y,3}}{\cos 27.6°} = \frac{0.2 \times 500}{\cos 27.6°} = 124.1kN \qquad \text{(select 125 kN)}$$

It was decided that a single device design will be used but the fluid initial pressure will be varied to achieve the desired preload for the two types of devices needed. The displacement capacity of the devices was calculated as *1.5x0.02h(R/C$_d$)cosθ* which is an upper bound estimate of the displacement in the MCE when the drift limit in the DE is 0.02*h* per ASCE 7-2010. The manufacturer of the devices was then contacted and asked to develop a design for a device that can be preloaded to either 300 or 125kN, have a displacement capacity of 165mm (6.5inch) and have linear viscous damping (could be of the half damping type) with a damping constant C=1,140kN-sec/m (6.5kip-sec/in). The manufacturer provided the following:

- Basic dimensions of the device (including the connection details) to be 216mm (8.5inch) in diameter and 1145mm (45inch) in length (pin to pin).
- The end-load of the device under quasi-static conditions at the displacement of 165mm, which was used to calculate the stiffness K_0 as follows

$$K_{0,1} = 2320 \text{ kN/m}$$
$$K_{0,2} = 2320 \text{ kN/m}$$
$$K_{0,3} = 1545 \text{ kN/m}$$

- Information on the force capacity of the device, including information that the peak damping force should not exceed 1,000kN, which effectively limits the peak device velocity to about 0.9m/sec.

Bracing for connecting this device to the frame was selected based on a compression force of three times the preload or 900 kN for an effective length of s9.1m (30ft). According to the AISC Construction Manual 14th Edition (2010), a section HSS8×8×1/2 with effective length KL=30ft has a design strength equal to 915kN, thus sufficient. Note that the effective length is actually equal to 8.5m (28ft) but the larger value of 9.1m is used for conservatism. The size of the bracing will be checked when the simplified analysis is completed and then verified when the response history analysis is completed.

Calculation of response in the Design Earthquake using the Response Spectrum Analysis (RSA) procedure

The steps described in Section 6.5 are followed.

1) The yield displacement of each story (relative displacement) is obtained either from the computed story shear – story displacement curves in Figure C-4 or from the calculated value of Δ_{yR} (Equations C-9, C-12) as follows where $\{\phi\}_{r1}$ is the modal drift in mode 1:

$$\{\delta\}_{\mathrm{y}} = \Delta_{\mathrm{yR}}\,\{\phi\}_{\mathrm{r1}} = 176.4 \cdot \begin{Bmatrix} 1.000 - 0.675 \\ 0.675 - 0.265 \\ 0.265 \end{Bmatrix} = \begin{Bmatrix} 57.6 \\ 72.3 \\ 46.7 \end{Bmatrix} \ \text{mm}$$

The calculated story yield displacements are in good agreement with the values obtained from pushover analysis of the frame in OpenSees where the values are 61, 75, and 47 mm, from the top to the bottom story (Figure C-4). The device stroke at the stage of initiation of story yield is calculated as follow:

$$\{\Delta\}_{\mathrm{y}}=\{\delta\}_{\mathrm{y}}\times\cos\theta=\begin{Bmatrix}57.3\times\cos 27.6\\72.3\times\cos 27.6\\46.7\times\cos 28.2\end{Bmatrix}=\begin{Bmatrix}50.8\\64.1\\41.1\end{Bmatrix}\quad\text{mm}$$

The effective stiffness of each device at initiation of yield $K_{\mathrm{eff},i}$ is approximately calculated as:

$$K_{\mathrm{eff},i}=\frac{F_{0,i}+\Delta_{\mathrm{y},i}\cdot K_{0,i}}{\Delta_{\mathrm{y},i}}$$

Thus (see Figure 6-2 for illustration),

$$K_{\mathrm{eff},1}=\frac{300+41.1\times 2320\times 10^{-3}}{41.1\times 10^{-3}}=9619.3\quad\text{kN/m}$$

$$K_{\mathrm{eff},2}=\frac{300+64.1\times 2320\times 10^{-3}}{64.1\times 10^{-3}}=7000.2\quad\text{kN/m}$$

$$K_{\mathrm{eff},3}=\frac{125+50.8\times 1545\times 10^{-3}}{50.8\times 10^{-3}}=4005.6\quad\text{kN/m}$$

2) The 3*S*-75 frame with diagonal bracing and with each self-centering device represented by a linear elastic spring with stiffness $K_{\mathrm{eff},i}$ (as calculated above) is analyzed to obtain the periods, mode shapes, participation factors and modal weights. The results are:

$$T_1=1.31\,\text{sec},\quad T_2=0.44\,\text{sec},\quad T_3=0.23\,\text{sec}$$

$$\{\phi\}_1=[1.000,0.681,0.274]^{\mathrm{T}},\quad\{\phi\}_2=[1.000,-0.521,-0.679]^{\mathrm{T}},\quad\{\phi\}_3=[1.000,-1.609,2.030]^{\mathrm{T}}$$

$$\overline{W}_1=6007.5\text{kN},\quad\overline{W}_2=990.2\text{kN},\quad\overline{W}_3=369.3\text{kN}$$

$$\Gamma_1=1.386,\quad\Gamma_2=-0.518,\quad\Gamma_3=0.133$$

The modal drifts $\{\phi_r\}_{\mathrm{j}}$ are calculated from modal displacements $\{\phi\}_{\mathrm{j}}$ as:

$$\{\phi\}_{r1}=[0.319,0.407,0.274]^{\mathrm{T}},\quad\{\phi\}_{r2}=[1.521,0.158,-0.679]^{\mathrm{T}},\quad\{\phi\}_{r3}=[2.609,-3.639,2.030]^{\mathrm{T}}$$

3) The damping ratio in each mode is calculated for the damping constant C_{j}=1,140 kN-s/m and angle of device inclination θ_{j} using Equation (6-36) (note that the damping constant was selected to provide a damping ratio in the fundamental mode equal to 0.1):

$$\beta_{v1}=\frac{1.31}{4\pi}\cdot\frac{1140\times 9.81\times\left(0.319^2\times\cos^2 27.6+0.407^2\times\cos^2 27.6+0.274^2\times\cos^2 28.2\right)}{2900\times 0.274^2+2900\times 0.681^2+1567\times 1.000^2}=0.100$$

$$\beta_{v2}=\frac{0.44}{4\pi}\cdot\frac{1140\times 9.81\times\left(1.521^2\times\cos^2 27.6+0.158^2\times\cos^2 27.6+(-0.679)^2\times\cos^2 28.2\right)}{2900\times(-0.679)^2+2900\times(-0.521)^2+1567\times 1.000^2}=0.233$$

$$\beta_{v3}=\frac{0.23}{4\pi}\cdot\frac{1140\times 9.81\times\left(2.609^2\times\cos^2 27.6+(-3.639)^2\times\cos^2 27.6+2.030^2\times\cos^2 28.2\right)}{2900\times 2.030^2+2900\times(-1.609)^2+1567\times 1.000^2}=0.184$$

4) The effective yield displacement in the spectral representation is calculated using Equation (6-42):

$$D_{\mathrm{y}}=\frac{\Delta_{\mathrm{yR}}}{\Gamma_1}=\frac{176.4}{1.386}=127.3\ \ \text{mm}$$

5) Assume the value of displacement D in the single-degree-of-freedom spectral representation of the pushover curve as D=185 mm. The ductility ratio μ is calculated using Equation (6-46):

$$\mu=\frac{D_{\mathrm{D}}}{D_{\mathrm{y}}}=\frac{154}{127.3}=1.21$$

6) The effective period T_{eff} is calculated using Equation (6-44):

$$T_{\mathrm{eff}}=T_1\sqrt{\mu}\sqrt{\frac{A_{\mathrm{y}}+A_{\mathrm{F0}}}{A_{\mathrm{y}}+2A_{\mathrm{F0}}}}=1.31\sqrt{1.21}\sqrt{\frac{0.216g+0.050g}{0.216g+2\times 0.050g}}=1.32\ \ \text{sec}$$

Quantities A_y and A_{F0} were calculated using Equations (6-41) and (6-45):

$$A_{\mathrm{y}}=\frac{V_{\mathrm{y}}g}{\overline{W}_1}=\frac{1300\times g}{6007.5}=0.216g$$

$$A_{\mathrm{F0}}=\frac{F_{01}g}{\overline{W}_1}=\frac{300\times g}{6007.5}=0.050g$$

The effective damping ratio is calculated using Equation (6-47):

$$\beta_{\mathrm{eff}}=\beta_i+\beta_{\mathrm{v1}}\times\frac{T_{\mathrm{eff}}}{T_1}+\frac{1.42q_{\mathrm{H}}}{\pi}\left(1-\frac{1}{\mu}\right)=0.05+0.1\times\frac{1.32}{1.31}+\frac{1.42\times 1.0}{\pi}\left(1-\frac{1}{1.21}\right)=0.229$$

Note that q_{H}=1.0. Using Table 18.6-1 of ASCE 7-2010 the damping factor is obtained as B=1.587.

7) Displacement D_D for the Design Earthquake is calculated using Equation (6-55):

$$D_{\mathrm{D}}=\frac{T_{\mathrm{eff}}^2 S_{\mathrm{a}}\left(T_{\mathrm{eff}},\beta=0.05\right)g}{4\pi^2 B}=\frac{1.32^2\times 0.448\times 9810}{4\pi^2\times 1.587}=122.2\ \ \text{mm}$$

Before proceeding to additional iterations for the calculation of the displacement, the elastic displacement demand is calculated.

8) The displacement demand is calculated again considering elastic conditions

$$D_{\mathrm{D}} = \frac{T_1^2 S_{\mathrm{a}}\left(T_1, \beta = 0.05\right) g}{4\pi^2 B_{\mathrm{E}}} = \frac{1.31^2 \times 0.4514 \times 9810}{4\pi^2 \times 1.35} = 142.6 \quad \mathrm{mm}$$

Note that the damping factor B=1.35 was obtained from Table 18.6-1 in ASCE 7-2010 for damping ratio $\beta_i+\beta_{v1}$=0.05+0.10=0.15. Since the elastic displacement D_{D} (=142.6 mm) is larger than the inelastic D_{D} (=122.2 mm), the elastic value is used so that D_{D} =142.6mm. Still the frame has yielded as the displacement exceeds the yield displacement D_{y}=127.3 mm.

9) The displacements contributed by the fundamental mode are given by Equation (6-56):

$$\{u\}_1 = \Gamma_1 \{\phi\}_1 D_{\mathrm{D}} = 1.386 \cdot \begin{Bmatrix} 1.000 \\ 0.681 \\ 0.274 \end{Bmatrix} \cdot 142.6 = \begin{Bmatrix} 197.6 \\ 134.6 \\ 54.2 \end{Bmatrix} \quad \mathrm{mm}$$

Story drifts are calculated as:

10) The displacements contributed by the higher modes are (Equation (6-57)):

$$\{u\}_2 = \frac{\Gamma_2 \{\phi\}_2 T_2^2 S_{\mathrm{a}}\left(T_2, \beta = 0.05\right) g}{4\pi^2 B_2} = \frac{\left|-0.518\right| \times 0.44^2 \times 1.2507 \times 9810}{4\pi^2 \times 1.749} \begin{Bmatrix} 1.000 \\ -0.521 \\ -0.679 \end{Bmatrix} = \begin{Bmatrix} 17.8 \\ -9.3 \\ -12.1 \end{Bmatrix} \quad \mathrm{mm}$$

$$\{u\}_3 = \frac{\Gamma_3 \{\phi\}_3 T_3^2 S_{\mathrm{a}}\left(T_3, \beta = 0.05\right) g}{4\pi^2 B_3} = \frac{\left|0.133\right| \times 0.23^2 \times 1.2507 \times 9810}{4\pi^2 \times 1.602} \begin{Bmatrix} 1.000 \\ -1.609 \\ 2.030 \end{Bmatrix} = \begin{Bmatrix} 1.4 \\ -2.2 \\ 2.8 \end{Bmatrix} \quad \mathrm{mm}$$

Note that the modal damping ratios were obtained by use of Equation (6-53):

$$\beta_2 = \beta_i + \beta_{\mathrm{v}2} = 0.05 + 0.233 = 0.283$$

$$\beta_3 = \beta_i + \beta_{\mathrm{v}3} = 0.05 + 0.184 = 0.234$$

The damping factors based on these values of damping ratio are B_2=1.749, B_3=1.602 (Table 18.6-1 in ASCE 7-2010).

Story drifts are calculated as:

$$\{\Delta u\}_2 = \begin{Bmatrix} 17.8 - (-9.3) \\ -9.3 - (-12.1) \\ -12.1 \end{Bmatrix} = \begin{Bmatrix} 27.1 \\ 2.8 \\ -12.1 \end{Bmatrix} \quad \mathrm{mm}$$

$$\{\Delta u\}_3 = \begin{Bmatrix} 1.4 - (-2.2) \\ -2.2 - 2.8 \\ 2.8 \end{Bmatrix} = \begin{Bmatrix} 3.6 \\ -5.0 \\ 2.8 \end{Bmatrix} \quad \mathrm{mm}$$

11) Combining the modal displacements and drifts by the SRSS rule:

$$\{u\}_{\mathrm{T}} = \begin{Bmatrix} \sqrt{197.6^2 + 17.8^2 + 1.4^2} \\ \sqrt{134.6^2 + (-9.3)^2 + (-2.2)^2} \\ \sqrt{54.2^2 + (-12.1)^2 + 2.8^2} \end{Bmatrix} = \begin{Bmatrix} 198.4 \\ 134.9 \\ 55.6 \end{Bmatrix} \text{ mm}$$

$$\{\Delta u\}_{\mathrm{T}} = \begin{Bmatrix} \sqrt{63.0^2 + 27.1^2 + 3.6^2} \\ \sqrt{80.4^2 + 2.8^2 + (-5.0)^2} \\ \sqrt{54.2^2 + (-12.1)^2 + 2.8^2} \end{Bmatrix} = \begin{Bmatrix} 68.7 \\ 80.6 \\ 55.6 \end{Bmatrix} \text{ mm}$$

For checking drift against the limits in ASCE 7-2010, the drift ratio is calculated as:

$$\{\Delta u\}_{\mathrm{T}} \cdot \frac{C_{\mathrm{d}}}{R} \cdot \frac{1}{h_{\mathrm{s},i}} = \begin{Bmatrix} 68.7/4304 \\ 80.6/4304 \\ 55.6/4420 \end{Bmatrix} \times \left(5.5/8\right) = \begin{Bmatrix} 0.011 \\ 0.013 \\ 0.009 \end{Bmatrix}$$

Thus the calculated drift is less that the maximum allowable drift $0.02h_{\mathrm{s}}$ per criteria in Table 12.12-1 in ASCE 7-2010.

12) Not used.

13) Not used.

14) Not used.

15) The relative velocity of each self-centering device for each mode is calculated using Equations (6-58) and (6-59):

$$\{\nabla\}_{j1} = \frac{2\pi}{T_1}\{\Delta u\}_1 \cos\theta_j CFV\left(T_1, \beta_1\right) = \frac{2\pi}{1.31}\begin{Bmatrix} 63.0 \cdot \cos 27.6 \\ 80.4 \cdot \cos 27.6 \\ 54.2 \cdot \cos 28.2 \end{Bmatrix} CFV\left(1.31, 0.15\right) = \begin{Bmatrix} 244.2 \\ 311.6 \\ 208.9 \end{Bmatrix} \text{ mm/sec}$$

$$\{\nabla\}_{j2}=\frac{2\pi}{T_2}\{\Delta u\}_2\cos\theta_j CFV\left(T_2,\beta_2\right)=\frac{2\pi}{0.44}\begin{Bmatrix}27.1\cdot\cos 27.6\\ 2.8\cdot\cos 27.6\\ -12.1\cdot\cos 28.2\end{Bmatrix}CFV\left(0.44,0.283\right)=\begin{Bmatrix}246.4\\ 25.5\\ -109.4\end{Bmatrix}\ \text{mm/sec}$$

$$\{\nabla\}_{j3}=\frac{2\pi}{T_3}\{\Delta u\}_3\cos\theta_j CFV\left(T_3,\beta_3\right)=\frac{2\pi}{0.23}\begin{Bmatrix}3.6\cdot\cos 27.6\\ -5.0\cdot\cos 27.6\\ 2.8\cdot\cos 28.2\end{Bmatrix}CFV\left(0.23,0.234\right)=\begin{Bmatrix}60.7\\ -84.3\\ 47.0\end{Bmatrix}\ \text{mm/sec}$$

Factor *CFV* was obtained from the data in Table 5-3: *CFV*(for T=1.31sec,β=0.15)=0.9118, *CFV*(for T=0.44sec, β=0.283)=0.7185 and *CFV*(for T=0.23sec, β=0.234)=0.6966, for the first, second and third mode, respectively.

16) The device velocities are obtained by combining the modal device velocities by the SRSS rule:

$$\{\nabla\}_{\mathrm{T}}=\begin{Bmatrix}\sqrt{244.2^2+246.4^2+60.7^2}\\ \sqrt{311.6^2+25.5^2+\left(-84.3\right)^2}\\ \sqrt{208.9^2+\left(-109.4\right)^2+47.0^2}\end{Bmatrix}=\begin{Bmatrix}352.2\\ 323.8\\ 240.5\end{Bmatrix}\ \text{mm/sec}$$

Also, the device displacements are calculated as $\Delta u_{iT}\cos\theta_i$, m=1, 2, and 3, where Δu_{iT} are the drifts calculated in step 11:

$$\{\Delta u\cos\theta\}_{\mathrm{T}}=\begin{Bmatrix}68.7\cdot\cos 27.6\\ 80.6\cdot\cos 27.6\\ 55.6\cdot\cos 28.2\end{Bmatrix}=\begin{Bmatrix}60.9\\ 71.4\\ 49.0\end{Bmatrix}\ \text{mm}$$

17) The peak damping force in each self-centering device is calculated by use of Equation (6-60):

$$\left\{F_{\mathrm{v},i}\right\}_{\mathrm{T}}=\left\{C_i\right\}\{\nabla\}_{\mathrm{T}}$$

Thus,

$$\left\{F_{\mathrm{v},i}\right\}=\begin{Bmatrix}1140.0\\ 1140.0\\ 1140.0\end{Bmatrix}\cdot\begin{Bmatrix}352.2\\ 323.8\\ 240.5\end{Bmatrix}\cdot\frac{1}{10^3}=\begin{Bmatrix}401.5\\ 369.1\\ 274.2\end{Bmatrix}\ \text{kN}$$

18) The peak self-centering device force is expressed using Equation (6-61):

$$\left\{F_{\mathrm{D},i\mathrm{MAX}}\right\}_{\mathrm{T}}=\left\{F_{\min,i}\right\}+\left\{F_{0,i}\right\}+\left\{K_{0,i}\right\}u+\left\{F_{\mathrm{v},i}\right\}\sqrt{1-\left(u/u_{\mathrm{D},i\mathrm{T}}\right)^2}$$

Thus,

$$\left\{F_{\mathrm{D},i\mathrm{MAX}}\right\}_{\mathrm{T}} = 0.05\times\begin{Bmatrix}125\\300\\300\end{Bmatrix}+\begin{Bmatrix}125\\300\\300\end{Bmatrix}+\begin{bmatrix}1545\\2320\\2320\end{bmatrix}\begin{Bmatrix}u_3\\u_2\\u_1\end{Bmatrix}+\begin{Bmatrix}401.5\\369.1\\274.2\end{Bmatrix}\begin{Bmatrix}\sqrt{1-\left(u_3/60.9\right)^2}\\\sqrt{1-\left(u_2/71.4\right)^2}\\\sqrt{1-\left(u_1/49.0\right)^2}\end{Bmatrix}=\begin{Bmatrix}543.6\\719.6\\611.8\end{Bmatrix}\ \mathrm{kN}$$

The maximum values of force were calculated for displacements $\{u_3, u_2, u_1\} = \{13.9, 29.2, 18.8\}$ (mm).

19) The peak shear force in each story is calculated as:

$$\left\{V_{\mathrm{D},i\mathrm{MAX}}\right\}_{\mathrm{T}} = \left\{V\right\}_{\mathrm{T}} + \left\{F_{\mathrm{D},i\mathrm{MAX}}\right\}_{\mathrm{T}}\cdot\cos\theta_i = \begin{Bmatrix}550\\1100\\1300\end{Bmatrix}+\begin{Bmatrix}543.6\cdot\cos 27.6°\\719.6\cdot\cos 27.6°\\611.8\cdot\cos 28.2°\end{Bmatrix}=\begin{Bmatrix}1031.7\\1737.7\\1839.2\end{Bmatrix}\ \mathrm{kN}$$

Calculation of response in the Design Earthquake using the Equivalent Lateral Force (ELF) procedure

The steps described in the corresponding part of Section 6.5 are followed.

1) Step 1 is the same as step 1 of the RSA procedure.

2) T_1, $\{\phi\}_1$ and Γ_1 are the same as those obtained in the RSA procedure: T_1=1.31 *sec*, $\{\phi\}_1$=$[1.000,0.681,0.274]^{\mathrm{T}}$ and Γ_1=1.386. The residual period T_{R} is calculated using Equation (6-28):

$$T_{\mathrm{R}} = 0.4T_1 = 0.4\cdot 1.31 = 0.524\ \ \mathrm{sec}$$

The residual modal participation factor Γ_{R} is calculated using Equation (6-26):

$$\Gamma_{\mathrm{R}} = 1-\Gamma_1 = 1-1.386 = -0.386$$

The residual modal shape is calculated using Equation (6-27):

$$\{\phi\}_{\mathrm{R}} = \frac{\{1\}-\Gamma_1\cdot\{\phi\}_1}{\Gamma_{\mathrm{R}}} = \frac{\{1\}-1.386\cdot\{\phi\}_1}{-0.386} = \left(\begin{bmatrix}1.000\\1.000\\1.000\end{bmatrix}-1.386\cdot\begin{bmatrix}1.000\\0.681\\0.274\end{bmatrix}\right)\cdot\frac{1}{-0.386}=\begin{bmatrix}1.000\\-0.145\\-1.607\end{bmatrix}$$

The modal drifts $\{\phi_{\mathrm{r}}\}_{\mathrm{R}}$ are calculated from the modal displacements $\{\phi\}_{\mathrm{R}}$ as:

$$\{\phi_{\mathrm{r}}\}_{\mathrm{R}} = \left[1.145, 1.462, -1.607\right]^{\mathrm{T}}$$

3) The damping ratio for m=1 is β_{V1}= 0.10 as obtained in step 3 of the RSA procedure.

For the residual mode,

$$\beta_{\mathrm{vR}} = \frac{0.524}{4\pi} \cdot \frac{1140 \times 9.81 \times \left(1.145^2 \times \cos^2 27.6° + 1.462^2 \times \cos^2 27.6° + \left(-1.607\right)^2 \times \cos^2 28.2°\right)}{2900 \times \left(-1.607\right)^2 + 2900 \times \left(-0.145\right)^2 + 1567 \times 1.000^2} = 0.241$$

4-9) Steps 4 to 9 are the same as steps 4 to 9 of the RSA procedure.

10) The displacements contributed by the residual mode are given by Equation (6-57) for m=R:

$$\{u\}_{\mathrm{R}} = \frac{\Gamma_{\mathrm{R}} \{\phi\}_{\mathrm{R}} T_{\mathrm{R}}^2 S_{\mathrm{a}}\left(T_{\mathrm{R}}, \beta = 0.05\right) g}{4\pi^2 B_{\mathrm{R}}} = \frac{\left|-0.386\right| \times 0.524^2 \times 1.1285 \times 9810}{4\pi^2 \times 1.773} \begin{Bmatrix} 1.000 \\ -0.145 \\ -1.607 \end{Bmatrix} = \begin{Bmatrix} 16.8 \\ -2.4 \\ -26.9 \end{Bmatrix} \text{ mm}$$

The modal damping ratio was obtained using Equation (6-53):

$$\beta_{\mathrm{R}} = \beta_i + \beta_{\mathrm{vR}} = 0.05 + 0.241 = 0.291$$

The damping coefficient is B_{R}=1.773 (Table 18.6-1 in ASCE 7-2010).

Story drifts for the residual mode are calculated as:

$$\{\Delta u\}_{\mathrm{R}} = \begin{Bmatrix} 16.8 - \left(-2.4\right) \\ -2.4 - \left(-26.9\right) \\ -26.9 \end{Bmatrix} = \begin{Bmatrix} 19.2 \\ 24.5 \\ -26.9 \end{Bmatrix} \text{ mm}$$

11) The total displacements and drifts are calculated by combining first mode and residual mode responses by SRSS:

$$\{u\}_{\mathrm{T}} = \begin{Bmatrix} \sqrt{197.6^2 + 16.8^2} \\ \sqrt{134.6^2 + \left(-2.4\right)^2} \\ \sqrt{54.2^2 + \left(-26.9\right)^2} \end{Bmatrix} = \begin{Bmatrix} 198.3 \\ 134.6 \\ 60.5 \end{Bmatrix} \text{ mm}$$

$$\{\Delta u\}_{\mathrm{T}} = \begin{Bmatrix} \sqrt{63.0^2 + 19.2^2} \\ \sqrt{80.4^2 + 24.5^2} \\ \sqrt{54.2^2 + \left(-26.9\right)^2} \end{Bmatrix} = \begin{Bmatrix} 65.9 \\ 84.1 \\ 60.5 \end{Bmatrix} \text{ mm}$$

For checking drift against the limits of ASCE 7-2010, the drift ratio is calculated as:

$$\{\Delta u\}_{\mathrm{T}} \cdot \frac{C_{\mathrm{d}}}{R} \cdot \frac{1}{h_{\mathrm{s},i}} = \begin{Bmatrix} 65.9/4304 \\ 84.1/4304 \\ 60.5/4420 \end{Bmatrix} . 5.5/8 = \begin{Bmatrix} 0.011 \\ 0.013 \\ 0.010 \end{Bmatrix}$$

Thus the design satisfies the maximum allowable drift criteria in Table 12.12-1 in ASCE 7-2010.

12) Not used.

13) Not used.

14) Not used.

15) The relative velocity in each self-centering device for the first mode has been calculated in the corresponding step of RSA. For the residual mode the relative velocity is calculated using Equation (6-59) for m=R:

$$\{\nabla\}_{\mathrm{R}} = \frac{2\pi}{T_{\mathrm{R}}} \cdot \{\Delta u\}_{\mathrm{R}} \cdot \cos\theta_j \cdot CFV\left(T_{\mathrm{R}}, \beta_{\mathrm{R}}\right) = \frac{2\pi}{0.524} \cdot \begin{Bmatrix} 19.2 \cdot \cos 27.6 \\ 24.5 \cdot \cos 27.6 \\ -26.9 \cdot \cos 28.2 \end{Bmatrix} \cdot CFV\left(0.524, 0.291\right) = \begin{Bmatrix} 150.2 \\ 191.6 \\ -209.2 \end{Bmatrix} \text{ mm/sec}$$

Factor CFV was obtained from the data in Table 5-3: CFV(0.524,0.291)=0.7361.

16) By combining the first and residual mode responses by SRSS, the device relative velocity is obtained:

$$\{\nabla\}_{\mathrm{T}} = \begin{Bmatrix} \sqrt{244.2^2 + 150.2^2} \\ \sqrt{311.6^2 + 191.6^2} \\ \sqrt{208.9^2 + \left(-209.2\right)^2} \end{Bmatrix} = \begin{Bmatrix} 286.7 \\ 365.8 \\ 295.6 \end{Bmatrix} \text{ mm/sec}$$

Also, the device relative displacements are calculated as $\Delta u_{iT} \cos\theta_i$, where Δu_{iT} are the drifts calculated in step 11:

$$\{\Delta u \cos\theta\}_{\mathrm{T}} = \begin{Bmatrix} 65.9 \cdot \cos 27.6° \\ 84.1 \cdot \cos 27.6° \\ 60.5 \cdot \cos 28.2° \end{Bmatrix} = \begin{Bmatrix} 58.4 \\ 74.5 \\ 53.3 \end{Bmatrix} \text{ mm}$$

17) The peak damping force in each self-centering device is calculated by use of Equation (6-60):

$$\{F_{\mathrm{v},i}\}_{\mathrm{T}} = \{C_i\}\{\nabla\}_{\mathrm{T}}$$

Thus,

$$\{F_{\mathrm{v},i}\}_{\mathrm{T}} = 1140 \cdot \begin{Bmatrix} 286.7 \\ 365.8 \\ 295.6 \end{Bmatrix} \cdot \frac{1}{10^3} = \begin{Bmatrix} 326.8 \\ 417.0 \\ 337.0 \end{Bmatrix} \text{ kN}$$

18) The peak self-centering device force is calculated using Equation (6-61):

$$\{F_{\mathrm{D},i\mathrm{MAX}}\}_{\mathrm{T}} = \{F_{\min,i}\} + \{F_{0,i}\} + \{K_{0,i}\}u + \{F_{\mathrm{v},i}\}\sqrt{1 - \left(u/u_{\mathrm{D},i\mathrm{T}}\right)^2}$$

Thus,

$$\left\{F_{\mathrm{D},i\mathrm{MAX}}\right\}_{\mathrm{T}} = 0.05\times\begin{Bmatrix}125\\300\\300\end{Bmatrix}+\begin{Bmatrix}125\\300\\300\end{Bmatrix}+\begin{Bmatrix}1545\\2320\\2320\end{Bmatrix}\begin{Bmatrix}u_3\\u_2\\u_1\end{Bmatrix}+\begin{Bmatrix}326.8\\417.0\\337.0\end{Bmatrix}\begin{Bmatrix}\sqrt{1-\left(u_3/58.4\right)^2}\\\sqrt{1-\left(u_2/74.5\right)^2}\\\sqrt{1-\left(u_1/53.3\right)^2}\end{Bmatrix}=\begin{Bmatrix}470.3\\766.4\\674.0\end{Bmatrix}\ \mathrm{kN}$$

The maximum values of force were calculated for displacements $\{u_3, u_2, u_1\} = \{15.5, 28.5, 18.4\}$ (mm).

19) The peak shear force in each story is calculated as:

$$\left\{V_{\mathrm{D},i\mathrm{MAX}}\right\}_{\mathrm{T}} = \left\{V\right\}_{\mathrm{T}}+\left\{F_{\mathrm{D},i\mathrm{MAX}}\right\}_{\mathrm{T}}\cdot\cos\theta_i=\begin{Bmatrix}550\\1100\\1300\end{Bmatrix}+\begin{Bmatrix}470.3\cdot\cos 27.6^\circ\\766.4\cdot\cos 27.6^\circ\\674.0\cdot\cos 28.2^\circ\end{Bmatrix}=\begin{Bmatrix}966.8\\1779.2\\1894.0\end{Bmatrix}\ \mathrm{kN}$$

Calculation of response in the Maximum Considered Earthquake using the Response Spectrum Analysis (RSA) procedure

The steps described in Section 6.5 are followed. Steps 1 to 4 are the same as those of the design example for Design Earthquake. Step 5 and thereafter are presented in the sequel.

5) Assume the value of displacement D_{M} in the single-degree-of-freedom spectral representation of the pushover curve as D_{M}=200 mm. The ductility ratio μ is calculated using Equation (6-46):

$$\mu=\frac{D_{\mathrm{M}}}{D_{\mathrm{y}}}=\frac{200}{127.3}=1.57$$

6) The effective period T_{eff} is calculated using Equation (6-44):

$$T_{\mathrm{eff}}=T_1\sqrt{\mu}\sqrt{\frac{A_{\mathrm{y}}+A_{\mathrm{F0}}}{A_{\mathrm{y}}+2A_{\mathrm{F0}}}}=1.31\sqrt{1.57}\sqrt{\frac{0.216g+0.050g}{0.216g+2\times 0.050g}}=1.51\ \ \mathrm{sec}$$

Quantities A_y and A_{F0} were calculated using Equations (6-41) and (6-45):

$$A_{\mathrm{y}}=\frac{V_{\mathrm{y}}g}{\overline{\overline{W}}_1}=\frac{1300\times g}{6007.5}=0.216g$$

$$A_{\mathrm{F0}}=\frac{F_{\mathrm{F0}}g}{\overline{\overline{W}}_1}=\frac{300\times g}{6007.5}=0.050g$$

The effective damping ratio is calculated using Equation (6-47):

$$\beta_{\text{eff}} = \beta_i + \beta_{\text{v1}} \times \frac{T_{\text{eff}}}{T_1} + \frac{1.42 q_{\text{H}}}{\pi}\left(1 - \frac{1}{\mu}\right) = 0.05 + 0.1 \times \frac{1.51}{1.31} + \frac{1.42 \times 1.0}{\pi}\left(1 - \frac{1}{1.57}\right) = 0.329$$

Note that q_{H}=1.0. Using Table 18.6-1 of ASCE 7-2010 the damping factor B=1.887.

7) Displacement D_D for the Maximum Considered Earthquake is calculated using Equation (6-55):

$$D_{\text{M}} = \frac{T_{\text{eff}}^2 (1.5) S_{\text{a}} (T_{\text{eff}}, \beta = 0.05) g}{4\pi^2 B} = \frac{1.51^2 \times 1.5 \times 0.3916 \times 9810}{4\pi^2 \times 1.887} = 176.4 \text{ mm}$$

Before proceeding to additional iterations for the calculation of the displacement, the elastic displacement demand is calculated.

8) The displacement demand is calculated again considering elastic conditions

$$D_{\text{M}} = \frac{T_1^2 (1.5) S_{\text{a}} (T_1, \beta = 0.05) g}{4\pi^2 B_{\text{E}}} = \frac{1.31^2 \times 1.5 \times 0.4514 \times 9810}{4\pi^2 \times 1.35} = 213.9 \text{ mm}$$

Note that the damping factor B=1.35 was obtained from Table 18.6-1 in ASCE 7-2010 for damping ratio $\beta_i + \beta_{\text{v1}}$=0.05+0.10=0.15. Since the elastic displacement D_{M} (=213.9 mm) is larger than the inelastic D_{D} (=176.4 mm), the elastic value is used so that D_{M}=213.9mm. Still the frame has yielded as the displacement exceeds the yield displacement D_{y}=127.3 mm.

9) The displacements contributed by the fundamental mode are given by Equation (6-56):

$$\{u\}_1 = \Gamma_1 \{\phi\}_1 D_{\text{M}} = 1.386 \cdot \begin{Bmatrix} 1.000 \\ 0.681 \\ 0.274 \end{Bmatrix} \cdot 213.9 = \begin{Bmatrix} 296.5 \\ 201.9 \\ 81.2 \end{Bmatrix} \text{ mm}$$

Story drifts are calculated as:

$$\{\Delta u\}_1 = \begin{Bmatrix} 296.5 - 201.9 \\ 201.9 - 81.2 \\ 81.2 \end{Bmatrix} = \begin{Bmatrix} 94.6 \\ 120.7 \\ 81.2 \end{Bmatrix} \text{ mm}$$

10) The displacements contributed by the higher modes are (Equation (6-57)):

$$\{u\}_2 = \frac{\Gamma_2 \{\phi\}_2 T_2^2 (1.5) S_{\text{a}} (T_2, \beta = 0.05) g}{4\pi^2 B_2} = \frac{|-0.518| \times 0.44^2 \times 1.5 \times 1.2507 \times 9810}{4\pi^2 \times 1.749} \begin{Bmatrix} 1.000 \\ -0.521 \\ -0.679 \end{Bmatrix} = \begin{Bmatrix} 26.7 \\ -13.9 \\ -18.1 \end{Bmatrix} \text{ mm}$$

$$\{u\}_3 = \frac{\Gamma_3 \{\phi\}_3 T_3^2 (1.5) S_{\text{a}} (T_3, \beta = 0.05) g}{4\pi^2 B_3} = \frac{|0.133| \times 0.23^2 \times 1.5 \times 1.2507 \times 9810}{4\pi^2 \times 1.602} \begin{Bmatrix} 1.000 \\ -1.609 \\ 2.030 \end{Bmatrix} = \begin{Bmatrix} 2.0 \\ -3.3 \\ 4.2 \end{Bmatrix} \text{ mm}$$

Note that the modal damping ratios were obtained by use of Equation (6-53):

$$\beta_2 = \beta_i + \beta_{v2} = 0.05 + 0.233 = 0.283$$

$$\beta_3 = \beta_i + \beta_{v3} = 0.05 + 0.184 = 0.234$$

The damping factors based on these values of damping ratio are B_2=1.749, B_3=1.602 (Table 18.6-1 in ASCE 7-2010).

Story drifts are calculated as:

$$\{\Delta u\}_2 = \begin{Bmatrix} 26.7-(-13.9) \\ -13.9-(-18.1) \\ -18.1 \end{Bmatrix} = \begin{Bmatrix} 40.6 \\ 4.2 \\ -18.1 \end{Bmatrix} \text{ mm}$$

$$\{\Delta u\}_3 = \begin{Bmatrix} 2.0-(-3.3) \\ -3.3-4.2 \\ 4.2 \end{Bmatrix} = \begin{Bmatrix} 5.3 \\ -7.5 \\ 4.2 \end{Bmatrix} \text{ mm}$$

11) Combining the modal displacements and drifts by the SRSS rule:

$$\{u\}_{\mathrm{T}} = \begin{Bmatrix} \sqrt{296.5^2 + 26.7^2 + 2.0^2} \\ \sqrt{201.9^2 + (-13.9)^2 + (-3.3)^2} \\ \sqrt{81.2^2 + (-18.1)^2 + 4.2^2} \end{Bmatrix} = \begin{Bmatrix} 297.7 \\ 202.4 \\ 83.3 \end{Bmatrix} \text{ mm}$$

$$\{\Delta u\}_{\mathrm{T}} = \begin{Bmatrix} \sqrt{94.6^2 + 40.6^2 + 5.3^2} \\ \sqrt{120.7^2 + 4.2^2 + (-7.5)^2} \\ \sqrt{81.2^2 + (-18.1)^2 + 4.2^2} \end{Bmatrix} = \begin{Bmatrix} 103.1 \\ 121.0 \\ 83.3 \end{Bmatrix} \text{ mm}$$

12) Not used.

13) Not used.

14) Not used.

15) The relative velocity of each self-centering device for each mode is calculated using Equations (6-58) and (6-59):

$$\{\nabla\}_{j1} = \frac{2\pi}{T_1}\{\Delta u\}_1 \cos\theta_j CFV\left(T_1,\beta_1\right) = \frac{2\pi}{1.31}\begin{Bmatrix} 94.6\cdot\cos 27.6 \\ 120.7\cdot\cos 27.6 \\ 81.2\cdot\cos 28.2 \end{Bmatrix} CFV\left(1.31, 0.15\right) = \begin{Bmatrix} 366.6 \\ 467.8 \\ 313.0 \end{Bmatrix} \text{ mm/sec}$$

$$\{\nabla\}_{j2} = \frac{2\pi}{T_2}\{\Delta u\}_2 \cos\theta_j CFV\left(T_2,\beta_2\right) = \frac{2\pi}{0.44}\begin{Bmatrix} 40.6\cdot\cos 27.6 \\ 4.2\cdot\cos 27.6 \\ -18.1\cdot\cos 28.2 \end{Bmatrix} CFV\left(0.44, 0.283\right) = \begin{Bmatrix} 369.2 \\ 38.2 \\ -163.7 \end{Bmatrix} \text{ mm/sec}$$

$$\{\nabla\}_{j3} = \frac{2\pi}{T_3}\{\Delta u\}_3 \cos\theta_j CFV\left(T_3,\beta_3\right) = \frac{2\pi}{0.23}\begin{Bmatrix} 5.3\cdot\cos 27.6 \\ -7.5\cdot\cos 27.6 \\ 4.2\cdot\cos 28.2 \end{Bmatrix} CFV\left(0.23, 0.234\right) = \begin{Bmatrix} 89.4 \\ -126.5 \\ 70.4 \end{Bmatrix} \text{ mm/sec}$$

Factor *CFV* was obtained from the data in Table 5-3: *CFV* (for T=1.31sec,β=0.15)=0.9118, *CFV* (for 0.44sec,0.283)=0.7185 and *CFV* (for 0.23sec,0.234)=0.6966, for the first, second and third mode, respectively.

16) The device velocities are obtained by combining the modal device velocities by the SRSS rule:

$$\{\nabla\}_{\mathrm{T}} = \begin{Bmatrix} \sqrt{366.6^2 + 369.2^2 + 89.4^2} \\ \sqrt{467.8^2 + 38.2^2 + \left(-126.5\right)^2} \\ \sqrt{313.0^2 + \left(-163.7\right)^2 + 70.4^2} \end{Bmatrix} = \begin{Bmatrix} 527.9 \\ 486.1 \\ 360.2 \end{Bmatrix} \text{ mm/sec}$$

Also, the device displacements are calculated as $\Delta u_{iT}\cos\theta_i$, m=1, 2, and 3, where Δu_{iT} are the drifts calculated in step 11:

$$\{\Delta u\cos\theta\}_{\mathrm{T}} = \begin{Bmatrix} 103.1\cos 27.6 \\ 121.0\cos 27.6 \\ 83.3\cos 28.2 \end{Bmatrix} = \begin{Bmatrix} 91.4 \\ 107.2 \\ 73.4 \end{Bmatrix} \text{ mm}$$

17) The peak damping force in each self-centering device is calculated by use of Equation (6-60):

$$\left\{F_{\mathrm{v},i}\right\}_{\mathrm{T}} = \{C_i\}\{\nabla\}_{\mathrm{T}}$$

Thus,

$$\left\{F_{\mathrm{v},i}\right\} = \begin{Bmatrix} 1140.0 \\ 1140.0 \\ 1140.0 \end{Bmatrix} \cdot \begin{Bmatrix} 527.9 \\ 486.1 \\ 360.2 \end{Bmatrix} \cdot \frac{1}{10^3} = \begin{Bmatrix} 601.8 \\ 554.2 \\ 410.6 \end{Bmatrix} \text{ kN}$$

18) The peak self-centering device force is expressed using Equation (6-61):

$$\left\{F_{\mathrm{M},i\mathrm{MAX}}\right\}_{\mathrm{T}} = F_{\mathrm{min},i} + F_{0,i} + K_{0,i}u + F_{\mathrm{v},i}\sqrt{1-\left(u/u_{\mathrm{D},i\mathrm{T}}\right)^2}$$

Thus,

$$\left\{F_{\mathrm{M},i\mathrm{MAX}}\right\}_{\mathrm{T}}=0.05\times\begin{Bmatrix}125\\300\\300\end{Bmatrix}+\begin{Bmatrix}125\\300\\300\end{Bmatrix}+\begin{Bmatrix}1545\\2320\\2320\end{Bmatrix}\begin{Bmatrix}u_3\\u_2\\u_1\end{Bmatrix}+\begin{Bmatrix}601.8\\554.2\\410.6\end{Bmatrix}\begin{Bmatrix}\sqrt{1-\left(u_3/91.4\right)^2}\\\sqrt{1-\left(u_2/107.2\right)^2}\\\sqrt{1-\left(u_1/73.4\right)^2}\end{Bmatrix}=\begin{Bmatrix}749.4\\922.4\\759.5\end{Bmatrix}\ \mathrm{kN}$$

The maximum values of force were calculated for displacements $\{u_3, u_2, u_1\}$ = {20.9, 43.9, 28.1} (*mm*).

19) The peak shear force in each story is calculated as:

$$\left\{V_{\mathrm{M},i\mathrm{MAX}}\right\}_{\mathrm{T}}=\left\{V\right\}_{\mathrm{T}}+\left\{F_{\mathrm{M},i\mathrm{MAX}}\right\}_{\mathrm{T}}\cdot\cos\theta_i=\begin{Bmatrix}550\\1100\\1300\end{Bmatrix}+\begin{Bmatrix}749.4\cdot\cos 27.6^\circ\\922.4\cdot\cos 27.6^\circ\\759.5\cdot\cos 28.2^\circ\end{Bmatrix}=\begin{Bmatrix}1214.1\\1917.4\\1969.3\end{Bmatrix}\ \mathrm{kN}$$

Calculation of response in the Maximum Considered Earthquake using the Equivalent Lateral Force (ELF) procedure

The steps described in the corresponding part of Section 6.5 are followed.

1) Step 1 is the same as step 1 of the RSA procedure.
2) T_1, $\{\phi\}_1$ and Γ_1 are the same as those obtained in the RSA procedure: T_1=1.31 *sec*, $\{\phi\}_1$=[1.000,0.681,0.274]$^{\mathrm{T}}$ and Γ_1=1.386. The residual period T_{R} is calculated using Equation (6-28):

$$T_{\mathrm{R}}=0.4T_1=0.4\cdot 1.31=0.524\ \ \mathrm{sec}$$

The residual modal participation factor Γ_R is calculated using Equation (6-26):

$$\Gamma_{\mathrm{R}}=1-\Gamma_1=1-1.386=-0.386$$

The residual modal shape is calculated using Equation (6-27):

$$\{\phi\}_{\mathrm{R}}=\frac{\{1\}-\Gamma_1\cdot\{\phi\}_1}{\Gamma_{\mathrm{R}}}=\frac{\{1\}-1.386\cdot\{\phi\}_1}{-0.386}=\left(\begin{bmatrix}1.000\\1.000\\1.000\end{bmatrix}-1.386\cdot\begin{bmatrix}1.000\\0.681\\0.274\end{bmatrix}\right)\cdot\frac{1}{-0.386}=\begin{bmatrix}1.000\\-0.145\\-1.607\end{bmatrix}$$

The modal drifts $\{\phi_{\mathrm{r}}\}_{\mathrm{R}}$ are calculated from modal displacements $\{\phi\}_{\mathrm{R}}$ as:

$$\left\{\phi_{\mathrm{r}}\right\}_{\mathrm{R}}=\left[1.145,1.462,-1.607\right]^{\mathrm{T}}$$

3) The damping ratio for m=1 is β_{V1}= 0.10 as obtained in step 3 of the RSA procedure.

   For the residual mode,

$$\beta_{\mathrm{vR}} = \frac{0.524}{4\pi} \cdot \frac{1140 \times 9.81 \times \left(1.145^2 \times \cos^2 27.6° + 1.462^2 \times \cos^2 27.6° + (-1.607)^2 \times \cos^2 28.2°\right)}{2900 \times (-1.607)^2 + 2900 \times (-0.145)^2 + 1567 \times 1.000^2} = 0.241$$

4-9) Steps 4 to 9 are the same as steps 4 to 9 of the RSA procedure.

10) The displacements contributed by the residual mode is (Equation (6-57)):

$$\{u\}_{\mathrm{R}} = \frac{\Gamma_{\mathrm{R}} \{\phi\}_{\mathrm{R}} T_{\mathrm{R}}^2 (1.5) S_{\mathrm{a}} (T_{\mathrm{R}}, \beta = 0.05) g}{4\pi^2 B_{\mathrm{R}}} = \frac{|-0.386| \times 0.524^2 \times 1.5 \times 1.1285 \times 9810}{4\pi^2 \times 1.773} \begin{Bmatrix} 1.000 \\ -0.145 \\ -1.607 \end{Bmatrix} = \begin{Bmatrix} 25.1 \\ -3.6 \\ -40.4 \end{Bmatrix} \text{ mm}$$

The modal damping ratios are obtained (Equation (6-53)):

$$\beta_{\mathrm{R}} = \beta_i + \beta_{\mathrm{vR}} = 0.05 + 0.241 = 0.291$$

The damping coefficient is B_2=1.773 (Table 18.6-1 in ASCE 7-2010).

Story drifts for the residual mode are calculated as:

$$\{\Delta u\}_{\mathrm{R}} = \begin{Bmatrix} 25.1 - (-3.6) \\ -3.6 - (-40.4) \\ -40.4 \end{Bmatrix} = \begin{Bmatrix} 28.7 \\ 36.8 \\ -40.4 \end{Bmatrix} \text{ mm}$$

11) The total displacements and drifts are calculated by combining first mode and residual mode responses by SRSS:

$$\{u\}_{\mathrm{T}} = \begin{Bmatrix} \sqrt{296.5^2 + 25.1^2} \\ \sqrt{201.9^2 + (-3.6)^2} \\ \sqrt{81.2^2 + (-40.4)^2} \end{Bmatrix} = \begin{Bmatrix} 297.6 \\ 201.9 \\ 90.7 \end{Bmatrix} \text{ mm}$$

$$\{\Delta u\}_{\mathrm{T}} = \begin{Bmatrix} \sqrt{94.6^2 + 28.7^2} \\ \sqrt{120.7^2 + 36.8^2} \\ \sqrt{81.2^2 + (-40.4)^2} \end{Bmatrix} = \begin{Bmatrix} 98.9 \\ 126.2 \\ 90.7 \end{Bmatrix} \text{ mm}$$

12) Not used.

13) Not used.

14) Not used.

15) The relative velocity in each self-centering device for the first mode has been calculated in the corresponding step of RSA. For the residual mode the relative velocity is calculated using Equation (6-59) for $m=R$:

$$\{\nabla\}_{\mathrm{R}} = \frac{2\pi}{T_{\mathrm{R}}} \cdot \{\Delta u\}_{\mathrm{R}} \cdot \cos\theta_j \cdot CFV\left(T_{\mathrm{R}}, \beta_{\mathrm{R}}\right) = \frac{2\pi}{0.524} \cdot \begin{Bmatrix} 28.7 \cdot \cos 27.6 \\ 36.8 \cdot \cos 27.6 \\ -40.4 \cdot \cos 28.2 \end{Bmatrix} \cdot CFV\left(0.524, 0.291\right) = \begin{Bmatrix} 224.5 \\ 287.9 \\ -314.3 \end{Bmatrix} \text{ mm/sec}$$

Factor *CFV* was obtained from the data in Table 5-3: *CFV* (0.524, 0.291) = 0.7361.

16) By combining the first and residual modes by SRSS, the device relative velocity is obtained:

$$\{\nabla\}_{\mathrm{T}} = \begin{Bmatrix} \sqrt{366.6^2 + 224.5^2} \\ \sqrt{467.8^2 + 287.9^2} \\ \sqrt{313.0^2 + (-314.3)^2} \end{Bmatrix} = \begin{Bmatrix} 429.9 \\ 549.3 \\ 443.6 \end{Bmatrix} \text{ mm/sec}$$

Also, the device relative displacements are calculated as $\Delta u_{iT} \cos\theta_i$, where Δu_{iT} are the drifts calculated in step 11:

$$\{\Delta u \cos\theta\}_{\mathrm{T}} = \begin{Bmatrix} 98.9 \cdot \cos 27.6^\circ \\ 126.2 \cdot \cos 27.6^\circ \\ 90.7 \cdot \cos 28.2^\circ \end{Bmatrix} = \begin{Bmatrix} 87.6 \\ 111.8 \\ 79.9 \end{Bmatrix} \text{ mm}$$

17) The peak damping force in each self-centering device is calculated by use of Equation (6-60):

$$\{F_{\mathrm{v},i}\}_{\mathrm{T}} = \{C_i\}\{\nabla\}_{\mathrm{T}}$$

Thus,

$$\{F_{\mathrm{v},i}\}_{\mathrm{T}} = 1140 \cdot \begin{Bmatrix} 429.9 \\ 549.3 \\ 443.6 \end{Bmatrix} \cdot \frac{1}{10^3} = \begin{Bmatrix} 490.1 \\ 626.2 \\ 505.7 \end{Bmatrix} \text{ kN}$$

18) The peak self-centering device force is calculated using Equation (6-61):

$$\{F_{\mathrm{M},i\mathrm{MAX}}\}_{\mathrm{T}} = F_{\min,i} + F_{0,i} + K_{0,i}u + F_{\mathrm{v},i}\sqrt{1-\left(u/u_{\mathrm{D},i\mathrm{T}}\right)^2}$$

$$\{F_{\mathrm{M},i\mathrm{MAX}}\}_{\mathrm{T}} = 0.05 \times \begin{Bmatrix} 125 \\ 300 \\ 300 \end{Bmatrix} + \begin{Bmatrix} 125 \\ 300 \\ 300 \end{Bmatrix} + \begin{Bmatrix} 1545 \\ 2320 \\ 2320 \end{Bmatrix}\begin{Bmatrix} u_3 \\ u_2 \\ u_1 \end{Bmatrix} + \begin{Bmatrix} 490.1 \\ 626.2 \\ 505.7 \end{Bmatrix}\begin{Bmatrix} \sqrt{1-(u_3/87.6)^2} \\ \sqrt{1-(u_2/111.8)^2} \\ \sqrt{1-(u_1/79.9)^2} \end{Bmatrix} = \begin{Bmatrix} 639.7 \\ 992.8 \\ 853.6 \end{Bmatrix} \text{ kN}$$

The maximum values of force were calculated for displacements $\{u_3, u_2, u_1\} = \{23.3, 42.8, 27.5\}$ (mm).

19) The peak shear force in each story is calculated as:

$$\{V_{\mathrm{M},i\mathrm{MAX}}\}_{\mathrm{T}} = \{V\}_{\mathrm{T}} + \{F_{\mathrm{M},i\mathrm{MAX}}\}_{\mathrm{T}} \cdot \cos\theta_i = \begin{Bmatrix} 550 \\ 1100 \\ 1300 \end{Bmatrix} + \begin{Bmatrix} 639.7 \cdot \cos 27.6° \\ 992.8 \cdot \cos 27.6° \\ 853.6 \cdot \cos 28.2° \end{Bmatrix} = \begin{Bmatrix} 1116.9 \\ 1979.8 \\ 2052.3 \end{Bmatrix} \text{ kN}$$

Table C-4 presents a summary of the calculated response.

Table C-4 Summary of RSA and ELF Analysis Results

Response Quantity	Story	RSA (DE)	ELF (DE)	RSA (MCE)	ELF (MCE)
Floor Displacement (mm)	3	198.4	198.3	297.7	297.6
	2	134.9	134.6	202.4	201.9
	1	55.6	60.5	83.3	90.7
Story Drift (mm)	3	68.7	65.9	103.1	98.9
	2	80.6	84.1	121.0	126.2
	1	55.6	60.5	83.3	90.7
Device Velocity (mm/sec)	3	352.2	286.7	527.9	429.9
	2	323.8	365.8	486.1	549.3
	1	240.5	295.6	360.2	443.6
Device Force (kN)	3	543.6	470.3	749.4	639.7
	2	719.6	766.4	922.4	992.8
	1	611.8	674.0	759.5	853.6
Maximum Story Shear Force (kN)	3	1031.7	966.8	1214.1	1116.9
	2	1737.7	1779.2	1917.4	1979.8
	1	1839.2	1894.0	1969.3	2052.3

The adequacy of the bracing is checked based on the results of the simplified analysis. The maximum device force in the MCE was calculated to be 992.8kN (MCE, ELF method). The nominal strength in compression of an HSS8x8x1/2 brace of effective length KL=8535mm (28ft) is 1216kN, thus sufficient. Results of response history analysis in the MCE (to be presented in Section 7) show a peak brace force (average of seven analyses) equal to 891.8kN. Sections 18.7.1.2 to 18.7.1.4 in ASCE 7-2010 specify the requirements for the design of damping systems and their connections, which presumably also apply to fluidic self-centering devices. The criteria require that the devices, bracing and connections are designed to resist the forces, displacements and velocities calculated in the MCE and assessed using strength design criteria with a redundancy factor ρ=1 and a resistance factor ϕ=1. Since compression is critical for the bracing, the design strength of the HSS8x8x1/2 tube (yield stress of 318MPa, or 46ksi) with KL=8535mm and ϕ=1 is 1216kN. The question at this point is what is the required strength? Is it the 891.8kN force calculated as the average of the seven analyses in the MCE or a multiple of this value to ensure adequacy? An appropriate value to use is 1.3 times the calculated average of the seven analyses, or 1.3x891.8=1159kN. Therefore, the HSS8x8x1/2 tube with KL=8535mm with design strength of 1216kN is sufficient.

C.5 Design of Frame 3*S*-85

Analysis following Chapter 12.8 of ASCE 7-2010 and presented in Appendix B established the seismic base shear for a single 3*S*-Reference frame, including the effect of torsion, to be V=735kN. The minimum base shear allowed for the 3*S*-85 frame per procedures of Section 6 is 0.85V=624.8kN. The required minimum base shear strength for the frame is

$$V_y = V \cdot \frac{C_d \cdot \Omega_o}{R} = 624.8 \times \frac{5.5 \times 3.0}{8} = 1,289\,kN\,(289.7kip)$$

The seismic base shear for a single frame V=624.8kN is distributed vertically using ASCE 7-2010 equations 12.8-11 and 12.8-12. The value of parameter k has been determined in Appendix B to be k =1.145. The calculated lateral seismic forces are summarized in Table C-5. Quantity $\sum_{i=1}^{n} w_i h_i^k$ is equal to 80,144.

Table C-5 Lateral Seismic Forces for 3-Story Frame 3*S*-85

Floor	w_x [kN]	h_x [m]	$w_x h_x^k$	C_{vx}	F_x [kN]
3	1567	13.03	29627	0.3697	231.0
2	2900	8.72	34617	0.4319	269.9
1	2900	4.42	15900	0.1984	124.0

Analysis of the frame for the critical loading combination (1.2+0.2S_{DS})D+0.5L+ρQ_E (which is equal to 1.45D+0.5L+1.3Q_E) resulted in the required strengths of the members of the frame. The frame with section properties for 3*S*-85 is shown in Figure C-5.

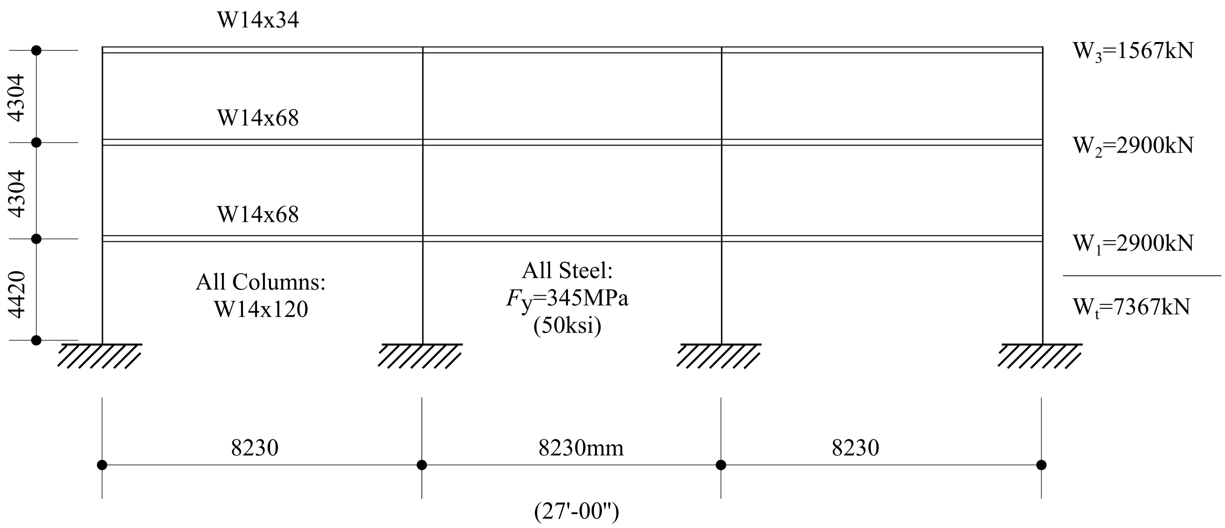

Figure C-5 Frame 3*S*-85 Geometry, Section Properties and Tributary Weights

A push-over analysis was conducted to obtain the relationship between base shear force and roof displacement. To validate the analysis results, a plastic analysis was conducted following the procedures described in Section C.2 in this appendix and using the following parameters:

Number and length of spans:		n=3; L_b=8230 mm
Number of stories:		N=3;
Material properties:		F_y=345 MPa (50 ksi)
Column sections:		W14×120 (d_c = 368 mm; M_{pc}= Z_x×F_y = 1197.2 kN-m)
Beam properties:		
	3rd floor:	W14×34 (d_b = 356 mm; M_{pc} = Z_x×F_y = 308.8 kN-m)
	2nd floor:	W14×68 (d_b = 356 mm; M_{pc}=Z_x×F_y= 648.6 kN-m)
	1st floor:	W14×68 (d_b = 356 mm; M_{pc}=Z_x×F_y= 648.6 kN-m)
Floor weights:		w_3=1567kN; w_2=w_1=2,900kN
Story heights:		h_3=12928 mm; h_2=8624 mm; h_1=4320 mm

It was assumed that plastic hinges form in the beams at a point located at a distance of half the depth of the column section $d_c/2$ from the column center (i.e., $\alpha_i = (d_c/2)/L_i$). Also, in columns a plastic hinge was assumed to develop near the base at a distance of one depth (d_c) of the column section from the base of the frame.

Values of parameters α_i, χ_i, and $M_{pbi}\chi_i$ are presented in Table C-6. Note that χ_i=1/(1-2α_{ij}).

Table C-6 Parameters α_i, χ_i, and $M_{pbi}\chi_I$ for Frame 3*S*-85

Level	M_{pbi} (kN-m)	α_i	χ_i	$M_{pbi}\chi_i$ (kN-m)
3	308.8	0.022	1.05	324.2
2	648.6	0.022	1.05	681.0
1	648.6	0.022	1.05	681.0
				$\Sigma M_{pbi}\chi_i$=1686.2 kN-m

Using data in Table C-6, the term $(n+1)M_{pc}+2n\sum_{i=1}^{N}(M_{pbi}\cdot\chi_i)$ in equation (C-8) was calculated as:

$$(n+1)M_{pc}+2n\sum_{i=1}^{N}(M_{pbi}\cdot\chi_i)=(3+1)\cdot 1197.2+2\cdot 3\cdot 1686.2=14906.0 \quad \text{kN}\cdot\text{m}$$

An eigenvalue analysis resulted in the following: T_1=1.41*sec*; $\{\phi_1\}^T$=[1.000, 0.677, 0.266]; $\overline{W}_1$=5966.4kN; Γ_1=1.387. The *k*-value (Section 12.8.3 in ASCE 7, 2010) was calculated to be *k*=1.455. The lateral loads were distributed in proportion to factor λ_i, which was calculated by the following equation:

$$\lambda_i=\frac{w_i h_i^k}{\sum_{m=1}^{N} w_m h_m^k}$$

where w_i is the weight of each floor. Results are presented in Table C-7.

Table C-7 Calculation of λ_I for Frame 3*S*-85

Level	w_i (kN)	h_i (mm)	$w_i h_i^k\times10^6$	λ_i	$\lambda_i h_i$ (mm)
3	1567	13027	1521.1	0.414	5393.2
2	2900	8724	1570.9	0.427	3725.1
1	2900	4420	584.1	0.159	702.8
			$\Sigma w_i h_i^k\times10^6$=3676.1		9821.1

The base shear strength V_y is calculated using equation (C-8) as:

$$V_y=\frac{14906.0\times10^3}{9821.1}=1517.8 \quad \text{kN}$$

The roof displacement when the plastic collapse mechanism develops Δ_{yR} is calculated using equation (C-9) as:

$$\Delta_{yR}=\left(\frac{g}{4\pi^2}\right)1.387\left(\frac{1517.8}{5966.4}\right)1.41^2=174.3 \quad \text{mm}$$

The push-over curves obtained by the plastic analysis is presented in Figure C-6 and compared to the pushover curve obtained computationally (program OpenSees) without consideration of P-Δ effects and assuming a small post-elastic stiffness (ratio of post-elastic to elastic stiffness equal to 0.01).

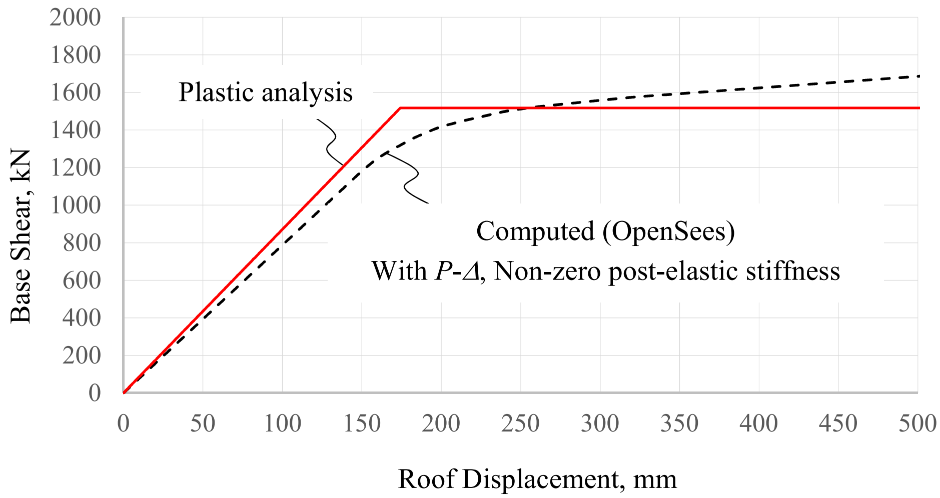

Figure C-6 Base Shear Force versus Roof Drift Relations for Frame 3*S*-85

The story shear force to story drift relations, as obtained by the computational model, are presented in Figure C-7. Based on the results in Figure C-7, the story yield strengths are obtained as: $F_{y,1}$=1,500kN, $F_{y,2}$=1,250kN and $F_{y,3}$=600kN. Note that the pushover curves in Figure C-7 have some small post-elastic stiffness so that the yield strength was defined as the force at initiation of inelastic action in bilinear representations of the pushover curves.

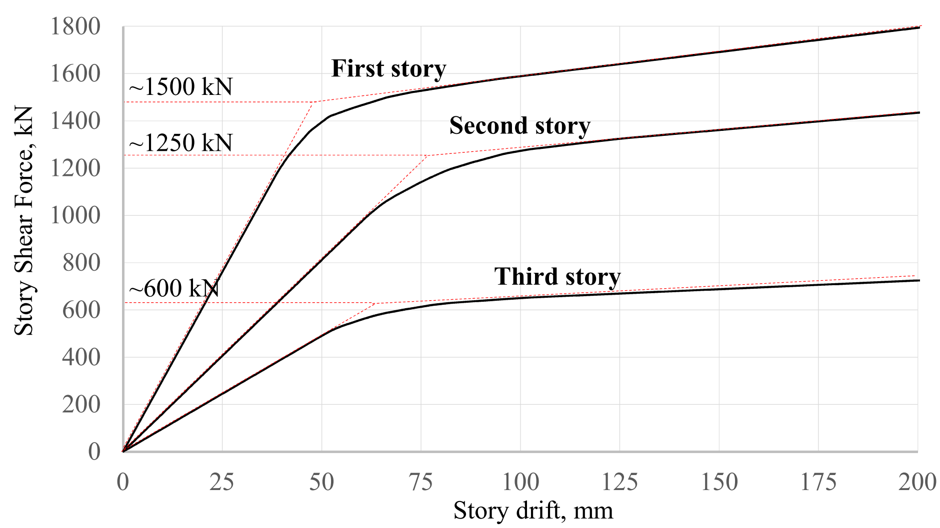

Figure C-7 Story Shear Force versus Story Drift Relations for Frame 3*S*-85

Parameters for fluidic self-centering devices for frame 3S-85

The component of preload in the horizontal direction is selected to be approximately equal to a 20% of the story shear yield strength. One device will be used at each story placed in a diagonal configuration at an angle θ. The preload for the device at story i, $F_{0,i}$ is calculated using equation (C-13):

$$F_{0,i} = \frac{0.2 \times F_{y,i}}{\cos\theta}$$

Accordingly,

$$F_{0,1} = \frac{0.2 \times F_{y,1}}{\cos 28.2°} = \frac{0.2 \times 1500}{\cos 28.2°} = 340.4 \text{ kN} \quad \text{(select 350 kN)}$$

$$F_{0,2} = \frac{0.2 \times F_{y,2}}{\cos 27.6°} = \frac{0.2 \times 1250}{\cos 27.6°} = 282.1 \text{ kN} \quad \text{(select 350 kN)}$$

$$F_{0,3} = \frac{0.2 \times F_{y,3}}{\cos 27.6°} = \frac{0.2 \times 600}{\cos 27.6°} = 135.4 \text{ kN} \quad \text{(select 150 kN)}$$

It was decided that a single device design will be used but the fluid initial pressure will be varied to achieve the desired preload for the two types of devices needed. The stiffness in each device $K_{0,i}$ was approximately calculated to be:

$$K_{0,1} = 2320 \text{ kN/m}$$

$$K_{0,2} = 2320 \text{ kN/m}$$

$$K_{0,3} = 1545 \text{ kN/m}$$

Calculation of response in the Design Earthquake using the Response Spectrum Analysis (RSA) procedure for frame 3S-85

The steps described in Section 6.5 are followed.

20) The yield displacement of each story (relative displacement) is obtained either from the computed story shear – story displacement curves in Figure C-7 or from the calculated value of $\Delta_{y,i}$ (Equation C-9, C-12) as follows, where $\{\phi\}_{r1}$ is the modal drift in mode 1:

$$\{\delta\}_y = \Delta_{yR}\{\phi\}_{r1} = 174.3 \cdot \begin{Bmatrix} 1.000 - 0.677 \\ 0.677 - 0.266 \\ 0.266 \end{Bmatrix} = \begin{Bmatrix} 56.3 \\ 71.6 \\ 46.4 \end{Bmatrix} \text{ mm}$$

The calculated story yield displacements are in good agreement with the values obtained from pushover analysis of the frame in OpenSees where the values are 61, 76, and 46 mm, from the top to the bottom story (Figure C-7). The device stroke at the stage of initiation of story yield is calculated as follows:

$$\{\Delta\}_{\mathrm{y}} = \{\delta\}_{\mathrm{y}} \times \cos\theta = \begin{Bmatrix} 56.3 \times \cos 27.6° \\ 71.6 \times \cos 27.6° \\ 46.4 \times \cos 28.2° \end{Bmatrix} = \begin{Bmatrix} 49.9 \\ 63.5 \\ 40.9 \end{Bmatrix} \text{ mm}$$

The effective stiffness of each device at initiation of yield $K_{\mathrm{eff},i}$ is approximately calculated as:

$$K_{\mathrm{eff},i} = \frac{F_{0,i} + \Delta_{\mathrm{y},i} \cdot K_{0,i}}{\Delta_{\mathrm{y},i}}$$

Thus (see Figure 6-2 for illustration),

$$K_{\mathrm{eff},1} = \frac{350 + 40.9 \times 2320 \times 10^{-3}}{40.9 \times 10^{-3}} = 10877.5 \text{ kN/m}$$

$$K_{\mathrm{eff},2} = \frac{350 + 63.5 \times 2320 \times 10^{-3}}{63.5 \times 10^{-3}} = 7831.8 \text{ kN/m}$$

$$K_{\mathrm{eff},3} = \frac{150 + 49.9 \times 1545 \times 10^{-3}}{49.9 \times 10^{-3}} = 4551.0 \text{ kN/m}$$

21) The 3*S*-85 frame with diagonal bracing and with each self-centering device represented by a linear elastic spring with stiffness $K_{\mathrm{eff},i}$ (as calculated above) is analyzed to obtain the periods, mode shapes, participation factors and modal weights. The results are:

$$T_1 = 1.23\text{sec},\ T_2 = 0.41\text{sec},\ T_3 = 0.22\text{sec}$$

$$\{\phi\}_1 = [1.000, 0.684, 0.275]^{\mathrm{T}},\ \{\phi\}_2 = [1.000, -0.516, -0.681]^{\mathrm{T}},\ \{\phi\}_3 = [1.000, -1.597, 2.004]^{\mathrm{T}}$$

$$\overline{W}_1 = 6017.4\text{kN},\ \overline{W}_2 = 982.9\text{kN},\ \overline{W}_3 = 366.7\text{kN}$$

$$\Gamma_1 = 1.383,\ \Gamma_2 = -0.516,\ \Gamma_3 = 0.133$$

The modal drifts $\{\phi_r\}_j$ are calculated from modal displacements $\{\phi\}_j$ as:

$$\{\phi\}_{r1} = [0.316, 0.409, 0.275]^{\mathrm{T}},\ \{\phi\}_{r2} = [1.516, 0.165, -0.681]^{\mathrm{T}},\ \{\phi\}_{r3} = [2.597, -3.601, 2.004]^{\mathrm{T}}$$

22) The damping ratio in each mode is calculated for the damping constant C_j=1,220 kN-s/m and angle of device inclination θ_j using Equation (6-36) (note that the damping constant was selected to provide a damping ratio in the fundamental mode equal to 0.1):

$$\beta_{v1} = \frac{1.23}{4\pi} \cdot \frac{1220 \times 9.81 \times \left(0.316^2 \times \cos^2 27.6 + 0.409^2 \times \cos^2 27.6 + 0.275^2 \times \cos^2 28.2\right)}{2900 \times 0.275^2 + 2900 \times 0.684^2 + 1567 \times 1.000^2} = 0.100$$

$$\beta_{v2} = \frac{0.41}{4\pi} \cdot \frac{1220 \times 9.81 \times \left(1.516^2 \times \cos^2 27.6 + 0.165^2 \times \cos^2 27.6 + (-0.681)^2 \times \cos^2 28.2\right)}{2900 \times (-0.681)^2 + 2900 \times (-0.516)^2 + 1567 \times 1.000^2} = 0.232$$

$$\beta_{v3} = \frac{0.22}{4\pi} \cdot \frac{1220 \times 9.81 \times \left(2.597^2 \times \cos^2 27.6 + \left(-3.601\right)^2 \times \cos^2 27.6 + 2.004^2 \times \cos^2 28.2\right)}{2900 \times 2.004^2 + 2900 \times \left(-1.597\right)^2 + 1567 \times 1.000^2} = 0.189$$

Response history analysis of 3S-85 with Fluidic Self-Centering devices under MCE motions

Response history analysis of frame 3*S*-85 with fluidic self-centering devices in MCE motions was conducted. The results of this analysis is summarized in Table C-8 where it is compared with the calculated response of frame 3*S*-75, also with a fluidic self-centering system. Moreover, Table C-9 compares the response of frame 3*S*-85 in DE and MCE motions.

Based on the calculated self-centering device peak force in the MCE (959.7kN), a brace of section HSS 8x8x5/8 was selected with ultimate capacity F_{Tension} = $F_{\text{Compression}}$ = 1435 kN (compressive strength for effective length of 8535mm). The device displacement capacity is D_{Capacity} = 165mm.

Table C-8 Comparison of Average Response Calculated in Response History Analysis for 3*S*-75 and 3*S*-85 in MCE

Response Quantity	Story	3*S*-75			3*S*-85		
		Near-Fault Pulse	Near-Fault Non-Pulse	Far-Field	Near-Fault Pulse	Near-Fault Non-Pulse	Far-Field
Peak Story Drift (mm)	3	80.2	71.8	76.5	73.9	67.2	70.9
	2	107.5	96.7	95.6	103.2	90.2	88.7
	1	97.6	86.2	79.4	92.3	76.4	72.7
Residual Story Drift (mm)	3	6.2	2.1	2.4	3.7	0.9	1.4
	2	8.4	2.7	2.3	6.4	1.4	1.7
	1	12.2	5.9	6.4	11.4	3.9	5.9
Story Shear Force (kN)	3	938.8	959.9	970.6	1073.8	1035.9	1034.2
	2	1791.1	1718.2	1768.6	1957.0	1866.8	1934.8
	1	2473.3	2347.9	2322.6	2667.5	2535.1	2452.8
Peak Floor Acceleration (g)	3	0.634	0.663	0.661	0.720	0.711	0.711
	2	0.466	0.525	0.516	0.528	0.553	0.549
	1	0.573	0.627	0.651	0.613	0.631	0.673
Peak Absolute Floor Velocity (mm/sec)	3	1689.4	1638.2	1844.1	1721.9	1676.8	1859.6
	2	1562.6	1526.6	1722.4	1597.6	1554.5	1752.9
	1	1578.8	1513.4	1645.1	1596.6	1514.6	1659.4
Device Velocity (mm/sec)	3	523.8	540.5	526.5	549.2	535.2	535.9
	2	525.4	533.6	515.0	560.7	537.8	524.4
	1	434.6	401.4	394.5	420.6	390.1	364.0
Device Force (kN)	3	663.2	721.2	715.2	750.4	776.9	784.9
	2	891.8	862.8	889.1	956.5	939.9	959.7
	1	854.8	780.6	753.7	893.7	848.8	798.0

Table C-9 Comparison of Average Response Calculated in Response History Analysis for 3*S*-85 in DE and MCE

Response Quantity	Story	DE			MCE		
		Near-Fault Pulse	Near-Fault Non-Pulse	Far-Field	Near-Fault Pulse	Near-Fault Non-Pulse	Far-Field
Peak Story Drift (mm)	3	52.2	46.1	48.7	73.9	67.2	70.9
	2	68.9	58.4	64.0	103.2	90.2	88.7
	1	52.3	45.0	45.5	92.3	76.4	72.7
Residual Story Drift (mm)	3	0.2	0.0	0.1	3.7	0.9	1.4
	2	0.5	0.2	0.2	6.4	1.4	1.7
	1	2.8	1.3	0.8	11.4	3.9	5.9
Story Shear Force (kN)	3	844.9	792.7	781.4	1073.8	1035.9	1034.2
	2	1610.3	1486.5	1570.0	1957.0	1866.8	1934.8
	1	2167.1	2079.8	1938.3	2667.5	2535.1	2452.8
Peak Floor Acceleration (g)	3	0.576	0.533	0.522	0.720	0.711	0.711
	2	0.453	0.437	0.416	0.528	0.553	0.549
	1	0.461	0.454	0.478	0.613	0.631	0.673
Peak Absolute Floor Velocity (mm/sec)	3	1241.5	1205.4	1294.4	1721.9	1676.8	1859.6
	2	1126.3	1079.0	1209.2	1597.6	1554.5	1752.9
	1	1098.3	1031.3	1129.2	1596.6	1514.6	1659.4
Device Velocity (mm/sec)	3	438.8	408.8	392.9	549.2	535.2	535.9
	2	441.0	405.3	383.4	560.7	537.8	524.4
	1	301.1	271.9	257.9	420.6	390.1	364.0
Device Force (kN)	3	646.4	612.7	606.9	750.4	776.9	784.9
	2	823.1	774.6	765.6	956.5	939.9	959.7
	1	672.1	669.6	659.5	893.7	848.8	798.0

APPENDIX D

DESIGN AND ANALYSIS OF EXAMPLE 6-STORY BUILDING WITH FLUIDIC SELF-CENTERING DEVICES

This appendix presents the design and simplified analysis of an example 6-story building with fluidic self-centering devices. The building is the one shown in Figure B-1 of Appendix B (but the number of stories is 6) and consists of two steel special moment frames in each principal direction. Each frame is designed for a base shear equal to $0.75V$, where V is determined in accordance with Section 12.8 of ASCE 7-2010 per design procedures of Section 6 of this report. This frame is designated as *6S-75*. Fluidic self-centering devices are added as diagonal elements to this frame. Similar to the comments in Appendix C for the 3-story example, the fluidic self-centering devices may be added to another frame (e.g., along lines 2, 5, B and E of plan in Figure B-1 of Appendix B) that is designed to remain elastic and with all simple connections. This is a preferred arrangement as it results in less force in the special moment frame and allows for easier assessment of adequacy of the structural system.

The frame exclusive of the fluidic self-centering system is first designed per procedures of Section 6 of this report. Then fluidic self-centering devices are added per procedures of Section 6 and analysis is performed again following the simplified ELF and RSA procedures of Section 6.

D.1 Design of Frame 6*S*-75

The geometry, material and gravity loading of the 6*S*-75 frame are the same as those of the 6*S*-Reference of Appendix B. Only difference between the two frames is the size of the member sections. Figure D-1 shows the geometry, section properties and the tributary weights of the 6*S*-75 frame. Note that the beam sections are slightly larger than those of the frame used by Ramirez et al. (2001) for buildings with damping systems and also designated as frame 6*S*-75. The reasons for the slight difference are: (a) the lateral distribution of lateral forces are slightly different, (b) the redundancy factor is larger in ASCE 7 than in the older version of NEHRP, and (c) the vertical earthquake and accidental torsion effects have been accounted for in the current design.

Analysis following Chapter 12.8 of ASCE 7-2010 and presented in Appendix B established the seismic base shear for a single 6*S*-Reference frame, including the effect of torsion, to be V=927.9kN. The minimum base shear allowed for the 6*S*-75 frame per procedures of Section 6 is $0.75V$=695.9kN. The required minimum base shear strength for the frame is

$$V_y = V \cdot \frac{C_d \cdot \Omega_o}{R} = 695.9 \times \frac{5.5 \times 3.0}{8} = 1,435\,kN\,(322.6\,kip)$$

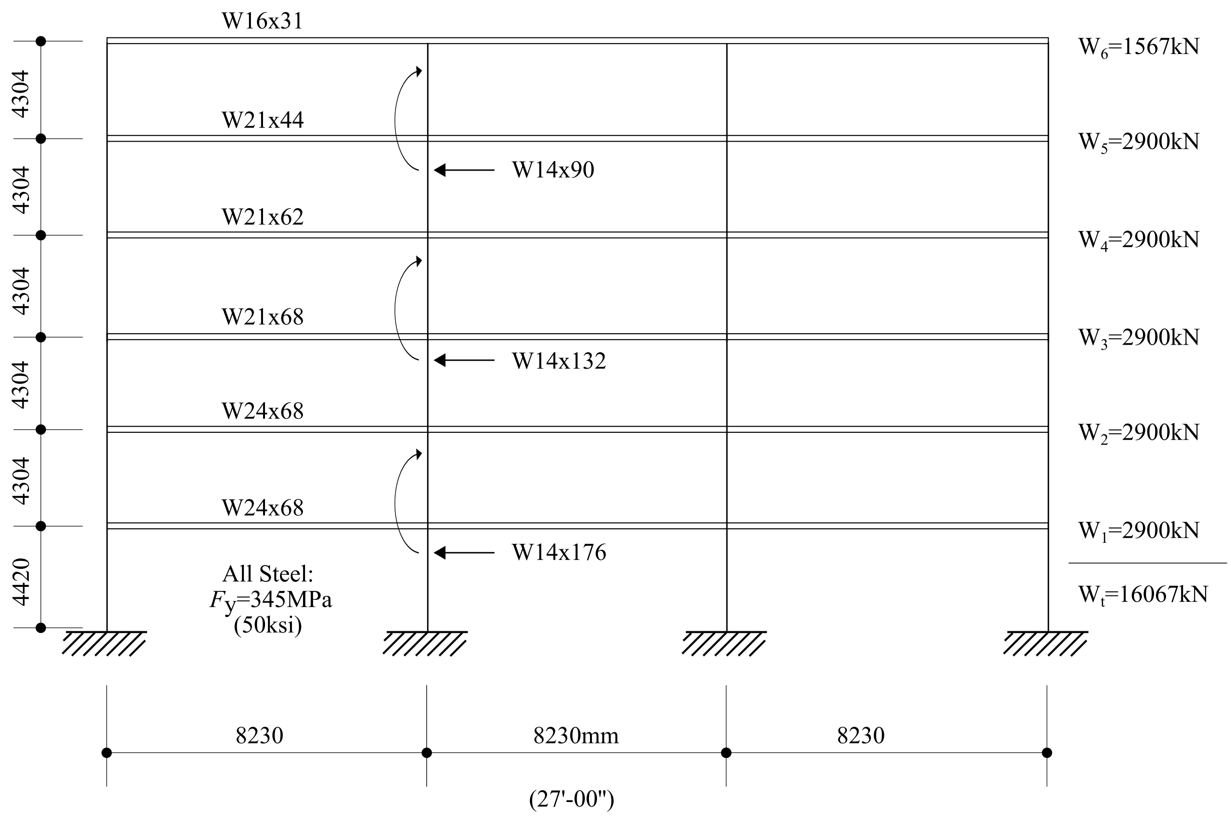

Figure D-1 Frame 6*S*-75 Geometry, Section Properties and Tributary Weights

Verification of the design is described below based on the procedures of Appendix B following ASCE 7-2010 and then by pushover analysis to obtain the force-displacement characteristics and verify the base shear strength. The parameters are: R=8, Ω_0=3, C_d=5.5, I_e=1.0, ρ=1.3, S_{MS}=1.875g, S_{M1}=0.9g, S_{DS}=1.25g and S_{D1}=0.6g. Also, the period for calculations of internal forces per ASCE 7-2010 is T=1.372sec (see Appendix B).

The seismic base shear for a single frame V=695.9kN is distributed vertically using ASCE 7-2010 equations 12.8-11 and 12.8-12:

$$F_y = C_{vx} V \tag{D-1}$$

$$C_{vx} = \frac{w_x h_x^k}{\sum_{i=1}^{n} w_i h_i^k} \tag{D-2}$$

The value of parameter k has been determined in Appendix B to be k =1.436. The calculated lateral seismic forces are summarized in Table D-1. Quantity $\sum_{i=1}^{n} w_i h_i^k$ is equal to 787,266.

Table D-1 Lateral Seismic Forces for 6-Story Frame 6*S*-75

Floor	w_i [kN]	h_i [m]	$w_i h_i^k$	C_{vx}	F_x [kN]
6	1567	25.94	168085	0.2135	148.6
5	2900	21.63	239629	0.3044	211.8
4	2900	17.33	174306	0.2214	154.1
3	2900	13.03	115733	0.1470	102.3
2	2900	8.72	65010	0.0826	57.5
1	2900	4.42	24503	0.0311	21.6

Analysis of the frame for the critical loading combination $(1.2+0.2S_{DS})D+0.5L+\rho Q_E$ (which is equal to $1.45D+0.5L+1.3Q_E$) resulted in the required strengths of the members of the frame. The required bending moment strengths are as follows: (a) sixth floor beam 168kN-m, (b) fifth floor beam 402kN-m, (c) fourth floor beam 566kN-m, (d) third floor beam 670kN-m, (e) second floor beam 754kN-m, (f) first floor beam 678kN-m and (g) sixth and fifth story columns 285kN-m, fourth and third columns 480kN-m and second and first story columns 775kN-m. The factored compressive axial force in the interior columns at the first story is P_u=1553kN, prior to the use of the Ω_0 factor.

D.2 Construction of Push-Over Curve of 6*S*-75 Based on Plastic Analysis

Plastic analysis may be used to calculate the base shear strength of the frame. Then with information on the fundamental mode period and mode shape, the push-over curve may be constructed. The method was detailed in Ramirez et al. (2001) and was reproduced in Appendix C. The application of the method is described below.

Frame parameters

Number and length of spans: n=3; L_b=8230 mm

Number of stories: N=6;

Material properties: F_y=345 MPa (50 ksi)

Column sections: 6th & 5th story: W14×90 (d_c = 356 mm; M_{pc}= Z_x×F_y = 886.7 kN-m)

4th & 3rd story: W14×132 (d_c = 373 mm; M_{pc}= Z_x×F_y = 1321.4 kN-m)

2nd & 1st story: W14×176 (d_c = 386 mm; M_{pc}= Z_x×F_y = 1807.8 kN-m)

Beam properties:

6^{th} floor: W16×31 (d_b = 404 mm; $M_{pb}=Z_x \times F_y$= 305.3 kN-m)

5^{th} floor: W21×44 (d_b = 526 mm; $M_{pb}=Z_x \times F_y$= 538.2 kN-m)

4^{th} floor: W21×62 (d_b = 533 mm; $M_{pb}=Z_x \times F_y$= 814.2 kN-m)

3^{rd} floor: W21×68 (d_b = 536 mm; $M_{pb}=Z_x \times F_y$= 903.9 kN-m)

2^{nd} floor: W24×68 (d_b = 602 mm; $M_{pb}=Z_x \times F_y$= 1000.5 kN-m)

1^{st} floor: W24×68 (d_b = 602 mm; $M_{pb}=Z_x \times F_y$= 1000.5 kN-m)

Floor weights: w_6=1,567kN; $w_5=w_4=w_3=w_2=w_1$=2,900kN

Story heights: h_6=25940 mm; h_5=21636 mm; h_4=17332 mm; h_3=13028 mm; h_2=8724 mm; h_1=4420 mm

Eigenvalue analysis: T_1=2.30*sec*; $\{\phi_1\}^T$=[1.000, 0.876, 0.701, 0.507, 0.298, 0.113]; $\overline{W}_1$ =12383.2kN; Γ_1=1.41

It is assumed that plastic hinges form in the beams at a point located at a distance of half the depth of the column section $d_c/2$ from the column center (i.e., $\alpha_i = (d_c/2)/L_i$). Also, in columns a plastic hinge develops near the base at a distance of one depth (d_c) of the column section from the base of the frame.

Evaluation of parameters α_i, χ_i, and $M_{pbi}\chi_i$

Parameters are presented in Table D-2.

Table D-2 Parameters α_i, χ_i, and $M_{pbi}\chi_i$

Level	M_{pbi} (kN-m)	α_i	χ_i	$M_{pbi}\chi_i$ (kN-m)
6	305.3	0.022	1.05	319.1
5	538.2	0.022	1.05	562.5
4	814.2	0.023	1.05	852.9
3	903.9	0.023	1.05	946.8
2	1000.5	0.023	1.05	1049.7
1	1000.5	0.023	1.05	1049.7
				$\Sigma M_{pbi}\chi_i$=4780.8 kN-m

From Table D-2, the term $(n+1)M_{pc} + 2n\sum_{i=1}^{N}(M_{pbi} \cdot \chi_i)$ in equation (C-8) is calculated as:

$$(n+1)M_{pc} + 2n\sum_{i=1}^{N}(M_{pbi} \cdot \chi_i) = (3+1)\cdot 1807.8 + 2\cdot 3\cdot 4780.8 = 35916.0 \quad \text{kN}\cdot\text{m}$$

The term $\sum_{i=1}^{N}(\lambda_i h_i)$ in equation (C-8) depends on the horizontal shear distribution λ_i. In this study, λ_i=C_{vx} as defined in section 12.8-12 in ASCE 7-2010. Thus,

$$\lambda_i = \frac{w_i h_i^k}{\sum_{m=1}^{N} w_m h_m^k} \tag{D-3}$$

Here, k is calculated to be k=1.90 (ASCE 7, 2010) based on the period of 2.30sec. Calculations are summarized in Table D-3.

Table D-3 Calculation of $\lambda_i h_i$

Level	w_i (kN)	h_i (mm)	$w_i h_i^k \times 10^8$	λ_i	$\lambda_i h_i$ (mm)
6	1567	25940	3816.0	0.252	6536.9
5	2900	21636	5003.0	0.330	7139.9
4	2900	17332	3282.5	0.217	3761.0
3	2900	13028	1908.4	0.126	1641.5
2	2900	8724	890.8	0.059	514.7
1	2900	4420	244.7	0.016	70.7
			$\Sigma w_i h_i^k \times 10^8$=15145.4		$\Sigma\lambda_i h_i$=19664.7

Thus, V_y is calculated from equation (C-8) as:

$$V_y = \frac{35916.0 \times 10^3}{19664.7} = 1826.4 \quad \text{kN} \tag{D-4}$$

Δ_{yR} is calculated from equation (C-9) as:

$$\Delta_{yR} = \left(\frac{g}{4\pi^2}\right)1.41\left(\frac{1826.4}{12383.2}\right)2.30^2 = 273.4 \quad \text{mm} \tag{D-5}$$

D.3 Push-Over Analysis of 6*S*-75 Frame and Comparison to Results of Plastic Analysis

A pushover analysis of frame 6*S*-75 was conducted in program OpenSees and the base shear-roof displacement relation was constructed. Lateral loads in the pushover analysis were distributed in proportion to parameter λ_i as shown in Table D-3. Figure D-2 presents the pushover curves computed in OpenSees with and without consideration of P-Δ effects and the pushover curve obtained in plastic analysis. The latter does not include P-Δ effects. Also, the computation when P-Δ effects are accounted for considers a small post-elastic stiffness of members (ratio of post-elastic to elastic stiffness equal to 0.01).

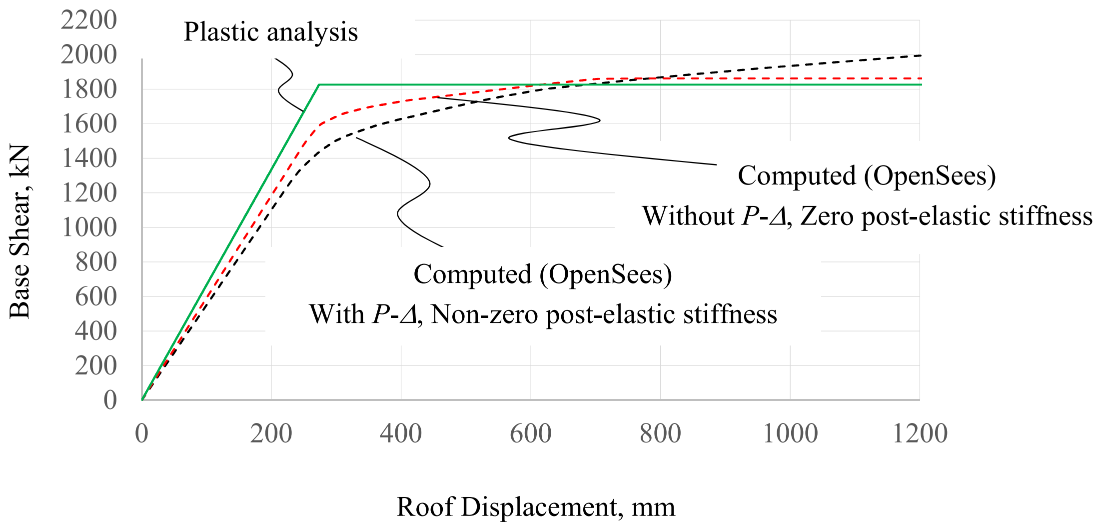

Figure D-2 Comparison of Pushover Curves of Frame 6*S*-75

Evidently, plastic analysis predicts well the pushover curve of the frame when P-Δ effects are neglected. Note that the calculated (OpenSees) base shear strength of 1,800 kN without P-Δ effects exceeds the minimum required for this frame, which is 1,435kN. Also, it is observed that the pushover curve is affected by P-Δ effects and this behavior will be accounted for in the analysis of the frame with added fluidic self-centering devices. The base shear strength including P-Δ effects is equal to about 1,750kN, thus more than the minimum required.

D.4 Design and Simplified Analysis of 6*S*-75 Frame with Fluidic Self-Centering Devices

The procedures of Section 6.5 are applied. The first step is to conduct a pushover analysis and determine the story shear-story drift relations of each story so that the story shear yield strengths are determined. This may be obtained by plastic analysis as described in Section D.3 but computational analysis including P-Δ effects is preferred to better capture the frame behavior. This analysis has been performed (see Section D.3) and Figure D-3 presents the results. Based on this figure, the story yield strengths are obtained as: $F_{y,1}$=1,750 kN, $F_{y,2}$=1,700 kN, $F_{y,3}$=1,550 kN, $F_{y,4}$=1,250 kN, $F_{y,5}$=1,000 kN and $F_{y,6}$= 400 kN. Note that the pushover curves in Figure D-3 have some small post-elastic stiffness so that the yield strength was defined as the force at initiation of inelastic action in bilinear representations of the pushover curves.

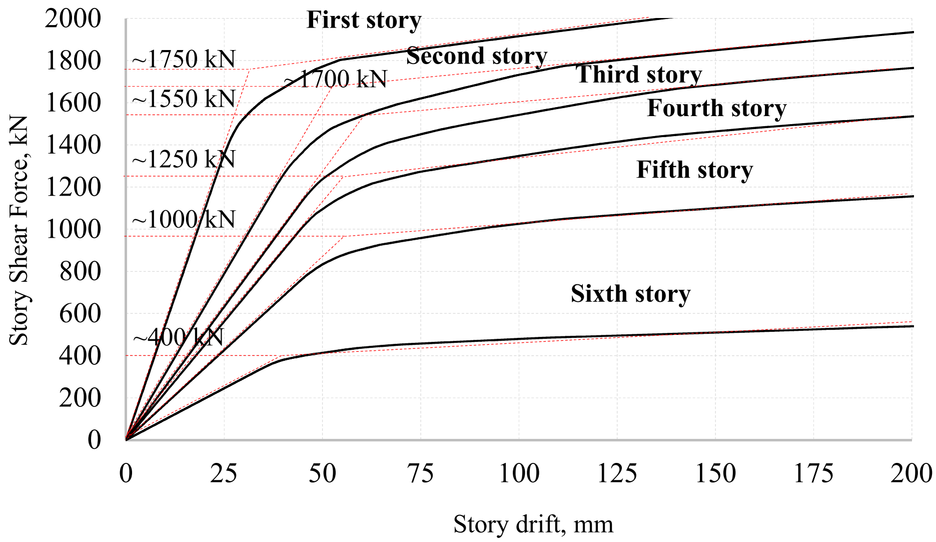

Figure D-3 Story Shear Force versus Story Drift Relations for Frame 6*S*-75

Parameters for fluidic self-centering devices

The component of preload in the horizontal direction is selected to be approximately equal to a 20% of the story shear yield strength. One device will be used at each story placed in a diagonal configuration at an angle θ. The preload for the device at story i, $F_{0,i}$ is calculated as:

$$F_{0,i} = \frac{0.2 \times F_{y,i}}{\cos\theta} \tag{C-13}$$

Accordingly,

$$F_{0,1} = \frac{0.2 \times F_{y,1}}{\cos 28.2°} = \frac{0.2 \times 1750}{\cos 28.2°} = 397 \quad \text{kN} \qquad \text{(select 400 kN)}$$

$$F_{0,2} = \frac{0.2 \times F_{y,2}}{\cos 27.6°} = \frac{0.2 \times 1700}{\cos 27.6°} = 384 \quad \text{kN} \qquad \text{(select 400 kN)}$$

$$F_{0,3} = \frac{0.2 \times F_{y,3}}{\cos 27.6°} = \frac{0.2 \times 1550}{\cos 27.6°} = 350 \quad \text{kN} \qquad \text{(select 400 kN)}$$

$$F_{0,4} = \frac{0.2 \times F_{y,4}}{\cos 27.6°} = \frac{0.2 \times 1250}{\cos 27.6°} = 282 \quad \text{kN} \qquad \text{(select 250 kN)}$$

$$F_{0,5} = \frac{0.2 \times F_{y,5}}{\cos 27.6°} = \frac{0.2 \times 1000}{\cos 27.6°} = 226 \quad \text{kN} \qquad \text{(select 250 kN)}$$

$$F_{0,6} = \frac{0.2 \times F_{y,6}}{\cos 27.6°} = \frac{0.2 \times 400}{\cos 27.6°} = 90 \quad \text{kN} \qquad \text{(select 100 kN)}$$

A single fluidic self-centering device design is possible that is suitable for all six stories with only the fluid initial pressure varied to achieve the desired preload for the three types of devices needed. The displacement capacity of the devices was calculated as $1.5x0.02h(R/C_d)cos\theta$ which is an upper bound estimate of the displacement in the MCE when the drift limit in the DE is 0.02h per ASCE 7-2010. The manufacturer of the devices was then contacted and asked to develop a design for a device that can be preloaded to either 400, 250 or 100kN, have a displacement capacity of 165mm (6.5inch) and have linear viscous damping (could be of the half damping type) with a damping constant C_1=C_2=C_3=C_4=C_5= C_6=2,900kN-sec/m (17kip-sec/in). The manufacturer provided the following:

- Basic dimensions of the device (including the connection details) to be 216mm (8.5inch) in diameter and 1145mm (45inch) in length (pin to pin).
- The end-load of the device under quasi-static conditions at the displacement of 165mm, which was used to calculate the stiffness K_0 as follows

$$K_{0,1} = 2230 \text{ kN/m}$$
$$K_{0,2} = 2230 \text{ kN/m}$$
$$K_{0,3} = 2230 \text{ kN/m}$$
$$K_{0,4} = 1790 \text{ kN/m}$$
$$K_{0,5} = 1790 \text{ kN/m}$$
$$K_{0,6} = 1350 \text{ kN/m}$$

- Information on the force capacity of the device, including information that the peak damping force should not exceed 1,000kN, which effectively limits the peak device velocity to about 0.35m/sec.

Bracing for connecting this device to the frame was selected based on a compression force of three times the preload or 300, 750 and 1200kN (top to bottom) for an effective length of 9.1m (30ft). Referring to the AISC Construction Manual 14th Edition (2010), the following brace sections are selected: HSS7×7×1/4 (6th story), HSS8×8×3/8 (4th and 5th stories) and HSS9×9×1/2 (1st to 3rd stories). These sections have sufficient design strength for the effective length of KL=9.1m (30ft): 362 kN, 774kN and 1357 kN, respectively.. Note that the effective length is actually equal to 8.5m (28ft) but the larger value of 9.1m is used for conservatism. The size of the bracing will be again checked when the MCE analysis is completed.

Calculation of response in the Design Earthquake using the Response Spectrum Analysis (RSA) procedure

The steps described in Section 6.5 are followed.

1) The yield displacement of each story (relative displacement) is obtained either from the computed story shear – story displacement curves in Figure D-4 or from the calculated value of D_y as follows where ϕ_{r1} is the modal drift in mode 1:

$$\{\delta\}_{\mathrm{y}} = \Delta_{\mathrm{yR}}\{\phi\}_{\mathrm{r1}} = 176.4\cdot\begin{Bmatrix} 1.000-0.876 \\ 0.876-0.701 \\ 0.701-0.507 \\ 0.507-0.298 \\ 0.298-0.113 \\ 0.113 \end{Bmatrix} = \begin{Bmatrix} 33.9 \\ 47.8 \\ 53.0 \\ 57.1 \\ 50.6 \\ 30.9 \end{Bmatrix} \text{ mm}$$

The calculated story yield displacements are in good agreement with the values obtained from pushover analysis of the frame in OpenSees where the values are 37, 55, 55, 59, 51 and 31 mm, from the top to the bottom story (Figure D-4). The device stroke at the stage of story initiation of yield is calculated as follow:

$$\{\Delta\}_{\mathrm{y}} = \{\delta\}_{\mathrm{y}} \times \cos\theta = \begin{Bmatrix} 33.9\times\cos 27.6^\circ \\ 47.8\times\cos 27.6^\circ \\ 53.0\times\cos 27.6^\circ \\ 57.1\times\cos 27.6^\circ \\ 50.6\times\cos 27.6^\circ \\ 30.9\times\cos 28.2^\circ \end{Bmatrix} = \begin{Bmatrix} 30.0 \\ 42.4 \\ 47.0 \\ 50.6 \\ 44.8 \\ 27.4 \end{Bmatrix} \text{ mm}$$

The effective stiffness of each device at initiation of yield $K_{\mathrm{eff},i}$ is approximately calculated as:

$$K_{\mathrm{eff},i} = \frac{F_{0,i} + \Delta_{\mathrm{y},i}\cdot K_{0,i}}{\Delta_{\mathrm{y},i}}$$

Thus (see Figure 6-2 for illustration),

$$K_{\mathrm{eff},1} = \frac{400 + 27.4\times 2230\times 10^{-3}}{27.4\times 10^{-3}} = 16828.5 \text{ kN/m}$$

$$K_{\mathrm{eff},2} = \frac{400 + 44.8\times 2230\times 10^{-3}}{44.8\times 10^{-3}} = 11158.6 \text{ kN/m}$$

$$K_{\mathrm{eff},3} = \frac{400 + 50.6\times 2230\times 10^{-3}}{50.6\times 10^{-3}} = 10135.1 \text{ kN/m}$$

$$K_{\mathrm{eff},4} = \frac{250 + 47.0\times 1790\times 10^{-3}}{47.0\times 10^{-3}} = 7109.1 \text{ kN/m}$$

$$K_{\mathrm{eff},5} = \frac{250 + 42.4\times 1790\times 10^{-3}}{42.4\times 10^{-3}} = 7686.2 \text{ kN/m}$$

$$K_{\mathrm{eff},6} = \frac{100 + 30.0\times 1350\times 10^{-3}}{30.0\times 10^{-3}} = 4683.3 \text{ kN/m}$$

2) The 6S-75 frame with diagonal bracing and with each self-centering device represented by a linear elastic spring with stiffness $K_{\mathrm{eff},i}$ (as calculated above) is analyzed to obtain the periods, mode shapes, participation factors and modal weights. The results are:

$$T_1 = 2.06\,\mathrm{sec},\ \ T_2 = 0.75\,\mathrm{sec},\ \ T_3 = 0.44\,\mathrm{sec},\ \ T_4 = 0.29\,\mathrm{sec},\ \ T_5 = 0.21\,\mathrm{sec},\ \ T_6 = 0.16\,\mathrm{sec}$$

$$\{\phi\}_1 = [1.000, 0.883, 0.713, 0.517, 0.307, 0.117]^{\mathrm{T}},$$

$$\{\phi\}_2 = [1.000, 0.305, -0.359, -0.662, -0.587, -0.266]^{\mathrm{T}},$$

$$\{\phi\}_3 = [1.000, -0.454, -0.691, 0.137, 0.736, 0.478]^{\mathrm{T}},$$

$$\{\phi\}_4 = [1.000, -1.199, 0.480, 0.912, -0.629, -0.871]^{\mathrm{T}},$$

$$\{\phi\}_5 = [1.000, -1.827, 2.923, -2.337, -0.328, 2.537]^{\mathrm{T}},$$

$$\{\phi\}_6 = [1.000, -2.357, 6.249, -11.980, 17.518, -17.880]^{\mathrm{T}}$$

$$\overline{W}_1 = 12464.1\mathrm{kN},\ \ \overline{W}_2 = 1900.3\mathrm{kN},\ \ \overline{W}_3 = 803.6\mathrm{kN},$$

$$\overline{W}_4 = 406.5\mathrm{kN},\ \ \overline{W}_5 = 270.0\mathrm{kN},\ \ \overline{W}_6 = 222.5\mathrm{kN}$$

$$\Gamma_1 = 1.397,\ \ \Gamma_2 = -0.637,\ \ \Gamma_3 = 0.371,\ \ \Gamma_4 = -0.183,\ \ \Gamma_5 = 0.062,\ \ \Gamma_6 = -0.010$$

The modal drifts $\{\phi_r\}_j$ are calculated from modal displacements $\{\phi\}_j$ as:

$$\{\phi\}_{r1} = [0.117, 0.170, 0.196, 0.210, 0.190, 0.117]^{\mathrm{T}},$$

$$\{\phi\}_{r2} = [0.695, 0.663, 0.304, -0.076, -0.320, -0.266]^{\mathrm{T}},$$

$$\{\phi\}_{r3} = [1.454, 0.237, -0.828, -0.598, 0.258, 0.478]^{\mathrm{T}},$$

$$\{\phi\}_{r4} = [2.199, -1.679, -0.432, 1.540, 0.242, -0.871]^{\mathrm{T}},$$

$$\{\phi\}_{r5} = [2.827, -4.750, 5.260, -2.009, -2.865, 2.537]^{\mathrm{T}},$$

$$\{\phi\}_{r6} = [3.357, -8.606, 18.229, -29.498, 35.397, -17.880]^{\mathrm{T}}$$

3) The damping constants were selected so that the added first mode damping ratio β_{v1} equals 0.1 (10%). This distribution of properties appears to be appropriate but not necessarily important as the damping force is linearly related to the velocity (it would have been more appropriate for nonlinear viscous dampers). The damping ratio of each mode was calculated as follows: using Equation (6-36):

$$\beta_{v1} = \frac{2.06}{4\pi} \cdot 9.81 \cdot \frac{\left[\left(0.117^2 + 0.170^2 + 0.196^2 + 0.210^2 + 0.190^2\right) \times \cos^2 27.6° + 0.117^2 \times \cos^2 28.2°\right] \times 2900}{1.000^2 \times 1567 + \left(0.883^2 + 0.713^2 + 0.517^2 + 0.307^2 + 0.117^2\right) \times 2900} = 0.100$$

$$\beta_{v2} = \frac{0.75}{4\pi} \cdot 9.81 \cdot \frac{\left[\left(0.695^2 + 0.663^2 + 0.304^2 + (-0.076)^2 + (-0.320)^2\right) \times \cos^2 27.6° + (-0.266)^2 \times \cos^2 28.2°\right] \times 2900}{1.000^2 \times 1567 + \left[0.305^2 + (-0.359)^2 + (-0.662)^2 + (-0.587)^2 + (-0.266)^2\right] \times 2900} = 0.340$$

$$\beta_{v3} = \frac{0.44}{4\pi} \cdot 9.81 \cdot \frac{\left[\left(1.454^2 + 0.237^2 + (-0.828)^2 + (-0.598)^2 + 0.258^2\right) \times \cos^2 27.6° + 0.478^2 \times \cos^2 28.2°\right] \times 2900}{1.000^2 \times 1567 + \left[(-0.454)^2 + (-0.691)^2 + 0.137^2 + 0.736^2 + 0.478^2\right] \times 2900} = 0.470$$

$$\beta_{v4} = \frac{0.29}{4\pi} \cdot 9.81 \cdot \frac{\left[\left(2.199^2 + (-1.679)^2 + (-0.432)^2 + 1.540^2 + 0.242^2\right) \times \cos^2 27.6° + (-0.871)^2 \times \cos^2 28.2°\right] \times 2900}{1.000^2 \times 1567 + \left[(-1.199)^2 + 0.480^2 + 0.912^2 + (-0.629)^2 + (-0.871)^2\right] \times 2900} = 0.467$$

$$\beta_{v5} = \frac{0.21}{4\pi} \cdot 9.81 \cdot \frac{\left[\left(2.827^2 + (-4.750)^2 + 5.260^2 + (-2.009)^2 + (-2.865)^2\right) \times \cos^2 27.6° + 2.537^2 \times \cos^2 28.2°\right] \times 2900}{1.000^2 \times 1567 + \left[(-1.827)^2 + 2.923^2 + (-2.337)^2 + (-0.328)^2 + 2.537^2\right] \times 2900} = 0.405$$

$$\beta_{v6} = \frac{0.16}{4\pi} \cdot 9.81 \cdot \frac{\left[\left(3.357^2 + (-8.606)^2 + 18.229^2 + (-29.498)^2 + 35.397^2\right) \times \cos^2 27.6° + (-17.880)^2 \times \cos^2 28.2°\right] \times 2900}{1.000^2 \times 1567 + \left[(-2.357)^2 + 6.249^2 + (-11.98)^2 + 17.518^2 + (-17.88)^2\right] \times 2900} = 0.344$$

4) The effective yield displacement in the spectral representation is calculated using Equation (6-42):

$$D_y = \frac{\Delta_{yR}}{\Gamma_1} = \frac{273.4}{1.397} = 195.7 \quad \text{mm}$$

5) Assume the value of displacement D in the single-degree-of-freedom spectral representation of the pushover curve as D_D=235 mm. Ductility ratio μ is calculated using Equation (6-46):

$$\mu = \frac{D_D}{D_y} = \frac{235}{195.7} = 1.20$$

6) The effective period T_{eff} is calculated using Equation (6-44):

$$T_{eff} = T_1\sqrt{\mu}\sqrt{\frac{A_y + A_{F0}}{A_y + 2A_{F0}}} = 2.06\sqrt{1.20}\sqrt{\frac{0.140g + 0.032g}{0.140g + 2 \times 0.032g}} = 2.07 \quad \text{sec}$$

Quantities A_y and A_{F0} were calculated using Equations (6-41) and (6-45):

$$A_y = \frac{V_y g}{\overline{\overline{W}}_1} = \frac{1750 \times g}{12464.1} = 0.140g$$

$$A_{F0} = \frac{F_{01} g}{\overline{\overline{W}}_1} = \frac{400 \times g}{12464.1} = 0.032g$$

The effective damping ratio is calculated using Equation (6-47):

$$\beta_{\text{eff}} = \beta_i + \beta_{\text{v1}} \times \frac{T_{\text{eff}}}{T_1} + \frac{1.42 q_{\text{H}}}{\pi}\left(1 - \frac{1}{\mu}\right) = 0.05 + 0.1 \times \frac{2.07}{2.06} + \frac{1.42 \times 1.0}{\pi}\left(1 - \frac{1}{1.20}\right) = 0.226$$

Note that q_{H}=1.0. Using Table 18.6-1 of ASCE 7-2010 the damping factor is obtained as B=1.578.

7) Displacement D_D for the Design Earthquake is calculated using Equation (6-55):

$$D_{\text{D}} = \frac{T_{\text{eff}}^2 S_{\text{a}}\left(T_{\text{eff}}, \beta = 0.05\right) g}{4\pi^2 B} = \frac{2.07^2 \times 0.2857 \times 9810}{4\pi^2 \times 1.578} = 192.8 \quad \text{mm}$$

Before proceeding to additional iterations for the calculation of the displacement, the elastic displacement demand is calculated.

8) The displacement demand is calculated again considering elastic conditions

$$D_{\text{D}} = \frac{T_1^2 S_{\text{a}}\left(T_1, \beta = 0.05\right) g}{4\pi^2 B_{\text{E}}} = \frac{2.06^2 \times 0.2871 \times 9810}{4\pi^2 \times 1.35} = 224.3 \quad \text{mm}$$

Note that the damping factor B=1.35 was obtained from Table 18.6-1 in ASCE 7-2010 for damping ratio $\beta_i+\beta_{\text{v1}}$=0.05+0.10=0.15. Since the elastic displacement D_{D} (=224.3 mm) is larger than the inelastic D_{D} (=192.8 mm), the elastic value is used so that D_{D}=224.3mm. Still the frame has yielded as the displacement exceeds the yield displacement D_{y}=195.7 mm.

9) The displacements contributed by the fundamental mode are given by Equation (6-56):

$$\{u\}_1 = \Gamma_1 \{\phi\}_1 D_{\text{D}} = 1.397 \cdot \begin{Bmatrix} 1.000 \\ 0.883 \\ 0.713 \\ 0.517 \\ 0.307 \\ 0.117 \end{Bmatrix} \cdot 224.3 = \begin{Bmatrix} 313.3 \\ 276.7 \\ 223.4 \\ 162.0 \\ 96.2 \\ 36.7 \end{Bmatrix} \quad \text{mm}$$

Story drifts are calculated as:

$$\{\Delta u\}_1 = \begin{Bmatrix} 313.3 - 276.7 \\ 276.7 - 223.4 \\ 223.4 - 162.0 \\ 162.0 - 96.2 \\ 96.2 - 36.7 \\ 36.7 \end{Bmatrix} = \begin{Bmatrix} 36.6 \\ 53.3 \\ 61.4 \\ 65.8 \\ 59.5 \\ 36.7 \end{Bmatrix} \quad \text{mm}$$

10) The displacements contributed by the higher modes are (Equation (6-57)):

$$\{u\}_2 = \frac{\Gamma_2 \{\phi\}_2 T_2^2 S_{\mathrm{a}}(T_2, \beta = 0.05) g}{4\pi^2 B_2} = \frac{|-0.637| \times 0.75^2 \times 0.7884 \times 9810}{4\pi^2 \times 2.070} \begin{Bmatrix} 1.000 \\ 0.305 \\ -0.359 \\ -0.662 \\ -0.587 \\ -0.266 \end{Bmatrix} = \begin{Bmatrix} 33.9 \\ 10.3 \\ -12.2 \\ -22.4 \\ -19.9 \\ -9.0 \end{Bmatrix} \text{ mm}$$

$$\{u\}_3 = \frac{\Gamma_3 \{\phi\}_3 T_3^2 S_{\mathrm{a}}(T_3, \beta = 0.05) g}{4\pi^2 B_3} = \frac{|0.371| \times 0.44^2 \times 1.2507 \times 9810}{4\pi^2 \times 2.460} \begin{Bmatrix} 1.000 \\ -0.454 \\ -0.691 \\ 0.137 \\ 0.736 \\ 0.478 \end{Bmatrix} = \begin{Bmatrix} 9.1 \\ -4.1 \\ -6.3 \\ 1.2 \\ 6.7 \\ 4.3 \end{Bmatrix} \text{ mm}$$

$$\{u\}_4 = \frac{\Gamma_4 \{\phi\}_4 T_4^2 S_{\mathrm{a}}(T_4, \beta = 0.05) g}{4\pi^2 B_4} = \frac{|-0.183| \times 0.29^2 \times 1.2507 \times 9810}{4\pi^2 \times 2.451} \begin{Bmatrix} 1.000 \\ -1.199 \\ 0.480 \\ 0.912 \\ -0.629 \\ -0.871 \end{Bmatrix} = \begin{Bmatrix} 2.0 \\ -2.3 \\ 0.9 \\ 1.8 \\ -1.2 \\ -1.7 \end{Bmatrix} \text{ mm}$$

$$\{u\}_5 = \frac{\Gamma_5 \{\phi\}_5 T_5^2 S_{\mathrm{a}}(T_5, \beta = 0.05) g}{4\pi^2 B_5} = \frac{|0.062| \times 0.21^2 \times 1.2507 \times 9810}{4\pi^2 \times 2.265} \begin{Bmatrix} 1.000 \\ -1.827 \\ 2.923 \\ -2.337 \\ -0.328 \\ 2.537 \end{Bmatrix} = \begin{Bmatrix} 0.4 \\ -0.7 \\ 1.1 \\ -0.9 \\ -0.1 \\ 1.0 \end{Bmatrix} \text{ mm}$$

$$\{u\}_6 = \frac{\Gamma_6 \{\phi\}_6 T_6^2 S_{\mathrm{a}}(T_6, \beta = 0.05) g}{4\pi^2 B_6} = \frac{|-0.010| \times 0.16^2 \times 1.2507 \times 9810}{4\pi^2 \times 2.082} \begin{Bmatrix} 1.000 \\ -2.357 \\ 6.249 \\ -11.980 \\ 17.518 \\ -17.880 \end{Bmatrix} = \begin{Bmatrix} 0.0 \\ -0.1 \\ 0.2 \\ -0.5 \\ 0.7 \\ -0.7 \end{Bmatrix} \text{ mm}$$

Note that the modal damping ratios were obtained by use of Equation (6-53):

$$\beta_2 = \beta_i + \beta_{\mathrm{v}2} = 0.05 + 0.340 = 0.390$$

$$\beta_3 = \beta_i + \beta_{\mathrm{v}3} = 0.05 + 0.470 = 0.520$$

$$\beta_4 = \beta_i + \beta_{\mathrm{v}4} = 0.05 + 0.467 = 0.517$$

$$\beta_5 = \beta_i + \beta_{\mathrm{v}5} = 0.05 + 0.405 = 0.455$$

$$\beta_6 = \beta_i + \beta_{v6} = 0.05 + 0.344 = 0.394$$

The damping factors based on these values of damping ratio are B_2=2.070, B_3=2.460, B_4=2.451, B_5=2.265, and B_6=2.082 (Table 18.6-1 in ASCE 7-2010).

Story drifts are calculated as:

$$\{\Delta u\}_2 = \begin{Bmatrix} 33.9-10.3 \\ 10.3-(-12.2) \\ -12.2-(-22.4) \\ -22.4-(-19.9) \\ -19.9-(-9.0) \\ -9.0 \end{Bmatrix} = \begin{Bmatrix} 23.6 \\ 22.5 \\ 10.2 \\ -2.5 \\ -10.9 \\ -9.0 \end{Bmatrix} \text{ mm}$$

$$\{\Delta u\}_3 = \begin{Bmatrix} 9.1-(-4.1) \\ -4.1-(-6.3) \\ -6.3-1.2 \\ 1.2-6.7 \\ 6.7-4.3 \\ 4.3 \end{Bmatrix} = \begin{Bmatrix} 13.2 \\ 2.2 \\ -7.5 \\ -5.5 \\ 2.4 \\ 4.3 \end{Bmatrix} \text{ mm}$$

$$\{\Delta u\}_4 = \begin{Bmatrix} 2.0-(-2.3) \\ -2.3-0.9 \\ 0.9-1.8 \\ 1.8-(-1.2) \\ -1.2-(-1.7) \\ -1.7 \end{Bmatrix} = \begin{Bmatrix} 4.3 \\ -3.2 \\ -0.9 \\ 3.0 \\ 0.5 \\ -1.7 \end{Bmatrix} \text{ mm}$$

$$\{\Delta u\}_5 = \begin{Bmatrix} 0.4-(-0.7) \\ -0.7-1.1 \\ 1.1-(-0.9) \\ -0.9-(-0.1) \\ -0.1-1.0 \\ 1.0 \end{Bmatrix} = \begin{Bmatrix} 1.1 \\ -1.8 \\ 2.0 \\ -0.8 \\ -1.1 \\ 1.0 \end{Bmatrix} \text{ mm}$$

$$\{\Delta u\}_6 = \begin{Bmatrix} 0.0-(-0.1) \\ -0.1-0.2 \\ 0.2-(-0.5) \\ -0.5-0.7 \\ 0.7-(-0.7) \\ -0.7 \end{Bmatrix} = \begin{Bmatrix} 0.1 \\ -0.3 \\ 0.7 \\ -1.2 \\ 1.4 \\ -0.7 \end{Bmatrix} \text{ mm}$$

11) Combining the modal displacements and drifts by the SRSS rule:

$$\{u\}_{\mathrm{T}}=\begin{Bmatrix}\sqrt{313.3^2+33.9^2+9.1^2+2.0^2+0.4^2+0.0^2}\\ \sqrt{276.7^2+10.3^2+(-4.1)^2+(-2.3)^2+(-0.7)^2+(-0.1)^2}\\ \sqrt{223.4^2+(-12.2)^2+(-6.3)^2+0.9^2+1.1^2+0.2^2}\\ \sqrt{162.0^2+(-22.4)^2+1.2^2+1.8^2+(-0.9)^2+(-0.5)^2}\\ \sqrt{96.2^2+(-19.9)^2+6.7^2+(-1.2)^2+(-0.1)^2+0.7^2}\\ \sqrt{36.7^2+(-9.0)^2+4.3^2+(-1.7)^2+1.0^2+(-0.7)^2}\end{Bmatrix}=\begin{Bmatrix}315.3\\276.9\\223.8\\163.6\\98.5\\38.1\end{Bmatrix}\ \text{mm}$$

$$\{\Delta u\}_{\mathrm{T}}=\begin{Bmatrix}\sqrt{36.6^2+23.6^2+13.2^2+4.3^2+1.1^2+0.1^2}\\ \sqrt{53.3^2+22.5^2+2.2^2+(-3.2)^2+(-1.8)^2+(-0.3)^2}\\ \sqrt{61.4^2+10.2^2+(-7.5)^2+(-0.9)^2+2.0^2+0.7^2}\\ \sqrt{65.8^2+(-2.5)^2+(-5.5)^2+3.0^2+(-0.8)^2+(-1.2)^2}\\ \sqrt{59.5^2+(-10.9)^2+2.4^2+0.5^2+(-1.1)^2+1.4^2}\\ \sqrt{36.7^2+(-9.0)^2+4.3^2+(-1.7)^2+1.0^2+(-0.7)^2}\end{Bmatrix}=\begin{Bmatrix}45.7\\58.0\\62.7\\66.2\\60.6\\38.1\end{Bmatrix}\ \text{mm}$$

For checking drift against the limits in ASCE 7-2010, the drift ratio is calculated as:

$$\{\Delta u\}_{\mathrm{T}}\cdot\frac{C_{\mathrm{d}}}{R}\cdot\frac{1}{h_{\mathrm{s},i}}=\begin{Bmatrix}45.7/4304\\58.0/4304\\62.7/4304\\66.2/4304\\60.6/4304\\38.1/4420\end{Bmatrix}\times\left(5.5/8\right)=\begin{Bmatrix}0.007\\0.009\\0.010\\0.011\\0.010\\0.006\end{Bmatrix}$$

Thus the calculated drift is less that the maximum allowable drift $0.02h_{\mathrm{s}}$ per criteria in Table 12.12-1 in ASCE 7-2010.

12) Not used.

13) Not used.

14) Not used.

15) The relative velocity of each self-centering device for each mode is calculated using Equations (6-58) and (6-59):

$$\{\nabla\}_{j1} = \frac{2\pi}{T_1}\{\Delta u\}_1 \cos\theta_j CFV(T_1,\beta_1) = \frac{2\pi}{2.06}\begin{Bmatrix} 36.6\cdot\cos 27.6 \\ 53.3\cdot\cos 27.6 \\ 61.4\cdot\cos 27.6 \\ 65.8\cdot\cos 27.6 \\ 59.5\cdot\cos 27.6 \\ 36.7\cdot\cos 28.2 \end{Bmatrix} CFV(2.06, 0.150) = \begin{Bmatrix} 108.6 \\ 158.1 \\ 182.2 \\ 195.2 \\ 176.5 \\ 108.3 \end{Bmatrix} \text{ mm/sec}$$

$$\{\nabla\}_{j2} = \frac{2\pi}{T_2}\{\Delta u\}_2 \cos\theta_j CFV(T_2,\beta_2) = \frac{2\pi}{0.75}\begin{Bmatrix} 23.6\cdot\cos 27.6 \\ 22.5\cdot\cos 27.6 \\ 10.2\cdot\cos 27.6 \\ (-2.5)\cdot\cos 27.6 \\ (-10.9)\cdot\cos 27.6 \\ (-9.0)\cdot\cos 28.2 \end{Bmatrix} CFV(0.75, 0.390) = \begin{Bmatrix} 136.9 \\ 130.5 \\ 59.2 \\ -14.5 \\ -63.2 \\ -51.9 \end{Bmatrix} \text{ mm/sec}$$

$$\{\nabla\}_{j3} = \frac{2\pi}{T_3}\{\Delta u\}_3 \cos\theta_j CFV(T_3,\beta_3) = \frac{2\pi}{0.44}\begin{Bmatrix} 13.2\cdot\cos 27.6 \\ 2.2\cdot\cos 27.6 \\ (-7.5)\cdot\cos 27.6 \\ (-5.5)\cdot\cos 27.6 \\ 2.4\cdot\cos 27.6 \\ 4.3\cdot\cos 28.2 \end{Bmatrix} CFV(0.44, 0.520) = \begin{Bmatrix} 111.5 \\ 18.6 \\ -63.3 \\ -46.5 \\ 20.3 \\ 36.1 \end{Bmatrix} \text{ mm/sec}$$

$$\{\nabla\}_{j4} = \frac{2\pi}{T_4}\{\Delta u\}_4 \cos\theta_j CFV(T_4,\beta_4) = \frac{2\pi}{0.29}\begin{Bmatrix} 4.3\cdot\cos 27.6 \\ (-3.2)\cdot\cos 27.6 \\ (-0.9)\cdot\cos 27.6 \\ 3.0\cdot\cos 27.6 \\ 0.5\cdot\cos 27.6 \\ (-1.7)\cdot\cos 28.2 \end{Bmatrix} CFV(0.29, 0.517) = \begin{Bmatrix} 51.6 \\ -38.4 \\ -10.8 \\ 36.0 \\ 6.0 \\ -20.3 \end{Bmatrix} \text{ mm/sec}$$

$$\{\nabla\}_{j5} = \frac{2\pi}{T_5}\{\Delta u\}_5 \cos\theta_j CFV(T_5,\beta_5) = \frac{2\pi}{0.21}\begin{Bmatrix} 1.1\cdot\cos 27.6 \\ (-1.8)\cdot\cos 27.6 \\ 2.0\cdot\cos 27.6 \\ (-0.8)\cdot\cos 27.6 \\ (-1.1)\cdot\cos 27.6 \\ 1.0\cdot\cos 28.2 \end{Bmatrix} CFV(0.21, 0.455) = \begin{Bmatrix} 18.9 \\ -30.9 \\ 34.4 \\ -13.7 \\ -18.9 \\ 17.1 \end{Bmatrix} \text{ mm/sec}$$

$$\{\nabla\}_{j6} = \frac{2\pi}{T_6}\{\Delta u\}_6 \cos\theta_j CFV(T_6,\beta_6) = \frac{2\pi}{0.16}\begin{Bmatrix} 0.1\cdot\cos 27.6 \\ (-0.3)\cdot\cos 27.6 \\ 0.7\cdot\cos 27.6 \\ (-1.2)\cdot\cos 27.6 \\ 1.4\cdot\cos 27.6 \\ (-0.7)\cdot\cos 28.2 \end{Bmatrix} CFV(0.16, 0.394) = \begin{Bmatrix} 2.3 \\ -7.0 \\ 16.4 \\ -28.0 \\ 32.7 \\ -16.3 \end{Bmatrix} \text{ mm/sec}$$

Factor *CFV* was obtained from the data in Table 5-3: *CFV*(for T=2.06sec,β=0.15)=1.0976, *CFV*(for 0.75sec,0.390)=0.7815, *CFV*(for 0.44sec,0.520)=0.6674, *CFV*(for 0.29sec,0.517)=0.6249, *CFV*(for 0.21sec,0.455)=0.6480 and *CFV* (for 0.16sec,0.394)=0.6712, for the first, second, third, fourth, fifth and sixth mode, respectively.

16) The device velocities are obtained by combining the modal device velocities by the SRSS rule:

$$\{\nabla\}_{\mathrm{T}} = \begin{Bmatrix} \sqrt{108.6^2+136.9^2+111.5^2+51.6^2+18.9^2+2.3^2} \\ \sqrt{158.1^2+130.5^2+18.6^2+(-38.4)^2+(-30.9)^2+(-7.0)^2} \\ \sqrt{182.2^2+59.2^2+(-63.3)^2+(-10.8)^2+34.4^2+16.4^2} \\ \sqrt{195.2^2+(-14.5)^2+(-46.5)^2+36.0^2+(-13.7)^2+(-28.0)^2} \\ \sqrt{176.5^2+(-63.2)^2+20.3^2+6.0^2+(-18.9)^2+32.7^2} \\ \sqrt{108.3^2+(-51.9)^2+36.1^2+(-20.3)^2+17.1^2+(-16.3)^2} \end{Bmatrix} = \begin{Bmatrix} 214.5 \\ 211.8 \\ 205.6 \\ 206.7 \\ 192.4 \\ 129.2 \end{Bmatrix} \text{ mm/sec}$$

Also, the device displacements are calculated as $\Delta u_{iT}\cos\theta_i$, m=1, 2, and 3, where Δu_{iT} are the drifts calculated in step 11:

$$\{\Delta u \cos\theta\}_{\mathrm{T}} = \begin{Bmatrix} 45.7\cdot\cos 27.6 \\ 58.0\cdot\cos 27.6 \\ 62.7\cdot\cos 27.6 \\ 66.2\cdot\cos 27.6 \\ 60.6\cdot\cos 27.6 \\ 38.1\cdot\cos 27.6 \end{Bmatrix} = \begin{Bmatrix} 40.5 \\ 51.4 \\ 55.6 \\ 58.7 \\ 53.7 \\ 33.6 \end{Bmatrix} \text{ mm}$$

17) The peak damping force in each self-centering device is calculated by use of Equation (6-60):

$$\{F_{\mathrm{v},i}\}_{\mathrm{T}} = \{C_i\}\{\nabla\}_{\mathrm{T}}$$

Thus,

$$\{F_{\mathrm{v},i}\} = \begin{Bmatrix} 2900 \\ 2900 \\ 2900 \\ 2900 \\ 2900 \\ 2900 \end{Bmatrix} \cdot \begin{Bmatrix} 214.5 \\ 211.8 \\ 205.6 \\ 206.7 \\ 192.4 \\ 129.2 \end{Bmatrix} \cdot \frac{1}{10^3} = \begin{Bmatrix} 622.1 \\ 614.2 \\ 596.2 \\ 599.4 \\ 558.0 \\ 374.7 \end{Bmatrix} \text{ kN}$$

18) The peak self-centering device force is expressed using Equation (6-61):

$$\left\{F_{\mathrm{D},i\mathrm{MAX}}\right\}_{\mathrm{T}}=\left\{F_{\min,i}\right\}+\left\{F_{0,i}\right\}+\left\{K_{0,i}\right\}u+\left\{F_{\mathrm{v},i}\right\}\sqrt{1-\left(u/u_{\mathrm{D},i\mathrm{T}}\right)^{2}}$$

Thus,

$$\left\{F_{\mathrm{D},i\mathrm{MAX}}\right\}_{\mathrm{T}}=0.05\times\begin{Bmatrix}100\\250\\250\\400\\400\\400\end{Bmatrix}+\begin{Bmatrix}100\\250\\250\\400\\400\\400\end{Bmatrix}+\begin{Bmatrix}1350\\1790\\1790\\2230\\2230\\2230\end{Bmatrix}\begin{Bmatrix}u_6\\u_5\\u_4\\u_3\\u_2\\u_1\end{Bmatrix}+\begin{Bmatrix}622.1\\614.2\\596.2\\599.4\\558.0\\374.7\end{Bmatrix}\begin{Bmatrix}\sqrt{1-\left(u_6/40.5\right)^2}\\\sqrt{1-\left(u_5/51.4\right)^2}\\\sqrt{1-\left(u_4/55.6\right)^2}\\\sqrt{1-\left(u_3/58.7\right)^2}\\\sqrt{1-\left(u_2/53.7\right)^2}\\\sqrt{1-\left(u_1/33.6\right)^2}\end{Bmatrix}=\begin{Bmatrix}769.4\\883.6\\867.0\\1033.5\\990.7\\802.1\end{Bmatrix}\ \mathrm{kN}$$

The maximum values of force were calculated for displacements $\{u_6, u_5, u_4, u_3, u_2, u_1\}$ = {3.3, 7.6, 9.2, 12.5, 11.3, 6.6} (mm).

19) The peak shear force in each story is calculated as:

$$\left\{V_{\mathrm{D},i\mathrm{MAX}}\right\}_{\mathrm{T}}=\left\{V\right\}_{\mathrm{T}}+\left\{F_{\mathrm{D},i\mathrm{MAX}}\right\}_{\mathrm{T}}\cdot\cos\theta_i=\begin{Bmatrix}400\\1000\\1250\\1550\\1700\\1750\end{Bmatrix}+\begin{Bmatrix}769.4\cdot\cos 27.6^\circ\\883.6\cdot\cos 27.6^\circ\\867.0\cdot\cos 27.6^\circ\\1033.5\cdot\cos 27.6^\circ\\990.7\cdot\cos 27.6^\circ\\802.1\cdot\cos 28.2^\circ\end{Bmatrix}=\begin{Bmatrix}1081.8\\1783.0\\2018.3\\2465.9\\2578.0\\2456.9\end{Bmatrix}\ \mathrm{kN}$$

Calculation of response in the Design Earthquake using the Equivalent Lateral Force (ELF) procedure

The steps described in the corresponding part of Section 6.5 are followed.

1) Step 1 is the same as step 1 of the RSA procedure.

2) T_1, $\{\phi\}_1$ and Γ_1 are the same as those obtained in the RSA procedure: T_1=2.06 *sec*, $\{\phi\}_1$=[1.000,0.883,0.713,0.517,0.307,0.117]$^{\mathrm{T}}$ and Γ_1=1.397. The residual period T_{R} is calculated using Equation (6-28):

$$T_{\mathrm{R}}=0.4T_1=0.4\cdot 2.06=0.82\ \ \mathrm{sec}$$

The residual modal participation factor Γ_R is calculated using Equation (6-26):

$$\Gamma_{\mathrm{R}} = 1 - \Gamma_1 = 1 - 1.397 = -0.397$$

The residual modal shape is calculated using Equation (6-27):

$$\{\phi\}_{\mathrm{R}} = \frac{\{1\} - \Gamma_1 \cdot \{\phi\}_1}{\Gamma_{\mathrm{R}}} = \frac{\{1\} - 1.397 \cdot \{\phi\}_1}{-0.397} = \left(\begin{bmatrix} 1.000 \\ 1.000 \\ 1.000 \\ 1.000 \\ 1.000 \\ 1.000 \end{bmatrix} - 1.397 \cdot \begin{bmatrix} 1.000 \\ 0.883 \\ 0.713 \\ 0.517 \\ 0.307 \\ 0.117 \end{bmatrix} \right) \cdot \frac{1}{-0.397} = \begin{bmatrix} 1.000 \\ 0.588 \\ -0.010 \\ -0.700 \\ -1.439 \\ -2.107 \end{bmatrix}$$

The modal drifts $\{\phi_{\mathrm{r}}\}_{\mathrm{R}}$ are calculated from the modal displacements $\{\phi\}_{\mathrm{R}}$ as:

$$\{\phi_{\mathrm{r}}\}_{\mathrm{R}} = [0.412, 0.598, 0.690, 0.739, 0.668, -2.107]^{\mathrm{T}}$$

3) The damping ratio for m=1 is β_{v1}= 0.10 as obtained in step 3 of the RSA procedure.

For the residual mode,

$$\beta_{\mathrm{vR}} = \frac{0.82}{4\pi} \cdot 9.81 \cdot \frac{\left[\left(0.412^2 + 0.598^2 + 0.690^2 + 0.739^2 + 0.668^2\right) \times \cos^2 27.6° + (-2.107)^2 \times \cos^2 28.2°\right] \times 2900}{1.000^2 \times 1567 + \left(0.588^2 + (-0.010)^2 + (-0.700)^2 + (-1.439)^2 + (-2.107)^2\right) \times 2900} = 0.407$$

4-9) Steps 4 to 9 are the same as steps 4 to 9 of the RSA procedure.

10) The displacements contributed by the residual mode are given by Equation (6-57) for m=R:

$$\{u\}_{\mathrm{R}} = \frac{\Gamma_{\mathrm{R}} \{\phi\}_{\mathrm{R}} T_{\mathrm{R}}^2 S_{\mathrm{a}}(T_{\mathrm{R}}, \beta = 0.05) g}{4\pi^2 B_{\mathrm{R}}} = \frac{|-0.397| \times 0.82^2 \times 0.7211 \times 9810}{4\pi^2 \times 2.271} \begin{Bmatrix} 1.000 \\ 0.588 \\ -0.010 \\ -0.700 \\ -1.439 \\ -2.107 \end{Bmatrix} = \begin{Bmatrix} 21.1 \\ 12.4 \\ -0.2 \\ -14.7 \\ -30.3 \\ -44.4 \end{Bmatrix} \text{ mm}$$

The modal damping ratio was obtained using Equation (6-53):

$$\beta_{\mathrm{R}} = \beta_i + \beta_{\mathrm{vR}} = 0.05 + 0.407 = 0.457$$

The damping coefficient is B_{R}=2.271 (Table 18.6-1 in ASCE 7-2010).

Story drifts for the residual mode are calculated as:

$$\{\Delta u\}_{\mathrm{R}} = \begin{Bmatrix} 21.1-12.4 \\ 12.4-(-0.2) \\ -0.2-(-14.7) \\ -14.7-(-30.3) \\ -30.3-(-44.4) \\ -44.4 \end{Bmatrix} = \begin{Bmatrix} 8.7 \\ 12.6 \\ 14.5 \\ 15.6 \\ 14.1 \\ -44.4 \end{Bmatrix} \text{ mm}$$

11) The total displacements and drifts are calculated by combining first mode and residual mode responses by SRSS:

$$\{u\}_{\mathrm{T}} = \begin{Bmatrix} \sqrt{313.3^2+21.1^2} \\ \sqrt{276.7^2+12.4^2} \\ \sqrt{223.4^2+(-0.2)^2} \\ \sqrt{162.0^2+(-14.7)^2} \\ \sqrt{96.2^2+(-30.3)^2} \\ \sqrt{36.7^2+(-44.4)^2} \end{Bmatrix} = \begin{Bmatrix} 314.0 \\ 277.0 \\ 223.4 \\ 162.7 \\ 100.9 \\ 57.6 \end{Bmatrix} \text{ mm}$$

$$\{\Delta u\}_{\mathrm{T}} = \begin{Bmatrix} \sqrt{36.6^2+8.7^2} \\ \sqrt{53.3^2+12.6^2} \\ \sqrt{61.4^2+14.5^2} \\ \sqrt{65.8^2+15.6^2} \\ \sqrt{59.5^2+14.1^2} \\ \sqrt{36.7^2+(-44.4)^2} \end{Bmatrix} = \begin{Bmatrix} 37.6 \\ 54.8 \\ 63.1 \\ 67.6 \\ 61.1 \\ 57.6 \end{Bmatrix} \text{ mm}$$

For checking drift against the limits of ASCE 7-2010, the drift ratio is calculated as:

$$\{\Delta u\}_{\mathrm{T}} \cdot \frac{C_{\mathrm{d}}}{R} \cdot \frac{1}{h_{\mathrm{s},i}} = \begin{Bmatrix} 37.6/4304 \\ 54.8/4304 \\ 63.1/4304 \\ 67.6/4304 \\ 61.1/4304 \\ 57.6/4420 \end{Bmatrix} . 5.5/8 = \begin{Bmatrix} 0.006 \\ 0.009 \\ 0.010 \\ 0.0011 \\ 0.010 \\ 0.009 \end{Bmatrix}$$

Thus the design satisfies the maximum allowable drift criteria in Table 12.12-1 in ASCE 7-2010.

12) Not used.

13) Not used.

14) Not used.

15) The relative velocity in each self-centering device for the first mode has been calculated in the corresponding step of RSA. For the residual mode the relative velocity is calculated using Equation (6-59) for m=R:

$$\{\nabla\}_{\mathrm{R}} = \frac{2\pi}{T_{\mathrm{R}}} \cdot \{\Delta u\}_{\mathrm{R}} \cdot \cos\theta_j \cdot CFV\left(T_{\mathrm{R}}, \beta_{\mathrm{R}}\right) = \frac{2\pi}{0.82} \cdot \begin{Bmatrix} 8.7 \cdot \cos 27.6 \\ 12.6 \cdot \cos 27.6 \\ 14.5 \cdot \cos 27.6 \\ 15.6 \cdot \cos 27.6 \\ 14.1 \cdot \cos 27.6 \\ (-44.4) \cdot \cos 28.2 \end{Bmatrix} \cdot CFV\left(0.82, 0.457\right) = \begin{Bmatrix} 47.7 \\ 69.1 \\ 79.5 \\ 85.6 \\ 77.3 \\ -242.1 \end{Bmatrix} \text{ mm/sec}$$

Factor CFV was obtained from the data in Table 5-3: CFV (for T_{R}=0.82sec, β_{R}=0.457) =0.8076.

16) By combining the first and residual mode responses by SRSS, the device relative velocity is obtained:

$$\{\nabla\}_{\mathrm{T}} = \begin{Bmatrix} \sqrt{108.6^2 + 47.7^2} \\ \sqrt{158.1^2 + 69.1^2} \\ \sqrt{182.2^2 + 79.5^2} \\ \sqrt{195.2^2 + 85.6^2} \\ \sqrt{176.5^2 + 77.3^2} \\ \sqrt{108.3^2 + (-242.1)^2} \end{Bmatrix} = \begin{Bmatrix} 118.6 \\ 172.5 \\ 198.8 \\ 213.1 \\ 192.7 \\ 265.2 \end{Bmatrix} \text{ mm/sec}$$

Also, the device relative displacements are calculated as $\Delta u_{iT} \cos\theta_i$, where Δu_{iT} are the drifts calculated in step 11:

$$\{\Delta u \cos\theta\}_{\mathrm{T}} = \begin{Bmatrix} 37.6 \cdot \cos 27.6^\circ \\ 54.8 \cdot \cos 27.6^\circ \\ 63.1 \cdot \cos 27.6^\circ \\ 67.6 \cdot \cos 27.6^\circ \\ 61.1 \cdot \cos 27.6^\circ \\ 57.6 \cdot \cos 28.2^\circ \end{Bmatrix} = \begin{Bmatrix} 33.3 \\ 48.6 \\ 55.9 \\ 59.9 \\ 54.1 \\ 50.8 \end{Bmatrix} \text{ mm}$$

17) The peak damping force in each self-centering device is calculated by use of Equation (6-60):

$$\left\{F_{\mathrm{v},i}\right\}_{\mathrm{T}}=\left\{C_i\right\}\left\{\nabla\right\}_{\mathrm{T}}$$

Thus,

$$\left\{F_{\mathrm{v},i}\right\}_{\mathrm{T}}=2900\cdot\begin{Bmatrix}118.6\\172.5\\198.8\\213.1\\192.7\\265.2\end{Bmatrix}\cdot\frac{1}{10^3}=\begin{Bmatrix}343.9\\500.3\\576.5\\618.0\\558.8\\769.1\end{Bmatrix}\ \mathrm{kN}$$

18) The peak self-centering device force is calculated using Equation (6-61):

$$\left\{F_{\mathrm{D},i\mathrm{MAX}}\right\}_{\mathrm{T}}=\left\{F_{\min,i}\right\}+\left\{F_{0,i}\right\}+\left\{K_{0,i}\right\}u+\left\{F_{\mathrm{v},i}\right\}\sqrt{1-\left(u/u_{\mathrm{D},i\mathrm{T}}\right)^2}$$

Thus,

$$\left\{F_{\mathrm{D},i\mathrm{MAX}}\right\}_{\mathrm{T}}=0.05\times\begin{Bmatrix}100\\250\\250\\400\\400\\400\end{Bmatrix}+\begin{Bmatrix}100\\250\\250\\400\\400\\400\end{Bmatrix}+\begin{Bmatrix}1350\\1790\\1790\\2230\\2230\\2230\end{Bmatrix}\begin{Bmatrix}u_6\\u_5\\u_4\\u_3\\u_2\\u_1\end{Bmatrix}+\begin{Bmatrix}343.9\\500.3\\576.5\\618.0\\558.8\\769.1\end{Bmatrix}\begin{Bmatrix}\sqrt{1-\left(u_6/33.3\right)^2}\\\sqrt{1-\left(u_5/48.6\right)^2}\\\sqrt{1-\left(u_4/55.9\right)^2}\\\sqrt{1-\left(u_3/59.9\right)^2}\\\sqrt{1-\left(u_2/54.1\right)^2}\\\sqrt{1-\left(u_1/50.8\right)^2}\end{Bmatrix}=\begin{Bmatrix}451.8\\770.3\\847.6\\1052.3\\991.7\\1197.4\end{Bmatrix}\ \mathrm{kN}$$

The maximum values of force were calculated for displacements $\{u_6, u_5, u_4, u_3, u_2, u_1\}$ = {4.3, 8.3, 9.6, 12.7, 11.4, 7.4} (*mm*).

19) The peak shear force in each story is calculated as:

$$\left\{V_{\mathrm{D},i\mathrm{MAX}}\right\}_{\mathrm{T}}=\left\{V\right\}_{\mathrm{T}}+\left\{F_{\mathrm{D},i\mathrm{MAX}}\right\}_{\mathrm{T}}\cdot\cos\theta_i=\begin{Bmatrix}400\\1000\\1250\\1550\\1700\\1750\end{Bmatrix}+\begin{Bmatrix}451.8\cdot\cos 27.6^\circ\\770.3\cdot\cos 27.6^\circ\\847.6\cdot\cos 27.6^\circ\\1052.3\cdot\cos 27.6^\circ\\991.7\cdot\cos 27.6^\circ\\1197.4\cdot\cos 28.2^\circ\end{Bmatrix}=\begin{Bmatrix}800.4\\1682.6\\2001.1\\2482.6\\2578.8\\2805.3\end{Bmatrix}\ \mathrm{kN}$$

Calculation of response in the Maximum Considered Earthquake using the Response Spectrum Analysis (RSA) procedure

The steps described in Section 6.5 are followed. The Steps 1) – 4) are same as the design example for Design Earthquake. Step 5) and thereafter are presented.

5) Assume the value of displacement D_{M} in the single-degree-of-freedom spectral representation of the pushover curve as D_{M}=280 mm. Ductility ratio μ is calculated using Equation (6-46):

$$\mu = \frac{D_{\mathrm{M}}}{D_{\mathrm{y}}} = \frac{280.0}{195.7} = 1.43$$

6) The effective period T_{eff} is calculated using Equation (6-44):

$$T_{\mathrm{eff}} = T_1\sqrt{\mu}\sqrt{\frac{A_{\mathrm{y}} + A_{\mathrm{F0}}}{A_{\mathrm{y}} + 2A_{\mathrm{F0}}}} = 2.06\sqrt{1.43}\sqrt{\frac{0.140g + 0.032g}{0.140g + 2\times 0.032g}} = 2.26 \quad \text{sec}$$

Quantities A_y and A_{F0} were calculated using Equations (6-41) and (6-45):

$$A_{\mathrm{y}} = \frac{V_{\mathrm{y}}g}{\overline{W}_1} = \frac{1750\times g}{12464.1} = 0.140g$$

$$A_{\mathrm{F0}} = \frac{F_{01}g}{\overline{W}_1} = \frac{400\times g}{12464.1} = 0.032g$$

The effective damping ratio is calculated using Equation (6-47):

$$\beta_{\mathrm{eff}} = \beta_i + \beta_{\mathrm{v1}} \times \frac{T_{\mathrm{eff}}}{T_1} + \frac{1.42q_{\mathrm{H}}}{\pi}\left(1 - \frac{1}{\mu}\right) = 0.05 + 0.1\times\frac{2.26}{2.06} + \frac{1.42\times 1.0}{\pi}\left(1 - \frac{1}{1.43}\right) = 0.296$$

Note that q_{H}=1.0. Using Table 18.6-1 of ASCE 7-2010 the damping factor B=1.788.

7) Displacement D_{M} for the Maximum Considered Earthquake is calculated using Equation (6-55):

$$D_{\mathrm{M}} = \frac{T_{\mathrm{eff}}^2 (1.5) S_{\mathrm{a}}\left(T_{\mathrm{eff}}, \beta = 0.05\right) g}{4\pi^2 B} = \frac{2.26^2 \times 1.5 \times 0.2617 \times 9810}{4\pi^2 \times 1.788} = 278.6 \quad \text{mm}$$

Before proceeding to additional iterations for the calculation of the displacement, the elastic displacement demand is calculated.

8) The displacement demand is calculated again considering elastic conditions

$$D_{\mathrm{M}} = \frac{T_1^2 (1.5) S_{\mathrm{a}}\left(T_1, \beta = 0.05\right) g}{4\pi^2 B_{\mathrm{E}}} = \frac{2.06^2 \times 1.5 \times 0.2871 \times 9810}{4\pi^2 \times 1.35} = 336.4 \quad \text{mm}$$

Note that the damping factor B=1.35 was obtained from Table 18.6-1 in ASCE 7-2010 for damping ratio $\beta_i+\beta_{v1}$=0.05+0.10=0.15. Since the elastic displacement D_M (=336.4mm) is larger than the inelastic D_M (=278.6 mm), the elastic value is used so that D_M=336.4mm. Still the frame has yielded as the displacement exceeds the yield displacement D_y=195.7mm.

9) The displacements contributed by the fundamental mode are given by Equation (6-56):

$$\{u\}_1 = \Gamma_1\{\phi\}_1 D_M = 1.397\cdot\begin{Bmatrix}1.000\\0.883\\0.713\\0.517\\0.307\\0.117\end{Bmatrix}\cdot 336.4 = \begin{Bmatrix}470.0\\415.0\\335.1\\243.0\\144.3\\55.0\end{Bmatrix} \text{ mm}$$

Story drifts are calculated as:

$$\{\Delta u\}_1 = \begin{Bmatrix}470.0-415.0\\415.0-335.1\\335.1-243.0\\243.0-144.3\\144.3-55.0\\55.0\end{Bmatrix} = \begin{Bmatrix}55.0\\79.9\\92.1\\98.7\\89.3\\55.0\end{Bmatrix} \text{ mm}$$

10) The displacements contributed by the higher modes are (Equation (6-57)):

$$\{u\}_2 = \frac{\Gamma_2\{\phi\}_2 T_2^2(1.5)S_a(T_2,\beta=0.05)g}{4\pi^2 B_2} = \frac{|-0.637|\times 0.75^2\times 1.5\times 0.7884\times 9810}{4\pi^2\times 2.070}\begin{Bmatrix}1.000\\0.305\\-0.359\\-0.662\\-0.587\\-0.266\end{Bmatrix} = \begin{Bmatrix}50.9\\15.5\\-18.3\\-33.7\\-29.9\\-13.5\end{Bmatrix} \text{ mm}$$

$$\{u\}_3 = \frac{\Gamma_3\{\phi\}_3 T_3^2(1.5)S_a(T_3,\beta=0.05)g}{4\pi^2 B_3} = \frac{|0.371|\times 0.44^2\times 1.5\times 1.2507\times 9810}{4\pi^2\times 2.460}\begin{Bmatrix}1.000\\-0.454\\-0.691\\0.137\\0.736\\0.478\end{Bmatrix} = \begin{Bmatrix}13.6\\-6.2\\-9.4\\1.9\\10.0\\6.5\end{Bmatrix} \text{ mm}$$

$$\{u\}_4 = \frac{\Gamma_4\{\phi\}_4 T_4^2(1.5)S_a(T_4,\beta=0.05)g}{4\pi^2 B_4} = \frac{|-0.183|\times 0.29^2\times 1.5\times 1.2507\times 9810}{4\pi^2\times 2.451}\begin{Bmatrix} 1.000 \\ -1.199 \\ 0.480 \\ 0.912 \\ -0.629 \\ -0.871 \end{Bmatrix} = \begin{Bmatrix} 2.9 \\ -3.5 \\ 1.4 \\ 2.7 \\ -1.8 \\ -2.5 \end{Bmatrix} \text{ mm}$$

$$\{u\}_5 = \frac{\Gamma_5\{\phi\}_5 T_5^2(1.5)S_a(T_5,\beta=0.05)g}{4\pi^2 B_5} = \frac{|0.062|\times 0.21^2\times 1.5\times 1.2507\times 9810}{4\pi^2\times 2.265}\begin{Bmatrix} 1.000 \\ -1.827 \\ 2.923 \\ -2.337 \\ -0.328 \\ 2.537 \end{Bmatrix} = \begin{Bmatrix} 0.6 \\ -1.0 \\ 1.6 \\ -1.3 \\ -0.2 \\ 1.4 \end{Bmatrix} \text{ mm}$$

$$\{u\}_6 = \frac{\Gamma_6\{\phi\}_6 T_6^2(1.5)S_a(T_6,\beta=0.05)g}{4\pi^2 B_6} = \frac{|-0.010|\times 0.16^2\times 1.5\times 1.2507\times 9810}{4\pi^2\times 2.082}\begin{Bmatrix} 1.000 \\ -2.357 \\ 6.249 \\ -11.980 \\ 17.518 \\ -17.880 \end{Bmatrix} = \begin{Bmatrix} 0.1 \\ -0.1 \\ 0.4 \\ -0.7 \\ 1.0 \\ -1.0 \end{Bmatrix} \text{ mm}$$

Note that the modal damping ratios were obtained by use of Equation (6-53):

$$\beta_2 = \beta_i + \beta_{v2} = 0.05 + 0.340 = 0.390$$

$$\beta_3 = \beta_i + \beta_{v3} = 0.05 + 0.470 = 0.520$$

$$\beta_4 = \beta_i + \beta_{v4} = 0.05 + 0.467 = 0.517$$

$$\beta_5 = \beta_i + \beta_{v5} = 0.05 + 0.405 = 0.455$$

$$\beta_6 = \beta_i + \beta_{v6} = 0.05 + 0.344 = 0.394$$

The damping factors based on these values of damping ratio are B_2=2.070, B_3=2.460, B_4=2.451, B_5=2.265, and B_6=2.082 (Table 18.6-1 in ASCE 7-2010).

Story drifts are calculated as:

$$\{\Delta u\}_2 = \begin{Bmatrix} 50.6-15.5 \\ 15.5-(-18.3) \\ -18.3-(-33.7) \\ -33.7-(-29.9) \\ -29.9-(-13.5) \\ -13.5 \end{Bmatrix} = \begin{Bmatrix} 35.4 \\ 33.8 \\ 15.4 \\ -3.8 \\ -16.4 \\ -13.5 \end{Bmatrix} \text{ mm}$$

$$\{\Delta u\}_3 = \begin{Bmatrix} 13.6-(-6.2) \\ -6.2-(-9.4) \\ -9.4-1.9 \\ 1.9-10.0 \\ 10.0-6.5 \\ 6.5 \end{Bmatrix} = \begin{Bmatrix} 19.8 \\ 3.2 \\ -11.3 \\ -8.1 \\ 3.5 \\ 6.5 \end{Bmatrix} \text{ mm}$$

$$\{\Delta u\}_4 = \begin{Bmatrix} 2.9-(-3.5) \\ -3.5-1.4 \\ 1.4-2.7 \\ 2.7-(-1.8) \\ -1.8-(-2.5) \\ -2.5 \end{Bmatrix} = \begin{Bmatrix} 6.4 \\ -4.9 \\ -1.3 \\ 4.5 \\ 0.7 \\ -2.5 \end{Bmatrix} \text{ mm}$$

$$\{\Delta u\}_5 = \begin{Bmatrix} 0.6-(-1.0) \\ -1.0-1.6 \\ 1.6-(-1.3) \\ -1.3-(-0.2) \\ -0.2-1.4 \\ 1.4 \end{Bmatrix} = \begin{Bmatrix} 1.6 \\ -2.6 \\ 2.9 \\ -1.1 \\ -1.6 \\ 1.4 \end{Bmatrix} \text{ mm}$$

$$\{\Delta u\}_6 = \begin{Bmatrix} 0.0-(-0.1) \\ -0.1-0.4 \\ 0.4-(-0.7) \\ -0.7-1.0 \\ 1.0-(-1.0) \\ -1.0 \end{Bmatrix} = \begin{Bmatrix} 0.2 \\ -0.5 \\ 1.1 \\ -1.7 \\ 2.0 \\ -1.0 \end{Bmatrix} \text{ mm}$$

11) Combining the modal displacements and drifts by the SRSS rule:

$$\{u\}_{\mathrm{T}} = \begin{Bmatrix} \sqrt{470.0^2+50.9^2+13.6^2+2.9^2+0.6^2+0.1^2} \\ \sqrt{415.0^2+15.5^2+(-6.2)^2+(-3.5)^2+(-1.0)^2+(-0.1)^2} \\ \sqrt{335.1^2+(-18.3)^2+(-9.4)^2+1.4^2+1.6^2+0.4^2} \\ \sqrt{243.0^2+(-33.7)^2+1.9^2+2.7^2+(-1.3)^2+(-0.7)^2} \\ \sqrt{144.3^2+(-29.9)^2+10.0^2+(-1.8)^2+(-0.2)^2+1.0^2} \\ \sqrt{55.0^2+(-13.5)^2+6.5^2+(-2.5)^2+1.4^2+(-1.0)^2} \end{Bmatrix} = \begin{Bmatrix} 473.0 \\ 415.4 \\ 335.7 \\ 245.4 \\ 147.7 \\ 57.1 \end{Bmatrix} \text{ mm}$$

$$\{\Delta u\}_{\mathrm{T}} = \begin{Bmatrix} \sqrt{55.0^2+35.4^2+19.8^2+6.4^2+1.6^2+0.2^2} \\ \sqrt{79.9^2+33.8^2+3.2^2+(-4.9)^2+(-2.6)^2+(-0.5)^2} \\ \sqrt{92.1^2+15.4^2+(-11.3)^2+(-1.3)^2+2.9^2+1.1^2} \\ \sqrt{98.7^2+(-3.8)^2+(-8.1)^2+4.5^2+(-1.1)^2+(-1.7)^2} \\ \sqrt{89.3^2+(-16.4)^2+3.5^2+0.7^2+(-1.6)^2+2.0^2} \\ \sqrt{55.0^2+(-13.5)^2+6.5^2+(-2.5)^2+1.4^2+(-1.0)^2} \end{Bmatrix} = \begin{Bmatrix} 68.7 \\ 87.0 \\ 94.1 \\ 99.2 \\ 90.9 \\ 57.1 \end{Bmatrix} \text{ mm}$$

12) Not used.

13) Not used.

14) Not used.

15) The relative velocity of each self-centering device for each mode is calculated using Equations (6-58) and (6-59):

$$\{\nabla\}_{j1} = \frac{2\pi}{T_1}\{\Delta u\}_1 \cos\theta_j CFV(T_1,\beta_1) = \frac{2\pi}{2.06}\begin{Bmatrix} 55.0\cdot\cos 27.6 \\ 79.9\cdot\cos 27.6 \\ 92.1\cdot\cos 27.6 \\ 98.7\cdot\cos 27.6 \\ 89.3\cdot\cos 27.6 \\ 55.0\cdot\cos 28.2 \end{Bmatrix} CFV(2.06, 0.150) = \begin{Bmatrix} 163.2 \\ 237.0 \\ 273.2 \\ 292.8 \\ 264.9 \\ 162.3 \end{Bmatrix} \text{ mm/sec}$$

$$\{\nabla\}_{j2} = \frac{2\pi}{T_2}\{\Delta u\}_2 \cos\theta_j CFV(T_2,\beta_2) = \frac{2\pi}{0.75}\begin{Bmatrix} 35.4\cdot\cos 27.6 \\ 33.8\cdot\cos 27.6 \\ 15.4\cdot\cos 27.6 \\ (-3.8)\cdot\cos 27.6 \\ (-16.4)\cdot\cos 27.6 \\ (-13.5)\cdot\cos 28.2 \end{Bmatrix} CFV(0.75, 0.390) = \begin{Bmatrix} 205.4 \\ 196.1 \\ 89.4 \\ -22.0 \\ -95.2 \\ -77.9 \end{Bmatrix} \text{ mm/sec}$$

$$\{\nabla\}_{j3} = \frac{2\pi}{T_3}\{\Delta u\}_3 \cos\theta_j CFV(T_3,\beta_3) = \frac{2\pi}{0.44}\begin{Bmatrix} 19.8\cdot\cos 27.6 \\ 3.2\cdot\cos 27.6 \\ (-11.3)\cdot\cos 27.6 \\ (-8.1)\cdot\cos 27.6 \\ 3.5\cdot\cos 27.6 \\ 6.5\cdot\cos 28.2 \end{Bmatrix} CFV(0.44, 0.520) = \begin{Bmatrix} 167.2 \\ 27.0 \\ -95.4 \\ -68.4 \\ 29.6 \\ 54.6 \end{Bmatrix} \text{ mm/sec}$$

$$\{\nabla\}_{j4}=\frac{2\pi}{T_4}\{\Delta u\}_4\cos\theta_j CFV\left(T_4,\beta_4\right)=\frac{2\pi}{0.29}\begin{Bmatrix}6.4\cdot\cos 27.6\\ (-4.9)\cdot\cos 27.6\\ (-1.3)\cdot\cos 27.6\\ 4.5\cdot\cos 27.6\\ 0.7\cdot\cos 27.6\\ (-2.5)\cdot\cos 28.2\end{Bmatrix}CFV\left(0.29,0.517\right)=\begin{Bmatrix}76.8\\ -58.8\\ -15.6\\ 54.0\\ 8.4\\ -30.0\end{Bmatrix}\text{ mm/sec}$$

$$\{\nabla\}_{j5}=\frac{2\pi}{T_5}\{\Delta u\}_5\cos\theta_j CFV\left(T_5,\beta_5\right)=\frac{2\pi}{0.21}\begin{Bmatrix}1.6\cdot\cos 27.6\\ (-2.6)\cdot\cos 27.6\\ 2.9\cdot\cos 27.6\\ (-1.1)\cdot\cos 27.6\\ (-1.6)\cdot\cos 27.6\\ 1.4\cdot\cos 28.2\end{Bmatrix}CFV\left(0.21,0.455\right)=\begin{Bmatrix}27.5\\ -44.7\\ 49.8\\ -18.9\\ -27.5\\ 23.9\end{Bmatrix}\text{ mm/sec}$$

$$\{\nabla\}_{j6}=\frac{2\pi}{T_6}\{\Delta u\}_6\cos\theta_j CFV\left(T_6,\beta_6\right)=\frac{2\pi}{0.16}\begin{Bmatrix}0.2\cdot\cos 27.6\\ (-0.5)\cdot\cos 27.6\\ 1.1\cdot\cos 27.6\\ (-1.7)\cdot\cos 27.6\\ 2.0\cdot\cos 27.6\\ (-1.0)\cdot\cos 28.2\end{Bmatrix}CFV\left(0.16,0.394\right)=\begin{Bmatrix}4.7\\ -11.7\\ 25.7\\ -39.7\\ 46.7\\ -23.2\end{Bmatrix}\text{ mm/sec}$$

Factor *CFV* was obtained from the data in Table 5-3: *CFV* (for T=2.06sec, β=0.15)=1.0976, *CFV* (for 0.75sec, 0.390)=0.7815, *CFV* (for 0.44sec, 0.520)=0.6674, *CFV* (for 0.29sec,0.517)=0.6249, *CFV* (for 0.21sec,0.455)=0.6480 and *CFV* (for 0.16sec, 0.394)=0.6712, for the first, second and third, fourth, fifth and sixth mode, respectively.

16) The device velocities are obtained by combining the modal device velocities by the SRSS rule:

$$\{\nabla\}_{\mathrm{T}}=\begin{Bmatrix}\sqrt{163.2^2+205.4^2+167.2^2+76.8^2+27.5^2+4.7^2}\\ \sqrt{237.0^2+196.1^2+27.0^2+(-58.8)^2+(-44.7)^2+(-11.7)^2}\\ \sqrt{273.2^2+89.4^2+(-95.4)^2+(-15.6)^2+49.8^2+25.7^2}\\ \sqrt{292.8^2+(-22.0)^2+(-68.4)^2+54.0^2+(-18.9)^2+(-39.7)^2}\\ \sqrt{264.9^2+(-95.2)^2+29.6^2+8.4^2+(-27.5)^2+46.7^2}\\ \sqrt{162.3^2+(-77.9)^2+54.6^2+(-30.0)^2+23.9^2+(-23.2)^2}\end{Bmatrix}=\begin{Bmatrix}321.6\\ 317.7\\ 308.4\\ 309.4\\ 288.3\\ 193.4\end{Bmatrix}\text{ mm/sec}$$

Also, the device displacements are calculated as $\Delta u_{iT}\cos\theta_i$, m=1, 2, and 3, where Δu_{iT} are the drifts calculated in step 11:

$$\left\{\Delta u\cos\theta\right\}_{\mathrm{T}}=\begin{Bmatrix}68.7\cdot\cos 27.6\\87.0\cdot\cos 27.6\\94.1\cdot\cos 27.6\\99.2\cdot\cos 27.6\\90.9\cdot\cos 27.6\\57.1\cdot\cos 27.6\end{Bmatrix}=\begin{Bmatrix}60.9\\77.1\\83.4\\87.9\\80.6\\50.6\end{Bmatrix}\ \text{mm}$$

17) The peak damping force in each self-centering device is calculated by use of Equation (6-60):

$$\left\{F_{\mathrm{v},i}\right\}_{\mathrm{T}}=\left\{C_i\right\}\left\{\nabla\right\}_{\mathrm{T}}$$

Thus,

$$\left\{F_{\mathrm{v},i}\right\}=\begin{Bmatrix}2900\\2900\\2900\\2900\\2900\\2900\end{Bmatrix}\cdot\begin{Bmatrix}321.6\\317.7\\308.4\\309.4\\288.3\\193.4\end{Bmatrix}\cdot\frac{1}{10^3}=\begin{Bmatrix}932.6\\921.3\\894.4\\897.3\\863.1\\560.9\end{Bmatrix}\ \text{kN}$$

18) The peak self-centering device force is expressed using Equation (6-61):

$$\left\{F_{\mathrm{M},i\mathrm{MAX}}\right\}_{\mathrm{T}}=\left\{F_{\min,i}\right\}+\left\{F_{0,i}\right\}+\left\{K_{0,i}\right\}u+\left\{F_{\mathrm{v},i}\right\}\sqrt{1-\left(u/u_{\mathrm{D},i\mathrm{T}}\right)^2}$$

Thus,

$$\left\{F_{\mathrm{M},i\mathrm{MAX}}\right\}_{\mathrm{T}}=0.05\times\begin{Bmatrix}100\\250\\250\\400\\400\\400\end{Bmatrix}+\begin{Bmatrix}100\\250\\250\\400\\400\\400\end{Bmatrix}+\begin{Bmatrix}1350\\1790\\1790\\2230\\2230\\2230\end{Bmatrix}\begin{Bmatrix}u_6\\u_5\\u_4\\u_3\\u_2\\u_1\end{Bmatrix}+\begin{Bmatrix}932.9\\921.9\\897.0\\906.0\\849.7\\565.8\end{Bmatrix}\begin{Bmatrix}\sqrt{1-\left(u_6/60.9\right)^2}\\\sqrt{1-\left(u_6/77.1\right)^2}\\\sqrt{1-\left(u_4/83.4\right)^2}\\\sqrt{1-\left(u_3/87.9\right)^2}\\\sqrt{1-\left(u_2/80.6\right)^2}\\\sqrt{1-\left(u_1/50.6\right)^2}\end{Bmatrix}=\begin{Bmatrix}1041.5\\1194.7\\1171.8\\1347.0\\1288.5\\996.9\end{Bmatrix}\ \text{kN}$$

The maximum values of force were calculated for displacements $\{u_6, u_5, u_4, u_3, u_2, u_1\}$ = {5.3, 11.4, 13.7, 18.6, 16.7, 9.9} (*mm*).

19) The peak shear force in each story is calculated as:

$$\{V_{\mathrm{M},i\mathrm{MAX}}\}_{\mathrm{T}} = \{V\}_{\mathrm{T}} + \{F_{\mathrm{M},i\mathrm{MAX}}\}_{\mathrm{T}} \cdot \cos\theta_i = \begin{Bmatrix} 400 \\ 1000 \\ 1250 \\ 1550 \\ 1700 \\ 1750 \end{Bmatrix} + \begin{Bmatrix} 1041.5\cdot\cos 27.6° \\ 1194.7\cdot\cos 27.6° \\ 1171.8\cdot\cos 27.6° \\ 1347.0\cdot\cos 27.6° \\ 1288.5\cdot\cos 27.6° \\ 996.9\cdot\cos 28.2° \end{Bmatrix} = \begin{Bmatrix} 1323.0 \\ 2058.7 \\ 2288.5 \\ 2743.7 \\ 2841.9 \\ 2628.6 \end{Bmatrix} \text{ kN}$$

Calculation of response in the Maximum Considered Earthquake using the Equivalent Lateral Force (ELF) procedure

The steps described in the corresponding part of Section 6.5 are followed.

1) Step 1 is the same as step 1 of the RSA procedure.

2) T_1, $\{\phi\}_1$ and Γ_1 are the same as those obtained in the RSA procedure: T_1=2.06 *sec*, $\{\phi\}_1$=[1.000,0.883,0.713,0.517,0.307,0.117]$^{\mathrm{T}}$ and Γ_1=1.397. The residual period T_{R} is calculated using Equation (6-28):

$$T_{\mathrm{R}} = 0.4T_1 = 0.4\cdot 2.06 = 0.82 \ \ \text{sec}$$

The residual modal participation factor Γ_R is calculated using Equation (6-26):

$$\Gamma_{\mathrm{R}} = 1 - \Gamma_1 = 1 - 1.397 = -0.397$$

The residual modal shape is calculated using Equation (6-27):

$$\{\phi\}_{\mathrm{R}} = \frac{\{1\} - \Gamma_1\cdot\{\phi\}_1}{\Gamma_{\mathrm{R}}} = \frac{\{1\} - 1.397\cdot\{\phi\}_1}{-0.397} = \left(\begin{bmatrix} 1.000 \\ 1.000 \\ 1.000 \\ 1.000 \\ 1.000 \\ 1.000 \end{bmatrix} - 1.397\cdot \begin{bmatrix} 1.000 \\ 0.883 \\ 0.713 \\ 0.517 \\ 0.307 \\ 0.117 \end{bmatrix} \right) \cdot \frac{1}{-0.397} = \begin{bmatrix} 1.000 \\ 0.588 \\ -0.010 \\ -0.700 \\ -1.439 \\ -2.107 \end{bmatrix}$$

The modal drifts $\{\phi_{\mathrm{r}}\}_{\mathrm{R}}$ are calculated from modal displacements $\{\phi\}_{\mathrm{R}}$ as:

$$\{\phi_{\mathrm{r}}\}_{\mathrm{R}} = [0.412, 0.598, 0.690, 0.739, 0.668, -2.107]^{\mathrm{T}}$$

3) The damping ratio for m=1 is β_{v1}= 0.10 as obtained in step 3 of the RSA procedure.

For the residual mode,

$$\beta_{\mathrm{vR}} = \frac{0.82}{4\pi}\cdot 9.81\cdot \frac{\left[\left(0.412^2 + 0.598^2 + 0.690^2 + 0.739^2 + 0.668^2\right)\times\cos^2 27.6° + (-2.107)^2\times\cos^2 28.2°\right]\times 2900}{1.000^2\times 1567 + \left(0.588^2 + (-0.010)^2 + (-0.700)^2 + (-1.439)^2 + (-2.107)^2\right)\times 2900} = 0.407$$

4-9) Steps 4 to 9 are the same as steps 4 to 9 of the RSA procedure.

10) The displacements contributed by the residual mode is (Equation (6-57)):

$$\{u\}_{\mathrm{R}} = \frac{\Gamma_{\mathrm{R}}\{\phi\}_{\mathrm{R}} T_{\mathrm{R}}^2 (1.5) S_{\mathrm{a}}(T_{\mathrm{R}}, \beta = 0.05) g}{4\pi^2 B_{\mathrm{R}}} = \frac{|-0.397| \times 0.82^2 \times 1.5 \times 0.7211 \times 9810}{4\pi^2 \times 2.271} \begin{Bmatrix} 1.000 \\ 0.588 \\ -0.010 \\ -0.700 \\ -1.439 \\ -2.107 \end{Bmatrix} = \begin{Bmatrix} 31.6 \\ 18.6 \\ -0.3 \\ -22.1 \\ -45.5 \\ -66.6 \end{Bmatrix} \text{ mm}$$

The modal damping ratios are obtained (Equation (6-53)):

$$\beta_{\mathrm{R}} = \beta_i + \beta_{\mathrm{vR}} = 0.05 + 0.407 = 0.457$$

The damping coefficient is B_2=2.271 (Table 18.6-1 in ASCE 7-2010).

Story drifts for the residual mode are calculated as:

$$\{\Delta u\}_{\mathrm{R}} = \begin{Bmatrix} 31.6 - 18.6 \\ 18.6 - (-0.3) \\ -0.3 - (-22.1) \\ -22.1 - (-45.5) \\ -45.5 - (-66.6) \\ -66.6 \end{Bmatrix} = \begin{Bmatrix} 13.0 \\ 18.9 \\ 21.8 \\ 23.4 \\ 21.1 \\ -66.6 \end{Bmatrix} \text{ mm}$$

11) The total displacements and drifts are calculated by combinin56.3g first mode and residual mode responses by SRSS:

$$\{u\}_{\mathrm{T}} = \begin{Bmatrix} \sqrt{470.0^2 + 31.6^2} \\ \sqrt{415.0^2 + 18.6^2} \\ \sqrt{335.1^2 + (-0.3)^2} \\ \sqrt{243.0^2 + (-22.1)^2} \\ \sqrt{144.3^2 + (-45.5)^2} \\ \sqrt{55.0^2 + (-66.6)^2} \end{Bmatrix} = \begin{Bmatrix} 471.1 \\ 415.4 \\ 335.1 \\ 244.0 \\ 151.3 \\ 86.4 \end{Bmatrix} \text{ mm}$$

$$\{\Delta u\}_{\mathrm{T}} = \begin{Bmatrix} \sqrt{55.0^2 + 13.0^2} \\ \sqrt{79.9^2 + 18.9^2} \\ \sqrt{92.1^2 + 21.8^2} \\ \sqrt{98.7^2 + 23.4^2} \\ \sqrt{89.3^2 + 21.1^2} \\ \sqrt{55.0^2 + (-66.6)^2} \end{Bmatrix} = \begin{Bmatrix} 56.5 \\ 82.1 \\ 94.6 \\ 101.4 \\ 91.8 \\ 86.4 \end{Bmatrix} \text{ mm}$$

12) Not used.

13) Not used.

14) Not used.

15) The relative velocity in each self-centering device for the first mode has been calculated in the corresponding step of RSA. For the residual mode the relative velocity is calculated using Equation (6-59) for *m*=*R*:

$$\{\nabla\}_{\mathrm{R}} = \frac{2\pi}{T_{\mathrm{R}}} \cdot \{\Delta u\}_{\mathrm{R}} \cdot \cos\theta_j \cdot CFV(T_{\mathrm{R}}, \beta_{\mathrm{R}}) = \frac{2\pi}{0.82} \cdot \begin{Bmatrix} 13.0 \cdot \cos 27.6 \\ 18.9 \cdot \cos 27.6 \\ 21.8 \cdot \cos 27.6 \\ 23.4 \cdot \cos 27.6 \\ 21.1 \cdot \cos 27.6 \\ (-66.6) \cdot \cos 28.2 \end{Bmatrix} \cdot CFV(0.82, 0.457) = \begin{Bmatrix} 71.3 \\ 103.6 \\ 119.6 \\ 128.3 \\ 115.7 \\ -363.2 \end{Bmatrix} \text{ mm/sec}$$

Factor *CFV* was obtained from the data in Table 5-3: *CFV* (for T_{R}=0.82sec, β_{R}=0.457) =0.8076.

16) By combining the first and residual modes by SRSS, the device relative velocity is obtained:

$$\{\nabla\}_{\mathrm{T}} = \begin{Bmatrix} \sqrt{163.2^2 + 71.3^2} \\ \sqrt{237.0^2 + 103.6^2} \\ \sqrt{273.2^2 + 119.6^2} \\ \sqrt{292.8^2 + 128.3^2} \\ \sqrt{264.9^2 + 115.7^2} \\ \sqrt{162.3^2 + (-363.2)^2} \end{Bmatrix} = \begin{Bmatrix} 178.1 \\ 258.7 \\ 298.2 \\ 319.7 \\ 289.1 \\ 397.8 \end{Bmatrix} \text{ mm/sec}$$

Also, the device relative displacements are calculated as $\Delta u_{iT} \cos\theta_i$, where Δu_{iT} are the drifts calculated in step 11:

$$\left\{\Delta u\cos\theta\right\}_{\mathrm{T}}=\begin{Bmatrix}56.5\cdot\cos 27.6^\circ\\82.1\cdot\cos 27.6^\circ\\94.6\cdot\cos 27.6^\circ\\101.4\cdot\cos 27.6^\circ\\91.8\cdot\cos 27.6^\circ\\86.4\cdot\cos 28.2^\circ\end{Bmatrix}=\begin{Bmatrix}50.1\\72.8\\83.8\\89.9\\81.4\\76.1\end{Bmatrix}\ \text{mm}$$

17) The peak damping force in each self-centering device is calculated by use of Equation (6-60):

$$\left\{F_{\mathrm{v},i}\right\}_{\mathrm{T}}=\left\{C_i\right\}\left\{\nabla\right\}_{\mathrm{T}}$$

Thus,

$$\left\{F_{\mathrm{v},i}\right\}_{\mathrm{T}}=2900\cdot\begin{Bmatrix}178.1\\258.7\\298.2\\319.7\\289.1\\397.8\end{Bmatrix}\cdot\frac{1}{10^3}=\begin{Bmatrix}516.5\\750.2\\864.8\\927.1\\838.4\\1153.6\end{Bmatrix}\ \text{kN}$$

18) The peak self-centering device force is calculated using Equation (6-61):

$$\left\{F_{\mathrm{M},i\mathrm{MAX}}\right\}_{\mathrm{T}}=\left\{F_{\min,i}\right\}+\left\{F_{0,i}\right\}+\left\{K_{0,i}\right\}u+\left\{F_{\mathrm{v},i}\right\}\sqrt{1-\left(u/u_{\mathrm{D},i\mathrm{T}}\right)^2}$$

Thus,

$$\left\{F_{\mathrm{M},i\mathrm{MAX}}\right\}_{\mathrm{T}}=0.05\times\begin{Bmatrix}100\\250\\250\\400\\400\\400\end{Bmatrix}+\begin{Bmatrix}100\\250\\250\\400\\400\\400\end{Bmatrix}+\begin{Bmatrix}1350\\1790\\1790\\2230\\2230\\2230\end{Bmatrix}\begin{Bmatrix}u_6\\u_5\\u_4\\u_3\\u_2\\u_1\end{Bmatrix}+\begin{Bmatrix}516.5\\750.2\\864.8\\927.1\\838.4\\1153.6\end{Bmatrix}\begin{Bmatrix}\sqrt{1-\left(u_6/50.1\right)^2}\\\sqrt{1-\left(u_5/72.8\right)^2}\\\sqrt{1-\left(u_4/83.8\right)^2}\\\sqrt{1-\left(u_3/89.9\right)^2}\\\sqrt{1-\left(u_2/81.4\right)^2}\\\sqrt{1-\left(u_1/76.1\right)^2}\end{Bmatrix}=\begin{Bmatrix}625.9\\1023.9\\1140.2\\1368.5\\1277.8\\1586.0\end{Bmatrix}\ \text{kN}$$

The maximum values of force were calculated for displacements $\{u_6, u_5, u_4, u_3, u_2, u_1\}=\{6.5, 12.5, 14.3, 18.7, 17.2, 11.1\}$ (*mm*).

19) The peak shear force in each story is calculated as:

$$\left\{V_{\mathrm{M},i\mathrm{MAX}}\right\}_{\mathrm{T}} = \left\{V\right\}_{\mathrm{T}} + \left\{F_{\mathrm{M},i\mathrm{MAX}}\right\}_{\mathrm{T}} \cdot \cos\theta_i = \begin{Bmatrix} 400 \\ 1000 \\ 1250 \\ 1550 \\ 1700 \\ 1750 \end{Bmatrix} + \begin{Bmatrix} 625.9 \cdot \cos 27.6° \\ 1023.9 \cdot \cos 27.6° \\ 1140.2 \cdot \cos 27.6° \\ 1368.5 \cdot \cos 27.6° \\ 1277.8 \cdot \cos 27.6° \\ 1586.0 \cdot \cos 28.2° \end{Bmatrix} = \begin{Bmatrix} 954.7 \\ 1907.4 \\ 2260.4 \\ 2762.8 \\ 2832.4 \\ 3147.7 \end{Bmatrix} \text{ kN}$$

Table D-4 presents a summary of the calculated response.

Table D-4 Summary of RSA and ELF Analysis Results

Response Quantity	Story	RSA (DE)	ELF (DE)	RSA (MCE)	ELF (MCE)
Floor Displacement (mm)	6	315.3	314.0	473.0	471.1
	5	276.9	277.0	415.4	415.4
	4	223.8	223.4	335.7	335.1
	3	163.6	162.7	245.4	244.0
	2	98.5	100.9	147.7	151.3
	1	38.1	57.6	57.1	86.4
Story Drift (mm)	6	45.7	37.6	68.7	56.5
	5	58.0	54.8	87.0	82.1
	4	62.7	63.1	94.1	94.6
	3	66.2	67.6	99.2	101.4
	2	60.6	61.1	90.9	91.8
	1	38.1	57.6	57.1	86.4
Device Velocity (mm/sec)	6	214.5	118.6	321.6	178.1
	5	211.8	172.5	317.7	258.7
	4	205.6	198.8	308.4	298.2
	3	206.7	213.1	309.4	319.7
	2	192.4	192.7	288.3	289.1
	1	129.2	265.2	193.4	397.8
Device Force (kN)	6	769.4	451.8	1041.5	625.9
	5	883.6	770.3	1194.7	1023.9
	4	867.0	847.6	1171.8	1140.2
	3	1033.5	1052.3	1347.0	1368.5
	2	990.7	991.7	1288.5	1277.8
	1	802.1	1197.4	996.9	1586.0
Maximum Story Shear Force (kN)	6	1081.8	800.4	1323.0	954.7
	5	1783.0	1682.6	2058.7	1907.4
	4	2018.3	2001.1	2288.5	2260.4
	3	2465.9	2482.6	2743.7	2762.8
	2	2578.0	2578.8	2841.9	2832.4
	1	2456.9	2805.3	2628.6	3147.7

The adequacy of the bracing needs to be checked. There is considerable difference between the results of the RSA and ELF analysis results for some of the bracing (6^{th} and 1^{st} stories) so instead the check is based on the response history analysis results for the MCE (Section 7). Sections 18.7.1.2 to 18.7.1.4 in ASCE 7-2010 specify the requirements for the design of damping systems and their connections, which presumably also apply to fluidic self-centering devices. The criteria require that the devices, bracing and connections are designed to resist the forces, displacements and velocities calculated in the MCE and assessed using strength design criteria with a redundancy factor ρ=1 and a resistance factor ϕ=1. Herein, the approach is followed (as in Appendix C) to use as the required strength the brace force calculated in the MCE (average of seven analyses) multiplied by factor 1.3 and then compare to the design strength of the brace in compression using ϕ=1. Table D-5 presents the calculated forces and strengths of the bracing of the 6-story frame and the required changes to meet the ASCE 7 criteria.

Table D-5 Bracing Forces, Required Strengths and Design Strengths

Story	Force in MCE (kN)	Required Strength[1] (kN)	Original Bracing		Modified Bracing	
			Brace	Design Strength[2] (kN)	Brace	Design Strength[2] (kN)
6	661.0	859.3	HSS7x7x1/4	461.8	HSS8x8x3/8	964.2
5	983.2	1278.2	HSS8x8x3/8	964.2	HSS8x8x5/8	1433.9
4	1001.2	1301.6	HSS8x8x3/8	964.2	HSS8x8x5/8	1433.9
3	1320.0	1716.0	HSS9x9x1/2	1656.4	HSS9x9x5/8	1982.7
2	1417.4	1842.6	HSS9x9x1/2	1656.4	HSS9x9x5/8	1982.7
1	1284.6	1670.0	HSS9x9x1/2	1656.4	HSS9x9x5/8	1982.7

1: 1.3xForce in MCE 2: Based on KL=8535mm, ϕ=1.

The original bracing was inadequate and it was modified to meet the criteria while keeping the required strength unchanged. Note that the effect of the change in the bracing size is immaterial in the calculation of the peak device forces and this has been confirmed by repeating selected analyses in the MCE with the modified bracing.

APPENDIX E
DETAILED COLLAPSE FRAGILITY DATA

This appendix presents detailed data obtained in the collapse fragility analysis. Data for each analyzed case are presented tables that contain the following:

1) Information on the analyzed system.
2) Computed Incremental Dynamic Analysis (IDA) curves.
3) Graph of the best-fit lognormal cumulative distribution function to the empirical data.
4) Information of the Collapse Margin Ratio (CMR), the dispersion factor, and spectral acceleration values at the fundamental period in the MCE and at collapse.
5) Number of collapses determined for each intensity level of the earthquake motions.

The procedure followed in the construction of the fragility curves followed the following steps.

1) Incremental dynamic analysis was conducted for the system using each of the 44 motions. The earthquake intensity was increased by a step of 0.05g in the spectral acceleration value at the fundamental period until collapse was observed. These resulted in the IDA curves for the 44 motions shown in the IDA graph.
2) The spectral acceleration at the fundamental period of each of the 44 motions that cause collapse was entered in a table and sorted in increasing spectral acceleration value as shown in the example below. A rank was assigned starting from 1 and ending at 44. The rank is the cumulative number of collapses. Note that for the same value of spectral acceleration there may be more than one entry in the table. For example, in the table below there are three entries at the acceleration of 1.95g. This means that one collapse was detected for each of three motions scaled at the intensity level of 1.95g. All three cases are considered in the construction of the fragility curve. It should be noted that had the increment in spectral acceleration value was extremely small (the analysis was performed with a step of 0.05g), the analysis would have differentiated between the three cases as collapse would occur at values of spectral acceleration slightly different than 1.95g for each of the three cases.

Table E-1 Assignment of Rank Number

$S_a(T_1)$ at Collapse, $S_{aCOL,i}$ (g)	Ground Motion	Rank i
$S_{aCOL,1}$=0.75	Loma Prieta; Capitola	1
$S_{aCOL,2}$=1.75	Chi-Chi; TCU045	2
$S_{aCOL,3}$=1.95	Northridge; Beverly Hills – Mulhol	3
$S_{aCOL,4}$=1.95	Kocaeli; Arcelik	4
$S_{aCOL,5}$=1.95	Landers; Coolwater	5
$S_{aCOL,6}$=2.30	Manjil; Abbar	6
$S_{aCOL,7}$=2.40	Imperial Valley; Delta	7
$S_{aCOL,8}$=2.80	Kobe; Shin-Osaka	8
etc.	etc.	etc.

3) The number of collapses for each level of earthquake intensity, as measured by the spectral acceleration value at the fundamental period, was reported.
4) The probability of collapse for each level of intensity (collapse fragility) was calculated as

$$P = \frac{i}{N+1}$$

where i is the rank and N is the number of ground motions (N=44). Note that N+1 is used instead of N to avoid a probability of 1 (certainty) for i=N. Data on the empirical probability of collapse are shown in the collapse fragility curves as circles.

5) The Collapse Margin Ratio (*CMR*) was calculated as the ratio of the spectral acceleration at which the number of collapses is at least half (22 or 23, corresponding to probability of collapse equal to 0.5) divided by the spectral acceleration at the MCE level.
6) A log-normal cumulative distribution function was constructed to best-fit the data using the following equation

$$CDF(x) = \int_{-\infty}^{x} \frac{1}{s\beta\sqrt{2\pi}} \exp\left[-\frac{\{\ln s - \ln m\}^2}{2\beta^2} \right] ds$$

Note that x is the random variable (now the spectral acceleration at the fundamental period of the structure), ln$m$ is the median of the 44 $S_{aCOL,i}$ (T_1) and β is the dispersion factor that is equal to the standard deviation of the sample of ln($S_{aCOL,1}$), ln($S_{aCOL,2}$), ln($S_{aCOL,3}$), …, ln($S_{aCOL,44}$).

Analyzed system	**3*S*-75** Linear Damping β_{v1} =0.10 α=1 Ultimate Capacity $1.3F_{MCE}$ T_1=1.31sec

Story	F_0 [kN]	K_0 [kN/m]	Braces	C or C_N [kN-(s/m)$^\alpha$]	D_{Cap} [mm]	Ultimate $F_{Tension}$ [kN]	Ultimate F_{Compr} [kN]
3rd	125	1545	HSS8x8×1/2	1140	165	1160	1215
2nd	300	2320	HSS8x8×1/2	1140	165	1160	1215
1st	300	2320	HSS8x8×1/2	1140	165	1160	1215

S_a-component scaling

IDA curves

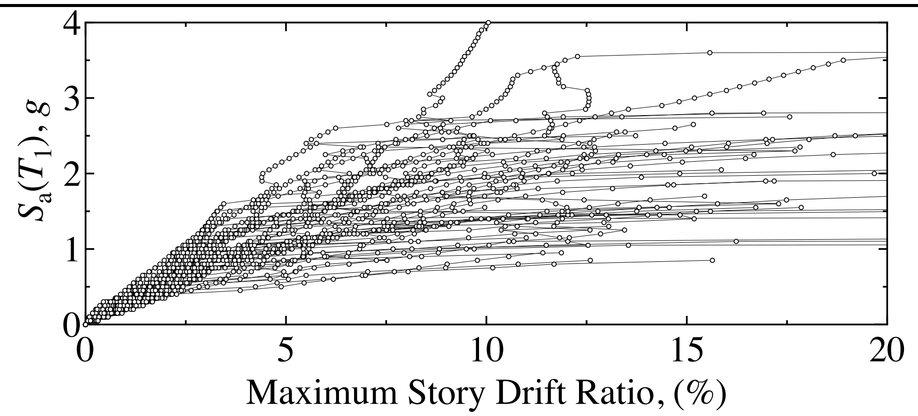

Collapse Fragility curve

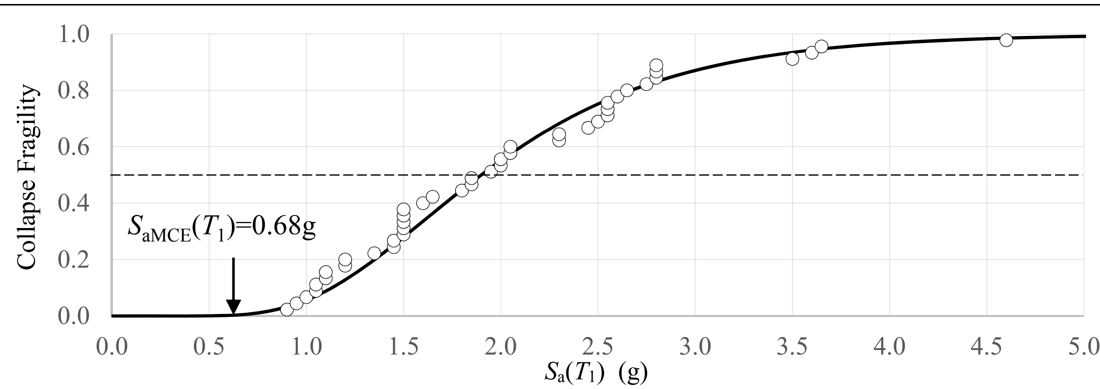

Detailed data

$S_{aMCE}(T_1)$	$S_{aCOL}(T_1)$	CMR	β
0.68g	1.90g	2.79	0.33

$S_a(T_1)$ (g)	Number of collapses	$S_a(T_1)$ (g)	Number of collapses
<0.90	0	1.90	23
0.90	1	1.95	24
1.00	2	1.95	25
1.05	3	1.95	26
1.10	4	1.95	27

1.20	5	2.05	28
1.25	6	2.05	29
1.25	7	2.05	30
1.30	8	2.10	31
1.30	9	2.15	32
1.40	10	2.15	33
1.45	11	2.20	34
1.50	12	2.30	35
1.50	13	2.45	36
1.50	14	2.50	37
1.55	15	2.65	38
1.55	16	2.75	39
1.65	17	2.90	40
1.65	18	3.00	41
1.65	19	3.00	42
1.85	20	3.10	43
1.90	21	3.55	44
1.90	22		

Analyzed system

3*S*-75 Linear Damping β_{v1}=0.10 α=1 Ultimate Capacity 1.3F_{MCE} Unbalanced (a) T_1=1.31sec	Story	F_0 [kN]	K_0 [kN/m]	Braces	C or C_N [kN-(s/m)$^{\alpha}$]	D_{Cap} [mm]	Ultimate $F_{Tension}$ [kN]	Ultimate F_{Compr} [kN]
	3rd	125	1545	HSS8x8×1/2	1140	165	2430	1215
	2nd	300	2320	HSS8x8×1/2	1140	165	2430	1215
	1st	300	2320	HSS8x8×1/2	1140	165	2430	1215
S_a-component scaling								

IDA curves

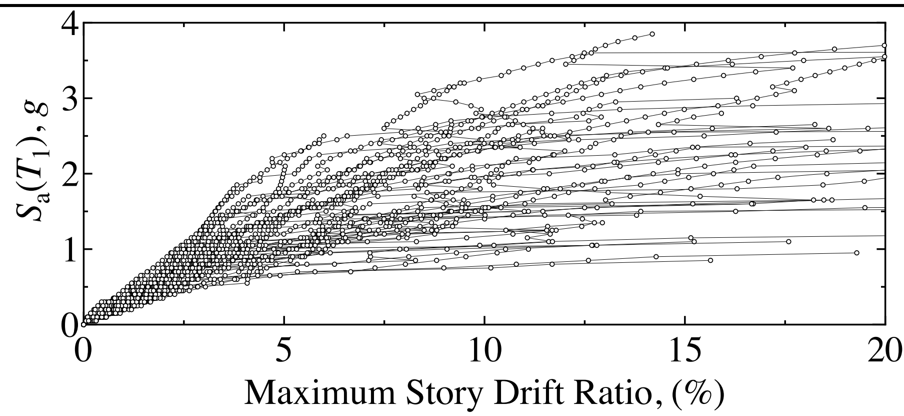

Collapse fragility curve

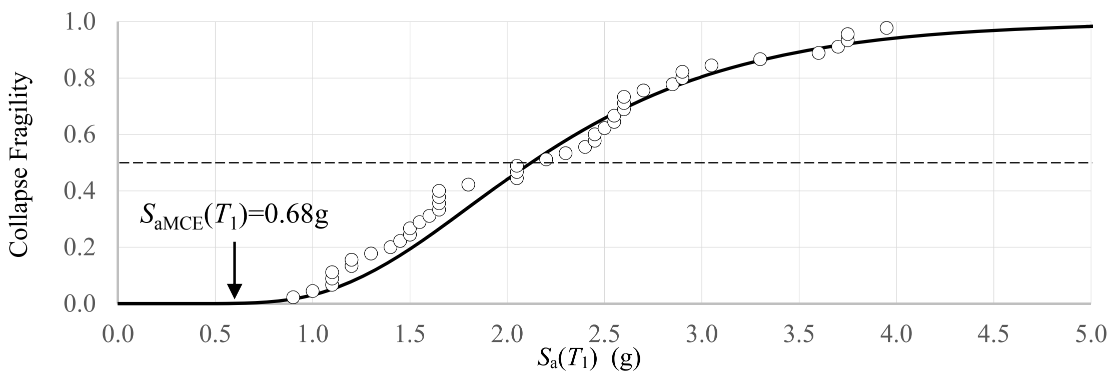

Detailed data

$S_{aMCE}(T_1)$	$S_{aCOL}(T_1)$	*CMR*	β
0.68g	2.13g	3.12	0.40

$S_a(T_1)$ (g)	Number of collapses	$S_a(T_1)$ (g)	Number of collapses
<0.90	0	2.20	23
0.90	1	2.30	24
1.00	2	2.40	25
1.10	3	2.45	26
1.10	4	2.45	27
1.10	5	2.50	28

1.20	6	2.55	29
1.20	7	2.55	30
1.30	8	2.60	31
1.40	9	2.60	32
1.45	10	2.60	33
1.50	11	2.70	34
1.50	12	2.85	35
1.55	13	2.90	36
1.60	14	2.90	37
1.65	15	3.05	38
1.65	16	3.30	39
1.65	17	3.60	40
1.65	18	3.70	41
1.80	19	3.75	42
2.05	20	3.75	43
2.05	21	3.95	44
2.05	22		

Analyzed system

3*S*-75 Linear Damping β_{v1}=0.10 α=1 Ultimate Capacity 1.3F_{MCE} Unbalanced (b) T_1=1.31sec	Story	F_0 [kN]	K_0 [kN/m]	Braces	C or C_N [kN-(s/m)$^{\alpha}$]	D_{Cap} [mm]	Ultimate $F_{Tension}$ [kN]	Ultimate F_{Compr} [kN]
	3rd	125	1545	HSS8x8×1/2	1140	165	2430	1215
	2nd	300	2320	HSS8x8×1/2	1140	165	2430	1215
	1st	300	2320	HSS8x8×1/2	1140	165	2430	1215
S_a-component scaling								

IDA curves

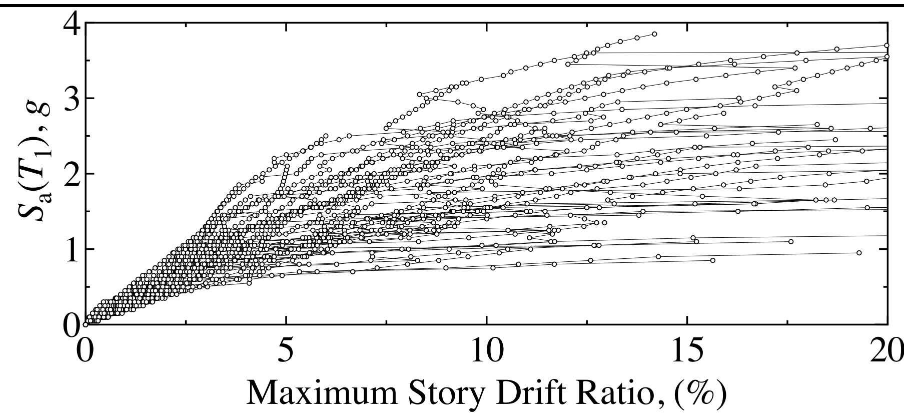

Collapse fragility curve

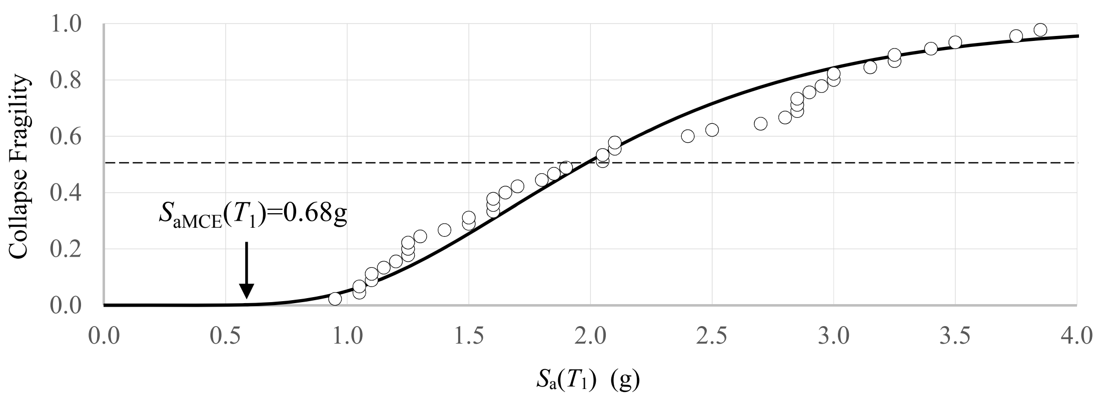

Detailed data

$S_{aMCE}(T_1)$	$S_{aCOL}(T_1)$	*CMR*	β
0.68g	1.98g	2.91	0.42

$S_a(T_1)$ (g)	Number of collapses	$S_a(T_1)$ (g)	Number of collapses
<0.95	0	2.05	23
0.95	1	2.05	24
1.05	2	2.10	25
1.05	3	2.10	26
1.10	4	2.40	27

1.10	5	2.50	28
1.15	6	2.70	29
1.20	7	2.80	30
1.25	8	2.85	31
1.25	9	2.85	32
1.25	10	2.85	33
1.30	11	2.90	34
1.40	12	2.95	35
1.50	13	3.00	36
1.50	14	3.00	37
1.60	15	3.15	38
1.60	16	3.25	39
1.60	17	3.25	40
1.65	18	3.40	41
1.70	19	3.50	42
1.80	20	3.75	43
1.85	21	3.85	44
1.90	22		

Analyzed system

3*S*-75 Linear Damping β_{v1} =0.10 α=1 Ultimate Capacity 1.3F_{MCE} Unbalanced (c) T_1=1.31sec	Story	F_0 [kN]	K_0 [kN/m]	Braces	C or C_N [kN-(s/m)$^\alpha$]	D_{Cap} [mm]	Ultimate $F_{Tension}$ [kN]	Ultimate F_{Compr} [kN]
	3rd	125	1545	HSS8x8×1/2	1140	165	2430	1215
	2nd	300	2320	HSS8x8×1/2	1140	165	2430	1215
	1st	300	2320	HSS8x8×1/2	1140	165	2430	1215

S_a-component scaling

IDA curves

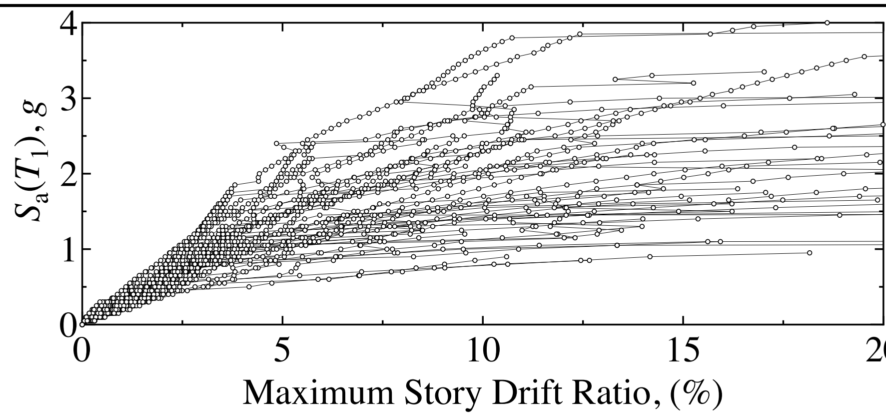

Collapse fragility curve

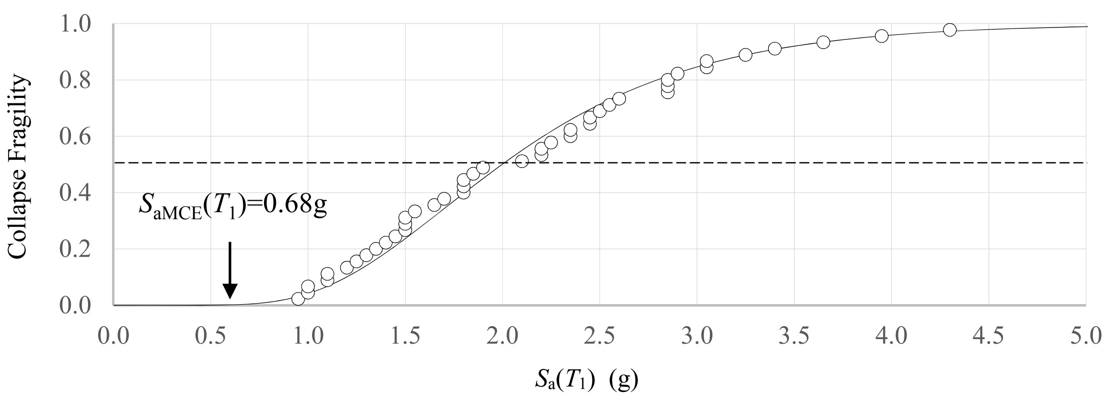

Detailed data

$S_{aMCE}(T_1)$	$S_{aCOL}(T_1)$	*CMR*	β
0.68g	2.00g	2.94	0.40

$S_a(T_1)$ (g)	Number of collapses	$S_a(T_1)$ (g)	Number of collapses
<0.95	0	2.10	23
0.95	1	2.20	24
1.00	2	2.20	25
1.00	3	2.25	26
1.10	4	2.35	27

1.10	5	2.35	28
1.20	6	2.45	29
1.25	7	2.45	30
1.30	8	2.50	31
1.35	9	2.55	32
1.40	10	2.60	33
1.45	11	2.85	34
1.50	12	2.85	35
1.50	13	2.85	36
1.50	14	2.90	37
1.55	15	3.05	38
1.65	16	3.05	39
1.70	17	3.25	40
1.80	18	3.40	41
1.80	19	3.65	42
1.80	20	3.95	43
1.85	21	4.30	44
1.90	22		

Analyzed system

3*S*-75 Linear Damping β_{v1}=0.10 α=1 Ultimate Capacity 1.3F_{MCE} Unbalanced (d) T_1=1.31sec	Story	F_0 [kN]	K_0 [kN/m]	Braces	C or C_N [kN-(s/m)$^\alpha$]	D_{Cap} [mm]	Ultimate $F_{Tension}$ [kN]	Ultimate F_{Compr} [kN]
	3rd	125	1545	HSS8x8×1/2	1140	165	2430	1215
	2nd	300	2320	HSS8x8×1/2	1140	165	2430	1215
	1st	300	2320	HSS8x8×1/2	1140	165	2430	1215
S_a-component scaling								

IDA curves

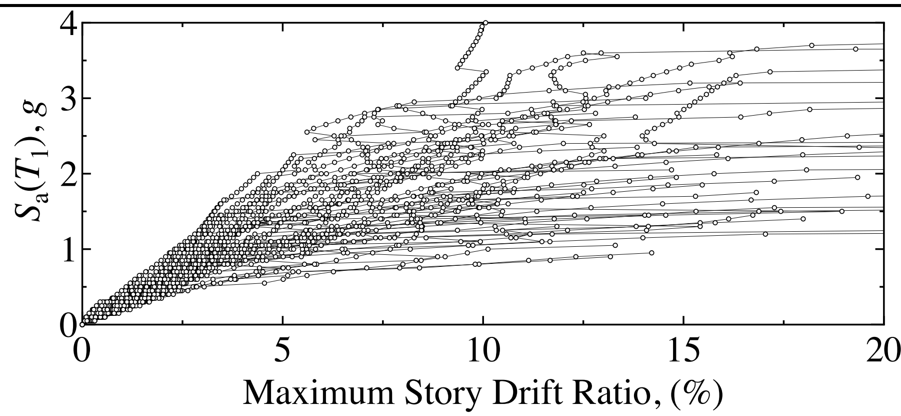

Collapse fragility curve

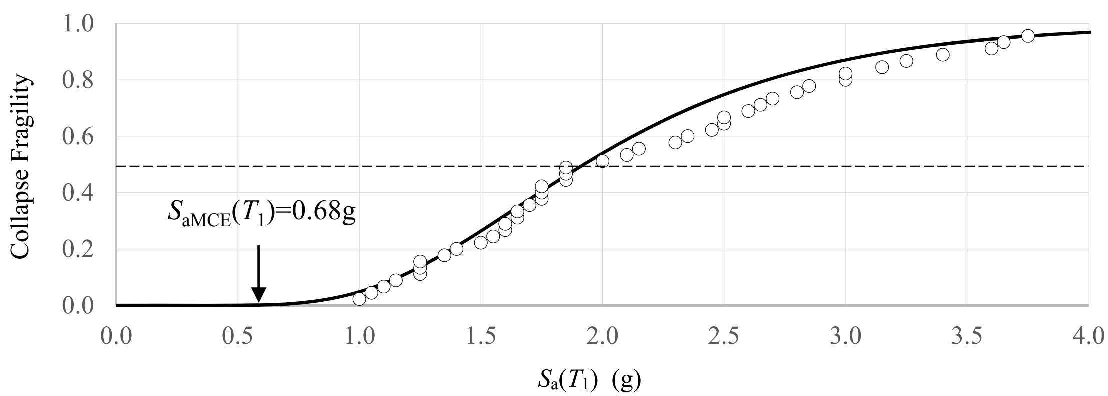

Detailed data

$S_{aMCE}(T_1)$	$S_{aCOL}(T_1)$	*CMR*	β
0.68g	1.93g	2.84	0.39

$S_a(T_1)$ (g)	Number of collapses	$S_a(T_1)$ (g)	Number of collapses
<1.00	0	2.00	23
1.00	1	2.10	24
1.05	2	2.15	25
1.10	3	2.30	26
1.15	4	2.35	27

		1.25	5	2.45	28	
		1.25	6	2.50	29	
		1.25	7	2.50	30	
		1.35	8	2.60	31	
		1.40	9	2.65	32	
		1.50	10	2.70	33	
		1.55	11	2.80	34	
		1.60	12	2.85	35	
		1.60	13	3.00	36	
		1.65	14	3.00	37	
		1.65	15	3.15	38	
		1.70	16	3.25	39	
		1.75	17	3.40	40	
		1.75	18	3.60	41	
		1.75	19	3.65	42	
		1.85	20	3.75	43	
		1.85	21	5.25	44	
		1.85	22			

Analyzed system

3*S*-75 Linear Damping β_{v1}=0.10 α=1 Ultimate Capacity 2.0F_{MCE} Increased Capacity T_1=1.31sec	Story	F_0 [kN]	K_0 [kN/m]	Braces	C or C_N [kN-(s/m)$^{\alpha}$]	D_{Cap} [mm]	Ultimate $F_{Tension}$ [kN]	Ultimate F_{Compr} [kN]
	3rd	125	1545	HSS9x9×5/8	1140	165	1983	1983
	2nd	300	2320	HSS9x9×5/8	1140	165	1983	1983
	1st	300	2320	HSS9x9×5/8	1140	165	1983	1983

S_a-component scaling

IDA curves

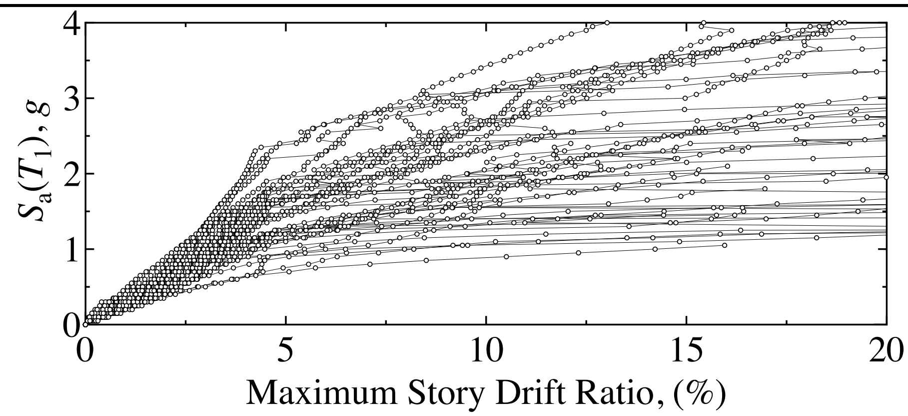

Collapse fragility curve

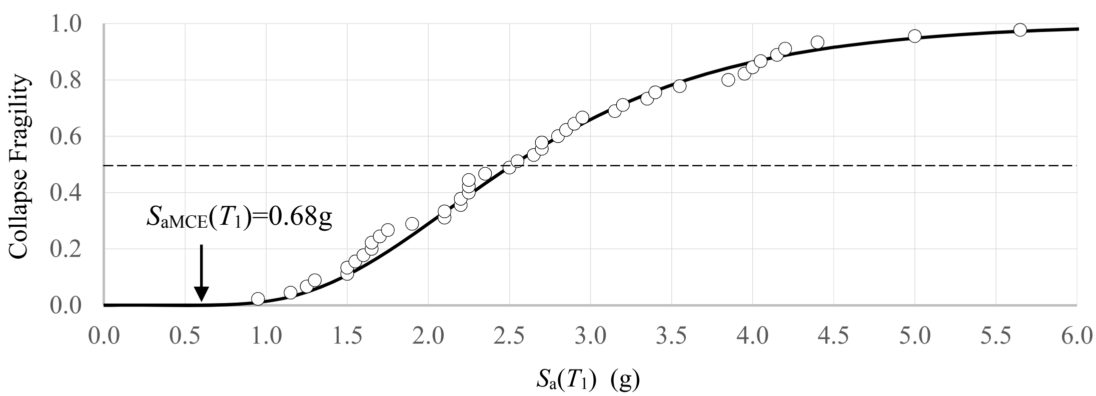

Detailed data

$S_{aMCE}(T_1)$	$S_{aCOL}(T_1)$	*CMR*	β
0.68g	2.53g	3.72	0.42

$S_a(T_1)$ (g)	Number of collapses	$S_a(T_1)$ (g)	Number of collapses
<0.95	0	2.55	23
0.95	1	2.65	24
1.15	2	2.70	25
1.25	3	2.70	26
1.30	4	2.80	27

		1.50	5	2.85	28	
		1.50	6	2.90	29	
		1.55	7	2.95	30	
		1.60	8	3.15	31	
		1.65	9	3.20	32	
		1.65	10	3.35	33	
		1.70	11	3.40	34	
		1.75	12	3.55	35	
		1.90	13	3.85	36	
		2.10	14	3.95	37	
		2.10	15	4.00	38	
		2.20	16	4.05	39	
		2.20	17	4.15	40	
		2.25	18	4.20	41	
		2.25	19	4.40	42	
		2.25	20	5.00	43	
		2.35	21	5.65	44	
		2.50	22			

Analyzed system

3*S*-75 Linear Damping β_{v1} =0.10 α=1 Ultimate Capacity $1.3F_{MCE}$ Increased Displacement Capacity T_1=1.31sec	Story	F_0 [kN]	K_0 [kN/m]	Braces	C or C_N [kN-(s/m)$^{\alpha}$]	D_{Cap} [mm]	Ultimate $F_{Tension}$ [kN]	Ultimate F_{Compr} [kN]
	3rd	125	1545	HSS8x8×1/2	1140	215	1160	1215
	2nd	300	2320	HSS8x8×1/2	1140	215	1160	1215
	1st	300	2320	HSS8x8×1/2	1140	215	1160	1215
S_a-component scaling								

IDA curves

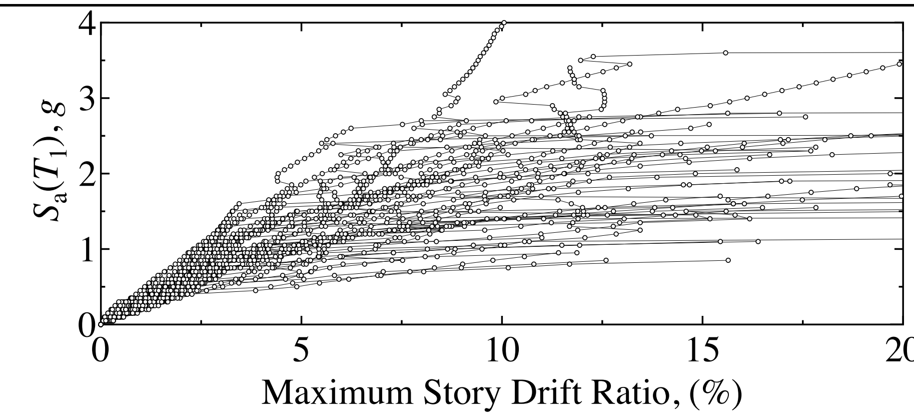

Collapse fragility curve

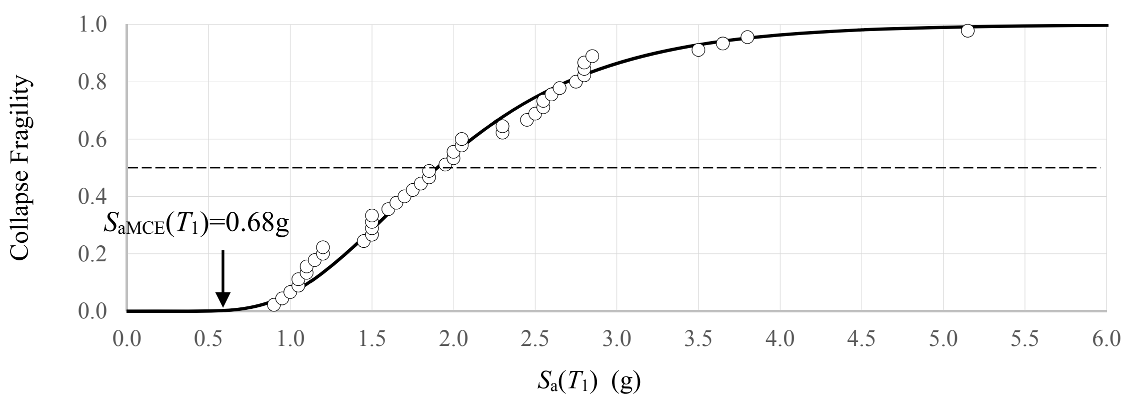

Detailed data

$S_{aMCE}(T_1)$	$S_{aCOL}(T_1)$	CMR	β
0.68g	1.90g	2.79	0.42

$S_a(T_1)$ (g)	Number of collapses	$S_a(T_1)$ (g)	Number of collapses
<0.90	0	1.95	23
0.90	1	2.00	24
0.95	2	2.00	25
1.00	3	2.05	26

		1.05	4	2.05	27	
		1.05	5	2.30	28	
		1.10	6	2.30	29	
		1.10	7	2.45	30	
		1.15	8	2.50	31	
		1.20	9	2.55	32	
		1.20	10	2.55	33	
		1.45	11	2.60	34	
		1.50	12	2.65	35	
		1.50	13	2.75	36	
		1.50	14	2.80	37	
		1.50	15	2.80	38	
		1.60	16	2.80	39	
		1.65	17	2.85	40	
		1.70	18	3.50	41	
		1.75	19	3.65	42	
		1.80	20	3.80	43	
		1.85	21	5.15	44	
		1.85	22			

Analyzed system

3*S*-75 Increased Linear Damping β_{v1} =0.15 α=1 Ultimate Capacity $1.3F_{MCE}$ T_1=1.31sec	Story	F_0 [kN]	K_0 [kN/m]	Braces	C or C_N [kN-(s/m)$^{\alpha}$]	D_{Cap} [mm]	Ultimate $F_{Tension}$ [kN]	Ultimate F_{Compr} [kN]
	3rd	125	1545	HSS8x8×5/8	1710	165	1435	1435
	2nd	300	2320	HSS8x8×5/8	1710	165	1435	1435
	1st	300	2320	HSS8x8×5/8	1710	165	1435	1435
S_a-component scaling								

IDA curves

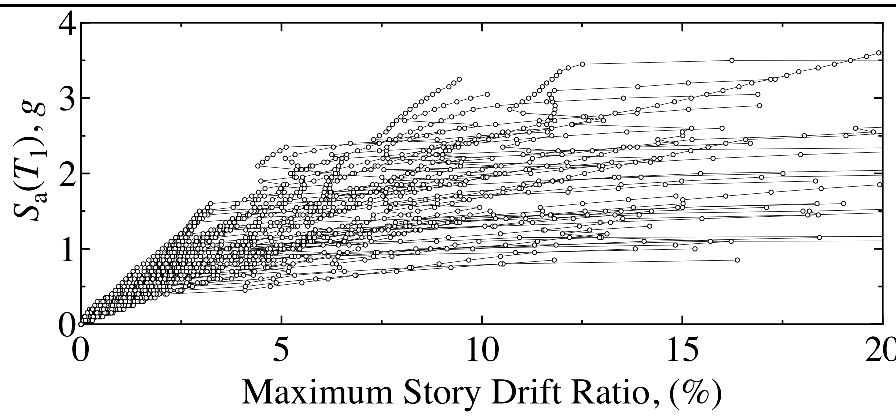

Collapse fragility curve

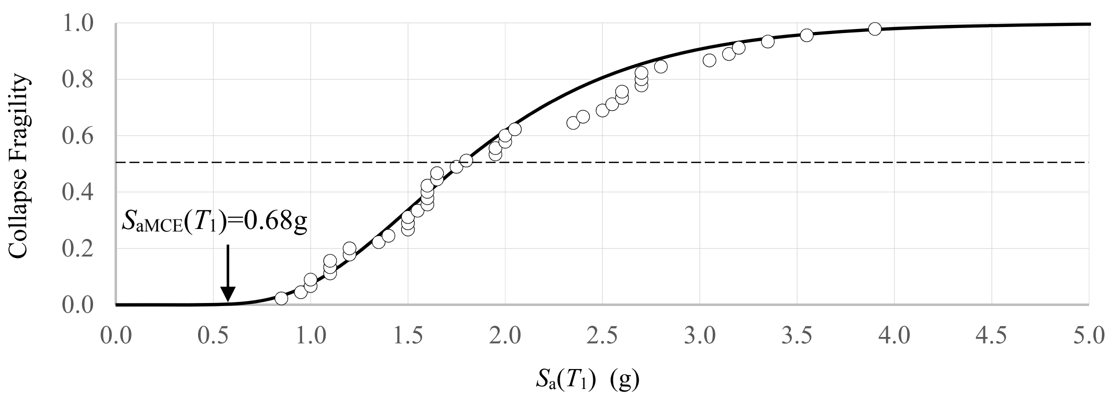

Detailed data

$S_{aMCE}(T_1)$	$S_{aCOL}(T_1)$	*CMR*	β
0.68g	1.78g	2.60	0.40

$S_a(T_1)$ (g)	Number of collapses	$S_a(T_1)$ (g)	Number of collapses
<0.85	0	1.80	23
0.85	1	1.95	24
0.95	2	1.95	25
1	3	2.00	26
1	4	2.00	27
1.1	5	2.05	28

		1.1	6	2.35	29	
		1.1	7	2.40	30	
		1.2	8	2.50	31	
		1.2	9	2.55	32	
		1.35	10	2.60	33	
		1.4	11	2.60	34	
		1.5	12	2.70	35	
		1.5	13	2.70	36	
		1.5	14	2.70	37	
		1.55	15	2.80	38	
		1.6	16	3.05	39	
		1.6	17	3.15	40	
		1.6	18	3.20	41	
		1.6	19	3.35	42	
		1.65	20	3.55	43	
		1.65	21	3.90	44	
		1.75	22			

Analyzed System

3S-75 Increased Preload β_{v1} = 0.10 α=1 Ultimate Capacity 1.3F_{MCE} T_1=1.28sec	Story	F_0 [kN]	K_0 [kN/m]	Braces	C or C_N [kN-(s/m)$^{\alpha}$]	D_{Cap} [mm]	Ultimate $F_{Tension}$ [kN]	Ultimate F_{Compr} [kN]
	3rd	160	1545	HSS8x8×5/8	1140	165	1435	1435
	2nd	390	2320	HSS8x8×5/8	1140	165	1435	1435
	1st	390	2320	HSS8x8×5/8	1140	165	1435	1435
S_a-component scaling								

IDA curves

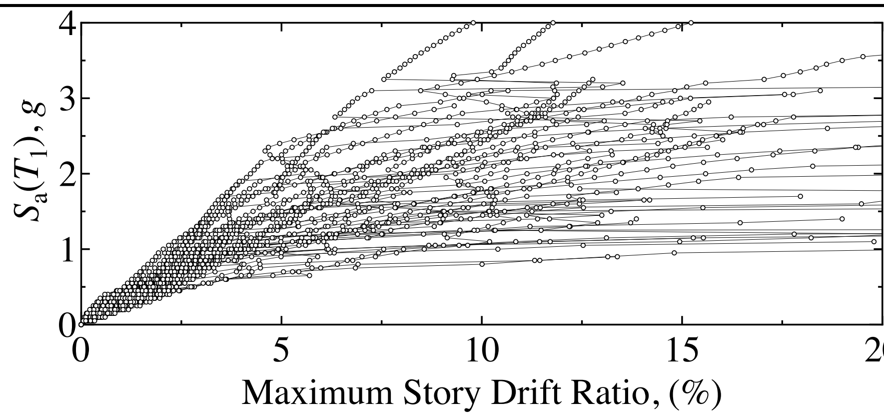

Collapse fragility curve

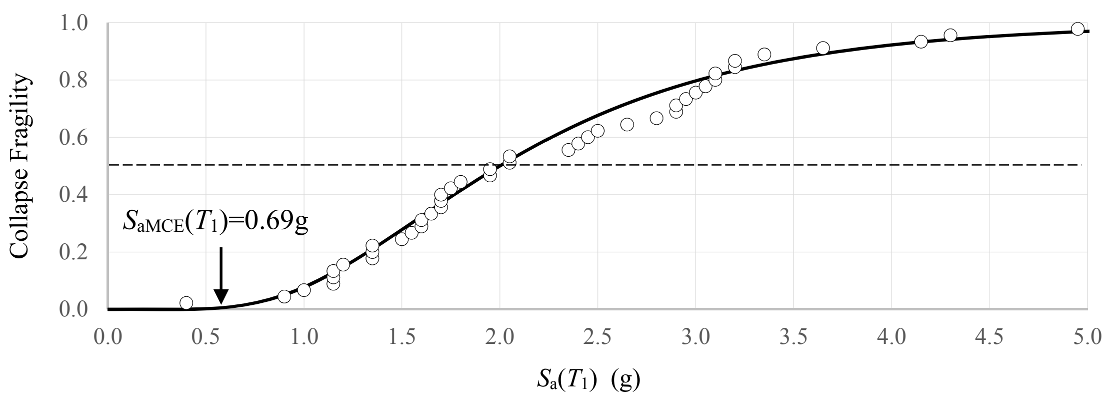

Detailed data

$S_{aMCE}(T_1)$	$S_{aCOL}(T_1)$	CMR	β
0.69g	2.00g	2.89	0.49

$S_a(T_1)$ (g)	Number of collapses	$S_a(T_1)$ (g)	Number of collapses
<0.40	0	2.05	23
0.40	1	2.05	24
0.90	2	2.35	25
1.00	3	2.40	26
1.15	4	2.45	27
1.15	5	2.50	28

1.15	6	2.65	29
1.20	7	2.80	30
1.35	8	2.90	31
1.35	9	2.90	32
1.35	10	2.95	33
1.50	11	3.00	34
1.55	12	3.05	35
1.60	13	3.10	36
1.60	14	3.10	37
1.65	15	3.20	38
1.70	16	3.20	39
1.70	17	3.35	40
1.70	18	3.65	41
1.75	19	4.15	42
1.80	20	4.30	43
1.95	21	4.95	44
1.95	22		

Analyzed system

3*S*-75 Nonlinear Damping $\beta_{v1} = 0.10$ α=0.5 Ultimate Capacity $1.3F_{MCE}$ T_1=1.31sec	Story	F_0 [kN]	K_0 [kN/m]	Braces	C or C_N [kN-(s/m)$^{\alpha}$]	D_{Cap} [mm]	Ultimate $F_{Tension}$ [kN]	Ultimate F_{Compr} [kN]
	3rd	125	1545	HSS8x8×1/2	551.3	165	1160	1215
	2nd	300	2320	HSS8x8×1/2	551.3	165	1160	1215
	1st	300	2320	HSS8x8×1/2	551.3	165	1160	1215

S_a-component scaling

IDA curves

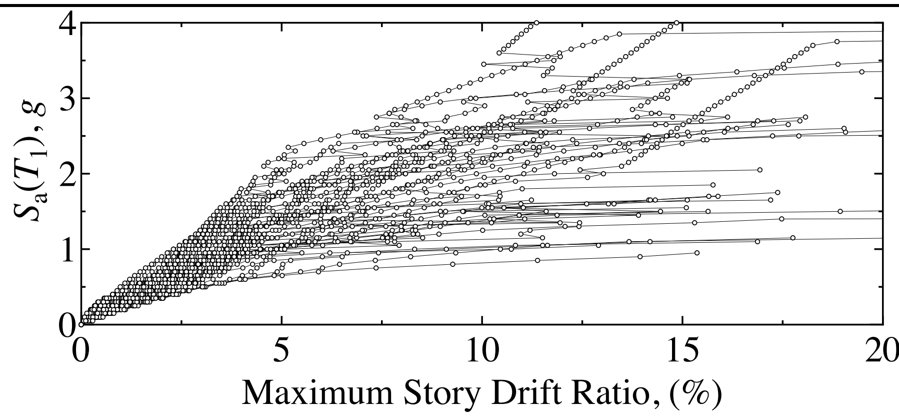

Collapse fragility curve

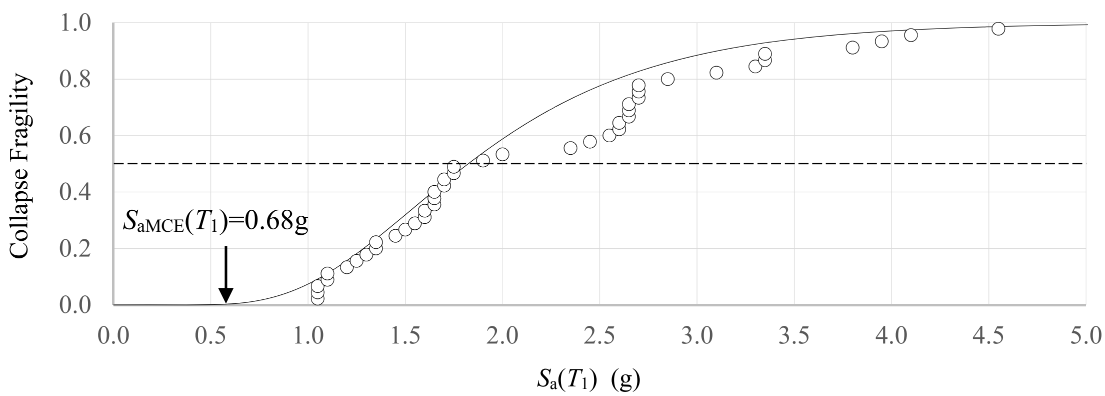

Detailed data

$S_{aMCE}(T_1)$	$S_{aCOL}(T_1)$	CMR	β
0.68g	1.83g	2.68	0.42

$S_a(T_1)$ (g)	Number of collapses	$S_a(T_1)$ (g)	Number of collapses
<1.05	0	1.90	23
1.05	1	2.00	24
1.05	2	2.35	25
1.05	3	2.45	26
1.10	4	2.55	27
1.10	5	2.60	28

		1.20	6	2.60	29	
		1.25	7	2.65	30	
		1.30	8	2.65	31	
		1.35	9	2.65	32	
		1.35	10	2.70	33	
		1.45	11	2.70	34	
		1.50	12	2.70	35	
		1.55	13	2.85	36	
		1.60	14	3.10	37	
		1.60	15	3.30	38	
		1.65	16	3.35	39	
		1.65	17	3.35	40	
		1.65	18	3.80	41	
		1.70	19	3.95	42	
		1.70	20	4.10	43	
		1.75	21	4.55	44	
		1.75	22			

Analyzed system

3*S*-75 Nonlinear Damping Increased Damping $\beta_{v1} = 0.15$ α=0.5 Ultimate Capacity $1.3F_{MCE}$ T_1=1.31sec	Story	F_0 [kN]	K_0 [kN/m]	Braces	C or C_N [kN-(s/m)$^{\alpha}$]	D_{Cap} [mm]	Ultimate $F_{Tension}$ [kN]	Ultimate F_{Compr} [kN]
	3rd	125	1545	HSS8x8×1/2	666.4	165	1160	1215
	2nd	300	2320	HSS8x8×1/2	666.4	165	1160	1215
	1st	300	2320	HSS8x8×1/2	666.4	165	1160	1215
S_a-component scaling								

IDA curves

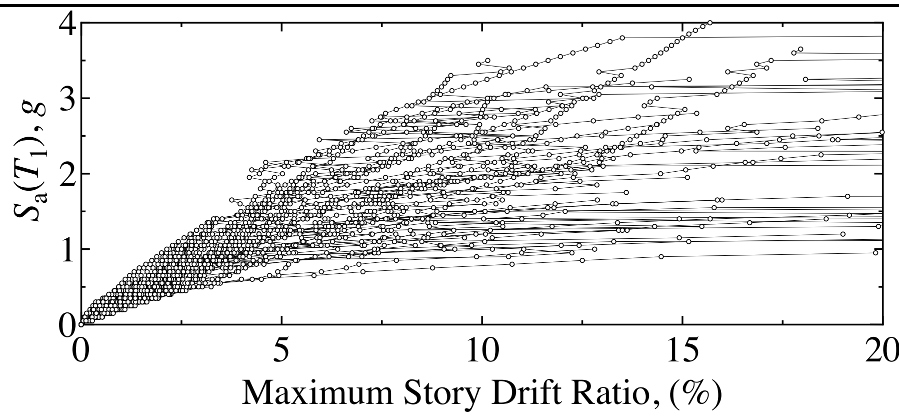

Collapse fragility curve

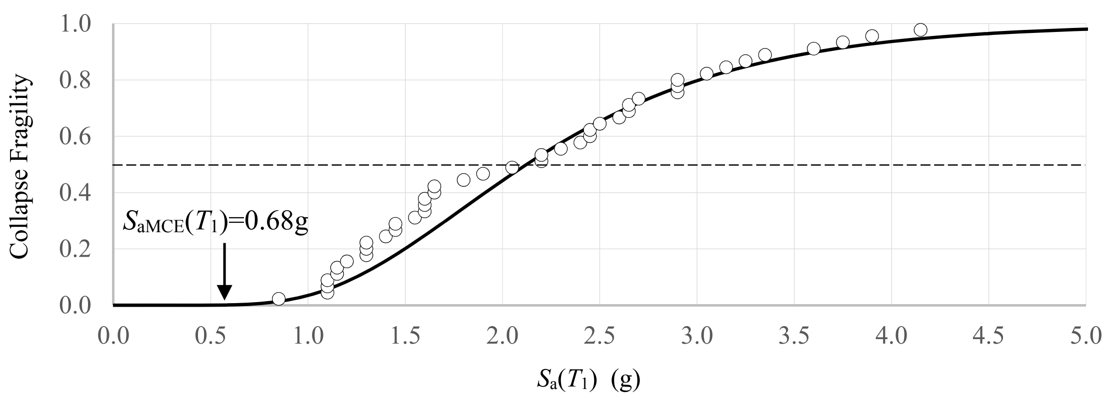

Detailed data

$S_{aMCE}(T_1)$	$S_{aCOL}(T_1)$	*CMR*	β
0.68g	2.13g	3.12	0.42

$S_a(T_1)$ (g)	Number of collapses	$S_a(T_1)$ (g)	Number of collapses
<0.85	0	2.20	23
0.85	1	2.20	24
1.10	2	2.30	25
1.10	3	2.40	26
1.10	4	2.45	27

1.15	5	2.45	28
1.15	6	2.50	29
1.20	7	2.60	30
1.30	8	2.65	31
1.30	9	2.65	32
1.30	10	2.70	33
1.40	11	2.90	34
1.45	12	2.90	35
1.45	13	2.90	36
1.55	14	3.05	37
1.60	15	3.15	38
1.60	16	3.25	39
1.60	17	3.35	40
1.65	18	3.60	41
1.65	19	3.75	42
1.80	20	3.90	43
1.90	21	4.15	44
2.05	22		

Analyzed system

3*S*-75 Nonlinear Damping Increased Damping β_{v1} = 0.15 α=0.5 Increased Ultimate Capacity T_1=1.31sec	Story	F_0 [kN]	K_0 [kN/m]	Braces	C or C_N [kN-(s/m)$^\alpha$]	D_{Cap} [mm]	Ultimate $F_{Tension}$ [kN]	Ultimate F_{Compr} [kN]
	3rd	125	1545	HSS9x9×5/8	666.4	165	1983	1983
	2nd	300	2320	HSS9x9×5/8	666.4	165	1983	1983
	1st	300	2320	HSS9x9×5/8	666.4	165	1983	1983
S_a-component scaling								

IDA curves

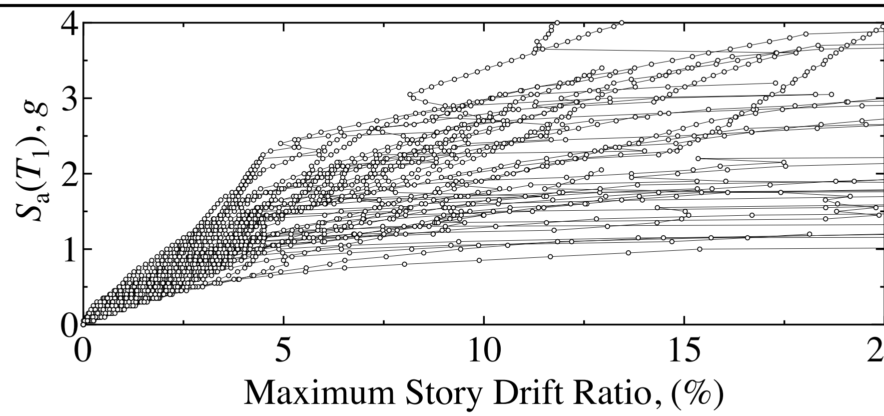

Collapse fragility curve

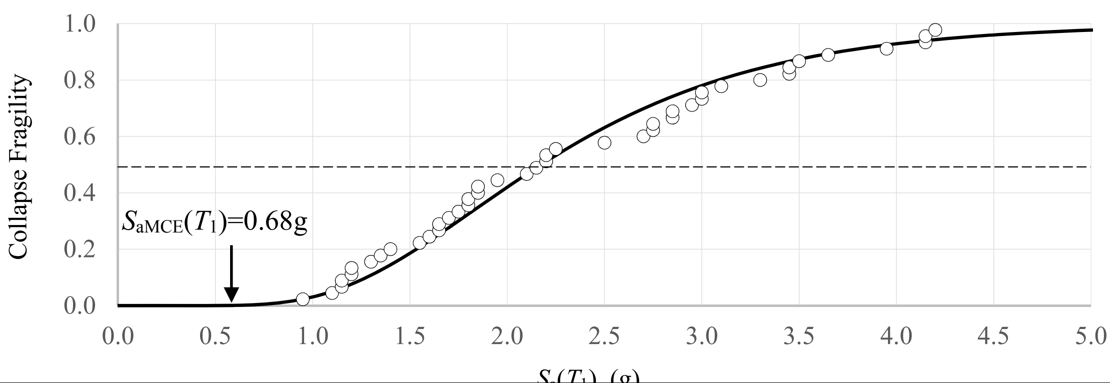

Detailed data

$S_{aMCE}(T_1)$	$S_{aCOL}(T_1)$	*CMR*	β
0.68g	2.18g	3.21	0.42

$S_a(T_1)$ (g)	Number of collapses	$S_a(T_1)$ (g)	Number of collapses
<0.95	0	2.20	23
0.95	1	2.20	24
1.10	2	2.25	25
1.15	3	2.50	26
1.15	4	2.70	27
1.20	5	2.75	28

1.20	6	2.75	29
1.30	7	2.85	30
1.35	8	2.85	31
1.40	9	2.95	32
1.55	10	3.00	33
1.60	11	3.00	34
1.65	12	3.10	35
1.65	13	3.30	36
1.70	14	3.45	37
1.75	15	3.45	38
1.80	16	3.50	39
1.80	17	3.65	40
1.85	18	3.95	41
1.85	19	4.15	42
1.95	20	4.15	43
2.10	21	4.20	44
2.15	22		

Analyzed system

3*S*-75 Nonlinear Increased Damping β_{v1} = 0.15 α=0.5 Low Stifness Ultimate Capacity 1.3F_{MCE} T_1=1.31sec	Story	F_0 [kN]	K_0 [kN/m]	Braces	C or C_N [kN-(s/m)$^\alpha$]	D_{Cap} [mm]	Ultimate $F_{Tension}$ [kN]	Ultimate F_{Compr} [kN]
	3rd	125	155	HSS8x8×1/2	666.4	165	1160	1215
	2nd	300	232	HSS8x8×1/2	666.4	165	1160	1215
	1st	300	232	HSS8x8×1/2	666.4	165	1160	1215

S_a-component scaling

IDA curves

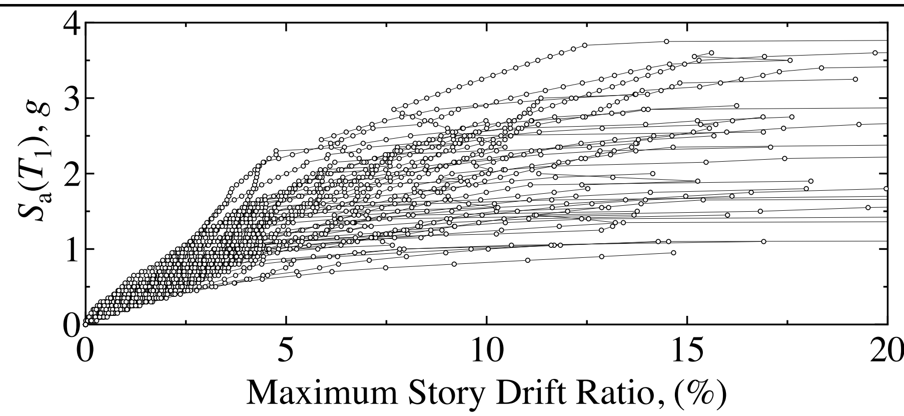

Collapse fragility curve

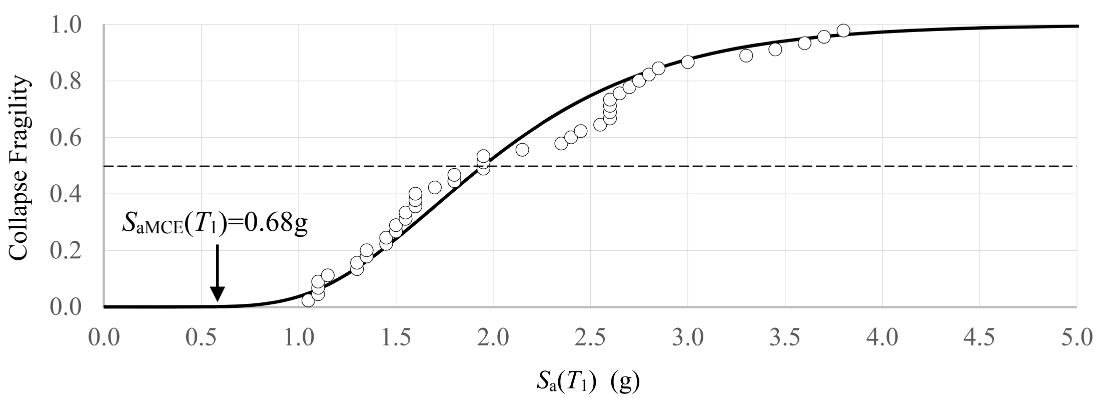

Detailed data

$S_{aMCE}(T_1)$	$S_{aCOL}(T_1)$	*CMR*	β
0.68g	1.95g	2.87	0.37

$S_a(T_1)$ (g)	Number of collapses	$S_a(T_1)$ (g)	Number of collapses
<1.05	0	1.95	23
1.05	1	1.95	24
1.10	2	2.15	25
1.10	3	2.35	26

1.10	4	2.40	27
1.15	5	2.45	28
1.30	6	2.55	29
1.30	7	2.60	30
1.35	8	2.60	31
1.35	9	2.60	32
1.45	10	2.60	33
1.45	11	2.65	34
1.50	12	2.70	35
1.50	13	2.75	36
1.55	14	2.80	37
1.55	15	2.85	38
1.60	16	3.00	39
1.60	17	3.30	40
1.60	18	3.45	41
1.70	19	3.60	42
1.80	20	3.70	43
1.80	21	3.80	44
1.95	22		

Analyzed system

	Story	F_0 [kN]	K_0 [kN/m]	Braces	C or C_N [kN-(s/m)$^\alpha$]	D_{Cap} [mm]	Ultimate $F_{Tension}$ [kN]	Ultimate F_{Compr} [kN]
3*S*-Reference T_1=1.07sec	3rd	-	-	-	-	-	-	-
	2nd	-	-	-	-	-	-	-
	1st	-	-	-	-	-	-	-

S_a-component scaling

IDA curves

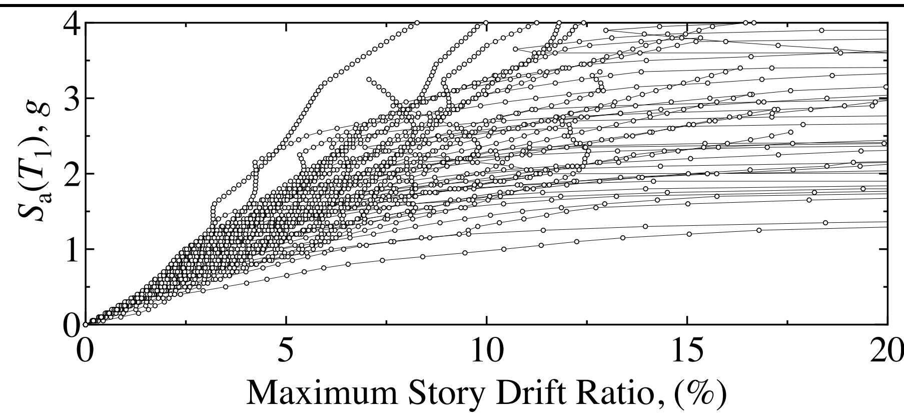

Collapse Fragility curve

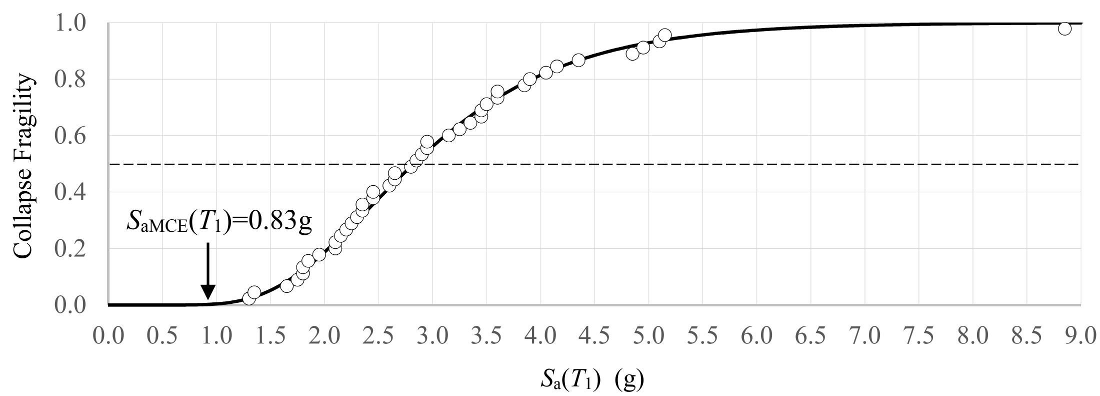

Detailed data

$S_{aMCE}(T_1)$	$S_{aCOL}(T_1)$	*CMR*	β
0.83g	2.83g	3.40	0.39

$S_a(T_1)$ (g)	Number of collapses	$S_a(T_1)$ (g)	Number of collapses
<1.30	0	2.85	23
1.30	1	2.90	24
1.35	2	2.95	25
1.65	3	2.95	26
1.75	4	3.15	27
1.80	5	3.25	28

		1.80	6	3.35	29	
		1.85	7	3.45	30	
		1.95	8	3.45	31	
		2.10	9	3.50	32	
		2.10	10	3.60	33	
		2.15	11	3.60	34	
		2.20	12	3.85	35	
		2.25	13	3.90	36	
		2.30	14	4.05	37	
		2.35	15	4.15	38	
		2.35	16	4.35	39	
		2.45	17	4.85	40	
		2.45	18	4.95	41	
		2.60	19	5.10	42	
		2.65	20	5.15	43	
		2.65	21	8.85	44	
		2.80	22			

Analyzed system

3*S*-75 Linear Damping β_{v1} =0.10 α=1 Ultimate Capacity 1.3F_{MCE} T_1=1.31sec	Story	F_0 [kN]	K_0 [kN/m]	Braces	C or C_N [kN-(s/m)$^{\alpha}$]	D_{Cap} [mm]	Ultimate $F_{Tension}$ [kN]	Ultimate F_{Compr} [kN]
	3rd	125	1545	HSS8x8×1/2	1140	165	1160	1215
	2nd	300	2320	HSS8x8×1/2	1140	165	1160	1215
	1st	300	2320	HSS8x8×1/2	1140	165	1160	1215
PGV Normalization scaling								

IDA curves

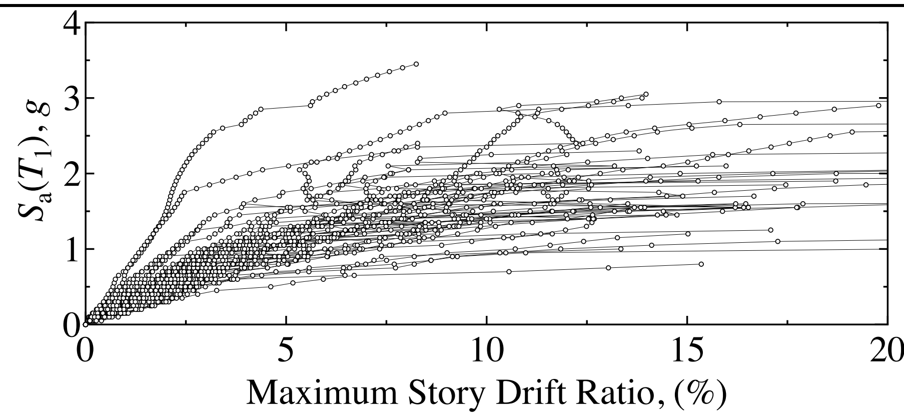

Collapse fragility curve

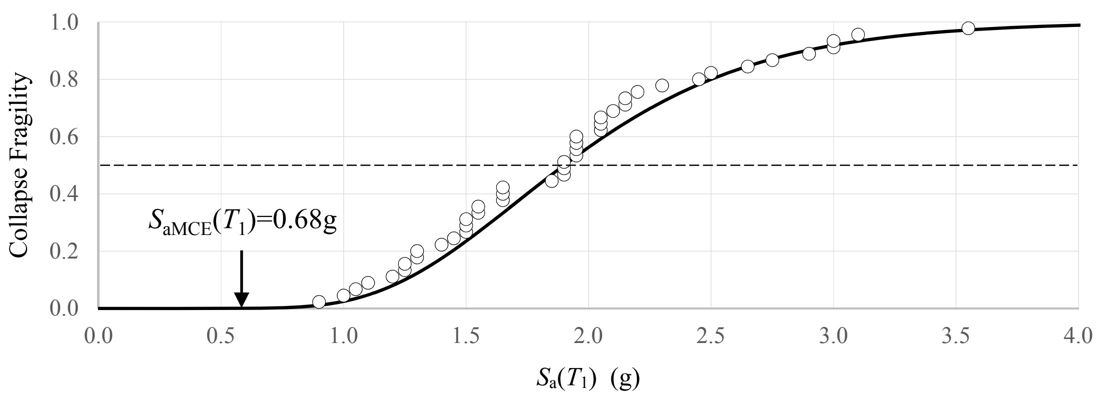

Detailed data

$S_{aMCE}(T_1)$	$S_{aCOL}(T_1)$	*CMR*	β
0.68g	1.90g	2.79	0.33

$S_a(T_1)$ (g)	Number of collapses	$S_a(T_1)$ (g)	Number of collapses
<0.90	0	1.90	23
0.90	1	1.95	24
1.00	2	1.95	25
1.05	3	1.95	26

		1.10	4	1.95	27	
		1.20	5	2.05	28	
		1.25	6	2.05	29	
		1.25	7	2.05	30	
		1.30	8	2.10	31	
		1.30	9	2.15	32	
		1.40	10	2.15	33	
		1.45	11	2.20	34	
		1.50	12	2.30	35	
		1.50	13	2.45	36	
		1.50	14	2.50	37	
		1.55	15	2.65	38	
		1.55	16	2.75	39	
		1.65	17	2.90	40	
		1.65	18	3.00	41	
		1.65	19	3.00	42	
		1.85	20	3.10	43	
		1.90	21	3.55	44	
		1.90	22			

Analyzed system

3*S*-75 Linear Damping β_{v1} =0.10 α=1 Ultimate Capacity 1.3F_{MCE} Unbalanced (a) T_1=1.31sec	Story	F_0 [kN]	K_0 [kN/m]	Braces	C or C_N [kN-(s/m)$^\alpha$]	D_{Cap} [mm]	Ultimate $F_{Tension}$ [kN]	Ultimate F_{Compr} [kN]
	3rd	125	1545	HSS8x8×1/2	1140	165	2430	1215
	2nd	300	2320	HSS8x8×1/2	1140	165	2430	1215
	1st	300	2320	HSS8x8×1/2	1140	165	2430	1215
PGV Normalization scaling								

IDA curves

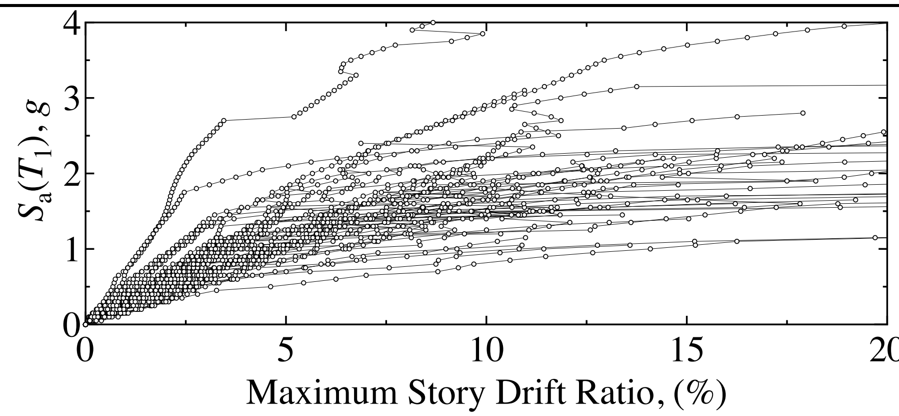

Collapse fragility curve

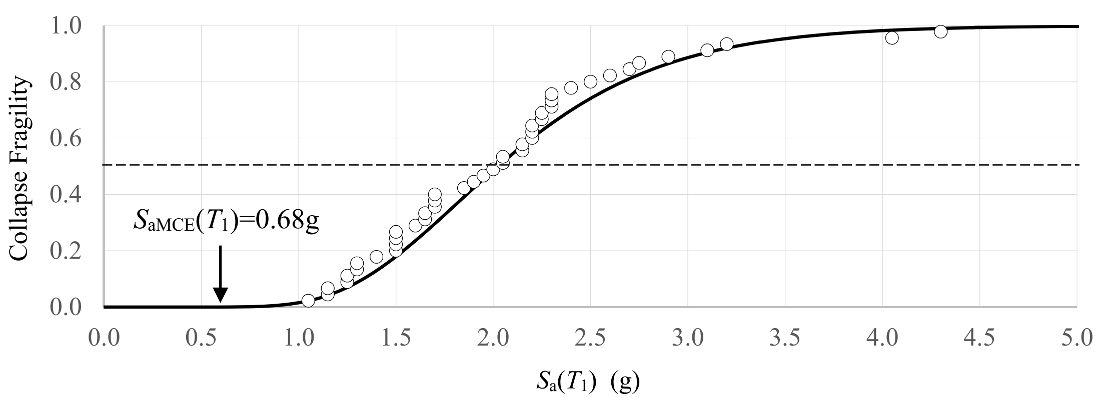

Detailed data

$S_{aMCE}(T_1)$	$S_{aCOL}(T_1)$	*CMR*	β
0.68g	2.03g	2.98	0.33

$S_a(T_1)$ (g)	Number of collapses	$S_a(T_1)$ (g)	Number of collapses
<1.05	0	2.05	23
1.05	1	2.05	24

		1.15	2	2.15	25	
		1.15	3	2.15	26	
		1.25	4	2.20	27	
		1.25	5	2.20	28	
		1.30	6	2.20	29	
		1.30	7	2.25	30	
		1.40	8	2.25	31	
		1.50	9	2.30	32	
		1.50	10	2.30	33	
		1.50	11	2.30	34	
		1.50	12	2.40	35	
		1.60	13	2.50	36	
		1.65	14	2.60	37	
		1.65	15	2.70	38	
		1.70	16	2.75	39	
		1.70	17	2.90	40	
		1.70	18	3.10	41	
		1.85	19	3.20	42	
		1.90	20	4.05	43	
		1.95	21	4.30	44	
		2.00	22			

Analyzed system

3*S*-85 Balanced T_1= 1.23sec	Story	F_0 [kN]	K_0 [kN/m]	Braces	C or C_N [kN-(s/m)$^\alpha$]	D_{Cap} [mm]	Ultimate $F_{Tension}$ [kN]	Ultimate F_{Compr} [kN]
	3rd	150	1545	HSS8x8×5/8	1220	165	1435	1435
	2nd	350	2320	HSS8x8×5/8	1220	165	1435	1435
	1st	350	2320	HSS8x8×5/8	1220	165	1435	1435

*S*a-component scaling

IDA curves

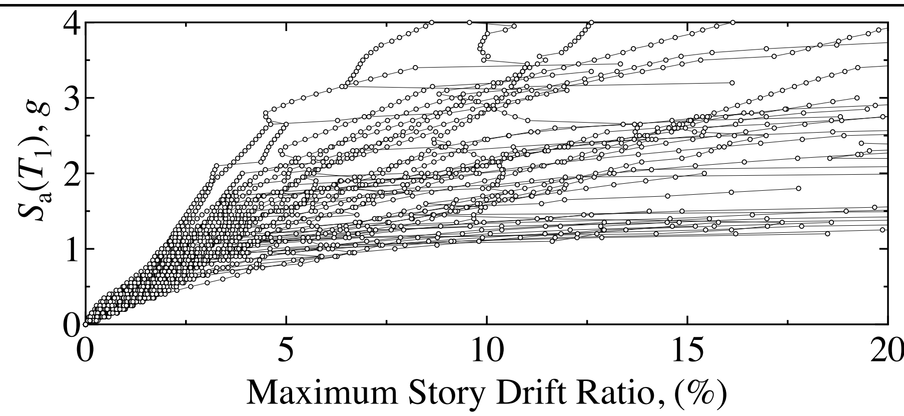

Collapse fragility curve

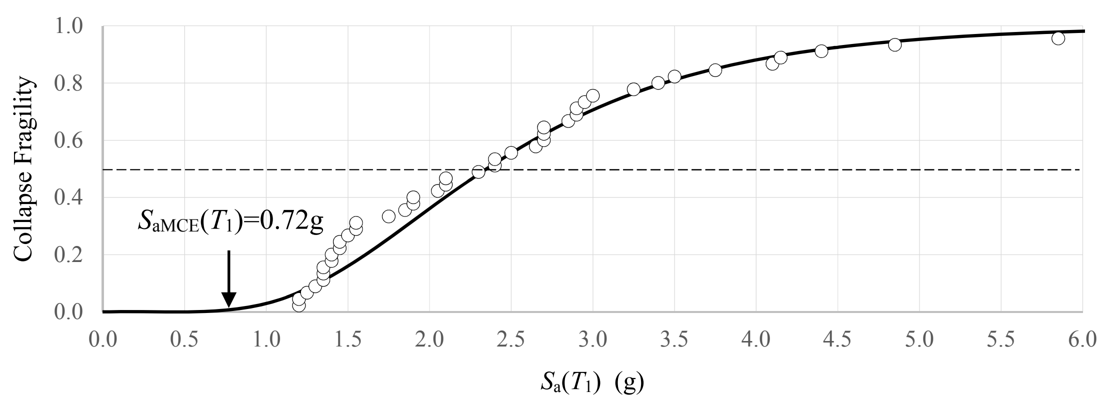

Detailed data

$S_{aMCE}(T_1)$	$S_{aCOL}(T_1)$	*CMR*	β
0.72g	2.35g	3.46	0.45

$S_a(T_1)$ (g)	Number of collapses	$S_a(T_1)$ (g)	Number of collapses
<1.20	0	2.40	23
1.20	1	2.40	24
1.20	2	2.50	25
1.25	3	2.65	26
1.30	4	2.70	27

1.35	5	2.70	28
1.35	6	2.70	29
1.35	7	2.85	30
1.40	8	2.90	31
1.40	9	2.90	32
1.45	10	2.95	33
1.45	11	3.00	34
1.50	12	3.25	35
1.55	13	3.40	36
1.55	14	3.50	37
1.75	15	3.75	38
1.85	16	4.10	39
1.90	17	4.15	40
1.90	18	4.40	41
2.05	19	4.85	42
2.10	20	5.85	43
2.10	21	6.60	44
2.30	22		

Analyzed system	**3*S*-Reference** T_1=1.07sec	Story	F_0 [kN]	K_0 [kN/m]	Braces	C or C_N [kN-(s/m)$^\alpha$]	D_{Cap} [mm]	Ultimate $F_{Tension}$ [kN]	Ultimate F_{Compr} [kN]
		3rd	-	-	-	-	-	-	-
		2nd	-	-	-	-	-	-	-
		1st	-	-	-	-	-	-	-
	PGV Normalization scaling								

IDA curves

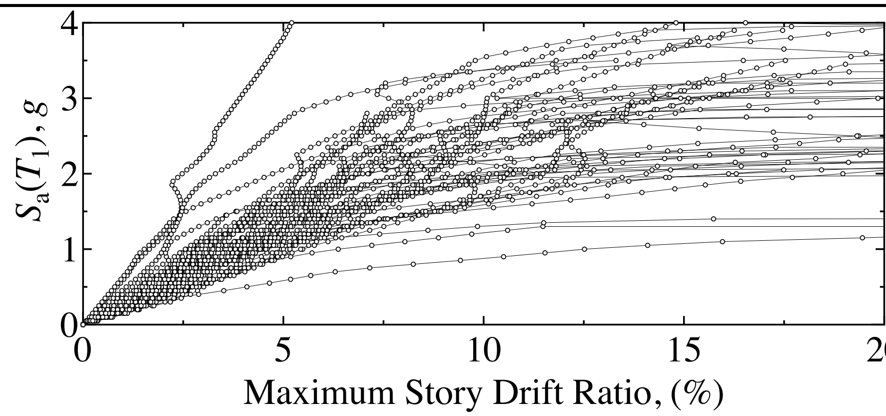

Collapse fragility curve

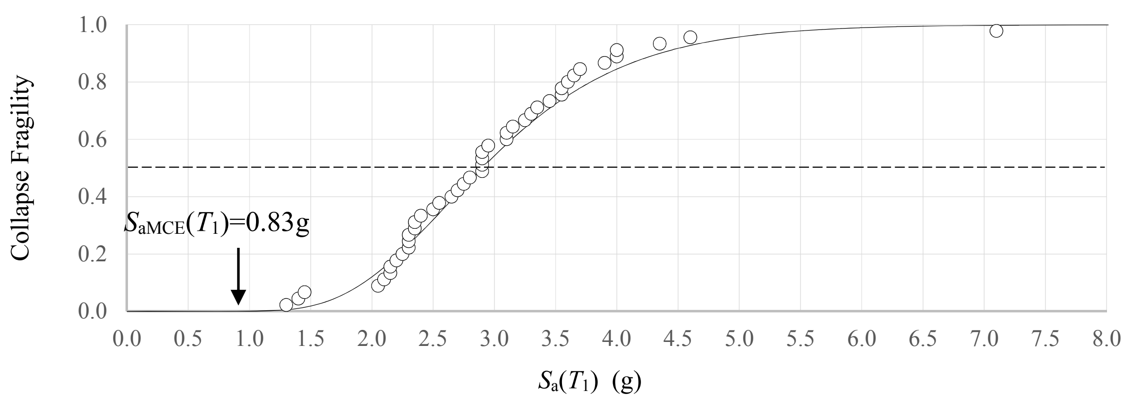

Detailed data

$S_{aMCE}(T_1)$	$S_{aCOL}(T_1)$	*CMR*	β
0.83g	2.90g	3.49	0.32

$S_a(T_1)$ (g)	Number of collapses	$S_a(T_1)$ (g)	Number of collapses
<1.30	0	2.90	23
1.30	1	2.90	24
1.40	2	2.90	25
1.45	3	2.95	26
2.05	4	3.10	27
2.10	5	3.10	28

2.15	6	3.15	29
2.15	7	3.25	30
2.20	8	3.30	31
2.25	9	3.35	32
2.30	10	3.45	33
2.30	11	3.55	34
2.30	12	3.55	35
2.35	13	3.60	36
2.35	14	3.65	37
2.40	15	3.70	38
2.50	16	3.90	39
2.55	17	4.00	40
2.65	18	4.00	41
2.70	19	4.35	42
2.75	20	4.60	43
2.80	21	7.10	44
2.90	22		

Analyzed system

6S-75 Linear Damping β_{v1}=0.10 α=1 Ultimate Capacity 1.3F_{MCE} T_1=2.06sec	Story	F_0 [kN]	K_0 [kN/m]	Braces	C or C_N [kN-(s/m)$^\alpha$]	D_{Cap} [mm]	Ultimate $F_{Tension}$ [kN]	Ultimate F_{Compr} [kN]
	6th	100	1350	HSS8x8x3/8	2900	165	859	964
	5th	250	1790	HSS8×8×5/8	2900	165	1302	1434
	4th	250	1790	HSS8×8×5/8	2900	165	1302	1434
	3rd	400	2320	HSS9x9×5/8	2900	165	1843	1983
	2nd	400	2320	HSS9x9×5/8	2900	165	1843	1983
	1st	400	2320	HSS9x9×5/8	2900	165	1843	1983
S_a-component scaling								

IDA curves

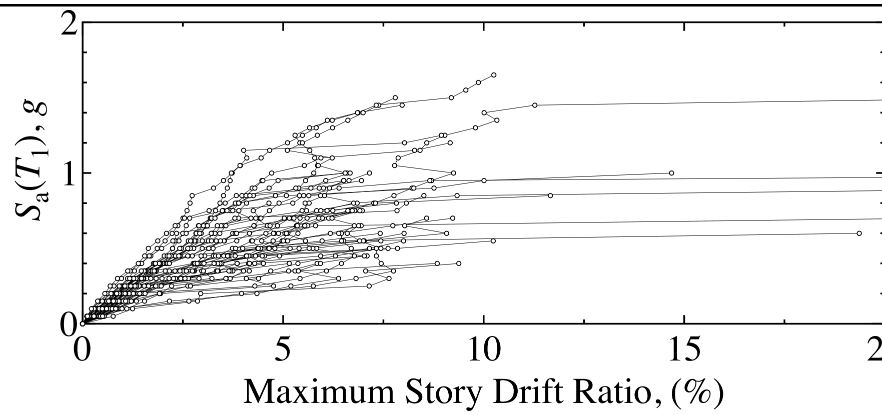

Collapse fragility curve

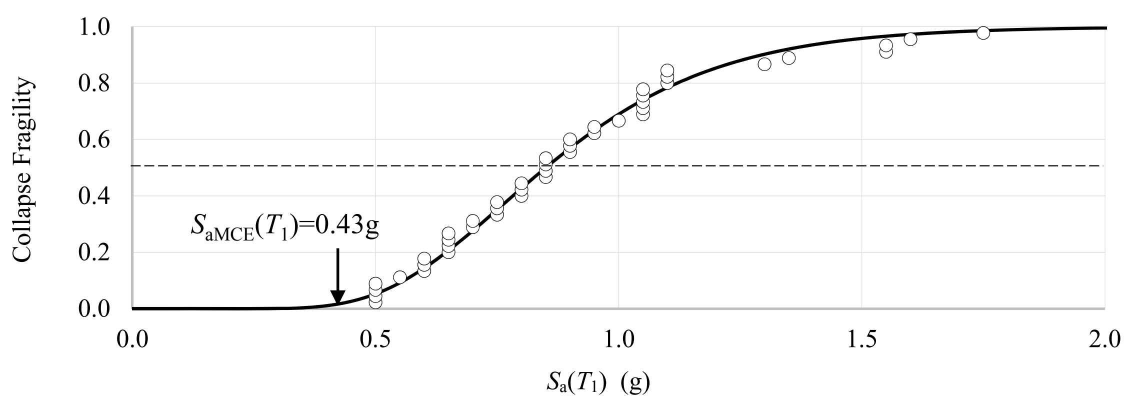

Detailed data

$S_{aMCE}(T_1)$, (g)	$S_{aCOL}(T_1)$, (g)	CMR	β
0.43	0.85	1.98	0.33

$S_a(T_1)$ (g)	Number of collapses	$S_a(T_1)$ (g)	Number of collapses
<0.50	0	0.85	23
0.50	1	0.85	24
0.50	2	0.90	25
0.50	3	0.90	26

0.50	4	0.90	27
0.55	5	0.95	28
0.60	6	0.95	29
0.60	7	1.00	30
0.60	8	1.05	31
0.65	9	1.05	32
0.65	10	1.05	33
0.65	11	1.05	34
0.65	12	1.05	35
0.70	13	1.10	36
0.70	14	1.10	37
0.75	15	1.10	38
0.75	16	1.30	39
0.75	17	1.35	40
0.80	18	1.55	41
0.80	19	1.55	42
0.80	20	1.60	43
0.85	21	1.75	44
0.85	22		

Analyzed system

6S-75 Nonlinear Damping β_{v1} =0.15 α=0.5 Ultimate Capacity $1.3F_{MCE}$ T_1=2.06sec	Story	F_0 [kN]	K_0 [kN/m]	Braces	C or C_N [kN-(s/m)$^{\alpha}$]	D_{Cap} [mm]	Ultimate $F_{Tension}$ [kN]	Ultimate F_{Compr} [kN]
	6th	100	1350	HSS8x8x3/8	1433	165	859	964
	5th	250	1790	HSS8×8×5/8	1433	165	1302	1434
	4th	250	1790	HSS8×8×5/8	1433	165	1302	1434
	3rd	400	2320	HSS9x9×5/8	1433	165	1843	1983
	2nd	400	2320	HSS9x9×5/8	1433	165	1843	1983
	1st	400	2320	HSS9x9×5/8	1433	165	1843	1983
S_a-component scaling								

IDA curves

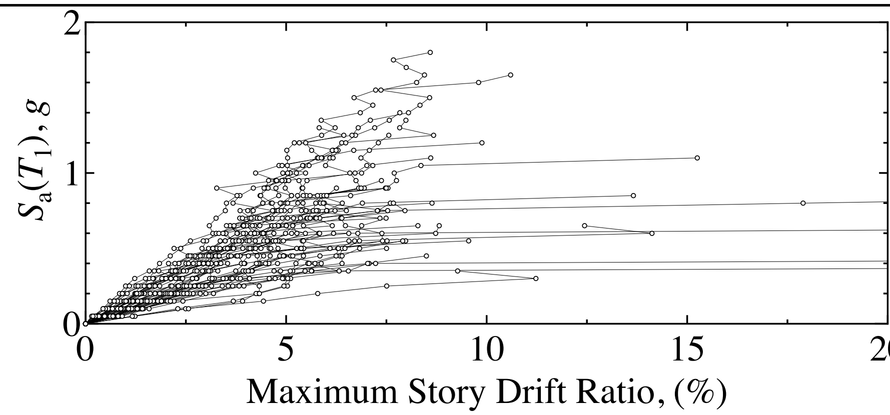

Collapse fragility curve

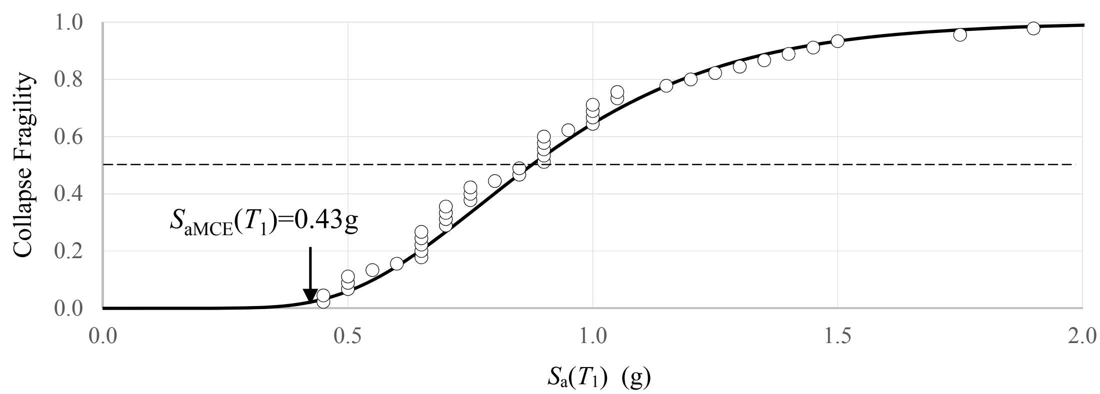

Detailed data

$S_{aMCE}(T_1)$, (g)	$S_{aCOL}(T_1)$, (g)	CMR	β
0.43	0.88	2.05	0.36

$S_a(T_1)$ (g)	Number of collapses	$S_a(T_1)$ (g)	Number of collapses
<0.45	0	0.90	23
0.45	1	0.90	24
0.45	2	0.90	25
0.50	3	0.90	26

0.50	4	0.90	27
0.50	5	0.95	28
0.55	6	1.00	29
0.60	7	1.00	30
0.65	8	1.00	31
0.65	9	1.00	32
0.65	10	1.05	33
0.65	11	1.05	34
0.65	12	1.15	35
0.70	13	1.20	36
0.70	14	1.25	37
0.70	15	1.30	38
0.70	16	1.35	39
0.75	17	1.40	40
0.75	18	1.45	41
0.75	19	1.50	42
0.80	20	1.75	43
0.85	21	1.90	44
0.85	22		

Analyzed system

6S-75 Linear Damping β_{v1} =0.10 α=1.0 Ultimate Capacity 2.0F_{MCE} T_1=2.06sec	Story	F_0 [kN]	K_0 [kN/m]	Braces	C or C_N [kN-(s/m)$^{\alpha}$]	D_{Cap} [mm]	Ultimate $F_{Tension}$ [kN]	Ultimate F_{Compr} [kN]
	6th	100	1350	HSS8x8x5/8	2900	165	1305	1305
	5th	250	1790	HSS9×9×5/8	2900	165	1983	1983
	4th	250	1790	HSS9×9×5/8	2900	165	1983	1983
	3rd	400	2320	HSS12x12×5/8	2900	165	3026	3026
	2nd	400	2320	HSS12x12×5/8	2900	165	3026	3026
	1st	400	2320	HSS12x12×5/8	2900	165	3026	3026
S_a-component scaling								

IDA curves

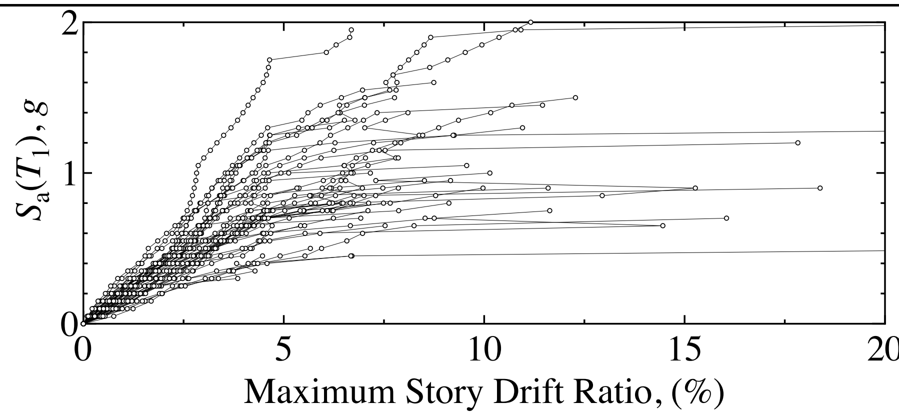

Collapse fragility curve

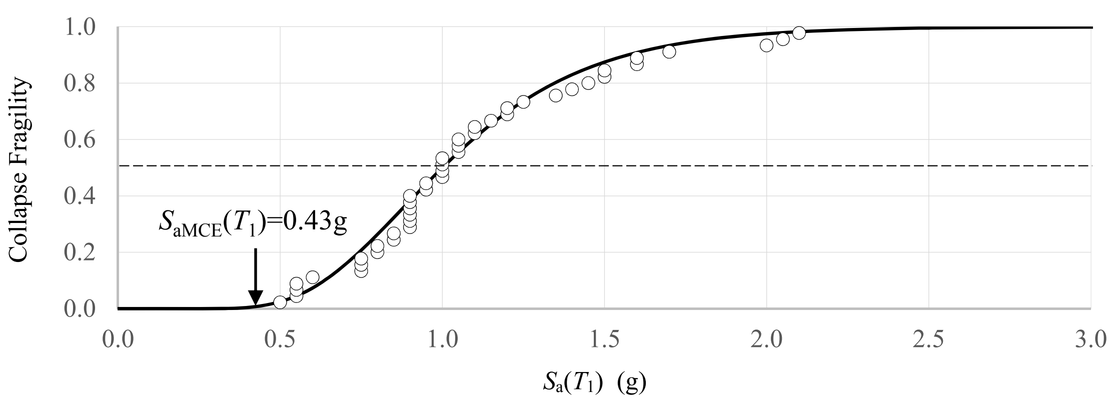

Detailed data

$S_{aMCE}(T_1)$, (g)	$S_{aCOL}(T_1)$, (g)	CMR	β
0.43	1.00	2.33	0.35

$S_a(T_1)$ (g)	Number of collapses	$S_a(T_1)$ (g)	Number of collapses
<0.50	0	1.00	23
0.50	1	1.00	24
0.55	2	1.05	25
0.55	3	1.05	26

		0.55	4	1.05	27	
		0.60	5	1.10	28	
		0.75	6	1.10	29	
		0.75	7	1.15	30	
		0.75	8	1.20	31	
		0.80	9	1.20	32	
		0.80	10	1.25	33	
		0.85	11	1.35	34	
		0.85	12	1.40	35	
		0.90	13	1.45	36	
		0.90	14	1.50	37	
		0.90	15	1.50	38	
		0.90	16	1.60	39	
		0.90	17	1.60	40	
		0.90	18	1.70	41	
		0.95	19	2.00	42	
		0.95	20	2.05	43	
		1.00	21	2.10	44	
		1.00	22			

Analyzed system

	Story	F_0 [kN]	K_0 [kN/m]	Braces	C or C_N [kN-(s/m)$^{\alpha}$]	D_{Cap} [mm]	Ultimate $F_{Tension}$ [kN]	Ultimate F_{Compr} [kN]
6S-Reference T_1=1.90sec	6th	-	-	-	-	-	-	-
	5th	-	-	-	-	-	-	-
	4th	-	-	-	-	-	-	-
	3rd	-	-	-	-	-	-	-
	2nd	-	-	-	-	-	-	-
	1st	-	-	-	-	-	-	-
S_a-component scaling								

IDA curves

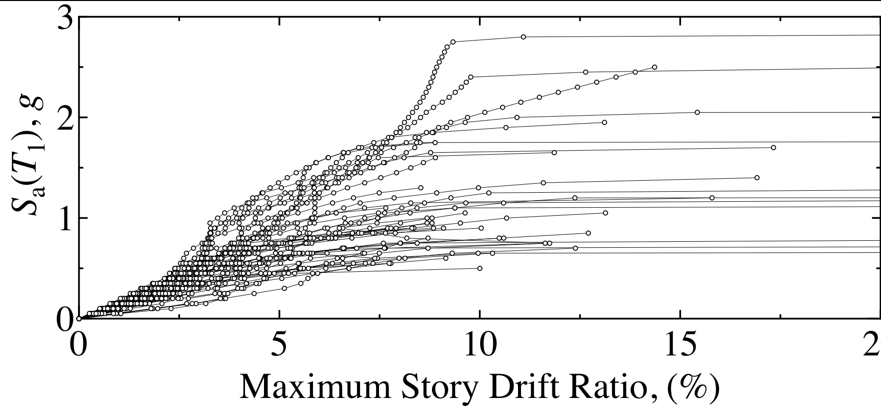

Collapse fragility curve

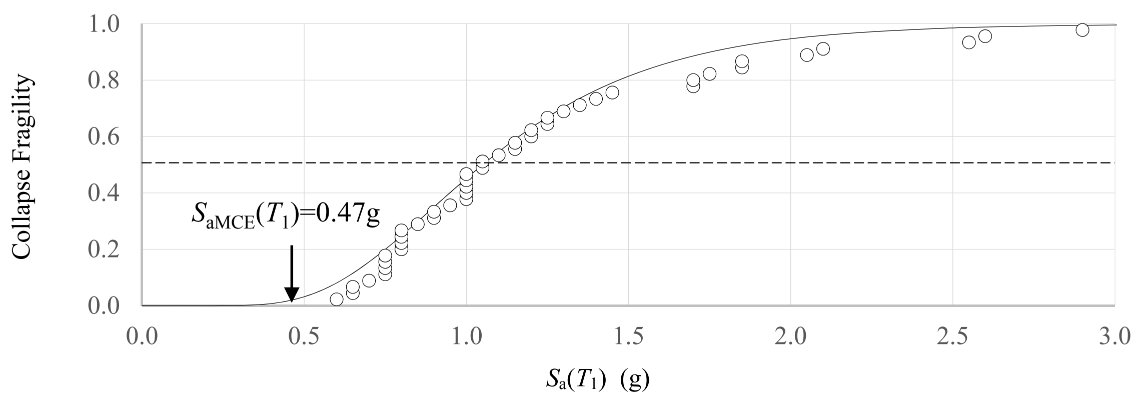

Detailed data

$S_{aMCE}(T_1)$, (g)	$S_{aCOL}(T_1)$, (g)	CMR	β
0.47	1.05	2.44	0.40

$S_a(T_1)$ (g)	Number of collapses	$S_a(T_1)$ (g)	Number of collapses
<0.60	0	1.05	23
0.60	1	1.10	24
0.65	2	1.15	25
0.65	3	1.15	26

	0.70	4	1.20	27	
	0.75	5	1.20	28	
	0.75	6	1.25	29	
	0.75	7	1.25	30	
	0.75	8	1.30	31	
	0.80	9	1.35	32	
	0.80	10	1.40	33	
	0.80	11	1.45	34	
	0.80	12	1.70	35	
	0.85	13	1.70	36	
	0.90	14	1.75	37	
	0.90	15	1.85	38	
	0.95	16	1.85	39	
	1.00	17	2.05	40	
	1.00	18	2.10	41	
	1.00	19	2.55	42	
	1.00	20	2.60	43	
	1.00	21	2.90	44	
	1.05	22			

Analyzed system

6S-75 Linear Damping	Story	F_0 [kN]	K_0 [kN/m]	Braces	C or C_N [kN-(s/m)$^\alpha$]	D_{Cap} [mm]	Ultimate $F_{Tension}$ [kN]	Ultimate F_{Compr} [kN]
β_{v1} =0.10	6th	100	1350	HSS8x8x3/8	2900	165	859	964
α=1	5th	250	1790	HSS8×8×5/8	2900	165	1302	1434
Ultimate	4th	250	1790	HSS8×8×5/8	2900	165	1302	1434
Capacity	3rd	400	2320	HSS9x9×5/8	2900	165	1843	1983
1.3F_{MCE}	2nd	400	2320	HSS9x9×5/8	2900	165	1843	1983
T_1=2.06sec	1st	400	2320	HSS9x9×5/8	2900	165	1843	1983

PGV Normalization scaling

IDA curves

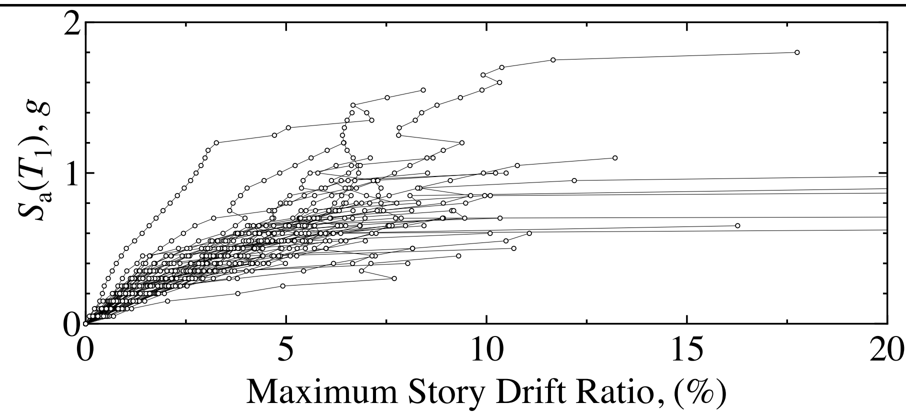

Collapse fragility curve

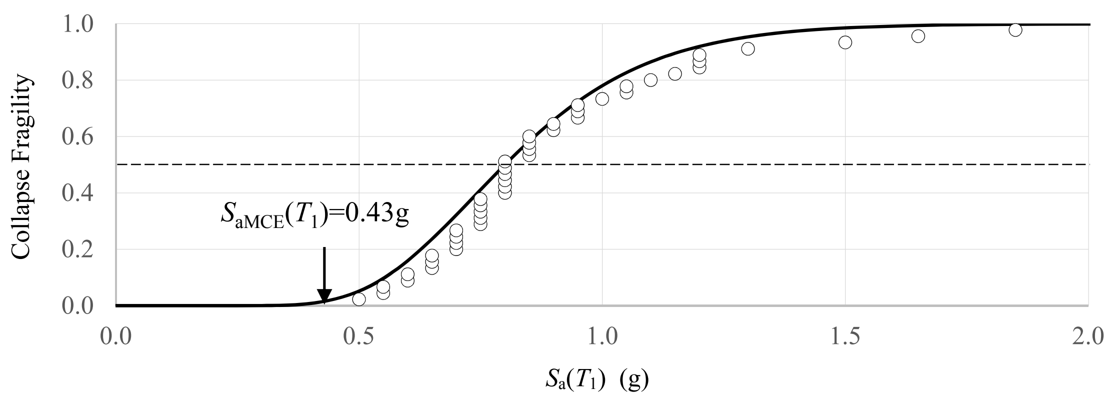

Detailed data

$S_{aMCE}(T_1)$, (g)	$S_{aCOL}(T_1)$, (g)	*CMR*	β
0.43	0.80	1.86	0.29

$S_a(T_1)$ (g)	Number of collapses	$S_a(T_1)$ (g)	Number of collapses
<0.50	0	0.80	23
0.50	1	0.85	24
0.55	2	0.85	25
0.55	3	0.85	26

0.60	4	0.85	27
0.60	5	0.90	28
0.65	6	0.90	29
0.65	7	0.95	30
0.65	8	0.95	31
0.70	9	0.95	32
0.70	10	1.00	33
0.70	11	1.05	34
0.70	12	1.05	35
0.75	13	1.10	36
0.75	14	1.15	37
0.75	15	1.20	38
0.75	16	1.20	39
0.75	17	1.20	40
0.80	18	1.30	41
0.80	19	1.50	42
0.80	20	1.65	43
0.80	21	1.85	44
0.80	22		

Analyzed system	6S-Reference T_1=1.90sec	Story	F_0 [kN]	K_0 [kN/m]	Braces	C or C_N [kN-(s/m)$^{\alpha}$]	D_{Cap} [mm]	Ultimate $F_{Tension}$ [kN]	Ultimate F_{Compr} [kN]
		6th	-	-	-	-	-	-	-
		5th	-	-	-	-	-	-	-
		4th	-	-	-	-	-	-	-
		3rd	-	-	-	-	-	-	-
		2nd	-	-	-	-	-	-	-
		1st	-	-	-	-	-	-	-
	PGV Normalization scaling								

IDA curves

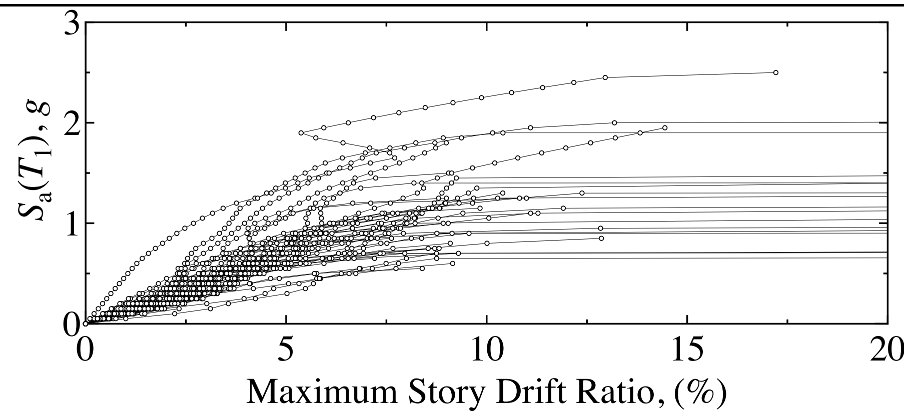

Collapse fragility curve

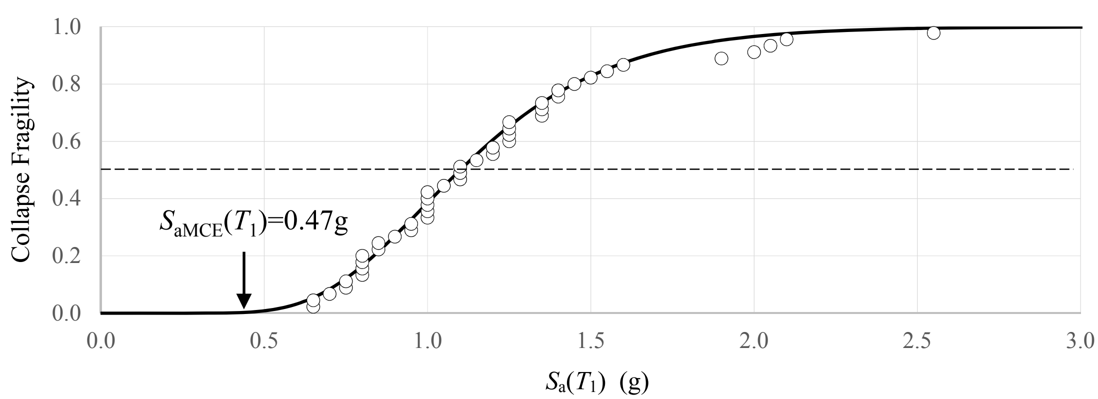

Detailed data

$S_{aMCE}(T_1)$, (g)	$S_{aCOL}(T_1)$, (g)	*CMR*	β
0.47	1.10	2.34	0.33

$S_a(T_1)$ (g)	Number of collapses	$S_a(T_1)$ (g)	Number of collapses
<0.65	0	1.10	23
0.65	1	1.15	24
0.65	2	1.20	25
0.70	3	1.20	26

		0.75	4	1.25	27	
		0.75	5	1.25	28	
		0.80	6	1.25	29	
		0.80	7	1.25	30	
		0.80	8	1.35	31	
		0.80	9	1.35	32	
		0.85	10	1.35	33	
		0.85	11	1.40	34	
		0.90	12	1.40	35	
		0.95	13	1.45	36	
		0.95	14	1.50	37	
		1.00	15	1.55	38	
		1.00	16	1.60	39	
		1.00	17	1.90	40	
		1.00	18	2.00	41	
		1.00	19	2.05	42	
		1.05	20	2.10	43	
		1.10	21	2.55	44	
		1.10	22			

APPENDIX F
DETAILED RESIDUAL DRIFT FRAGILITY DATA

This appendix presents detailed data obtained in the residual drift fragility analysis. Data for each analyzed case are presented in tables that contain the following:

1) Information on the analyzed system.
2) Computed Incremental Dynamic Analysis (IDA) curves.
3) Graph of the best-fit lognormal cumulative distribution function to the empirical data.
4) Values of the median of the spectral acceleration at the fundamental period of structure and the dispersion factor for specified values of the residual drift, and of the spectral acceleration at the fundamental period in the MCE.
5) Number of ground motions in which the peak residual drift ratio exceeded the specified limits of 0.2%, 0.5%, 1% and 2%.

The procedure followed in the construction of the fragility curves followed the steps below.

1) Incremental dynamic analysis was conducted for the system using each of the 44 motions. The earthquake intensity was increased by a step of 0.05g in the spectral acceleration value at the fundamental period until either collapse was observed or a specified value of the residual drift was exceeded, whoever occurred first. These resulted in the curves for the 44 motions shown in the IDA graphs.
2) The duration of the ground motions was increased with 10 seconds of zero acceleration to allow for calculation of the residual deformations.
3) The spectral acceleration at the fundamental period of the structure at which a specified value of the residual drift was exceeded was determined. This required the use of interpolation to obtain values of the spectral acceleration as the increment in acceleration of 0.05g often caused to exceed both limits of 0.2% and 0.5% in residual drift in the same step. The process utilized is illustrated in the IDA curve schematic below (Figure F-1). Linear interpolation was used. The values reported are $S_{a,A}$ for residual drift of 0.2% and $S_{a,B}$ for residual drift of 0.5%. Otherwise, the spectral acceleration value of $S_{a,i+2}$ would have been reported for both events.

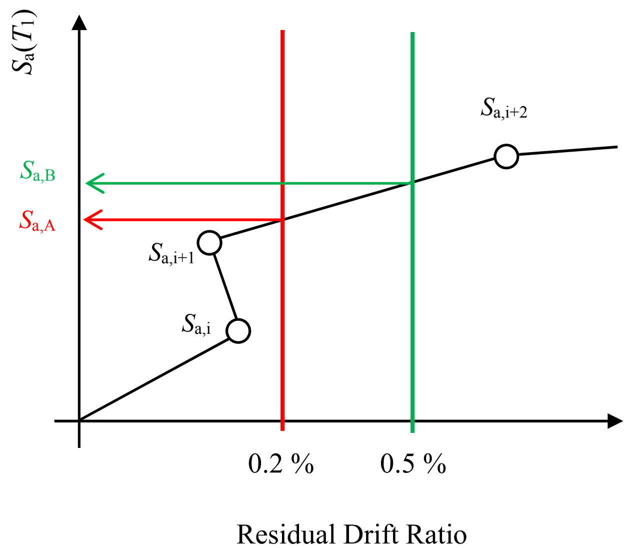

Figure F-1 Spectral Acceleration at Exceedance of Specified Residual Drift Ratio

4) Steps 2 to 6 of Appendix E were followed.

Analyzed system

3*S*-75 Linear Damping β_{v1} =0.10 α=1 Ultimate Capacity 1.3F_{MCE} T_1=1.31sec	Story	F_0 [kN]	K_0 [kN/m]	Braces	C or C_N [kN-(s/m)$^\alpha$]	D_{Cap} [mm]	Ultimate $F_{Tension}$ [kN]	Ultimate F_{Compr} [kN]
	3rd	125	1545	HSS8x8×1/2	1140	165	1160	1215
	2nd	300	2320	HSS8x8×1/2	1140	165	1160	1215
	1st	300	2320	HSS8x8×1/2	1140	165	1160	1215
S_a-component scaling								

IDA curves

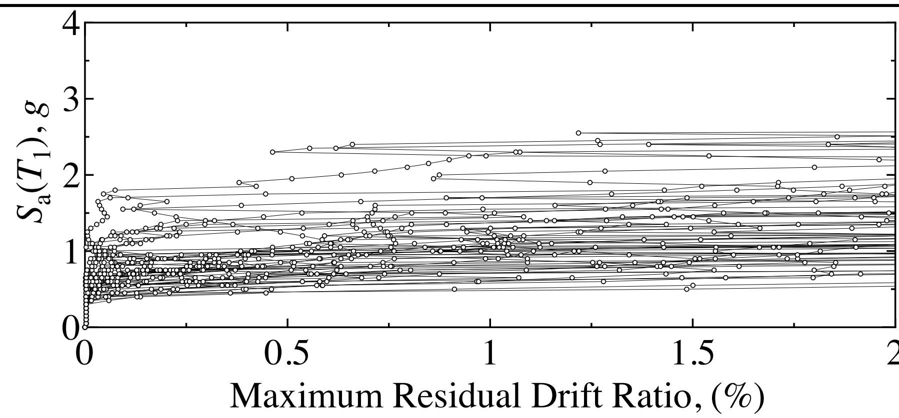

Residual drift fragility curves (Probability of exceeding the specified value of residual drift)

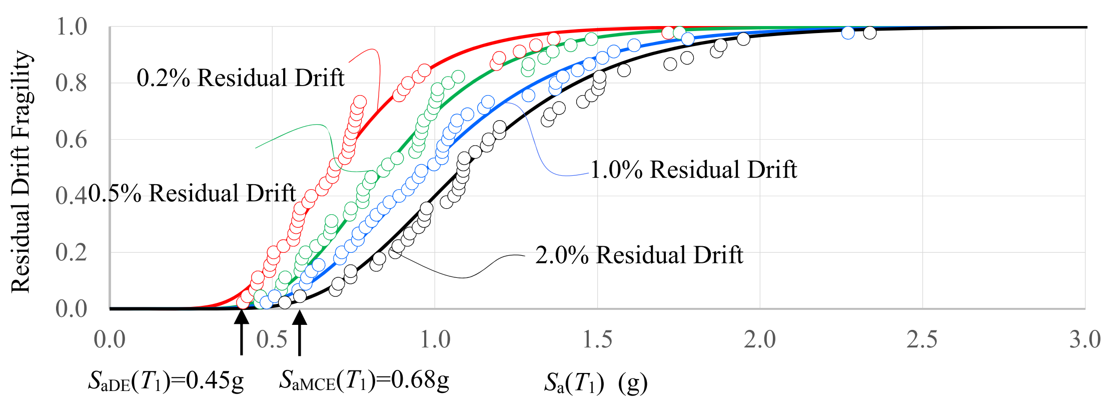

Detailed data

Residual Drift Ratio, %	$S_{aMCE}(T_1)$	Median $S_a(T_1)$	Median $S_a(T_1)$ / $S_{aMCE}(T_1)$	β
0.2	0.68g	0.69g	1.01	0.34
0.5		0.85g	1.25	0.32
1.0		0.98g	1.44	0.35

2.0		1.09g	1.60	0.33

$S_a(T_1)$ (g) for 0.2 % Residual Drift	$S_a(T_1)$ (g) for 0.5 % Residual Drift	$S_a(T_1)$ (g) for 1.0 % Residual Drift	$S_a(T_1)$ (g) for 2.0 % Residual Drift	Number of Exceedances
<0.41	<0.46	<0.48	<0.54	0
0.41	0.46	0.48	0.54	1
0.42	0.46	0.51	0.59	2
0.45	0.53	0.58	0.69	3
0.45	0.53	0.60	0.70	4
0.46	0.54	0.61	0.74	5
0.49	0.59	0.62	0.74	6
0.49	0.59	0.64	0.82	7
0.50	0.59	0.71	0.83	8
0.50	0.60	0.71	0.88	9
0.53	0.64	0.74	0.89	10
0.56	0.66	0.76	0.92	11
0.57	0.68	0.77	0.92	12
0.57	0.68	0.79	0.95	13
0.58	0.68	0.81	0.97	14
0.58	0.74	0.82	0.97	15
0.59	0.74	0.84	0.98	16
0.61	0.78	0.86	1.04	17
0.62	0.78	0.89	1.06	18
0.65	0.78	0.92	1.07	19
0.66	0.80	0.93	1.07	20
0.68	0.80	0.95	1.08	21
0.69	0.84	0.96	1.09	22
0.70	0.86	1.00	1.09	23
0.72	0.88	1.02	1.09	24
0.73	0.94	1.02	1.12	25
0.74	0.95	1.03	1.16	26
0.74	0.95	1.04	1.17	27
0.74	0.96	1.04	1.20	28
0.75	0.96	1.06	1.20	29
0.75	0.97	1.07	1.35	30
0.76	0.99	1.10	1.35	31
0.76	1.00	1.15	1.38	32
0.77	1.00	1.16	1.46	33
0.89	1.01	1.29	1.48	34
0.90	1.01	1.37	1.50	35
0.92	1.04	1.37	1.51	36
0.95	1.07	1.39	1.51	37
0.97	1.29	1.44	1.58	38

	1.19	1.29	1.48	1.72	39
	1.20	1.34	1.52	1.78	40
	1.26	1.36	1.55	1.87	41
	1.31	1.42	1.61	1.88	42
	1.37	1.48	1.78	1.95	43
	1.72	1.75	2.27	2.34	44

Analyzed system								
3*S*-75, Increased Preload Capacity 1.3F_{MCE} Linear Viscous Damping β_{v1} =0.10 T_1= 1.28sec	Story	F_0 [kN]	K_0 [kN/m]	Braces	C or C_N [kN-(s/m)$^\alpha$]	D_{Cap} [mm]	Ultimate $F_{Tension}$ [kN]	Ultimate F_{Compr} [kN]
	3rd	160	1545	HSS8x8×5/8	1140	165	1435	1435
	2nd	390	2320	HSS8x8×5/8	1140	165	1435	1435
	1st	390	2320	HSS8x8×5/8	1140	165	1435	1435
S_a-component scaling								

IDA curves

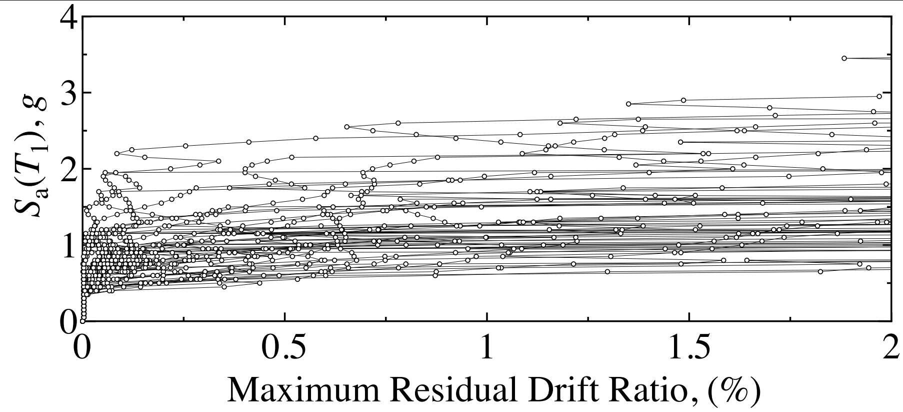

Residual drift fragility curves (Probability of exceeding the specified value of residual drift)

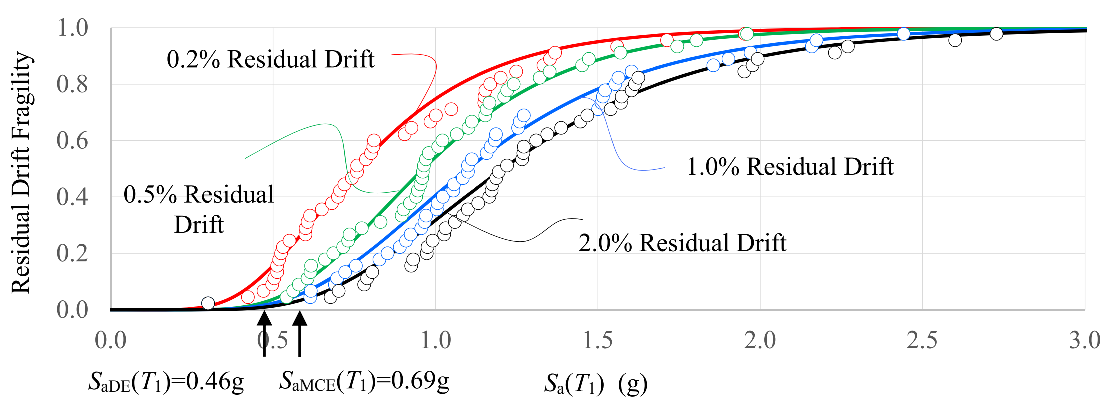

Detailed data

Residual Drift Ratio, %	$S_{aMCE}(T_1)$	Median $S_a(T_1)$	Median $S_a(T_1)$ / $S_{aMCE}(T_1)$	β
0.2	0.69g	0.76g	1.10	0.41
0.5		0.96g	1.39	0.37
1.0		1.10g	1.59	0.40

2.0		1.21g	1.75	0.40

$S_a(T_1)$ (g) for 0.2 % Residual Drift	$S_a(T_1)$ (g) for 0.5 % Residual Drift	$S_a(T_1)$ (g) for 1.0 % Residual Drift	$S_a(T_1)$ (g) for 2.0 % Residual Drift	Number of Exceedances
<0.30	<0.30	<0.30	<0.30	0
0.30	0.30	0.30	0.30	1
0.42	0.54	0.62	0.68	2
0.47	0.56	0.62	0.70	3
0.50	0.58	0.69	0.78	4
0.50	0.61	0.70	0.79	5
0.51	0.62	0.72	0.81	6
0.51	0.62	0.76	0.93	7
0.52	0.66	0.83	0.93	8
0.53	0.69	0.85	0.97	9
0.53	0.72	0.89	0.98	10
0.55	0.73	0.91	0.99	11
0.60	0.74	0.92	1.03	12
0.60	0.77	0.96	1.03	13
0.61	0.83	0.97	1.06	14
0.61	0.90	0.97	1.09	15
0.65	0.90	1.00	1.10	16
0.68	0.92	1.01	1.13	17
0.70	0.94	1.02	1.17	18
0.71	0.95	1.06	1.17	19
0.72	0.95	1.06	1.18	20
0.74	0.96	1.08	1.19	21
0.76	0.96	1.10	1.20	22
0.76	0.96	1.10	1.22	23
0.79	0.97	1.11	1.27	24
0.80	0.98	1.16	1.27	25
0.81	1.01	1.17	1.27	26
0.81	1.02	1.18	1.31	27
0.91	1.07	1.19	1.34	28
0.93	1.10	1.25	1.39	29
0.98	1.11	1.26	1.45	30
1.00	1.15	1.27	1.47	31
1.05	1.16	1.50	1.54	32
1.15	1.17	1.51	1.57	33
1.15	1.21	1.52	1.57	34
1.15	1.22	1.52	1.60	35
1.17	1.24	1.55	1.61	36
1.20	1.32	1.56	1.63	37
1.25	1.35	1.60	1.95	38

	1.33	1.45	1.86	1.98	39
	1.35	1.47	1.90	1.99	40
	1.37	1.57	1.97	2.23	41
	1.56	1.74	2.16	2.27	42
	1.71	1.80	2.17	2.60	43
	1.95	1.96	2.44	2.73	44

Analyzed system

3S-75, Increased Capacity 2.0 F_{MCE} Linear Viscous Damping β_{v1} =0.10 T_1= 1.31sec	Story	F_0 [kN]	K_0 [kN/m]	Braces	C or C_N [kN-(s/m)$^{\alpha}$]	D_{Cap} [mm]	Ultimate $F_{Tension}$ [kN]	Ultimate F_{Compr} [kN]
	3rd	125	1545	HSS9x9×5/8	1140	165	1983	1983
	2nd	300	2320	HSS9x9×5/8	1140	165	1983	1983
	1st	300	2320	HSS9x9×5/8	1140	165	1983	1983

S_a-component scaling

IDA curves

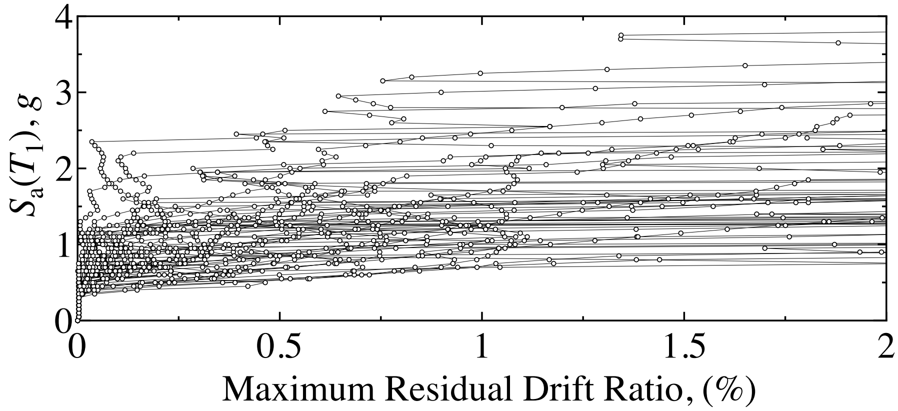

Residual drift fragility curves (Probability of exceeding the specified value of residual drift)

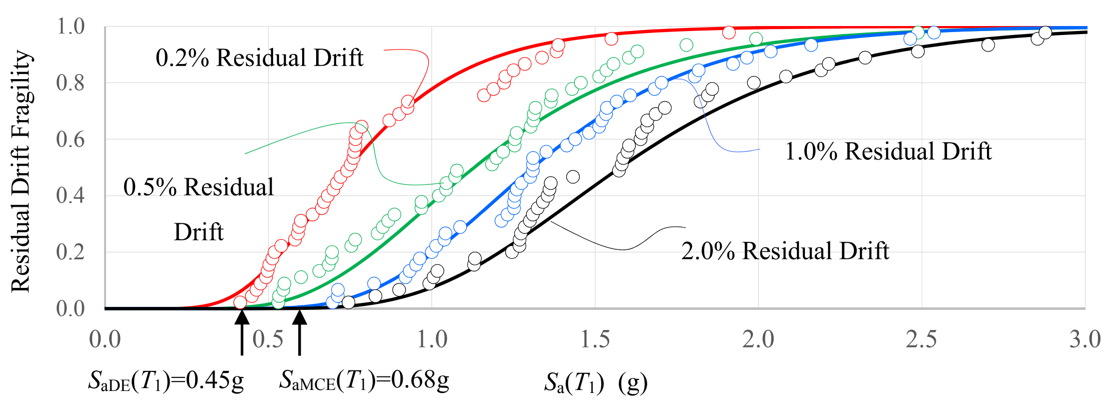

Detailed data

Residual Drift Ratio, %	$S_{aMCE}(T_1)$	Median $S_a(T_1)$	Median $S_a(T_1)$ / $S_{aMCE}(T_1)$	β
0.2	0.68g	0.75g	1.10	0.38
0.5		1.13g	1.66	0.38
1.0		1.31g	1.93	0.31
2.0		1.58g	2.32	0.32

$S_a(T_1)$ (g) for 0.2 % Residual Drift	$S_a(T_1)$ (g) for 0.5 % Residual Drift	$S_a(T_1)$ (g) for 1.0 % Residual Drift	$S_a(T_1)$ (g) for 2.0 % Residual Drift	Number of Exceedances
<0.41	<0.53	<0.70	<0.75	0
0.41	0.53	0.70	0.75	1
0.45	0.53	0.71	0.83	2
0.46	0.55	0.71	0.90	3
0.48	0.55	0.82	0.99	4
0.49	0.60	0.92	1.01	5
0.50	0.66	0.93	1.02	6
0.50	0.69	0.95	1.13	7
0.51	0.69	0.96	1.13	8
0.52	0.69	1.00	1.25	9
0.54	0.75	1.01	1.27	10
0.58	0.77	1.04	1.27	11
0.59	0.83	1.04	1.27	12
0.59	0.85	1.09	1.28	13
0.60	0.87	1.21	1.30	14
0.64	0.89	1.23	1.31	15
0.66	0.97	1.25	1.32	16
0.67	0.97	1.25	1.34	17
0.68	1.02	1.25	1.35	18
0.70	1.04	1.26	1.36	19
0.71	1.05	1.27	1.36	20
0.72	1.07	1.30	1.43	21
0.74	1.08	1.31	1.57	22
0.75	1.18	1.31	1.58	23
0.76	1.20	1.31	1.59	24
0.76	1.22	1.35	1.60	25
0.77	1.25	1.41	1.60	26
0.77	1.25	1.44	1.64	27
0.77	1.26	1.48	1.64	28
0.79	1.30	1.51	1.66	29
0.87	1.31	1.52	1.66	30
0.90	1.31	1.53	1.69	31
0.93	1.32	1.54	1.71	32
0.93	1.36	1.57	1.82	33
1.16	1.37	1.61	1.85	34
1.19	1.43	1.68	1.86	35
1.22	1.46	1.70	1.99	36
1.23	1.51	1.80	2.08	37
1.25	1.53	1.82	2.19	38
1.28	1.56	1.92	2.22	39

	1.34	1.60	1.96	2.33	40
	1.38	1.63	2.04	2.49	41
	1.39	1.78	2.16	2.70	42
	1.55	1.99	2.46	2.85	43
	1.91	2.49	2.54	2.88	44

Analyzed system	3*S*-75, Capacity $1.3F_{MCE}$ Increased Nonlinear Damping $\beta_{v1}=0.15$ in DE (α=0.5) T_1= 1.31sec							
	Story	F_0 [kN]	K_0 [kN/m]	Braces	C or C_N [kN-(s/m)$^\alpha$]	D_{Cap} [mm]	Ultimate $F_{Tension}$ [kN]	Ultimate F_{Compr} [kN]
	3rd	125	1545	HSS8x8x1/2	666.4	165	1160	1215
	2nd	300	2320	HSS8x8x1/2	666.4	165	1160	1215
	1st	300	2320	HSS8x8x1/2	666.4	165	1160	1215
	S_a-component scaling							

IDA curves

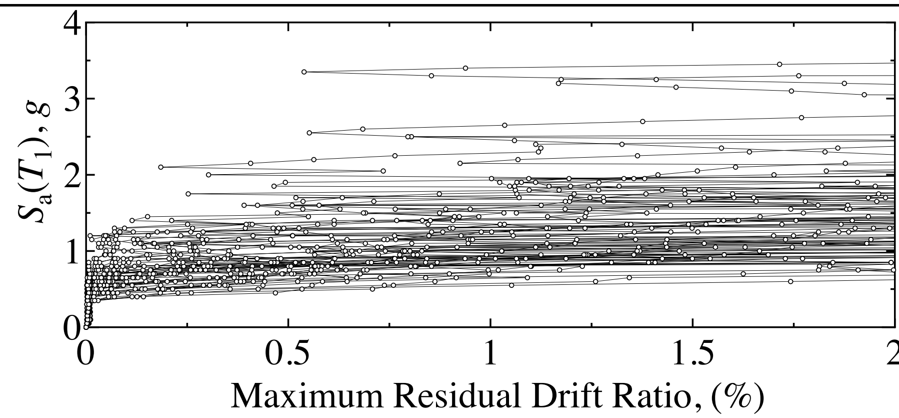

Residual drift fragility curves (Probability of exceeding the specified value of residual drift)

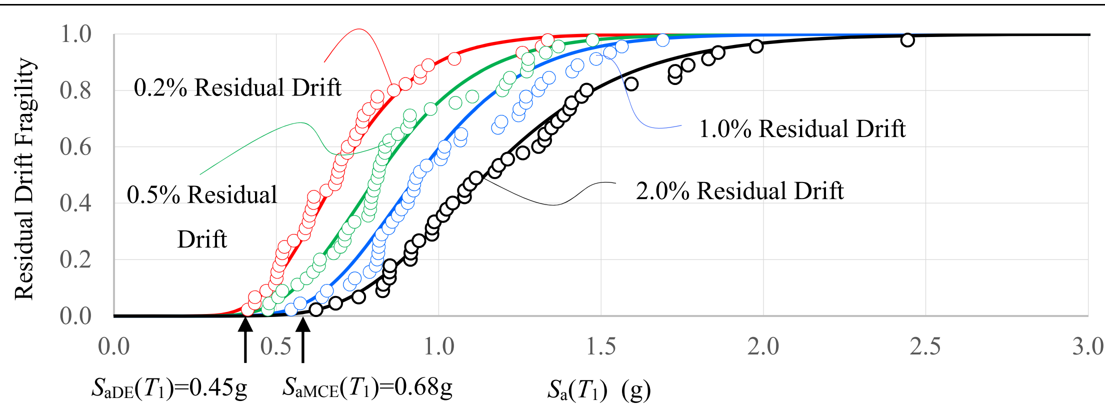

Detailed data

Residual Drift Ratio, %	$S_{aMCE}(T_1)$	Median $S_a(T_1)$	Median $S_a(T_1)$ / $S_{aMCE}(T_1)$	β
0.2	0.68g	0.69g	1.01	0.29
0.5		0.81g	1.19	0.29
1.0		0.94g	1.37	0.28

2.0		1.14g	1.68	0.30

$S_a(T_1)$ (g) for 0.2 % Residual Drift	$S_a(T_1)$ (g) for 0.5 % Residual Drift	$S_a(T_1)$ (g) for 1.0 % Residual Drift	$S_a(T_1)$ (g) for 2.0 % Residual Drift	Number of Exceedances
<0.41	<0.47	<0.55	<0.62	0
0.41	0.47	0.55	0.62	1
0.43	0.48	0.57	0.68	2
0.43	0.51	0.64	0.75	3
0.47	0.52	0.66	0.83	4
0.50	0.57	0.73	0.83	5
0.50	0.59	0.74	0.85	6
0.50	0.61	0.79	0.85	7
0.51	0.63	0.81	0.85	8
0.52	0.63	0.81	0.91	9
0.52	0.68	0.81	0.91	10
0.53	0.70	0.82	0.92	11
0.55	0.71	0.82	0.94	12
0.59	0.71	0.82	0.98	13
0.59	0.72	0.85	0.98	14
0.60	0.74	0.86	0.99	15
0.60	0.78	0.87	1.01	16
0.61	0.79	0.89	1.02	17
0.61	0.79	0.90	1.04	18
0.62	0.79	0.91	1.08	19
0.65	0.80	0.92	1.08	20
0.68	0.80	0.92	1.10	21
0.69	0.81	0.93	1.12	22
0.69	0.82	0.94	1.17	23
0.70	0.82	0.96	1.19	24
0.70	0.83	1.01	1.21	25
0.72	0.83	1.01	1.26	26
0.72	0.84	1.02	1.31	27
0.74	0.85	1.07	1.33	28
0.75	0.87	1.07	1.33	29
0.76	0.90	1.18	1.35	30
0.77	0.91	1.19	1.37	31
0.77	0.91	1.25	1.39	32
0.78	0.98	1.25	1.40	33
0.81	1.05	1.27	1.41	34
0.81	1.10	1.27	1.44	35
0.86	1.20	1.31	1.46	36
0.90	1.21	1.32	1.59	37
0.94	1.22	1.34	1.73	38

	0.94	1.27	1.41	1.73	39
	0.97	1.28	1.43	1.77	40
	1.05	1.28	1.48	1.83	41
	1.26	1.33	1.53	1.86	42
	1.32	1.37	1.56	1.98	43
	1.34	1.47	1.69	2.44	44

Analyzed system	3*S*-Reference T_1= 1.07sec	Story	F_0 [kN]	K_0 [kN/m]	Braces	C or C_N [kN-(s/m)$^\alpha$]	D_{Cap} [mm]	Ultimate $F_{Tension}$ [kN]	Ultimate F_{Compr} [kN]
		3rd	-	-	-	-	-	-	-
		2nd	-	-	-	-	-	-	-
		1st	-	-	-	-	-	-	-
	S_a-component scaling								

IDA curves

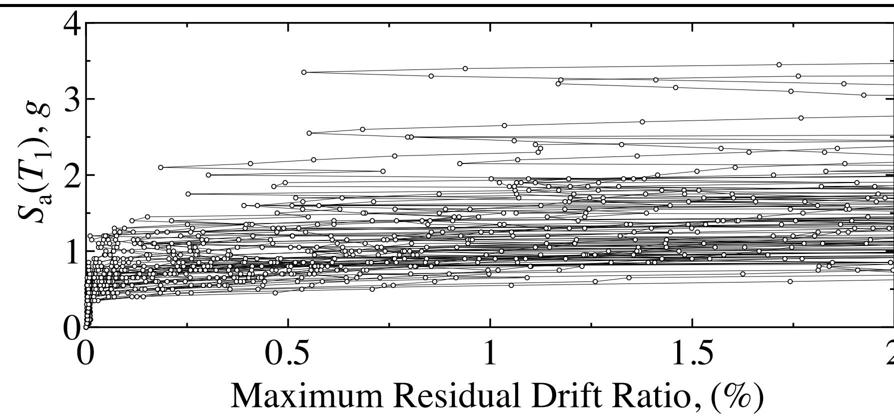

Residual drift fragility curves (Probability of exceeding the specified value of residual drift)

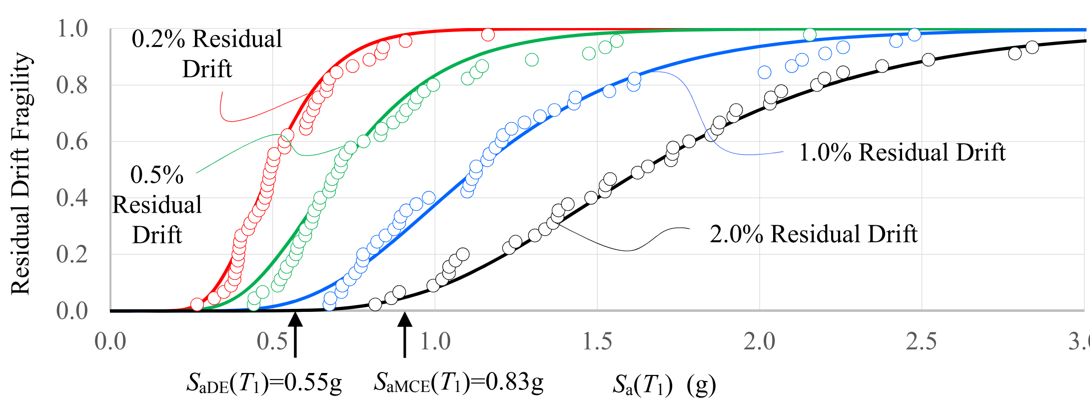

Detailed data

Residual Drift Ratio, %	$S_{aMCE}(T_1)$	Median $S_a(T_1)$	Median $S_a(T_1)$ / $S_{aMCE}(T_1)$	β
0.2	0.83g	0.49g	0.59	0.39
0.5		0.71g	0.85	0.39
1.0		1.13g	1.36	0.38
2.0		1.64g	1.98	0.37

$S_a(T_1)$ (g) for 0.2 % Residual Drift	$S_a(T_1)$ (g) for 0.5 % Residual Drift	$S_a(T_1)$ (g) for 1.0 % Residual Drift	$S_a(T_1)$ (g) for 2.0 % Residual Drift	Number of Exceedances
<0.27	<0.44	<0.67	<0.82	0
0.27	0.44	0.67	0.82	1
0.32	0.44	0.68	0.87	2
0.35	0.47	0.71	0.89	3
0.37	0.52	0.71	1.00	4
0.38	0.52	0.74	1.02	5
0.38	0.54	0.75	1.04	6
0.39	0.54	0.77	1.04	7
0.39	0.56	0.78	1.06	8
0.39	0.57	0.78	1.09	9
0.40	0.58	0.81	1.23	10
0.40	0.58	0.82	1.25	11
0.40	0.60	0.85	1.31	12
0.42	0.60	0.87	1.34	13
0.43	0.62	0.89	1.36	14
0.45	0.62	0.89	1.38	15
0.46	0.63	0.91	1.38	16
0.47	0.64	0.94	1.41	17
0.48	0.65	0.98	1.48	18
0.48	0.67	1.10	1.52	19
0.48	0.68	1.11	1.53	20
0.49	0.68	1.11	1.54	21
0.49	0.70	1.13	1.62	22
0.50	0.71	1.13	1.66	23
0.50	0.71	1.16	1.73	24
0.50	0.72	1.17	1.73	25
0.54	0.74	1.19	1.73	26
0.54	0.78	1.21	1.78	27
0.55	0.83	1.21	1.85	28
0.60	0.84	1.24	1.87	29
0.60	0.87	1.28	1.88	30
0.61	0.90	1.32	1.92	31
0.62	0.91	1.37	1.93	32
0.63	0.94	1.43	2.03	33
0.64	0.94	1.43	2.04	34
0.67	0.97	1.54	2.07	35
0.67	0.99	1.61	2.18	36
0.68	1.10	1.62	2.20	37
0.70	1.13	2.02	2.26	38
0.75	1.15	2.10	2.38	39

	0.80	1.30	2.13	2.52	40
	0.83	1.47	2.20	2.79	41
	0.84	1.52	2.26	2.84	42
	0.91	1.56	2.42	3.13	43
	1.16	2.15	2.48	3.65	44

Analyzed system

	Story	F_0 [kN]	K_0 [kN/m]	Braces	C or C_N [kN-(s/m)$^{\alpha}$]	D_{Cap} [mm]	Ultimate $F_{Tension}$ [kN]	Ultimate F_{Compr} [kN]
6*S*-75, Capacity 1.3F_{MCE} Linear Viscous Damping β_{v1} =0.10 T_1= 2.06sec	6th	100	1350	HSS8x8x3/8	2900	165	859	964
	5th	250	1790	HSS8×8×5/8	2900	165	1302	1434
	4th	250	1790	HSS8×8×5/8	2900	165	1302	1434
	3rd	400	2320	HSS9x9×5/8	2900	165	1843	1983
	2nd	400	2320	HSS9x9×5/8	2900	165	1843	1983
	1st	400	2320	HSS9x9×5/8	2900	165	1843	1983

S_a-component scaling

IDA curves

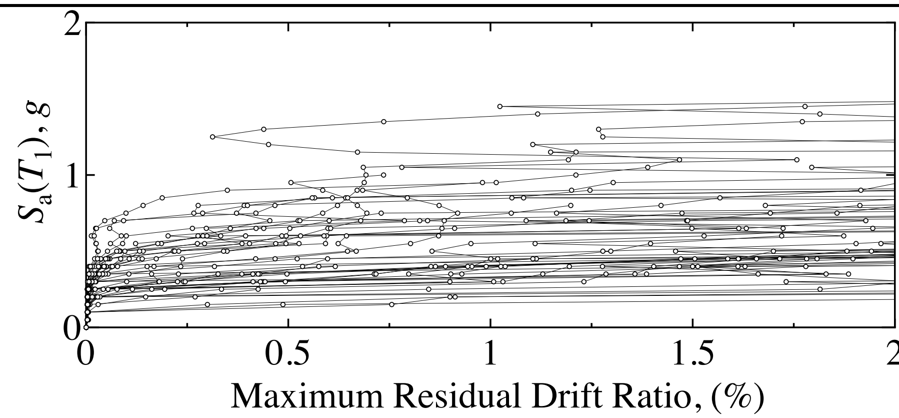

Residual drift fragility curves (Probability of exceeding the specified value of residual drift)

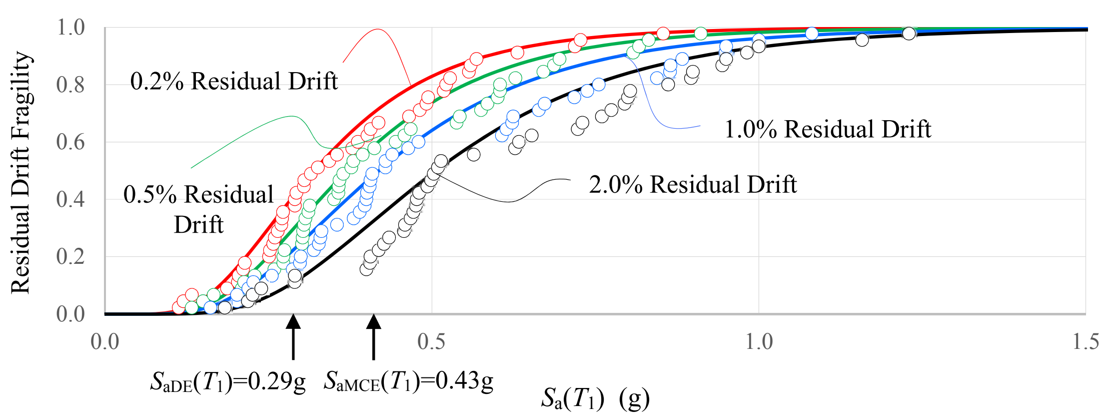

Detailed data

Residual Drift Ratio, %	$S_{aMCE}(T_1)$	Median $S_a(T_1)$	Median $S_a(T_1)$ / $S_{aMCE}(T_1)$	β

0.2	0.43g	0.32g	0.74	0.47
0.5		0.37g	0.86	0.47
1.0		0.42g	0.98	0.49
2.0		0.51g	1.19	0.46

$S_a(T_1)$ (g) for 0.2 % Residual Drift	$S_a(T_1)$ (g) for 0.5 % Residual Drift	$S_a(T_1)$ (g) for 1.0 % Residual Drift	$S_a(T_1)$ (g) for 2.0 % Residual Drift	Number of Exceedances
<0.11	<0.13	<0.16	<0.18	0
0.11	0.13	0.16	0.18	1
0.12	0.15	0.20	0.22	2
0.13	0.17	0.20	0.23	3
0.19	0.21	0.22	0.24	4
0.20	0.21	0.23	0.29	5
0.20	0.23	0.26	0.29	6
0.21	0.26	0.29	0.40	7
0.21	0.27	0.30	0.41	8
0.25	0.27	0.30	0.41	9
0.25	0.27	0.32	0.42	10
0.26	0.30	0.33	0.43	11
0.26	0.30	0.33	0.43	12
0.26	0.30	0.33	0.46	13
0.27	0.30	0.36	0.46	14
0.27	0.31	0.38	0.47	15
0.27	0.31	0.39	0.47	16
0.29	0.31	0.40	0.48	17
0.29	0.35	0.40	0.48	18
0.29	0.36	0.40	0.48	19
0.30	0.36	0.41	0.49	20
0.30	0.36	0.41	0.50	21
0.32	0.36	0.41	0.50	22
0.33	0.38	0.43	0.51	23
0.34	0.38	0.43	0.51	24
0.36	0.39	0.44	0.56	25
0.38	0.41	0.46	0.63	26
0.39	0.44	0.48	0.63	27
0.40	0.46	0.61	0.65	28
0.41	0.47	0.61	0.72	29
0.42	0.54	0.62	0.73	30
0.47	0.54	0.62	0.76	31
0.48	0.58	0.66	0.77	32
0.49	0.59	0.67	0.79	33
0.49	0.60	0.72	0.80	34

	0.52	0.60	0.74	0.80	35
	0.52	0.60	0.76	0.86	36
	0.53	0.63	0.84	0.90	37
	0.56	0.67	0.86	0.90	38
	0.56	0.69	0.86	0.94	39
	0.57	0.70	0.88	0.95	40
	0.63	0.81	0.95	0.98	41
	0.72	0.82	0.95	1.00	42
	0.73	0.83	1.00	1.16	43
	0.85	0.91	1.08	1.23	44

Analyzed system

6S-75, Capacity $1.3F_{MCE}$ Increased Nonlinear Damping $\beta_{v1}=0.15$ in DE (α=0.5) T_1= 2.06sec	Story	F_0 [kN]	K_0 [kN/m]	Braces	C or C_N [kN-(s/m)$^\alpha$]	D_{Cap} [mm]	Ultimate $F_{Tension}$ [kN]	Ultimate F_{Compr} [kN]
	6th	100	1350	HSS8x8x3/8	1433	165	859	964
	5th	250	1790	HSS8×8×5/8	1433	165	1302	1434
	4th	250	1790	HSS8×8×5/8	1433	165	1302	1434
	3rd	400	2320	HSS9x9×5/8	1433	165	1843	1983
	2nd	400	2320	HSS9x9×5/8	1433	165	1843	1983
	1st	400	2320	HSS9x9×5/8	1433	165	1843	1983
S_a-component scaling								

IDA curves

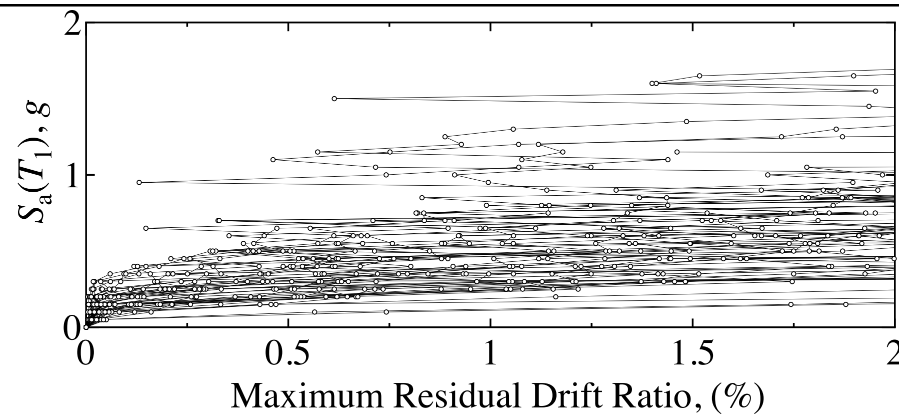

Residual drift fragility curves (Probability of exceeding the specified value of residual drift)

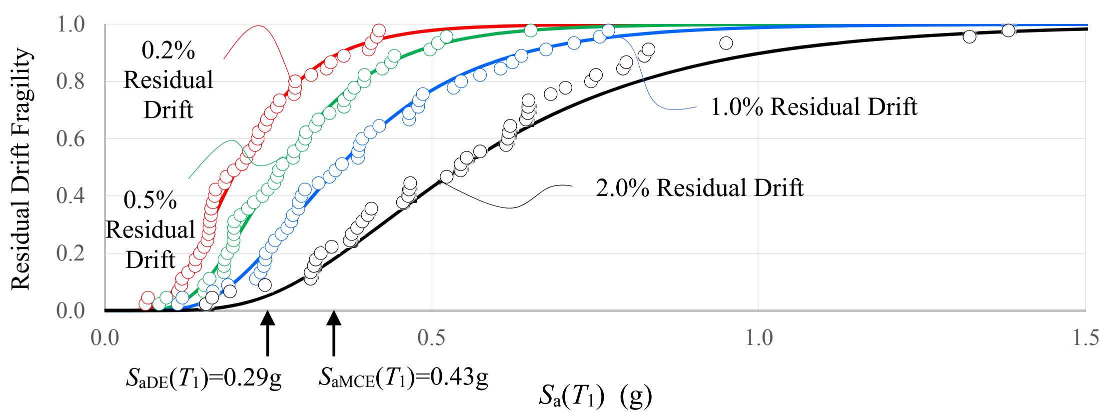

Detailed data

Residual Drift Ratio, %	$S_{aMCE}(T_1)$	Median $S_a(T_1)$	Median $S_a(T_1)$ / $S_{aMCE}(T_1)$	β
0.2	0.43g	0.20g	0.47	0.45

0.5		0.27g	0.63	0.44
1.0		0.36g	0.83	0.46
2.0		0.54g	1.27	0.48

$S_a(T_1)$ (g) for 0.2 % Residual Drift	$S_a(T_1)$ (g) for 0.5 % Residual Drift	$S_a(T_1)$ (g) for 1.0 % Residual Drift	$S_a(T_1)$ (g) for 2.0 % Residual Drift	Number of Exceedances
<0.06	<0.08	<0.11	<0.15	0
0.06	0.08	0.11	0.15	1
0.07	0.09	0.12	0.16	2
0.11	0.15	0.17	0.19	3
0.12	0.15	0.19	0.24	4
0.12	0.16	0.23	0.31	5
0.13	0.18	0.24	0.31	6
0.14	0.18	0.24	0.32	7
0.14	0.18	0.25	0.32	8
0.15	0.19	0.25	0.33	9
0.15	0.20	0.26	0.35	10
0.16	0.20	0.26	0.37	11
0.16	0.20	0.27	0.38	12
0.16	0.20	0.28	0.39	13
0.16	0.20	0.28	0.39	14
0.16	0.21	0.29	0.40	15
0.16	0.22	0.30	0.41	16
0.17	0.23	0.30	0.46	17
0.17	0.24	0.30	0.46	18
0.17	0.25	0.31	0.47	19
0.18	0.26	0.33	0.47	20
0.19	0.26	0.34	0.52	21
0.20	0.27	0.35	0.54	22
0.21	0.27	0.36	0.54	23
0.22	0.29	0.39	0.55	24
0.22	0.29	0.39	0.57	25
0.23	0.30	0.39	0.61	26
0.23	0.31	0.39	0.62	27
0.23	0.31	0.41	0.62	28
0.24	0.32	0.42	0.62	29
0.25	0.33	0.47	0.64	30
0.25	0.34	0.47	0.65	31
0.26	0.37	0.48	0.65	32
0.27	0.37	0.48	0.65	33
0.29	0.37	0.49	0.68	34
0.29	0.38	0.53	0.70	35

	0.29	0.40	0.54	0.74	36
	0.32	0.40	0.57	0.75	37
	0.34	0.42	0.61	0.79	38
	0.35	0.44	0.62	0.80	39
	0.37	0.44	0.64	0.83	40
	0.40	0.50	0.67	0.83	41
	0.41	0.51	0.72	0.95	42
	0.42	0.52	0.76	1.32	43
	0.42	0.65	0.77	1.38	44

Analyzed system

6S-75, Capacity $2.0F_{MCE}$ Linear Damping β_{v1}=0.10 in DE T_1= 2.06sec	Story	F_0 [kN]	K_0 [kN/m]	Braces	C or C_N [kN-(s/m)$^{\alpha}$]	D_{Cap} [mm]	Ultimate $F_{Tension}$ [kN]	Ultimate F_{Compr} [kN]
	6th	100	1350	HSS8x8x5/8	1433	165	859	964
	5th	250	1790	HSS9×9×5/8	1433	165	1302	1434
	4th	250	1790	HSS9×9×5/8	1433	165	1302	1434
	3rd	400	2230	HSS12x12×5/8	1433	165	1843	1983
	2nd	400	2230	HSS12x12×5/8	1433	165	1843	1983
	1st	400	2230	HSS12x12×5/8	1433	165	1843	1983
S_a-component scaling								

IDA curves

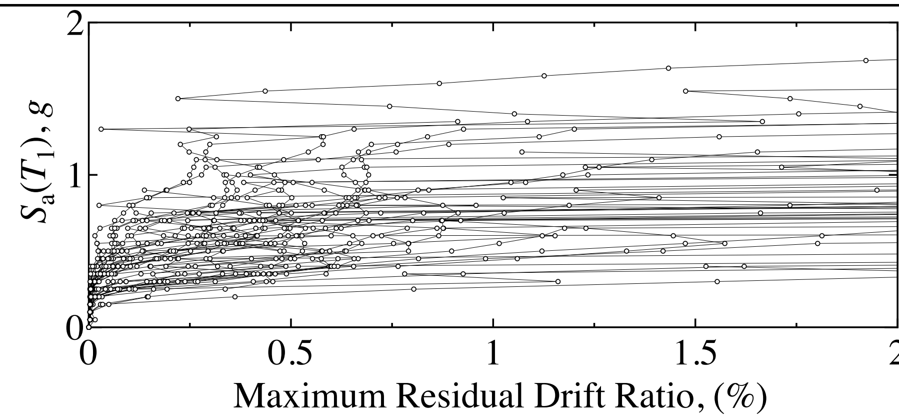

Residual drift fragility curves (Probability of exceeding the specified value of residual drift)

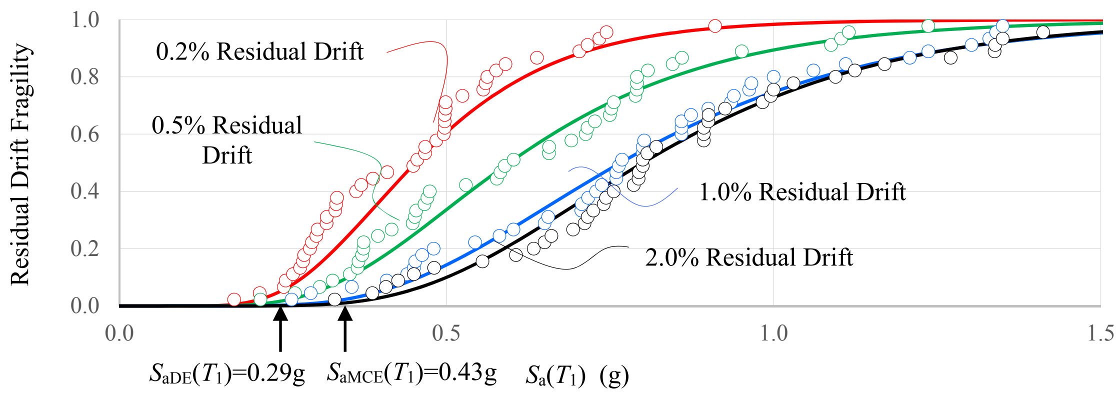

Detailed data

Residual Drift Ratio, %	$S_{aMCE}(T_1)$	Median $S_a(T_1)$	Median $S_a(T_1)$ / $S_{aMCE}(T_1)$	β
0.2	0.43g	0.45g	1.05	0.37

0.5		0.60g	1.39	0.42
1.0		0.77g	1.78	0.40
2.0		0.80g	1.86	0.37

$S_a(T_1)$ (g) for 0.2 % Residual Drift	$S_a(T_1)$ (g) for 0.5 % Residual Drift	$S_a(T_1)$ (g) for 1.0 % Residual Drift	$S_a(T_1)$ (g) for 2.0 % Residual Drift	Number of Exceedances
<0.18	<0.22	<0.26	<0.33	0
0.18	0.22	0.26	0.33	1
0.21	0.27	0.29	0.39	2
0.25	0.31	0.36	0.41	3
0.25	0.33	0.41	0.43	4
0.27	0.35	0.44	0.45	5
0.28	0.36	0.45	0.48	6
0.28	0.37	0.45	0.56	7
0.28	0.37	0.46	0.61	8
0.29	0.37	0.48	0.63	9
0.29	0.37	0.54	0.65	10
0.30	0.40	0.58	0.66	11
0.30	0.42	0.60	0.69	12
0.32	0.45	0.65	0.71	13
0.32	0.45	0.66	0.72	14
0.33	0.45	0.71	0.72	15
0.33	0.47	0.71	0.74	16
0.33	0.47	0.72	0.74	17
0.36	0.47	0.73	0.76	18
0.37	0.53	0.74	0.79	19
0.39	0.58	0.76	0.79	20
0.41	0.58	0.76	0.79	21
0.45	0.59	0.76	0.80	22
0.46	0.60	0.77	0.80	23
0.47	0.66	0.80	0.81	24
0.47	0.66	0.80	0.82	25
0.48	0.69	0.80	0.89	26
0.50	0.71	0.86	0.89	27
0.50	0.72	0.86	0.89	28
0.50	0.73	0.86	0.90	29
0.50	0.75	0.87	0.90	30
0.50	0.75	0.90	0.93	31
0.50	0.76	0.93	0.98	32
0.52	0.79	0.94	1.00	33
0.56	0.79	0.96	1.00	34
0.56	0.79	0.97	1.03	35

0.56	0.79	1.00	1.09	36
0.58	0.81	1.06	1.12	37
0.59	0.85	1.11	1.17	38
0.64	0.86	1.21	1.27	39
0.70	0.95	1.24	1.34	40
0.72	1.09	1.30	1.34	41
0.73	1.10	1.33	1.35	42
0.74	1.11	1.34	1.41	43
0.91	1.24	1.35	1.76	44

Analyzed system		Story	F_0 [kN]	K_0 [kN/m]	Braces	C or C_N [kN-(s/m)$^\alpha$]	D_{Cap} [mm]	Ultimate $F_{Tension}$ [kN]	Ultimate F_{Compr} [kN]
	6*S*-Reference T_1= 1.90sec	6th	-	-	-	-	-	-	-
		5th	-	-	-	-	-	-	-
		4th	-	-	-	-	-	-	-
		3rd	-	-	-	-	-	-	-
		2nd	-	-	-	-	-	-	-
		1st	-	-	-	-	-	-	-
	S_a-component scaling								

IDA curves

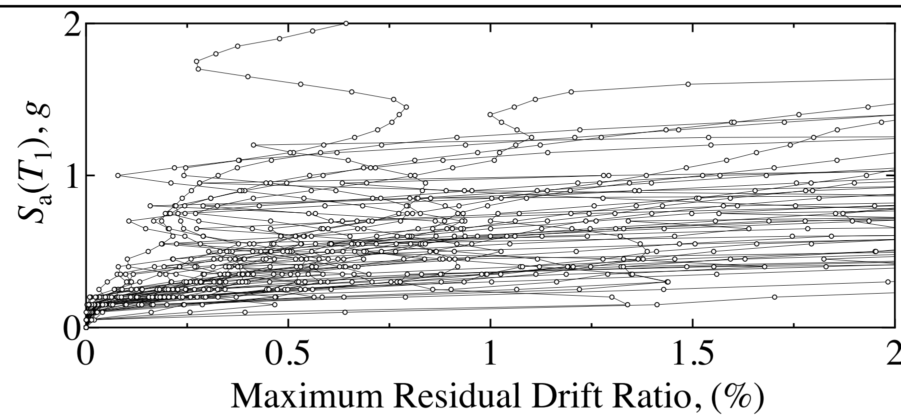

Residual drift fragility curves (Probability of exceeding the specified value of residual drift)

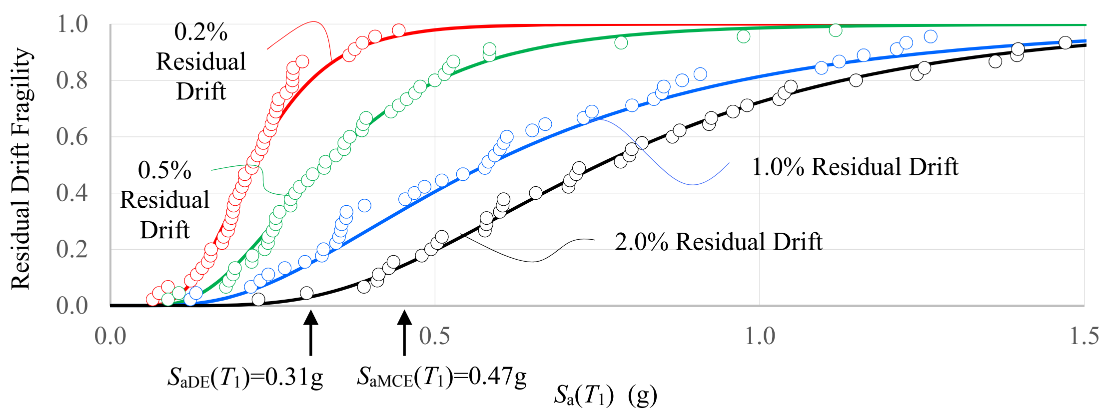

Detailed data	Residual Drift Ratio, %	$S_{aMCE}(T_1)$	Median $S_a(T_1)$	Median $S_a(T_1)$ / $S_{aMCE}(T_1)$	β
	0.2	0.47g	0.22g	0.47	0.41

0.5		0.33g	0.70	0.50
1.0		0.58g	1.23	0.61
2.0		0.75g	1.60	0.48

$S_a(T_1)$ (g) for 0.2 % Residual Drift	$S_a(T_1)$ (g) for 0.5 % Residual Drift	$S_a(T_1)$ (g) for 1.0 % Residual Drift	$S_a(T_1)$ (g) for 2.0 % Residual Drift	Number of Exceedances
<0.07	<0.09	<0.12	<0.23	0
0.07	0.09	0.12	0.23	1
0.07	0.11	0.13	0.30	2
0.09	0.18	0.22	0.39	3
0.12	0.18	0.23	0.41	4
0.13	0.19	0.24	0.41	5
0.14	0.19	0.27	0.43	6
0.15	0.22	0.30	0.44	7
0.15	0.22	0.33	0.48	8
0.16	0.24	0.33	0.49	9
0.17	0.24	0.35	0.50	10
0.17	0.24	0.35	0.51	11
0.18	0.25	0.35	0.58	12
0.18	0.25	0.36	0.58	13
0.19	0.25	0.36	0.58	14
0.19	0.26	0.36	0.60	15
0.19	0.28	0.39	0.60	16
0.19	0.28	0.45	0.61	17
0.20	0.28	0.47	0.66	18
0.20	0.29	0.48	0.71	19
0.21	0.30	0.51	0.71	20
0.21	0.31	0.54	0.72	21
0.22	0.33	0.58	0.72	22
0.22	0.33	0.58	0.79	23
0.23	0.35	0.59	0.80	24
0.23	0.36	0.60	0.80	25
0.24	0.36	0.61	0.82	26
0.24	0.37	0.61	0.87	27
0.25	0.39	0.65	0.88	28
0.25	0.39	0.67	0.92	29
0.25	0.39	0.73	0.93	30
0.26	0.43	0.74	0.96	31
0.26	0.44	0.80	0.98	32
0.26	0.46	0.84	1.03	33
0.27	0.47	0.85	1.04	34
0.28	0.48	0.85	1.05	35

	0.28	0.50	0.88	1.15	36
	0.28	0.51	0.91	1.24	37
	0.28	0.52	1.10	1.25	38
	0.30	0.53	1.12	1.36	39
	0.37	0.58	1.16	1.40	40
	0.38	0.58	1.21	1.40	41
	0.39	0.79	1.23	1.47	42
	0.41	0.98	1.26	1.63	43
	0.44	1.12	2.18	2.41	44

APPENDIX G
DETAILED RISK ASSESSMENT DATA

This appendix presents detailed data obtained in the risk assessment analysis. The following data are presented for each analyzed case:

1) Collapse fragility curve.
2) Residual drift fragility curves (for residual drift ratio of 0.2, 0.5, 1.0, and 2.0 %).
3) Absolute value of slope of the seismic hazard curve.
4) De-aggregation curves for calculating λ_C and λ_{RD} (product of fragility curve and seismic hazard curve slope).
5) Values of the mean annual frequencies λ_C and λ_{RD}.
6) Values of the probability of collapse P_C in 50 years.
7) Values of the probability of exceeding a specified value of residual drift P_{RD} in 50 years.

System	Limit State Parameter	0.2% Res. Drift	0.5% Res. Drift	1.0% Res. Drift	2.0% Res. Drift	Collapse
3*S*-75, Capacity 1.3F_{MCE} Linear Viscous Damping	λ_C or λ_{RD}	1.91×10^{-3}	1.04×10^{-3}	7.19×10^{-4}	4.80×10^{-4}	8.25×10^{-5}
β_{v1} =0.10 T_1= 1.31sec	P_C or P_{RD} (in 50 years)	0.0910	0.0507	0.0353	0.0237	0.0041

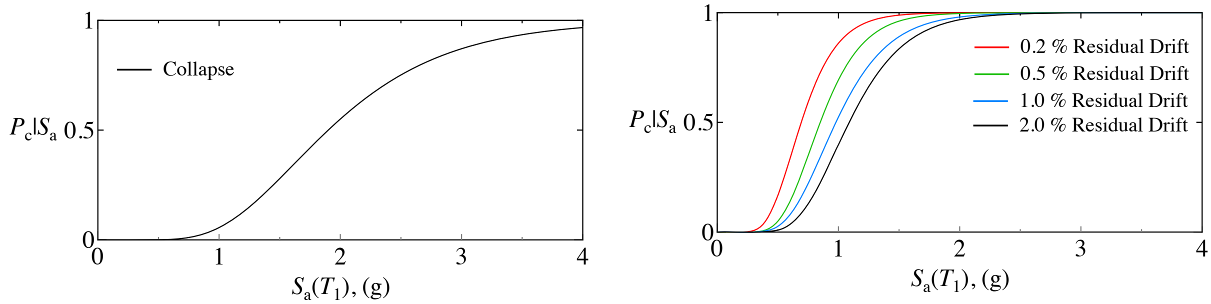

Fragility Curves

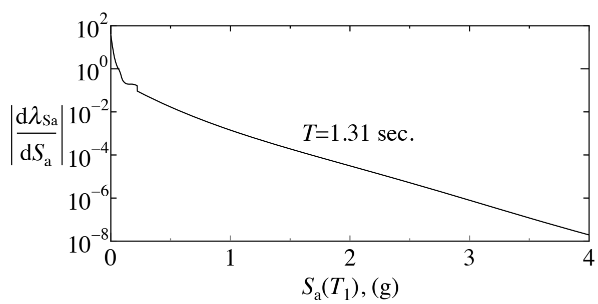

Slope of Seismic Hazard Curve

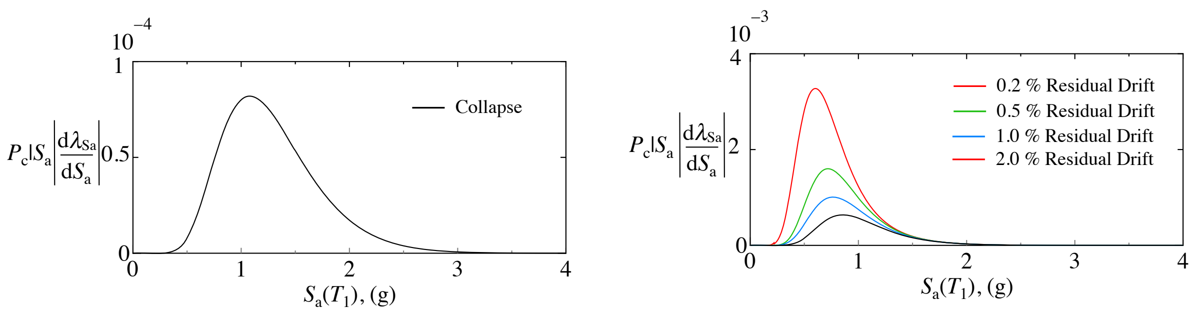

De-aggregation Curves

System	Limit State Parameter	0.2% Res. Drift	0.5% Res. Drift	1.0% Res. Drift	2.0% Res. Drift	Collapse
3*S*-75, Increased Preload Capacity 1.3F_{MCE} Linear Viscous Damping β_{v1} =0.10 T_1= 1.28sec	λ_C or λ_{RD}	1.84×10^{-3}	8.49×10^{-4}	6.15×10^{-4}	4.55×10^{-4}	1.20×10^{-4}
	P_C or P_{RD} (in 50 years)	0.0878	0.0416	0.0303	0.0225	0.0060

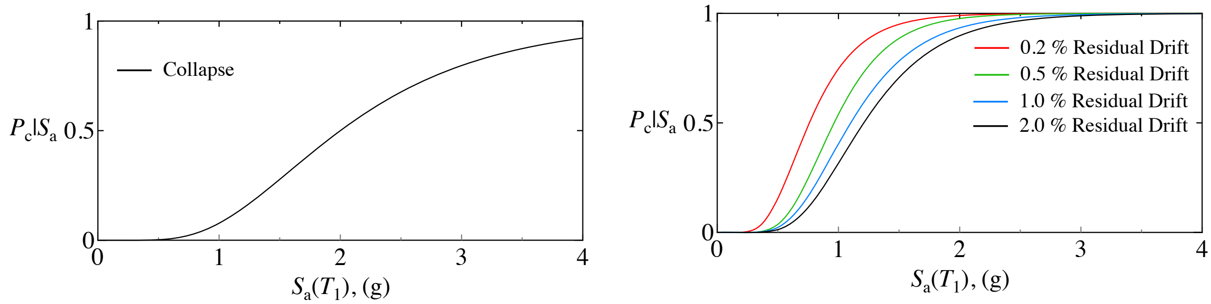

Fragility Curves

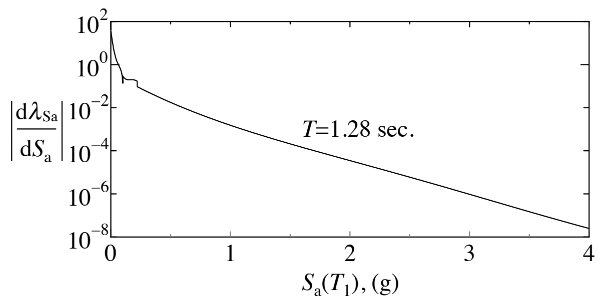

Slope of Seismic Hazard Curve

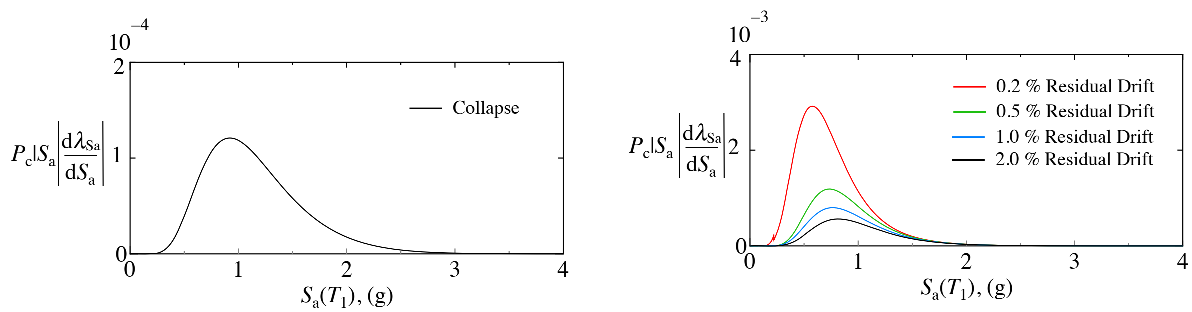

De-aggregation Curves

System	Limit State Parameter	0.2% Res. Drift	0.5% Res. Drift	1.0% Res. Drift	2.0% Res. Drift	Collapse
3*S*-75, Increased Capacity 2.0 F_{MCE} Linear Viscous Damping β_{v1} =0.10 T_1= 1.31sec	λ_C or λ_{RD}	1.70×10^{-3}	4.97×10^{-4}	2.31×10^{-4}	1.10×10^{-4}	2.65×10^{-5}
	P_C or P_{RD} (in 50 years)	0.0817	0.0246	0.0115	0.0055	0.0013

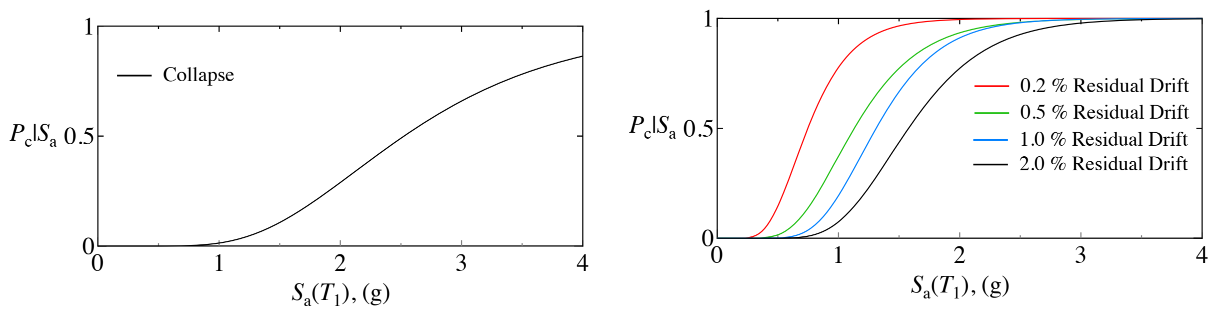

Fragility Curves

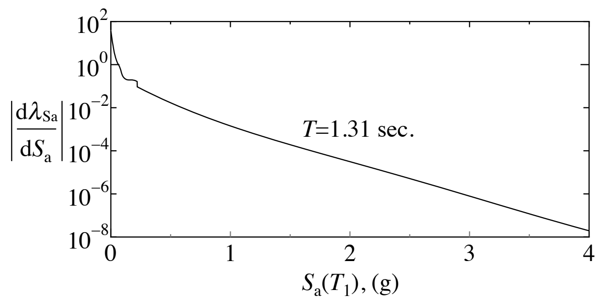

Slope of Seismic Hazard Curve

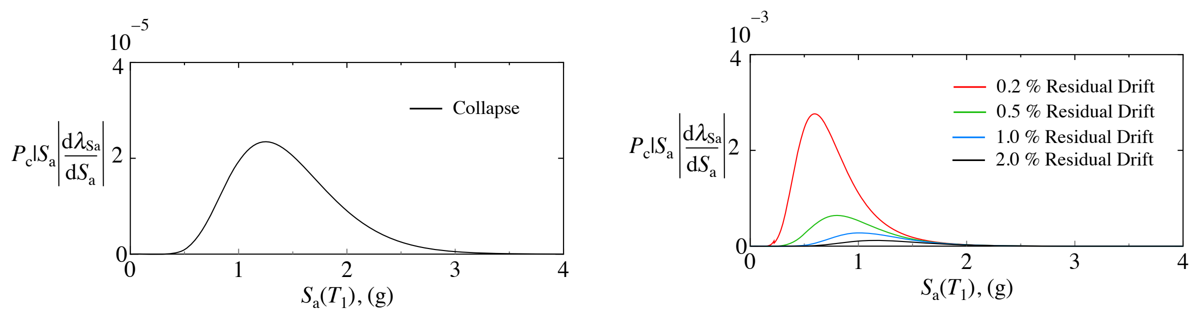

De-aggregation Curves

System	Limit State Parameter	0.2% Res. Drift	0.5% Res. Drift	1.0% Res. Drift	2.0% Res. Drift	Collapse
3*S*-75, Capacity 1.3F_{MCE} Increased Nonlinear Damping β_{v1} =0.15 in DE (α=0.5) T_1= 1.31sec	λ_C or λ_{RD}	1.77×10^{-3}	1.11×10^{-3}	6.79×10^{-4}	3.67×10^{-4}	5.53×10^{-5}
	P_C or P_{RD} (in 50 years)	0.0848	0.0539	0.0334	0.0182	0.0028

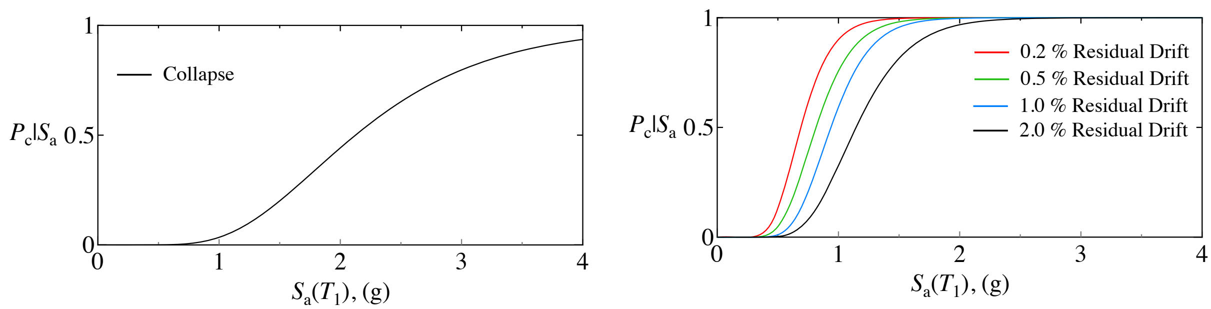

Fragility Curves

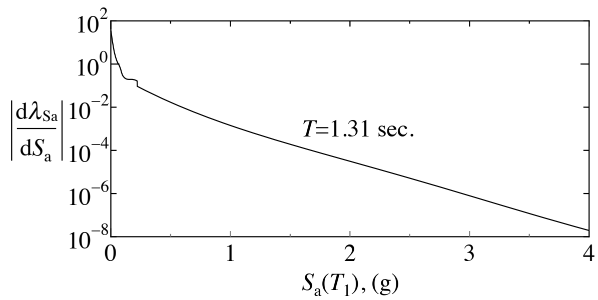

Slope of Seismic Hazard Curve

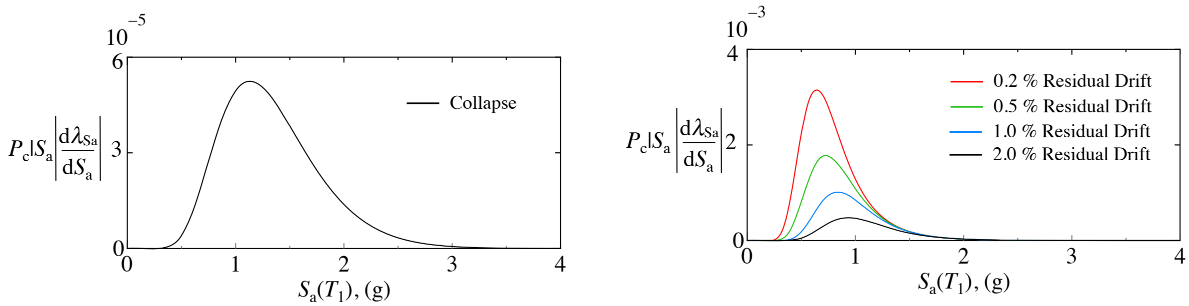

De-aggregation Curves

System	Limit State Parameter	0.2% Res. Drift	0.5% Res. Drift	1.0% Res. Drift	2.0% Res. Drift	Collapse
3S-85, Capacity 1.3F_{MCE} Linear Viscous Damping β_{v1} =0.10 T_1= 1.23sec	λ_C or λ_{RD}	1.80×10^{-3}	6.04×10^{-4}	4.80×10^{-4}	3.09×10^{-4}	5.76×10^{-5}
	P_C or P_{RD} (in 50 years)	0.0862	0.0298	0.0237	0.0153	0.0029

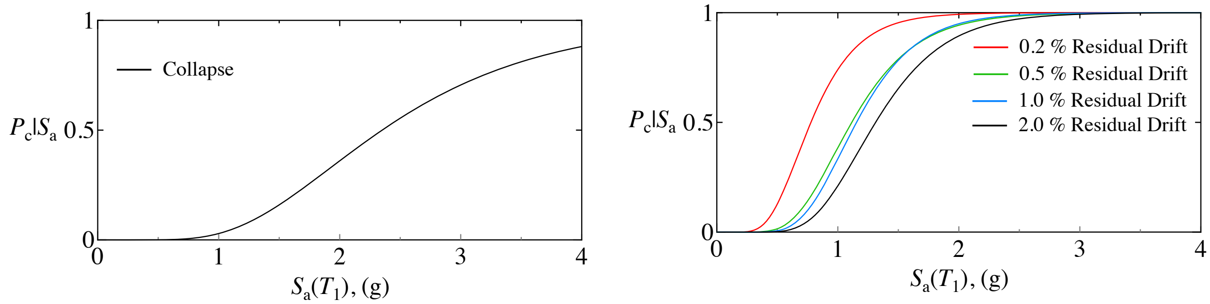

Fragility Curves

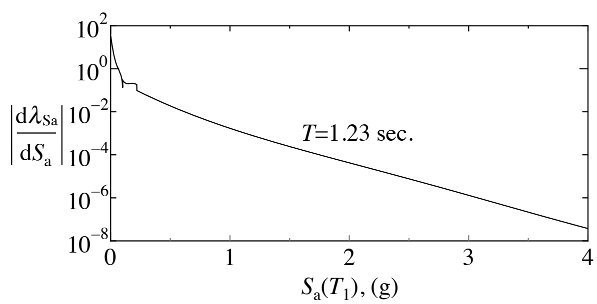

Slope of Seismic Hazard Curve

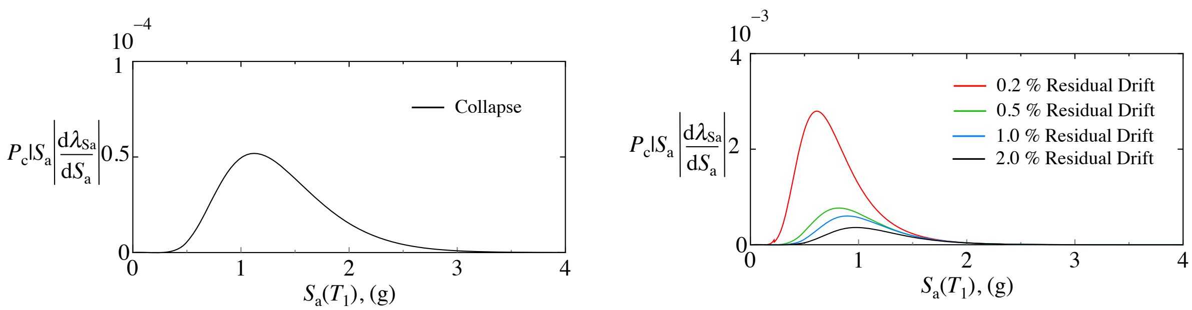

De-aggregation Curves

System	Limit State Parameter	0.2% Res. Drift	0.5% Res. Drift	1.0% Res. Drift	2.0% Res. Drift	Collapse
3*S*-Reference T_1= 1.07sec	λ_C or λ_{RD}	5.93×10^{-3}	2.90×10^{-3}	8.44×10^{-4}	2.16×10^{-4}	2.62×10^{-5}
	P_C or P_{RD} (in 50 years)	0.2567	0.1351	0.0413	0.0108	0.0013

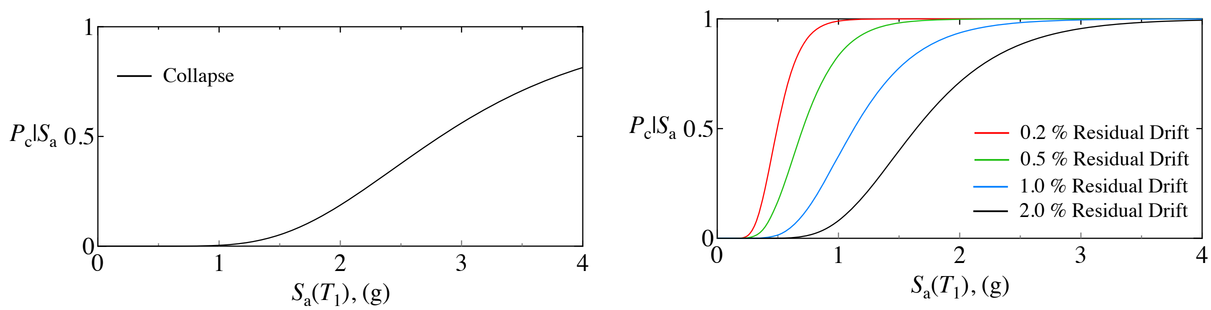

Fragility Curves

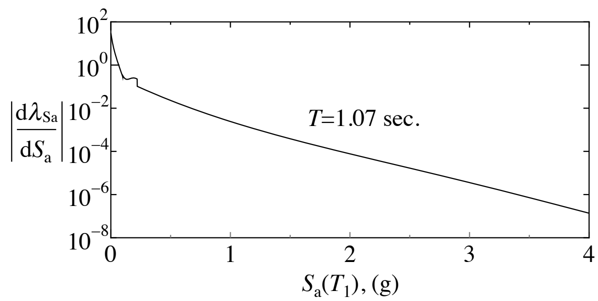

Slope of Seismic Hazard Curve

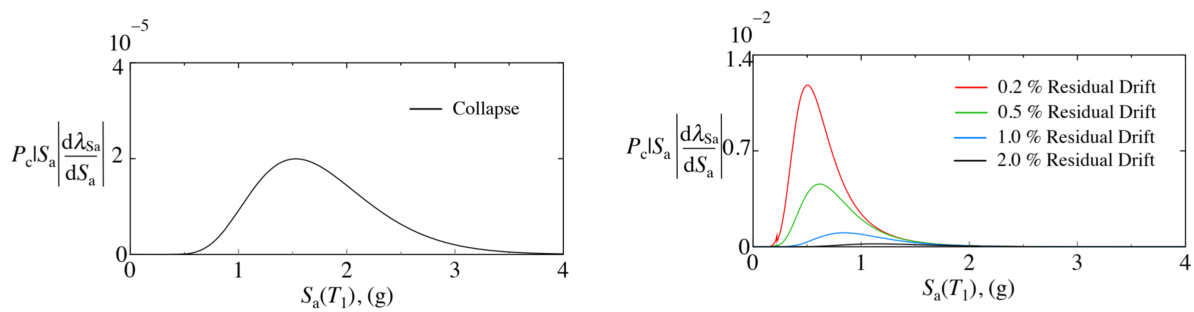

De-aggregation Curves

System	Limit State Parameter	0.2% Res. Drift	0.5% Res. Drift	1.0% Res. Drift	2.0% Res. Drift	Collapse
6*S*-75, Capacity 1.3F_{MCE} Linear Viscous Damping	λ_C or λ_{RD}	4.64×10^{-3}	3.50×10^{-3}	2.81×10^{-3}	1.72×10^{-3}	2.42×10^{-4}
β_{v1} =0.10 T_1= 2.06sec	P_C or P_{RD} (in 50 years)	0.2070	0.1607	0.1310	0.0824	0.0120

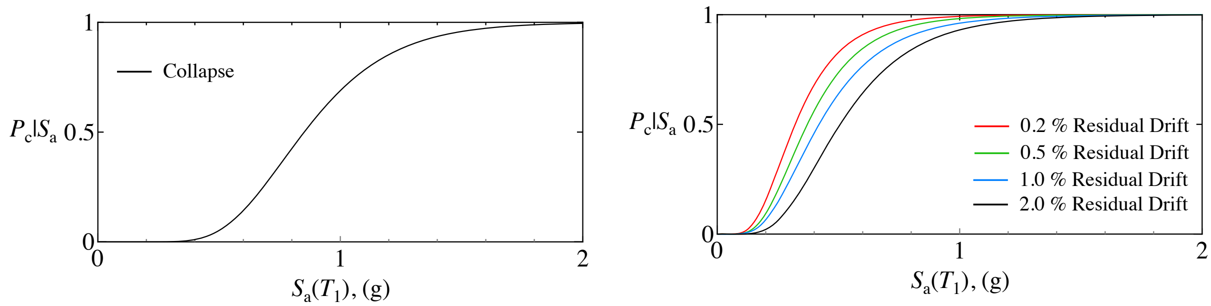

Fragility Curves

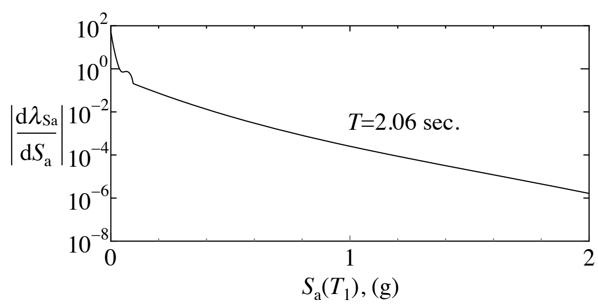

Slope of Seismic Hazard Curve

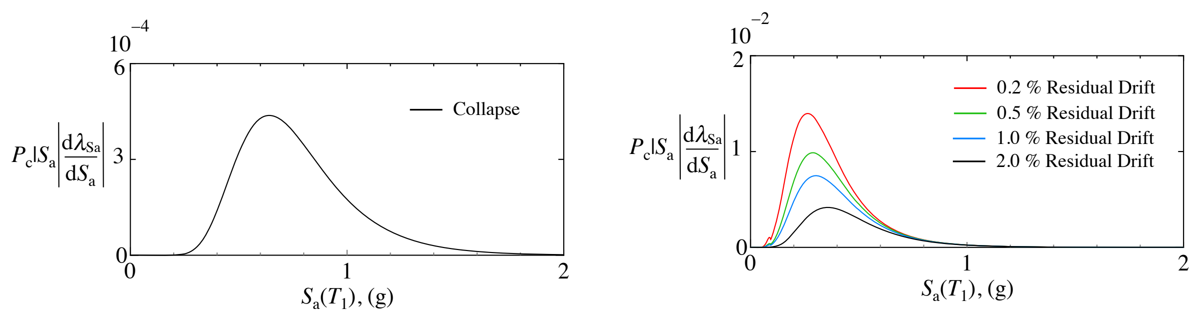

De-aggregation Curves

System	Limit State Parameter	0.2% Res. sDrift	0.5% Res. Drift	1.0% Res. Drift	2.0% Res. Drift	Collapse
6S-75, Capacity 1.3F_{MCE} Increased Nonlinear Damping	λ_C or λ_{RD}	9.70×10^{-3}	6.17×10^{-3}	3.70×10^{-3}	1.51×10^{-3}	2.47×10^{-4}
β_{v1} =0.15 in DE (α=0.5) T_1= 2.06sec	P_C or P_{RD} (in 50 years)	0.3843	0.2654	0.1687	0.0727	0.0122

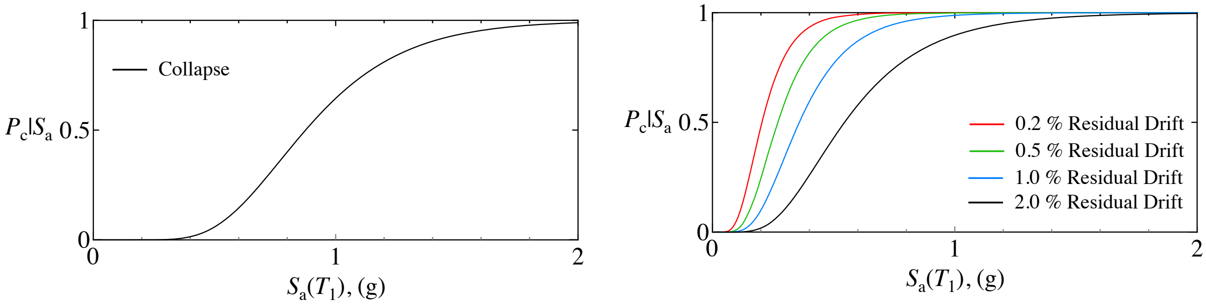

Fragility Curves

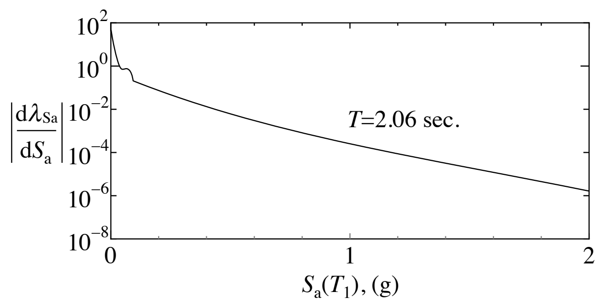

Slope of Seismic Hazard Curve

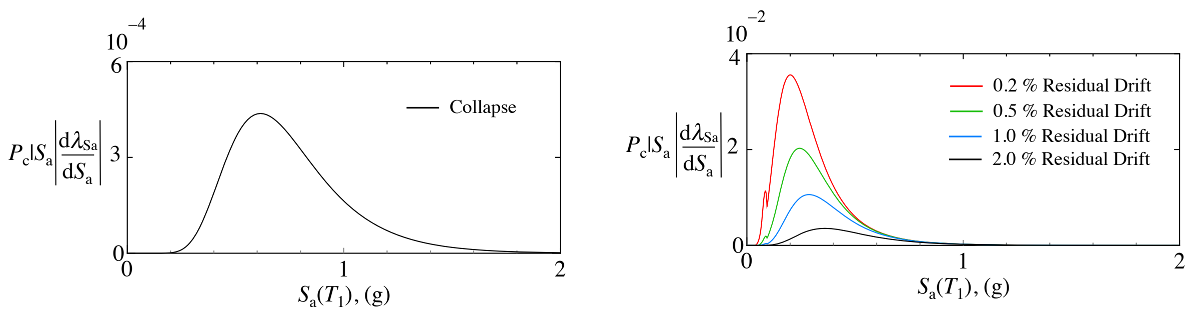

De-aggregation Curves

System	Limit State Parameter	0.2% Res. Drift	0.5% Res. Drift	1.0% Res. Drift	2.0% Res. Drift	Collapse
6*S*-75, Capacity 2.0F_{MCE} Linear Damping	λ_C or λ_{RD}	1.92×10^{-3}	1.01×10^{-3}	4.56×10^{-4}	3.49×10^{-4}	1.45×10^{-4}
β_{v1} =0.10 in DE T_1= 2.06sec	P_C or P_{RD} (in 50 years)	0.0913	0.0494	0.0225	0.0173	0.0072

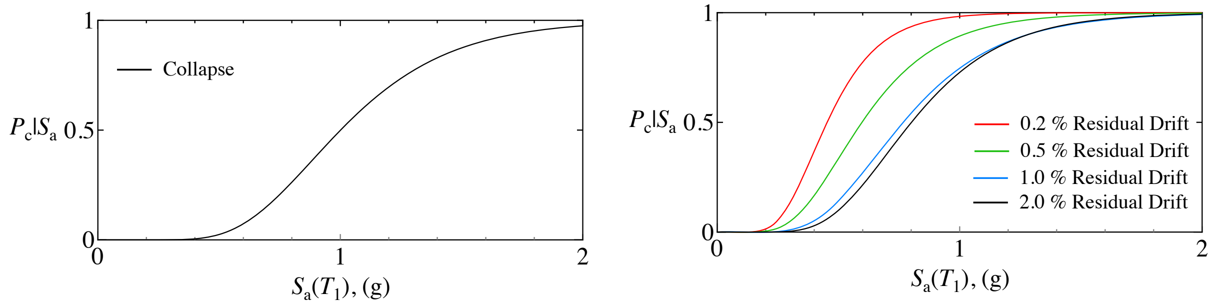

Fragility Curves

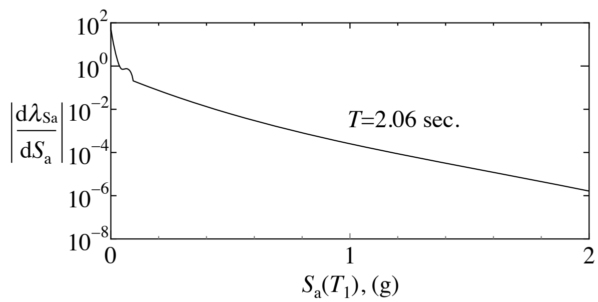

Slope of Seismic Hazard Curve

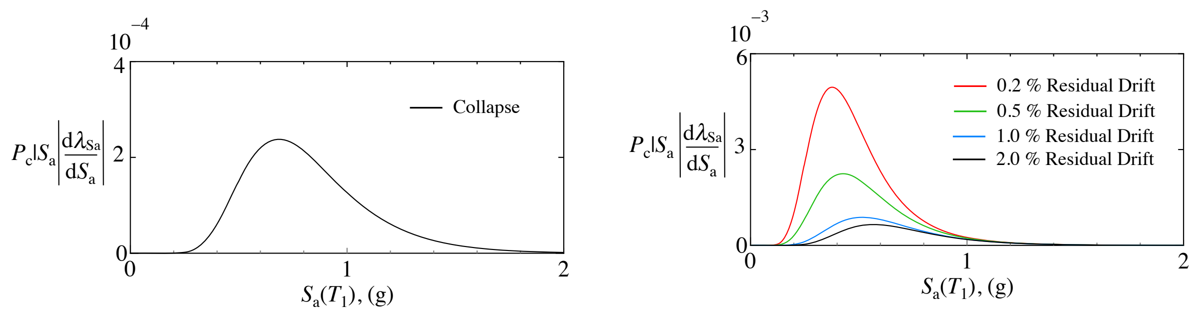

De-aggregation Curves

System	Limit State Parameter	0.2% Res. Drift	0.5% Res. Drift	1.0% Res. Drift	2.0% Res. Drift	Collapse
6*S*-Reference T_1= 1.90sec	λ_C or λ_{RD}	9.95×10^{-3}	5.46×10^{-3}	2.16×10^{-3}	8.07×10^{-4}	2.07×10^{-4}
	P_C or P_{RD} (in 50 years)	0.3920	0.2390	0.1026	0.0395	0.0103

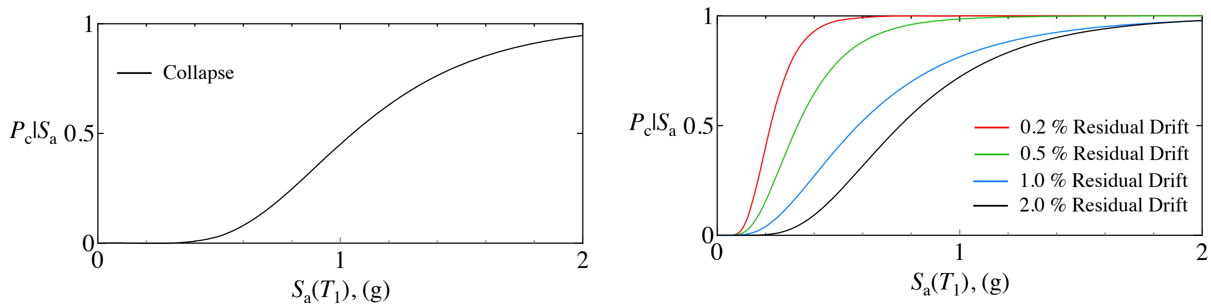

Fragility Curves

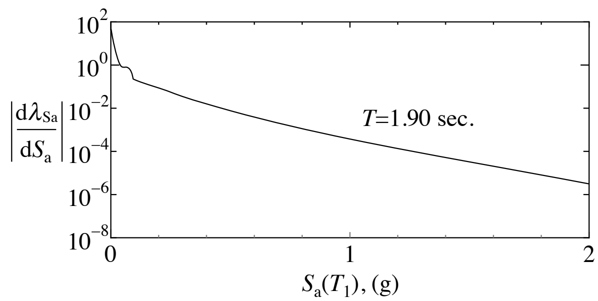

Slope of Seismic Hazard Curve

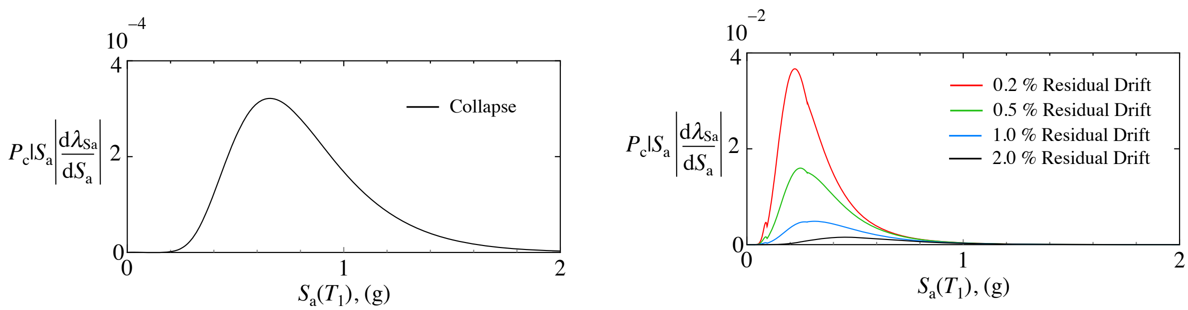

De-aggregation Curves

MCEER Technical Reports

MCEER publishes technical reports on a variety of subjects written by authors funded through MCEER. These reports are available from both MCEER Publications and the National Technical Information Service (NTIS). Requests for reports should be directed to MCEER Publications, MCEER, University at Buffalo, State University of New York, 133A Ketter Hall, Buffalo, New York 14260. Reports can also be requested through NTIS, P.O. Box 1425, Springfield, Virginia 22151. NTIS accession numbers are shown in parenthesis, if available.

NCEER-87-0001 "First-Year Program in Research, Education and Technology Transfer," 3/5/87, (PB88-134275, A04, MF-A01).

NCEER-87-0002 "Experimental Evaluation of Instantaneous Optimal Algorithms for Structural Control," by R.C. Lin, T.T. Soong and A.M. Reinhorn, 4/20/87, (PB88-134341, A04, MF-A01).

NCEER-87-0003 "Experimentation Using the Earthquake Simulation Facilities at University at Buffalo," by A.M. Reinhorn and R.L. Ketter, not available.

NCEER-87-0004 "The System Characteristics and Performance of a Shaking Table," by J.S. Hwang, K.C. Chang and G.C. Lee, 6/1/87, (PB88-134259, A03, MF-A01). This report is available only through NTIS (see address given above).

NCEER-87-0005 "A Finite Element Formulation for Nonlinear Viscoplastic Material Using a Q Model," by O. Gyebi and G. Dasgupta, 11/2/87, (PB88-213764, A08, MF-A01).

NCEER-87-0006 "Symbolic Manipulation Program (SMP) - Algebraic Codes for Two and Three Dimensional Finite Element Formulations," by X. Lee and G. Dasgupta, 11/9/87, (PB88-218522, A05, MF-A01).

NCEER-87-0007 "Instantaneous Optimal Control Laws for Tall Buildings Under Seismic Excitations," by J.N. Yang, A. Akbarpour and P. Ghaemmaghami, 6/10/87, (PB88-134333, A06, MF-A01). This report is only available through NTIS (see address given above).

NCEER-87-0008 "IDARC: Inelastic Damage Analysis of Reinforced Concrete Frame - Shear-Wall Structures," by Y.J. Park, A.M. Reinhorn and S.K. Kunnath, 7/20/87, (PB88-134325, A09, MF-A01). This report is only available through NTIS (see address given above).

NCEER-87-0009 "Liquefaction Potential for New York State: A Preliminary Report on Sites in Manhattan and Buffalo," by M. Budhu, V. Vijayakumar, R.F. Giese and L. Baumgras, 8/31/87, (PB88-163704, A03, MF-A01). This report is available only through NTIS (see address given above).

NCEER-87-0010 "Vertical and Torsional Vibration of Foundations in Inhomogeneous Media," by A.S. Veletsos and K.W. Dotson, 6/1/87, (PB88-134291, A03, MF-A01). This report is only available through NTIS (see address given above).

NCEER-87-0011 "Seismic Probabilistic Risk Assessment and Seismic Margins Studies for Nuclear Power Plants," by Howard H.M. Hwang, 6/15/87, (PB88-134267, A03, MF-A01). This report is only available through NTIS (see address given above).

NCEER-87-0012 "Parametric Studies of Frequency Response of Secondary Systems Under Ground-Acceleration Excitations," by Y. Yong and Y.K. Lin, 6/10/87, (PB88-134309, A03, MF-A01). This report is only available through NTIS (see address given above).

NCEER-87-0013 "Frequency Response of Secondary Systems Under Seismic Excitation," by J.A. HoLung, J. Cai and Y.K. Lin, 7/31/87, (PB88-134317, A05, MF-A01). This report is only available through NTIS (see address given above).

NCEER-87-0014 "Modelling Earthquake Ground Motions in Seismically Active Regions Using Parametric Time Series Methods," by G.W. Ellis and A.S. Cakmak, 8/25/87, (PB88-134283, A08, MF-A01). This report is only available through NTIS (see address given above).

NCEER-87-0015 "Detection and Assessment of Seismic Structural Damage," by E. DiPasquale and A.S. Cakmak, 8/25/87, (PB88-163712, A05, MF-A01). This report is only available through NTIS (see address given above).

NCEER-87-0016 "Pipeline Experiment at Parkfield, California," by J. Isenberg and E. Richardson, 9/15/87, (PB88-163720, A03, MF-A01). This report is available only through NTIS (see address given above).

NCEER-87-0017 "Digital Simulation of Seismic Ground Motion," by M. Shinozuka, G. Deodatis and T. Harada, 8/31/87, (PB88-155197, A04, MF-A01). This report is available only through NTIS (see address given above).

NCEER-87-0018 "Practical Considerations for Structural Control: System Uncertainty, System Time Delay and Truncation of Small Control Forces," J.N. Yang and A. Akbarpour, 8/10/87, (PB88-163738, A08, MF-A01). This report is only available through NTIS (see address given above).

NCEER-87-0019 "Modal Analysis of Nonclassically Damped Structural Systems Using Canonical Transformation," by J.N. Yang, S. Sarkani and F.X. Long, 9/27/87, (PB88-187851, A04, MF-A01).

NCEER-87-0020 "A Nonstationary Solution in Random Vibration Theory," by J.R. Red-Horse and P.D. Spanos, 11/3/87, (PB88-163746, A03, MF-A01).

NCEER-87-0021 "Horizontal Impedances for Radially Inhomogeneous Viscoelastic Soil Layers," by A.S. Veletsos and K.W. Dotson, 10/15/87, (PB88-150859, A04, MF-A01).

NCEER-87-0022 "Seismic Damage Assessment of Reinforced Concrete Members," by Y.S. Chung, C. Meyer and M. Shinozuka, 10/9/87, (PB88-150867, A05, MF-A01). This report is available only through NTIS (see address given above).

NCEER-87-0023 "Active Structural Control in Civil Engineering," by T.T. Soong, 11/11/87, (PB88-187778, A03, MF-A01).

NCEER-87-0024 "Vertical and Torsional Impedances for Radially Inhomogeneous Viscoelastic Soil Layers," by K.W. Dotson and A.S. Veletsos, 12/87, (PB88-187786, A03, MF-A01).

NCEER-87-0025 "Proceedings from the Symposium on Seismic Hazards, Ground Motions, Soil-Liquefaction and Engineering Practice in Eastern North America," October 20-22, 1987, edited by K.H. Jacob, 12/87, (PB88-188115, A23, MF-A01). This report is available only through NTIS (see address given above).

NCEER-87-0026 "Report on the Whittier-Narrows, California, Earthquake of October 1, 1987," by J. Pantelic and A. Reinhorn, 11/87, (PB88-187752, A03, MF-A01). This report is available only through NTIS (see address given above).

NCEER-87-0027 "Design of a Modular Program for Transient Nonlinear Analysis of Large 3-D Building Structures," by S. Srivastav and J.F. Abel, 12/30/87, (PB88-187950, A05, MF-A01). This report is only available through NTIS (see address given above).

NCEER-87-0028 "Second-Year Program in Research, Education and Technology Transfer," 3/8/88, (PB88-219480, A04, MF-A01).

NCEER-88-0001 "Workshop on Seismic Computer Analysis and Design of Buildings With Interactive Graphics," by W. McGuire, J.F. Abel and C.H. Conley, 1/18/88, (PB88-187760, A03, MF-A01). This report is only available through NTIS (see address given above).

NCEER-88-0002 "Optimal Control of Nonlinear Flexible Structures," by J.N. Yang, F.X. Long and D. Wong, 1/22/88, (PB88-213772, A06, MF-A01).

NCEER-88-0003 "Substructuring Techniques in the Time Domain for Primary-Secondary Structural Systems," by G.D. Manolis and G. Juhn, 2/10/88, (PB88-213780, A04, MF-A01).

NCEER-88-0004 "Iterative Seismic Analysis of Primary-Secondary Systems," by A. Singhal, L.D. Lutes and P.D. Spanos, 2/23/88, (PB88-213798, A04, MF-A01).

NCEER-88-0005 "Stochastic Finite Element Expansion for Random Media," by P.D. Spanos and R. Ghanem, 3/14/88, (PB88-213806, A03, MF-A01).

NCEER-88-0006 "Combining Structural Optimization and Structural Control," by F.Y. Cheng and C.P. Pantelides, 1/10/88, (PB88-213814, A05, MF-A01).

NCEER-88-0007 "Seismic Performance Assessment of Code-Designed Structures," by H.H-M. Hwang, J-W. Jaw and H-J. Shau, 3/20/88, (PB88-219423, A04, MF-A01). This report is only available through NTIS (see address given above).

NCEER-88-0008 "Reliability Analysis of Code-Designed Structures Under Natural Hazards," by H.H-M. Hwang, H. Ushiba and M. Shinozuka, 2/29/88, (PB88-229471, A07, MF-A01). This report is only available through NTIS (see address given above).

NCEER-88-0009 "Seismic Fragility Analysis of Shear Wall Structures," by J-W Jaw and H.H-M. Hwang, 4/30/88, (PB89-102867, A04, MF-A01).

NCEER-88-0010 "Base Isolation of a Multi-Story Building Under a Harmonic Ground Motion - A Comparison of Performances of Various Systems," by F-G Fan, G. Ahmadi and I.G. Tadjbakhsh, 5/18/88, (PB89-122238, A06, MF-A01). This report is only available through NTIS (see address given above).

NCEER-88-0011 "Seismic Floor Response Spectra for a Combined System by Green's Functions," by F.M. Lavelle, L.A. Bergman and P.D. Spanos, 5/1/88, (PB89-102875, A03, MF-A01).

NCEER-88-0012 "A New Solution Technique for Randomly Excited Hysteretic Structures," by G.Q. Cai and Y.K. Lin, 5/16/88, (PB89-102883, A03, MF-A01).

NCEER-88-0013 "A Study of Radiation Damping and Soil-Structure Interaction Effects in the Centrifuge," by K. Weissman, supervised by J.H. Prevost, 5/24/88, (PB89-144703, A06, MF-A01).

NCEER-88-0014 "Parameter Identification and Implementation of a Kinematic Plasticity Model for Frictional Soils," by J.H. Prevost and D.V. Griffiths, not available.

NCEER-88-0015 "Two- and Three- Dimensional Dynamic Finite Element Analyses of the Long Valley Dam," by D.V. Griffiths and J.H. Prevost, 6/17/88, (PB89-144711, A04, MF-A01).

NCEER-88-0016 "Damage Assessment of Reinforced Concrete Structures in Eastern United States," by A.M. Reinhorn, M.J. Seidel, S.K. Kunnath and Y.J. Park, 6/15/88, (PB89-122220, A04, MF-A01). This report is only available through NTIS (see address given above).

NCEER-88-0017 "Dynamic Compliance of Vertically Loaded Strip Foundations in Multilayered Viscoelastic Soils," by S. Ahmad and A.S.M. Israil, 6/17/88, (PB89-102891, A04, MF-A01).

NCEER-88-0018 "An Experimental Study of Seismic Structural Response With Added Viscoelastic Dampers," by R.C. Lin, Z. Liang, T.T. Soong and R.H. Zhang, 6/30/88, (PB89-122212, A05, MF-A01). This report is available only through NTIS (see address given above).

NCEER-88-0019 "Experimental Investigation of Primary - Secondary System Interaction," by G.D. Manolis, G. Juhn and A.M. Reinhorn, 5/27/88, (PB89-122204, A04, MF-A01).

NCEER-88-0020 "A Response Spectrum Approach For Analysis of Nonclassically Damped Structures," by J.N. Yang, S. Sarkani and F.X. Long, 4/22/88, (PB89-102909, A04, MF-A01).

NCEER-88-0021 "Seismic Interaction of Structures and Soils: Stochastic Approach," by A.S. Veletsos and A.M. Prasad, 7/21/88, (PB89-122196, A04, MF-A01). This report is only available through NTIS (see address given above).

NCEER-88-0022 "Identification of the Serviceability Limit State and Detection of Seismic Structural Damage," by E. DiPasquale and A.S. Cakmak, 6/15/88, (PB89-122188, A05, MF-A01). This report is available only through NTIS (see address given above).

NCEER-88-0023 "Multi-Hazard Risk Analysis: Case of a Simple Offshore Structure," by B.K. Bhartia and E.H. Vanmarcke, 7/21/88, (PB89-145213, A05, MF-A01).

NCEER-88-0024 "Automated Seismic Design of Reinforced Concrete Buildings," by Y.S. Chung, C. Meyer and M. Shinozuka, 7/5/88, (PB89-122170, A06, MF-A01). This report is available only through NTIS (see address given above).

NCEER-88-0025 "Experimental Study of Active Control of MDOF Structures Under Seismic Excitations," by L.L. Chung, R.C. Lin, T.T. Soong and A.M. Reinhorn, 7/10/88, (PB89-122600, A04, MF-A01).

NCEER-88-0026 "Earthquake Simulation Tests of a Low-Rise Metal Structure," by J.S. Hwang, K.C. Chang, G.C. Lee and R.L. Ketter, 8/1/88, (PB89-102917, A04, MF-A01).

NCEER-88-0027 "Systems Study of Urban Response and Reconstruction Due to Catastrophic Earthquakes," by F. Kozin and H.K. Zhou, 9/22/88, (PB90-162348, A04, MF-A01).

NCEER-88-0028 "Seismic Fragility Analysis of Plane Frame Structures," by H.H-M. Hwang and Y.K. Low, 7/31/88, (PB89-131445, A06, MF-A01).

NCEER-88-0029 "Response Analysis of Stochastic Structures," by A. Kardara, C. Bucher and M. Shinozuka, 9/22/88, (PB89-174429, A04, MF-A01).

NCEER-88-0030 "Nonnormal Accelerations Due to Yielding in a Primary Structure," by D.C.K. Chen and L.D. Lutes, 9/19/88, (PB89-131437, A04, MF-A01).

NCEER-88-0031 "Design Approaches for Soil-Structure Interaction," by A.S. Veletsos, A.M. Prasad and Y. Tang, 12/30/88, (PB89-174437, A03, MF-A01). This report is available only through NTIS (see address given above).

NCEER-88-0032 "A Re-evaluation of Design Spectra for Seismic Damage Control," by C.J. Turkstra and A.G. Tallin, 11/7/88, (PB89-145221, A05, MF-A01).

NCEER-88-0033 "The Behavior and Design of Noncontact Lap Splices Subjected to Repeated Inelastic Tensile Loading," by V.E. Sagan, P. Gergely and R.N. White, 12/8/88, (PB89-163737, A08, MF-A01).

NCEER-88-0034 "Seismic Response of Pile Foundations," by S.M. Mamoon, P.K. Banerjee and S. Ahmad, 11/1/88, (PB89-145239, A04, MF-A01).

NCEER-88-0035 "Modeling of R/C Building Structures With Flexible Floor Diaphragms (IDARC2)," by A.M. Reinhorn, S.K. Kunnath and N. Panahshahi, 9/7/88, (PB89-207153, A07, MF-A01).

NCEER-88-0036 "Solution of the Dam-Reservoir Interaction Problem Using a Combination of FEM, BEM with Particular Integrals, Modal Analysis, and Substructuring," by C-S. Tsai, G.C. Lee and R.L. Ketter, 12/31/88, (PB89-207146, A04, MF-A01).

NCEER-88-0037 "Optimal Placement of Actuators for Structural Control," by F.Y. Cheng and C.P. Pantelides, 8/15/88, (PB89-162846, A05, MF-A01).

NCEER-88-0038 "Teflon Bearings in Aseismic Base Isolation: Experimental Studies and Mathematical Modeling," by A. Mokha, M.C. Constantinou and A.M. Reinhorn, 12/5/88, (PB89-218457, A10, MF-A01). This report is available only through NTIS (see address given above).

NCEER-88-0039 "Seismic Behavior of Flat Slab High-Rise Buildings in the New York City Area," by P. Weidlinger and M. Ettouney, 10/15/88, (PB90-145681, A04, MF-A01).

NCEER-88-0040 "Evaluation of the Earthquake Resistance of Existing Buildings in New York City," by P. Weidlinger and M. Ettouney, 10/15/88, not available.

NCEER-88-0041 "Small-Scale Modeling Techniques for Reinforced Concrete Structures Subjected to Seismic Loads," by W. Kim, A. El-Attar and R.N. White, 11/22/88, (PB89-189625, A05, MF-A01).

NCEER-88-0042 "Modeling Strong Ground Motion from Multiple Event Earthquakes," by G.W. Ellis and A.S. Cakmak, 10/15/88, (PB89-174445, A03, MF-A01).

NCEER-88-0043 "Nonstationary Models of Seismic Ground Acceleration," by M. Grigoriu, S.E. Ruiz and E. Rosenblueth, 7/15/88, (PB89-189617, A04, MF-A01).

NCEER-88-0044 "SARCF User's Guide: Seismic Analysis of Reinforced Concrete Frames," by Y.S. Chung, C. Meyer and M. Shinozuka, 11/9/88, (PB89-174452, A08, MF-A01).

NCEER-88-0045 "First Expert Panel Meeting on Disaster Research and Planning," edited by J. Pantelic and J. Stoyle, 9/15/88, (PB89-174460, A05, MF-A01).

NCEER-88-0046 "Preliminary Studies of the Effect of Degrading Infill Walls on the Nonlinear Seismic Response of Steel Frames," by C.Z. Chrysostomou, P. Gergely and J.F. Abel, 12/19/88, (PB89-208383, A05, MF-A01).

NCEER-88-0047 "Reinforced Concrete Frame Component Testing Facility - Design, Construction, Instrumentation and Operation," by S.P. Pessiki, C. Conley, T. Bond, P. Gergely and R.N. White, 12/16/88, (PB89-174478, A04, MF-A01).

NCEER-89-0001 "Effects of Protective Cushion and Soil Compliancy on the Response of Equipment Within a Seismically Excited Building," by J.A. HoLung, 2/16/89, (PB89-207179, A04, MF-A01).

NCEER-89-0002 "Statistical Evaluation of Response Modification Factors for Reinforced Concrete Structures," by H.H-M. Hwang and J-W. Jaw, 2/17/89, (PB89-207187, A05, MF-A01).

NCEER-89-0003 "Hysteretic Columns Under Random Excitation," by G-Q. Cai and Y.K. Lin, 1/9/89, (PB89-196513, A03, MF-A01).

NCEER-89-0004 "Experimental Study of `Elephant Foot Bulge' Instability of Thin-Walled Metal Tanks," by Z-H. Jia and R.L. Ketter, 2/22/89, (PB89-207195, A03, MF-A01).

NCEER-89-0005 "Experiment on Performance of Buried Pipelines Across San Andreas Fault," by J. Isenberg, E. Richardson and T.D. O'Rourke, 3/10/89, (PB89-218440, A04, MF-A01). This report is available only through NTIS (see address given above).

NCEER-89-0006 "A Knowledge-Based Approach to Structural Design of Earthquake-Resistant Buildings," by M. Subramani, P. Gergely, C.H. Conley, J.F. Abel and A.H. Zaghw, 1/15/89, (PB89-218465, A06, MF-A01).

NCEER-89-0007 "Liquefaction Hazards and Their Effects on Buried Pipelines," by T.D. O'Rourke and P.A. Lane, 2/1/89, (PB89-218481, A09, MF-A01).

NCEER-89-0008 "Fundamentals of System Identification in Structural Dynamics," by H. Imai, C-B. Yun, O. Maruyama and M. Shinozuka, 1/26/89, (PB89-207211, A04, MF-A01).

NCEER-89-0009 "Effects of the 1985 Michoacan Earthquake on Water Systems and Other Buried Lifelines in Mexico," by A.G. Ayala and M.J. O'Rourke, 3/8/89, (PB89-207229, A06, MF-A01).

NCEER-89-R010 "NCEER Bibliography of Earthquake Education Materials," by K.E.K. Ross, Second Revision, 9/1/89, (PB90-125352, A05, MF-A01). This report is replaced by NCEER-92-0018.

NCEER-89-0011 "Inelastic Three-Dimensional Response Analysis of Reinforced Concrete Building Structures (IDARC-3D), Part I - Modeling," by S.K. Kunnath and A.M. Reinhorn, 4/17/89, (PB90-114612, A07, MF-A01). This report is available only through NTIS (see address given above).

NCEER-89-0012 "Recommended Modifications to ATC-14," by C.D. Poland and J.O. Malley, 4/12/89, (PB90-108648, A15, MF-A01).

NCEER-89-0013 "Repair and Strengthening of Beam-to-Column Connections Subjected to Earthquake Loading," by M. Corazao and A.J. Durrani, 2/28/89, (PB90-109885, A06, MF-A01).

NCEER-89-0014 "Program EXKAL2 for Identification of Structural Dynamic Systems," by O. Maruyama, C-B. Yun, M. Hoshiya and M. Shinozuka, 5/19/89, (PB90-109877, A09, MF-A01).

NCEER-89-0015 "Response of Frames With Bolted Semi-Rigid Connections, Part I - Experimental Study and Analytical Predictions," by P.J. DiCorso, A.M. Reinhorn, J.R. Dickerson, J.B. Radziminski and W.L. Harper, 6/1/89, not available.

NCEER-89-0016 "ARMA Monte Carlo Simulation in Probabilistic Structural Analysis," by P.D. Spanos and M.P. Mignolet, 7/10/89, (PB90-109893, A03, MF-A01).

NCEER-89-P017 "Preliminary Proceedings from the Conference on Disaster Preparedness - The Place of Earthquake Education in Our Schools," Edited by K.E.K. Ross, 6/23/89, (PB90-108606, A03, MF-A01).

NCEER-89-0017 "Proceedings from the Conference on Disaster Preparedness - The Place of Earthquake Education in Our Schools," Edited by K.E.K. Ross, 12/31/89, (PB90-207895, A012, MF-A02). This report is available only through NTIS (see address given above).

NCEER-89-0018 "Multidimensional Models of Hysteretic Material Behavior for Vibration Analysis of Shape Memory Energy Absorbing Devices, by E.J. Graesser and F.A. Cozzarelli, 6/7/89, (PB90-164146, A04, MF-A01).

NCEER-89-0019 "Nonlinear Dynamic Analysis of Three-Dimensional Base Isolated Structures (3D-BASIS)," by S. Nagarajaiah, A.M. Reinhorn and M.C. Constantinou, 8/3/89, (PB90-161936, A06, MF-A01). This report has been replaced by NCEER-93-0011.

NCEER-89-0020 "Structural Control Considering Time-Rate of Control Forces and Control Rate Constraints," by F.Y. Cheng and C.P. Pantelides, 8/3/89, (PB90-120445, A04, MF-A01).

NCEER-89-0021 "Subsurface Conditions of Memphis and Shelby County," by K.W. Ng, T-S. Chang and H-H.M. Hwang, 7/26/89, (PB90-120437, A03, MF-A01).

NCEER-89-0022 "Seismic Wave Propagation Effects on Straight Jointed Buried Pipelines," by K. Elhmadi and M.J. O'Rourke, 8/24/89, (PB90-162322, A10, MF-A02).

NCEER-89-0023 "Workshop on Serviceability Analysis of Water Delivery Systems," edited by M. Grigoriu, 3/6/89, (PB90-127424, A03, MF-A01).

NCEER-89-0024 "Shaking Table Study of a 1/5 Scale Steel Frame Composed of Tapered Members," by K.C. Chang, J.S. Hwang and G.C. Lee, 9/18/89, (PB90-160169, A04, MF-A01).

NCEER-89-0025 "DYNA1D: A Computer Program for Nonlinear Seismic Site Response Analysis - Technical Documentation," by Jean H. Prevost, 9/14/89, (PB90-161944, A07, MF-A01). This report is available only through NTIS (see address given above).

NCEER-89-0026 "1:4 Scale Model Studies of Active Tendon Systems and Active Mass Dampers for Aseismic Protection," by A.M. Reinhorn, T.T. Soong, R.C. Lin, Y.P. Yang, Y. Fukao, H. Abe and M. Nakai, 9/15/89, (PB90-173246, A10, MF-A02). This report is available only through NTIS (see address given above).

NCEER-89-0027 "Scattering of Waves by Inclusions in a Nonhomogeneous Elastic Half Space Solved by Boundary Element Methods," by P.K. Hadley, A. Askar and A.S. Cakmak, 6/15/89, (PB90-145699, A07, MF-A01).

NCEER-89-0028 "Statistical Evaluation of Deflection Amplification Factors for Reinforced Concrete Structures," by H.H.M. Hwang, J-W. Jaw and A.L. Ch'ng, 8/31/89, (PB90-164633, A05, MF-A01).

NCEER-89-0029 "Bedrock Accelerations in Memphis Area Due to Large New Madrid Earthquakes," by H.H.M. Hwang, C.H.S. Chen and G. Yu, 11/7/89, (PB90-162330, A04, MF-A01).

NCEER-89-0030 "Seismic Behavior and Response Sensitivity of Secondary Structural Systems," by Y.Q. Chen and T.T. Soong, 10/23/89, (PB90-164658, A08, MF-A01).

NCEER-89-0031 "Random Vibration and Reliability Analysis of Primary-Secondary Structural Systems," by Y. Ibrahim, M. Grigoriu and T.T. Soong, 11/10/89, (PB90-161951, A04, MF-A01).

NCEER-89-0032 "Proceedings from the Second U.S. - Japan Workshop on Liquefaction, Large Ground Deformation and Their Effects on Lifelines, September 26-29, 1989," Edited by T.D. O'Rourke and M. Hamada, 12/1/89, (PB90-209388, A22, MF-A03).

NCEER-89-0033 "Deterministic Model for Seismic Damage Evaluation of Reinforced Concrete Structures," by J.M. Bracci, A.M. Reinhorn, J.B. Mander and S.K. Kunnath, 9/27/89, (PB91-108803, A06, MF-A01).

NCEER-89-0034 "On the Relation Between Local and Global Damage Indices," by E. DiPasquale and A.S. Cakmak, 8/15/89, (PB90-173865, A05, MF-A01).

NCEER-89-0035 "Cyclic Undrained Behavior of Nonplastic and Low Plasticity Silts," by A.J. Walker and H.E. Stewart, 7/26/89, (PB90-183518, A10, MF-A01).

NCEER-89-0036 "Liquefaction Potential of Surficial Deposits in the City of Buffalo, New York," by M. Budhu, R. Giese and L. Baumgrass, 1/17/89, (PB90-208455, A04, MF-A01).

NCEER-89-0037 "A Deterministic Assessment of Effects of Ground Motion Incoherence," by A.S. Veletsos and Y. Tang, 7/15/89, (PB90-164294, A03, MF-A01).

NCEER-89-0038 "Workshop on Ground Motion Parameters for Seismic Hazard Mapping," July 17-18, 1989, edited by R.V. Whitman, 12/1/89, (PB90-173923, A04, MF-A01).

NCEER-89-0039 "Seismic Effects on Elevated Transit Lines of the New York City Transit Authority," by C.J. Costantino, C.A. Miller and E. Heymsfield, 12/26/89, (PB90-207887, A06, MF-A01).

NCEER-89-0040 "Centrifugal Modeling of Dynamic Soil-Structure Interaction," by K. Weissman, Supervised by J.H. Prevost, 5/10/89, (PB90-207879, A07, MF-A01).

NCEER-89-0041 "Linearized Identification of Buildings With Cores for Seismic Vulnerability Assessment," by I-K. Ho and A.E. Aktan, 11/1/89, (PB90-251943, A07, MF-A01).

NCEER-90-0001 "Geotechnical and Lifeline Aspects of the October 17, 1989 Loma Prieta Earthquake in San Francisco," by T.D. O'Rourke, H.E. Stewart, F.T. Blackburn and T.S. Dickerman, 1/90, (PB90-208596, A05, MF-A01).

NCEER-90-0002 "Nonnormal Secondary Response Due to Yielding in a Primary Structure," by D.C.K. Chen and L.D. Lutes, 2/28/90, (PB90-251976, A07, MF-A01).

NCEER-90-0003 "Earthquake Education Materials for Grades K-12," by K.E.K. Ross, 4/16/90, (PB91-251984, A05, MF-A05). This report has been replaced by NCEER-92-0018.

NCEER-90-0004 "Catalog of Strong Motion Stations in Eastern North America," by R.W. Busby, 4/3/90, (PB90-251984, A05, MF-A01).

NCEER-90-0005 "NCEER Strong-Motion Data Base: A User Manual for the GeoBase Release (Version 1.0 for the Sun3)," by P. Friberg and K. Jacob, 3/31/90 (PB90-258062, A04, MF-A01).

NCEER-90-0006 "Seismic Hazard Along a Crude Oil Pipeline in the Event of an 1811-1812 Type New Madrid Earthquake," by H.H.M. Hwang and C-H.S. Chen, 4/16/90, (PB90-258054, A04, MF-A01).

NCEER-90-0007 "Site-Specific Response Spectra for Memphis Sheahan Pumping Station," by H.H.M. Hwang and C.S. Lee, 5/15/90, (PB91-108811, A05, MF-A01).

NCEER-90-0008 "Pilot Study on Seismic Vulnerability of Crude Oil Transmission Systems," by T. Ariman, R. Dobry, M. Grigoriu, F. Kozin, M. O'Rourke, T. O'Rourke and M. Shinozuka, 5/25/90, (PB91-108837, A06, MF-A01).

NCEER-90-0009 "A Program to Generate Site Dependent Time Histories: EQGEN," by G.W. Ellis, M. Srinivasan and A.S. Cakmak, 1/30/90, (PB91-108829, A04, MF-A01).

NCEER-90-0010 "Active Isolation for Seismic Protection of Operating Rooms," by M.E. Talbott, Supervised by M. Shinozuka, 6/8/9, (PB91-110205, A05, MF-A01).

NCEER-90-0011 "Program LINEARID for Identification of Linear Structural Dynamic Systems," by C-B. Yun and M. Shinozuka, 6/25/90, (PB91-110312, A08, MF-A01).

NCEER-90-0012 "Two-Dimensional Two-Phase Elasto-Plastic Seismic Response of Earth Dams," by A.N. Yiagos, Supervised by J.H. Prevost, 6/20/90, (PB91-110197, A13, MF-A02).

NCEER-90-0013 "Secondary Systems in Base-Isolated Structures: Experimental Investigation, Stochastic Response and Stochastic Sensitivity," by G.D. Manolis, G. Juhn, M.C. Constantinou and A.M. Reinhorn, 7/1/90, (PB91-110320, A08, MF-A01).

NCEER-90-0014 "Seismic Behavior of Lightly-Reinforced Concrete Column and Beam-Column Joint Details," by S.P. Pessiki, C.H. Conley, P. Gergely and R.N. White, 8/22/90, (PB91-108795, A11, MF-A02).

NCEER-90-0015 "Two Hybrid Control Systems for Building Structures Under Strong Earthquakes," by J.N. Yang and A. Danielians, 6/29/90, (PB91-125393, A04, MF-A01).

NCEER-90-0016 "Instantaneous Optimal Control with Acceleration and Velocity Feedback," by J.N. Yang and Z. Li, 6/29/90, (PB91-125401, A03, MF-A01).

NCEER-90-0017 "Reconnaissance Report on the Northern Iran Earthquake of June 21, 1990," by M. Mehrain, 10/4/90, (PB91-125377, A03, MF-A01).

NCEER-90-0018 "Evaluation of Liquefaction Potential in Memphis and Shelby County," by T.S. Chang, P.S. Tang, C.S. Lee and H. Hwang, 8/10/90, (PB91-125427, A09, MF-A01).

NCEER-90-0019 "Experimental and Analytical Study of a Combined Sliding Disc Bearing and Helical Steel Spring Isolation System," by M.C. Constantinou, A.S. Mokha and A.M. Reinhorn, 10/4/90, (PB91-125385, A06, MF-A01). This report is available only through NTIS (see address given above).

NCEER-90-0020 "Experimental Study and Analytical Prediction of Earthquake Response of a Sliding Isolation System with a Spherical Surface," by A.S. Mokha, M.C. Constantinou and A.M. Reinhorn, 10/11/90, (PB91-125419, A05, MF-A01).

NCEER-90-0021 "Dynamic Interaction Factors for Floating Pile Groups," by G. Gazetas, K. Fan, A. Kaynia and E. Kausel, 9/10/90, (PB91-170381, A05, MF-A01).

NCEER-90-0022 "Evaluation of Seismic Damage Indices for Reinforced Concrete Structures," by S. Rodriguez-Gomez and A.S. Cakmak, 9/30/90, PB91-171322, A06, MF-A01).

NCEER-90-0023 "Study of Site Response at a Selected Memphis Site," by H. Desai, S. Ahmad, E.S. Gazetas and M.R. Oh, 10/11/90, (PB91-196857, A03, MF-A01).

NCEER-90-0024 "A User's Guide to Strongmo: Version 1.0 of NCEER's Strong-Motion Data Access Tool for PCs and Terminals," by P.A. Friberg and C.A.T. Susch, 11/15/90, (PB91-171272, A03, MF-A01).

NCEER-90-0025 "A Three-Dimensional Analytical Study of Spatial Variability of Seismic Ground Motions," by L-L. Hong and A.H.-S. Ang, 10/30/90, (PB91-170399, A09, MF-A01).

NCEER-90-0026 "MUMOID User's Guide - A Program for the Identification of Modal Parameters," by S. Rodriguez-Gomez and E. DiPasquale, 9/30/90, (PB91-171298, A04, MF-A01).

NCEER-90-0027 "SARCF-II User's Guide - Seismic Analysis of Reinforced Concrete Frames," by S. Rodriguez-Gomez, Y.S. Chung and C. Meyer, 9/30/90, (PB91-171280, A05, MF-A01).

NCEER-90-0028 "Viscous Dampers: Testing, Modeling and Application in Vibration and Seismic Isolation," by N. Makris and M.C. Constantinou, 12/20/90 (PB91-190561, A06, MF-A01).

NCEER-90-0029 "Soil Effects on Earthquake Ground Motions in the Memphis Area," by H. Hwang, C.S. Lee, K.W. Ng and T.S. Chang, 8/2/90, (PB91-190751, A05, MF-A01).

NCEER-91-0001 "Proceedings from the Third Japan-U.S. Workshop on Earthquake Resistant Design of Lifeline Facilities and Countermeasures for Soil Liquefaction, December 17-19, 1990," edited by T.D. O'Rourke and M. Hamada, 2/1/91, (PB91-179259, A99, MF-A04).

NCEER-91-0002 "Physical Space Solutions of Non-Proportionally Damped Systems," by M. Tong, Z. Liang and G.C. Lee, 1/15/91, (PB91-179242, A04, MF-A01).

NCEER-91-0003 "Seismic Response of Single Piles and Pile Groups," by K. Fan and G. Gazetas, 1/10/91, (PB92-174994, A04, MF-A01).

NCEER-91-0004 "Damping of Structures: Part 1 - Theory of Complex Damping," by Z. Liang and G. Lee, 10/10/91, (PB92-197235, A12, MF-A03).

NCEER-91-0005 "3D-BASIS - Nonlinear Dynamic Analysis of Three Dimensional Base Isolated Structures: Part II," by S. Nagarajaiah, A.M. Reinhorn and M.C. Constantinou, 2/28/91, (PB91-190553, A07, MF-A01). This report has been replaced by NCEER-93-0011.

NCEER-91-0006 "A Multidimensional Hysteretic Model for Plasticity Deforming Metals in Energy Absorbing Devices," by E.J. Graesser and F.A. Cozzarelli, 4/9/91, (PB92-108364, A04, MF-A01).

NCEER-91-0007 "A Framework for Customizable Knowledge-Based Expert Systems with an Application to a KBES for Evaluating the Seismic Resistance of Existing Buildings," by E.G. Ibarra-Anaya and S.J. Fenves, 4/9/91, (PB91-210930, A08, MF-A01).

NCEER-91-0008 "Nonlinear Analysis of Steel Frames with Semi-Rigid Connections Using the Capacity Spectrum Method," by G.G. Deierlein, S-H. Hsieh, Y-J. Shen and J.F. Abel, 7/2/91, (PB92-113828, A05, MF-A01).

NCEER-91-0009 "Earthquake Education Materials for Grades K-12," by K.E.K. Ross, 4/30/91, (PB91-212142, A06, MF-A01). This report has been replaced by NCEER-92-0018.

NCEER-91-0010 "Phase Wave Velocities and Displacement Phase Differences in a Harmonically Oscillating Pile," by N. Makris and G. Gazetas, 7/8/91, (PB92-108356, A04, MF-A01).

NCEER-91-0011 "Dynamic Characteristics of a Full-Size Five-Story Steel Structure and a 2/5 Scale Model," by K.C. Chang, G.C. Yao, G.C. Lee, D.S. Hao and Y.C. Yeh," 7/2/91, (PB93-116648, A06, MF-A02).

NCEER-91-0012 "Seismic Response of a 2/5 Scale Steel Structure with Added Viscoelastic Dampers," by K.C. Chang, T.T. Soong, S-T. Oh and M.L. Lai, 5/17/91, (PB92-110816, A05, MF-A01).

NCEER-91-0013 "Earthquake Response of Retaining Walls; Full-Scale Testing and Computational Modeling," by S. Alampalli and A-W.M. Elgamal, 6/20/91, not available.

NCEER-91-0014 "3D-BASIS-M: Nonlinear Dynamic Analysis of Multiple Building Base Isolated Structures," by P.C. Tsopelas, S. Nagarajaiah, M.C. Constantinou and A.M. Reinhorn, 5/28/91, (PB92-113885, A09, MF-A02).

NCEER-91-0015 "Evaluation of SEAOC Design Requirements for Sliding Isolated Structures," by D. Theodossiou and M.C. Constantinou, 6/10/91, (PB92-114602, A11, MF-A03).

NCEER-91-0016 "Closed-Loop Modal Testing of a 27-Story Reinforced Concrete Flat Plate-Core Building," by H.R. Somaprasad, T. Toksoy, H. Yoshiyuki and A.E. Aktan, 7/15/91, (PB92-129980, A07, MF-A02).

NCEER-91-0017 "Shake Table Test of a 1/6 Scale Two-Story Lightly Reinforced Concrete Building," by A.G. El-Attar, R.N. White and P. Gergely, 2/28/91, (PB92-222447, A06, MF-A02).

NCEER-91-0018 "Shake Table Test of a 1/8 Scale Three-Story Lightly Reinforced Concrete Building," by A.G. El-Attar, R.N. White and P. Gergely, 2/28/91, (PB93-116630, A08, MF-A02).

NCEER-91-0019 "Transfer Functions for Rigid Rectangular Foundations," by A.S. Veletsos, A.M. Prasad and W.H. Wu, 7/31/91, not available.

NCEER-91-0020 "Hybrid Control of Seismic-Excited Nonlinear and Inelastic Structural Systems," by J.N. Yang, Z. Li and A. Danielians, 8/1/91, (PB92-143171, A06, MF-A02).

NCEER-91-0021 "The NCEER-91 Earthquake Catalog: Improved Intensity-Based Magnitudes and Recurrence Relations for U.S. Earthquakes East of New Madrid," by L. Seeber and J.G. Armbruster, 8/28/91, (PB92-176742, A06, MF-A02).

NCEER-91-0022 "Proceedings from the Implementation of Earthquake Planning and Education in Schools: The Need for Change - The Roles of the Changemakers," by K.E.K. Ross and F. Winslow, 7/23/91, (PB92-129998, A12, MF-A03).

NCEER-91-0023 "A Study of Reliability-Based Criteria for Seismic Design of Reinforced Concrete Frame Buildings," by H.H.M. Hwang and H-M. Hsu, 8/10/91, (PB92-140235, A09, MF-A02).

NCEER-91-0024 "Experimental Verification of a Number of Structural System Identification Algorithms," by R.G. Ghanem, H. Gavin and M. Shinozuka, 9/18/91, (PB92-176577, A18, MF-A04).

NCEER-91-0025 "Probabilistic Evaluation of Liquefaction Potential," by H.H.M. Hwang and C.S. Lee," 11/25/91, (PB92-143429, A05, MF-A01).

NCEER-91-0026 "Instantaneous Optimal Control for Linear, Nonlinear and Hysteretic Structures - Stable Controllers," by J.N. Yang and Z. Li, 11/15/91, (PB92-163807, A04, MF-A01).

NCEER-91-0027 "Experimental and Theoretical Study of a Sliding Isolation System for Bridges," by M.C. Constantinou, A. Kartoum, A.M. Reinhorn and P. Bradford, 11/15/91, (PB92-176973, A10, MF-A03).

NCEER-92-0001 "Case Studies of Liquefaction and Lifeline Performance During Past Earthquakes, Volume 1: Japanese Case Studies," Edited by M. Hamada and T. O'Rourke, 2/17/92, (PB92-197243, A18, MF-A04).

NCEER-92-0002 "Case Studies of Liquefaction and Lifeline Performance During Past Earthquakes, Volume 2: United States Case Studies," Edited by T. O'Rourke and M. Hamada, 2/17/92, (PB92-197250, A20, MF-A04).

NCEER-92-0003 "Issues in Earthquake Education," Edited by K. Ross, 2/3/92, (PB92-222389, A07, MF-A02).

NCEER-92-0004 "Proceedings from the First U.S. - Japan Workshop on Earthquake Protective Systems for Bridges," Edited by I.G. Buckle, 2/4/92, (PB94-142239, A99, MF-A06).

NCEER-92-0005 "Seismic Ground Motion from a Haskell-Type Source in a Multiple-Layered Half-Space," A.P. Theoharis, G. Deodatis and M. Shinozuka, 1/2/92, not available.

NCEER-92-0006 "Proceedings from the Site Effects Workshop," Edited by R. Whitman, 2/29/92, (PB92-197201, A04, MF-A01).

NCEER-92-0007 "Engineering Evaluation of Permanent Ground Deformations Due to Seismically-Induced Liquefaction," by M.H. Baziar, R. Dobry and A-W.M. Elgamal, 3/24/92, (PB92-222421, A13, MF-A03).

NCEER-92-0008 "A Procedure for the Seismic Evaluation of Buildings in the Central and Eastern United States," by C.D. Poland and J.O. Malley, 4/2/92, (PB92-222439, A20, MF-A04).

NCEER-92-0009 "Experimental and Analytical Study of a Hybrid Isolation System Using Friction Controllable Sliding Bearings," by M.Q. Feng, S. Fujii and M. Shinozuka, 5/15/92, (PB93-150282, A06, MF-A02).

NCEER-92-0010 "Seismic Resistance of Slab-Column Connections in Existing Non-Ductile Flat-Plate Buildings," by A.J. Durrani and Y. Du, 5/18/92, (PB93-116812, A06, MF-A02).

NCEER-92-0011 "The Hysteretic and Dynamic Behavior of Brick Masonry Walls Upgraded by Ferrocement Coatings Under Cyclic Loading and Strong Simulated Ground Motion," by H. Lee and S.P. Prawel, 5/11/92, not available.

NCEER-92-0012 "Study of Wire Rope Systems for Seismic Protection of Equipment in Buildings," by G.F. Demetriades, M.C. Constantinou and A.M. Reinhorn, 5/20/92, (PB93-116655, A08, MF-A02).

NCEER-92-0013 "Shape Memory Structural Dampers: Material Properties, Design and Seismic Testing," by P.R. Witting and F.A. Cozzarelli, 5/26/92, (PB93-116663, A05, MF-A01).

NCEER-92-0014 "Longitudinal Permanent Ground Deformation Effects on Buried Continuous Pipelines," by M.J. O'Rourke, and C. Nordberg, 6/15/92, (PB93-116671, A08, MF-A02).

NCEER-92-0015 "A Simulation Method for Stationary Gaussian Random Functions Based on the Sampling Theorem," by M. Grigoriu and S. Balopoulou, 6/11/92, (PB93-127496, A05, MF-A01).

NCEER-92-0016 "Gravity-Load-Designed Reinforced Concrete Buildings: Seismic Evaluation of Existing Construction and Detailing Strategies for Improved Seismic Resistance," by G.W. Hoffmann, S.K. Kunnath, A.M. Reinhorn and J.B. Mander, 7/15/92, (PB94-142007, A08, MF-A02).

NCEER-92-0017 "Observations on Water System and Pipeline Performance in the Limón Area of Costa Rica Due to the April 22, 1991 Earthquake," by M. O'Rourke and D. Ballantyne, 6/30/92, (PB93-126811, A06, MF-A02).

NCEER-92-0018 "Fourth Edition of Earthquake Education Materials for Grades K-12," Edited by K.E.K. Ross, 8/10/92, (PB93-114023, A07, MF-A02).

NCEER-92-0019 "Proceedings from the Fourth Japan-U.S. Workshop on Earthquake Resistant Design of Lifeline Facilities and Countermeasures for Soil Liquefaction," Edited by M. Hamada and T.D. O'Rourke, 8/12/92, (PB93-163939, A99, MF-E11).

NCEER-92-0020 "Active Bracing System: A Full Scale Implementation of Active Control," by A.M. Reinhorn, T.T. Soong, R.C. Lin, M.A. Riley, Y.P. Wang, S. Aizawa and M. Higashino, 8/14/92, (PB93-127512, A06, MF-A02).

NCEER-92-0021 "Empirical Analysis of Horizontal Ground Displacement Generated by Liquefaction-Induced Lateral Spreads," by S.F. Bartlett and T.L. Youd, 8/17/92, (PB93-188241, A06, MF-A02).

NCEER-92-0022 "IDARC Version 3.0: Inelastic Damage Analysis of Reinforced Concrete Structures," by S.K. Kunnath, A.M. Reinhorn and R.F. Lobo, 8/31/92, (PB93-227502, A07, MF-A02).

NCEER-92-0023 "A Semi-Empirical Analysis of Strong-Motion Peaks in Terms of Seismic Source, Propagation Path and Local Site Conditions, by M. Kamiyama, M.J. O'Rourke and R. Flores-Berrones, 9/9/92, (PB93-150266, A08, MF-A02).

NCEER-92-0024 "Seismic Behavior of Reinforced Concrete Frame Structures with Nonductile Details, Part I: Summary of Experimental Findings of Full Scale Beam-Column Joint Tests," by A. Beres, R.N. White and P. Gergely, 9/30/92, (PB93-227783, A05, MF-A01).

NCEER-92-0025 "Experimental Results of Repaired and Retrofitted Beam-Column Joint Tests in Lightly Reinforced Concrete Frame Buildings," by A. Beres, S. El-Borgi, R.N. White and P. Gergely, 10/29/92, (PB93-227791, A05, MF-A01).

NCEER-92-0026 "A Generalization of Optimal Control Theory: Linear and Nonlinear Structures," by J.N. Yang, Z. Li and S. Vongchavalitkul, 11/2/92, (PB93-188621, A05, MF-A01).

NCEER-92-0027 "Seismic Resistance of Reinforced Concrete Frame Structures Designed Only for Gravity Loads: Part I - Design and Properties of a One-Third Scale Model Structure," by J.M. Bracci, A.M. Reinhorn and J.B. Mander, 12/1/92, (PB94-104502, A08, MF-A02).

NCEER-92-0028 "Seismic Resistance of Reinforced Concrete Frame Structures Designed Only for Gravity Loads: Part II - Experimental Performance of Subassemblages," by L.E. Aycardi, J.B. Mander and A.M. Reinhorn, 12/1/92, (PB94-104510, A08, MF-A02).

NCEER-92-0029 "Seismic Resistance of Reinforced Concrete Frame Structures Designed Only for Gravity Loads: Part III - Experimental Performance and Analytical Study of a Structural Model," by J.M. Bracci, A.M. Reinhorn and J.B. Mander, 12/1/92, (PB93-227528, A09, MF-A01).

NCEER-92-0030 "Evaluation of Seismic Retrofit of Reinforced Concrete Frame Structures: Part I - Experimental Performance of Retrofitted Subassemblages," by D. Choudhuri, J.B. Mander and A.M. Reinhorn, 12/8/92, (PB93-198307, A07, MF-A02).

NCEER-92-0031 "Evaluation of Seismic Retrofit of Reinforced Concrete Frame Structures: Part II - Experimental Performance and Analytical Study of a Retrofitted Structural Model," by J.M. Bracci, A.M. Reinhorn and J.B. Mander, 12/8/92, (PB93-198315, A09, MF-A03).

NCEER-92-0032 "Experimental and Analytical Investigation of Seismic Response of Structures with Supplemental Fluid Viscous Dampers," by M.C. Constantinou and M.D. Symans, 12/21/92, (PB93-191435, A10, MF-A03). This report is available only through NTIS (see address given above).

NCEER-92-0033 "Reconnaissance Report on the Cairo, Egypt Earthquake of October 12, 1992," by M. Khater, 12/23/92, (PB93-188621, A03, MF-A01).

NCEER-92-0034 "Low-Level Dynamic Characteristics of Four Tall Flat-Plate Buildings in New York City," by H. Gavin, S. Yuan, J. Grossman, E. Pekelis and K. Jacob, 12/28/92, (PB93-188217, A07, MF-A02).

NCEER-93-0001 "An Experimental Study on the Seismic Performance of Brick-Infilled Steel Frames With and Without Retrofit," by J.B. Mander, B. Nair, K. Wojtkowski and J. Ma, 1/29/93, (PB93-227510, A07, MF-A02).

NCEER-93-0002 "Social Accounting for Disaster Preparedness and Recovery Planning," by S. Cole, E. Pantoja and V. Razak, 2/22/93, (PB94-142114, A12, MF-A03).

NCEER-93-0003 "Assessment of 1991 NEHRP Provisions for Nonstructural Components and Recommended Revisions," by T.T. Soong, G. Chen, Z. Wu, R-H. Zhang and M. Grigoriu, 3/1/93, (PB93-188639, A06, MF-A02).

NCEER-93-0004 "Evaluation of Static and Response Spectrum Analysis Procedures of SEAOC/UBC for Seismic Isolated Structures," by C.W. Winters and M.C. Constantinou, 3/23/93, (PB93-198299, A10, MF-A03).

NCEER-93-0005 "Earthquakes in the Northeast - Are We Ignoring the Hazard? A Workshop on Earthquake Science and Safety for Educators," edited by K.E.K. Ross, 4/2/93, (PB94-103066, A09, MF-A02).

NCEER-93-0006 "Inelastic Response of Reinforced Concrete Structures with Viscoelastic Braces," by R.F. Lobo, J.M. Bracci, K.L. Shen, A.M. Reinhorn and T.T. Soong, 4/5/93, (PB93-227486, A05, MF-A02).

NCEER-93-0007 "Seismic Testing of Installation Methods for Computers and Data Processing Equipment," by K. Kosar, T.T. Soong, K.L. Shen, J.A. HoLung and Y.K. Lin, 4/12/93, (PB93-198299, A07, MF-A02).

NCEER-93-0008 "Retrofit of Reinforced Concrete Frames Using Added Dampers," by A. Reinhorn, M. Constantinou and C. Li, not available.

NCEER-93-0009 "Seismic Behavior and Design Guidelines for Steel Frame Structures with Added Viscoelastic Dampers," by K.C. Chang, M.L. Lai, T.T. Soong, D.S. Hao and Y.C. Yeh, 5/1/93, (PB94-141959, A07, MF-A02).

NCEER-93-0010 "Seismic Performance of Shear-Critical Reinforced Concrete Bridge Piers," by J.B. Mander, S.M. Waheed, M.T.A. Chaudhary and S.S. Chen, 5/12/93, (PB93-227494, A08, MF-A02).

NCEER-93-0011 "3D-BASIS-TABS: Computer Program for Nonlinear Dynamic Analysis of Three Dimensional Base Isolated Structures," by S. Nagarajaiah, C. Li, A.M. Reinhorn and M.C. Constantinou, 8/2/93, (PB94-141819, A09, MF-A02).

NCEER-93-0012 "Effects of Hydrocarbon Spills from an Oil Pipeline Break on Ground Water," by O.J. Helweg and H.H.M. Hwang, 8/3/93, (PB94-141942, A06, MF-A02).

NCEER-93-0013 "Simplified Procedures for Seismic Design of Nonstructural Components and Assessment of Current Code Provisions," by M.P. Singh, L.E. Suarez, E.E. Matheu and G.O. Maldonado, 8/4/93, (PB94-141827, A09, MF-A02).

NCEER-93-0014 "An Energy Approach to Seismic Analysis and Design of Secondary Systems," by G. Chen and T.T. Soong, 8/6/93, (PB94-142767, A11, MF-A03).

NCEER-93-0015 "Proceedings from School Sites: Becoming Prepared for Earthquakes - Commemorating the Third Anniversary of the Loma Prieta Earthquake," Edited by F.E. Winslow and K.E.K. Ross, 8/16/93, (PB94-154275, A16, MF-A02).

NCEER-93-0016 "Reconnaissance Report of Damage to Historic Monuments in Cairo, Egypt Following the October 12, 1992 Dahshur Earthquake," by D. Sykora, D. Look, G. Croci, E. Karaesmen and E. Karaesmen, 8/19/93, (PB94-142221, A08, MF-A02).

NCEER-93-0017 "The Island of Guam Earthquake of August 8, 1993," by S.W. Swan and S.K. Harris, 9/30/93, (PB94-141843, A04, MF-A01).

NCEER-93-0018 "Engineering Aspects of the October 12, 1992 Egyptian Earthquake," by A.W. Elgamal, M. Amer, K. Adalier and A. Abul-Fadl, 10/7/93, (PB94-141983, A05, MF-A01).

NCEER-93-0019 "Development of an Earthquake Motion Simulator and its Application in Dynamic Centrifuge Testing," by I. Krstelj, Supervised by J.H. Prevost, 10/23/93, (PB94-181773, A-10, MF-A03).

NCEER-93-0020 "NCEER-Taisei Corporation Research Program on Sliding Seismic Isolation Systems for Bridges: Experimental and Analytical Study of a Friction Pendulum System (FPS)," by M.C. Constantinou, P. Tsopelas, Y-S. Kim and S. Okamoto, 11/1/93, (PB94-142775, A08, MF-A02).

NCEER-93-0021 "Finite Element Modeling of Elastomeric Seismic Isolation Bearings," by L.J. Billings, Supervised by R. Shepherd, 11/8/93, not available.

NCEER-93-0022 "Seismic Vulnerability of Equipment in Critical Facilities: Life-Safety and Operational Consequences," by K. Porter, G.S. Johnson, M.M. Zadeh, C. Scawthorn and S. Eder, 11/24/93, (PB94-181765, A16, MF-A03).

NCEER-93-0023 "Hokkaido Nansei-oki, Japan Earthquake of July 12, 1993, by P.I. Yanev and C.R. Scawthorn, 12/23/93, (PB94-181500, A07, MF-A01).

NCEER-94-0001 "An Evaluation of Seismic Serviceability of Water Supply Networks with Application to the San Francisco Auxiliary Water Supply System," by I. Markov, Supervised by M. Grigoriu and T. O'Rourke, 1/21/94, (PB94-204013, A07, MF-A02).

NCEER-94-0002 "NCEER-Taisei Corporation Research Program on Sliding Seismic Isolation Systems for Bridges: Experimental and Analytical Study of Systems Consisting of Sliding Bearings, Rubber Restoring Force Devices and Fluid Dampers," Volumes I and II, by P. Tsopelas, S. Okamoto, M.C. Constantinou, D. Ozaki and S. Fujii, 2/4/94, (PB94-181740, A09, MF-A02 and PB94-181757, A12, MF-A03).

NCEER-94-0003 "A Markov Model for Local and Global Damage Indices in Seismic Analysis," by S. Rahman and M. Grigoriu, 2/18/94, (PB94-206000, A12, MF-A03).

NCEER-94-0004 "Proceedings from the NCEER Workshop on Seismic Response of Masonry Infills," edited by D.P. Abrams, 3/1/94, (PB94-180783, A07, MF-A02).

NCEER-94-0005 "The Northridge, California Earthquake of January 17, 1994: General Reconnaissance Report," edited by J.D. Goltz, 3/11/94, (PB94-193943, A10, MF-A03).

NCEER-94-0006 "Seismic Energy Based Fatigue Damage Analysis of Bridge Columns: Part I - Evaluation of Seismic Capacity," by G.A. Chang and J.B. Mander, 3/14/94, (PB94-219185, A11, MF-A03).

NCEER-94-0007 "Seismic Isolation of Multi-Story Frame Structures Using Spherical Sliding Isolation Systems," by T.M. Al-Hussaini, V.A. Zayas and M.C. Constantinou, 3/17/94, (PB94-193745, A09, MF-A02).

NCEER-94-0008 "The Northridge, California Earthquake of January 17, 1994: Performance of Highway Bridges," edited by I.G. Buckle, 3/24/94, (PB94-193851, A06, MF-A02).

NCEER-94-0009 "Proceedings of the Third U.S.-Japan Workshop on Earthquake Protective Systems for Bridges," edited by I.G. Buckle and I. Friedland, 3/31/94, (PB94-195815, A99, MF-A06).

NCEER-94-0010 "3D-BASIS-ME: Computer Program for Nonlinear Dynamic Analysis of Seismically Isolated Single and Multiple Structures and Liquid Storage Tanks," by P.C. Tsopelas, M.C. Constantinou and A.M. Reinhorn, 4/12/94, (PB94-204922, A09, MF-A02).

NCEER-94-0011 "The Northridge, California Earthquake of January 17, 1994: Performance of Gas Transmission Pipelines," by T.D. O'Rourke and M.C. Palmer, 5/16/94, (PB94-204989, A05, MF-A01).

NCEER-94-0012 "Feasibility Study of Replacement Procedures and Earthquake Performance Related to Gas Transmission Pipelines," by T.D. O'Rourke and M.C. Palmer, 5/25/94, (PB94-206638, A09, MF-A02).

NCEER-94-0013 "Seismic Energy Based Fatigue Damage Analysis of Bridge Columns: Part II - Evaluation of Seismic Demand," by G.A. Chang and J.B. Mander, 6/1/94, (PB95-18106, A08, MF-A02).

NCEER-94-0014 "NCEER-Taisei Corporation Research Program on Sliding Seismic Isolation Systems for Bridges: Experimental and Analytical Study of a System Consisting of Sliding Bearings and Fluid Restoring Force/Damping Devices," by P. Tsopelas and M.C. Constantinou, 6/13/94, (PB94-219144, A10, MF-A03).

NCEER-94-0015 "Generation of Hazard-Consistent Fragility Curves for Seismic Loss Estimation Studies," by H. Hwang and J-R. Huo, 6/14/94, (PB95-181996, A09, MF-A02).

NCEER-94-0016 "Seismic Study of Building Frames with Added Energy-Absorbing Devices," by W.S. Pong, C.S. Tsai and G.C. Lee, 6/20/94, (PB94-219136, A10, A03).

NCEER-94-0017 "Sliding Mode Control for Seismic-Excited Linear and Nonlinear Civil Engineering Structures," by J. Yang, J. Wu, A. Agrawal and Z. Li, 6/21/94, (PB95-138483, A06, MF-A02).

NCEER-94-0018 "3D-BASIS-TABS Version 2.0: Computer Program for Nonlinear Dynamic Analysis of Three Dimensional Base Isolated Structures," by A.M. Reinhorn, S. Nagarajaiah, M.C. Constantinou, P. Tsopelas and R. Li, 6/22/94, (PB95-182176, A08, MF-A02).

NCEER-94-0019 "Proceedings of the International Workshop on Civil Infrastructure Systems: Application of Intelligent Systems and Advanced Materials on Bridge Systems," Edited by G.C. Lee and K.C. Chang, 7/18/94, (PB95-252474, A20, MF-A04).

NCEER-94-0020 "Study of Seismic Isolation Systems for Computer Floors," by V. Lambrou and M.C. Constantinou, 7/19/94, (PB95-138533, A10, MF-A03).

NCEER-94-0021 "Proceedings of the U.S.-Italian Workshop on Guidelines for Seismic Evaluation and Rehabilitation of Unreinforced Masonry Buildings," Edited by D.P. Abrams and G.M. Calvi, 7/20/94, (PB95-138749, A13, MF-A03).

NCEER-94-0022 "NCEER-Taisei Corporation Research Program on Sliding Seismic Isolation Systems for Bridges: Experimental and Analytical Study of a System Consisting of Lubricated PTFE Sliding Bearings and Mild Steel Dampers," by P. Tsopelas and M.C. Constantinou, 7/22/94, (PB95-182184, A08, MF-A02).

NCEER-94-0023 “Development of Reliability-Based Design Criteria for Buildings Under Seismic Load,” by Y.K. Wen, H. Hwang and M. Shinozuka, 8/1/94, (PB95-211934, A08, MF-A02).

NCEER-94-0024 “Experimental Verification of Acceleration Feedback Control Strategies for an Active Tendon System,” by S.J. Dyke, B.F. Spencer, Jr., P. Quast, M.K. Sain, D.C. Kaspari, Jr. and T.T. Soong, 8/29/94, (PB95-212320, A05, MF-A01).

NCEER-94-0025 “Seismic Retrofitting Manual for Highway Bridges,” Edited by I.G. Buckle and I.F. Friedland, published by the Federal Highway Administration (PB95-212676, A15, MF-A03).

NCEER-94-0026 “Proceedings from the Fifth U.S.-Japan Workshop on Earthquake Resistant Design of Lifeline Facilities and Countermeasures Against Soil Liquefaction,” Edited by T.D. O’Rourke and M. Hamada, 11/7/94, (PB95-220802, A99, MF-E08).

NCEER-95-0001 "Experimental and Analytical Investigation of Seismic Retrofit of Structures with Supplemental Damping: Part 1 - Fluid Viscous Damping Devices," by A.M. Reinhorn, C. Li and M.C. Constantinou, 1/3/95, (PB95-266599, A09, MF-A02).

NCEER-95-0002 "Experimental and Analytical Study of Low-Cycle Fatigue Behavior of Semi-Rigid Top-And-Seat Angle Connections," by G. Pekcan, J.B. Mander and S.S. Chen, 1/5/95, (PB95-220042, A07, MF-A02).

NCEER-95-0003 "NCEER-ATC Joint Study on Fragility of Buildings," by T. Anagnos, C. Rojahn and A.S. Kiremidjian, 1/20/95, (PB95-220026, A06, MF-A02).

NCEER-95-0004 "Nonlinear Control Algorithms for Peak Response Reduction," by Z. Wu, T.T. Soong, V. Gattulli and R.C. Lin, 2/16/95, (PB95-220349, A05, MF-A01).

NCEER-95-0005 "Pipeline Replacement Feasibility Study: A Methodology for Minimizing Seismic and Corrosion Risks to Underground Natural Gas Pipelines," by R.T. Eguchi, H.A. Seligson and D.G. Honegger, 3/2/95, (PB95-252326, A06, MF-A02).

NCEER-95-0006 "Evaluation of Seismic Performance of an 11-Story Frame Building During the 1994 Northridge Earthquake," by F. Naeim, R. DiSulio, K. Benuska, A. Reinhorn and C. Li, not available.

NCEER-95-0007 "Prioritization of Bridges for Seismic Retrofitting," by N. Basöz and A.S. Kiremidjian, 4/24/95, (PB95-252300, A08, MF-A02).

NCEER-95-0008 "Method for Developing Motion Damage Relationships for Reinforced Concrete Frames," by A. Singhal and A.S. Kiremidjian, 5/11/95, (PB95-266607, A06, MF-A02).

NCEER-95-0009 "Experimental and Analytical Investigation of Seismic Retrofit of Structures with Supplemental Damping: Part II - Friction Devices," by C. Li and A.M. Reinhorn, 7/6/95, (PB96-128087, A11, MF-A03).

NCEER-95-0010 "Experimental Performance and Analytical Study of a Non-Ductile Reinforced Concrete Frame Structure Retrofitted with Elastomeric Spring Dampers," by G. Pekcan, J.B. Mander and S.S. Chen, 7/14/95, (PB96-137161, A08, MF-A02).

NCEER-95-0011 "Development and Experimental Study of Semi-Active Fluid Damping Devices for Seismic Protection of Structures," by M.D. Symans and M.C. Constantinou, 8/3/95, (PB96-136940, A23, MF-A04).

NCEER-95-0012 "Real-Time Structural Parameter Modification (RSPM): Development of Innervated Structures," by Z. Liang, M. Tong and G.C. Lee, 4/11/95, (PB96-137153, A06, MF-A01).

NCEER-95-0013 "Experimental and Analytical Investigation of Seismic Retrofit of Structures with Supplemental Damping: Part III - Viscous Damping Walls," by A.M. Reinhorn and C. Li, 10/1/95, (PB96-176409, A11, MF-A03).

NCEER-95-0014 "Seismic Fragility Analysis of Equipment and Structures in a Memphis Electric Substation," by J-R. Huo and H.H.M. Hwang, 8/10/95, (PB96-128087, A09, MF-A02).

NCEER-95-0015 "The Hanshin-Awaji Earthquake of January 17, 1995: Performance of Lifelines," Edited by M. Shinozuka, 11/3/95, (PB96-176383, A15, MF-A03).

NCEER-95-0016 "Highway Culvert Performance During Earthquakes," by T.L. Youd and C.J. Beckman, available as NCEER-96-0015.

NCEER-95-0017 "The Hanshin-Awaji Earthquake of January 17, 1995: Performance of Highway Bridges," Edited by I.G. Buckle, 12/1/95, not available.

NCEER-95-0018 "Modeling of Masonry Infill Panels for Structural Analysis," by A.M. Reinhorn, A. Madan, R.E. Valles, Y. Reichmann and J.B. Mander, 12/8/95, (PB97-110886, MF-A01, A06).

NCEER-95-0019 "Optimal Polynomial Control for Linear and Nonlinear Structures," by A.K. Agrawal and J.N. Yang, 12/11/95, (PB96-168737, A07, MF-A02).

NCEER-95-0020 "Retrofit of Non-Ductile Reinforced Concrete Frames Using Friction Dampers," by R.S. Rao, P. Gergely and R.N. White, 12/22/95, (PB97-133508, A10, MF-A02).

NCEER-95-0021 "Parametric Results for Seismic Response of Pile-Supported Bridge Bents," by G. Mylonakis, A. Nikolaou and G. Gazetas, 12/22/95, (PB97-100242, A12, MF-A03).

NCEER-95-0022 "Kinematic Bending Moments in Seismically Stressed Piles," by A. Nikolaou, G. Mylonakis and G. Gazetas, 12/23/95, (PB97-113914, MF-A03, A13).

NCEER-96-0001 "Dynamic Response of Unreinforced Masonry Buildings with Flexible Diaphragms," by A.C. Costley and D.P. Abrams," 10/10/96, (PB97-133573, MF-A03, A15).

NCEER-96-0002 "State of the Art Review: Foundations and Retaining Structures," by I. Po Lam, not available.

NCEER-96-0003 "Ductility of Rectangular Reinforced Concrete Bridge Columns with Moderate Confinement," by N. Wehbe, M. Saiidi, D. Sanders and B. Douglas, 11/7/96, (PB97-133557, A06, MF-A02).

NCEER-96-0004 "Proceedings of the Long-Span Bridge Seismic Research Workshop," edited by I.G. Buckle and I.M. Friedland, not available.

NCEER-96-0005 "Establish Representative Pier Types for Comprehensive Study: Eastern United States," by J. Kulicki and Z. Prucz, 5/28/96, (PB98-119217, A07, MF-A02).

NCEER-96-0006 "Establish Representative Pier Types for Comprehensive Study: Western United States," by R. Imbsen, R.A. Schamber and T.A. Osterkamp, 5/28/96, (PB98-118607, A07, MF-A02).

NCEER-96-0007 "Nonlinear Control Techniques for Dynamical Systems with Uncertain Parameters," by R.G. Ghanem and M.I. Bujakov, 5/27/96, (PB97-100259, A17, MF-A03).

NCEER-96-0008 "Seismic Evaluation of a 30-Year Old Non-Ductile Highway Bridge Pier and Its Retrofit," by J.B. Mander, B. Mahmoodzadegan, S. Bhadra and S.S. Chen, 5/31/96, (PB97-110902, MF-A03, A10).

NCEER-96-0009 "Seismic Performance of a Model Reinforced Concrete Bridge Pier Before and After Retrofit," by J.B. Mander, J.H. Kim and C.A. Ligozio, 5/31/96, (PB97-110910, MF-A02, A10).

NCEER-96-0010 "IDARC2D Version 4.0: A Computer Program for the Inelastic Damage Analysis of Buildings," by R.E. Valles, A.M. Reinhorn, S.K. Kunnath, C. Li and A. Madan, 6/3/96, (PB97-100234, A17, MF-A03).

NCEER-96-0011 "Estimation of the Economic Impact of Multiple Lifeline Disruption: Memphis Light, Gas and Water Division Case Study," by S.E. Chang, H.A. Seligson and R.T. Eguchi, 8/16/96, (PB97-133490, A11, MF-A03).

NCEER-96-0012 "Proceedings from the Sixth Japan-U.S. Workshop on Earthquake Resistant Design of Lifeline Facilities and Countermeasures Against Soil Liquefaction, Edited by M. Hamada and T. O'Rourke, 9/11/96, (PB97-133581, A99, MF-A06).

NCEER-96-0013 "Chemical Hazards, Mitigation and Preparedness in Areas of High Seismic Risk: A Methodology for Estimating the Risk of Post-Earthquake Hazardous Materials Release," by H.A. Seligson, R.T. Eguchi, K.J. Tierney and K. Richmond, 11/7/96, (PB97-133565, MF-A02, A08).

NCEER-96-0014 "Response of Steel Bridge Bearings to Reversed Cyclic Loading," by J.B. Mander, D-K. Kim, S.S. Chen and G.J. Premus, 11/13/96, (PB97-140735, A12, MF-A03).

NCEER-96-0015 "Highway Culvert Performance During Past Earthquakes," by T.L. Youd and C.J. Beckman, 11/25/96, (PB97-133532, A06, MF-A01).

NCEER-97-0001 "Evaluation, Prevention and Mitigation of Pounding Effects in Building Structures," by R.E. Valles and A.M. Reinhorn, 2/20/97, (PB97-159552, A14, MF-A03).

NCEER-97-0002 "Seismic Design Criteria for Bridges and Other Highway Structures," by C. Rojahn, R. Mayes, D.G. Anderson, J. Clark, J.H. Hom, R.V. Nutt and M.J. O'Rourke, 4/30/97, (PB97-194658, A06, MF-A03).

NCEER-97-0003 “Proceedings of the U.S.-Italian Workshop on Seismic Evaluation and Retrofit,” Edited by D.P. Abrams and G.M. Calvi, 3/19/97, (PB97-194666, A13, MF-A03).

NCEER-97-0004 "Investigation of Seismic Response of Buildings with Linear and Nonlinear Fluid Viscous Dampers," by A.A. Seleemah and M.C. Constantinou, 5/21/97, (PB98-109002, A15, MF-A03).

NCEER-97-0005 "Proceedings of the Workshop on Earthquake Engineering Frontiers in Transportation Facilities," edited by G.C. Lee and I.M. Friedland, 8/29/97, (PB98-128911, A25, MR-A04).

NCEER-97-0006 "Cumulative Seismic Damage of Reinforced Concrete Bridge Piers," by S.K. Kunnath, A. El-Bahy, A. Taylor and W. Stone, 9/2/97, (PB98-108814, A11, MF-A03).

NCEER-97-0007 "Structural Details to Accommodate Seismic Movements of Highway Bridges and Retaining Walls," by R.A. Imbsen, R.A. Schamber, E. Thorkildsen, A. Kartoum, B.T. Martin, T.N. Rosser and J.M. Kulicki, 9/3/97, (PB98-108996, A09, MF-A02).

NCEER-97-0008 "A Method for Earthquake Motion-Damage Relationships with Application to Reinforced Concrete Frames," by A. Singhal and A.S. Kiremidjian, 9/10/97, (PB98-108988, A13, MF-A03).

NCEER-97-0009 "Seismic Analysis and Design of Bridge Abutments Considering Sliding and Rotation," by K. Fishman and R. Richards, Jr., 9/15/97, (PB98-108897, A06, MF-A02).

NCEER-97-0010 "Proceedings of the FHWA/NCEER Workshop on the National Representation of Seismic Ground Motion for New and Existing Highway Facilities," edited by I.M. Friedland, M.S. Power and R.L. Mayes, 9/22/97, (PB98-128903, A21, MF-A04).

NCEER-97-0011 "Seismic Analysis for Design or Retrofit of Gravity Bridge Abutments," by K.L. Fishman, R. Richards, Jr. and R.C. Divito, 10/2/97, (PB98-128937, A08, MF-A02).

NCEER-97-0012 "Evaluation of Simplified Methods of Analysis for Yielding Structures," by P. Tsopelas, M.C. Constantinou, C.A. Kircher and A.S. Whittaker, 10/31/97, (PB98-128929, A10, MF-A03).

NCEER-97-0013 "Seismic Design of Bridge Columns Based on Control and Repairability of Damage," by C-T. Cheng and J.B. Mander, 12/8/97, (PB98-144249, A11, MF-A03).

NCEER-97-0014 "Seismic Resistance of Bridge Piers Based on Damage Avoidance Design," by J.B. Mander and C-T. Cheng, 12/10/97, (PB98-144223, A09, MF-A02).

NCEER-97-0015 “Seismic Response of Nominally Symmetric Systems with Strength Uncertainty,” by S. Balopoulou and M. Grigoriu, 12/23/97, (PB98-153422, A11, MF-A03).

NCEER-97-0016 “Evaluation of Seismic Retrofit Methods for Reinforced Concrete Bridge Columns,” by T.J. Wipf, F.W. Klaiber and F.M. Russo, 12/28/97, (PB98-144215, A12, MF-A03).

NCEER-97-0017 “Seismic Fragility of Existing Conventional Reinforced Concrete Highway Bridges,” by C.L. Mullen and A.S. Cakmak, 12/30/97, (PB98-153406, A08, MF-A02).

NCEER-97-0018 “Loss Asssessment of Memphis Buildings,” edited by D.P. Abrams and M. Shinozuka, 12/31/97, (PB98-144231, A13, MF-A03).

NCEER-97-0019 “Seismic Evaluation of Frames with Infill Walls Using Quasi-static Experiments,” by K.M. Mosalam, R.N. White and P. Gergely, 12/31/97, (PB98-153455, A07, MF-A02).

NCEER-97-0020 “Seismic Evaluation of Frames with Infill Walls Using Pseudo-dynamic Experiments,” by K.M. Mosalam, R.N. White and P. Gergely, 12/31/97, (PB98-153430, A07, MF-A02).

NCEER-97-0021 “Computational Strategies for Frames with Infill Walls: Discrete and Smeared Crack Analyses and Seismic Fragility,” by K.M. Mosalam, R.N. White and P. Gergely, 12/31/97, (PB98-153414, A10, MF-A02).

NCEER-97-0022 "Proceedings of the NCEER Workshop on Evaluation of Liquefaction Resistance of Soils," edited by T.L. Youd and I.M. Idriss, 12/31/97, (PB98-155617, A15, MF-A03).

MCEER-98-0001 "Extraction of Nonlinear Hysteretic Properties of Seismically Isolated Bridges from Quick-Release Field Tests," by Q. Chen, B.M. Douglas, E.M. Maragakis and I.G. Buckle, 5/26/98, (PB99-118838, A06, MF-A01).

MCEER-98-0002 "Methodologies for Evaluating the Importance of Highway Bridges," by A. Thomas, S. Eshenaur and J. Kulicki, 5/29/98, (PB99-118846, A10, MF-A02).

MCEER-98-0003 "Capacity Design of Bridge Piers and the Analysis of Overstrength," by J.B. Mander, A. Dutta and P. Goel, 6/1/98, (PB99-118853, A09, MF-A02).

MCEER-98-0004 "Evaluation of Bridge Damage Data from the Loma Prieta and Northridge, California Earthquakes," by N. Basoz and A. Kiremidjian, 6/2/98, (PB99-118861, A15, MF-A03).

MCEER-98-0005 "Screening Guide for Rapid Assessment of Liquefaction Hazard at Highway Bridge Sites," by T. L. Youd, 6/16/98, (PB99-118879, A06, not available on microfiche).

MCEER-98-0006 "Structural Steel and Steel/Concrete Interface Details for Bridges," by P. Ritchie, N. Kauhl and J. Kulicki, 7/13/98, (PB99-118945, A06, MF-A01).

MCEER-98-0007 "Capacity Design and Fatigue Analysis of Confined Concrete Columns," by A. Dutta and J.B. Mander, 7/14/98, (PB99-118960, A14, MF-A03).

MCEER-98-0008 "Proceedings of the Workshop on Performance Criteria for Telecommunication Services Under Earthquake Conditions," edited by A.J. Schiff, 7/15/98, (PB99-118952, A08, MF-A02).

MCEER-98-0009 "Fatigue Analysis of Unconfined Concrete Columns," by J.B. Mander, A. Dutta and J.H. Kim, 9/12/98, (PB99-123655, A10, MF-A02).

MCEER-98-0010 "Centrifuge Modeling of Cyclic Lateral Response of Pile-Cap Systems and Seat-Type Abutments in Dry Sands," by A.D. Gadre and R. Dobry, 10/2/98, (PB99-123606, A13, MF-A03).

MCEER-98-0011 "IDARC-BRIDGE: A Computational Platform for Seismic Damage Assessment of Bridge Structures," by A.M. Reinhorn, V. Simeonov, G. Mylonakis and Y. Reichman, 10/2/98, (PB99-162919, A15, MF-A03).

MCEER-98-0012 "Experimental Investigation of the Dynamic Response of Two Bridges Before and After Retrofitting with Elastomeric Bearings," by D.A. Wendichansky, S.S. Chen and J.B. Mander, 10/2/98, (PB99-162927, A15, MF-A03).

MCEER-98-0013 "Design Procedures for Hinge Restrainers and Hinge Sear Width for Multiple-Frame Bridges," by R. Des Roches and G.L. Fenves, 11/3/98, (PB99-140477, A13, MF-A03).

MCEER-98-0014 "Response Modification Factors for Seismically Isolated Bridges," by M.C. Constantinou and J.K. Quarshie, 11/3/98, (PB99-140485, A14, MF-A03).

MCEER-98-0015 "Proceedings of the U.S.-Italy Workshop on Seismic Protective Systems for Bridges," edited by I.M. Friedland and M.C. Constantinou, 11/3/98, (PB2000-101711, A22, MF-A04).

MCEER-98-0016 "Appropriate Seismic Reliability for Critical Equipment Systems: Recommendations Based on Regional Analysis of Financial and Life Loss," by K. Porter, C. Scawthorn, C. Taylor and N. Blais, 11/10/98, (PB99-157265, A08, MF-A02).

MCEER-98-0017 "Proceedings of the U.S. Japan Joint Seminar on Civil Infrastructure Systems Research," edited by M. Shinozuka and A. Rose, 11/12/98, (PB99-156713, A16, MF-A03).

MCEER-98-0018 "Modeling of Pile Footings and Drilled Shafts for Seismic Design," by I. PoLam, M. Kapuskar and D. Chaudhuri, 12/21/98, (PB99-157257, A09, MF-A02).

MCEER-99-0001 "Seismic Evaluation of a Masonry Infilled Reinforced Concrete Frame by Pseudodynamic Testing," by S.G. Buonopane and R.N. White, 2/16/99, (PB99-162851, A09, MF-A02).

MCEER-99-0002 "Response History Analysis of Structures with Seismic Isolation and Energy Dissipation Systems: Verification Examples for Program SAP2000," by J. Scheller and M.C. Constantinou, 2/22/99, (PB99-162869, A08, MF-A02).

MCEER-99-0003 "Experimental Study on the Seismic Design and Retrofit of Bridge Columns Including Axial Load Effects," by A. Dutta, T. Kokorina and J.B. Mander, 2/22/99, (PB99-162877, A09, MF-A02).

MCEER-99-0004 "Experimental Study of Bridge Elastomeric and Other Isolation and Energy Dissipation Systems with Emphasis on Uplift Prevention and High Velocity Near-source Seismic Excitation," by A. Kasalanati and M. C. Constantinou, 2/26/99, (PB99-162885, A12, MF-A03).

MCEER-99-0005 "Truss Modeling of Reinforced Concrete Shear-flexure Behavior," by J.H. Kim and J.B. Mander, 3/8/99, (PB99-163693, A12, MF-A03).

MCEER-99-0006 "Experimental Investigation and Computational Modeling of Seismic Response of a 1:4 Scale Model Steel Structure with a Load Balancing Supplemental Damping System," by G. Pekcan, J.B. Mander and S.S. Chen, 4/2/99, (PB99-162893, A11, MF-A03).

MCEER-99-0007 "Effect of Vertical Ground Motions on the Structural Response of Highway Bridges," by M.R. Button, C.J. Cronin and R.L. Mayes, 4/10/99, (PB2000-101411, A10, MF-A03).

MCEER-99-0008 "Seismic Reliability Assessment of Critical Facilities: A Handbook, Supporting Documentation, and Model Code Provisions," by G.S. Johnson, R.E. Sheppard, M.D. Quilici, S.J. Eder and C.R. Scawthorn, 4/12/99, (PB2000-101701, A18, MF-A04).

MCEER-99-0009 "Impact Assessment of Selected MCEER Highway Project Research on the Seismic Design of Highway Structures," by C. Rojahn, R. Mayes, D.G. Anderson, J.H. Clark, D'Appolonia Engineering, S. Gloyd and R.V. Nutt, 4/14/99, (PB99-162901, A10, MF-A02).

MCEER-99-0010 "Site Factors and Site Categories in Seismic Codes," by R. Dobry, R. Ramos and M.S. Power, 7/19/99, (PB2000-101705, A08, MF-A02).

MCEER-99-0011 "Restrainer Design Procedures for Multi-Span Simply-Supported Bridges," by M.J. Randall, M. Saiidi, E. Maragakis and T. Isakovic, 7/20/99, (PB2000-101702, A10, MF-A02).

MCEER-99-0012 "Property Modification Factors for Seismic Isolation Bearings," by M.C. Constantinou, P. Tsopelas, A. Kasalanati and E. Wolff, 7/20/99, (PB2000-103387, A11, MF-A03).

MCEER-99-0013 "Critical Seismic Issues for Existing Steel Bridges," by P. Ritchie, N. Kauhl and J. Kulicki, 7/20/99, (PB2000-101697, A09, MF-A02).

MCEER-99-0014 "Nonstructural Damage Database," by A. Kao, T.T. Soong and A. Vender, 7/24/99, (PB2000-101407, A06, MF-A01).

MCEER-99-0015 "Guide to Remedial Measures for Liquefaction Mitigation at Existing Highway Bridge Sites," by H.G. Cooke and J. K. Mitchell, 7/26/99, (PB2000-101703, A11, MF-A03).

MCEER-99-0016 "Proceedings of the MCEER Workshop on Ground Motion Methodologies for the Eastern United States," edited by N. Abrahamson and A. Becker, 8/11/99, (PB2000-103385, A07, MF-A02).

MCEER-99-0017 "Quindío, Colombia Earthquake of January 25, 1999: Reconnaissance Report," by A.P. Asfura and P.J. Flores, 10/4/99, (PB2000-106893, A06, MF-A01).

MCEER-99-0018 "Hysteretic Models for Cyclic Behavior of Deteriorating Inelastic Structures," by M.V. Sivaselvan and A.M. Reinhorn, 11/5/99, (PB2000-103386, A08, MF-A02).

MCEER-99-0019	"Proceedings of the 7th U.S.- Japan Workshop on Earthquake Resistant Design of Lifeline Facilities and Countermeasures Against Soil Liquefaction," edited by T.D. O'Rourke, J.P. Bardet and M. Hamada, 11/19/99, (PB2000-103354, A99, MF-A06).
MCEER-99-0020	"Development of Measurement Capability for Micro-Vibration Evaluations with Application to Chip Fabrication Facilities," by G.C. Lee, Z. Liang, J.W. Song, J.D. Shen and W.C. Liu, 12/1/99, (PB2000-105993, A08, MF-A02).
MCEER-99-0021	"Design and Retrofit Methodology for Building Structures with Supplemental Energy Dissipating Systems," by G. Pekcan, J.B. Mander and S.S. Chen, 12/31/99, (PB2000-105994, A11, MF-A03).
MCEER-00-0001	"The Marmara, Turkey Earthquake of August 17, 1999: Reconnaissance Report," edited by C. Scawthorn; with major contributions by M. Bruneau, R. Eguchi, T. Holzer, G. Johnson, J. Mander, J. Mitchell, W. Mitchell, A. Papageorgiou, C. Scaethorn, and G. Webb, 3/23/00, (PB2000-106200, A11, MF-A03).
MCEER-00-0002	"Proceedings of the MCEER Workshop for Seismic Hazard Mitigation of Health Care Facilities," edited by G.C. Lee, M. Ettouney, M. Grigoriu, J. Hauer and J. Nigg, 3/29/00, (PB2000-106892, A08, MF-A02).
MCEER-00-0003	"The Chi-Chi, Taiwan Earthquake of September 21, 1999: Reconnaissance Report," edited by G.C. Lee and C.H. Loh, with major contributions by G.C. Lee, M. Bruneau, I.G. Buckle, S.E. Chang, P.J. Flores, T.D. O'Rourke, M. Shinozuka, T.T. Soong, C-H. Loh, K-C. Chang, Z-J. Chen, J-S. Hwang, M-L. Lin, G-Y. Liu, K-C. Tsai, G.C. Yao and C-L. Yen, 4/30/00, (PB2001-100980, A10, MF-A02).
MCEER-00-0004	"Seismic Retrofit of End-Sway Frames of Steel Deck-Truss Bridges with a Supplemental Tendon System: Experimental and Analytical Investigation," by G. Pekcan, J.B. Mander and S.S. Chen, 7/1/00, (PB2001-100982, A10, MF-A02).
MCEER-00-0005	"Sliding Fragility of Unrestrained Equipment in Critical Facilities," by W.H. Chong and T.T. Soong, 7/5/00, (PB2001-100983, A08, MF-A02).
MCEER-00-0006	"Seismic Response of Reinforced Concrete Bridge Pier Walls in the Weak Direction," by N. Abo-Shadi, M. Saiidi and D. Sanders, 7/17/00, (PB2001-100981, A17, MF-A03).
MCEER-00-0007	"Low-Cycle Fatigue Behavior of Longitudinal Reinforcement in Reinforced Concrete Bridge Columns," by J. Brown and S.K. Kunnath, 7/23/00, (PB2001-104392, A08, MF-A02).
MCEER-00-0008	"Soil Structure Interaction of Bridges for Seismic Analysis," I. PoLam and H. Law, 9/25/00, (PB2001-105397, A08, MF-A02).
MCEER-00-0009	"Proceedings of the First MCEER Workshop on Mitigation of Earthquake Disaster by Advanced Technologies (MEDAT-1), edited by M. Shinozuka, D.J. Inman and T.D. O'Rourke, 11/10/00, (PB2001-105399, A14, MF-A03).
MCEER-00-0010	"Development and Evaluation of Simplified Procedures for Analysis and Design of Buildings with Passive Energy Dissipation Systems, Revision 01," by O.M. Ramirez, M.C. Constantinou, C.A. Kircher, A.S. Whittaker, M.W. Johnson, J.D. Gomez and C. Chrysostomou, 11/16/01, (PB2001-105523, A23, MF-A04).
MCEER-00-0011	"Dynamic Soil-Foundation-Structure Interaction Analyses of Large Caissons," by C-Y. Chang, C-M. Mok, Z-L. Wang, R. Settgast, F. Waggoner, M.A. Ketchum, H.M. Gonnermann and C-C. Chin, 12/30/00, (PB2001-104373, A07, MF-A02).
MCEER-00-0012	"Experimental Evaluation of Seismic Performance of Bridge Restrainers," by A.G. Vlassis, E.M. Maragakis and M. Saiid Saiidi, 12/30/00, (PB2001-104354, A09, MF-A02).
MCEER-00-0013	"Effect of Spatial Variation of Ground Motion on Highway Structures," by M. Shinozuka, V. Saxena and G. Deodatis, 12/31/00, (PB2001-108755, A13, MF-A03).
MCEER-00-0014	"A Risk-Based Methodology for Assessing the Seismic Performance of Highway Systems," by S.D. Werner, C.E. Taylor, J.E. Moore, II, J.S. Walton and S. Cho, 12/31/00, (PB2001-108756, A14, MF-A03).

MCEER-01-0001 "Experimental Investigation of P-Delta Effects to Collapse During Earthquakes," by D. Vian and M. Bruneau, 6/25/01, (PB2002-100534, A17, MF-A03).

MCEER-01-0002 "Proceedings of the Second MCEER Workshop on Mitigation of Earthquake Disaster by Advanced Technologies (MEDAT-2)," edited by M. Bruneau and D.J. Inman, 7/23/01, (PB2002-100434, A16, MF-A03).

MCEER-01-0003 "Sensitivity Analysis of Dynamic Systems Subjected to Seismic Loads," by C. Roth and M. Grigoriu, 9/18/01, (PB2003-100884, A12, MF-A03).

MCEER-01-0004 "Overcoming Obstacles to Implementing Earthquake Hazard Mitigation Policies: Stage 1 Report," by D.J. Alesch and W.J. Petak, 12/17/01, (PB2002-107949, A07, MF-A02).

MCEER-01-0005 "Updating Real-Time Earthquake Loss Estimates: Methods, Problems and Insights," by C.E. Taylor, S.E. Chang and R.T. Eguchi, 12/17/01, (PB2002-107948, A05, MF-A01).

MCEER-01-0006 "Experimental Investigation and Retrofit of Steel Pile Foundations and Pile Bents Under Cyclic Lateral Loadings," by A. Shama, J. Mander, B. Blabac and S. Chen, 12/31/01, (PB2002-107950, A13, MF-A03).

MCEER-02-0001 "Assessment of Performance of Bolu Viaduct in the 1999 Duzce Earthquake in Turkey" by P.C. Roussis, M.C. Constantinou, M. Erdik, E. Durukal and M. Dicleli, 5/8/02, (PB2003-100883, A08, MF-A02).

MCEER-02-0002 "Seismic Behavior of Rail Counterweight Systems of Elevators in Buildings," by M.P. Singh, Rildova and L.E. Suarez, 5/27/02. (PB2003-100882, A11, MF-A03).

MCEER-02-0003 "Development of Analysis and Design Procedures for Spread Footings," by G. Mylonakis, G. Gazetas, S. Nikolaou and A. Chauncey, 10/02/02, (PB2004-101636, A13, MF-A03, CD-A13).

MCEER-02-0004 "Bare-Earth Algorithms for Use with SAR and LIDAR Digital Elevation Models," by C.K. Huyck, R.T. Eguchi and B. Houshmand, 10/16/02, (PB2004-101637, A07, CD-A07).

MCEER-02-0005 "Review of Energy Dissipation of Compression Members in Concentrically Braced Frames," by K.Lee and M. Bruneau, 10/18/02, (PB2004-101638, A10, CD-A10).

MCEER-03-0001 "Experimental Investigation of Light-Gauge Steel Plate Shear Walls for the Seismic Retrofit of Buildings" by J. Berman and M. Bruneau, 5/2/03, (PB2004-101622, A10, MF-A03, CD-A10).

MCEER-03-0002 "Statistical Analysis of Fragility Curves," by M. Shinozuka, M.Q. Feng, H. Kim, T. Uzawa and T. Ueda, 6/16/03, (PB2004-101849, A09, CD-A09).

MCEER-03-0003 "Proceedings of the Eighth U.S.-Japan Workshop on Earthquake Resistant Design f Lifeline Facilities and Countermeasures Against Liquefaction," edited by M. Hamada, J.P. Bardet and T.D. O'Rourke, 6/30/03, (PB2004-104386, A99, CD-A99).

MCEER-03-0004 "Proceedings of the PRC-US Workshop on Seismic Analysis and Design of Special Bridges," edited by L.C. Fan and G.C. Lee, 7/15/03, (PB2004-104387, A14, CD-A14).

MCEER-03-0005 "Urban Disaster Recovery: A Framework and Simulation Model," by S.B. Miles and S.E. Chang, 7/25/03, (PB2004-104388, A07, CD-A07).

MCEER-03-0006 "Behavior of Underground Piping Joints Due to Static and Dynamic Loading," by R.D. Meis, M. Maragakis and R. Siddharthan, 11/17/03, (PB2005-102194, A13, MF-A03, CD-A00).

MCEER-04-0001 "Experimental Study of Seismic Isolation Systems with Emphasis on Secondary System Response and Verification of Accuracy of Dynamic Response History Analysis Methods," by E. Wolff and M. Constantinou, 1/16/04 (PB2005-102195, A99, MF-E08, CD-A00).

MCEER-04-0002 "Tension, Compression and Cyclic Testing of Engineered Cementitious Composite Materials," by K. Kesner and S.L. Billington, 3/1/04, (PB2005-102196, A08, CD-A08).

MCEER-04-0003 "Cyclic Testing of Braces Laterally Restrained by Steel Studs to Enhance Performance During Earthquakes," by O.C. Celik, J.W. Berman and M. Bruneau, 3/16/04, (PB2005-102197, A13, MF-A03, CD-A00).

MCEER-04-0004 "Methodologies for Post Earthquake Building Damage Detection Using SAR and Optical Remote Sensing: Application to the August 17, 1999 Marmara, Turkey Earthquake," by C.K. Huyck, B.J. Adams, S. Cho, R.T. Eguchi, B. Mansouri and B. Houshmand, 6/15/04, (PB2005-104888, A10, CD-A00).

MCEER-04-0005 "Nonlinear Structural Analysis Towards Collapse Simulation: A Dynamical Systems Approach," by M.V. Sivaselvan and A.M. Reinhorn, 6/16/04, (PB2005-104889, A11, MF-A03, CD-A00).

MCEER-04-0006 "Proceedings of the Second PRC-US Workshop on Seismic Analysis and Design of Special Bridges," edited by G.C. Lee and L.C. Fan, 6/25/04, (PB2005-104890, A16, CD-A00).

MCEER-04-0007 "Seismic Vulnerability Evaluation of Axially Loaded Steel Built-up Laced Members," by K. Lee and M. Bruneau, 6/30/04, (PB2005-104891, A16, CD-A00).

MCEER-04-0008 "Evaluation of Accuracy of Simplified Methods of Analysis and Design of Buildings with Damping Systems for Near-Fault and for Soft-Soil Seismic Motions," by E.A. Pavlou and M.C. Constantinou, 8/16/04, (PB2005-104892, A08, MF-A02, CD-A00).

MCEER-04-0009 "Assessment of Geotechnical Issues in Acute Care Facilities in California," by M. Lew, T.D. O'Rourke, R. Dobry and M. Koch, 9/15/04, (PB2005-104893, A08, CD-A00).

MCEER-04-0010 "Scissor-Jack-Damper Energy Dissipation System," by A.N. Sigaher-Boyle and M.C. Constantinou, 12/1/04 (PB2005-108221).

MCEER-04-0011 "Seismic Retrofit of Bridge Steel Truss Piers Using a Controlled Rocking Approach," by M. Pollino and M. Bruneau, 12/20/04 (PB2006-105795).

MCEER-05-0001 "Experimental and Analytical Studies of Structures Seismically Isolated with an Uplift-Restraint Isolation System," by P.C. Roussis and M.C. Constantinou, 1/10/05 (PB2005-108222).

MCEER-05-0002 "A Versatile Experimentation Model for Study of Structures Near Collapse Applied to Seismic Evaluation of Irregular Structures," by D. Kusumastuti, A.M. Reinhorn and A. Rutenberg, 3/31/05 (PB2006-101523).

MCEER-05-0003 "Proceedings of the Third PRC-US Workshop on Seismic Analysis and Design of Special Bridges," edited by L.C. Fan and G.C. Lee, 4/20/05, (PB2006-105796).

MCEER-05-0004 "Approaches for the Seismic Retrofit of Braced Steel Bridge Piers and Proof-of-Concept Testing of an Eccentrically Braced Frame with Tubular Link," by J.W. Berman and M. Bruneau, 4/21/05 (PB2006-101524).

MCEER-05-0005 "Simulation of Strong Ground Motions for Seismic Fragility Evaluation of Nonstructural Components in Hospitals," by A. Wanitkorkul and A. Filiatrault, 5/26/05 (PB2006-500027).

MCEER-05-0006 "Seismic Safety in California Hospitals: Assessing an Attempt to Accelerate the Replacement or Seismic Retrofit of Older Hospital Facilities," by D.J. Alesch, L.A. Arendt and W.J. Petak, 6/6/05 (PB2006-105794).

MCEER-05-0007 "Development of Seismic Strengthening and Retrofit Strategies for Critical Facilities Using Engineered Cementitious Composite Materials," by K. Kesner and S.L. Billington, 8/29/05 (PB2006-111701).

MCEER-05-0008 "Experimental and Analytical Studies of Base Isolation Systems for Seismic Protection of Power Transformers," by N. Murota, M.Q. Feng and G-Y. Liu, 9/30/05 (PB2006-111702).

MCEER-05-0009 "3D-BASIS-ME-MB: Computer Program for Nonlinear Dynamic Analysis of Seismically Isolated Structures," by P.C. Tsopelas, P.C. Roussis, M.C. Constantinou, R. Buchanan and A.M. Reinhorn, 10/3/05 (PB2006-111703).

MCEER-05-0010 "Steel Plate Shear Walls for Seismic Design and Retrofit of Building Structures," by D. Vian and M. Bruneau, 12/15/05 (PB2006-111704).

MCEER-05-0011 "The Performance-Based Design Paradigm," by M.J. Astrella and A. Whittaker, 12/15/05 (PB2006-111705).

MCEER-06-0001 "Seismic Fragility of Suspended Ceiling Systems," H. Badillo-Almaraz, A.S. Whittaker, A.M. Reinhorn and G.P. Cimellaro, 2/4/06 (PB2006-111706).

MCEER-06-0002 "Multi-Dimensional Fragility of Structures," by G.P. Cimellaro, A.M. Reinhorn and M. Bruneau, 3/1/06 (PB2007-106974, A09, MF-A02, CD A00).

MCEER-06-0003 "Built-Up Shear Links as Energy Dissipators for Seismic Protection of Bridges," by P. Dusicka, A.M. Itani and I.G. Buckle, 3/15/06 (PB2006-111708).

MCEER-06-0004 "Analytical Investigation of the Structural Fuse Concept," by R.E. Vargas and M. Bruneau, 3/16/06 (PB2006-111709).

MCEER-06-0005 "Experimental Investigation of the Structural Fuse Concept," by R.E. Vargas and M. Bruneau, 3/17/06 (PB2006-111710).

MCEER-06-0006 "Further Development of Tubular Eccentrically Braced Frame Links for the Seismic Retrofit of Braced Steel Truss Bridge Piers," by J.W. Berman and M. Bruneau, 3/27/06 (PB2007-105147).

MCEER-06-0007 "REDARS Validation Report," by S. Cho, C.K. Huyck, S. Ghosh and R.T. Eguchi, 8/8/06 (PB2007-106983).

MCEER-06-0008 "Review of Current NDE Technologies for Post-Earthquake Assessment of Retrofitted Bridge Columns," by J.W. Song, Z. Liang and G.C. Lee, 8/21/06 (PB2007-106984).

MCEER-06-0009 "Liquefaction Remediation in Silty Soils Using Dynamic Compaction and Stone Columns," by S. Thevanayagam, G.R. Martin, R. Nashed, T. Shenthan, T. Kanagalingam and N. Ecemis, 8/28/06 (PB2007-106985).

MCEER-06-0010 "Conceptual Design and Experimental Investigation of Polymer Matrix Composite Infill Panels for Seismic Retrofitting," by W. Jung, M. Chiewanichakorn and A.J. Aref, 9/21/06 (PB2007-106986).

MCEER-06-0011 "A Study of the Coupled Horizontal-Vertical Behavior of Elastomeric and Lead-Rubber Seismic Isolation Bearings," by G.P. Warn and A.S. Whittaker, 9/22/06 (PB2007-108679).

MCEER-06-0012 "Proceedings of the Fourth PRC-US Workshop on Seismic Analysis and Design of Special Bridges: Advancing Bridge Technologies in Research, Design, Construction and Preservation," Edited by L.C. Fan, G.C. Lee and L. Ziang, 10/12/06 (PB2007-109042).

MCEER-06-0013 "Cyclic Response and Low Cycle Fatigue Characteristics of Plate Steels," by P. Dusicka, A.M. Itani and I.G. Buckle, 11/1/06 06 (PB2007-106987).

MCEER-06-0014 "Proceedings of the Second US-Taiwan Bridge Engineering Workshop," edited by W.P. Yen, J. Shen, J-Y. Chen and M. Wang, 11/15/06 (PB2008-500041).

MCEER-06-0015 "User Manual and Technical Documentation for the REDARS™ Import Wizard," by S. Cho, S. Ghosh, C.K. Huyck and S.D. Werner, 11/30/06 (PB2007-114766).

MCEER-06-0016 "Hazard Mitigation Strategy and Monitoring Technologies for Urban and Infrastructure Public Buildings: Proceedings of the China-US Workshops," edited by X.Y. Zhou, A.L. Zhang, G.C. Lee and M. Tong, 12/12/06 (PB2008-500018).

MCEER-07-0001 "Static and Kinetic Coefficients of Friction for Rigid Blocks," by C. Kafali, S. Fathali, M. Grigoriu and A.S. Whittaker, 3/20/07 (PB2007-114767).

MCEER-07-0002 "Hazard Mitigation Investment Decision Making: Organizational Response to Legislative Mandate," by L.A. Arendt, D.J. Alesch and W.J. Petak, 4/9/07 (PB2007-114768).

MCEER-07-0003 "Seismic Behavior of Bidirectional-Resistant Ductile End Diaphragms with Unbonded Braces in Straight or Skewed Steel Bridges," by O. Celik and M. Bruneau, 4/11/07 (PB2008-105141).

MCEER-07-0004 "Modeling Pile Behavior in Large Pile Groups Under Lateral Loading," by A.M. Dodds and G.R. Martin, 4/16/07(PB2008-105142).

MCEER-07-0005 "Experimental Investigation of Blast Performance of Seismically Resistant Concrete-Filled Steel Tube Bridge Piers," by S. Fujikura, M. Bruneau and D. Lopez-Garcia, 4/20/07 (PB2008-105143).

MCEER-07-0006 "Seismic Analysis of Conventional and Isolated Liquefied Natural Gas Tanks Using Mechanical Analogs," by I.P. Christovasilis and A.S. Whittaker, 5/1/07, not available.

MCEER-07-0007 "Experimental Seismic Performance Evaluation of Isolation/Restraint Systems for Mechanical Equipment – Part 1: Heavy Equipment Study," by S. Fathali and A. Filiatrault, 6/6/07 (PB2008-105144).

MCEER-07-0008 "Seismic Vulnerability of Timber Bridges and Timber Substructures," by A.A. Sharma, J.B. Mander, I.M. Friedland and D.R. Allicock, 6/7/07 (PB2008-105145).

MCEER-07-0009 "Experimental and Analytical Study of the XY-Friction Pendulum (XY-FP) Bearing for Bridge Applications," by C.C. Marin-Artieda, A.S. Whittaker and M.C. Constantinou, 6/7/07 (PB2008-105191).

MCEER-07-0010 "Proceedings of the PRC-US Earthquake Engineering Forum for Young Researchers," Edited by G.C. Lee and X.Z. Qi, 6/8/07 (PB2008-500058).

MCEER-07-0011 "Design Recommendations for Perforated Steel Plate Shear Walls," by R. Purba and M. Bruneau, 6/18/07, (PB2008-105192).

MCEER-07-0012 "Performance of Seismic Isolation Hardware Under Service and Seismic Loading," by M.C. Constantinou, A.S. Whittaker, Y. Kalpakidis, D.M. Fenz and G.P. Warn, 8/27/07, (PB2008-105193).

MCEER-07-0013 "Experimental Evaluation of the Seismic Performance of Hospital Piping Subassemblies," by E.R. Goodwin, E. Maragakis and A.M. Itani, 9/4/07, (PB2008-105194).

MCEER-07-0014 "A Simulation Model of Urban Disaster Recovery and Resilience: Implementation for the 1994 Northridge Earthquake," by S. Miles and S.E. Chang, 9/7/07, (PB2008-106426).

MCEER-07-0015 "Statistical and Mechanistic Fragility Analysis of Concrete Bridges," by M. Shinozuka, S. Banerjee and S-H. Kim, 9/10/07, (PB2008-106427).

MCEER-07-0016 "Three-Dimensional Modeling of Inelastic Buckling in Frame Structures," by M. Schachter and AM. Reinhorn, 9/13/07, (PB2008-108125).

MCEER-07-0017 "Modeling of Seismic Wave Scattering on Pile Groups and Caissons," by I. Po Lam, H. Law and C.T. Yang, 9/17/07 (PB2008-108150).

MCEER-07-0018 "Bridge Foundations: Modeling Large Pile Groups and Caissons for Seismic Design," by I. Po Lam, H. Law and G.R. Martin (Coordinating Author), 12/1/07 (PB2008-111190).

MCEER-07-0019 "Principles and Performance of Roller Seismic Isolation Bearings for Highway Bridges," by G.C. Lee, Y.C. Ou, Z. Liang, T.C. Niu and J. Song, 12/10/07 (PB2009-110466).

MCEER-07-0020 "Centrifuge Modeling of Permeability and Pinning Reinforcement Effects on Pile Response to Lateral Spreading," by L.L Gonzalez-Lagos, T. Abdoun and R. Dobry, 12/10/07 (PB2008-111191).

MCEER-07-0021 "Damage to the Highway System from the Pisco, Perú Earthquake of August 15, 2007," by J.S. O'Connor, L. Mesa and M. Nykamp, 12/10/07, (PB2008-108126).

MCEER-07-0022 "Experimental Seismic Performance Evaluation of Isolation/Restraint Systems for Mechanical Equipment – Part 2: Light Equipment Study," by S. Fathali and A. Filiatrault, 12/13/07 (PB2008-111192).

MCEER-07-0023 "Fragility Considerations in Highway Bridge Design," by M. Shinozuka, S. Banerjee and S.H. Kim, 12/14/07 (PB2008-111193).

MCEER-07-0024 "Performance Estimates for Seismically Isolated Bridges," by G.P. Warn and A.S. Whittaker, 12/30/07 (PB2008-112230).

MCEER-08-0001 "Seismic Performance of Steel Girder Bridge Superstructures with Conventional Cross Frames," by L.P. Carden, A.M. Itani and I.G. Buckle, 1/7/08, (PB2008-112231).

MCEER-08-0002 "Seismic Performance of Steel Girder Bridge Superstructures with Ductile End Cross Frames with Seismic Isolators," by L.P. Carden, A.M. Itani and I.G. Buckle, 1/7/08 (PB2008-112232).

MCEER-08-0003 "Analytical and Experimental Investigation of a Controlled Rocking Approach for Seismic Protection of Bridge Steel Truss Piers," by M. Pollino and M. Bruneau, 1/21/08 (PB2008-112233).

MCEER-08-0004 "Linking Lifeline Infrastructure Performance and Community Disaster Resilience: Models and Multi-Stakeholder Processes," by S.E. Chang, C. Pasion, K. Tatebe and R. Ahmad, 3/3/08 (PB2008-112234).

MCEER-08-0005 "Modal Analysis of Generally Damped Linear Structures Subjected to Seismic Excitations," by J. Song, Y-L. Chu, Z. Liang and G.C. Lee, 3/4/08 (PB2009-102311).

MCEER-08-0006 "System Performance Under Multi-Hazard Environments," by C. Kafali and M. Grigoriu, 3/4/08 (PB2008-112235).

MCEER-08-0007 "Mechanical Behavior of Multi-Spherical Sliding Bearings," by D.M. Fenz and M.C. Constantinou, 3/6/08 (PB2008-112236).

MCEER-08-0008 "Post-Earthquake Restoration of the Los Angeles Water Supply System," by T.H.P. Tabucchi and R.A. Davidson, 3/7/08 (PB2008-112237).

MCEER-08-0009 "Fragility Analysis of Water Supply Systems," by A. Jacobson and M. Grigoriu, 3/10/08 (PB2009-105545).

MCEER-08-0010 "Experimental Investigation of Full-Scale Two-Story Steel Plate Shear Walls with Reduced Beam Section Connections," by B. Qu, M. Bruneau, C-H. Lin and K-C. Tsai, 3/17/08 (PB2009-106368).

MCEER-08-0011 "Seismic Evaluation and Rehabilitation of Critical Components of Electrical Power Systems," S. Ersoy, B. Feizi, A. Ashrafi and M. Ala Saadeghvaziri, 3/17/08 (PB2009-105546).

MCEER-08-0012 "Seismic Behavior and Design of Boundary Frame Members of Steel Plate Shear Walls," by B. Qu and M. Bruneau, 4/26/08 . (PB2009-106744).

MCEER-08-0013 "Development and Appraisal of a Numerical Cyclic Loading Protocol for Quantifying Building System Performance," by A. Filiatrault, A. Wanitkorkul and M. Constantinou, 4/27/08 (PB2009-107906).

MCEER-08-0014 "Structural and Nonstructural Earthquake Design: The Challenge of Integrating Specialty Areas in Designing Complex, Critical Facilities," by W.J. Petak and D.J. Alesch, 4/30/08 (PB2009-107907).

MCEER-08-0015 "Seismic Performance Evaluation of Water Systems," by Y. Wang and T.D. O'Rourke, 5/5/08 (PB2009-107908).

MCEER-08-0016 "Seismic Response Modeling of Water Supply Systems," by P. Shi and T.D. O'Rourke, 5/5/08 (PB2009-107910).

MCEER-08-0017 "Numerical and Experimental Studies of Self-Centering Post-Tensioned Steel Frames," by D. Wang and A. Filiatrault, 5/12/08 (PB2009-110479).

MCEER-08-0018 "Development, Implementation and Verification of Dynamic Analysis Models for Multi-Spherical Sliding Bearings," by D.M. Fenz and M.C. Constantinou, 8/15/08 (PB2009-107911).

MCEER-08-0019 "Performance Assessment of Conventional and Base Isolated Nuclear Power Plants for Earthquake Blast Loadings," by Y.N. Huang, A.S. Whittaker and N. Luco, 10/28/08 (PB2009-107912).

MCEER-08-0020 "Remote Sensing for Resilient Multi-Hazard Disaster Response – Volume I: Introduction to Damage Assessment Methodologies," by B.J. Adams and R.T. Eguchi, 11/17/08 (PB2010-102695).

MCEER-08-0021 "Remote Sensing for Resilient Multi-Hazard Disaster Response – Volume II: Counting the Number of Collapsed Buildings Using an Object-Oriented Analysis: Case Study of the 2003 Bam Earthquake," by L. Gusella, C.K. Huyck and B.J. Adams, 11/17/08 (PB2010-100925).

MCEER-08-0022 "Remote Sensing for Resilient Multi-Hazard Disaster Response – Volume III: Multi-Sensor Image Fusion Techniques for Robust Neighborhood-Scale Urban Damage Assessment," by B.J. Adams and A. McMillan, 11/17/08 (PB2010-100926).

MCEER-08-0023 "Remote Sensing for Resilient Multi-Hazard Disaster Response – Volume IV: A Study of Multi-Temporal and Multi-Resolution SAR Imagery for Post-Katrina Flood Monitoring in New Orleans," by A. McMillan, J.G. Morley, B.J. Adams and S. Chesworth, 11/17/08 (PB2010-100927).

MCEER-08-0024 "Remote Sensing for Resilient Multi-Hazard Disaster Response – Volume V: Integration of Remote Sensing Imagery and VIEWS^{TM} Field Data for Post-Hurricane Charley Building Damage Assessment," by J.A. Womble, K. Mehta and B.J. Adams, 11/17/08 (PB2009-115532).

MCEER-08-0025 "Building Inventory Compilation for Disaster Management: Application of Remote Sensing and Statistical Modeling," by P. Sarabandi, A.S. Kiremidjian, R.T. Eguchi and B. J. Adams, 11/20/08 (PB2009-110484).

MCEER-08-0026 "New Experimental Capabilities and Loading Protocols for Seismic Qualification and Fragility Assessment of Nonstructural Systems," by R. Retamales, G. Mosqueda, A. Filiatrault and A. Reinhorn, 11/24/08 (PB2009-110485).

MCEER-08-0027 "Effects of Heating and Load History on the Behavior of Lead-Rubber Bearings," by I.V. Kalpakidis and M.C. Constantinou, 12/1/08 (PB2009-115533).

MCEER-08-0028 "Experimental and Analytical Investigation of Blast Performance of Seismically Resistant Bridge Piers," by S.Fujikura and M. Bruneau, 12/8/08 (PB2009-115534).

MCEER-08-0029 "Evolutionary Methodology for Aseismic Decision Support," by Y. Hu and G. Dargush, 12/15/08.

MCEER-08-0030 "Development of a Steel Plate Shear Wall Bridge Pier System Conceived from a Multi-Hazard Perspective," by D. Keller and M. Bruneau, 12/19/08 (PB2010-102696).

MCEER-09-0001 "Modal Analysis of Arbitrarily Damped Three-Dimensional Linear Structures Subjected to Seismic Excitations," by Y.L. Chu, J. Song and G.C. Lee, 1/31/09 (PB2010-100922).

MCEER-09-0002 "Air-Blast Effects on Structural Shapes," by G. Ballantyne, A.S. Whittaker, A.J. Aref and G.F. Dargush, 2/2/09 (PB2010-102697).

MCEER-09-0003 "Water Supply Performance During Earthquakes and Extreme Events," by A.L. Bonneau and T.D. O'Rourke, 2/16/09 (PB2010-100923).

MCEER-09-0004 "Generalized Linear (Mixed) Models of Post-Earthquake Ignitions," by R.A. Davidson, 7/20/09 (PB2010-102698).

MCEER-09-0005 "Seismic Testing of a Full-Scale Two-Story Light-Frame Wood Building: NEESWood Benchmark Test," by I.P. Christovasilis, A. Filiatrault and A. Wanitkorkul, 7/22/09 (PB2012-102401).

MCEER-09-0006 "IDARC2D Version 7.0: A Program for the Inelastic Damage Analysis of Structures," by A.M. Reinhorn, H. Roh, M. Sivaselvan, S.K. Kunnath, R.E. Valles, A. Madan, C. Li, R. Lobo and Y.J. Park, 7/28/09 (PB2010-103199).

MCEER-09-0007 "Enhancements to Hospital Resiliency: Improving Emergency Planning for and Response to Hurricanes," by D.B. Hess and L.A. Arendt, 7/30/09 (PB2010-100924).

MCEER-09-0008 “Assessment of Base-Isolated Nuclear Structures for Design and Beyond-Design Basis Earthquake Shaking,” by Y.N. Huang, A.S. Whittaker, R.P. Kennedy and R.L. Mayes, 8/20/09 (PB2010-102699).

MCEER-09-0009 “Quantification of Disaster Resilience of Health Care Facilities,” by G.P. Cimellaro, C. Fumo, A.M Reinhorn and M. Bruneau, 9/14/09 (PB2010-105384).

MCEER-09-0010 “Performance-Based Assessment and Design of Squat Reinforced Concrete Shear Walls,” by C.K. Gulec and A.S. Whittaker, 9/15/09 (PB2010-102700).

MCEER-09-0011 “Proceedings of the Fourth US-Taiwan Bridge Engineering Workshop,” edited by W.P. Yen, J.J. Shen, T.M. Lee and R.B. Zheng, 10/27/09 (PB2010-500009).

MCEER-09-0012 “Proceedings of the Special International Workshop on Seismic Connection Details for Segmental Bridge Construction,” edited by W. Phillip Yen and George C. Lee, 12/21/09 (PB2012-102402).

MCEER-10-0001 “Direct Displacement Procedure for Performance-Based Seismic Design of Multistory Woodframe Structures,” by W. Pang and D. Rosowsky, 4/26/10 (PB2012-102403).

MCEER-10-0002 “Simplified Direct Displacement Design of Six-Story NEESWood Capstone Building and Pre-Test Seismic Performance Assessment,” by W. Pang, D. Rosowsky, J. van de Lindt and S. Pei, 5/28/10 (PB2012-102404).

MCEER-10-0003 “Integration of Seismic Protection Systems in Performance-Based Seismic Design of Woodframed Structures,” by J.K. Shinde and M.D. Symans, 6/18/10 (PB2012-102405).

MCEER-10-0004 “Modeling and Seismic Evaluation of Nonstructural Components: Testing Frame for Experimental Evaluation of Suspended Ceiling Systems,” by A.M. Reinhorn, K.P. Ryu and G. Maddaloni, 6/30/10 (PB2012-102406).

MCEER-10-0005 “Analytical Development and Experimental Validation of a Structural-Fuse Bridge Pier Concept,” by S. El-Bahey and M. Bruneau, 10/1/10 (PB2012-102407).

MCEER-10-0006 “A Framework for Defining and Measuring Resilience at the Community Scale: The PEOPLES Resilience Framework,” by C.S. Renschler, A.E. Frazier, L.A. Arendt, G.P. Cimellaro, A.M. Reinhorn and M. Bruneau, 10/8/10 (PB2012-102408).

MCEER-10-0007 “Impact of Horizontal Boundary Elements Design on Seismic Behavior of Steel Plate Shear Walls,” by R. Purba and M. Bruneau, 11/14/10 (PB2012-102409).

MCEER-10-0008 “Seismic Testing of a Full-Scale Mid-Rise Building: The NEESWood Capstone Test,” by S. Pei, J.W. van de Lindt, S.E. Pryor, H. Shimizu, H. Isoda and D.R. Rammer, 12/1/10 (PB2012-102410).

MCEER-10-0009 “Modeling the Effects of Detonations of High Explosives to Inform Blast-Resistant Design,” by P. Sherkar, A.S. Whittaker and A.J. Aref, 12/1/10 (PB2012-102411).

MCEER-10-0010 “L’Aquila Earthquake of April 6, 2009 in Italy: Rebuilding a Resilient City to Withstand Multiple Hazards,” by G.P. Cimellaro, I.P. Christovasilis, A.M. Reinhorn, A. De Stefano and T. Kirova, 12/29/10.

MCEER-11-0001 “Numerical and Experimental Investigation of the Seismic Response of Light-Frame Wood Structures,” by I.P. Christovasilis and A. Filiatrault, 8/8/11 (PB2012-102412).

MCEER-11-0002 “Seismic Design and Analysis of a Precast Segmental Concrete Bridge Model,” by M. Anagnostopoulou, A. Filiatrault and A. Aref, 9/15/11.

MCEER-11-0003 ‘Proceedings of the Workshop on Improving Earthquake Response of Substation Equipment,” Edited by A.M. Reinhorn, 9/19/11 (PB2012-102413).

MCEER-11-0004 “LRFD-Based Analysis and Design Procedures for Bridge Bearings and Seismic Isolators,” by M.C. Constantinou, I. Kalpakidis, A. Filiatrault and R.A. Ecker Lay, 9/26/11.

MCEER-11-0005 "Experimental Seismic Evaluation, Model Parameterization, and Effects of Cold-Formed Steel-Framed Gypsum Partition Walls on the Seismic Performance of an Essential Facility," by R. Davies, R. Retamales, G. Mosqueda and A. Filiatrault, 10/12/11.

MCEER-11-0006 "Modeling and Seismic Performance Evaluation of High Voltage Transformers and Bushings," by A.M. Reinhorn, K. Oikonomou, H. Roh, A. Schiff and L. Kempner, Jr., 10/3/11.

MCEER-11-0007 "Extreme Load Combinations: A Survey of State Bridge Engineers," by G.C. Lee, Z. Liang, J.J. Shen and J.S. O'Connor, 10/14/11.

MCEER-12-0001 "Simplified Analysis Procedures in Support of Performance Based Seismic Design," by Y.N. Huang and A.S. Whittaker.

MCEER-12-0002 "Seismic Protection of Electrical Transformer Bushing Systems by Stiffening Techniques," by M. Koliou, A. Filiatrault, A.M. Reinhorn and N. Oliveto, 6/1/12.

MCEER-12-0003 "Post-Earthquake Bridge Inspection Guidelines," by J.S. O'Connor and S. Alampalli, 6/8/12.

MCEER-12-0004 "Integrated Design Methodology for Isolated Floor Systems in Single-Degree-of-Freedom Structural Fuse Systems," by S. Cui, M. Bruneau and M.C. Constantinou, 6/13/12.

MCEER-12-0005 "Characterizing the Rotational Components of Earthquake Ground Motion," by D. Basu, A.S. Whittaker and M.C. Constantinou, 6/15/12.

MCEER-12-0006 "Bayesian Fragility for Nonstructural Systems," by C.H. Lee and M.D. Grigoriu, 9/12/12.

MCEER-12-0007 "A Numerical Model for Capturing the In-Plane Seismic Response of Interior Metal Stud Partition Walls," by R.L. Wood and T.C. Hutchinson, 9/12/12.

MCEER-12-0008 "Assessment of Floor Accelerations in Yielding Buildings," by J.D. Wieser, G. Pekcan, A.E. Zaghi, A.M. Itani and E. Maragakis, 10/5/12.

MCEER-13-0001 "Experimental Seismic Study of Pressurized Fire Sprinkler Piping Systems," by Y. Tian, A. Filiatrault and G. Mosqueda, 4/8/13.

MCEER-13-0002 "Enhancing Resource Coordination for Multi-Modal Evacuation Planning," by D.B. Hess, B.W. Conley and C.M. Farrell, 2/8/13.

MCEER-13-0003 "Seismic Response of Base Isolated Buildings Considering Pounding to Moat Walls," by A. Masroor and G. Mosqueda, 2/26/13.

MCEER-13-0004 "Seismic Response Control of Structures Using a Novel Adaptive Passive Negative Stiffness Device," by D.T.R. Pasala, A.A. Sarlis, S. Nagarajaiah, A.M. Reinhorn, M.C. Constantinou and D.P. Taylor, 6/10/13.

MCEER-13-0005 "Negative Stiffness Device for Seismic Protection of Structures," by A.A. Sarlis, D.T.R. Pasala, M.C. Constantinou, A.M. Reinhorn, S. Nagarajaiah and D.P. Taylor, 6/12/13.

MCEER-13-0006 "Emilia Earthquake of May 20, 2012 in Northern Italy: Rebuilding a Resilient Community to Withstand Multiple Hazards," by G.P. Cimellaro, M. Chiriatti, A.M. Reinhorn and L. Tirca, June 30, 2013.

MCEER-13-0007 "Precast Concrete Segmental Components and Systems for Accelerated Bridge Construction in Seismic Regions," by A.J. Aref, G.C. Lee, Y.C. Ou and P. Sideris, with contributions from K.C. Chang, S. Chen, A. Filiatrault and Y. Zhou, June 13, 2013.

MCEER-13-0008 "A Study of U.S. Bridge Failures (1980-2012)," by G.C. Lee, S.B. Mohan, C. Huang and B.N. Fard, June 15, 2013.

MCEER-13-0009 "Development of a Database Framework for Modeling Damaged Bridges," by G.C. Lee, J.C. Qi and C. Huang, June 16, 2013.

MCEER-13-0010 "Model of Triple Friction Pendulum Bearing for General Geometric and Frictional Parameters and for Uplift Conditions," by A.A. Sarlis and M.C. Constantinou, July 1, 2013.

MCEER-13-0011 "Shake Table Testing of Triple Friction Pendulum Isolators under Extreme Conditions," by A.A. Sarlis, M.C. Constantinou and A.M. Reinhorn, July 2, 2013.

MCEER-13-0012 "Theoretical Framework for the Development of MH-LRFD," by G.C. Lee (coordinating author), H.A Capers, Jr., C. Huang, J.M. Kulicki, Z. Liang, T. Murphy, J.J.D. Shen, M. Shinozuka and P.W.H. Yen, July 31, 2013.

MCEER-13-0013 "Seismic Protection of Highway Bridges with Negative Stiffness Devices," by N.K.A. Attary, M.D. Symans, S. Nagarajaiah, A.M. Reinhorn, M.C. Constantinou, A.A. Sarlis, D.T.R. Pasala, and D.P. Taylor, September 3, 2014.

MCEER-14-0001 "Simplified Seismic Collapse Capacity-Based Evaluation and Design of Frame Buildings with and without Supplemental Damping Systems," by M. Hamidia, A. Filiatrault, and A. Aref, May 19, 2014.

MCEER-14-0002 "Comprehensive Analytical Seismic Fragility of Fire Sprinkler Piping Systems," by Siavash Soroushian, Emmanuel "Manos" Maragakis, Arash E. Zaghi, Alicia Echevarria, Yuan Tian and Andre Filiatrault, August 26, 2014.

MCEER-14-0003 "Hybrid Simulation of the Seismic Response of a Steel Moment Frame Building Structure through Collapse," by M. Del Carpio Ramos, G. Mosqueda and D.G. Lignos, October 30, 2014.

MCEER-14-0004 "Blast and Seismic Resistant Concrete-Filled Double Skin Tubes and Modified Steel Jacketed Bridge Columns," by P.P. Fouche and M. Bruneau, June 30, 2015.

MCEER-14-0005 "Seismic Performance of Steel Plate Shear Walls Considering Various Design Approaches," by R. Purba and M. Bruneau, October 31, 2014.

MCEER-14-0006 "Air-Blast Effects on Civil Structures," by Jinwon Shin, Andrew S. Whittaker, Amjad J. Aref and David Cormie, October 30, 2014.

MCEER-14-0007 "Seismic Performance Evaluation of Precast Girders with Field-Cast Ultra High Performance Concrete (UHPC) Connections," by G.C. Lee, C. Huang, J. Song, and J. S. O'Connor, July 31, 2014.

MCEER-14-0008 "Post-Earthquake Fire Resistance of Ductile Concrete-Filled Double-Skin Tube Columns," by Reza Imani, Gilberto Mosqueda and Michel Bruneau, December 1, 2014.

MCEER-14-0009 "Cyclic Inelastic Behavior of Concrete Filled Sandwich Panel Walls Subjected to In-Plane Flexure," by Y. Alzeni and M. Bruneau, December 19, 2014.

MCEER-14-0010 "Analytical and Experimental Investigation of Self-Centering Steel Plate Shear Walls," by D.M. Dowden and M. Bruneau, December 19, 2014.

MCEER-15-0001 "Seismic Analysis of Multi-story Unreinforced Masonry Buildings with Flexible Diaphragms," by J. Aleman, G. Mosqueda and A.S. Whittaker, June 12, 2015.

MCEER-15-0002 "Site Response, Soil-Structure Interaction and Structure-Soil-Structure Interaction for Performance Assessment of Buildings and Nuclear Structures," by C. Bolisetti and A.S. Whittaker, June 15, 2015.

MCEER-15-0003 "Stress Wave Attenuation in Solids for Mitigating Impulsive Loadings," by R. Rafiee-Dehkharghani, A.J. Aref and G. Dargush, August 15, 2015.

MCEER-15-0004 "Computational, Analytical, and Experimental Modeling of Masonry Structures," by K.M. Dolatshahi and A.J. Aref, November 16, 2015.

MCEER-15-0005 "Property Modification Factors for Seismic Isolators: Design Guidance for Buildings," by W.J. McVitty and M.C. Constantinou, June 30, 2015.

MCEER-15-0006 “Seismic Isolation of Nuclear Power Plants using Sliding Bearings,” by Manish Kumar, Andrew S. Whittaker and Michael C. Constantinou, December 27, 2015.

MCEER-15-0007 “Quintuple Friction Pendulum Isolator Behavior, Modeling and Validation,” by Donghun Lee and Michael C. Constantinou, December 28, 2015.

MCEER-15-0008 “Seismic Isolation of Nuclear Power Plants using Elastomeric Bearings,” by Manish Kumar, Andrew S. Whittaker and Michael C. Constantinou, December 29, 2015.

MCEER-16-0001 “Experimental, Numerical and Analytical Studies on the Seismic Response of Steel-Plate Concrete (SC) Composite Shear Walls,” by Siamak Epackachi and Andrew S. Whittaker, June 15, 2016.

MCEER-16-0002 “Seismic Demand in Columns of Steel Frames,” by Lisa Shrestha and Michel Bruneau, June 17, 2016.

MCEER-16-0003 “Development and Evaluation of Procedures for Analysis and Design of Buildings with Fluidic Self-Centering Systems” by Shoma Kitayama and Michael C. Constantinou, July 21, 2016.

MCEER
EARTHQUAKE ENGINEERING TO EXTREME EVENTS
University at Buffalo, The State University of New York
133A Ketter Hall ▪ Buffalo, New York 14260-4300
Phone: (716) 645-3391 ▪ Fax: (716) 645-3399
Email: *mceer@buffalo.edu* ▪ Web: *http://mceer.buffalo.edu*
University at Buffalo *The State University of New York*

ISSN 1520-295X